

MATERIALS
RESEARCH
SOCIETY
SYMPOSIUM PROCEEDINGS

VOLUME 332

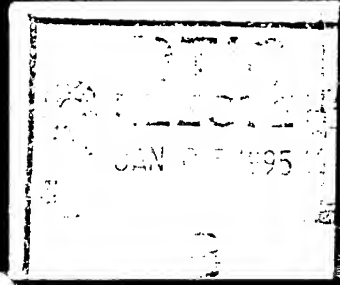
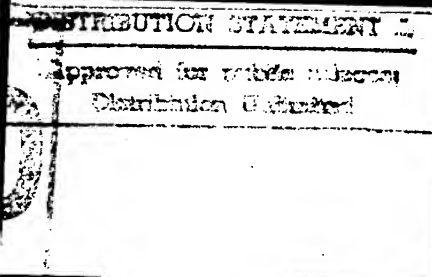
Determining Nanoscale Physical Properties of Materials by Microscopy and Spectroscopy

EDITORS

Mehmet Sarikaya

H. Kumar Wickramasinghe

Michael Isaacson



19950103 080

Determining Nanoscale Physical Properties of
Materials by Microscopy and Spectroscopy

Accession For	
NTIS GRA&I	<input checked="" type="checkbox"/>
DTIC TAB	<input type="checkbox"/>
Unannounced	<input type="checkbox"/>
Justification	
By _____	
Distribution/	
Availability Codes	
Avail and/or	
Dist	Special
A-1	

Determining Nanoscale Physical Properties of Materials by Microscopy and Spectroscopy

Symposium held November 29-December 3, 1993, Boston, Massachusetts, U.S.A.

EDITORS:

Mehmet Sarikaya

University of Washington
Seattle, Washington, U.S.A.

H. Kumar Wickramasinghe

IBM T.J. Watson Research Center
Yorktown Heights, New York, U.S.A.

Michael Isaacson

Cornell University
Ithaca, New York, U.S.A.



MATERIALS RESEARCH SOCIETY
Pittsburgh, Pennsylvania

DTIC QUALITY INSPECTED 3

This work was supported in part by the Office of Naval Research under Grant Number N00014-1-94-0076. The United States Government has a royalty-free license throughout the world in all copyrightable material contained herein.

Single article reprints from this publication are available through
University Microfilms Inc., 300 North Zeeb Road, Ann Arbor, Michigan 48106

CODEN: MRSPDH

Copyright 1994 by Materials Research Society.
All rights reserved.

This book has been registered with Copyright Clearance Center, Inc. For further information, please contact the Copyright Clearance Center, Salem, Massachusetts.

Published by:

Materials Research Society
9800 McKnight Road
Pittsburgh, Pennsylvania 15237
Telephone (412) 367-3003
Fax (412) 367-4373

Library of Congress Cataloging in Publication Data

Determining nanoscale physical properties of materials by microscopy and spectroscopy /
editors Mehmet Sarikaya, H. Kumar Wickramasinghe, and Michael Isaacson.

p. cm.—(Materials Research Society symposium proceedings, ISSN 0272-9172 ;
v. 332)

Includes bibliographical references and index.

ISBN 1-55899-231-6

1. Nanostructures—Analysis—Congresses. 2. Microscopy—Technique—
Congresses. 3. Spectrum analysis—Congresses. I. Sarikaya, Mehmet
II. Wickramasinghe, H. Kumar III. Isaacson, Michael IV. Series: Materials
Research Society symposium proceedings ; v. 332.

Q176.8.N35D48 1994
620.1'1299'0287—dc20

94-23255
CIP

Manufactured in the United States of America

Contents

PREFACE	xiii
MATERIALS RESEARCH SOCIETY SYMPOSIUM PROCEEDINGS	xiv
PART I: LOCAL SPECTROSCOPY AND IMAGING	
*SPATIALLY RESOLVED LOCAL ATOMIC STRUCTURE FROM EXELFS	3
E.A. Stern, M. Qian, and M. Sarikaya	
*CROSS-SECTIONAL SCANNING TUNNELING MICROSCOPY OF III-V SEMICONDUCTOR STRUCTURES	15
R.M. Feenstra, A. Vaterlaus, J.M. Woodall, D.A. Collins, and T.C. McGill	
*CHALLENGES AND OPPORTUNITIES IN MAGNETIC RESONANCE FORCE MICROSCOPY	25
John A. Sidles and Joseph L. Garbini	
*TRENDS IN ATOMIC RESOLUTION ELECTRON MICROSCOPY	43
David J. Smith and M.R. McCartney	
PART II: DYNAMIC PROPERTIES AT NANOSCALE	
*FLUX LINE DYNAMICS WITH ELECTRON HOLOGRAPHY	55
Akira Tonomura	
*ANALYSIS OF INTERFACE DYNAMICS IN SOLID-STATE PHASE TRANSFORMATIONS BY <i>IN SITU</i> HOT-STAGE HIGH-RESOLUTION TRANSMISSION ELECTRON MICROSCOPY	65
James M. Howe, W.E. Benson, A. Garg, and Y.-C. Chang	
*EPITAXIAL GROWTH OF TWO-DIMENSIONAL DICHALCOGENIDES AND MODIFICATION OF THEIR SURFACES WITH SCANNING PROBE MICROSCOPES	79
Bruce A. Parkinson	
MICROSTRUCTURAL IMAGING OF LOCALIZED CHEMICAL REACTIONS USING VALENCE PHOTOELECTRONS	87
S. Liang, A.K. Ray-Chaudhuri, W. Ng, and F. Cerrina	
MICROTRIBOLOGICAL STUDIES BY USING ATOMIC FORCE AND FRICTION FORCE MICROSCOPY AND ITS APPLICATIONS	93
Bharat Bhushan, Vilas N. Koinkar, and J. Ruan	
MOLECULAR DYNAMICS SIMULATION OF THE ELASTIC DEFORMATION OF NANOMETER DIAMETER METAL CLUSTERS	99
Dilip Y. Paithankar, Julian Talbot, and Ronald P. Andres	
A THERMAL STAGE FOR NANOSCALE STRUCTURE STUDIES WITH THE SCANNING FORCE MICROSCOPE	105
W.J. Kulnis, Jr. and W.N. Unertl	
DYNAMIC BEHAVIOUR OF LEAD NANOPARTICLES IN A DIELECTRIC MATRIX	109
P. Cheyssac, R. Kofman, P.G. Merli, A. Migliori, and A. Stella	

*Invited Paper

<i>IN-SITU</i> DYNAMIC HIGH-RESOLUTION TRANSMISSION ELECTRON MICROSCOPY INVESTIGATION OF GUEST-LAYER BEHAVIOR DURING DEINTERCALATION OF MERCURY TITANIUM DISULFIDE	115
M. McKelvy, M. Sidorov, A. Marie, R. Sharma, and W.S. Glaunsinger	

<i>IN-SITU</i> OBSERVATION OF OXIDE MONOLAYER FORMATION ON COPPER SOLID-LIQUID INTERFACES	121
John R. LaGraff, Brandon J. Cruickshank, and Andrew A. Gewirth	

PART III: LOCAL STRUCTURES AND PROPERTIES

*APPLICATION OF HIGH SPATIAL RESOLUTION ELECTRON DIFFRACTION TECHNIQUES TO THE STUDY OF LOCAL PROPERTIES OF CRYSTALLINE SOLIDS	129
J.W. Steeds, X.F. Duan, P.A. Midgley, P. Spellward, and R. Vincent	

*HOLOGRAPHIC ATOM IMAGING FROM EXPERIMENTAL PHOTOELECTRON ANGULAR DISTRIBUTION PATTERNS	141
L.J. Terminello, D.A. Lapiiano-Smith, J.J. Barton, B.L. Petersen, and D.A. Shirley	

A CBED PROCEDURE FOR DETERMINING LOCAL RESIDUAL STRESSES FROM NANOSCALE AREAS IN CERMETS	151
Gyeung Ho Kim and Mehmet Sarikaya	

ELECTRONIC STRUCTURE AND BONDING AT INTERFACES BETWEEN CVD DIAMOND AND SILICON	163
David A. Muller, Yujun Tzou, Rishi Raj, and John Silcox	

QUANTITATIVE ELECTRONIC STRUCTURE ANALYSIS OF α -Al ₂ O ₃ USING SPATIALLY RESOLVED VALENCE ELECTRON ENERGY-LOSS SPECTRA	169
Harald Millejans, J. Bruley, R.H. French, and P.A. Morris	

HIGH RESOLUTION TEM APPLIED TO NANOSCALE STRUCTURE STUDIES	177
L. Beltran Del Rio, M. Jose Yacaman, S. Tehuacanero, and A. Gomez	

MOIRE PATTERNS IN HIGH RESOLUTION ELECTRON MICROSCOPY IMAGES	183
J. Reyes-Gasga, S. Tehuacanero, and C. Zorrilla	

NANOSTRUCTURES DETECTED BY CONDUCTIVITY SPECTROSCOPY	189
K. Funke, K. El-Egili, R. Reichelt, M. Amrein, and C. Cramer	

SYNTHESIS AND CHARACTERIZATION OF STRUCTURED METAL/SILICA CLUSTERS	195
A.N. Patil, N. Otsuka, and R.P. Andres	

POROUS SILICON LUMINESCENCE STUDY BY IMAGING METHODS: RELATIONSHIP TO PORE DIMENSIONS	201
Anna Kontkiewicz, Andrzej M. Kontkiewicz, Sidhartha Sen, Marek Wesolowski, Jacek Lagowski, Piotr Edelman, and Tomasz Kowalewski	

*Invited Paper

TEM STUDIES ON THE MORPHOLOGY, SIZE DISTRIBUTION AND STRUCTURE OF NANOCRYSTALLINE IRON PARTICLES USING A FORMVAR EMBEDDED PREPARATION TECHNIQUE	207
Hengfei Ni, Xiangxin Bi, and John M. Stencel	
COMPOSITION AND STRAIN ANALYSIS OF SEMICONDUCTOR HETEROSTRUCTURES USING THICKNESS FRINGES ON TEM IMAGES	213
H. Kakibayashi, R. Tsuneta, and F. Nagata	
ELECTRON HOLOGRAPHY OF FLUX LATTICES IN NIOBIUM	219
J.E. Bonevich, K. Harada, T. Matsuda, H. Kasai, T. Yoshida, G. Pozzi, and A. Tonomura	
NANOINDENTATION ON CONTAMINATION-FREE GOLD FILMS USING THE ATOMIC FORCE MICROSCOPE	225
D.M. Schaefer and R. Reifenberger	
OBSERVATION AND MEASUREMENT OF ATOMIC SCALE IMPERFECTIONS IN MATERIALS USING CBED+EBI/H	231
Rodney A. Herring, John E. Bonevich, Takayoshi Tanji, and Akira Tonomura	
IMAGING OF BURIED Si AND Si:Ge SURFACE STRUCTURE UNDER AMORPHOUS Ge FILMS BY PLAN VIEW TRANSMISSION ELECTRON MICROSCOPY	237
Olof C. Hellman	
STRUCTURAL INVESTIGATION OF NaNO_3 NANOPHASE CONFINED IN POROUS SILICA	243
R. Mu, D.O. Henderson, and F. Jin	
INTERFACIAL ROUGHNESS IN GaAs/AlGaAs MULTILAYERS: INFLUENCE OF CONTROLLED IMPURITY ADDITION	249
S. Nayak, J.M. Redwing, T.F. Kuech, D.E. Savage, and M.G. Lagally	
DIRECT OBSERVATION OF DIFFRACTION ARCS FROM NANOSCALE PRECIPITATES IN STEELS BY HIGHLY BRILLIANT AND FOCUSED SYNCHROTRON RADIATION BEAM AND IMAGING PLATE	255
Yasuo Takagi, Yoshitaka Okitsu, and Toshiyasu Ukena	
NANOSTRUCTURAL STUDIES BY MÖSSBAUER SPECTROSCOPY	261
Georgia C. Papaefthymiou	
NMR STUDIES OF ELECTRONIC AND LOCAL STRUCTURE IN Cu-Au ALLOYS	267
James Chepin and Joseph H. Ross, Jr.	
PART IV: LOCAL CHEMISTRY AND COMPOSITION DETERMINATION	
*ATOMIC RESOLUTION ELECTRONIC STRUCTURE USING SPATIALLY RESOLVED ELECTRON ENERGY LOSS SPECTROSCOPY	275
P.E. Batson	
TRACE ANALYSIS OF NANOSCALE MATERIALS BY ANALYTICAL ELECTRON MICROSCOPY	287
Dale E. Newbury and Richard D. Leapman	

*Invited Paper

SELECTIVE IMAGING OF METAL ATOMS IN THE SEMICONDUCTING LAYERED COMPOUND MoS ₂ BY STM/STS	293
S. Inoue, H. Kawami, M. Yoshimura, and T. Yao	
ATOMIC-RESOLUTION CHEMICAL ANALYSIS AT 100 kV IN THE SCANNING TRANSMISSION ELECTRON MICROSCOPE	297
N.D. Browning, M.F. Chisholm, and S.J. Pennycook	
NANOANALYTICAL CHARACTERIZATION OF GRANULAR Ag-Fe FILMS WITH GIANT MAGNETORESISTANCE	303
J. Liu, Z.G. Li, H. Wan, A. Tsoukatos, and G.C. Hadjipanayis	
AEM INVESTIGATION OF TETRAHEDRALLY COORDINATED Ti ⁴⁺ IN NICKEL-TITANATE SPINEL	309
Ian M. Anderson, Jim Bentley, and C. Barry Carter	
QUANTITATIVE X-RAY MICROANALYSIS FOR THE STUDY OF NANOMETER-SCALE PHASES IN THE AEM	315
Ian M. Anderson, Jim Bentley, and C. Barry Carter	
DETERMINATION OF THE NUMBER OF MOLECULES BONDED TO A CdSe NANOCRYSTALLITE SURFACE	321
Sara Majetich, Jennifer Newbury, and Dale Newbury	
TEM STUDY OF THE Pt-Ru BI-METALLIC CATALYST FORMATION	327
Chaoying Ma, A.D. Kowalak, and Changmo Sung	
RAMAN SPECTROSCOPY OF SIZE SELECTED, MATRIX ISOLATED Si CLUSTERS	333
A. Ogura, E.C. Honea, C.A. Murray, K. Raghavachari, W.O. Sprenger, M.F. Jarrold, and W.L. Brown	
PART V: ELEMENTAL IMAGING	
*ELEMENTAL MAPPING BY ENERGY-FILTERED ELECTRON MICROSCOPY	341
Ondrej L. Krivanek, Michael K. Kundmann, and Xavier Bourrat	
*EELS IMAGING OF BIOLOGICAL MATERIALS	351
R.D. Leapman, S. Sun, J.A. Hunt, and S.B. Andrews	
*ANNULAR DARK FIELD IMAGING IN STEM	361
Sean Hillyard and John Silcox	
*QUANTITATIVE HRTEM: MEASURING PROJECTED POTENTIAL, SURFACE ROUGHNESS AND CHEMICAL COMPOSITION	373
P. Schwander, C. Kisielowski, F.H. Baumann, Y.O. Kim, and A. Ourmazd	
COMPOSITIONS AND CHEMICAL BONDING IN CERAMICS BY QUANTITATIVE ELECTRON ENERGY-LOSS SPECTROMETRY	385
J. Bentley, L.L. Horton, C.J. McHargue, S. McKernan, C.B. Carter, A. Revcolevschi, S. Tanaka, and R.F. Davis	

*Invited Paper

PART VI: MOLECULAR IMAGING

*STM STUDIES AT ELECTROCHEMICALLY CONTROLLED INTERFACES	393
S.M. Lindsay, J. Pan, and T.W. Jing	
*LOW VOLTAGE POINT PROJECTION MICROSCOPY AND TIME OF FLIGHT STM—TWO NEW MICROSCOPIES	405
J.C.H. Spence, W. Qian, W. Lo, S. Mo, U. Knipping, and X. Zhang	
*IMAGING SINGLE NACREOUS TABLETS WITH THE ATOMIC FORCE MICROSCOPE	413
R. Giles, S. Manne, C.M. Zaremba, A. Belcher, S. Mann, D.E. Morse, G.D. Stucky, and P.K. Hansma	
SCANNING TUNNELING MICROSCOPY (STM) AND SCANNING FORCE MICROSCOPY (SFM) OF LIQUID CRYSTALS AND POLYMERS	423
K.D. Jandt, T.J. McMaster, D.G. McDonnell, J.M. Blackmore, and M.J. Miles	
VISUALIZING LANGMUIR-BLODGETT FILMS WITH THE ATOMIC FORCE MICROSCOPE	429
Ravi Viswanathan, D.K. Schwartz, L.L. Madsen, and J.A. Zasadzinski	

PART VII: SURFACE STRUCTURES AND PHYSICAL PROPERTIES

*POLARIZATION, INTERFERENCE CONTRAST, AND PHOTOLUMINESCENCE IMAGING IN NEAR FIELD OPTICAL MICROSCOPY	437
M. Vaez-Iravani, R. Toledo-Crow, and J.K. Rogers	
*PHOTON TUNNELING MICROSCOPY APPLICATIONS	449
John M. Guerra	
*THE FIELD EMISSION GUN SCANNING ELECTRON MICROSCOPE— HIGH RESOLUTION AT LOW BEAM ENERGIES	461
David C. Joy	
*STRUCTURAL AND MAGNETIC PROPERTIES OF EPITAXIALLY GROWN FCC Fe/Cu(100) AND Fe/CaF ₂ /Si(111)	473
M.R. Scheinfein, S.D. Healy, K.R. Heim, Z.J. Yang, J.S. Drucker, and G.G. Hembree	
SURFACE MORPHOLOGY OF DIAMOND THIN FILMS USING PHOTO-INDUCED SCANNING TUNNELING MICROSCOPY	483
D.L. Carroll, T. Mercer, Y. Liang, N.J. DiNardo, and D.A. Bonnell	
ATOMIC SCALE CHARACTERIZATION OF (NH ₄) ₂ S _x -TREATED GaAs (100) SURFACE	489
Naoki Yokoi, Hiroya Andoh, and Mikio Takai	
RELATIONSHIPS BETWEEN PHOTOLUMINESCENCE SPECTRA AND POROSITY OF POROUS SILICON	495
H.Z. Song, L.Z. Zhang, B.R. Zhang, and G.G. Qin	

*Invited Paper

EXPERIMENTAL AND SIMULATED SCANNING TUNNELING MICROSCOPY OF THE CLEAVED $Rb_{1/3}WO_3$ (0001) SURFACE	501
Weier Lu and Gregory S. Rohrer	
IMAGING THE ATOMIC-SCALE STRUCTURE OF MOLYBDENUM AND VANADIUM OXIDES BY SCANNING TUNNELING MICROSCOPY	507
Gregory S. Rohrer, Weier Lu, and Richard L. Smith	
CHARACTERIZATION OF InP/GaInAs NANOMETER-SIZED COLUMNS PRODUCED BY AEROSOL DEPOSITION AND PLASMA ETCHING	513
I. Maximov, K. Deppert, L. Montelius, L. Samuelson, S. Gray, M. Johansson, H.-C. Hansson, and A. Wiedensohler	
NANOMETER SCALE STRUCTURES RESULTING FROM GRAPHITE OXIDATION	519
Marilyn J. Nowakowski, John M. Vohs, and Dawn A. Bonnell	
GRAZING INCIDENCE X-RAY REFLECTANCE MEASUREMENT OF SURFACE AND INTERFACE ROUGHNESS ON THE SUB-NANOMETRE SCALE	525
M. Wormington, K. Sakurai, D.K. Bowen, and B.K. Tanner	
SIZE-EFFECT STABILIZATION OF THE LOW-T FERROELECTRIC PHASE IN NANOCRYSTALLINE WO_3	531
Xiang-Xin Bi, W.T. Lee, Kai-An Wang, D.F. Collins, S. Bandow, and P.C. Eklund	
STRENGTH-FLAW RELATIONSHIP OF CORRODED PRISTINE SILICA STUDIED BY ATOMIC FORCE MICROSCOPY	537
Qian Zhong, Daryl Inniss, and Charles R. Kurkjian	
PHOTON SCANNING TUNNELING MICROSCOPY OF OPTICAL WAVEGUIDE STRUCTURES	543
Ahn Goo Choo, Mona H. Chudgar, Howard E. Jackson, Gregory N. De Brabander, Mukesh Kumar, and Joseph T. Boyd	
SPECTROSCOPIC CHARACTERIZATION OF NANOSCALE MODIFICATION OF PASSIVATED Si(100) SURFACE BY STM	549
F. Pérez-Murano, N. Barniol, and X. Aymerich	
INVESTIGATION OF THE VICINAL Ge(001) SURFACE WITH STM	555
Bart A.G. Kersten, Lianda Sjerps-Koomen, Harold J.W. Zandvliet, and Dave H.A. Blank	
PART VIII: CROSS-SECTIONAL AND 3-D IMAGING AT ATOMIC RESOLUTION	
*3-D IMAGING OF CRYSTALS AT ATOMIC RESOLUTION	563
M.A. O'Keefe, K.H. Downing, H-R. Wenk, and Hu Meisheng	
*ELECTRONIC STRUCTURE OF LAYERED AND LINEAR CHAIN MATERIALS BY SCANNING PROBE MICROSCOPY	573
R.V. Coleman, Z. Dai, Y. Gong, C.G. Slough, and Q. Xue	
*ATOM PROBE MICROSCOPY AND ITS FUTURE	587
T.F. Kelly, P.P. Camus, D.J. Larson, and L.M. Holzman	

*Invited Paper

*CROSS-SECTIONAL SCANNING TUNNELING MICROSCOPY OF III-V QUANTUM STRUCTURES	599
M.B. Johnson, M. Pfister, S.F. Alvarado, and H.W.M. Salemink	
*INCOHERENT IMAGING BY Z-CONTRAST STEM: TOWARDS 1 Å RESOLUTION	607
S.J. Pennycook, D.E. Jesson, and A.J. McGibbon	
AUTHOR INDEX	615
SUBJECT INDEX	619

*Invited Paper

Preface

As the capabilities of microscopy techniques to investigate materials at smaller dimensions improve, processing techniques advance in parallel. In fact, materials synthesis with better-controlled spatial variations at a smaller scale has been demonstrated in many areas of materials and biological sciences. The major purpose of this symposium was not only to use microscopy and spectroscopy techniques for imaging, and compositional and chemical analysis of bulk and surface structures, but also to show that these newly emerging techniques are now capable of directly measuring physical and chemical properties of nanostructured biological and synthetic materials at a local scale. The concept of determining nanoscale properties of materials by microscopy and spectroscopy, therefore, can be expected to open up new avenues for science and engineering of materials, as firmly demonstrated by this symposium.

Microscopy techniques included those that use photons, x-rays, electrons, and scanning probe techniques at their highest resolutions, all less than 1000 Å down to nanometer and molecular levels, and in some cases 1 Å and smaller. Similarly, spectroscopy techniques included local measurements of bonding, electronic, optical, and magnetic properties, again using probes at the nanometer scale.

All of the invited presentations, and many of the extraordinary contributed papers, represented the latest applications of the techniques at the highest resolution levels. Highlights among the presentations included the following. Breaking the resolution limit in the light optical microscope, traditionally limited by aberration due to light scattering, we witnessed that the near-field scanning optical microscope (NSOM) can now image surfaces (wet or dry) of materials at an order of better resolution, and with ease (represented by Michael Paesler, NCSU, Jay Trautman, AT&T, and Mehdi Vaez-Iravani, Rochester Institute of Technology). X-ray microscopy (XRM) and chemical contrast (Janos Kirz, SUNY and Harald Ade, NCSU) were shown to produce structural and chemical bulk-imaging from wet synthetic and biological materials with resolution down to a few hundred nanometers, with a potential for further reduction.

We learned from David Smith (ASU) and Michael O'Keefe that *conventional* atomic resolution transmission electron microscopy (AREM) provides images at better than 2 Å resolution, both in projection and in 3-D. With coherent imaging, provided by the new field emission TEM instruments (Hannes Lichte) and incoherent imaging, with dedicated STEM instruments (Steve Pennycook, Oak Ridge National Laboratory, and John Silcox, Cornell), resolution limits seem to have gone down to 1 Å in the electron microscope. Furthermore, as beautifully demonstrated by Pennycook and Peter Schwander/Abbas Ourmazd et al. (AT&T, Holmdel) it is now possible to chemically image atoms in projection by STEM and TEM, respectively, both with FEG sources. Universally the most practical of all imaging techniques, i.e., scanning electron microscopy (SEM), now at the subnanometer-level resolution, was demonstrated, with great humor, by David Joy (U. Tennessee). We now know from Philip Batson's (IBM, Yorktown Heights) and Edward Stern's (U. Washington) presentations that using electron energy loss spectroscopy (EELS) in the transmission electron microscope, it is possible to obtain information about: bonding energies and oxidation states; and short range ordering in areas from 1000 Å down to as small as 2 Å diameter (defined by the electron probe), using energy loss near edge structure analysis (ELNES) and extended energy loss fine structure analysis (EXELFS), respectively. Parts-per-million level elemental analysis by energy dispersive x-ray (EDXS) and EELS were discussed heatedly by David Williams (Lehigh), Dale Newbury (NIST) and Anthony Garrat-Reed (MIT). Elemental imaging at the highest resolution levels using energy filtering was skillfully illustrated by Ondrej Krivanek (Gatan) in engineering materials with

a conventional TEM and, with the same rigor, by Richard Leapman (NIH) in biological samples with a STEM. With an FEG-TEM, we learned that it is now possible to obtain diffraction directly from nanoscale areas (interfaces, multilayers, and defects), and to decipher structures using convergent beam electron diffraction (CBED). This was well represented by John Steeds (U. Bristol).

The latest developments in imaging and spectroscopy with scanning probe microscopies were also well represented. Imaging and interface structure at Å dimensions, and electrical properties at less than eV level with scanning tunneling microscopy (STM), were demonstrated by Randy Feenstra (IBM, Yorktown Heights), Huub Salemink (IBM, Zurich) and Robert Coleman (U. Virginia). Hans Hallen, et al. (NCSU) and Michael Scheinfein (ASU) demonstrated measurements of magnetic and dynamic superconducting properties with STM, respectively. Molecular imaging with STM and atomic force microscopy (AFM) in fluids was demonstrated by enthusiastic speakers and experimentalists Stuart Lindsay (ASU) and Paul Hansma (UCSB), respectively, and the problems in STM imaging of proteins were discussed by Buddy Ratner (U. Washington). Imaging of electron standing waves, enclosed in a *quantum corral* on the surface of Fe, was elegantly demonstrated by Donald Eigler (IBM, Almaden) showing us directly for the first time that electrons are really waves!

Although limited by sample preparation to conductive materials, current status and future prospects of 3-D imaging by atom probe was demonstrated by Thomas Kelly (U. Wisconsin). Dynamic imaging, in projection, of atomic diffusion in precipitate growth in metals was demonstrated by James Howe (U. Virginia). Flux-line dynamics in low- and, surprisingly, high-temperature superconductors was clearly demonstrated by Akira Tonomura (Hitachi). Dynamic properties of surfaces (dynamic properties of phase states of fluids at interfaces) were discussed by Jacob Israelachvili (UCSB). Bruce Parkinson (Colorado State) discussed 2-D growth with STM, and a number of contributed talks discussed elastic, thermal, and tribological studies.

It was exciting to hear about relatively new techniques in molecular imaging. John Spence (ASU) demonstrated the possibilities of imaging thin membranes (<20 Å) with a low-voltage point-projection microscope (PPM!). A truly revolutionary technique, NMR imaging, both in theory and experiment (represented, respectively, by John Sidles, U. Washington and Donald Rugar, IBM, Almaden), appeared to have set a new era in the quest for imaging structures at sub-Å level and in 3-D (meaning recognizing atoms and their bonding states and biological molecules).

The symposium constituted 42 invited speakers and over 120 contributed papers, both as platform and as poster presentations (these proceedings represent almost all of the invited papers and about half of the contributed papers). The symposium started on Monday afternoon and continued until noon on Friday, with poster sessions on Tuesday and Thursday evenings. From the beginning to the end, the symposium was well attended, often with the audience spreading out into the corridors, and discussions continuing well into the late-night hours. The quality of the symposium was kept at a high standard that was made possible by generous grants from NSF (Division of Materials Research) and ONR (Materials Division), our company sponsors (Digital Instruments, Inc. and JEOL, Ltd.), and by the professional assistance of the MRS staff.

Mehmet Sarikaya
H. Kumar Wickramasinghe
Michael Isaacson

December 1993

MATERIALS RESEARCH SOCIETY SYMPOSIUM PROCEEDINGS

Volume 297— Amorphous Silicon Technology—1993, E.A. Schiff, M.J. Thompson, P.G. LeComber, A. Madan, K. Tanaka, 1993, ISBN: 1-55899-193-X

Volume 298— Silicon-Based Optoelectronic Materials, R.T. Collins, M.A. Tischler, G. Abstreiter, M.L. Thewalt, 1993, ISBN: 1-55899-194-8

Volume 299— Infrared Detectors—Materials, Processing, and Devices, A. Appelbaum, L.R. Dawson, 1993, ISBN: 1-55899-195-6

Volume 300— III-V Electronic and Photonic Device Fabrication and Performance, K.S. Jones, S.J. Pearton, H. Kanber, 1993, ISBN: 1-55899-196-4

Volume 301— Rare-Earth Doped Semiconductors, G.S. Pomrenke, P.B. Klein, D.W. Langer, 1993, ISBN: 1-55899-197-2

Volume 302— Semiconductors for Room-Temperature Radiation Detector Applications, R.B. James, P. Siffert, T.E. Schlesinger, L. Franks, 1993, ISBN: 1-55899-198-0

Volume 303— Rapid Thermal and Integrated Processing II, J.C. Gelpey, J.K. Elliott, J.J. Wortman, A. Ajmera, 1993, ISBN: 1-55899-199-9

Volume 304— Polymer/Inorganic Interfaces, R.L. Opila, A.W. Czanderna, F.J. Boerio, 1993, ISBN: 1-55899-200-6

Volume 305— High-Performance Polymers and Polymer Matrix Composites, R.K. Eby, R.C. Evers, D. Wilson, M.A. Meador, 1993, ISBN: 1-55899-201-4

Volume 306— Materials Aspects of X-Ray Lithography, G.K. Celler, J.R. Maldonado, 1993, ISBN: 1-55899-202-2

Volume 307— Applications of Synchrotron Radiation Techniques to Materials Science, D.L. Perry, R. Stockbauer, N. Shinn, K. D'Amico, L. Terminello, 1993, ISBN: 1-55899-203-0

Volume 308— Thin Films—Stresses and Mechanical Properties IV, P.H. Townsend, J. Sanchez, C-Y. Li, T.P. Weihs, 1993, ISBN: 1-55899-204-9

Volume 309— Materials Reliability in Microelectronics III, K. Rodbell, B. Filter, P. Ho, H. Frost, 1993, ISBN: 1-55899-205-7

Volume 310— Ferroelectric Thin Films III, E.R. Myers, B.A. Tuttle, S.B. Desu, P.K. Larsen, 1993, ISBN: 1-55899-206-5

Volume 311— Phase Transformations in Thin Films—Thermodynamics and Kinetics, M. Atzmon, J.M.E. Harper, A.L. Greer, M.R. Libera, 1993, ISBN: 1-55899-207-3

Volume 312— Common Themes and Mechanisms of Epitaxial Growth, P. Fuoss, J. Tsao, D.W. Kisker, A. Zangwill, T.F. Kuech, 1993, ISBN: 1-55899-208-1

Volume 313— Magnetic Ultrathin Films, Multilayers and Surfaces/Magnetic Interfaces—Physics and Characterization (2 Volume Set), C. Chappert, R.F.C. Farrow, B.T. Jonker, R. Clarke, P. Grünberg, K.M. Krishnan, S. Tsunashima, E.E. Mariner, T. Egami, C. Rau, S.A. Chambers, 1993, ISBN: 1-55899-211-1

Volume 314— Joining and Adhesion of Advanced Inorganic Materials, A.H. Carim, D.S. Schwartz, R.S. Silbergliitt, R.E. Loehman, 1993, ISBN: 1-55899-212-X

Volume 315— Surface Chemical Cleaning and Passivation for Semiconductor Processing, G.S. Higashi, E.A. Irene, T. Ohmi, 1993, ISBN: 1-55899-213-8

MATERIALS RESEARCH SOCIETY SYMPOSIUM PROCEEDINGS

Volume 316—Materials Synthesis and Processing Using Ion Beams, R.J. Culbertson, K.S. Jones, O.W. Holland, K. Maex, 1994, ISBN: 1-55899-215-4

Volume 317—Mechanisms of Thin Film Evolution, S.M. Yalisove, C.V. Thompson, D.J. Eaglesham, 1994, ISBN: 1-55899-216-2

Volume 318—Interface Control of Electrical, Chemical, and Mechanical Properties, S.P. Murarka, T. Ohmi, K. Rose, T. Seidel, 1994, ISBN: 1-55899-217-0

Volume 319—Defect-Interface Interactions, E.P. Kvam, A.H. King, M.J. Mills, T.D. Sands, V. Vitek, 1994, ISBN: 1-55899-218-9

Volume 320—Silicides, Germanides, and Their Interfaces, R.W. Fathauer, L. Schowalter, S. Mantl, K.N. Tu, 1994, ISBN: 1-55899-219-7

Volume 321—Crystallization and Related Phenomena in Amorphous Materials, M. Libera, T.E. Haynes, P. Cebe, J. Dickinson, 1994, ISBN: 1-55899-220-0

Volume 322—High-Temperature Silicides and Refractory Alloys, B.P. Bewlay, J.J. Petrovic, C.L. Briant, A.K. Vasudevan, H.A. Lipsitt, 1994, ISBN: 1-55899-221-9

Volume 323—Electronic Packaging Materials Science VII, R. Pollak, P. Børgesen, H. Yamada, K.F. Jensen, 1994, ISBN: 1-55899-222-7

Volume 324—Diagnostic Techniques for Semiconductor Materials Processing, O.J. Glembocki, F.H. Pollak, S.W. Pang, G. Larrabee, G.M. Crean, 1994, ISBN: 1-55899-223-5

Volume 325—Physics and Applications of Defects in Advanced Semiconductors, M.O. Manasreh, M. Lannoo, H.J. von Bardeleben, E.L. Hu, G.S. Pomrenke, D.N. Talwar, 1994, ISBN: 1-55899-224-3

Volume 326—Growth, Processing, and Characterization of Semiconductor Heterostructures, G. Gumbs, S. Luryi, B. Weiss, G.W. Wicks, 1994, ISBN: 1-55899-225-1

Volume 327—Covalent Ceramics II: Non-Oxides, A.R. Barron, G.S. Fischman, M.A. Fury, A.F. Hepp, 1994, ISBN: 1-55899-226-X

Volume 328—Electrical, Optical, and Magnetic Properties of Organic Solid State Materials, A.F. Garito, A. K-Y. Jen, C. Y-C. Lee, L.R. Dalton, 1994, ISBN: 1-55899-227-8

Volume 329—New Materials for Advanced Solid State Lasers, B.H.T. Chai, T.Y. Fan, S.A. Payne, A. Cassanho, T.H. Allik, 1994, ISBN: 1-55899-228-6

Volume 330—Biomolecular Materials By Design, H. Bayley, D. Kaplan, M. Navia, 1994, ISBN: 1-55899-229-4

Volume 331—Biomaterials for Drug and Cell Delivery, A.G. Mikos, R. Murphy, H. Bernstein, N.A. Peppas, 1994, ISBN: 1-55899-230-8

Volume 332—Determining Nanoscale Physical Properties of Materials by Microscopy and Spectroscopy, M. Sarikaya, M. Isaacson, H.K. Wickramasighe, 1994, ISBN: 1-55899-231-6

Volume 333—Scientific Basis for Nuclear Waste Management XVII, A. Barkatt, R. Van Konynenburg, 1994, ISBN: 1-55899-232-4

Volume 334—Gas-Phase and Surface Chemistry in Electronic Materials Processing, T.J. Mountziaris, P.R. Westmoreland, F.T.J. Smith, G.R. Paz-Pujalt, 1994, ISBN: 1-55899-233-2

Volume 335—Metal-Organic Chemical Vapor Deposition of Electronic Ceramics, S.B. Desu, D.B. Beach, B.W. Wessels, S. Gokoglu, 1994, ISBN: 1-55899-234-0

PART I

Local Spectroscopy and Imaging

SPATIALLY RESOLVED LOCAL ATOMIC STRUCTURE FROM EXELFS

E. A. Stern*, M. Qian† and M. Sarikaya,†

Departments of *Physics and †Materials Science and Engineering,
University of Washington, Seattle, WA 98115, USA

Abstract

EXELFS, extended energy loss fine structure, is one of the spectroscopic techniques provided by electron energy loss spectrometer in the transmission electron microscope. Here, EXELFS is described for its potential use for determining nanoscale physical properties of complex materials. It is demonstrated that EXELFS analysis, like EXAFS, extended X-ray absorption fine structure in bulk materials, provides short-range structural information such as atomic nearest-neighbors and their distances in amorphous and crystalline samples. Some of the problems that hindered the development and wide use of EXELFS were discussed and their solutions are presented. Further solutions and future prospects are discussed.

1.0 Introduction

The technique of X-ray absorption fine structure (XAFS) has proven over the years to be an important tool to determine the local atomic structures in condensed matter.^{1,2} The technique has been developed so that, presently, sophisticated methods of measurement and analysis are employed to determine the local atomic structure of various classes of materials. Recently, the capability to analyze accurately the structure out to fourth nearest neighbors and further was made possible by the introduction of accurate theoretical calculations³ of the multiple scattering suffered by the excited photoelectrons and software to utilize these calculations to fit the data.⁴ For example, these advances have allowed the determination, for the first time, of the structure of a mixed salt with an average NaCl type lattice, which include the deviations of the atoms about the average lattice.⁵

It had been appreciated some time ago that the same information as in the XAFS spectra is also present in the extended electron loss fine structure from high energy electrons passing through matter.^{6,7} However, in spite of the promise, the EXELFS technique has not yet been exploited for structure determination. The reasons for this are varied but the most important is the need to collect very high statistics to accurately measure the weak fine structure. Until the commercial availability of parallel electron energy loss (PEEL) detectors⁸ it was not feasible to collect such statistics because of both time and radiation damage considerations. The PEEL detectors collect the EXELFS spectra two orders of magnitude more rapidly than the series

detectors, making the necessary statistics collection feasible.⁹ Moreover, to obtain accurately the full quantitative structural information from the spectra it is necessary to utilize the sophisticated analysis programs of XAFS and to correct the data for systematic errors, as discussed in Section 3.

In this paper we describe our progress in making EXELFS a quantitative technique for structure determination. Section 2 gives a summary of what XAFS is and what information can be obtained from it. Section 3 discusses EXELFS and the cases where it can complement XAFS and even have advantages over it. Some examples of quantitative structure determination from EXELFS are given in Section 4. Conclusions and Summary are given in Section 5 while future prospects are discussed in Section 6.

2.0 XAFS

XAFS is the fine structure on the high energy side of absorption edges suffered by X-rays interacting with matter. The absorption edges occur when the X-ray photon energy is just sufficient to excite core electrons free from an atom. As the X-ray photon energy is increased further, the excess energy is imparted to the photoelectron, consequently varying the wavelength of its wave function. The final state wave function of the photoelectron is the interference of the outgoing portion of the wave function with the portion backscattered from the surrounding atoms. The phase difference between these two portions varies as the photoelectron wavelength changes, introducing the fine structure in the absorption.

An analysis of the XAFS gives quantitative information on the partial pair distribution function of the atoms surrounding the absorbing atom. The features of XAFS are:¹⁰

- i. The local atomic arrangement is determined about each type of atom, separately, by tuning the X-rays to its characteristic absorption energy edge.
- ii. Long range order is not required. Both amorphous and crystalline materials can be analyzed equally well.
- iii. The numbers and types of surrounding atoms up to the 4th nearest neighbors and beyond can be determined. The average distance of atoms can be ascertained to typically $\pm 0.01\text{\AA}$ and the distribution about the average can be determined to a typical resolution of 0.1\AA .
- iv. Angular dependence of the distribution of atoms can be obtained in some special cases. Also, when three or more atoms are near collinear, three-body correlations can be measured including the angle from collinearity.
- v. The analysis is relatively straightforward and simple so that only small computers are required and the analysis can be accomplished in a short time.

- vi. Near edge fine structure adds electronic binding information such as valence of the absorbing atom.
- vii. The XAFS technique is limited to determining only short range order and loses its capabilities if the rms distribution of atoms about their average position is greater than about 0.15 Å. Fortunately, the short range order is rarely that disordered, at least for first neighbors.

3.0 EXELFS

In spite of the fact that it has been recognized for about 20 years that EXELFS contains the same structure information as XAFS, it has not been exploited as yet. As mentioned above, now is an opportune time to develop EXELFS as a quantitative technique for structure determination as the instrumental requirements of the TEM are rapidly advancing. When applicable, EXELFS has several advantages over XAFS. It has greater spatial resolution (determined by the electron probe size,) which can be used to an advantage to investigate phenomena that are spatially inhomogeneous such as in nanograined materials. In addition, the region being investigated can be characterized by the full capabilities of the transmission electron microscope such as imaging and diffraction. The EXELFS technique is optimized for measuring losses in the 0-1500 eV range. This is just the soft X-ray range which is most difficult to investigate using synchrotron radiation sources. It has been estimated¹¹ that in this energy range, the radiation damage to samples by high energy electron measurements of EXELFS is not much more severe than that produced by soft X-rays when measuring XAFS.

To develop EXELFS as a standard tool for structure determination several problems must be overcome. New problems that have not been addressed previously are:

- i. Obtaining high statistics: it is required to accumulate, for each energy interval of approximately 3 eV, a million or more counts so as to obtain statistical accuracy of 0.1%
- ii. The systematic errors introduced by the channel-to-channel variation of the parallel energy loss detector must be reduced to less than the statistical errors.
- iii. The radiation damage to the sample must be monitored and kept below values that can produce detectable changes in the structure.
- iv. The EXELFS data must be normalized by the correct background.

Besides addressing the new issues listed above, other issues must also be accounted for. The techniques for doing so are already known and will not be discussed here. They are:

- Corrections for plural scattering of the high energy electrons as they transverse the sample.
- Producing samples thin enough to decrease plural scattering effects, typically < 500 Å.

- Surface effects, such as oxide coating and hydrocarbon contamination, have to be minimized and taken into account.
- The sample has to retain its integrity under the high vacuum conditions of the TEM.
- Insulating samples have to be prepared so as to eliminate charging effects which can produce energy loss shifts as a function of time.
- The thickness of the sample must be quite uniform over the beam.

In the following, we first outline how the new problems listed above have been overcome.¹² For (i) the parallel detector does not have the dynamic range to collect the required statistics. Each pixel saturates after 16×10^3 counts. In addition, even if each pixel could accumulate enough counts, the collection time to do so is typically in the hours and it is necessary to have the electron beam energy, typically at 200 or 300 KeV, to be stabilized to within a pixel width of less than 3 eV during this period. This very stringent requirement of beam stability is quite difficult to attain. In our case, these problems are overcome by breaking the accumulation time into many shorter time intervals during which drifts in the energy are small. The spectra for successive time intervals are aligned on-line (in real time) to correct for any energy shifts and then summed to accumulate the required statistics. The correction of channel-to-channel variations (item (ii) above) can be performed using the procedure and software provided by GATAN, the manufacturer of the PEELS detector.¹³ In this procedure, electron beam uniformly illuminates the parallel detector and measures, by this means, the pixel-to-pixel response variation, which then can be divided out. Such a procedure is not always sufficiently accurate because under actual operating conditions the electron beam illuminates only the center region of the pixels while in the calibration technique of GATAN, the full length of the pixels are illuminated. To calibrate under the actual operating conditions we measure the energy loss excitation somewhat above the plasma loss peaks. In that region, the spectra of amorphous carbon, for example, are smooth and intense. After accumulating enough statistics, which typically takes less than an hour, the spectra are fitted with a smooth spline and the fluctuations from the spline are used as the correction for channel-to-channel gain variations. For item (iii), the radiation damage is monitored by dividing the sum of the various scans into a small number of separate sums to have a record of the time dependence of the spectra. Radiation damage would be revealed by a time dependent change in the spectra.

To obtain an EXELFS spectrum which can be analyzed, the data must be normalized by the background signal contributed solely by the core electron being excited, as mention in item (iv). For low energy edges, this normalization varies quite dramatically with energy past the edge, in contrast to the quite slow variation for the high energy edges. It requires an extremely accurate method to determine the correct background. To model the correct background it is necessary to separate the contribution of the excited core electron from that contributed by all

the rest of the processes. One possible way to accomplish this is to very accurately fit the pre-edge background and then extrapolate this pre-edge background beyond the edge and then subtract it from the total signal. Unfortunately, the core electron background decreases by more than an order of magnitude for the energy range of interest past the edge. Whereas for carbon atoms it is possible to have an edge step about equal to the pre-edge background, by the desired energy range beyond the edge, the core electron background decays to less than 10% of the extrapolated pre-edge. Thus, small errors in the extrapolated background can give serious errors in the core electron background. To overcome this difficulty, we use the subtracted extrapolated pre-edge background only for an energy range within 100 eV of the edge where the core electron background is large and then splice this onto a theoretical calculation of the background which is accurate beyond 100 eV of the edge.

The background so obtained has a different energy dependence than that obtained by X-ray absorption if the maximum electron wave number transverse to the beam introduced by scattering is much less than $\hbar\omega/v$, where $\hbar\omega$ is the electron energy loss and v is the speed of the electrons. In some cases it is standard to normalize the χ by the edge step instead of the background as a function of energy because the background is not accurately determined. To normalize correctly to the X-ray absorption χ it is necessary in such a case to multiply the χ obtained from EXELFS by E^2/E_0^2 where E is the energy loss and E_0 is the edge energy.¹³

4.0 Example of Al

There have been a number of investigations of the EXELFS of various materials such as Al,¹⁴⁻¹⁶ Si,¹⁷ SiC,¹⁸⁻²¹ and Al₂O₃,²² during the past decade. To calibrate our improved EXELFS technique, Al was investigated by us.²³ A 99.999% pure aluminum sample was rolled to a 75 nm thin film and annealed 48 hours at 280 °C after it was placed in a quartz tube, evacuated by a mechanical pump, and sealed. The thin film was then removed from the tube, a 3 mm diameter disk was punched out, polished on both sides with number 600 sand paper, and cleaned with acetone. The aluminum disk was given a final thinning by jet electropolishing with 33% HNO₃ + 67% methanol solution at -35 °C.

The sample was immediately put into a Philips 430T TEM/STEM to avoid further oxidizing. GATAN parallel detector EELS 666 system and EL/P 2.1 acquisition software were used which included as additions our custom software for CCGV (channel-to-channel-gain-variation) correction and on-line alignment and summation. The TEM was operated in the image (diffraction coupling) mode at 200 KeV electron energy with an objective aperture of 40 μm diameter and 10 KX magnification. This combination accepts scattering angles of the incident electrons from the sample of 1.3 mrad. This correspond for Al to a value of

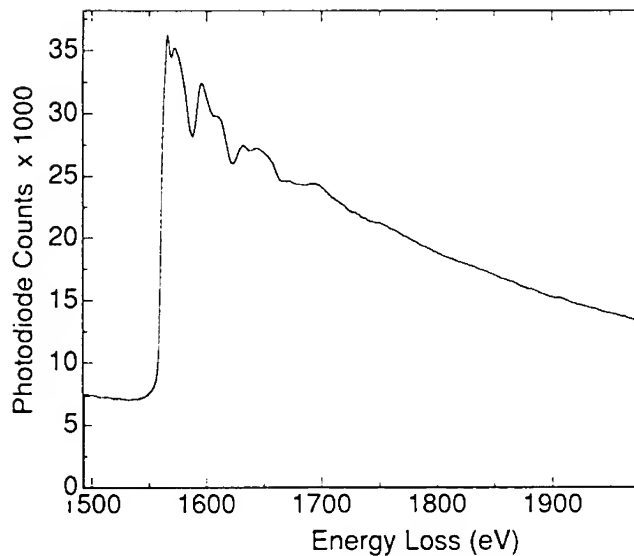


Fig. 1- One of the Al K-edge EELS spectra acquired at room temperature by using a GATAN EL/P 2.1 parallel electron energy loss detector with addition of our AcqLong custom function. Acquiring conditions: image mode with 40 μ m diameter objective aperture, 5 sec. acquisition time, 2 mm entrance aperture, 10 KX magnification. The final spectrum is a sum of 500 of such scans divided into ten subsums of 50 scans.

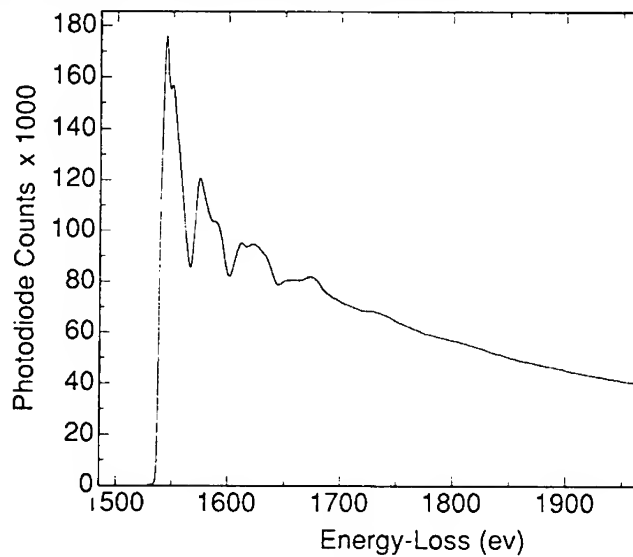


Fig. 2. The preprocessed Al K-edge EELS data. For each group of raw data, sharpened resolution, pre-edge background removal, and removal of plural scattering were applied. Then the preprocessed data were aligned and summed up.

$qa \approx 0.013$ where q is the wave number (Δk) transverse to the electron beam introduced in the scattering process and a is the size of the orbit of the 1s electrons in Al that are excited at the K-edge. Since $qa \ll 1$, the dipole approximation is satisfied in our measurements as required to use the XAFS analysis programs. In the case of the Al, since the XAFS background was not accurately determined, the data were normalized by the edge step. We also normalized the EXELFS data by the edge step and then, because such small values of q require it, the E^2/E_0^2 factor was used to normalize the EXELFS χ to the XAFS one. The EELS system was set up to a 2 mm entrance aperture, and 0.5 eV/Ch (per channel) dispersion rate. The beam was focused to cover a 5 mm circle area at the viewing screen. The total electron current was 2 nA. The acquisition time was set to 5 sec per readout, which gave a count level of 500 counts/Ch. To accumulate 10^5 counts/Ch, 500 spectra were needed. To monitor the time effects, we divided the 500 spectra into 10 groups, each containing 50 spectra. Low energy loss spectra were also taken for each group. Fig. 1 shows the raw data.

The GATAN EL/P 2.1 sharpened resolution function was used first to recover some of the spectrum details which were lost due to the instrument broadening. Although the thickness was about $0.3 - 0.4 \lambda$ (mean free path) there were still considerable multiple scattering contributions. Removal of plural scattering therefore, has to be performed for each of the ten spectra. Then the ten spectra were aligned and summed over, giving the result shown in Fig. 2. Using the procedures for background subtraction and normalization described in the previous section, the EXELFS spectra as shown in Fig. 3 are then exactly equivalent to XAFS spectra χ^{23} and can be analyzed by the same software as used for XAFS.²³

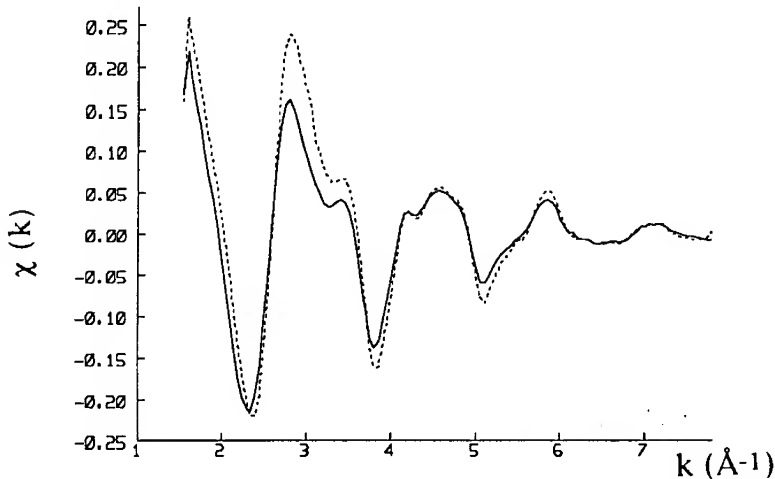


Fig. 3. $\chi(k)$ The EXELFS data of Al K-edge (dot). Also shown is the XAFS $\chi(k)$ data (solid, from P. LaGarde²⁴)

Fig. 3 displays χ as a function of the photoelectron wave number k given by

$$\frac{h^2 k}{2m} = E - E_0, \quad (1)$$

where E_0 is the edge step energy and E is the electron energy loss. Also shown in the same figure is the $\chi(k)$ as determined from XAFS²⁴ measurements. As can be seen, the shape of the of both $\chi(k)$ is similar while the EXELFS is somewhat smaller at low k . At present we do not understand this small difference. A Fourier transform of $\chi(k)$ with respect to k (Fig. 4) was performed, and the magnitude of this transform, $\chi(R)$, is displayed in Fig. 5 as a function of R , real space. It can be seen that the first shell has a large amplitude whereas the second shell is quite small. In order to obtain quantitative structural information, an R-space non-linear least square fit was performed using the program UWXAFS2.0.⁴ We used theoretical FEFF5 XAFS as a standard since it is convenient and it has been greatly improved to a level that its results can be as good as experimental standards.³ Fig. 5 shows the FEFF calculated Al $\chi(R)$ data. The fitting R-range was 1.5 - 3.7 Å, which covers the first and second shell. The k -range used was 2.0 - 8.0 Å⁻¹ and the Fourier transform was performed on $k^2\chi(k)$. The number of independent points in the data was 10, more than the 5 fitting parameters used. The five parameters were: S_0^2 (many body effect), ΔE_0 (edge energy shift), R (first shell distance), σ_1^2 (Debye-Waller-factor, of the first shell), σ_2^2 (DW-factor of the second shell). The fcc structure was assumed so the second shell distance is determined by the first shell value. As we mentioned before, the second shell is small and it is known that it contains a considerable contribution from multiple scattering. We do not expect to get accurate information from a fit on the second shell. We included it in the fit mainly because we want to account for any leakage of the second shell into the first shell. The fit results are show in Fig. 5 and Table I.

Table I: Al fit results

parameters	fit results	ref. values ²⁵
r_1 (Å)	2.84 ± 0.01	2.85
r_2 (Å)	4.01 ± 0.02	4.03
σ_1^2 (Å ²)	0.011 ± 0.001	
σ_2^2 (Å ²)	0.023 ± 0.002	

The theoretical calculations have to be normalized by a constant $s_0^2 \approx 1$ to correct for many-body effects.¹⁰ The s_0^2 value obtained from the EXELFS data agrees with that obtained by analyzing Al-XAFS data. As one can note from the Table, the structure determined by EXELFS agrees well with the known structure of Al.

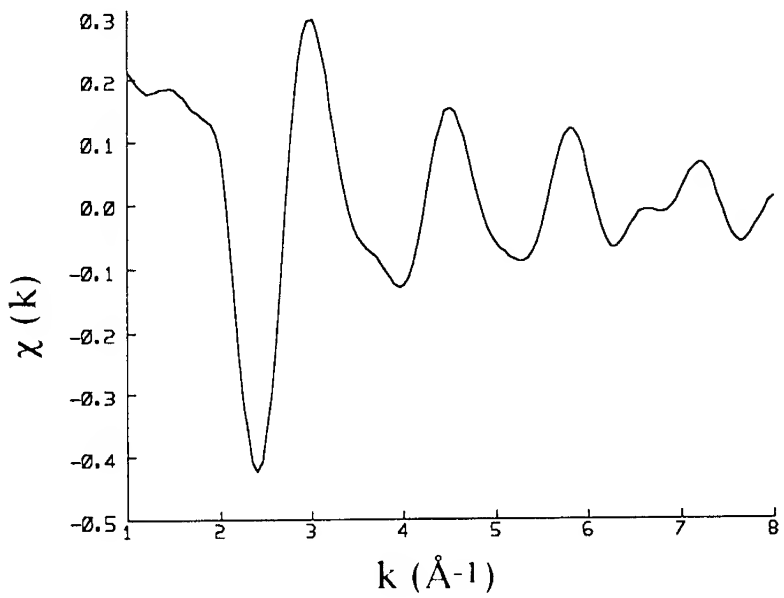


Fig. 4. The FEFF calculated Al K-edge $\chi(k)$ data. $s_0^2 = 1$, and $\sigma^2 = 0$ were assumed.

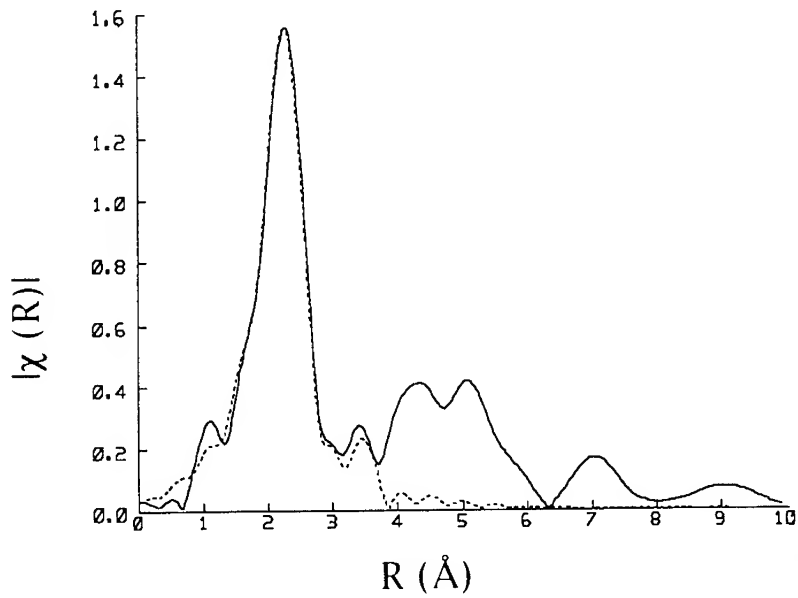


Fig. 5. The magnitude of the Fourier transform of $k^2\chi(k)$. The dotted line is the fit result.

5.0 Summary and Conclusions

We have shown that it is possible to obtain quantitative structure information from EXELFS taken in a transmission electron microscope on an Al sample. The quality of the Al data obtained from EXELFS is comparable to that obtained at a synchrotron source. In general, one expects¹³ these two techniques to give comparable quality of spectra from samples whose edges are below 1500 eV. Radiation damage was not a problem for Al but this issue must be assessed for each case since it will be material dependent (especially severe in ionic crystals and biological composites).

EXELFS has important advantages over XAFS measurements. The measurements can be performed in one's laboratory (avoiding a clearly inconvenient trip to a synchrotron source) if it contains the correctly instrumented transmission electron microscope. The spatial resolution is 100 nm or less in current TEMs with LaB₆ electron sources²⁶ and down to subnanometer in STEM²⁷ that have a field emission (FE) source, which is far superior to that of the present X-ray sources, although the energy resolution is somewhat limited (about 1.2 eV LaB₆ and 0.5 eV in TEM, but can be improved down to less than 0.1 eV in STEM²⁷). In addition, the sample can be characterized by high spatial resolution imaging, electron diffraction, and microspectroscopy techniques provided by TEM or STEM,²⁸ e.g., conventional and atomic resolution imaging, micro- and nano-diffraction, and EELS and energy dispersive X-ray compositional analyses, respectively. A disadvantage of EXELFS is that for dilute impurities, the large background cannot be reduced, as this can be for XAFS by detecting the signal in fluorescence instead of transmission. This limits the EXELFS technique to detecting atoms which are substantially more concentrated than the limit of XAFS detection.

Whereas it is usually stated that EXELFS contains the same information as XAFS and this statement is correct qualitatively, there are quantitative differences that need to be accounted for in order to obtain correct quantitative structure information, as discussed here. In particular, the EXELFS spectra may require an E² correction to account for the different backgrounds in X-ray absorption and electron energy loss spectra.

6.0 Future Prospects

We expect that it is possible to develop EXELFS so as to be a routine technique on every electron microscope with a parallel electron energy loss detector. This opens up the possibility of applying the technique to many materials (both crystalline and amorphous) especially those with inhomogeneities at the nanometer scale and obtain their local atomic structure. The EXELFS technique can be utilized in some crystalline samples to obtain angular structure

information. By appropriate alignment of crystalline samples it is possible to produce standing electron waves which can then be used to obtain site-specific EXELFS data to distinguish the same atom type at different crystalline sites.²⁹ The superior spatial resolution opens up many possibilities for investigation which can be illustrated by a specific example. In some bacteria single-domain magnetite particles of about 500 Å linear dimension are grown and then aligned to produce a dipole moment which is used to align the axes of the bacteria along the earth's magnetic field. This alignment allows the bacteria to move along the magnetic field lines either forward or backwards, so as to adjust their depth in the water at the optimum for feeding purposes. The electron microscope permits imaging of the particles and picking those which have not matured and reached their final size.³⁰ Investigating the magnetite particles as a function of their size from when they just start growing to maturity, by imaging, EXELFS, and diffraction, would give detailed information on the changes that occur from initiation of the growth to its termination, giving insight into the mechanism of control of the formation of these particles.

7.0 Acknowledgment

This work was partially supported by the University of Washington, through the Royalty Research Fund, and by the Japan-NEDO Grant, entitled Pan Pacific Ceramic Yacht.

8.0 References

1. D. E. Sayers, E. A. Stern and F. W. Lytle, *Phys. Rev. Lett.*, **27**, 1204 (1971).
2. E. A. Stern and W. M. Heald, in *Handbook on Synchrotron Radiation.*, Vol. 1, Ch. 10 (North Holland, Publisher, New York, 1983).
3. J. J. Rehr, R. C. Albers, and S. I. Zabinsky, *Phys. Rev. Lett.*, **69**, 3397 (1992); J. Mustre de Leon, J. J. Rehr, S. I. Zabinsky, and R. C. Albers, *Phys. Rev. B*, **44**, 4146 (1991); J. J. Rehr, J. Mustre de Leon, S. I. Zabinsky, and R. C. Albers, *J. Am. Chem. Soc.*, **113**, 5135 (1991).
4. For example, the copyrighted UWXAFS 2.0 software. Information regarding this software may be obtained from E. A. Stern, University of Washington.
5. A. I. Frenkel, E. A. Stern, M. Qian, and M. Newville, *Phys. Rev. B*, **49**, 1249 (1994); *Phys. Rev. Lett.*, **71**, 3485 (1993).
6. R. D. Leapman, and V. E. Cosslett, *J. Phys. D*, **9 L**, 29-32 (1976);
7. D. E. Johnson, S. Csillag and E. A. Stern, *Scanning Electr. Microsc.*, **1**, 105-115 (1981).
8. *Electron Energy Loss Spectroscopy in the Electron Microscope*, R. G. Egerton (Plenum Press, New York, 1986) pp. 246-255.
9. O. L. Krivanek, C. C. Ahn, and R. B. Keeney, *Ultramicroscopy*, **22**, 103-110 (1987).

10. E. A. Stern, *Optik* **61**, 45 (1982).
11. M. Utlauf, *EXAFS Spectroscopy Techniques and Applications*, B. K. Tao and D. C. Joy (eds.) (Plenum, New York, 1981) pp. 255-267.
12. M. Qian, M. Sarikaya, and E. A. Stern, in *Proceedings of the 51st Annual Meeting of Microscopy Society of America* (San Francisco Press, San Francisco, 1993) pp. 578-579.
13. M. Kundman, *Instructions for EELS Acquisition* (GATAN Inc., Pleasanton, CA, USA, 1993).
14. S. Csillag, D. E. Johnson, and E. A. Stern, in *EXAFS Spectroscopy Techniques and Applications*, B. K. Teo and D. C. Joy (eds.) (Plenum, New York, 1981) pp. 241-254.
15. M. M. Disko, C. C. Ahn, G. Meitzner, and O. L. Krivanek, in *Microbeam Anal.*, 1988 , (San Francisco Press, San Francisco, 1988) pp. 47-49.
16. J. K. Okamoto, C. C. Ahn, and B. Fultz, in *Microbeam Analysis, 1991* (San Francisco Press, San Francisco, 1991) pp. 273-276.
17. M. De Crescenzi, Lozzi, P. Picozzi, and S. Santucci, *Phys. Rev.*, **39** [12] 8409 (1989).
18. P. Angelini, P. S. Sklad, J. C. Sevely and D. K. Hssein, in *Proc. 46th Ann. Meeting of Electron Microsc. Soc. of Am.*, (San Francisco Press, San Francisco, 1988) pp. 466-467.
19. J. M. Martin and J. L. Mansot, *J. Microsc.*, **162** [1] 171-178 (1991).
20. V. Serin, G. Zanchi, and J. Sevely, *Microsc. Microanal. Microstruct.*, **3**, 201-212 (1992).
21. M. Qian, M. Sarikaya, and E. A. Stern, to be published.
22. K. Hssein, G. Zanchi, J. Sevely, X. Devaux and A. Rousset, in *Inst. Phys. Conf. Ser.*, **98** (EMAG-MICRO '89, Vol. 1, 1990) pp. 75-78 .
23. M. Qian, M. Sarikaya, and E. A. Stern, in *Proceedings of the 55th Annual Meeting of the Microscopy Society of America* (San Francisco Press, San Francisco, 1993) pp. 584-585.
24. P. LaGarde, measured in 1992, unpublished.
25. *Crystal Structures*, R. W. Wyckoff (Interscience Publication, New York, NY, 1963).
26. D. Newbury and R. D. Leapman, these Proceedings.
27. P. E. Batson, these Proceedings.
28. See, for example, these Proceedings: D. J. Smith for HREM, J. W. Steeds and R. Vincent for convergent beam techniques, O. L. Krivanek et al. and R. D. Leapman for EELS compositional analysis, and ref. 26 for energy dispersive X-ray analysis.
29. J. C. H. Spence, *Optik*, **57**, 451-456 (1980); J. C. H. Spence and J. Taftø, *J. Microsc.*, **130**, 147-154 (1993); K. M. Krishnan, *Scanning Electron Microsc.*, Supplement, **4**, 157-170 (1990).
30. *Iron Biominerals*, R. B. Frankel and R. P. Blakemore (Plenum, New York, NY, 1992).

CROSS-SECTIONAL SCANNING TUNNELING MICROSCOPY OF III-V SEMICONDUCTOR STRUCTURES

R. M. FEENSTRA*, A. VATERLAUS*, J. M. WOODALL*, D. A. COLLINS** AND T. C. McGILL**

*IBM Research Division, T. J. Watson Research Center, Yorktown Heights, NY 10598

**T. J. Watson Sr. Laboratory of Applied Physics, California Institute of Technology, Pasadena, CA 91125

ABSTRACT

The method of cross-sectional scanning tunneling microscopy (STM) is described. Illustrative examples are given of studies of III-V semiconductor systems, including low-temperature-grown (LT) GaAs, and InAs/GaSb superlattices. In each case, the STM permits the observation of structural features on an atomic scale. The associated electronic spectroscopy for states a few eV on either side of the Fermi-level can be determined. Such information is relevant for the operation of devices constructed from these layered semiconductor systems.

1. INTRODUCTION

The method of *cross-sectional* scanning tunneling microscopy (STM) has been utilized in the past several years for studying a variety of epitaxial semiconductor structures [1-4]. Such structures generally consist of a number of layers, with thickness ranging from angstroms to microns, grown by molecular-beam epitaxy (MBE) on a single crystal substrate. In the method, a cross-section of the structure is prepared by cleaving, and STM studies are performed on this cleavage face. For layered systems (*i.e.* superlattices), one gains information on the interfaces between layers, as well as the properties of the individual layers themselves. Most studies to date have been performed on III-V semiconductors (GaAs and related materials), although some work has appeared on the group IV materials (Si and Ge) [2]. For GaAs, the cleavage face is a (110) plane, and, for cleavage in ultra-high-vacuum (UHV), this face has the convenient property that the dangling bond energies do *not* lie within the band gap. Thus, spectroscopic studies of this surface reveal bulk-like properties for the band gap, band offsets, and other features. Alternatively, for Si, cleavage can be accomplished on either the (110) or (111) faces, but in both cases the spectroscopy of as-cleaved surfaces are dominated by dangling bond surface states. Thus, some chemical treatment is required to passivate these states, and perfect passivation may be difficult to attain. Passivation for the GaAs cleavage face is also possible, and is a viable alternative to UHV cleaving [4].

In addition to the requirements for sample preparation, discussed above, another requirement for cross-sectional STM is the ability to conveniently position the STM probe-tip over the epitaxial layers of interest. These layers are located, of course, at one edge of the cleavage face. Thus, they are found by stepping the probe-tip over to this edge in a controlled fashion. This stepping motion, which operates in the sub- μ m to mm length range, was a limitation in implementing the technique in the early years. However, with the commercial availability of UHV-compatible piezo-electric steppers [5] (and improved knowledge for constructing home built versions), this no longer presents a significant problem. One other technical detail of the measurements concerns the ability to perform detailed spectroscopic measurements. For studies of bulk-related spectral features, high dynamic range (about 6 orders-of-magnitude) in current and conductance is required to properly define band edges and other features. Such a high dynamic range is not attainable with a routine, quick current-voltage measurement. Thus, spe-

cial techniques have been developed to acquire and analyze such spectra, and these technique are described below.

In this paper, we describe the cross-sectional STM method, and present results from several systems which we have studied. Section 2 presents details of STM data acquisition, and specifies the growth parameters for the MBE-grown samples. Section 3 describes our results for low-temperature-grown (LT) GaAs. This material, grown at temperatures near 200°C, contains about 1 atomic % excess arsenic, leading to the formation of point defects (in unannealed films) or arsenic precipitates (in annealed films) [6]. The electronic properties of these defects have been determined in our studies [7,8]. Section 4 described results obtained from InAs/GaSb superlattices. This system has application for use as infra-red photodetectors, and a number of materials related issues affect the operation of such devices [9]. Using spectroscopy, we resolve the quantum subband structures in the superlattices. Also, details of the interface structure between InAs and GaSb, including interface roughness and intermixing, are determined in our studies [10].

2. EXPERIMENTAL

The LT-GaAs structures discussed in Section 3 were grown by MBE in a Varian GEN II system, at a growth temperature of 225°C. The structures generally consist of a *n*- or *p*-type layer 500–1000 Å thick grown at low-temperature, surrounded on both sides by layers of the opposite doping grown at high-temperature (> 350°C). These neighboring layers serve as markers to help locate the LT layer. High doping levels, around 10^{19} cm^{-3} , are used for all the layers. The LT layers have been studied in both as-grown unannealed form (denoted LTU) and in annealed form (denoted LTA). Annealing was performed at 600°C for 30 min under an As pressure of 10^{-6} Torr. The InAs/GaSb superlattices discussed in Section 3 were grown on a Perkin-Elmer 430 MBE system, at a growth temperature of ~ 380 °C. The growth surface was exposed to an Sb₂ flux for 5 s at the termination of each InAs and GaSb layer. The superlattices are Si doped at concentrations of $3 \times 10^{17} \text{ cm}^{-3}$ *p*-type in GaSb and $3 \times 10^{17} \text{ cm}^{-3}$ *n*-type in InAs. The superlattices have a period of 42 Å InAs and 24 Å GaSb, and total growth of 30–60 periods.

Samples cut from the above wafers were cleaved *in situ*, at pressure of 4×10^{-11} Torr. Single crystal <111> oriented tungsten probe tips were prepared by electrochemical etching and *in situ* electron beam heating, and were characterized *in situ* by field-emission microscopy. STM images were acquired with constant current of 0.1 nA and at various voltages specified below. Spectroscopic measurements were performed using a method previously developed for obtained a large dynamic range in the tunnel current and conductance [11,12]. An example of raw spectral data is shown in Fig. 1, for a clean *n*-type GaAs sample (doped at $1 \times 10^{19} \text{ cm}^{-3}$). We measure the tunnel current I_m and conductance $(dI/dV)_m$, Figs. 1(a) and (b), where the subscript *m* refers to *measured* quantity. The conductance is determined using a lock-in amplifier, with typically 50 mV modulation on the bias voltage. While the voltage *V*, is being scanned, we simultaneously vary the tip-sample separation *s* according to $\Delta s = -a |V|$, with $a \approx 1 \text{ \AA/V}$, as shown in Fig. 1(c). This variation in separation amplifies the current and conductance at low voltages, so that it is measurable above the noise level. Typically we use several seconds to acquire such a spectrum, during which time the STM feedback loop is disabled. Unintentional drift of the tip-sample separation during this time must be small, < 0.1 Å. This is routinely achieved in our STM because of the symmetric design, and also with the use of drift compensation [13,14].

The first step in the analysis of the spectral data is to transform it to constant-*s*, accomplished by multiplying the measured current or conductance by $\exp(2\kappa\Delta s)$, where 2κ is the inverse decay constant of the current and conductance. We measure κ during each experiment, and it has values in the range $0.7 - 1.1 \text{ \AA}^{-1}$. For simplicity, a voltage-independent value of κ

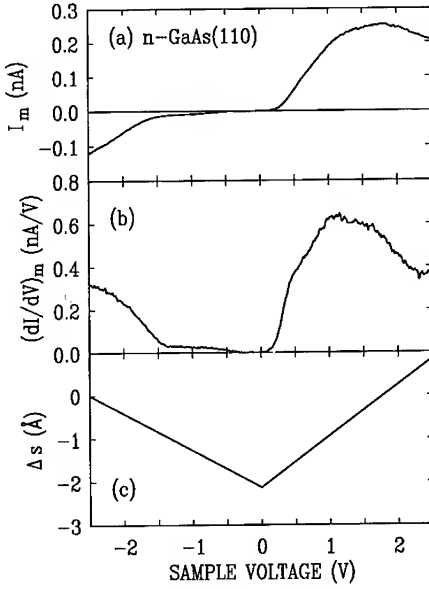


FIG. 1. Measured data for (a) the tunneling current, and (b) the conductance, as a function of sample voltage, obtained from a *n*-type GaAs(110) surface. The applied variation in tip-sample separation is shown in (c), illustrating a V-shaped Δs contour. The zero in tip-height is arbitrary.

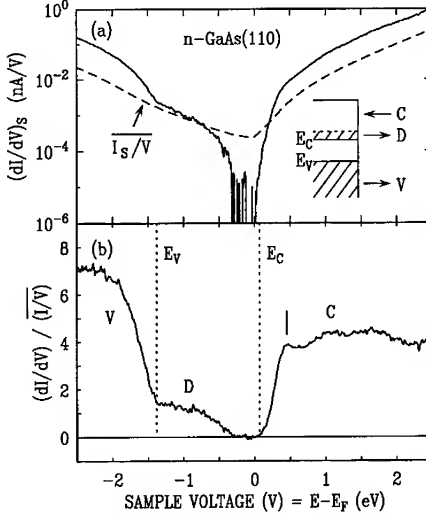


FIG. 2. Analyzed spectral data, obtained from the measured data of Fig. 1. (a) Constant-*s* conductance, obtained by multiplying the measured conductance by $\exp(2\kappa\Delta s)$. A background term I_s/V is shown by the dashed line. (b) Ratio of differential to total conductance, computed as described in the text using either the constant-*s* data of (a), or the measured data of Fig. 1.

is generally used, although more sophisticated methods to exist which allow us to include its complete voltage-dependence [12]. An example of such constant-*s* data is shown in Fig. 2(a). With the 6 orders-of-magnitude dynamic range, we see a clear definition of the band edges, near 0 and -1.4 V. Smaller features are also present in the spectrum, but are difficult to discern because of the logarithmic scale used in Fig. 2(a). Thus, we perform a second step in the analysis, normalizing the constant-*s* data to some quantity which acts as a "background" subtraction on the logarithmic scale, thus suppressing the large variation in conductance arising from both the presence of the semiconductor band gap and the voltage dependence of the tunneling transmission term. This normalization quantity is taken to be I_s/V , which is the total conductance I_s at constant-*s*, broadened over an energy range of width 1.5 V. This quantity is shown by the dashed line in Fig. 2(a). As an explanation of this term, we note that I/V with no broadening has been demonstrated to be a convenient normalization term in many studies involving metal or small-gap semiconductor systems [12]. For the case of large-gap semiconductors, it is necessary to perform the broadening of I/V , since, without it, $(dI/dV)/(I/V)$ diverges at the band edges because the current approaches zero faster than the conductance. The final form for the normalized spectrum is shown in Fig. 2(b). As in Fig. 1(a), the band edges, marked E_V and E_C are very well defined. Various components in the tunneling current are indicated: C-conduction-band, V-valence-band, and D-dopant-induced (arising from electrons tunneling out of conduction band state in this *n*-type material [15]). In addition, small features are visible in the spectrum, *e.g.* the peak located at 0.45 V which arises from a surface state.

It should also be noted that the subscripts m (measured) or s (constant-separation) have been dropped from the y -axis label in Fig. 2(b). This is because, for the particular choice of V-shaped Δs contour used here, the normalization can be performed using *either* the measured data or the constant- s data, and the results obtained are identical due to the form used for the broadening function [12].

3. LOW-TEMPERATURE-GROWN GaAs

The properties of GaAs grown at low temperatures near 200°C has been the subject of numerous recent studies [6]. The as-grown (unannealed) material is known to contain an excess arsenic concentration of about 1 atomic %, leading to a concentration of point defects (mainly arsenic antisite defects) of about $1 \times 10^{20} \text{ cm}^{-3}$. Subsequent annealing causes this excess arsenic to agglomerate and form precipitates. In both the as-grown and the annealed material, the Fermi-level is generally found to be pinned near midgap, leading to relatively high resistivities which are useful for device applications. For as-grown material this pinning is attributed to the arsenic-related point defects, but for annealed material some controversy has arisen as to the relative role of the arsenic precipitates in the pinning compared to that of residual point defects [16,17]. Below, we present STM images and spectra of both the unannealed (LTU) and annealed (LTA) material.

In Fig. 3 we show STM images of a LTU-GaAs layer. These images are acquired with negative sample bias, so that the background atomic corrugation arises from the As-sublattice of the GaAs. Numerous defects are visible in the images, and these defects can be classified into several types as labelled in Fig. 3. The largest apparent defect is type A, and the next largest is type B. Note the presence of two distinct satellite features on the left-hand side of the type B defects, and these satellites can be faintly seen around the type A defects as well. Other smaller types of defects are labelled C and D in Fig. 3, and most unlabeled defects in the images can be seen to fall within one of these four classes. As discussed in detail elsewhere [7], we interpret these various types of images as all arising from the same type of defect, with the core of the defect being located in differing planes relative to the (110) cleavage plane. Specifically, the image types A, B, C, and D are interpreted as arising from arsenic-related defects located 0, 1, 2, or 3 planes (2.0 Å spacing) below the surface. Since the dominant defect in this material is known to involve an arsenic antisite (As on a Ga site, As_{Ga}), and this defect is consistent with both the structure and spectroscopy of our observed defects, we identify the point defects in the STM images as being arsenic antisites. The satellite features seen around the defects are interpreted in terms of tails of the antisite wave-function, probably arising from strain-related variations in surface buckling [7]. Similar effects, though not so long-range, have been seen in recent computations for Si donors at the GaAs(110) surface [18].

Spectroscopic results, obtained from samples of various doping ($p^{++} = 5 \times 10^{19} \text{ cm}^{-3}$, n^+ and $p^+ = 1 \times 10^{19} \text{ cm}^{-3}$), are shown in Fig. 4. These results show typical spectra, averaged over about 10 point defects for each sample. The spectra reveal tunneling out of valence-band states at large negative voltages and into conduction-band states at large positive voltages, with the band edges denoted by E_V and E_C respectively. These bands are separated by the bulk band gap of 1.43 eV. On a region of the LT-layer which is *not* on a point defect, the spectra reveal zero current and conductance within the gap. If the probe-tip is positioned on top of a point defect, then the spectra reveal large peaks within the gap region as seen in Fig. 4. Focussing first on Fig. 4(a), we find a band of states centered near $E_V + 0.5$ eV, and the Fermi-level (0 V) is located above this band. The location of this band is close to that for the donor states of an arsenic antisite defect [19], as shown in the top of Fig. 4 relative to the band edges of spectrum (a). Moving to Figs. 4(b) and (c), we see that as shallow acceptors are introduced into the material the Fermi-level moves into the band of deep defect states. Thus,

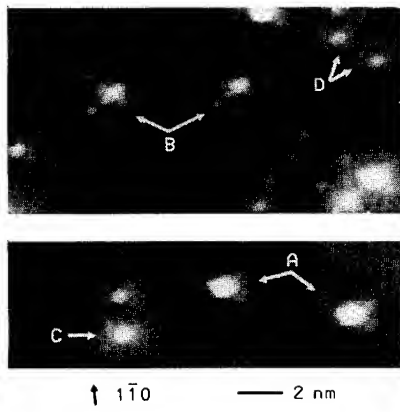


FIG. 3. STM images of the (110) cleaved surface of LT-GaAs, acquired at a sample voltage of -2.0 V. Various point defects can be seen, and they are classified as types A, B, C, and D as indicated. The grey-scale range is 4.3 Å.

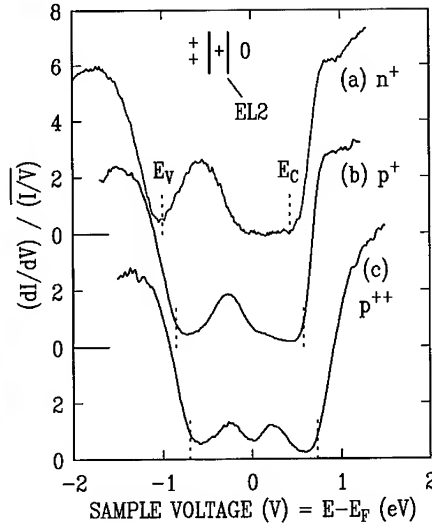


FIG. 4. Tunneling spectra acquired from layers of LT-GaAs containing varying amount of compensating shallow dopants. The valence-band maximum (E_V) and conduction-band minimum (E_C) are indicated by dashed lines in each spectrum. An intense band of states, arising from arsenic-related defects, appears within the band gap. The states of a bulk arsenic antisite defect are shown in the upper part of the figure, relative to the band edges of spectrum (a). The upper (0/+) state is the well-known EL2 level.

these states are donors. For spectrum (c), in which the Fermi-level is roughly in the middle of the deep defect band, a distinct minimum in conductance forms at the Fermi-level, indicating a gap of about 0.4 eV in the state-density. This conductance minimum observed in Fig. 4(c) is interpreted in terms of Coulomb interactions, both onsite and offsite, at the defects [7].

Figure 5 shows STM images obtained from the LTA-GaAs annealed at 600°C , showing topography and conductance in (a) and (b) respectively. As marked in the conductance image, the LTA layer extends over most of the image, with the neighboring p -layers seen at the right and left-hand sides of the image. Two steps occur on the cleavage face in the LTA layer, as marked by the arrows at the top of Fig. 5(a), and these steps lead to some local pinning of the surface Fermi-level as seen by the dark lines occurring at the same spatial location in Fig. 5(b). Small protrusions can be seen in the LTA layer, appearing as white circular areas in Fig. 5(a). These protrusions have typical diameter of about 50 Å and height of 15 Å (the observed diameter is sometimes larger due to tip convolution effects; the 50 Å value is derived from measurements with relatively sharp probe tips). Such protrusions are never seen on n - or p -type material grown at temperatures of 350°C or higher, and thus we identify the protrusions with the arsenic precipitates which are known to occur in this material [6,16]. In addition to the precipitates present in Fig. 5(a), several depressions or "holes" are visible in the image, appearing as the dark circular areas with typical diameter of 50 Å. We association these holes

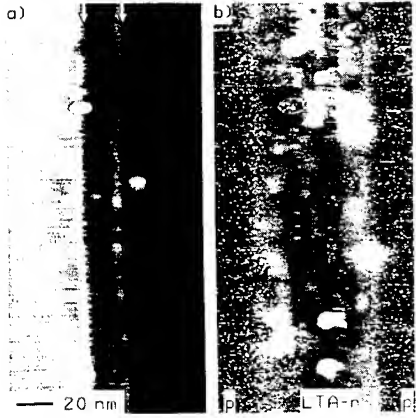


FIG. 5. STM image of a cleaved GaAs structure, showing (a) topography and (b) conductance, acquired at a sample voltage of -2.5 V. The grey-scale range in (a) is 8 Å. As indicated in (b), the structure contains an LTA *n*-type layer, surrounded by *p*-type layers grown at higher temperature. The sample was annealed at 600 °C. Two steps occur in the LTA-layer, as marked by arrows in (a).

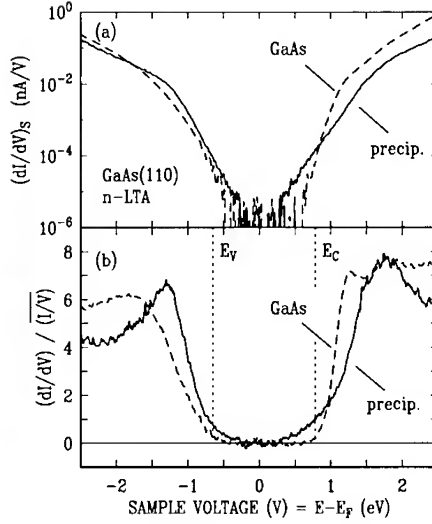


FIG. 6. STM spectra acquired from the LTA *n*-type layer. Spectra are shown acquired on the arsenic precipitates (solid line) and on regions of bare GaAs in between the precipitates (dashed line). The valence and conduction band edges are marked by E_V and E_C respectively.

with regions where an arsenic precipitate has been pulled out of the material during the cleave (in general, one expects the same number of protrusions as depressions in the images). Based on the observed number of protrusions and holes, we estimate a precipitate density of $12 \times 10^{16} \text{ cm}^{-3}$, in reasonable agreement with that found in transmission-electron microscopy (TEM) studies [16].

Figure 6 shows spectroscopy results obtained from the LTA-layer. Spectra were acquired on the precipitates themselves, and on regions of the bare GaAs in between the precipitates. The results shown are the average of about 10 such spectra at each type of location. On the bare GaAs, we see a band gap extending from about -0.65 to $+0.8$ eV, indicating a pinned Fermi-level at $E_F = E_V + 0.65$ eV. No states are visible in the gap for the GaAs spectra. On the precipitates, we observe a band gap at about the same location, but now tails of states are observed extending into the gap. These gap states are most pronounced on the conduction band side of the spectrum, but can also be seen on the valence band side. Since these gap states are only observed on the precipitates, and are the only source of gap states anywhere within the LTA-layer, we identify the precipitates as being responsible for the Fermi-level pinning observed throughout this *n*-type LTA-layer.

4. InAs/GaSb SUPERLATTICES

In Fig. 7 we display an STM image obtained from the InAs/GaSb superlattice. For filled state images such as this, the GaSb layers are bright and InAs layers dark (as established by spectroscopy, below, or by imaging the adjoining GaSb substrate). Faint fringes, with spacing

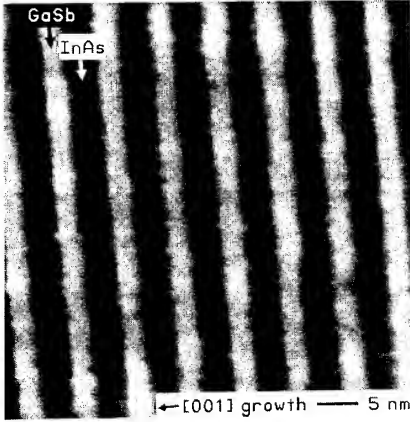


FIG. 7. Constant-current STM image of InAs/GaSb superlattice, consisting of 42 Å thick InAs and 24 Å thick GaSb layers. Image was acquired at a sample voltage of -1.3 V. The $[001]$ growth direction is indicated. Grey-scale range is 2.1 Å.

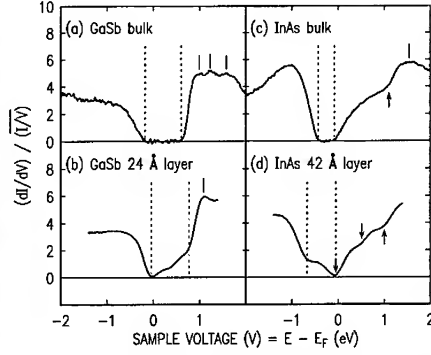


FIG. 8. Typical tunneling spectra, acquired from (a) bulk GaSb, (b) bulk InAs, (c) GaSb superlattice layer, and (d) InAs superlattice layer. Apparent band gaps are indicated by dashed lines, surface states by tic marks, and L-valley conduction band onsets by upward pointing arrows. Downward pointing arrows indicate subband onset energies in panel (d).

of 6.1 Å (2 bilayers) arise from the atomic planes in the superlattice (most clearly seen in the GaSb layers in Fig. 7). The interfaces between InAs and GaSb layers are seen not to be smooth, but rather, interface roughness is visible with step heights of 3–6 Å. This interface roughness can be seen more clearly by enhancing the grey-scale in the images, and from that a quantitative spectrum of interface roughness has been determined [10]. We find that the roughness contains two components, a low frequency component (length scale ~ 50 Å) which determines the carrier mobility in the material, and a higher frequency component (~ 5 Å) which appears to be related to the "microroughness" discussed in prior work [20].

Spectroscopic results are shown in Fig. 8, where we compare typical spectra acquired near the center of the superlattice layers compared with those obtained from bulk InAs and GaSb. Spectral features are indicated in Fig. 8, where the energetic positions are determined using peak locations for surface states, and assuming linear onsets for the bulk bands, with a precision of ± 0.03 eV. Possible systematic errors due to tip-induced band bending could result in positions which are too large by 0.1–0.2 eV [21]. For bulk GaSb, Fig. 8(a), we find a band gap of 0.78 eV (compared with known value of 0.72 eV) and surface state locations in good agreement with inverse photoemission results [22]. For bulk InAs, we find a band gap of 0.35 eV and L-valley onset located 1.18 eV above the Γ -valley minimum (compared with known values of 0.36 and 1.08 eV respectively). Turning now to the superlattice spectra, Fig. 8(c) and (d), we see some new features. First, significant conductance is observed within the apparent band gap regions. Based on the intensity and spatial dependence of this feature, we interpret it as arising from electron (hole) states tailing out from neighboring InAs (GaSb) layers. Second, we find that the apparent band gaps are slightly larger for the superlattice compared with the bulk, with observed gaps of 0.82 and 0.62 eV for the GaSb and InAs layers respectively. We attribute the significantly larger gap for InAs to confinement effects in the quantum well (this effect is smaller for GaSb due to the much larger heavy hole mass); subtracting the known InAs gap yields an energy for the first electron subband of 0.26 eV. The third feature seen in the superlattice spectra is an additional onset at 0.51 V, which we attribute to the second electron

subband. Relative to the observed InAs valence-band edge, it is located at 1.18 eV, and subtracting the InAs bulk gap yields an energy of 0.82 eV. These subband energies (0.26 and 0.82 eV) are in reasonable agreement with theoretical estimates based on an 8-band tight binding model [10,23] of 0.19 and 0.73 eV, thus confirming the above identification.

A detailed spectroscopic study of the interfaces between InAs and GaSb has been performed [10]. In voltage-dependent imaging, it is found that the two types of interfaces (InAs grown on GaSb vs. GaSb grown on InAs) have different properties, with the former having a significantly larger empty-state density. In addition, spectra acquired at the interfaces reveal that certain spectral features for the InAs on GaSb interfaces are smeared out, thus implying the existence of some grading or intermixing at these interfaces. Based on the growth conditions used in the superlattices, it is argued that this intermixing involves Sb incorporation into the InAs overlayer. Further studies on material grown under different conditions are in progress, in an effort to confirm this conclusion.

5. SUMMARY

In this paper, we have described the technique of cross-sectional STM, and given several illustrative examples of III-V semiconductor systems which have been studied by this method. The results obtained provide unique information concerning both geometric structure of defects and interfaces, and their associated electronic spectroscopy. For the case of the unannealed LT-GaAs, considerable discussion existed in the literature over the identity of the point defects: were they simply isolated antisites, or were additional defects involved [24,25]. The structure and spectroscopy seen in our STM studies is consistent with the isolated antisite, thus providing evidence for that interpretation. For the annealed LT-GaAs, a controversy existed over the relative role of antisites compared with precipitates in determining the electrical properties (*i.e.* Fermi-level position) in the material [16,17]. In our work we find, for *n*-type material, that only precipitates are present, and thus they determine the Fermi-level position. In other studies of *p*-type material, we find the coexistence of antisites and precipitates, and they both make contributions to the electrical properties of the material [26]. For the InAs/GaSb studied here, the STM studies allowed, for the first time in any system, a quantitative determination of interface roughness. Furthermore, spectroscopic differences were seen between the properties of InAs grown on GaSb compared with GaSb on InAs, thus indicating some different chemistry at these interfaces.

ACKNOWLEDGEMENTS

One of us (A.V.) gratefully acknowledges financial support from the Swiss National Fond. The InAs/GaSb portion of this work was supported in part by Advanced Research Projects Agency under contract N00014-93-1-0881 and Air Force Office of Scientific Research under contract F49620-93-1-0258.

REFERENCES

1. H. W. M. Salemink, O. Albrektsen, and P. Koenraad, Phys. Rev. B45, 6946 (1992).
2. E. T. Yu, M. B. Johnson, and J.-M. Halbout, Appl. Phys. Lett. 61, 201 (1992).
3. A. Vaterlaus, R. M. Feenstra, P. D. Kirchner, J. M. Woodall, and G. D. Pettit, J. Vac. Sci. Technol. B 11, 1502 (1993).
4. S. Gwo, K.-J. Chao, C. K. Shih, K. Sadra, and B. G. Streetman, Phys. Rev. Lett. 71, 1883 (1993).
5. Burleigh Instruments, Fishers, New York.

6. See, *e.g.*, M. Kaminska and E. R. Weber, *Mat. Sci. Forum* **83-87**, 1033 (1992) and references therein.
7. R. M. Feenstra, J. M. Woodall, and G. D. Pettit, *Phys. Rev. Lett.* **71**, 1176 (1993).
8. R. M. Feenstra, A. Vaterlaus, J. M. Woodall, and G. D. Pettit, *Appl. Phys. Lett.* **63**, 2528 (1993).
9. See, *e.g.*, R. H. Miles, J. N. Schulman, D. H. Chow, and T. C. McGill, *Semicond. Sci. Technol.* **8**, S102, (1993), and references therein.
10. R. M. Feenstra, D. A. Collins, D. Z.-Y. Ting, M. W. Wang, and T. C. McGill, submitted to *Phys. Rev. Lett.*
11. P. Mårtensson and R. M. Feenstra, *Phys. Rev. B* **39**, 7744 (1988).
12. *Methods of Experimental Physics*, Vol. 27, *Scanning Tunneling Microscopy*, eds. J. A. Stroscio and W. J. Kaiser (Academic Press, Boston, 1993), chapter 4.
13. R. M. Feenstra, in *21st International Conference on the Physics of Semiconductors*, eds. Ping Jiang and Hou-Zhi Zheng (World Scientific, Singapore, 1992), p. 357.
14. R. M. Feenstra and M. A. Lutz, *J. Vac. Sci. Technol. B* **9**, 716 (1991).
15. R. M. Feenstra and J. A. Stroscio, *J. Vac. Sci. Technol. B* **5**, 923 (1987).
16. A. C. Warren, J. M. Woodall, P. D. Kirchner, X. Yin, F. Pollack, M. R. Melloch, N. Otsuka, and K. Mahalingam, *Phys. Rev. B* **46**, 4617 (1992).
17. D. C. Look, *J. Appl. Phys.* **70**, 3148 (1991).
18. J. Wang, T. A. Arias, J. D. Joannopoulos, G. W. Turner, and O. L. Alerhand, *Phys. Rev. B* **47**, 10326 (1993).
19. E. R. Weber, H. Ennen, U. Kaufman, J. Windscheif, J. Schneider, and T. Wosinski, *J. Appl. Phys.* **53**, 6140 (1982).
20. D. S. Katzer, D. Gammon, and B. V. Shanabrook, *J. Vac. Sci. Technol. B* **10**, 800 (1992).
21. As shown in Ref. 15, tip-induced band bending effects are greatly reduced due to tunneling through the space charge region of the semiconductor. For bulk spectral features (band and subband onsets), corrections to the observed energies are thus less than 0.1–0.2 eV for doping levels near 10^{18} cm^{-3} . Corrections to surface state related features can, in certain cases, be larger.
22. H. Cartensen, R. Manzke, I. Schäfer, and M. Skibowski, in *Proc. 18th Int. Conf. on the Physics of Semiconductors*, ed. O. Engström (World Scientific, Singapore, 1987), p. 125.
23. D. Z.-Y. Ting, E. T. Yu, and T. C. McGill, *Phys. Rev. B* **45**, 3583 (1992).
24. B. K. Meyer, D. M. Hofmann, J. R. Niklas, and J.-M. Spaeth, *Phys. Rev. B* **36**, 1332 (1987).
25. M. K. Nissen, A. Villemaire, and M. L. W. Thewalt, *Phys. Rev. Lett.* **67**, 112 (1991).
26. R. M. Feenstra, M. A. Lutz, A. Vaterlaus, J. M. Woodall, and M. R. Melloch, to be published.

CHALLENGES AND OPPORTUNITIES IN MAGNETIC RESONANCE FORCE MICROSCOPY

JOHN A. SIDLES* and JOSEPH L. GARBINI**

* Department of Orthopaedics RK-10, School of Medicine
University of Washington, Seattle WA 98195 (sidles@u.washington.edu)
** Department of Mechanical Engineering FM-15,
University of Washington, Seattle WA 98195 (garbini@u.washington.edu)

ABSTRACT

Recently the first experiments in magnetic resonance force microscopy (MRFM) have been conducted. In these experiments a force microscope cantilever is used to detect the magnetic force exerted by electrons and nuclei in a sample. The magnetization of the sample is modulated at the resonant frequency of the cantilever, using standard magnetic resonance techniques. The resulting excitation of the cantilever is detected optically. This article reviews the present status of MRFM technology, emphasizing the physical principles involved and the opportunities for further research and development. Particular emphasis is placed on single spin detection by MRFM and potential applications in biomolecular imaging.

INTRODUCTION

Recent experiments by Dan Rugar, Nino Yannoni, and colleagues at IBM Almaden Research Laboratories [1-3] have demonstrated the detection and imaging of magnetic resonance signals using the new method of magnetic resonance force microscopy (MRFM). In these experiments, a microscale force microscope cantilever is used to detect the magnetic force exerted by electrons and nuclei in the sample. The magnetization of the sample is modulated at the resonant frequency of the cantilever, using standard magnetic resonance techniques. The excitation of the cantilever is detected by optical means.

Recent theoretical calculations [4-7] suggest that MRFM might be developed into a nearly ideal technique for studying biomolecular structure. Like medical magnetic resonance imaging, MRFM is inherently three-dimensional and nondestructive. Like x-ray crystallography, MRFM in principle can achieve subangstrom resolution. And like atomic force microscopy and scanning tunneling microscopy, MRFM in principle is able to image individual biological molecules *in situ* [6].

However, it should be clearly understood that MRFM technology is still in its infancy, and that the ultimate limits of MRFM sensitivity are not known at present. Existing instruments have not yet achieved the sensitivity needed for molecular imaging. A key issue is whether MRFM noise levels can be made small enough to allow the detection of individual electrons and nucleons.

This article reviews the present status of MRFM research, with particular attention to:

- (1) the limits of present methods for determining molecular structure,
- (2) the basic physical principles involved in MRFM,
- (3) MRFM experiments that have been conducted to date, and
- (4) opportunities for further research and development in MRFM.

PRESENT METHODS FOR DETERMINING BIOMOLECULAR STRUCTURE

Early theoretical work in MRFM [4-6] was motivated by the need of the biomedical research community for better information about the three-dimensional structure of biological molecules. This structural information is of substantial scientific and medical interest, for example in the rational design of drugs and vaccines. The following paragraphs review existing techniques for determining biomolecular structure.

Known and Unknown Biomolecular Structures

The Brookhaven Protein Data Bank [8,9] serves as an international repository of known structures of biological molecules. As of October 1993, there were 1,777 entries in the Data Bank, comprising 519 differently named molecules [10]. New entries are continually being added to the Data Bank by a large and vigorous community of structural molecular biologists.

Compared to the diversity of molecules produced by living organisms, the present-day Data Bank contains relatively few entries. Only a few hundred human proteins appear in the Data Bank, yet the human genome codes for approximately 100,000 proteins. Thus a truly comprehensive data bank would encompass many millions of structures, not hundreds. It would include structures for all the proteins coded in the human genome, and also would include structures for many viral, bacterial, plant, and animal proteins, as well as nonprotein molecules.

Clinical Significance

Some of the gaps in the present-day Data Bank have immediate clinical significance. For example, the entire gene sequence of the HIV-1 virus is known, and by extension the sequence of all the proteins that it encodes. Yet as of the present writing [10] the Data Bank contains structures for only four HIV-1 proteins, namely, the entries entitled (1) "HIV-1 gp120 (16-residue peptide)," (2) "HIV-1 p7 nucleocapsid protein," (3) "HIV-1 protease," and (4) "HIV-1 reverse transcriptase ribonuclease h domain."

The structure of the remaining HIV-1 proteins has not been determined as yet. Recent research on the rational design of HIV-protease inhibitors [11] has demonstrated that structural information for the remaining HIV-1 proteins would be useful in developing effective treatments for HIV infection.

Many additional examples could be given of proteins that are biologically and medically important, and whose sequence is known, but whose structure has not been determined. For example, the tumor suppressor gene p53 encodes a DNA-binding protein that is thought to play a fundamental role in regulating human cell growth and differentiation. From a medical point of view, p53 is interesting because approximately half of all human cancer patients carry a p53 mutation [12]. p53 was the subject of approximately 1000 new scientific articles in 1993, and the number is likely to increase in coming years [13].

Despite this intense scientific and medical interest, there is at present no structural entry for p53 in the Brookhaven Protein Data Bank [10]. In the absence of detailed structural information, the functional significance of specific p53 mutations is difficult to assess, except by studying the epidemiology of patients carrying various mutations.

Existing Methods for Determining Structure

The main reason for our limited structural knowledge is that existing methods for determining molecular structure are not applicable in all cases of interest. For example, microscopic imaging of atomic-scale biological structure is possible using scanning tunneling microscopy (STM) and atomic force microscopy (AFM). However, these techniques respond mainly to the topmost layer of atoms, and thus cannot readily determine the three-dimensional structure of binding sites in biological molecules. Yet it is precisely the structure of binding sites which is of greatest interest in the rational design of drugs and vaccines.

More detailed information, including the three-dimensional structure of binding sites, can be obtained by x-ray crystallography and by multidimensional NMR. However, these techniques require careful preparation of purified solutions and crystals containing the molecule of interest. For many biological molecules the required purification is not readily achieved, or else the molecules crystallize in a disordered manner. In such cases the three-dimensional structure cannot be readily determined by any present technology.

STRUCTURAL IMAGING BY MAGNETIC RESONANCE FORCE MICROSCOPY

An ideal technology for determining biomolecular structure would be:

- nondestructive,
- three dimensional,
- have subangstrom spatial resolution, and
- image individual molecules *in situ*.

A technology with these combined characteristics could aptly be called "molecular microscopy," because it would have the same practical utility as optical microscopy.

The goal of our research program at the University of Washington has been to determine whether molecular microscopy is achievable by MRFM, both in theoretical principle and in experimental practice.

As discussed in this article, there are several engineering strategies by which the sensitivity of existing MRFM experiments can be substantially increased, and there is reasonable grounds for optimism that single-spin detection can be achieved.

One of the main challenges in MRFM research is to assimilate the existing noise-related literature, and apply it to the practical design, fabrication, and operation of MRFM devices. More than a dozen noise-related mechanisms are relevant to MRFM. These encompass many standard topics in materials science and engineering, such as techniques for fabricating microscale structures, optimal design of low-noise oscillators, dislocation mobility in crystal lattices, nonlinear phonon interactions, the effects of atoms adsorbed on cryogenic surfaces, thermoelastic damping, vacuum engineering, mechanical and electrical properties of amorphous materials, and optical interferometry.

The present research strategy in MRFM emphasizes doable and scalable experiments. Here "doable" means that a working experiment can be built on a benchtop using off-the-shelf equipment. "Scalable" means that making the apparatus smaller makes the experiment work better. This reflects our pragmatic judgment that a practical molecular imaging technology is most likely to be achieved by making cumulative improvements in working devices.

EXPERIMENTS IN MAGNETIC RESONANCE FORCE MICROSCOPY

To date, all MRFM experiments have operated in a similar manner, as shown at right [1-3].

A sample in which magnetic resonance is to be observed is fixed to a force microscope cantilever. A permanent magnet is brought nearby. The gradient of the magnetic field then exerts a force on the cantilever. This magnetic force derives either from paramagnetic centers in the sample, or alternatively from magnetic moments of nuclei. A nearby radio-frequency coil modulates the sample magnetization at the resonant frequency of the cantilever, by any of the large number of techniques that have been described in the magnetic resonance literature [14,15]. The resulting excitation of the cantilever is sensed by optical means.

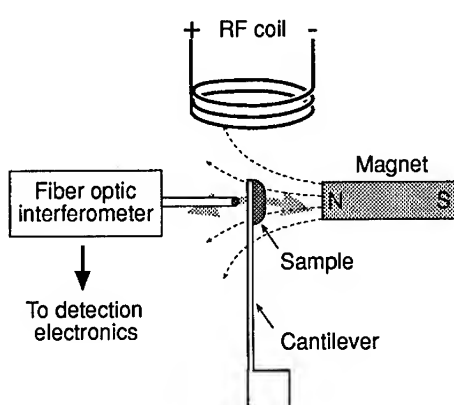


Fig. 1 A representative MRFM experiment.

The first MRFM experiment was performed by Dan Rugar, Nino Yannoni, and collaborators at IBM Almaden Research Laboratories [1]. This experiment involved the detection of paramagnetic resonance by cyclic saturation of DPPH. The sample size was 30 ng and the detected force was 10^{-14} N. The magnetic resonance theory was provided by a 1955 article by Garstens and Kaplan [47]. As shown in Fig. 2, there was reasonably good agreement between theory and MRFM experimental data.

Soon after the first detection of magnetic resonance by MRFM, Zuger and Rugar [2] demonstrated the first image reconstructions. The same basic experimental apparatus was employed, and the magnetic tip was raster-scanned over a paramagnetic sample of DPPH. The image was reconstructed using standard Fourier transform techniques. The image resolution was 5 microns laterally and 1 micron axially.

PRACTICAL ASPECTS OF IMAGING BY MRFM

Usually in force and tunneling microscopy, the tip-sample interaction increases rapidly in strength as the tip moves closer to the sample. But in MRFM experiments the strongest interaction involves spins located at a determinate distance from the tip, such that their spin precession frequency is resonant with the applied RF field (see Fig. 3). Similar slice selectivity is an essential element of medical magnetic resonance imaging, which MRFM resembles in many respects.

For imaging applications, the aspects of MRFM that distinguish it from conventional scanning force and tunneling microscopy are:

1. The imaging process is noncontact and nondestructive.
2. The imaging field is three-dimensional, and reaches below the scanned surface. This is desirable when imaging subsurface structures.
3. The theory of magnetic resonance interactions provides a reliable basis for designing experiments and deconvolving images from raw data.

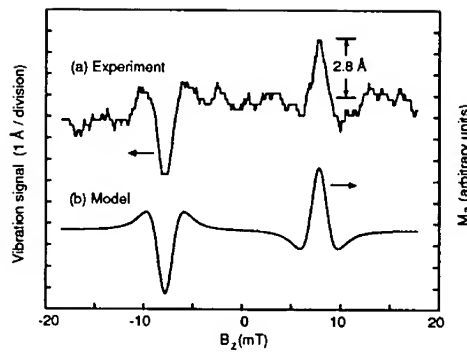


Fig. 2 Experimental data vs. theoretical predictions (from ref. [1]).

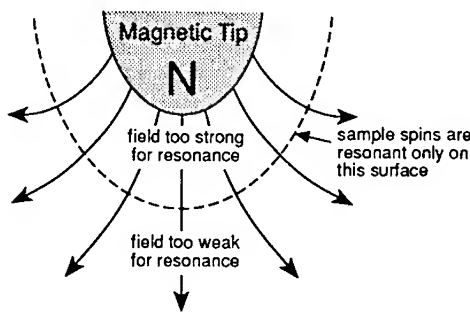


Fig. 3 Spatial extent of tip-sample interaction in MRFM.

SIGNAL-TO-NOISE CONSIDERATIONS IN MRFM

There is a price to be paid for the practical advantages of MRFM imaging. Namely, MRFM signal levels are relatively weak, just as they are in conventional magnetic resonance imaging.

Comparison with Inductive Detection Methods

Sidles and Rugar [7] have compared MRFM sensitivity with that of conventional inductive coil-based magnetic resonance detection.

A key idea is that MRFM and coil-based detection both involve the magnetic coupling of a sample to an oscillator. In MRFM the oscillator is a mechanical cantilever, which is coupled to the sample by a magnetic force. In coil-based detection the oscillator is a tuned LC pickup coil, which is coupled to the sample by a magnetic flux.

Physically speaking, an inductive coil creates and then annihilates its magnetic field twice during each cycle, and this entails an energy cost that is in proportion

to the volume of the coil. A mechanical oscillator avoids this energy cost by a trick; the field source is moved to another location instead of being annihilated. This exchanges one energy cost for another; the field source still must be vibrated back and forth, which entails the expenditure and storage of kinetic energy. However, as the cantilever is made smaller, it gets easier to move, such that sufficiently small cantilevers can have quite good detection capabilities.

The motional mass of Rugar et al.'s cantilever is only ~40 ng, and its velocity is of order ~2 cm/hr (corresponding to a vibration amplitude of one angstrom at 8 KHz). Thus very little energy is required to excite a microscale cantilever. This is the physical reason why even the first MRFM experiment achieved a magnetic moment sensitivity comparable to the sensitivity of the best available room temperature inductive coils [7].

Ref. [7] works through these ideas quantitatively. It is shown that three parameters suffice to characterize both types of oscillator. Two of the parameters are familiar ones: the resonant frequency ω_0 and the quality factor Q . The third parameter is a "magnetic spring constant" k_{mag} , which is defined as follows. When excited, both mechanical and electrical oscillators create an oscillating magnetic field $B(t)$ at the sample. In a Hamiltonian formalism this energy appears as a potential energy term:

$$(\text{potential energy}) = \frac{1}{2} k_{\text{mag}} B^2. \quad (1)$$

This implicitly defines the magnetic spring constant k_{mag} , which has SI units of Joules/Tesla². Physically, small values of k_{mag} mean that an oscillator requires little energy to generate an oscillating magnetic field.

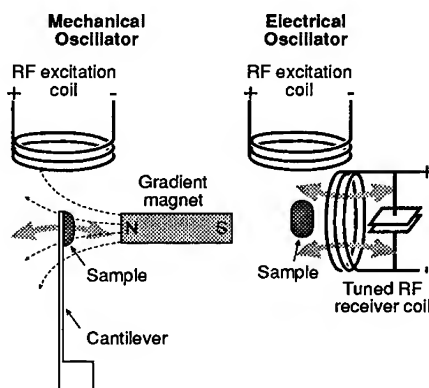


Fig. 4 Mechanical vs. electrical detection of magnetic resonance.

The thermal noise in the oscillator is dynamically equivalent [7] to a fluctuating magnetic moment with spectral density S_m :

$$S_m = \frac{k_{mag}}{Q\omega_0} 4 k_B T . \quad (2)$$

Here T is the temperature, k_B is Boltzman's constant, and ω_0 is expressed in radians/sec (not Hz). We will adopt an engineering bandwidth convention such that the mean square magnetic moment noise $\langle m^2 \rangle$ in a bandwidth b (in Hz) is $\langle m^2 \rangle = S_m b$.

For a receiver coil, the magnetic spring constant is determined solely by the volume V_{coil} inside the coil, and (to a reasonable approximation) is independent of the number of coil windings and the coil aspect ratio:

$$k_{mag} = \frac{2}{\mu_0} V_{coil} \text{ (SI units)} = \frac{1}{2\pi} V_{coil} \text{ (gaussian units)} . \quad (3)$$

For a mechanical cantilever, the magnetic spring constant k_{mag} is related to the mechanical spring constant k_{mech} by

$$k_{mag} = k_{mech}/g^2 \quad (4)$$

Here g is the local magnetic field gradient generated by the MRFM device.

Force Sensitivity

Another useful noise-related quantity is the force sensitivity of a cantilever. The thermal noise in the cantilever appears as Brownian motion equivalent to that generated by a Langevin force $F(t)$ with spectral density S_F :

$$S_F = g^2 S_m = \frac{k_{mech}}{Q\omega_0} 4 k_B T . \quad (5)$$

Here ω_0 is expressed in radians/sec. The bandwidth convention is that the minimum detectable force F_{min} in a bandwidth b (in Hz), with unit signal-to-noise ratio, is $F_{min} = [S_F b]^{1/2}$.

We can write F_{min} in three equivalent ways:

$$F_{min} = \left[\frac{k_{mech}}{Q\omega_0} 4 k_B T b \right]^{1/2} = \left[m_{eff} \frac{\omega_0}{Q} 4 k_B T b \right]^{1/2} = \left[\frac{m_{eff}}{\tau} 4 k_B T b \right]^{1/2} . \quad (6)$$

Here m_{eff} is the motional mass, $k_{mech} = m_{eff} \omega_0^2$, and $\tau = Q/\omega_0$ is the damping time.

Of these expressions, the rightmost offers the simplest design insights, because it contains only two oscillator parameters, while the other expressions have three. It states that for oscillator damping time τ held constant, the mass of the oscillator should be minimized, while the spring constant and the frequency of the oscillator are immaterial. In this respect neither high-frequency nor low-frequency mechanical oscillators offer an intrinsic advantage in force sensitivity.

Cantilever Design Considerations

The figure at right shows a cantilever of length l , width w , and thickness t . For a cantilever material of density ρ and Young's modulus E , the motional mass $m_{eff} = \rho l w t/4$, and the resonant frequency ω_0 is given by [6,16,17]

$$\omega_0 = 3.516 \frac{t}{l^2} \left[\frac{E}{12 \rho} \right]^{1/2} . \quad (7)$$

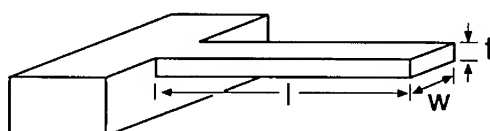


Fig. 5 Cantilever dimensions

The dimensionless factor 3.516 is a modal eigenvalue. The spring constant k_{mech} , as measured at the cantilever tip, is:

$$k_{\text{mech}} = m_{\text{eff}} \omega_0^2 = 1.03 \cdot \frac{1}{4} \frac{E}{\rho} \frac{w t^3}{l^3}. \quad (8)$$

The factor 1.03 has been extracted to indicate that the fundamental mode of the cantilever is about 3% stiffer than a statically bent cantilever. In practical calculations it is usually reasonable to omit this factor.

These results are readily generalized to higher order cantilever modes. The eigenfrequencies of the first four flexural modes are:

$$\omega_0 = \left[\frac{3.516}{22.03} \frac{t}{l^2} \left[\frac{E}{12 \rho} \right] \right]^{1/2} \quad (9)$$

The motional mass is the same for all modes, namely $m_{\text{eff}} = \rho l w t / 4$, and the effective spring constant is $k_{\text{mech}} = m_{\text{eff}} \omega_0^2$. The second mode is 6.3 times higher in frequency than the fundamental mode, so the spring constant k_{mech} is effectively $6.3^2 \approx 40$ times greater.

If all modes have the same damping time τ , then all modes will exhibit the same force sensitivity, regardless of their differing frequency, as per eq. 6. But more typically the higher modes have shorter damping times than the fundamental mode, so their magnetic moment sensitivity is reduced. For this reason the fundamental mode has been used in all MRFM experiments to date.

This completes our review of the basic results needed to predict signal-to-noise ratios in cantilever-based MRFM devices.

OPPORTUNITIES IN MRFM TECHNOLOGY

How Can MRFM Sensitivity Be Improved?

The results already reviewed in this article imply that the minimum detectable magnetic moment m_{min} in a bandwidth b is

$$m_{\text{min}} = \frac{1}{9} \left[\frac{m_{\text{eff}}}{\tau} 4k_B T b \right]^{1/2} \quad (\text{in SI units of A-m}^2). \quad (10)$$

From this expression it is clear that MRFM sensitivity can be systematically improved by fabricating cantilevers with (1) longer damping times and (2) smaller motional mass, then equipping the cantilevers with (3) stronger gradients and operating them at (4) lower temperatures.

Research Issues in Cantilever Relaxation Mechanisms

Achieving a reliable and practically useful understanding of cantilever damping mechanisms is an important issue in MRFM design and fabrication research. There is an abundance of literature on the general subject of acoustic and mechanical relaxation mechanisms. Mason's multivolume series *Physical Acoustics* [18-22] lists many hundreds of references. Blair's *Gravity Wave Detection* [23,24] similarly reviews a large body of theoretical and experimental literature relevant to the operation of macroscale resonant bar detectors.

Among the known loss mechanisms that deserve attention are (1) mechanical losses associated with the gas damping, (2) losses due to the mounting of the cantilever, (3) Rayleigh waves propagating into the substrate from the base of the cantilever, (4) photon shot noise associated with the interferometer, (5) three-phonon and four-phonon anelastic scattering,

(6) thermoelastic damping, (7) metallic coating damping, (8) dislocation damping, (9) surface contaminant damping, and (10) heating of the cantilever due to optical absorption.

With specific reference to relaxation mechanisms in micromechanical oscillators, Roszhart [25] has published an analysis of thermoelastic friction in single crystal silicon resonators, referencing Zener's pioneering work in the field [26-28]. Pitcher et al. [29], Langdon and Dowe [30], and Zhange et al. [31] have investigated optothermal interactions between laser light and silicon cantilevers. Buser and Rooij [32] have fabricated very high-Q resonators in monocrystalline silicon, achieving Q of $6 \cdot 10^5$ at room temperature, but in a millimeter-scale oscillator which is too massive for MRFM use. Zook et al. [33] review the mechanical characteristics of polysilicon resonant microbeams.

As yet, no authors have investigated damping mechanisms in oscillators that are optimized for MRFM applications, that is to say, oscillators designed to have the lowest possible mass and the longest possible damping time, and operated at the lowest possible temperature. Partly for this reason, the quality Q of MRFM cantilevers is determined empirically at present, rather than being a well-controlled design parameter.

It is not known whether cantilevers are the optimal design choice for MRFM oscillators. Conceivably torsional mechanical oscillators or shear mode oscillators could offer superior performance. To date, relatively little work has been done in considering alternative micromechanical designs for MRFM applications.

Recent IBM Work in Cantilever Design and Fabrication

Hoen and other members of the IBM group have recently published a description of cantilevers whose design has been optimized for MRFM work [16]. An important insight of the IBM group is that the easiest cantilever dimension to make small is the thickness of the cantilever, because this dimension is under evaporative control (as opposed to lithographic control) for the amorphous silicon nitride cantilevers described in their article.

The smallest cantilever described is 55 μm long, 5 μm long, and only 200 \AA thick. Assuming a density of 3 gm/cm^3 , a modulus of 140 GPa, and a quality factor of 3000, this cantilever would achieve a room-temperature force sensitivity of $3.2 \cdot 10^{-17} \text{ N}/\sqrt{\text{Hz}}$.

Recent IBM Experimental Demonstration of Nuclear Spin MRFM

Using 900 \AA thick cantilevers having a force sensitivity of $4.3 \cdot 10^{-16} \text{ N}/\sqrt{\text{Hz}}$, the IBM group has experimentally demonstrated the detection of nuclear magnetism at room temperature, in a sample size of a few nanograms. The magnetic resonance modulation technique used in this experiment was cyclic adiabatic inversion of the proton spins in the sample. A description of this experiment is in press [3], and therefore it is not reviewed here.

What Experiments Can Be Done?

Any experiment in the magnetic resonance literature in principle can be repeated as an MRFM experiment. There are many thousands of such experiments. The question then arises, which experiments are predicted to have a reasonable signal-to-noise ratio?

Sidles et al. [6] have considered in some detail the prospects for directly imaging individual nuclei in biological molecules by MRFM. For reasons set forth at the beginning of this article, there is a biomedical need for such an imaging capability.

We therefore are motivated to define a sequence of successively more sensitive MRFM experiments that lead toward a true molecular imaging capability.

We will consider three magnetic phenomena that exhibit resonance; in order of decreasing strength these are ferromagnetism, paramagnetism, and nuclear magnetism. We then consider three means of cyclically modulating the magnetization at the resonant frequency of a mechanical oscillator; these are cyclic saturation, cyclic adiabatic inversion, and precession resonance.

The focus of this article is on the sequence of entries (1)-(4) below, and particularly the detection of individual electron and nuclear spins. However, it is important to appreciate that MRFM potentially has important applications in the study of ferromagnetism and superconductivity, outside of the highlighted boxes below.

	Ferromagnetism	Paramagnetism	Nuclear Magnetism
Cyclic Saturation	definitely feasible; requires GHz RF.	1 successfully demonstrated at IBM Almaden [1,2].	T1 is inconveniently long.
Cyclic Inversion	potentially feasible at cryogenic temps; requires coherent manipulation of single domain magnetization.	3 feasible at low temperatures; easiest route to single spin detection; not yet demonstrated.	2 successfully demonstrated at IBM Almaden [3].
Spin Precession	potentially feasible; FMR frequencies tend to be inconveniently high.	potentially feasible; ESR frequencies tend to be inconveniently high.	4 feasible but challenging; important for biomedical applications; not yet demonstrated.

Table 1. Experiments in MRFM organized by type of magnetization and method of modulation.

PROSPECTS FOR SINGLE SPIN IMAGING

In this section, we will consider whether MRFM might in principle be used to detect individual spins. In the process, we will develop an understanding of how MRFM devices bypass some of the limitations of SQUIDs and other inductive devices for detecting magnetic resonance.

Analysis of SQUID-based Detection of Single Electron Magnetic Resonance

Fig. 6 shows a single paramagnetic center (i.e., an unpaired electron spin) which is located 50 Å deep below a sample surface.

For purposes of discussion, we will assume that a thin film de SQUID [34,35] has been placed on the sample surface, directly above the electron. For a pickup loop of radius r_{loop} imaging a vertically oriented magnetic moment m^e located at a depth h_{depth} , the captured magnetic flux Φ is readily shown to be

$$\Phi = \frac{\mu_0 m^e}{2\pi} \frac{\pi r_{\text{loop}}^2}{(r_{\text{loop}}^2 + h_{\text{depth}}^2)^{3/2}}. \quad (11)$$

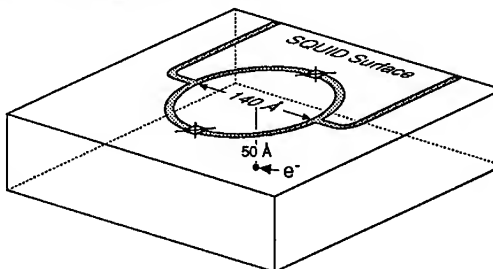


Fig. 6 Single electron located 50 Å deep below a dc SQUID loop.

The electron magnetic moment m^e satisfies $m^e = \hbar\gamma^e/2$, where \hbar is Planck's constant and γ^e is the gyromagnetic ratio of the electron, $\gamma^e = 2.8 \text{ MHz/Gauss}$. The radius of the loop can be optimized to capture the maximum possible flux. According to eq. 11 the optimal radius is $r_{\text{loop}} = \sqrt{2}h_{\text{depth}}$. We therefore specify a pickup loop of radius 70 Å.

For this optimally sized SQUID, the captured flux Φ is $2.2 \cdot 10^{-7} \Phi_0$, where Φ_0 is the flux quantum $\Phi_0 = \pi \hbar/q^e = 2.067 \cdot 10^{-15} \text{ T-m}^2$. Here q^e is the electron charge. As far as SQUID-based detection of single spins is concerned, this result is sobering. The best available macroscopic SQUIDs achieve a flux sensitivity of approximately $10^{-7} \Phi_0/\sqrt{\text{Hz}}$. It would be an impressive

technical feat to match this sensitivity using a pickup loop with radius 70 Å. Yet the loop cannot be made bigger without sacrificing signal strength, due to the $1/r_{\text{loop}}$ dependence of the captured flux. We are therefore committed to a SQUID pickup loop that is roughly the size of a large protein molecule.

To resolve an interferometric phase of $\alpha = 10^{-7}$ with unit signal-to-noise ratio, an intuitive argument suggests that roughly $\alpha^2 = 10^{14}$ electrons must be pushed through the SQUID loop. Otherwise the signal will be lost in shot noise.

This result is consistent with the formalism presented by Tesche and Clarke [36-38] for optimizing the design of thin film dc SQUIDs. We assume that the pickup loop has been fabricated of superconducting wire with radius $r_{\text{wire}} = 20 \text{ \AA}$. The inductance L of such a loop is [39]

$$L = \mu_0 r_{\text{loop}} \ln \left[\frac{8r_{\text{loop}}}{r_{\text{wire}}} \right] = 3.6 \cdot 10^{-14} \text{ H} . \quad (12)$$

Let I_0 be the critical current of the Josephson junctions in the SQUID. We assume that the reduced inductance $\beta = 2Ll_0/\Phi_0$ satisfies $\beta \ll 1$ (and we check the consistency of this assumption later). As per Tesche and Clarke's analysis of dc SQUID performance in the low-temperature limit, we further assume that the temperature is low enough that Johnson noise in the shunt resistances of the SQUID is reduced to negligible levels. The junctions are assumed to be operated at a current bias of twice the critical current.

Under these conditions, eq. 29 of Tesche and Clarke's analysis [36] yields (after some reorganization) a simple and physically illuminating expression for the noise flux spectral density S_Φ :

$$S_\Phi = \Phi_0^2 \frac{1}{4} \frac{q^2}{l_0} \quad (\text{SI units of T-m}^2/\sqrt{\text{Hz}}) . \quad (13)$$

Note that S_Φ is independent of all SQUID parameters except I_0 . According to Tesche and Clarke, this represents the ultimate performance limit of small β , low T dc SQUID designs.

To achieve the desired flux sensitivity of $10^{-7} \Phi_0/\sqrt{\text{Hz}}$, our SQUID junctions must support a critical current of at least $I_0 = 1/4 \cdot 10^{14} \text{ q/sec} = 4.0 \mu\text{A}$. This implies that $\beta = 2Ll_0/\Phi_0 = 1.3 \cdot 10^{-4}$, so the condition $\beta \ll 1$ is consistently satisfied. In operation, each of the two junctions is biased at twice the critical current, so the total current is $I_{\text{tot}} = 4I_0 = 16 \mu\text{A} = 10^{14} \text{ q/sec}$, which is in agreement with our previous simple estimate. In turn, this implies that the 20 Å-diameter loop wires (and the junctions themselves) must support a current density of order $2.6 \cdot 10^8 \text{ A/cm}^2$, which is well above the limit that existing superconducting materials can support even in bulk.

If proton detection is attempted the situation is even more sobering. The intercepted flux is 650 times smaller, so the required critical current is 650^2 times greater, which yields a necessary critical current of $I_0 = 1.7 \text{ A}$. It is not clear that a nanoscale junction could support such a large tunneling current.

It therefore appears unlikely that thin film dc SQUIDs of the type most commonly used can achieve single spin detection. However, other types of SQUIDs have been used to detect magnetic fields [35], and it is possible that some of these might be more suitable. Effective methods for minimizing shot noise in tunnel junctions and shunt resistances would be required of any SQUID technology used to detect single electron or single proton magnetic moments.

The goal of the above analysis is not to assert that SQUID-based imaging of individual electron moments is impossible *per se*, but merely to make the general points that: (1) single spin detection would be technically challenging to achieve with SQUIDs, (2) the required flux sensitivity is of order $10^{-7} \Phi_0/\sqrt{\text{Hz}}$ or better, and (3) the main technical challenges arise from the necessity of pushing a large current density through a small device.

MRFM Detection of Single Spin Magnetic Resonance

To illustrate how MRFM devices sidestep some of the difficulties that SQUIDs encounter, we will design an MRFM device that is capable in principle of resolving individual electron moments at room temperature, with reasonably good signal-to-noise ratio.

The physical principles and engineering parameters of this example device are taken directly from the MRFM literature. Specifically, the cantilever design [16] and the method of spin modulation (nominally cyclic adiabatic inversion [3]) are borrowed from experiments done by the IBM group, and the field gradient source is as described in ref. [6].

The IBM group has already recognized the suitability of their new ultrathin cantilevers for detecting single electron moments [16]. The main challenge in present-day MRFM research is the fabrication and successful operation of such devices.

Our purpose in working out a specific MRFM design in some detail is to illustrate the basic physical mechanisms and technical challenges involved in MRFM. Interestingly, we will find that although MRFM appears to be a relatively simple technology, it is in many respects just as sophisticated as SQUID technology in its use of a coherent quantum phenomenon (namely ferromagnetism) as the basis for sensing small magnetic signals.

The MRFM Field Source

We begin our design of a single-spin MRFM imaging device by fixing a single-domain ferromagnetic sphere [6,40] to the cantilever. The sphere radius r_{sphere} is chosen to maximize the field gradient g at a depth $h_{\text{depth}} = 50 \text{ \AA}$ below the sample surface. For a spherical dipole source with magnetization axis oriented vertically, as shown below, the magnetic field gradient g is:

$$g = 2 \mu_0 M \frac{r_{\text{sphere}}^3}{(r_{\text{sphere}} + h_{\text{depth}})^4}. \quad (14)$$

For an electron at a $h_{\text{depth}} = 50 \text{ \AA}$, the gradient is maximal when $r_{\text{sphere}} = 3 h_{\text{depth}} = 150 \text{ \AA}$.

The sphere magnetization M is taken to be $M = 2 \text{ Tesla}$, which is typical of Fe and similar strongly ferromagnetic materials. At a distance of 50 \AA below the sphere, the electron experiences a field gradient $g = 84 \text{ Gauss/\AA}$, and the force on the sphere is

$$\begin{aligned} F_{\text{electron}} &= g h \gamma^2 / 2 \\ &= 7.8 \cdot 10^{-16} \text{ N}. \end{aligned} \quad (15)$$

This is comparable to the force sensitivity of $F_{\text{min}} = 9 \cdot 10^{-16} \text{ N}$ attained in the first MRFM experiments, in a 0.1 Hz bandwidth [1]. Thus even the first MRFM experiment in principle could have achieved single-spin sensitivity at room temperature, if the cantilever had been equipped with a strong ferromagnetic gradient of the type shown in Fig. 7.

From a physical point of view, much of the sensitivity of MRFM arises from the extraordinarily large current density associated with the electron spins in the ferromagnet.

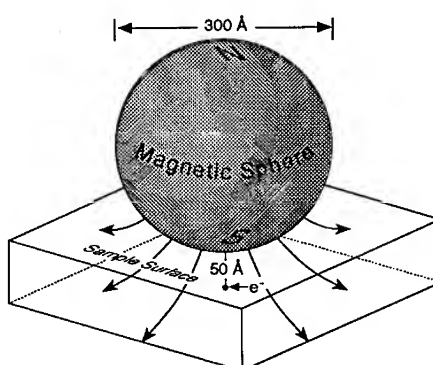


Fig. 7 The ferromagnetic gradient source.

Suppose we were to replace the ferromagnetic sphere with a classical current distribution having the same magnetic moment, consisting of a spatially uniform current density j_{eff} oriented circumferentially within the sphere. This would require a current density of

$$j_{\text{eff}} = \frac{32}{3\pi} \frac{M}{r_{\text{sphere}}} = 3 \cdot 10^{10} \text{ A/cm}^2, \quad (16)$$

corresponding to a net circulating current of 0.13 A.

This ferromagnetic current density is considerably larger than existing superconducting materials can sustain. The current is sustained because ferromagnetism is a collective quantum phenomenon, similar in many respects to superconductivity, in which the ground state of the ferromagnetic spins is macroscopically coherent. Like a superconductor, a ferromagnet can sustain a strong yet completely nondissipative current indefinitely.

We see that for purposes of single-spin detection, ferromagnetic materials provide a uniquely large current density in a conveniently small package.

Cantilever Design and Operation

Having coupled the electron spin to a ferromagnetic current density, the next task is to couple the current density to the outside world. This is accomplished in two stages: (1) we mechanically couple the ferromagnetic current to the cantilever by physically mounting the ferromagnetic sphere on the cantilever [40], and (2) we monitor the cantilever motion with an optical interferometer.

As previously discussed, the IBM group has fabricated ultrathin cantilevers that are optimized for MRFM applications [16]. For purposes of illustration, we will analyze a silicon nitride cantilever described in their article. The cantilever is 55 μm long, 5 μm wide, and 200 \AA thick, with density of 3 gm/cm^3 , modulus of 140 GPa, and quality factor of $Q = 3000$. The ambient temperature is assumed to be 295 K. The field source is the 300 \AA diameter Fe sphere described in the previous section, which exerts a local field gradient of 84 G/ \AA .

The predicted operating parameters of this MRFM device are readily found, using the results presented earlier:

resonant frequency	= 7300 Hz
cantilever mass	= 4.1 picogram
spring constant	= 8.6 $\mu\text{N/m}$
damping time	= 65 msec
single electron force	= $7.8 \cdot 10^{-16} \text{ N}$
force sensitivity	= $3.2 \cdot 10^{-17} \text{ N}/\sqrt{\text{Hz}}$
SNR for single electron	= 28 dB in one Hz bandwidth

Here the signal-to-noise ratio (SNR) is defined to be $\text{SNR} = 10 \log_{10}[\text{signal power} / \text{noise power}]$.

In theory the sensitivity of this room temperature MRFM design would easily suffice to detect an individual electron moment, with an SNR of 28 dB at room temperature in a one Hz bandwidth. At cryogenic temperature, $T = 4.2 \text{ K}$, the predicted SNR is improved from 28 dB to 46 dB. This would suffice to detect individual electron spins with an SNR of 16 dB in a bandwidth of 10^3 Hz. Thus detection could in principle occur rapidly enough to allow rapid scanning and imaging of samples containing many individual spins.

These relatively large SNR values indicate that a single spin MRFM experiment has reasonable leeway to behave in nonideal fashion and still maintain an acceptable SNR. This is important because (in our experience) MRFM experiments are not easy to accomplish, especially the first time out, and a surplus of SNR is therefore very welcome.

It is plausible that MRFM cantilevers could be made even smaller, colder, and with a longer damping time than the above example, as discussed in [6]. This would further improve the magnetic moment sensitivity. The ultimate limits of MRFM sensitivity are not known at present.

Interferometric Detection

To date, all MRFM experiments have used fiber-optic interferometry to detect cantilever excitation, as described by Rugar et al. [41,42] (see Fig. 1). Fiber-optic interferometers achieve their best force sensitivity when the optical power is set to a specific optimal value P_{opt} . Rugar and Grutter [42] give the optimal power as

$$P_{\text{opt}} = \frac{c\lambda k_{\text{mech}}}{4\sqrt{2}\pi Q} . \quad (17)$$

If optical power is less than this value, then shot noise in the photodiodes is excessive, and if greater, then photon backaction on the cantilever is excessive. For the example at hand, we find $P_{\text{opt}} = 32 \text{ nW}$. The corresponding force sensitivity is

$$S_F^{1/2} = \left[\sqrt{8} \frac{\hbar k_{\text{mech}}}{Q} \right]^{1/2} = 2.9 \cdot 10^{-21} \text{ N}/\sqrt{\text{Hz}} , \quad (18)$$

which is more than adequate for our purposes.

How is it that a simple fiber optic interferometer can achieve such remarkable force sensitivity? To answer this question, it is instructive to rewrite S_F as an energy uncertainty relation. Suppose we measure the mean noise energy $\langle E \rangle$ in the oscillator in its effective bandwidth $b = f_0/Q$, where f_0 is the frequency of the oscillator in Hz. The mean value of the energy $\langle E \rangle$ can be expressed in units of oscillator quanta $\langle n \rangle$:

$$\langle E \rangle = \langle n \rangle \hbar \omega_0 . \quad (19)$$

The number of energy quanta contributed by interferometer noise then is:

$$\langle n \rangle = \frac{E}{\hbar \omega_0} = \frac{k_{\text{mech}} S_F b}{\hbar \omega_0} = \frac{Q^2}{k_{\text{mech}}^2} \frac{k_{\text{mech}} S_F b}{\hbar \omega_0} = 2\sqrt{2} \quad (20)$$

This implies that an optimized interferometer can resolve any external force that is large enough to contribute more than about three quanta of energy to the oscillator during its natural damping time. This result is independent of cantilever design parameters.

So if an MRFM device experiences signal forces that are large enough to make the cantilever behave classically, then an optimized interferometer will contribute negligible noise to the system. It is remarkable that a technology as simple and robust as a fiber optic interferometer can achieve near quantum-limited performance.

Some Remarks on MRFM as an Exotic Technology

On first acquaintance, MRFM seems to be a fairly mundane technology in which ordinary magnetic forces are sensed by simple mechanical oscillators. But as we have illustrated in our design exercise, it is more appropriate to regard MRFM as an exotic technology consisting of four linked physical mechanisms, namely:

- (1) The spin being observed is strongly coupled to a dissipation-free current density in the ferromagnetic source, whose strength cannot be matched by classical or even superconducting current sources.
- (2) The ferromagnetic current is strongly coupled to the fundamental mode of the cantilever, again in a dissipation-free manner, by virtue of the physical motion of the cantilever.
- (3) The fundamental cantilever mode is separated from higher modes by a frequency gap, which serves to isolate the fundamental mode from ambient thermal fluctuations.
- (4) Relatively simple interferometric techniques provide nearly quantum-limited sensing of the cantilever excitation.

The only intrinsically dissipative link in this chain, and hence the only intrinsically noisy link, is the optical interferometer. But we have seen that a fiber optic interferometer can approach quantum-limited sensitivity.

We recognize that these four MRFM mechanisms form a linked chain connecting a microscopic spin to a macroscopic observer. Each link functions in a nearly noise-free manner. This is why single spin detection with MRFM is a realistic possibility.

QUANTUM ASPECTS OF SINGLE-SPIN DETECTION

For sufficiently small samples, sample polarization occurs in MRFM by a mechanism that is different than in conventional magnetic resonance imaging. If we consider an ensemble of N individual spin one half particles in a polarizing field, such that the mean polarization is $\langle p \rangle$, then the mean square polarization $\langle p^2 \rangle$ is readily shown to be

$$\langle p^2 \rangle = \langle p \rangle^2 + (1 - \langle p \rangle^2)/N. \quad (21)$$

Here the $1/N$ term is the contribution of statistical fluctuations to the mean square polarization.

In typical macroscopic experiments $N \approx 10^{13}$ or greater, so the fluctuations in $\langle p^2 \rangle$ are usually negligible. But for experiments detecting a single spin, we find $\langle p^2 \rangle = 1$. Physically speaking, the particle is always measured to be 100% polarized, even in the absence of an external polarizing field. The sign of the polarization is random in the limit $\langle p \rangle = 0$.

This statistical argument indicates that sufficiently small spin ensembles are effectively self-polarizing. This effect is particularly important in MRFM detection of individual nuclear spins, as it is difficult to achieve large nuclear spin polarizations in a macroscopic sample.

As discussed by Sidles et al. [5,6], this simple statistical analysis agrees with a more rigorous quantum analysis of MRFM measurements. The self-polarization exhibited by MRFM is shown to be equivalent to the familiar Stern-Gerlach effect, now manifested in the cyclic phase space of the mechanical oscillator of the MRFM.

A 1982 article by Wootters and Zurek [43] shows that Stern-Gerlach self-polarization will be observed by any device that measures the polarization of individual spins. It therefore should be observed in cyclic adiabatic inversion experiments [3], as well as in precession-resonant experiments [6].

BIOMOLECULAR APPLICATIONS OF SINGLE-SPIN MRFM

It is standard laboratory practice to spin label proteins and DNA with unpaired electrons, by attaching tempol and other compounds that have unpaired electrons (here tempol = 2,2,6,6-tetramethyl-4-piperidinol-1-oxyl [44,45,46]).

MRFM imaging of spin labeled structures, if it can be achieved, will have a broad range of applications in biological research. By spin labeling a membrane-bound receptor and also labeling the proteins which bind to the receptor, the combined system of protein plus receptor might be directly imaged, and information regarding the location of the binding site within the protein and receptor sequences may be obtained. Similarly, by spin labeling lipids within a bilayer, the lattice structure of the bilayer might be directly imaged, and the diffusion of labeled lipids within a bilayer may be studied.

Speaking more generally, the three-dimensional structure of any self-assembling protein/DNA/RNA complex might be studied by spin labeling the individual components, then using MRFM to image the assembled complex. Examples of such complexes which are of substantial scientific/medical interest include ribosomes, polymerase/DNA complexes, actin/integrin/membrane assemblies, the light harvesting complex, and viral architectures. Some metalloproteins are naturally spin labeled, and thus might be directly imaged by MRFM. Examples of important metalloproteins include chlorophyll, hemoglobin, and nitrogenase.

The reason for spin labeling is the large magnetic moment of the unpaired electron in a spin label. The longer-term goal of MRFM research is the direct imaging of individual proton magnetic moments. This would obviate the need for spin labeling, and by virtue of the ubiquity of hydrogen in biological molecules would be applicable to all biological structures.

DISCUSSION

The Role of Microscopy in Studying Structure

To better appreciate the essential role that microscopy plays in the study of biological structure, it is useful to imagine a world in which optical and electron microscopy had never been invented. In this hypothetical world, how would biologists study cell structure?

Structural cell biology would prosper as a scientific discipline, even in the absence of microscopy. Biologists would study cell structure using indirect techniques. For example, they would homogenize, centrifuge, and filter cell extracts, prior to running the extracts through gels. After many ingenious experiments, biologists would be able to demonstrate that cells are surrounded by membranes, and contain nuclei that carry genetic information. All aspects of cell structure could be studied in this indirect way.

Cell biologists would not feel particularly handicapped by the absence of microscopy. Rather, they would compete for access to newer and more ingenious filtering techniques. In this hypothetical world, the need for a microscopic imaging technology might not be readily apparent.

It is arguably the case that we live in an analogous world, which has a pressing need for a microscopic imaging technology that can directly image the three-dimensional structure of individual molecules, *in situ*, with the subangstrom spatial resolution required for the rational design of drugs and vaccines.

MRFM Research Goals

MRFM represents one possible approach to achieving the goal of direct molecular imaging, and there is reasonable grounds for optimism that this goal can be achieved.

The last two years have seen rapid experimental progress in MRFM, led by Dan Rugar and Nino Yannoni at IBM Almaden Laboratories. The design path to the detection of individual electron magnetic moments is reasonably clear. Up to the present time, both signal and noise in every MRFM experiment have been in reasonable accordance with theoretical expectations. If this continues to be true of future MRFM experiments, then single spin experiments will become practical in the next few years.

If successful, MRFM imaging of individual electron magnetic moments will serve as a bridge technology leading to a more difficult, but more broadly applicable, technology for MRFM imaging of individual proton magnetic moments.

The practical applications of single spin MRFM imaging are sufficiently important, and the technical issues sufficiently well defined, that a serious and sustained MRFM development effort is indicated. However, it should be clearly understood that MRFM technology is still in the early stages of development. A key priority is the reduction of MRFM noise to a level consistent with the detection of individual electrons and nucleons. For this reason, over the next two or three years the most important MRFM research will be in the area of instrument design, control, and noise. This research will provide a foundation for the biomedical applications described above.

Although our discussion has emphasized biomolecular applications of MRFM, existing MRFM devices are already sensitive enough to be useful in a number of nonbiological applications. Examples include studying the dynamical behavior of magnetization states in individual ferromagnetic and ferrimagnetic particles, and determining the local penetration depth and coherence length of superconducting samples.

ACKNOWLEDGEMENTS

We acknowledge many helpful conversations with Frederick A. Matsen III, Dan Rugar, Nino Yannoni, Othmar Zuger, Stoers Hoen, Gary Drobny, Bruce Robinson, Bill Lytollis, Rob Kaiser, and Kelly Bruland, Jurek Krzystek, Al Kwiram, Lowell Brown, David Thouless, Sam Fain, Cliff Slaughterbeck, and Rob Van Dyck. The support of the Department of Orthopaedics of the University of Washington School of Medicine, the University of Washington Royalty Research Fund, and the NIH National Center for Research Resources under R01-RR08820 is gratefully acknowledged.

REFERENCES

1. D. Rugar, C.S. Yannoni, and J.A. Sidles; Mechanical detection of magnetic resonance. *Nature* 360, 563-566 (1992).
2. O. Zuger and D. Rugar; First images from a magnetic resonance force microscope. *Appl. Phys. Lett.* 63, 2496-2498 (1993).
3. D. Rugar, O. Zuger, C. S. Yannoni, S. Hoen, H.-M. Vieth, and R. D. Kendrick; Force detection of nuclear magnetic resonance. *Science* (in press).
4. J. A. Sidles; Noninductive detection of single-proton magnetic resonance. *Appl. Phys. Lett.* 58, 2854-2856 (1991).
5. J. A. Sidles; Folded Stern-Gerlach experiment as a means of detecting magnetic resonance in individual nuclei. *Phys. Rev. Lett.* 68-70, 1124 (1992).
6. J. A. Sidles, J. L. Garbini, and G. P. Drobny; The theory of oscillator-coupled magnetic resonance with potential applications to molecular imaging. *Rev. Sci. Instr.* 63, 3881-3899 (1992).
7. J. A. Sidles and D. Rugar; Signal-to-noise ratios in electrical and mechanical detection of magnetic resonance. *Phys. Rev. Lett.* 70, 3506-3509 (1993).
8. F. C. Bernstein, T. F. Koetzle, G. J. B. Williams, E. F. Meyer, Jr., M.D. Brice, J. R. Rodgers, O. Kennard, T. Shimanouchi, and M. Tasumi; The protein data bank: a computer-based archival file for macromolecular structures. *J. Mol. Biol.* 112, 535-542 (1977).
9. F. H. Allen, G. Bergerhoff, and R. Sievers; *Data Commission of the International Union of Crystallography*. Bonn/Cambridge/Chester (1987), pp. 107-132.
10. All entries in the October 1993 full release index file 'compounds.lst' were reviewed. This list was obtained by ftp from the Brookhaven Protein Data Bank gopher server 'pdb.pdb.bnl.gov'. This was the most recent list on the server as of January 1994.
11. Y. S. Lam et al.; Rational design of potent, bioavailable, nonpeptide cyclic ureas as HIV protease inhibitors. *Science* 262, 380-384 (1994).
12. C. C. Harris; p53: at the crossroads of molecular carcinogenesis and risk assessment. *Science* 262, 1980-1991 (1984).
13. D. E. Koshland and E. Culotta; p53 sweeps through cancer research. *Science* 262, 1958-1961 (1984).
14. A. Abragam; *Principles of Nuclear Magnetism*. Clarendon Press, Oxford (1982). For examples of cyclic adiabatic inversion, see page 86 and page 548.
15. C. P. Slichte; *Principles of Magnetic Resonance*. Harper & Row, New York, (1963).
16. S. Hoen, O. Zuger, C. S. Yannoni, H. J. Mamin, K. Wago, and D. Rugar; Fabrication of ultrasensitive force detectors. in *Technical Digest of the 1994 Solid State Sensor and Actuator Workshop*, Hilton Head, SC (June 1994) , pp. 13-199 (in press).
17. W. P. Mason; *Electromechanical Transducers and Wave Filters*, Van Nostrand, New York (1942), pp. 90.

18. D. B. Fraser; Impurities and anelasticity in crystalline quartz. in *Physical Acoustics Vol. V*. W. P. Mason (ed.), Academic Press, NY (1968). See pp. 59-110.
19. A. V. Granato and K. Lucke; The vibrating string model of dislocation damping. in *Physical Acoustics Vol. IVA*. W. P. Mason (ed.), Academic Press, NY (1966). See pp. 225-276.
20. W. P. Mason; Effect of impurities and phonon processes on the ultrasonic attenuation of germanium, crystal quartz, and silicon. in *Physical Acoustics Vol IIIB*. W. P. Mason (ed.), Academic Press, NY (1966). see pp. 235-286.
21. P. G. Klemens; Effect of thermal and phonon processes on ultrasonic attenuation. in *Physical Acoustics Vol. IIIB*. W. P. Mason (ed.), Academic Press, NY (1966). see pp. 201-234.
22. B. S. Berry and A. S. Nowick: Anelasticity and internal friction due to point defects in crystals. in *Physical Acoustics Vol. IIIA*. W. P. Mason WP (ed.), Academic Press, NY (1966). See pp. 1-42.
23. J. Ferreira; Internal friction in high Q materials. in *The Detection of Gravity Waves*. D. G. Blair (ed.) Cambridge Univ. Press, Cambridge (1991). See pp 116-166.
24. D. G. Blair; Resonant bar detectors. in *The Detection of Gravity Waves*. D. G. Blair (ed.) Cambridge Univ. Press, Cambridge (1991) . see pp 73-98.
25. T. V. Roszhart; The effect of thermoelastic friction on the Q of micromachined silicon resonators. in *IEEE Sensor and Actuator Workshop*. Hilton Head Island, SC (1990). see pp. 13-16.
26. C. Zener; Internal friction in solids: theory of internal friction in reeds). *Phys. Rev.* 52, 230 (1937).
27. C. Zener; Internal friction in solids II: general theory of thermoelastic internal friction. *Phys. Rev.* 53, 90 (1938).
28. Randall, Roce, and Zener; Intercrystalline thermal currents as a source of internal friction. *Phys. Rev.* 56, 343 (1939).
29. R. J. Pitcher and K. W. H. Foulds; Optothermal drive of silicon resonators: the influence of surface coatings. *Sensors and Actuators A21-A23*, 387-390 (1990).
30. R. M. Langdon and D. L. Dowe; Photoacoustic oscillator sensors. *SPIE vol. 798; Fiber Optic Sensors II* (1987). see pp. 86-93.
31. L. M. Zhange, D. Uttamchandani, and B. Culshaw; Excitation of silicon microresonators using short optical pulses. *Sensors and Actuators A21-A23*, 391-393 (1990).
32. R. A. Buser and N. F. De Rooij; Very high-Q resonators in monocrystalline silicon. *Sensors and Actuators A21-A23*, 323-327 (1990).
33. J. D. Zook, D. W. Burns, H. Guckel, J. J. Sniegowski, R. L. Engelstad, and Z. Feng; Characteristics of polysilicon resonant microbeams. *Sensors and Actuators A35*, 51-19 (1992).
34. R. C. Jaklevic, J. Lambe, A. H. Silver, and J. E. Mercereau; Quantum interference effects in Josephson tunneling. *Phys. Rev. Lett.* 12, 159-160 (1964).
35. J. Clarke; SQUIDs: principles, noise, and applications. in *Superconducting Devices*. S. T. Ruggiero and D. A. Rudman (eds), Academic Press, NY (1990). see pp 51-101.
36. C. D. Tesche and J. Clarke; dc SQUID: noise and optimization. *J. Low Temp. Phys.* 29, 301-331 (1977).
37. J. J. P. Bruines, V. J. de Waal, and J. E. Mooij; Comment on " dc SQUID noise and optimization" by Tesche and Clarke. *J. Low Temp. Phys.* 46, 382-396 (1982).
38. V. J. de Waal, P. Schrijner, and R. Llurba; Simulation and optimization of a dc SQUID with finite capacitance. *J. Low Temp. Phys.* 54, 215-232 (1984).
39. W. R. Smythe; *Static and Dynamic Electricity (third edition)*. McGraw-Hill, New York (1968). see pp. 339-340.

40. A. D. Kent, T. M. Shar, S. von Molnar, and D. D. Awschalom; Growth of high aspect-ratio nanometer-scale magnets with chemical vapor deposit tunneling microscopy. *Science* 262, 1249-1252 (1993).
41. D. Rugar, H.J. Mamin, and P. Guethner; Improved fiber-optic interferometer for atomic force microscopy. *Appl. Phys. Lett.* 55, 2588-2590 (1989).
42. D. Rugar and P. Grutter; Mechanical parametric amplification and thermomechanical noise squeezing. *Phys. Rev. Lett.* 67, 699-702 (1989).
43. W. K. Wootters and W. H. Zurek; A single quantum cannot be cloned. *Nature* 299, 802-803 (1982).
44. B. Robinson, H. Thomann, A. H. Beth, P. Fajer, and L. Dalton; The phenomenon of magnetic resonance: theoretical considerations. in *EPR and Advanced EPR Studies of Biological Systems*, L. R. Dalton (ed.), CRC Press, Boca Raton (1985). see pp. 12-108.
45. B. Robinson, H. Thomann, A. H. Beth, P. Fajer, and L. Dalton; The application of EPR techniques to the study of DNA. in *EPR and Advanced EPR Studies of Biological Systems*, L. R. Dalton (ed.), CRC Press, Boca Raton, (1985). see pp. 296-301.
46. B. H. Robinson, D. A. Haas, and C. Mailer; Molecular dynamics in liquids: spin-lattice relaxation of nitroxide spin labels. *Science* 263, 490-493 (1994).
47. M. A. Garstens and J. I. Kaplan; Low field magnetic resonance. *Phys. Rev.* 99, 459-463 (1955).

TRENDS IN ATOMIC RESOLUTION ELECTRON MICROSCOPY

DAVID J. SMITH* AND M.R. MCCARTNEY

Center for Solid State Science, Arizona State University, Tempe, AZ 85287

*also at: Department of Physics and Astronomy, Arizona State University, Tempe, AZ 85287

ABSTRACT

Structural information on the atomic scale is readily accessible from thin samples using the technique of high-resolution electron microscopy. Electron micrographs recorded under well-defined operating conditions can be directly interpreted in terms of atomic arrangements around defects of interest such as dislocations and interfaces. Digital image recording with slow-scan CCD cameras and quantitative comparisons with image simulations based on structural models are starting to lead to improved accuracy and reliability in structure determinations. Techniques based upon holographic methods are utilizing the superior illumination coherence of the field emission electron source to enhance resolution beyond the conventional extended Scherzer limit. Innovative methods for combining image and diffraction pattern information are also leading to improved levels of resolution for periodic objects. Care is needed to ensure that electron irradiation damage and surface cleanliness do not impose unnecessary restrictions on the details that can be extracted from recorded micrographs. It is proposed that the complex wavefunction emerging from the exit-surface of the sample should be considered as a basis for comparing the differences between experimental micrographs and image simulations.

BACKGROUND

It has long been realized that the electron microscope should have the capability of resolving atomic-scale detail as a direct result of the sub-Ångstrom wavelength of its high-energy electron beam [1]. Whilst this potential has not been fully realized because of unavoidable aberrations in the imaging or objective lens, instrumental developments over the last decade or so have led to high-resolution electron microscopes (HREMs) that can routinely provide images with 2-3 Å resolution. Individual atomic columns can be resolved in several low-index zones of many common semiconductors, metals and ceramics, making the HREM an invaluable tool for structural characterization. The diversity of results from many fields of science being reported on an almost daily basis from laboratories around the world testifies to its widespread usefulness. In this overview of the field, however, no serious attempt is made to provide a comprehensive survey of these multitudinous applications. The interested reader is referred to several recent MRS Symposium Proceedings [2-4], as well as to the proceedings of more specialized electron microscopy conferences, for further details. We concentrate our emphasis here upon the technique of high-resolution electron microscopy, in particular the recent progress that has been made towards improving resolution limits for perfect and defective materials and quantifying the determination of atomic arrangements at unknown defects.

In the early years of electron microscopy, technical factors such as electrical and mechanical instabilities represented severe practical limitations on attainable microscope resolving power. Direct observation of lattice planes was first achieved by Menter [5] in studies of phthalocyanine crystals, and later studies of large-unit-cell oxides established the first direct correlations between crystal structure and recorded images [6]. The discrimination of individual tunnels in block oxides opened up the practice of what came to be known as structure imaging [7,8]. With the validity of image interpretation initially being justified from a prior knowledge of the observed crystal's structure, sufficient confidence in the technique was quickly established and many fruitful studies of defects in nonstoichiometric oxides and minerals soon followed [9]. With assistance from prior chemical and structural knowledge, models for several novel types of defects were developed primarily on the basis of structure images. Concurrently, image simulation programs were developed [10] that utilized the multislice algorithm [11], so-called because it involved projections of the crystal structure onto many thin slices along the incident

electron beam direction. Images computed with these programs were used more and more frequently as a basis for justifying image interpretation although, as we discuss in more detail below, comparisons between computed and experimental images have mostly remained on a rather subjective and qualitative basis.

EXPERIMENTAL APPROACH

Over many years, the electron microscope has evolved into a highly sophisticated and complex instrument, with much attention being given to high-resolution imaging theory [12] as well as to various aspects of instrumentation [13]. The main principles of the high-resolution imaging technique are easily understood by reference to the transfer function (TF) of the objective lens for axial incident illumination. The TF is specimen- and microscope-independent and it can be represented in generalized units. Different microscopes and lenses can be easily compared since a single set of universal curves describes the transfer behavior of all objective lenses. For the ideal weak-phase object, the TF can be replaced by the phase contrast transfer function (PCTF) which is given by:

$$\begin{aligned} T(k) &= 2\sin \gamma(k) \\ &= 2\sin \pi k^2 (k^2/2 - D) \end{aligned} \quad (1)$$

where k is a coordinate representing the generalized spatial frequency ($k = |2\sin\theta/\lambda|/(C_s\lambda^3)^{1/4}$, θ = scattering half-angle) and D ($= \Delta f/C_s\lambda^{1/2}$) is the generalized objective lens defocus [13]. The final image is a product of the PCTF and the wavefunction emerging from the exit-surface of the specimen. The PCTF becomes increasingly oscillatory at higher spatial frequencies (i.e. higher resolution) so that electrons scattered to higher angles will suffer reversals in phase with respect to those scattered at smaller angle. Corresponding artefactual detail in the final image is thus likely to occur. The focus dependence of this function will lead to periodic phase reversals, again complicating the issue of image interpretation. Examples of calculated PCTFs for HREMs operating at 300keV at the so-called optimum defocus ($D = -1.22$), with a spherical aberration coefficient, C_s , for the objective lens of 1.00mm, are shown in Figs. 1a-c. The first PCTF corresponds to an ideal Microscope A with fully coherent incident illumination, meaning that there is no electron energy spread or focal spread due to lens current or high voltage instabilities, and no angular spread in the incident electron beam direction. The second PCTF corresponds to a typical HREM (Microscope B) with a lanthanum hexaboride electron source (focal spread, Δf , of 7nm, beam divergence, α , of 0.5mrad), and the third is for a Microscope C equipped with a highly coherent field emission gun (FEG) as its electron source ($\Delta f = 2\text{nm}$, $\alpha = 0.05\text{mrad}$). The extent of the higher frequency oscillations depends on the coherency of the illumination, with the FEG offering the prospect of substantial information transfer occurring beyond the first zero crossover of the PCTF.

The most critical point on all of these PCTF curves is the first zero crossover which has the approximate value

$$d \sim 0.66 (C_s\lambda^3)^{1/4} \quad (2)$$

The broad band of spatial frequencies without phase reversals occurring on the left of the crossover means that, in the case of thin samples, it is often possible to interpret intuitively any images that have been recorded at this defocus in terms of the projected crystal structure. This crossover point thus defines what is usually known as the "interpretable" or "structure image" resolution. Table I gives a list of typical values. The difference in damping for Microscopes B and C is a measure of the coherence of the incident illumination. Given that the PCTF behavior as a function of angle is well-established, the oscillations could be removed by suitable deconvolution, thereby allowing the resolution of the image to be further improved, albeit with missing information corresponding to the positions of the PCTF zeroes. In the case of Microscope C, *a posteriori* image processing for this purpose would be clearly worthwhile since substantial additional information about the specimen might then be retrievable [14]. Until quite recently (see below), this objective had only been achieved for a few simple objects [15].

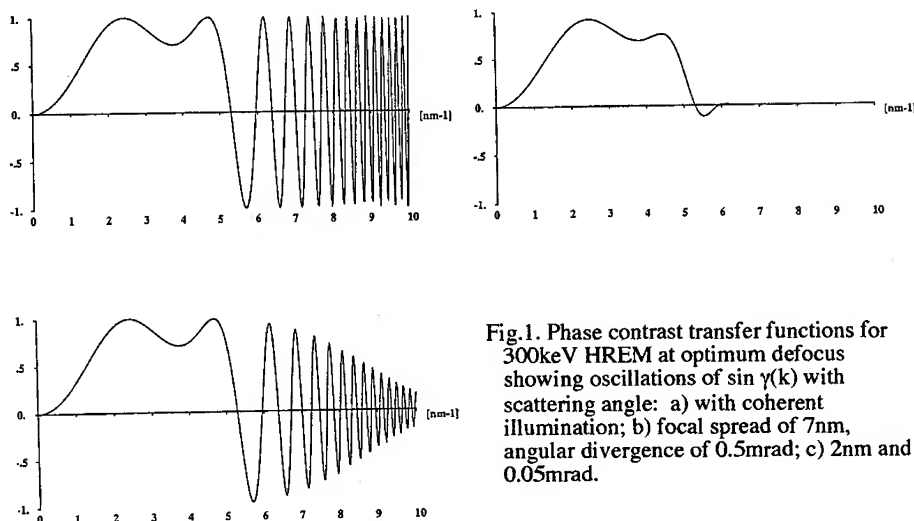


Fig.1. Phase contrast transfer functions for 300keV HREM at optimum defocus showing oscillations of $\sin \gamma(k)$ with scattering angle: a) with coherent illumination; b) focal spread of 7nm, angular divergence of 0.5mrad; c) 2nm and 0.05mrad.

Equation (2) is inescapable. For bright-field imaging of thin samples, with incident illumination parallel to the optic axis of the objective lens, improvements in interpretable resolution can only be achieved by reducing the spherical aberration coefficient or by decreasing the electron wavelength (higher accelerating voltage). The latter possibility is limited by very practical considerations such as the extreme cost of a high-voltage, high-resolution instrument (perhaps \$US10M for a 1MeV machine at 1993 prices!) and the increasing likelihood of electron irradiation effects causing irreversible damage to the sample. (However, some notable successes have recently been reported for microscopes operating at 1.0MeV [16] and 1.2MeV [17].) Very little gain can be anticipated with the former approach because of the already highly advanced state of objective lens and specimen stage design. With the continuing lack of progress in achieving correction of spherical aberration, the most promising avenue for enhanced resolution currently appears to be through deconvolution of the effects of the transfer function in the event of sufficiently coherent imaging conditions, such as for Microscope C depicted above. Progress that has recently been made in this direction, in particular towards extraction of the complex phase and amplitude of the specimen exit-surface wavefunction, using electron holography [18] and focal series restoration [19,20] is described briefly below.

Table I. Interpretable resolution for different electron energies and objective lenses

Energy (keV)	Wavelength (Å)	Spherical aberration (mm)	Resolution (Å)
100	0.0370	0.7	3.0
200	0.0251	0.8	2.3
300	0.0197	0.9	2.0
400	0.0164	1.0	1.7
1000	0.0087	2.3	1.3
2000	0.0050	4.0	0.99

RESULTS

The macroscopic properties of most materials usually depend on their nanostructure. Because of its extreme resolving power which allows individual atomic columns to be discriminated, the high resolution electron microscope has an invaluable role to play in the characterization of materials. The structure of many different types of irregularities such as dislocations and interfaces can be extracted from (a series of) high-resolution electron micrographs provided that the imaging conditions are sufficiently well defined. In this section we briefly survey some recent high-resolution structural studies and the progress that has been made towards quantification of structure determination using the HREM, and we conclude by considering some of the experimental factors that can limit the reliability of the refinement process.

Determination of defect structures

Before progressing to determining the structure of some unknown defect, it is useful to begin by calculating a "map" or "tableau" of high-resolution images of the perfect crystal lattice as a function of both defocus and thickness [21]. For small-unit-cell materials, focus recognition is, however, complicated by Fourier or self images of the crystal which recur periodically as the objective lens defocus is altered [22,23]. For selection of focus, the microscopist may then need to refer to the amorphous material or Fresnel fringe along a nearby sample edge if available. In large-unit-cell materials, focus recognition is not usually such a problem because the optimum defocus image generally has a very characteristic appearance. Finally, recent work has demonstrated that cross-correlation coefficients in Fourier space could be used to determine defocus and thickness automatically with high speed and precision provided that a tableau of images of the perfect crystal has first been generated [24].

The determination of defect structures in small-unit-cell materials using the HREM has historically relied upon qualitative comparisons between experimental micrographs and image simulations, usually upon the basis of a finite number of postulated structural models. Some past examples are listed in Table II [16, 25-45]. Figure 2 shows two micrographs from a focal series of images of an inversion domain boundary in aluminum nitride, with corresponding image simulations inset. Structural models have normally been considered as being more acceptable if an image "match" is obtained for two or more members of such a through-focal series [25,28,33, 36-38,41-43]. However, one always needs to be aware of the possibility of positioning errors arising from direct visual interpretation of experimental images since the apparent positions of closely-spaced atomic columns at aperiodic features may vary by as much as 0.3 Å [46]. In several recent studies [31,39,44], projected atomic column positions were overlaid on the experimental and/or simulated images, and superposition [39] or subtraction [26] of experimental and simulated image pairs has been used in the refinement process. Increased accuracy in the structure refinement process has recently been obtained using least-squares refinement methods [47,48] to iterate between the experimental and simulated images.

Table II. Examples of defect modelling in small-unit-cell materials.

Material	Defect	Ref.	Material	Defect	Ref.
SnO ₂	(001) glide twin	[25]	CdTe	2x1, 3x1 (001) surface	
NiO	Σ5 (210) and 13 (320) tilt GB	[26]		reconstruction	[35]
α-Al ₂ O ₃	Σ11 (0111)/(0111) 35.2° tilt GB	[16]	C(diamond)	{100} nitrogen platelet	[36]
SiTiO ₃	Σ5 (130)/[001] 36.8° tilt GB	[27]	Nb	Σ5 (310)/[001] 36.9° tilt GB	[37]
Si	Σ13 (510)/[001] GB	[28]	Nb	Σ25 (710)/[001] tilt GB	[38]
Si, Ge	Lomer edge dislocation	[29]	Mo	Σ41 (910)/[001] tilt GB	[39]
Ge	Σ9 twin	[30]	Al	Σ3 {112} incoherent twin	[40]
Ge	Σ5 (130)/[001] tilt GB	[31]	Al	Σ99 {557} <110> tilt GB	[41]
Ge	Σ27 tilt GB	[32]	Al	Σ11 (113) and Σ9 (221) tilt GB	[42]
NiSi ₂ /Si(111)	7-fold Ni A-type	[33]	AlN	Inversion domain boundary	[43]
CoSi ₂ /Si(111)	7-fold Co A-type		Pd/NiO	O-terminated (111) interface	[44]
	7-fold/8-fold Co B-type	[34]	Au	2x1 (110) surface reconstruction	[45]

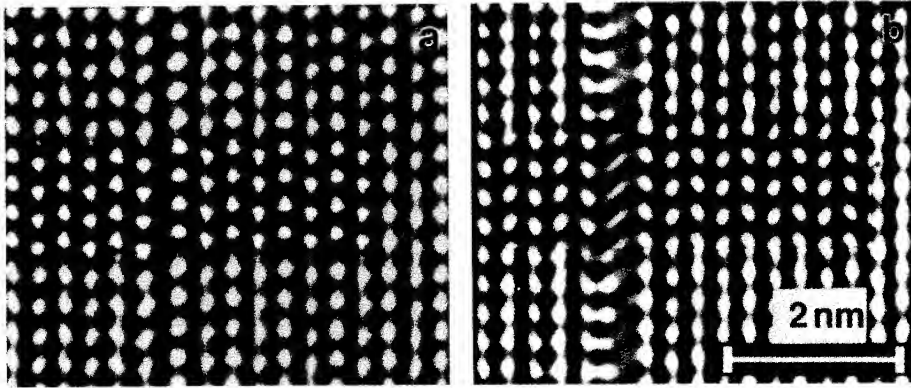


Fig. 2. Experimental high-resolution electron micrographs of oxygen-containing inversion domain boundary (IDB) defect in AlN, recorded at 400keV with a JEM-4000EX. (a) inset simulated for 3.1nm thickness and -45nm defocus; (b) inset simulated for 5.3nm thickness and -72nm defocus [43].

Recent attention has been given to innovative approaches which combine image plane and diffraction pattern information, such as the maximum entropy method [49,50]. In one sense, these methods may be considered as having limited applicability because they cannot be used for aperiodic features such as interfaces or dislocations. Nevertheless, recent studies of oxides [51,52], minerals [53] and beam-sensitive hydrocarbons [49] demonstrate that the structural resolution in perfect crystals can be substantially enhanced beyond that available from the image alone. Moreover, it is important to appreciate that the volumes of material involved are many orders of magnitude less than those accessible to most bulk characterization techniques. Hence, it can be anticipated that the (unknown) structures of many small crystalline phases will become amenable to fruitful study.

Enhanced structural resolution can, in principle, also be attained by removing the oscillations of the PCTF that occur at higher spatial frequencies. This possibility becomes feasible as a result of the reduced energy spread and increased source brightness available with the field-emission electron source. The complex image wavefunction can be extracted from a focal series of images and then the exit-surface wavefunction can be recovered by compensating for aberrations of the imaging lens. Two different image reconstruction algorithms have recently been proposed that lend themselves to computer processing. The so-called paraboloid method [19], which appears to be a variant of an earlier method [54], works well for comparatively thin, weakly scattering objects. The maximum-likelihood method (MAL) utilizes linear and non-linear imaging contributions [20]: it has been used to striking effect in overcoming the 2.4 Å structural resolution of a 200keV HREM to achieve reliable structural information at the 1.4 Å level which then enabled resolution, for the first time, of the positions of individual oxygen atomic columns in a high-temperature superconductor [20].

Quantification.

In order to carry out structure determinations for unknown defects, including quantitative comparisons between experiment and simulations for final verification of any proposed structural models, electron microscopists must first ensure that their HREMs are properly adjusted. Several instrumental parameters should be pre-determined and the microscope operating conditions must be carefully chosen. It will also be helpful if quantitative recording facilities are available to avoid consuming time with corrections for photographic film nonlinearities.

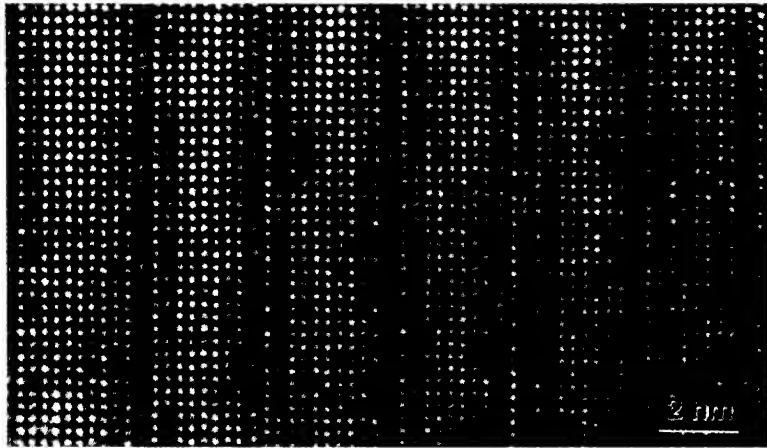


Fig. 3. High-resolution electron micrograph of large-unit-cell Al-O-N polypyridoid recorded at 400keV with slow-scan CCD camera attached to JEM-4000EX HREM. Digital recording facilitates quantitative comparison with image simulations.

The most relevant microscope parameters are the spherical aberration coefficient of the objective lens, the defocus step size and the actual defocus value. These can be determined in several ways using experimental micrographs [13], for example from the Fourier oscillation period of the dominant lattice spacing [23] or by referring to optical diffractograms from images of amorphous materials [55]. Cross-correlation techniques involving comparisons of coefficients in Fourier space have recently also been proposed [24]. Standard deviation values of less than 1% have been attained using methods based on least-squares fitting of PCTF zeroes [56,57]. These parameters depend sensitively on the objective lens current, so care should be taken to ensure that all subsequent images are recorded at very similar lens current settings. The appearance of high-resolution electron micrographs is relatively insensitive to the absolute value of C_s , but it might not be possible to utilize any image information occurring at spatial frequencies beyond the interpretable resolution limit unless even higher accuracy is attained [58].

Progress towards more accurate quantification is being achieved by several other means which include control of microscope operation by online computer [59-61], as well as image recording with slow-scan CCD cameras [61-63]. As an example of the latter, Fig.3 shows a digital micrograph of a large-unit-cell Al-O-N polypyridoid that was recorded recently as part of a quantitative structure determination study (McCartney et al, unpublished). Experimentally, computer control enables focus setting, astigmatism and incident beam alignment to be adjusted routinely to accuracies usually beyond the capabilities of experienced microscopists, thereby simplifying subsequent attempts at structure refinement. The criteria that have been used for autotuning include image variance (contrast) [59], beam-induced displacement (BID) which works for crystalline materials [60], and automatic diffractogram analysis (ADA) [61]. Slow-scan CCD cameras provide excellent linearity of the exit signal over a wide dynamic range of the input signal intensity (~4 orders of magnitude) provided that the camera has been correctly adjusted for the prevailing conditions. Highly efficient recording, with a detection quantum efficiency (DQE) close to unity, can be achieved for imaging purposes at reasonable intensity levels [63]. Higher electron-optical magnification with the camera is, however, usually necessary because of the finite pixel size, and holographic reconstructions should preferably utilize CCD pixel arrays greater than 1024x1024 in size [58]. The geometry of the imaging/detection system remains fixed, unlike the mechanical movement involved in normal photographic recording, so that geometric distortions that are present can be substantially compensated [64]. This correction must be made as a necessary preliminary step in the process of carrying out off-axis electron holography studies requiring accurate phase measurements [65].

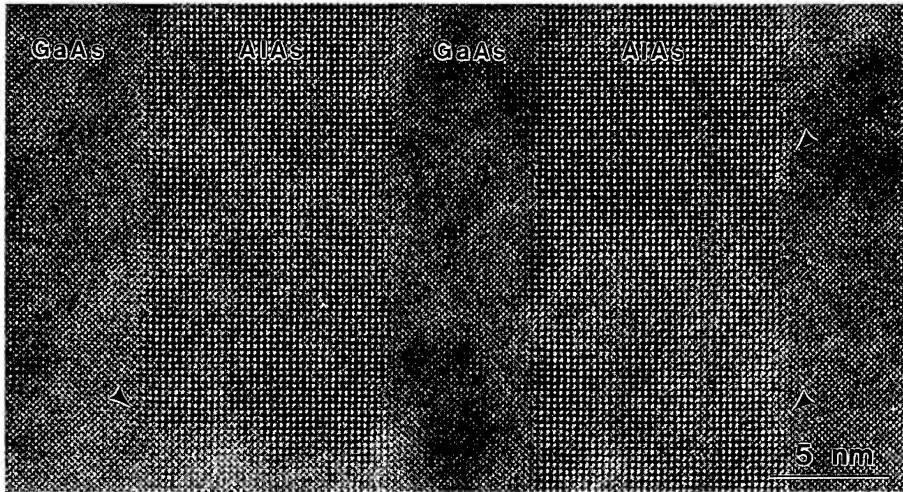


Fig. 4. High-resolution electron micrograph of [001]-oriented GaAs/AlAs heterostructure. Compare the different contrast motifs of crossed 0.20nm {220} lattice fringes in GaAs and the 0.28nm {200} lattice fringes in AlAs, and note interface steps (arrowed).

Compositional variations that cause subtle changes in image contrast have recently received much attention [66-69]. Several groups of lattice-matched materials, such as the GaAs/AlAs heterostructures [66] and Ni₃Al intermetallic alloys [67] have subsets of reflections in some projections that depend upon structure-factor differences, i.e. the reflections can be considered as being "chemically sensitive". For example, the {200} reflections in [001]-oriented GaAs have amplitudes that are very low even for crystal thicknesses in excess of 200Å, whereas these reflections are relatively strong, although oscillatory with thickness, for AlAs. As shown in Fig.4, thickness and defocus values can be found that facilitate differentiation between these two materials because of the resulting characteristic contrast motif. An algorithm for vector pattern recognition in these materials has also been developed that attempts to quantify the local composition on the unit-cell scale. The recognition of single-atom, and double-atom, substitution in individual atomic columns at AlAs/GaAs heterojunctions with confidence levels of 60% and 90%, respectively, has been reported [68] (see also these proceedings).

Experimental concerns

In any experimental technique, there are invariably extraneous practical effects that must be taken into account. High-resolution electron microscopy is no exception. The presence of amorphous surface overlayers, the occurrence of multiple and inelastic scattering, and the likelihood of electron irradiation damage to the sample during observation are all likely to affect the integrity of the imaging process. These factors result either in image blurring or effective loss of true image detail, so their influence should be minimized as much as possible.

Amorphous overlayers are present on almost all specimens prepared for electron microscopy: these overlayers must impact the appearance of the final image because it is formed by electron transmission through the whole sample. This expectation is clearly evident from comparing any matched pair of simulated image and experimental micrograph. Image-averaging techniques offer obvious benefits for enhanced signal quality but they cannot be applied to aperiodic defects [69]. Elimination, or at least reduction, of the surface-generated noise has been shown to result in significant improvements in image quantification [70]. Overall, the electron microscopist has no alternative except to pay careful attention to sample preparation to avoid loss of signal quality.

Inelastic electron scattering has serious implications for HREM structural studies, especially in thick samples, but it is not easily incorporated into image simulations because of lack of knowledge of angular and energy spreads associated with scattering from defects, and it has therefore, to a large extent, been (deliberately?) ignored. Electron-energy-imaging filters could be used to form high-resolution images with electrons that have not lost energy when passing through the specimen [71], or reference could be made to complex wavefunctions reconstructed from off-axis electron holograms which are energy-filtered [72]. Accounting for multiple scattering also remains problematical, except for special channeling conditions [73], so structure determinations using high-resolution imaging must be restricted to very thin regions.

Structural modification as a result of electron irradiation is inevitable. Atomic displacements in the bulk of materials as high as copper ($Z=29$) in the Periodic Table will occur at an electron energy of 400keV, while atoms at lattice defects and surfaces, which are not so tightly bound, will be even more susceptible to displacement [74]. Moreover, high beam current densities, and hence electron doses, are required for imaging at very high magnification at the highest resolution levels. Beam damage thus has the overall effect that the final recorded micrograph may not be representative of the original microstructure of the sample. The microscopist must be continually aware of this, and do whatever possible to restrict the total dose sustained.

PERSPECTIVE AND OUTLOOK

High-resolution electron microscopy has slowly evolved into a mature technique, and only small improvements in performance levels have occurred over recent years. Nevertheless, these gains will continue to make significant differences in the analyses of particular materials and/or defects. As an example, Fig.5 shows again the oxygen-containing IDB in AlN. At current resolution levels of $\sim 1.6\text{\AA}$ (Fig.5a), individual Al and N atomic columns are not resolved in the perfect crystal, nor are any O atomic columns visible along the defect [43]. With a resolution improvement to $\sim 1.0\text{\AA}$ (Fig.5b), it should be possible to discriminate between atomic columns in all regions of the perfect and defective crystal. Significant insights into many other materials, and a variety of physical and chemical processes, can likewise be expected as a result of better knowledge of atomic structure and chemical composition. Moreover, improved accuracy in determining relative atomic locations, perhaps to within $\sim 0.05\text{\AA}$, would, for example, greatly impact theoretical modelling of interfaces. HREM should retain its important role in structural characterization studies.

One topic that has been attracting increasing attention lately is the unresolved question of how best to assign some sort of reliability or R-factor to structure determinations of defects such as grain boundaries. The problem is that, unlike the case for X-ray diffraction where this factor usually refers to the entire contents of the particular unit cell, in grain boundary studies no such well-defined entity exists. Several parameters that were initially proposed [75] proved to be unsatisfactory due to their defocus dependence. A non-linear, least-squares optimization approach that compared experimental and simulated boundary images was successfully used to refine atomic positions at Nb grain boundaries [47]. In a very recent paper [76], the so-called "normalized Euclidean distance (NED)" was proposed as an alternative criterion for quantifying the discrepancy between simulated and experimental images: it was also pointed out that further discrepancies could arise as a result of non-structural differences, such as approximations made in the image simulation programs. We have recently proposed [77] that comparisons should be made on the basis of the complex exit-surface wavefunction so that microscope parameters are removed as variables in the optimization process. Discussion in the electron microscopy community is clearly needed in order to reach some sort of consensus agreement.

In summary, state-of-the-art electron microscopy involves structural studies on the atomic scale. With facilities for computer-controlled microscope operation and digital recording becoming commercially available, future work is likely to be increasingly quantitative. High resolution electron microscopists are likely to become more concerned about refining complementary techniques, such as small probe microdiffraction and microanalysis, preferably with the same instrument, to augment their structural information. Atomic arrangements and locations at interfaces and defects will be determined with high degrees of accuracy, and better insights into the physical behavior of many materials should be achieved.

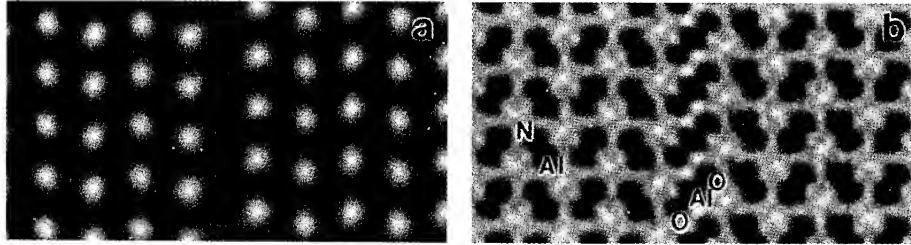


Fig. 5. (a) Experimental high-resolution ($\sim 1.6\text{\AA}$) image of O-containing IDB in AlN [43].
 (b) Simulated image for 1.0\AA resolution. Separate Al, N and O atomic columns are resolved.

Acknowledgement: Electron microscopy at Arizona State University was conducted at the Center for High Resolution Electron Microscopy supported by NSF Grant DMR-9115680.

References

- [1] E. Ruska, *Adv. Opt. El. Microsc.* 1 (1965) 115.
- [2] High Resolution Microscopy of Materials, Eds. W. Krakow, F.A. Ponce and D.J. Smith, *Materials Research Society Symposium Proceedings*, Vol. 139 (Materials Research Society, Pittsburgh, 1989).
- [3] High Resolution Electron Microscopy of Defects in Materials, Eds. R. Sinclair, D.J. Smith and U. Dahmen, *Materials Research Society Symposium Proceedings*, Vol. 183 (Materials Research Society, Pittsburgh, 1990).
- [4] Atomic-Scale Imaging of Surfaces and Interfaces, Eds. D.K. Biegelsen, D.J. Smith and S.Y. Tong, *Materials Research Society Symposium Proceedings*, Vol. 295 (Materials Research Society, Pittsburgh, Pittsburgh, 1993).
- [5] J.W. Menter, *Proc. Roy. Soc. A236* (1956) 119.
- [6] J.G. Allpress and J.V. Sanders, *J. Appl. Cryst.* 6 (1969) 165.
- [7] S. Iijima, *J. Appl. Phys.* 42 (1971) 5891.
- [8] J.L. Hutchison and J.S. Anderson, *Phys. status solidi (a)* 9 (1972) 207.
- [9] J.S. Anderson, *Chemica Scripta* 14 (1978/79) 129, 287.
- [10] P.R. Self and M.A. O'Keefe, in *High-Resolution Transmission Electron Microscopy*, Eds. P.R. Buseck, J.M. Cowley and L. Eyring (Oxford University Press, New York, 1988) Chap.8.
- [11] P.A. Goodman and A. F. Moodie, *Acta Cryst. A30* (1974) 280.
- [12] J.M. Cowley, see Ref. 10, Chaps. 1-4.
- [13] D.J. Smith, *Adv. Opt. El. Microsc.* 11 (1989) 1.
- [14] C.J. Humphreys and J.C.H. Spence, *Optik* 58 (1981) 125.
- [15] W.O. Saxton, A. Howie, A. Mistry and A. Pitt, *Inst. Phys. Conf. Ser.* 36 (1977) 119.
- [16] T. Hoche, P.R. Kenway, H.-J. Kleebe and M. Ruhle, *MRS Symp. Proc.* 295 (1993) 103.
- [17] S. Horiuchi, T. Matsui, Y. Kitami, M. Yokoyama, S. Suehara, X.J. Wu, I. Matsui, and T. Katsuta, *Ultramicroscopy* 39 (1991) 231.
- [18] H. Lichte, *Ultramicroscopy* 38 (1991) 13.
- [19] D. Van Dyck, M. Op de Beeck and W. Coene, *Optik* 93 (1993) 103.
- [20] W. Coene, G. Janssen, M. Op de Beeck and D. Van Dyck, *Phys. Rev. Lett.* 69 (1992) 3743.
- [21] M.A. O'Keefe, U. Dahmen and C.J.D. Hetherington, *MRS Symp. Proc.* 159 (1990) 453.
- [22] J.M. Cowley and A.F. Moodie, *Proc. Phys. Soc. (London)* B70 (1957) 486.
- [23] S. Iijima and M.A. O'Keefe, *J. Microscopy* 117 (1979) 347.
- [24] A. Thust and K. Urban, *Ultramicroscopy* 45 (1992) 23.
- [25] D.J. Smith, L.A. Bursill and G.J. Wood, *J. Solid State Chem.* 50 (1983) 51.
- [26] K.L. Merkle and D.J. Smith, *Ultramicroscopy* 22 (1987) 57.
- [27] V. Ramikumar and V. Dravid, *MRS Symp. Proc.* 295 (1993) 115.
- [28] M.J. Kim, R.W. Carpenter, Y.L. Chen and G.H. Schwutke, *Ultramicroscopy* 40 (1992) 258.
- [29] A. Bourret, J. Desseaux and A. Renault, *Phil. Mag. A45* (1982) 1.

[30] C. D'Anterroches and A. Bourret, *Phil. Mag. A* 49 (1984) 783.

[31] A. Bourret, J.L. Rouviere and J.M. Penisson, *Acta Cryst. A* 44 (1988) 838.

[32] S. McKernan and C.B. Carter, *MRS Symp. Proc.* 295 (1993) 173.

[33] D. Cherns, J.C.H. Spence, G.R. Anstis and J.L. Hutchison, *Phil. Mag. A* 46 (1982) 849.

[34] A. Catana, P.E. Schmid, P. Lu and D.J. Smith, *Phil. Mag. A* 66 (1992) 933.

[35] P. Lu and D.J. Smith, *Surf. Sci.* 254 (1991) 119.

[36] J.C. Barry, *Phil. Mag. A* 64 (1991) 111.

[37] W.E. King and G.H. Campbell, *MRS Symp. Proc.* 295 (1993) 83.

[38] G.H. Campbell, W.L. Wien, W.E. King, S.M. Foiles and M. Ruhle, *Ultramicroscopy* 51 (1993) 247.

[39] J.M. Penisson, T. Nowicki and M. Biscondi, *Phil. Mag. A* 58 (1988) 947.

[40] D.L. Medlin, M.J. Mills, W.M. Stobbs, M.S. Daw and F. Cosandey, *MRS Symp. Proc.* 295 (1993) 91.

[41] U. Dahmen, C.J.D. Hetherington, M.A. O'Keefe, K.H. Westmacott, M.J. Mills, M.S. Daw and V. Vitek, *Phil. Mag. Letts.* 62 (1990) 327.

[42] M.J. Mills, M.S. Daw, G.J. Thomas and F. Cosandey, *Ultramicroscopy* 40 (1992) 247.

[43] M.R. McCartney, R.A. Youngman and R.G. Teller, *Ultramicroscopy* 40 (1992) 291.

[44] M.I. Buckett, J.P. Shaffer and K.L. Merkle, *MRS Symp. Proc.* 295 (1993) 109.

[45] L.D. Marks, *Surf. Sci.* 139 (1983) 281.

[46] W.O. Saxton and D.J. Smith, *Ultramicroscopy* 18 (1985) 39.

[47] W.E. King and B.S. Lamver, in: *Microbeam Analysis - 1991*, Ed. D.G. Howitt (San Francisco Press, San Francisco, 1991) p. 217.

[48] J.F. Banfield, D.R. Veblen and D.J. Smith, *Amer. Mineral.* 76 (1991) 343.

[49] W. Dong, T. Baird, J.R. Fryer, C.J. Gilmore, D.D. MacNicol, G. Bricogne, D.J. Smith, M.A. O'Keefe and S. Hovmøller, *Nature* 355 (1992) 605.

[50] J.J. Hu and F.H. Li, *Ultramicroscopy* 35 (1991) 339.

[51] S. Hovmøller, A. Sjogren, G. Farrants, M. Sundberg and B.-O. Marinder, *Nature* 311 (1984) 238.

[52] J.J. Hu, F.H. Li and H.F. Fan, *Ultramicroscopy* 41 (1992) 387.

[53] K.H. Downing, H. Meisheng, H.-R. Wenk and M.A. O'Keefe, *Nature* 348 (1992) 525.

[54] W.O. Saxton, *Computer Techniques for Image Processing in Electron Microscopy* (Academic, New York, 1978).

[55] O.L. Krivanek, *Optik*, 45 (1976) 97.

[56] A.R. Glanville, A.F. Moodie, H.J. Whitfield and I.J. Wilson, *Aust. J. Phys.* 39 (1985) 71.

[57] W.M.J. Coene and T.J. Denteneer, *Ultramicroscopy* 38 (1991) 225.

[58] H. Lichte, *Ultramicroscopy* 51 (1993) 15.

[59] W.O. Saxton, D.J. Smith and S.J. Erasmus, *J. Microscopy* 130 (1983) 187.

[60] A.J. Koster and W.J. de Ruijter, *Ultramicroscopy* 40 (1992) 89.

[61] O.L. Krivanek and P.E. Mooney, *Ultramicroscopy* 49 (1993) 95.

[62] I. Daberkow, K.-H. Herrmann, L.B. Liu and W.D. Rau, *Ultramicroscopy* 38 (1991) 215.

[63] W.J. de Ruijter and J.K. Weiss, *Rev. Sci. Insts.* 63 (1992) 4314.

[64] W.J. de Ruijter and J.K. Weiss, *Ultramicroscopy* 50 (1993) 269.

[65] M. Gajdardziska-Josifovska, W.J. de Ruijter, M.R. McCartney, D.J. Smith, J.K. Weiss and J.M. Zuo, *Ultramicroscopy* 50 (1993) 285.

[66] A. Ourmazd, F.H. Baumann, M. Bode and Y. Kim, *Ultramicroscopy* 34 (1990) 237.

[67] J.M. Penisson, F.H. Baumann, M. Bode and A. Ourmazd, *Phil. Mag. Letts.* 64 (1991) 239.

[68] A. Ourmazd, D.W. Taylor, M. Bode and Y. Kim, *Science* 246 (1989) 1571.

[69] S. Paciornik, R. Kilaas and R. Gronsky, *Ultramicroscopy* 50 (1993) 255.

[70] J.M. Gibson and M.L. McDonald, *MRS Symp. Proc.* 82 (1987) 109.

[71] W.M. Stobbs and W.O. Saxton, *J. Microscopy* 151 (1988) 88.

[72] M.R. McCartney and M. Gajdardziska-Josifovska, *Ultramicroscopy*, in press.

[73] D. Van Dyck, in: *Proc XIth. Int Cong. E. M. (Seattle, 1990)* Vol.1, 26.

[74] L.W. Hobbs, in: *Quantitative Electron Microscopy*, Eds. J.N. Chapman and A.J. Craven (SUSSP Publications, Edinburgh, 1984) Chapter 11.

[75] A.R. Smith and L. Eyring, *Ultramicroscopy* 8 (1982) 65.

[76] D. Hofmann and F. Ernst, *Ultramicroscopy*, in press.

[77] D.J. Smith, W.J. de Ruijter, M.R. McCartney and J.K. Weiss, *Ultramicroscopy* 52 (1993) 591.

PART II

Dynamic Properties at Nanoscale

FLUX LINE DYNAMICS WITH ELECTRON HOLOGRAPHY

AKIRA TONOMURA

Advanced Research Laboratory, Hitachi, Ltd. &
Tonomura Electron Wavefront Project, ERATO, JRDC
Hatoyama, Saitama 350-03, Japan

ABSTRACT

Flux lines in superconducting thin films are observed statically in a holographic electron interference micrograph, and dynamically in a Lorentz micrograph with a "coherent" and 300kV electron beam. In interference microscopy, projected magnetic lines of force in a tilted Nb thin film are observed quantitatively as contour fringes drawn on an in-focus electron micrograph. Whereas in Lorentz microscopy, flux lines are observed as spots with bright and dark contrast pairs due to defocusing of the image. Although the image is blurred due to a large amount of defocusing, this method is suitable for real-time observation. By making the best use of this feature, flux line movement can be observed when the applied magnetic field or the film temperature changes.

INTRODUCTION

Magnetic flux penetrates type-II superconductors in the form of a thin filament called a "flux line" or a "vortex". Flux lines prevent the superconductive state from breaking down until when a superconductor is filled with flux lines with the application of a higher magnetic field. The applied current exerts a Lorentz force on the flux lines. When this force overcomes the pinning force, flux lines begin to flow and the superconductive state breaks down. The study of flux-line behavior is important for practical applications of superconductivity in that this behavior determines the critical current of a superconductor. Unfortunately, flux lines are difficult to observe directly because they are extremely thin filaments, 300Å in radius in the case of Nb, and have a small flux value of $h/2e$. So far, several methods of observation have been developed. For example, in the Bitter method [1] magnetic powder is sprinkled on the superconductor surface, and the accumulated powder is then observed as a replica by using electron microscopy. A scanning tunneling microscope can distinguish normal and superconducting regions by detecting the tunneling current between a tip and a superconductor surface [2]. Magnetic fields above a superconductor surface are measured by a scanning Hall probe microscope [3].

The present paper describes observation results for individual flux lines obtained by using electron holography and Lorentz microscopy.

EXPERIMENTAL METHOD

Flux lines appear as phase objects to illuminating electron beams, and consequently, cannot be observed in electron micrographs, where only the electron intensity is detected. The phase shift caused by a flux line can be observed by directly measuring the phase distribution in a holographic interference micrograph [4].

In the first step of holography (Fig. 1(a)), an interference pattern is formed between an object wave and a reference wave in a field-emission electron microscope, and recorded on film as a hologram. This film hologram is subsequently illuminated by a collimated laser beam (Fig. 1(b)). The exact image is produced three-dimensionally in a diffracted beam. An additional image called a "conjugate image" is also produced in holography, which has the same amplitude in magnitude, but has the opposite sign.

An interference micrograph, or contour map of the wavefront, can be obtained by simply overlapping an optical plane wave with this reconstructed wave (see Fig. 2(a)). If a conjugate image instead of a plane wave overlaps this wavefront, the phase difference becomes twice as large, and is as if the phase distribution were amplified two times, as shown in Fig. 2(b). By repeating this technique, a phase shift can be detected even as small as 1/100 of the wavelength. This phase-amplified interference electron microscopy provides information about microscopic distribution of electromagnetic fields.

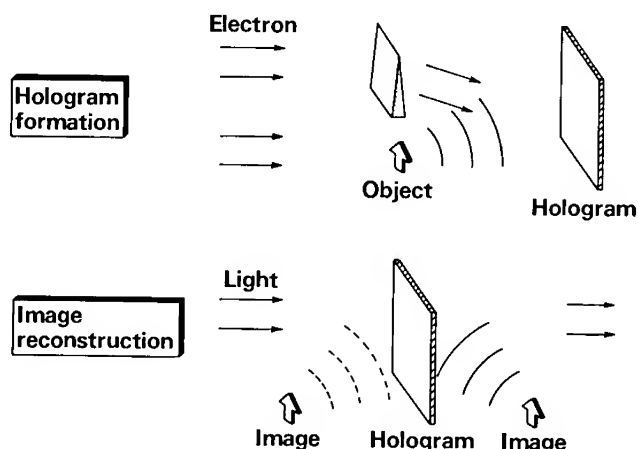


Fig. 1 Principle behind electron holography.

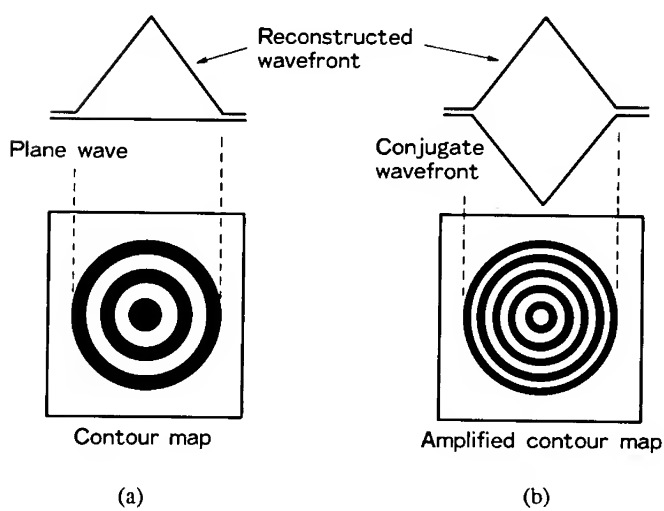


Fig. 2 Principle behind phase amplification.
(a) Contour map. (b) Twice-amplified contour map.

When a parallel electron beam is incident on a uniform magnetic field, the beam is deflected to the right by the Lorentz force which acts perpendicular to the direction of the magnetic field as shown in Fig. 3. When the electron beam is viewed as a wave, the introduction of a wavefront perpendicular to the electron trajectory will suffice. The incident electron beam is a plane wave, but the outgoing beam becomes a plane wave with the right side up. In other words, the wavefront is viewed as having revolved around a revolving axis, the magnetic line of force. From the contour map of this wavefront, we see that the contour lines follow the magnetic line of force. This is because the height of the wavefront is the same along the magnetic line of force. Thus, we reach this very simple conclusion. When a magnetic field is observed as an interference electron micrograph, the contour fringe can be considered to be a magnetic line of force.

To be more exact, we have to calculate a phase shift of an electron beam from the Schrödinger equation: The phase difference $\Delta\phi$ between two beams passing through two points A and B in a magnetic object is given by

$$\Delta\phi = \frac{e}{\hbar} \oint A ds = \frac{e}{\hbar} \int B ds = -\frac{e}{\hbar} \Phi, \quad (1)$$

where the first integral of vector potential A is carried out along a closed loop connecting the two electron paths and the second integral of magnetic field B is carried out over the surface enclosed by the closed loop.

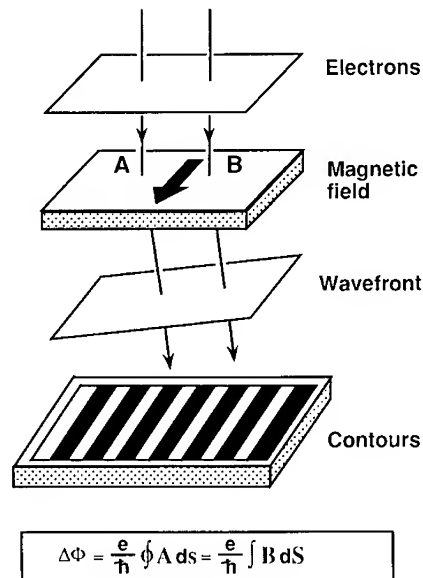


Fig. 3 Principle behind magnetic line observation by interference electron microscopy.

It can be concluded from this equation that the electron interference micrograph is quantitative. A constant amount of minute magnetic flux, h/e , is flowing between adjacent contour fringes. This is, in a sense, quite natural. A superconductive flux meter, SQUID, can measure the flux units of $h/2e$ by using Cooper pair interference. The electron interference micrograph is formed due to the interference, not of Cooper pairs, but of electrons. In our case, the flux unit becomes h/e , since the electric charge is changed from $2e$ to e . The principle is the same between the two. When a magnetic field is observed in a twice phase-amplified interference micrograph, contour fringes in the micrograph indicate projected magnetic lines of force in $h/2e$ flux units.

Although the holography process is an off-line process, phase modulation can also be observed by defocusing an electron micrograph in the case of the observation of flux lines in a superconductor. The principle behind this observation method can be roughly explained as follows. When an electron beam is incident perpendicular to a flux line, the beam is deflected by a Lorentz force. Therefore, when the electron intensity distribution is observed in the defocused plane, the electron beam transmitted through the flux line is shifted and produces a pair of bright and dark regions.

EXPERIMENTAL RESULTS

Flux lines were statically and dynamically observed through both interference microscopy and Lorentz microscopy.

Observation of flux lines penetrating a superconductor

Magnetic lines of force leaking out from flux lines in a superconductor can be directly observed as contour fringes in a twice phase-amplified interference micrograph [5]. The experimental arrangement is shown in Fig. 4. A magnetic field of a few gauss or less was applied perpendicularly to an evaporated lead film. The specimen was then cooled to 4.5 K. In a weak magnetic field, magnetic lines are excluded from the superconductor by the Meissner effect, but if the magnetic field is strong, the magnetic lines of force penetrate the superconductor in the form of flux lines. By applying an electron beam to the specimen from above, we can observe the magnetic lines of force through electron holography.

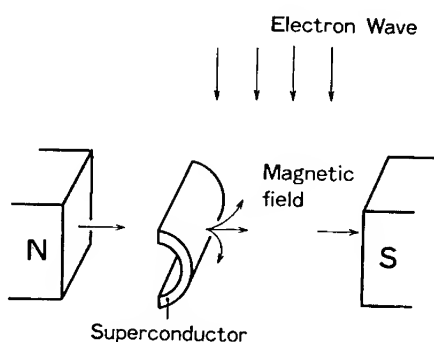


Fig. 4 Experimental arrangement for observing flux lines.

Figure 5(a) shows the flux lines observed when the superconducting film was 0.2 μm thick. In this figure, the phase difference is amplified by a factor of two. Therefore, one interference fringe corresponds to one flux line. A single flux line is captured at the right side of this photograph. The magnetic line of force is produced from an extremely small area of the lead surface, then spreads out into free space.

In addition to observing isolated flux lines, we found a pair of flux lines oriented in opposite directions and connected by magnetic lines of force (left side in Fig. 5 (a)). When the specimen is cooled below the critical temperature, the lead becomes superconductive. During the cooling, however, the specimen experiences a state where the flux-line pair appears and disappears repeatedly due to thermal excitation. Finally, it is pinned by some imperfection in the superconductor, and eventually results in the flux being frozen.

What happens when the thickness of the superconducting thin film is increased? Figure 5 (b) shows the state of the magnetic lines of force when the thickness is 1 μm . We can see that the flux state changes completely. Magnetic flux penetrates the superconductor not as individual flux lines, but in a bundle. This figure does not show any flux-line pairs. Since lead is a type-I superconductor, the strong magnetic field applied to it partially destroys the superconductive state in some parts of the specimen (intermediate state). Figure 5 (b) shows that the magnetic lines of force penetrate the parts of the specimen where superconductivity has been destroyed. However, since the surrounding parts are still superconductive, the total amount of penetrating magnetic flux is an integral multiple of the flux quantum, $h/2e$. Thin superconductor film (Fig. 5(a)) is an exception and flux penetrates the superconductor in the form of individual flux lines.

Since the flux itself can be observed by using electron holography, its dynamic behavior can also be observed. In this case, after the electron holograms were dynamically recorded on videotape, a twice phase-amplified contour map of each frame was numerically reconstructed and again recorded on videotape. After this process, flux-line dynamics could be observed with a time resolution of 1/30 of a second.



Fig. 5 Interference micrographs of flux lines leaking from Pb film
(Phase amplification: $\times 2$). (a) Thickness = 0.2 μm . (b) Thickness = 1 μm .

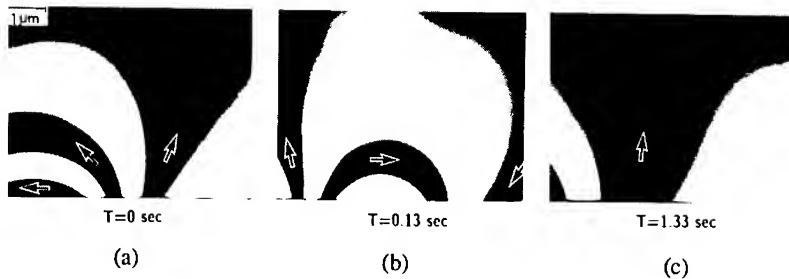


Fig. 6 Dynamic observation of trapped flux lines near T_c .
 (a) 0 seconds. (b) 0.13 seconds later. (c) 1.33 seconds later.

While trapped fluxes in a Pb thin film remained stationary at 5 K, when the sample temperature was raised, the flux diameter gradually increased. The fluxes began to move just below the critical temperature. Figure 6 shows a section from the videotape of this movement.

Although flux movement due to thermal activation is random, a similar experiment was made where a current was applied to a superconductor [6]. A Lorentz force, as determined by the current, was exerted in opposite directions for upward and downward fluxes. The pinning force at each pinning site could thus be measured.

Direct observation of flux lines in a superconducting thin film

In the above-mentioned method, an electron beam passes near the superconductor surface so that we can observe magnetic flux sticking out from the surface. However, neither a two-dimensional array of flux lines nor the inside structure of the superconductor can be observed.

Recently, our 350-kV holography electron microscope [7], has been enhanced to provide a more "coherent" electron wave. This has made it possible to observe both the static images of flux-line arrays by using holographic interference microscopy and their dynamic behavior using by Lorentz microscopy.

The experimental arrangement is shown in Fig. 7. A Nb thin film, set on a low-temperature stage, was tilted 45° to an incident beam of 300-keV electrons so that the electrons could be affected by the flux-line magnetic fields. An external magnetic field of up to 150 gauss was applied horizontally. An example of a flux-line array in a single-crystalline Nb thin film [8] is shown in Fig. 8. In this interference micrograph, projected magnetic lines of force are observed. They become dense in the localized regions indicated by circles in the photograph, which correspond to individual flux lines.

Lorentz microscopy is more convenient for observing the dynamic behavior of flux lines. In this experiment, the sample was first cooled down to 4.5 K and the applied magnetic field, B , was gradually increased. As B increased, flux lines suddenly began to penetrate the film at $B = 32$ gauss, and their number increased as B increased. Their dynamic behavior was quite interesting. At first, only a few flux lines appeared here and there in the field of view, $15 \times 10 \mu\text{m}^2$. They oscillated around their own pinning centers and occasionally hopped from one center to another. These movements continued as long as the flux lines were not closely packed ($B \leq 100$ gauss).

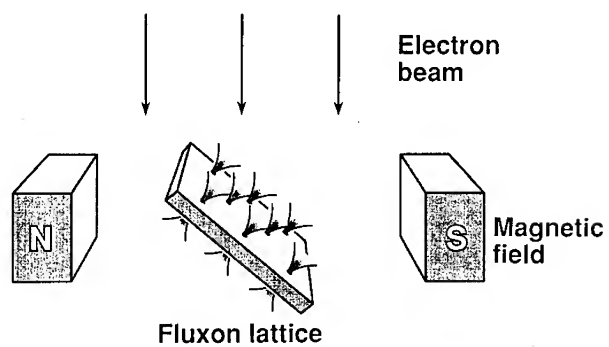


Fig. 7 Schematic diagram for flux-line lattice observation.

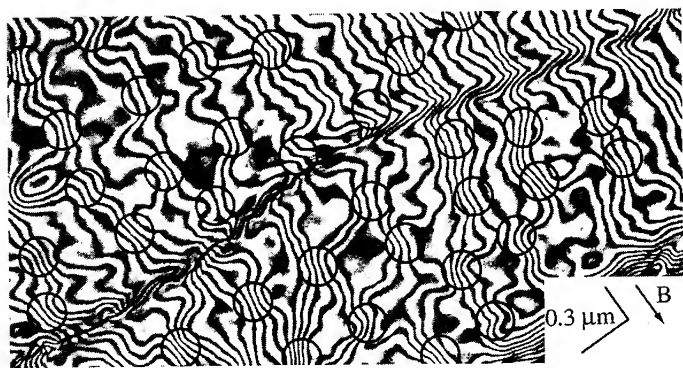


Fig. 8 Interference micrograph of a superconducting Nb film at $B = 100$ gauss
(Phase amplification: $\times 16$).

An equilibrium Lorentz micrograph at $B = 100$ gauss [9] is shown in Fig. 9. The film has a fairly uniform thickness in the region shown, but is bent along the black curves, called bend contours, which are due to Bragg reflections at the atomic plane brought to a favorable angle by bending. Each spot with black and white contrast is the image of a single flux line. This contrast reversed, as expected, when the applied magnetic field was reversed. The tilt direction of the sample can be read from the line dividing the black and white parts of the spots. Since the black part is on the same side of all the spots, the polarities of all the flux lines seen in the region are the same.

At low B , i.e., up to 30 - 50 gauss, the flux lines are too sparse to form a lattice, even in equilibrium. At $B = 100$ gauss, where the flux-line density is so high that it cannot be anything but a hexagonal lattice, the flux-line configuration and movement are influenced by structural defects.

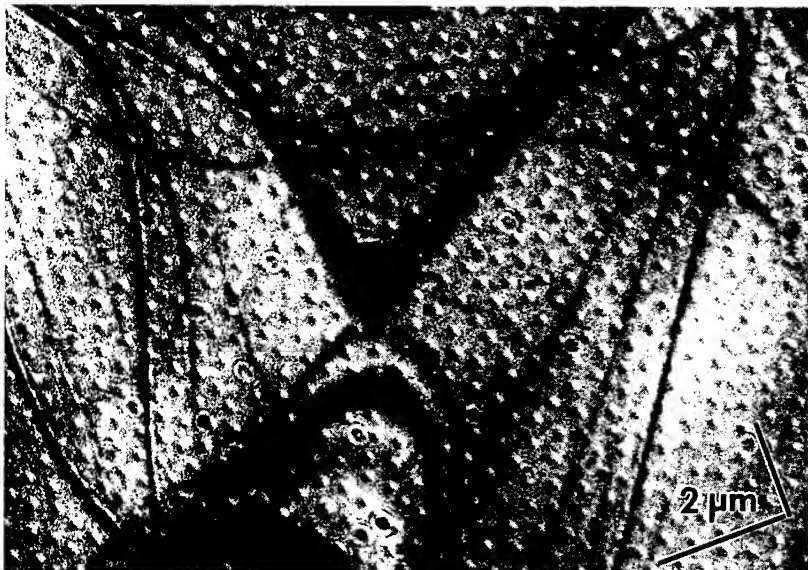


Fig. 9 Lorentz micrograph of a two-dimensional array of flux lines in a superconducting Nb film.

CONCLUSION

Individual flux lines in a superconductor have been directly and dynamically observed for the first time by using a "coherent" field-emission electron beam. This technique can be used to clarify the fundamentals and practical applications of superconductivity, especially in the field of high-T_c superconductors.

REFERENCES

- [1] V. Essman and H. Träuble, Phys. Lett., **A24**, 526 (1967).
- [2] H. F. Hess, et al., Phys Rev. Lett., **62**, 214 (1989).
- [3] H. D. Hallen, et al., Phys. Rev. Lett., **71**, 3007 (1993).
- [4] A. Tonomura, Rev. Mod. Phys., **59**, 637 (1987).
- [5] T. Matsuda et al., Phys. Rev. Lett., **62**, 2519 (1989).
- [6] T. Yoshida, et al., in Proc. 50th Ann. Meet. Electron Microsc. Soc. Amer., edited by G. W. Bailey (San Francisco Press, San Francisco, 1992) pp. 68-69.
- [7] T. Kawasaki, et al., Jpn. Appl. Phys., **29**, L508 (1990).
- [8] J. Bonevich, et al., Phys. Rev. Lett., **70**, 2952 (1993).

ANALYSIS OF INTERFACE DYNAMICS IN SOLID-STATE PHASE TRANSFORMATIONS BY *IN SITU* HOT-STAGE HIGH-RESOLUTION TRANSMISSION ELECTRON MICROSCOPY

JAMES M. HOWE, W. E. BENSON, A. GARG* and Y.-C. CHANG**

Department of Materials Science and Engineering, University of Virginia, Charlottesville, VA 22903, U.S.A.

*NASA Lewis Research Center, 21000 Brookpark Road, Cleveland, OH 44135, U.S.A.

**Aeronautical Research Laboratory, Chung-Shan Institute of Science and Technology, P.O. Box 90008-11-12, Taichung City, Taiwan, R.O.C.

ABSTRACT

In situ hot-stage high-resolution transmission electron microscopy (HRTEM) provides unique capabilities for quantifying the dynamics of interfaces at the atomic level. Such information is critical for understanding the theory of interfaces and solid-state phase transformations. This paper provides a brief description of particular requirements for performing *in situ* hot-stage HRTEM, summarizes different types of *in situ* HRTEM investigations and illustrates the use of this technique to obtain quantitative data on the atomic mechanisms and kinetics of interface motion in precipitation, crystallization and martensitic reactions. Some limitations of *in situ* hot-stage HRTEM and future prospects of this technique are also discussed.

INTRODUCTION

The purpose of this paper is to demonstrate the capabilities of *in situ* high-resolution transmission electron microscopy (HRTEM) for quantifying interface dynamics in solid-state phase transformations, as well as to point out limitations and future prospects of this technique. The availability of single and double-tilt hot-stage specimen holders for medium-voltage transmission electron microscopes with point-to-point resolutions of about 0.2 nm means that many laboratories can perform *in situ* HRTEM studies. However, this technique has not yet achieved widespread use in materials science. This may be due to difficulties often encountered in performing *in situ* experiments [1] such as surface effects and limited specimen tilt, or to anticipated detrimental effects on the microscope such as contamination and prolonged high-temperature exposure. These are potential problems, but like most experimental techniques, *in situ* hot-stage HRTEM can be performed for a wide variety of important materials science problems that can be readily interpreted and which do not degrade the microscope quality.

REQUIREMENTS

The specimen and microscope requirements for *in situ* hot-stage HRTEM imaging are no different from those of static HRTEM, except that one must have a heating holder and some method of recording and analyzing dynamic images. At present, most HRTEMs are equipped with a TV-rate camera containing a fiber optically coupled yttrium aluminum garnet (YAG) crystal, possibly combined with a charge-coupled device (CCD) camera [2,3]. The simplest and least expensive way to record *in situ* HRTEM images is to send the output from the TV-rate camera directly into a standard videocassette recorder (VCR) [4]. The quality and cost of this method of storage varies with the type of recorder, but a reasonably good VHS format VCR with videocassette tapes can be used to store hours of *in situ* studies for very low cost. The images can then be analyzed directly during playback or sent to a computer for image processing and analysis. More expensive digital recording methods are necessary if quantitative image intensities are required for analysis.

It is important to note that TV-rate cameras acquire 30 frames per second, so that the time resolution of the videorecording is 1/30th of a second. Since 30 frames are acquired per second, drift is not much of a problem unless it is severe. In order to obtain static images, it is often necessary to average over several frames, either by photographing the TV screen at exposures of about 1/8th of a second, or by superimposing several frames in the computer. This limits the time resolution of an *in situ* study to 1/30th of a second at best and often less. As shown in a later example, this may not be sufficient to capture the desired atomic processes involved in a reaction.

The most versatile specimen holder for materials science applications is a double-tilt hot-stage and a few manufacturers offer such holders. The specifications vary, but a holder of this type can usually achieve a temperature of about 800°C with ± 10 degrees tilt. This type of holder was used in the example studies which follow. Single-tilt hot-stages are more common and available for most HRTEMs [5]. These generally possess a wider range of tilt, at least ± 25 degrees along one axis, and slightly higher temperature capability (1000°C for example), but the lack of a second axis of tilt can preclude many potential materials science studies. As in static HRTEM, the area of interest must be in a zone axis orientation in order to interpret the atomic structure in the images and therefore, tilting capability is critical for *in situ* hot-stage HRTEM. Specimens such as metals often bend during heating, further emphasizing the need for double-tilt capability. Knowing the specimen temperature in the area of interest is critical for quantitative studies and this can vary from the hot-stage thermocouple output depending on the thermal conductivity of the sample and how well it is in contact with the furnace base. Fortunately, in some cases the sample itself can be used to calibrate the temperature, as in the example of the Al-Cu-Mg-Ag system discussed below, where the solvus temperature of the alloy is well known [6] and can be used to provide an internal calibration. Except in unusual cases, the sample temperature is usually within about 25°C of the thermocouple readout.

TYPES OF *IN SITU* HOT-STAGE HRTEM STUDIES

The number of different types of phase transformation studies that can be examined by *in situ* hot-stage HRTEM is almost endless and a list of some possibilities is shown in Table I below. References are also provided for areas which have been investigated by *in situ* HRTEM. It is important to note that many of these areas have been previously investigated by *in situ* hot-stage TEM, but not at high-resolution, and the book by Butler and Hale [1] summarizes a number of studies. Much of the research employing *in situ* hot-stage HRTEM has been performed by Sinclair et al. [7] on Si, compound semiconductors and multilayer materials, where the orientation could be controlled to facilitate analysis in a single-tilt holder.

Table I. Some types of transformation amenable to study by *in situ* hot-stage HRTEM.

Order/disorder reactions	Twin/martensite motion [16]
Grain-boundary motion [8]	Oxidation/reduction [17,18]
Melting/freezing of materials [9]	Dislocation motion
Precipitation/dissolution [10,11]	Faceting/roughening transitions [19]
Interfacial reaction [4,12]	Decomposition and nucleation in solids
Crystallization [13-15]	Coarsening/Sintering [20]

QUANTITATIVE *IN SITU* HOT-STAGE HRTEM

Examples of three different types of *in situ* hot-stage HRTEM studies, which illustrate the quantitative nature of this technique and also some limitations, are shown below. The samples in these studies were examined at 400 kV in a JEOL 4000EX microscope equipped with a UHP40X hot-stage pole piece ($C_s = 1.1$ mm, point-to-point resolution 0.18 nm) and a top-entry double-tilt

($\pm 10^\circ$) specimen holder using temperatures generally in the range of 180-450°C. Images were recorded on a Sony BetaCam videocassette recorder connected to a Gatan fiber-optically coupled TV camera with an image intensifier. A 35 mm camera with a 1/8 s exposure was used to obtain photographs directly from the TV monitor during playback of the videocassettes and kinetic data were obtained during playback of the videocassettes. Further details regarding the alloys and specimen preparation are provided elsewhere [10,12,16].

Precipitation in the Al-Cu-Mg-Ag System

It is now well established that precipitate plates usually grow by some type of ledge mechanism [21,22] and that atomic attachment to ledges can occur at highly localized sites such as at kinks in the ledges [23], i.e., the so-called terrace-ledge-kink mechanism [24]. This picture has emerged from a combination of data obtained by conventional and *in situ* hot-stage TEM and static HRTEM studies on a variety of alloy systems [25]. However, to date, there have been no direct *in situ* HRTEM studies of precipitate plate growth mechanisms and interface dynamics at the atomic level. This section describes initial results on the atomic mechanisms of θ -Al₂Cu precipitate plate growth in an Al-Cu-Mg-Ag alloy obtained by *in situ* hot-stage HRTEM experiments performed both parallel and perpendicular to the plate faces. It is particularly useful to examine interfaces from several different orientations in order to determine their three-dimensional structure, as demonstrated in this study. The θ plates in this alloy have a $\{111\}_\alpha$ habit plane due to the addition of Mg and Ag to the alloy [26] and are often referred to as Ω phase [26-28].

The experimental results are divided into two parts, the first dealing with structural aspects of the θ plates and the second, concerning kinetic aspects of plate growth. Further, within each of these parts, observations made along a $\langle 121 \rangle_\alpha$ matrix direction parallel to the plate faces are discussed first, followed by experimental results obtained by examining the plates perpendicular to the faces along a $\langle 111 \rangle_\alpha$ matrix direction. The orientation relationship (OR) for this $\{111\}_\alpha$ variant of θ -Al₂Cu phase is $(\bar{1}10)_\theta \parallel (111)_\alpha$, $[110]_\theta \parallel [10\bar{1}]_\alpha$ and $[001]_\theta \parallel [1\bar{2}1]_\alpha$, which is a low-energy OR relationship for θ phase found previously by Vaughan and Silcock [29] and designated as a Vaughan II (V.II) type OR. The relationship between the Ω and θ phase has been discussed previously [30,31].

Structural Analysis Along $[001]_\theta \parallel [1\bar{2}1]_\alpha$

Figure 1 shows a HRTEM image of a ledge on the face of a θ plate viewed edge-on along a $[001]_\theta \parallel [1\bar{2}1]_\alpha$ direction. The ledge is approximately two $\{111\}_\alpha$ matrix planes high, or half of a unit cell of the θ (or Ω) structure (0.424 nm). This was the smallest ledge size that was observed on the faces of the θ plates and higher ledges were often observed [31,32]. The image was photographed from the videocassette during *in situ* growth at about 220°C and the ledge was observed to oscillate several times per second over a distance of about two unit-cells of the θ phase along the precipitate face while moving slowly across the face with constant overall velocity toward the precipitate edge in the direction indicated by an arrow. *In situ* experiments performed perpendicular to the plate face indicate that the oscillatory motion is due to the formation and annihilation of kinks along the ledge, as demonstrated in the next section. The videocassette recording also revealed direct experimental evidence of enhanced atomic motion in the matrix just ahead of the ledge and this leads to slight blurring in the photograph [33], which is visible in the enclosed area in Fig. 1. It is important to note that the precipitate structure only one unit cell behind the ledge appears completely transformed, indicating that the structural and compositional changes which are necessary for diffusional growth occur simultaneously within a few atomic distances of the ledge. This is further confirmed by the results in the next section. *In situ* HRTEM studies of ledges that were stacked vertically at the precipitate edges revealed similar features such as enhanced atomic motion at the interface and oscillatory motion of ledges, but the oscillatory motion appeared to occur cooperatively among groups of ledges, with the edge moving by

intermittent rapid motion of all of the ledges at the edge simultaneously rather than by smooth, constant motion.

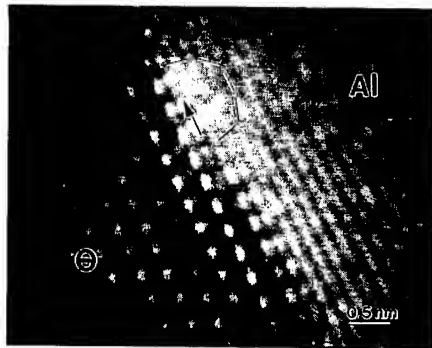


Figure 1. HRTEM image of a ledge on a θ plate during growth at about 220°C.

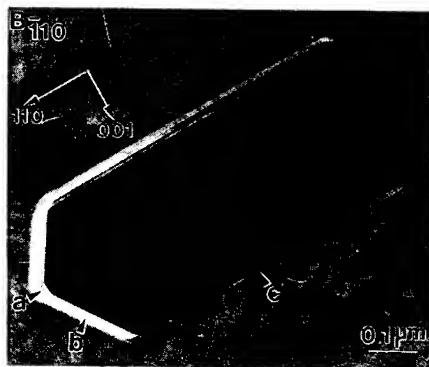


Figure 2. TEM image of a θ plate showing facets and elongation along the $[110]_\theta$ direction.

Structural Analysis Along $[110]_\theta \parallel [111]_\alpha$

Figure 2 shows a bright-field TEM image of a θ plate viewed face-on along a $[110]_\theta \parallel [111]_\alpha$ direction during an *in situ* hot-stage experiment at about 275°C. The $\{111\}_\alpha$ θ plates tend to form with two types of morphology, the most common being a hexagonal shape with facets along the $\langle 121 \rangle_\alpha$ matrix directions [28], and the other being octagonal, often with a long direction along $[110]_\theta \parallel [10\bar{1}]_\alpha$ and a $(001)_\theta \parallel (1\bar{2}1)_\alpha$ facet perpendicular to this direction [32,34]. The plate shown in Fig. 2 is of the second type, as indicated by the θ directions labelled on the figure, and images of the three facets labelled a, b and c in Fig. 2 taken during the *in situ* hot-stage HRTEM experiment are shown together in Fig. 3. The contrast from the matrix and precipitate in the three images is not identical due to the slightly different defocus values of the objective lens in each image but the prominent rectangular pattern of white spots which is outlined in each of the three images in Fig. 3 relates directly to positions of Cu atoms in the θ structure, as determined by HRTEM image simulation [35] and illustrated by the inset $[110]_\theta \parallel [111]_\alpha$ projection of the θ structure on the right side of Fig. 3, where the rectangular pattern of the Cu atoms, which are shown as filled circles, is also outlined.

In the *in situ* hot-stage HRTEM experiments, the θ plate was observed to grow by the nucleation of half unit-cell high (0.429 nm) double kinks along the $(110)_\theta \parallel (10\bar{1})_\alpha$ edge of the plate in Fig. 3(a), which then propagated along the edge until they reached the intersection of the $(332)_\theta \parallel (2\bar{1}1)_\alpha$ facet, where they then stopped about one and a half unit-cells (0.731 nm) behind the previous kink to preserve the $(332)_\theta$ orientation, as shown in Fig. 3(b). The smallest kinks were one-half of the θ unit cell in height (one rectangular pattern of white spots about 0.429 nm long) but sometimes two or three kinks nucleated and/or dissolved in rapid succession in an oscillatory manner about an average position, similar to the behavior described for the ledge in Fig. 1. Evidence of this oscillatory behavior is visible by the diffuse kink indicated by an arrow in Fig. 3(a). The $(001)_\theta \parallel (1\bar{2}1)_\alpha$ facet in Fig. 3(c) is roughly flat and composed of kinks which lie adjacent to one another along the interface. The information provided by the three images in Fig. 3 shows that the morphology of the θ plate within the $\{111\}_\alpha$ habit plane is determined by the density of kinks along a particular interface [23,36] and that nucleation of kinks along the $(110)_\theta$ edge is necessary for lengthening of the precipitate.

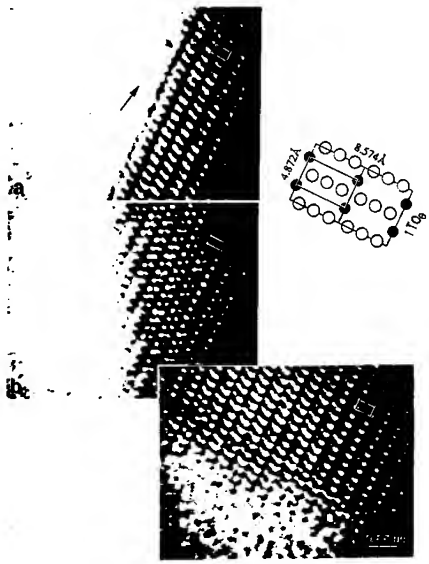


Figure 3. Three HRTEM images taken at locations a, b, and c in Fig. 2.

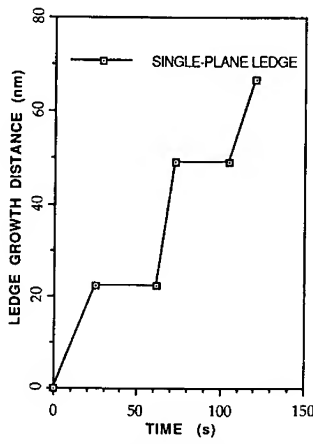


Figure 4. Growth behavior of a half unit-cell ledge (0.424 nm high) on a θ plate face.

Kinetic Analysis Along $[001]_{\theta} \parallel [1\bar{2}1]_{\alpha}$

The velocities of a number of different ledges which migrated across the plate faces during the *in situ* HRTEM studies were measured from the videocassette recordings and four are shown in Table II.

Table II. Velocities and conditions of ledges migrating across θ plate faces.

Ledge Sequence	Temperature (°K)	Ledge Height (nm)	Ledge Velocity (nm/s)	Experimental Diffusivity (cm ² /s)
1	455	0.424	1.92	5.2×10^{-12}
		1.270	1.53	1.2×10^{-11}
2	488	1.690	1.02	1.1×10^{-11}
3	492	0.848	0.03	1.7×10^{-13}
4	493	0.424	0.90	2.4×10^{-12}
			2.54	6.7×10^{-12}
			1.14	3.1×10^{-12}

In some cases, such as for sequences 2 and 3, the velocities represent smooth constant motion of the ledges across the plate faces for the entire recording except for the local atomic motion at the edges mentioned previously. Other ledges, such as that in sequence 4, displayed periods of varying velocity in between times of little or no movement (Fig. 4). Such periodic lack of mobility during the migration of ledges has been observed previously and attributed to a lack of sites for atomic attachment along the ledges as they align along low-energy matrix directions, in this case $\langle 121 \rangle_{\alpha}$ [23]. In sequence 1, the velocity of a 0.424 nm leading ledge was faster than that of a

1.270 nm trailing ledge as theory would predict, although the velocity of the trailing ledge was not as slow as given by theory, which indicates that the velocity should vary inversely with the ledge height [37-39]. Several other types of behavior were observed and all ledges shared the common feature that they moved at rates that were too fast for volume diffusion control. For example, in the temperature range in Table I, the bulk diffusivity of Cu in Al is on the order of 10^{-15} to 10^{-16} cm²/s [40]. This is about 3 to 4 orders of magnitude less than most of the experimental diffusivities shown in Table I, which were back-calculated from the measured ledge velocities, v_l , using the simple expression in Eqn. (1) below [22,23,41]:

$$v_l = D (C_o - C_e) / [h_l \alpha(p) (C_p - C_e)] \quad (1)$$

where D is the solute interdiffusivity, C_o is the average matrix composition far from the interface, C_e is the matrix composition in equilibrium with the precipitate, C_p is the precipitate composition, h_l is the ledge height and $\alpha(p)$ is a parameter which represents an effective diffusion distance (~2). This result indicates that surface diffusion may be dominating the kinetic process of the ledges when the precipitates are edge on and intersect the surface of the thin foil in the *in situ* hot-stage HRTEM experiments. Such behavior has been observed in previous *in situ* hot-stage TEM studies on precipitate plates in Al-Ag and Al-Cu alloys [1, 42,43], where plate lengthening occurred 1 to 2 orders of magnitude faster than expected when precipitates intersected the foil surface.

Kinetic Analysis Along $[\bar{1}10]_{\theta} \parallel [111]_{\alpha}$

The velocity of the $(110)_{\theta}$ edge was measured as 0.047 nm/s at 275 °C (548 °K), the velocity of the $(001)_{\theta}$ edge was 0.025 nm/s and the velocity of the facet along $(322)_{\theta}$ was intermediate between these two values at 0.044 nm/s. At 275 °C the bulk diffusivity of Cu in Al is 3.5×10^{-13} cm²/s, which is substantially higher than the experimental diffusivity of 4.2×10^{-15} cm²/s, back-calculated from the lengthening rate of the $(110)_{\theta}$ plate edge using the Zener-Hillert equation [22] (Eqn. (1) with $h_l \alpha(p)$ replaced by $4r$, where r is the edge radius) and assuming a precipitate thickness of only one or two unit cells. Since the *in situ* hot-stage HRTEM results showed that nucleation and propagation of kinks along the $(110)_{\theta}$ edge are necessary for growth, the slow lengthening rate of the plate in this orientation can be attributed to the rate of nucleation of kinks on the $(110)_{\theta}$ edge. This nucleation process presents an interfacial barrier to lengthening, resulting in a growth rate that is slower than volume diffusion control [22,23]. Hence, it appears that when θ plates do not intersect the foil surface, reliable kinetic and mechanistic data can be obtained from the *in situ* HRTEM analyses. It is interesting to note that while the average lengthening rate of the $(110)_{\theta}$ plate edge was slower than volume diffusion control, the videocassette recordings indicate that oscillatory nucleation and dissolution (local fluctuations) of kinks along the interface may occur on a time scale that is much faster than diffusion control.

The results from the *in situ* hot-stage HRTEM analyses performed both parallel and perpendicular to the $\{111\}_{\alpha}$ θ plate faces demonstrate that the precipitates grow by a terrace-ledge-kink mechanism and that the structural and compositional changes in the diffusional reaction occur along a growing ledge simultaneously (at least within the resolution limits of the *in situ* HRTEM technique) within a volume as small as one-half of a unit cell of the θ phase along the $[\bar{1}10]_{\theta}$ and $[110]_{\theta}$ directions. This volume contains no more than about two atoms of Cu and ten atoms of Al. Lengthening of the precipitate along the $[110]_{\theta}$ direction requires the nucleation and propagation of kinks along the $(110)_{\theta}$ precipitate edge and the shape of the precipitate within the habit plane is obtained by varying the density of these kinks around the periphery. While the overall lengthening rate of the elongated plate studied was consistent with diffusion control limited by nucleation of kinks at the edge, the *in situ* hot-stage HRTEM studies of individual ledges and the plate edges indicate that local interface dynamics involve the cooperative motion of many atoms and occur at very rapid rates, and that the kinetics of precipitate interfaces which intersect the foil surface may be dominated by surface effects.

Crystallization in the Pd-Si System

Previous HRTEM studies revealed the presence of unit-cell ledges on the tips of Pd_3Si lamellae growing into the amorphous matrix during crystallization of a $\text{Pd}_{80}\text{Si}_{20}$ alloy [44]. These ledges were thought to accomplish growth by nucleating on the (010) terrace planes of the faceted Pd_3Si lamellae and spreading laterally across this plane. The purpose of the present study was to perform *in situ* hot-stage HRTEM experiments of the crystallization process at the tips of growing Pd_3Si lamellae, in order to verify the mechanism of growth previously proposed and to quantify this process by comparing kinetic data obtained from the *in situ* experiments with those predicted from nucleation and growth theory.

Figure 5 shows an image at the tip of a growing lamella of Pd_3Si oriented such that the viewing direction is [001] and the terrace plane at the tip is (010) [44-46]. The temperature was about 225°C and two-dimensional nuclei one unit-cell high (0.76 nm) were observed to form and propagate laterally across the (010) plane. The width of the smallest visible nucleus was about 1.5 nm (3 unit-cells wide) along the [100] direction and one such nucleus is outlined in Fig. 5. In some cases it appeared that rearrangement of the amorphous phase occurred ahead of the growing crystalline interface and that compositional changes occurred in the crystalline phase subsequent to the initial structural change. The latter effect is evident from the difference in contrast between the areas labelled A and B in Fig. 5, where the darkness of the Pd_3Si lamella increases with order. These effects could also be due to projection problems associated with amorphous matrix superimposed on crystalline Pd_3Si and this is an area of interpretation which needs further investigation.



Figure 5. *In situ* HRTEM image of Pd_3Si lamella tip.

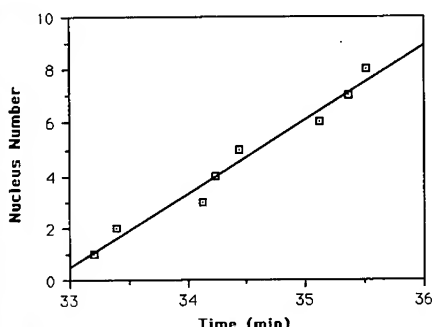


Figure 6. Nucleation data obtained from the same lamella.

Figure 6 shows the number of nuclei as a function of time obtained for the Pd_3Si lamella in Fig. 5 from the videocassette. The nucleation rate (J) at the tip of the lamella was determined as $1.1 \times 10^{14} \text{ s}^{-1} \cdot \text{m}^{-2}$ by dividing the number of nuclei per unit time by the area of the (010) terraces. The area was determined from the width of the terrace measured in the HRTEM image (40 nm) and assuming a sample thickness of 10 nm. A theoretical analysis of nucleation and growth was then performed according to Cahn, Hillig and Sears [47] using the experimental data above and thermodynamic and diffusion data for the Pd-Si system available in the literature [48,49]. The results are shown below.

For classical two-dimensional nucleation and growth (2DNG) to occur

$$-\Delta G_v = L \Delta T / V_m T_m < \gamma g / h \quad (2)$$

where ΔG_v is the free-energy change per unit volume, L is the latent heat of fusion per mole, V_m is the molar volume of the solid, T is the temperature, T_m is the melting temperature, $\Delta T = (T - T_m)$ is the undercooling, γ is the interfacial free energy, g is a diffuseness parameter and h is the step height. Using thermodynamic data for the Pd-Si system [47] where $L = 5,797.6 \text{ J/mol}$, $\gamma = 76 \text{ mJ/m}^2$, $V_m = 3.4 \times 10^{-5} \text{ m}^3/\text{mol}$, $T_m = 1233 \text{ K}$, $T = 498 \text{ K}$, $h = 7.5 \times 10^{-10} \text{ m}$ and letting $g=1$ for faceted Pd_3Si gives

$$-\Delta G_v = 1.0 \times 10^8 \text{ J/m}^3 \quad \text{and} \quad \gamma g/h = 1.0 \times 10^8 \text{ J/m}^3.$$

Therefore, the reaction is just within the 2DNG regime. The step free-energy per unit length

$$\epsilon = \gamma h(g)^{1/2} = 5.7 \times 10^{-11} \text{ J/m} \quad (3)$$

and the theoretical energy barrier for 2DNG is given by

$$W_{\text{theo}} = -\pi \epsilon^2 / h \Delta G_v = 1.4 \times 10^{-19} \text{ J} (0.84 \text{ eV}). \quad (4)$$

Since $W_{\text{theo}} = \pi r_c \epsilon$, where r_c is the radius of the critical nucleus, rearranging yields

$$r_c = -\epsilon / h \Delta G_v = 7.5 \times 10^{-10} \text{ m} (0.75 \text{ nm}). \quad (5)$$

Hence, the diameter of the critical nucleus at 225°C (498 K) is about three units-cells of Pd_3Si along the [100] direction, and this is about the dimension of the nucleus visible in Fig. 5. The nucleation rate of new steps per unit area is approximately

$$J \cong v N / V_m (L \Delta T / RTT_m)^{1/2} e^{-W/RT} \quad (6)$$

where N is Avogadro's number, R is the universal gas constant and v is the velocity of a straight step, given as

$$v = DL \Delta T \beta (2+g^{-1/2}) / hRTT_m \cong 3DL \Delta T / hRTT_m \quad (7)$$

where D is the diffusivity and β is a factor that relates the liquid and interfacial transport properties (~ 10 for metals). From bulk experiments [49], the diffusivity of Si in amorphous Pd-Si alloy at 498 K ($T_g/T=1.31$) is $D \cong 3 \times 10^{-22} \text{ m}^2/\text{s}$, which is about four orders of magnitude higher than that of Pd at the same temperature, and thus

$$v_{\text{theo}} = 1.0 \times 10^{-12} \text{ m/s.}$$

From measurement of the lateral velocity of the ledges in the *in situ* experiments

$$v_{\text{expt}} = 4.9 \times 10^{-10} \text{ m/s.}$$

Therefore, the diffusivity in the *in situ* experiments ($D_{\text{expt}} = 1.5 \times 10^{-19} \text{ m}^2/\text{s}$) is about 490 times greater than the diffusivity reported for Si in bulk samples. Using v_{theo} and the previous thermodynamic data, the theoretical nucleation rate per unit area at 498 K is

$$J_{\text{theo}} = 2.9 \times 10^7 \text{ s}^{-1} \cdot \text{m}^{-2}.$$

The experimental nucleation rate obtained from Fig. 6 was

$$J_{\text{expt}} = 1.1 \times 10^{14} \text{ s}^{-1} \cdot \text{m}^{-2}$$

and this experimental nucleation rate is about a factor of 10^7 greater than J_{theo} . The energy barrier for nucleation and growth in the *in situ* HRTEM experiment can be calculated from

$$W_{\text{expt}} = RT \{ \ln [v_{\text{expt}} N/V_m (L \Delta T/RTT_m)^{1/2}] - \ln J_{\text{expt}} \} \quad (8)$$

$$= 7.6 \times 10^{-20} \text{ J (0.47 eV)},$$

with the result that $W_{\text{expt}} = 0.56 W_{\text{theo}}$. The low activation energy barrier for nucleation combined with the high diffusivity obtained in the *in situ* hot-stage HRTEM studies indicate that heterogeneous nucleation and surface diffusion may be controlling the kinetics of this reaction, as in the case of Al-Cu-Mg-Ag when precipitates intersected the foil surfaces. However, further kinetic studies using thicker foils and an understanding of the rearrangements in the amorphous phase ahead of the growing crystal are necessary in order to fully understand the *in situ* HRTEM data.

In summary, it is possible to investigate the crystallography, growth mechanisms and kinetics of crystal/amorphous interfaces in Pd-Si alloys at dimensions approaching the atomic level by *in situ* HRTEM. This alleviates many of the uncertainties associated with more indirect methods of investigation and allows direct comparison with nucleation and growth theory. However, possible surface effects associated with the use of thin foils in the *in situ* hot-stage HRTEM experiment and superposition of amorphous matrix on crystalline features are two factors which need to be understood in order to obtain a fully quantitative comparison with nucleation and growth theory.

Martensitic Transformation in the Co-Ni System

The f.c.c. \rightarrow h.c.p. martensitic transformation in Co-Ni alloys involves one of the simplest crystal structure changes in phase transformations [50,51], requiring only a change in stacking sequence of the close-packed planes from ABCABC... in the high-temperature f.c.c. α phase to ABABAB... in the low-temperature h.c.p. ϵ phase, accompanied by a slight decrease in volume (~0.3%). This stacking change can be accomplished by the passage of $a/6<112>$ Shockley partial dislocations on alternate {111} planes of the f.c.c. phase or by $a/3<1\bar{1}0>$ partial dislocations for the reverse transformation in the h.c.p. phase [52,53]. The resulting orientation relationship between the two phases is $\{111\}_{\text{fcc}} \parallel \{0001\}_{\text{hcp}}$ and $<110>_{\text{fcc}} \parallel <11\bar{2}0>_{\text{hcp}}$, which is called the Shoji-Nishiyama (S-N) relation. In this study, a Co-32wt.%Ni alloy was chosen because the martensite start temperature (M_s) is below room temperature while the austenite start temperature (A_s) is above room temperature [54]. Thus, it is possible to observe the interfacial structure between the two phases by partially transforming the high temperature f.c.c. phase to h.c.p. martensite by cooling, and then to study the dynamics of the reverse transformation by *in situ* hot-stage HRTEM.

Figure 7 shows an image of the f.c.c./h.c.p. interface on the face of a martensite plate in a $<110> \parallel <11\bar{2}0>$ orientation at about 350°C in the *in situ* heating experiment. At this temperature, the thin foil had bent such that it was not possible to orient the foil exactly on the $<110> \parallel <11\bar{2}0>$ zone axis within the $\pm 10^\circ$ tilt capabilities of the specimen holder. This led to a loss of detail in the image since not all of the fundamental frequencies were contributing equally to the image contrast and also created a strong (0001) periodicity in the h.c.p. phase due to excitation of the forbidden (0001) reflections from the tilt [55]. Nevertheless, the ABCABC... and ABABAB... stacking sequences in the f.c.c. and h.c.p. phases are still visible and the $\{111\} \parallel \{0001\}$ interface plane is perfectly coherent and atomically flat in this figure.

Suddenly, a six-plane lamella of f.c.c. phase propagated through the h.c.p. phase four (0002) planes below the interface, as shown in Fig. 8. This lamella appeared to nucleate in the thicker region of the foil on the left and propagate toward the thin edge on the right. Nucleation of f.c.c. lamellae in thicker regions of TEM foils was reported to occur during *in situ* weak-beam dark-field (WBDF) studies of the h.c.p. \rightarrow f.c.c. transformation in Co-Ni [56]. The f.c.c. lamella propagated across the field of view in one frame (1/30th sec) indicating that it had a velocity of at

least 440 nm/sec. Previous research has shown that the interface velocity in Co-Ni alloys is temperature dependent but generally in the range of 1-100 mm/sec [57]. The much slower velocity in the present *in situ* hot-stage HRTEM study may be because the lamella propagated across the field of view in less than the 1/30th sec resolution of the VCR or it could be due to interaction with the surface of the thin foil. Frame by frame playback of the videotape showed that a shock wave propagated through the field of view beginning 29 frames (approximately one second) ahead of the actual structural transformation in the image and the structural change occurred immediately after the shock wave had passed.

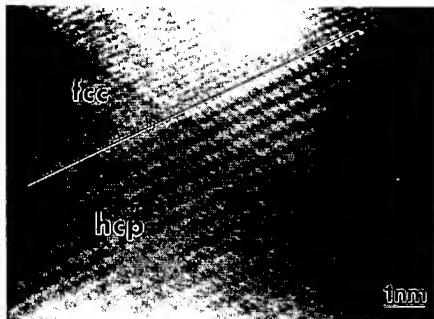


Figure 7. HRTEM image of $\{111\}_{\text{fcc}}||\{0001\}_{\text{hcp}}$ interface taken during the *in situ* hot-stage experiment at about 350°C.



Figure 8. Same area as in Fig. 7 after propagation of a six-plane f.c.c. lamella (indicated in the figure) through the h.c.p. phase.

The fact that the f.c.c. lamella in Fig. 8 is six planes thick and does not contain any stacking faults indicates that the f.c.c. nucleus also had this thickness. This result agrees with the WBDT studies of Hitzenberger et al. [53,56], where lamellae with minimum thicknesses on the order of six to ten close-packed planes were observed. Observation of a six-plane thick defect-free lamella supports nucleation models which are based on the simultaneous formation of several overlapping stacking faults on alternate basal planes [58-60] rather than by other mechanisms [61-63]. A six-plane thick nucleus is a particularly favorable size if three transformation dislocations with each type of $a/3<1\bar{1}00>$ Burgers vector form on alternate (0002) planes so that their long-range stress fields largely cancel at the plate edge. Although the transformation dislocations could not be seen in this experiment due to the limited time resolution of the TV camera, the six-plane height of the lamella indirectly indicates that the three type of dislocations may have been present. This phenomenon has been clearly demonstrated for the f.c.c. \rightarrow h.c.p. diffusional transformation in Al-Ag [36,64].

FUTURE DIRECTIONS

As in static HRTEM, superposition of atomic features occurs through the sample thickness during *in situ* hot-stage HRTEM, and this makes it difficult to analyze the three-dimensional structure of interfaces and structural features approaching the atomic level [4,65,66]. However, techniques of image analysis are being developed to improve this situation [67-70] and atomic modelling, quantitative image acquisition, HRTEM simulation and image processing are all becoming increasingly easy as computational speeds increase, so this situation is likely to continue to improve [3,4,66,71-73]. Image processing is just beginning to be used to analyze *in situ* hot-stage HRTEM results. When this capability is applied to sequences of images obtained fractions of a second apart, it may facilitate analysis of the three-dimensional structure of some interfaces as features such as ledges and kinks propagate through the thickness of a foil. The increase in

brightness and coherency of the new generation of medium-voltage field-emission gun (FEG) HRTEMs also promises to improve the possibilities for quantitative image analysis and this is expected to facilitate *in situ* HRTEM studies [74,75].

CONCLUSIONS

The results from recent *in situ* hot-stage HRTEM studies demonstrate that it is possible to obtain quantitative, atomic level data on interface dynamics in solid-state phase transformations for comparison with interface and transformation theory. This technique alleviates many of the uncertainties associated with more indirect methods of investigation. As in static HRTEM, superposition of surrounding matrix and the two-dimensional nature of HRTEM complicate image interpretation. In addition, surface effects associated with the use of very thin foils in HRTEM and the time resolution of current TV-rate cameras may limit quantitative comparison of *in situ* HRTEM experiments with interface and transformation theory.

ACKNOWLEDGEMENTS

The authors gratefully acknowledge the support of the National Science Foundation under Grant DMR-9302493. The authors are also grateful to Dr. L. M. Angers for providing the Al-Cu-Mg-Ag alloy, to Drs. L. E. Tanner and H. H. Liebermann for providing the Pd-Si ribbon, to Dr. H. C. Baxi and Prof. T. B. Massalski for providing thermodynamic data on the Pd-Si system and to Prof. A. V. Granato for providing the Co-Ni alloy.

REFERENCES

1. E. P. Butler and K. F. Hale, Dynamic Experiments in the Electron Microscope (North-Holland Publishing Co., New York, 1981) p. 135.
2. L. Reimer, Transmission Electron Microscopy: Physics of Image Formation and Microanalysis, 2nd Ed. (Springer-Verlag, Berlin, 1989) p. 125.
3. O. L. Krivanek, A. J. Gubbens, N. Delby and C. E. Meyer, in Proc. 50th Ann. Meeting Electron Microsc. Soc. of Amer., edited by G. W. Bailey et al. (San Francisco Press, Inc., San Francisco, 1992) p. 1192.
4. High-Resolution Transmission Electron Microscopy and Associated Techniques, edited by P. R. Buseck, J. M. Cowley and L. Eyring (Oxford University Press, New York, 1988) p. 237, 456, 464.
5. Refer to Gatan, Inc. or microscope manufacturer catalogs, for example.
6. Y.C. Chang and J. M. Howe, Metall. Trans., **24A**, 1462 (1993).
7. R. Sinclair, T. Yamashita, M. A. Parker, K. B. Kim, K. Holloway and A. F. Schwartzman, Acta Cryst., **A44**, 965 (1988).
8. H. Ichinose, T. Kizuka and Y. Ishida, in Proc. XIIth Inter. Cong. Electron Microsc., edited by L. D. Peachey and D. B. Williams (San Francisco Press, Inc., San Francisco, 1990) p. 514.
9. H. Saka, A. Sakai, T. Kamino and T. Imura, Philos. Mag. Lett., **52**, L29 (1985).
10. J. M. Howe, W. E. Benson, A. Garg and Y. C. Chang, in Proc. Interfaces II Conference, Ballarat, Victoria, Australia, November, 1993 (in press).
11. Y. C. Chang and J. M. Howe, Ultramicroscopy, **51**, 46 (1993).
12. K. Holloway and R. Sinclair, J. Less-Common Metals, **140**, 139 (1988).
13. J. M. Howe, Mater. Sci. Forum, **126-128**, 467 (1993).
14. R. Sinclair, J. Morgiel, A. S. Kirtikar, I.-W. Wu and A. Chiang, Ultramicroscopy, **51**, 41 (1993).
15. J. Batstone, Philos. Mag. A, **67**, 51 (1993).
16. J. M. Howe, in Proc. Inter. Conf. on Martensitic Transformations '92 (ICOMAT '92), Monterey, CA, July, 1992 (in press).

17. Z. Kang and L. Eyring, *Metall. Trans.*, **22A**, 1323 (1991).
18. N. Thangaraj and B. W. Wessels, *J. Appl. Phys.*, **67**, 1535 (1990).
19. J. M. Howe (unpublished research).
20. H. Fujita, *J. Electron Microscopy Tech.*, **12**, 201 (1989).
21. H. I. Aaronson, C. Laird and K. R. Kinsman, in Phase Transformations, edited by H.I. Aaronson (Amer. Soc. for Metals, Ohio, 1970) p. 313.
22. C. Laird and H. I. Aaronson, *Acta Metall.*, **17**, 505 (1969).
23. J. M. Howe and N. Prabhu, *Acta Metall. Mater.*, **38**, 881, 889 (1990).
24. W. K. Burton, N. Cabrera and F. C. Frank, *Phil. Trans. Roy. Soc.*, **A243**, 299 (1950-52).
25. H. I. Aaronson, T. Furuhara, J. M. Rigsbee, W. T. Reynolds, Jr. and J. M. Howe, *Metall. Trans.*, **21A**, 2369 (1990).
26. R. J. Chester and I. J. Polmear, in The Metallurgy of Light Alloys (Inst. of Metallurgists, London, 1983) p. 75.
27. K. M. Knowles and W. M. Stobbs, *Acta Cryst.*, **B44**, 207 (1988).
28. B.C. Muddle and I. J. Polmear, *Acta Metall.*, **37**, 777 (1989).
29. D. Vaughan and J. M. Silcock, *Phys. Stat. Sol.*, **20**, 725 (1967).
30. A. Garg and J. M. Howe, *Acta Metall. Mater.*, **39**, 1939 (1991).
31. A. Garg, Y. C. Chang and J. M. Howe, *Acta Metall. Mater.*, **41**, 235 (1993).
32. R. W. Fonda, W. A. Cassada and G. J. Shiflet, *Acta Metall. Mater.*, **40**, 2539 (1992).
33. S. Iijima, in High-Resolution Electron Microscopy of Defects in Materials, edited by R. Sinclair, D. J. Smith and U. Dahmen (Mater. Res. Soc. Symp. Proc. **183**, Pittsburgh, PA, 1990) p. 349.
34. S. P. Ringer, B. C. Muddle and Polmear, in Proc. 3rd Inter. Conf. on Aluminum Alloys, edited by L. Arnborg et al. (Norwegian Inst. Tech., Trondheim, 1992) p. 214.
35. Y. C. Chang, Ph.D. Thesis, Carnegie Mellon Univ., Pittsburgh, 1992.
36. J. M. Howe, U. Dahmen and H. I. Aaronson, *Philos. Mag. A*, **56**, 31 (1987).
37. G. J. Jones and R. Trivedi, *J. Cryst. Growth*, **29**, 155 (1975).
38. C. Atkinson, *Proc. Roy. Soc. London*, **A384**, 107 (1982).
39. M. Enomoto, *Acta Metall.*, **35**, 935, 947 (1987).
40. Handbook of Chemistry and Physics, 63rd Edition, edited by R.C. Weast (CRC Press, Boca Raton, 1982) p. F-52.
41. R. Trivedi, in Proc. Inter. Conf. on Solid-Solid Phase Transformations, edited by H.I. Aaronson et al. (Metall. Soc. AIME, Warrendale, PA, 1982) p. 477.
42. S. K. Kang and C. Laird, *Acta Metall.*, **23**, 35 (1975).
43. C. Laird and H. I. Aaronson, *Acta Metall.*, **14**, 171 (1966).
44. Brearley, W.H., Shieh, P.-C. and Howe, J.M.: *Metall. Trans.*, 1991, **22A**, 1287.
45. J. A. Wysocki and P. E. Duwez, *Metall. Trans.*, **12A**, 1455 (1981).
46. P.-C. Shieh, C. O. Stanwood and J. M. Howe, *Ultramicroscopy*, **35**, 99 (1991).
47. J. W. Cahn, W. B. Hillig and J. W. Sears, *Acta Metall.*, **12**, 1421 (1964).
48. H. C. Baxi and T. B. Massalski, *J. Phase Equilibria*, **12**, 349 (1991).
49. B. Cantor, in Rapidly Quenched Metals, edited by S. Steeb and H. Warlimont (Elsevier Science Publishers, 1991) p. 595.
50. Z. Nishiyama, Martensitic Transformation, (Academic Press, New York, 1978) p. 48.
51. J. W. Christian, in Dislocations and Properties of Real Crystals, (The Institute of Metals, London, 1985) p. 94.
52. E. Votava, *Acta Metall.*, **8**, 901 (1960).
53. C. Hitzenberger and H. P. Kärnthal, *Acta Metall.*, **64**, 151 (1991).
54. M. Hansen and K. Anderko, Constitution of Binary Alloys, (McGraw-Hill Book Company, New York, 1958) p. 485.
55. J. M. Howe and S. J. Rozeveld, *J. Micros. Res. Tech.*, **23**, 230 (1992).
56. C. Hitzenberger, H. P. Kärnthal and A. Körner, *Acta Metall.*, **36**, 2719 (1988).
57. S. Takeuchi, and T. Honma, *Sci. Rep. RITU*, **A9**, 492 (1957).
58. E. de Lamotte and C. Altstetter, *Trans. Amer. Inst. Min. Engrs.*, **245**, 651 (1969).
59. G. B. Olson and M. Cohen, *Metall. Trans.*, **7A**, 1897 (1976).
60. S. Mahajan, M. L. Green, and D. Brasen, *Metall. Trans.*, **8A**, 283 (1977).
61. H. Fujita and S. Ueda, *Acta Metall.*, **20**, 759 (1972).
62. B. A. Bilby, *Philos. Mag.*, **44**, 782 (1953).

63. A. Seeger, *Z. Metallk.*, **47**, 653 (1956).

64. N. Prabhu and J. M. Howe, *Scripta Metall.*, **22**, 425 (1988).

65. J. C. H. Spence, Experimental High-Resolution Electron Microscopy, 2nd ed. (Oxford University Press, New York, 1988) p. 103.

66. P.C. Shieh, C. O. Stanwood and J. M. Howe, *Ultramicroscopy*, **35**, 99 (1991).

67. A. Ourmazd, D. W. Taylor, M. Bode and Y. Kim, *Science*, **246**, 1571 (1989).

68. T. Nakamura, M. ikeda, S. Muta and I. Umebu, *Appl. Phys. Lett.*, **53**, 379 (1988).

69. S. Thoma and H. Cerva, *Ultramicroscopy*, **38**, 265 (1991).

70. J. Planes, A. Loiseau and F. Ducastelle, *J. Phys. I France*, **2**, 1507 (1992).

71. P. R. Buseck, Y. Epelboin and A. Rimsky, *Acta Cryst. A***44**, 975 (1988).

72. R. Kilaas and M. A. O'Keefe, in Computer Simulation of Electron Microscope Diffraction and Images, edited by W. Krakow and M. O'Keefe (The Minerals, Metals and Materials Soc., Warrendale, PA, 1989) p. 171.

73. W. E. King and G. H. Campbell, *Ultramicroscopy*, **51**, 128 (1993).

74. Max T. Otten and Wim M. J. Coene, *Ultramicroscopy*, **48**, 77 (1993).

75. W. Coene, A. J. E. M. Janssen, M. Op de Beeck and Van Dyck, *Philips Electron Optics Bull.*, **132**, 15 (1992).

Epitaxial Growth of Two-Dimensional Dichalcogenides and Modification of Their Surfaces with Scanning Probe Microscopes

Bruce A. Parkinson
Department of Chemistry, Colorado State University, Fort Collins, CO 80523

Abstract

Methods for epitaxial growth of two dimensional materials are described. The lack of interlayer bonding in these materials allows for epitaxial growth with large lattice mismatches. Growth of MoSe_2 on MoS_2 (a 5% mismatch) or on SnS_2 (10% mismatch) can be demonstrated. Scanning tunneling microscopy (STM) revealed remarkable structures in the epilayer as a result of the large mismatches. A technique using the STM or atomic force microscope (AFM) to selectively remove single molecular layers from the surface of layered materials is also described. The combination of these two technologies may result in the ability to produce nanoscale devices exhibiting quantum size effects.

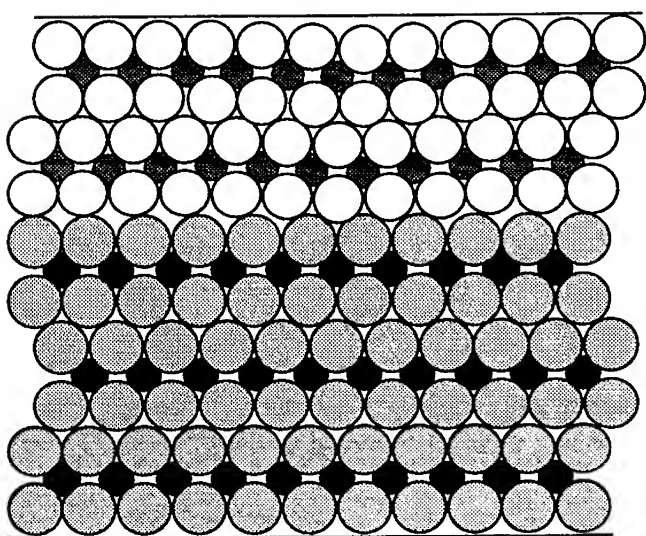
Introduction

This contribution will focus on the combination of two new technologies being developed in our laboratory. Both these technologies are concerned with materials which have a two dimensional (2-D) structure. The materials which crystallize in 2-D structures include many transition metal dichalcogenides, indium and gallium chalcogenides and tin disulfide and diselenide. The electronic properties of these materials range from large bandgap semiconductors to metallic conductors (and superconductors) providing all the required properties for device fabrication. The weak interlayer bonding is evident by the easy cleavage of crystals of these materials to produce clean and atomically flat surfaces composed of hexagonally-closest-packed (HCP) chalcogenide atoms. We and others have demonstrated the inertness of many of these cleavage surfaces towards oxidation and hydrolysis [1] making them ideal substrates for fundamental surface chemistry in air and electrolytes [2]. Herein we discuss methods for deposition of these materials in an epitaxial fashion and for precisely etching them away a layer at a time from extremely small regions of the surface using either a scanning tunneling microscope or an atomic force microscope.

Epilayer Structure

Modern epitaxial growth techniques have been valuable for the preparation of high quality thin films of electronic materials for device applications [3]. A severe requirement for the production of high quality epilayers has been that the substrate and epilayer must have the same symmetry and very nearly the same lattice constant. Violation of these conditions produces interfaces with strain and dislocations degrading the performance of a device. The concept of van der Waals epitaxy (VDWE) has recently been introduced where the lattice matching requirement is removed by using materials which have strong bonding only in two dimensions [4-7]. Although there is no covalent bonding between these layers the van der Waals forces, which hold the layers together in the pure crystal, still operate on the epilayer (Figure 1a). The most stable site for the a chalcogenide atom of the epilayer is in the trigonal site between chalcogenide atoms of the substrate and above one of the trigonal sites containing a metal atom. Subsequent deposition will produce a strongly 2-D bonded epilayer with the two HCP lattices going in and out of phase. A 2-D model of the interface with the substrate and epilayer represented as different sized hexagonal packed circles is shown in Figure 1b.

a.)



b.)

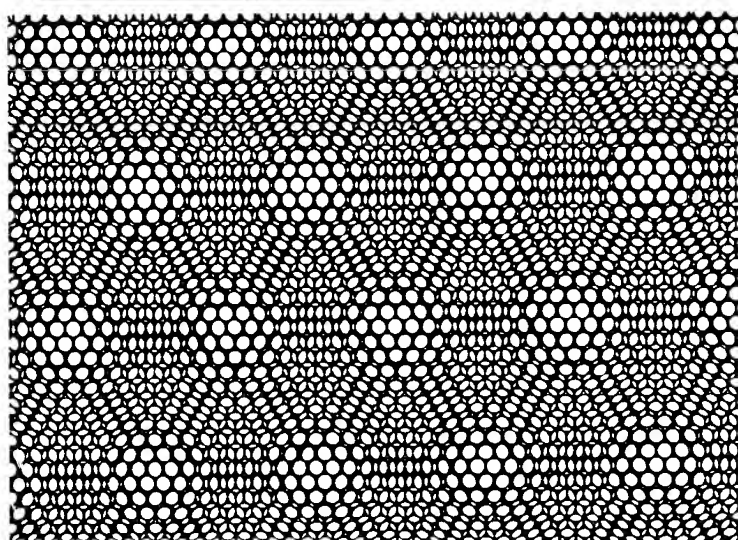


Figure 1 Side view (a) and top view (b) of the interface between two mismatched layered materials. The mismatch for the Moiré pattern is about 6%. Notice slight lattice distortions are possible due to atoms of the epilayer occupying 1 (atop), 2 and 3 fold sites in the substrate

The lattice of the epilayer is distorted by some of the atoms falling into the three-fold sites while others are sitting directly on top of the substrate atoms. We attempted to measure this distortion using the scanning tunneling microscope (STM) since the z resolution (out of plane) of the STM can in principal be less than the width of an atom[9]. STM images of several molecular layers of MoSe₂ grown on a MoS₂ substrate [8] (lattice mismatch 5%) are shown in Figure 2. Triangular regions where the epilayer atoms have relaxed into the trigonal sites can be clearly seen and appear to be commensurate even when a molecular step is present. The size of these "wagon wheel" structures can be predicted using the Moiré equation resulting in a value of 78 Å whereas the actual size varies between 72 Å and 80 Å. We have also prepared epilayers of MoSe₂ on SnS₂ where the lattice mismatch is 10%. Superstructures were also observed on these surfaces but they were much smaller (35 Å) as would be expected from the Moiré equation [10].

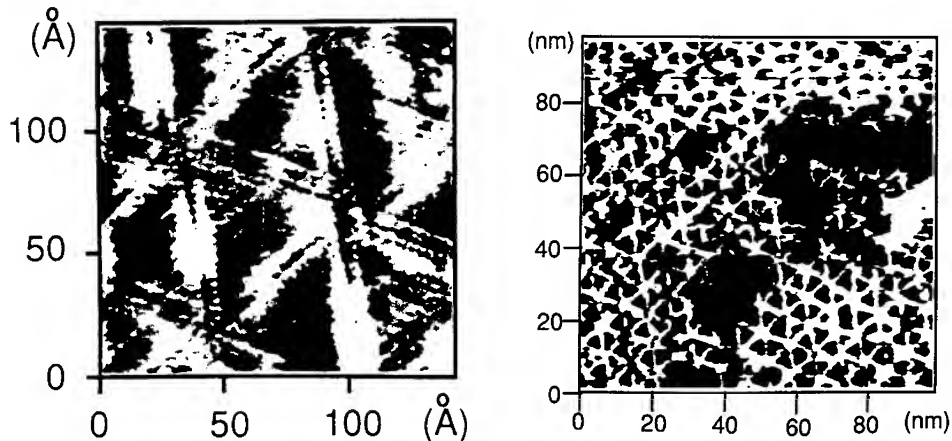


Figure 2 Atomic resolution constant current STM image of an epilayer of MoSe₂ grown on MoS₂ (left). A larger scale STM image in the constant height mode showing the network of "wagon wheel" structures.

The measured apparent height of the "wagon wheel" structures observed in this study (0.2 to 0.7 nm) was surprisingly large since it was expected that the difference in height between the epitaxial atoms in the three-fold sites when compared to those in atop sites would produce structures much less than an atom high [9]. There are several possible explanations for this amplified height modulation. One explanation is the higher compressibility of the structure above the three-fold sites when compared the atop sites. Forces from the tip can push the three-fold site atoms down more easily. The other explanation is that the structures are due to new electronic states as a result of the removal of the degeneracy of the normally planar HCP lattice of the transition metal dichalcogenide. The new electronic states, as a result of a unit cell twenty times larger than of the bulk crystalline material, are prominently imaged with the STM. Experiments in our laboratory showed that it is very difficult to see these structures with the atomic force microscope (AFM) suggesting the electronic nature of this phenomena.

STM and AFM Modification of Surfaces

The STM and AFM have become useful tools for not only imaging the surfaces of materials but for modification of surfaces at an extremely small level. We have observed the etching of various transition metal dichalcogenides, via nucleation and growth of holes, by simply scanning an STM tip over the surface of the layered material in air at usual imaging conditions of tip bias and current [11]. No systematic variation of the etching rate on experimentally accessible parameters (scan rate, tip bias, tunneling current...) was observed allowing us to only speculate about the mechanism of the etching process at that time. When the identical process was observed with an AFM [12] it provided the experimental handle needed, i.e. the applied force, to ascertain various aspects of the mechanism for the etching process.

Figure 3 shows a series of AFM images taken by continuously scanning a $0.5 \mu \times 0.5 \mu$ area of a NbSe_2 crystal with the AFM tip.

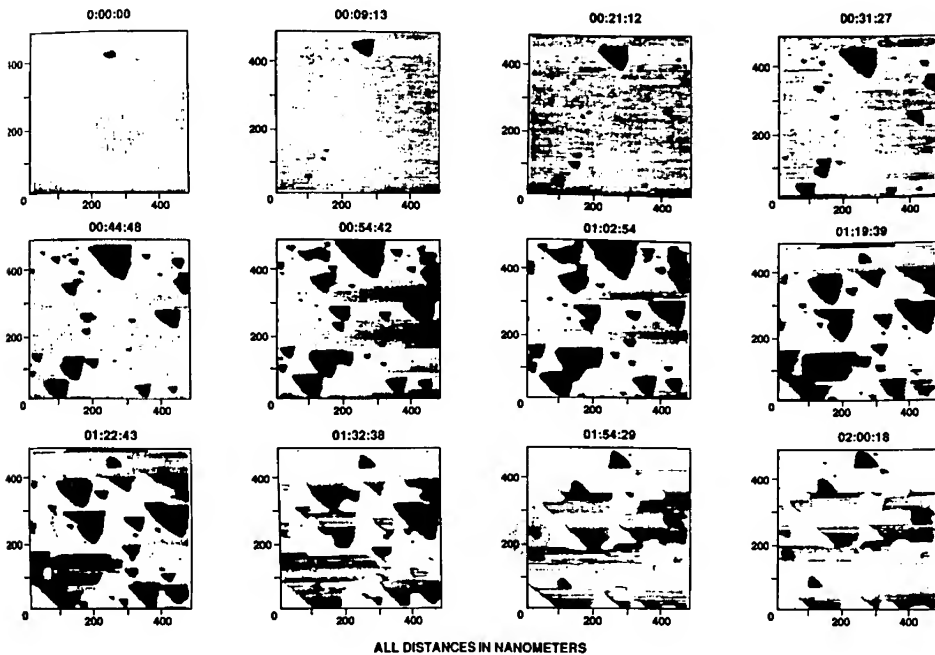


Figure 3 A sequence of 12 AFM images at different elapsed times for the removal of a layer of NbSe_2 and subsequent nucleation and initial removal of a second layer. Note the rotation of the triangular holes in the subsequent layer. The force was $19 \pm 5 \text{ nN}$.

Figure 3 shows the nucleation and growth of triangular holes in the top layer of material resulting in the nearly complete removal of this layer and subsequent nucleation of the second layer. Continued scanning would result in the removal of many additional layers. Note the 180° rotation of the triangles in the second layer due to the 2H polytype of the NbSe_2 where alternate layers are rotated 180° with respect to each other. The process is completely analogous to that observed on the same substrate with an STM tip. SnSe_2 and SnS_2 , when etched with the STM, produced rounded (almost hexagonal) holes. The etched structures are completely stable over periods of at least several days exposure to laboratory air, and presumably longer, if they are not scanned by the AFM tip. Other layered structure dichalcogenides were also observed to etch in the AFM or STM including TaS_2 , SnS_2 , ZrSe_2 , MoSe_2 , HfSe_2 and TiSe_2 . MoTe_2 , WSe_2 , WTe_2 , ReSe_2 and WS_2 crystals, grown in our lab, were not observed to etch. Graphite was also not observed to etch in the fashion described but high forces did produce some wrinkling of the graphite surface.

Variation of the force applied to the cantilever, via the piezoelectric elements of the AFM, resulted in the observation that the rate of removal of material was directly related to the applied force. This could also be demonstrated by toggling the applied force between two values while scanning the upper or lower half of an image. The part of the image with the higher applied force was always observed to etch faster than the area with the lower force. Cratering, or build-up of material on the sides of the etched areas, was only observed at very high applied forces (>150 nN) on SnSe_2 . On NbSe_2 a force of 100 nN produced fast etching but no cratering was observed. Higher applied forces did not produce etching in materials listed above which show no etching. Forces lower than 5 nN are difficult to study due to drifts in the apparatus over the long times needed to remove a layer at such low applied forces.

Figure 4 shows several structures which could be fabricated by custom rastering of the AFM tip. The 300 nm "X" in Figure 4a has lines which are only 20 nm wide and are one unit cell of SnSe_2 deep (0.6135 nm). This structure was created by disabling one of the scan axis of the microscope and then rotating the scan. The line width apparently is controlled by the thermal drift in the microscope during the time it takes to etch the line (less than 2 minutes) and perhaps the bluntness of the tip although these tips are routinely capable of atomic resolution on these substrates.

Figure 4b illustrates a structure on a single material which is a useful model for etching tiny device structures. In figure 4c a single layer mesa of about 100 x 100 x 0.6 nm has been isolated from the surrounding material of the top layer but retains a connection with the second layer down. This structure suggests an interesting technology if the AFM/STM patterning is combined with the aforementioned van der Waals epitaxy. If the top layer was an epitaxially deposited semiconducting material (MoS_2 , SnSe_2 etc.) deposited on several layers of metallic NbSe_2 and all these layers were deposited on an insulating substrate such as SnS_2 , a very small semiconductor diode structure which could be contacted with an STM tip is the result. Other combinations of deposited layers and etching patterns could be used to produce other device structures. Construction of single quantum sized devices with these technologies would be of considerable research interest although any practical applications of this technology would require multiplexing of AFM and/or STM tips.

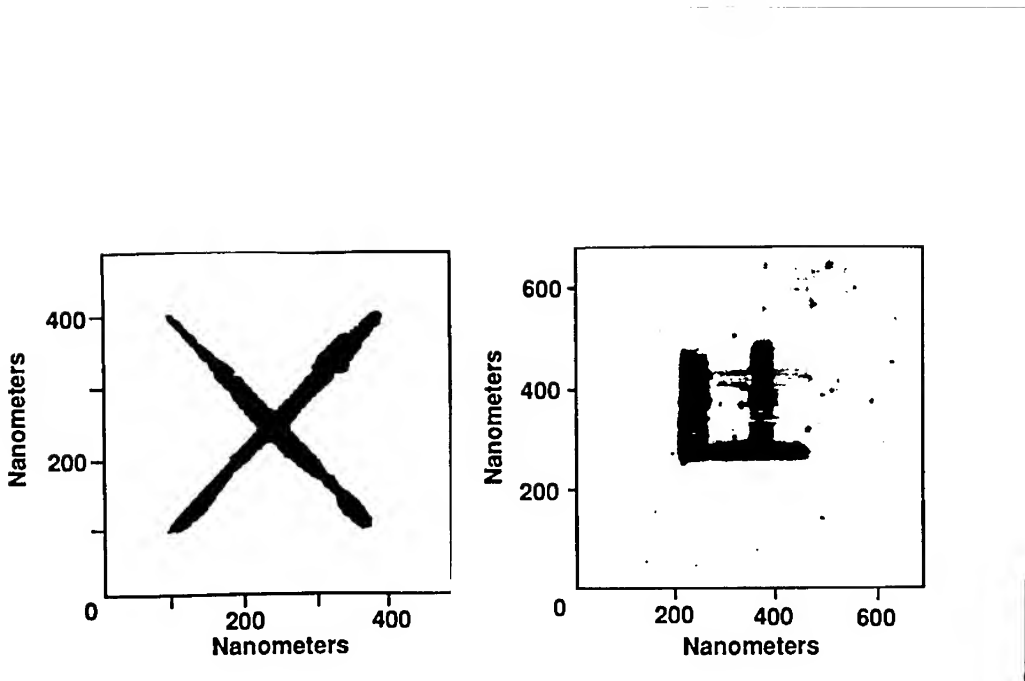


Figure 4 Several etched structures which were created by disabling one scan axis and moving and rotating the scan. See text for significance of various features.

Conclusion and Summary

We have described a two technologies, developed in our laboratories, for the growth and patterning of epitaxial layers of two dimensional materials. The use of two dimensional materials removes the lattice matching constraint, which usually limits the choice of materials for epitaxial growth, and provides for true layer-by-layer growth of the epilayers. Scanning probe microscopes can then be used to pattern the epilayers. In the future we hope to produce devices exhibiting quantum confinement effects with the combination of these two technologies.

References

- (1) J. L. Stickney, S.D. Rosasco, B. C. Schardt, T. Solomun, A. T. Hubbard, and B. A. Parkinson, *Surf. Sci.*, **136**, 15 (1984).
- (2) B. A. Parkinson, *Langmuir*, **4**, 967 (1986).
- (3) P. S. Peercy, E. G. Bauer, B. W. Dodson, D. J. Ehrlich, L. C. Feldman, C. P. Flynn, M. W. Geis, J. P. Harbison, R. J. Matyi, P. M. Petroff, J. M. Phillips, G. B. Stringfellow, A. Zangwill, *J. Mater. Res.*, **5**, 852(1990).
- (4) A. Koma and K. Yoshimura, *Surface Science* , **174**, 556 (1986).
- (5) A. Koma, K. Saiki, K. and Y. Sato, *Appl. Surface Science*, **41/42**, 451 (1989)

- (6) K. Ueno, T. Shimada, K. Saiki and A. Koma, *Appl. Phys. Lett.*, **56**, 327 (1990).
- (7) K. Ueno, K. Saiki, T. Shimada and A. Koma, *J. Vac. Sci. Technol. A.*, **8**, 68 (1990).
- (8) The MoSe₂ films were deposited on SnS₂ and MoS₂ substrates using a three chamber UHV-MBE system equiped with a Knudsen cell for selenium evaporation and an electrostatic focusing electron beam evaporator for a molybdenum source. The films were deposited at a rate of about 2 Å-min⁻¹ resulting in a complete Se-Mo-Se layer (crystallographic layer thickness = 6.45 Å) in about 3 minutes.
- (9) K. Ueno, A. Koma, F. S. Ohuchi and B. A. Parkinson, *Appl. Phys. Letters*, **58**, 472 (1991)
- (10) F. S. Ohuchi, B. A. Parkinson, K. Ueno and A. Koma, *J. Appl. Physics*, **68**, 2168 (1990)
- (11) B. A. Parkinson, *Journal of the American Chemical Society*, **112**, 7498 (1990)
- (12) Ed Delawski and B. A. Parkinson, *Journal of the American Chemical Society*, **114**, 1661 (1992)

MICROSTRUCTURAL IMAGING OF LOCALIZED CHEMICAL REACTIONS USING VALENCE PHOTOELECTRONS

S. Liang, A.K. Ray-Chaudhuri, W. Ng, and F. Cerrina
Center for X-ray Lithography, University of Wisconsin - Madison,
3731 Schneider Dr., Stoughton, WI 53589

ABSTRACT

We have utilized scanning soft X-ray photoelectron spectromicroscopy-MAXIMUM to investigate the microstructural evolution induced by localized corrosion in the Al-Cu-Si alloy thin films. We present energy-specific photoelectron micrographs showing the distribution of Cu-rich precipitates and corrosion products for the thin films after corrosion. Micro-spectroscopy performed across a corrosion site reveals that the O 2p valence band shifts in energy with location and the amount of shift can be related to the degree of corrosion. The photoelectron micrographs also show that the Cu-rich phase precipitates near the surface region and grows with annealing temperature.

INTRODUCTION

Chemical reactions at the surface of alloy thin films often result in a spatially inhomogeneous chemical system. The microstructural non-uniformity is usually on the length scale of microns to nanometers. In order to characterize such systems, surface sensitive techniques with both *spatial* and *chemical* resolution are required. With the advent of high resolution soft X-ray photoelectron spectromicroscopy[1], it is now possible to examine the localized non-uniform chemical process by imaging photoelectrons of specific energy as represented as peaks in an electron energy distribution curve (EDC) as well as performing micro-spectroscopy.

One system of particular interest is the micro-corrosion process on Al-Cu-Si alloy thin films which are widely utilized as metallization materials for interconnects and contacts in microelectronic devices[2]. One major drawback of adding Cu (0.5-4wt.%) is the increased corrosion susceptibility of the thin films[3-5]. Corrosion can take place *in-process* during device fabrication[6], or *in-service* when the device is used in a humid environment[7]. It is generally accepted that Cu-rich precipitates (designated as θ -Al₂Cu) form upon annealing during device fabrication[2, 8]. The cathodic Cu-rich phase promotes localized corrosion via pitting and galvanic mechanisms[3, 4, 9].

In this paper, we extend previous efforts[9] to characterize in detail the corrosion induced microstructural evolution and investigate factors such as annealing temperature and Cu concentration. Particularly, we focus on valence band photoelectron spectra. Based on the results gathered from this study, we can describe in more detail the corrosion process and its induced microstructure in Al-Cu-Si thin films.

EXPERIMENTAL

Al-Cu-Si thin films with 1wt.% Cu and 2wt.%Cu deposited on a Si(100) wafer (with surface native oxide) were studied. The Al-1%Cu-1%Si film was magnetron-sputter deposited from a composite target. The Al-2%Cu-1.5%Si film was evaporated from the alloy placed in a W boat. The films were then furnace annealed at 320°C or 400°C under flowing N₂ for 20 minutes. The thin film wafers were cut into pieces for corrosion tests. The accelerated corrosion tests presented in this paper were executed as follows: The wafer was dipped in 1wt% HNO₃ (diluted from 70% w/w A.C.S. reagent) at room temperature for 20 minutes, rinsed by DI water 5 times, dried by blowing N₂, and stored in an environmental chamber

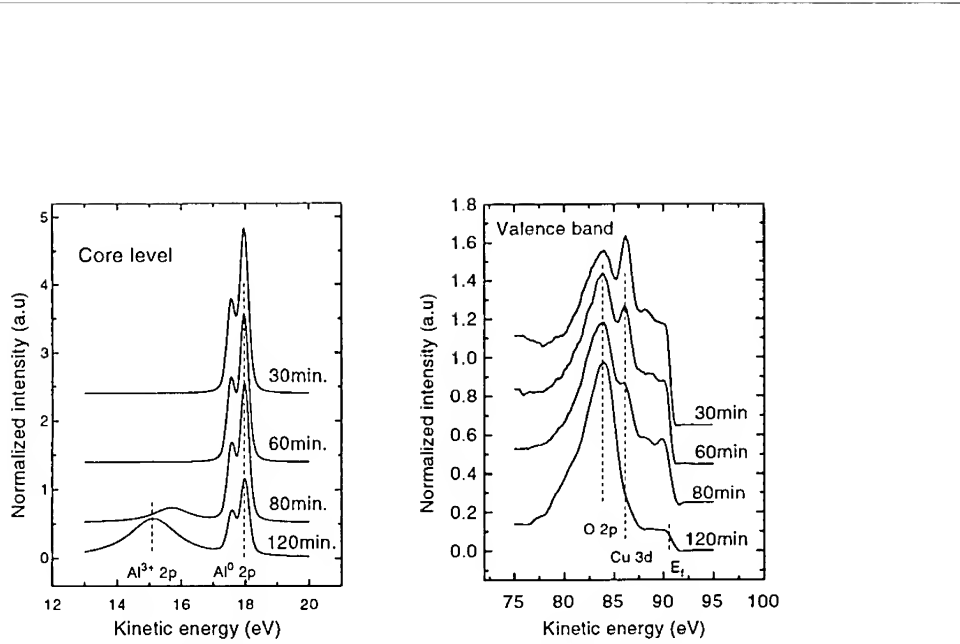


Figure 1: Al 2p core level and valence band EDCs for 800 Å Al-2%Cu-1.5%Si thin film deposited on Si(100). The spectra were recorded at different times after deposition. Valence band spectra are clearly more sensitive than core levels to chemical change at the thin film surface.

kept at 85% relative humidity and 85°C for 80 minutes. After this accelerated corrosion test, the sample was mounted to the sample holder and ion sputtered slightly to clean off the gaseous contamination on the surface before transferring to the microscope's scanning stage for examination using MAXIMUM.

The details of the MAXIMUM project and its performance can be found elsewhere[1]. Briefly, it is a scanning soft X-ray photoelectron microscope employing a Mo/Si multilayer-coated Schwarzschild objective (SO) to focus X-rays of 95eV from the undulator beamline. A mechanical scanning stage rasteres the sample under focus, and the sample position is measured by laser interferometers with a precision of 10nm. Photoelectrons emitted from the sample are energy analyzed by an cylindrical mirror electron energy analyzer (CMA). The microscope provides 1000 Å spatial resolution and 300meV energy resolution. The entire microscope system is under 5×10^{-10} torr UHV.

RESULTS AND DISCUSSION

We first studied both the core level and valence band photoelectron spectra of a 800 Å thick Al-2%Cu-1.5%Si thin film deposited under UHV condition for the following reasons: (1) To the best of our knowledge, there was no report on the photoelectron spectra (particularly the valence band EDCs) for this system using soft X-rays around 95eV. Therefore, we start with these spectra as reference for later studies; (2) This paper focuses on the role of Cu and its precipitation in the corrosion reaction, so we need first to identify and then choose the spectral features which represent both Cu and the corrosion product-oxides.

In Fig. 1, the core level and valence band EDCs are presented for the Al-2%Cu-1.5%Si thin film after different degrees of oxidation, as represented by various exposure times in 2×10^{-9} torr vacuum after deposition. The core level EDCs show the Al 2p peaks for metallic ($E_k(2p_{3/2})=18$ eV) and oxidized (at $E_k=15.1$ eV) states. There are no observable Cu 3p peaks because the photoionization cross section of Cu 3p core level (binding energy

around 75eV) is just near the Cooper minimum [10] for 95eV photon energy. These values are in agreement with the values for pure Al, suggesting that the small amount of Cu has negligible effect on the Al 2p core EDCs. The broad oxide peak at 15.1eV indicates that the surface oxide is Al_2O_3 with different stoichiometry and structure. Two main features are noticed in the valence band spectra. The sharp peak at 86.3eV is the Cu 3d band, which is 4.4eV below the Fermi edge ($E_f=90.7\text{eV}$). This is 2eV higher in energy than that of the bulk Cu [12]. This suggests that the Cu is in the Al-rich alloy[11]. The broad peak at 84eV is the O 2p band (6.7eV below E_f) with a shoulder at 80eV[13]. With oxidation, the oxygen peak grows and the Cu 3d band diminishes. This suggests that the oxygen reacts mostly with Al to form surface oxide, Al_2O_3 , covering the Cu. By comparing the core and valence band EDCs, it is clear that valence band is much more sensitive to chemical changes than the core level spectra (Also, the broad core level peak precludes the detailed oxide information). Therefore, valence band EDCs are utilized in this paper in the chemical mapping of microstructures in the corroded thin films.

If we take an image by tuning the CMA to only accept the Cu 3d photoelectrons, we can map the distribution of the Cu-rich precipitates as represented by the intensity (the brightness) in the image. For the thin films before the accelerated corrosion test, we have not observed any surface microstructures by imaging with photoelectrons of any kinetic energy. This suggests that the surface of the film under such conditions is rather uniform. The next step is to examine the surface of the thin films after corrosion.

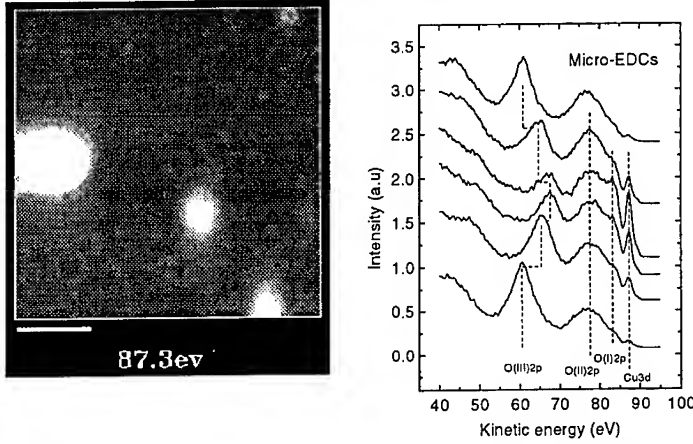


Figure 2: Left: Micrograph of corrosion induced microstructure in a 1000\AA Al-1%Cu-1%Si thin film. The image was formed by Cu 3d valence electrons with $E_k=87.3\text{eV}$, thus representing the distribution of Cu-rich phase in the film. The scale bar is $5\mu\text{m}$. Right: A series of valence band EDCs recorded by stepping the sample under the focused X-ray beam across the Cu-rich region at the far left of the micrograph.

In Fig. 2, the image is produced by photoelectrons with 87.3eV kinetic energy, representing the Cu 3d band. The image size is $19\mu\text{m} \times 19\mu\text{m}$. In order to get spectroscopic information about the 'disc-like' structure, micro-spectroscopy is performed. The plot on the right panel of Fig. 2 is a series of EDCs recorded by stepping the sample under the X-ray focus, in equivalent to scanning the X-ray beam vertically across the feature on the left side of the image (the bottom and top curves are taken just outside the 'disk'). There are four sets of peaks with distinct characteristics: (1) The sharp peak at 87.3ev becomes

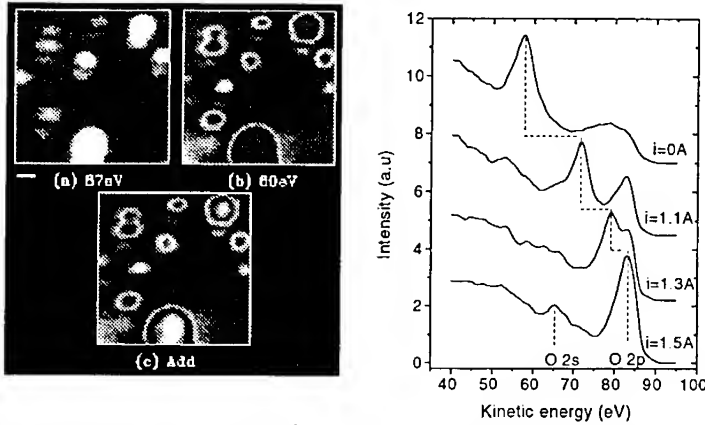


Figure 3: Micrographs taken of a 5000\AA Al-1%Cu-1%Si thin film after corrosion at mapping energies of (a) 87eV and (b) 60eV. (c) Superposition of (a) and (b) to show their relative position (See text for details). The scale bar in $3\mu\text{m}$. The four EDCs on the right are recorded at the same sample position with varying compensation to the surface charge.

strongest at the central region of the disc; (2) Also appearing in this region is the oxygen 2p band at 83.1eV, designated as O(I) 2p in the plot. The position of these two peaks remains unchanged and only the intensity varies with location. This O(I) 2p valence band is from the oxide in contact with the Cu-rich precipitates possibly formed with Al within the precipitates; (3) The broad peaks at 77.5eV labeled as O(II) 2p remain almost constant across the entire surface of the thin film. They are from the photoelectrons generated by the scattered X-rays from the multilayer-coated SO, and act as background signals; (4) The last set of peaks shift in energy from 67.2eV in the central region to 60.4eV outside the region. The shifts are *stable* and *repeatable*. A careful scrutiny of the lineshape of these peaks suggests that they are the shifted oxygen 2p valence bands in the oxides formed during corrosion. The shifts are due to the surface electrostatic charging effect of the highly resistive oxides. The amount of the shift indicates the degree of micro-corrosion. Imaging with the shifted peaks should thus produce maps of the oxide distribution. Micrograph (b) in Figure 3 is such a map with 60eV photoelectrons.

It is interesting to see that the oxide forms a circular structure. By simply superimposing the images taken at 87eV and 60eV in Fig. 3, the relative location of the Cu-rich region and the oxide is shown clearly in micrograph (c). The precipitate phase is within the circular oxide. This is the first spectromicroscopic evidence that the Cu-rich precipitates act as a cathode in the reaction process such that the surrounding Cu-deficit Al matrix corrodes to form a oxide layer.

To further confirm the spectral assignment associated with the shifted O 2p bands in the oxide, an experiment was performed to examine the effect of surface charge compensation. The neutralizing electrons (with 1-2eV energy) were generated by heating up a 1mil W filament placed in front of the sample. EDCs in Fig. 3 shows variation of the valence band spectra when current is passed through the filament. The peak at 58eV gradually shifts to 82.3eV, the final position for the O 2p band in a conducting film (The O 2s peak is also visible in the final spectrum).

The growth of Cu-rich precipitates, and thus the corrosion induced microstructures de-

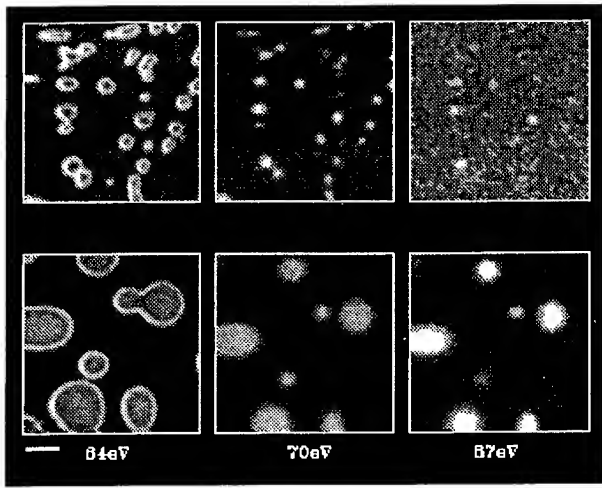


Figure 4: Micrographs taken of the corroded Al-2%Cu-1.5%Si thin film (1500Å thick) annealed at 320°C (upper panel) and 400°C (lower panel). The mapping energies are 64eV, 70eV and 87eV. The scale bar is 5 μ m.

pend on the annealing temperature. Fig. 4 shows photoelectron images taken at various energies for the corroded Al-2%Cu-1.5%Si thin film annealed at two different temperatures. With 320°C annealing, the images (upper panel) show dense and small microstructures. When the film is annealed at 400°C (still below the solvus temperature), the precipitates grow bigger and so do the corrosion induced microstructures as shown in the lower panel in Fig. 4. The images also show that the larger precipitates grow at the expense of smaller ones, indicating that part of the growth is by coalescence[14]. This demonstrates that the spectromicroscope can be utilized to characterize the dynamic process of microstructure evolution in the Al-Cu-Si thin films. Fig. 4 shows again the existence of Cu-rich precipitates in every corrosion induced microstructure. This demonstrates that the formation of Cu precipitates is solely responsible for the increased corrosion in the Al-Cu-Si metallization thin films. Images taken with 70eV photoelectrons show that the Cu-rich phase is also reacted, but to a less degree than its surroundings (mapped at 64eV).

From the energy-specific photoelectron images and microspectroscopic valence band EDCs presented, the evolution of corrosion induced microstructures can be proposed. The relative amount of Cu-rich phase as shown by the bright areas in the images taken at 87eV suggests that the precipitates form near the surface region. Because our technique is highly composition sensitive, the Cu precipitates exhibit relative large sizes as compared with TEM observations[8]. With the influence of precipitation, the native oxide formed on the thin film surface is less protective towards corrosion initiation as compared to the otherwise very protective oxide layer on pure Al or Cu-deficit Al regions. Thus, corrosion is initiated at these affected regions and the underlying precipitates further promote the reaction through a galvanic mechanism. The reaction will slow down and stop with the formation of Al oxide surrounding the Cu-rich sites.

Summary

We have employed a scanning X-ray photoelectron spectromicopic technique in the investigation of technologically important, thin films of Al-Cu-Si alloys. Both spectromicroscopy and microspectroscopy are necessary in order to characterize the details of the microstructural chemistry. We have found through this study that Cu diffuses to form Cu-rich precipitates near the surface and their precipitates grow with annealing at higher temperatures. Corrosion only takes place at these Cu-rich regions. We also show that valence band spectral shifts can be used to gauge the degree of corrosion.

ACKNOWLEDGEMENTS

We would like to thank our collaborators J.H. Underwood, J.B. Kortright and R.C.C. Perera at Lawrence berkeley Laboratory, and G. Margaritondo at EPFL, Lausanne, Switzerland. This work was supported by NSF under Grand No. DMR-8919297 and partially supported by DOE.

REFERENCES

1. C. Capasso, A. Ray-Chaudhuri, W. Ng, S. Liang, R. Cole, J. Wallace, and F. Cerrina, *J. Vac. Sci. Technol.*, **A9**(3), 1248(1991).
2. S. Wolf, Silicon Processing for the VLSI Era, Vol. 2, (Lattice Press, Sunset Beach, CA), Chapt.3(1990).
3. S. Thomas and H.M. Berg, *IEEE Trans. Components, Hybrids, Manufact. Technol.*, **10**, 252 (1987).
4. J.R. Scully, D.E. Peebles, A.D. Romig,Jr., D.R. Frear, and C.R. Hills, *Metall. Trans.*, **23A**, 2641(1992).
5. B.R. Rogers and S.R. Wilson, *J. Vac. Sci. Technol.*, **A9**(3), 1616(1991).
6. V. Brusic, G.S. Frankel, C.K. Hu, M.M. Plechaty, and B.M. Rush, *Corrosion*, **47**(1), 35(1991).
7. J.D. Sinclair, *J. Electrochem. Soc.*, **135**, 89C(1988).
8. D.R. Frear, J.R. Michael, C. Kim, A.D. Romig, and J.W. Morris, *SPIE*, **1596**, 72(1991).
9. S. Liang, A.K. Ray-Chaudhuri, W. Ng, S. Singh, J.T. Welnak, and F. Cerrina, *MRS Symp. Proc.*, **309**, 449(1993).
10. J.W. Cooper, *Phys. Rev.*, **128**, 681(1962).
11. V. Di Castro and G. Polzonetti, *Surf. Sci.*, **186**, 383(1987).
12. Unpublished results on thin films of Cu.
13. I.P. Batra, *J. Elect. Spect. Rel. Phen.*, **33**, 175(1984).
14. L.C. Brown, *Scripta Metallurgica*, **21**, 693(1987).

MICROTRIBOLOGICAL STUDIES BY USING ATOMIC FORCE AND FRICTION FORCE MICROSCOPY AND ITS APPLICATIONS

BHARAT BHUSHAN, VILAS N. KOINKAR AND J. RUAN
Computer Microtribology and Contamination Laboratory, Department of Mechanical Engineering, The Ohio State University, Columbus, OH 43210-1107

ABSTRACT

We have used atomic force microscopy (AFM) and friction force microscopy (FFM) techniques for microtribological studies including microscale friction, nanowear, nanoscratching and nanoindentation hardness measurements. The microscale friction studies on a gold ruler sample demonstrated that the local variation in friction correspond to a change of local surface slope, and this correlation is explained by a friction mechanism. Directionality effect is also observed as the sample was scanned in either direction. Nanoscratching, nanowear and nanoindentation hardness studies were performed on single-crystal silicon. Wear rates of single crystal silicon are approximately constant for various loads and test duration. Nanoindentation hardness studies show that AFM technique allows the hardness measurements of surface monolayers and ultra thin films in multilayered structures at very shallow depths and low loads. The AFM technique has also been shown to be useful for nanofabrication.

INTRODUCTION

Scanning tunneling microscopy (STM) [1], atomic force microscopy (AFM) [2] and the modifications of AFMs such as friction force microscopy (FFM) [3] are becoming increasingly important in the understanding of fundamental mechanisms of friction [3-5], wear and lubrication and in studying the interfacial phenomena in micro- and nanostructures used in magnetic devices and micro-electromechanical systems (MEMS). The need for ever increasing recording densities requires that the head and medium surfaces be as smooth as possible and flying height be near zero (contact recording). The size of the components in magnetic storage devices is miniaturized to minimize friction and wear at the head medium interface. The advantage of miniaturization and low-cost are resulting in an increasing use of silicon as a mechanical material [6,7]. Read-write sliders made of silicon have been fabricated using integrated circuit technology [8,9]. Integrated circuit technology offers the advantages of low cost and high volume production. However, limited data exist on the tribological behavior of silicon for use in the disk drives [9-12]. In this paper, we describe atomic force microscopy and its modifications developed for microtribological studies to conduct microscale friction, nanoscratching, nanowear, nanoindentation and its application for nanofabrication.

EXPERIMENTAL

Microtribological experiments have been performed using a modified atomic force microscope (AFM)/friction force microscope (FFM) (NanoScope III from Digital Instruments, Inc.), to conduct studies of microfriction, nanoscratching, nanowear and nanoindentation [5,13]. Simultaneous measurements of friction force and surface roughness can be made using this instrument. A Si_3N_4 tip fabricated using plasma-enhanced chemical-vapor-deposition (PECVD) on an integral Si_3N_4 cantilever beam having a normal stiffness 0.4 N/m was used for friction

force and topography measurements at loads ranging from 10 to 100 nN. The sample was scanned over a $4 \mu\text{m} \times 4 \mu\text{m}$ area in a direction orthogonal to the long axis of the cantilever beam with a scan rate of 1 Hz (scanning speed of $4.0 \mu\text{m/s}$). For nanoscratching, nanowear and nanoindentation hardness measurements, a three-sided pyramidal single-crystal natural diamond tip with an apex angle of 80° and a tip radius of about 100 nm (determined by scanning electron microscopy imaging) was used at relatively higher loads ($10 \mu\text{N}$ - $150 \mu\text{N}$). The tip was mounted on a stainless steel beam with normal stiffness of about 30 N/m [13]. For scratching and wear, the sample was scanned in a direction of a long axis of the cantilever beam at a scanning speed of $1 \mu\text{m/s}$. For wear, an area of $2 \mu\text{m} \times 2 \mu\text{m}$ was scanned. Sample surfaces were scanned before and after the scratches or wear to obtain the initial and the final surface topography, in this case, at a lower vertical load of $0.5 \mu\text{N}$ using the same diamond tip, over an area larger than the scratched or worn region to observe the scratch or wear scars. The operation procedures for nanoindentation were similar to those used for nanowear except that the scan size was set to zero in the case of nanoindentation, in order for the tip to continuously press the sample surface for about two seconds at various indentation forces (loads) which will be presented later. The surface was also imaged before and after the indentation at a normal load of about $0.5 \mu\text{N}$ as in the case of imaging of the scratch or wear scars. Nanohardness was calculated by dividing the indentation load by the projected residual area. The Si(111) samples used in our study were ultrasonically cleaned in methanol for 15-20 minutes and dried in dry nitrogen atmosphere before mounting on AFM. A gold ruler sample having 1000 lines/mm was used for friction force measurements. All measurements were carried out in the ambient atmosphere.

RESULTS AND DISCUSSION

Figure 1 shows the surface profiles, the slope of the surface profiles taken along the sample sliding direction, and the friction profile for the gold ruler. No direct correlation between the surface profile and the corresponding friction profile is observed in this figure, e.g., high and low points on the friction profile do not correspond to high and low points on the surface roughness profile, respectively. However there is a correlation between the slope of the roughness profile and the corresponding friction profile. In a paper by Bhushan and Ruan [5], we have presented similar correlation on a microscale of $500 \text{ nm} \times 500 \text{ nm}$ for magnetic tape and disk samples. We note that the Si_3N_4 tip has a radius typically about 30 to 50 nm which is smaller than that of most asperities present on the sample surface, therefore, the slope of the sample surface taken in the sample sliding direction is expected to affect the local friction. According to a friction mechanism (ratchet mechanism) developed by Makinson [14] and Bowden and Tabor [15], the variation of friction is strongly correlated to the variation of local surface slope, with ascending edge of an asperity having a larger friction force than that at the descending edge. Therefore, we believe that the good correlation between the surface slope and friction profiles can be explained by the ratchet mechanism. We have also observed the directionality in the local variation of micro-scale friction data as the sample was scanned in either direction, resulting from the scanning direction and the anisotropy in the surface topography (data not shown here).

Figure 2 shows the scratching marks on a single-crystal (111) silicon generated by using a diamond tip. The normal loads used for scratching were in the range of 10 - $80 \mu\text{N}$. All scratches were done with ten scratching cycles. A shallow scratch mark is visible at a normal load of $10 \mu\text{N}$ with depth of about 2 nm. The scratch depth increases linearly with an increase of normal load.

By scanning the sample (in 2D) while scratching, wear scars were generated on the Si(111) sample surface. Figure 3 shows the plot of wear depth as a function of number of cycles. The wear profiles generated at an applied normal load of $30 \mu\text{N}$ using a diamond tip and at various number of cycles are shown in Fig. 4. We observed wear debris in the wear zone just after wear tests that could be easily removed by scanning the worn region at a much lower load ($0.5 \mu\text{N}$). These suggest that wear debris are not adhered strongly to the silicon surface. These results

show that the wear depth increases with the number of cycles with almost the same wear rate. This is very useful method to determine the wear resistance of different surfaces.

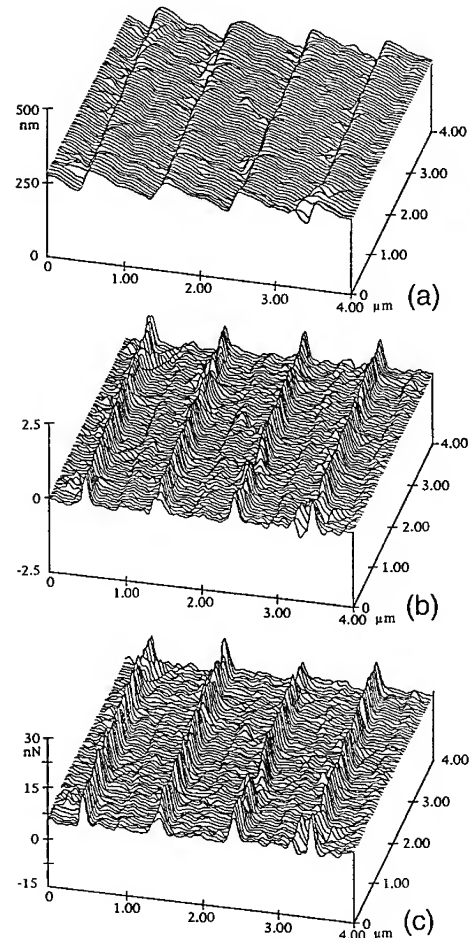


Fig.1. A $4 \mu\text{m} \times 4 \mu\text{m}$ scan of gold ruler.
 (a) surface roughness profile ($\sigma=22.0 \text{ nm}$),
 (b) slope of the roughness profile ($\tan\theta$) taken in the sample sliding direction (mean=0.0, $\sigma=0.25$) and (c) friction profile (mean=7.0 nN, $\sigma=2.9 \text{ nN}$) for a normal load of 150 nN.

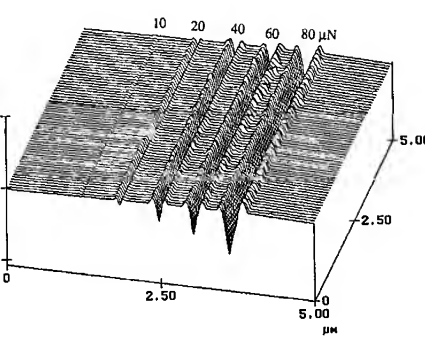


Fig.2. Scratch profile for scratched Si(111). Samples were scratched for 10 cycles. The normal load used for various scratches are indicated in the plot.

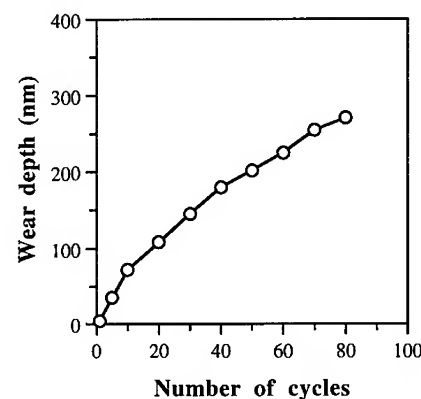


Fig.3. Wear depth as a function of number of cycles for Si(111) at normal load of 30 μN .

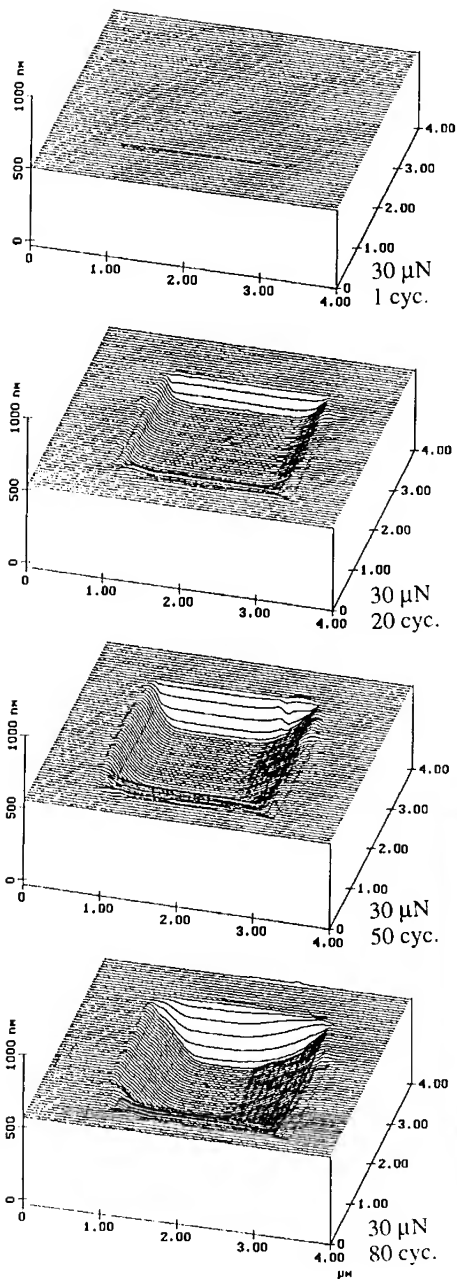


Fig.4. Surface profiles of Si(111) sample showing the worn region (center 2 $\mu\text{m} \times 2 \mu\text{m}$). The normal load and number of cycles are indicated in the figure.

We have measured the nanoindentation hardness of a single-crystal silicon. Figure 5 shows the gray scale plot of an indentation mark generated on Si(111) surface at a 70 μN vertical load. Triangular indent can be clearly observed with a depth of indentation of about 3 nm. The depth of indentation increases with an increase in normal load. The calculated hardness value for Si(111) at indentation depth of about 3 nm is about 15.8 GPa and drops to a value of 11.5 GPa at a depth of 12 nm and normal load of 130 μN , Fig. 6. The hardness data at a depth of 12 nm is comparable to the nanohardness data reported by Pharr et al. [16] with depth of indentations exceeding 20 nm. High hardness obtained at shallow depth probably arises from the hard surface films. If the silicon is to be used at very light load such as in microsystems, high hardness of surface films would protect the surface until worn.

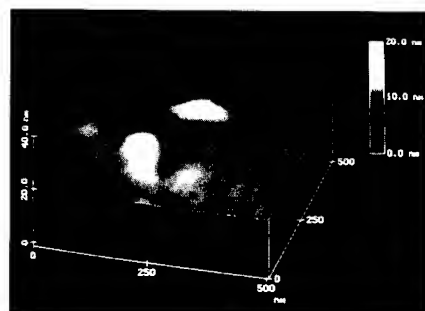


Fig.5. Gray scale plot of indentation mark generated on Si(111) at normal load of 70 μN .

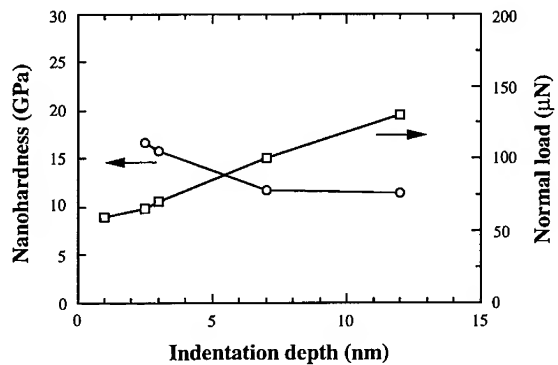


Fig. 6. Hardness value at different indentation depths with different indentation loads for Si(111).

An extension of nanoscratching is nanofabrication using AFM. Figure 7 shows such an example. The letters "OHIO" were written on a single-crystal silicon using a diamond tip under a 50 μ N normal load. The writing was done at slow speed (100 nm/s for scratching each line). Small shift in the marks occurred because of the thermal drift of the PZT tube. With a totally automated operation, it is possible to significantly reduce the drifting effect and to improve the nanofabrication quality.

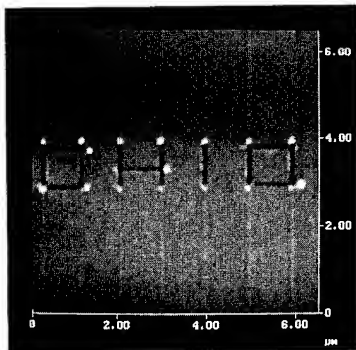


Fig. 7. Example of nanofabrication. The letters "OHIO" (which stands for the Ohio state) were generated by scratching a Si(111) surface using a diamond tip at an applied vertical (scratching) load of 50 μ N. The white spots observed at the corners are due to debris generated during scratching.

CONCLUSIONS

It has been shown that atomic force microscopy and friction force microscopy can be used for various microtribological studies: Friction measurements were carried out at microscale and the data show that the slope of sample surfaces is responsible for the variation of microscale friction for a gold ruler. Atomic force microscopy is successfully employed for nanoscratching, nanowear and nanoindentation hardness measurements. Nanoindentations made on silicon at very light load (~70 μ N) and shallow depth (~3 nm) indicate that the surface films on silicon are harder as compared to the bulk. Nanoindentation hardness measurements by using atomic force microscopy has a potential of measuring the hardness of monolayers and ultra thin film in multilayered structures. AFM has also been shown to be useful for nanofabrication.

REFERENCES

1. G. Binning, H. Rohrer, Ch. Gerber and E. Weibel, Phys. Rev. Lett., 49 (1), 57 (1982).
2. G. Binning, C.F. Quate and Ch. Gerber, Phys. Rev. Lett., 56 (9), 930 (1986).
3. C.M. Mate, G.M. McClelland, R. Erlandsson and S. Chiang, Phys. Rev. Lett., 59 (17), 1942 (1987).
4. J. Ruan and B. Bhushan, J. Trib., Trans. ASME (1994) (in press).
5. B. Bhushan and J. Ruan, J. Trib., Trans. ASME (1994) (in press).
6. K.E. Petersen, Proc. IEEE, 70 (5), 420 (1982).
7. B. Bhushan and S. Venkatesan, Adv. Info. Storage Syst., 5, 211 (1993).
8. J.P. Lazzari and P. Deroux-Dauphin, IEEE Trans. Mag., 25 (5), 3190 (1989).
9. B. Bhushan, M. Dominiak and J.P. Lazzari, IEEE Trans. Mag., 28, 2874 (1992).
10. B. Bhushan and S. Venkatesan, J. Mater. Res., 8, 1611 (1993).
11. S. Venkatesan and B. Bhushan, Adv. Info. Storage. Syst., 5, 243 (1993); Wear (1994) (in press).
12. B.K. Gupta, J. Chevallier and B. Bhushan, J. Trib. Trans. ASME, 115, 392 (1993); Trib. Trans. (1994) (in press).
13. B. Bhushan, V.N. Koinkar and J. Ruan, J. Eng. Trib., Proc. I. Mech. E.(1994) (in press).
14. K.R. Makinson, Trans. Faraday Soc., 44, 279 (1948).
15. F.P. Bowden and D. Tabor, The Friction and Lubrication of Solids, (Clarendon Press , Oxford, 1950), p. 172.
16. G.M. Pharr, W.C. Oliver and D.R. Clarke, J. Electronic Mat., 19 (9), 881 (1990).

MOLECULAR DYNAMICS SIMULATION OF THE ELASTIC DEFORMATION OF NANOMETER DIAMETER METAL CLUSTERS

DILIP Y. PAITHANKAR, JULIAN TALBOT, AND RONALD P. ANDRES
School of Chemical Engineering, Purdue University, West Lafayette, IN 47907

ABSTRACT

Indentation using the AFM is a powerful method for determining elastic properties of small supported clusters. However, a theoretical framework has yet to be developed to interpret such measurements. The elastic deformation of nanometer sized gold clusters are modeled using the Embedded Atom Method (EAM) potential of Foiles *et al.* [1]. Force versus deformation curves are obtained for a series of truncated octahedral clusters having FCC symmetry ($N=38, 201, 586, 1289, 2406$). It is found that the MD results both for static compression and for harmonic vibration can be analytically estimated by using an elastic constant for the clusters analogous to the elastic modulus of a bulk material. However MD predictions for static compression are not in agreement with the deformation results of Schaefer *et al.* [2].

INTRODUCTION

Molecular dynamics (MD) studies have been undertaken to complement the indentation experiments on nanometer sized clusters by Schaefer *et al.* [2]. With a SiO_2 tip having a radius of curvature larger than the cluster radius and maximum loads of only a few nN, the authors obtain linear force versus deformation curves. In the present study we model the elastic compression of nanometer sized gold clusters by means of MD simulations. The purpose of these calculations is twofold: (1) to compare with the experimental results of Schaefer *et al.* and (2) to develop an analytical model for estimating the size dependence of the elastic deformation curves for nanometer diameter metal clusters.

COMPUTATIONAL DETAILS

MD calculations have been carried out by integrating Newton's equations of motion for the gold atoms constituting a cluster with the velocity Verlet algorithm [3]. We use a time step of 0.007 ps which gives acceptable energy conservation for a constant energy simulation of an isolated gold cluster. The forces between gold atoms are calculated using the semi-empirical EAM potential developed by Foiles *et al.* [1]. It has been experimentally observed that gold clusters that have been well annealed in the gas phase are face centered cubic (FCC) crystals [4]. Energy minimization with the EAM potential reveals that the most stable shape for these clusters is that of a truncated octahedron with square (100) and hexagonal (111) faces [4, 5]. The smallest clusters with this structure contain 38, 201, 586, 1289, and 2406 atoms. These are the clusters we have studied. Key geometric characteristics of these clusters are tabulated in Table 1. Here N is the number of atoms in the cluster, n_e is the number of atoms along an edge, and n_s is the number of atoms in a hexagonal (111) face. The clusters were oriented so that two opposite hexagonal faces were perpendicular to the z-direction and n_z is the number of (111) planes in a cluster counting from the bottom face to the top face.

In the first set of simulations, equal and opposite forces were applied to the top and bottom faces of the cluster. The total force was distributed evenly over each of the atoms in the face. At each time step, the net force on each atom in the top and bottom faces is the sum of the force due to other atoms and this external force. In the compression studies, the external force was applied downward on the top face and upward on the bottom face while the directions were reversed in tension studies. The net external force on the cluster is always zero and hence there is no net translational motion of the cluster. Simulations were performed for successively higher values of force. At each value of force, a simulated annealing calculation was carried out. This calculation involved performing MD calculations for a block of 40 time steps and then setting the velocity of all the atoms to zero. This process was

Table 1: Geometric properties of fcc truncated octahedra.

N	n_e	N_s	n_z
38	2	7	4
201	3	19	7
586	4	37	10
1289	5	61	13
2409	6	91	16

repeated until the energy of the cluster became constant. The last configuration at a given value of force was used as the first configuration for the next higher value of force. The height of the cluster was defined as the difference in the average of the z-coordinates of atoms in the top layer and the bottom layer. Plots of force versus the cluster deformation were then

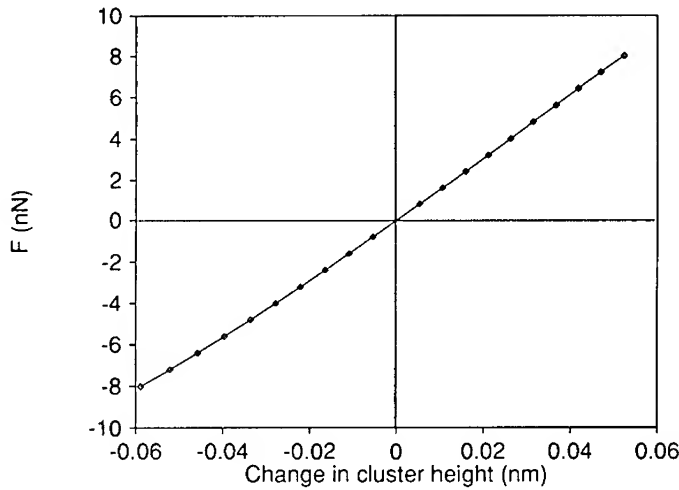


Figure 1: Force-deformation curve for a 201 atom gold cluster as determined from MD simulations.

constructed. Figure 1 presents the force-deformation curve for $N=201$.

In the second set of MD simulations, a cluster at its equilibrium configuration was perturbed by symmetric compression and then released from all external forces. A plot of cluster height versus time for such a simulation is shown in Figure 2. The average of the z-coordinates of the atoms in each of the (111) layers from the bottom face to the top face varied in phase revealing the primary mode of vibration to be a symmetric stretch along the z-axis. The frequency of this vibration was determined for each size cluster.

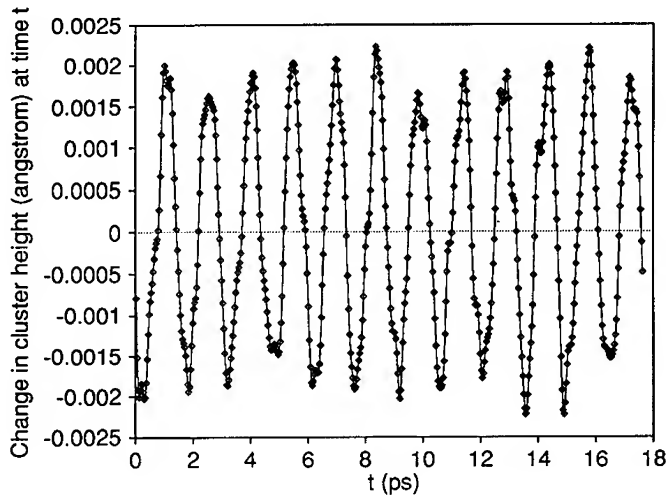


Figure 2: Difference between cluster height at time t and height of unperturbed cluster versus time t for a 201 atom gold cluster.

RESULTS AND DISCUSSION

INDENTATION OF BULK GOLD

In order to check the accuracy of our calculations, molecular dynamics with simulated annealing was performed on a slab of atoms with adjustable periodic boundary conditions in the lateral directions. The system was composed of 13 (111) layers, each layer consisting of 100 atoms. External force was applied to the atoms in the top and bottom faces. The lattice dimensions in both lateral directions were adjusted so as to minimize the energy of the equilibrium configuration at each value of force. This allows for Poisson expansion. The slope of the normalized force versus deformation curve for this slab should be approximately equal to $E_{111}/(1-v^2)$, where E_{111} is Young's modulus in the [111] direction and v is Poisson's ratio. Taking $v = 0.3$ yields a value for E_{111} of 130 GPa. Foiles *et al.* [1] report values of C_{11} , C_{12} , and C_{44} , the elastic constants of gold. The Young's modulus, E_{111} calculated from the above elastic constants is 124 GPa. Thus, there is a reasonably good match between the value of E_{111} obtained from our simulations and that reported by Foiles *et al.* [1].

INDENTATION OF GOLD CLUSTERS

The slopes, S , of the force-deformation curves obtained from the MD simulations for each cluster size are shown in Table 2. Schaefer *et al.* [2] modeled their cluster deformation by an equation of the form:

$$S = \frac{F}{\Delta h_c} = \frac{EA_c}{h_c} \quad [1]$$

where E is an elastic modulus, A_c is the area of a (111) face, and h_c is the cluster height.

$$A_c = N_s \times a_{111} \quad \text{and} \quad h_c = n_z \times d_{111} \quad [2]$$

Here, $a_{111} = 0.0721 \text{ nm}^2$ is the area per atom in a (111) plane and $d_{111} = 0.236 \text{ nm}$ is the distance between (111) planes in bulk gold. Substitution of the S values obtained by MD simulations into Eq. [1] yields the E values shown in Table 2. These values of E are plotted

Table 2: Elastic deformation results for gold clusters.

N	S (nN/nm)	E (GPa)	E_{111}^S (GPa)
38	108.6	202.7	104
201	145.9	175.7	98
586	194.8	172.0	98
1289	246.4	171.6	99
2406	290.5	166.9	98

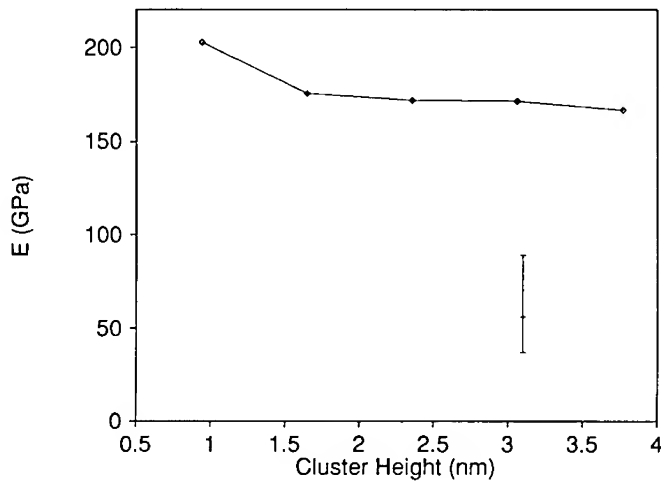


Figure 3: Elastic modulus determined from MD simulations; "+" with an error bar indicates experimental value from Schaefer *et al.* [2].

as a function of cluster height in Figure 3. The values of E determined from the MD simulations are much greater than the experimental E value estimated by Schaefer *et al.* [2]. There are several possible explanations for this lack of agreement. Both the model used by Schaefer *et al.* and the model underlying the MD simulations assume elastic deformation of an ideal truncated octahedral cluster under simple contact forces. The experimental cluster may not have been an ideal truncated octahedron and may not have been oriented with a (111) face perpendicular to the surface normal. Any deviation in the shape of the cluster or its orientation will serve to decrease E. Furthermore, although the adhesive interactions between Au and HOPG and SiO_2 do not appear to cause any plastic deformation of the cluster, the net effect of these adhesive forces is to soften the force-deformation curve and this may be especially important for the small clusters and low loads of interest. MD simulations that model the effects of adhesive forces are currently being run [5].

It is seen from Table 2 that E, as determined by the MD simulations, is size dependent. The question arises whether this is due to the fact that Eq. [1] models the cluster as having a constant cross-sectional area equal to the area of a (111) face or is it due to an increase in the effective elastic modulus of these small clusters brought about by their high surface-to-

volume ratios. In an attempt to answer this question an analytical model that accounts for the actual variation in cluster cross-section with cluster height was developed. The cluster is regarded as a series of (111) planes and the compression of the region between each atomic plane is modeled by the equation

$$\Delta h_{i,i+1} = F \left[\frac{d_{111}}{E_{111} a_{111}} \right] \left[\frac{2}{N_i + N_{i+1}} \right] \quad [3]$$

where $\Delta h_{i,i+1}$ = deformation of the region between the i th and $i+1$ st (111) planes, N_i = number of atoms in i th plane, and E_{111} = effective elastic modulus in the [111] direction. The elastic deformation of a cluster is then given by the expression

$$\Delta h_c = F \left[\frac{d_{111}}{E_{111} a_{111}} \right] \sum_{i=1}^{n_z-1} \frac{2}{N_i + N_{i+1}} \quad [4]$$

which assumes constant E_{111} for different size planes.

Substituting the values of S obtained from the MD simulations into Eq. [4] and taking into account the number of atoms in each (111) plane yields the values for E_{111}^S shown in Table 2. It is apparent that Eq. [4] reproduces the size dependence in the MD force-deformation data with a single adjustable parameter, $E_{111}^S \approx 100$ GPa. Equation [4] is proposed as a simple analytical model for estimating elastic deformation curves for small FCC clusters oriented with their (111) planes perpendicular to the applied force. The usefulness of this model is of course contingent on developing methods for determining the equilibrium shape of a supported cluster and for estimating the effects of adhesive forces between the cluster and its support and between the cluster and the AFM tip.

HARMONIC VIBRATION OF GOLD CLUSTERS

The vibrational frequency of the symmetric stretch for different size clusters is shown in Table 3.

Table 3: Frequency of symmetric stretch vibration of gold clusters

N	f (THz)	E_{111}^D (GPa)
201	0.684	71
586	0.478	70
1289	0.365	69
2406	0.295	68

Modeling the motion of the (111) layers in the cluster in a manner analogous to that used in deriving Eq. [4] yields

$$N_1 m \frac{d^2}{dt^2}(\theta_1) = \left[\frac{E_{111} a_{111}}{d_{111}} \right] \left[\frac{N_1 + N_2}{2} \right] [\theta_2 - \theta_1] \quad [5(a)]$$

$$N_i m \frac{d^2}{dt^2}(\theta_i) = \left[\frac{E_{111} a_{111}}{d_{111}} \right] \left[\left(\frac{N_i + N_{i+1}}{2} \right) [\theta_{i+1} - \theta_i] + \left(\frac{N_i + N_{i-1}}{2} \right) [\theta_{i-1} - \theta_i] \right] \quad [5(b)]$$

$$N_{n_z} m \frac{d^2}{dt^2}(\theta_{n_z}) = \left[\frac{E_{111} a_{111}}{d_{111}} \right] \left[\frac{N_{n_z-1} + N_{n_z}}{2} \right] [\theta_{n_z-1} - \theta_{n_z}] \quad [5(c)]$$

Here, m is the mass of an atom and θ_i is the deviation between the z -position of the i th plane of atoms at time t and its z position in an undeformed cluster. Writing Eq. [5] in vector form

Solving the eigenvalue problem for this equation for the smallest non-zero eigenvalue and using the frequency of vibration obtained by MD simulations, one can calculate E_{111}^D for each cluster size. The E_{111}^D values calculated in this manner are tabulated in Table 3. Again, the model accounts for the size dependence of the vibrational frequency with a single adjustable parameter, $E_{111}^D \approx 70$ GPa. However, this parameter is not equal to the effective elastic modulus obtained by static deformation.

SUMMARY

Molecular dynamics simulations of the static and dynamic elastic deformation of nanometer sized gold clusters containing 38, 201, 586, 1289, and 2406 atoms are adequately modeled by analytical expressions which take into account the detailed variation in the cluster's cross section as a function of cluster height and represent the elastic behavior of the cluster in terms of an effective elastic modulus. The agreement between MD simulations of static deformation and the experimental deformation of a gold cluster measured by Schaefer *et al.* [2] is poor. While there are several possible reasons for this lack of agreement, the most probable seems to be the need to account for the effects of adhesive surface forces both in the MD simulations and in the nanoindentation model used to invert the experimental data.

ACKNOWLEDGEMENTS

This work was partially funded by the National Science Foundation under grant ECS-9117691 and by National Center for Supercomputing Applications, University of Illinois at Urbana-Champaign under grant CBT-920035N and utilized the computer system CRAY Y-MP4/464.

REFERENCES

1. S.M. Foiles, M.I. Baskes, and M.S. Daw, Phys. Rev. B., **33**, 7983 (1986).
2. D.M. Schaefer, A. Patil, R.P. Andres, and R. Reifenberger, Appl. Phys. Lett., **63**, 1492 (1993).
3. W.C. Swope, H.C. Andersen, P.H. Berens, and K.R. Wilson, J. Chem. Phys., **76**, 637 (1982).
4. A.N. Patil, D.Y. Paithankar, N. Otsuka, and R.P. Andres, Z. Phys. D, **26**, 135 (1993).
5. D.Y. Paithankar (unpublished results).

A Thermal Stage For Nanoscale Structure Studies With the Scanning Force Microscope

W. J. Kulnis, Jr. and W. N. Unertl, University of Maine, Orono, ME 04469

Abstract:

We have constructed an inexpensive sample mounting stage for studies of temperature dependent processes in a surface force microscope (SFM). The stage is constructed from a Peltier thermoelectric heater secured to a standard SFM mounting stage with silver paint. The sample temperature can be varied from room temperature to about 100 °C thus making it possible to use the SFM to observe thermally activated processes at lateral spatial resolutions of 10-20 nm. Approximately 10 minutes is required to reach thermal equilibrium following a 5 °C temperature change. The lateral magnification must be calibrated at each temperature. We illustrate the capabilities of the stage with images of polystyrene spheres just below their glass transition temperature of 100 °C.

Introduction:

In this paper, we describe a thermal stage designed for studies of latex wetting using the scanning force microscope (SFM). This stage, is inexpensive and easily adaptable to the study of many other materials using the SFM. Developed in 1986 by Binnig et al.,¹ the SFM has proven to be a useful tool for investigating surfaces at high spatial resolution. Since 1986 the SFM has been used to study many different materials and processes.²⁻⁸ One such process is the behavior of latex during film formation.^{9,10,11}

Synthetic latexes are of great importance in the adhesive, paint, paper, and coating industries. A better understanding of the film formation and wetting and spreading phenomena of latex is needed to improve production and design of commercial latex. To date, SFM studies of latex film formation could only be done by imaging the latex after thermal treatment above the film formation temperature.^{9,10} Studies also have been done on latexes that have not been allowed to reach film formation temperature.¹¹ We have constructed a simple, inexpensive "hot stage" for the SFM that allows us to investigate processes *in situ* at temperatures ranging from room temperature to about 100 °C. Here we illustrate the capabilities of the hot stage by presenting preliminary results of a study of latex film formation and the investigation of wetting and spreading of individual latex spheres imaged through a temperature range from 20 °C to approximately 80 °C. We will also address some of the difficulties and problems that occur while imaging with the hot stage.

Experimental:

I.) Hot Stage:

Figure 1 shows the "hot stage" which has been constructed from a Peltier device¹² and a standard sample stub¹³. The Peltier device is secured to the sample stub, cold side down, by silver paint. An epoxy with low thermal conductivity would improve the thermal response. The substrate to be used is then attached to the hot side of the Peltier device with the silver paint to obtain a contact with high thermal conductivity. A conducting epoxy could also be used but it would be more difficult to change the sample. The Peltier device is powered by a dc current source capable of providing up to 1.5 A at about 2.5 mV. Passing a current through the hot stage produces a temperature range from room temperature to approximately 80 °C. The maximum temperature is limited to about 100 °C by materials used to fabricate the Peltier device. Copper wire of 0.015 inch diameter is used as leads for the hot stage. The

leads are run from the stage to the current source which is placed on a table next to the air table that the SFM sits on. The leads do not affect the images in any way. Total cost of a stage is about \$12.00.

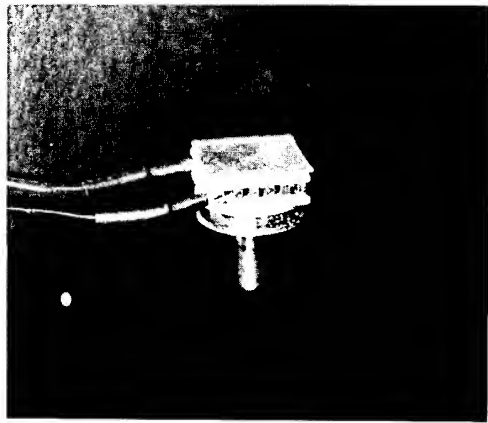


Fig. 1. Hot stage constructed from Peltier thermoelectric heater secured to standard SFM stage with silver paint. Mica sheet with latex sample mounted on top. The Peltier heater has a 12 mm x 12 mm surface area and is 3.2 mm thick.

II.) Latex Sample:

Freshly cleaved mica was used as the substrate for the latex particles. The mica surface is smooth on the atomic scale. This makes it an ideal substrate for studies of film surfaces. After securing the substrate to the hot stage with conductive silver paint, a drop of 0.1% solution by volume of Lytron 2503 latex in deionized water was applied from a standard laboratory pipette. After application to the mica, the solution was left to dry in air for several hours. The samples were imaged in air with a commercial atomic force microscope¹⁴ operating in the constant force contact mode.¹⁵ Humidity was controlled by placing the SFM head into a dry box purged with a flow of dry air from a commercial air drying system.¹⁶ Images were taken with the sample at temperatures ranging from about 20 °C (room temperature) up to around 80 °C.

Results and Discussion:

Figure 2a shows a 10 µm x 10 µm image of polystyrene particles at room temperature. The 10 µm x 10 µm image was clipped from a larger 35 µm x 35 µm image using image processing software supplied with the SFM. The images were taken with the SFM in a mode of operation that eliminates any sample tilt in the y-direction. A monolayer thick band of close-packed particles is seen running from the left side of the image to the upper right corner with a section of another band joining at the lower left. A small island of particles can also be seen in the lower right of the image. A few single particle voids can be seen. The edges of the band show a step-like profile.

Figure 2b shows roughly the same $10 \mu\text{m} \times 10 \mu\text{m}$ area of the same sample. This image was also clipped from a larger $35 \mu\text{m} \times 35 \mu\text{m}$ image. This image was taken at approximately 82°C , which is below the glass transition temperature ($T_g = 100^\circ\text{C}$) of the latex. Images were taken at 5°C intervals beginning with room temperature and ending at 82°C . Approximately 10 minutes are required for the sample to reach thermal equilibrium after every current change. The particles appear to have lost their row orientation in places such as the point labeled (1) in Fig. 2b. Also, some of the particle size voids (e.g.; that labeled (2) in Fig. 2b) are no longer visible. The island of particles on the right side of Figure 2a can no longer be seen (3). The edges of the main band of particles has a less jagged profile due to motion of latex particles during the heating process. This is particularly evident if the top edges of Fig. 2(a) and 2(b) are compared. The dimensions of the main band of particles appear to have changed with heating. The band seems wider in the upper right, becoming narrower toward the lower left. This may be due to particle migration which is suggested by the movement of the small island out of the field of view (3) and changes in edge structure.

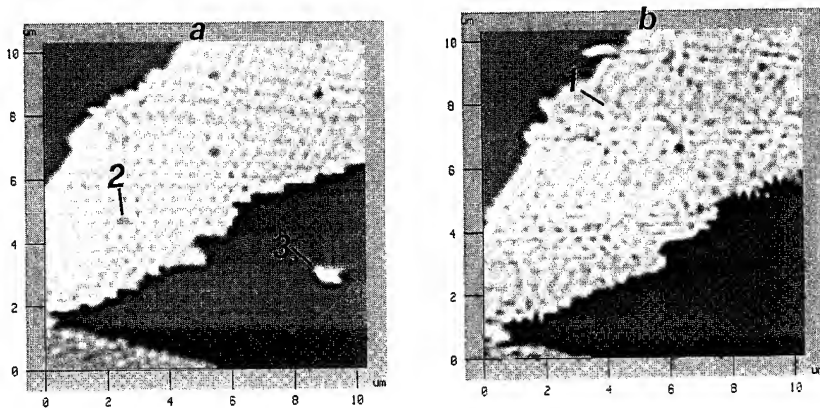


Fig. 2(a) $10 \mu\text{m} \times 10 \mu\text{m}$ image of latex particles on mica taken at room temperature.
 (b) $10 \mu\text{m} \times 10 \mu\text{m}$ image of latex particles on mica taken with the sample at 82°C .
 Gray scale, going from dark to light, runs from 0 \AA - $10,000 \text{ \AA}$.

References:

1. G. Binnig, C.F. Quate, and Ch. Gerber, Phys. Rev. Lett. **56**, 930 (1986).
2. T.R. Albrecht and C.F. Quate, J. Appl. Phys. **62** 2599 (1987).
3. C.M. Mate, G.M. McClelland, R. Erlandsson, and S. Chiang, Phys. Rev. Lett. **59**, 1942 (1987).
4. Y. Martin and H.K. Wickranainghe, Appl. Phys. Lett. **50**, 1455 (1987).
5. M.D. Kirk, T.R. Albrecht, C.F. Quate, Rev. Sci. Instrum. **59**, 833 (1988).

6. S. Gould, O. Marti, B. Drake, L. Hellemans, C.E. Bradker, P.K. Hansma, N.L. Keder, M.M. Eddy, and G.D. Stucky, *Nature* **332**, 332 (1988).
7. T.R. Albrecht, M.N. Dovek, C.A. Lang, P. Grutter, C.F. Quate, S.W.J. Kvan, C.W. Frank, P.F.W. Pease, *J. Appl. Phys.* **64**, 1178 (1988).
8. A.L. Weisenhorn, J.E. MacDougall, S.A.C. Gould, S.D. Cox, M.S. Wise, J. Massie, P. Maivald, V.B. Elings, G.D. Stucky and P.K. Hansma, *Science* **247**, 1330 (1990).
9. M.C. Goh, D. Juhue, O.M. Leumg, Y.C. Wang and M.A. Winnik, *Langmuir* **9**, 1319 (1993).
10. V. Granier, A. Sartre, M. Joanicot, preprint 1993.
11. D. Juhue and J. Lang, *Langmuir* **9**, 792 (1993).
12. Melcor Materials Electronics Products Corp. CAT# CP1.0-17-05TL, 990 Spruce Street Trenton, NJ 08648.
13. Ted Pella INC., CAT# 16112, P.O. Box 492477, Redding, CA. 96049.
14. Park Scientific Instruments model# SFM-BD2, 1171 Borregas Ave. Sunnyvale, CA 94089.
15. N.A. Burnham and R.J. Coulton, in Scanning Tunneling Microscopy and Spectroscopy, D.A. Bonnell, ed.(VCH Publishers, New York, 1993) p. 232.
16. Puregas Heatless Dryer, Model PCDA1-120-B032 from General Cable Corp., Westminster, CO.

DYNAMIC BEHAVIOUR OF LEAD NANOPARTICLES IN A DIELECTRIC MATRIX

P. CHEYSSAC*, R. KOFMAN*, P. G. MERLI**, A. MIGLIORI**, A. STELLA***

* Laboratoire de Physique de la Matière Condensée, URA 190, Université de Nice Sophia Antipolis, 06108 Nice Cedex 2, France.

** Istituto di Chimica e Tecnologie dei Materiali e dei Componenti dell' Elettronica del Consiglio Nazionale delle Ricerche, Via di Castagnoli 1, I-40126 Bologna, Italy

*** Dipartimento di Fisica A. Volta, Università degli Studi di Pavia, Via A. Bassi 6, 27100 Pavia, Italy .

ABSTRACT

In this paper we present electron microscopy results near and below the melting temperature, both in dark field and high resolution mode, of lead nanoparticles embedded in a dielectric matrix of amorphous SiO_x . Three different size dependent regimes are distinguished. Indications of solid particles rotations as well as of a new phenomenon amenable to spontaneous solid-liquid phase fluctuations will be briefly discussed.

I - INTRODUCTION

Small metal particles show some remarkable deviations from bulk properties when the size is decreased down to a few nm. Actually, when the surface atoms become a relevant fraction of the total volume, important consequences are expected on the main physical features of the system: in particular, a strong decrease of the melting temperature T_M with size has been observed in some metals like Au and Pb [1,2]. Predictions of a progressive decrease also of the latent heat of fusion with size have been given on the basis of empirical molecular dynamics simulations [3].

Furthermore, from recent theoretical work the interplay between short and long range forces has been shown to affect drastically, in specific cases, the phase configuration both of flat bulk surfaces and of small particles even well below T_M [4]. Recent experiments have shown that a very thin liquid film may form at the crystal vapour (or crystal-matrix) interface, whose thickness grows as a function of temperature and, in the case of the particles, also as a function of curvature [5].

This behaviour, known as surface melting, depends strictly on the material and on the crystal orientation. For instance in the case of Au and Pb, the surfaces (110) melt whereas the more close-packed (111) do not. In order to have surface melting, the following necessary condition must be fulfilled [6,7]:

$$\gamma_{sv} - \gamma_{sl} - \gamma_{lv} > 0 \quad (1)$$

where the three terms represent respectively free energies per unit area of solid-vapour, solid-liquid and liquid-vapour interfaces. In (1) the vapour is replaced by the matrix if particles surrounded by a solid environment are considered, as shown below. In this paper the attention will be focused on generally spherical Pb particles having diameters in the range $2 \text{ nm} \leq d \leq 20 \text{ nm}$, where their dynamic behaviour exhibits large variations.

II - EXPERIMENTAL

The samples were prepared by evaporation-condensation in ultrahigh vacuum on carefully cleaned substrates of sapphire; copper grids coated with carbon were subsequently attached on top of them to make electron microscopy measurements. After evaporation of a film of $\text{SiO} \sim 15$ nm thick on such substrates, lead was deposited at temperatures from 77 to 473 K. Metal particles were thus formed, having dimensions which can be controlled in the above referred range with a size dispersion of about 1/4 the average diameter; they were subsequently covered with an additional layer of SiO about 15 nm thick. In fig.1 a sketch of the samples is shown. The Pb particles are completely encased inside the SiO matrix which doesn't induce any preferential orientation on the metal grains since it is amorphous. The melting temperature for bulk lead is 601 K and it has been ascertained to decrease down to values of 392 K for diameters of 8.4 nm. This makes the choice of the coupling $\text{Pb} - \text{SiO}$ as particles-matrix system particularly suitable, since the melting temperature of SiO is 1978 K: in other words melting of Pb particles can be studied in a temperature range characterized by a good stability of the matrix. Also the interaction $\text{Pb} - \text{SiO}$ is negligible below 600 K, as proved by the absence of any detectable ageing after several runs between 300 and 600 K. It should also be added that Pb doesn't wet SiO , the contact angle being $\theta \sim 112^\circ$ [8]

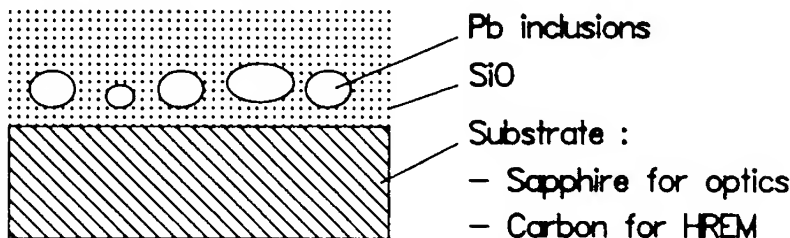


Fig. 1: Schematic presentation of the sample.

By performing *in-situ* dark field electron microscopy (DFEM) experiments it is possible to study changes in the state (solid or liquid) of the lead particles. The objective aperture is between the (200) and (220) rings of polycrystalline lead, so that most of the electrons passing through the aperture are scattered from the liquid part of the clusters. In fig.2 a DFEM picture sequence is reported. In the first picture the central big particles (diameter ≈ 10 nm), being still solid, look dark and are surrounded by a white ring indicating the presence of a thin liquid layer. The other clusters are melted, so that they have a bright look. The left bottom side of the big central and asymmetric solid cluster looks already nearly liquid at the lower temperatures shown. By increasing the temperature the two portions of the cluster join and the thickness of the surrounding liquid layer grows. A further temperature increase produces a quick melting of the solid particle core.

In summary, DF data versus temperature show that:

- The particles tend to melt at a temperature T_M below the bulk melting temperature (601 K).
- In the same picture at a given temperature showing a distribution of particles it is evident that smaller particles entirely liquid coexist with bigger solid particles surrounded by a liquid layer.
- At a given temperature as a function of time a rotation of the solid core is evident, apparently made possible by the existence of the liquid layer. Rotations have also been detected in the high resolution mode.

High resolution electron microscopy (HREM) measurements were made with a Philips CM30 electron microscope, equipped with a TV system, image intensifier and video recording facilities, that was operated at 300 kV.

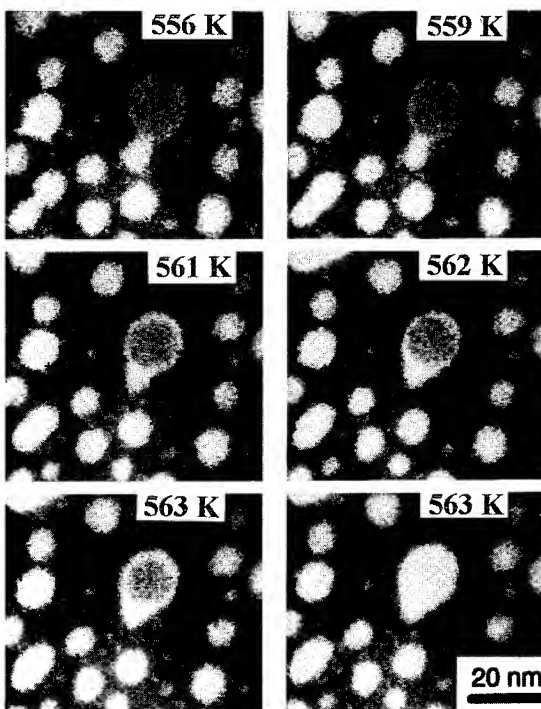


Fig. 2: DFEM picture sequence reporting the solid to liquid transition of a Pb particle with a diameter of ~ 10 nm. The time interval between the last two photographs is 40 ms.

Such measurements have been performed at room temperature with the purpose of making a comparative study on a distribution of particles of different size in order to have a deeper insight into their dynamic behaviour just below and around T_M (depending on the dimensions). The current density was varied in the range 10-20 Amp / cm^2 , as measured by means of a Faraday cage. The maximum temperature rise due to inelastic scattering however was calculated to be less than 10 K, so that the beam heating should play a negligible role in the physical processes investigated.

Three different regimes can be distinguished :

- i) $d > 10$ nm. The particles show a crystalline or multiply twinned structure, and the movements observed take place in a few seconds, as previously observed in similar cases.
- ii) $d \approx 10-5$ nm (see fig.3). Fluctuations in the exhibited structure of the particle take place in fractions of a second, with a frequency that increases by reducing the cluster size. The time separation between successive frames in fig.4 is 0.04 sec. It is shown that in 0.08 sec. a cluster having a diameter $d \sim 5$ nm changes from a liquid globule look to a crystalline one and then turns back to an image characterized by the absence of any structure.
- iii) The clusters having $d < 5$ nm never display an ordered structure. The combined examination of the contrast in DF images gives strong indications that here we are in presence of liquid particles [5].

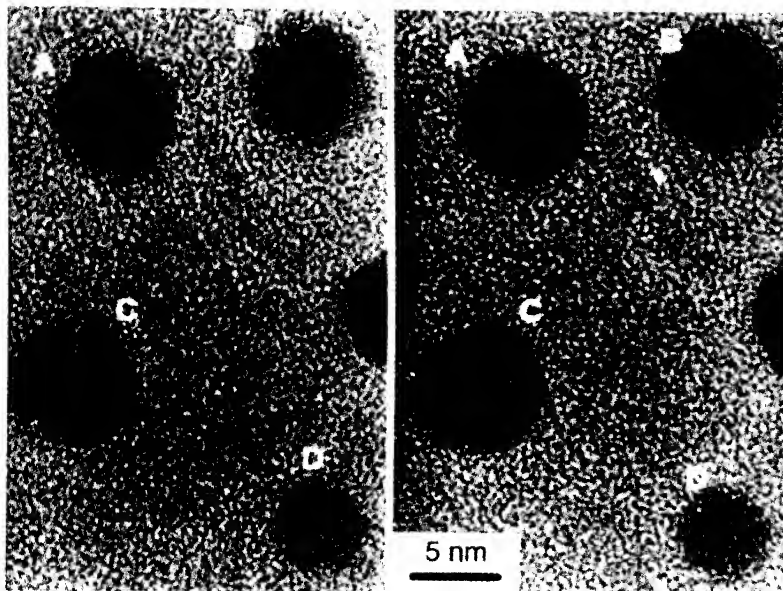


Fig. 3: a) HREM image of four Pb clusters; b) image of the same region after ~ 10 s

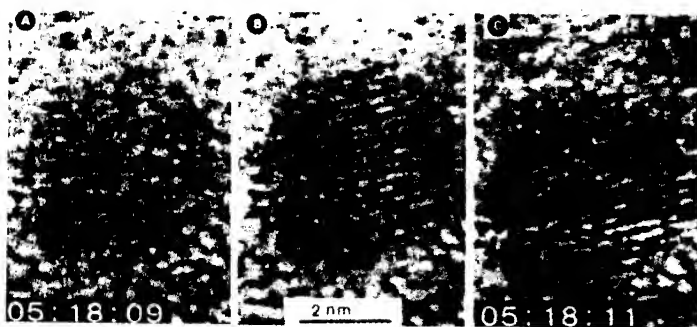


Fig.4: a, b, c) Single frames from videotape; numbers on the bottom report minutes, seconds and frame number. The time interval between the successive frames is 40 ms.

III - DISCUSSION

From the several thousands of frames examined two clear indications can be obtained on statistical basis:

- i) images of particles having $d < 5$ nm have been recorded for a few minutes and no crystal structure has been observed.

ii) the fluctuations relative to particles (or their portions) in the range 5-10 nm show a completely different character with respect to twins or fragments of comparable size belonging to bigger grains ($d > 10$ nm): in the latter case crystal order is always present, and rotations are slow enough to be detected without ambiguity.

In order to clarify the physical nature of the above described fluctuations, which appear to be due to a mechanism distinct from rotation, additional investigations were performed along two different lines :

A) Analysis of previously obtained optical data [5,9]: the reflectivity rise[10] which marks the onset of the solid to liquid transition has been normalized to the number of Pb atoms. Such a normalized reflectivity rise decreases rapidly as a function of size, and its extrapolation tends to zero when $d \sim 2-3$ nm. This means that the dielectric functions in the two phases for sufficiently small particles are no longer distinguishable and the system approaches the conditions for spontaneous melting (see fig.5).

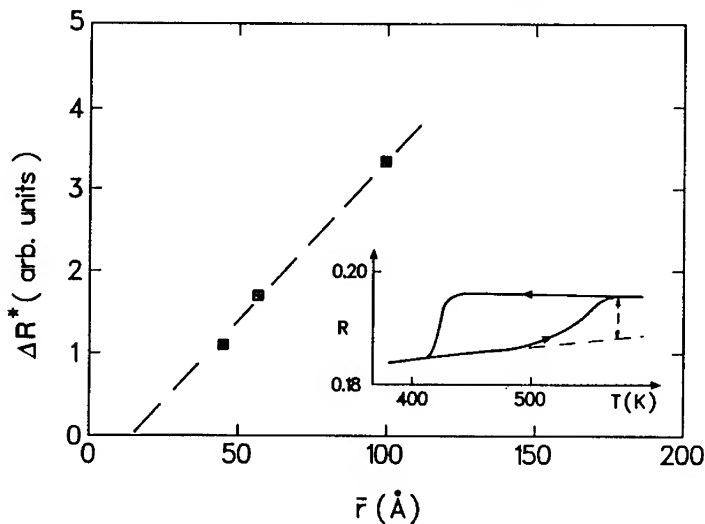


Fig. 5: The reflectivity rise marking the onset of the transition normalized to the number of Pb atoms is reported as a function of the average radius of the particles.

B) A further check on the possible spontaneous fluctuations between the two phases was carried out by means of a computer simulation of premelting along the lines of previous works of classical thermodynamics [11,12]. The free energy difference ΔG between solid-thin liquid-vapour (matrix) and solid-vapour (matrix) configurations is calculated as a function of δ / r (δ is the thickness of the liquid layer and r is the radius of the particle). Using the data known from the literature for the physical quantities involved (essentially free energies, correlation length, chemical potentials and latent heat of fusion), a minimum in ΔG (δ / r) is obtained for $\delta / r \approx 0.1$ only if $r > 3$ nm; below that value the particle is entirely liquid [13] (see fig.6).

From the analysis of the results here reported the following conclusions can be drawn :

- The decrease of T_M with size, the existence of a thin liquid layer below T_M with the consequent rotations are clearly evidenced and shown to be in general agreement with what is expected from previous theoretical and experimental works.

- A new phenomenon which can be explained in terms of spontaneous phase fluctuations may take place for particles of very small size. Optical data and classical thermodynamics calculations support this interpretation.

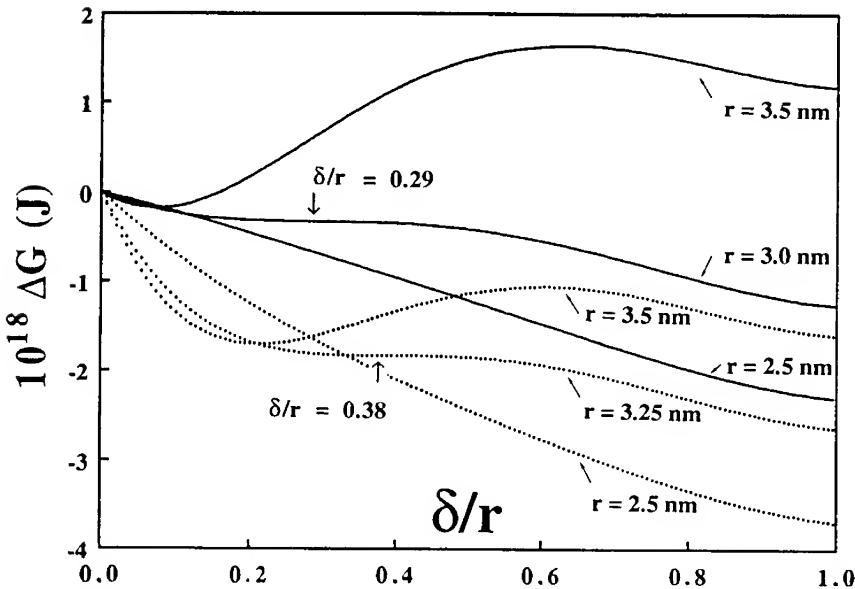


Fig. 6. Solid lines: Free energy difference ΔG between solid-thin liquid-vapour and solid-vapour configurations as a function of δ/r (δ is the thickness of the liquid layer and r the radius of the particle), using $\gamma_{sl} = 0.05 \text{ Jm}^{-2}$, $\gamma_{sv} = 0.61 \text{ Jm}^{-2}$, $\gamma_{lv} = 0.48 \text{ Jm}^{-2}$ and $T = 300 \text{ K}$.
 Dotted lines: same curves as varied by introducing a 3% increase on γ_{sv} .

- 1 - Ph. Buffat and J.P. Borel, Phys. Rev. 13, 2287 (1976)
- 2 - Y. Lereah, G. Deutscher, P. Cheyssac and R. Kofman, Europhysics Letters 12, 709 (1990)
- 3 - F. Ercollessi, W. Andreoni and E. Tosatti, Phys. Rev. Letters 66, 911, (1991)
- 4 - X.J. Chen, A.C. Levi and E. Tosatti, Il Nuovo Cimento 13D (1991) 919
- 5 - R. Kofman, P. Cheyssac, A. Aouaj, Y. Lereah, G. Deutscher, T. Ben-David, J.M. Pénisson and A. Bourret, Surf. Sci. in press
- 6 - J.G. Dash, Contemporary Physics, 30, 89, (1989)
- 7 - J.W.M. Frenken, P.M.J. Maree and J.F. Van der Veen, Phys. Rev. B 34, 7506, (1986)
- 8 - N.I. Gladkikh, S.P. Chizik, V.L. Larin, L.K. Grigoreva and V.N. Sukhov, Izv. Acad. Nauk SSSR Met., 5, 196, (1982)
- 9 - R. Garrigos, P. Cheyssac and R. Kofman, Z. Phys. D 12, 497 (1989)
- 10 - The reflectivity rise at the transition temperature is generally considered a very reliable indicator of the solid to liquid transition. (See D.H. Auston *et al* in Appl. Phys. Lett. 34, 365, (1978)).
- 11 - D Beaglehole, J. of Crystal Growth, 112, 663, (1991)
- 12 - J.Q. Broughton and G.H. Gilmer, Acta Metall. 31, 854, (1983)
- 13 - The calculation was performed under the assumption of spherical particles (as confirmed by DF and HREM data) and of a relatively not too strong perturbation at RT due to the presence of the matrix instead of the vapour. It was checked in any case that variations up to 8% in the free energies due to such perturbation do not change the main features of the curves in fig 6.

IN-SITU DYNAMIC HIGH-RESOLUTION TRANSMISSION ELECTRON MICROSCOPY
INVESTIGATION OF GUEST-LAYER BEHAVIOR DURING DEINTERCALATION OF
MERCURY TITANIUM DISULFIDE

M. MCKELVY*, M. SIDOROV*, A. MARIE#, R. SHARMA*, and W.S.
GLAUNSINGER**

*Center for Solid State Science and **Department of Chemistry and Biochemistry
Arizona State University, Tempe, AZ (USA) 85287-1704.

#Institut des Matériaux, UMR 110, University of Nantes, 44072 Nantes, France.

ABSTRACT

Deintercalation processes for the model neutral intercalation system Hg_xTiS_2 ($1.25 \geq x > 0.00$) have been investigated using dynamic high-resolution transmission electron microscopy. X-ray powder diffraction and thermogravimetric analysis demonstrated the intercalation process is thermally reversible, both structurally and compositionally. *In situ* deintercalation of stage-1 compounds was induced by thermal/electron-beam heating during DHRTEM observation. The resulting deintercalation processes were followed with 0.03 second time resolution. The deintercalation processes observed possess a strong similarity to nucleation and growth processes. Deintercalation was observed to "nucleate" by the initial deintercalation of an external-most or internal guest layer, with further deintercalation of the guest layers generally "growing" away from the onset layers. This results in generally randomly staged regions, occasionally containing regions of short-range order, that expand away from the deintercalation onset layers.

INTRODUCTION

The intercalation of transition-metal dichalcogenides (TMDs) and graphite offers a unique soft-chemistry route to a vast array of compounds that are of broad interest both scientifically and technologically¹⁻³. Their intercalation reactions and intercalates have substantial chemical and structural similarities⁴⁻⁶. Chemically, TMD and graphite intercalation compounds (TMDICs and GICs) can range in character from ionic, containing only ionic guests, to neutral, where all of the guests are essentially uncharged, but may experience weak covalent guest-host electron exchange^{4,7}. Structurally, both TMDICs and GICs have relatively thin, flexible host layers. Such layers enhance the interlayer electrostatic and elastic repulsions that lead to the interlayer (stage) ordering observed for these compounds^{5,6}.

In order to fully exploit the synthetic potential of intercalation a sound understanding of intercalation/deintercalation processes is needed. Even though TMDICs and GICs have been widely investigated for many years, relatively little is known about their intercalation/deintercalation processes, particularly at the atomic level. Recently, we used environmental-cell DHRTEM to observe intercalation processes at the atomic level for the first time⁸. We have also used DHRTEM to make the first atomic-level observations of model ionic and neutral intercalate staging transitions⁹. Herein, we focus on our study of the layer-by-layer deintercalation behavior of the model neutral intercalates: Hg_xTiS_2 ($1.25 \geq x > 0.00$)⁷.

EXPERIMENTAL PROCEDURES

$Hg_{1.25}TiS_2$ samples were prepared by Hg intercalation of highly-stoichiometric TiS_2 ($Ti_{1.002}S_2$)⁷. All synthesis and handling was carried out under inert conditions⁷. X-ray powder diffraction (XPD) showed the intercalates were single-phase and stage-1, with a 8.7 Å

interlayer repeat. Thermogravimetric analysis (TGA) of Hg deintercalation was used to determine intercalate compositions, $Hg_{1.25 \pm 0.01}TiS_2$ ⁷. The complete reversibility of the intercalation process was verified both structurally and compositionally by XPD and oxidative TGA of the thermally-deintercalated host⁷.

DHRTEM samples were prepared as described previously, with XPD verifying no significant structural change occurred during sample preparation⁹. The DHRTEM studies were performed using a JEOL 2000FX electron microscope (2.5 Å pt.-to-pt. resolution) interfaced to a 0.03 s resolution video recording system. DHRTEM samples were loaded under nitrogen into a Gatan model 626SP cryotransfer holder, isolated from the surrounding atmosphere, slowly cooled to -170°C, and loaded into the microscope. Deintercalation of the initially stage-1 intercalates was brought about by slow, controlled thermal/electron-beam heating. The images are taken directly from videotape and show the intercalates parallel to their TiS_2 layers. The broad and narrow dark lines in each image correspond to Hg-intercalated and empty guest-layer regions, respectively.

RESULTS AND DISCUSSION

General Observations

8.7 Å and 5.7 Å interlayer spacings were observed for mercury-intercalated and empty guest galleries, respectively, consistent with XPD observations of the layer spacings of the stage-1 intercalate and host⁷. Deintercalation was only observed parallel to the host layers.

The Onset of Deintercalation

The deintercalation process was most frequently observed to start with deintercalation of the outermost guest layer(s), as shown in Figure 1a. This follows from their neighboring host layers being the most flexible, resulting in the lowest deintercalation activation energy, E_a^d , for the outermost guest layers. However, the onset of deintercalation can also occur at internal guest layer(s), as shown in Figure 1b. In this case, the initiation of the deintercalation process at internal guest layers can be correlated with the presence of internal defects, such as host-edge dislocations (HEDs) and interlayer defects (e.g., interlamellar shear) and surface defects, including steps and irregular termination of the host-layer edges¹⁰. The strain energy associated with such defects can reduce the E_a^d of internal guest layers to the point that deintercalation is initiated at an internal guest layer.

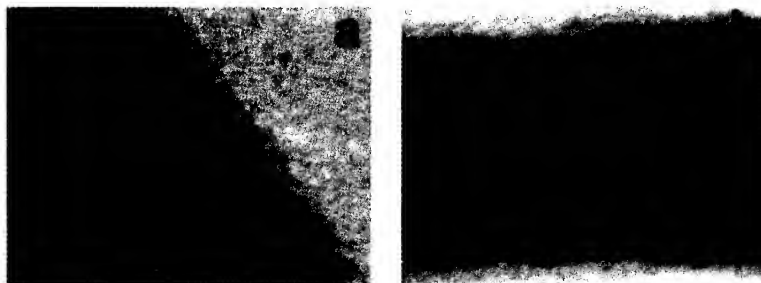


Figure 1. Onset of guest-layer deintercalation: a) at the external-most guest layers; and b) at internal guest layers.

Progressive Deintercalation Away from the Onset Layers

After the initiation of deintercalation at the external-most guest layer(s), the deintercalation process generally continued inward from the external-most layer(s). Figure 2 shows the progress of deintercalation for a well-formed crystal in the middle of its deintercalation process. As shown in Figure 2a, the outer guest layers exhibited preferential deintercalation early on in the deintercalation process, as was generally observed following the onset of deintercalation at external-most guest layers. Two guest-edge dislocations (GEDs) in neighboring guest layers have also formed a staggered domain wall boundary in the left of Figure 2a. These elastically-stabilized boundaries were often observed to form and persist during the deintercalation process, substantially impeding the progress of deintercalation, as predicted theoretically⁶. Deintercalation then progresses with the preferential deintercalation of the outermost remaining guest layers. First, the outermost lower guest layer deintercalates, as shown in Figure 2b. This is followed by the deintercalation of the central layer of the three-layer stage-1 (a stage-n intercalate has n host layers between nearest neighbor guest layers) region to form the longest-range, locally-ordered deintercalated region observed in these studies, as shown in Figure 2c. Deintercalation continues with the deintercalation of the lower and upper external-most remaining guest layers, as illustrated in Figures 2d and e, respectively. Then the second and third from the top remaining guest layers deintercalate to the right and left, respectively, to form another stable GED staggered domain wall. The presence of a host layer between the GEDs indicates their elastic stabilization is not confined to neighboring guest layers.

After the onset of deintercalation at internal guest layer(s), the deintercalation process generally continued with the deintercalation of nearby guest layers progressively outward from the onset layer(s). Figure 3 shows the progress of deintercalation after internal onset in a crystal containing a host-edge dislocation (HED). Figure 3a shows the deintercalated guest layer and GED that initially formed above the HED. This GED serves to stabilize the intercalate elastically by reducing the interlayer mismatch between the left and right sides of the HED termination from 8.7 Å to 5.7 Å. Its stability is evidenced by its persistence, with minor deintercalation, as shown in Figures 3b-d. Next, two guest layers below and near to the HED completely and partially deintercalate, as shown in Figure 3b. Deintercalation continues to progress outward, away from the HED, with the partial and complete deintercalation of the third from the external-most guest layers, as seen in Figure 3c. This is accompanied by the deintercalation of the GED seen below the HED in Figure 3b. Next, the deintercalation process reaches the outermost upper guest layer, yielding the randomly-staged intercalate in Figure 3d.

The deintercalation processes observed show substantial similarity to nucleation and growth processes. Independent of its onset location, deintercalation generally proceeds away from the onset layer(s). This occurs with the formation of randomly-staged regions, with occasional short-range order, that "grow" away from the onset layer(s). Thus, after the initial guest layer has deintercalated, the remaining guest layers nearby become more susceptible to deintercalation. This apparently results from a combination of factors. The presence of defects, or the enhanced flexibility of an adjacent external host layer, can also lower the E_a^d for nearby guest layers as well as the onset layer(s)¹⁰. Also, the slight in-plane host-layer mismatch between adjoining intercalated and deintercalated host layers (about 0.0-0.3%, as a function of the in-plane direction for $Hg_{1.25}TiS_2$ and TiS_2)⁷ should favor the deintercalation of the adjoining intercalate layers. However, the elastic and electrostatic interlayer repulsive forces that lead to stage ordering should promote ordered periodic guest-layer deintercalation^{5,6}. Thus, it appears that no dominant force is responsible for the observed progression of deintercalation away from the onset layers.

CONCLUSIONS

The onset and progression of deintercalation has been followed at the atomic level by DHRTEM, providing new insight into lamellar deintercalation processes for the model neutral

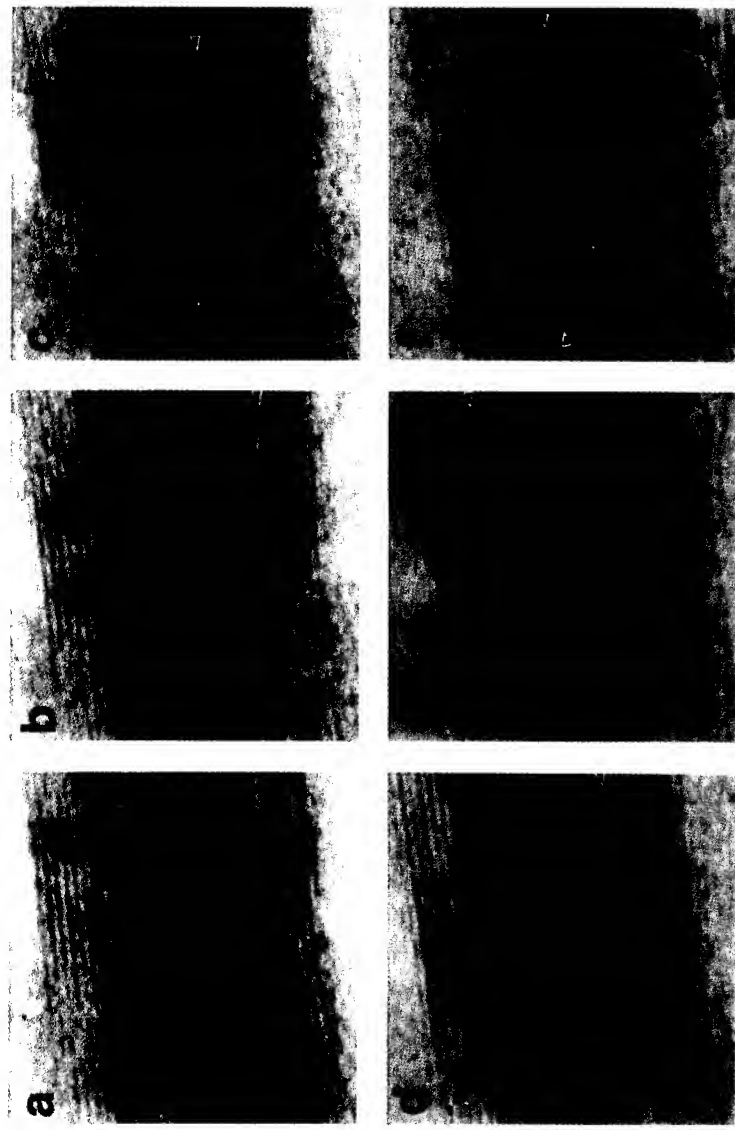


Figure 2. Typical $\text{Hg}_{1.25}\text{TiS}_2$ deintercalation progression following external-most guest layer onset: a) preferential deintercalation of the outer guest layers; b) deintercalation of the outermost remaining guest layer; c) deintercalation of the central guest layer of the remaining stage-1 region to form a short-range stage-2 ordered region internally; d and e) successive deintercalation of outermost guest layers; and f) partial deintercalation of two internal guest layers to form a GED staggered domain wall. The broad and narrow dark lines in each image correspond to Hg-intercalated and empty guest layer regions, respectively. The arrows indicate the layers that have experienced deintercalation since the previous frame.

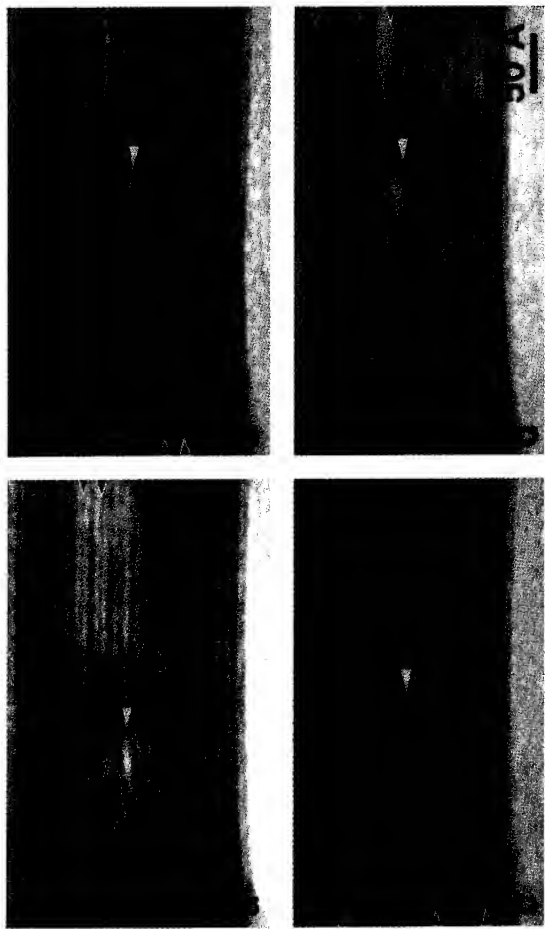


Figure 3. Typical $\text{Hg}_{1.25}\text{TiS}_2$ deintercalation progression after internal onset: a) internal onset of deintercalation. Note the GED and deintercalated guest layer above the HED; b) subsequent deintercalation of guest layers below the HED; and c and d) continued layer-by-layer deintercalation away from the HED. The broad and narrow dark lines in each image correspond to Hg-intercalated and empty guest layer regions, respectively. The white arrows indicate the position of the HED. The black on white arrows indicate the layers that have experienced deintercalation since the previous frame.

intercalate Hg_xTiS_2 ($1.25 \geq x > 0.00$). The onset and early progression of deintercalation bears a close similarity to nucleation and growth processes. In this case, "nucleation" occurs via the deintercalation of either an external-most or internal guest layer. After "nucleation", continued deintercalation results in primarily randomly-staged regions "growing" away from the onset layer. These regions contain only occasional local stage ordering, which is consistent with the lack of electrostatic interlayer repulsions for this neutral intercalation compound^{5,7}.

ACKNOWLEDGEMENTS

We wish to acknowledge the National Science Foundation for support through grant DMR 91-06792 and acknowledgement is made to the Petroleum Research Fund, administered by the ACS, for partial support of this research. We also wish to thank the Center for Solid State Science for use of its Materials Science Electron Microscope Laboratory and Materials Preparation Facility.

REFERENCES

1. Intercalation Chemistry, edited by M.S. Whittingham and A.J. Jacobson (Academic Press, New York, 1982).
2. Chemical Physics of Intercalation, edited by A.P. Legrand and S. Flandrois (Plenum Press, New York, 1987).
3. Graphite Intercalation Compounds I, edited by H. Zabel and S.A. Solin (Springer Verlag, Berlin, 1990).
4. M. McKelvy and W. Glaunsinger, *Ann. Rev. Phys. Chem.* **41**, 497 (1990).
5. S.A. Safran, *Solid State Phys.* **40**, 183 (1987).
6. G. Kirczenow, in reference 3, pp. 59-100.
7. E.W. Ong, M.J. McKelvy, G. Ouvrard, and W.S. Glaunsinger, *Chem. Mater.* **4**, 14 (1992).
8. M. McKelvy, R. Sharma and W. Glaunsinger, *Solid State Ionics* **63-65**, 369 (1993).
9. M. McKelvy, R. Sharma, E. Ong, G. Burr, and W. Glaunsinger, *Chem. Mater.* **3**, 783 (1991).
10. M. McKelvy, M. Sidorov, A. Marie, R. Sharma, and W. Glaunsinger, *Chem. Mater.*, (submitted).

IN-SITU OBSERVATION OF OXIDE MONOLAYER FORMATION ON COPPER SOLID-LIQUID INTERFACES

JOHN R. LaGRAFF, BRANDON J. CRUICKSHANK, AND ANDREW A. GEWIRTH
Department of Chemistry and Materials Research Laboratory, The University of Illinois at
Urbana-Champaign, Urbana, IL 61801

ABSTRACT

It is extremely important to characterize the various bare copper surfaces *in situ* before any subsequent corrosion or deposition chemistry can be understood. In this paper, *in situ* Atomic Force Microscopy (AFM) was used to image the low-index faces of Cu single crystals in H_2SO_4 and $HClO_4$ acidic solutions. Cu(100) surfaces exhibited potential-dependent $c(2\times 2)$ adlayers in pH=1 solutions which were attributed to oxide (or hydroxide) overayers. Images of Cu(110) obtained in pH 2.5-2.7 solutions revealed the growth of primarily [001] oriented ($n\times 1$) adlayer chain structures, where n is an integer. Preliminary measurements on Cu(111) did not reveal any adlayer structures between pH's of 1-3. The oxide monolayers on Cu(100) and Cu(110) crystals were observed in the thermodynamically forbidden region of the pH-potential phase diagram, which indicates that stable oxide adlayers develop prior to bulk oxide formation.

INTRODUCTION

A fundamental understanding of adlayer structure on single crystal metal surfaces immersed in liquids is extremely important in developing a structural basis for electrochemical reactivity, including, corrosion and catalysis. Nowhere is this understanding more important than in the study of the initial stages of corrosion of Cu. While significant progress has been made in imaging electrochemical processes with atomic resolution on Au [1] and Ag [2] surfaces, Cu has received scant attention owing to its tendency to oxidize and for its narrow (ca. 400-600 mV) double-layer (ideally polarizable) region.

Copper single crystal surfaces immersed in aqueous solutions have been studied by a variety of techniques [3-5]. However, the results are extremely sensitive to surface preparation, ostensibly due to adventitious oxide species. Oxide monolayers have been observed on Cu surfaces in the ultra high vacuum (UHV) environment [6-8], but their existence in the acidic electrochemical environment remains problematic. In particular, thermodynamic potential-pH considerations suggest that bulk oxide is unstable at pH < 3.5 at the rest potential [9]. Consequently, the determination of atomic-level oxide structure evolution on copper single crystal surfaces is invaluable in helping develop an atomic-level understanding of copper oxidation and corrosion in aqueous environments.

In this paper, we summarize the oxide (or hydroxide) adlayer structures observed on the three low index faces of Cu solid-liquid interfaces in acidic aqueous solutions [10,11].

EXPERIMENTAL

The working electrodes were formed from Cu(100), Cu(110), and Cu(111) single crystals (1 cm dia., 99.999%, Monocrystals Company). These surfaces were mechanically polished down to 0.3 μ m with Al_2O_3 , rinsed with Millipore-Q-purified water, dried in flowing air, and then electropolished with an applied current of ~1.5 A/cm² in a solution containing H_3PO_4 (85%): H_2SO_4 (96%): H_2O in a 6:1:3 by volume ratio [3]. The reference electrodes were formed from either a Pt wire or a Hg/Hg_2SO_4 (MSE) cell (0.64V vs. a normal hydrogen electrode, NHE) connected to the AFM cell through a Luggin capillary. All potentials are reported relative to the MSE cell. The counter electrode was a 0.5 mm dia. Au wire prepared by

flame annealing followed by quenching into a solution containing the appropriate supporting electrolyte. Electrolytes were prepared with Millipore-Q water, H_2SO_4 (J.T. Baker, Ultrex), $HClO_4$ (J.T. Baker, Ultrex), and $NaCl$ (reagent grade, Fisher). The electrolytes were not deoxygenated prior to use.

In situ AFM images were obtained with a Nanoscope II AFM [12] equipped with a glass cell and operating in constant force mode. Tips were microfabricated with integral pyramidal Si_3N_4 tips. The instrument was calibrated using the known spacings and structures for mica and either $Cu(100)$, $Cu(110)$, or $Cu(111)$. Upon completion of the experiments, the in-plane crystal orientations measured by the AFM were confirmed by using Laue x-ray backscattering.

RESULTS AND DISCUSSION

Cu(100)

Fig. 1a shows an AFM image of an electropolished $Cu(100)$ sample in 0.1 M $HClO_4$ solution obtained at -1000 mV versus MSE [10]. The atoms are arranged in a square configuration with an atomic spacing of 0.26 ± 0.02 nm; the correct structure and spacing for the (100) orientation. The images at these potentials are generally not as sharp due to incipient H_2 evolution. Upon sweeping to more positive potentials (-450mV), a square lattice is also evident, however, it is rotated 45° with respect to the underlying Cu substrate with an interatomic separation of 0.36 ± 0.02 nm (Fig. 1b). A similar structure was also seen in H_2SO_4 solutions of the same concentration. This structure is consistent with a c(2x2) overlayer as shown in Fig. 1c. The adatoms are arranged in four-fold hollow sites to give the expected 1/2 monolayer coverage for a c(2x2) structure.

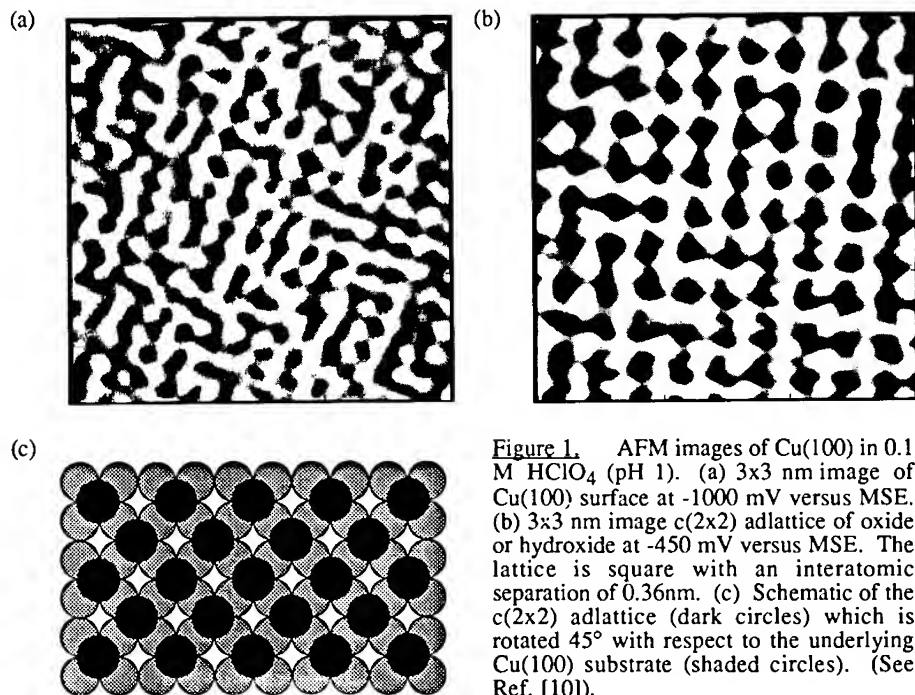


Figure 1. AFM images of $Cu(100)$ in 0.1 M $HClO_4$ (pH 1). (a) 3x3 nm image of $Cu(100)$ surface at -1000 mV versus MSE. (b) 3x3 nm image c(2x2) adlattice of oxide or hydroxide at -450 mV versus MSE. The lattice is square with an interatomic separation of 0.36nm. (c) Schematic of the c(2x2) adlattice (dark circles) which is rotated 45° with respect to the underlying $Cu(100)$ substrate (shaded circles). (See Ref. [10]).

Cu(110)

Figure 2a shows an image of the Cu(110) surface in dilute (0.003 M, pH=2.5) HClO_4 obtained at a potential of -500 mV which was 160 mV negative of the rest potential, E_0 (-340 ± 10 mV in this electrolyte). This surface exhibited a rectangular array of atoms separated by 0.36 ± 0.03 in the [001] direction and 0.25 ± 0.02 nm in the [1 $\bar{1}$ 0] direction [11]. While other structures were also observed in this potential range (*vide infra*) this was the dominant lattice structure seen. The spacing and structure of this lattice correspond well with that expected for the bare, unreconstructed Cu(110) surface.

Sweeping the potential back to E_0 caused additional structures to form on the Cu(110) surface. Fig. 2b shows a region of the surface which developed 10-20 min. after stepping from -550 mV to E_0 [11]. In the upper right there are atomic scale features exhibiting the same spacing and structure as the Cu(110) surface seen in Fig. 2a. However, the lower left of Fig. 2b reveals atomic scale chains with a 0.34 ± 0.02 nm spacing in the [001] direction and a 0.49 ± 0.05 nm spacing in the [1 $\bar{1}$ 0] direction. The height of the chains above the Cu(110) surface was 0.15 ± 0.08 nm; these correspond to atomic scale heights. This is equivalent to a (2x1) overlayer and the image shows this overlayer growing in on top of the bare Cu(110) lattice. $n \times 1$ overlayers ($n=2,3,4$) have also been observed in this potential regime.

The two-domain image, Fig. 2b, allows determination of the registry of the overlayer with the [001] direction of the Cu(110) surface. This was determined to correspond to the (2x1) overlayer bound on, rather than in between, the close-packed copper rows (Fig. 2c). However, the registry in the [1 $\bar{1}$ 0] direction from Fig. 2b was indeterminate. Figure 2c is a schematic of the Cu(110) surface with [001] chains of atoms arranged in one possible 2x1 structure.

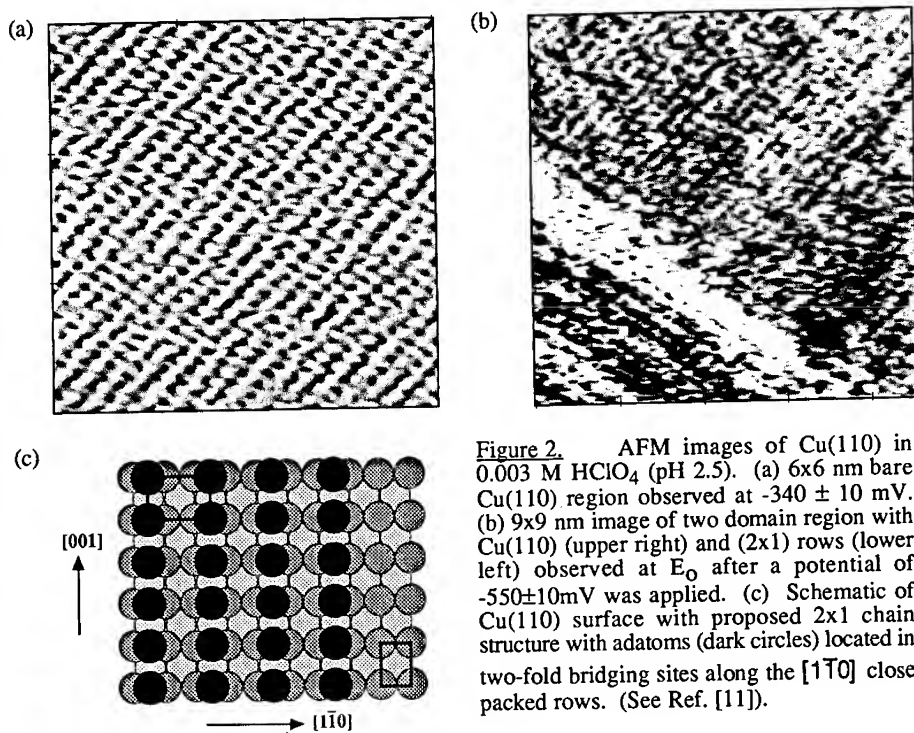


Figure 2. AFM images of Cu(110) in 0.003 M HClO_4 (pH 2.5). (a) 6x6 nm bare Cu(110) region observed at -340 ± 10 mV. (b) 9x9 nm image of two domain region with Cu(110) (upper right) and (2x1) rows (lower left) observed at E_0 after a potential of -550 ± 10 mV was applied. (c) Schematic of Cu(110) surface with proposed 2x1 chain structure with adatoms (dark circles) located in two-fold bridging sites along the [1 $\bar{1}$ 0] close packed rows. (See Ref. [11]).

We assign the 2x1 and 3x1 chain structures observed in Fig. 2b to an adsorbed oxide or hydroxide species growing on the bare Cu(110) surface. These chains represent the initial stage of oxide formation on Cu(110). The images in Fig. 2 were obtained in the pH-potential region of the Pourbaix diagram where bulk Cu₂O oxide formation is thermodynamically unfavorable. Consequently, the observation of oxide chain structures at pH values between 2.5 and 2.7 indicates that prior to bulk oxide formation, a partial oxide monolayer develops. This is equivalent to saying that the oxide forms at underpotentials, and the oxide monolayer can be thought of thermodynamically in the same manner as are monolayers of metal adatoms which form via underpotential deposition [13]. Lowering the pH to 1 or applying a potential negative of E_O removed the chain structures which enabled resolution of only Cu(110) surfaces [14]. This is in qualitative agreement with the Pourbaix diagram [9].

Cu(111)

Preliminary investigations in acidic solutions (pH~1-3) did not reveal any adlayer structures different from the expected hexagonal arrangement and spacing of the bare Cu(111) surface [10,14]. This suggests that the (111) face of copper is less reactive than Cu(100) and Cu(110) towards oxide monolayer formation.

Possible Adsorbates

There are three species which may be responsible for the adlayer structures observed on the Cu(100) and Cu(110) surfaces: (1) Cl⁻ impurity, (2), electrolyte anion, and (3) oxide (hydroxide) [11]. The first two possibilities have been discussed extensively elsewhere [10,11]. To summarize, there is not enough Cl⁻ in solution (according to the solution assays) to form a complete monolayer. Also, control experiments for Cu(110) in 1 mM NaCl solutions at the same pH revealed different adlayer structures than the (nx1) chains [11]. Briefly, the possibility of electrolyte anion (bisulfate versus perchlorate) causing the adlayers was ruled out by the similarity in structures observed in H₂SO₄ and HClO₄ solutions [10,11]. The remaining, and most likely, source of the adlayer structures is an oxide adlayer. However, the lack of chemical specificity in the AFM does not yet allow a definitive choice to be made regarding oxide versus hydroxide.

The Pourbaix Diagram

The pH-potential phase diagram (Pourbaix diagram) for the system Cu-H₂O indicates that bulk Cu₂O is unstable below a pH of approximately 3.5 [9]. Consequently, the observation of ordered oxide adlayer structures on Cu(100) and Cu(110) at lower pH values is significant with regards to how copper corrodes and how it reacts with other possible adsorbates [10,11]. We did not observe any ordered overlayer on Cu(111) in similar pH-potential ranges. This suggests that Cu(100) and Cu(110) are more reactive towards oxide monolayer formation than Cu(111). As the (111) face exhibits the largest work function of the three low Miller index faces it is also the most electronegative. This implies that the strength of the Cu-O bond will be lower on the (111) face than the (100) and (110) faces. In fact, the Cu-O stretching frequency in UHV is lowest on the (111) face and only a disordered oxygen structure is observed [15]. Again, this suggests that Cu(111) is the least reactive towards ordered oxide monolayer formation.

CONCLUSION

In summary, ordered oxide monolayers have been observed on Cu(100) and Cu(110) surfaces in aqueous solutions with pH values as low as 1 and 2.5, respectively. These structures

correspond to c(2x2) and (nx1) adlayers for the (100) and (110) surfaces, respectively, and are removed by negative potentials to reveal bare Cu. These structures exist in the thermodynamically forbidden regime of the Pourbaix diagram for bulk Cu₂O development indicating that these are likely precursor structures to eventual bulk oxide formation. These oxide monolayers are analogous with monolayers of metal adatoms formed by underpotential deposition. Preliminary measurements on the Cu(111) surface, however, did not show any adlayer structures between pH values from 1 to 3. An understanding of monolayer oxide structures on copper raises possibilities in controlling either these structures or inhibiting their development in order to halt copper oxidation and corrosion.

ACKNOWLEDGMENTS

JRL acknowledges a National Science Foundation Postdoctoral Fellowship in Chemistry (CHE-9302406). AAG acknowledges a Presidential Young Investigator Award (CHE-9027593) with matching funds provided by Digital Instruments, Inc. and is an A.P. Sloan Foundation Fellow. This work was funded by the Department of Energy (DE -FG02-91ER45349) through the Materials Research Laboratory at the University of Illinois.

REFERENCES

- [1] O.M. Magnussen *et al.*, *Phys. Rev. Lett.* **64**, 2929 (1990); X. Gao, A. Hamelin and M.J. Weaver, *Phys. Rev. Lett.* **67**, 618 (1991); S. Manne *et al.*, *Science* **251**, 183 (1991).
- [2] U. Muller *et al.*, *Phys. Rev. B*, **46**, 12899 (1992).
- [3] H. Siegenthaler and K. Juttner, *J. Electroanal. Chem.* **163**, 327 (1984).
- [4] J.R. Vilche and K. Juttner, *Electrochim. Acta* **32**, 1567 (1987).
- [5] R.A. Bradley *et al.*, *J. Electroanal. Chem.* **309**, 319 (1991).
- [6] D.J. Coulman *et al.*, *Phys. Rev. Lett.* **64**, 1761 (1990).
- [7] F.M. Chua, Y. Kuk and P.J. Silverman, *Phys. Rev. Lett.* **63**, 386 (1989); F. Jensen *et al.*, *Phys. Rev. B* **41**, 10233 (1990); R. Feidenhans'l *et al.*, *Phys. Rev. Lett.* **65**, 2027 (1990).
- [8] A. Spitzer and H. Luth, *Surf. Sci.* **120**, 376 (1982).
- [9] M. Pourbaix, *Atlas of Electrochemical Equilibria in Aqueous Solutions* (Pergamon Press, New York, 1966), p. 387.
- [10] B.J. Cruickshank, D.D. Sneddon, and A.A. Gewirth, *Surf. Sci.* **281**, L308 (1993).
- [11] J.R. LaGraff and A.A. Gewirth, *Phys. Rev. Lett.* (submitted, 1993)
- [12] Digital Instruments 6780 Cortona Drive, Santa Barbara, CA 93117.
- [13] D.M. Kolb, *Advances in Electrochemistry and Electrochemical Engineering*, Vol. 11, edited by H. Gerischer C.W. Tobias (Wiley; New York, 1978), pp 125-271.
- [14] J.R. LaGraff and A.A. Gewirth (unpublished).
- [15] F. Besenbacher and J.K. Norskov, *Prog. in Surf. Sci.* **44**, 5 (1993).

PART III

Local Structures and Properties

APPLICATION OF HIGH SPATIAL RESOLUTION ELECTRON DIFFRACTION TECHNIQUES TO THE STUDY OF LOCAL PROPERTIES OF CRYSTALLINE SOLIDS

J W STEEDS, X F DUAN, P A MIDGLEY, P SPELLWARD & R VINCENT
Physics Department, University of Bristol, Bristol BS8 1TL, UK.

ABSTRACT

The addition of a Gatan imaging parallel electron-energy loss spectrometer (IPEELS) to a Hitachi HF 2000 cold field emission TEM has allowed us to produce high quality energy-filtered coherent electron diffraction patterns and electron holograms from a wide variety of materials. In this paper we review the recent achievements and make an assessment of the use of coherent electron diffraction in solving problems at high spatial resolution in materials science.

1. PRESENT STATE OF PERFORMANCE

a) Reduction of Fringe Spacing

Our first successful experiments in coherent electron diffraction were performed on SiC polytypes with relatively long c axis repeat distances¹. With increased experience and control of the instrument, and in particular, with the addition of a Gatan imaging parallel electron energy loss system (IPEELS) steady improvements have been achieved. The IPEELS system brought two distinct effects. First, it became possible to form elastic (or energy selected) coherent electron diffraction patterns with consequent improvement of the fringe visibility². Second, the required control over the microscope operating voltage and associated spectral analysis revealed that our instrument performs much better at an operating voltage of slightly less than 200kV. In particular, smaller focused probes can be formed. As a result of this discovery, together with the

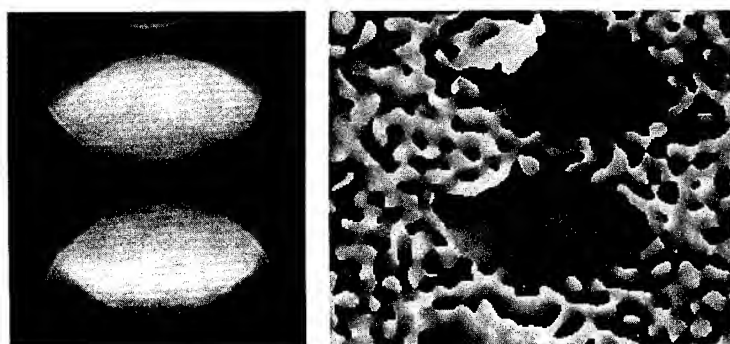


Fig 1. 0.28nm fringes in the overlap regions of the direct beam with the $\pm\{200\}$ reflections of InGaAs (left). The phasing of the fringes in the overlap regions is shown in the micrograph on the right.

experience we have gained, it has now been possible to obtain clear fringes in the {200} reflections of III-V semiconductors and their alloys. An example is shown in Fig 1. This is an exciting development because it opens to us a whole range of experiments on semiconductor materials which are of considerable potential interest. Moreover, these are the materials which can be produced with the greatest degree of control and a wide range of other sensitive experimental techniques are regularly applied to them.

b) Two Dimensional Fringe Patterns

As the SiC polytypes had a single long-period direction, the fringes that we observed were necessarily one dimensional. With the reduction in fringe periodicity a number of zone axes have been studied with two-dimensional fringe patterns. The first of these was the [001] zone axis of BaCuO₂³. The results are complicated by the degree of overlap which can occur that is not immediately apparent on studying the micrograph. Computer simulations of the results are necessary to clarify the situation (Fig 2). A second result, shown in Fig 3, is for the [001] axis of Er₂Ge₂O₇. Interference fringes may be seen in the overlaps of reflections with spacings of 0.68 and 0.48nm. The most recent result, shown in Fig 4, gives the two-dimensional overlap of {111} fringes in silicon at the <110> zone axis; the fringe spacings are 3.1Å.

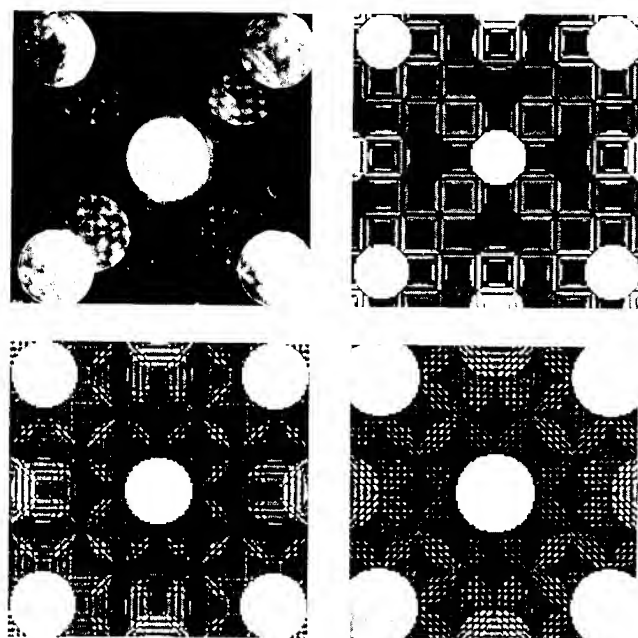


Fig 2.

Composite of an experimental [001] coherent diffraction pattern of BaCaO₂ (top left) with simulations for overlaps of 41.4% (top right) 70% (bottom left) and 100% (bottom right).

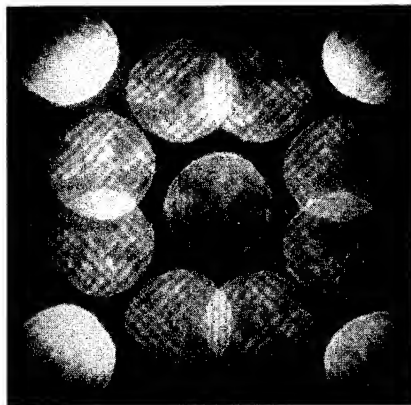


Fig 3.

Coherent electron diffraction from the [001] axis of $\text{Er}_2\text{Ge}_2\text{O}_7$.

c) Coherent Large Angle Convergent Beam Electron Diffraction (LACBED)

It was demonstrated⁴ that, by use of a $1\mu\text{m}$ selected area aperture, coherent LACBED patterns could be produced that contained more than 100 fringes created by the overlap of two adjoining reflections. The images can be analyzed and at least partially corrected for spherical aberration by performing digital Fourier transformation of the results. The work has now been extended to samples of SiC containing stacking abnormalities.

d) LACBED

In LACBED experiments the spatial resolution is limited by the probe cross-over size that, no longer residing in the specimen plane, acts as a pin-hole camera. By use of the cold field emission source with a restricted angle of convergence it has been demonstrated⁵ that a spatial resolution of 1nm can now be achieved with this technique. This resolution should be effective in studying local changes associated with defects or interfaces. It has already been used⁵ to study the strains in 20nm period Si/SiGe superlattices.

e) Energy-filtered Results

The chief purpose of adding the IPEELS system to our instrument was to generate elastic-only zone axis CBED patterns for detailed analysis to generate information about bonding charge distributions and redistributions in materials. Our first results are now being analyzed. However, the system also allows us to form energy filtered coherent electron diffraction patterns, LACBED and coherent LACBED patterns, high resolution images and electron holograms. We have recently demonstrated that the fringe visibility in coherent electron diffraction patterns is greatly enhanced by energy filtering but is greatly reduced for plasmon scattered electrons². Other advantages of this system include:

- (i) the formation of an immediate record of the experiment so that unforeseen aberrations can be detected and the results replaced immediately by better ones.

- (ii) image intensification which aids the process of alignment and stigmation, leading to smaller more symmetrical probes.
- (iii) the image or diffraction pattern is recorded directly in digital form and can be processed immediately to test its quality.

(f) Phase Extraction Routines

Given the digital form of the electron diffraction patterns they can be processed directly to extract phase information. Several essentially distinct operations have been performed. The first involves pixel averaging to improve the accuracy of phase measurement (Fig 5a). The second involves Fourier transformation of a cross grating coherent electron diffraction pattern, just as was performed previously for coherent LACBED patterns⁴. The relative phases of the overlapping neighbouring pairs of reflections are simply displayed by selecting a first order maximum in the transform corresponding to the lines of overlapping reflections and plotting the phase as a grey level in each of the separate overlap regions in a back transformation (Fig 5b). This step

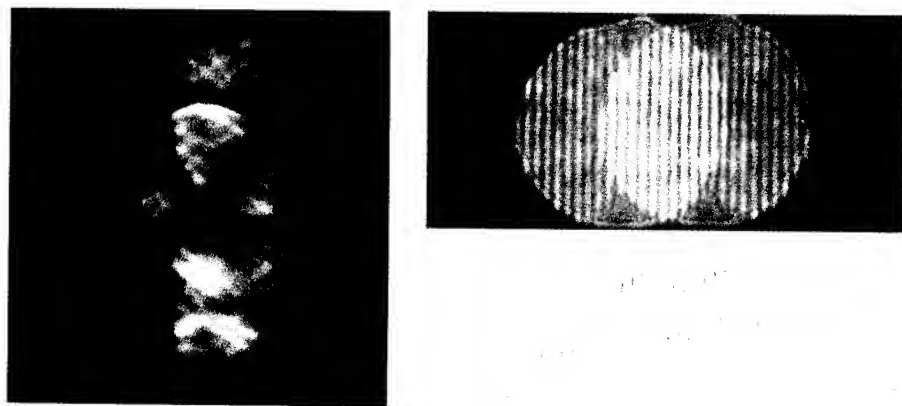


Fig 4. Two sets of {111} fringes with Fig 5a. A line profile across coherent spacings of 0.31nm at the <110> zone axis of silicon

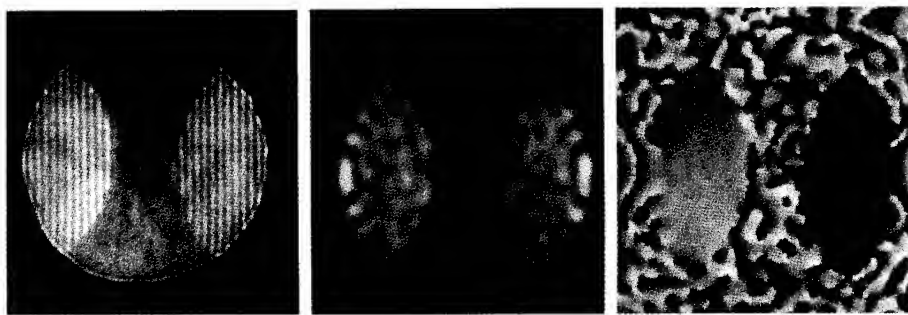


Fig 5b. Phase determination by Fourier transformation; the energy-filtered 0.45nm fringes from mica on the left produce the amplitude distribution (centre) and phases (right) illustrated.

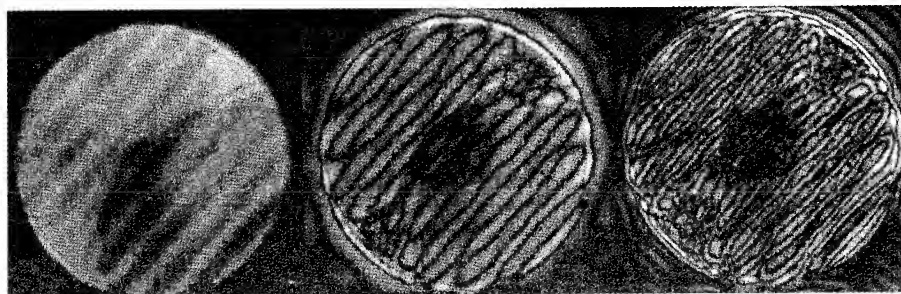


Fig 5c. Phase amplification of fringes in a coherent electron diffraction pattern.

facilitates preliminary phasing of the pattern. To enhance the accuracy of phase determination, phase enhancement techniques can be used, as they have in the past for electron holograms. An example of this technique is illustrated in Fig 5c.

The phases determined will be relative phases of the overlapping diffracted waves. In order to make straightforward use of this phase information it is advantageous if this relative phase is that of the associated structure factors. The rate of departure of a particular reflection from a kinematical approximation with increase of specimen thickness will depend greatly on the material being studied and its orientation. For the c reflection overlaps of SiC, we have shown, by dynamical calculations, that the kinematical approximation holds for thicknesses of a few tens of nm but starts to break down quite seriously for some reflections at a thickness of 50

nm. On the other hand Spence⁶ calculated that for certain reflections in ZnS a thickness of about 7 nm was an upper limit for validity of the kinematical theory.

One obvious application of coherent electron diffraction from complex structures is the use of two-dimensional overlapping cross-grating patterns to evaluate the amplitudes and phases of the reflections from thin crystals. Fourier transformation of the results offers the prospect of determination of the charge distribution in the appropriate projection to higher resolution than can be obtained by HREM at the same axis. By extending the coherent diffraction to HOLZ reflections and use of a precession camera⁷ even greater accuracy could be obtained.

2. STUDY OF INTERFACES AND BOUNDARIES - WHICH TECHNIQUES?

One prospect for energy filtered high-quality transmission electron microscopy is the study of microscopic fields not previously accessible to detailed study. It is of considerable interest in several areas of research to be able to separate out and study independently the nature and existence of strain fields, electric fields, magnetic fields, and state of order. One example would be {111} strained layers of ternary III-V alloys. The strain, piezo-electric fields and state of order will each affect the optical properties. The effectiveness of TEM related techniques has already been demonstrated in identifying the separate contributions in the case of InGaP layers on GaAs⁸ but there were no piezo-electric fields in that case. Other examples include the investigation of electric fields at dislocations, planar faults, interfaces and grain boundaries.

The TEM now has a wide variety of techniques available for study of such problems. Strain may be investigated by HOLZ lines in CBED, or by LACBED, projected atom positions may be determined to better than 0.2 nm resolution by high resolution electron microscopy (HREM), the state of order may be investigated by diffraction contrast microscopy and large angle studies in CBED. Bonding effects may be studied by detailed analysis of CBED data. However, our present concern is with the relative merits of electron holography, coherent electron diffraction and coherent LACBED for obtaining new information not previously available by the other techniques mentioned above.

3. COMPARISON OF ELECTRON HOLOGRAPHY, COHERENT DIFFRACTION AND COHERENT LACBED

In order to make the comparison it may be helpful to consider in more detail the use of an out-of-focus probe of small dimensions in diffraction experiments. The probe size will be determined by a number of factors, particularly the demagnification of the source, the source size, and the spherical aberration of the pre-field of the condenser-objective lens. An oversimplified representation of the situation is given in Fig 6. There are two chief points to notice. First, position in the specimen within the defocused probe is correlated with angle of incidence. Paraxial rays come to the centre of the probe, extreme rays to the extremes of the probe. Second, the resultant amplitude at a particular point in the overlap region of convergent beam discs is the result of the sum of the complex amplitudes (for a coherently filled aperture) of a direct wave and diffracted wave which have different entry points and taken different trajectories

through the crystal. There is a sense therefore in which coherent diffraction is very close to electron holography. Suppose, for example, the point B (Fig 6a) is at the straight edge B'B'' of a specimen. Then the rays at on the left of the diagram will pass outside the edge of the specimen while rays to right of the diagram will pass through the specimen and become diffracted. Some of these diffracted rays will end up propagating at the same angle as the rays which pass outside the specimen to interfere in the overlap region between the two discs in the diagram. We have created by diffraction a situation closely resembling that achieved by a Möllenstedt biprism.

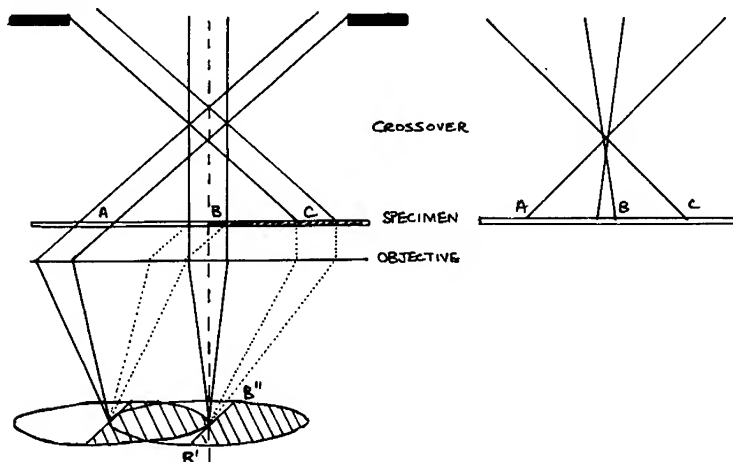


Fig 6. Schematic ray diagram for out-of-focus coherent electron diffraction with a finite probe. Regions A and B of the specimen plane interfere at the extreme left hand side of the direct disc and regions B and C interfere at the centre of the direct disc. The argument may be carried over to the case of spherical aberration as indicated in the right of the figure.

It is of interest to examine some relevant magnitudes. For SiC with twelve 1.5 nm fringes in the region of overlap, at an operating voltage of 200kV, the angle between the reference and diffracted beams in $\alpha (= 2\theta_B) = \frac{0.025}{15} \sim 2.10^{-3}$. The amount of defocus

required to achieve this result is $\Delta f = \frac{18}{2.10^{-3}} \text{ nm} = 9 \mu\text{m}$. For twelve 0.3nm fringes of Si in the region of overlap the new angle between the diffracted and reference beams is 10^{-2} and the defocus required in this case is $\Delta f = \frac{3}{10^{-2}} = 0.3 \mu\text{m}$. This range of angles and focal distances is comparable with the biprism angles of incidence and the distance of the quartz fibre from the specimen when converted to a virtual image near the specimen plane.

There are nevertheless a large number of differences between electron holography and coherent diffraction. In electron holography the biprism wire can be oriented at will with respect to the specimen, the convergence angle can be externally controlled, at will, and as the technique does not rely on diffraction from the specimen it can be used alike on crystalline or non-crystalline specimens. Coherent diffraction, relying on diffraction, is constrained by crystallographic considerations and has no absolute reference by which to measure large phase shifts; there is an uncertainty of phase therefore modulo 2π . As against these disadvantages, the diffraction contrast in the coherent CBED patterns can be used to characterize defects, the diffraction geometry immediately fixes crystallographic directions in the specimen, and no additional equipment is required. Electron holography, involving operations at two independent levels in the column at a high level of perfection would appear to be a much more demanding technique. Electron holograms are affected by lens aberrations differently from coherent diffraction patterns and the ability to record information at large diffraction angles, beyond the information limit for HREM, suggests that higher resolution information might be available by coherent diffraction.

Coherent LACBED patterns give a larger field of view at a larger defocus but are limited in terms of the number of reflections involved.

4. EXAMPLES OF APPLICATION

a) Linear and Planar Defects

There are many reports of electric or magnetic fields associated with extended defects in crystals or deliberately induced by novel growth procedures. Most of these reports depend on indirect methods and lack direct evidence of their validity. It is therefore very attractive to attempt direct verification of some of these conclusions using electron holography or coherent diffraction. An example of the application of this technique to the study of faults in 6H SiC is shown in Fig 7. In this case, a planar fault

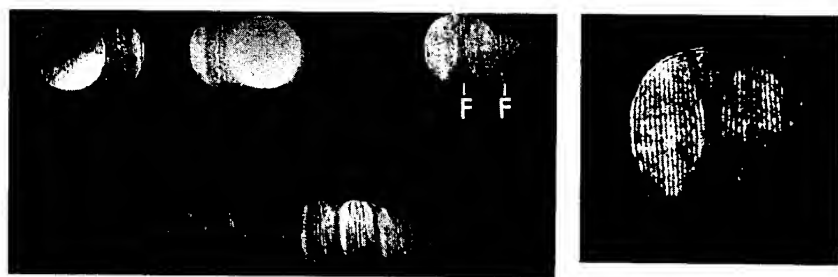


Fig 7. Coherent electron diffraction pattern from faulted SiC showing a planar fault (F) in the regions between the overlapping orders of reflection. The micrograph on the right is a higher magnification of the top right corner of the micrograph on the left.

can be seen in projection (F) in the overlap region of the diffraction discs. It is apparent that the orientation of F and the value of the associated fault displacement vector can be determined from such patterns. By moving the fault into the overlap region, information about associated electric fields might be acquired. Some limitations are apparent. The faults must be well separated so that only one fault occurs within the out-of-focus probe. Without this restriction there would be no unaffected reference beam. With high fault densities, streaking or additional Bragg reflections could occur confusing the situation greatly. By use of a cross-grating coherent electron diffraction pattern a wide variety of fringe orientations relative to the line of the defect can be achieved.

b) Electric and Magnetic Fields

The general expression for the phase change introduced into the electron beam in traversing a specimen with associated \underline{E} and \underline{B} fields is

$$\Delta\phi = \frac{\pi}{\lambda E_0} V_0 t + \frac{\pi}{\lambda E_0 \text{path}} \int V(\underline{R}, z) dz - \frac{e}{\hbar \text{path}} \int A_z(\underline{R}, z) dz \quad (1)$$

where the beam is propagating along the z direction and \underline{R} is a two dimensional vector in the perpendicular plane, E_0 is the accelerating voltage, V_0 the mean potential of the specimen of thickness t , λ is the electron wavelength, $V(\underline{R}, z)$ is the electrostatic potential and $A_z(\underline{R}, z)$ the z component of the vector potential \underline{A} from which \underline{B} may be derived.

c) Electric Fields

If the electric field E_z in a specimen is constant and perpendicular to the specimen surface (parallel to the beam direction), then the additional resulting phase change is $\frac{E_z t^2}{\lambda E_0}$. For in-plane fields the phase change is introduced because of the existence of a field between the two regions of the specimen (separated by Δx) contributing to a given point in the interference pattern (Fig 6a). For fringes created in a systematic row of reflections in the x direction and for a z independent electric field, the phase change is given by

$$\phi_E = \frac{\pi t}{\lambda E_0} \int_{x-\Delta x/2}^{x+\Delta x/2} E_x(x) dx \quad (2)$$

Suppose a vertical boundary exists where the electric field changes direction. If the boundary is parallel to the fringes, they will adjust their separation near the boundary as dictated by the above equation (2). If the fringes are perpendicular to the boundary and if, as is likely, E_x is constant, then $\phi_E = \frac{\pi t E_x \Delta x}{\lambda E_0}$ and an appropriate sideways displacement of the fringes will occur at the boundary (which can only be

determined modulo 2π). The magnitude of this phase change will depend on the defocus, increasing as the defocus increases and as Δx increases.

As, is well known, in reality, account must be taken on the resultant phase changes of the tendency of electric fields to become compensated, and the effect of fringing fields outside the specimen. An important question is the sensitivity of the effect. Tonomura and coworkers⁹ were able to detect monolayer changes of thickness of a specimen by measuring phase changes down to about $\pi/50$. For a 0.6 nm step and a mean potential of 5V the voltage/thickness product is 3Vnm. For a TEM experiment on a specimen of thickness 20nm, with 3 nm separation between the interfering beams, the potential/thickness product would be $E_x 3.20(\text{Vnm})$. Hence we estimate sensitivity to fields down to $E_x \geq \frac{10^9}{20} = 5.10^7 \text{ Vm}^{-1}$ (5.10^5 Vcm^{-1}). For a specimen of 100nm thickness a sensitivity five times greater could be achieved.

d) Magnetic Fields

Both electron holography and coherent electron diffraction require immersion of the specimen in a large magnetic field for high resolution observations. Such strong magnetic fields are likely to have a major effect on the magnetic field distribution in the specimen. If any field variation remains it is only components of magnetic field that are perpendicular to the beam which produce phase changes.

For fringes created in a systematic row of reflections in the x direction and for a z independent magnetic field, the phase change is given by

$$\phi_m = \frac{-te}{\hbar} \int_{x-\Delta x/2}^{x+\Delta x/2} B_y(x) dx \quad (3)$$

For a vertical boundary where the magnetic field changes direction, the resulting effect on the fringes will once again depend on the relative orientation of the fringes to the boundary. For fringes parallel to the boundary the fringe separation will adjust according to equation 3. If the boundary is perpendicular to the fringes then it is likely

that B_y is independent of x and so $\phi_m = -\frac{te\Delta x}{\hbar} B_y$

The variations of magnetic field associated with fluxons in superconductors have recently been used to reveal the fluxon pinning and motion by electron holography¹⁰.

5. CHOICE OF SPECIMEN ORIENTATION

The specimen to be studied will normally be prepared with its planar boundary of interest parallel to the electron beam direction. This geometry facilitates the study of changes associated with the boundary. Unfortunately it also produces a large stress relaxation where stresses exist near the boundary, and a reduction of any resulting electric fields. To minimise stress relaxation effects, we have performed a large number of experiments on specimens with the boundaries parallel to the specimen surface and

perpendicular to the beam¹¹. The great sensitivity of rocking curves in LACBED experiments has made possible a wide range of sensitive investigations by this technique. It may also have advantages for coherent diffraction experiments. As a further alternative, specimens can be prepared with inclined boundaries so that by tilting edge-on or flat-on orientations to the beam can be achieved.

6. CONCLUSIONS

Coherent electron diffraction has now been developed to the point where it can be applied effectively to a wide range of materials. Procedures for phase extraction have been worked out. There exists as a result exciting prospects for investigating several topics of interest in materials science connected with local electric or magnetic fields in specimens. Moreover unknown structures can be solved to high spatial resolution.

Using energy filtered CBED patterns bonding effects can be investigated and LACBED experiments have been performed at a spatial resolution of 1nm.

ACKNOWLEDGEMENTS

The authors wish to acknowledge the support of the Science and Engineering Research Council for various aspects of this work and one of us (XFD) acknowledges the support of the Royal Society and the Academia Sinica.

REFERENCES

- [1] J.W. Steeds, R. Vincent, W. J. Vine, P. Spellward & D. Cherns, *Acta Microscopica* **1** (1992)1 (also abridged in *Hitachi News* **24** (1992)).
- [2] R. Vincent, P. A. Midgley & P. Spellward, *Proceedings of EMAG 93*, Institute of Physics: in the press.
- [3] J.W. Steeds, R. Vincent, P. Spellward & X. F. Duan, *Proc 51st Annual Meeting of MSA* 1054 (1993).
- [4] R. Vincent, W.J. Vine, P.A. Midgley, P. Spellward & J.W. Steeds, *Ultramicroscopy*, **50** 365 (1993).
- [5] X.F. Duan, N. Grigorjeff, D. Cherns, J.W. Steeds & C. Sheng. *Proc. 8th Conf. on Microscopy of Semiconducting Materials* Inst. of Phys. 1993, in the press.
- [6] J.C.H. Spence. *Scanning Electron Microscopy* Vol 1, SEM Inc., AMF O'Hare 1978, p61.
- [7] R. Vincent & P.A. Midgley. *Ultramicroscopy*, in the press.
- [8] J.N. Wang, J.W. Steeds & M. Hopkinson. *Semicond. Sci. Tech.* **8** 502 (1993).
- [9] A. Tonomura, T. Matsuda, T. Kawasaki, J. Endo & N. Osakabe. *Phys. Rev.Lett.* **54** 60 (1985).
- [10] J.E. Bonevich, K. Harada, T. Matsuda, H. Kasai, T. Yoshida, G. Pozzi & A. Tonomura. *Proceedings of 51st Annual Meeting of MSA* 1096 (1993).
- [11] N. Grigorjeff, D. Cherns, M.J. Yates, M. Hockly, S.D. Perrin & M.R. Aylett. *Phil. Mag. A68*, (1993) 121.

HOLOGRAPHIC ATOM IMAGING FROM EXPERIMENTAL PHOTOELECTRON ANGULAR DISTRIBUTION PATTERNS

L. J. TERMINELLO,¹ D. A. LAPIANO-SMITH,² J. J. BARTON², B. L. PETERSEN³, and D. A. SHIRLEY⁴

1. Lawrence Livermore National Laboratory, M/S L-357, Livermore, CA 94550
2. IBM T. J. Watson Research Center, Yorktown Heights, NY 10598
3. Lawrence Berkeley Laboratory, M/S 2-300, 1 Cyclotron Rd. Berkeley, CA 94720
4. Pennsylvania State University, Kern Graduate Building, University Park, PA 16802

ABSTRACT

One of the most challenging areas of materials research is the imaging of technologically relevant materials with microscopic and atomic-scale resolution. As part of the development of these methods, near-surface atoms in single crystals were imaged using core-level photoelectron holograms. The angle-dependent electron diffraction patterns that constitute an electron hologram were two-dimensionally transformed to create a three dimensional, real-space image of the neighboring scattering atoms. We have made use of a multiple-wavenumber, phased-summing method to improve the atom imaging capabilities of experimental photoelectron holography using the Cu(001) and Pt(111) prototype systems. These studies are performed to evaluate the potential of holographic atom imaging methods as structural probes of unknown materials.

INTRODUCTION

In the hopes of developing new, direct methods for probing the structure of novel materials, the atom imaging technique of photoelectron holography has generated much interest as a probe of single crystal materials and, eventually, more challenging abrupt interfaces. Suggested by Szöke,¹ and subsequently formulated by Barton,² the electron holography technique has undergone a series of refinements to improve the quality and reliability of the atom images. Most of these improvements - such as scattering factor compensation, reduced angular windowing, and Gaussian elimination methods³⁻⁵ - have been demonstrated mainly on simulated data, but some of the experimental demonstrations to date of the holography technique have also benefited.⁶⁻¹⁰ However, most of these image improvement methods require *a priori* knowledge of the system being studied to achieve image improvement, particularly the suppression of conjugate atom images.

Another method for improving the quality of holographically derived atom images was developed by Barton.^{11,12} He showed with simulated holograms that a third-axis transform-approximation - a phased-sum of multiple-wavenumber holograms - can suppress twin images and multiple scattering artifacts that are a natural consequence of hologram inversion. It was later demonstrated with experimental work^{13,14} that this approach for near surface atom imaging held much promise. We show in this work the application of this image improvement method on experimental holograms and have chosen the Cu(001) and Pt(111) bulk systems using the photoejected Cu 3p and Pt 4f core-states as the coherent wave source for atom illumination. This method is well served by vacuum ultra-violet and soft x-ray synchrotron radiation because of the tunability of the monochromatic light. One attractive

feature of the multiple-wavenumber, phase-summing formalism is that it requires only experimentally observable information (the hologram and its energy) to create a higher fidelity atom image.

(PHOTO) ELECTRON HOLOGRAPHY

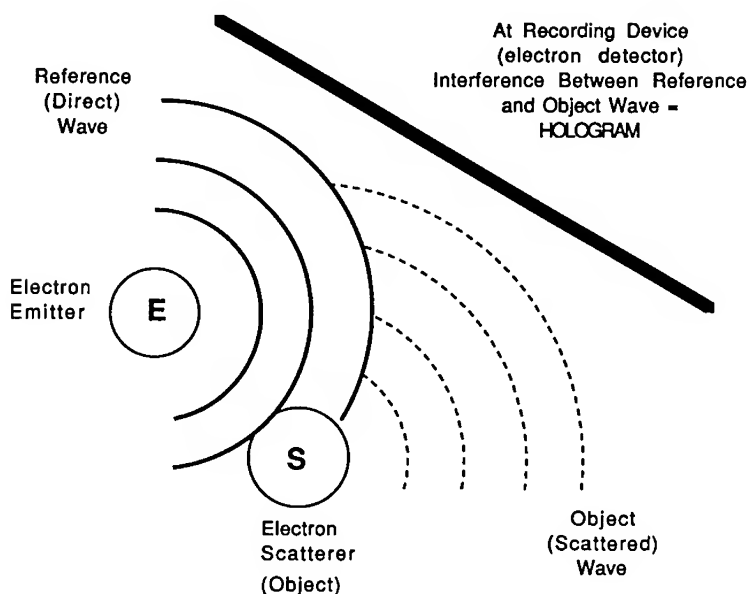


Figure 1: A schematic that illustrates the diffraction process that forms an electron hologram is shown. A localized electron is ejected from an atom (electron emitter) at some fixed kinetic energy and propagates towards an angle resolved electron detector. Part of that same electron wave scatters off of neighboring atoms *en route* to the electron detector. The interference between these two waves contains the structural information in the form of the path length difference incurred during the scattering process.

BACKGROUND

The electron scattering physics that produces a photoelectron hologram is experimentally the same as photoelectron diffraction.¹⁵ This technique for probing the atomic structure of surfaces, adsorbates, epitaxial overlayers, and interfaces examines the photoelectron intensity measured from ordered materials in order to isolate the structurally significant modulations in intensity that arise from local diffraction. Several excellent reviews of this now well established and utilized technique have been written.¹⁶ When electron emission is measured as an electron angular distribution, the diffraction (interference) between the core-level electron measured directly from the emitter (i.e., the reference beam), and the same

photoelectron wave that has scattered off neighboring atoms (i.e., the object wave), form a true hologram. The electron scattering physics that forms a hologram is shown schematically in Fig. 1. A hologram's chemical specificity is a consequence of using element-specific core-level photoelectrons, and oxidation-state and interfacial sensitivity can be achieved when high-resolution, synchrotron-radiation photoelectron spectroscopy is used to select the oxidation-state or interfacially shifted core-level electron.

The elegance of the holography technique permits the multiple-angle photoelectron interference pattern to be two-dimensionally transformed² to produce a real-space, three-dimensional intensity map of the electron-scattering atoms neighboring the photoemitter.⁵⁻⁸ Even without transforming the holograms, the electron forward scattering, which is implicit in patterns measured from buried systems, yields important structural information. The powerful combination of synchrotron radiation and photoelectron holography also enables higher resolution images of atoms to be created through multiple-energy filtering of the resultant images.¹²⁻¹⁴

EXPERIMENTAL

We measured copper 3p photoelectron holograms from a clean, Cu(001) crystal face using well established cleaning and annealing procedures.¹⁷ The surface was checked with core-level photoelectron spectroscopy for contaminants, and the Cu valence-band photoemission features were used to orient the sample with respect to the analyzer. All photoemission spectra were recorded using an Eastman ellipsoidal mirror analyzer that has been described previously.¹⁸ This angle-resolving, energy-band-pass electron analyzer characterized the Cu sample as an angle-integrating detector and also measured the 3p photoelectron holograms in an angle-resolved mode.

Measuring the Cu 3p multiple-energy electron angular distribution patterns at several energies mandated the use of monochromatic synchrotron radiation as the excitation source so that photoelectron holograms over a wide kinetic energy range could be obtained. We conducted these measurements at the National Synchrotron Light Source on the IBM/U8 beamline¹⁹ This facility provided the 316 - 560 eV photons needed for ejecting the Cu 3p core electrons. Electron angular distributions were measured at nine kinetic energies ranging from 244 to 477 eV. This range had several experimental advantages over a higher energy which could produce better resolution:⁶ the cross section for Cu 3p photoemission is well matched with the flux throughput of the monochromator, and non-forward scattering intensities are large in this region of k-space.²⁰ This implies that electron back scattering atoms as well as forward scatterers may be observed through this choice of energy range.

The Pt(111) sample was prepared using well established cleaning procedures¹⁴ and was examined for cleanliness using photoelectron spectroscopy. Initial spectra were measured and continually compared to spectra taken during the experiment in order to monitor the cleanliness of the sample. The sample normal was positioned directly into the center of the angle-resolving analyzer and resulted in the synchrotron radiation polarization vector being 45° with respect to the sample surface. Crystal positioning was done by observing the symmetry of the Fermi surface map obtained from angular distribution patterns.

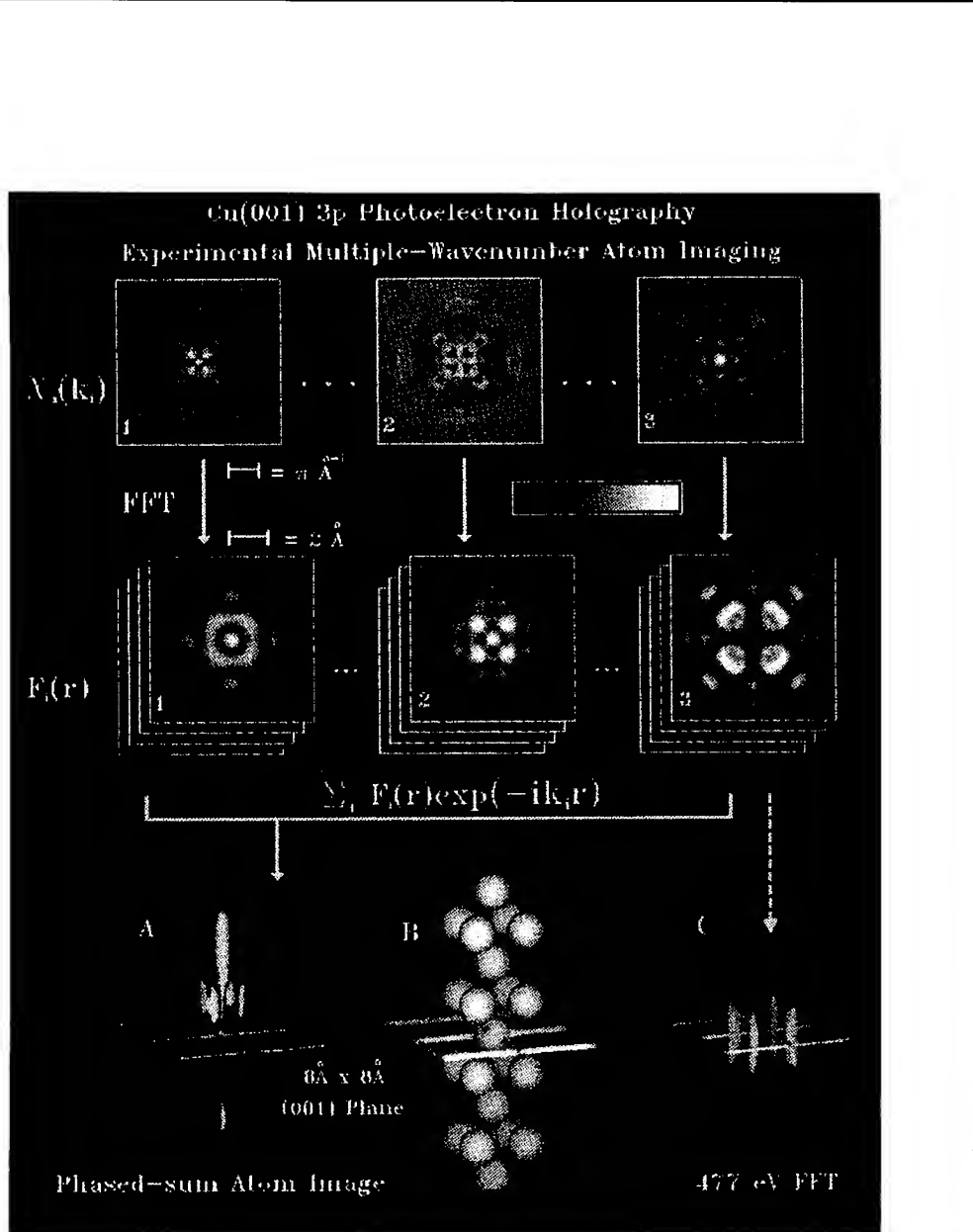


Figure 2: Several steps in the experimental multiple-wavenumber atom imaging method are shown. A series of holograms (Cu 3p $\chi_i(k_i)$) measured at several wavenumbers k_i , $1 = 244$ eV, $2 = 322$ eV, $3 = 477$ eV are numerically inverted to form a series of real space atom images $F_i(r)$. The amplitude of a nine wavenumber phase-summed reconstruction for Cu(001) is shown in panel A. This iso-contour volume rendering has an $8 \times 8 \text{ \AA}$ reference plane parallel to the (001) face passing through the emitter and is shown next to an ideal atom rendering of the Cu(001) lattice (Panel B) with an identical reference plane. The volume contour depiction of the atom image intensity for 3 is shown in Panel C.

Electron emission patterns of the Pt 4f_{5/2} photoelectron were measured at eight equally spaced wavenumbers from $k=8.8\text{\AA}^{-1}$ to 10.2\AA^{-1} . Background spectra were taken at the high energy side of the photoelectron peak and were used for analyzer signature and photon flux normalization. We found that the backgrounds were interchangeable and it was sufficient to measure a few at well chosen energies. All eight images were taken at the same sample position. The method of extracting the structural information from the electron angular distribution patterns from Pt(111) were similar to those used for the Cu(001) sample.

RESULTS

Simple, two-dimensional background removal methods were used for each electron angular distribution pattern to isolate the holographic interference information from the raw data. It should be noted that many aspects of our background removal also eliminate the strong forward peak upon which the structure-containing interference fringes reside,⁸ which improved the image quality. Each Cu hologram was then four-fold symmetry averaged and multiplied by a Gaussian window to eliminate truncation errors. The Cu(001) hologram measured at 322 eV is shown in the inset to Fig. 2. Each of the nine copper holograms were then two-dimensionally transformed.² The resultant volume of Fourier-like intensities ideally have local maxima that are located at scattering atom positions, but in practice, the reconstructed atom intensities appear shifted from their ideal position by as much as 1 \AA . Other work has shown that this result of direct transformation of the hologram, without any other treatment, also produces shifted atom images.⁵⁻⁷ It is only a fortunate selection of energy that produces unshifted atom images.¹⁴

From the raw electron angular distribution patterns, holograms were extracted using methods that have been described elsewhere.²¹ Three of the holograms measured in this work are pictured in Fig. 2 where χ_1 was measured at 244 eV, χ_2 at 322 eV, and χ_3 at 477 eV. Fourier-like, two-dimensional transforms were used to invert all nine holograms into three-dimensional, real-space, atom intensity volumes. The numerical inversions of the three holograms pictured in Fig. 2 are shown schematically below their respective source data. The visible slice in each case is a cut through the Fourier volume taken through the first layer of electron forward scatterers. Note the four high intensity spots around the center (the surface normal) that can be assigned to the four scatterers. Also note that going from lower to higher kinetic energy, the lateral resolution of each atom image improves.

Phase-summing of the hologram reconstructions was achieved using the simple, multiple-energy transform approximation presented by Barton.¹² Briefly, this approximation can be described as:

$$A(r) = \sum_i F_i(k_i, \chi_i, r) e^{-ik_i r}$$

where the resultant real-space r scattering atom intensity, $A(r)$, is given by a sum over the individual atom reconstructions $F_i(k_i, \chi_i, r)$ - which were computed from the holograms χ_i measured at each wave vector value k_i times $\exp(-ik_i r)$ - the phase term that isolates the real, single-scattering contribution to the reconstruction. The phase-dependence as a function of wavenumber is different for the conjugate image than the true image thereby leading to suppression of the twin image.

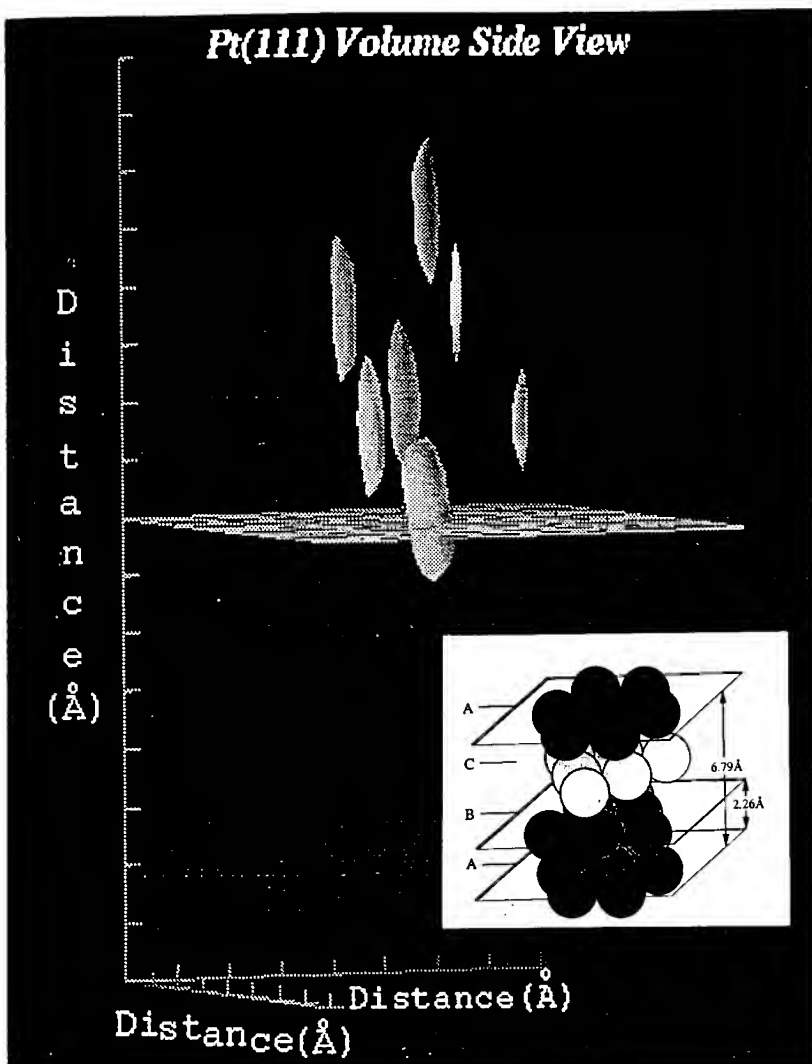


Figure 3: Multiple-wavenumber symmetry averaged volume side view of the Pt(111) $4f_{5/2}$ hologram reconstructions. Atoms are shown as iso-density surfaces in a three-dimensional space above the photoelectron emitting atom. Seven atoms are shown in their expected atomic positions. Each tick mark is 1 Å. The inset depicts the ideal atom geometry with the black sphere representing the emitter atom (bottom layer).

The result of the Cu(001) nine-energy phased sum is shown as a volume contour at 70 % of maximum in Panel A of Fig. 2. The five atoms directly above the emitter are visible in this image and are the highest intensity features. When compared to the ideal atom image of the Cu(001) lattice in panel B, and to the 477 eV result in Panel C, it is apparent that the quality of the atom imaging has been improved mostly through suppression of the conjugate image below the reference plane. In the phase-summed image we also note that the conjugate image is approximately 0.1 the intensity of the real image.

Scattering atoms appear shifted from their nominal lattice location in the multiple-energy (A) and all single-energy images^{6,8,22} because of the additional phase introduced by the scattering physics. This has been observed in earlier experimental electron holography studies⁶ and Fourier-transformed, energy-dependent, photoelectron diffraction.^{15,23} Forward scattering amplitudes are greater than back scattering intensities throughout the structurally-useful range of wavenumbers and determines why atoms that lie between the emitter and the detector dominate the Fourier reconstruction. In our multiple-energy, phase-summed image, we obtain a radial shift of 0.4 Å for the first layer atoms, and a 0.9 Å shift for the second layer atom located directly above the emitter.

The results obtained from the Pt(111) multiple wavenumber phased-summing procedure are even more striking.¹⁴ Figure 3 shows an iso-density, three-dimensional image of atoms above a given Pt emitter, which is shown in the center of the reference grid. Three atoms are seen near their ideal location one layer above the emitter, three more two layers above, and one three layers up, directly above the emitter. This image was generated by phase-summing eight patterns together in the fashion described above.² Notice, that compared to the Cu(001) results, there is some improvement in Z-resolution for the Pt(111) image with the main effect being a loss of twin images and artifacts. We note that all of the information shown here has been averaged rotationally for ease of presentation, and that most of the information can be realized without averaging. Variations in position intensity for different directions due to final state wave effects encourage this method of presentation.

CONCLUSIONS

We have shown that the recently developed technique of photoelectron holography can be used to image single-crystal materials with atomic resolution. Using the prototype, single-crystal surfaces of Cu(001) and Pt(111), we can improve upon the early accomplishments in the field by using a multiple-wavenumber phase-summing algorithm that suppresses the conjugate images that are a result of the numerical transform. This method also acts to suppress the multiple-scattering contributions to the resultant reconstructed atom images.² In our examples, it is not clear that the intensity below the emitter in Figure 2, Panel A is entirely attributable to the twin image of the second layer, (forward scattering) atom above the emitter, or to the second layer (back scattering) atom below the emitter; the expected intensities for both should be the same. However, we see that in Figure 3, the twin image problem can almost entirely be removed. When the multiple-wavenumber, phase-summing method can be coupled with an adsorbate system imaging demonstration, we can then consider using photoelectron holography on challenging abrupt interfaces, such as buried heterojunctions.

ACKNOWLEDGMENTS

We would like to thank C. Costas and J. Yurkas for technical assistance with the experiment. This work was conducted under the auspices of the US Department of Energy, Office of Basic Energy Sciences, Division of Materials Sciences by the Lawrence Livermore National Laboratory under contract No. W-7405-ENG-48, and was conducted at the National Synchrotron Light Source, Brookhaven National Laboratory, which is supported by the Department of Energy (Division of Materials Sciences and Division of Chemical Sciences of Basic Energy Sciences) under Contract No. DE-AC02-76CH0016.

REFERENCES

1. A. Szöke in *Short Wavelength Coherent Radiation: Generation and Applications*, AIP Conference Proceedings No. 147, American Institute of Physics, New York, 1986.
2. J. J. Barton, *Phys. Rev. Lett.* **61**, 1356 (1988).
3. B. P. Tonner, Zhi-Lan Han, G. R. Harp, and D. K. Saldin, *Phys. Rev. B* **43**, 14423 (1991).
4. S. Y. Tong, C. M. Wei, T. C. Zhao, H. Huang, and Hua Li, *Phys. Rev. Lett.* **66**, 60 (1991).
5. G. S. Herman, S. Thevuthasan, Y. J. Kim, T. T. Tran, and C. S. Fadley, *Phys. Rev. Lett.* **68**, 650 (1992).
6. G. R. Harp, D. K. Saldin, and B. P. Tonner, *Phys. Rev. Lett.* **65**, 1012 (1990); G. R. Harp, D. K. Saldin, and B. P. Tonner, *Phys. Rev. B* **42**, 9199 (1990).
7. Z. L. Han, S. Hardcastle, G. R. Harp, H. Li, X. D. Wang, J. Zhang, and B. P. Tonner, *Surf. Sci.* **258**, 313 (1991).
8. S. Thevuthasan, G. S. Herman, A. P. Kaduwela, R. S. Saiki, Y. J. Kim, and C. S. Fadley, *Phys. Rev. Lett.* **67**, 469 (1991).
9. H. Huang, Hua Li, and S. Y. Tong, *Phys. Rev. B* **44**, 3240 (1991).
10. C. M. Wei, T. C. Zhao, and S. Y. Tong, *Phys. Rev. Lett.* **65**, 2278 (1990).
11. J. J. Barton and L. J. Terminello, In S. Y. Tong, M. A. Van Hove, X. Xide, and K. Takayanagi, editors, *Structure of Surfaces III*, Milwaukee, WI, USA Springer-Verlag, 1991.
12. J. J. Barton, *Phys. Rev. Lett.* **67**, 3106 (1991).
13. L. J. Terminello, D. A. Lapiano-Smith, and J. J. Barton, *J. Vac. Sci. and Technol. B* **10**, 2088 (1992), and L. J. Terminello, J. J. Barton, and D. A. Lapiano-Smith, *Phys. Rev. Lett.* **70**, 599 (1993).
14. B. L. Petersen, L. J. Terminello, J. J. Barton, and D. A. Shirley, *Chem Phys. Lett.* **213** (3,4), 412 (1993), and Mater. Res. Soc. Symp. Proc. **307**, 285 (1993).
15. L. J. Terminello, X. S. Zhang, Z. Q. Huang, S. H. Kim, A. E. Schach von Wittenau, K. T. Leung, and D. A. Shirley, *Phys. Rev. B* **38**, 3879 (1988).

16. C. S. Fadley, in *Synchrotron Radiation Research: Advances in Surface Science*, edited by R. Z. Bachrach (Plenum, New York, 1993); S. A. Chambers, *Surf. Sci. Reports* **16**, 261 (1992); W. F. Egelhoff, Jr. in *Critical Reviews in Solid State and Materials Sciences*, **16**, 213 (1990); H. P. Bonzel, *Prog. in Surf. Sci.* **42**, 219 (1993); A. M. Bradshaw and D. P. Woodruff, *Applications of Synchrotron Radiation: High-Resolution Studies of Molecules and Molecular Adsorbates on Surfaces*, edited by W. Eberhardt (Springer-Verlag, Berlin, 1993).
17. C. C. Bahr, J. J. Barton, Z. Hussain, S. W. Robey, J. G. Tobin, and D. A. Shirley, *Phys. Rev. B* **35**, 3773 (1987).
18. D. E. Eastman, J. J. Donelon, N. C. Hien, and F. J. Himpsel, *Nucl. Instrum. and Meth.* **172**, 327 (1980).
19. F. J. Himpsel, Y. Jugnet, D. E. Eastman, J. J. Donelon, D. Grimm, G. Landgren, A. Marx, J. F. Morar, C. Oden, R. A. Pollack, J. Schneir, and C. Crider, *Nucl. Instrum. Methods Phys. Res.* **222**, 107 (1984).
20. J. J. Barton and D. A. Shirley, *Phys. Rev. A* **32**, 1019 (1985).
21. L. J. Terminello and J. J. Barton, to be published.
22. D. Hardcastle, Z.-L. Han, G. R. Harp, J. Zhang, B. L. Chen, D. K. Saldin, and B. P. Tonner, *Surf. Sci.* **245**, L190 (1991).
23. J. J. Barton, C. C. Bahr, S. W. Robey, Z. Hussain, E. Umbach, and D. A. Shirley, *Phys. Rev. B* **34**, 3807 (1986).

A CBED PROCEDURE FOR DETERMINING LOCAL RESIDUAL STRESSES FROM NANOSCALE AREAS IN CERMETS

Gyeung Ho Kim and Mehmet Sarikaya,

Materials Science and Engineering, University of Washington, Seattle, WA 98195, USA

Abstract

A convergent beam electron diffraction method was used in a transmission electron microscope to determine residual thermal stresses from nanometer-scale areas in a ceramic-metal (cermet) composite material. It is demonstrated that the method is simple, but requires a standard sample for each of the phases in the composite. The principle of the technique is that the stresses are determined by comparing higher order Laue zone line shifts, due to lattice strain, in high-symmetry zone-axis electron diffraction patterns recorded under the same experimental conditions from the unknown phases and the standards. The application of the method to composite systems containing dissimilar phases, such as ceramic-metal composite systems, demonstrates the universality of the technique in obtaining local structural information of anisotropic strain unambiguously with a high accuracy. The procedure involved is described in detail with application to B₄C-Al, a three-dimensional intertwined ceramic-metal composite.

1.0 Introduction

A technique that can provide local information of stress distribution from a complex, fine-scale microstructure would be an indispensable tool to understand the role of thermal stress on mechanical behavior and other physical properties.¹⁻² One such technique is convergent beam electron diffraction (CBED)³⁻⁷ which is best suited to meet the requirements for stress measurements in single and multi-phase materials with complex microstructures by providing a high spatial resolution with an accuracy in lattice parameter of $\pm 5 \times 10^{-5}$ nm. Modern transmission electron microscopes (TEM) allow focusing of an electron probe to a diameter as small as 10 nm with sufficient probe currents (down to 0.5 nm dia. probe with 0.5 nAmp probe current in TEMs with field emission electron sources).⁸ Because of the sample-electron beam geometry, as shown in Figure 1, the strain perpendicular to the specimen surface is determined at high diffraction angles by higher order Laue Zone (HOLZ) diffraction lines.⁸ Since electron diffraction takes place in transmission through the sample (Fig. 1), the magnitude of the strain measured becomes σ/E . This indicates, in a cermet material, that the metal phase with small E is more favorable for high accuracy-thermal strain determination.

HOLZ line analysis in a ceramic phase is rather difficult since ceramic phases, compared a metal phase, normally yields complicated HOLZ patterns and smaller shifts in their position due to smaller strain under a given stress. Unlike X-ray diffraction technique,⁹ however, CBED can measure thermal stress using metal phase without the loss of accuracy at higher diffraction angles. Besides the capability of obtaining information from areas as small as the size of electron probe, the distinctive advantage of using electron diffraction technique is that a correlation between measured strain and the microstructural detail can directly be made.

There are several procedures used in the literature in determining strain or lattice parameter changes by CBED.³⁻⁷ The method applied in this work uses a standard sample with identical structure and composition, and compares the HOLZ patterns obtained from the unknown and the standard samples recorded in the same z.a. orientations for differences in the HOLZ-line positions. The major differences between this and the standardless method are that in this technique, a high symmetry z.a. is used for accurate determination of the "center of the pattern." Secondly, a so-called strain equation is derived for each phase in the microstructure for a given diffraction condition, for example the (hkl) lines used and the position of the (hkl) HOLZ lines as described below. The technique is applied to a cermet system, i.e., B₄C-Al, since cermets are known to exhibit high toughness and especially high strength above those predicted by the rule-of-mixtures. One reason for this would be residual stresses that originate from differences in thermal contraction in metal and ceramic phases as they are cooled from the processing temperatures (above 1000°C) to room temperature. A standard sample is used for HOLZ-line measurements for each phase in the microstructure, i.e., for pure Al and pure B₄C, and the errors associated with measurements, and the procedures of conversion from strain to stress values are described.¹⁰

2.0 Experimental Procedures

The TEM samples were prepared from B₄C-Al cermet containing 36 vol. % of Al. This composition corresponds to the maximum strength observed in the B₄C-Al system.¹⁰ Processing of B₄C-Al cermet involves presintering of B₄C at 1900 °C and subsequent infiltration of Al into the porous B₄C skeleton at 1200 °C.¹¹ Al content in the cermet is controlled by the porosity of the presintered B₄C skeleton.¹²

Electron transparent cermet samples were prepared for TEM by ion-beam milling using a low-temperature holder. For a B₄C standard, single crystalline powders, that were suspended on a carbon film, were used. Standard Al sample was prepared by electropolishing using nitric-methanol solution at -30 °C. The CBED experiments were done using a Philips 430T TEM/STEM equipped with a LaB₆ electron source in the TEM mode of operation at 100 kV

accelerating voltage. The samples were always kept in a liquid-nitrogen-cooled double-tilt holder. Specimen cooling was necessary to damp thermal vibrations to reduce background and increase the sharpness of the HOLZ lines and, hence, to enhance their visibility and the accuracy of the measurements. Samples were tilted to $<111>$ orientation for the Al phase and to the only 3-fold symmetry axis, [111] for the rhombohedral phase of B₄C. The diffraction patterns were obtained with a convergence angle of 10.5 mrad and typical spot size of approximately 30 nm. The recorded HOLZ patterns were measured with a measuring microscope within an accuracy of ± 0.01 mm.

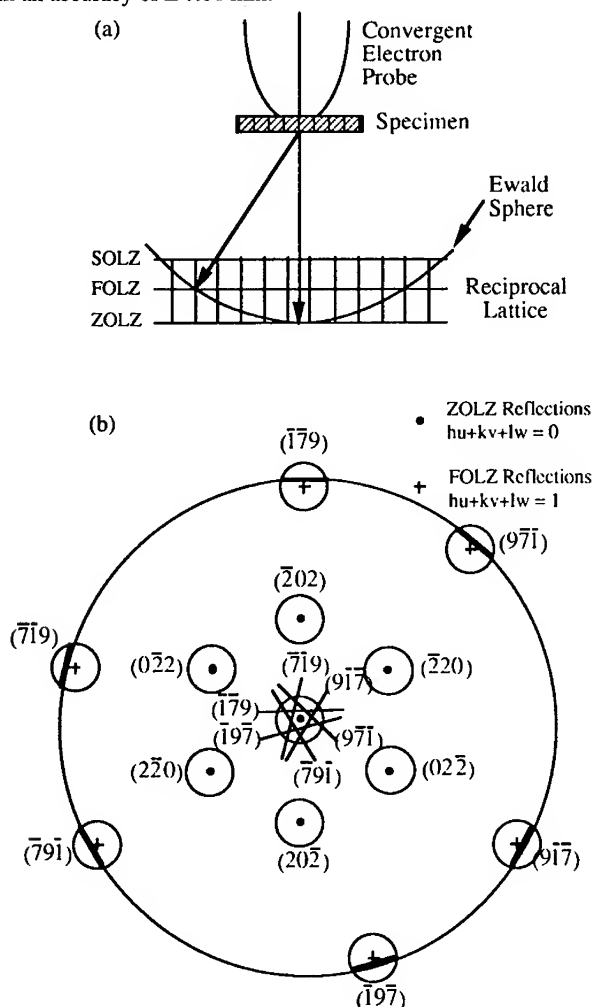


Fig. 1 - Principles of CBED and formation of HOLZ lines in Al [111] z.a. (a) Geometry of reciprocal lattice-Ewald Sphere; (b) pairs of indexed HOLZ lines in (000) disk and FOLZ ring.

3.0 Derivation of the Strain Equation

The detailed procedures of derivation of strain equations that are used to evaluate the magnitude of strain in the specimen for Al and B₄C phases are given elsewhere.^{10,13} Here, basic points in the procedure and the equations will be given. The geometrical description of diffraction condition is given in Fig. 2. In these derivations, the kinematical approximation of higher order Laue zone diffraction is used. In the figure, θ is the Bragg angle for the reflection (hkl), and ψ is the angle from the center of pattern or optic axis to the intersection of g_{hkl} with higher order Laue zone. The actual angle is δ ; the value of Δ is the distance of dark or deficient (hkl) HOLZ-line from the optic axis in the transmitted disk. H is the spacing of the reciprocal lattice planes that are normal to the [uvw] excited z.a. The wave vector is denoted by \mathbf{k} whose magnitude is the reciprocal of the operating wavelength of the incident electron beam; g_{hkl} is reciprocal vector corresponding to the (hkl) reflection that gives the dark line in the transmitted disk. From the geometry presented in Fig. 2, the Bragg angle θ can be expressed as:

$$\theta = \sin^{-1}\left(\frac{\lambda}{2d}\right) \equiv \frac{g}{2k} \quad (1) \text{ and the angle } \omega \text{ is defined as: } \omega = \sin^{-1}\left(\frac{H}{g}\right) \equiv \frac{H}{g} \quad (2)$$

Two cases can be considered as shown in Fig. 2(a) and (b). In Fig. 1 (a), $\theta > \omega$ and consequently the following relationships are established.

$$\delta = 2(\theta - \psi) \quad (3)$$

$$\delta + (90^\circ - \theta) + \omega = 90^\circ \quad (4)$$

$$\delta = \theta - \omega. \quad (5)$$

Combining all relationships to find a proper expression for δ , one gets:

$$\delta = \frac{g}{2k} - \frac{H}{g}. \quad (6)$$

The actual distances in the diffraction pattern can be found by multiplying the camera length L with the angle δ , and the expression for Δ becomes:

$$\Delta = L \left(\frac{g}{2k} - \frac{H}{g} \right). \quad (7)$$

On the other hand, if $\omega > \theta$ as shown in Fig. 2 (b), then the following relationships hold:

$$\delta = 2(\psi - \theta) \quad (8)$$

$$(90^\circ - \theta) - \delta + \omega = 90^\circ, \quad (9)$$

$$\delta = \omega - \theta \quad (10)$$

$$\delta = \frac{H}{g} - \frac{g}{2k}. \quad (11)$$

Final expression for the actual distance of a (hkl) HOLZ line from the center of (000) disk in the diffraction pattern becomes:

$$\Delta = L \left(\frac{H}{g} - \frac{g}{2k} \right) \quad (12)$$

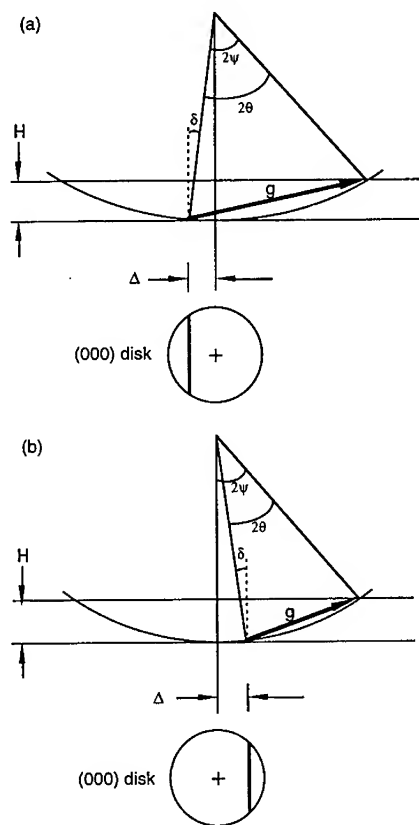


Figure 2. The geometry of formation of deficient HOLZ lines in (000) disk in CBED:
 (a) $\theta > \psi$ and (b) $\psi > \theta$.

The strain equations for the Al and B₄C phases are as follows:

(a) Al phase in [111] z.a. orientation for $\{9\bar{7}\bar{1}\}$ HOLZ lines (equations for other planes can be derived similarly):

If $g_{9\bar{7}\bar{1}}$ HOLZ line is used for the measurement of strain at [111] orientation, as shown in Fig.

3(a) for Al standard, then Eqn. 12 is applicable, and substitution gives the following:

$$\frac{Q_{\text{STD}}}{3} = \frac{P_{\text{STD}} \cdot k}{g_{2\bar{2}0}} \left(\frac{g_{9\bar{7}\bar{1}}}{2k} - \frac{H_{111}}{g_{9\bar{7}\bar{1}}} \right) \quad (14)$$

$$\frac{Q_{\text{STD}}}{P_{\text{STD}}} = \frac{3\sqrt{131}}{4\sqrt{2}} - \frac{\sqrt{3}}{2\sqrt{2}} \cdot \frac{k \cdot a_0}{\sqrt{131}} ; \quad (15)$$

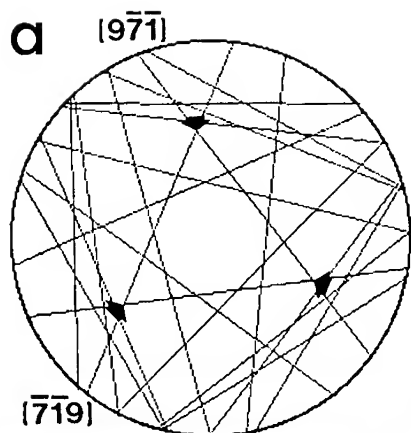
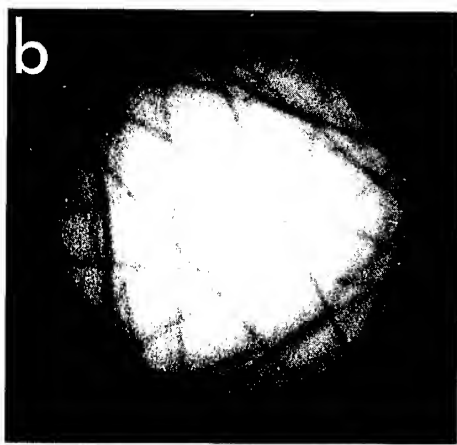
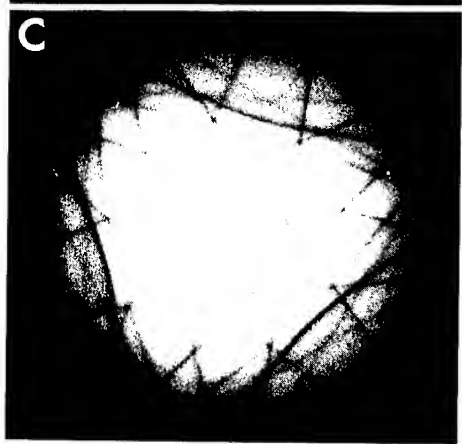


Figure 3

(a) Geometry of HOLZ line pattern in Al in $\langle 111 \rangle$ z.a. orientation.



(b) HOLZ diffraction lines in ZOLZ (000) diffraction disk obtained from a pure Al standard in a $\langle 111 \rangle$ z.a.



(c) HOLZ diffraction lines in (000) diffraction disk obtained from Al region of the B₄C-Al cermet in a $\langle 111 \rangle$ z.a. HOLZ lines in (c) display small and distorted triangular feature compared to that of that in (b).

or solving for a_0 , one gets: $a_0 = \frac{2\sqrt{2} \cdot \sqrt{131}}{\sqrt{3} \cdot k} \left(\frac{3\sqrt{131}}{4\sqrt{2}} - \frac{Q_{STD}}{P_{STD}} \right)$. (16)

A similar equation holds for $a (= a_0 + \Delta a)$ of the Al phase with a strain in the cermet sample:

$$\frac{Q}{P} = \frac{3\sqrt{131}}{4\sqrt{2}} - \frac{\sqrt{3}}{2\sqrt{2}} \cdot \frac{k \cdot (a_0 + \Delta a)}{\sqrt{131}}. \quad (17)$$

Combining this with Eqn. 15 and solving for Δa , one gets:

$$\Delta a = \frac{2\sqrt{2} \cdot \sqrt{131}}{\sqrt{3} \cdot k} \left(\frac{Q_{STD}}{P_{STD}} - \frac{Q}{P} \right). \quad (18)$$

Finally, the expression for strain ϵ is obtained from Eqn. 16 and Eqn. 18:

$$\frac{\Delta a}{a_0} = \frac{\frac{Q_{STD}}{P_{STD}} - \frac{Q}{P}}{\frac{3\sqrt{131}}{4\sqrt{2}} - \frac{Q_{STD}}{P_{STD}}}. \quad (19)$$

(b) B₄C phase in [111] z.a. orientation for $\{2\bar{7}\bar{4}\}$ HOLZ lines:

The triangles in B₄C [111] HOLZ pattern are made of six $\{2\bar{7}\bar{4}\}$ HOLZ lines giving two triangles rotated with respect to each other by 19.64 ° as shown in Fig. 4(a). The height of the triangle formed by the $\{2\bar{7}\bar{4}\}$ lines, however, is difficult to measure due to overlapping between two triangles producing a 6-sided polygons of HOLZ pattern as shown by the thick lines in Fig. 4(a). It is, therefore, necessary to derive a relationship between an easily measurable quantity (the height of the polygon, $Q = \overline{GH}$) and the true distance of $\{2\bar{7}\bar{4}\}$ HOLZ lines from the center of the pattern ($\Delta = \frac{\overline{DI}}{3} = \overline{OI}$). Again, a simple trigonometric relationship exists between the two distances, i.e., $Q = 3.913 \Delta$. The value of a geometrical factor, Φ , for B₄C phase is 0.767, ($\Phi = 1$ for Al phase) and for Δ , one gets: $\Delta = \frac{Q}{3} \cdot \Phi$. (20)

By following similar steps as in Al, for a_0 , one gets:

$$a_R = \frac{F(1\bar{1}0) \cdot F(\bar{2}7\bar{4})}{3k \cdot (0.428)} \left(\frac{3F(\bar{2}7\bar{4})}{2F(1\bar{1}0)} - \frac{Q_{STD} \cdot \Phi}{P_{STD}} \right) \quad (21)$$

and $\Delta a = \frac{F(1\bar{1}0) \cdot F(\bar{2}7\bar{4})}{3k \cdot (0.428)} \left(\frac{Q_{STD}}{P_{STD}} - \frac{Q}{P} \right) \cdot \Phi. \quad (22)$

Finally, the expression for strain ϵ is obtained from Eqns. 21 and 22,

$$\frac{\Delta a}{a_0} = \frac{\frac{Q_{STD}}{P_{STD}} - \frac{Q}{P}}{\frac{3F(\bar{2}7\bar{4})}{2F(1\bar{1}0) \cdot \Phi} - \frac{Q_{STD}}{P_{STD}}}. \quad (23)$$

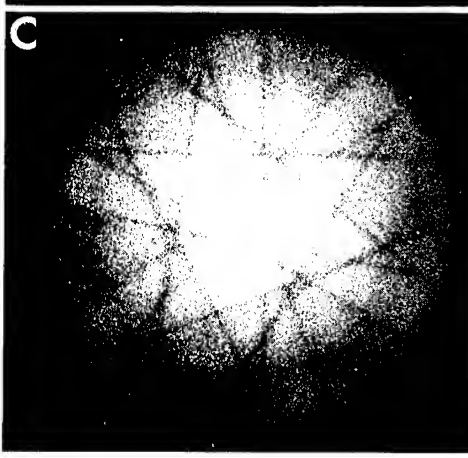
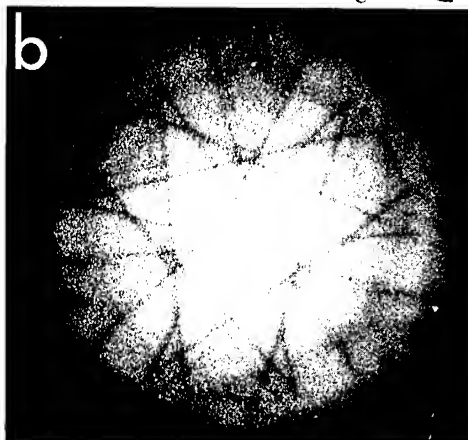
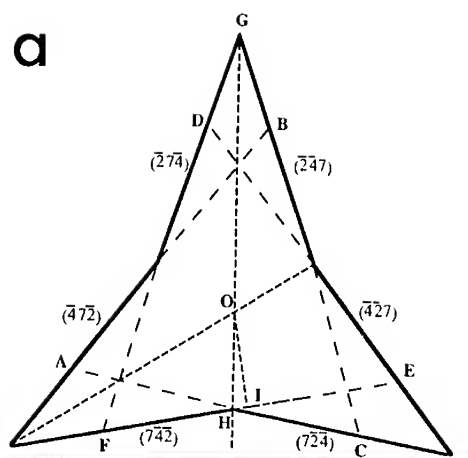


Figure 4

(a) Geometry of HOLZ line pattern in B_4C in $[111]$ z.a. orientation.

(b) HOLZ diffraction lines in ZOLZ (000) diffraction disk obtained from a pure B_4C standard (powder) in a $<111>$ z.a.

(c) HOLZ diffraction lines in (000) diffraction disk obtained from B_4C region of the B_4C -Al cermet in a $<111>$ z.a.

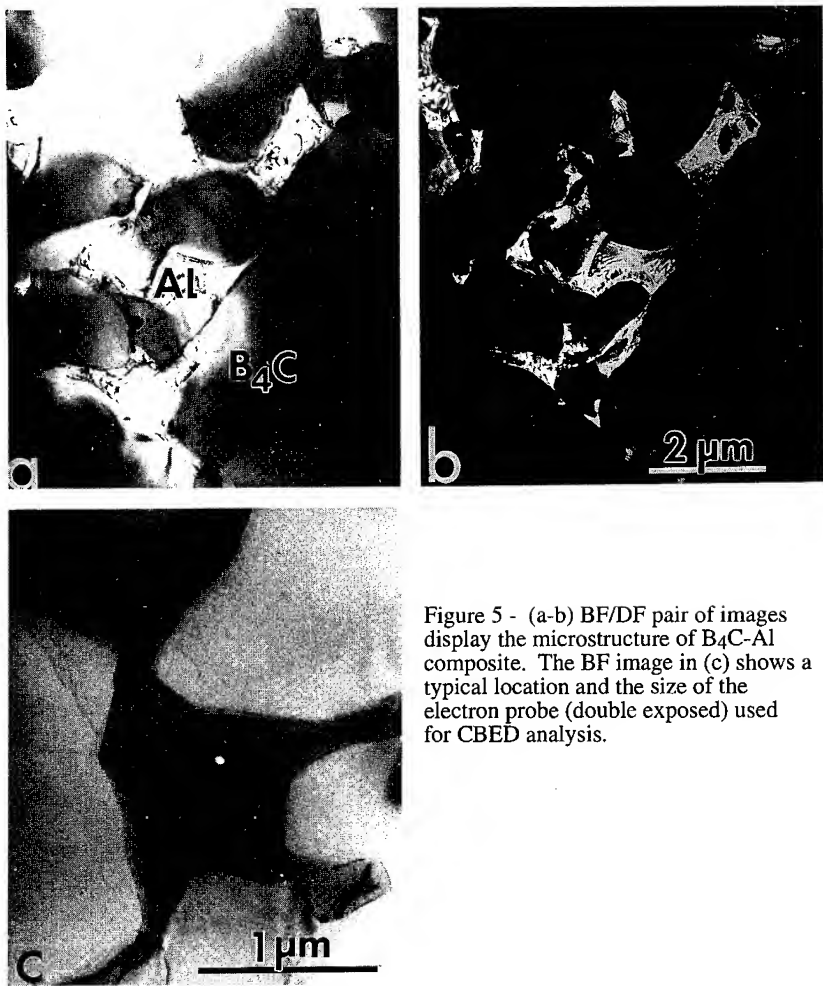


Figure 5 - (a-b) BF/DF pair of images display the microstructure of B₄C-Al composite. The BF image in (c) shows a typical location and the size of the electron probe (double exposed) used for CBED analysis.

5.0 Results and Discussion

A typical area in B₄C for analysis is shown in Fig. 5 with the electron probe (about 30 nm diameter) double exposed onto the image. An example that compares HOLZ patterns from the standard and strained sample is given in Fig. 3 (b-c), where the strain in the Al phase in B₄C-Al cermet not only reduces the size of the triangle but also destroys the 3-fold symmetry. Compared to the Al phase, the effect of strain in the B₄C phase is not so apparent as shown in Fig. 4 (b-c) in which HOLZ line patterns taken from the B₄C powder standard and from B₄C grain in the cermet sample are compared. This is due to high elastic modulus of B₄C phase which causes much smaller strain under a given stress level. The values of strain in B₄C-Al

cermet are calculated from the measured Q/P values using Eqns. 19 and 23; 2.23×10^{-3} in Al (tensile) and -0.246×10^{-3} in B₄C (compressive); corresponding average stresses, using the elastic moduli of Al and B₄C phases, are +156 MPa and -108 MPa, respectively.¹³

The unique additional advantages of this method are that, first, by measuring the heights of distorted triangle along three apexes, strains can be measured in three directions (120° apart), i.e., 3-dimensional strain distribution. Secondly, a simple rotation calibration of the image about the diffraction pattern will relate the image to the directional strain in the sample. Only one CBED pattern can reveal two-dimensional stress state in the metal phase surrounded by the ceramic phase. Thirdly, it may be possible to measure the local interfacial strength of a ceramic/metal interface. For this, the shear stress at the interface can be estimated from the measured thermal stress values of the metal and ceramic phase across the interface.¹⁴

There are errors associated with the CBED technique described here that can be classified into two categories. First one originates from the assumptions used in the derivation of the strain equations, primarily from the kinematical approximation of HOLZ line position. Main sources of error involved in kinematical approximation have been extensively studied,¹⁵⁻¹⁷ and in some cases, full scale dynamic calculation was proposed.¹⁶⁻¹⁷ The second sources of errors come from the practical aspects of the technique. For example, errors in measuring the height of the triangle in Al pattern, uncertainty in the elastic constant values, and surface stress relaxation in TEM samples (These are discussed in detail in references 10 and 13).

The procedure for converting strains from the HOLZ line measurements to corresponding thermal stresses is, in principle, straightforward and does not require Poisson's ratio, since measured strain is σ/E . The accuracy of strain measurement with a strain-free standard is expected to be very good; it is only affected by the error in measurements made on the actual diffraction patterns. In the present B₄C-Al case, measurement uncertainties lead to an approximately $\pm 10\%$ of error in the values of nominal strain. The error value, for example, in the Al phase would be about ± 30 MPa. The conversion of the measured strain to stress can be performed in three different ways.^{10,13} The simplest approach is to assume biaxial stress state and to use Young's modulus of the metal phase. The second approach is to use the elastic modulus of a single crystal standard along certain crystallographic directions calculated from the compliance constants.¹⁸ The difference between the first and the second approach comes out to be about 3% for E_{971} and Young's modulus of polycrystalline Al phase. If a hydrostatic state of stress is assumed, then the values of bulk modulus and the dilation of Al phase are used to calculate the hydrostatic stresses in Al. Using the bulk modulus of Al, this approach gives hydrostatic tensile stress of about 2.2 times higher than the biaxial stress value.¹⁰

6. Conclusions

A CBED procedure was discussed that uses standard samples and examines the shifts in HOLZ-line positions as compared to those from an unknown sample to determine residual stresses in engineering materials. The simple strain equations were developed for the calculation of stresses that develop due to differential thermal contraction of phases in a B₄C-Al composite with three-dimensional interpenetrating microstructure. The major advantages of the procedure are that strain equation has a simple form, there is no need for a prior knowledge of operating condition of the microscope, and that the technique allows a direct examination of anisotropic elastic deformation in a local region of an otherwise complex microstructure.

The largest error in the residual stress determination by this CBED procedure comes from the uncertainty in elastic constant and measurements of HOLZ positions. The errors that are associated with the dynamic effects are insignificant.^{10,13} The measured strain of Al in B₄C-Al cermet was as high as $+5.2 \times 10^{-3}$, and the thermal stress is about three times the bulk yield strength of Al. The corresponding compressive strain was also determined in the B₄C phase. The ability of the Al phase to withstand the high strain without considerable plastic deformation is attributed to the effective constraint of Al phase by the rigid three-dimensional B₄C skeleton. This result may help explain the high toughness values achieved in this successful cermet. The technique is simple to apply, and has unique advantages to provide local strain profiles at nanometer dimensions in complex microstructures and should be applicable to other materials systems with structural variations at the nanometer scale.

7.0 Acknowledgments

We appreciate the valuable discussions with I. A. Aksay, M. Yasrebi, and D. L. Milius. The financial support (GHK) was provided by AFOSR under a Grant # AFOSR-91-0040.

8.0 References

1. J. Gurland, "Temperature Stresses in the Two-Phase Alloy, WC-Co," *Trans. ASM*, **50** 1063-1071(1958)
2. A. D. Krawitz, M. L. Crapenhoft, D. G. Reichel and R. Warren, "Residual Stress Distribution in Cermets," *Mat. Sci. and Eng. A***105/106** 275-281(1988).
3. P. M. Jones, G. M. Rackham, and J. W. Steeds, "Higher Order Laue Zone Effects in Electron Diffraction and Their Use in Lattice Parameter Determination," *Proc. R. Soc. Lond. A*, **354** 197-222 (1977).

4. R. C. Ecob, M. P. Shaw, A. J. Porter and B. Ralph, "The Application Of Convergent-Beam Electron Diffraction to the Detection of Small Symmetry Changes Accompanying Phase Transformations, I. General and Methods," *Phil. Mag. A* **44** [5] 1117-1133 (1981).
5. P. Chemelle, A. Ribes, R. Potier and B. Thomas, "Introduction a Quelques Applications de la Diffraction a Faisceau Convergent," *Microsc. Spectrosc. Electron.*, **8**, 401-418 (1983).
6. C. De Blasi, M. Di Giulio and D. Manno, "Numerical Evaluation of Lattice Parameters From High-Order Laue Zone Lines in Convergent-Beam Electron Diffraction Disks," *Ultramicroscopy*, **26**, 377-384 (1988).
7. I. N. Yachikov and S. K. Marksimov, "Dynamics of CBED Patterns", *Sov. Phys. Crystallogr.* **36** [3] 308-312 (1991).
8. J. W. Steeds and R. Vincent, see These Proceedings, and also, J. W. Steeds, "Convergent Beam Electron Diffracton and Its Applications," in *Introduction to Analytical Electron Microscopy*, J. J. Hren, J. I. Goldstein, and D. C. Joy (eds.) (Plenum Press, New York, 1979) pp. 387-422.
9. D. N. French, "X-Ray Stress Analysis of WC-Co Cermets: II - Temperature Stresses," *J. Am. Ceram. Soc.*, **52** [4] 271-275 (1969).
10. G. H. Kim and M. Sarikaya, to be published (1994).
11. D. C. Halverson, A. J. Pyzik, I. A. Aksay, and W. E. Snowden, "Processing of Boron Carbide-Aluminum Composites," *J. Am. Ceram. Soc.*, **72** [5] 775-780 (1980).
12. A. J. Pyzik, I. A. Aksay, and M. Sarikaya, "Microdesigning of Ceramic-Metal Composites," in *Ceramic Microstructures '86*, J. A. Pask and A. G. Evans (eds.) Plenum Press, New York, 1987) pp. 45-54.
13. G. H. Kim, "The Effects of Metallic Phase and Microstructure on the Strengthening Behavior of B₄C-Al Cermets," Ph. D. Thesis, University of Washington, March, 1993
14. G. H. Kim and M. Sarikaya, "Determining the Local Interfacial Strength in Cermets by Convergent Beam Electron Diffraction Technique," to be published.
15. Y. P. Lin, D. M. Bird, and R. Vincent, "Errors and Correction Term For Holz Line Simulations", *Ultramicroscopy* **27**, 233-240 (1989).
16. E. G. Bithell and W. M. Stobbs, "The Simulation of HOLZ Line Positions in Electron Diffraction Patterns: First Order Dynamic Corrections," *J. Microsc.*, **153** [1] 39-49 (1987).
17. *Microdiffraction and Convergent Beam Electron Diffraction*, J. C. H. Spence and J. M. Zuo (Plenum, New York, 1992).
18. *Physical Properties fo Crystals*, J. F. Nye (Oxford Science Publ., New York, 1989).

ELECTRONIC STRUCTURE AND BONDING AT INTERFACES BETWEEN CVD DIAMOND AND SILICON

DAVID A. MULLER*, YUJIUN TZOU⁺, RISHI RAJ⁺, AND JOHN SILCOX[&]

*Physics Dept., Cornell University, Ithaca, N.Y., U.S.A., 14853.

⁺Dept. of Mat. Sci. and Eng., Cornell University, Ithaca, N.Y., U.S.A., 14853.

[&]School of App. and Eng. Physics, Cornell University, Ithaca, N.Y., U.S.A., 14853.

ABSTRACT

The interfacial structure of CVD diamond grown on silicon was studied using spatially resolved electron energy loss spectroscopy (EELS) in a UHV STEM with a subnanometer probe size. Both the plasmon and core excitations in the bulk appear to be localized on this scale. Spatial maps of the different bonding configurations of carbon were obtained by forming images from transmitted electrons that had undergone energy losses characteristic of threefold and fourfold coordinated carbon. Films grown on both prescratched silicon and intermediate amorphous carbon layers were examined. In the latter case, diamond nucleation on a narrow sp² a-C occurred. For diamond grown directly on silicon, at some regions of the interface, threefold coordinated defect states smaller than 1nm are observed on the diamond side of the interface while at other regions along the interface the presence of an intermediate 2nm thick SiC layer preserves the fourfold coordination of the carbon.

INTRODUCTION

The potential for diverse applications of diamond¹ has been enhanced by the discovery of a simple chemical vapor deposition (CVD) process^{2,3}. While polycrystalline films with special orientations⁴ have been made, the possibility of growing heteroepitaxial films on silicon remains an exciting though elusive goal. Diamond growth on silicon often involves interlayers⁵ because of the large (50%) lattice mismatch between diamond and silicon. These thin interlayers may contain crystalline (SiC)^{6,7} or amorphous compounds (a-SiC, sp² a-C⁸ or SiO₂). An understanding of how the diamond initially nucleates (e.g., on silicon⁹ or via interlayers of SiC⁵ or graphite^{10,11}) is a fundamental question that requires knowledge of the arrangements of the sp² and sp³ bonds at the interface.

EXPERIMENTAL APPROACH

Film Growth and Preparation for Microscopy

Two specimens were selected from a previous TEM study⁹ as typical of two different growth regimes. Both specimens were grown on (001) silicon substrates that had been scratched with 1μ diamond paste. The first diamond film, Specimen A, was prepared by microwave decomposition of a methane (1%) hydrogen (99%) mixture deposited first for one hour at 640°C and then one hour more at 750°C and thinned as a cross-section sample. The gas pressure was held at 50 Torr. This type of growth led to nanocrystalline diamond overgrowth on a 2-4nm thick amorphous layer between the diamond and the silicon substrate⁹.

Specimen B was grown at 900°C for 15 minutes. At this temperature the growth rate was roughly 1μm/hour. Specimens of this type showed both amorphous interlayers as in specimen A and also many regions where no third phase could be seen between the diamond and the silicon in a CTEM(conventional electron microscope).

EELS Imaging

A scanning transmission electron microscope (STEM) equipped with an electron energy spectrometer, can select a specific energy loss and scan the focused 0.3nm wide electron probe on the sample¹² thereby mapping the locations at which that loss occurs¹³. We report here observations that use the carbon K-edge (i.e., excitations from the carbon 1s orbital to states above the Fermi level). From Fermi's golden rule and dipole selection rules, the observed intensity is proportional to the local density of states (LDOS) with p-like symmetry in the conduction band^{14,15}. Fig. 1 shows the background stripped¹⁶ carbon K-edge loss spectra taken from the diamond and a-C labelled regions of specimen A and recorded in spot mode (see Fig 3). In a molecular orbital picture, carbon in the diamond structure has four unoccupied σ^* orbitals whereas in graphite or sp^2 a-C there are 3 σ^* and one π^* states separated by about 5eV which can be identified in the EELS near edge structure^{17,18,19}. A feature characteristic of graphite but not a-C is a sharp peak at the onset of the σ^* band (See Fig.2. The absence of this peak in the interface region suggests that if microcrystallites of graphite are present, they must be smaller than 1.5nm (XANES cluster calculations show that cluster sizes of about 80 carbon atoms are needed before the LDOS of a graphite cluster resembles that of the bulk material²⁰).

To ensure the high mechanical and electrical stability needed to obtain maps of details of the core loss spectra, the Vacuum Generators HB501A 100 kV STEM was located in a shielded room²¹. The spatial drift is less than 0.05nm/minute and the energy drift is under 0.06eV/minute. The EELS signal is recorded digitally in an electron counting mode with single electron sensitivity and a DQE of roughly 90%²². This stability and high detector efficiency meant that a slit width (resolution) of 2eV was sufficient to allow the π^* state (285eV) and the σ^* state (290 eV) to be separated in spatial maps at a subnanometer resolution. At least one pre-edge spectrum must also be recorded to subtract the background. The annular dark field (ADF)^{12,23} signal was recorded simultaneously with the EELS and used to check the spatial alignment of the different energy loss images.

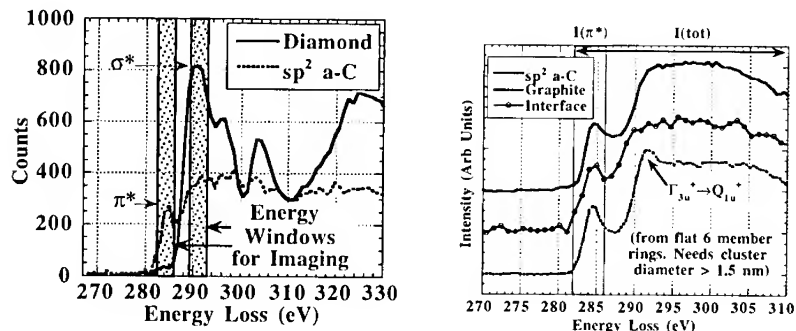


Figure 1. Carbon K edge, after background subtraction, taken from the diamond bulk and a-C interlayer of specimen A. The boxes placed over the π^* and σ^* peaks at 285 and 290eV respectively represent the energy windows used to record the spatial maps of fig.4.

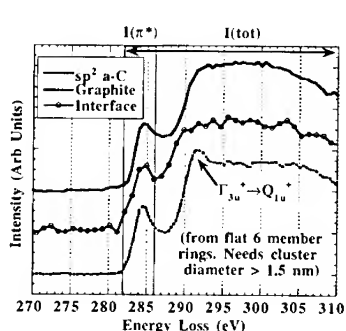


Figure 2. Carbon K edge, after background subtraction, taken from the a-C layer of specimen A and compared with reference spectra from graphitized Carbon and 90% sp^2 a-C.

RESULTS

Specimen A: Diamond/ Amorphous Carbon/Silicon

The chemical bonding maps²⁴ of Fig.4 should be compared with the area of the interface between the silicon and diamond shown in the bright field (BF) image of Fig.3. An amorphous area of approximately 10 nm seen between the two crystalline regions in Fig.3 contains the high intensity area seen in the energy filtered high spatial resolution map obtained from the $\pi^*(285 \text{ eV})$ peak (see Fig.1) shown in Fig.4a. The corresponding map for the $\sigma^*(290 \text{ eV})$ peak (see Fig.1), is shown in Figs 4b and the spatial distribution of the sp^3 states (in this case diamond) is shown in Fig 3c.

Figure 5 shows horizontal line scans from the π^* and diamond images of figures 4a. and 4c. Chemical shifts of the silicon $\text{L}_{2,3}$ edge^{25,26} were used to identify the various silicon compounds present (the $\text{Si L}_{2,3}$ edge moves from 100 eV in pure Si to 103 eV in a-SiC²⁵ and 106 eV in a- SiO_2 ²⁶). Thus, the presence of a-SiC and a- SiO_2 in addition to a-C can be seen in the interlayer region.

Changes in the chemical bonding at the heterointerface can be identified in Fig.4. The a-C/diamond interface is rough, but the transition is very sharp, limited to a layer less than 1 nm thick showing that the diamond nucleated directly on the a-C. In contrast with this, specimens prepared under a 250 V negative bias to increase the nucleation density^{5,6}, diamond was found to nucleate on SiC. In the present work, there is no connection between the SiC layer and the diamond overgrowth, suggesting that the diamond nucleation occurred on the a-C.

It has been postulated that microcrystalline graphite^{10,11} or turbostratic carbon with a suitable orientation could be a nucleation site for diamond. In the present study, the presence of such crystallites larger than 1.5nm in the interlayer could be ruled out from the shape of the carbon K-edge. Instead, analysis¹⁸ of this edge (Fig. 2) shows the carbon sites in the interlayer to be typical of sp^2 a-C with little or no hydrogen (See Table I), i.e., similar to that found in general CVD diamond grain boundaries^{27,28}.

TABLE I. Comparison of carbon interlayer in specimen A with Graphite and sp^2 a-C

	% sp^2 bonded	Plasmon Energy (eV)
sp^2 a-C	90%	22.8
Interface Carbon	85±5%	23±0.5
Graphite	100%	27

Specimen B: Diamond/Silicon

Regions of specimen B where a sharp diamond/silicon interface was present could be subdivided into regions where no third phase could be detected in ADF or in plasmon images and regions where a 23 eV plasmon was present at the interface and the ADF signal suggested a region of intermediate intensity. An EELS map of the former region is shown in Fig. 6 and a line scan perpendicular to this interface is shown in Fig. 7. A series of threefold coordinated defect states narrower than 1nm FWHM are visible at the interface.

Fig. 8 shows a line scan through a latter type of region where a 2nm intermediate layer could be detected in ADF but only with extreme difficulty in BF. No sp^2 defect states are visible at the interface. From a $\text{Si L}_{2,3}$ edge recorded in spot mode, this interlayer was identified as containing SiC which is consistent with a 23 eV plasmon energy.

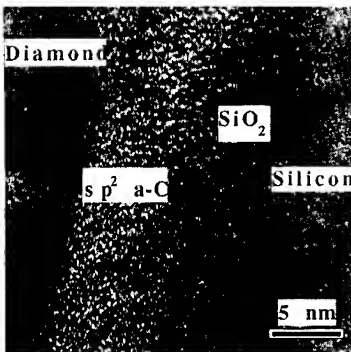


Figure 3. Bright field STEM image of the CVD diamond/silicon interface of Specimen A recorded with a 10 mrad objective aperture and 10 mrad collection angle, giving a probe size of 0.3 nm and a beam current of 0.12 nA. These are the same conditions used for the energy filtered imaging. The various regions have been identified using EELS (See fig. 5).

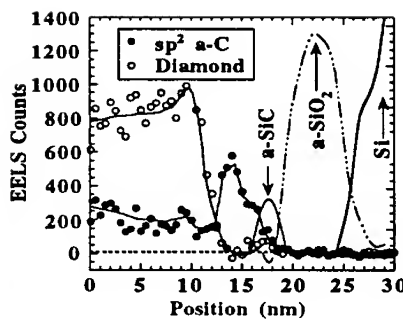


Figure 5. A line scan through figure 4 showing the relative intensities of the diamond and sp^2 a-C signals. Also shown are silicon line scans which were recorded at intervals of 1 nm. The carbon images were taken with a 0.5 nm pixel size. The thin layer of a-C on the diamond side is probably surface damage from the ion milling.

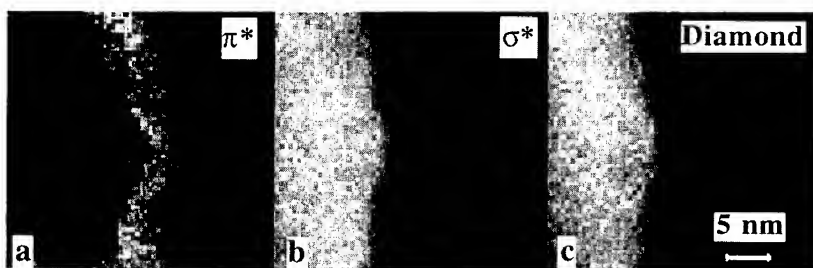


Figure 4. Energy selected images of specimen A in the (a) π^* and (b) σ^* excitations at 285 eV and 290 eV after background subtraction. (c) is a map of the diamond region, obtained by removing the sp^2 contribution to the σ^* states. This was done by subtracting 1.6 times the $ls \rightarrow 2\pi^*$ image from the $ls \rightarrow 2\sigma^*$ image. The weighting of 1.6 was determined from the areas in the π^* and σ^* windows of figure 1 for sp^2 a-C. A weighting of less than the ideal 2:1 value is to be expected since the band resulting from the σ^* states is broader than the energy window while the π^* band is not. Each pixel is 0.5x0.5 nm and the dwell time was 70 msec.

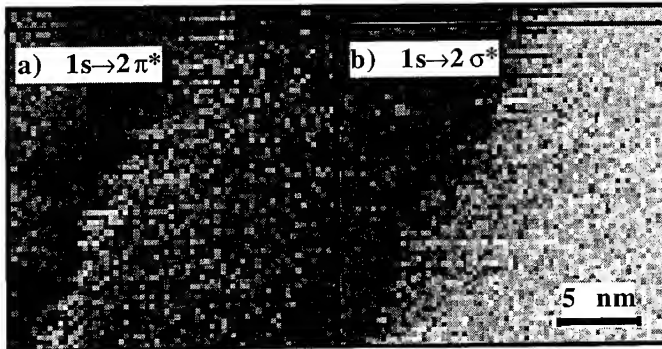


Figure 6. Energy Selected images in the (a) π^* and (b) σ^* excitations of the interface in specimen B where no interlayer is apparent in BF. The diamond/silicon interface is seen to be abrupt, but π^* states are visible along the interface. Dwell time is 50 ms per pixel and the pixel size is 0.4 nm.

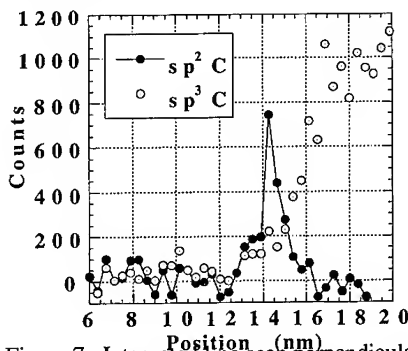


Figure 7. Integrated line scan perpendicular to the interface in Fig. 6. The sp^2 defect states at the interface are readily apparent.

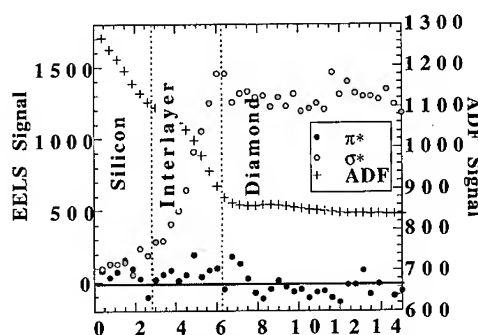


Figure 8. A region of specimen B where a narrow SiC interlayer is present between the diamond and the silicon substrate. No threefold coordinated defect states are seen at the interface. As the specimen is tilted, only an upper limit of 2-3 nm can be placed on the width of the interlayer.

CONCLUSIONS

Two dimensional and subnanometer resolution images of different bonding states of carbon have been obtained from various diamond/silicon interfaces using spatially resolved EELS. The amorphous layer between the nanocrystalline diamond and the silicon substrate of specimen A was identified as $85 \pm 5\%$ sp^2 a-C. Graphite clusters larger than 1.5 nm or comprising more than 5% of the interlayer were not seen (but could be detected.) In the present case diamond nucleation had occurred on the a-C layer rather than SiC or graphite. The regions of specimen B where sharp diamond/silicon interfaces could be found showed either regions of threefold coordinated carbon atoms at the interface or a 2 nm thick SiC layer which preserved the tetrahedral coordination of the carbon. This suggests that for electronic applications a SiC buffer may be desirable.

ACKNOWLEDGMENTS

Special thanks are due to E. J. Kirkland for his implementation of the STEM data acquisition system and to M. Thomas for maintenance of the STEM. This research was supported by the Department of Energy (D.A.M. and J.S.) and by the Office of Naval Research (Y.T. and R.R.). Funding for the purchase of the UHV STEM and operation through the Materials Science Center was provided by the National Science Foundation.

REFERENCES

1. R. Davis, Z. Sitar, B.E. Williams, H.S. Kong, H.J. Kim, J.W. Palmour, J.A. Edmond, J. Ryu, J.T. Glass and C.H. Carter Jr., *Mat.Sci.and Eng.*, **B1** 77-104 (1988)
2. S. Matsumoto, Y. Sato, M. Kamo and N. Setaka, *Jpn.J.Appl. Phys.* **21**, L183-185 (1982)
3. J.C. Angus and C.C. Hayman, *Science*, **241** 913-921 (1988)
4. X. Jiang, C.P. Klages, R. Zachai, M. Hartweg and H.J. Fusser *Appl. Phys. Lett.* **62**, 3438-3440 (1993)
5. B.R. Stoner, G-H. M. Ma, S.D. Wolter and J.T. Glass, *Phys. Rev.*, **B45** 11067-11084 (1992)
6. S.D. Wolter, B.R. Stoner, J.T. Glass, P.J. Ellis, D.S. Buhaendo, C.E. Jenkins and P. Southworth, *Appl. Phys. Lett.* **62**, 1215-1217 (1993)
7. B.E. Williams, J.T. Glass, *J. Mater.Res.*, **4**, 373-384 (1988).
8. P.E. Pehrsson, J. Glesener, A. Morrish, *Thin Solid Films*, **212**, 81-90 (1992)
9. Y. Tzou, J. Bruley, F. Ernst, M. Ruhle and R. Raj, submitted to *J.Mat.Res.* (1993)
10. W.R.L. Lambrecht, C.H. Lee, B. Segall, J.C. Angus, Z. Li, M. Sunkara, *Nature* **364**, 607-610 (1993).
11. Z. Li, L. Wang, T. Suzuki, A Argotia, P. Pirouz, J.C. Angus, *J.App.Phys* **73**, 711-715 (1993).
12. A.V. Crewe, J. Wall, J. Langmore, *Science* **168** 1338-1340 (1970)
13. R.D. Leapman and J.A. Hunt, in 'Microscopy: The Key Research Tool' eds. Lyman, C. E., Peachey, L.D., and Fisher, M.J., E.M.S.A., Woods Hole, Ma., 39-49 (1992)
14. D.H. Tomboulian, and D.E. Bedo, *Phys. Rev.* **104** 590-597 (1956)
15. C. Collie and B. Jouffrey, *Phil. Mag.* **25** 491-511 (1972)
16. R.F. Egerton, "EELS in the Electron Microscope", Plenum, New York (1986)
17. R.F. Egerton, and M.J. Whelan, *J.Elect.Spect.* **3** 232-236 (1974)
18. S.D. Berger, D.R. McKenzie and P.J. Martin, *Phil.Mag. Letters* **6** 285-290 (1988)
19. R.D. Leapman, P.L. Fejes, and J. Silcox, *Phys.Rev.*, **B28** 2361-2373 (1983)
20. D.D. Vvedensky, in 'Topics in Applied Physics: Unoccupied Electronic States', eds J.C. Fuggle and J.E. Inglesfield **69**, Springer Verlag (New York) 152 (1992).
21. J. Silcox, P. Xu and R.F. Loane, *Ultramicroscopy*, **47** 173-186 (1992)
22. E.J. Kirkland, *Ultramicroscopy*, **32** 349-364 (1990)
23. S.J. Pennycook, and L.A. Boatner, *Nature* **336** 565-567 (1988)
24. D.A. Muller, Y. Tzou, R. Raj, J. Silcox, to Appear in *Nature* (1993)
25. D. R. McKenzie, J. Bruley and G.B. Smith, *Appl. Phys. Lett.* **53**, 2284-2286 (1988).
26. P.E. Batson, *Inst. Phys. Conf. Ser. No 177: Section 2, Paper presented at Micros. Semicond. Mater. Conf.*, Oxford, 55-62 (1991)
27. J. Bruley, J.J. Cuomo, R.C. Guanieri, S.J. Whitehair, *M.R.S. Extended Abstracts EA-19* 99-100 (1989).
28. P.J. Fallon, L.M. Brown, *Diamond and Related Materials*, **2** 1004-1011 (1994).

QUANTITATIVE ELECTRONIC STRUCTURE ANALYSIS OF α - Al_2O_3 USING SPATIALLY RESOLVED VALENCE ELECTRON ENERGY-LOSS SPECTRA

HARALD MÜLLEJANS*, J. BRULEY**, R. H. FRENCH*** AND P. A. MORRIS***

*Max-Planck-Institut für Metallforschung, Seestraße 92, D-70174 Stuttgart, Germany

**Lehigh University, Materials Science Department, Bethlehem, PA 18015-3195, USA

***DuPont Central Research and Development, Wilmington, DE 19880-0356, USA

ABSTRACT

Valence electron energy-loss (EEL) spectroscopy in a dedicated scanning transmission electron microscope (STEM) has been used to study the $\bar{\Sigma}11$ grain boundary in α - Al_2O_3 in comparison with bulk α - Al_2O_3 . The interband transition strength was derived by Kramers-Kronig analysis and the electronic structure followed from quantitative critical point (CP) modelling. Thereby differences in the acquired spectra were related quantitatively to differences in the electronic structure at the grain boundary. The band gap at the boundary was slightly reduced and the ionicity increased. This work demonstrates for the first time that quantitative analysis of spatially resolved (SR) valence EEL spectra is possible. This represents a new avenue to electronic structure information from localized structures.

1. INTRODUCTION

The real and imaginary part of the dielectric function can be obtained from valence EEL spectroscopy by Kramers-Kronig analysis [1]. Such results have been compared qualitatively to optical data [2] but to date there has not been a quantitative evaluation of these measured optical properties or the electronic structure. By comparison quantitative CP analysis [3] [4] of vacuum ultraviolet (VUV) spectra has provided a detailed understanding of interband transitions and the electronic structure of ceramics such as α - Al_2O_3 [5] [6] and AlN [7]. VUV measurements are, however, limited to the determination of the bulk properties of a material, due to the large size of the optical probe. The importance of the electronic structure of localized features such as dislocations, twins and grain boundaries has motivated the combination of this quantitative analysis with SR spectroscopy.

Here we present our results from combining SR-EEL spectroscopy in a dedicated STFM, providing information on a nanometer scale, with quantitative analysis to investigate the electronic structure of α - Al_2O_3 in the bulk material and at the $\bar{\Sigma}11$ grain boundary. Although EEL spectroscopy in a dedicated STEM has been available for some time such studies were hindered by the lack of analytical tools for interpreting and comparing the electronic structure information content of the EEL data. Recent improvements in analytical techniques for VUV spectroscopy, namely CP analysis of the interband transition strength, have rendered such problems tractable. We believe that the present work is the first successful quantitative analysis of the electronic structure of a grain boundary. It leads the way to further work in this area, proving that analysis at nanometer dimensions is possible.

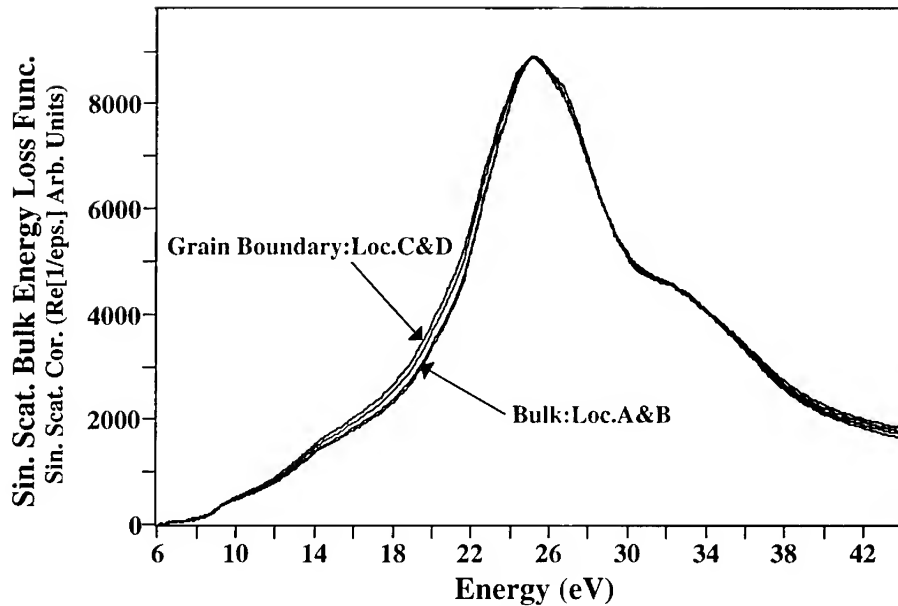


Figure 1. Single scattering corrected bulk energy-loss functions, acquired using STEM SR-EEL spectroscopy, taken at locations A and B in the bulk of each grain of the α -Al₂O₃ sample and at locations C and D along the $\Sigma 11$ grain boundary.

2. EXPERIMENTS

A cross-section transmission electron microscopy sample of the near $\Sigma 11$ grain boundary in α -Al₂O₃ [8] was prepared by standard methods [9]. EEL spectra were acquired with a Gatan 666 parallel EEL spectroscopy system fitted to a Vacuum Generators HB501 dedicated STEM operating at 100 keV. The incident beam convergence and the collection semi-angle were both 7 mrad and the energy resolution was better than 0.7 eV. Spectra were acquired while the electron beam was scanning an area of 3 nm x 4.5 nm on the specimen, reducing beam damage and allowing for manual correction of specimen drift. Data analysis was done by the Gatan software El/P version 2.1, Kramers-Kronig analysis and CP modelling were performed by programs [10] [11] running under GRAMS/386 [12]. Four sets of spectra were taken, two with the electron beam on bulk α -Al₂O₃ on either side of the grain boundary (A and B) and two with the electron beam located on the $\Sigma 11$ grain boundary (C and D). To increase the dynamic range of the detector system each set contained three spectra (50 eV wide), with the following features just below saturation: the Al-L edge, the bulk plasmon and the zero loss. After correction of readout pattern and dark current of the detector the three spectra of each set were spliced together to give a single spectrum from -10 to 80 eV energy loss. The specimen was about 60 nm thick as determined by the ratio of inelastic to total spectrum intensity. The multiple scattering (MS) was removed by Fourier-log deconvolution [1]. There always remained a finite band-gap absorption intensity which may be caused in part by the zero-loss removal procedure employed by the Gatan routine, and in part due to energy losses resulting from relativistic retardation effects (Cerenkov and

transition radiation). A power law of the form A^*E^{-r} , where A and r are constants and E the energy loss, was fitted in the band-gap region, extrapolated to 80 eV and subtracted from the data to remove the intensity arising from these effects. The resulting spectrum was corrected for the incident beam convergence and the finite collection angle at each energy loss with a program based on Egerton's CONCOR routine [1]. The four spectra resulting from this analysis are the single scattering distribution, two for bulk α -Al₂O₃ and two for the $\Sigma 11$ grain boundary (fig. 1). They show that changes in the energy-loss function of the bulk and boundary appear most prominently in the energy range from 14 to 26 eV on the low energy side of the bulk plasmon peak at 25 eV.

3. ANALYSIS

To enable quantitative analysis of the valence EEL spectra for interband electronic structure information it is important to understand any experimental and analytical artifacts which can arise in the data. The quantitative analysis presented here is based on an accurate knowledge of the amplitude of the single scattering EEL spectra so as to derive the interband transition strengths for CP analysis, permitting the accurate use of spectral strengths and amplitudes and for example the partial optical sum rules. Therefore here we consider the effects of the MS correction routines and the use of the index sum rule to scale the amplitude of the EEL spectra.

3.1 Multiple scattering analysis

The acquired EEL spectra must be corrected for MS events to derive the single scattering bulk energy-loss function. The routines used here for MS correction determine the scattering power by comparison of the zero loss peak to the rest of the EEL spectrum. By artificially multiplying the zero loss peak by factors of 0.5, 0.8, 0.9, 0.95, 1.0, 1.05, 1.1, 1.2 and 1.5 we can vary the imputed scattering power in the analysis. The results (fig. 2) demonstrate that the effect is appreciable only at energy losses beyond 34 eV. Upon Kramers-Kronig analysis of these EEL spectra, only for large MS errors changes are seen in the interband transition strengths (fig. 3) in the region from 8 to 26 eV where the band structure information appears in the data. Therefore the quantitative analysis is not very sensitive even to gross errors in the MS correction. Here have we used the accurate MS correction in all subsequent analysis.

3.2 Index Sum Rule

The complex optical property J_{cv} is defined by [7]

$$J_{cv}(E) = \frac{m^2}{8 \pi^2 h^2 e^2} E^2 \epsilon(E) \quad (1)$$

where m is the mass of the electron, h is Planck's constant and E is the energy loss. The complex dielectric function ϵ was calculated by Kramers-Kronig analysis with an FFT based algorithm [13] originally developed for VUV data and modified for EEL spectra. The real part of J_{cv} is called the interband transition strength. Since the EEL spectra are acquired as scattering counts versus energy, the data is in arbitrary units and during Kramers-Kronig analysis the index sum

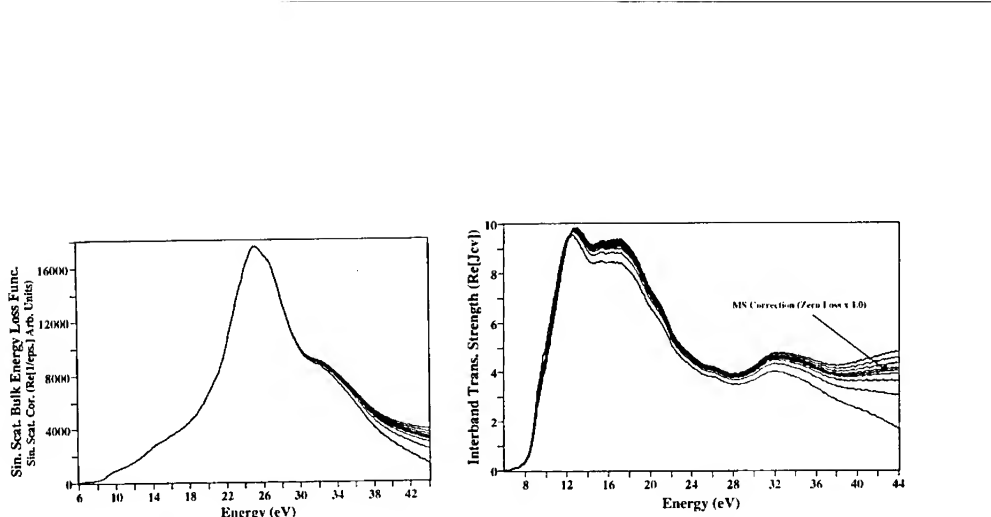


Figure 2. The effect of varying the multiple scattering correction on the single scattering distribution for the bulk α -Al₂O₃ SR-EEL spectrum taken at site A.

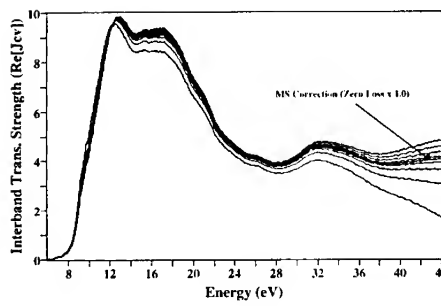


Figure 3. The effect of varying the multiple scattering correction on the interband transition strength J_{cv} determined from Kramers-Kronig analysis for the bulk α -Al₂O₃ SR-EEL spectrum taken at site A.

rule (Eq. 4.29 in [1]) is used to scale the y axis values of the EEL spectra. The J_{cv} spectra are very sensitive to varying the index of refraction from 1.5 to 2.2 (fig. 4). With large index errors the interband transition strength does change shape, emphasizing the importance of accurate knowledge of the index of refraction for analysis of EEL spectra. The index of refraction for α -Al₂O₃ used here is 1.767 at 633 nm (determined from optical spectroscopy), and is a constant for all spectra, so that consistent changes among the spectra are meaningful. For more complex systems where the index is unknown the use of the sum rule for scaling can be problematic and we are considering alternative methods for EEL spectra scaling.

After Kramers-Kronig analysis, a linear baseline was found to be present in the real part of the interband transition strength. The power law fit used to remove the intensity in the band gap region might cause such an offset at higher energies, since the extrapolation extends beyond the energies for which the effects of Čerenkov and transition radiation occur. This error might then propagate to yield the linear baseline in the real part of J_{cv} but at present the exact origin is still under investigation. For the following analysis in this work we have subtracted a linear baseline so that the intensity at 40 eV is reduced to zero. The interband transition strength then agrees closely with data determined from VUV spectroscopy [6]. Although this cannot be accepted as a full justification, it seems a reasonable way to proceed for the moment. Also it does not seem to be important for the comparison between bulk and grain boundary which is the main concern of this paper.

4. RESULTS

The interband transition strengths determined for bulk α -Al₂O₃ and the $\Sigma 11$ grain boundary are shown in fig. 5. The interband transitions in the bulk are identical while the two grain boundary results are different from the bulk and very similar to each other. The major difference seen in these spectra is a reduction of the interband transitions in the region of 14 to 22 eV. This demonstrates that the EEL spectra are accurate and reproducible and show the changes in the electronic structure between the bulk and the grain boundary. The interband transition strength for all four spectra was modeled with CPs for one exciton and three 3D bands in analogy to the analysis of VUV data [6]. The contributions from individual pairs of valence and conduction

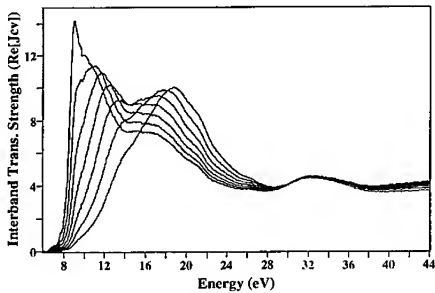


Figure 4. Effect of variation of the index of refraction in the sum rule used for scaling the EEL function on the resulting J_{cv} spectra.

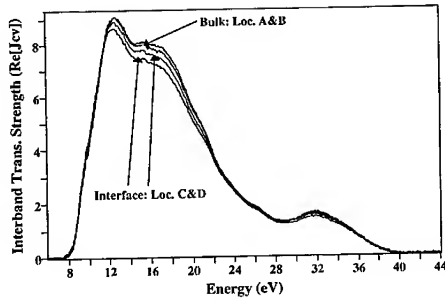


Figure 5. Comparison of the interband transition strengths of $\alpha\text{-Al}_2\text{O}_3$ taken in the bulk at location A and B and at the $\Sigma 11$ grain boundary at location C and D, showing the changes in the interband electronic structure at the boundary.

bands can be deduced from this analysis. In fig. 6 and 7 the individual CP models for the bulk and grain boundary are shown while these models are overlaid in fig. 8 and summarized in table I to highlight the changes in the interband transitions of the grain boundary. The EEL data agree with the interband transition strength obtained from VUV spectroscopy for bulk $\alpha\text{-Al}_2\text{O}_3$ [6]. The exciton is a bound state of the excited electron and appears at ~ 9.1 eV. The three other sets of CPs used for modeling of the electronic structure correspond to transitions from the valence bands to the empty Al 3p band. The first set (lowest in energy) are transitions from the filled O 2p levels which represent the ionic bonding of the material. The next interband transition set arises from the hybridized Al=O level and can be thought of as the covalent part of the bonding in $\alpha\text{-Al}_2\text{O}_3$. The third set are the interband transitions from the atomic like O 2s band.

Table I: Critical point parameters from STEM SR-EELS for bulk $\alpha\text{-Al}_2\text{O}_3$ (location A and B, average) and the $\Sigma 11$ grain boundary (location C and D, average).

CP Set	Type	Energy (eV)		Amplitude		Width (eV)	
		Bulk	$\Sigma 11$ GB	Bulk	$\Sigma 11$ GB	Bulk	$\Sigma 11$ GB
Exciton		9.10	9.02	1.86	1.59	0.35	0.38
O2p	M_0	9.20	9.13	1.14	1.13	0.07	0.07
	M_1	11.64	11.50	0.43	0.43	0.07	0.08
	M_2	13.18	13.07	3.07	3.06	0.55	0.57
	M_3	22.53	22.58	1.49	1.52	0.86	0.94
Al=O	M_0	14.04	14.13	2.04	2.01	0.99	1.00
	M_1	16.50	17.72	0.19	0.16	0.35	0.56
	M_2	18.67	18.32	1.26	1.23	0.60	0.64
	M_3	27.87	28.20	0.63	0.65	0.85	0.85
O2s	M_0	18.45	18.21	0.05	0.05	0.19	0.10
	M_1	31.20	31.29	0.48	0.45	0.60	0.67
	M_2	32.83	33.30	0.27	0.34	0.79	0.83
	M_3	36.69	36.71	0.20	0.17	0.46	0.43

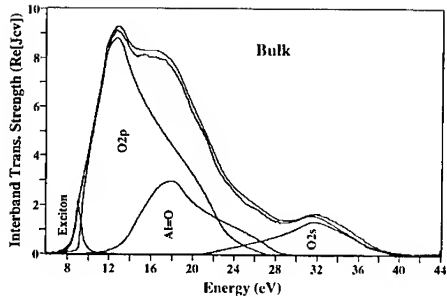


Figure 6. Interband CP models for bulk α - Al_2O_3 determined from STEM SR-EEL spectroscopy taken at location A and B.

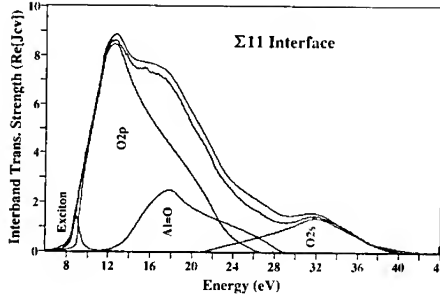


Figure 7. Interband CP models for the $\Sigma 11$ grain boundary of α - Al_2O_3 from STEM SR-EEL spectroscopy determined at location C and D.

Partial optical sum rules (the oscillator strength sum rules) were calculated (table II) from the CP sets to determine the electron occupancy of the interband transitions in the bulk and at the boundary. These are calculated assuming a primitive unit cell volume of 84.9 angstroms³ and 1 formula unit per unit cell. These results show that the electron occupancy of the Al=O hybridized bonding set is reduced in the boundary, and this can be seen by the changes in the % ionicity defined as $\text{Occ.}(\text{O}2\text{p})/\{\text{Occ.}(\text{O}2\text{p}) + \text{Occ.}(\text{Al=O})\}$ which changes from 78.9 % ionic for the bulk to 80.8 % ionic at the $\Sigma 11$ grain boundary.

5. DISCUSSION

The results for bulk α - Al_2O_3 and the $\Sigma 11$ grain boundary show differences in the width of the band gap, the position of the exciton and in the strengths of the CP sets of interband transitions, most prominently in the A=O hybridized set. The latter is equivalent to an increase in ionicity at the grain boundary.

The decrease in the band gap width is less than 0.1 eV. In SR experiments investigating the energy-loss near-edge structure [14], it was found that the transition energy from the aluminium L shell to the conduction band was reduced by more than 1 eV. Hence the latter has to be attributed mainly to a shift in the core level energy. Such a combination of core and valence EEL spectroscopy gives full information about the electronic structure of materials. This could complement information obtained from various other spectroscopies, always with the added benefit of high spatial resolution.

Table II. Total and partial optical sum rules for bulk and $\Sigma 11$ grain boundary of α - Al_2O_3 , averaged for bulk and grain boundary locations						
Electrons	Exper. Total	Model Total	Exciton	O2p	Al=O	O2s
Bulk	21.6	22.6	0.7	15.2	4.1	1.5
$\Sigma 11$ GB	20.9	21.0	0.6	15.0	3.6	1.6

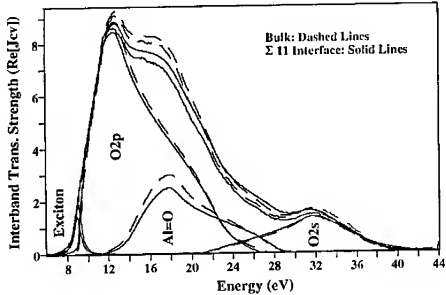


Figure 8 Interband CP models for the bulk (dashed) and $\Sigma 11$ grain boundary (solid) of $\alpha\text{-Al}_2\text{O}_3$ from STEM SR-EEL spectroscopy determined at location A and C, showing changes in exciton and the $\text{Al}=\text{O}$ hybridized bonding CP set.

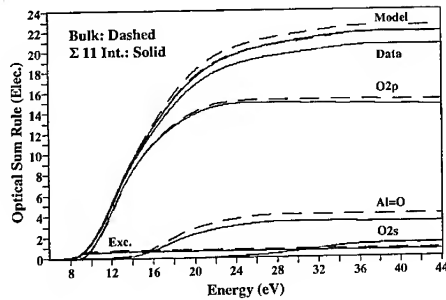


Figure 9. Total and partial optical sum rules showing the electron occupancies of the data, the model and each individual CP set for the bulk and $\Sigma 11$ grain boundary in $\alpha\text{-Al}_2\text{O}_3$.

In order to deduce relevant information about the electronic structure extensive data analysis has to be performed. It is important to ensure that the results of each step are reliable and reproducible as artefacts introduced in one step might give unreliable results concerning the electronic structure. The data analysis is analogous to the, now well established, analysis of VUV data once the dielectric function has been obtained. In the EEL specific part of the analysis the errors in the MS correction, while changing the interband transition strength, do not have a major influence on the final result. The index of refraction on the other hand has to be known accurately, which will be a problem for materials where no other information is available *a priori*. At two points in the analysis an intensity occurred which was subtracted ad hoc: in the band gap region of the single scattering distribution by a power law fit and in the real part of the interband transition strength by a linear baseline. The second effect might actually be caused by the first. Although the modifications used in the analysis cannot be fully justified, it seems to be reasonable to apply them because the data are then very similar to the results of VUV spectroscopy on bulk $\alpha\text{-Al}_2\text{O}_3$.

The determination of the electronic structure without any prior information will only be reliable if the data analysis can made fully comprehensive. To achieve this the study of bulk $\alpha\text{-Al}_2\text{O}_3$ is an ideal test case as its electronic structure is well known from VUV experiments. Nevertheless it is already possible now to deduce information about the relative electronic structure of localized features, i. e. in comparison to the bulk properties. All the influences of data analysis are expected to be similar, if not identical, for such spectra, which are similar to each other. Hence it is possible to deduce differences in electronic structure from differences seen in the EEL spectra taken at different locations on the specimen.

If we consider that the atomic structure at the $\Sigma 11$ grain boundary is only changed in a region 0.6 - 0.8 nm wide at the grain boundary, as deduced from high resolution transmission electron microscopy [15], atomistic modelling [16] and the energy-loss near-edge structure [14], then only 20 - 25 % of the atoms in the probed volume contribute to the difference in electronic structure at the boundary. This means that the changes in electronic structure at the boundary are 4 - 5 times stronger than is seen directly from the data. Since the experiment is obviously sensitive to such small variations, it should be straightforward to investigate other, more extended inhomogeneities.

An important question concerns the reliability of the measurements (fig. 1) and the resulting differences (fig. 5). EEL measurements were reproducible, including the small shift in band gap energy. The system is stable to much less than 0.1 eV and an internal absolute energy reference is provided in each spectrum through the zero loss. Variations in spectra from the grain boundary represent variations in grain boundary structure. CP modelling is well established and numerically

stable. For the comparison of two spectra the present stability of data analysis is sufficient, whereas improvement is needed for fully quantitative results from a single spectrum. Noise is negligible compared to systematic errors. The work presented is a successful first attempt to investigate the electronic structure of a model grain boundary, demonstrating feasibility and suggesting ways for improvement. The boundary chosen is well characterized by HREM and atomistic structure modelling and work is in progress to calculate the electronic structure for a comparison with the present experimental results.

6. CONCLUSION

We have shown that it is possible to analyze SR-EEL spectra taken from bulk material and a grain boundary quantitatively. Differences in the raw experimental data have been translated into differences in the electronic structure. While the data analysis is not fully developed yet, we are confident that, in the application presented here and similar cases, the combination of SR-EEL spectroscopy and quantitative analysis yields valuable insight into the local electronic properties of materials. This opens up the quantitative analysis on a nanometer scale, for example of dislocations, defects, interfaces and intergranular glass films or materials which only exist as thin films or small particles. The knowledge of the electronic structure of small features is the key to our understanding of the mechanical and electrical properties of materials or devices incorporating them.

ACKNOWLEDGEMENTS

We acknowledge financial support from the Volkswagen-Stiftung contract I/ 66 790 for the Gatan PEELS and one of us (HM). We thank M. Rühle, P. Kenway and T. Höche for helpful discussions and S. Loughin, D. J. Jones and L. K. Denoyer for assistance.

REFERENCES

1. R. F. Egerton, Electron energy-loss spectroscopy in the electron microscope, (Plenum Press, New York, 1986).
2. M. G. Walls, PhD thesis, University of Cambridge, 1987.
3. S. Loughin, R. H. French, W. Y. Ching, Y. N. Xu and G. A. Slack, *Appl. Phys. Lett.* **63**, 1182 (1993).
4. S. Loughin, L. DeNoyer and R. H. French, *Phys. Rev. B* to be submitted, (1993).
5. R. H. French, *J. Am. Ceram. Soc.* **73**, 477 (1990).
6. R. H. French, D. J. Jones and S. Loughin, *J. Am. Ceram. Soc.* submitted to *Topical Issue on the Science of Alumina*, (1994).
7. S. Loughin, PhD thesis, University of Pennsylvania, 1992.
8. P. A. Morris, PhD thesis, MIT, 1986.
9. B. D. Flinn, M. Rühle and A. G. Evans, *Acta metall.* **37**, 3001 (1989).
10. Cript, v. 7.7, Spectrum Square Associates, Ithaca NY 14850 USA.
11. KKgrams, v. 3.4, Spectrum Square Associates, Ithaca NY 14850 USA.
12. Grams/386, v. 2.03, Galactic Industries, Salem NH.
13. M. L. Bortz and R. H. French, *Appl. Spectr.* **43**, 1498 (1989).
14. J. Bruley, *Microsc. Microanal. Microstruct.* **4**, 23 (1993).
15. T. Höche, P. R. Kenway, H.-J. Kleebe, M. Rühle and P. A. Morris, *J. Am. Ceram. Soc.* submitted to *Topical Issue on the Science of Alumina*, (1994).
16. P. R. Kenway, *J. Am. Ceram. Soc.* submitted to *Topical Issue on the Science of Alumina*, (1994).

HIGH RESOLUTION TEM APPLIED TO NANOSCALE STRUCTURE STUDIES

L. BELTRAN DEL RIO, M.JOSE YACAMAN, S. TEHUACANERO AND A. GOMEZ
Universidad Nacional Autónoma de México, Departamento de
Materia Condensada, Apartado Postal 20-364 México 01000 D.F.

ABSTRACT

In this work, digital image processing techniques are used to study the structure of small metallic particles imaged under high resolution conditions. An algorithm is devised to extract directly from the micrographs the coordinates of columns of atoms in such a way that the crystal structure of the particles and their boundaries can be determined. For distorted regions (such as grain boundaries) the actual positions can be compared to the ones in the ideal lattice so that a general trend of the distortion field can be elucidated.

1. INTRODUCTION

When imaging nanoparticles at a high resolution the observed image is known to be a projection of the actual structure along the direction of the incoming electron beam. It is also known that, under certain conditions (Scherzer defocus, a condition that produces a basically flat transfer function for a large

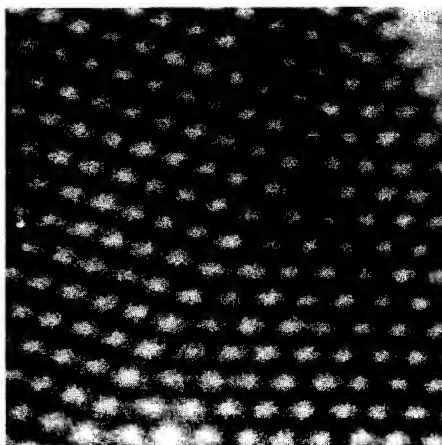


Figure 1. Original unprocessed HRTEM image of a silver particle.

range of spatial frequencies), individual atoms appear as bright dots in the image [1].

In a particular case where the material is oriented along high symmetry low-index directions, whole columns of atoms become aligned giving an image consisting of dots where each dot actually represents an atomic column (figure 1).

Under these circumstances it is of interest to determine accurately the coordinates of each column with respect to the real lattice. For instance it may happen that atoms close to free boundaries of a crystallite or in the vicinity of a grain boundary become displaced with respect to their "official" positions.

In most published works, atomic positions are determined by purely visual methods [2]. The question arises of whether this can be done automatically from a digitized micrograph.

2. PROCEDURE

Silver and platinum nanoparticles were prepared by evaporation under ultra-high vacuum conditions as follows: the metal was evaporated from a tungsten filament onto a sodium chloride single crystal that had been previously vacuum cleaved; the crystal with the particles was later covered with a carbon film deposited from a carbon arc. Subsequently the sodium chloride crystal was dissolved in water and the carbon film with the metal was mounted on copper grids [3].

The particles were observed and photographed in a JEOL 4000 EX microscope making sure that imaging conditions (Scherzer defocus) were such that atoms would display as bright dots.

The micrographs were digitized and subjected to the processing as described in the following section.

2.1 Preliminary processing

In the images, high frequency noise components were removed by light low-pass filtering. Also an histogram expansion algorithm was used to improve image quality [4].

2.2 Peak position determination

In order to evaluate a coordinate set that represents accurately the position of an atomic column, it is necessary first to define a neighborhood such that it includes the whole area of the intensity peak representing the position of an atomic column and excludes any other peak. It is necessary first to generate an image that includes all such neighborhood masks (binary images in which zero value pixels represent a general background and groups of contiguous non-zero value

pixels represent neighborhoods).

If the image includes edges from the structure, it is useful to generate also a border definition mask such that it includes the particle as a whole, as a means of eliminating spurious peaks clearly outside the structure. By working selectively on each of the neighborhood masks, an algorithm can evaluate the position of each peak and elaborate a list of coordinates.

A mask defining the border of a particle can be obtained by applying several methods; in some cases low-pass filtering can define the border appropriately, Fourier transform methods can also be used [5]. In order to insure that the whole nanostructure is included in the mask, sometimes it is necessary to expand the border with binary morphological erosion algorithms [6].

It is often necessary to obtain an enhanced image from the original micrograph more suitable for mask segmentation [7]. A selective enhancement of the atomic column can be achieved by targeting the Gaussian nature of these peaks and applying geometrical filters with Gaussian templates or correlation algorithms with Gaussian auxiliary functions.

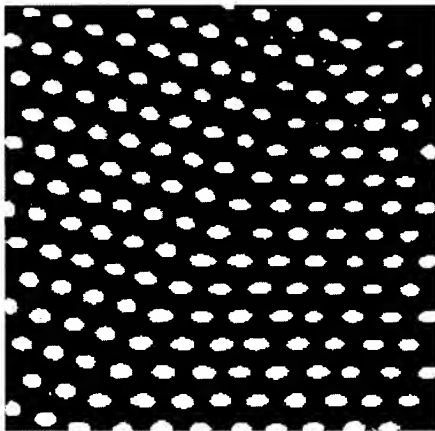


Figure 2. Binary neighborhood mask image.

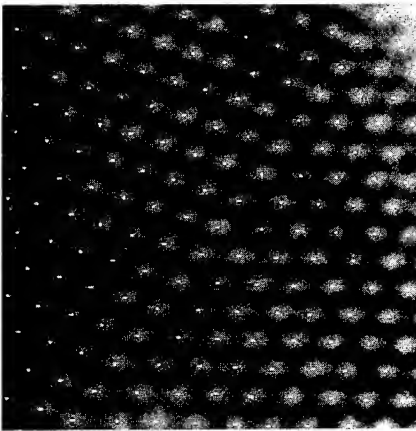


Figure 3. Image with positions of atomic columns superimposed.

The final neighborhood mask is obtained by simple segmentation with a threshold [8] or with an Otsu algorithm [9] (figure 2). Even though the enhancement is done selectively, very often a neighborhood of nonexistent atomic columns is going to be present in the mask, it can be eliminated almost totally by applying the border mask in an OR (logical Boolean "or" operation) fashion. Later on, other geometrical algorithms can be applied to even further reduce the occurrence of a noisy peak that does not belong to the actual structure.

For each neighborhood the contribution of the position of the pixels can be averaged with different weighting criteria in order to obtain a representative set of coordinates (figure 3).

Once the list is obtained, with the help of geometric selection algorithms, columns can be classified as belonging to different domains, planes, particles etc. and the adequate sub-lists can be generated; these lists can be useful in processes like automatic crystalline structure characterization.

2.3 Matching to lattices

In the crystalline regions, the atoms can be fitted to a two-dimensional lattice. In order to perform this task three non-collinear atoms, far from boundaries, are selected.

From these non-collinear points the corresponding lattice can be calculated in the following way: 1) label the points as A, B, C; 2) form the vectors D (from A to B) and E (from A to C), these vectors are lattice vectors and they are linearly independent; 3) Count how many atoms are between A and B (call this m) and between A and C (call this n); a basis for the lattice is, then, given by C/m and D/n .

In this way the image processing program can also simultaneously display the actual positions of the atoms and the ideal lattice positions. This is useful to study, for example, the distortions close to grain boundaries.

3. EXAMPLES

In the case of silver thin film structures with twin boundaries, lists of atomic column coordinates have been obtained. The first immediate application has been the generation of diagrams where the crystalline structure of the domains is calculated and the real position of the atomic columns are added for visual comparison.

The next step consists on the creation of an algorithm that assigns each column to one of the lattices according to its position and distances in order to minimize the error. Once this is done, the difference in position vectors can be calculated and superimposed on the diagram in order to visualize tendencies in the displacement in the neighborhood of the grain boundary (figure 4).

In order to perceive this differences more clearly, a scale factor can be added to exaggerate this displacements between the theoretical lattices on both sides of the boundary and the real positions of the columns in the micrographs.

In either domain of the structure, an atom column is represented by two positions, the first one belongs to the theoretical lattice modeling the domain and the second position belongs to the real image, these two positions generate a displacement vector. An exaggerated image can be generated by representing the actual positions of the micrograph and creating new positions of the theoretical lattice using the

real positions as reference with the addition of the displacement vectors scaled at twice (or more) their size. It seems important to emphasize that this kind of image serves only the purpose of enhancing the distortions visually.

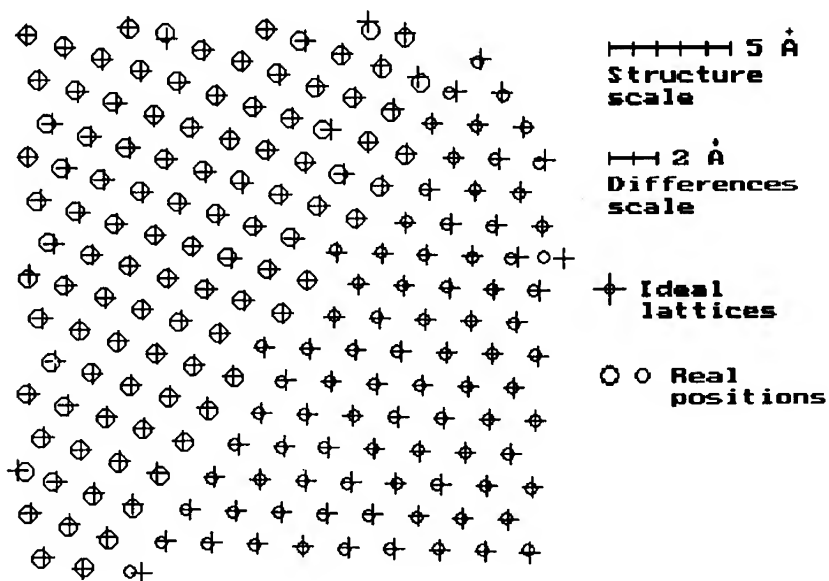


Figure 4. Schematic representation of a twin boundary showing ideal positions and displacements.

4. DISCUSSION AND CONCLUSIONS

In this work we have shown how, given a micrograph with "atoms" (dots on the image), the coordinates of these atomic columns can be extracted. This requires micrographs taken at known imaging conditions (Scherzer defocus) and samples oriented in highly symmetric positions along low index directions so atomic columns project as single dots on the image.

The procedure involves several kinds of image processing (filtering, histogram equalization and segmentation among others) and yields a simplified version of the image in which single points represent atomic columns.

If in addition there are points far from boundaries, for which it can be assumed that they are in their undistorted positions, the (average) lattices (for the two crystals

comprising a bi-crystal with a boundary) can be found . In this way a map of the distortions close to boundaries can be obtained. Of course, this can be done only if the boundary is seen edge-on so there is no crystal overlap in the image (in this case the atomic columns of the two grains can be seen separately).

These techniques are relevant to problems in nanoaterials such as distortions (presumably due to finite size effects) and distortions at or close to grain boundaries.

ACKNOWLEDGEMENTS

The authors wish to thank A. Sánchez for his help with the photographic work.

REFERENCES

1. J. M. Cowley. Principles of Image formation. In:Introduction to analytical electron microscopy; J. J. Hren, J.I. Goldstein, D. C. Joy eds. Plenum Press, New York andLondon 1979
2. W. Krakow Acta metall. mater. Vol. 40, #5, 977 (1992).
3. S. Ino, S. Ogawa. Journal of the Physical Society of Japan 22 (1967) 1365.
4. R.C. González, P. Wintz. Digital Image processing (second edition) Addison-Wesley (1987).
5. A. De Jong, W. Coene, D. Van Dyck; Ultramicroscopy 27 (198) 53
6. J. Song and E. J. Delp, Computer vision, graphics, and image processing 50, 308-328 (1990).
7. A. Beghdadi and A. Le Negrate, Computer vision, graphics, and image processing 46, 162 (1989).
8. M.I. Sezan, Computer vision, graphics, and image processing 49, 36 (1990).
9. J. Otsu, IEEE Transactions on systems, man, and cybernetics Vol 9, 1 (1979).

MOIRE PATTERNS IN HIGH RESOLUTION ELECTRON MICROSCOPY IMAGES

J. Reyes-Gasga, S. Tehuacanero and C. Zorrilla.
Instituto de Física, UNAM.
Apartado Postal 20-364, 01000 México D. F., MEX

ABSTRACT

Moiré patterns are so often observed in the HREM images and they could be mistaken as the direct image of the atomic structure of the sample under analysis. In this work we presented some examples of these patterns and their computer graphic simulations.

INTRODUCTION

Atomic-level details are easily resolved in the latest generations of intermediate voltage electron microscopes, but structural information on the same scale can only be extracted under certain specific conditions. Some of these conditions are: (i) the crystal must be oriented with a prominent zone axis along the electron beam direction, (ii) the crystal must be very thin, (iii) the objective aperture must allow through only those diffracted beams which correspond to distances within the point resolution of the microscope, (iv) the imaging must be carried out at a specific value of defocus, and (v) any crystal defect must lie along the electron beam direction. In most of the cases some understanding of imaging theory, as well as an awareness of correct operating conditions, is required for reliable image interpretation [1]. In general for the interpretation of any high resolution electron microscope (HREM) image detailed computer calculations must be carried out and several microscope operation parameters used to take the micrograph, together with a structural model of the sample, have to be taken in account. The image is interpreted by comparing the simulated image with the experimental one. This step although simple must be done very carefully because the contrast the micrograph shows is also sample dependent (thickness, atomic number, orientation respecting the electron beam direction, etc.). Only having an exact idea of what we are looking at the HREM micrographs we will be sure of their correct interpretation.

It is common to observe in some HREM images a contrast consisted of periodic arrays of features whose dimensions are bigger than the atomic dimensions of the sample under observation and which could be mistaken as the direct image of the atomic structure. However in most of the cases they are a result of a interference phenomenon produced by the overlapping of two crystals. This is, they are the well known periodic arrays called "Moiré patterns".

The importance of the Moiré patterns in electron microscopy is the possibility of resolving the periodicity of the atomic planes in a indirect way using electron microscopes whose resolution is not of the atomic order. In fringe resolution images the Moiré patterns are easily recognized [2], but at atomic-level scale, in the HREM images, a little more effort has to be done. In this work we present a series of examples of Moiré patterns frequently observed in HREM images and their simple computer graphic simulations.

Experimental Procedure

Several samples were observed at high resolution level using a JEOL 4000EX electron microscope. These samples were prepared for electron microscope observation by different methods, depending upon which one gives the best results. For example, some of them were powdered and supporting on copper grids previously covered with holey carbon. For others, thin films were evaporated on salt and their preparation was straightforward. Some others were mechanical and ion milling polished.

The computer graphic simulation method of the Moiré patterns is done very easy. The network under analysis is digitally processed with a CCD camera system AT200. These data are loaded in a PC-486 computer. Using a computer program developed by one of our colleagues (L. Beltran del Rio), two images of this network are overlapped, rotating one of them with respect to the other and the Moiré pattern is observed.

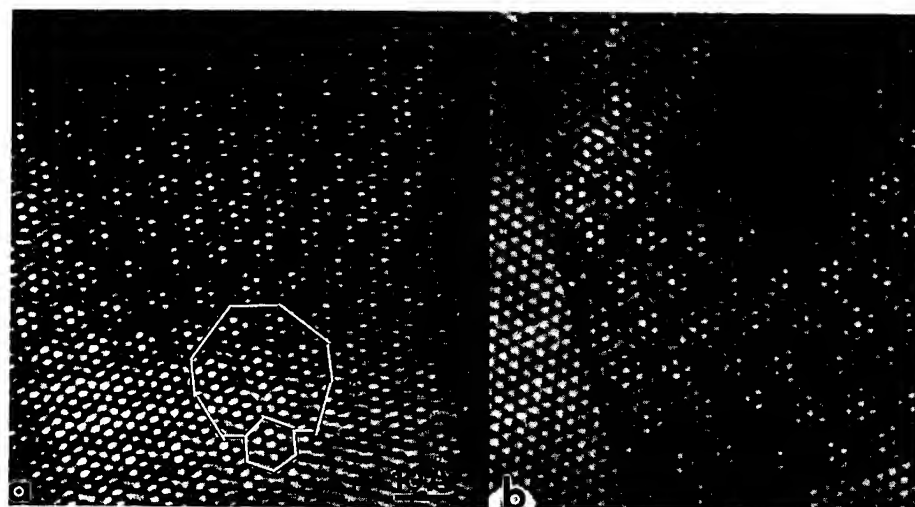


Fig. 1. a) High resolution image of the catalytic $\text{MoS}_2:\text{Co}$.
b) Moiré pattern from two hexagonal networks rotated by 16° .
All the contrast features observed in (a) are reproduced in (b)

HREM Images and the Simulated Moiré Patterns

Figure 1a presents a high resolution image of the catalytic compound MoS₂:Co where two hexagonal arrays are shown. At first sight this image can be thought as produced by an arrays of hexagonal domains separating the atomic columns. However the distances observed do not correspond to the interatomic distances for this compound and a simple model consisting in the rotation of two hexagonal networks by a given angle (fig. 1b) shows that these images are the result of the overlapping of two very thin crystals along the hexagonal axis.

If these networks are rotated a little bit more a beautiful hexagonal arrangement is observed (fig. 2c). The Fourier spectrum of this arrangement shows an almost dodecagonal motif of points (fig. 2d) which reminds us the one presented by Reyes-Gasga et al. [3] for the dodecagonal quasicrystalline phase observed in a thin film of the Bi-Mn alloy. In fact at first sight the HREM image of this thin film (figs. 2a) seems to be identical to the Moiré pattern. However in this case the Moiré pattern is completely periodic whereas the HREM image is not. This aperiodicity suggest that the phase observed in the Bi-Mn thin film is a real dodecagonal phase [4].

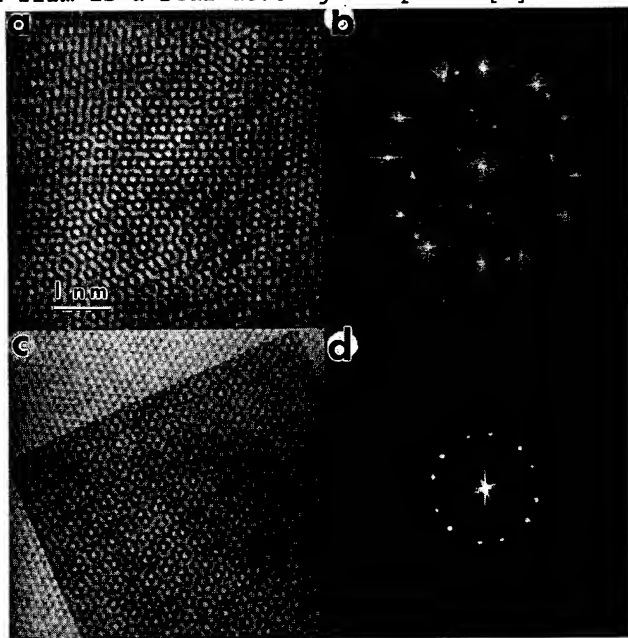


Fig. 2. a) High resolution image of the dodecagonal quasicrystalline phase observed in thin films of the alloy BiMn. b) Fourier transform spectrum from (a). c) Moiré pattern from two hexagonal networks rotated by 24°. d) Fourier transform spectrum from (c). At first sight the contrast features observed in (a) could be reproduced in (c) but the image of the Moiré pattern is periodic whereas (a) is not.

In the high resolution images of small particles the observation of Moiré patterns occurs very often. This is because they are built by polyhedral units which are joined each to the other by a twin relationship, and the orientation of these boundaries with respect the electron beam direction is inclined. Figure 3 shows the HREM image of a chain of gold small particles where the Moiré patterns are easily recognized (compare them with the Moiré patterns shown in figure 3b of reference 5).

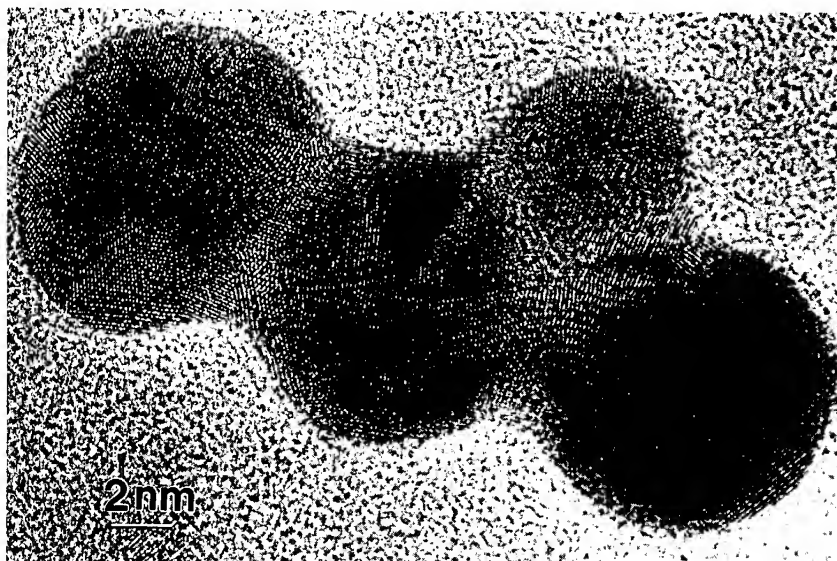


Fig.3. High resolution image of small particles of Au. Different Moiré patterns are easily observed (compare them with the ones shown in figure 3b of reference 5).

When the rotated networks are squares instead of hexagons also some interesting Moiré patterns are observed (fig. 4). These images are also presented in some HREM of samples with a square arrangement along the electron beam direction. For example, figure 4a shows the HREM image of a Ni particle covered by an oxygen layer and whose square arrangements produce the square Moiré pattern shown in figure 4b. Many more Moiré patterns can be produced using other geometrical shape networks. The most important thing to do is to model them when there is a suspect of their existance in some HREM images.

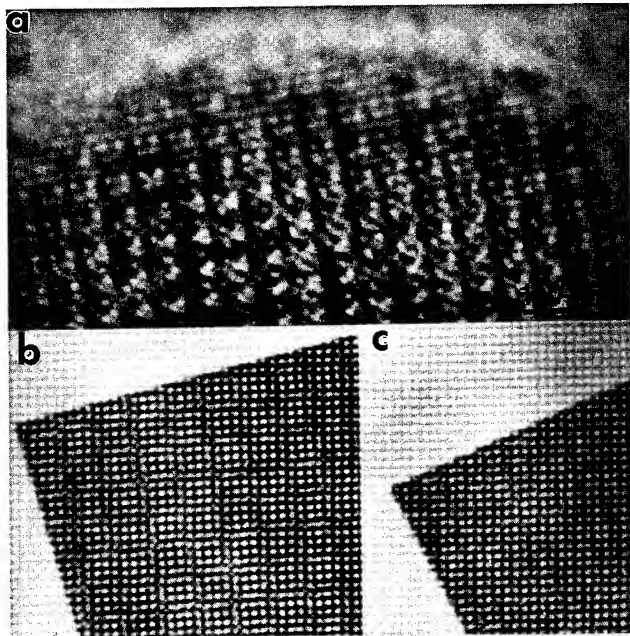


Fig. 4. a) High resolution of a Ni particle covered by a oxygen layer. The contrast observed in this image can be reproduced by square Moiré patterns produced from two square networks rotated (b) by 14° and (c) by 25° .

Final Remarks

Moiré patterns can easily be observed in images of layered structures and planar structural defects, such as grain boundaries, when they are inclined with respect to the electron beam direction. The reason why a particular sample shows Moiré patterns is related to its structure and properties and this represents another important question to resolve. Of course, we have to bear in mind that generally lengthy image simulations must be required before the nature of any image contrast can be fully and unambiguously characterized [1], but the existence of Moiré patterns gives the first sight on the structural characteristics of the sample.

ACKNOWLEDGEMENTS

We want to thank to L. Rendón, L. Beltrán del Rio, A. Sánchez, J. A. Ramírez for technical help. We want also thank to Dr. P. Schabes and Fis. J. Arenas for allowing us to use the HREM image shown in figure 4. This work supported by CONACYT, under project 0564-E9108.

REFERENCES

1. D. J. Smith, J. Elect. Microsc. Tech. **12**, 11 (1989).
2. A. Hirsch et al., "Electron microscopy of thin crystals", Butterworths, London 1965.
3. J. Reyes-Gasga, R. Hernández and M. José-Yacamán Script. Metall. et Mater. **25**, 325 (1991).
4. K. Yoshida and Y. Taniguchi, Phil. Mag. Lett. **63**, 127 (1991).
5. D. Shechtman et al., Appl. Phys. Lett. **62**, 487 (1993).

NANOSTRUCTURES DETECTED BY CONDUCTIVITY SPECTROSCOPY

K. FUNKE*, K. EL-EGILI**, R. REICHELT***, M. AMREIN*** AND C. CRAMER*

*University of Münster, Institute of Physical Chemistry, 48149 Münster, Germany

**Mansoura University, Department of Physics, Mansoura, Egypt

***University of Münster, Institute of Medical Physics and Biophysics, 48149 Münster, Germany

ABSTRACT

Measurement of frequency dependent ionic conductivities is shown to be a simple and effective means for the detection and characterization of nanostructures in solid electrolytes. As an example, the conclusions drawn from the conductivity spectrum of a silver-iodide/silver-borate glass are compared with scanning electron and scanning tunneling micrographs. The results consistently prove the existence of nanoscale heterogeneities about 25 nm in diameter.

INTRODUCTION

The existence or non-existence of nanoscale heterogeneities in glass has been a subject of animated and controversial discussion over the years [1]. Lately Börjesson et al. have been searching for evidence in favor of microheterogeneities in AgI containing glassy electrolytes. However, applying low momentum transfer neutron diffraction techniques, they have not been able to detect any clustering of more than about 1 nm in diameter [2].

The purpose of our present paper is twofold.

(i) We wish to report on the detection and characterization of nanoscale heterogeneities in a silver-iodide/silver-borate glass. The microclusters detected here are typically some 25 nm across. Their existence has now been verified by application of three independent techniques, see below.

(ii) We wish to demonstrate that measurement of frequency dependent ionic conductivities is a cheap, simple and effective means for the detection of nanostructures in solid electrolytes. In particular, it is well suited for determining their typical sizes in units of the elementary hopping distance of the mobile ions.

In the following, the conductivity technique will be described and exemplified. The conclusions drawn from the conductivity spectra of glassy $B_2O_3 \cdot 0.50Ag_2O \cdot 0.75AgI$ will then be compared with the information contained in scanning electron and scanning tunneling micrographs. It will be shown that our conductivity spectroscopic and microscopic data consistently prove the existence of nanoscale heterogeneities about 25 nm in diameter.

CONDUCTIVITY SPECTRA

Ionic conductivities of solid electrolytes – crystalline or glassy – are known to display a characteristic dispersion. As an example, conductivity spectra of glassy $B_2O_3 \cdot 0.56Li_2O \cdot 0.45LiBr$ are shown in Fig. 1 [3].

Here the conductivity is constant at low frequency, e.g., up to about 10 MHz at 373 K. (The deviation below 10 kHz is an artifact due to electrode polarization.) At higher frequencies there is dispersion, and a power-law behavior, $\sigma - \sigma_{dc} \propto \nu^p$, $0 < p < 1$, is observed. Features occurring at still higher frequencies are of no importance in the

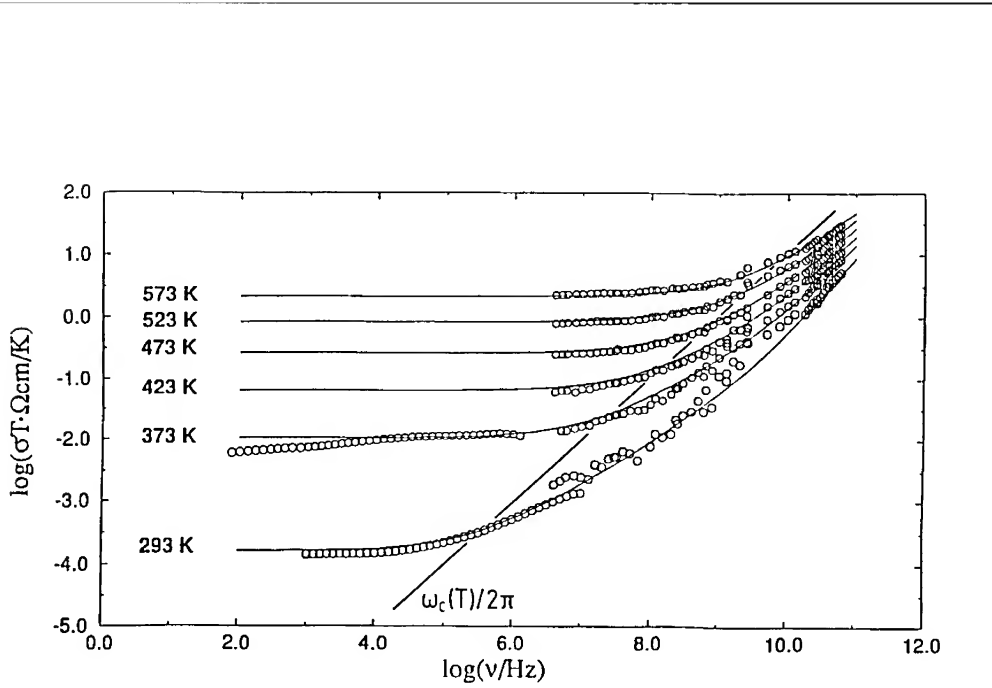


Fig. 1. Conductivity spectra of glassy $B_2O_3 \cdot 0.56Li_2O \cdot 0.45LiBr$ at different temperatures, in a log-log representation of σT versus frequency. The solid lines result from a fit described in ref. 3. For the straight line, see text.

present context. The crossover angular frequency at which the power-law dispersion sets in is denoted by ω_c . At ω_c the conductivity is twice as large as at low frequencies.

Dispersive conductivities are a hallmark of non-random hopping. In particular, the power-law behavior is explained by the jump relaxation model, which traces it back to many-particle Coulomb interactions, time dependent single-particle potentials, and correlated back-and-forth hopping processes [4]. The back-and-forth hopping has recently been seen most vividly in Monte-Carlo simulations [5].

In the jump relaxation model as well as in other approaches [6], ω_c is the inverse average time between two consecutive successful hops of a mobile ion. As opposed to the back-and-forth hopping, which is observed in the power-law frequency regime, these hops have to be regarded as random, yielding no further dispersion at lower frequencies. Therefore, the crossover angular frequency is at the same time the random-hopping rate and thus plays the role of a time marker in the conductivity spectrum. Note that the random-hopping rate determines the value of the coefficient of self-diffusion and, according to the Nernst-Einstein relation, of $\sigma_{dc} \cdot T$, see Fig. 1. In a plot like Fig. 1, a straight line intersecting the spectra at ω_c will, therefore, have a slope of one.

The time-marker property of ω_c can be exploited for the detection of nanostructures. Suppose the conductivity is dispersionless at $\omega < \omega_c$ for at least n decades. Then this implies that a mobile ion will perform at least 10^n consecutive hops in a random fashion. In doing so it explores a spatial regime whose size is at least $10^{n/2}$ elementary hopping distances. As the hopping is random we infer that the material is homogeneous on a scale of at least $10^{n/2}$ hopping distances. In fact, no indication of nanoscale heterogeneities has been found when the glass of Fig. 1 was analyzed by scanning tunneling microscopy (STM).

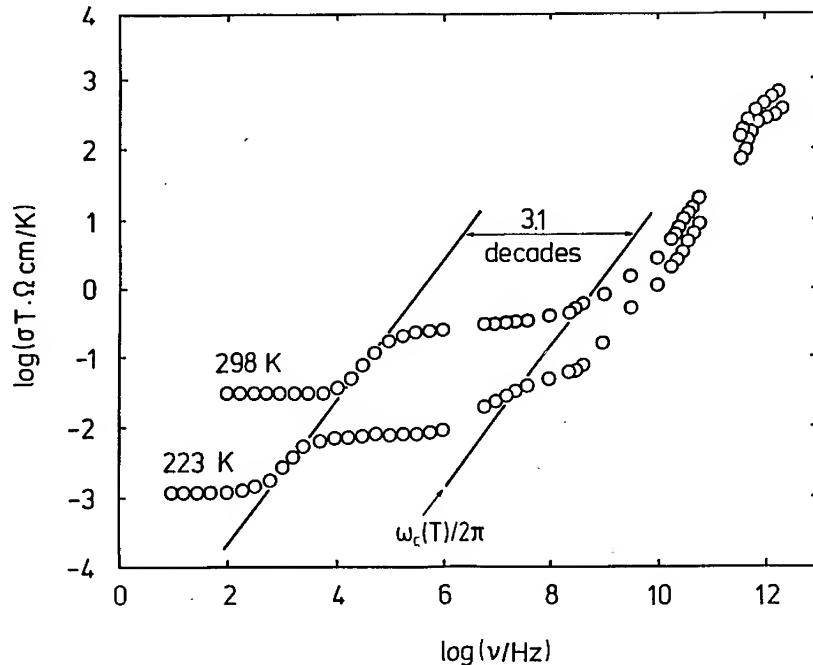


Fig. 2. Conductivity spectra of glassy $B_2O_3 \cdot 0.50Ag_2O \cdot 0.75AgI$ at two temperatures, in a log-log representation of σT versus frequency. For the straight lines, see text.

A different situation is encountered in the case of glassy $B_2O_3 \cdot 0.50Ag_2O \cdot 0.75AgI$. Fig. 2 shows conductivity spectra taken at two temperatures. Here, a marked relaxation step is observed in the kHz frequency regime. In Fig. 2, a straight line, with a slope of one, intersects the spectra at those frequencies where the conductivity is reduced by a factor of two. This line is parallel to the crossover line intersecting the spectra at ω_c . On the frequency scale, the two straight lines are 3.1 orders of magnitude apart. This implies that a hopping silver ion typically encounters some obstacle after roughly 1300 successful hops. In jump diffusion this corresponds to about 36 elementary hopping distances. We, therefore, have to assume that the glass is made up of easy-hopping regimes with an extension of the order of 100 elementary hopping distances, i.e., of roughly 20 nm. Those regimes probably have to be identified with AgI-rich clusters or microheterogeneities.

SEM AND STM

In order to investigate the glass structure on a nanometer scale, both high resolution SEM (scanning electron microscopy) and STM have been applied, see Figs. 3 and 4.

Two types of field emission SEM (Hitachi S-4100 and S-4500) have been employed, using an acceleration voltage of 5 kV. The samples were mounted in the usual way on a stub using conductive carbon. Subsequently, they were coated with a thin amorphous carbon film (10 nm to 20 nm thickness) by means of a commercial sputter coater.

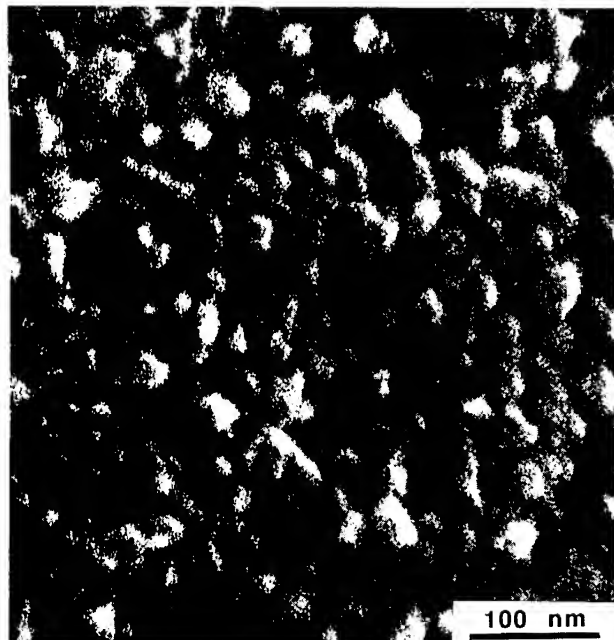


Fig. 3.
Secondary electron micrograph of glassy $B_2O_3\cdot0.50Ag_2O\cdot0.75AgI$ recorded with a field emission SEM S-4100 (Hitachi/Japan) at 5 kV acceleration voltage. The glass was coated with a thin amorphous carbon film having a thickness of 10 nm to 20 nm.

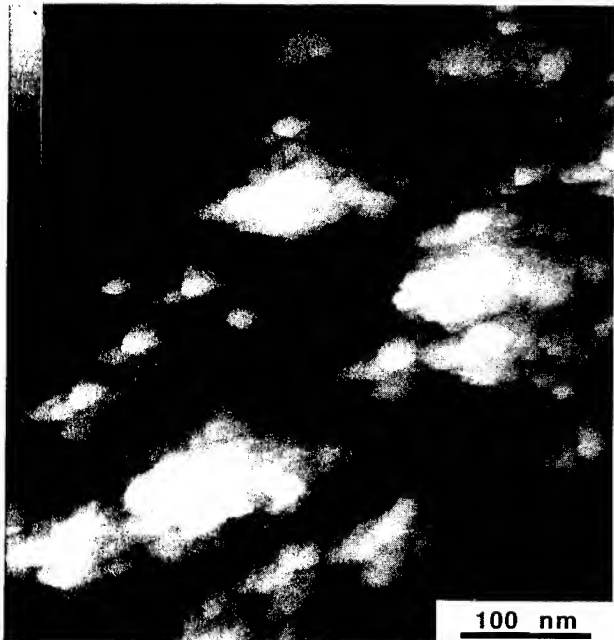


Fig. 4.
Scanning tunneling microscopic image of glassy $B_2O_3\cdot0.50Ag_2O\cdot0.75AgI$ recorded in the constant current mode. The glass was coated with an extremely thin Pt/Ir/C film having a thickness of 1 nm to 2 nm. The brightness range of the image corresponds to a height range of 22 nm (black: height = 0 nm, white: height = 22 nm; see brightness scale on the top left side).

In our STM experiments, a tungsten tip serves as a probe. Imaging was performed in the "constant current mode", i.e., the distance is kept constant by a constant tunneling current. Therefore, the tip follows the topographic features of the surface revealing its three-dimensional structure with high precision. As the tunneling of electrons requires conductive specimens, our samples were coated with a very thin layer of Pt/Ir/C (thickness 1 nm to 2 nm) in an oilfree high vacuum. The grain size of the Pt/Ir/C film is extremely small (very few nm only), cf. [7].

The $B_2O_3 \cdot 0.50Ag_2O \cdot 0.75AgI$ samples used in our conductivity experiments and for SEM and STM were all taken from the same batch. Fig. 3 shows a secondary electron micrograph of the surface of the silver-iodide/silver-borate glass. It proves the actual existence of the AgI-rich clusters or microheterogeneities. The typical cluster size is, indeed, about 20 nm to 30 nm, the size distribution being rather narrow.

The results obtained by STM, see e.g. Fig. 4, are consistent with Fig. 3. Again, the preferential cluster sizes are in a range of roughly 20 nm to 30 nm. The clusters are found all over the glass surface. This has been verified by optimizing the optical-imaging contrast with regard to areas of different height. Note, however, that the largest difference in height within the whole field of view (500 nm x 500 nm) amounts to only 22 nm.

As mentioned before, STM micrographs have also been prepared for the lithium-bromide/lithium-borate glass of Fig. 1. In this case, the largest difference in height within the whole field of view (500 nm x 500 nm) amounts to less than 10 nm, i.e., the surface is very flat and structureless. In particular, there is no indication of nanoscale heterogeneities, in accordance with our expectations on the basis of Fig. 1.

DISCUSSION AND CONCLUSION

Data obtained by application of three independent techniques, viz. conductivity spectroscopy, SEM, and STM, consistently prove the existence of nanoscale heterogeneities in glassy $B_2O_3 \cdot 0.50Ag_2I \cdot 0.75AgI$, the preferential cluster size being about 20 nm to 30 nm. The consequences of our results are twofold, concerning

- (i) nanoscale structures of glassy electrolytes and
- (ii) conductivity spectroscopy as a novel technique for their detection and characterization.

(i) Interestingly, nanoscale heterogeneities have been observed in a silver-iodide/silver-borate glass, but not in a lithium-bromide/lithium-borate glass. This might have been expected on the basis of the AgI and LiBr lattice energies which differ significantly.

Naturally, the extent of the formation of nanoscale concentration gradients may depend on sample preparation. Our silver-iodide/silver-borate samples were obtained from the melt and annealed for one hour at 280 °C before cooling to room temperature. However, quenched samples yielded very similar results from all three techniques. We, therefore, conclude that the nanoscale clustering is already present in the melt (at 750 °C).

(ii) The conductivity spectroscopic method has been shown to be well suited for studying nanostructures in solid electrolytes. Two particular advantages are worth mentioning. First, the technique can be used for *in-situ* observations of kinetic changes of nanoscale properties at elevated temperatures. This is not normally possible in SEM and STM. Second, the conductivity spectra need not cover broad frequency ranges as in Figs. 1 and 2, but may be restricted to the range below a few MHz, which is easily accessible in ordinary impedance spectroscopy. This is possible by extending the measurements to lower temperatures. The crossover angular frequency, which serves as a time marker, will then be shifted to sufficiently low frequencies. In a plot like Fig. 1, extrapolation along a straight line of slope one readily yields values of ω_c at any temperature at which the structure induced relaxation is observed. The cluster size is then determined as described

earlier in this paper. Thus nanoscale structures in solid electrolytes can be well studied with the help of a commercial impedance analyzer. This makes the technique cheap and easy to apply.

References

1. See, e.g., M.D. Ingram, M.A. Mackenzie, W. Müller and M. Torge, *Solid State Ionics* 40/41, 671 (1990).
2. L. Börjesson and W.S. Howells, *Solid State Ionics* 40/41, 702 (1990).
3. C. Cramer, K. Funke, C. Vortkamp-Rückert and A.J. Dianoux, *Physica A* 191, 358 (1992).
4. K. Funke, *Prog. Solid St. Chem.* 22, 111 (1993).
5. P. Maass, J. Petersen, A. Bunde, W. Dieterich and H.E. Roman, *Phys. Rev. Lett.* 66, 52 (1991).
6. D.P. Almond, G.K. Duncan and A.R. West, *Solid State Ionics* 8, 159 (1983).
7. M. Amrein, A. Stasiak, H. Gross, E. Stoll and G. Travaglini, *Science* 240, 514 (1988).

SYNTHESIS AND CHARACTERIZATION OF STRUCTURED METAL/SILICA CLUSTERS

A.N. PATIL*, N. OTSUKA**, R.P. ANDRES*

* School of Chemical Engineering,

** School of Materials Science and Engineering,

Purdue University, West Lafayette, Indiana 47906, U.S.A.

ABSTRACT

The synthesis of two component clusters of Au/SiO_2 , Ag/SiO_2 and $\text{Cu}_2\text{O/SiO}_2$ is described. These heteronuclear clusters are synthesized as metal/silicon clusters of controlled composition and controlled size using a novel gas aggregation source and by means of gas phase annealing are transformed into 'structured' particles. The final metal/oxide and oxide/oxide clusters are formed by air exposure. The structure of these nanostructured particles is determined by electron diffraction and transmission electron microscopy (TEM). The clusters exhibit two distinct structural forms: (1) clusters consisting of a metal rich core surrounded by a silicon rich skin and (2) clusters having a metal rich domain and a silicon rich domain separated by a sharp interface.

INTRODUCTION

Understanding and controlling the structure of nanometer size clusters is the key to understanding and synthesizing a wide class of novel nanostructured materials. [1, 2] These materials have potential applications as catalysts, electro-optical materials, thin films and high strength ceramics [3]. While much is known about synthesis of one component and two component homogeneous clusters [4, 5, 6], little is known about the synthesis of clusters with two components which exhibit atomic segregation. Such segregated or structured clusters have several potential applications. Metal clusters surrounded by a thin metal oxide layer have potential as novel catalysts [7]. Metal clusters surrounded by a thin insulating sheath also have potential as coulomb blockade devices [8, 9].

We have used aerosol techniques to produce structured metal/silicon clusters. Exposure of these clusters to O_2 leads to the production of M/SiO_2 and MO_x/SiO_2 clusters. The results of our experiments with Au/Si , Ag/Si and Cu/Si are reported in this article.

EXPERIMENTAL

Figure 1 shows a schematic diagram of a gas aggregation source known as a Multiple Expansion Cluster Source (MECS), developed at Purdue University. A detailed description of the MECS can be found elsewhere. [10, 11].

In order to produce metal/silicon clusters using the MECS, separate carbon crucibles containing metal and silicon were placed in the oven section of the source, and metal and silicon were coevaporated in the oven in the presence of inert gas. The inert gas used in this study was He (99.995 % pure) that was passed through a trap containing Cu turnings at 400 °C. The oven was maintained in the temperature range of 1200 °C - 1600 °C, depending on the metal/silicon system used. There is a temperature gradient along the length of the oven. Hence the evaporation rate from a crucible depends on the position of the crucible in the oven. By placing the crucibles at appropriate positions, the relative evaporation of metal and silicon can be controlled, thereby controlling the composition of the metal/silicon clusters synthesized. The superheated vapor mixture from the oven is cooled by mixing with inert quench gas in the reactor region. Upon quenching, cluster growth starts. The residence time in the reactor zone is

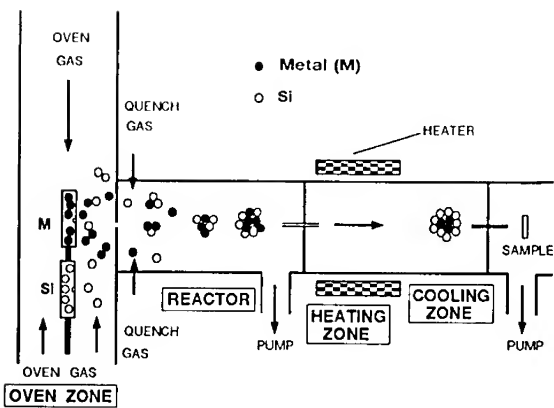


Figure 1 Schematic diagram of the MECS for synthesis of metal/silicon clusters

10^{-3} to 10^{-2} seconds. By controlling the residence time in the reactor, the size of the clusters can be controlled. The clusters form initially by addition of single atoms of metal or silicon and finally by cluster-cluster agglomeration. The diameters of the clusters synthesized in the MECS can be easily varied in the range 1-30 nm.

The clusters formed in the reactor region are annealed in the gas phase by passing the cluster aerosol through a Lindberg furnace [General Signal, Watertown, WI]. The furnace temperature can be as high as 1500°C . The residence time of the clusters in the heating region is about 0.5 seconds. The clusters are then cooled. The residence time in the cooling region is also about 0.5 seconds.

The resulting cluster aerosol flows through a capillary into a vacuum chamber maintained at 10^{-6} torr. The clusters are deposited on 5 nm thick amorphous carbon films supported on 400 mesh nickel or copper grids [Ernest Fullam Inc., Latham, NY] for TEM analysis. The samples were analyzed using a JEOL 2000FX analytical transmission electron microscope. In transferring the samples to the microscope, they are exposed to the air and the M/Si clusters are oxidized as discussed below.

RESULTS AND DISCUSSION

Figure 2 shows a bright field micrograph of unannealed Au/Si clusters that have been exposed to air. Electron diffraction analysis of annealed Au/Si clusters exposed to air indicates that the gold is in the Au^0 state [12]. X-ray photoelectron spectroscopic analysis of thin films of Au/Si clusters exposed to air reveals oxidation of the silicon to SiO_2 [13]. The distribution of metal and silicon in the unannealed clusters is uniform. From the morphology of the unannealed clusters, their formation through agglomeration of smaller Au/Si clusters is evident (See Figure 2).

Figure 3 shows the effect of annealing on the structure of Au/Si clusters. The Au/SiO_2 clusters shown in Figure 3 were annealed at 1200°C and then exposed to air. Atomic

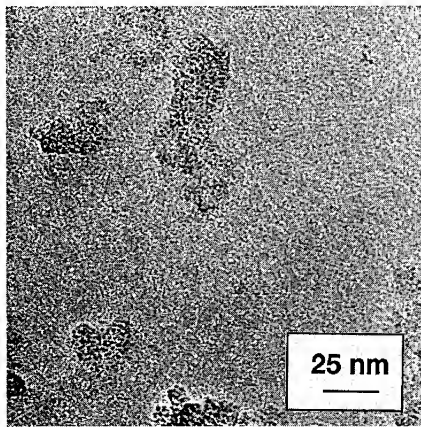


Figure 2 Bright field micrograph of unannealed Au/SiO₂ clusters

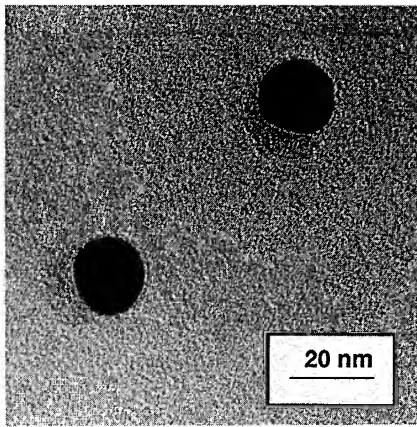


Figure 3 Bright field micrograph of Au/SiO₂ clusters annealed at 1200 °C.

segregation into Au and Si rich regions can be clearly identified in the micrograph. The Au and Si domains segregate side by side.

In previous studies with Au clusters, we have shown the effect of annealing temperature on cluster crystal structure [4]. To investigate the effect of different annealing conditions on the structure of metal/Si particles, we annealed the Au/Si clusters at 1350 °C. The bright field micrograph of one of these clusters after air exposure is shown in Figure 4. The cluster has a core of gold surrounded by a layer of silica. During synthesis of these particles, there was a relatively high partial pressure of silicon in the heating zone. At furnace temperatures above 1400 °C, under similar flow and evaporation conditions, the silicon partial pressure is high enough to induce homogeneous nucleation of secondary silicon clusters. The fairly thick SiO₂ layer on the Au/SiO₂ cluster in Figure 4 was possibly formed by condensation of silicon from the gas phase onto a Au/Si cluster as it cools.

We believe that the structure observed in Figure 3 is an intermediate state that is less stable than the structure in Figure 4 and that the segregation process leading to formation of the structure in Figure 4 is incomplete under the conditions of Figure 3 due to the slow solid-solid diffusion in the Au/Si system. In order to confirm our hypothesis regarding the lowest energy structure of metal/silicon clusters, we also synthesized and annealed Cu/Si and Ag/Si clusters. Silver and copper have higher solid-solid diffusivities in Si than does gold [14,15]. Hence the lowest energy structure should form more easily in Ag/Si and Cu/Si clusters than in Au/Si clusters.

A bright field transmission electron micrograph of a Ag/Si cluster annealed at 960 °C and then exposed to air is shown in Figure 5. At this annealing temperature, evaporation in the heating zone is insignificant. In the micrograph, segregation of silver and silica phases is clearly seen. Silver forms the cluster core and silica forms the outer layer. Thus, the structure consisting of a metal core and a silicon outer layer is observed for the Ag/Si system in absence of silicon condensation onto the cluster during segregation.

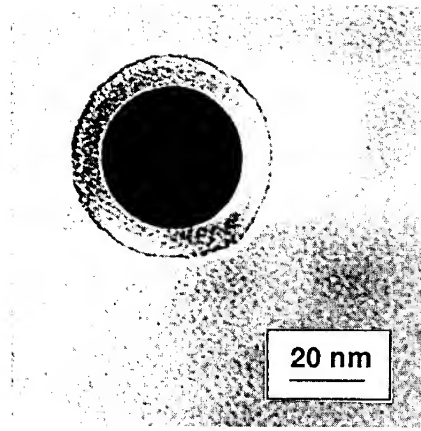


Figure 4 Bright field micrograph of Au/SiO_2 clusters annealed at $1350\text{ }^\circ\text{C}$.

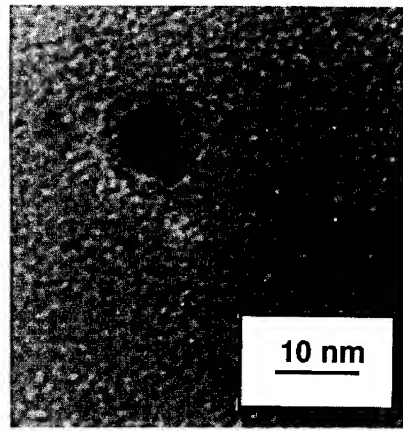
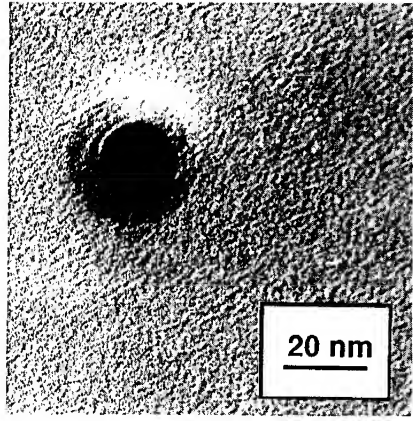
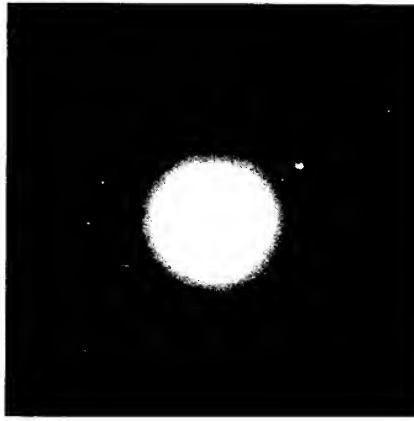


Figure 5 Bright field micrograph of Ag/SiO_2 clusters annealed at $960\text{ }^\circ\text{C}$.



(a)



(b)

Figure 6 (a) bright field micrograph (b) microdiffraction pattern of $\text{Cu}_2\text{O}/\text{SiO}_2$ clusters annealed at $1200\text{ }^\circ\text{C}$.

Figures 6a and 6b show a bright field micrograph and a microdiffraction pattern of a Cu/Si cluster annealed at 1200 °C and then exposed to air. At this annealing temperature, evaporation from the clusters in the heating zone is insignificant. From the bright field micrograph in Figure 6a, it is clear that the Cu/Si clusters also exhibit a metal rich core surrounded by a silicon rich layer. Analysis of the microdiffraction pattern indicates that after air exposure the core of the cluster is Cu₂O.

CONCLUSIONS

Two component clusters of metal/silicon of controlled composition and controlled size can be produced in the MECS. To transform these particles into structured particles, high temperature annealing of the clusters in the gas phase is required. For annealed metal/Si clusters, a structure consisting of a metal rich core and a silicon rich outer layer seems to be favored thermodynamically. On exposure to air these clusters are oxidized. In the case of Au/Si and Ag/Si clusters this leads to Au/SiO₂ and Ag/SiO₂ clusters. In the case of Cu/Si clusters this yields Cu₂O/SiO₂ clusters.

ACKNOWLEDGEMENTS

This work was partially funded by the National Science Foundation under grant ECS-9117691.

REFERENCES

- [1] R. P. Andres, R. S. Averback, W. L. Brown, L. E. Brus, W. A. Goddard, A. E. Kaldor, S. G. Louie, M. Mascovits, P. S. Peercy, S. J. Riely, R. W. Siegel, F. Spaepen and Y. Wang, *J. Mat. Res.*, **4**, 704 (1989).
- [2] R. W. Siegel, *MRS Bulletin*, **25**, 60 (1990).
- [3] H. Gleiter, *Nanostructured Materials*, **1**, 1 (1992).
- [4] A. N. Patil, D. Paithankar, N. Otsuka and R. P. Andres, *Z. Phys. D*, **26**, 137 (1993).
- [5] A. Hartman and K.G. Weil, *High Temperature Science*, **27**, 31 (1990).
- [6] N. Toshima, *J. Macromol. Sci.*, **A27** (9-11), 1225 (1990).
- [7] L. C. Chao, A. N. Patil and R. P. Andres (unpublished results).
- [8] J. B. Barner and S. T. Ruggiero, *Physical Review Letters*, **59**, 807 (1987).
- [9] M. A. Reed, *Scientific American*, **269**, 118 (1993).
- [10] E. Choi and R. P. Andres in *Physics and Chemistry of Small Clusters*, edited by P. Jena, B. K. Rao and S. N. Khanna (Plenum Press, New York, 1987) p. 61.
- [11] S. B. Park, PhD Thesis, Purdue University (1988).
- [12] A. N. Patil and R. P. Andres (unpublished results).
- [13] R. Crane, A. N. Patil and R. P. Andres (unpublished results).
- [14] F. Rollert, N. A. Stolwijk and H. Mehrer, *J. Phys. D*, **20**, 1148 (1987).
- [15] W. Frank, U. Gosele, H. Mehrer and A. Seeger in *Diffusion in Crystalline Solids*, edited by Murch G. F. and Nowick A.S. (Academic Press, New York, 1984) p. 63.

POROUS SILICON LUMINESCENCE STUDY BY IMAGING METHODS: RELATIONSHIP TO PORE DIMENSIONS

ANNA KONTKIEWICZ*, ANDRZEJ M. KONTKIEWICZ*, SIDHARTHA SEN*,
MAREK WESOŁOWSKI*, JACEK LAGOWSKI*, PIOTR EDELMAN**
AND TOMASZ KOWALEWSKI***

*Center for Microelectronics Research, University of South Florida, Tampa, FL 33620

**Semiconductor Diagnostics, Tampa, FL 33610

***Chemistry Dept., Washington University, St. Louis, MO 63130

ABSTRACT

In a photoluminescence and surface photovoltage study of porous silicon films with crystallite dimensions assessed with the Atomic Force Microscope, we have found cases when the blue shifts of the luminescence spectrum and the optical absorption edge take place upon increasing crystallite dimensions, which is contrary to quantum size effects. Fourier transform infrared spectroscopy analysis of these samples shows significant differences in hydrogen and oxygen bonding, which imply that the origin of the luminescence is of chemical nature. Our results show that porous silicon luminescence is not a consequence of one mechanism, but rather results from several mechanisms with contributions depending on the chemistry and structure of porous silicon.

BACKGROUND

Visible light luminescence of porous silicon films formed by anodic etching of silicon wafers has recently attracted a great deal of attention. The origin of this luminescence has been intensely studied since this phenomenon was first observed [1]. Two main possible mechanisms of photoluminescence (PL) have been proposed. Most authors relate this phenomenon to quantum size effects in crystalline silicon dots or wires [2-4]. Some attribute it to surface localized states or complex formation on porous silicon surface during anodization and subsequent treatment [5-7]. The purpose of the present study is to present the results of luminescence behavior of porous silicon and their relation to pore size as observed by atomic force microscope (AFM). We also address the role of surface passivation and discuss the likely origin of PL in porous films. In this study we observed many cases where the shift of PL wavelength did not follow the quantum confinement model.

EXPERIMENTAL PROCEDURES

Porous silicon films on both p- and n-type (100) silicon wafers with resistivities between 3-20 Ωcm were obtained using anodization process in a teflon cell. To ensure uniform distribution of anodic current, a metallic contact was formed on the back surface of the wafer. The electrolyte was a mixture of HF and $\text{C}_2\text{H}_5\text{OH}$ with HF concentration varying from 10 wt% to 49 wt%, 25 wt% HF being typical composition. Anodization of p-type substrates was usually done under ambient light, while for n-type substrates additional illumination was provided by a halogen light source. The anodization parameters such as current density and time were varied between 10-100 mA/cm² and 1-70 min, respectively. Photoluminescence from as-anodized porous layers is known to be unstable [8]. To stabilize PL, some of our samples were subjected to a two step dry-oxidation process following anodization. The first step - long time annealing at 350°C in O_2 as suggested previously [9] for improving the structure of porous silicon, was followed by a rapid thermal annealing in O_2 at temperature in the range 800 - 1000°C. In the range of parameters investigated, porous layers with best PL were obtained after anodization in 25 wt% HF ethanol solution at current density of 20 mA/cm² and subsequent oxidation at 850°C for 20 secs.

The porous layers characteristics were investigated using photoluminescence, surface photovoltage (SPV) and Fourier transform infrared absorption (FTIR) spectroscopy at room

temperature. Photoluminescence was measured using 514.5 nm Ar laser as an excitation source. SPV spectroscopy was performed in a non-contact manner similar to one used for characterization of optical transitions in silicon-on-sapphire (SOS) [10]. FTIR measurements were recorded using NICOLET 60SXR spectrometer at 4 cm⁻¹ resolution.

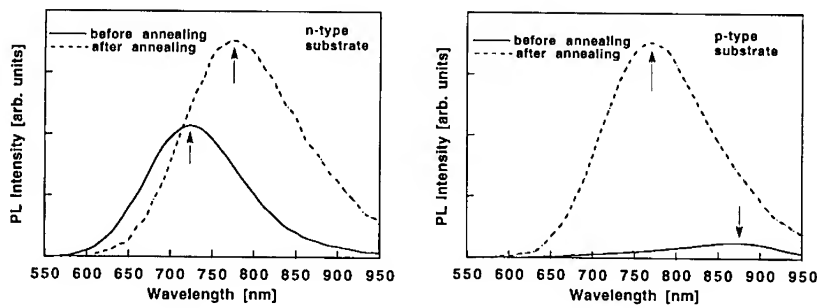


Fig. 1 Photoluminescence spectra of porous silicon layers on n-type (a) and p-type (b) substrates, before and after annealing

RESULTS AND DISCUSSIONS

As shown in Fig. 1 the peak wavelength for as-anodized porous films obtained in 25 wt% HF solution was 800 nm for p-type substrate and 700 nm for n-type substrate. Annealing enhances and stabilizes PL and shifts the PL peak position. The "blue" shift of PL peak was characteristic of films on p-type substrates. Similar annealing of films on n-type substrates resulted in a "red" luminescence shift. However, the final peak position following RTO treatment was the same, about 770-780 nm, for both p- and n-type substrates. It is worthwhile to note that when lower HF concentrations (<20 wt%) were used than the as-anodized layers on p-type substrates exhibited shorter PL peak wavelength. In such samples RTO treatment caused "red" shift of PL peak to the same "after annealing" position (770-780 nm) as mentioned above. Dry oxidation reduces feature size of the porous layer and based on quantum confinement theory one would expect the "blue" shift of PL for both types of substrates. The final PL peak position after RTO should also depend on the initial peak wavelength of the as-anodized sample. Our PL results after dry oxidation are contrary to what is expected from quantum model.

A micro-pore structure of porous films was analyzed using 3-D imaging of porous silicon surfaces, with nm resolution, using atomic force microscope (AFM). The first part of our investigation was concerned with the effects of anodic current. A series of films were prepared on p-type substrates using 25wt% HF and different current densities. We observed the behavior similar to that previously reported [2-4], namely, films with smaller crystallites showed higher luminescence intensity and shorter wavelengths than films with larger crystallites. The same tendency was observed with as anodized and annealed films. Later, we encountered completely opposite behavior in porous silicon films prepared using solutions with different HF:H₂O:C₂H₅OH ratios. By lowering HF concentration we were able to lower the PL peak wavelength. AFM measurements have shown that in these films lower PL wavelength corresponded to larger crystallite sizes rather than smaller ones. An example of such behavior is shown in Figure 2. AFM 3-D surface images were measured in the tapping mode. Films #307 and #328 were prepared using 21% HF and 25% HF, respectively. Film #307, which corresponds to the lower HF concentration, clearly shows large crystallite dimensions. This conclusion was confirmed by enhanced resolution imaging and linear profiling shown in Fig. 3. The 300K PL spectra of Films #307 and #328 are shown in Figure 4. It is evident that PL peak energy for Film #328, with smaller crystallites, is lower than that of Film #307 with about twice larger crystallite diameter. This "red" luminescence shift is opposite to the "blue" shift expected

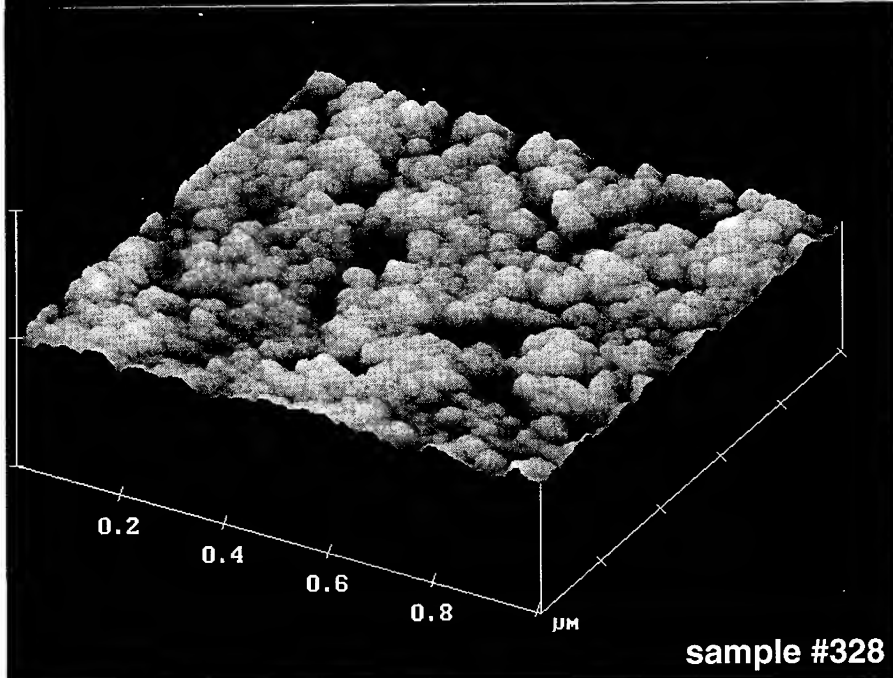
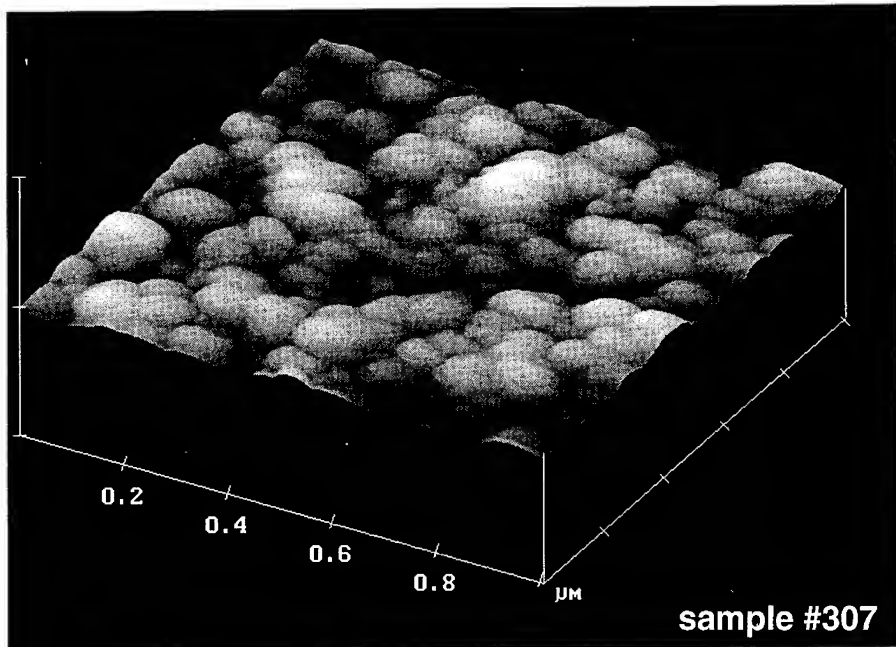


Fig. 2 AFM images of porous silicon prepared using 21% HF (#307) and 25% HF (#328)

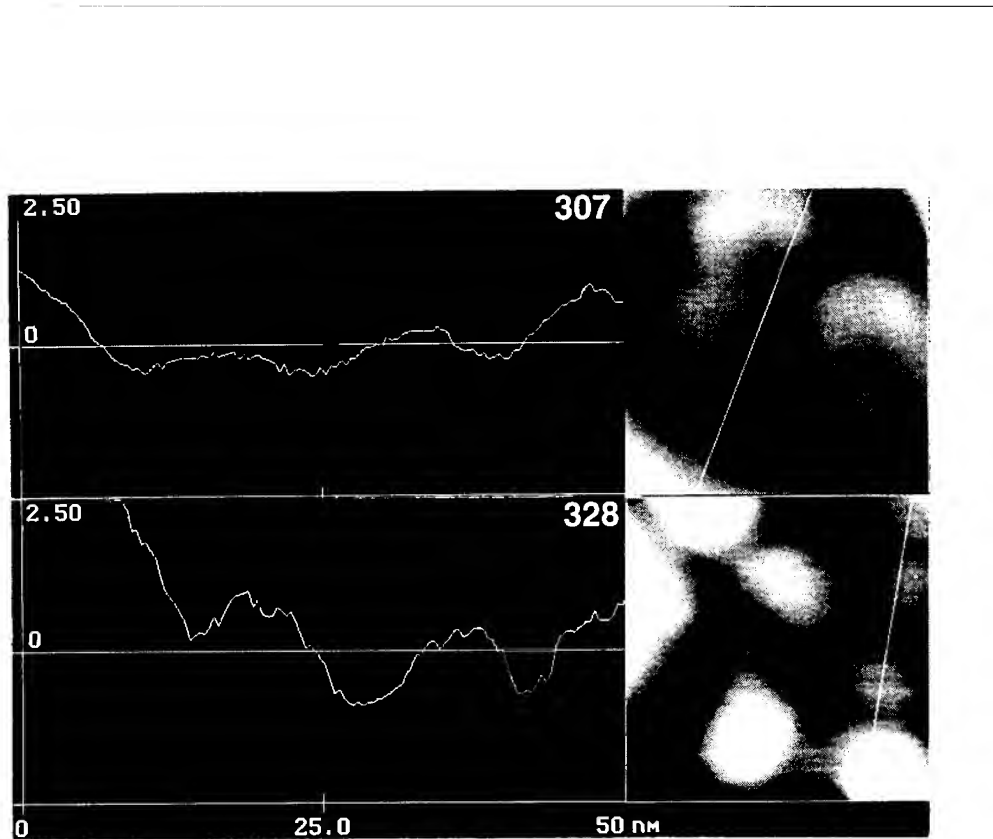


Fig. 3 Enhanced AFM surface profiles.

from the quantum size effect. This result is of significance, especially that the enhanced AFM measurements exclude the existence of small pores sub-structure within the large pores of Film #307. According to the theoretical calculations, to observe visible luminescence resulting from quantum size effects the characteristic dimensions of silicon wires need to be less than 5 nm [11]. In case of Films #307 and #328 these dimensions were 25 nm and 12 nm respectively. This result is again contrary to quantum size model.

The optical transitions in porous silicon which are not present in crystalline silicon were studied using SPV spectroscopy. In this technique the chopped light generates excess carriers which alter the surface potential. Corresponding AC photovoltage signal is picked up by a semitransparent

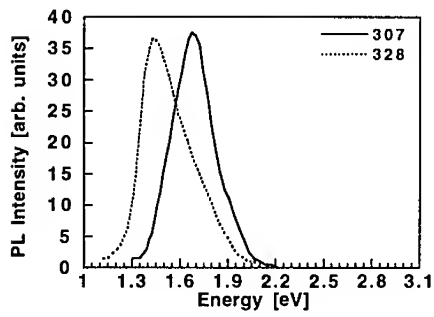


Fig. 4 Photoluminescence spectra of porous silicon layers.

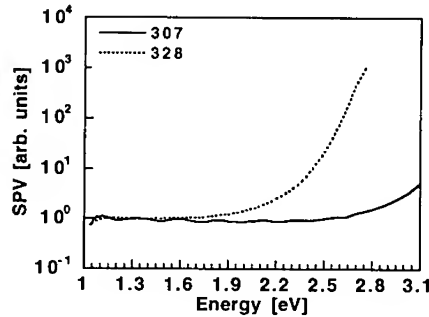


Fig. 5 Surface photovoltaic spectra of porous silicon layers.

reference electrode capacitively coupled to the measured wafer. For films with a short minority carrier diffusion length the spectral dependence of surface photovoltage reflects the variation of the absorption coefficient. The differences between porous and crystalline silicon can be best seen in the surface photovoltage spectrum normalized to spectrum of crystalline silicon. The "red" shift is very pronounced for the spectra of normalized surface photovoltage of Films #307 and #328 (see Figure 5) which reveals high energy optical transitions rather than recombination transitions.

In Fig. 6 the photovoltage data for films #307 and #328 are plotted in a form which is often used for determination of the optical energy gap. It is seen that the film #328 seems to have two thresholds. Low energy threshold, E_1 , at about 1.7 eV is close to the optical gap in amorphous silicon. The high energy threshold, E_2 , at about 2.4 eV is present in both films. The complex character of optical transitions in porous silicon and the red shift of the photovoltage threshold do not seem to be consistent with the quantum confinement model of the porous silicon energy spectrum. The annealing-induced blue luminescence shift in films formed on p-type substrate was also accompanied by the blue shift of the photovoltage. This indicates that indeed new optical transitions occur, which are not present in crystalline silicon. The absolute magnitude of photovoltage for rapid thermal oxidized porous silicon in the high energy region was greater by more than an order of magnitude than the as-anodized porous silicon. The corresponding increase after RTP was less pronounced for films formed on n-type substrates. This difference may be attributed to the difference in the morphology of the porous layer formed on p- and n-type substrates [12].

FTIR spectra for samples #307 and #328 presented in Fig. 7 show significant differences in hydrogen and oxygen bonding in these two samples which seem to us to be the main reason of the observed blue shift of the luminescence.

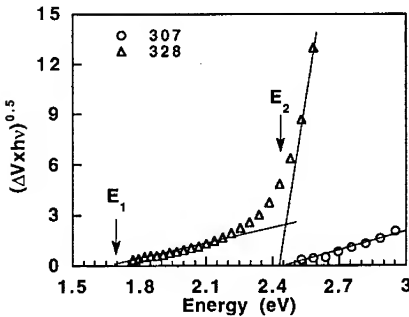


Fig. 6 Photovoltage data for films #307 and #328.

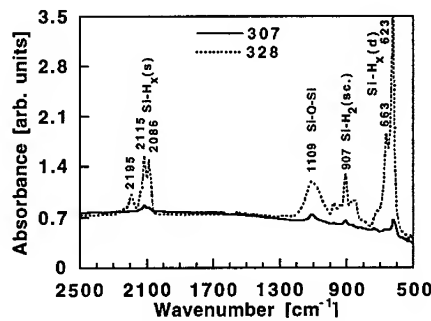


Fig. 7 FTIR spectra of porous silicon layers.

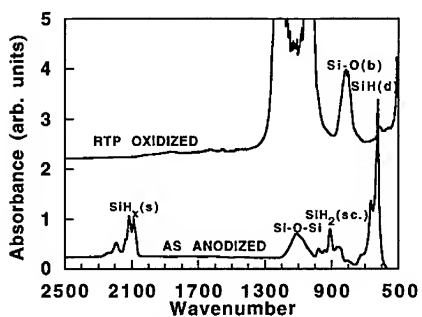


Fig. 8 FTIR spectra for porous silicon layers before and after rapid thermal oxidation.

FTIR measurements have also revealed hydrogen bonding peaks dominant in as-anodized films formed on both p- and n-substrates. Rapid thermal oxidation at 850°C has resulted in hydrogen desorption and the appearance of SiO_x peaks and surface oxygen peaks (as shown in Fig. 8). This behavior is true for porous films on p- and n-substrates and is consistent with previous findings [13]. The main compositional change in the as-anodized and annealed porous films is in the magnitude of 810 cm^{-1} (Si-O bonding) and 887 cm^{-1} (H-Si-O₃ bonding) peaks. The unstable luminescence from the as-anodized samples under laser irradiation is likely to be due to the photo-oxidation of SiH_x bonds. The

rapid thermal processing of porous layers on both p- and n-type substrates in oxygen at temperatures $> 750^{\circ}\text{C}$ results in a high quality oxide layer which enhances and stabilizes PL intensity. Lower temperature RTP treatments in oxygen were not effective in stabilizing the porous surface. FTIR measurements in these samples have shown a prominent peak near 880 cm^{-1} (due to H-Si-O₃ bonding absorption) other than a broad peak near 1100 cm^{-1} (due to interstitial oxygen and surface oxide species). The 810 cm^{-1} peak was systematically absent in all low temperature RTP oxidized porous films. We may therefore suggest that the presence of a strong 810 cm^{-1} absorbance peak is a good indicator of surface passivation favoring stable luminescence. It is worthwhile to add that other means of surface passivation such as one step low temperature ($\sim 350^{\circ}\text{C}$) RTP in O₂, one (350°C) and two step (350°C and 850°C) RTP in N₂ have all resulted in unstable and in some cases no luminescence from the porous layers. High temperature ($\sim 850^{\circ}\text{C}$) furnace oxidation for short time was also found effective in causing surface passivation for stable luminescence.

CONCLUSIONS

We have observed cases where the PL wavelength and luminescence shift in annealed porous silicon were not consistent with the quantum confinement model. It is evident from the AFM observations that the both structure of porous films and crystallite dimensions cannot be always correlated with theoretical expectations. We have established cases where blue shifts of luminescence and surface photovoltage threshold coincide with increasing crystallite diameters. We have also established unambiguous cases where strong visible luminescence was observed for films with crystallite sizes much larger than expected from quantum size theory. We consider these observations as proof that, in porous silicon films, optical transitions and radiative recombination transitions are not always determined by the quantum size effect. It is most likely that the differences in the chemical surface composition clearly seen in FTIR spectra are a dominant cause for the observed differences in optical and electrical properties.

ACKNOWLEDGMENT

This work was founded in part by the Advanced Research Project Agency.

- [1] L.T. Canham, *Appl. Phys. Lett.* **54**, 1046 (1990)
- [2] V. Lehmann and U. Goesele, *Appl. Phys. Lett.* **58**, 856 (1991)
- [3] Y.H. Xie, W.L. Wilson, F.M. Ross, J.A. Mucha, E.A. Fitzgerald, J.M. Macaulay and D. Harris, *J. Appl. Phys.* **71**, 2403 (1992)
- [4] J.P. Proot, C. Delerue and G. Allan, *Appl. Phys. Lett.* **61**, 1948 (1992)
- [5] K.H. Li, C. Tsai, J. Sarathy and J.C. Campbell, *Appl. Phys. Lett.* **62**, 3192 (1993)
- [6] S. Banerjee, K.L. Narasimhan, P. Ayyub, A.K. Srivastava and A. Sardesai, *SolidState Comm.* **84**, 691 (1992)
- [7] S.M. Prokes, *J. Appl. Phys.* **73**, 407 (1992)
- [8] L.T. Canham, M.R. Houlton, W.Y. Leong, C. Pickering and J.M. Keen, *J. Appl. Phys.* **70**, 422 (1991)
- [9] S. Shih, C. Tsai, K.-H. Li, K.H. Jung, J.C. Campbell and D.L. Kwong, *Appl. Phys. Lett.* **60**, 633 (1992)
- [10] J. Lagowski, L. Jastrzebski and G.W. Cullen, *J. Electrochem. Soc.* **128**, 2665 (1981)
- [11] G.D. Sanders and Yia-Chung Chang, *Appl. Phys. Lett.* **60**, 2525 (1992)
- [12] P.C. Searson and J.M. Macaulay, *Nanotechnology* **3**, 188 (1992)
- [13] H. Lik, C. Tsai, J.C. Campbell, B.K. Hance and J.M. White, *Appl. Phys. Lett.* **62**, 3501 (1993)

TEM STUDIES ON THE MORPHOLOGY, SIZE DISTRIBUTION AND STRUCTURE
OF NANOCRYSTALLINE IRON PARTICLES USING A FORMVAR
EMBEDDED PREPARATION TECHNIQUE

HENGFEI NI, XIANGXIN BI AND JOHN M. STENCEL
University of Kentucky, Center for Applied Energy Research, Lexington, KY 40511-8433

ABSTRACT

A new, simple and effective method was developed for preparing specimens of Fe-carbide ultrafine particles (UFP), by suspending them in Formvar films. Various samples of Fe-carbide UFP's were obtained by a laser pyrolysis process by varying the process parameters. The UFP samples were mixed with different concentrations of Formvar in ethylene dichloride solution. The sample particles were embedded in ultra-thin Formvar films with thickness of 20 nm or more and mounted on the 200 mesh copper TEM grids. The influences of the concentration of the Formvar solution and the amount of sample powder on the UFP distribution in the micrographs were investigated to determine the optimal film-making parameters. The different sizes and same spherical morphology for the various UFP samples were revealed, indicating the main diameters to be between 5-20 nm. Compared with the size values obtained by using XRD, the UFP size measurements by the new process are in good agreement. The crystalline features and the surface of the UFP's are presented and confirmed by micro-diffraction studies.

INTRODUCTION

The study of ultrafine particles (UFP) has attracted increasing attention in many fields, including catalyst chemistry, solid state physics, biology, medical science, and advanced functional materials research because of their unusual physical and chemical behavior. In this regard, there is special interest in their use as catalysts[1-6]. Morphology, size distribution and crystalline structure of UFP's are crucial for understanding size-dependent activity and for selecting optimal production conditions. Transmission electron microscopy (TEM) is a particularly useful tool for the study of ultrafine particles. However, obtaining useful TEM information on morphology, size and microstructure of UFP's requires the development of appropriate procedures for specimen preparation[7-9]. Few procedures have been found to be suitable for UFP's, because they are very reactive and can, for example, be easily oxidized. Holey carbon film is the most common UFP TEM specimen preparation technique but its use causes problems with the specimen preparation and TEM observation[10-12].

To prepare samples that produce high quality TEM images, it is necessary to reduce interactions between the UFP and the electron beam, which can cause small particles to disappear, and to eliminate possible contamination on the high resolution electron lens. Some modifications to conventional techniques have been carried out using Formvar embedded films. The technique that has been developed enables highly dispersed and embedded UFP films to be prepared with controlled thicknesses. As a result, reliable data on morphology, size and crystalline structure of the UFP samples can be obtained.

In this paper, an improved method of preparing TEM specimens is described, and relationships between the morphology, size and crystalline structure of UFP's produced by laser pyrolysis are discussed.

EXPERIMENTAL

TEM Specimen Preparation

The laser pyrolysis of $\text{Fe}(\text{CO})_5$ in C_2H_4 was employed to synthesize iron carbide UFP's. The processing details have been reported in the literature[13-14]. The size and composition of the UFP's were controlled by varying the reactant flow rates, reaction chamber pressure and laser irradiation intensity. These parameters range from 10-100 sccm for the flow rate, 300 to 600 torr for pressure, 30-110 W for laser power. The samples contain Fe_3C , Fe_7C_3 and metallic Fe depending on the different synthesis conditions[14].

Formvar polymeric matrix films containing highly dispersed monolayer UFP were made, and supported on 200 mesh copper TEM grid, with and without a carbon substrate. The procedure for making these specimens is given below.

Add 20-40 mg of UFP's sample to a 2ml volume small tubule containing 0.5 ml solution of 0.25 % Formvar in ethylene dichloride. Stir Formvar and particle mixture efficiently using the ultrasonic bath for 10 minutes. For getting the appropriate film thickness to embed the monolayer UFP individuals and to attain good strength and stability for electron beam irradiation, the embedding medium must have proper viscosity and an appropriate concentration of Formvar and particles. Add another 0.5 ml solution with 2.5 % Formvar in ethylene dichloride to the above mixed sample tubule. As a result, a 1.38 % Formvar colloidal solution with the uniform black color is obtained after stirring in the ultrasonic bath for 10 minutes. Then, dilution was conducted in 1.38% Formvar solution of ethylene dichloride for getting 0.04-2 % UFP's suspension concentrations, followed by mixing in the ultrasonic bath for 15 minutes.

Place a small droplet(about 0.02 ml) onto distilled water. Lay TEM 200 mesh grid on the film. Using a filter paper, carefully pick up the sample from the water. Dry the filter paper with Formvar film and grid in an oven at 45 C for 60 min.

Characterization of Morphology, size distribution and crystalline structure

The TEM observations were carried out with a H-7000 Electron microscope using 125 KV and the magnification of 100-600 KX. Electron microdiffraction for the UFP single crystalline structure analysis was performed in a H-800NA using 200 KV in the NANO operation mode. XRD was used to identify the UFP phases and to compare the measured size data with TEM.

RESULTS AND ANALYSIS

TEM BF Image Contrast Analysis

Typical TEM BF images are presented in Figure 1. The different intensities shown in the Figure 1 are due to the different size and the orientation of the UFP. The contrast of BF

images is determined by diffraction and phase effects. Various factors such as the phase average Z, particle size, and Formvar film thickness, particle crystal orientation with the incident beam, and particle coating substance composition and structure affect the contrast of BF images. For a given particle, the contrast in BF will be a maximum when the particle is in the Bragg condition. For the small particles, especially in the 1-4nm size range, the contrast is low because the elastic scattering is small from these particles.

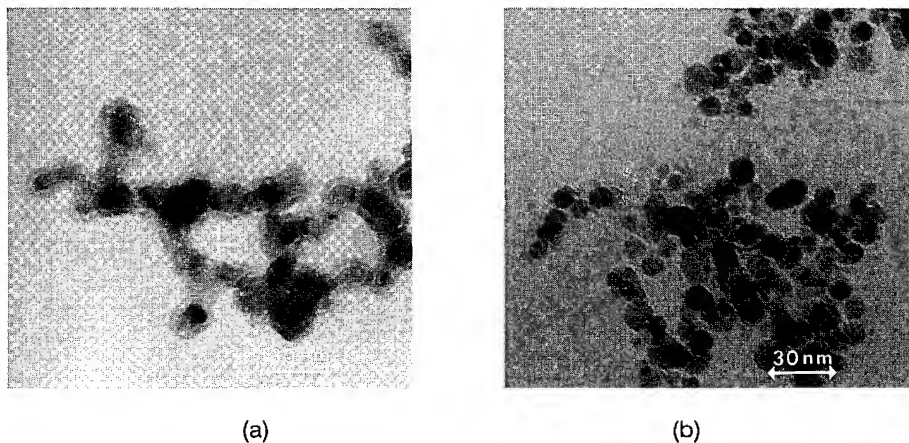


Fig.1. Typical TEM BF Image of UFP Fe Carbide Samples (a). Coating Structure of $\text{Fe}_3\text{C}+\text{Fe}_2\text{O}_3$; (b). No-Coating Structure of $\text{Fe}_7\text{C}_3+\text{Fe}$.

The surface carbon coating on the particles and the oxidation structures are highlighted by BF contrast variation. Oxide bands of UFP's are separated by the light-colored regions. It is also possible that the brightness enhanced regions consist largely of voids created by oxidation. Characteristic changes in the image contrast using defocused TEM confirmed the presence of a substantial surface carbon film on the UFP's.

Different concentrations of Formvar films, in the range of 0.25-2.5 % were examined to determine the optimal concentration for quality images. The optimal contrast, strength and stability were obtained using 1.38 % Formvar film. At higher concentrations, a rippled film surface formed and particles overlapped which decreased contrast. Our experience indicates that the 1.0% Formvar solution resulted in the 10 nm thickness film, and 2.0 % gave a 20 nm film. Low concentrations cause maximum contrast and highly dispersion, but also results in a tendency to decompose, shrink and break during irradiation from the electron beam.

UFP Morphology and Electron Beam Irradiation Effect

In the most cases when examining UFP embedded Formvar films, negligible effects of the electron beam on the UFP's were noted. The thin Formvar films possess a composite structure that consists of the UFP covered by a protective overcoat of polymers. It offers

a beneficial function of preventing exposure to air during preparation and decreasing direct irradiation from the electron beam.

It has been suggested that an important aspect of the physics of UFP's is a quasi-melting phenomenon[15-16]. This configurational instability is the result of the large number of free energy states in which the UFP particles can populate. These energy states are close and jumps between them are likely. It is a phenomenon that requires a certain activation energy for its onset. The value of the activation barrier for quasi-melting is very low but in general will strongly depend on the substrate. Formvar/UFP composite films apparently provide the strong interaction between the UFP and the support. No particle motion or the disappearance of small particles during TEM measurements have been observed.

Most Fe carbide UFP samples were nearly spherical and chain-like. The latter property may be related to a dipolar magnetic effect. Niklasson and his co-workers also observed the formation of chains of Fe and Co UFP's[17]. Previously, the spherical morphology was noted for UFP's of size less than 30 nm. Our experiments prove the same trend for Fe carbides with the size less than 20 nm. Their small size implies that particles are single domain.

In some cases of weak interactions between the UFP's and Formvar film, a significant UFP configurational instability was found. This resulted in a change of particle shape from spherical to polygonal thin flakes having low contrast.

Single Crystalline Structure Confirmation

The electron microdiffraction results obtained from the individual particle show single crystal structure (Fig.2). The sample crystalline structure has been identified as Fe_7C_3 structure. Comparison of XRD data with the TEM data showed good agreement, as shown in Table I. The XRD diffraction peaks are significantly broadened, a known consequence of the small crystallite size. It is suggested that the UFP's consist of stressed particles with a complicated distorted structure. Figure 3 shows the moire image caused by two single overlapping crystals, indicating defects or bending crystalline planes.

Table I. Comparison of TEM measured Size with those by XRD

Sample Number	Size (nm)	
	TEM	XRD
Run-1	23.8	19.8
Run-2	10.8	8.4
Run-3	5.6	5.2

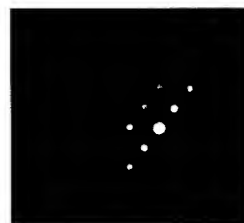


Fig. 2. Micro-Electron Diffraction Pattern obtained from the individual particle of UFP sample.

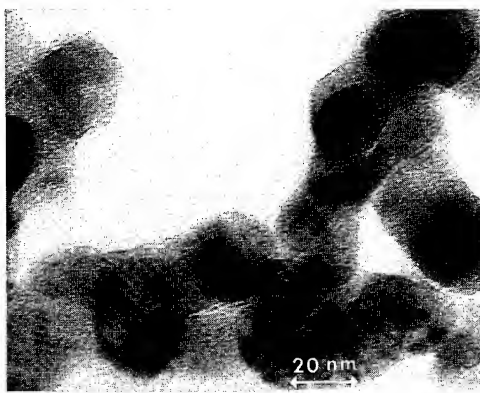


Fig. 3. Moire Fringes resulted from two single overlapping crystals in UFP samples.

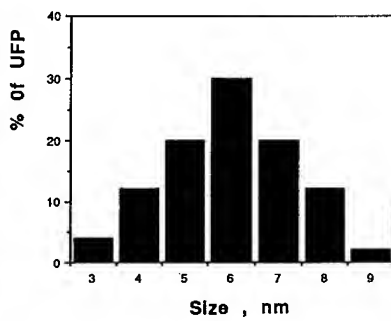


Fig. 4. Size Distribution Diagram by Counting 100 Particles.

UFP Size Variation

A number of samples of Fe carbide UFP produced with different reactant gas flow rate, chamber pressure and laser power were analyzed by TEM for their size and size distribution. Figure 4 shows the typical size distribution diagram. From the results shown in Table 1, it is clear that increasing the gas flow rate as the increase of the run number caused decreased size due to a decreased time in the reaction zone. For run-3 sample with the highest gas flow rate, is indicated the smallest size, 5.6 nm. In addition, the different crystalline structures of UFP's appear to be of different size.

CONCLUSIONS

1. Formvar embedded film is a feasible TEM specimen preparation method suitable for the UFP characterization, providing observable and individual UFP's, efficiently preventing their exposure to air, and decreasing the interaction between the electron beam and UFP.
2. Optimal concentration of the Formvar solution for the film preparation is 1.38 %.
3. Iron carbide UFP's have spherical morphology and chain structure with sizes between 5-20 nm. The single crystalline structure of the Fe carbides was confirmed.
4. Sizes of iron carbide UFP's depends on the laser pyrolysis condition and crystalline structure.

ACKNOWLEDGEMENTS

The authors would like to thank Dr. Peter C. Eklund for UFP samples and Dr. Robert J. Jacob for use of the TEM. One of us (H.F.N.) wishes to thank them for their helpful discussion and Mr. Larry A. Rice for the microdiffraction work. H.F.N. gratefully acknowledge Dr. Frank. J. Derbyshire for his valuable comments on the manuscript preparation.

This work was performed at the CAER, University of Kentucky. We acknowledge the financial support of the Commonwealth of Kentucky and the U.S. Department of Energy.

REFERENCES

1. C. Hayashi, Physics Today, **12**, 44 (1987).
2. E. R. Buckle, P. Tsakirooulos, and K. C. Poiton, International Metals Reviews, **31** (6), 258 (1986).
3. T. Sato, T. Iijima, M. Seki and N. Inagaki, J. of Mag. Mater. **65**, 252 (1986).
4. F. J. Derbyshire, B. H. Davis, P. C. Eklund, R. Keogh, J. M. Stencel and M. Thwaites, Proc. Symp. S. Mater. Res. Soc. Mtg., 171 (1990).
5. P. C. Eklund, J. M. Stencel, X. X. Bi, R. A. Keogh and F. J. Derbyshire, Preprints, ACS Mtg., Fuel Chemistry Div., **36** (2), 551 (1991).
6. D. Girardin and M. Maurer, Mat. Res. Bull. **25**, 119 (1990).
7. R. J. Matyi, L. H. Schwartz and J. B. Butt, Cat. Rev.-Sci. Eng. **29** (1), 41 (1991).
8. M. M. Morra and R. R. Biederman, Mater. Sci. and Eng., **A124**, 55 (1990).
9. M. Seki, T. Sato and S. Usui, J. Appl. Phys., **63** (5), 1424 (1988).
10. R. Srinivasan, R. A. Keogh and B. H. Davis, Preprints, ACS Mtg., Fuel Chemistry Div., **38** (1), 203 (1993).
11. S. Iijima and T. Ichihashi, Phys. Rev. Lett., **56** (6), 616 (1986).
12. D. J. Smith, A. K. Petford-Long, L. R. Wallenberg and J.-O. Bovin, Science, **233**, 872 (1986).
13. J. M. Stencel, P. C. Eklund, X-X. Bi and F. J. Derbyshire, Catalysis Today, **15**, 285 (1992).
14. X-X. Bi, B. Ganguly, G. P. Huffman, F. E. Huggins, M. Endo and P. C. Eklund, J. Mater. Res. **8** (7), 1666 (1993).
15. J. Dundurs, L. D. Marks and P. M. Ajayan, Phil. Mag., **A57**, 605 (1988).
16. M. Jose-Yacaman and M. Avalos-Borja, Catal. Rev.-Sci. Eng. **34** (1&2), 55 (1992).
17. G. A. Niklasson, A. Torebring, C. Larsson, C. G. Grangqvist and T. Farestam, Phys. Rev. Lett., **60** (17), 1735 (1988).

COMPOSITION AND STRAIN ANALYSIS OF SEMICONDUCTOR HETEROSTRUCTURES USING THICKNESS FRINGES ON TEM IMAGES

H. KAKIBAYASHI*, R. TSUNETA* AND F. NAGATA**

*Hitachi, Ltd., Central Research Laboratory, Kokubunji, Tokyo 185, Japan

**Hitachi Instrument Engineering, Ltd., Katsuta, Ibaraki 312, Japan

ABSTRACT

Composition and strain depth profiles in heterostructures such as AlGaAs/GaAs, InGaAs/InP and SiGe/Si have been analyzed with a high resolution of 0.5 nm by using the thickness fringes in a transmission electron microscope image. This diagnostic method is found to successfully evaluate the compositional disordering caused by annealing multiple quantum well structures with abrupt interfaces, and determine the difference in strain distribution in the strained-layers with various lattice mismatches. Both the composition and strain depth-profiles are analyzed quantitatively by the image simulation based on the dynamical theory of electron diffraction. This method is also useful for sensitively detecting ion-implantation-induced defects.

INTRODUCTION

High-performance electronic and optical devices have been developed utilizing both disordered and strained heterostructures.¹ The former are formed locally by destroying the abrupt heterointerface by annealing and ion implantation. The latter consist of layers in which the lattice is mismatched to the substrate without forming misfit dislocations. Disorder reduces parasitic resistance in the electron devices, which originates from the band discontinuity at the heterointerfaces. Lattice strain enhances the splitting of heavy and light holes, and improves lasing characteristics such as threshold current and differential gain.

It has been very difficult to measure the composition and strain distributions in nanometer-scale areas near the heterointerface because of the poor spatial resolution inherent in conventional analytical methods such as Auger electron spectroscopy and X-ray diffraction. A cross-sectional image taken with a high-resolution transmission electron microscope (TEM), which can directly observe heterointerface structure on an atomic order,² is shown in Fig. 1. In this image, InGaAs and InP layers can be identified by scattering and/or diffraction contrast. However, it is not clear why the abruptness seems to be different in the upper and lower heterointerfaces.

The authors have proposed a new method for evaluating these lattice-matched and strained heterostructures based on thickness fringes in the TEM image.³ This method allows the composition and strain profiles to be measured with a high spatial resolution of 0.5 nm. In this study, the method is applied to evaluate the heterostructures of both compound and Si semiconductors formed under various growth conditions.

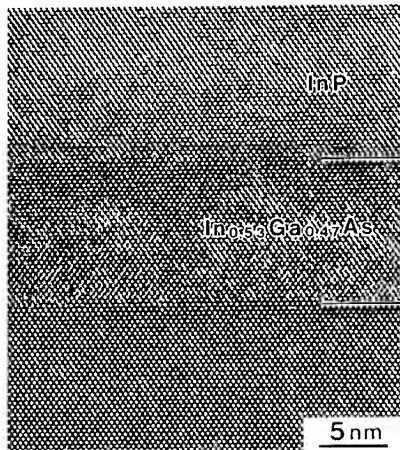


Figure 1. Cross-sectional high-resolution TEM image of the InGaAs/InP heterostructure.

METHODOLOGY

Principle of composition and strain analysis based on thickness fringe

This method uses wedge-shaped specimens prepared by cleaving along the (110) and (110) crystal planes. A 1.0 x 0.5 x 0.2-mm specimen is mounted on a TEM specimen holder with a tilting stage. The geometry of the TEM imaging condition is shown in Fig. 2. The incident electron is multiple-scattered in the crystal and the intensity distribution of transmitted electrons oscillates with a period D (extinction distance). D is inversely proportional to the product of the crystal structure factor and the function of the electron diffraction condition, as shown in Fig. 2. The structure factor is a function of composition and the diffraction condition changes according to the bending of crystal planes induced by lattice strain. As a result, the composition and strain are detected as fringe shifts in the TEM image corresponding to changes in D .

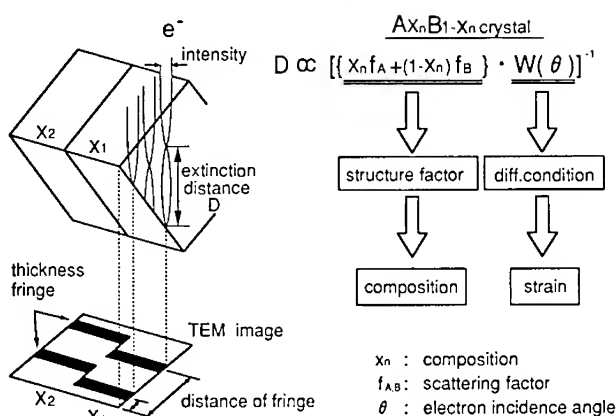


Figure 2. Geometry of TEM imaging condition of the cleaved specimen, and the principle of the composition and strain analysis based on thickness fringe.

Specimen preparation and TEM observation

Si-doped $\text{Al}_{0.3}\text{Ga}_{0.7}\text{As}/\text{GaAs}$, $\text{In}_{1-x}\text{Ga}_x\text{As}/\text{InP}$, and $\text{Si}_{1-x}\text{Ge}_x/\text{Si}$ heterostructures were grown by molecular beam epitaxy and metalorganic vapor phase epitaxy. $\text{AlGaAs}/\text{GaAs}$ was grown on a $\text{GaAs}(100)$ substrate at 650 °C, InGaAs/InP on an $\text{InP}(100)$ at 600 °C, and SiGe/Si on $\text{Si}(100)$ at 520 °C. The alloy ratios x were varied from 0.4 to 0.54 for $\text{In}_{1-x}\text{Ga}_x\text{As}$ and from 0.06 to 0.2 for $\text{Si}_{1-x}\text{Ge}_x$. $\text{AlGaAs}/\text{GaAs}$ was annealed in ambient H_2 at 750–800 °C using a CVD SiO_2 cap (20-nm thick) deposited on top of the samples. $\text{Si}(100)$ substrates were also prepared by B^+ and P^+ ion implantation from the surface. A Hitachi H-800 TEM with a specially designed specimen holder was operated at 175 kV. The electron beam was illuminated from the [100] direction to the edge of the cleaved specimen, resulting in bright- and dark-field images.

RESULTS AND DISCUSSIONS

Composition analysis of disordered AlGaAs/GaAs heterostructures

Si-doped ($3 \times 10^{18} \text{ cm}^{-3}$) $\text{Al}_{0.3}\text{Ga}_{0.7}\text{As}$ (10-nm thick)/un-doped GaAs (10-nm thick) structures are observed before and after annealing for 15 min at 750 °C and 800 °C, as shown in Fig. 3. The left end of each image is the edge of the wedge-shaped specimen. The heterostructure is grown vertically. The GaAs and AlGaAs layers are visible as horizontal stripes. The thickness fringes run in the vertical direction and their positions shift according to the Al compositions of each layer. In the as-grown state, thickness fringes shift sharply at the heterointerfaces. After 750 °C annealing, they incline and broaden. The change in the thickness fringes suggests a change in the compositional transition width caused by the interdiffusion of Ga and Al atoms between the GaAs and AlGaAs layers. It is well known that Ga atoms diffuse from GaAs into the SiO_2 cap

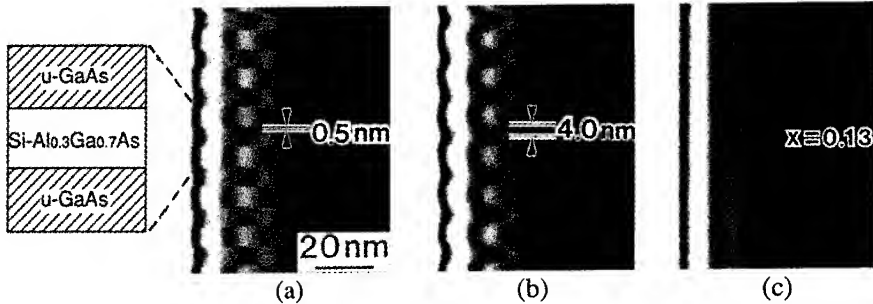


Figure 3. Cross-sectional TEM images of cleaved specimens including Si-doped ($3 \times 10^{18} \text{ cm}^{-3}$) $\text{Al}_{0.3}\text{Ga}_{0.7}\text{As}$ / un-doped GaAs heterostructures before (a) and after annealing for 15 min at 750 °C (b) and 800 °C (c).

during annealing.⁴ Outdiffusion of Ga atoms suggests that Ga vacancies form in the crystal. This Ga vacancy seems to play an important role in the Si-induced disordering.⁵

The compositional depth-profile in the transition region can be analyzed quantitatively by computer simulation of thickness fringes based on the dynamical electron diffraction theory, as shown in Fig. 4. The simulated thickness fringes with various transition widths are calculated as the Al composition changes linearly from 0.0 to 3.0 in the transition region, as shown in the right-hand figure. By comparing the observed to the simulated images, the transition widths are determined to be less than 0.5 nm in the as-grown condition and 4 nm after 750 °C annealing. After 800 °C annealing, the thickness fringes through the heterostructure straighten out, as shown in Fig. 3(c). This figure also shows that the heterostructure becomes perfectly disordered. The Al composition x of the disordered structure is analyzed and found to be 0.13 from the intensity distribution of thickness fringes.

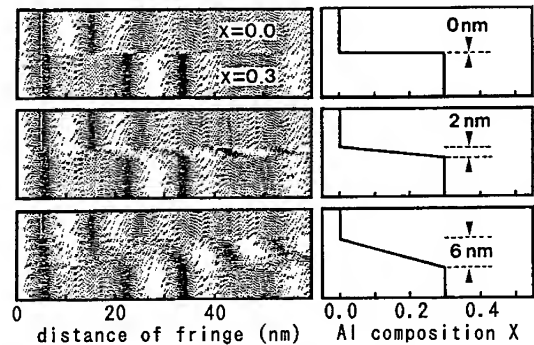


Figure 4. Simulated thickness fringes of $\text{Al}_{0.3}\text{Ga}_{0.7}\text{As}/\text{GaAs}$ heterointerfaces with various compositional transition widths. Simulated images are shown on the left, and compositional depth-profiles are shown on the right.

Strain analysis of InGaAs/InP strained heterostructures

Figure 5 shows TEM images of two kinds of $\text{In}_{1-x}\text{Ga}_x\text{As}/\text{InP}$ strained heterostructures with +0.5% compressive strain in the $\text{In}_{0.6}\text{Ga}_{0.4}\text{As}$ layers (a) and with mixed +0.5% compressive and -0.5% tensile strain in the $\text{In}_{0.6}\text{Ga}_{0.4}\text{As}$ and $\text{In}_{0.46}\text{Ga}_{0.54}\text{As}$ layers (b). The $\text{In}_{1-x}\text{Ga}_x\text{As}$ layers are 75-nm thick. The thickness fringes bend near the upper and lower InP/multiple quantum-wells (MQW) interfaces in (a). The region of fringe bending in the InP layer is about 40-nm thick. The compositional transition widths of the heterostructures in both (a) and (b) are confirmed to be less than a few nm wide by other analytical methods such as Auger electron spectroscopy and secondary ion mass spectroscopy. Therefore, the fringe bending in this case results from changes in the Bragg condition caused by the distortion in the crystal planes around the interface having a lattice mismatch between the InP layer and MQW.⁶ Thus, the fringe shape corresponds to the strain distribution. The amount of fringe bending reduces with increasing distance from the interface and decreasing strain. On the other hand, no fringe bending appears in the image of specimen (b)

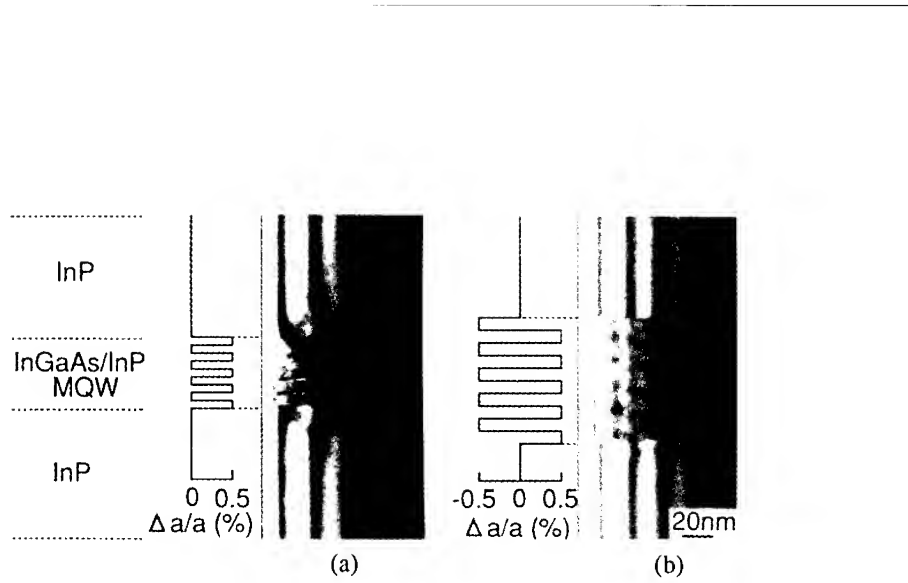


Figure 5. Cross-sectional TEM images of $In_{1-x}Ga_xAs/InP$ heterostructures with $+0.5\%$ strain (a) and $\pm 0.5\%$ mixed strain (b) in multiple quantum wells (MQW).

in spite of a $\pm 0.5\%$ strain. This indicates that there is no bending of crystal planes changing the Bragg condition.

The strained lattice structures of the specimens are interpreted as shown in Fig. (6) (a) and (b). Both the InP and MQW lattices are distorted continuously until a lattice match occurs in (a). This structure is characterized by crystal planes bending in the transition region with thickness T . The inclination angle θ of the bending plane is highest at the InP/MQW interface and decreases with increasing distance from the interface. Simulated thickness fringes in the transition regions T for various θ distributions are shown in Fig. 7. The effect of a potential difference at the interface is assumed to be negligible. θ is considered to be the deviation angle of the incident electron beam from the [100] axis. The distribution of θ in the growth direction is assumed to be triangular, as shown in the right-hand figure. Fringe bending increases with increasing the maximum θ , which corresponds to the degree of strain. By comparing the simulated and observed thickness fringes, the maximum θ in specimen (a) is estimated to be about 5 mrad. Simulation suggests that the

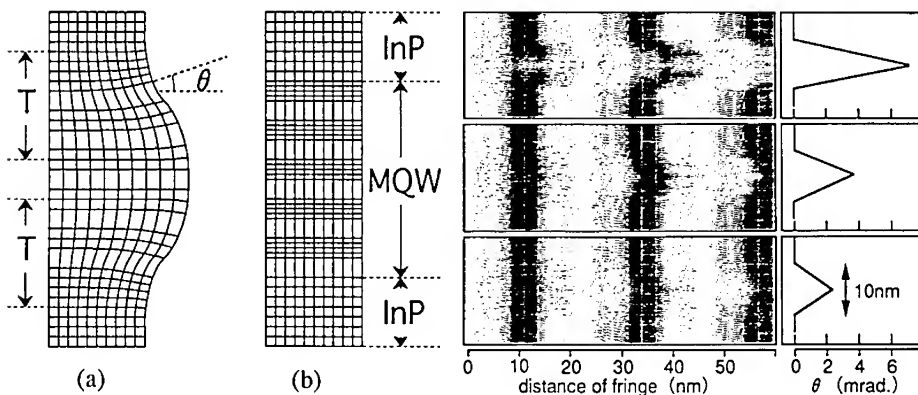


Figure 6. Strained lattice structures at the InP/MQW interface. (a) is distorted continuously near the interface until a lattice match occurs. (b) is based on the expansion and/or shrinkage of the lattice constant in a MQW.

Figure 7. Simulated thickness fringe in the strain transition region T shown in Fig. 6(a). Simulated images are shown on the left, and the distributions of the crystal plane's inclination angle are shown in the right.

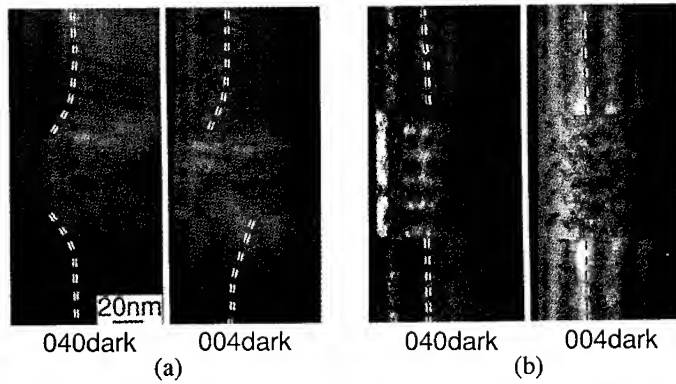


Figure 8. 040 and 004 dark-field images of $In_{1-x}Ga_xAs/InP$ heterostructures with $+0.5\%$ strain (a) and $\pm 0.5\%$ mixed strain (b) in a MQW.

minimum θ detectable as a fringe shift is less than 1.0 mrad. Therefore, the strained lattice structure of specimen (b) is considered to have a MQW whose lattice changes from cubic to tetragonal, as shown in Fig. 6(b). Namely, a MQW lattice is completely elastic-strained by the mixed compressive and tensile strain.

Figure 8 shows 040 and 004 dark-field images of the same specimens at [100] axial incidence. The 040 lattice plane is parallel to the InP/MQW interface, while the 004 plane is vertical to it. In the case of specimen (b), thickness fringes in both the upper and lower InP layers bend to the left-hand side in the 040 dark-field image, but to opposite sides in the 004 dark-field image. The fringe shift to the left-hand side indicates an increase in the deviation from the Bragg condition of 040 and 004 reflections. Each fringe shift is interpreted as a crystal plane's rotation around a crystal axis.⁷ The 040 planes in both the upper and lower InP layers rotate counterclockwise around the [100] axis, while the 004 planes rotate around the [010] axis, counterclockwise for the upper and clockwise for the lower. It is clear that there is no crystal-plane rotation in the case of specimen (b). In this way, the strained lattice structure is analyzed in three dimensions using dark-field images of various reflections.

Structure analysis of ion-implanted Si substrates and SiGe/Si heterostructures

Damaged layers near the surface of Si(100) substrates are formed by B^+ and P^+ ion implantation (50 keV, $1 \times 10^{16} \text{ cm}^{-2}$), as shown in Fig. 9(a) and (b), respectively. In the case of P^+ ion implantation (a), the thickness fringes disappear between the surface and a 120-nm depth. This indicates that the crystal structure of the damaged layer is amorphous. In the interface between amorphous and crystalline Si, there are many dotted contrasts resulting from defects formed by the knock-on damage. The density of these dotted contrasts decreases with increasing distance from the interface. Such defect contrast is enhanced in the thickness fringe image more than in the usual TEM image. The amorphous damaged layer is not observed in the case of B^+ ion implantation (b). Only the defect contrast exists between the surface and a 180-nm depth. The different crystal structures in B^+ and P^+ ion implantation are considered to depend on the mass of the implanted ion. The projected range and its straggling are generally larger in a light ion (in this case B^+) than a heavy ion (in this case P^+) at the same acceleration energy. Therefore, light-ion implantation results in the formation of defects because of a low probability of nuclear collisions weakening Si-Si bonding.

Figure 9(c) and (d) show TEM images of 90-nm-thick $Si_{1-x}Ge_x/Si$ heterostructures. Their lattice mismatches to the Si substrate are 0.25 % in Ga composition $x=0.06$ and 0.8 % in $x=0.2$. Because the differences in the crystal structure factors for low Ga compositions are not sufficiently large, there is scarcely any difference in the thickness-fringe position between the $Si_{1-x}Ge_x$

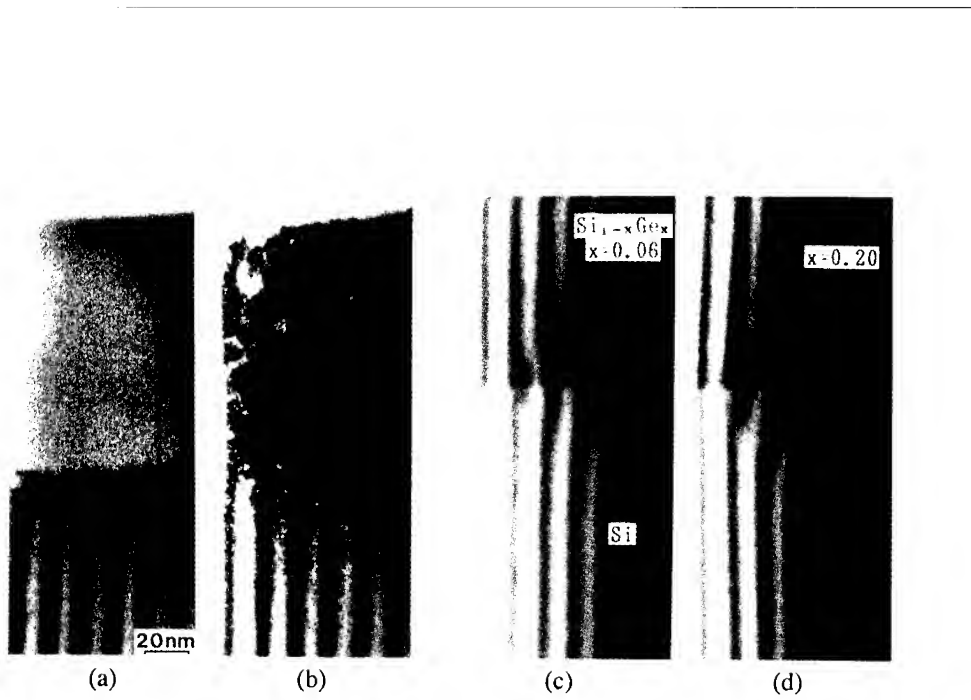


Figure 9. Cross-sectional TEM images of Si(100) substrates implanted with P⁺ ion (a) and B⁺ ion (b), and Si_{1-x}Ge_x/Si heterostructures with Ga composition x=0.06 (c) and x=0.2 (d).

bulk crystal and the Si substrate. The fringe bending near the interface indicates strain distribution in Si_{1-x}Ge_x and Si crystals as well as in InGaAs/InP (Fig. 5). Fringe bending is more extensive at x=0.2 (b) than x=0.06 (a). It is found that the inclination angle of the bending crystal planes is larger in (b) than (a), based on their lattice mismatches.

SUMMARY

The thickness-fringe method has facilitated direct observation of the composition and strain distributions in nanometer-scale areas, which are difficult to measure by conventional analytical methods. Although this method has been used for compound semiconductors such as GaAs and InP as before, the present study shows that applying it to Si is also very useful. Therefore, this method also satisfies the requirement for a valid form of diagnosis for advanced memory devices, such as DRAM and SRAM, which require detailed structural characterization.

ACKNOWLEDGMENTS

The authors would like to thank Mr. T. Tsuchiya, Mr. S. Goto and Mr. A. Nishida for providing the samples, and Prof. N. Tanaka and Prof. K. Mihama for their valuable comments. Thanks are also due to Dr. M. Miyao and Dr. Y. Mitsui for their encouragement during this study.

REFERENCES

1. P. J. A. Thijs, L. F. Tiemeijer, P. T. Kuindersma, J. I. M. Binsma and T. V. Dongen, IEEE J. Quantum Electron. **27**, 1426 (1991).
2. P. M. Petroff, A. C. Gossard, W. Wiegmann and A. Savage, J. Crystal Growth **44**, 5 (1978).
3. H. Kakibayashi and K. Itoh, Jpn. J. Appl. Phys. **30**, L52 (1991).
4. X. Wang, J. Electrochem. Soc. **130**, 950 (1983).
5. S. Goto, H. Kakibayashi, M. Kawata and T. Usagawa, Appl. Surf. Sci. **41/42**, 480 (1989).
6. T. Tsuchiya, T. Taniwatari and T. Kawano, Int. Symp. Gallium Arsenide and Related Compounds, 1992, Inst. Phys. Conf. Ser. No. 129, 269 (1993).
7. N. Tanaka, K. Mihama and H. Kakibayashi, Jpn. J. Appl. Phys. **30**, L959 (1991).

ELECTRON HOLOGRAPHY OF FLUX LATTICES IN NIOBIUM

J.E. BONEVICH, K. HARADA, T. MATSUDA, H. KASAI, T. YOSHIDA, G. POZZI[†]

and A. TONOMURA

Hitachi Advanced Research Laboratory, Hatoyama, Saitama 350-03 JAPAN

[†]Dept. of Physics, Univ. of Bologna, via Iternio 46, 40126 Bologna, ITALIA

ABSTRACT

Magnetic lines of force penetrating a superconducting thin foil have been investigated by means of electron holography. A field-emission TEM with a specially constructed cold stage was used to cool a Nb thin foil down to 4.5 K and apply magnetic fields up to 100 G. The specimen is tilted by 45° to both the electron beam and the magnetic field (applied horizontally) allowing the 2-D lattice of penetrating flux-lines to be discerned. The phase distribution of electrons transmitted through the specimen were quantitatively measured. Interference micrographs revealed tiny regions where the phase distribution rapidly changed. These regions coincided spatially with the spot-like contrast observed by Lorentz microscopy and were found to be quantized vortices containing a flux of $h/2e$. The experimental results were in good agreement with those predicted by theoretical simulations. Experiments exploring the vortex inner core structure at high resolution are presented.

INTRODUCTION

Superconductors are of widespread interest in materials science and many research efforts have concentrated on exploring the behavior of these materials while in the superconducting state. In the past, various methods have been used to detect the presence of quantized magnetic flux lines (henceforth called fluxons or vortices) in superconducting specimens. For example, static images of the vortices have been provided by the Bitter magnetic decoration [1,2] or scanning tunneling microscopy [3] methods. Electron holography [4] has been previously used to investigate the dynamic behavior of magnetic fields close to the surface of a superconductor [5], but the 2-D vortex lattice could not be observed.

Recently, we succeeded in observing for the first time the fluxon lattice in a thin specimen by means of transmission electron microscopy. Lorentz microscopy has been employed to study the dynamic behavior of vortices [6,7]. In this technique, the phase difference produced by the fluxons in a tilted specimen [8] is manifested in a defocused plane as spots of bright and dark contrast. In the Lorentz mode, we have observed the behavior of fluxons in response to applied magnetic fields and temperature, as well as the interaction of fluxons with specimen defects such as dislocations and grain boundaries.

However, a disadvantage of the Lorentz mode, as well as of the other standard phase contrast methods in electron microscopy [9], is that it is very difficult to extract quantitative information from the experimental data. For instance, the Lorentz micrograph indicates both the location and the polarity of the fluxons, but not the degree of flux quantization ($h/2e$), which plays an important role in the field of superconductivity, being composed of the ratio of two fundamental physical constants. In contrast, electron holography measures the amplitude and phase information of the entire object and it is possible to quantitatively extract this information from the holograms. Therefore it can be used to measure the flux quantitatively and with a higher spatial resolution than the Lorentz mode. For these reasons it is important to apply electron holography to the investigation of the flux-line distribution in superconductors [10]. This paper presents the results obtained in observation of thin superconducting Nb specimens at high resolution.

EXPERIMENTAL METHOD

The thin foil specimens used for transmission observation were prepared by chemically polishing $2 \times 2 \text{ mm}^2$ wide by $7 \mu\text{m}$ thick Nb ($T_c = 9.2 \text{ K}$, resistance ratio $R_{300 \text{ K}} / R_{10 \text{ K}} \approx 20$) sections that had been annealed to $\sim 2000^\circ\text{C}$ in a vacuum of 10^{-6} Pa . The annealing resulted in a grain size of 200 to $300 \mu\text{m}$ with a [110] texture.

The experiments were conducted in a 300 keV cold-tip field emission holography electron microscope developed to provide a highly coherent and bright source of electrons [11]. The FE-HEM is equipped with a specially constructed cold stage that allows magnetic fields to be applied while the specimen, tilted at 45° with respect to the electron beam and the magnetic field, can be maintained at temperatures from 4.5 K to 26 K. This cold stage enables the user to study the behavior of superconductors under both equilibrium and dynamic conditions. The microscope is also equipped with a standard rotatable electron biprism [12] used to form the holograms, shown schematically in Fig. 1. The holography method is a two-step process [4]. First, a hologram containing the amplitude and phase information of the object is recorded on electron microscope film. The holograms were then digitized and reconstructed to extract and quantitatively analyze the phase information. During the reconstruction process, a comparison wave is interfered with the object wave (hologram) to produce contour fringes of constant phase. By choosing the appropriate interference conditions, i.e., tilting

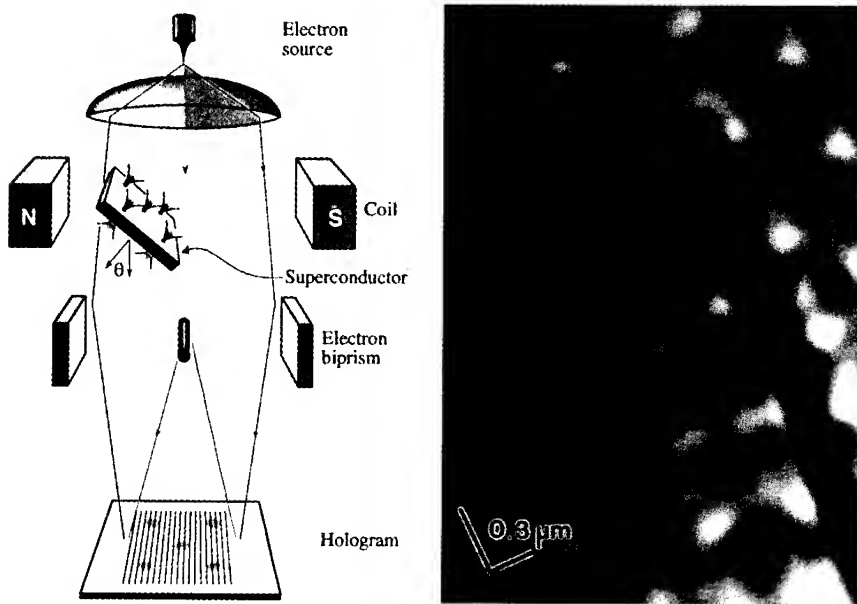


FIG.1. Experimental configuration. The superconducting specimen is tilted by 45° with respect to the electron beam. The magnetic field is applied in the horizontal plane. The electrons passing through the specimen (object wave) are interfered with the vacuum (reference wave) via the biprism forming a hologram.

FIG.2. Lorentz image of the flux line lattice at 100 G and 4.5 K. The phase differences produced by the fluxons are revealed in a 20 mm defocused image. The vortex core is located in the intersection between bright and dark contrast spots.

the comparison wave, a phase map of the vortex lattice is created. The phase differences produced by the flux line lattices are quite small and for this reason the hologram is phase-amplified [13] to increase the sensitivity to the phase distribution.

However, to satisfy in the electron microscope the ideal condition of having an unperturbed reference (plane) wave coming from the vacuum region, an interference distance as large as possible between the object and the reference wave should be chosen [14]. In addition, the biprism interference fringe spacing referred to the specimen should be as small as possible, as this parameter affects the hologram resolution, roughly given by three times the above spacing. Given that the interference distance and inverse fringe spacing are both proportional to the biprism voltage, by increasing the latter the ideal conditions can be approached. Unfortunately, this is possible only to a limited extent owing to the lateral coherence of the electron beam, which diminishes the fringe contrast and hence the hologram quality as the interference distance is increased.

A compromise between these opposing requirements, and the limitations set by the recording medium and the mechanical and electrical stability, can be reached by carrying out the observations with the objective lens switched-off, and imaging with the intermediate lens, so that the hologram has an overall electron optical magnification of 1800 \times , with a carrier fringe spacing referred to the specimen of about 30 nm. These optical conditions comprise relatively low resolution electron holograms as their information limit is approximately 100 nm. The resolution can be increased by using the objective lens to focus on the specimen and subsequently forming a hologram in the usual fashion. Since the objective lens magnifies the specimen with respect to the biprism (by a factor of 3-4), the hologram resolution can be improved to better than 30 nm. However, it is important to remember that the interference width of the corresponding hologram will be reduced (to $\sim 1\mu\text{m}$) and therefore the reference wave in the hologram will be more strongly attenuated by the long-range magnetic fields surrounding the specimen. Holograms with both of these optical configurations have been taken with exposure times of about 30 sec.

RESULTS AND DISCUSSION

The detection of the fluxon lattice in the specimen was first made by means of Lorentz microscopy. A typical example is shown in Fig. 2 where the Nb foil was cooled to 4.5 K in a field of 100 G. This Lorentz image was defocused by 20 mm to reveal the presence of the vortices. Each vortex is composed of adjacent spots of light and dark contrast with the vortex core being oriented in between them. Bend contours are present due to the slight deformation of the self-supporting thin foil. The vortices have arranged themselves along the direction of the applied magnetic field.

Holograms were then taken of the same specimen region under the in-focus condition. The interference micrograph shown in Fig. 3 is 16 \times phase amplified so that the phase difference between each dark contour line, given by $\Delta\phi = (2\pi/n)$ where n is the phase amplification, is $\Delta\phi = \pi/8$. The tilt of the plane wave in the reconstruction was chosen in such a way that the contour fringes were running in the same direction as the magnetic field. With this choice it is important to note that the fringe contours become narrowly spaced at the regions corresponding to the vortex location. Comparison with the Lorentz image reveals that the spot-like vortex contrast spatially coincides with the regions of finely spaced contours. In regions between vortex cores the fringe contours are widely spaced.

A smaller region containing a few fluxons was processed via a computer with dedicated software. Before digitizing the hologram, it was aligned so that the fluxon axis was parallel to the vertical axis. The tilt of the wave in the reconstruction was first chosen in such a way to have the overall phase as flat as possible over the whole region. Then an additional tilt was introduced, so that the phases on both sides of the fluxon were as flat as possible: in this

condition the contour map, Fig. 4, best resembles the expected contour map and the phase difference due to the fluxon can be evaluated.

The Aharonov-Bohm effect [15] predicts that a magnetic flux Φ causes a phase difference $\Delta\phi$ between two coherent electron wavefronts passing on either side of the flux;

$$\Delta\phi = 2\pi \frac{\Phi}{h/e} \quad . \quad (1)$$

Therefore, a singly quantized flux (2.07×10^{-15} Wb, or $h/2e$) produces an electron phase difference of exactly π . However, the phase differences produced by fluxons in this study have been measured to be about $\sim 0.5\pi$. At first glance, the measured phase difference would appear in conflict with the theoretical expectations, but it is important to recall that the specimen is tilted to the electron beam. That is, the AB effect predicts a phase difference in proportion to the flux that is enclosed by the electron paths, i.e., only the flux that *penetrates* the plane of the electron paths contributes to a phase difference. The discrepancy between theory and experiment arising from specimen tilt [8] can be accounted for by a simple geometrical model.

Consider the case of a very thin superconductor that has been penetrated by a single fluxon. While the total enclosed flux penetrating the superconductor is Φ_0 not all of this flux is also enclosed by the electron paths. Consequently, the phase difference measured is reduced when the specimen is tilted with respect to the electron beam as;

$$\Delta\phi = 2(2\theta) \frac{\Phi}{h/e} \quad , \quad (2)$$

where θ is the angle between the superconductor and the electron beam, see Fig. 1. Thus in the present study ($\theta = 45^\circ$), the phase difference is expected to be $\pi/2$. Previously in holography [5], the specimen was parallel to the electron beam ($\theta = 90^\circ$) and the expected phase difference of π is recovered. When the plane of the specimen lays perpendicular to the electron beam (untilted, transmission case), no phase difference is expected [8].

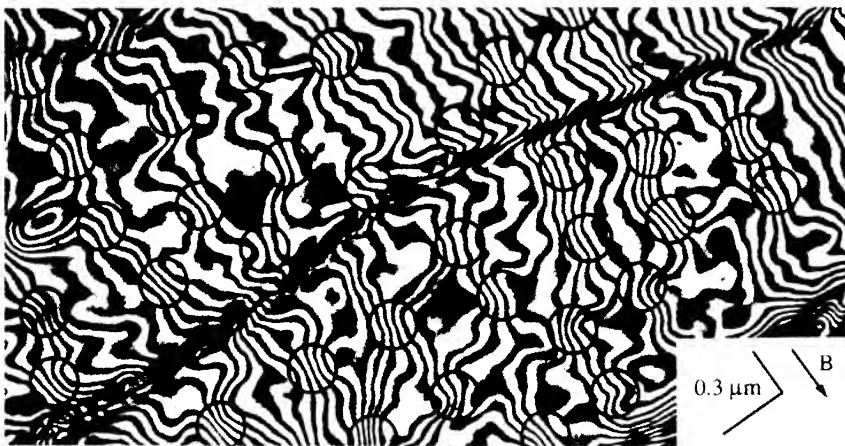


FIG.3. Interference micrograph of the flux-line lattice at 4.5 K and 100 G (16x phase map). Equiphase contours become narrowly spaced (circled) indicating the presence of vortices.

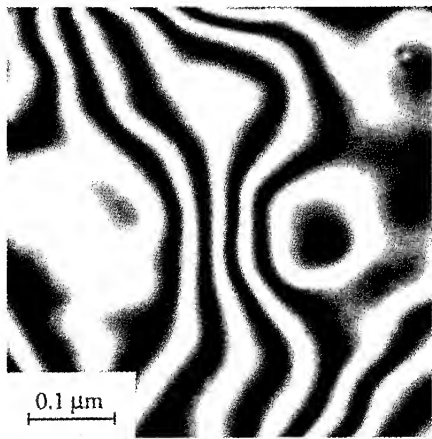


FIG.4. Single flux vortex at 4.5 K and 100 G. The phase difference produced is 0.55π .

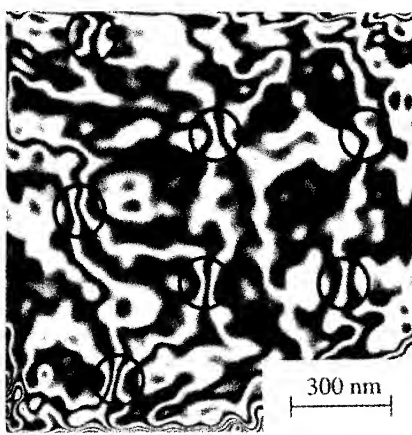


FIG.5. Vortices at 4.5 K and 10 G. Phase is corrected to compensate reference wave.

Equation (2) assumes a very thin superconductor, and so the contribution from the vortex core can be neglected. However, a real specimen has a thickness on the order of the penetration depth ($t \approx 2\lambda_L$) and in this case we must consider the structure of the vortex core. In this situation, the presence of a finite *length* of core will increase the amount of flux enclosed by the electron paths and the resulting phase differences will be greater than $\pi/2$.

Ideally, the high resolution of holography is a unique tool to investigate the structure of vortex cores in superconductors. Indeed, the reconstructions in this study have shown the magnetic flux to be well aligned in the core and the cores themselves measure ~ 100 nm in dimension. However, it must be noted that the resolution limit of these reconstructions is of the same order of magnitude and thus the size of the flux cores may, in fact, be resolution-limited. For example, simulations of vortex lattices [16] predict cores with smaller sizes and sharper contrast features than those measured in the low resolution holograms.

Higher Resolution Holography

Therefore, we have endeavored to examine the flux-line lattice under higher resolution conditions by employing the objective as the focusing lens. However, there are drawbacks to this approach. By effectively magnifying the specimen with respect to the biprism the interference width of the corresponding hologram will be reduced to ~ 1.5 μm . This means that the “reference” wave interfered with the object wave can no longer be assumed to be an unperturbed plane wave. In fact, the magnetic field applied to the specimen strongly perturbs the reference wave complicating the reconstruction process. Furthermore, the narrow interference width means that only those vortices near the specimen edge may be examined increasing the possibility of vortex motion and core broadening due to thin film effects, etc.

Holograms formed under these higher resolution conditions were taken and compared with low resolution holograms. The reconstruction process was as follows: a region of the

hologram containing vortices was digitized with the fluxon axis oriented vertically. The tilt of the comparison wave was then adjusted so that the phase across the entire field of view was as flat as possible (because of the attenuation of the reference wave, substantial phase modulation remained). Then this phase map was fitted to a 3rd-order polynomial: the difference between them resulting in a corrected phase map. The corrected phase map could then be evaluated for the presence of vortices.

Fluxons reconstructed from a higher resolution hologram (Fig. 5) show several features. Firstly, while the equiphaseline contour lines flow smoothly through the vortex and spread out above and below the core, as expected, the shape of the core is somewhat sharper than in Fig. 4 supporting the results of the proposed model for the phase difference. Also the fluxon appears broader than the low resolution ones. This is most likely due to thin film effects as the narrow interference width restricts observable vortices to those near the edge where the specimen is only 30-50 nm ($\sim \lambda_L$) thick. Still, the measured phase difference from the hologram is $\sim 0.5\pi$ indicating no change in the degree of flux quantization in the vortices. One obvious drawback in the higher resolution holograms is that with the field of view limited to the specimen edge, bend contours in the thin foil affect the reconstructions. Vortices typically can be found near bend contours and the resulting interference micrographs show phase differences due to the both vortices and bend contours complicating unambiguous measurements of the phase. Consequently, only vortices well separated from specimen artifacts are suitable for phase reconstruction.

CONCLUSIONS

In summary, we have observed the 2-D flux line lattice in a Nb superconductor by means of electron holography. This technique is highly sensitive to the phase differences produced by singly quantized fluxes. Typical SQFs in thin regions of the specimen had measured phase differences of about $0.5\pi \pm 0.05\pi$, equivalent to $0.5(h/2e)$, in agreement with the theoretical predictions. The flux-line lattices examined with both high and low resolution holography were found to be in agreement, the latter requiring polynomial fitting of the phase to observe wide fields of view. The success of electron holography in detecting and evaluating the flux-line lattice in Nb holds promise for similar investigations in high T_c superconductors.

REFERENCES

1. V. Essman and H. Träuble, *Phys. Lett. A* **24**, 526 (1967).
2. G.J. Dolan et al., *Phys. Rev. Lett.* **62**, 2184 (1989).
3. H.F. Hess et al., *Phys. Rev. Lett.* **62**, 214 (1989).
4. A. Tonomura, *Rev. Mod. Phys.* **59**, 639 (1987).
5. T. Matsuda et al., *Phys. Rev. Lett.* **66**, 457 (1991).
6. K. Harada et al., *Nature* **360**, 51 (1992).
7. K. Harada et al., *Phys. Rev. Lett.* **71**, 3371 (1993).
8. A. Migliori, G. Pozzi and A. Tonomura, *Ultramicroscopy* **49**, 87 (1993).
9. J.N. Chapman, *J. Phys. D* **17**, 623 (1984).
10. J.E. Bonevich et al., *Phys. Rev. Lett.* **70**, 2952 (1993).
11. T. Kawasaki et al., *Jpn. J. Appl. Phys.* **29**, L508 (1990).
12. G. Möllenstedt and H. Düker, *Naturwissenschaften* **42**, 41 (1955).
13. J. Endo, T. Kawasaki, T. Matsuda, N. Osakabe and A. Tonomura, *Proc. of the 13th Internat'l. Comm. for Optics*, edited by H. Ohzu (ICO, Sapporo, 1984), p. 480.
14. G. Matteucci et al., *J. Appl. Phys.* **69**, 1835 (1991).
15. Y. Aharonov and D. Bohm, *Phys. Rev.* **115**, 485 (1959).
16. G. Pozzi, J. Bonevich and A. Tonomura, *Proc. 51th Ann. Meet. Microsc. Soc. Amer.*, edited by G.W. Bailey (San Francisco Press, San Francisco, 1993), p. 1224.

NANOINDENTATION ON CONTAMINATION-FREE GOLD FILMS USING THE ATOMIC FORCE MICROSCOPE

D. M. SCHAEFER AND R. REIFENBERGER
Purdue University, Department of Physics, W. Lafayette IN 47907

ABSTRACT

Nanoindentation experiments on high quality Au films were performed in vacuum using an atomic force microscope. In these experiments, elastic behavior was observed until loading forces greater than ~ 20 nN were applied. For loads larger than this, systematic changes in the jump-to-contact, loading/unloading and lift-off regions of the data occur. These observations are consistent with a transition from elastic to inelastic behavior during indentation.

INTRODUCTION

Non-contact force measurements using the atomic force microscope (AFM) can provide information about the attractive forces acting between a sharp tip and a surface.^{1,2} Contact data give localized measurements of the elastic properties of bulk materials³ as well as nanometer-size objects like supported gold clusters.⁴ Extensions of these techniques have permitted the study of adhesion between micron-size objects placed on an AFM cantilever and various substrates.^{5,6}

A common problem that plagues nanoindentation experiments at low loads is the presence of an uncontrolled contamination layer that is always present when operating under ambient conditions. To better understand nanoindentation data, it is essential to eliminate effects due to contamination which can hide interesting atomistic effects. It is for this reason that a series of systematic nanoindentation experiments were performed under vacuum conditions on a high quality Au film evaporated onto a mica substrate. Au was the material of choice in this study because of its known inertness to oxidation and because high quality films can be prepared in a relatively easy fashion.^{7,8}

EXPERIMENTAL APPARATUS AND FILM PREPARATION

The AFM used in these studies was a custom built instrument that has been described elsewhere.⁹ Si ultralevers¹⁰ were used exclusively during the course of this study. A determination of the tip radius was made after the acquisition of force data using standard TEM cross-section imaging techniques. Detection of the cantilever displacement was done using a laser deflection method.¹¹⁻¹³ A 68030 CPU based computer system similar to that described previously¹⁴ was used to handle all data acquisition and system control. Finally, a hysteresis correction system was employed to eliminate piezotube hysteresis and ensure linear motion of the sample.

The Au film was evaporated onto a mica substrate at 10^{-7} Torr. Prior to deposition, the freshly cleaved mica substrate was outgassed at a temperature of ~ 330 C. The Au was

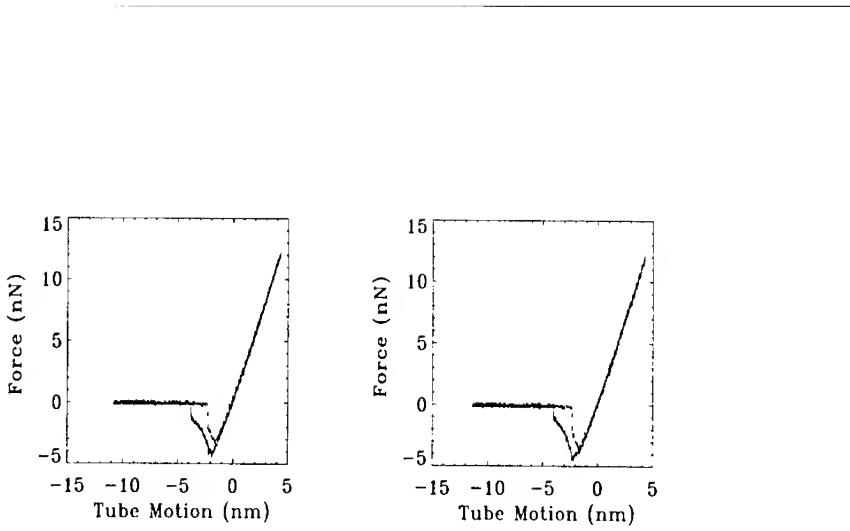


Figure 1: Two consecutive nanoindentation experiments performed on a 200nm thick Au film in vacuum.

evaporated onto the mica substrate until a film thickness of 200 nm was reached. After deposition was complete, the film was cooled to room temperature, removed from the evaporator and stored in a vacuum dessicator until placed in the AFM. STM scans of typical films grown in this way have revealed a surface morphology comprised of inter-locking, atomically flat, crystalline grains.

To eliminate unwanted contamination during these experiments, the AFM was mounted inside a stainless steel chamber which was evacuated to forepump pressures (~ 500 mTorr). This procedure was required to minimize contamination due to water vapor. As shown by Krim and co-workers,¹⁵ a water film with a thickness determined by the relative humidity forms on Au surfaces. By mounting our AFM in a vacuum chamber, thick layers of absorbed water (plus additional hydrocarbon adsorption) are eliminated.

RESULTS

The indentation of a gold film was studied under vacuum conditions by increasing the maximum loading force and sequentially repeating a nanoindentation experiment. Maximum loads of 6.4, 12.5, 19.0, 25.3, and 31.4 nN were used in succession. For maximum loads below ~ 20.0 nN, the nanoindentation data exhibit repeatable elastic behavior. This is illustrated in Fig. 1 which shows data from two sequential nanoindentation experiments performed at the same place on the 200 nm thick gold film under a 12.5 nN maximum loading force.

Several interesting observations can be made from the data obtained in this study. First, for loading forces less than 12.5 nN, the Au film responds elastically in a reproducible way (see Fig. 1). This should be contrasted to data obtained in air at lower forces, such as that shown in Fig. 2, which show evidence for large plastic deformation.

The plastic deformation observed in air but absent in vacuum is explained by the capillary force between the tip and sample due to water contamination. The capillary force, F_{cap} , between a spherical tip of radius R_{tip} and a flat surface covered by a thin liquid film can be expressed as¹⁶

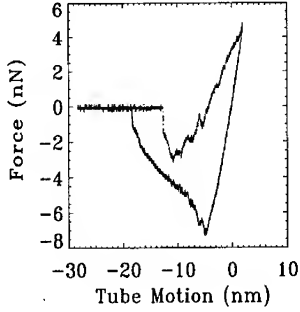


Figure 2: Nanoindentation data taken on Au in air at loading forces comparable to that used in Fig. 1.

$$F_{\text{cap}} = \frac{2\pi\gamma R_{\text{tip}}\Delta\mathcal{L}}{r_m} , \quad (1)$$

where γ is the surface tension of the liquid, $\Delta\mathcal{L}$ is the height of the water meniscus up the shank of the AFM tip, and r_m is the radius of curvature of the meniscus. For our experiment, typical values are $R_{\text{tip}} = 25$ nm, $\gamma(\text{H}_2\text{O}) = 72$ mJ/m², $\Delta\mathcal{L} = 2$ nm, and $r_m = 1$ nm, leading to a capillary force of ~ 25 nN. This additional force delivered across the contact area of the tip produces stresses which exceed the elastic limit of Au. Under these conditions, nanoindentation data taken on thin films in air will generally exhibit plastic behavior. In vacuum, the contamination layer is absent and elastic behavior is expected (and observed) for small applied loads.

For nanoindentation data taken at higher loads, a distinct transition is observed. This transition is illustrated in Fig. 3 which was obtained immediately after the data in Fig. 1 with a maximum applied load of ~ 19.0 nN. Several changes occur during this sequence of experiments. First, the jump to contact distance is observed to increase in a systematic way after each data run. This behavior is summarized in Fig. 4 (a) and implies a permanent modification to the Au film's surface. Secondly, the removal force increases after each nanoindentation experiment (see Fig. 4 (b)). Also, the pull off region is observed to change from a gradual separation to an abrupt jump from contact. Finally, the slope of the loading/unloading data increases with each successive indentation. All of these observations are consistent with an inelastic deformation of the Au surface.

These features can be analyzed in a semi-quantitative way by considering a van der Waals interaction between the AFM tip and the Au film. The jump to contact of the AFM tip occurs whenever the interaction force gradient based on the van der Waals interaction exceeds k , the cantilever spring constant. This will occur when

$$k = \frac{HR}{6z_{\text{jtc}}^3} \quad (2)$$

where H is the Hamaker constant, z_{jtc} is the jump to contact distance, and R is the effective

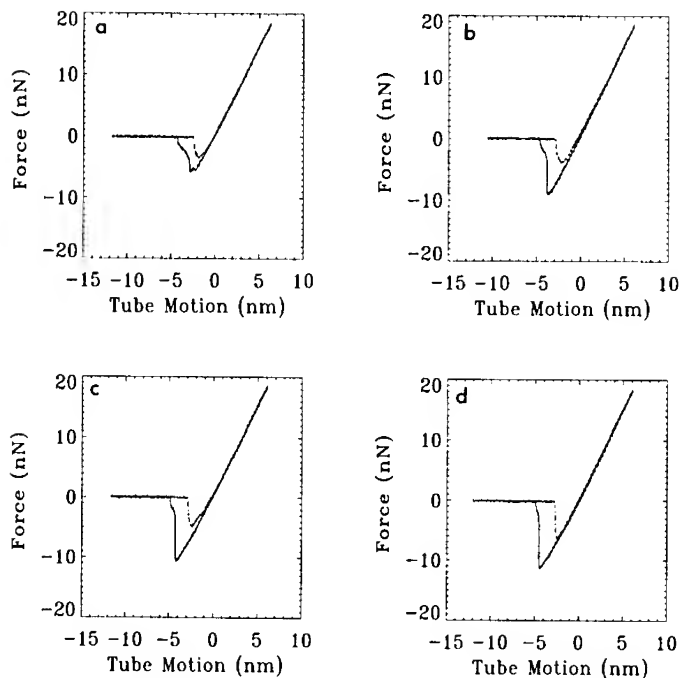


Figure 3: Sequential nanoindentation data obtained in vacuum from the same place on a 200 nm thick Au film.

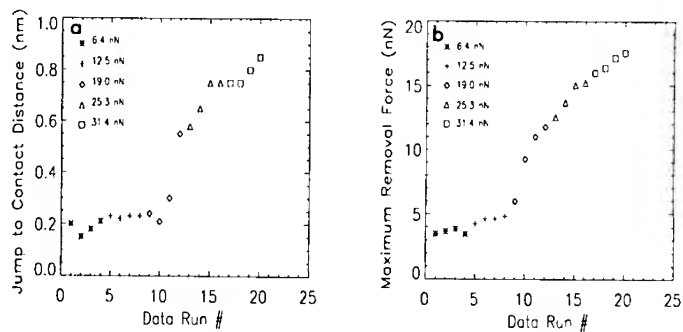


Figure 4: (a) Jump to contact distance vs. data run number on a 200 nm thick Au film deposited on mica. (b) Removal force vs. data run number on the same Au film.

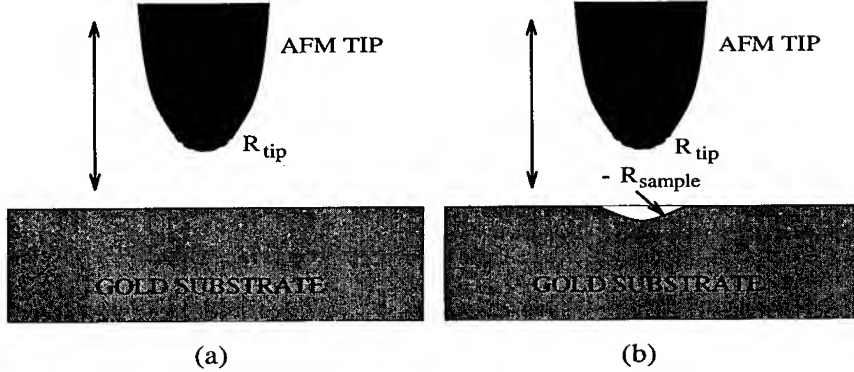


Figure 5: Schematic depicting the result of plastic deformation on the gold surface. (a) For low loading forces, no plastic deformation is observed and the sample surface remains flat. (b) Plastic deformation produces a surface with a negative radius of curvature.

radius of the system, given by

$$\frac{1}{R} = \frac{1}{R_{tip}} + \frac{1}{R_{sample}} . \quad (3)$$

In Eq. 3, R_{sample} is the radius of the substrate and R_{tip} is the tip radius. For flat substrates, $R_{sample} = \infty$ and $R = R_{tip}$ (see Fig. 5 (a)). If a permanent deformation of the flat Au film by the tip occurs (see Fig. 5 (b)), R_{sample} will change from infinity to a value approaching $-R_{tip}$. As a consequence, the parameter R will increase. Since the spring constant k remains fixed, an increase in the jump to contact distance observed experimentally can be explained by an increase in R . Experience has shown that the tip radius is constant throughout, implying that a change in R_{sample} is required to explain the observed behavior. This requirement implies a permanent deformation of the film surface.

The systematic increase in the removal force (see Fig. 4 (b)) can also be accounted by a deformation of the Au film. The removal force, F_{rem} , can be estimated by the JKR theory¹⁷ and is given by $F_{rem} = 3\pi WR$, where W is the work of adhesion. As discussed above, a permanent deformation of the Au film will cause R to increase, again providing a qualitative explanation for the increase in F_{rem} .

For small loads (less than 12 nN), the release of the tip from contact is found to exhibit a continuous behavior. Because measurements are performed in vacuum, this is interpreted as evidence for the formation of a thin neck of atoms between the tip and Au film, leading to a gradual separation from contact. It is interesting that as the contact area increases, evidence for the necking behavior disappears (see Fig. 3) and the lift-off resembles that predicted for macroscopic objects.¹⁷ It is well known that the JKR theory predicts two bodies will separate *abruptly* when a removal force is reached. Evidently, atomistic effects appropriate for small contact areas disappear as the contact area increases.

CONCLUSIONS

Force measurements have been performed on a high quality, 200 nm thick Au film in vacuum using an atomic force microscope. Under vacuum conditions, elastic nanoindentation

behavior is observed until a load greater than ~ 20 nN is applied. As the loading force increases beyond this value, the onset of inelastic deformation of the Au film occurs. When contamination effects are minimal, atomistic process are observed in the removal data for small contact areas.

ACKNOWLEDGMENTS

The authors would like to thank M. Dorogi for making the gold film on mica. In addition, the authors would like to thank R. P. Andres for many helpful discussions. This work was partially funded by the National Science Foundation under contract ECS-9117691.

References

- [1] N. A. Burnham, R. J. Colton, and H. M. Pollock, *Nanotechnology*, **4**, 64 (1993).
- [2] D.M. Schaefer, R.P. Andres, and R. Reifenberger (in preparation) (1993).
- [3] N.A. Burnham and R.J. Colton, *J. Vac. Sci. Technol.*, **A7**, 2906 (1989).
- [4] D.M. Schaefer, A. Patil, R.P. Andres, and R. Reifenberger, *Appl. Phys. Lett.*, **63**, 1492 (1993).
- [5] H.A. Mizes, M.L. Ott, K.G. Loh, and R.J.D. Miller (submitted to *J. Adhes. Sci. Technol.*, 1994).
- [6] D.M. Schaefer, M. Carpenter, R. Reifenberger, L.P. DeMejo, and D.S. Rimai (submitted to *J. Adhes. Sci. Technol.*, 1994).
- [7] J.A. Derose, T. Thundat, L.A. Nagahara, and S.M. Lindsay, *Surf. Sci.*, **256**, 102 (1991).
- [8] J. Hwang and M.A. Dubson, *J. Appl. Phys.*, **72**, 1852 (1992).
- [9] D.M. Schaefer, A. Ramachandra, R.P. Andres, and R. Reifenberger, *Z. Phys. D*, **26**, 249 (1993).
- [10] Available from Park Scientific Instruments, Sunnyvale CA 94089.
- [11] G. Meyer and N.M. Amer, *Appl. Phys. Lett.*, **53**, 1045 (1988).
- [12] G. Meyer and N.M. Amer, *Appl. Phys. Lett.*, **53**, 2400 (1988).
- [13] S. Alexander, L. Hellemans, O. Marti, J. Schneir, V. Elings, P.K. Hansma, M. Longmire, and J. Gurley, *J. Appl. Phys.*, **65**, 164 (1989).
- [14] R. Piner and R. Reifenberger, *Rev. Sci. Instrum.*, **60**, 3123 (1989).
- [15] J. Krim, private communication.
- [16] J.N. Israelachvili, *Intermolecular and Surface Forces* (Academic Press, New York, 1985).
- [17] K.L. Johnson, K. Kendall, and A.D. Roberts, *Proc. R. Soc. London*, **A324**, 301 (1971).

OBSERVATION AND MEASUREMENT OF ATOMIC SCALE IMPERFECTIONS IN MATERIALS USING CBED+EBI/H

Rodney A. Herring, John E. Bonevich, Takayoshi Tanji and Akira Tonomura, Tonomura
Electron Wavefront Project, ERATO, JRDC, P.O. Box 5, Hatoyama, Saitama 350-03
Japan

ABSTRACT

A new method of electron interferometry/holography (CBED+EBI/H) has been realized which produces interference between convergent beam electron diffracted beams. An electron biprism placed between the diffracted beams compensates for their diffraction angle by an induced potential. When overlaid the diffracted beams interfere to produce an interferogram. Holography is possible due to coherency of the electron beam. Reconstruction of the hologram by standard methods enables the phase change around the defects to be measured. These methods are very easy to apply and examples are given for small defects and defect clusters in heavy-ion implanted Si.

INTRODUCTION

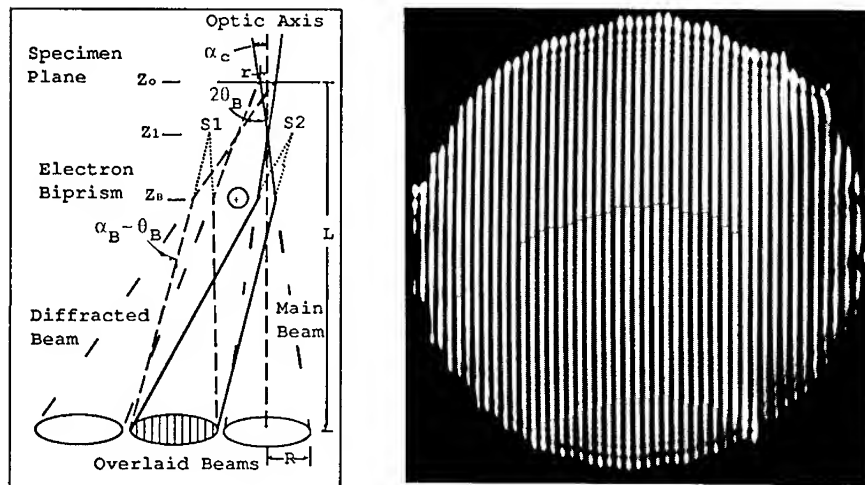
New methods of microscopy which enable us to see nanoscale structures are constantly being invented such as the many forms of STM, SFM and electron holography. Electron holography was invented by Gabor in 1949 [1] in order to improve the resolution of electron microscopes by enabling aberration to be corrected external of the microscope. Due to the complex nature of aberration, only recently has the development of phase masks using liquid-crystal spatial light modulators enabled its correction [2], although still requiring a priori knowledge of the aberration. Nevertheless, the highest resolution of electron microscopy has been made possible by off-axis holography with the achievement of a minimum carrier fringe spacing of 9.3 pm [3] which gives a theoretical point resolution of 0.03 nm [4]. Off-axis holography was made possible by the invention of the electron biprism in 1955 [5]. Recently, a new method of interferometry/holography has been realized using the electron biprism [6,7,8]. The electron biprism, being placed below the specimen and usually in the selected area aperture position, is placed in between diffracted beams. An applied potential on the electron biprism deflects the electron beams sufficiently to cause their interference. High resolution is made possible by decreasing the carrier fringe spacing, with respect to the specimen, by using a combination of a small electron beam probe size, defocusing and high ordered diffracted beams [9]. One of the advantages of using CBED+EBI over conventional holography includes being able to produce high resolution images in small to very large specimens (or far from the vacuum area, i.e., specimen edge).

This paper provides an introduction to the CBED+EBI/H technique. It has been used to see and characterize very small defects in heavy-ion implanted Si in accordance with the theme of this MRS conference.

METHOD

A Hitachi HF-2000 FEG microscope equipped with a rotatable electron biprism holder was used. The CBED+EBI/H method was possible with this microscope being fitted with many different pole pieces having spherical aberration, C_s , values ranging from 0.6 mm to 3.3 mm. Interferograms were produced in the microscope's diffraction mode by using the electron biprism to overlay, by deflection, slightly-convergent ($\alpha \sim 2$ mrad, depending on condenser aperture) diffracted beams (Fig. 1). In Fig. 1, the labels Z_0 , Z_1 , Z_B , S_1 , and S_2

are the specimen plane, focused plane, biprism position and apparent focused probe positions, respectively. The electron biprism ($\sim 0.3 \mu\text{m}$ dia.) used an applied voltage ranging from 15 to 270 eV to compensate the diffracted beam(s) angle of $2\theta_B$ (Fig. 1) with the larger biprism potentials being used with the higher order diffracted beams. In Fig. 1, the virtual image of a biprism is shown with respect to the specimen plane. It is reduced in size by the (de)magnification of the post-specimen lens which enables it to be placed in between and perpendicular to the diffracted beams without intersecting them. The convergent electron beam probe size is varied with the condenser lens excitation and is an important parameter for the magnification of the fringes with respect to the specimen. The probe sizes used were typically between 3.7 nm to 50 nm. Thus the image within the CBED disk of the specimen strongly depends on the convergence angle (C1 and C2 current), objective (de)focus, and $\text{I} \text{I}$ lens current and lies in the back-focal-plane between the Fraunhofer plane (the in-focus diffraction condition) and the near-image plane, i.e., Fresnel image. For lens conditions which give Fraunhofer imaging a typical diffraction pattern is seen and CBED+EBI can be used to extract structure factor information from the crystal. For lens conditions which give Fresnel imaging, an out-of-focus image is produced which is sometimes referred to as convergent beam imaging, CBIM [10], and can be used to extract information of "objects" or regions of interest. CBIM was produced by exciting the intermediate lens in the diffraction mode to shift the imaging plane from the Fraunhofer to a Fresnel image plane. High resolution CBIM images have the same limitations as those governing standard high resolution imaging.

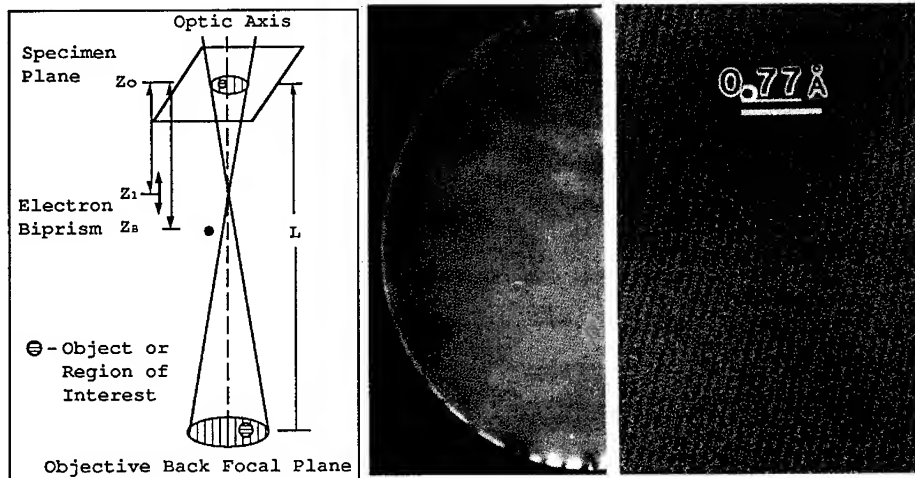


a) Figure 1 *Interference of the main beam with the diffracted beam by use of an electron biprism showing in a) a schematic of the CBED+EBI method, and in b) the main beam interfering with the 111 diffracted beam of GaAs.*

As can be seen in Fig. 1a, by directly overlaying the two beams, the apparent source of the beams come from the same point within the specimen. This fact cancels out any coherency requirement necessary for interference and thus the CBED+EBI/II method should be possible with any electron source. Having coherency is preferred though, as it allows interference to be possible even if the beams are not directly overlaid and it is likely to extend the visibility range of the fringes during defocusing due to the van Cittert/Zernike theorem [11], enhancing resolution. In addition, for symmetrically opposing beams, such as the 111 and the -1-1-1, which suffer equal but opposite Cs interfering them results in the reduction of Cs within the interferogram, reducing to zero

at the optical axis, and for non-symmetric interfering beams C_s is reduced to zero away from the optic axis.

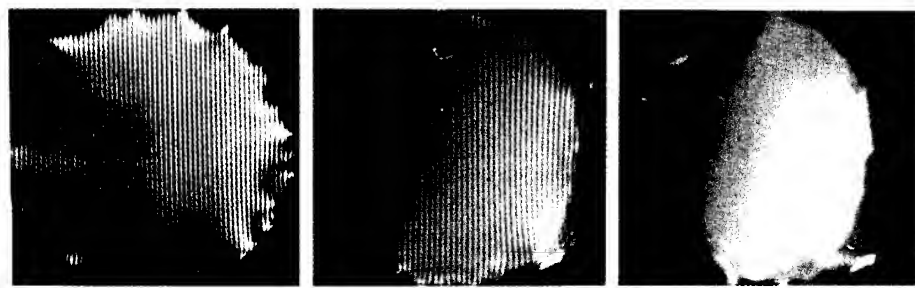
A typical interferogram is shown in Figure 1b for an electron beam spot size of ~ 3.5 nm, and for the main beam interfering with the 111 of GaAs which shows straight, fine fringes having good contrast. The spacing of the fringes within the interferogram can be made very fine. Figure 2a shows a simplified diagram illustrating the magnification relationship between the fringes within the interferogram, $M_f = L/Z_B$, and an object, $M_o = L/Z_1$. For the condition of $Z_1 = Z_B$, the spacing of the fringes in the interferogram equals the spacing of the atomic planes in the specimen. For the condition of $Z_1 \gg Z_B$, the spacing of the fringes in the interferogram are much less than the spacing of the atomic planes in the specimen. By exciting the objective lens which defocused (by $\sim 4 \mu\text{m}$) Z_1 and then refocusing the electron beam spot size on the specimen to 3.7 nm by using the C1 lens, the fringe spacing was reduced to $\sim 10 \text{ pm}$, Fig. 2b. Thus, very high resolution microscopy is made possible by decreasing the carrier fringe spacing with respect to the specimen and imaging the specimen in the Fresnel image plane.



^aFigure 2 In a) a simplified schematic showing the magnification relationship between an object in the specimen and the fringes seen in the interferogram is shown, and b) fine fringes using the main beam and 200 beam of a Au specimen and c) magnified fringes from b) showing an extremely fine fringe width of $\sim 10 \text{ pm}$.

Holography is made possible by the fact that the beams continue to interfere as they are displaced from each other slightly, Figure 3. This fact also enables the coherency of the electron beam to be accurately measured (Figure 3c) since the transverse coherency width, which equals $2\pi\lambda/\theta_c$ where θ_c is the angle at which the beams no longer interfere, is easily measured. For holography an object beam is taken from one part of a crystal (e.g. a crystal defect) and a reference beam is taken from another part of the crystal (e.g. the perfect crystal). Their interference results in a phase shift around the dissimilar region. As well, for small defects which do not disturb or phase shift one beam significantly, say the main beam, but do so with another beam, say the diffracted beam, directly overlaying the two beams results in a significant phase shift at the defect. Because convergent beams, rather than plane waves, are being used the interfering beams have a curved phase surface. The reconstruction process of the object [9] then requires a good reference hologram. The reference can be a hologram taken from a region close to the region of

interest or, if the object is small enough, from an adjacent region within the same hologram. Compensation for defocusing effects of the object are possible and methods to measure defocusing are being investigated. These methods are very easy to apply for crystal structures such as interfaces, dislocations, etc. [8], although the interpretation of the phase shifted regions still requires knowledge of the crystal and its diffraction characteristics.



a **b** **c**
Figure 3 Disappearance of the interference fringes as the beams are separated by reducing the biprism potential. See text.

RESULTS

Applying CBED+EBI/II to a cross-sectional region of a 111 oriented single crystal Si specimen which had previously been irradiated by MeV As-ions, as reported earlier [11], showed no fringes in regions which had been amorphized and large fringe shifts at amorphous/crystal interfaces (Fig. 4). These holograms were produced in crystal thicknesses varying between the edge of the TEM thin foil to the first extinction distance ~ 50 nm. Reconstruction of the holograms showed that the phase shifts of amorphous regions are connected to each other (Fig. 5a and 5b). Some phase shifted regions were isolated and extremely small and are around the size of the Si unit cell (Figure 5c and 5d). The reconstruction of a hologram containing only one amorphous zone which was also very small (~ 3 Si unit cells in diameter) and buried inside the Si crystal is shown in Figure 6.

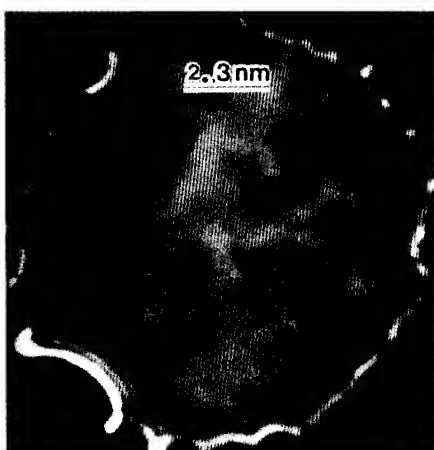


Figure 4 A hologram of an As-ion implanted Si region showing amorphous and crystal regions and fringe shifts at their interfaces.

DISCUSSION

As has been shown, CBED+EBI/II is a very powerful method for measuring the phase shifts at small dissimilar regions in crystals. CBED+EBI/II is an inherently high-resolution method, being able to easily produce fine fringes with respect to the specimen. Unlike the standard off-axis holography method which uses $\sim 1\text{-}3\%$ of the electron beam's intensity for holography, CBED+EBI/II can use more than 90% for crystal orientations giving good two beam conditions, producing high contrast fringes, required for high resolution holography.

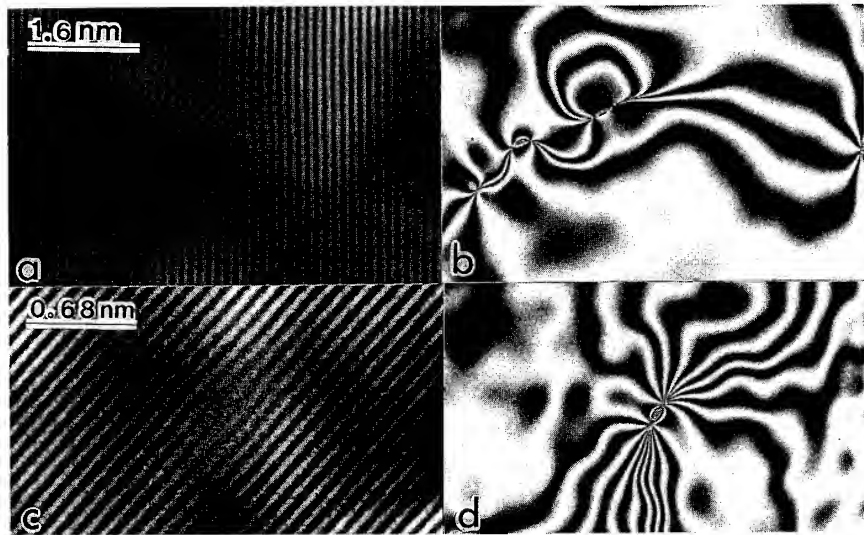


Figure 5 As-ion implanted Si showing in a) and c) holograms of amorphous/crystal regions and their reconstructed $\pi/4$ and $\pi/8$ phase images in b) and d), respectively.

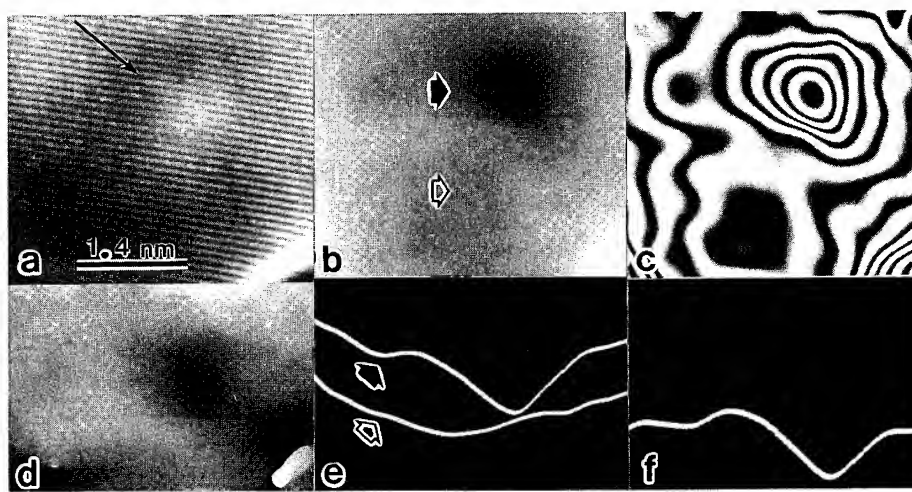


Figure 6 Reconstruction of an amorphous zone buried in the Si crystal (dark arrow) using an adjacent region (light arrow) as a reference to determine the absolute maximum phase shift of $-2\pi/5$ where a) is the hologram, b) is a 2π phase image, c) is a $\pi/8$ phase image of b), d) is the 2π phase image with the background phase removed, e) is the line profiles of the phase passing from side to side in b), and f) is the line profile passing through the amorphous zone in d) which gives the absolute phase shift of the amorphous zone.

For the results reported here, the absence of fringes in the amorphous zones is a consequence of the Si 004 structure factor being zero or undefined, i.e., the 004 beam's intensity is zero, and thus interference with any other beam is not possible. The phase shifts at the amorphous/crystal interfaces are due to a mean inner potential change due to the volumetric strain between the amorphous and crystal regions. The strain within the crystal planes shifts the angle of diffraction of the 004 beam slightly which in turn shifts the interference fringes. The results show that CBED+EBI is very sensitive to strain in crystals. It is interesting to note that the measured phase shift or strain within the crystal is connected from one amorphous region to another. This paper is the first to report this finding. This information is important for understanding the diffusion mechanism of point defects during recrystallization of the amorphous regions and for the subsequent formation of secondary defects. At some amorphous/crystal interfaces (Fig. 4), phase shifts greater than 2π , which is equivalent to a spatial shift of $1/4a$ (Si lattice constant), are shown. Thus some of these interfaces will have sufficient strain energy to form dislocations, as their strain is greater than $1/2[110]$, the dislocation's Burgers vector. This has been confirmed experimentally [11]. In addition, Fig. 5 and Fig. 6 show that CBED+EBI is very sensitive to small defects and clusters which vary in size from a cluster having a diameter of a few unit cells to ~ 1 unit cell, i.e., on the order of a point defect. The small cluster in Fig. 6 has a maximum phase shift of $\sim 2\pi/5$ which is equivalent to $\sim 5\%$ strain in the crystal, which is slightly larger than a 3% strain measured experimentally for the bulk crystal [11].

In summary, a new method of electron interferometry/holography, CBED+EBI/H, has been demonstrated and it is shown that high resolution holograms of small defect regions, on the order of the Si unit cell, can be reconstructed to reveal good phase information.

References

1. D. Gabor, Proc. R. Soc. London **A197**, 454 (1949); **B64**, 449 (1951).
2. N. Konforti, E. Maron and S.T. Wu, Opt. Lett. **13**, 251 (1988).
3. T. Kawasaki, Q.X. Ru, T. Matsuda, Y. Bando and A. Tonomura, Jpn. J Appl. Phys. **30**, 1830 (1991).
4. K.J. Hanszen, J. Phys. D: Appl. Phys. **19**, 373 (1986).
5. G. Möllenstedt and H. Düker, Naturwissenschaften **42**, 41 (1955).
6. R.A. Herring, G. Pozzi, T. Tanji and A. Tonomura, Ultramicroscopy **50**, 94 (1993).
7. R.A. Herring, G. Pozzi, T. Tanji and A. Tonomura, Proc. 51st Ann. Meeting of MSA, Eds. G.W. Bailey and C.L. Rieder, 1056 (1993).
8. R.A. Herring and T. Tanji, Proc. 51st Ann. Meeting of MSA, Eds. G.W. Bailey and C.L. Rieder, 1086 (1993).
9. R.A. Herring et. al., Ultramicroscopy, To be submitted.
10. C.J. Humphreys, D.J. Eaglesham, D.M. Maher and H.L. Fraser, Ultramicroscopy **26**, 13 (1988).
10. J. Thompson and E. Wolf, J. Optical Soc. of Am. **47**, 895 (1957).
11. R.A. Herring and E. Fiore, Mater. Res. Soc. Symp. Proc. **100**, 441 (1988).

IMAGING OF BURIED SI AND SI:GE SURFACE STRUCTURE UNDER AMORPHOUS GE FILMS BY PLAN VIEW TRANSMISSION ELECTRON MICROSCOPY

OLOF C. HELLMAN

Electrotechnical Laboratory, 1-1-4 Umezono, Tsukuba, Ibaraki, 305 Japan, and
NTT Basic Research Laboratories, 3-9-11 Midori-cho, Musashino, Tokyo, 180 Japan

ABSTRACT

Real space plan-view Transmission Electron Microscopy (TEM) of the interfacial structure at the amorphous-Ge / Si (111) interface is presented. Ge is deposited at between room temperature and 150°C on either a 5x5 or 7x7 reconstructed surface. Conventional Plan-view TEM analysis reveals microstructural details such as surface steps, reconstruction phase shift boundaries and the reconstruction itself buried under the amorphous film, features which have previously been seen only as clean surfaces in UHV. Also imaged are small regions where Ge grows epitaxially on the Si surface above room temperature. These are seen to appear preferentially at steps and phase shift boundaries.

INTRODUCTION

Recently, the study of surface structures by plan-view high resolution Transmission Electron Microscopy (TEM) has been shown to possible for a wide range of systems.¹⁻¹¹ All of these studies have been restricted to Ultra High Vacuum (UHV) microscopes, wherein surface cleaning is tedious and there are many constraints on the types of samples made, and which is expensive and not available to most researchers. This paper demonstrates that it is possible to use a conventional (non-UHV) TEM to study some surface structures prepared ex-situ and capped to preserve the surface features.

The present study is concerned with 5x5 and 7x7 reconstructions on a Si (111) surface. Gossmann et al. used ion scattering to show that the number of atomic displacements on the Si(111) 7x7 reconstruction was unchanged after deposition of an amorphous Ge film.¹² Gibson et al. used Transmission Electron Diffraction (TED) to show that a 7x7 periodic structure was preserved under a-Si deposition on Si(111)7x7.¹³ In situ annealing which would be expected to cause about 15Å of SPE growth destroyed this periodic structure.¹³⁻¹⁵

High resolution cross-section TEM images of the preserved Si (111) 7x7 structure have been published.^{13,15} These images show the stacking fault from the original reconstruction, but provide no more information due to difficulties in cross-section image interpretation. X-ray scattering experiments show more clearly the preserved dimer-stacking fault structure and disruption of the adatom structure, with a partial ordering of the first and second deposited layers.¹⁶

UHV-TEM has proven to be a powerful technique for atomic structure determination of Si surface reconstructions,² in situ surface studies,^{6,9} imaging of surface reconstruction defects^{6,7} and single atom imaging.⁸ Silicon interfacial structures have also been studied by TEM, for example the step structure at the Si(111)-silicide interface¹⁷, and the propagation of the Si(111)/SiO₂ interface during oxidation⁹.

This paper differs from previous work in that an ordinary TEM is used to observe surface structures. There are three major motivations for doing so. First, ex-situ sample preparation widens greatly the experimental possibilities for surface analysis by TEM, and allows for greater precision and reproducibility in surface preparation. Secondly, samples cleaned in the UHV-TEM necessarily have two surfaces, whose images can interfere with each other. A capped surface is immune to this two-image effect. Lastly, the structure of buried surfaces and the role they play in thin film evolution is itself of interest. Thus, while other surface analysis techniques such as

LEEM,¹⁸ REM¹⁹ or STM²⁰ are clearly superior to TEM in resolution or ease of sample preparation, they are incapable of imaging solid-solid interfaces. Good real space images of buried surfaces, comparison of their structure to bare surfaces and examination of their effect on thin film phase transformations can only be performed by TEM.

EXPERIMENT

In the experiment, 14mm x 16mm (111) Si wafers ($\pm 0.4^\circ$) are cleaned in $\text{H}_2\text{SO}_4:\text{H}_2\text{O}_2$ 4:1, followed by oxide stripping in $\text{HF}:\text{H}_2\text{O}$ 1:20 and oxidation in boiling nitric acid. After a final oxide strip, a thin oxide is grown in room temperature nitric acid for 20 seconds. The substrate is then washed in water, blown dry with nitrogen and loaded into the UHV chamber. The sample and sample holder are outgassed for 1 hour at 550°C , after which the oxide is desorbed by heating to about 900°C for two minutes. Si and Ge can be evaporated from e-gun sources. Sample heating is supplied by resistive heaters from the backside of the sample. Temperature is measured using a thermocouple mounted in the sample holder and by infrared pyrometer: both temperatures are calibrated at the 830°C 1x1/7x7 transition of the Si (111) surface, as observed using RHEED.

Base pressure in the deposition chamber is 2×10^{-11} Torr. For all samples, 200Å of silicon is grown epitaxially on the cleaned surface. Samples may be annealed at 800°C for five minutes to produce sharp 7x7 RHEED spots, or may be annealed at 550°C after deposition of one monolayer (1.5×10^{15}) Ge and 1/2 monolayer Si to form a mixed 5x5 and 7x7 surface, and cooled to near room temperature. 40Å Ge is then deposited at a rate of between 4 and 10Å/minute, and is capped by 10Å of silicon. This sample is taken from the vacuum and cut into 3mm disks. These are dimpled and polished from the backside to optical transparency, washed in acetone, and fastened with wax to a fused quartz slide. Reactive ion etching with CF_4 is used to thin to electron transparency. This etching produces microdimples in the sample, resulting in a partially perforated disk, with some areas which are exceedingly thin. Samples are removed from the quartz slides by soaking in acetone overnight. TEM observation is performed using a JEOL 4000 TEM operating at 200 kV.

RESULTS

Fig. I shows a step and PSB array in dark field on the $(02\bar{2})$ beam with the electron beam incident near [111], producing a three-beam condition with the transmitted beam, $(20\bar{2})$ and $(02\bar{2})$. Steps run horizontally, and PSBs run vertically. At intersections of PSBs with the lower side of steps, a triangular region where there is no buried reconstruction can be seen. High temperature UHV-TEM observation of the 1x1 to 7x7 phase transition of the surface can identify the step direction because 7x7 regions are known to nucleate and grow from the upper side of the steps.^{19,20} Subsequent observation of the 7x7 surface shows the same triangular structure as observed here.²¹

Figure II shows a PSB running vertically between two 7x7 domains of the sample in Figure I. The spotty structure is due to the strain and amplitude contrast resulting from having a thin sample and from the beam being exactly aligned along [111]. The diffraction pattern shows the amorphous ring from the Ge film, the main Si substrate spots and the 7x7 superstructure spots.

Figure III shows a bright field image from a mixed 5x5 and 7x7 surface. The objective aperture is at least large enough to include 7x7 superlattice spots closest to the transmitted beam (i.e. the $\{1/7, 0\}$ spots²²). Both 5x5 and 7x7 fringes can be imaged, and features such as phase boundaries can be identified, although it is often difficult to identify precisely the location of phase boundaries. Further, steps may not be differentiated from phase boundaries or PSBs because there is no identifiable step pattern, and the reconstruction domain sizes can be small in comparison to the step terrace width, as is not the case for the previous sample. Nevertheless, individual domains can be delineated, and the surface coverage of each reconstruction can be estimated at near 50%. For comparison of these results to those using a UHV-TEM, see work by Kajiyama, et al.²³

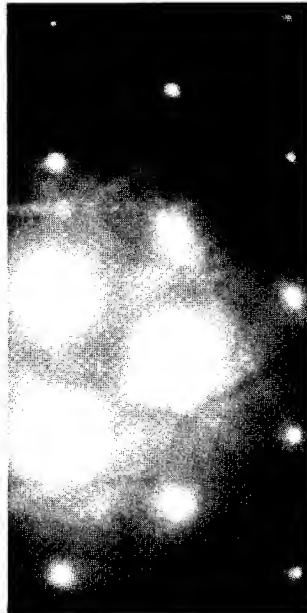
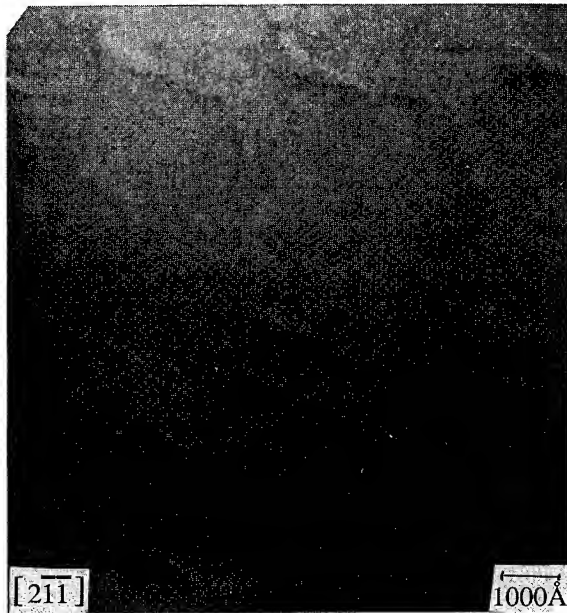


Fig. Ia. Step and PSB array imaged in dark field on the $(2\bar{2}0)$ beam in a three beam condition. The light triangular regions at half of the step/PSB intersections are regions where the 7x7 structure has been destroyed. 7x7 superlattice spots appear in the TED pattern

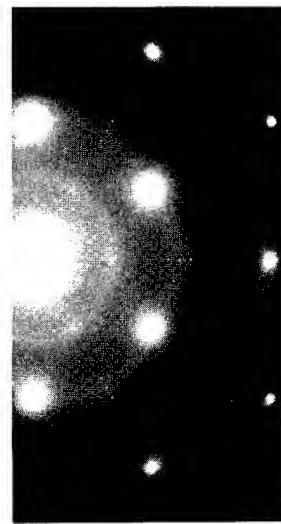
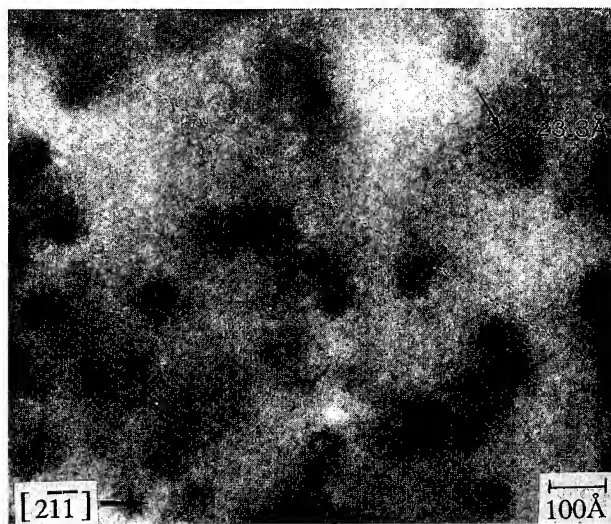


Figure IIa. Phase shift boundary in the 7x7 buried reconstruction runs vertically. 7x7 fringes can be easily seen. IIb. TED pattern

Figure IV shows a dark field image of a Ge film deposited at 120°C on a Si (111) 7x7 substrate, taken on the 1/3 (422) forbidden reflection. Ge crystallites appear dark in this micrograph because local variation in the number of (111) planes cause extinction of this reflection; where the interface is flat, the intensity of the 1/3 (422) is more likely to be non-zero. The crystallites decorate the surface step and PSB structure. Figure V shows a bright field image of a Ge film deposited at 150°C. Interference between the Si and Ge {220} beams causes contrast at each crystallite, although they are not large enough to show moiré fringes. At 150°C, the Ge crystallites are larger, and do not show a preference for growth at surface steps and reconstruction defects.

DISCUSSION

These results show that conventional TEM can rival UHV-TEM in imaging some surface structures.^{3,4,7} There are a number of reasons why UHV-TEM can result in lesser quality images. First, there is the possibility of contamination in the TEM, which is easier to control in a UHV system dedicated to thin film deposition. Secondly, thin sample preparation in the TEM is rather difficult. However, a buried surface structure is insensitive to ordinary sample preparation techniques. Third, a thin sample will have some degree of strain, which alter the surface structure itself. Burying the surface ensures that the structure will not change in the TEM. The primary disadvantage is that the amorphous film deposition can alter the structure of the surface. For example, the Si (100) 2x1 reconstruction is destroyed upon deposition of an amorphous film.¹² It is interesting to note that silicon surface features were first seen using conventional TEM as long ago as 1968.²⁴

Furthermore, the power of plan-view TEM in comparison with cross-sectional TEM or non-imaging techniques is shown. These techniques, x-ray diffraction¹⁶, ion scattering¹² or X-TEM¹⁴ are at a disadvantage analyzing non-uniform interfacial structures, because different structures are probed simultaneously. The preferential crystallization of Ge at surface steps and reconstruction defects would be impossible with these techniques, although similar information might be obtained by LEEM¹⁸ or STM.²⁵ Figures IV and V essentially show the structure of the surface at its transition between epitaxial growth and amorphous deposition. Using the framework of limited

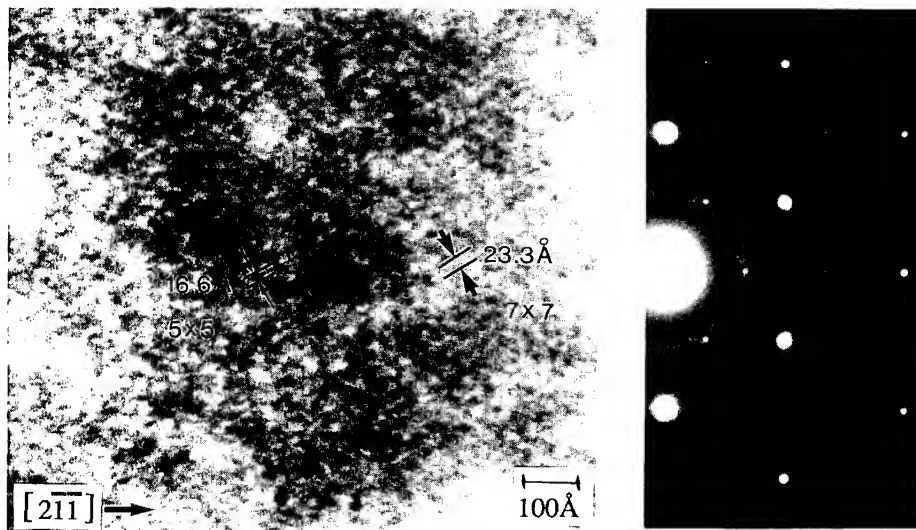


Fig. IIIa. A mixed 5x5 and 7x7 reconstructed Si(111):Ge surface capped with amorphous Ge. Both 5x5 and 7x7 areas are imaged, and a phase boundary is indicated. IIb. TED pattern.

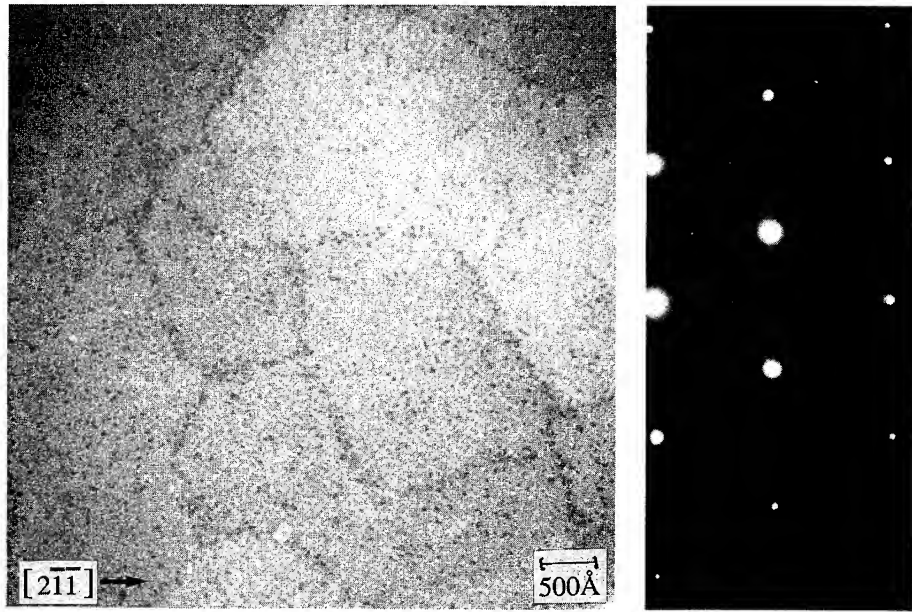


Figure IV. A dark field image from the $1/3 (4\bar{2}\bar{2})$ beam, taken of a sample with a Ge film deposited at 120°C . Ge crystallites appear dark. 7x7 superlattice spots appear faintly in TED

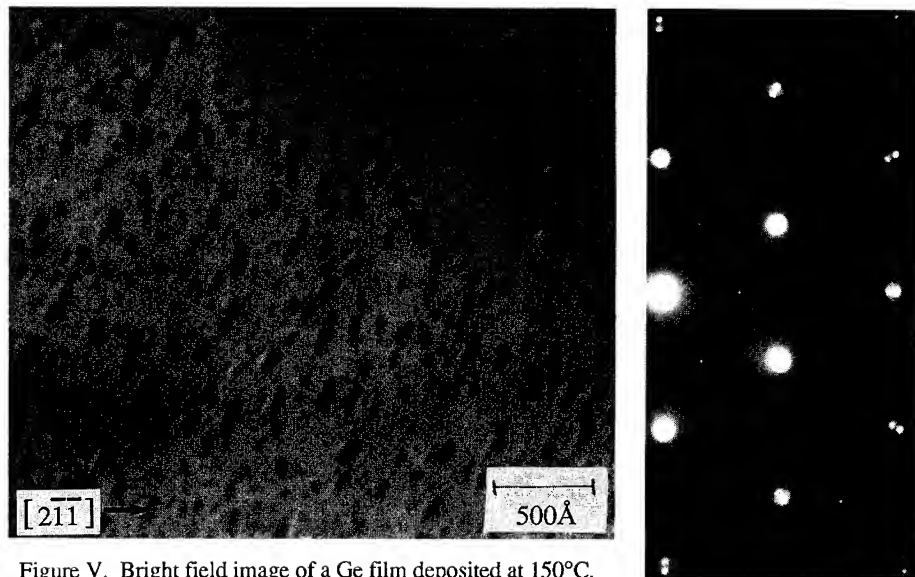


Figure V. Bright field image of a Ge film deposited at 150°C . The Ge crystallites are large enough to show moiré fringes.

thickness epitaxy,²⁶ films grown at low temperature will grow a certain thickness epitaxially before entering the amorphous growth regime. These micrographs show that for heterogrowth of Ge on Si (111), this thickness varies greatly at different sites on the surface. The appearance of 7x7 superlattice spots in the diffraction patterns shows that the original Si surface structure is preserved, implying no epitaxial growth of Ge in some areas. However, the appearance of the crystallites in the TEM images show that many layers of Ge grow epitaxially at other sites, especially those sites near steps and reconstruction domain boundaries. This is consistent with a model for epitaxial growth on the Si (111) surface in which the limiting step in growth is the reordering of the reconstruction.²⁷

CONCLUSION

In summary, images of the buried surface structure of Si (111) 7x7 and Si:Ge (111) 7x7+5x5 acquired using conventional TEM have been shown. Defects in the buried structure such as reconstruction phase shift boundaries can be seen. In addition, small Ge epitaxial crystallites are observed for films deposited at above room temperature; they occur preferentially at defects in the buried surface.

REFERENCES

1. K. Takayanagi, Jap. J. Appl. Phys. **22** (1) L4 (1983).
2. K. Takayanagi, Y. Tanishiro, S. Takahashi and M. Takahashi, Surf. Sci. **164** 367 (1985).
3. K. Takayanagi, Y. Tanishiro, M. Takahashi and S. Takahashi, J. Vac. Sci. Tech. **A3** (3) 1502 (1985).
4. J.M. Gibson, M.L. McDonald and F.C. Unterwald, Phys. Rev. Lett., **55** (17) 1765 (1985).
5. K. Akiyama, K. Takayanagi and Y. Tanishiro, Surf. Sci., **205** 177 (1988).
6. K. Takayanagi, Y. Tanishiro, T. Ishitsuka and K. Akiyama, Appl. Surf. Sci. **41/42** 337 (1989).
7. K. Yagi, A. Yamanaka, H. Sato, M. Shima, H. Ohse, S. Ozawa and Y. Tanishiro, Prog. Theor. Phys. **106** 303 (1991).
8. Y. Haga and K. Takayanagi, Ultramicroscopy **45** 95 (1992).
9. F.M. Ross and J.M. Gibson, Phys. Rev. Lett., **68** (11) 1782 (1992).
10. P. Xu, D. Dunn, J.P. Zhang and L.D. Marks, Surf. Sci. Lett., **285** L479 (1993).
11. O. Pohland, X. Tong and J.M. Gibson, J. Vac. Sci. Tech. **A11** (4) 1837 (1993).
12. H.J. Gossman, L.C. Feldman and W.M. Gibson, Phys. Rev. Lett. **53** (3) 294 (1984).
13. J.M. Gibson, H.J. Gossman, J.C. Bean, R.T. Tung and L.C. Feldman Phys. Rev. Lett. **56** (4) 355 (1986).
14. A. Sakai, T. Tatsumi, I. Hirosawa, H. Ono and K. Ishida, Surf. Sci. **249** L300 (1991).
15. A. Sakai, T. Tatsumi and K. Ishida, Surf. Sci. **224** L956 (1989).
16. I.K. Robinson, W.K. Waskewicz, R.T. Tung and J. Bohr, Phys. Rev. Lett., **57** (21) 2714 (1986).
17. R.T. Tung and F. Schrey, Phys. Rev. Lett., **63** (12) 1277 (1989).
18. W. Telieps and E. Bauer, Surf. Sci., **162** 163 (1985).
19. N. Osakabe, Y. Tanishiro, K. Yagi and G. Honjo, Surf. Sci., **109** 353 (1981).
20. K. Miki, Y. Morita, H. Tokumoto, T. Sato, M. Iwatsuki, M. Suzuki and T. Fukuda, Ultramicroscopy, **42-44** 851 (1992).
21. J.M. Gibson, unpublished.
22. This is indexed using the surface hexagonal notation. In the Si diamond cubic structure, this would be the 1/21 {422} spots.
23. K. Kajiyama, Y. Tanishiro and K. Takayanagi, Surf. Sci. **222** 47 (1989).
24. H.C. Abbink, R.M. Broudy and G.P. McCarthy, J. Appl. Phys. **39** (10) 4637 (1968).
25. U. Köhler, J.E. Demuth and R.J. Hamers, J. Vac. Sci. Tech. **A7** (4) 2860 (1989).
26. D.J. Eaglesham, H.J. Gossman and M. Cerullo, Phys. Rev. Lett. **65** (10) 1227 (1990).
27. H. Tochihara and W. Shimada, Surf. Sci. **296** 186 (1993).

STRUCTURAL INVESTIGATION OF NaNO_3 NANOPHASE CONFINED IN POROUS SILICA

R. MU, D. O. HENDERSON, AND F. JIN
Physics Department, Fisk University, Nashville, TN 37208

ABSTRACT

We have demonstrated that thermal and vibrational investigations of sodium nitrate (NaNO_3) physically confined in the porous silica hosts is an effective approach to mimic the solute clustering effects in aqueous solution. The results show that the structure of the NaNO_3 confined in nanopores can be divided into three regions, i.e., the regular solid phase region, solution-like molecular aggregates region, and a new solid-like phase region. Depending upon the pore size of the porous host, the physical range of the three regions varies accordingly. For pore size $d < 2.5$ nm, only the solution-like molecular aggregates phase remains.

INTRODUCTION

It is difficult and sometimes impossible to grow sufficient size and high quality single crystals from solution. The bottleneck associated with the problem is a poor understanding of the solution structure, dynamic equilibrium, and kinetic rate constants which govern the crystal nucleation and growth from solution. It has been commonly accepted that there are four possible species present in solution. They are aquated ions, solvent-separated-ion pairs, contacted ion pairs, and clusters. Based on the classical homogeneous nucleation theory, the new solid phase formed from a supersaturated solution is by the growth of clusters via monomer addition. However, a Raman study of a model system of the NaNO_3 solution¹⁻⁴ indicates that i) the solute clustering occurs in undersaturated, saturated, as well as supersaturated solutions, ii) as the solution become supersaturated, some of the solute clusters coalesce into larger clusters, iii) the mechanisms governing crystallization from solution are associated with the coalescence of solvated solute clusters. A recent ATR-FTIR study⁵ of NaNO_3 solution enabled us to identify the four concentration dependent species in aqueous solution. The results also suggest that as the concentration increases, the average cluster size increases via coalescing of smaller clusters together rather than via monomer addition. From the detailed analysis of the NO_3 symmetric vibration, we are able to estimate, for the first time, the cluster size and number of the clusters as a function of the concentration. Further, the systematic intensity deviation associated with the solution clusters at high concentration from Beer's law may suggest that the structure of the NO_3 in the interior of the clusters has solid-like structure (D_{3d}), while the NO_3 in or close to the surface possesses C_{2v} symmetry. In order to explore the relationship between the cluster formation and crystal nucleation and growth in solution, attempts were made in the present study to demonstrate the possible crossover effects between solid bulk and clusters by impregnating NaNO_3 into various pore-sized silica, and to characterize the structure of the clusters which may be formed in aqueous solution.

EXPERIMENTAL

In order to elucidate the possible link between the clusters in solution and the solid phase in nanometer scale, we have carefully prepared three sets of NaNO_3 samples. They are the bulk NaNO_3 polycrystalline phase, NaNO_3 solutions with various molar concentrations, and NaNO_3 impregnated in four different-sized pores of porous glass. The polycrystals were obtained by slow evaporation of the water from the saturated solution in a desiccator. No special effort was made to obtain a single crystal in the present work. The solutions with different molar concentrations were prepared by dissolving a known amount of NaNO_3 in deionized and doubly distilled water.

Four different pore-sized silica from Geltech were chosen as the confining host for the present study. The nominal pore diameters are 2.5, 5.0, 10, and 20 nm, respectively. The procedure of the impregnation of the NaNO_3 into porous silica has been reported elsewhere.⁶ However, one important process is still necessary to address in this paper. It is known that under ordinary conditions, the porous silica can adsorb much of the water from its environment. The structure of the retained water can be roughly classified into three types as illustrated in figure 1. They are surface hydroxyl (Si-OH), surface hydrogen bonded water, and the bulk water at the pore center. Therefore, in order to use the physically confined NaNO_3 in nanopores to mimic the clusters formed in solution, the NaNO_3 impregnated in porous silica was dried in an oven at 120 °C for 2-3 days to ensure no bulk water left inside the pores before being subjected to the measurements. It was estimated that about 40 per cent pores were filled with the NaNO_3 solid.

In order to evaluate the water content inside the pores and the thermodynamic properties of the confined NaNO_3 in different pore-sized glass, a section of the porous disk impregnated with NaNO_3 was cut with a diamond saw and measured in the region 25 °C < T < 350 °C using Perkin-Elmer Differential Scanning Calorimetry (DSC) 4. The typical scanning rate in both heating and cooling modes was 10 °C/min. The accuracy of the calibrated DSC system is estimated to be ± 2 °C. Aluminum pans were used throughout the measurements.

Raman scattering measurements of the NaNO_3 in its bulk, confined in porous glass, and solution phases were carried out with Spex Raman spectrometer, which is equipped with double-grating monochromator and Ar ion Laser. The scattered light was collected at 90° to the incident laser beam for the silica impregnated samples, bulk NaNO_3 and the solutions contained in capillaries. Typically a resolution of 2 cm^{-1} and an integration time of 0.5 s were used throughout the measurements. Spectra were recorded scanning between 10 cm^{-1} from the excitation line (488 nm) to 4000 cm^{-1} at laser power of ~ 1 W.

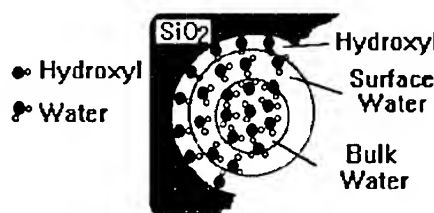


Figure 1. A simple schematic illustration of types water present in silica pores.

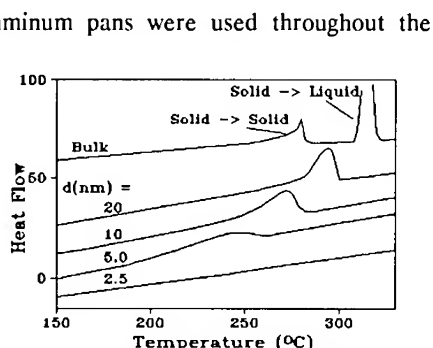


Figure 2. DSC thermograms of NaNO_3 in its bulk and physically confined phases in porous silica upon heating.

RESULTS AND DISCUSSION

The DSC measurements for NaNO_3 in its bulk phase and impregnated in 2.5, 5.0, 10, and 20 nm pore-sized silica disks show no water evaporation peak around 100 °C upon the heating run. However, the melting transition of the bulk and the confined NaNO_3 is observed as shown in figure 2. For the bulk, there were two observed endothermic peaks at 280 °C and 417 °C, respectively, as shown in fig. 2a. These two peaks are identified as solid orientational order-disorder ($T = 280$ °C) and solid melting ($T_m = 417$ °C) transitions.^{7,9, 13-15} As expected, when the NaNO_3 is confined in different pore-sized silica glasses, as illustrated in fig. 2b-2e, the melting transition of the NaNO_3 depressed. The amount of depression was increased as the average pore size of the silica glass decreased. However, no indication of the solid-solid phase transition was observed within our experimental sensitivity.

It has been recognized that when the fluids and/or solids are physically confined in small pores, both their solid-to-solid and solid melting transitions are depressed.¹⁰⁻¹³ The amount of depression of the transition temperatures can be quantitatively scaled with $1/d$, where the d is defined as the average pore size of the porous host. However, when NaNO_3 is confined in small pores ($d < 20$ nm), no indication of the solid structural order-disorder phase transition was observed. The temperatures of the solid melting transition of NaNO_3 confined in the pores were systematically depressed except for the NaNO_3 inside 2.5 nm pores. Interestingly, the amount of depression, shown in figure 3, does not quite follow the linear relation with $1/d$. In order to further study the observed depressed temperature deviation from the $1/d$ relation, Raman measurements were conducted.

Figs. 4-6 show the Raman spectra of NaNO_3 in its bulk, confined in silica pores, and solution forms. In order to make a systematic comparison among the spectra, the intensity of the spectra was normalized against the symmetric N-O stretch vibration (v_2) since this mode is Raman active both in the solid phase ($v_2 = 1068$ cm⁻¹) and in the solution phase ($v_2 = 1050$ cm⁻¹). As shown in fig. 4, the internal vibrations of the confined nitrate groups show two different trends for the pore size $d > 2.5$ and $d < 2.5$ nm. For $d > 2.5$ nm, the bands at 1386 cm⁻¹ (v_3) and 724 cm⁻¹ (v_4) are similar with that of the bulk. For $d = 2.5$ nm, however, these two modes resemble the spectrum of the solution rather than

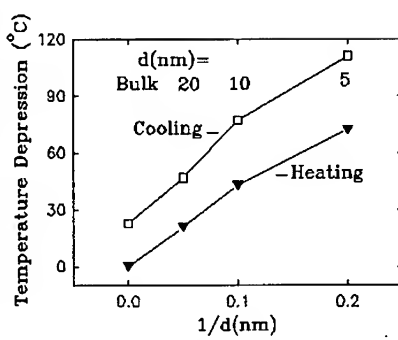


Figure 3. Graph showing the depression of the melting temperature with the pore size of the porous host.

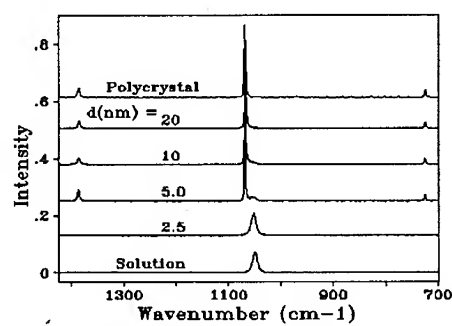


Figure 4. Raman spectra of NaNO_3 in the bulk, the confined, and solution states in 1450 - 700 cm⁻¹ region.

that of bulk solid phase. On the other hand, as illustrated in fig. 5, the band at 1070 cm^{-1} (v_1) exhibited an additional peak at about 1050 cm^{-1} for $d < 20\text{ nm}$. The intensity of this peak increases as the pore size decreases at the expense of the intensity of the 1070 cm^{-1} peak. For the pore size $d = 2.5\text{ nm}$, the band at 1070 cm^{-1} disappeared and the whole spectrum closely intimates the spectrum of the NaNO_3 solution. For the external vibrations of the NaNO_3 system in fig. 6, however, more interesting features can be observed. As the NaNO_3 changes from the bulk state to the confined ones, i.e., $d = 20, 10, 5.0$, and 2.5 nm pores, the absorbance of the long-wavelength librational mode of NO_3 groups at 175 cm^{-1} decreased in intensity and the linewidth of the band broadened. This mode disappeared when the NaNO_3 was confined in 2.5 nm pores. The transverse optical (TO) mode of the confined NaNO_3 at 100 cm^{-1} exhibited the similar behavior as the band at 175 cm^{-1} , that is, the intensity decreased and linewidth broadened as the pore size decreased, more strikingly, there appeared a new band at 70 cm^{-1} which began to develop for $d < 20\text{ nm}$. And both modes at 100 cm^{-1} and 70 cm^{-1} disappeared when the NaNO_3 was confined in 2.5 nm pores and in solution. The other feature is that the Raman scattering below 200 cm^{-1} showed a system dependent Rayleigh wing. The wing broadened as the pore size of the silica host became smaller. However, the Rayleigh wing for the confined NaNO_3 in porous silica was nearly bracketed by the wing observed in polycrystal (small wing) and in NaNO_3 solution (large wing).

Vibrational properties of the sodium nitrate crystal have been extensively studied in the past.^{7-9, 13-15} The Raman spectra reported here for the internal and external modes are in good agreement with the literature except for the one at 70 cm^{-1} . It is known that when a system's physical dimension is reduced, the finite size effect can cause the broadening of the vibrational modes which may be partly due to the fact that the lattice of the system is not able to sustain low wave-vector modes below the physical size of the particle size, i.e., confined phonon^{17,18} (here it will be the pore size). Broadening can also arise from the surface perturbation of the host material, i.e., the porous silica surface. In addition, the observed broadening of the librational and TO modes at 175 and 100 cm^{-1} can also be related with the pore size distribution of the porous host. However, the sudden

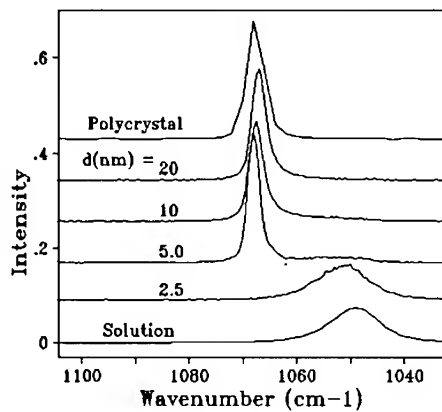


Figure 5. Expanded Raman spectra in fig. 5 to illustrate the effects of pore confinement on NO_3 symmetric vibration.

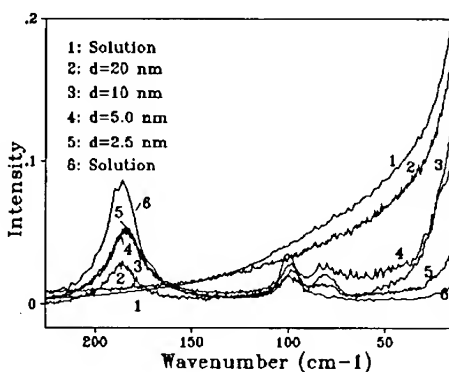


Figure 6. Raman spectra of NaNO_3 in the bulk, the confined, and solution states in $500 - 10\text{ cm}^{-1}$ region.

appearance of the band at 70 cm^{-1} can not account for the physical confinement due to the pore size of the host. If one assumes that the band at 70 cm^{-1} is due to physical confinement of the TO mode, based upon the phonon confinement model,¹⁶⁻¹⁹ one would then expect the TO mode to shift down (note: it may also shift up depending on the dispersion relation of the system) and broaden continuously as the physical dimension of the confined phase decreases, which is not consistent with the sudden appearance nature of the 70 cm^{-1} band. Therefore we discount phonon confinement as the rational explanation. Consequently, this experimental observation can only suggest the existence of a new solid phase of NaNO_3 in the confined system. As we will discuss further in the following section, the formation of the new phase may be associated not only with the physical confinement but more importantly with the surface effect of the host.

As stated in experimental section, the confined NaNO_3 in porous host was controlled in such way that it replaced the bulk water and was surrounded by surface adsorbed water. Based on the observation of the internal modes of the NO_3 vibrations shown in figs. 4 and 5, one would argue that the spectrum change is only due to the NO_3 situated in a solution-like phase since it is known that the system still retains surface adsorbed water. The surface adsorbed water and surface hydroxyl will interact with some of the NO_3 groups close to the substrate surface which in turn gives rise to the typical "solvated" NO_3 symmetric vibration at 1050 cm^{-1} . As the pore size decreases, the surface to volume ratio increases which corresponds to an increase of the surface adsorbed water. Thus, the band at $\sim 1050\text{ cm}^{-1}$ is enhanced. Therefore, the NaNO_3 confined in the porous silica can be considered as two zones. One is the crystal-like solid at the pore center, and the solution-like molecular "aggregates" at and or near the interface between the surface water and the crystal-like NaNO_3 at the pore center. However, the presence of new mode appears at 70 cm^{-1} strongly suggesting an additional phase with ordered solid structure. Therefore, it is plausible that the structure of the confined NaNO_3 can be divided into three regions which is illustrated in fig. 7. They are the regular solid phase region at the pore center, the solution-like disordered molecular aggregates region at or near the substrate surface which is partially hydrated by the surface adsorbed water, and the new solid phase region between the regular solid phase region and the solution-like molecular aggregates region. The physical range of the region is clearly dependent upon the pore size of the host and the sample preparation condition. For the pore size $d < 2.5\text{ nm}$, only the solution-like molecular aggregates region remains.

Finally, the Rayleigh wing of the polycrystals, impregnated phase, and solution form of the NaNO_3 show a continuous broadening. Based upon our above-mentioned model for the NaNO_3 physically confined in pores, the observed Rayleigh wing broadening may indicate that the system changes from ordered homogeneous phase to disordered inhomogeneous state. However, the present Raman study is not sufficient to conclude the above hypothesis. More experiments are underway to explore the Rayleigh wing of NaNO_3 confined in porous silica.

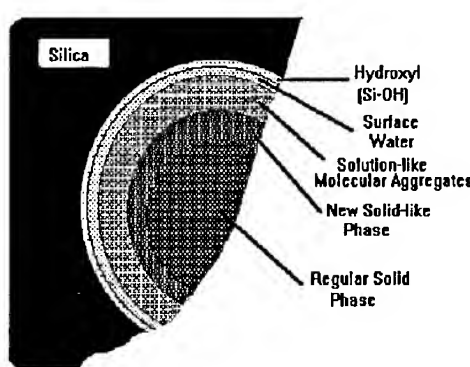


Figure 7. The proposed phase formation model of NaNO_3 confined in nanopores of porous silica.

CONCLUSION

Confining the NaNO_3 into the well-defined porous silica hosts provides an excellent model system to understand the clustering phenomena in aqueous solution. The comparative thermal and vibrational study of NaNO_3 in its bulk, confined, and solution phases suggests that the physically confined NaNO_3 nanophase under the present experimental conditions can be generally divided into three structural regions. They are regular solid phase at the pore center, the solution-like molecular aggregates at or near the substrate surface, and a new solid phase between the two. The physical range of each region varies with the pore size of the host. For a pore size $d < 2.5$ nm, only the solution-like molecular aggregates survive, which is consistent with our suggested solute clustering model investigated via ATR-FTIR spectroscopy.

REFERENCES

1. R. L. Frost and D. W. James, *Faraday Discuss. Chem. Soc.* **78**, 3223(1982).
2. F. Koussinsa, F. Bertin, and J. Bouix, *J. Raman Spectrosc.* **20**, 227 (1989).
3. C. E. Bugg, *J. Crystal Growth* **76**, 535 (1986); F. Rosenberger and E. J. Meehan, *J. Crystal Growth*, **90**, 74(1988).
4. I. T. Rusli, G. L. Schrader, and M. A. Larson, *J. Crystal Growth*, **97**, 345(1989).
5. F. Jin,
5. R. Mu, F. Hua, D. O. Henderson, *J. Crystal Growth*. (submitted) (1993).
6. R. Mu, F. Jin, S. H. Morgan, D. O. Henderson, and E. Silberman, *J. Chem. Phys.* (accepted for publication) (1993).
7. W. W. Schmahl and E. Salje, *Phys. Chem. Minerals*, **16**, 790 (1989); R. M. Lynden-Bell, M. Ferrario, I. R. McDonald, and E. Salje, *J. Phys.: Condens. Matter*, **1**, 6523(1989); R. J. Reeder, S. A. T. Redfern, and E. Salje, *Phys. Chem. Minerals*, **15**, (605)(1988); M. J. Harris, E. K. H. Salje, and B. Guttler, *J. Phys.: Condens. Matter* **2**, 5517(1990).
8. F. Brehat and B. Wynche, *J. Phys.* **18**, 4247(1985).
9. H. Terauchi and Y. Yamada, *J. Phys. Soc. Jpn.* **33**, 446(1972).
10. J. Warnock, D. D. Awschalom, and M. W. Shafer, *Phys. Rev. Lett.* **57**, 1753(1986); D. Awschalom and J. Warnock, *Phys. Rev. B* **35**, 6779(1987).
11. R. Mu and Malhotra, *Phys. Rev. B* **44**, 4296(1991); R. Mu and Malhotra, *Phys. Rev. B* [Rapid Comm.] **46**, 532 (1992) (and references therein).
12. C. L. Jackson and G. B. Mckenna, *J. Chem. Phys.* **93**, 9002(1990).
13. S. F. Trevino and H. Prask, *Phys. Rev. B* **10**, 739(1974).
14. T. R. Lettiteri and E. M. Brody, *Solid State Comm.* **26**, 235(1978).
15. G. Neumann and H. Vogt, *Phys. Status Solidi B* **85**, 179(1978).
16. H. Yasaka, A. Sakai, and T. Yagi, *J. Phys. Soc. Japan* **54**, 3697(1985).
17. H. Richter, Z. P. Wang, and L. ley, *Solid State Comm.* **39**, 625 (1981).
18. W. H. Yang, T. E. Huber, J. A. Lubin, G. E. Walrafen, and C. A. Huber, *Mat. Res. Soc. Symp. Proc* **286** (in press)(1992).
18. M. Multani, P. Ayyub, V. Palkar and P. Guptasarma, *Phase Transitions* **24-26**, 91 (1990).
19. L. T. Zhuravlev, *Langmuir* **3**, 316(1987).

Interfacial Roughness in GaAs/AlGaAs Multilayers: Influence of Controlled Impurity Addition

**S. Nayak, *J.M. Redwing, *T.F. Kuech, **D.E. Savage, **M.G. Lagally, *Dept. of Chemical Engineering, **Materials Science Program, University of Wisconsin, Madison, WI-53706

Impurities at heterointerfaces can alter the interfacial structure resulting in changes in physical, electrical and optical properties. We present a study of the interfacial roughness of GaAs/Al_xGa_{1-x}As superlattices which were grown using controlled addition of oxygen at the interface. The interfacial properties were characterized by x-ray diffraction. The morphology of the surface was determined by Atomic Force Microscopy (AFM). X-ray diffraction measurements, both θ -2 θ and rocking curves, were used to analyze the correlated and uncorrelated component of the interfacial roughness. A strong difference in the interfacial roughness was observed depending on whether the intentional oxygen incorporation occurred at the GaAs-to-AlGaAs interface or at both interfaces. When oxygen is incorporated at both interfaces, the x-ray reflectivity of the superlattice is decreased considerably resulting from a much higher interfacial roughness. The substrate miscut has a significant effect on RMS roughness, correlated roughness and its correlation length when oxygen is incorporated at the GaAs-to-Al_xGa_{1-x}As interface.

INTRODUCTION

Multilayer structures of GaAs/Al_xGa_{1-x}As grown by metal organic vapor phase epitaxy (MOVPE) have a wide variety of applications in electronic and optoelectronics devices. Quantum wells currently find increasing applications in areas such as lasers, modulators, waveguides as well as in the study of electronic transport and quasi-two-dimensional systems. The ability of quantum wells to provide such diverse and novel uses depends critically on the compositional uniformity and interfacial abruptness. The detailed determination of the interfacial structure is difficult when the typical spatial dimension of the roughness is on the nanometer scale. A number of physical methods have been used to extract interfacial roughness in semiconductors structures. Small angle x-ray diffraction and cross sectional transmission electron microscopy (CTEM) are conventionally used to ascertain interfacial roughness [1-4]. The average roughness can be obtained from low angle x-ray diffraction by measuring the specular reflectivity of the sample as a function of incidence angle. Photoluminescence measurements are also done to determine the electronic structure of the quantum well [5-6]. PL line broadening is typically used as a measure of the interfacial roughness. PL line broadening can, however, be due to the imperfections in the interface, fluctuations in alloy composition of wells and barriers and the presence of impurities. It is this last contribution to interfacial structure which is investigated in this paper.

Oxygen has been established as an important impurity in Al_xGa_{1-x}As epitaxial layers which can impact both the structure and properties of GaAs/Al_xGa_{1-x}As based interfaces. Surface and interface roughness, during the MOVPE growth process, can occur due to the deposition chemistry, thermal roughening, interdiffusion between the heterolayers and the presence of impurities at the interface. An understanding of the fundamental growth process that gives rise to interfacial roughness can enable us to control the morphology of the interface. We

present a study of how the structure of the interface is affected by the controlled addition of oxygen at the interface during growth by the MOVPE process.

THEORY

Small angle x-ray diffraction experiments on superlattices are used to determine the total RMS interfacial roughness, the correlated roughness and its lateral correlation length. The theory of x-ray diffraction from superlattices has been discussed by several authors [9-11]. The details of the kinematic model used here have been discussed in reference 9. X-ray reflectivity from superlattices at small angles arises from the constructive interference from individual layers of the superlattice. Typically, x-ray reflectivity consists of a diffused background with intense peaks, which are referred to as Bragg peaks. In a θ -2 θ scan, the reduction in the intensity of the Bragg peaks is mainly due to interfacial roughness. The grazing angle used in these measurements minimizes the influence of x-ray absorption in the superlattice. The RMS interfacial roughness is assumed here to follow a Gaussian distribution in the direction perpendicular to the growth front. The measured specular intensity of the superlattice peak I_{Spec} following these assumptions [9] can be written as:

$$I_{\text{Spec}} = I_0 \exp(-s_z^2 \sigma^2),$$

where I_0 is the reflectivity of the perfect mirror, $s_z = 4 \pi \sin \theta / \lambda$ is the momentum transfer vector in the vertical or substrate normal direction and σ is the RMS roughness. I_0 cannot be measured directly but it can be calculated using Fresnel diffraction theory. The RMS interfacial roughness is treated as a reduction in the superlattice peak intensity of a perfect mirror, which is equivalent to a frozen Debye Waller factor. Since the kinematic theory is insufficient to predict reflectance when the scattering is significant, then a recursion method is used.

The total RMS interfacial roughness cannot yield information about the correlated roughness. Correlated roughness is a result of morphology that is replicated from layer to layer. Because shorter wavelength features are more likely to be perturbed during growth, it is expected that longer wavelengths are preferentially replicated [7]. The diffuse background in a x-ray spectrum contains information about correlated roughness and correlation length associated with it. Intensity distribution of the diffuse background in a x-ray Bragg peak can be mapped by performing a transverse scan around a specific Bragg peak. Comparison of transverse scan and theoretical calculations allow extraction of interfacial parameters.

EXPERIMENTAL PROCEDURE

$\text{Al}_x\text{Ga}_{1-x}\text{As}/\text{GaAs}$ multilayer samples were grown by the MOVPE at 650°C on GaAs substrates [12]. Buffer layers of GaAs, 0.05 μm in thickness were initially grown on GaAs substrate, followed by 0.6 μm of $\text{Al}_{0.3}\text{Ga}_{0.7}\text{As}$. A superlattice consisting of 40 periods of GaAs and $\text{Al}_{0.3}\text{Ga}_{0.7}\text{As}$ was grown at the growth rate of 0.02 and 0.0286 $\mu\text{m}/\text{min}$, respectively. Each layer in the superlattice was 70 Å. Oxygen was introduced at the interface through exposure to an oxygen bearing precursor ($(\text{C}_2\text{H}_5)_2\text{AlOC}_2\text{H}_5$) during the growth [13]. Most samples are fabricated with only the GaAs-to- $\text{Al}_{0.3}\text{Ga}_{0.7}\text{As}$ interface exposed to the oxygen bearing precursor and not the $\text{Al}_{0.3}\text{Ga}_{0.7}\text{As}$ -to-GaAs interface. An additional sample was grown in which both interfaces were exposed to the oxygen bearing precursor. These superlattice samples were grown on substrates with various miscut angles in order to ascertain the influence

of miscut derived steps on the interfacial roughness with and without oxygen at the interface. The miscut angle of the substrate was 0° , 2° , $>4^\circ$. X-ray (Cu-K α) measurements were carried out using a conventional x-ray diffractometer. The rotation of the detector and sample can be controlled to an accuracy better than 0.01° and 0.005° respectively. The aperture of the entrance slit limits the divergence of the incident beam to 0.03° in the diffraction plane. Two types of scans were measured: θ - 2θ scans, which maps out reflected intensity in the reciprocal space perpendicular to the interface, and rocking curves on transverse scans, which measures the reflected intensity parallel to the interface. In this case, the detector slit integrates the scattered intensity perpendicular to the diffraction plane. All scans were made at a grazing incident angle ($0^\circ \leq \theta \leq 3^\circ$). AFM images were obtained using a commercial AFM at constant height mode.

RESULT ANALYSIS

The results were analyzed using the model discussed in detail in reference 9 and therefore limited by the assumptions inherent in that model. In the RMS roughness measurement, roughness is assumed to be isotropic within the plane of the interface. The RMS roughness of the interface is determined by comparing the calculated and measured integrated specular intensity of each of the 3rd, 5th and 7th order peaks in the x-ray spectrum. When intensity due to the diffused background is significant, the specular intensity in a θ - 2θ scan can be much smaller and therefore the calculated RMS roughness is the lower limit of roughness. The probed depth of the sample is $1 \mu\text{m}$ at $\theta=2^\circ$. The first order peak is omitted from analysis because of the depth of the sample probed near the grazing angle is very small and it is not accurately modeled by kinematic theory. The even order peaks are neglected because their lower intensity. The lower limit and upper limit of roughness is therefore determined by fitting the integrated intensity of 7th order peak and 3rd peak respectively. Fig. 1 shows a typical calculated and measured x-ray intensity profile. The RMS interfacial roughness of the superlattice is 5\AA .

Intensity of the superlattice peaks is strongly affected by the addition of oxygen at the interface as shown in fig. 2 and table I. All the samples were grown on substrates with 2° miscut angle. Oxygen added at the GaAs-to- $\text{Al}_x\text{Ga}_{1-x}\text{As}$ has a minimal effect on RMS roughness but it reduces the correlation length of correlated roughness. When oxygen is added to both interfaces the roughness increases significantly. The increase in roughness corresponds to a higher rate of oxygen incorporation at the $\text{Al}_x\text{Ga}_{1-x}\text{As}$ interface.

The effect of substrate step density, in the presence of oxygen, on the RMS interfacial roughness was investigated through the growth of superlattices on substrates with 0° , 2° and $>4^\circ$ miscut angles towards $<110>$ direction. Superlattices were grown with and without the addition of oxygen at GaAs-to- $\text{Al}_x\text{Ga}_{1-x}\text{As}$ interface. The results are tabulated in table II. The RMS roughness of the superlattices decreases with the addition of oxygen at the GaAs-to- $\text{Al}_x\text{Ga}_{1-x}\text{As}$ interface. The RMS roughness changes very little between superlattices grown on substrates with 0° and 2° miscut angles without any oxygen incorporation at the interface. The correlation length of correlated roughness gets smaller with the addition of oxygen at the interface except for the superlattice with $>4^\circ$ miscut angle. If oxygen is incorporated at the GaAs-to- $\text{Al}_x\text{Ga}_{1-x}\text{As}$ interface, the RMS roughness increases and correlation length decreases, with increasing miscut angle. A significant contribution to the superlattice peak intensity in the x-ray spectrum of superlattices grown on substrates with $>4^\circ$ miscut angle, with and without oxygen at the interface, is due to a strong diffused background. The reported roughness in this case is

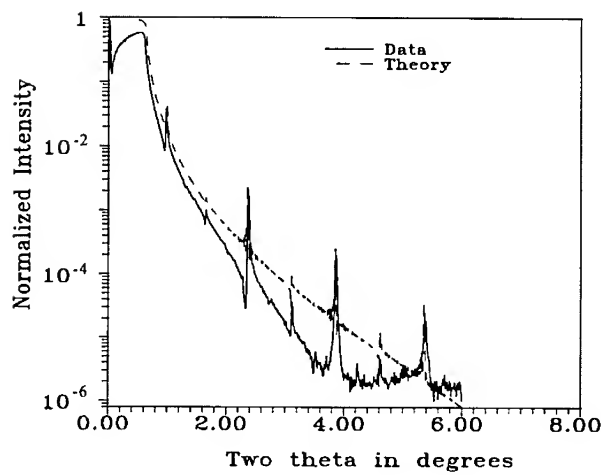


Fig.1 The calculated and measured x-ray intensity from GaAs/AlGaAs superlattice grown at 650°C.

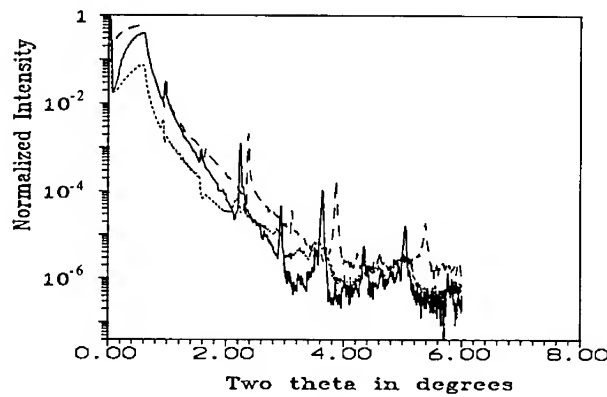


Fig.2 The measured x-ray profile of no doping (solid line), oxygen doping at GaAs to AlGaAs interface (dashed line) and oxygen doping at both interfaces (dotted line).

therefore the lower limit of roughness. The surface roughness of the superlattices was studied by AFM. These measurements yield a final surface roughness of 1 and 3 nm when averaged over a 5 μm by 5 μm area on the 0° and 2° miscut sample respectively. The AFM measurements reflect both the roughness evolved during growth as well as any roughness generated by surface oxidation of the GaAs. The general trends in the lateral scale or correlation length of the AFM-derived roughness agree qualitatively with the x-ray measurements.

TABLE I: The total RMS roughness (σ_{tot}) and correlated roughness (σ_{corr}) of the $\text{Al}_x\text{Ga}_{1-x}\text{As}/\text{GaAs}$ superlattices. The thickness of each layer and the RMS roughness are obtained by fitting the conventional 0-2θ scans. The correlated roughness and correlation length (ξ) is determined by fitting the diffuse component of the intensity of the 3rd order of rocking curves. The uncorrelated roughness can be determined from the relationship: $\sigma_{\text{tot}}^2 = \sigma_{\text{corr}}^2 + \sigma_{\text{uncorr}}^2$. All samples were grown at 650°C.

40 Periods $\text{Al}_{0.3}\text{Ga}_{0.7}\text{As}/\text{GaAs}$ layer thickness	Oxygen doping at the interface	Total RMS Roughness σ_{tot} (Å)	Correlated Roughness σ_{corr} (Å)	Correlation Length ξ (Å)
59/62 Å	No doping	5.0±0.5 Å	1.2 Å	2500 Å
57/61 Å	GaAs to AlGaAs interface	5.0±0.5 Å	*	**
62/63 Å	Both interfaces	6.8±0.5 Å	*	*

TABLE II: The effect of oxygen doping at the interface of $\text{GaAs}/\text{Al}_{0.3}\text{Ga}_{0.7}\text{As}$ superlattices grown on GaAs substrates with various miscut angles.

Miscut angle	Oxygen doped at $\text{GaAs}/\text{Al}_{0.3}\text{Ga}_{0.7}\text{As}$			No doping		
	σ_{tot} (Å)	σ_{corr} (Å)	ξ (Å)	σ_{tot} (Å)	σ_{corr} (Å)	ξ (Å)
0°	3.8±0.5 Å	1.5 Å	1500 Å	4.8±0.5 Å	1.2 Å	2000 Å
2°	†5.0	*	**	5.0±0.5 Å	1.2 Å	1500 Å
>4°	†7.0	*	***	†10 Å	*	***

* Could not be determined with the present model.

** Correlation length is less than 1000 Å.

*** Correlation length is less than 100 Å.

† The RMS roughness is the lower limit of roughness.

These results indicate that the incorporation of oxygen at these superlattice interfaces can alter the structure of the growing surface. Since the samples were grown at high temperatures, the growing surface is assumed to progress in a step-flow growth mode. The impurities incorporated into the growing surface appears to alter this flow of steps across the surface. The changes in the character of interfacial roughness with miscut angle are most directly related to the higher oxygen incorporation found when increasing the substrate miscut angle. In addition, the theoretical density of surface steps is also increasing with miscut angle. The RMS or overall roughness does not seem to be strongly affected by oxygen addition in the case of the GaAs-to-Al_xGa_{1-x}As interface. The lateral correlation length does, however, dramatically decreases. The effect of oxygen appears to break up the coherence of the step flow across the surface. Step pinning or island or layer nucleation can arise from the impurity addition to the surface yielding the observed roughness.

Conclusions

The controlled addition of oxygen to GaAs/Al_xGa_{1-x}As interfaces was carried out during MOVPE-based growth. The samples were characterized by glancing angle x-ray diffraction and AFM. The incorporation of oxygen at the GaAs-to-Al_xGa_{1-x}As interface results in a decrease in the lateral correlation length of the roughness. Addition of oxygen to both interfaces results in a large increase in the interfacial roughness of the superlattice. These techniques yield quantitative measurements of the interfacial roughness which can now be used to interpret other measurements, such as photoluminescence and electrical properties.

ACKNOWLEDGMENT

The authors would like to acknowledge the support of NSF through the Materials Research Group on Chemical Vapor Deposition (DMR-9121074).

REFERENCES

1. D. Gammon, B.V. Shanabrook, and D.S. Katzer, *Phys. Rev. Lett.* **67**, 1547 (1991).
2. A. Ourmarzd, D.W. Talyor, J. Cunningham and C.W. Tu, *Phys. Rev. Lett.* **62**, 933 (1989).
3. C.A. Warwick, W.Y. Jan, A. Ourmarzd, and T.D. Harris, *Appl. Phys. Lett.* **56**, 2666 (1990).
4. D. Chrzan and P. Dutta, *J. Appl. Phys.* **59**, 1504 (1986).
5. J. Singh and K.K. Bajaj, *J. Appl. Phys.* **57** (12), 5433, (1985)
6. J. Singh and K.K. Bajaj, *Appl. Phys. Lett.* **44** (11), 1075, (1985)
7. See for example, R. Brusina, R.P.U. Karunasiri and J. Rudnick, *Kinetics of Ordering and Growth at Surfaces*, edited by M.G. Lagally (Plenum, New York, 1990), p. 395 and references therein
8. S.K. Sinha, E.B. Sirota, S. Garoff and H.B. Stanley, *Phys. Rev. B* **38**, 2297 (1988).
9. D.E. Savage, J. Kleiner, N. Schimke, Y.H. Phang, T. Jankowski, J. Jacobs, R. Kariotis, and M.G. Lagally, *J. Appl. Phys.* **69**, 1411 (1991).
10. D.E. Savage, N. Schonke, Y.H. Phang, and M.G. Lagally, *J. Appl. Phys.* **71**, 3283 (1992)
11. Y.H. Phang, D.E. Savage, T.F. Kuech, M.G. Lagally, J.S. Park and K.L. Wang, *Appl. Phys. Lett.* **60**, 2988 (1992).
12. T.F. Kuech, E. Veuhoff, T.S. Kuan, V. Deline, and R. Potemski, *J. Crystal Growth* **77**, 257 (1986)
13. J.M. Huang, D.F. Gaines, T.F. Kuech, R.M. Potemski and F. Cardone presented at 1993 EMC, Santa Barbara, CA, (1993) to be published
14. S. Nayak, J.M. Redwing, T.F. Kuech, Y.-H. Phang, D.E. Savage, and M.G. Lagally, *Mat. Res. Soc. Symp. Proc.* Vol. 312 (1993)

**DIRECT OBSERVATION OF DIFFRACTION ARCS
FROM NANOSCALE PRECIPITATES IN STEELS
BY HIGHLY BRILLIANT AND FOCUSED SYNCHROTRON RADIATION BEAM
AND IMAGING PLATE**

Yasuo Takagi*, Yoshitaka Okitsu,** and Toshiyasu Ukena**

*R & D Laboratories for Advanced Materials and Technology, Nippon Steel Corp.,
Kawasaki, Kanagawa 211, JAPAN

**Hirohata R & D Laboratories, Nippon Steel Corp., Himeji, Hyogo 671-11, JAPAN

ABSTRACT

Direct observation of diffraction arcs by X-ray from nanoscale precipitates in steels has become possible for the first time by using a highly brilliant and focused synchrotron radiation beam at BL3A of Photon Factory, and also by using an "imaging plate", a two dimensional X-ray detector which has a wide dynamic range and high sensitivity. For examples, most of the diffraction arcs from ϵ -Cu precipitates (~ 200 Å in diameter and ~ 1 at. % in concentration) in Cu-added steels were observed. The method can apply to non-destructive and *in-situ* observation of creation and growth processes of the precipitates which has close relationships to various physical properties of the matrix steels.

INTRODUCTION

It is well known that nanoscale precipitates included in various types of steels have very important roles on their physical properties [1]. Structural studies of the precipitates have been performed mainly by electron diffraction (ED) method by using transmission electron microscope (TEM) because a highly focused and brilliant electron beam is necessary for the analyses. Although accurate determination of the crystal structure of each precipitates is possible by using the ED method, it has some weak points. One of them is that samples must be prepared to be thin enough to transmit the electron beam. Therefore, the method is usually destructive. Such destructive measurements sometimes arouse questions about whether observed phenomena are exactly the same ones occurring in the real bulk materials.

X-ray diffraction (XRD) technique is another popular method for various structural analyses of materials [2]. However, few studies on applications of XRD to the structural analysis of the precipitates in steels have been reported till now because no such highly brilliant and focused x-ray sources equivalent to TEM and sensitive x-ray two-dimensional area directors have been available. In principle, if such difficulties can be overcome, the XRD method has some advantage over the ED method because the diffraction measurements can be carried out not only by transmission (Laue case) but also by reflection (Debye case) which enables to observe a bulk properties without thinning sample [3].

Advent of synchrotron radiation (SR) as a highly brilliant x-ray source and also that of imaging plate (IP) as a highly sensitive two-dimensional area detector eliminated such difficulties and enabled the direct observation of diffraction arcs from small and dilute particles in matrix like nanoscale precipitates in steels.

The purpose of this report is to introduce the new method of the structural analysis of nanoscale precipitates by using XRD, showing some examples taken at PF-BL3A. The SR experimental station, PF-BL3A, equips a very unique X-ray optics system by which a highly brilliant and focused SR beam can be generated. "Cu-added steels" [4] were chosen as idealistic test samples to examine the detection limit of the crystal size from which the diffraction arcs can be observed because the sizes of the Cu-precipitates subsequently increase on the aging process in the steels.

EXPERIMENTAL

The SR beam at BL3A of Photon Factory, Tsukuba, Japan was used as an X-ray source. Among various beamlines (SR experimental stations) using a normal bending magnet (BM) as an SR source, BL-3A has an unique x-ray optics system[5]. Figure 1 shows the optics of BL3A schematically. It has a pair of total reflection mirrors on the both side of a double-crystal monochromator. By bending its surface parabolically the first mirror collimates the SR beam and improves parallelness of the beam. It also eliminates the X-ray having shorter wavelength than a critical wavelength, λ_c (the cut-off wavelength). The second mirror having identical mechanism to the first one focuses the beam vertically onto the sample. By bending the second crystal of the monochromator cylindrically, a focusing of the horizontal direction of the beam is possible. By using such optics the brilliance of the beam becomes more than 100 times higher than that in other conventional BM beamlines. The beam size also can be reduced down to 1 x 1 mm size. SR beam having rectangular size (1 x 6 mm) was used in the experiment.

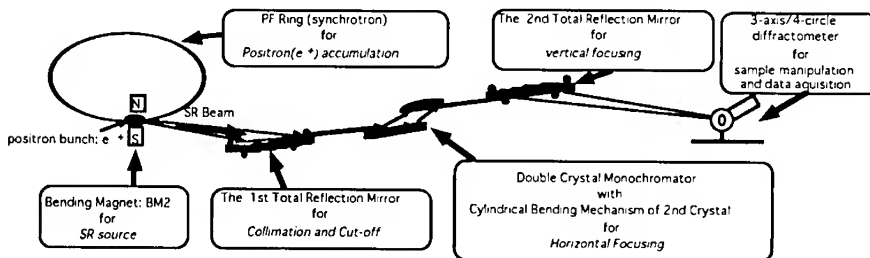


Fig. 1 Schematic drawing of x-ray optics of PF-BL3A (modified and added to Ref. [5])

A new type of two-dimensional (area) detector, imaging plate (IP) was used for the measurements [6] & [7]. The detector utilizes x-ray induced photo-stimulated luminescence phenomena. The imaging plate which has ~ 0.5 mm in thickness is a flexible plastic plate on which photo-stimulable BaFBr:Eu⁺ crystal is coated. By X-ray excitation a part of the Eu⁺ ions are ionized to Eu³⁺ while electrons liberated to the conduction band are trapped at F⁻ center. By the laser (a visual light) beam the trapped electron at F-centers are again liberated to the conduction band and return to Eu³⁺ ions converting them to excited Eu²⁺. At the same time photo-induced luminescence is emitted and detected by a photo-multiplier(s). By scanning an laser beam and photo-multiplier(s) on each spot on the IP plate, the recorded IP image by X-ray can be observed.

The sensitivity is as high as 1 (luminescence) photon per pixel (a unit size of IP, usually $100 \times 100 \mu\text{m}$). It has also a wide dynamic range and a linearity (more than 10^5). As the IP reader of the recorded information *BAS 2000* of *Fuji Films Co., Ltd.* was used.

The sample was mounted at the 4-circle goniometer of the triple axis/four circle diffractometer installed at BL3A [8]. The measurements of the diffraction arcs were performed by using a typical Debye-Scherrer type method [2] by using IP instead of a conventional film as described in Fig. 2. The imaging plate was mounted onto 2θ axis and ϕ , θ and/or χ axes were used to oscillate the sample to increase the number of the crystals which satisfy the Bragg condition.

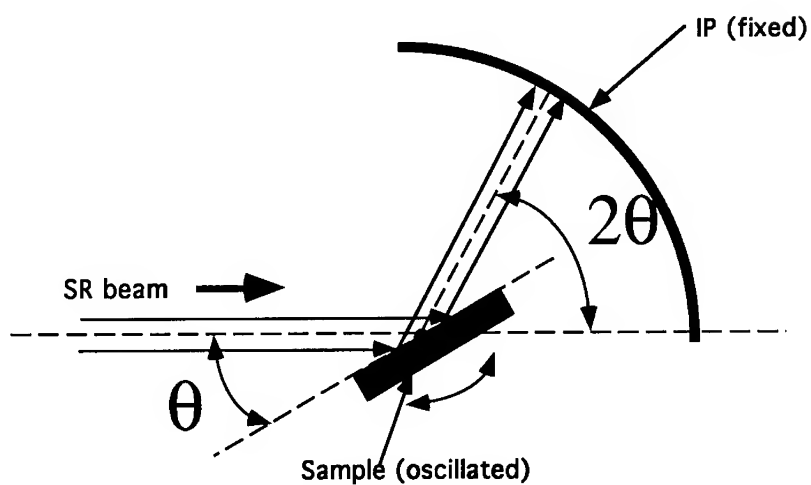


Fig. 2 Instrumentation of the experiment. The sample was oscillated along ϕ , θ and/or χ axes, while IP was fixed on the 2θ axis.

The samples used were so-called "Cu-added steels", a typical composition of which is shown in Table I.

Table I A typical composition of the extra-low carbon Cu-added steel (wt. %)

Cu	Si	Mn	P	S	sol. Al	N	Ti	C
1.60	0.02	0.25	0.017	0.004	0.055	0.0013	0.045	0.0013

The samples were prepared by the following rolling and aging processes described in Fig. 3. The Cu-precipitates were formed at the last process of aging at around 550 - 700 °C. As the aging proceeded, the Cu-precipitates were formed and transformed into the ϵ -Cu structure and subsequently increase their sizes. The process provides an idealistic test sample for checking the detection limit of the crystal sizes from which the diffraction arcs are observed. The following six samples on the several aging stage were chosen for the experiments. The formation of the Cu-precipitates in the samples were confirmed by TEM experiments in advance. The aging temperatures and times, and also estimated average sizes of precipitates are shown in Table II. A typical sample size used in the present study was about 50 x 50 x 2 mm.

Table II Aging temperatures and times, and also the sizes of the precipitates in the sample used for the experiments.

Sample No.	I	II	III	IV
Temp. (°C)	550	550	550	700
Time (hrs.)	5	10	25	65
size (Å)	~100	~200	~200	~800

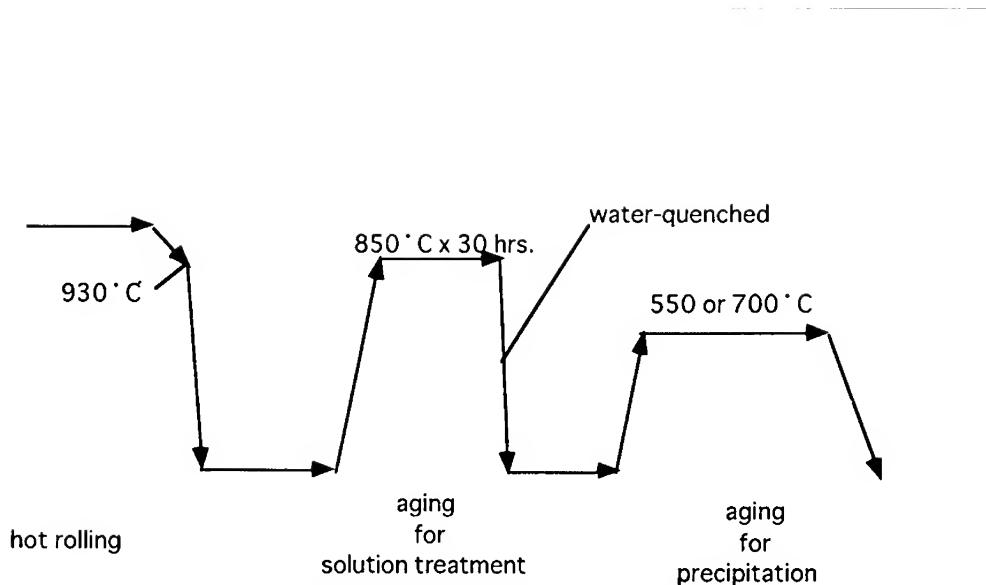


Fig. 3 Formation processes of a typical Cu-added steel

The wavelength of incident SR beam was chosen as 1.80 \AA which is a little longer than that of Fe K absorption edge ($\lambda = 1.74346 \text{ \AA}$) to avoid an increase of background level due to emission of fluorescence related to the Fe K-edge ($K_{\alpha 1}$, $K_{\alpha 2}$, & K_{β} emission).

RESULTS

While only several diffraction arcs identified to be those from Fe-matrix were observed in the IP images of the sample I (no figure), some other arcs identified to those from ϵ -Cu were also observed in the other samples (II, III, & IV). Figures 4 & 5 show the IP images from the sample II & IV, respectively. The horizontal direction corresponds to the 2θ axis in the images. The d-spacings were determined by the Bragg law from the coordinate of the 2θ axis. The vertical axis corresponds to the vertical direction of 2θ axis usually called χ axis. The orientation of the crystal plane toward the incident beam can be estimated from the coordinate of χ axis.

Several diffuse but clear diffraction arcs identified to be those from ϵ -Cu precipitates were observed in Sample II. A similar image was observed from the sample III (no figure), indicating the precipitates in both samples have a similar structure.

The feature of the image from the sample IV (Fig. 5) which was aged much longer (65 hrs.) and at a slightly higher temperature than other samples were very different. Although the 2θ coordinates of the arcs observed were similar to those from sample II, each arc is not continuous but consisted of some "spotty" areas which have very characteristic shapes.

The results of d-space evaluation of ϵ -Cu precipitates in all the samples are summarized in Table III.

Table III The d-spacings (in \AA) calculated from the diffraction arcs on the IP images and corresponding indices of ϵ -Cu.

II	III	VI	ϵ -Cu	indices
2.088	2.090	2.092	2.088	(111)
1.810	1.830	1.809	1.808	(200)
1.282	not observed	1.277	1.278	(220)
1.099	not observed	1.095	1.090	(311)

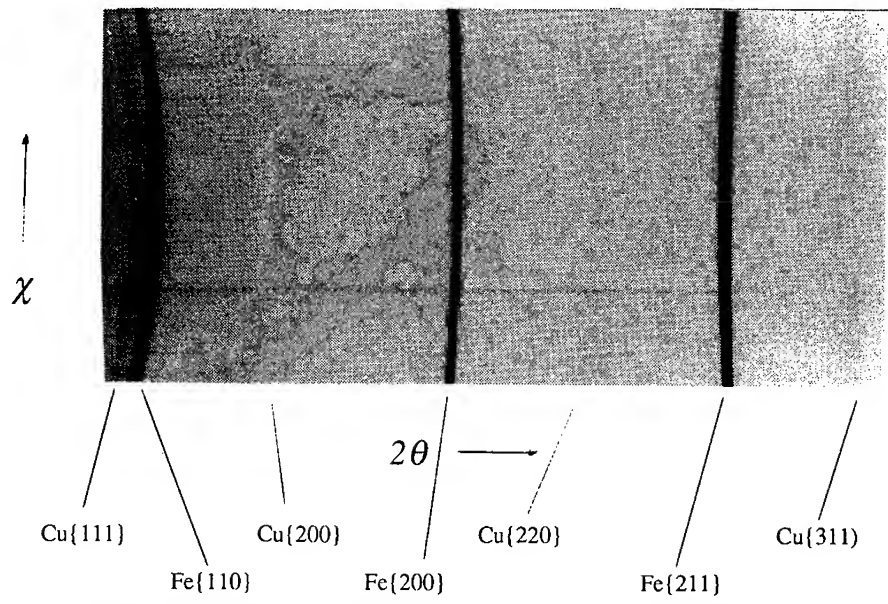


Fig. 4 The IP image of diffraction arcs from the sample II (aged for 10 hrs. at 550 °C)

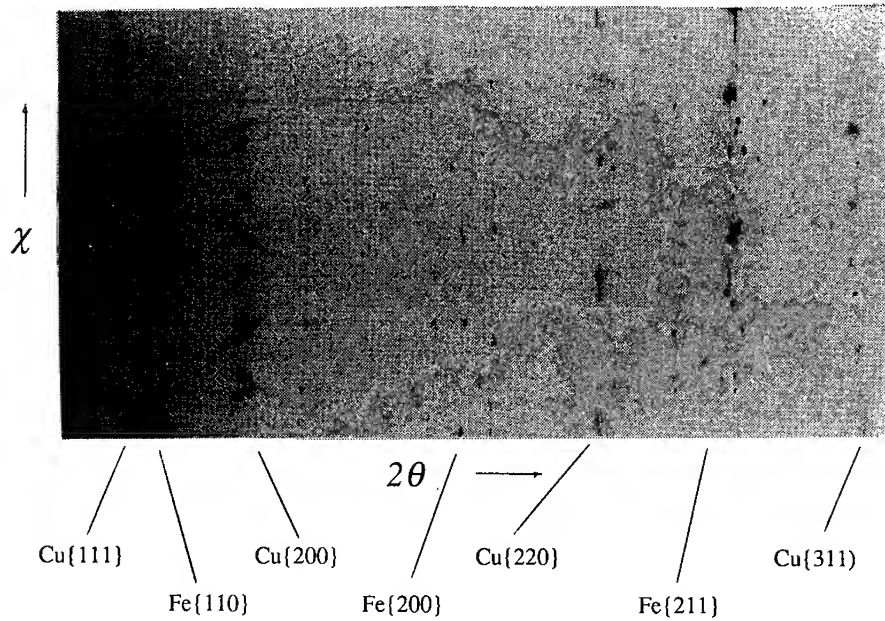


Fig. 5 The IP image of diffraction arcs from the sample IV (aged for 65 hrs. at 700 °C).

DISCUSSION

Various information on the structures of the precipitates were recorded in the IP image of the diffraction arcs observed in the present study. Not only the information of d-spacings of the crystal structure but those on crystal shapes, sizes, and their distribution (real space information), crystal lattice strains and orientation (k-space information) are also recorded. However, extraction and separation of such information are not very easy because there are various factors like the beam shape and divergence which are necessary to take into consideration for the analyses.

For example, the diffuse and broad nature of the arcs observed in the image of the sample II & III might be due to the natural broadening of the diffraction arcs from the small crystals. However, some lattice distortions of the formation and growth processes of the precipitates can also contribute to form such diffuse images.

On the other hand, the spotty nature of the arcs in the image of Sample IV can be interpreted as the results of the crystal coarsening of the precipitates. It is probable each area in the arcs corresponds to the reflection from a "single" crystal of the precipitates. Such direct observation of crystal shapes and sizes are not unusual by the XRD method using SR [9]. A "streak-like" shapes of the spots (see Fig. 5) indicates the distribution of the d-spacings in a crystallite of the precipitates, indicating some distorted minor areas were included in the crystallite.

Further analyses are necessary for more quantitative interpretation of the images.

CONCLUSIONS

Based on the above findings, the following can be concluded at the present stage. By using focused and highly brilliant SR beam and imaging plate, diffraction arcs from nanoscale precipitates in steels, the average diameters of which were larger than 200 Å, were successfully observed. The d-spacings of them were determined from the arcs.

- (1) When the average diameter of the precipitates were small (~200 Å), diffuse and continuous diffraction arcs were observed. The separation of the diffraction spots from each crystallite of precipitants was not possible.
- (2) If the average diameter was large enough (~800 Å), diffraction arcs consisted of some spotty areas. Each area corresponds to a diffraction spot from each crystallite of the precipitates.

REFERENCES

1. W.C. Leslie, *The Physical Metallurgy of Steels*, (Hemisphere Publishing Corporation, Washington, New York, London, 1981) pp. 97-103.
2. B.D. Cullity, *Elements of X-Ray Diffraction*, 2nd Ed. (Addison-Wesley Publishing Company, Inc., Reading, Massachusetts, Menlo Park, California, London, Amsterdam, Don Mills, Ontario, Sydney, 1978).
3. W.H. Zachariasen, *Theory of X-Ray Diffraction in Crystal* (Dover Publishing Inc., New York, 1945) pp.120 - 123.
4. E. Hornbogen and R.C. Glenn, *Trans. Metall. Soc. AIME*, **218**, 1064 (1960).
5. S. Sasaki, T. Mori, A. Mikuni, H. Iwasaki, K. Kawasaki, Y. Takagi, and K. Nose, *Rev. Sci. Instrum.*, **63**, 1047 (1992).
6. J. Miyahara, K. Takahashi, Y. Amemiya, N. Kamiya, and Y. Satow: *Nucl. Instrum. & Method in Phys. Res.*, **A246**, 572 (1986).
7. Y. Amemiya, Y. Satow, T. Matsushita, J. Chikawa, K. Wakabayashi, and J. Miyahara, *Topics in Current Chemistry*, **147**, 121 (1988).
8. K. Kawasaki, Y. Takagi, K. Nose, H. Morikawa, S. Yamazaki, T. Kikuchi and S. Sasaki, *Rev. Sci. Instrum.*, **63**, 1023 (1992).
9. K. Kawasaki, H. Iwasaki, H. Kawata and K. Nose: *Rev. Sci. Instrum.*, **63**, 1110 (1992).

NANOSTRUCTURAL STUDIES BY MÖSSBAUER SPECTROSCOPY

GEORGIA C. PAPAEFTHYMIOU

Francis Bitter National Magnet Laboratory, Massachusetts Institute of Technology, Cambridge, MA 02139

ABSTRACT

Application of ^{57}Fe Mössbauer spectroscopy to the determination of magnetic structural parameters relevant to nanostructural studies is discussed. Variable temperature and applied magnetic field strength investigations are considered in order to illustrate the power of the technique in rendering a microscopic picture of the internal spin structure and dynamical spin relaxation phenomena associated with nanoscale systems. Examples from biology and chemistry, where iron aggregates of nanometer dimensions are encountered, are presented.

INTRODUCTION

The application of ^{57}Fe Mössbauer spectroscopy for the determination of magnetic nanostructural parameters dates back to the classical work by Kündig et al. [1] on the superparamagnetic properties of supported $\alpha\text{-Fe}_2\text{O}_3$ fine particles. For small 2-20 nm diameter, non-interacting magnetic particles the observation of the transition from superparamagnetic to ferromagnetic behavior by variable temperature Mössbauer spectroscopy, coupled with a measurement of the average particle size by electron microscopy or X-ray line broadening, leads to calculation of the average magnetic anisotropy of the particles. The latter is of fundamental importance in determining the overall magnetic response of the particles to thermal and magnetic excitations. A large number of Mössbauer investigations on the magnetic properties of iron microcrystals have since been reported, including the observation of surface-sensitive magnetic anisotropy barriers [2] and the pinning of surface spins [3] when the Mössbauer spectra are examined in the presence of externally applied magnetic fields. Recent applications of the technique encompass a diverse range of investigations, from the study of monocrystalline iron oxide nanocompounds used as targeted diagnostic pharmaceuticals [4] to nanophase molecular antiferromagnets which help delineate the molecular/solid state boundary [5] to the iron nucleation processes in the ferritin mineral iron core [6]. There have also been some new and exciting applications in materials such as the investigations of critical magnetic transitions in ultra-thin granular films of iron [7] and the excellent soft magnetic properties of iron-based nanocrystalline materials [8]. However, the Mössbauer study of the second application is further complicated by the presence of interacting magnetic grains, a discussion of which is beyond the scope of this article limited to the study of isolated, non-interacting nanostructures. Furthermore, this presentation does not attempt to review the field but only to highlight the basic principles and illustrate them with examples from the author's own and collaborative work.

THEORETICAL CONSIDERATIONS

The total interaction energy that determines the magnetic behavior of iron nanophases in the presence of an external magnetic field is given by

$$E = E_{\text{ex}} + E_h + E_{\text{ani}} \quad (1)$$

where $E_{\text{ex}} = -J \sum_{ij} \mathbf{S}_i \cdot \mathbf{S}_j$ within the Heisenberg model. J gives the strength of the exchange interactions present between neighboring spins that determine the Néel temperature, T_N , in an extended system of a corresponding lattice structure. $E_h = -\mu \mathbf{H}_0$ gives the magnetic orientational energy of the total uncompensated moment, μ , of the nanostructure in an externally applied field H_0 . E_{ani} is the magnetic anisotropy energy which fixes the magnetization along an easy direction within the nanocrystal. For a cluster or particle of volume V and uniaxial symmetry, $E_{\text{ani}}(\theta) = 2KV \sin^2(\theta)$ where θ is the angle between the magnetization \mathbf{M} and the easy

axis, and K is the magnetic anisotropy constant. There are two contributions to K : one arising from the inner core lattice magnetocrystalline anisotropy, the other from strain anisotropy due to the particle shape and structural discontinuity at the surface. The magnetic anisotropy energy barrier $2KV$ determines the superparamagnetic relaxation properties of the nanostructures which exhibit technique-dependent blocking temperatures

$$T_B = 2KV/(k_B \ln(\tau_m/\tau_0)) \quad (2)$$

where τ_m is the characteristic measurement response time of the experimental technique used, k_B is Boltzmann's constant and τ_0 is a constant of the order of 10^{-9} sec. Mössbauer measurements over a wide range of temperatures and applied magnetic field strengths can be used to study the interplay among the three terms of Eq.(1) in determining the magnetic behavior of small magnetic structures.

What makes Mössbauer spectroscopy particularly powerful in the study of nanoscale systems is the relatively short characteristic measurement time of the technique $\tau_m \sim 10^{-8}$ sec as compared to bulk susceptibility and magnetization measurements with $\tau_m \geq 1$ sec. Most mesoscopic systems of one to several tens of nanometers in diameter possess blocking temperatures commonly accessible by Mössbauer spectroscopy, allowing examination of magnetic order below T_B and direct measurement of magnetic anisotropy energies. For nanostructures at the lower limit of the mesoscopic range bordering molecular sizes Mössbauer offers a window into the investigation of short-range intramolecular order and dynamical spin correlation and relaxation phenomena [5].

The fundamental physical process that records the Mössbauer spectrum is the resonant γ -ray absorption by the ^{57}Fe nucleus to its first excited metastable state lying at 14.4 keV above the ground state (Fig. 1). The high nuclear spin Larmor precession frequency v_L of this excited state in an effective field, \mathbf{H}_{eff} , arising from unpaired electronic spins and typically 500 KOe for ferric ions is what gives the technique its exceptionally short response time

$$v_L = (g_n \mu_n / \hbar) H_{\text{eff}} \approx 3.9 \times 10^7 \text{ sec}^{-1}; \quad \tau_m = 1/v_L \quad (3)$$

Here g_n is the nuclear g-factor, μ_n is the nuclear magneton and \hbar is Planck's constant.

For magnetically ordered nanophases, there exists a critical temperature above which thermal energies kT overcome the magnetic anisotropy barrier $2KV$ and produce rapid reversals of the net magnetic moment along opposite directions of the symmetry axis which are energetically equivalent, inducing a behavior analogous to that of paramagnetic atoms, i.e. superparamagnetism[9]. In the presence of a distribution of particle sizes there exists, equivalently, a critical volume below which, at a certain temperature, superparamagnetic relaxation will occur. For superparamagnetic relaxation times $\tau_s < \tau_m$, the rapid spin fluctuations produce a vanishing average $\langle H_{\text{eff}} \rangle$ at the nucleus, which results in paramagnetic spectra, while for $\tau_s > \tau_m$ magnetically split Mössbauer spectra are obtained (Fig. 1). The transition from paramagnetic (doublet) to magnetic (sextet) spectra with decreasing temperature determines the blocking temperature T_B , and therefore K , through Eq.(2).

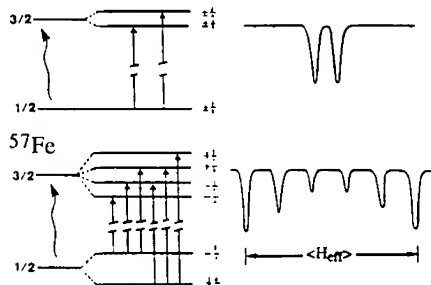


Figure 1. Fundamentals of Mössbauer Spectroscopy. The resonant γ -ray absorption by the ^{57}Fe nucleus records the Mössbauer spectra. Resonance is achieved by Doppler-shifting the γ -ray energy, $E = E_0 (1 \pm v/c)$ ($E_0 = 14.4$ KeV) allowing observation of the hyperfine structure of the nuclear energy levels. An internal fluctuating magnetic field with $\tau_s < \tau_m$ (top) gives a paramagnetic spectrum, while a static magnetic field during the time of the measurement $\tau_s > \tau_m$ (bottom) gives a magnetic spectrum.

In addition to the internal effective field, H_{eff} , an external magnetic field, H_0 , may be applied. If H_0 is parallel to the γ -ray propagation direction, selection rules for the magnetic dipole Mössbauer transition dictate that the $\Delta m = 0$ lines (Lines 2 and 5 of the sextet) approach zero intensity if a colinear spin alignment relative to H_0 is obtained. Deviations from zero intensity can be used to measure the degree of non-colinearity or spin canting in the structures.

APPLICATIONS

Three examples follow which serve to illustrate the use of the technique in determining (a) the magnetic anisotropy constant K of a magnetite-based pharmaceutical nanocompound, (b) the particle size distribution of iron deposits due to a hemolytic iron overloading disease and (c) the internal spin structure of a one nanometer diameter undecanuclear iron cluster that suggests the presence of collective magnetic correlations among iron spins.

(a) Magnetopharmaceuticals for MRI Contrast Enhancement: Estimation of K — Magnetic resonance imaging (MRI) promises to compliment, if not eventually compete with computerized tomography in the detection and diagnosis of cancer associated with the reticuloendothelial system i.e., liver, spleen and bone marrow. Its potential lies in the use of ferrite particles for image contrast enhancement of cancer tumors and lymphomas. Image enhancement has been achieved by taking advantage of the phagocytotic property of healthy reticuloendothelial cells which is lost upon invasion by cancer [10].

Ferrites are ferrimagnetic crystalline iron oxides of a spinel structure with the general formula $Fe_2^{3+}O_3 \cdot M^{2+}O$, where M is a divalent metal ion such as Mn^{2+} , Ni^{2+} , Co^{2+} and Mg^{2+} . Of these, magnetite -- where the divalent ion is iron -- is most commonly used. Polymeric stabilization of magnetite in small aggregates can be achieved by coating the particles with a variety of hydrophylic substances. The resulting particles are superparamagnetic. The H^+ T_2 (transverse) relaxation time of water molecules in the vicinity of such magnetic impurities is drastically shortened (owing to the dephasing of their Larmor precessional frequency by the magnetic field gradient present around a magnetic particulate) with a concomitant loss of magnetic resonance signal intensity. Since tumor cells are not phagocytes for foreign particles, H^+ signals originating from their vicinity are not affected and tumor imaging is enhanced. Current research in the field focuses on generalizing the use of these magnetopharmaceuticals as contrast enhancement agents for different organs beyond the reticuloendothelial system [4].

Figure 2 shows temperature-dependent Mössbauer spectra and a transmission electron microscopy (TEM) image of such a magnetopharmaceutical [4]. These are magnetite-based nanoparticulates, surface-coated by dextran molecules. TEM analysis indicates that the average size of the inner magnetic core of the particles is 4.6 ± 1.2 nm. The overall magnetic splitting of the Mössbauer spectrum gives a saturated effective magnetic field $H_{eff} = 505$ KOe which

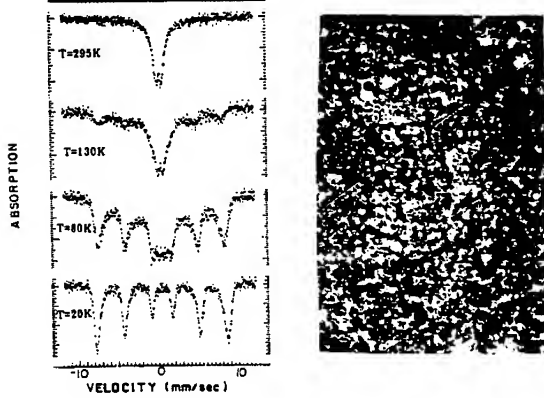


Figure 2. (Left) Mössbauer spectra of magnetite-based magnetopharmaceuticals at various temperatures showing typical superparamagnetic relaxation phenomena associated with small magnetically ordered particles. (Right) Bright field TEM image of these particles at 76,000 magnification.

determines $\tau_m = 2.58 \times 10^{-8}$ sec from Eq.(3). Spectral absorption analysis gives a blocking temperature, $T_B = 100$ K. T_B is operationally defined as the temperature at which the doublet and sextet intensities are equal. Assuming τ_0 to have a value similar to that observed for single-domain magnetite particles [11], $\tau_0 = 0.95 \times 10^{-9}$ sec, we solve Eq.(2) for K to obtain an anisotropy constant $K = 4.47 \times 10^5$ erg/cm³. This value is much larger than those of macroscopic crystals. This is due to the contribution of surface anisotropy which increases with decreasing particle size and can be strongly affected by different surface coatings of the particles [2]. Experimentation with such magnetically well characterized pharmaceuticals is necessary in order to maximize their image contrasting characteristics and to test transverse relaxation theories modeling their mechanism of action [12].

(b) Particle Size Distribution of Iron Deposits on Thalassemic Heart Tissue — Thalassemic hemoglobin disorders are accompanied by an excess amount of unbound iron in the red blood cells due to globin chain denaturation and precipitation [13]. This eventually leads to the formation of iron granules deposited on different internal organs, primarily the spleen, heart, liver, pancreas and lymph nodes. Life expectancy is short and mortality is most frequently associated with congestive heart failure due to myocardial hemosiderosis [14]. Iron-chelation therapy with different agents such as desferrioxamine, which allows the removal and excretion of iron deposits, offers the possibility of alleviating fatal iron-loading states. The complex chemistry involved in the possible removal of these siderotic deposits in a non-toxic way requires the detailed physicochemical characterization of these deposits.

In this example we present the Mössbauer results of a study of the heart tissue obtained at post-mortem from two β -thalassemia patients [15]. An identification of the nature of iron deposits as hemosiderin and an estimation of the particle size distribution was carried out. Mössbauer spectra were obtained between 77 and 4.2 K. The spectra exhibited typical superparamagnetic behavior. The distribution of particle volumes was obtained from the measurement at various temperatures of the fraction $f(T)$ of particles with volume greater than the critical volume for superparamagnetism. This fraction is just the ratio of the integrated intensity in the magnetic hyperfine spectrum divided by the total intensity, assuming the Debye-Waller factors are equal. This is shown in Fig. 3 where f is plotted versus T . The solid line is an

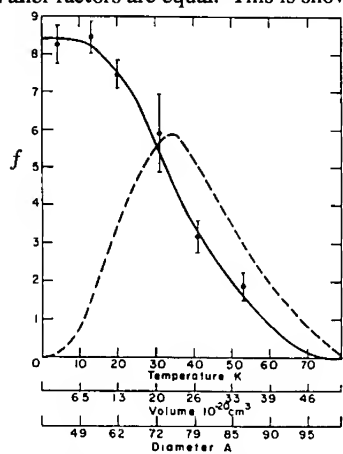


Figure 3. The fraction f of particles with volume greater than the critical volume for superparamagnetism given by the ratio of the integrated intensity of the magnetic hyperfine component of the spectrum over the total intensity as a function of temperature or, equivalently, volume or diameter of particles. The solid line gives an eye fit to the experimental points. The dashed line is proportional to $n(V)$ the particle volume distribution in the sample (from Reference 15).

eye fit to the data. Assuming a particle volume distribution $n(V)$, $f(T)$ is given by

$$f(T) = \int_{V(T)}^{\infty} n(V') d(V') / \int_0^{\infty} n(V') d(V') = 1 - \frac{1}{N} \int_0^{V(T)} n(V') dV' \quad (4)$$

where $V(T)$ corresponds to the critical particle volume for superparamagnetic behavior at temperature T , and N is the total number of particles present.

Since V and T are interdependent, $2KV = k_B T \ln(\tau/\tau_0)$, we can equivalently consider f as a function of the particle volume $V(f(T) \geq f(V))$. Then from Eq.(4) we conclude that the particle volume distribution is proportional to the negative volume derivative of f , i.e. $n(V) \propto -df(V)/dV$. $n(V)$ is shown by the dashed line in Fig. 3 obtained from a graphical evaluation of the slope of the $f(V)$ versus V curve at different values of V . It is observed that the distribution peaks at approximately 75 Å (see Reference 15) with a half-width at half-maximum of 12 Å.

(c) Collective Magnetic Correlations in Molecular Systems and the Internal Spin Structure of $\text{Fe}_{11}\text{O}_6(\text{OH})_6(\text{O}_2\text{CPh})_{15-6}\text{THF}$ — Large molecular complexes lie at the boundary between the molecular and the solid state, providing appropriate experimental systems for the investigation of the onset of collective magnetic phenomena associated with extended structures. Theoretical predictions on metallic clusters place the onset of incipient solid state phenomena — such as the emergence of a conduction band and collective magnetic interactions responsible for magnetic ordering in solids — in the vicinity of $n \geq 10$, where n is the number of atoms or interacting spins in a cluster [16].

The undecanuclear complex of the title compound shown in Fig. 4 contains 11 strongly superexchange-coupled iron ions forming a central magnetic core of ~ 1 nm diameter encapsulated within 15 benzoate ligands and six tetrahydrofuran molecules [17]. Mössbauer

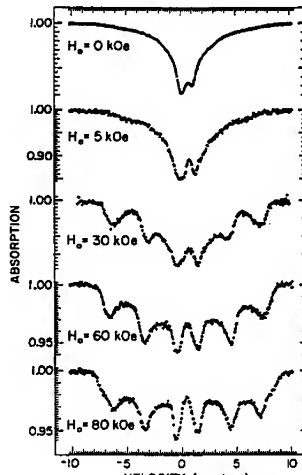
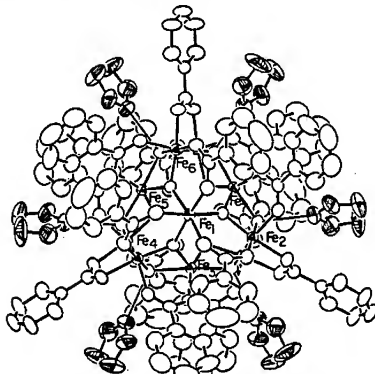


Figure 4. (Above) Crystal structure of $\text{Fe}_{11}\text{O}_6(\text{OH})_6(\text{O}_2\text{CPh})_{15-6}\text{THF}$ showing 40% probability thermal ellipsoids. Only 7 of the 11 Fe ions are discernible in this view of the molecule. (Right) Mössbauer spectra of Fe_{11} at 4.2 K in zero and various applied fields H_0 parallel to the γ -ray propagation direction. (from Reference 17).

and magnetization studies indicate that the iron ions are high spin ferric ($S = 5/2$, Fe^{3+}) and the exchange interactions are antiferromagnetic [5]. At 4.2 K in zero field the Mössbauer spectrum of Fe_{11} is dominated by intermediate spin relaxation phenomena (Fig. 4, Right, top spectrum). It is significantly broadened, with wings that extend from about -7 to +7 mm/sec, but no magnetic hyperfine lines are defined. The net moment of the Fe_{11} aggregate does not have a fixed spatial orientation in zero field but fluctuates with a certain frequency with respect to the crystal axis. The broadening of the Mössbauer spectrum implies that the relaxation time is of the order of the Mössbauer time scale. When an external magnetic field, H_0 , is applied parallel to the direction of the 14.4 KeV γ -ray, the orientational magnetic energy of the total spin of the cluster, $E_h = -\mu B H_0$, forces the spin to precess about H_0 , further reducing its relaxation time and a full magnetic hyperfine structure is developed (Fig. 4, Right) [17]. It is most notable that (a) in the presence of the external field the middle $\Delta m = 0$ absorption lines persist and (b) the overall magnetic splitting, which is a measure of the total magnetic field at the iron nucleus $H_n = H_0 + H_{\text{eff}}$, does not change significantly with increasing applied field strength.

The non-vanishing $\Delta m = 0$ lines indicate that although the total uncompensated moment μ of the cluster may be oriented along the direction of the magnetic field, the effective fields and therefore, the local magnetic moments, at the different iron sites are not colinear with the total moment or \mathbf{H}_0 . That is, internal magnetic anisotropies dominate. Since high spin ferric ions are highly isotropic this non-colincarity can hardly be due to single-ion anisotropies. It suggests the presence of collective magnetic interactions producing short-range magnetic order and the existence of easy directions of magnetization within the crystalline solid. It points to a non-colinear structure or canted antiferromagnetic order of the type observed on the surface atoms of antiferromagnetic small particles [3]. It could also be a result of frustration in the network of magnetic interactions present, resulting in a spin glass-like structure [18]. The bulky benzoate ligands surrounding the 11 iron magnetic cores keep them separated by a distance of ~ 20 Å, over which long-range dipole-dipole interactions are negligible [19]. Thus, there is no long-range spatial correlation of the antiferromagnetic axis of a cluster with its neighbors and the magnetic correlations must be confined within the Fe_{11} core. This observation places this cluster at the molecular/solid state boundary of magnetic behavior.

ACKNOWLEDGEMENTS — The author wishes to thank Dr. R. Weissleder, Massachusetts General Hospital, for providing the MRI nanocompound and T. Shen, Department of Health Sciences and Technology, MIT, for the TEM picture. The research reported herein was partially supported by the Office of Naval Research and the National Science Foundation.

REFERENCES

1. W. Kündig, H. Bömmel, G. Constabaris, and R.H. Lindquist, Phys. Rev. **142**, 327 (1966).
2. S. Mørup, H. Topsøe, and J. Lipka, J. de Phys. **37**, C6-287 (1976).
3. J.M.D. Coey, Phys. Rev. Lett. **27**, 1140 (1971); A.E. Berkowitz et al., *ibid* **34**, 594 (1975).
4. T. Shen, R. Weissleder, M. Papisov, A. Bogdanov, Jr., and T.J. Brady, Magn. Res. in Med. **29**, 599 (1993).
5. G.C. Papaeftymiou, Phys. Rev. B **46**, 10366 (1992); in On Clusters and Clustering, From Atoms to Fractals, Ch. 16, P.J. Reynolds, Ed. (North-Holland, Amsterdam, 1993) pp. 209-220, and references therein.
6. C. Yang, A. Meagher, B.H. Huynh, D.E. Sayers, and E.C. Theil, Biochemistry **26**, 497 (1987); R.B. Frankel, G.C. Papaeftymiou, and G.D. Watt, Hyperfine Inter. **66**, 71 (1991).
7. A.A. Hirsch, T. Massalha, and G. Galecki, JMMM **75**, 209 (1988).
8. X.Z. Zhou, A.H. Morris, D.G. Naugle, and R. Pan, J. Appl. Phys. **73**, 6597 (1993).
9. W.J. Schuele, S. Strikman, and D. Treves, J. Appl. Phys. **36**, 101 (1965); W.F. Brown, Jr., J. Appl. Phys. **30**, 1305 (1959).
10. D.D. Stark et al., Radiology **168**, 297 (1988); R. Weissleder et al., *ibid* **166**, 423 (1988); S. Saini et al., *ibid* **162**, 217 (1987).
11. T.K. MacNabb et al., J. Appl. Phys. **39**, 5703 (1968).
12. P.A. Hardy and R.M. Henkelman, Mag. Res. Imag. **7**, 265 (1989); P. Gillis and S.H. Koenig, Magn. Res. in Med. **4**, 323 (1984); S. Majamdar and J.C. Gore, J. Magn. Res. **77**, 41 (1988).
13. D.J. Weatherall and J.B. Clegg, The Thalassemia Syndromes, 2nd ed. (Blackwell Sci. Publ., Oxford, 1972).
14. A. Polliack et al., Br. J. Haematol. **26**, 201 (1974); L.M. Buja and W.C. Roberts, Am. J. Med. **51**, 209 (1971); M.A. Engle, Am. NY Acad. Sci. **119**, 694 (1961).
15. K.S. Kaufman, G.C. Papaeftymiou, R.B. Frankel, and A. Rosenthal, Biochim. Biophys. Acta **629**, 522 (1980).
16. R.P. Messmer et al., Phys. Rev. B. **13**, 1396 (1976); C.Y. Yang et al., *ibid* **24**, 5673 (1981); G.M. Pastor et al., *ibid* **40**, 7642 (1989).
17. S.M. Gorun, G.C. Papaeftymiou, R.B. Frankel, and S.J. Lippard, J. Am. Chem. Soc. **109**, 3337 (1987).
18. D. Chowdhury, Spin Glasses and Other Frustrated Systems (Princeton University Press, Princeton, NJ, 1986).
19. The dipole-dipole interaction energy $\mu_1 \cdot \mu_2 / r^3 \sim 10^{-20}$ ergs for two magnetic dipoles of $1\mu_B$ each separated by a distance $r = 20$ Å, which is much weaker than either thermal energies $k_B T$ for the lowest temperature used in these experiments, or the orientation energy of each dipole — $\mu \cdot \mathbf{H}_0$ in the external field of 80 kOe, both of which are of the order of 10^{-16} ergs.

NMR STUDIES OF ELECTRONIC AND LOCAL STRUCTURE IN CU-AU ALLOYS

JAMES CHEPIN AND JOSEPH H. ROSS, JR.
Department of Physics, Texas A&M University, College Station, TX 77843-4242

ABSTRACT

We have studied ordered and disordered Cu-Au alloys via ^{63}Cu NMR, probing local electronic structure in the bulk and near anti-phase boundaries in CuAuII. A line-shape model has provided good agreement for disordered and partially ordered alloys, and we thus have obtained a measure of local site symmetries, and Knight shifts and local densities of states within the alloys. We have combined Knight shift and relaxation measurements to obtain detailed local information. We report effects of the ordering process in Cu_3Au , CuAu, and CuAu₃ intermetallics. We find enhanced susceptibility at the CuAuII anti-phase boundary which is heavily anti-site populated. We compare these results to other measurements of these properties.

INTRODUCTION

The factors determining the phase stability and microstructure of binary alloy systems remain elusive. A great deal of light was shed on the subject by William Hume-Rothery.¹ His ideas provided a basis of understanding of alloy formation. More recently, first principles studies, which model the periodic potential of the alloy and the electronic wave function, have been used to determine alloy properties.²

The distinct properties of the Cu-Au phase system coupled with the relative simplicity of the noble metal electronic structure have led to extensive studies of this system. The Cu-Au alloy system is completely miscible at high temperatures and forms three ordered superlattice phases, Cu_3Au , CuAu, and CuAu₃ at lower temperatures. The equiatomic phase exhibits both an ordered structure (CuAuI) and a long period ordered structure (CuAuII). Numerous calculations of band structure and Fermi surface characteristics have been done. Experimental measurements of this system include specific heat,³ susceptibility,⁴ de Haas-van Alphen,⁵ as well as x-ray studies,⁶ however questions of local structure properties and ordering energetics remain.

NMR can be used as an atomic probe in metal alloys yielding information on the site occupation and Fermi surface structure. For example, NMR studies of copper metal indicated non-s type states at the Fermi Surface,⁷ and measurements of Hg-Cd-Te provide insight into to the clustering of near neighbors.⁸ Early NMR measurements of the Cu-Au system exist,⁹ however with advances in magnetic field strength and instrumentation, more precise measurements can be made. Here we have used NMR to study the local electronic structure and site occupation.

PROCEDURE

Samples for this experiment were prepared using 99.999% pure elements, weighed to within 0.5% stoichiometry. The preparation was accomplished in two steps. First an ingot was formed in argon by arc melting the constituents. Second, a ribbon was formed out of the ingot by melt spinning. The resulting material was in the disordered crystal state. Each specimen was confirmed to be within 0.5 at.% using wavelength-dispersive spectroscopy, WDS. The phases were formed by annealing in an evacuated borosilicate tube. In order to obtain the disordered state or

the CuAuII structure it is necessary to quench the anneal. This was accomplished by a water quench. A water quench above the disorder temperature gave essentially identical NMR results as the melt spin. Thus we have shown that our material could be ordered and subsequently disordered while maintaining the integrity of the data. In order to insure against the possibility of preferential orientation in the multicrystalline structure the ribbons were finely chopped. The result was a "powdered" specimen for NMR studies.

The measurements were taken using a 400 MHz magnet and home-built spectrometer. Both the line shape and the spin-lattice relaxation time, T_1 , were measured for each sample at room temperature and 77 K. It was necessary to modify the apparatus for wide line measurements, central transitions being over 100 kHz while satellites were several MHz. The T_1 's measured at room temperature were very short (less than 10 ms) and their accuracy was somewhat limited.

LINE SHAPES: ORDERED AND DISORDERED ANALYSIS

In solid state NMR the nuclear states in the magnetic field are perturbed by local magnetic and electrostatic interactions. The former is responsible for the Knight shift and the latter produces the quadrupole shift. In the Cu-Au system the Knight shift is a result of both the Fermi contact interaction and an orbital term caused by non-s electronic states. The Fermi contact term has no angular dependence so it will simply shift the resonant frequency, however the orbital term can exhibit angular dependence. The quadrupole shift affects the central transition only in second order, which proves to be substantial for this study. The line shape is complicated further since the sample is in powdered form. By fitting the line shape to the theory behind these perturbations, properties of local structure can be determined.

Ordered Phases

The copper nucleus has a spin of 3/2 and the quadrupole interaction will affect the non-central transitions to first order forming satellites which are symmetric about the central transition. The first order quadrupole shift is the dominant effect shaping the satellite line, and for this reason the quadrupole frequency, v_q , was determined using this line. Figure 1 shows the lower half of the satellite line shape and the fit that determined v_q for CuAuI.

The central transition line shape is a result of both the quadrupole interaction and the angular part of the orbital Knight shift. For both CuAuI and Cu₃Au the angular dependence of the Knight shift and the quadrupole shift is axial due to the copper site symmetry. The dependence of the frequency shift, Δv , for this case is

$$\Delta v = \frac{3v_q^2}{16v_i} (1 - \cos^2 \theta)(1 - 9\cos^2 \theta) + K_{ax} \left(\frac{3}{2} \cos^2 \theta - \frac{1}{2} \right), \quad (1)$$

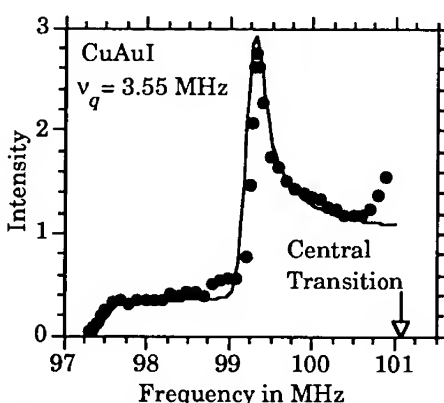


FIG. 1. CuAuI satellite line showing the fit to the first order quadrupole line shape.

where v_l is the Lamor frequency, K_{ax} is the magnitude of the axial part of the orbital Knight shift, and θ is the angle between the crystal symmetry axis and the external magnetic field. The result for v_q determined from the satellite line in Figure 1 was used in eq 1 to determine K_{ax} . Figure 2 shows the fit determined by eq 1 to the central line shape of the CuAuI structure. The fit to the central line also provides the center frequency of the line enabling an accurate measure of the isotropic Knight shift, K . Knowing the center frequency of the line is essential as the linewidth is of the same order as the Knight shift. The copper site symmetry for CuAu₃ is cubic so both K_{ax} and v_q vanish.

Disordered Phases

In the disordered state the line shape is composed of a wide range of electrostatic and magnetic interactions. The resulting line shape lacks the sharp detail seen in the ordered line. Our fit assumed that the quadrupole interaction is dominated by nearest-neighbor sites only and that the quadrupole shift was a superposition of the shift produced by each single site. The statistics for a random site occupation were used to construct the line shape. This method did not account for the angular Knight shift, however the center frequency of the line is not altered by the asymmetric Knight shift so the determination of the isotropic Knight shift was not compromised. The single-Au near-neighbor values of v_q for each of the compositions Cu₃Au, CuAu, CuAu₃ were found to be 3.12, 2.65, and 2.41 MHz respectively. A NMR study of dilute Au in Cu gave a near neighbor v_q of 2.65 MHz and a second-nearest neighbor value of 0.823 MHz.¹⁰

T_1 and Knight Shift

The T_1 was measured using the inversion recovery method. Though the T_1 can be of either a magnetic or electrostatic nature, each having well known multi-exponential behavior, the magnetic process agreed well with the data, while the temperature dependence of the electrostatic process was not consistent with the data.

The results of the T_1 and Knight shift measurements for each composition in both the ordered and disordered state are summarized in Figure 3. The theoretical Korringa value, K^2T_1T , for copper, calculated assuming strictly s-state valence structure, is shown as a straight line. The high Korringa values for each composition, including the pure copper value, indicate the Knight shift has a significant orbital part.⁷ The consistent value of K^2T_1T indicates the contribution of the s:p:d type valence states does not change much with composition. The smooth dependence of the Knight shift for the disordered structures and the consistent Korringa value further validate the disordered line shape analysis.

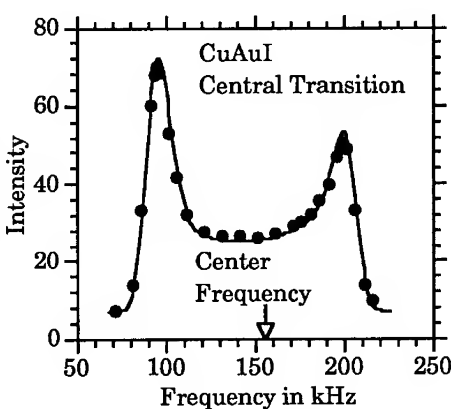


FIG. 2. CuAuI central line showing the fit determined by eq 1. The bare Cu resonance would occur at 0 kHz. The offset frequency is 101 MHz.

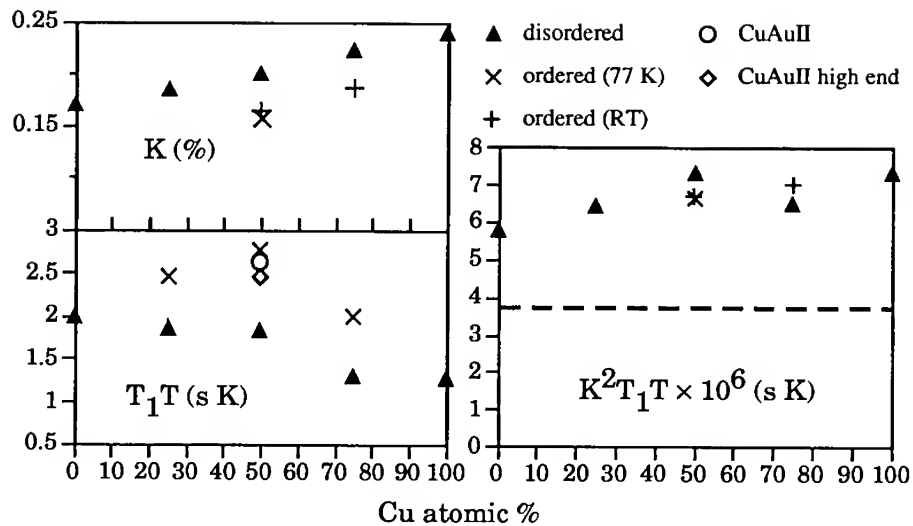


FIG. 3. Measured isotropic Knight shift (K), T_1T , and K^2T_1T . The symbols denote the phase and temperature of the measurement. The values for pure copper and dilute copper in gold were taken from Carter, Bennett, and Kahan.¹¹

The T_1 in Cu is determined mainly by the s DOS at the Fermi level due to the large hyperfine field produced by these electronic states. It has been shown that the hyperfine field scales with the inverse of the volume expansion of the lattice.¹² Using a value calculated for the Fermi contact hyperfine field of pure Cu¹³ and adjusting for the expansion of the lattice with composition the hyperfine fields for Cu₃Au, CuAu, and CuAu₃ can be estimated. Assuming that the ratio of the s DOS to the total DOS at the Fermi level remains constant in the Cu-Au system, which is indicated by the small change of K^2T_1T with composition and has also been demonstrated in the Cu-Pd system,¹² the s DOS found using our T_1 value can be scaled into a total DOS at the Fermi level. This was done for each of the three compositions and the results are summarized in Table 1.

TABLE 1. Calculated Cu DOS, in states/(eV atom), using the experimental values of T_1T and the hyperfine field value and s contribution to the total density of states found by Oja et al.¹³ The 77 K T_1T values were used. The two results for CuAuII are from two T_1 's measured at different frequencies.

	Disordered	Ordered	CuAuII
Cu ₃ Au	0.307	0.248	
CuAu	0.282	0.229	
CuAu ₃	0.315	0.274	0.236, 0.243

The CuAuII Structure

The satellite line shape for the long period superlattice structure, CuAuII, is shown in Figure 4. The line clearly retains the sharp structure of the CuAuI satellite

line (Figure 2) with an added component which we believe to be the result of a smoothly varying distribution of quadrupole shifts at anti-phase boundaries, APB's. It is believed that in this structure the APB is not a sharp planar structure, instead the boundary is "wavy".¹⁴ The fit to the data in Figure 4 is comprised of the same quadrupole fit of Figure 2 (slightly broadened) and a smooth curve representing the APB contribution. The relative intensity of the two terms is what would be expected given that half the period of the structure is five unit cells, the middle three being the CuAuI-like and the outer two are at APB's.

The Knight shift for CuAuII has not been determined exactly as the APB contribution has not been modeled. However an estimate of the Knight shift can be found by comparing the central line shape of CuAuII to that of CuAuI and the disordered CuAu composition, as in Figure 5. This figure shows the Knight shift is very near that of the CuAuI structure, while it is certainly lower than that of disordered CuAu. The CuAuII line shape is more intense than CuAuI in the high frequency region, however the line shape does not suggest the structure is a result of mixing CuAuI and disordered CuAu as the susceptibility of disordered CuAu is too great. Furthermore, the $T_1 T$ falls between the values for CuAuI and disordered CuAu, being much closer to the CuAuI value. The T_1 was measured at both the middle and the upper end of the line shape, which is shown in Figure 3. The DOS calculated from these T_1 's are listed in Table 1.

DISCUSSION OF RESULTS

Table 1 shows that our results yield a ubiquitous decrease in the DOS at the Fermi level upon ordering throughout the composition range. Our Knight shift measurements mimic this behavior, giving further conformation that the DOS is lowered at the copper sites upon ordering. The sharp features of the ordered line shapes indicate these samples were highly ordered. The CuAu₃ system is an exception; as is well known this composition is difficult to order.³ A comprehensive measure of the specific heat in Cu-Au alloys shows a decrease in only the Cu₃Au electronic density of states upon ordering, with an increase in both the CuAu and CuAu₃ compositions.³ An electronic structure calculation¹⁵ agrees with the trends of the experimental specific heat

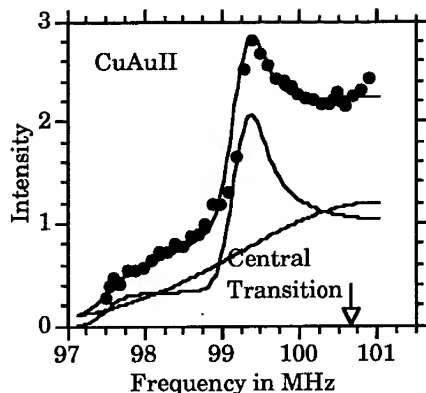


FIG. 4. CuAuII satellite line showing the fit to the quadrupole line shape used for the CuAuI satellite added to a smooth line shape representing the APB's.

FIG. 5. Comparison of the three Cu-Au phases. The designation is CuAuI(●), CuAuII(○), and disordered CuAu(▲).

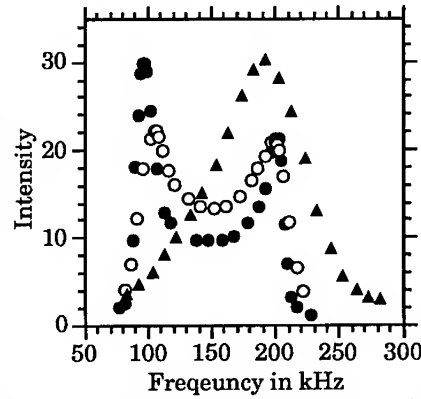


FIG. 5. Comparison of the three Cu-Au phases. The designation is CuAuI(●), CuAuII(○), and disordered CuAu(▲).

measurements, where the author suggests that sharp features in the DOS near the Fermi level explain the results. For instance, the small lattice contraction of CuAuI shifts the feature so as to increase the DOS near the Fermi level, thus the increase in specific heat. Our results point to a narrow dip, rather than a peak, in the DOS structure at the Fermi level of CuAuI; this is indicated by an increase of Knight shift with temperature (See Figure 3). We attribute the discrepancies, in part, to changes in the electron-phonon enhancement of the specific heat upon ordering. Our measurement is Cu site specific, so particularly for Cu₃Au the large DOS change we observed upon ordering does not seem consistent with the small DOS change extracted directly from the specific heat result.

In the CuAuII phase both the satellite and central line have the CuAuI character with an added term caused by a wide variation of anti-site defects near the APB's. If the APB's were planar we would expect two distinct structure patterns in the line shape. A high resolution electron microscopy study also shows the APB structure to be "wavy" with a great deal of atomic disorder.¹⁴ However, contrary to the specific heat studies we have seen an increase in the DOS in CuAuII compared to CuAuI. Also, we find the DOS in the APB regions to be enhanced, possibly due to the disorder in these regions.

CONCLUSION

NMR is an effective probe for local electronic as well as physical properties in these materials. Our Knight shift and T₁ results show a decrease in the Cu DOS upon ordering for all compositions. The structure of the APB's in CuAuII is non-uniform and we find an enhanced Cu DOS in these regions.

ACKNOWLEDGMENTS

Partial support was provided by the Donors of the Petroleum Research Fund administered by the American Chemical Society.

REFERENCES

1. W. Hume-Rothery and B. R. Coles, *Atomic Theory for Students of Metallurgy* (Institute of Metals, London, 1988).
2. F. Ducastelle, *Order and Phase Stability in Alloys* (North-Holland, Amsterdam, 1991).
3. D. L. Martin, Phys. Rev. B **14**, 369 (1976).
4. G. Airoldi and M. Drosi, Philos. Mag. **19**, 349 (1969).
5. P. P. Deimel and R. J. Higgins, Phys. Rev. B **25**, 7117 (1982).
6. T. K. Sham, *et al.*, Phys. Rev. B **41**, 11881 (1990).
7. R. E. Walstedt and Y. Yafet, Solid State Commun. **15**, 1855 (1974).
8. J. Shi, M. Wessels and J. H. Ross Jr., Phys. Rev. B **48**, 8742 (1993).
9. D. L. Weinberg, J. Phys. Chem. Solids **15**, 249 (1960).
10. R. Nevald, B. L. Jensen and P. B. Fynbo, J. Phys. F **4**, 1320 (1974).
11. G. C. Carter, L. H. Bennett and D. J. Kahan, ed., *Metallic Shifts in NMR* (Pergamon, Oxford, 1977).
12. H. Ebert, H. Winter and J. Voitländer, J. Phys. F **14**, 2433 (1984).
13. A. S. Oja, X. W. Wang and B. N. Harmon, Phys. Rev. B **39**, 4009 (1989).
14. K. Yasuda and M. Nakagawa, J. Less-Common Metals **135**, 169 (1987).
15. K. Kokko, E. Ojala and K. Mansikka, J. Phys.: Condens. Matter **2**, 4587 (1990).

PART IV

Local Chemistry and Composition Determination

ATOMIC RESOLUTION ELECTRONIC STRUCTURE USING SPATIALLY RESOLVED ELECTRON ENERGY LOSS SPECTROSCOPY

P.E. BATSON,
IBM Thomas J. Watson Research Center,
Yorktown Heights, New York, 10598.

ABSTRACT

Electronic structure in small areas is obtainable by inspection of near edge fine structure of core excitations. We can accomplish this today with near atomic resolution, using EELS at high energy. At IBM, we have obtained results using a sub-0.2nm probe at 120KeV with enough current to allow 200meV resolution studies at the Si L_{2,3} edge. It is especially crucial for Si-based structures that this allows us to obtain Z-contrast dark field images of the Si lattice at an acceleration voltage that is low enough to minimize radiation damage, but with a high enough current to allow good quality spectra to be obtained. A review of instrumental requirements, spectral interpretation, and applications to Si-Ge alloys is presented.

INTRODUCTION

Increasingly, electrical properties of practical devices depend on atomic-scale heterogeneity. For instance, the speed of electrical carriers in a field effect transistor can be increased if the silicon conduction channel is grown as a thin layer embedded in an alloy of 30-40% germanium in silicon.¹ This causes a distortion of the silicon crystal structure to match bonds at the interface with the alloy, which has a slightly larger lattice constant. The distortion makes it particularly easy for carriers to move parallel to the silicon/alloy interface, giving them a very high mobility and consequently allowing very fast operation of the transistor. In a typical structure, the silicon layer is about 10 nanometers thick, while the carriers are confined by electrostatic fields to within about 0.5 nanometers of the silicon/alloy interface. Within this very thin, buried region, electrical properties depend on the atomic structure, averaged over some length scale determined by screening and modulation doping density.

High resolution electron microscopy is a very effective tool for revealing atomic structure. In addition, recent progress in Annular Dark Field (ADF) imaging using a 0.2 nanometer electron beam in the Scanning Transmission Electron Microscope has allowed limited interpretation of high resolution images in terms of average composition of individual atom columns.²⁻⁴ To date, however, there has been no way to determine the atomically local electrical properties so that we may relate the observed electrical behavior with structure at the atomic level. In part, the success of the Scanning Tunneling Microscope has resulted from its ability to do this for the same area of a surface. This report describes results using high energy EELS in transmission to obtain similar information from buried structures.

X-ray Absorption Near Edge Fine Structure (XANES) can reveal the electronic structure of bulk conduction bands, provided suitable theoretical modeling is available

to allow interpretation. Electron Energy Loss Spectroscopy can also obtain Electron Loss Near Edge Fine Structure (ELNES) revealing similar information. In principle, EELS should provide a useful compliment to the ADF imaging in the same instrument, because it uses mainly the small angle scattering that is not so useful for the imaging.

There have been several kinds of barriers against this use. Foremost, is the fact that the spectroscopy equipment having the needed resolution and accuracy is difficult to build. There exists no commercial equipment that can routinely resolve electronic structure in semi-conductor systems at high accelerating voltage. For instance, high mobility in a modulation doped Si quantum well depends on the existence of a precisely controlled heterojunction band offset -- in the range 0.16-0.18 eV. This band offset can be measured, in some cases, as a shift in the Si L_{2,3} core excitation at 99.84 eV. Obviously, this variation is unobservable using a typically available resolution and energy axis stability of 0.4-0.5 eV. At IBM, I have constructed a simple device⁵ that utilizes ideas developed during the 1960's and 1970's at Cornell.⁶ The IBM instrument has achieved a 170 meV resolution with a reproducible accuracy of ± 20 meV at 120 KeV accelerating voltage. This performance is marginally adequate to resolve the band shifts in the Si-Ge alloy system.

Secondly, in the 100 KeV energy range, differential scattering cross sections for soft x-ray core excitations is of order $10^{-19} \text{ cm}^2 \text{ eV}^{-1} \text{ atom}^{-1}$. With 0.1 nanoampere of current in a 0.2 nanometer diameter probe incident on a 500 Å thick sample, we obtain a few hundred counts per eV-sec. An energy bin size of 100 meV then produces about 40-100 counts per second, giving a 3% statistical accuracy in about 10-25 seconds of integration per spectral point. This is an acceptable time for atom column resolution experiments, provided parallel detection is used. In addition, with as few as a thousand scattered electrons per energy bin, we must have single electron sensitivity so that the statistical uncertainty of the measurement is dominated by counting statistics and not by the detector gain or background. For this reason a CCD-based detector appears to offer advantages over diode arrays because its very much lower noise limits allow detection of single scintillator impact events. These counting requirements are similar to those derived for single atom sensitivity, using higher currents and wider energy collection windows.⁷ However, in this case we do not seek to identify a particular atomic species, but rather, the electronic environment of a species known to be present.

Thirdly, the scattering physics governing inelastic scattering within 0.2-0.5 nanometers of a high energy electron is far from clear. Simple rules, derived from Uncertainty Principle ideas relating to the characteristic scattering angles do not reproduce observed behavior. For instance, a few years ago, Scheinfein showed that a 0.5 nanometer lateral spatial resolution was observable using bulk plasmons at the Al/AlF₃ interface.⁸ This is in spite of the fact that the quantity $\hbar/K_0\theta_E$ (where K_0 is the incident electron wavevector, and θ_E is the characteristic scattering angle) is of order of 100 nanometers for a 15eV loss. He also found that the Si L_{2,3} edge displayed a similar sensitivity to position. In more recent work, Batson has shown experimental data for the Si core edge⁹ and discussed current theoretical understanding of the spatially resolved EELS scattering geometry.¹⁰ The result of this work is that a very high lateral spatial

resolution is possible, although some difficulties in spectral interpretation do occur in very thin sections of samples.

Finally, once we have obtained good quality spectra from well defined, small areas, the complexities of interpretation are quite daunting. These include proper inclusion of core excitonic interactions, dipole selection rules, matrix element weighting, core lifetime broadening, and instrumental resolution, in order to obtain a local Conduction Band Density of States (DOS). All of these must be considered through a spectral modeling procedure, because the DOS contribution to the scattering can be subtle. The methods used to evaluate spectra in this work have been published in detail elsewhere.^{11,12}

In the end, all of these needed advances in the acquisition and understanding of spatially resolved EELS data result in an entirely new capability: to acquire direct information about the local electronic structure near an interface or defect within the bulk of the material which has been imaged in high resolution.

THE IBM SPATIALLY RESOLVED EELS INSTRUMENT

The Microscope

The IBM instrument is based on the 100 KV VG Microscopes HB501 STEM, equipped with a high resolution objective lens pole piece. This instrument has been extensively modified over the years to improve its performance and to allow computer control. Recently, the accelerating voltage has been increased to 120 KV, and the objective lens pole piece has been raised by about 125 micrometers. This improves the spherical aberration coefficient to about 1.2 mm from the nominally obtained 1.3 mm. With the higher voltage, a theoretical spot size of 1.95 Å is obtainable. Although there remain some problems with mechanical and electrical instabilities, the instrument has resolved in the ADF image the three crossing 1.92 Å Si [220] fringes in the [111] zone axis orientation. Figure 1 shows a [110] zone axis ADF image for silicon, showing in some cases the 1.4 Å projected spacing of the Si dimer. This image has been smoothed and contrast enhanced to display small intensity variations. Although, the presence of dimers are obvious, the dimer spacing is difficult to obtain accurately at this spatial resolution. In addition, since the point resolution of the instrument is greater than the 1.4 Å fringe spacing, there may be difficulty in preserving the positions of various fringes. For Bright Field (BF) imaging, this leads to shifts in observed fringes. It remains to be seen whether similar shifts are present in the ADF images.

A second point to make is that much detail in these images can be enhanced through smoothing, contrast expansion, and resolution enhancement numerical techniques, but these methods will probably fail for analytical signals. For instance, the uniform background subtraction used in Figure 1 to bring out the small contrast variations, implies that spectra taken under these conditions need to be corrected by subtraction of a background reference spectrum to show spectral variations resulting from passage of the electron beam down different regions of the specimen. At this point, therefore, Spatially Resolved EELS studies should be limited to probe displacements larger than the theoretical point resolution limit.

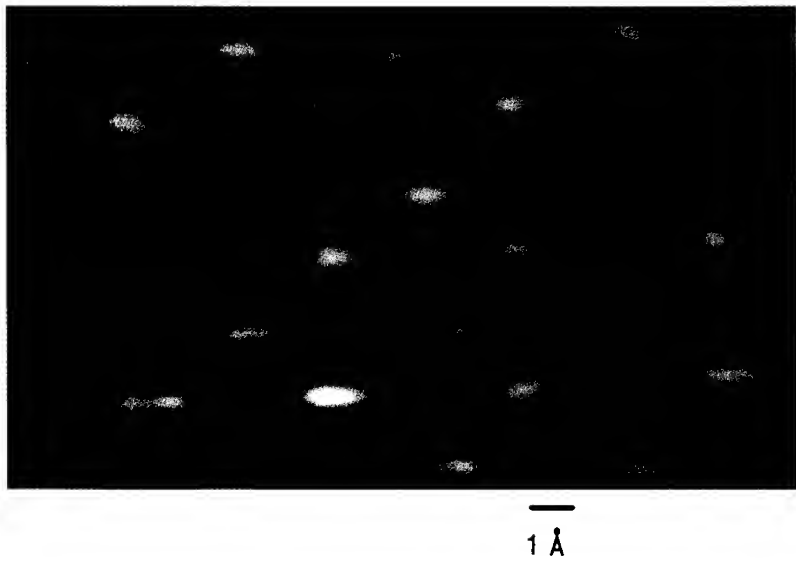


Figure 1. Contrast enhanced ADF image of the [110] zone axis oriented silicon. Although the point resolution is about 1.95 \AA , the projected Si dimer distance of 1.4 \AA is occasionally visible. Care must be exercised for interpretation of images such as this, in spite of their dark field nature, because of the disparity between the fringe spacing and the instrumental point resolution.

While the modifications described above are relatively minor, there is risk involved in their implementation. The 20% increase in accelerating voltage presents a danger to the equipment for extraordinary overvoltage situations. These can occur during electron gun conditioning and during electrical supply interruptions. Power dissipation in the objective lens is also an issue. The increase in voltage and raising of the objective lens pole piece require a 40% increase in the objective lens power dissipation to about 800 watts. This must be carefully monitored during operation to ensure the safety of the lens windings.

The Spectrometer

The electron spectrometer is a 4 cm long Wien Filter, which consists of crossed electric magnetic fields, adjusted so as to null the total Lorentz force for electrons that traverse the filter at 100 eV energy. It is situated within a high voltage electrode which is electrically offset from the gun potential by 100 V, so that electrons which do not lose energy within the specimen are decelerated to 100 eV on entering the filter, and traverse it undeflected. As these electrons leave the filter, they are reaccelerated to 120 KeV before striking a viewing screen. The fundamental advantage of this arrangement is that

high voltage fluctuations do not interfere with the measurement, because the spectrometer potential follows the gun potential precisely. In addition, the needed fractional resolution is much relaxed to about 1×10^{-3} to attain 0.1 eV resolution. This is easily obtained with a simple design.

A key need in these experiments is to calibrate the energy loss spectrum as accurately as possible. This is accomplished by scanning the difference in the center potential of the spectrometer relative to the gun. This if 10 V is subtracted from the spectrometer potential, a 10 eV loss electron will be at the correct energy to pass undeflected through the spectrometer. Therefore, if axially located slits are positioned so as to catch only undeflected electrons, these may be used to define the origin of the energy loss spectrum. In the IBM system, these slits define the energy axis to ± 20 meV. A corollary to this is that BF images taken with this instrument are energy filtered elastic images with an energy width of about 50 meV.

Between the specimen and spectrometer, there are two quadrupole field lenses which transfer the spot at the specimen position to within about 1 cm of the spectrometer electrode. These lenses, in conjunction with the post-lens compression of the STEM objective lens, and the deceleration field of the spectrometer electrode, allow an angular demagnification of about 3 between the specimen and spectrometer. Thus, a collection semi-angle of 15 mrad at the specimen gives a 5 mrad semi-angle at the spectrometer. This controls the main energy axis aberration giving a low limit on spectrometer resolution of about 70 meV.

After reacceleration, electrons strike a YAG scintillator, and the resulting light is coupled through fiber optics directly to a CCD detector. Since the energy dispersion of the Wien Filter is very high at the 100eV analysis energy (several hundred microns per eV), no post spectrometer magnification is needed to match the spectrum to the CCD detector. A typical dispersion at the array is 15 meV per pixel. In the IBM system, BF slits are placed on axis for imaging. The CCD scintillator is positioned immediately off axis. Thus the zero in energy is positioned using the BF slits, then a small, precisely known deflection places the energy loss spectrum at the CCD detection plane. Even though the energy zero is known, there is still a need to know the dispersion at the CCD in eV/pixel. In the present arrangement, this can change during daily operation. Therefore, from time to time the unscattered beam is shifted across the CCD to give a set of calibrated peak positions which are evaluated by software to establish the energy dispersion.

There are also large gain variations across the array, some having to do with the array function and some having to do with non-ideal behavior of the spectrometer. Correction of these requires a multiple scanning arrangement to ensure that all energy loss bins are evaluated at identical gains. This is accomplished with a variation of the method introduced by Shuman and Kruit.¹³ Viewing the CCD as an array of single detectors, the energy loss spectrum is scanned across the whole array to generate as many spectra as there are CCD pixels. These are then shift to match energy axes and added to obtain one spectrum that has been averaged over all pixels in the array. This averages background and gain variations, and converts any energy axis irregularities into a small

energy resolution degradation. Reference 14 describes this process for an earlier, diode array based system. As the spectrum is being stepped across the array, the electron beam current is also monitored and recorded so that a normalization can be made prior to averaging. Thus, beam current fluctuations are reduced, and a result proportional to scattering power of the specimen is produced. This turns out to be convenient, because thickness variations as a function of position can be easily identified by the variations in the absolute magnitude of acquired spectra, without regard to electron beam fluctuations. Finally, this multiple Serial-Parallel scanning system allows a separation of the desired scanning properties from the physical size of the CCD array. For instance in the present system, the physical array covers only a 6eV window. Scanning the spectrum across the array allows us to generate a spectrum that is wider than this. Software keeps track of the necessary calibrations, freeing the operator from the need to worry about peculiarities of the array detection.

Typical Results for Silicon

Figure 1 shows a summary of the low energy loss regime for silicon, including the soft x-ray $L_{2,3}$ core excitation at 99.84 eV, reproduced from reference 15. In general, with this system, the no-loss electrons are defined by the field emission tunneling distribution at the tungsten field emission tip. This can be as narrow as 0.28 eV for low emission currents, but is typically closer to 0.4 eV for normal STEM operation (in this case 0.15 nanoamps into a 2 Å probe). Bulk and surface plasmons are present in the 10-40 eV range, and the $L_{2,3}$ edge is present on a background composed largely of multiple single particle excitations.

Figure 2. Typical low loss spectrum for silicon, reproduced from reference 15.

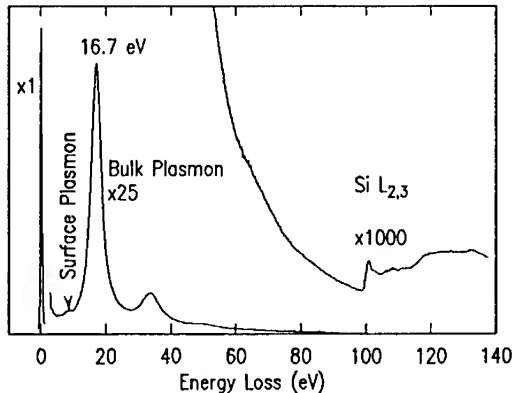
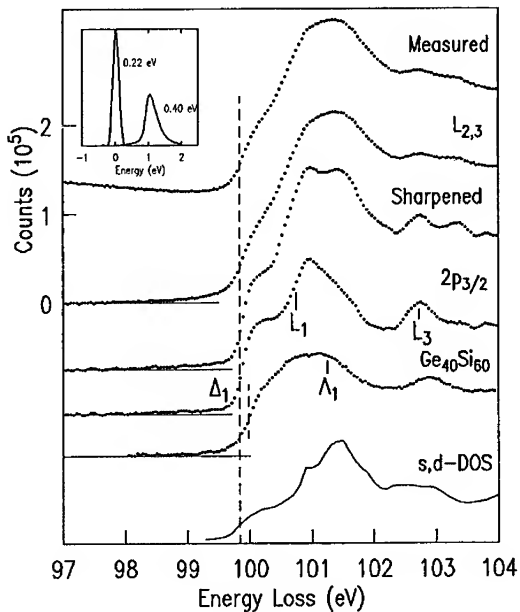


Figure 3. shows only the region around the Si $L_{2,3}$ core excitation reproduced from reference 9. It summarizes the various processing steps which are required to extract ELNES structure from the as-measured spectrum. Briefly, from top to bottom, I show the measured data, a background subtraction using the standard power law form, a resolution enhanced spectrum¹⁶ (with the resulting improved no-loss distribution displayed in the inset), and the extracted $2p_{3/2}$ part of the spectrum, obtained by deconvolution of a spin-orbit splitting function consisting of two δ -functions separated by 0.608eV and weighted by 2/1. The resolution enhancement works because the field emission distrib-

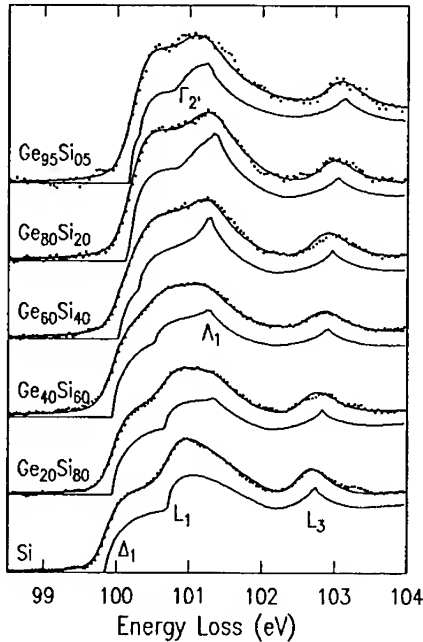
ution (in the inset, shifted to the right by 1 eV) has a sharp low energy onset. This provides for adequate high resolution information in the spectra to allow extraction of a 0.22 eV wide resolution (having a shape as depicted by the peak at 0 eV). Thus the weak spin orbit doubling of the peak at 102.7 eV in the core loss spectrum becomes obvious on sharpening.

Figure 3. Summary of silicon $L_{2,3}$ spectra, reproduced from reference 9. Top to bottom -- As-measured; background stripped; sharpened to 0.22 eV resolution; $2p_{3/2}$ part of the scattering; $2p_{3/2}$ results for a 40% Ge-Si alloy, showing that the onset is shifted and the overall shape is discernibly different; and an s,d projected DOS calculation from reference 17, showing the good degree of understanding of the ELNES structure.



In general, the s- and d-projected DOS gives a good explanation for the three main structure observed in the $2p_{3/2}$ spectrum. However, reference to the Ge-Si alloy result shows that it also gives a reasonably good explanation of the alloy. Thus, the easily observed variations in the experimental spectra lie within the range of variation tolerated by the calculation. This situation can be dealt with by inspection of the silicon bandstructure, followed by detailed modeling of the spectra based on this inspection. It turns out that there are only three or four dipole allowed contributions to the scattering. These include transitions to (1) the s-like band minimum at Δ_1 in the Brillouin Zone, (2) the s-like band minimum at L_1 , (3) a d-like flat band at L_3 , and (4) a saddle point in the Λ_1 branch between L_1 and Γ_2 in Ge containing alloys. These occur at 99.84 eV (Δ_1), 100.7 eV (L_1), 102.7 eV (L_3), in silicon, and 101.1 eV (Λ_1) in the 40% Ge-Si alloy. The appearance of Λ_1 is the cause of the apparent broadening in the 101 eV feature in the spectra. These four contributions can be modeled using various shapes characteristic of minima, maxima and saddle points of parabolic bands, provided some care is taken to include matrix element effects. This procedure is given in detail in Reference 9.

Figure 4. Summary of silicon $2p_{3/2}$ spectra, for a range of Ge-Si alloys. The trial DOS (lower solid curves) are used with a detailed scattering theory, including core excitonic interactions, lifetime broadening and instrumental resolution, to fit the observed spectral shape. This data shows that Δ_1 shifts smoothly upwards, while L_1 shifts downwards, until they cross near 85% Ge. In addition, the Ge-like saddle point Λ_1 is necessary to explain the data even for alloys having as little as 5% Ge.

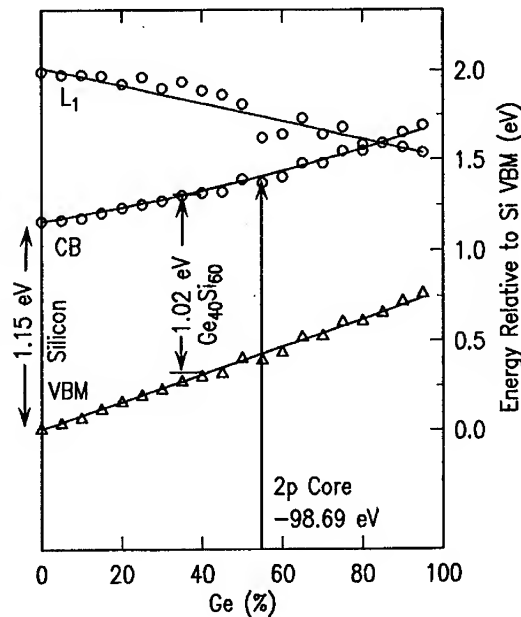


In Figure 4, data for a range of Ge-Si alloy composition are shown (dots), compared with the modeled DOS (dashed lines) and the resulting spectral fits (solid lines). Briefly, the DOS modeling scheme produces a guess for the final states in the material. It is generally agreed that the measured spectra will not directly reproduce this result due to the distorting influence of core excitons, core hole lifetime broadening and instrumental resolution. Therefore, these must be included in a scattering theory that takes into account the details of a particular experimental situation. This work is built upon several years of effort solely aimed at obtaining a reasonable treatment for this scattering theory for the case of Spatially Resolved EELS. Details of this work are available.^{9,11,12} For the purposes of this discussion, two things need to be said. First, the spectra are not understandable without including the core excitonic enhancement that distorts the shape of the results away from the ideal parabolic behavior. On the other hand, once reasonable excitonic behavior is included, remarkably detailed fits to the measured data are possible using the very simple shapes allowed by consideration of the topologies and symmetries of the various bands. Secondly, even in the absence of detailed fits, some features of the data are obvious. For instance, in Figure 3, the shift upwards of the core edge on going from Si to 40% Ge-Si is unmistakable even though it amounts to only 150 meV. In Figure 4, this shift is seen to be part of a smooth trend which continues throughout the alloy series.

In Figure 5, the positions of Δ_1 and L_1 are plotted as a function of alloy composition. This figure is similar to that shown in Reference 18. In this plot, the $2p_{3/2}$ core level is

assumed to be constant at -98.69 eV relative to the silicon valence band maximum (VBM). Then, Δ_1 moves smoothly from the silicon conduction band position at 1.15 eV up to 1.7 eV at 95% Ge content. At the same time, L_1 shifts down from about 1.9 eV to 1.55 eV, becoming the conduction band minimum (CBM) near 85% Ge. If the measured optical gap¹⁹ is subtracted from the measured CBM, the VBM can be inferred, provided that the core level is, in fact, constant as assumed. The solid lines Figure 5 are predictions given by theoretical estimates derived from deformation potential theory.²⁰ Thus it would appear that the core level is constant in this alloy system. This can be understood by realizing that the major effect that might shift a Si core level in the presence of a Ge neighbor is through the change in electrostatic potential. Although the Ge potential is slightly deeper than for Si, the Si-Ge bond length is slightly longer, so that the potential at the Si atom is nearly independent of the identity of its neighbor. The stunning result in this alloy system is that a heterojunction band offset can be obtained simply by measuring the absolute position of the $L_{2,3}$ edge.

Figure 5. Positions of Δ_1 and L_1 as a function of Ge content in the Ge-Si alloy system. Δ_1 and L_1 shift smoothly towards each other until they cross near 85% Ge. The core level is found to be constant at -98.68 eV. If the measured optical gap is subtracted from the position of the band edge, the valence band maximum can be derived. It is found to vary linearly with composition, in agreement with the theoretical prediction (solid line through triangles).



APPLICATION TO A SINGLE 10NM SI QUANTUM WELL

If this result is correct, the pieces are now in place to measure the absolute energy of the conduction band edge as a function of position through a single Si quantum well, and to relate this to the atomic positions and, possibly, composition by use of ADF atom column imaging. The first step in this process, a map of bi-axial strain splitting in a Ge-Si alloy quantum well has been reported recently.²¹ That work required more de-

tailed EELS analysis to include the bi-axial strain, but was performed using an 8 Å probe with a low resolution objective lens pole piece at 100 KeV. In Figure 6, there is an example of a single silicon quantum well placed between 30% Ge alloy substrate and cap layers. The well composition has been deliberately graded over a 5nm length scale from 30% to 0% Ge on the substrate side. In this [110] oriented specimen, the ADF image clearly shows the elongated atom "dimer" pairs. A line scan, taken along the dotted line, is superposed at the top of the photo to show the variation in intensity that signifies the change in composition. The composition grading is clearly present on the left. The vertical, solid lines are parallel to the [001] direction.

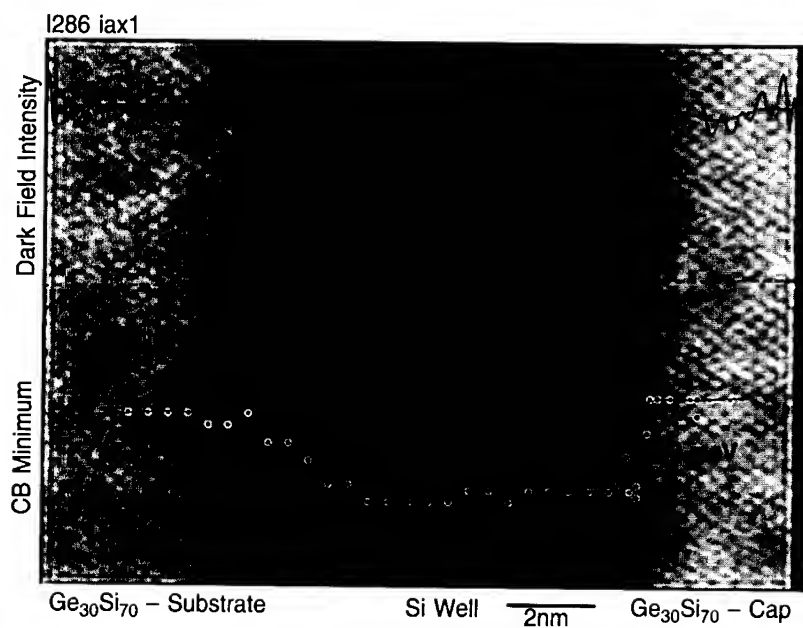


Figure 6. A silicon quantum well. The Annular Dark Field (ADF) image shows the elongated spots due to the atomic "dimers" in the [110] projection. The probe size was 1.95 Å at 120 KeV. The upper solid curve shows the ADF intensity along the dotted line. The composition is deliberately graded from the substrate up into the well. The lower data points reveal the heterojunction band offset to be 170 meV at the Si/alloy interface.

In the bottom half of the image, the conduction band edge position is plotted. These are the fitted positions of Δ_1 using spectra similar to those shown above. Each spectrum, in this case, was a sum of 5-10 30 second acquisitions. Between each acquisition, the ADF image was inspected to correct mechanical drift and probe focus. The conduction band edge moves smoothly with the composition profile at the substrate/well interface. At the well/cap interface, the heterojunction band offset is found to be 170 meV and occurs within one unit cell of Si (about 0.54 nm). Curiously, the shift in the band edge appears to be sharper than the ADF composition profile. The reason for this is not clear at this

time. But it can be noted that the ADF compositional variation is reasonable for the growth conditions, and is consistent with the junction roughness estimated from other ADF images taken in thinner areas. The surprise here is the relative sharpness of the band edge variation.

CONCLUSIONS AND FUTURE DIRECTION

This work opens new opportunities for relating electronic properties to atomic structure. Thus far it has demonstrated that the spectra are obtainable and interpretable using a probe which is small enough to adequately image atom columns in zone axis orientations. The spectral results promise to be extremely rich in detail using the small probe, because much detail has been lost in the past by spatial averaging when using a probe that covers many unit cells. This new detail has allowed the first observation of the Si^{2+} oxidation state recently at a buried $\text{Si}-\text{SiO}_2$ interface using the 1.95\AA probe.²²

Today, the IBM instrument can routinely obtain spectra whose quality equals that shown above, making it uniquely valuable for investigating nanometer sized semiconductor structures and heterogeneous interfaces. For instance small isolated Si particles show strong band edge shifts in the sub-4nm diameter regime.²³ In addition, it provides a world class spectroscopy tool for bulk crystalline materials that have imperfect macroscopic morphology. Recently, an unexpectedly sharp peak at the σ^* transition of the 1s core excitation in graphite was observed.²⁴ Thus, even familiar materials can harbor surprises when new methods of observation are employed. Use of the very small probe should allow detailed maps of the silicon conduction band edge within the strain field of single dislocations or near stacking faults. Clues to the origin of observed cathodoluminescence may result from this type of study. In sum, Spatially Resolved EELS should be regarded as an exciting new probe of bulk materials, providing new information that is unobtainable in any other way.

Many parts of this work owe a debt of gratitude to F.K. LeGoues, for providing access to many varied types of relevant specimens. Various parts of the work were also done in collaboration with J.F. Morar, J. Tersoff, S.F. Nelson, K. Ismail, and P. Mooney.

REFERENCES

1. K. Ismail, S.F. Nelson, J.O. Chu, and B.S. Meyerson, *J. Appl. Phys.*, **63** 660 (1993).
2. A.V. Crewe, M. Isaacson and D. Johnson, *Rev. Sci. Inst.*, **42** 411 (1971).
3. S.J. Pennycook, and L.A. Boatner, *Nature* **336** 565 (1988).
4. R.F. Loane, E.J. Kirkland, and J. Silcox, *Act. Crys.* **A44** 912 (1988).
5. P.E. Batson, *Rev. Sci. Inst.*, **57** 43 (1986).
6. G.H. Curtis and J. Silcox, *Rev. Sci. Inst.*, **42** 630 (1971).
7. M. Isaacson and D. Johnson, *Ultramicroscopy* **1** 33 (1975).
8. M. Scheinfein, in *Physical Aspects of Microscopic Characterization of Materials*, edited by J. Kirschner, K. Murata, and J.A. Venables, (Scanning Microscopy Supplement 1, Scanning Microscopy International, Chicago, 1987), pp. 161-177.

9. P.E. Batson, Ultramicroscopy, **50** 1 (1993).
10. P.E. Batson, Ultramicroscopy, **47** 133 (1992).
11. P.E. Batson and J. Bruley, Phys. Rev. Lett., **67** 350 (1991).
12. P.E. Batson, Phys. Rev. B, **47** 6898 (1993).
13. H. Shuman and P. Kruit Rev. Sci. Inst., **56** 231 (1985).
14. P.E. Batson, Rev. Sci. Inst., **59** 1132 (1988).
15. P.E. Batson, Mat. Sci. and Eng. B, **14** 297 (1992).
16. P.E. Batson, D.W. Johnson, and J.C.H. Spence, Ultramicroscopy, **41** 137 (1992).
17. X. Weng, P. Rez, and P.E. Batson, Sol. Stat. Comm., **74** 1013 (1990).
18. J.F. Morar, P.E. Batson and J. Tersoff, Phys. Rev. B, **47** 4107 (1993).
19. J. Weber and M. Alonso, Phys. Rev. B **40** 5683 (1989).
20. C. Van de Walle, Phys. Rev. B **39** 1871 (1989).
21. P.E. Batson and J.F. Morar, Phys. Rev. Lett., **71** 609 (1993).
22. P.E. Batson, Nature, in press.
23. P.E. Batson and J.R. Heath, Phys. Rev. Lett., **71** 911 (1993).
24. P.E. Batson Phys. Rev. B **48** 2608 (1993).

TRACE ANALYSIS OF NANOSCALE MATERIALS BY ANALYTICAL ELECTRON MICROSCOPY

DALE E. NEWBURY* AND RICHARD D. LEAPMAN**

*National Institute of Standards and Technology, Gaithersburg, MD 20899

** National Institutes of Health, Bethesda, MD 20892

ABSTRACT

Trace analysis of nanometer-scale objects can be performed with parallel-detection electron energy loss spectrometry in the analytical electron microscope. Spectra are collected in the second difference mode with the beam current chosen to maximize the spectral count rate. Numerous elements can be detected at trace levels below 100 parts per million atomic, including transition metal, alkali metal, alkaline earth, and rare earth elements, provided they have a "white line" resonance structure at the ionization edge. Trace nanoanalysis by AEM/PEELS permits direct examination of the microscopic distribution of trace constituents.

INTRODUCTION

The characterization of individual nanoscale objects in the size range from 1 - 500 nm raises special challenges to microbeam techniques. Of the wide variety of techniques currently available based on beams of electrons, ions, and photons, one of the most successful in attacking problems involving particles in the nanometer size range is analytical electron microscopy (AEM).¹ The AEM is ideally suited to the comprehensive characterization of nanoscale objects through the determination of morphology, crystal structure, and chemical composition. Morphology is accessible through high resolution imaging in the transmission electron microscope (TEM), scanning transmission electron microscope (STEM), and scanning electron microscope (SEM) modes. Structural information is available through a variety of electron diffraction techniques in the TEM and STEM modes. Elemental composition can be determined by spectroscopies based on inner shell ionization (electron energy loss spectrometry, EELS) and subsequent de-excitation with the emission of x-rays (energy dispersive spectrometry, EDS), and in special cases, compound information is also accessible with EELS.

An inevitable consequence of decreasing the primary beam diameter in the AEM is a decrease in the beam current, following a power law, $i \propto d^2$. The current delivered into the focused probe controls the rate of production of characteristic secondary radiation in the EELS and EDS spectra. As the probe size decreases, the consequent decrease in the spectral counting statistics results in a deterioration in the limit of detection. Two important concepts for understanding the limitations imposed on the measurement are the minimum detectable mass and the minimum mass fraction. The minimum detectable mass (MDM) is the smallest absolute mass that can be detected. For a particle consisting only of a pure element, the MDM depends on several factors: (1) the physics of signal generation and measurement, including any processes contributing to the background; (2) the source brightness as it influences the smallest primary beam size that can provide sufficient current to yield a statistically useful signal in a reasonable measurement time (e.g., arbitrarily taken as 100 seconds, in view of the need for positional stability on an extremely fine scale); and (3) the scattering of the primary radiation to excite regions adjacent to the cylindrical volume defined by the circular beam cross section and the specimen thickness. Achieving the lowest possible value of the MDM depends on having high beam brightness, minimum scattering of the signal out of the cylindrical beam volume, and efficient collection and detection of the secondary radiation. For a pure target of thickness t , a probe of radius r , and assuming that at least 100 counts must be accumulated to provide detection with a measurement statistic of 10% relative standard deviation, the MDM can be estimated in the absence of primary scattering and of a background process as:

$$(\pi r^2 t \rho N_A \sigma \epsilon j \tau) / A > 100, \text{ or } MDM = \pi r^2 t \rho > 100 A / (N_A \sigma \epsilon j \tau) \quad (1)$$

where A is the atomic weight, ρ is the density, N_A is Avogadro's number, σ is the cross section for production of secondary radiation, ϵ is the efficiency of secondary radiation collection and detection, j is the source current density, and τ is the measurement time.

When the MDMs for EELS and EDS are compared for pure materials, EELS has the advantage for excitation edges in the ionization energy range from 0 - 3 keV. EELS makes use of most of the cross section while for EDS the ionization events are reduced by the fluorescence yield, ω (x-rays/ionization event), which is low, $\approx 0.01 - 0.1$, for the low ionization energy range. The efficiency with which the radiation is detected is also strongly in favor of EELS. The maximum geometric efficiency for EDS is approximately 0.02 (a detector solid angle of 0.2 steradian detector/4 π steradians for isotropic x-ray emission), and the detection efficiency is 0.01 - 0.7 for the x-ray energy range from 0.1 - 3 keV, depending on the spectrometer window. For EELS, the mean inelastic scattering angle $\alpha \approx \Delta E/E_0 = 0.01$ (for $\Delta E = 1$ keV and $E_0 = 100$ keV), a value that is smaller than the acceptance angle of the spectrometer ($\beta = 0.02$), so that a large fraction of the EELS signal is accepted, thus yielding a collection efficiency near unity. The EELS detection efficiency is also close to unity, and parallel collection eliminates the loss of information incurred by sequential scanning. As ΔE increases above 3 keV, the advantage shifts to EDS because the inelastic scattering angle becomes greater than the spectrometer acceptance angle and signal is lost.

For a target with multiple constituents, the MDM depends on the mass of the excited specimen multiplied by the fractional sensitivity. The minimum mass fraction (MMF) is the smallest fractional constituent of a multi-component sample that can be measured. The ability to measure a minor (1-10%) or trace (<1%) fractional constituent depends strongly on the character of the spectrum, particularly on the presence of a spectral background beneath the characteristic peaks. As derived by Wittry², the concentration limit of detection, C_{MMF} , is given by the expression:

$$C_{MMF} = (P/B)^{-1} (\sigma \epsilon j \tau)^{-1/2} \quad (2)$$

where P is the intensity integrated across the peak and B is the background under the peak window, as measured on a pure element target. The strong influence of P/B is evident in its appearance in equation (2) as a linear term, whereas the other factors appear to a fractional power.

When the MDMs for EELS and EDS are compared for multielement materials, the advantage seems to be clearly in favor of EDS, even when the most favorable edge energy for each technique is chosen. Standard Reference Material (SRM) 2063a, a multielement glass film 76 nm thick, has been used to compare EDS and EELS.³ For EDS, a $P/B = 44/1$ was obtained for the Si K α peak from a concentration of $C_a = 0.20$ (atomic). The corresponding EELS spectrum gave a much lower P/B ratio of 1.46 for the Si K-edge across an energy interval of 100 eV. Observations of the P/B for EDS and EELS led Wittry to suggest that the limiting C_{MMF} would be about 0.001 for AEM/EDS, but would have a substantially poorer value, > 0.01 , for AEM/EELS.²

TRACE NANOANALYSIS

Despite this state of affairs, true trace concentrations $<< 0.01$ can be measured with EELS for some elements.³ To achieve trace detection with EELS, a spectral feature with an inherently much higher P/B than the extended ionization edge must be sought. Certain elements display an effect at the ionization edge energy known as a "white line", which is due to a resonance in the unfilled density of states.⁴ White lines are the peak-like structures seen for the Ca L_{2,3}-edges in Figure 1. Such sharp features could be enhanced against the slowly varying background by means of a derivative, but derivative processing would also enhance the channel-to-channel gain variations that inevitably occur in the parallel EELS detector array, leading to interference with low intensity features. An alternative approach which suppresses channel gain variations is the "2nd difference" spectral collection/processing procedure, in which three EELS spectra are recorded with sequential shifting on the detector array above and below the nominal value by an amount δE , which is comparable to the width of the white line features that are sought.⁵ The final spectrum is obtained by subtracting the shifted spectra from twice the value of the unshifted (central) spectrum. This action has the effect of a derivative filter, emphasizing high frequency white line features while suppressing the slowly varying background. Most importantly, the gain variations are quantitatively eliminated, as shown in Figure 2, where trace constituents (Ce, Cs) in NIST glass K-1012 are easily found in the 2nd difference spectrum but are difficult to even detect in the direct

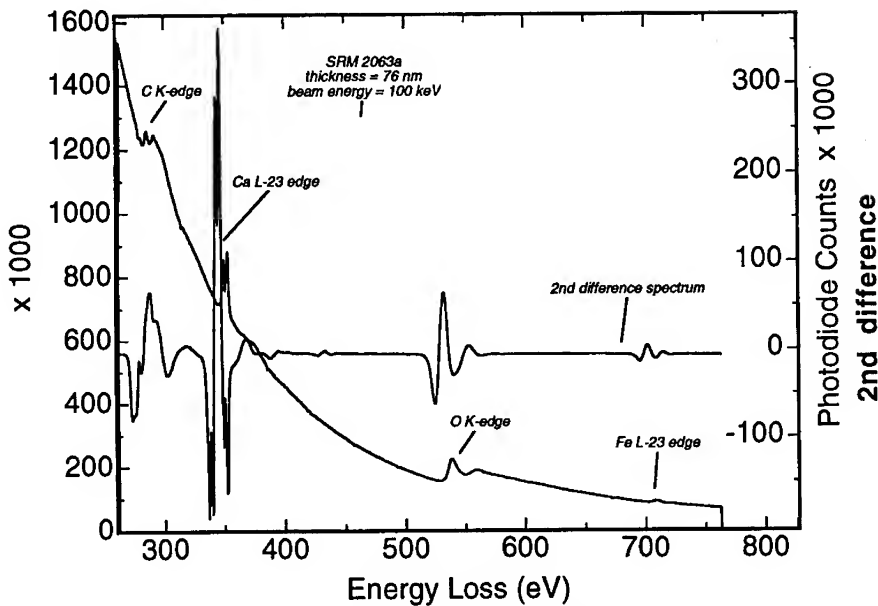


Figure 1 Direct and 2nd difference EELS spectra of NIST SRM 2063a, 76 nm thick glass film.

spectrum. By recording EELS spectra with sufficiently high counting statistics, the fundamental detection limit imposed by counting statistics can be reduced to levels below 100 parts per million atomic for elements with strong white line features. Figure 3 shows an example of the detection of trace constituents by AEM/EELS in the NIST trace element glass, SRM 610. The AEM used was a field emission scanning transmission electron microscope (FE-STEM) equipped with a parallel collection electron energy loss spectrometer (PEELS). The spectrum was recorded in 200 s with a beam current of 10 nA (beam size 5 nm) to maximize the count rate within the limitations of the detector response. The spectral resolution was ~ 0.4 eV and the dispersion was chosen to view a 1000 eV wide energy band on the 1024 channel detector array. The spectrum demonstrates the detection of several transition metal elements, alkaline earth elements, and rare earth elements present at levels ranging from 75 to 200 parts per million atomic. The region sampled had dimensions of 10×10 nm (defined by the scan) $\times \sim 100$ nm thick (estimated maximum based on multiple scattering limitations) and contained only about 10^6 total atoms. Thus, the peaks shown in Figure 3 represent the detection of 75 - 200 atoms in a nanometer-sized target. This level of detection has been designated "trace nanoanalysis".

THE MICROSCOPIC DISTRIBUTION OF TRACE ELEMENTS

Trace nanoanalysis by AEM/PEELS provides a new approach to a difficult microstructure characterization problem, namely determining the distribution of trace constituents on a microscopic scale. The inevitable deterioration in the limit of detection which can be achieved at high spatial resolution prohibits most microanalytical techniques from directly determining if a target such as a nanoscale particle actually contains a constituent at a trace level. If a macroscopic analysis of a particle sample indicates the presence of a trace constituent and if the microscopic distribution of that trace is of interest, the analysis strategy currently available is to assess if the trace constituent is localized at a high concentration in a minority particle species or inclusion. Finding such a localized "needle-in-a-haystack" depends on having an analytical technique with an acceptably low MDM for major species, rapid analysis time per particle, and computer-assisted analysis for automatic detection and analysis in unattended operation. A "brute force" approach

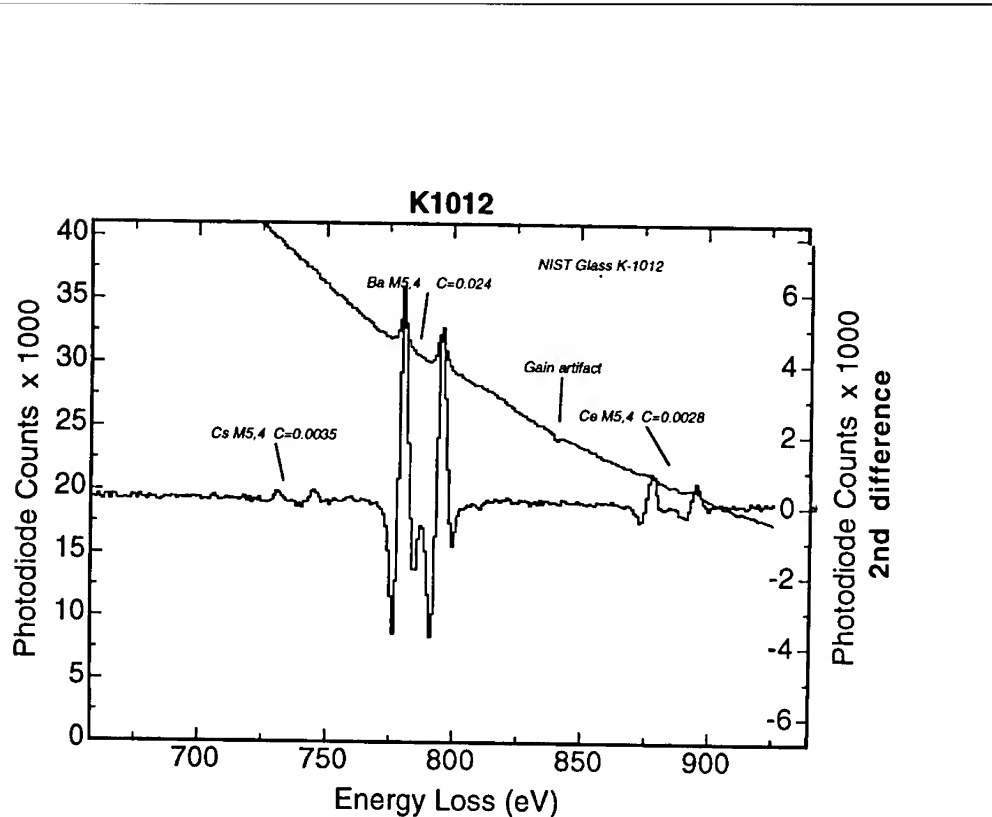
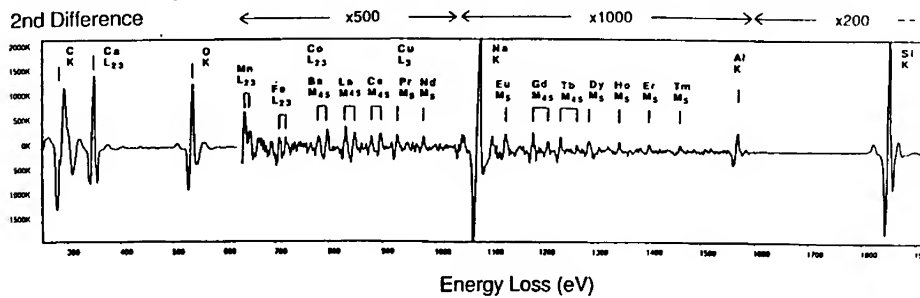


Figure 2 Direct and 2nd difference EELS spectra from a nanoscale particle of NIST glass K1012.

may then permit interrogation of a sufficiently large number of particles to find the rare particle. As a new alternative to time-consuming searching, trace nanoanalysis by AEM/PEELS achieves a sufficiently low MMF to permit direct examination of particles for trace constituents. By directly measuring the presence or absence of trace constituents down to a definable limit of detection, the possible localization of a constituent can be inferred, even if detailed searching to find such a localization is unsuccessful or impractical.

An example of the application of trace nanoanalysis by AEM/PEELS to assess the degree of localization of a trace constituent is shown in Figures 4 - 6. The sample consisted of nanoscale yttria particles (approximately 5 - 20 nm) which had been co-evaporated with europia. Bulk trace analysis by neutron activation (performed by R. Lindstrom, NIST) revealed that the overall sample loading of europium was approximately 0.0035 (3500 ppm). AEM/PEELS examination of a series of individual nanoscale particles revealed no detectable europium, as shown in Figure 4; however, a trace level of lanthanum was unexpectedly found, confirming that trace analysis conditions were

Figure 3 EELS spectrum (2nd difference) from NIST SRM 610, Trace Elements in Glass.



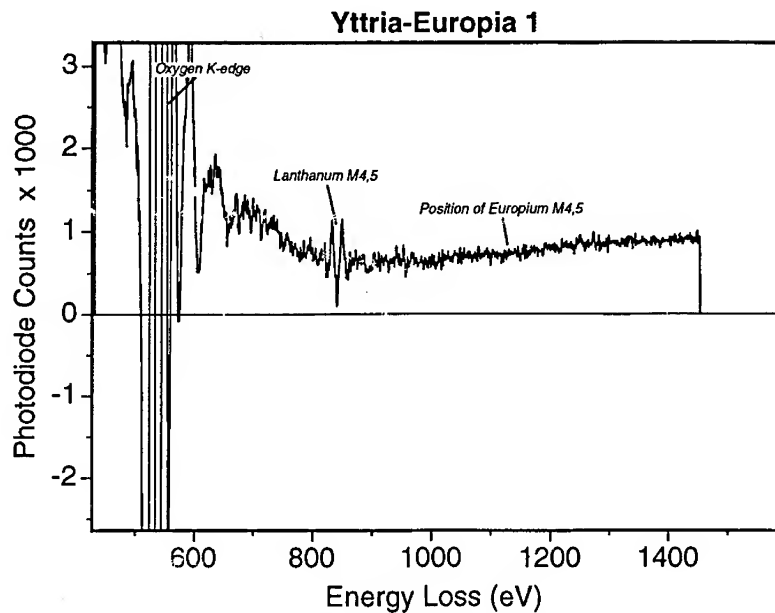


Figure 4 2nd difference EELS spectrum from a nanoscale particle of an yttria-europia sample showing detection of trace La but the absence of Eu above a detection limit of 100 ppm a.

being achieved. Further searching revealed a few particles with minor levels of europium, in the range 0.001 - 0.01, as shown in Figure 5, but there were not enough of these particles to account for the overall europium loading of the sample as determined by bulk analysis. Finally, by sampling several hundred locations, particles were located in which the major constituent was europium, as shown in Figure 6. These europium-rich particles were also found to contain a large fraction of tungsten, shown in Figure 6 and confirmed by EDS, which was apparently transferred from a reaction with the evaporation source.

CONCLUSIONS

Trace nanoanalysis by AEM/PEELS offers new characterization capabilities for nanoscale objects and complements AEM/EDS by extending sensitivity to the trace level for the first time. The microstructural distribution of trace constituents can be examined to much finer scales than previously possible. In conjunction with other information derived from microscopy and phase identification, the AEM can provide comprehensive characterization on the nanoscale.

ACKNOWLEDGMENT

The authors wish to thank Dr. John C. Parker of Nanophase Technologies Corp. for the nanoscale yttria-europia particle sample and Dr. Richard Lindstrom of NIST for the bulk trace analysis.

REFERENCES

1. D. C. Joy, A. D. Romig, and J. I. Goldstein, *Principles of Analytical Electron Microscopy*, (Plenum Press, New York, 1986).
2. D. B. Wittry, Proc. 9th Intl. Conf. X-ray Optics and Microanalysis, 14 (1980).
3. R. D. Leapman and D. E. Newbury, *Analytical Chem.*, **65**, 2409 (1993).
4. R. F. Egerton, *Electron Energy-Loss Spectroscopy in the Electron Microscope* (Plenum Press, New York, 1986) 205.
5. H. Shuman and P. Kruit, *Rev. Sci. Instrum.*, **56**, 231, (1985).

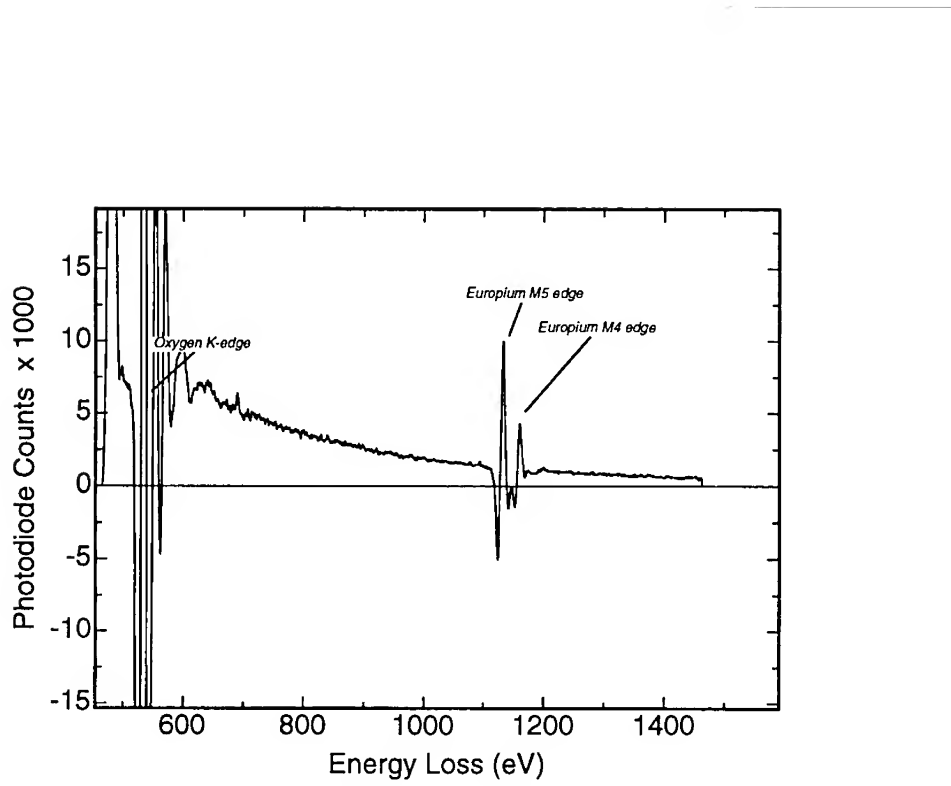


Figure 5 2nd difference EELS spectrum from a nanoscale particle of an yttria-europia sample showing detection of europium as a minor constituent at a level of approximately 0.01 atomic.

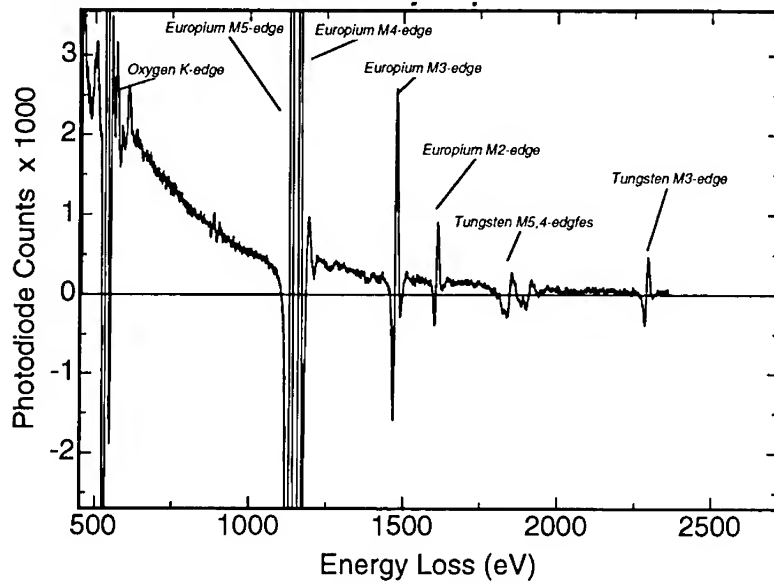


Figure 6 2nd difference EELS spectrum from a nanoscale particle of an yttria-europia sample showing detection of europium as a major constituent, and the presence of significant tungsten.

SELECTIVE IMAGING OF METAL ATOMS IN THE SEMICONDUCTING LAYERED COMPOUND MoS_2 BY STM/STS

S. INOUE, H. KAWAMI, M. YOSHIMURA AND T. YAO
Department of Electrical Engineering, Hiroshima University
Higashi-hiroshima 724, Japan

ABSTRACT

We have investigated the valence band structure of MoS_2 , a transition-metal dichalcogenide, using scanning tunneling microscopy (STM) and scanning tunneling spectroscopy (STS) for the first time. We have found characteristic peaks in the $(dI/dV)/(I/V)$ -V characteristic at -1.0 and -1.4V below the fermi level, which correspond to the S p_z state and Mo d_{z^2} state, respectively. Mo atoms are accessible only at the sample voltage of -1.4V in the range of -1.0 through -1.5V, due to the strong localization of the Mo d_{z^2} state with very small bandwidth.

INTRODUCTION

Since the invention of scanning tunneling microscopy (STM), 2H- MoS_2 , a semiconducting layered compound of transition-metal dichalcogenide, has been widely used as a test sample for STM instruments and as a substrate for organic materials such as liquid crystals[1]. This is because one can easily get an atomically-flat surface by cleavage and the surface is very stable even in air.

Figure 1 shows the (001) surface structure of MoS_2 as determined by X-ray diffraction. The topmost layer is a hexagonal lattice of S atoms with lattice constant of 3.16Å. The second layer is an identical hexagonal lattice of Mo atoms laterally displaced relative to the top layer. The distance between the Mo and S layers is 1.59Å. To date, only a few STM studies have paid attention to the electronic structure of transition-metal dichalcogenides. Weimer et al.[2] claimed from their vacuum STM study that both Mo and S atoms could be simultaneously imaged at a positive sample bias. Mori et al.[3] suggested that the metal layer in MoSe_2 (the crystal structure is almost the same as that of MoS_2) contributed greatly to the STM image at the unoccupied state, while the chalcogen atom layer contributed at the occupied state. However detailed examinations such as the tunneling voltage dependence on the image were not described in either paper.

The electronic band-structure of MoS_2 has been investigated by photoelectron spectroscopy[4,5] and inverse photoemission spectroscopy[6], together with band-calculations[7,8]. According to these studies, the valence band near the fermi level, which contributes to the tunneling current in STM, consists mainly of the Mo d_{z^2} state but is overlapped with the sulfur p_z state. Since both states extend perpendicular to the surface and each type of atom forms in a hexagonal arrangement, detailed STM/STS study is needed to elucidate which atom layer contributes more to the STM image.

In this paper we present a detailed STM/STS study of the MoS_2 surface to clarify the valence band structure and understand which layer is responsible for the STM image. At -1.4V below the fermi level we have found a strongly localized d_{z^2} state of metal atoms, while the S p_z state is around -1.0V.

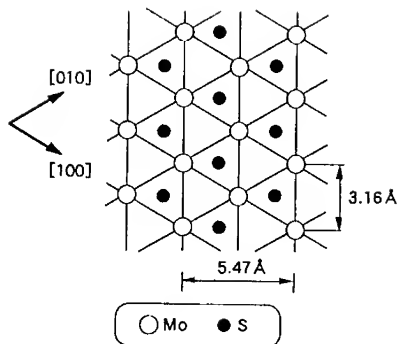


Fig.1. Crystal structure of MoS₂ (001) surface. The distance between Mo and S layers is 1.59 Å.

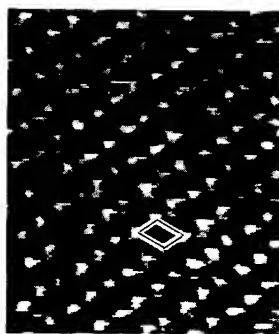


Fig.2. Topograph of MoS₂ surface at -1.0V. A unit cell is drawn.

EXPERIMENTAL

We have utilized a home-made STM operated in air which uses a dc motor for coarse motion and a tube-type piezo actuator for fine approach[9]. Spectroscopic data of 64 preset points are acquired with 128 voltage steps into a computer memory (PC9801), together with a simultaneous STM topographic image. Electrochemically sharpened tungsten tips ($\phi = 0.5\text{mm}$) are used as probes for the tunneling current. The clean surface of MoS₂ is prepared by cleavage just before observation.

RESULTS AND DISCUSSION

Figure 2 shows a constant-current topograph of the MoS₂ surface obtained at a sample voltage of -1.0V, which probes the occupied state. The hexagonal lattice structure is observed in the image where the unit cell is drawn. We tentatively assign the observed protrusions to the sulfur atoms in the topmost layer, although at this stage the protrusions are not identified as Mo or S atoms. Figures 3 shows the simultaneously obtained STS spectra, which are averaged over the equivalent sites. Negative energies indicate occupied states, while positive energies indicate empty states. All of the curves have stronger intensity in the empty states than that in the occupied states, and have a semiconducting band gap. Curve *a*, obtained at the S sites, has a strong peak at around -1.0V. Curves *b* and *c* were obtained at the center of one half and the other half of the unit cell. Curve *b* has a characteristic peak at around -1.4V and curve *c* has no appreciable peaks. We tentatively assign the curves *b* and *c* to the Mo site and the hollow site, respectively, on the assumption that an absence of peaks corresponds to an absence of atoms. Then Mo atoms have a state (probably d_{z^2}) at -1.4V below the fermi level, and S atoms have a state (p_z) at -1.0V. As a result, Mo atoms are expected to be imaged around a tunneling voltage of -1.4V.

Figure 4 shows a topograph obtained at a sample voltage of -1.4V. One can see clearly a subsidiary spot (indicated by arrow) in one half of the unit cell and a

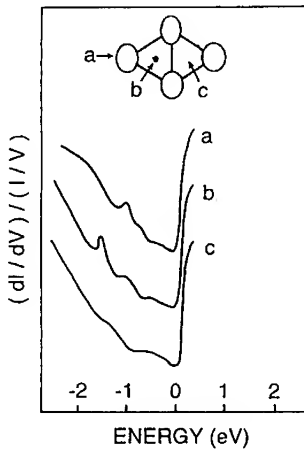


Fig.3. STS spectra simultaneously obtained with Fig.2. Curves *a*, *b* and *c* are obtained and averaged at S sites, Mo sites and hollow sites, respectively.

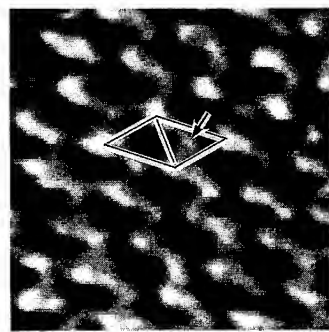


Fig.4. Topograph obtained at -1.4V. Sulfur atoms and Mo atoms are observed simultaneously.

hollow in the other half, which is in agreement with the surface structure of the bulk crystal. Namely, at this voltage we observe both Mo and S atoms at the same time. Since our operation system does not have enough memory to get STS in every pixel (more than sixty-four), we have tried to image at some different voltages around -1.4V in order to determine which atoms correspond to the subsidiary spots. All the images obtained at -1.1~1.3 and -1.5~1.6 are reproducible and have no such subsidiary spots. Since the Mo d_{z^2} state is considered to be localized with a smaller band-width than the sulfur p_z state[5], it may appear as spots within a small range of the tunneling voltage. Moreover, the difference in vertical atomic position between sulfur atoms in the topmost layer and Mo atoms in the second layer is so large (1.59Å) that the Mo atoms seem to contribute little to the tunneling current. In fact, simulation of the STM image on the MoS₂ surface shows that only sulfur atoms can be imaged at around -0.2V [10]. Based on these facts, we conclude that the peaks at -1.0V and -1.4V correspond to the S p_z and Mo d_{z^2} states, respectively. The subsidiary spots shown in Fig.4 are Mo atoms which are accessible only around this tunneling voltage. At voltages of -1.0 through -1.5 except around -1.4V, we image only sulfur atoms, the state of which is distributed widely enough in energy to include the Mo d_{z^2} state.

CONCLUSIONS

We performed a STM/STS study of the valence-band structure of the MoS₂ surface. Characteristic peaks are observed at -1.0V and -1.4V for the S p_z and Mo d_{z^2} states, respectively. The STM image at -1.4V reveals both S and Mo atoms simultaneously. We image only sulfur atoms at voltages of -1.0 through -1.5V

except at -1.4V. This is because the p_z and d_{z^2} states overlap in the valence band, and d_{z^2} is strongly localized at -1.4V while the S p_z state is widely distributed.

REFERENCES

1. M. Hara, Y. Iwakabe, K. Tochigi, H. Sasabe, A. F. Garito and A. Yamada, *Nature* 344, 228 (1990).
2. M. Weimer, J. Kramar, C. Bai, and J. D. Baldeschwieler, *Phys. Rev. B* 37, 4292 (1988).
3. T. Mori, K. Saiki, and A. Koma, *Jpn. J. Appl. Phys.* 31, L1370 (1992).
4. R. Coehoorn, C. Haas, J. Dijkstra, and C. J. F. Flipse, *Phys. Rev. B* 35, 6195 (1987).
5. J. C. McMenamin and W. E. Spicer, *Phys. Rev. Lett.* 29, 1501 (1972).
6. M. Sancrotti, L. Braicovich, C. Chemelli, and G. Trezzi, *Solid. State. Commun.* 66, 593 (1988).
7. R. V. Kasowski, *Phys. Rev. Lett.* 30, 1175 (1973).
8. L. F. Mattheiss, *Phys. Rev. B* 8, 3719 (1973).
9. H. Kawami, S. Inoue, M. Yoshimura, and T. Yao, *Solid State Phys.* 28, 177 (1993). (in Japanese)
10. K. Kobayashi (private communication)

ATOMIC-RESOLUTION CHEMICAL ANALYSIS AT 100 KV IN THE SCANNING TRANSMISSION ELECTRON MICROSCOPE.

N. D. BROWNING, M. F. CHISHOLM AND S. J. PENNYCOOK
Solid State Division, Oak Ridge National Laboratory, Oak Ridge, TN 37831-6030 USA

ABSTRACT

In a 100 kV VG HB501 UX dedicated scanning transmission electron microscope, the 2.2 Å probe size allows the atomic structure to be observed with compositional sensitivity in the Z-contrast image. As this image requires only the high-angle scattering, it can be used to position the probe for simultaneous electron energy loss spectroscopy. Energy loss signals in the core loss region of the spectrum (>300 eV) are sufficiently localized that the spatial resolution is limited only by the probe. The electronic structure of the material at the interface can thus be determined on the same scale as the changes in composition, and atomic structure can be observed in the image, allowing the structure and chemical bonding at interfaces and boundaries to be characterized at the atomic level.

INTRODUCTION

It is becoming increasingly evident that many of the most technologically important bulk properties of materials are governed by the atomic structure of internal interfaces or the distribution and nature of microscopic defects. Determination of the nature of these interfaces and defects on the atomic scale, therefore, represents a key element in a fundamental understanding of the structure and properties of materials. In this paper, we describe a technique which utilizes the 2.2 Å probe of the 100 kV VG HB501 dedicated scanning transmission electron microscope (STEM) to characterize the structure, composition, and electronic structure of crystalline materials on the atomic scale. This is achieved by using the combination of the high-resolution Z-contrast imaging technique [1] and electron energy loss spectroscopy (EELS) which, due to the detector geometry in the STEM, can be performed simultaneously [2]. By selecting experimental conditions for detection of the energy loss spectrum which cause the inelastic signal to be localized at the probe, the image and spectrum can have the same atomic resolution [3]. This ability is demonstrated in the study of a CoSi₂-Si {111} interface, where both the image and energy loss spectrum indicate the interface to be atomically abrupt. The use of the spectral fine structure to characterize interface bonding with atomic resolution is discussed, with particular reference to the effects of increasing accelerating potential on the spatial resolution of both the image and spectrum.

EXPERIMENTAL TECHNIQUE

The basis of obtaining electron energy loss spectra (EELS) with atomic resolution is the high-resolution Z-contrast imaging technique in the STEM (Fig. 1). At high angles, thermal diffuse scattering is the dominant contribution to the detected intensity in the annular dark field detector. This allows us to consider each atom as scattering independently with a cross section that approaches the Z^2 dependence on atomic number, so for thin specimens, where there is no dynamical diffraction, the detected intensity consists of a convolution of the probe profile and an object function which is strongly peaked at the atom sites. The width of the object function is typically ~0.1 Å, which means that the spatial resolution is limited only by the 2.2 Å probe size of the microscope. In zone-axis orientations where the probe size is smaller than the atomic spacing, the individual atomic columns can therefore be excited individually and an atomic resolution compositional map of the specimen generated. Experimental results show that this high resolution also holds for thicker specimens where dynamical diffraction would be expected to significantly broaden the probe [4,5]. This is due to the local nature of the high-angle scattering events resulting in a preferential scattering from *s*-type Bloch states. Dynamical diffraction then manifests itself simply as a columnar channeling effect which scales the scattering cross section

according to thickness[4-8]. Differences in intensity due to channeling effects are always less than differences due to compositional changes, so the intuitive interpretability of the image is retained.

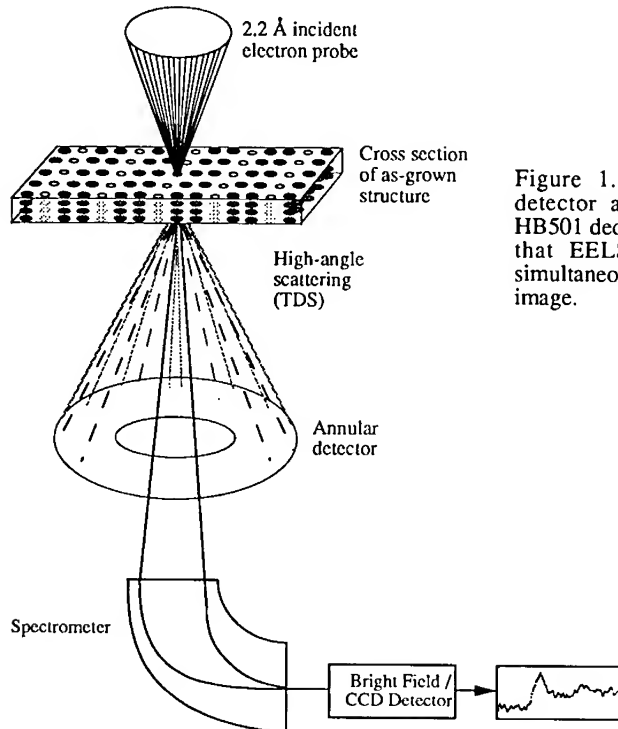


Figure 1. A schematic of the detector arrangement in a VG HB501 dedicated STEM, showing that EELS can be performed simultaneously with the Z-contrast image.

The nature of the image, therefore, approaches that of an ideal incoherent image, and it is this that makes it an ideal reference signal on which to base atomic-resolution microanalysis. The effect of increasing thickness is easily interpretable as there is no strong change in the form of the image, and in general, as the number of atoms increases in each column, the detected signal intensity increases until eventually, the beam is depleted by the scattering events. Similarly, the effect of changing focus is also intuitively understandable as the focus control effectively alters the probe profile. As the focus is altered away from the Scherzer condition, the probe either broadens for lower defocus causing the individual columns not to be resolved, or narrows with the formation of more intense tails for higher defocus causing sharper image features but compositional averaging over several columns. The optimum focus condition, therefore, represents a compromise between high resolution (narrow central peak profile) and the desire for a highly local image (no significant tails to the probe). Changes in focus and thickness therefore do not cause contrast reversals in the atomic resolution image allowing the unambiguous identification of atomic column sites. In addition to this ease of interpretation of the Z-contrast image, it is formed only from high-angle scattering, allowing the lower angle signal to be used simultaneously for energy loss spectroscopy. The high-resolution image can thus be used to position the probe on a particular atomic column or plane, upon which the spectroscopy can be performed.

For the energy loss spectrum to have the same atomic resolution as the image, the range of the excitation event must be less than the interatomic spacing. This range can be described classically by the impact parameter, b , and in similar terms to the Z-contrast theory, it effectively describes the object function of the energy loss signal. The experimental spatial resolu-

tion limit for EELS can therefore be defined by consideration of the spatial resolution of this object function and the distribution of the probe, which is achieved in practice by the summation of the two in quadrature. For a collection angle of 30 mrad, limited by the inner angle of the dark field detector, the energy loss signal is effectively localized at the probe for energy losses of 300 eV and above [3] (Note that this is a classical free space calculation; dielectric screening may reduce the impact parameter and allow atomic resolution at lower energy losses [9]).

The impact parameter description of spatial resolution deals only with the generation of the signal, assumes a very thin sample and ignores any beam broadening effects. However, for a zone-axis orientation, the Z-contrast result shows that for scattering events located close to the atomic cores, beam channeling preserves the spatial resolution of the signal (Fig. 2). This beam channeling effect allows the use of the large 30 mrad aperture, whereas traditionally, small collector apertures are used to reduce the effects of multiple scattering and preserve spatial resolution. Collecting over a large angular range also averages over dynamical effects on the outgoing inelastically scattered electrons, thus ensuring that they too carry an incoherent atomic resolution signal. Note that by complementarity alone, we would expect that the outer collection angle for EELS would need to be equal to the inner collection angle of the Howie detector to provide an equally local signal. This would be necessary for example, to provide an incoherent bright field signal. It is the additional localization due to the transfer of energy that allows us to reduce this angle substantially and still maintain sufficient localization.

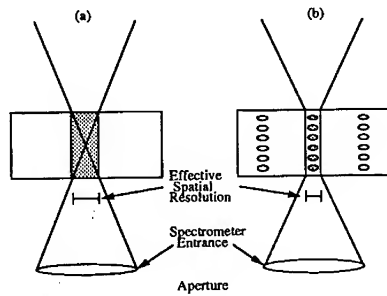


Figure 2. The beam broadening seen in energy loss studies of amorphous materials or crystalline materials away from zone-axis orientation (a) is reduced in the case of a crystalline material in zone-axis orientation by the channeling of the electron beam down the atomic columns (b).

ATOMIC-RESOLUTION CHARACTERIZATION OF COBALT DISILICIDE-SILICON INTERFACES

The extent that these theoretical estimates of spatial resolution applies to the experimental study of interfaces and boundaries can be examined by the study of a CoSi_2 -Si (111) interface. The interface was produced by implanting Co^+ ions in a heated Si(001) substrate followed by a two stage anneal [10], with cross-sectional samples prepared for electron microscopy by mechanical polishing and ion-milling. A typical Z-contrast image of this interface is shown in Fig. 3, with the brighter region corresponding to the increased scattering power of the heavier cobalt atoms in the silicide. The stacking fault visible at the interface causes the separation of the planes across the boundary to be reduced to 2.7 Å from the 3.1 Å planar spacing of the bulk, and means that the microscopic orientation of the interface is the twinned "B"-type, in which the cobalt atoms in the interface plane have the same 8-fold coordination as the bulk [11]. As the Z-contrast image of the interface is used to select a region where the interface is abrupt for the full width of the scan, no change in spectral intensity is expected in moving along the interface and the linescan mode of the microscope can be used to acquire spectra, thus reducing beam damage. The cobalt $\text{L}_{2,3}$ spectra obtained plane-by-plane in this way are shown in Fig. 4. Each spectrum is limited to a 5 second exposure, reducing the effects of specimen drift ($\sim 2-3$ Å/minute). The CCD detector used [12] has very low thermal and output noise, so that the noise of the spectra is due only to shot noise in the spectrum itself ($\sim 10\%$).

The total intensity of the cobalt L-edge from planes close to the interface was calculated by fitting a reference spectrum obtained from the bulk of the silicide (Fig. 5). This reference spectrum was obtained by summing 20 linescan spectra from single planes of similar thickness 4–6 atomic planes from the interface and confirmed to be representative of bulk CoSi_2 by the characteristic 2:1 $\text{L}_3:\text{L}_2$ intensity ratio [13] (the coordination of cobalt at the interface did not appear to vary from that in the bulk, though the signal-to-noise ratio is insufficient to accurately address this point). Figure 5 shows the experimental changes (x) in the total L-edge intensity agree well with those expected theoretically from calculations of the probe intensity profile at the surface (o), with an intensity variation that drops from 86% to 7% in a single atomic plane. This change in intensity across the interface clearly demonstrates that the resolution of the energy loss signal corresponds to a single atomic plane.



Figure 3. Z-contrast image of a CoSi_2 -Si {111} interface.

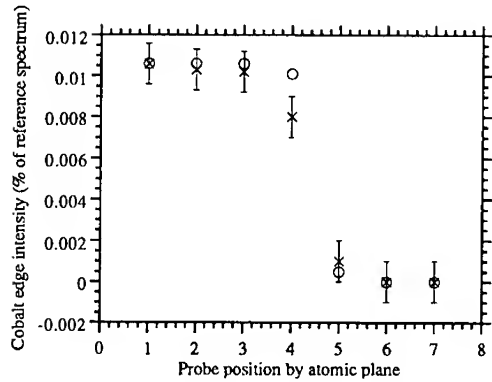


Figure 5. The experimental changes (x) in the L-edge intensity (Fig. 4) agree well with those expected theoretically from calculations of the probe intensity profile at the surface (o), and demonstrate clearly that atomic-resolution analysis has been achieved at the interface.

DISCUSSION AND CONCLUSIONS

Figure 5 shows that obtaining atomic-resolution microanalysis from selected atomic columns (theoretically even a single column) defined by the image is now a practical possibility. The results also indicate aspects of the scattering process which require further study, such as the slight reduction in the contrast at the two planes either side of the interface. This is most likely due to a combination of amorphous surface layer broadening the probe, and some elastic scattering of the probe out of the channeling condition. The fact that the composition profile is asymmetric supports the idea of some elastic scattering out of the channeling condition, as this

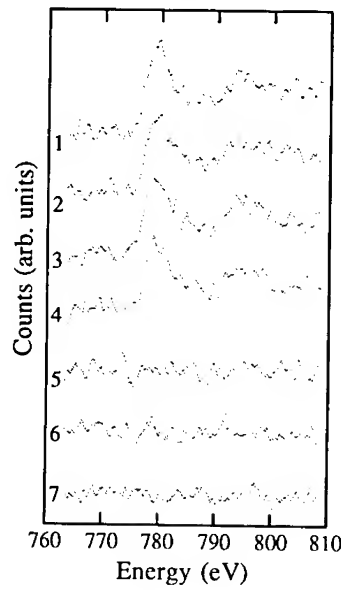


Figure 4. Background stripped cobalt $\text{L}_{2,3}$ spectra obtained plane by plane across the interface.

effect would be expected to be more pronounced in the silicide. However, as only the interface plane itself is significantly affected ($\sim 10\%$ less than predicted by the probe profile) these effects are small in this particular instance. It is important to note that for thicker specimens and for elements with higher atomic number, the effect of the elastic scattering may become more pronounced.

Compositional information can be obtained in principle column-by-column and directly related to the interface structure seen in the image. This overcomes problems caused by beam broadening and uncertainties in the interface structure that occur in microanalysis without the benefit of a high-resolution reference image. At an amorphous/crystal interface of course, the usual beam broadening will occur when the probe is in the amorphous layer, but the last atomic column of the crystal can still be analyzed with atomic resolution. Additionally, by increasing the number of spectra taken from each plane, it should be possible to interpret the fine structure of the spectrum in terms of the chemical bonding on the atomic scale [14]. (An increase in the number of spectra rather than a single longer exposure is needed so that the effects of beam damage can be monitored.) Such measurements will aid in the determination of the interface structure, something that is difficult to do from the image alone, even with the intuitive Z-contrast image. How localized this band structure information will be has yet to be seen, but a knowledge of the exact crystallographic location of the probe greatly reduces some of the ambiguities in interpretation of spectral fine structure [15].

The orientation of the specimen in this well-defined manner also offers the possibility of using the microscope to obtain angle resolved spectra [16]. By obtaining spectra from the specimen in different orientations or with different collection angles, the orientation dependence of the transitions making up the fine structure of the spectrum can be probed. Though it is possible to perform such a treatment in conventional TEM and STEM, the signal to noise ratio of the spectrum makes changes in fine structure difficult to observe in any sample other than ideal anisotropic specimens such as graphite. By using the Z-contrast image to position the probe, spectra from different sites within the unit cell can be obtained with the collection conditions selected to promote transitions of a certain symmetry. This would reduce the background intensity from transitions with different symmetry and enable spectra to be obtained with comparable quality to dedicated spectrometers but, provided sufficient localization is maintained, with a spatial resolution that is far superior.

The recent development of VG 300 kV dedicated STEM, with its 1.4 \AA probe size, presents the means of achieving even higher spatial resolution in the future. From the classical impact parameter argument, we would expect the spatial resolution of the energy loss spectrum to decrease with increasing acceleration voltage. However, as the voltage is increased, the decrease in probe size proceeds at a faster rate than the increase in impact parameter, causing an improvement in the resolution of the energy loss spectrum. This is demonstrated in Fig. 6, where the expected resolution of both the image and the energy loss spectrum is shown for a

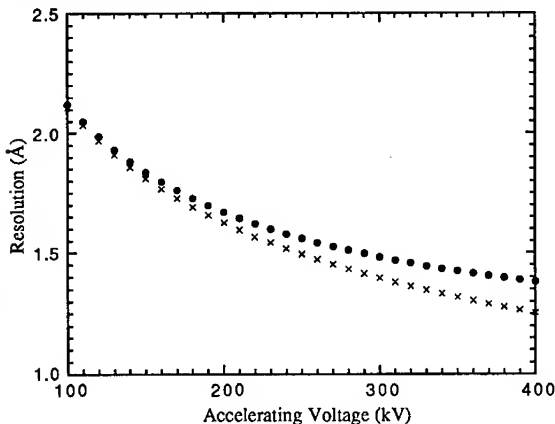


Figure 6. The predicted spatial resolution for the image (x) and the energy loss spectrum (●) improves for higher accelerating potentials, though there is an increased discrepancy between the two.

range of acceleration potentials between 100 kV and 400 kV. The image resolution is calculated for a lens with $C_s = 1.0$ mm [4] and the resolution of the energy loss spectrum is obtained by adding the impact parameter and probe size in quadrature[12]. For a 300 kV STEM the spatial resolution of the energy loss spectrum is expected to be $\sim 1.5\text{\AA}$, which offers the potential to resolve individual atomic columns in a much wider variety of materials, including metals.

This atomic-resolution chemical analysis capability offers the opportunity to address many of the long standing problems in materials science. For example, locating the impurities at dislocation cores would aid the understanding of how alloying elements improved the strength of high-temperature materials, how dopant segregation controls the electronic properties of semiconductor nanostructures, and how diffusion along grain boundaries causes grain growth and brittleness. Furthermore it offers the possibility of mapping a materials electronic structure at atomic resolution, with direct correlation to the atomic structure, linking electronic properties such as local Schottky barrier heights or the density of superconducting charge carriers to the local atomic structure.

ACKNOWLEDGMENTS

We would like to thank D. McMullan and the staff of the MP group at the Cavendish Laboratory for helping design, build and test the EELS system; S. Mantl for supplying the sample; and T. C. Estes, J. T. Luck and S. L. Carney for technical assistance. This research was sponsored by the Division of Materials Sciences, US Department of Energy, under contract No. DE-AC05-84OR21400 with Martin Marietta Energy Systems, Inc., and supported in part by an appointment to the Oak Ridge National Laboratory Postdoctoral Research Program administered by the Oak Ridge Institute for Science and Education.

REFERENCES

1. Pennycook, S. J. and Boatner, L. A., *Nature* **336**, 565 (1988)
2. Crewe, A. V., Wall, J. and Langmore, J., *Science* **168**, 1338 (1970)
3. Browning, N. D., Chisholm, M. F. and Pennycook, S. J., *Nature* **366**, 143 (1993)
4. Pennycook, S. J. and Jesson, D. E., *Ultramicroscopy* **37**, 14 (1991), *Acta Metall Mater* **40**, (1992), S149-159
5. Jesson, D. E and Pennycook, S. J., *51st Annual Proc Micrs Soc America* , eds G. W. Bailey and C. L. Rieder, San Francisco Press, San Francisco, 978 (1993)
6. Fertig, J. & Rose, H., *Optik* **59**, 407 (1981)
7. Loane, R. F., Xu, P. and Silcox J, *Ultramicroscopy* **40**, 121 (1992)
8. Loane, R. F., Kirkland, E. J. and Silcox J, *Acta Cryst A* **44**, 912 (1988)
9. Batson, P. E., *Ultramicroscopy* , **47**, 133 (1992)
10. Schüppen, A., Mantl, S., Vescan, L., Woiwod, S., Jebasinski, R. and Lüth, H, *Materials Science and Engineering B* **12**, 157 (1992)
11. Chisholm, M. F., Jesson, D. E, Pennycook, S. J. & Mantl, S., in press *Appl. Phys. Lett*
12. Browning, N. D. and Pennycook, S. J. *Microbeam Analysis* **2**, 81 (1993)
13. De Crescenzi, M., Derrien, J., Chainet, E. and Orumchian, K., *Phys. Rev. B* **39**, 5520 (1989)
14. Batson, P. E., *Phys. Rev. B* **44**, 5556-5561 (1991)
15. Browning N. D., Chisholm, M. F., Pennycook, S. J., Norton, D. P. and Lowndes, D. H., *Physica C* **212**, 185(1993)
16. Browning, N. D., Yuan, J. and Brown, L. M, *Ultramicroscopy* **38**, 291 (1991), *Philosophical Magazine A* **67**, 261(1993)

NANOANALYTICAL CHARACTERIZATION OF GRANULAR Ag-Fe FILMS WITH GIANT MAGNETORESISTANCE

J. LIU*, Z. G. LI**, H. WAN#, A. TSOUKATOS# AND G. C. HADJIPANAYIS#

* Center for Solid State Science, Arizona State University, Tempe, AZ 85287

** Du Pont Company., P. O. Box 80356, Wilmington, DE 19880

Department of Physics and Astronomy, University of Delaware, Newark, DE 19716

ABSTRACT

Dedicated scanning transmission electron microscopy and associated techniques were used to extract microstructural and compositional information about granular Ag-Fe magnetic films produced by sputtering. Nanometer-resolution compositional analysis by energy dispersive X-ray spectroscopy (EDS), showed that Ag-Fe granular films consist of two separate phases. It has been found that nanometer size Fe particles are separated by small as well as large Ag particles. Nanodiffraction patterns showed that a large proportion of small Ag particles have an icosahedral shape and that the Fe particles are highly disordered. The nanostructure of the Ag-Fe system and its relation to the giant magnetoresistance of granular films are discussed.

INTRODUCTION

The recent demonstration of giant magnetoresistance (GMR) in granular magnetic films has stimulated intense research activity [1-8]. The GMR of granular films was found to depend strongly on the chemical composition and the size distribution of ferromagnetic particles in the film. It has also been proposed that the magnetoresistance in granular films originates primarily from the spin-dependent scattering at the interfaces, similar to that for multilayered structures [8]. The GMR models in granular films, however, have not been well-established due to the lack of microstructural information about the fabricated magnetic films.

GMR and its evolution in granular Fe_xAg_{100-x} system have been recently investigated [3-6]. The GMR is found to be very sensitive to the Fe volume fraction and it becomes negligible in both the Fe-poor and Fe-rich regions of the system. The maximum GMR is achieved in the Fe volume fraction range of 10%-25%.

The structure and phases of Ag-Fe granular films, fabricated by sputtering technique, have been previously studied by X-ray and electron diffraction and transmission electron microscopy (TEM) [3,4]. It has been found that only one type of crystalline phase exists in the as-deposited Ag-Fe granular films. TEM images of Ag-Fe magnetic films showed the existence of nanometer size grains. But direct observation of phase separation in as-deposited Ag-Fe granular magnetic films has not been reported. In the work presented here we used nanometer resolution analytical electron microscopy techniques to investigate the microstructure of granular Ag-Fe magnetic films.

EXPERIMENTAL PROCEDURES

Details of the preparation of magnetic Fe_xAg_{100-x} films by a tandem sputtering method are described in a previous publication [9]. Thin films with thickness varying from 3 to 20 nm were deposited onto carbon coated copper grids with or without a

SiN coating layer. The magnetic properties of the fabricated Fe_xAg_{100-x} system have been reported elsewhere [4,5]. High-angle annular dark-field (HAADF) imaging technique was used to identify Ag/Fe particles and to examine the compositional variations in granular Ag-Fe films because of its high sensitivity to the atomic number of the scatters [10]. HAADF images were obtained on a high resolution scanning transmission electron microscopy (STEM) instrument (100 kV), VG HB-501, with an image resolution ~ 0.5 nm. EDS spectra were acquired with a windowless energy dispersive X-ray spectrometer. Nanodiffraction patterns were recorded on a video tape and played back frame by frame for photographic reproduction and digital analysis. The incident probe used for EDS analysis and nanodiffraction was approximately 1 nm in diameter. All the HAADF images were acquired digitally. Particle analysis was performed on digitally stored HAADF images with a Semper 6+ software.

RESULTS AND DISCUSSION

Nanoanalysis of $Fe_{25}Ag_{75}$ Granular Film

Figures 1a-1c show a series of HAADF images of an as-deposited $Fe_{25}Ag_{75}$ sample with increasing magnification. Figure 1d shows another HAADF image obtained from a different area of the same sample. The HAADF images reveal three levels of image contrast: bright particles, gray patches and dark areas. In order to identify the different phases present in the $Fe_{25}Ag_{75}$ granular film EDS spectra were obtained from different areas with a nanometer size probe. Figure 2a shows a EDS spectrum obtained from a bright particle indicated by B in Figure 1c. This spectrum shows that the bright particle is pure Ag. It has been found by EDS point analysis that Ag particles have distinct bright contrast in HAADF images. Silver particles as small as 1 nm in diameter were formed during the fabrication process.

Figure 2b shows a EDS spectrum obtained from the gray area in the HAADF image (indicated by G in Figure 1c). Based on this spectrum and many other EDS spectra we concluded that the granular features with gray contrast in HAADF images represent Fe clusters. The dark areas in the HAADF images represent areas of carbon film substrate.

The HAADF images and the EDS spectra clearly show that Ag and Fe are separated from each other and that uniform Ag-Fe alloy does not exist in the as-deposited granular Ag-Fe films. The Ag particles have large and small sizes and can be easily recognized in HAADF images. The clustering of small Fe particles makes it difficult to determine their sizes. However, by reducing the inner collection angle of the annular dark-field (ADF) detector it is possible to observe small Fe particles by diffraction contrast. Figure 3 shows a low-angle ADF image of a patch of Fe film revealing small Fe particles with bright contrast. The sizes of the small Fe particles are approximately 1 nm in diameter.

Ag-Fe thin films with a SiN protection layer were also examined and quite similar results were obtained. Thicker granular films were investigated by X-ray diffraction, TEM and HAADF techniques. For very thick films many Ag and Fe particles superpose in electron microscopy images. Thus, it is not possible to analyze the individual particles by EDS technique. X-ray diffraction data, however, showed that the main structural characteristics of thick and thin films are quite similar.

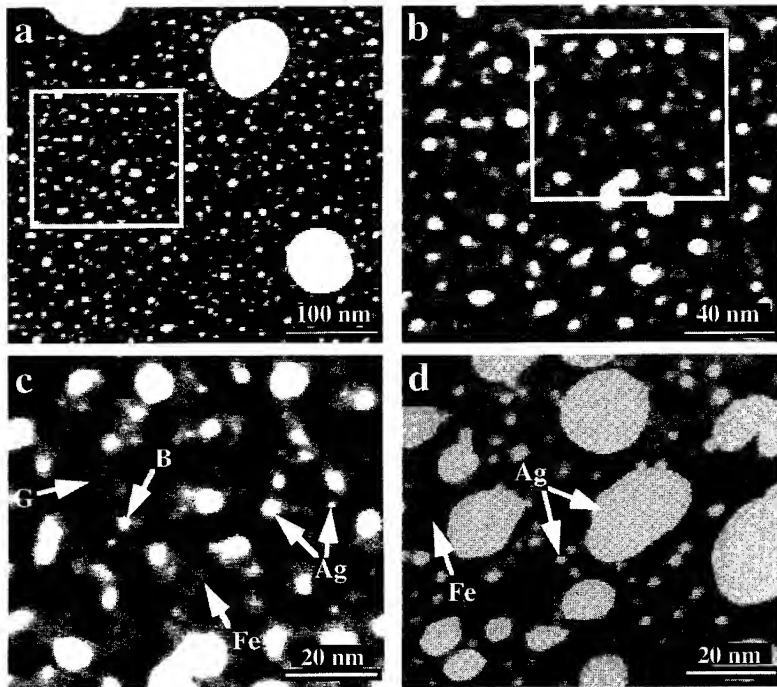


Figure 1. HAADF images of $\text{Fe}_{25}\text{Ag}_{75}$ granular magnetic film revealing Ag and Fe particles.

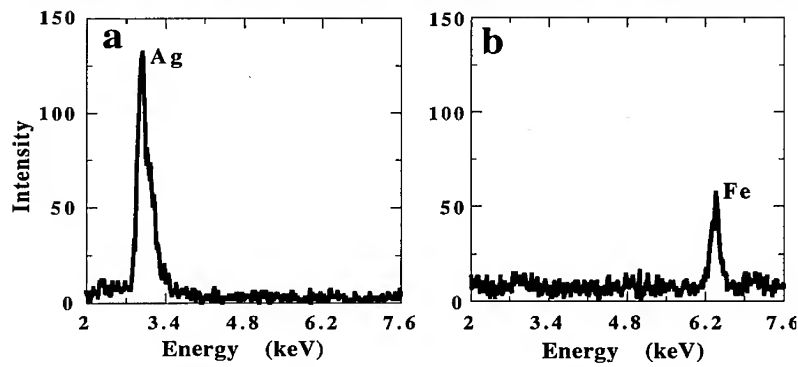


Figure 2. EDS spectra obtained from (a) bright particles and (b) gray areas shown in Figure 1.

Particle Size Distribution

The size and spatial distribution of ferromagnetic Fe particles plays an important role in determining the GMR of the Ag-Fe granular films since the GMR is primarily caused by spin-dependent scattering at the interfaces between ferromagnetic

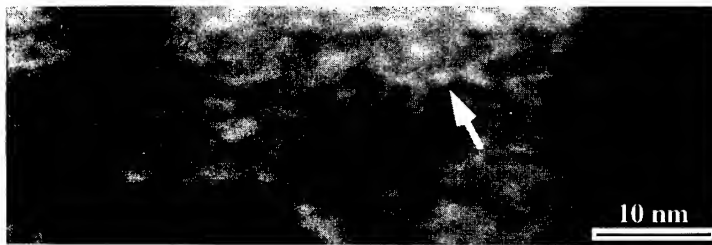


Figure 3. Low-angle ADF image of $\text{Fe}_{25}\text{Ag}_{75}$ granular film showing small Fe particles.

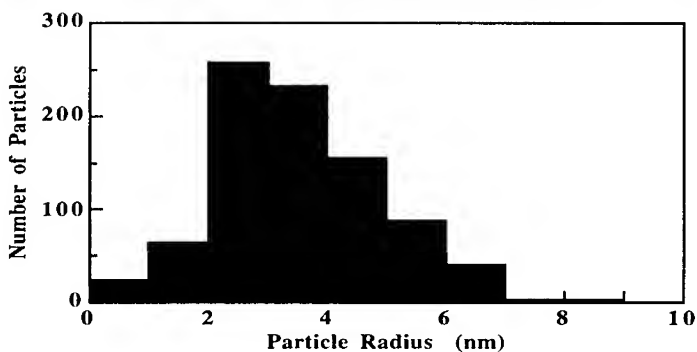


Figure 4. Size distribution of Ag particles in as-prepared $\text{Fe}_{25}\text{Ag}_{75}$ granular magnetic film.

particles and the non-ferromagnetic phases. HAADF images of granular $\text{Fe}_{25}\text{Ag}_{75}$ films showed that the Ag particles are clearly separated from each other. The size distribution of these Ag particles is shown in Figure 4. A total of 583 Ag particles were analyzed. Silver particles have a broad size distribution with a mean particle size approximately 6 nm in diameter.

The Fe particles were clustered to form patches of Fe film, which makes it impossible to analyze each particle to give a statistically meaningful particle size distribution. Based on Figure 3 and other low-angle ADF images we deduced that the Fe particles have a narrow size distribution with an average particle size approximately 1 nm in diameter.

The GMR of granular magnetic films depends on the size distribution and the interparticle distances of the ferromagnetic particles. With increasing Fe content large Fe particles may be formed and multiple domains within a single Fe particle may occur which will reduce the GMR effect. With too small Fe content the interparticle distance of Fe particles becomes large which could also reduce the GMR effect. Uniform mixing of nanometer size Ag and Fe particles could be the ideal situation for highest GMR values providing that the GMR is predominantly determined by spin-dependent interphase interface scattering.

The broad size distribution of Ag particles and the clustering of small Fe particles could have several effects on the GMR of the system. The formation of large Ag particles may adversely affect the GMR and should be avoided by optimizing

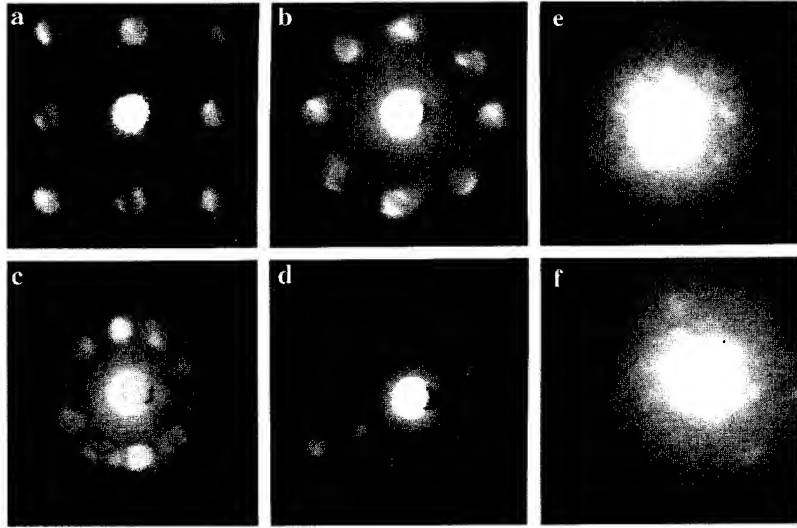


Figure 5. Coherent electron nanodiffraction patterns from Ag and Fe Particles: (a) from a large fcc Ag particle; (b) from a rotationally twinned Ag particle; (c) and (d) from icosahedral Ag particles; (e) from highly disordered Fe particles and (f) from a Fe crystallite.

the fabrication conditions. The aggregation of small Fe particles reduces the total portion of scattering at interphase interfaces. The surface area to volume ratio of the clustered Fe particles is still high as compared to that of large Fe particles. Further work is needed to evaluate the effect of Fe clustering on the GMR of the system.

Nanodiffraction From Ag And Fe Particles

Coherent electron nanodiffraction from small particles contain information about the particle size, shape, structure and defects. Nanodiffraction technique has been widely used for identifying crystallographic structures of small particles.

Nanodiffraction patterns from Ag particles showed a variety of effects illustrated in Figures 5a-5d. In many cases the spot patterns from larger particles can be attributed to single crystals of fcc Ag as shown in Figure 5a. Many nanodiffraction patterns showed spots from several crystallites in twinned orientations. For example, Figure 5b shows a nanodiffraction pattern from a Ag particle, with a pseudo-eightfold symmetry. This pattern can be attributed to a small Ag particle containing 45° rotational twins with the incident beam along the [001] axis.

The most interesting result obtained by analyzing nanodiffraction patterns is that a large proportion of the small Ag particles have an icosahedral shape. Figures 5c and 5d show nanodiffraction patterns from such Ag particles, obtained with the incident beam along the five-fold and three-fold symmetry axis, respectively. It has been found that nanometer size Ag particles tend to have a shape of icosahedron [11]. The icosahedral arrangement of atoms is not a fcc packing but it is the stable form for the smallest sizes of fcc metals and provides the nuclei from which larger particles grow. With the increase in particle size a transition from icosahedral packing to fcc

packing will occur and thus large Ag particles have a regular fcc structure.

The X-ray diffraction results showed that the (111)Ag peak shifts slightly to higher angles with increasing Fe. But the shift is so small that it cannot be directly related to a Ag-Fe alloy with similar composition [3-5]. This shift in peak position with the change of Fe composition could be related to the formation of icosahedral Ag particles. With increasing Fe composition the Ag particles become smaller and thus more icosahedral Ag particles are formed in the Ag-Fe granular film.

Nanodiffraction patterns obtained from Fe particles showed considerable spottiness, as shown in Figure 5e, reflecting the extent of local positional correlation of the atoms. In very rare occasions a crystalline diffraction pattern can be obtained from small Fe particles as shown in Figure 5f. These Fe crystallites are very unstable under electron beam irradiation. The Fe particles, in general, are highly disordered and this may be the main reason why x-ray and selected area electron diffraction patterns show only one type of crystalline phase present in the Ag-Fe granular films.

SUMMARY

Two separate phases in the as-deposited granular Ag-Fe thin films were observed using high spatial resolution analytical electron microscopy techniques. The highly disordered Fe particles are very small, approximately 1 nm in size, and they are separated by large and small crystalline Ag particles. Nanometer size Ag particles tend to have an icosahedral shape, which could be responsible for the observed (111)Ag peak shift to higher angles in the X-ray diffraction patterns. The clustering of nanometer size Fe particles may affect the GMR of the system in a complicated way. The combination of HAADF imaging with EDS analysis has proved very useful for extracting nanostructural and compositional information in heterogeneous samples such as granular magnetic thin films.

ACKNOWLEDGMENTS

This work was supported by Shell Development Company (JLIU) and NSF DMR-8917028 and was conducted at Center for HREM at Arizona State University, supported by the National Science Foundation under grant No. DMR-9115680.

REFERENCES

- [1] A.E. Berkowitz, J.R. Mitchell, M.J. Carey, A.P. Young, S. Zhang, F.E. Spada, F.T. Parker, A. Hutton and G. Thomas, *Phys. Rev. Lett.* **68**, 3745 (1992).
- [2] J. Q. Xiao, J. S. Jiang and C. L. Chien, *Phys. Rev. Lett.* **68**, 3749 (1992).
- [3] G. Xiao, J. Q. Wang and P. Xiong, *Appl. Phys. Lett.* **62**, 420 (1993).
- [4] A. Tsoukatos, H. Wan, G.C. Hadjipanayis, K.M. Unruh and Z.G. Li, *J. Appl. Phys.* **73**, 5509 (1993).
- [5] H. Wan, A. Tsoukatos, G.C. Hadjipanayis, Z.G. Li, J. Liu, *Phys. Rev. B.* (Dec., 1993).
- [6] Z.G. Li, H. Wan, J. Liu, A. Tsoukatos, G.C. Hadjipanayis and L. Liang, *Appl. Phys. Lett.* (Dec., 1993).
- [7] M.L. Watson, J.A. Banard, S. Hossain, M.R. Parker, *J. Appl. Phys.* **73**, 5506 (1993).
- [8] S. Zhang and P. M. Levy, *J. Appl. Phys.* **73**, 5315 (1993).
- [9] A. Tsoukatos, H. Wan, G.C. Hadjipanayis, Z.G. Li, *Appl. Phys. Lett.* **61**, 3059 (1992).
- [10] J. Liu and J. M. Cowley, *Ultramicroscopy* **34**, 119 (1990); *ibid.*, **37**, 50 (1991).
- [11] J. Liu, M. Pan and G. E. Spinnler, *Proc. 51st MSA Meeting* (1993) pp. 1058-1059.

AEM INVESTIGATION OF TETRAHEDRALLY COORDINATED Ti^{4+} IN NICKEL-TITANATE SPINEL

IAN M. ANDERSON*,†, JIM BENTLEY*, AND C. BARRY CARTER†

*Oak Ridge National Laboratory, Metals and Ceramics Division, P.O. Box 2008, M.S. 6376, Oak Ridge, TN 37831-6376; †University of Minnesota, Department of Chemical Engineering and Materials Science, 421 Washington Ave. S.E., Minneapolis, MN 55455-0132

ABSTRACT

The stoichiometry and site distribution of metastable nickel-titanate spinel has been studied with AEM. The results of EDXS and EELS agree that the metastable spinel is nonstoichiometric and titanium-deficient relative to its hypothetical endmember composition, " Ni_2TiO_4 ". The titanium deficiency has been determined by EELS to be $\Delta = 0.025 \pm 0.005$. Channeling-enhanced microanalysis and ELNES studies indicate that the Ti^{4+} and Ni^{2+} cations are in tetrahedral and octahedral coordination, respectively, so that the metastable spinel has the normal cation distribution: $Ti_{1-\Delta}[Ni_{2(1+\Delta)}]O_4$. This result is consistent with neutron powder-diffraction studies and SiO_2 -solubility measurements of similar equilibrated and quenched spinel-containing specimens. Metastable nickel-titanate spinel therefore contrasts with stable stoichiometric spinels which tend to the inverse cation distribution, $Me[MeTi]O_4$.

INTRODUCTION

As the characteristic scale of the microstructures of engineering materials and devices approaches the nanometer level,¹ the characterization of these structures becomes increasingly challenging. Analytical electron microscopy (AEM) offers a variety of characterization techniques for the structural and chemical analysis of materials with nanometer-scale resolution.² Among chemical analysis techniques, X-ray microanalysis (or energy-dispersive X-ray spectrometry, EDXS) and electron energy loss spectroscopy (EELS) can be used to extract not only quantitative local compositions, but also local site distributions and elemental oxidation states.^{3,4}

The spinel-structured phase in the system $NiO-TiO_2$ is a model material for chemical analysis with the high spatial resolution of AEM. The equilibrium spinel phase, $Ni_{2(1+x)}Ti_{1-x}O_4$, exists only above 1425°C and with a large cation excess.^{5,6} During quenching, the nonstoichiometric phase decomposes into a more stoichiometric spinel, $Ni_{2(1+\Delta)}Ti_{1-\Delta}O_4$, and a periclase-structured phase, of nominal composition NiO . The quenched-in metastable spinel always coexists with nanometer-scale periclase-structured inclusions.⁷ The high spatial resolution of AEM is therefore necessary in order to characterize the metastable quenched-in spinel phase directly. Stable stoichiometric titanate spinels tend to the inverse cation distribution, $Me_{(tet)}[MeTi]_{(oct)}O_4$, with $Me = Mg, Mn, Fe, Co$, and Zn . Neutron powder diffraction⁸ and SiO_2 -solubility studies⁹ indicate that in the metastable nickel-titanate spinel the Ti^{4+} cation is tetrahedrally coordinated; the site distribution is therefore apparently $Ti_{1-\Delta}[Ni_{2(1+\Delta)}]O_4$. However, these earlier studies did not have sufficient spatial resolution to isolate the spinel phase in the nanometer-scale microstructure nor did they provide spectroscopic analyses of the metastable spinel.

Tetrahedral coordination of Ti^{4+} in crystalline oxides is rare. Nickel-titanate spinel is the only known nearly close-packed oxide with the Ti^{4+} cation in tetrahedral coordination. A rare stable stoichiometric compound with tetrahedral Ti^{4+} is Ba_2TiO_4 .¹⁰ However, this latter compound is of lower symmetry than spinel and the four oxygen anions surrounding the Ti^{4+} cation do not form a regular tetrahedron.¹¹ Titanium can be made to coordinate tetrahedrally in amorphous oxides. The strong octahedral site preference of the Ti^{4+} cation is exploited technologically in the production of glass-ceramics¹² in which the cation, initially made to assume tetrahedral coordination as a network modifier in the glass, achieves octahedral coordination by precipitating in the form of TiO_2 crystallites; these tiny crystals then serve as sites for the controlled nucleation and growth of the fine ceramic grains from the glass. A nearly close-packed crystalline oxide with tetrahedral Ti^{4+} may also exhibit novel properties that can be exploited technologically.

EXPERIMENTAL PROCEDURE

Powders with the composition NiO-20wt.% TiO₂ were equilibrated in air at 1488°C for 142 h and quenched in water, as has been detailed elsewhere.⁶ The quenched specimens were subsequently annealed in air at 1200°C for 30 minutes and air quenched. The loosely sintered specimens were embedded in epoxy¹³ and then cut into 200 µm-thick slices with a low-speed diamond saw. Thin-foil specimens suitable for AEM investigation were prepared with standard mechanical techniques: embedded slices were cut into 3 mm disks with an ultrasonic drill; these disks were lapped to ~100 µm, dimpled to ~20 µm, and ion-milled to perforation. The final stage of ion-milling was performed at a relatively low energy (3 keV) and incident angle (12°). A thin coat of carbon was applied in order to mitigate charging effects.

The specimens were examined at ORNL with a Philips EM400T AEM equipped with a field-emission electron gun (FEG) and operated at 100 kV. X-ray microanalysis and EELS were performed with an EDAX 9100 energy-dispersive X-ray spectrometer and a Gatan 666 parallel-collection electron energy-loss spectrometer, respectively. The specimens were cooled to -130°C during spectrum acquisition using a Gatan double-tilt cooling holder. For X-ray microanalysis, the majority of the self-supporting disc specimen was masked by a gold washer with a 0.5 mm × 2.0 mm slot in order to minimize secondary excitation effects.

RESULTS

Figure 1 shows EDX spectra characteristic of the three different phases composing the specimen. Spectra characteristic of the periclase-, spinel-, and corundum-structured phases, of nominal compositions NiO, Ni₂TiO₄, and NiTiO₃, respectively, are shown in Fig. 1a-c. The spectrum of the periclase-structured phase, Fig. 1a, is also shown at 20× magnification in order to show the Ti K_α peak. (The two other small peaks visible in this enlargement are the Ni K_α escape peak and the Fe K_α peak, the latter probably due to secondary excitation of the objective pole-piece.) The sum of the number of counts in the K_α peaks of titanium and nickel exceeds 5×10⁵ for all three spectra. The ratio of the intensities of the Ti K_α to the Ni K_α characteristic peaks in Fig. 1 are:

$$\left(\frac{N_{Ti}}{N_{Ni}}\right)_{(per)} = 0.0050; \left(\frac{N_{Ti}}{N_{Ni}}\right)_{(sp)} = 0.463; \left(\frac{N_{Ti}}{N_{Ni}}\right)_{(cor)} = 1.055. \quad (1)$$

so that, in particular,

$$\left(\frac{N_{Ti}}{N_{Ni}}\right)_{(cor)} / \left(\frac{N_{Ti}}{N_{Ni}}\right)_{(sp)} = 2.28. \quad (2)$$

EEL spectra of the spinel- and corundum-structured phases are shown in Figure 2. These spectra were acquired with a detector dispersion of ~1 eV per channel and show the Ti L_{2,3}, O K, and Ni L_{2,3} edges after background subtraction. The two spectra are normalized such that the areas beneath their Ti edges are identical. The number of counts above the L-edges of the transition-metal ions were measured for two sets of spinel and corundum spectra with several different background-subtraction windows. In all spectra, the number of counts measured above the Ni L edges was ~5×10⁴; the number of counts above the Ti L edge exceeded 1×10⁵. Based on these measurements:

$$\left(\frac{N_{Ti}}{N_{Ni}}\right)_{(cor)} / \left(\frac{N_{Ti}}{N_{Ni}}\right)_{(sp)} = 2.10 \pm 0.02. \quad (3)$$

Figure 3 shows EDX spectra of the spinel-structured phases (a) Ni_{2(1+Δ)}Ti_{1-Δ}O₄ (NT) and (b) ZnNiTiO₄ (ZNT) with the specimens oriented for strong dynamical diffraction conditions at a {200} systematic row. Two spectra are superimposed in each part of the figure: (1) the shaded spectrum was recorded with the specimen oriented at the Laue (symmetric) orientation of the systematic row, whereas (2) the line spectrum (which appears black-on-white and white-on-black) was recorded near the Bragg orientation of the first-order allowed reflection, {400}, but with a positive excitation error. The relative sizes of the characteristic peaks in the spectra can be quantified with the ratio⁴ R(X/Y) = (N_X⁽¹⁾/N_Y⁽¹⁾) / (N_X⁽²⁾/N_Y⁽²⁾), where N_X⁽ⁿ⁾ is the number of

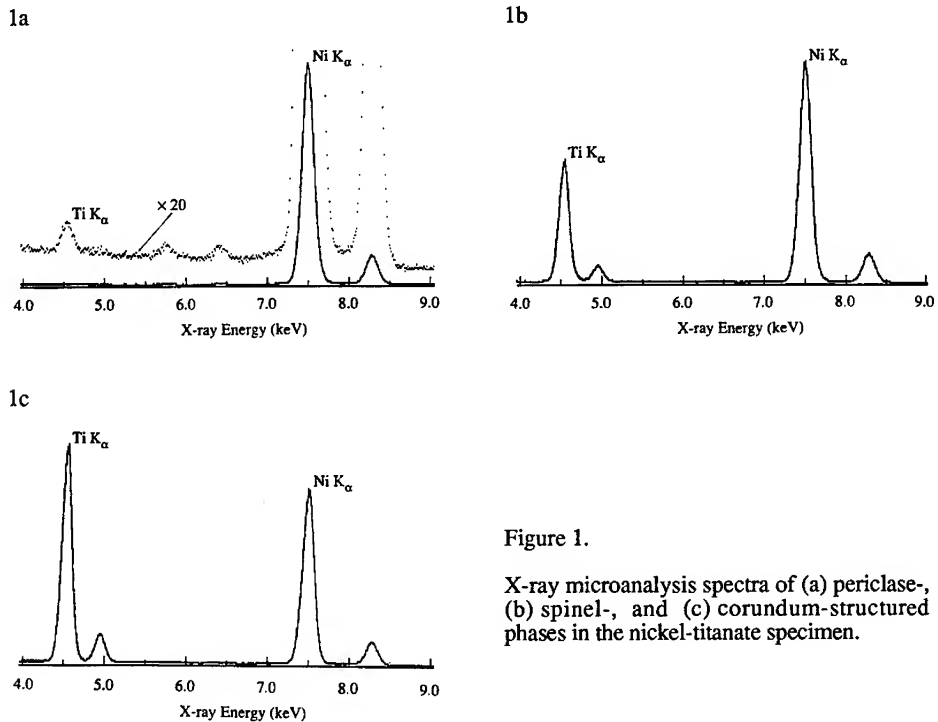


Figure 1.
X-ray microanalysis spectra of (a) periclase-,
(b) spinel-, and (c) corundum-structured
phases in the nickel-titanate specimen.

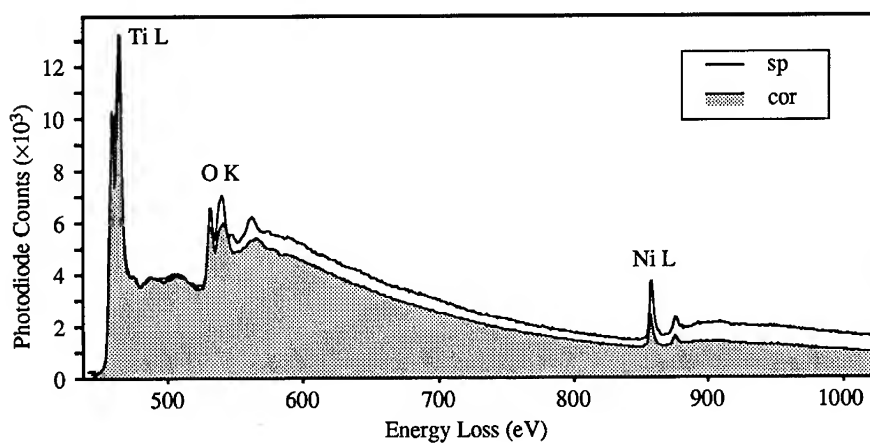


Figure 2. EEL spectra of the spinel- and corundum-structured phases. These spectra were acquired with a detector dispersion of ~ 1 eV per channel and are shown after background subtraction. The scales of the two spectra were adjusted such that the areas beneath the Ti L edges are equal.

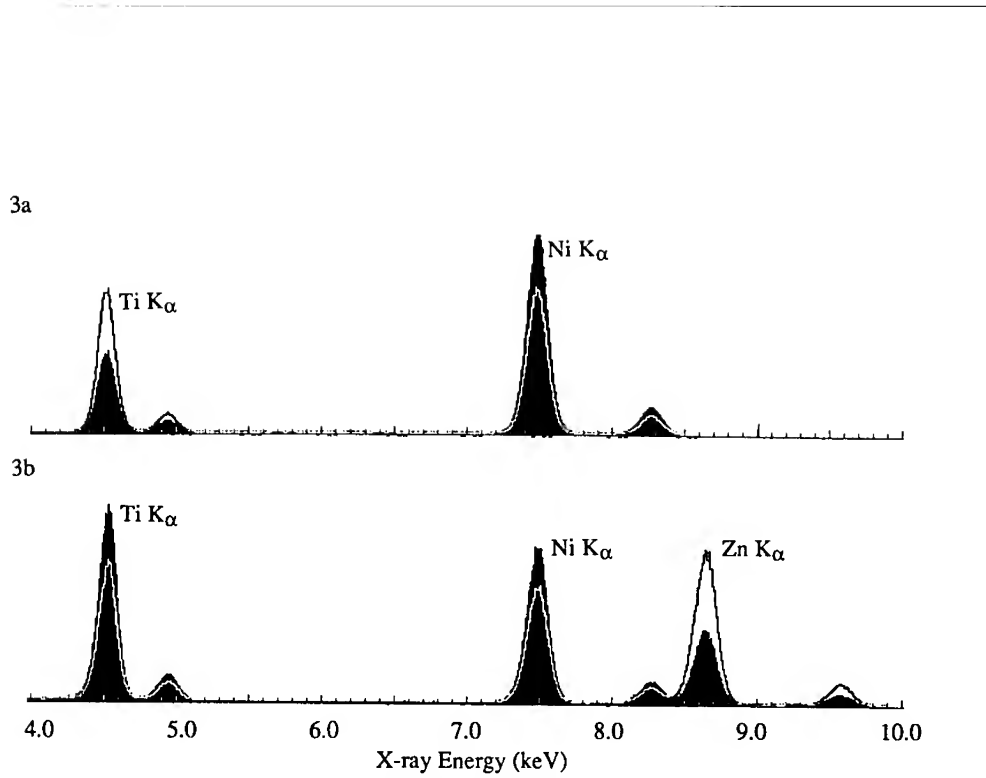


Figure 3. X-ray microanalysis spectra of (a) nickel-titanate spinel and (b) zinc-nickel-titanate-spinel, acquired under planar channeling conditions. The shaded spectra were acquired with the specimen at the Laue (symmetric) orientation; the superimposed line spectra were acquired with the specimen near the Bragg condition for the (400) reflection with a slightly positive excitation error.

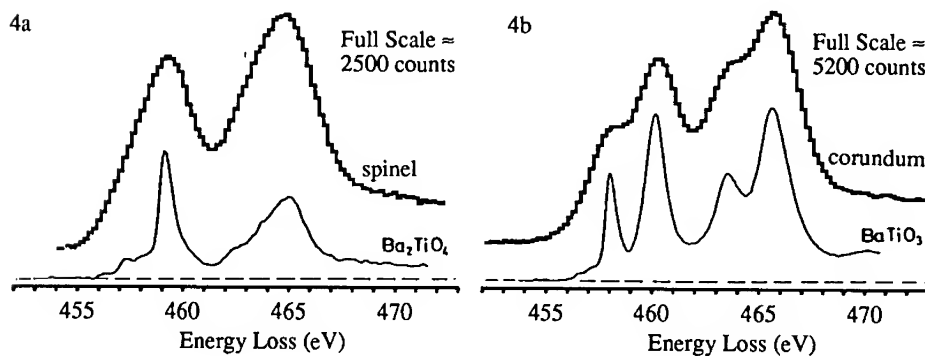


Figure 4. EEL spectra showing the near-edge fine structure of the Ti L_{2,3} edge of (a) the spinel- and (b) the corundum-structured phase. Inset are spectra reported by Brydson *et al.*¹⁴ for (a) Ba₂TiO₄ and (b) BaTiO₃, respectively.

counts recorded in the K_{α} peak of element X in the n^{th} spectrum. Here, $R_{\text{NT}}(\text{Ni}/\text{Ti}) = 2.50$, $R_{\text{ZNT}}(\text{Ni}/\text{Ti}) = 0.97$, and $R_{\text{ZNT}}(\text{Ni}/\text{Zn}) = 2.79$.

Figure 4 shows EEL spectra of the $\text{Ti L}_{2,3}$ edge of the (a) spinel- and (b) corundum-structured phase, after background subtraction. These spectra were acquired with a detector dispersion of ~ 0.2 eV per channel and show the near-edge fine structure (ELNES) of the $\text{Ti L}_{2,3}$ edges for these two phases. Comparable spectra of Brydson *et al.*¹⁴ for (a) Ba_2TiO_4 and (b) BaTiO_3 are inset.

DISCUSSION

The ratios calculated in equations (2) and (3) should reflect the relative nickel to titanium concentrations in the spinel- and corundum-structured phases. X-ray microanalysis yields a value which is $\sim 10\%$ higher than that yielded by EELS. The measured intensities of the characteristic peaks in the spectra shown in Fig. 1 are, however, expected to be representative of those excited in the primary excitation volume during analysis; corrections for absorption and secondary excitation effects should be modest. Since spectra are acquired in portions of the specimen such that only one phase is present through the thickness of the foil, the maximum thickness of the specimen should be ~ 100 nm. Characteristic absorption lengths of Ni K_{α} and Ti K_{α} X rays in $\text{NiO}-20\text{wt.\% TiO}_2$ are $(\mu^{\text{Ni}})^{-1} \approx 97$ μm and $(\mu^{\text{Ti}})^{-1} \approx 39$ μm . The absorption correction¹⁵ for these two X-ray lines should therefore be $\sim 0.15\%$. The secondary fluorescence correction is quite modest for masked dimpled and ion-milled specimens,^{7,16} even for strongly fluorescing specimens. Given that Ni K_{α} fluoresces Ti K X rays relatively weakly, the fluoresced intensity of Ti K_{α} is expected to be $\sim 0.1\%$ of the Ni K_{α} intensity and therefore negligible. This expectation is supported by the spectrum of the periclase-structured phase (Fig. 1a): the measured Ti K_{α} intensity is $\sim 0.5\%$ of the Ni K_{α} intensity; the contributions of *all* secondary excitation effects cannot exceed this value. It is possible that beam broadening may be responsible for the higher nickel-to-titanium ratio of the spinel for X-ray microanalysis; however, the intensity ratio of the characteristic peaks was found to be consistent among a number of spectra. Most likely, channeling effects are responsible for the higher nickel-to-titanium ratio in the spinel measured by X-ray microanalysis: as shown by Fig. 3a, a variation in the intensity ratio by a factor of 2.5 can be achieved under extreme diffraction¹⁷ conditions; a residual 10% effect is therefore conceivable and consistent with other studies.¹⁷ EELS is less susceptible to the effects of channeling because those electrons which contribute to the effect tend to be scattered through angles larger than that subtended by the collection aperture.

Assuming that the corundum-structured phase is stoichiometric NiTiO_3 , the nonstoichiometry of nickel-titanate spinel, $\text{Ni}_{2(1+\Delta)}\text{Ti}_{1-\Delta}\text{O}_4$, consistent with equation (3) is:

$$\Delta = 0.025 \pm 0.005, \quad (4)$$

a deficit of one of forty titanium cations (one in every fifth conventional unit cell) and with an average separation of ~ 14 \AA . Residual nonstoichiometry in the spinel would be accommodated by point defects, which should introduce either diffuse reflections or superstructure reflections in the diffraction patterns of the spinel, neither of which are observed. However, the amount of diffuse scattering produced by a point defect concentration as dilute as that suggested by equation (4) may not be pronounced enough to be detected. If the corundum-structured phase is not stoichiometric, it would be expected to be NiO -rich; the value of Δ would then be greater than 2.5%. However, any reasonable amount of nonstoichiometry falls well within the standard deviation in equation (4).

The values $R_{\text{ZNT}}(\text{Ni}/\text{Ti}) = 0.97$ and $R_{\text{ZNT}}(\text{Ni}/\text{Zn}) = 2.79$ show that the site distribution of zinc-nickel-titanate spinel is $\text{Zn}[\text{NiTi}]\text{O}_4$: an R-value near unity indicates a similar site distribution whereas a value far removed from unity indicates that the cations occupy different lattice sites. ZnNiTiO_4 is a good standard for estimating the size of the channeling effect since Zn^{2+} has a strong tetrahedral site-preference whereas the Ni^{2+} and Ti^{4+} cations have strong octahedral site-preferences. The channeling-enhanced microanalysis of nickel-titanate spinel therefore strongly supports the normal cation distribution, $\text{Ti}_{1-\Delta}[\text{Ni}_{2(1+\Delta)}]\text{O}_4$, since $R_{\text{NT}}(\text{Ni}/\text{Ti}) = 2.50$ is of the order of $R_{\text{ZNT}}(\text{Ni}/\text{Zn})$. The results of ELNES also substantiate the normal site distribution for metastable nickel-titanate spinel. The spectral features of the spinel- and corundum-structured phases in Fig. 4 are in good agreement with the superimposed spectra reported¹⁴ for Ba_2TiO_4 and BaTiO_3 , which feature tetrahedrally and octahedrally coordinated Ti^{4+} , respectively.

CONCLUSIONS

Metastable nickel-titanate spinel is characterized by the chemical formula, $Ti_{1-\Delta}[Ni_{2(1+\Delta)}]O_4$. The phase is titanium-deficient relative to its hypothetical endmember composition, "Ni₂TiO₄", and has the normal cation distribution. The degree of nonstoichiometry has been determined by EELS to be $\Delta = 0.025 \pm 0.005$. X-ray microanalysis, which yields a significantly larger nickel-to-titanium cation ratio in the spinel, was deemed less reliable than EELS. The probable reason for the inaccuracy is the large channeling effect for $Ti_{1-\Delta}[Ni_{2(1+\Delta)}]O_4$.

The high spatial resolution of the AEM was necessary to determine the stoichiometry and the site distribution of the spinel directly because of the nanometer-scale distribution of the periclase-structured NiO phase within the spinel. Larger regions of single-phase Ni_{2(1+\Delta)}Ti_{1-\Delta}O₄ might be stabilized in thin-films deposited by a nonequilibrium technique such as sputtering or pulsed-laser deposition (PLD), which can be used¹⁸ to deposit thermodynamically unstable phases given a suitable choice of substrate material. Thin films of Ni_{2(1+\Delta)}Ti_{1-\Delta}O₄ might exhibit unusual properties given the unusual tetrahedral coordination of the Ti⁴⁺ cation in this compound.

ACKNOWLEDGMENTS

This research was supported by the Division of Materials Sciences, U.S. Department of Energy, under contract DE-AC05-84OR21400 with Martin Marietta Energy Systems, Inc. and through the SHaRE Program under contract DE-AC05-76OR00033 with the Oak Ridge Institute of Science and Education; and by the National Science Foundation through grant number DMR-8901218. This research is also supported in part by an appointment to the Oak Ridge National Laboratory Postdoctoral Research Associates Program, which is administered jointly by the Oak Ridge Institute for Science and Education and Oak Ridge National Laboratory.

REFERENCES

1. R. W. Siegel, *Annu. Rev. Mater. Sci.* **21**, 559-578 (1991).
2. *Principles of Analytical Electron Microscopy*, edited by D. C. Joy, A. D. Romig Jr., and J. I. Goldstein (Plenum Press, New York, 1986).
3. O. L. Krivanek, M. M. Disko, J. Taftø, and J. C. H. Spence, *Ultramicrosc.* **9**, 249-254 (1982).
4. J. C. H. Spence and J. Taftø, *J. Microsc.* **130**, 147-154 (1983).
5. W. Laqua, E. W. Schulz, and B. Reuter, *Z. anorgan. allg. Chem.* **433**, 167-180 (1977).
6. A. Muan, *J. Amer. Ceram. Soc.* **75**, 1357-1360 (1992).
7. I. M. Anderson, Ph. D. thesis, Cornell University, 1993.
8. G. A. Lager, T. Armbruster, F. K. Ross, F. J. Rotella, and J. D. Jorgensen, *J. Appl. Cryst.* **14**, 261-264 (1981).
9. N. F. Roberts and A. Muan, *J. Amer. Ceram. Soc.* **75**, 1382-1389 (1992).
10. P. Tarte, *Nature* **191**, 1002-1003 (1961).
11. J. A. Bland, *Acta Cryst.* **14**, 875-881 (1961).
12. W. D. Kingery, H. K. Bowen, and D. R. Uhlmann, *Introduction to Ceramics*, 2nd ed. (John Wiley and Sons, New York, 1976).
13. A. R. Spurr, *J. Ultrastr. Res.* **26**, 31-43 (1969).
14. R. Brydson, H. Sauer, and W. Engel, in *Transmission Electron Energy Loss Spectrometry in Materials Science*, edited by M. M. Disko, C. C. Ahn, and B. Fultz (The Minerals, Metals, and Materials Society, Warrendale, PA, 1992), pp. 131-154.
15. J. I. Goldstein, D. B. Williams, and G. Cliff, in reference (2), pp. 155-217.
16. I. M. Anderson, J. Bentley, and C. B. Carter, in preparation.
17. I. M. Anderson, in *Proceedings of the 50th Annual Meeting of the Electron Microscopy Society of America*, edited by G. W. Bailey, J. Bentley, and J. A. Small (San Francisco Press, San Francisco, CA, 1992), pp. 1240-1241.
18. I. M. Anderson, L. A. Tietz, and C. B. Carter, in *Structure and Properties of Interfaces in Materials*, edited by W. A. T. Clark, U. Dahmen, and C. L. Briant (Mater. Res. Soc. Proc. **238**, Pittsburgh, PA, 1992), pp. 807-814.

QUANTITATIVE X-RAY MICROANALYSIS FOR THE STUDY OF NANOMETER-SCALE PHASES IN THE AEM

IAN M. ANDERSON*,†, JIM BENTLEY*, AND C. BARRY CARTER†

*Oak Ridge National Laboratory, Metals and Ceramics Division, P. O. Box 2008, M. S. 6376, Oak Ridge, TN 37831-6376; †University of Minnesota, Department of Chemical Engineering and Materials Science, 421 Washington Ave. S. E., Minneapolis, MN 55455-0132

ABSTRACT

Secondary excitation can be a large source of inaccuracy in quantitative X-ray microanalysis of inhomogeneous specimens in the AEM. The size of the secondary excitation component in the measured X-ray spectrum is sensitive to the geometry of the thin foil specimen. Secondary excitation has been examined in a self-supporting disc specimen of composition NiO-20 wt.% TiO₂ which has been partially masked by a gold slot washer. The ratio of the intensities of the characteristic K_α peaks of Ti and Ni in X-ray spectra from a periclase-structured phase, of nominal composition NiO, has been measured to be N_{Ti} / N_{Ni} ≈ 0.005. There is no apparent Ti L_{2,3} signal in the corresponding electron energy-loss spectrum. The secondary excitation contribution to the characteristic Ti K_α-peak from all sources can therefore be no larger than 0.5%. It should be possible to reduce this modest level of secondary excitation still further with a better masking arrangement.

INTRODUCTION

For compositional analysis, the principal strength of X-ray microanalysis or energy-dispersive X-ray spectroscopy (EDXS) in the analytical electron microscope (AEM) relative to electron probe microanalysis is its high spatial resolution. However, when the composition of the volume being analyzed is markedly different than the average composition of the specimen, the relative contribution of the extraneous signal from the remainder of the specimen to a characteristic X-ray peak can be significant.¹ This extraneous signal arises from the excitation of characteristic X rays by fast electrons that have been scattered through large angles or by X rays that have been excited in the probed volume.² Especially when a major constituent of the specimen is a minor or dilute constituent of a phase being analyzed, the characteristic X-ray intensity of this element that emanates from locations in the specimen that are remote from the analysis volume can be comparable to that excited in the analysis volume itself.³

The size of the secondary excitation component in the measured X-ray spectrum is sensitive to the geometry of the thin foil specimen. The most effective strategy for minimizing secondary excitation is to restrict the amount of material that can be so excited. To this end, Williams et al.^{4,5} have advocated a specimen-geometry consisting of thin flakes of the material to be analyzed that have been dispersed in low concentrations on a beryllium grid. The thin flake specimen-geometry is suitable for EDXS when all portions of the specimen are equally suitable for examination. However, this specimen geometry is impractical for many microanalysis problems. When only a limited portion of the specimen is of interest, such as when a thin film is analyzed in cross-section, the analyst may have difficulty finding a flake of the specimen containing the area of interest. The thin flake specimen-geometry may also be inappropriate when the position of the region being analyzed must be known relative to a microstructural feature of the specimen; this information may be lost. In such situations, the analyst must rely on a geometry that leaves the specimen intact.

Recently, it has been shown that one type of secondary excitation, secondary fluorescence, is expected to be small for self-supporting disc specimens and for the dimpled and ion-milled specimen in particular.⁶⁻⁸ Basic geometrical considerations indicate that the secondary fluoresced intensity from self-supporting disc specimens should be modest relative to that from specimens with other geometries since the fractional solid angle subtended by the self-supporting disc specimen relative to the thin edge being analyzed is small.

The drawback of the self-supporting disc specimen relative to, for example, a cleaved wedge specimen is that it subtends a large area from the perspective of both the electron-optical column and the EDX spectrometer. A just-perforated specimen presents to the column a 3 mm disc (area $\sim 7 \text{ mm}^2$), whereas a cleaved wedge of thickness 100 μm protruding 0.5 mm from a supporting washer presents a target of area 0.05 mm^2 , more than two orders of magnitude smaller. The large target provided by the disc specimen increases the contribution to the measured spectrum of X rays excited by uncollimated radiation (in the hole count) and potentially by high-angle-scattered electrons when the specimen is tilted with respect to the beam.²

The area of the specimen presented to the electron-optical column and to the EDXS detector can be substantially reduced by partially covering the self-supporting disc specimen with a masking washer. For a specimen with a small perforation, the exposed area of the disc specimen can be easily reduced by a factor of 50. As long as the characteristic X-ray lines of the washer material do not overlap with the X-ray lines characteristic of the analysis volume, the reduction in the area of the specimen exposed to the detector leads to a corresponding reduction in the extraneous contributions to the X-ray lines of interest. Furthermore, it has been shown that the secondary fluorescence contribution to the measured EDX spectrum can be kept to a fraction of a percent if the dimpled and ion-milled specimen is suitably masked with an "X ray opaque" washer having an aperture of a few hundred micrometers diameter.⁸

The purpose of the present paper is to study the level of secondary excitation in the measured EDX spectrum characteristic of the masked dimpled and ion-milled specimen-geometry. A model specimen for this study would have a phase that contains little (or none) of an element that is one of the major constituents of the overall specimen. A specimen of average composition NiO-20 wt.% TiO₂ has been chosen for this purpose. When a specimen of this composition is equilibrated at $\sim 1500^\circ\text{C}$, quenched, and subsequently annealed, periclase-structured regions of $\sim 100 \text{ nm}$ dimension and nominal composition NiO are found throughout the specimen.⁶ These regions provide nanometer-scale volumes of the specimen containing little titanium in a specimen with a large relative titanium concentration.

EXPERIMENTAL PROCEDURE

Powders with the composition NiO-20 wt.% TiO₂ were equilibrated in air at 1488°C for 142 h and quenched in water, as has been detailed elsewhere.⁹ The quenched specimens were subsequently annealed in air at 1200°C for 30 minutes and air quenched. The loosely sintered specimens were embedded in epoxy¹⁰ and then cut into 200 μm -thick slices with a low-speed diamond saw. Thin-foil specimens suitable for AEM investigation were prepared with standard mechanical techniques: embedded slices were cut into 3 mm disks with an ultrasonic drill; these disks were lapped to $\sim 100 \mu\text{m}$, dimpled to $\sim 20 \mu\text{m}$, and ion-milled to perforation. The final stage of ion-milling was performed at a relatively low energy (3 keV) and incident angle (12°). A thin coat of carbon was applied in order to mitigate charging effects.

The specimens were examined at ORNL with a Philips EM400T AEM equipped with a field-emission electron gun (FEG) and operated at 100 kV. X-ray microanalysis and electron energy-loss spectrometry (EELS) were performed with an EDAX 9100 energy-dispersive X-ray spectrometer and a Gatan 666 parallel-collection electron energy-loss spectrometer, respectively. The specimens were cooled to -130°C during spectrum acquisition using a Gatan double-tilt cooling holder. For X-ray microanalysis, the majority of the specimen was masked by a gold washer with a 0.5 mm \times 2.0 mm slot, as shown schematically in Figure 1a. Care was taken to avoid shadowing effects. An alternative masking geometry is shown in Fig. 1b.

RESULTS

The nickel-titanate specimens were found to contain phases of the periclase, spinel, and corundum structures with a microstructure of dimension $\sim 100 \text{ nm}$.¹¹

Figure 2 shows the EDX spectrum measured from the periclase-structured phase and the corresponding hole count, in the energy range 2 - 12 keV. This energy range contains the Ti K and Ni K lines characteristic of the specimen and the Au L and Au M lines of the masking washer.

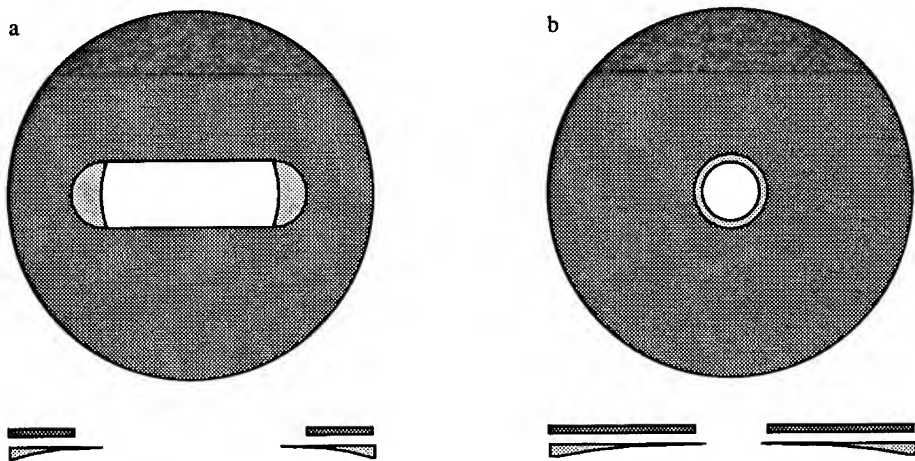


Figure 1. Schematic representations of masking geometries for self-supporting disc specimens: (a) the geometry used for this study, with the specimen masked by a washer with a $0.5\text{ mm} \times 2.0\text{ mm}$ slot; (b) the specimen masked by a circular aperture. Plan view and cross-sectional views of these geometries are shown.

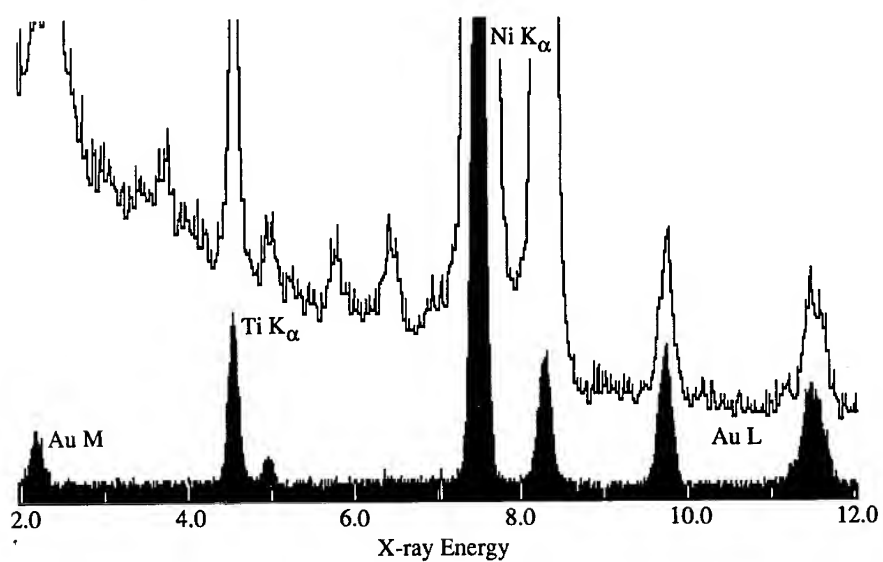


Figure 2. EDX spectra in the energy range 2 - 12 keV show the intensities characteristic of the hole count (shaded) relative to those acquired from the periclase-structured phase. The two spectra are of the same scale.

Figure 3 shows an EDX spectrum characteristic of the periclase-structured phase, after hole-count subtraction, in the energy range 4 - 9 keV and at two vertical scales. When the spectrum is scaled such that the entire Ni K_α peak is depicted (line), no Ti K_α peak is apparent; the spectrum is therefore also depicted with the vertical scaling increased by a factor of twenty (dots). The ratio of the Ti K_α to Ni K_α intensities, $N_{\text{Ti}} / N_{\text{Ni}}$, is 0.0050.

Electron energy loss spectra of the periclase- and corundum-structured phases, acquired in the second-difference collection mode, are shown in Figure 4. The portion of the spectra shown is the energy range between 425 eV and 575 eV and depicts both the $\text{Ti L}_{2,3}$ edge at ~456 eV and the O K edge at ~532 eV. The scales of the two spectra are such that the sums of the absolute values of the number of counts recorded across the O K edges of the two spectra are equal. There is no apparent $\text{Ti L}_{2,3}$ edge in the spectrum of the periclase-structured phase.

DISCUSSION

Analysis of the periclase-structured phase by EELS, Fig. 4, indicates the apparent absence of any titanium, whereas the EDX spectrum shown in Fig. 3 has a distinct Ti K_α peak which is 0.5% of the Ni K_α intensity. Linear superposition of the two spectra in Fig. 4 suggests that a titanium concentration of even 0.2% would have yielded a detectable $\text{Ti L}_{2,3}$ signal given the level of the noise in the spectra; therefore, most if not all of the Ti K_α intensity in the EDX spectrum in Fig. 3 is the result of secondary excitation. Other normalization schemes for the EEL spectra, such as equating the peak to valley ratios of the O K edges, do not substantially change these conclusions.

The secondary excitation component to the measured Ni K_α intensity may be greater or smaller than that of the Ti K_α peak depending upon the predominant type of secondary excitation. Secondary fluorescence would yield only a Ti K_α peak since Ni K X rays can fluoresce Ti K X rays but not *vice versa*. Conversely, excitation by high-angle-scattered electrons would be expected to yield secondary excitation peaks for both nickel and titanium with intensities comparable to their relative concentrations (~4:1). Therefore, if the measured Ti K_α peak in Fig. 3 is due primarily to secondary fluorescence, the extraneous Ni K_α intensity may be smaller than 0.5 %, whereas if high-angle-scattered electrons are primarily responsible for the measured Ti K_α intensity, then the extraneous Ni K_α intensity may be as much as 2 %. These levels of inaccuracy are nevertheless modest and suggest that secondary excitation would not limit the accuracy of the compositional analysis of the spinel- or corundum-structured phases in the specimen.¹¹

The masking geometry shown in Fig. 1a is only partially successful at reducing the intensities of the characteristic lines of interest in the hole count spectrum, as shown in Fig. 2. Optimally, the Au L lines in this spectrum should be larger than the Ti K and Ni K lines. Whereas the Ni K_α intensity in the hole count is just a few percent of the corresponding intensity in the spectrum of the periclase-structured phase, the Ti K_α intensity in the hole count spectrum is about half that in the measured EDX spectrum of the periclase-structured phase. A better masking geometry, such as shown in Fig. 1b, would reduce the characteristic intensities both in the hole count and due to secondary excitation. In addition, formulae are available for the calculation of the secondary fluorescence intensity of dimpled and ion-milled specimens that have been masked with a washer having a circular aperture.⁸

There is potential concern that the use of a high-Z masking material like gold may unduly increase the continuum background level, thus degrading the quality of the EDX spectrum and, in particular, leading to reduced detectability limits. In Fig. 2, the Au L signal in the raw spectrum (line) is comparable to that in the hole count (shaded) so that the characteristic lines of the gold are mostly due to the hole count with only a small secondary excitation component; the residual continuum background due to secondary excitation of the gold washer may be expected to be similarly small. The level of the continuum background in the hole count relative to that in the measured spectrum increases with increasing X-ray energy from ~5% at 2 keV to ~20% at 12 keV. However, particularly if the residual increase in the background level after background subtraction is only a small fraction of these percentages, the background levels are not sufficiently increased by the use of the high-Z masking washer to affect practical detectability limits.

The choice of masking material is dependent upon the elements composing the specimen. Gold was chosen as a washer material for this study because it is a strong absorber of X rays and because its characteristic peaks are not in the energy range of interest for the specimen, namely that

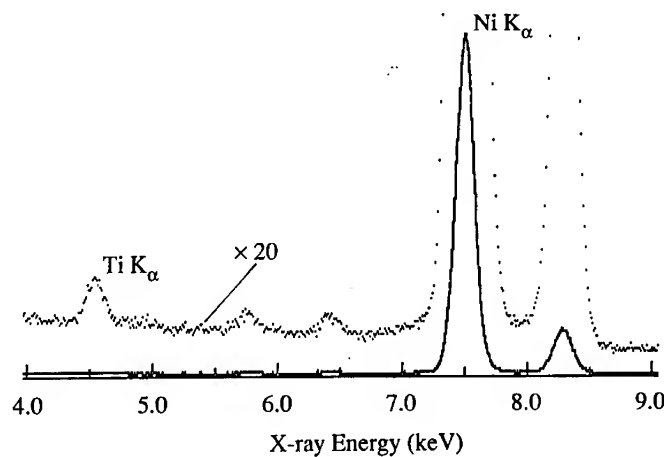


Figure 3. X-ray spectrum of the periclase-structured phase, of nominal composition NiO , in the specimen of overall composition $\text{NiO}-20$ wt.% TiO_2 ; the spectrum is also magnified 20 \times to show the relative size of the titanium K_α peak. Also visible are a small Ni K_α "escape peak" (at 5.74 keV) and a small Fe K_α peak (at 6.40 keV), the latter presumably due to secondary excitation of the objective pole-piece.

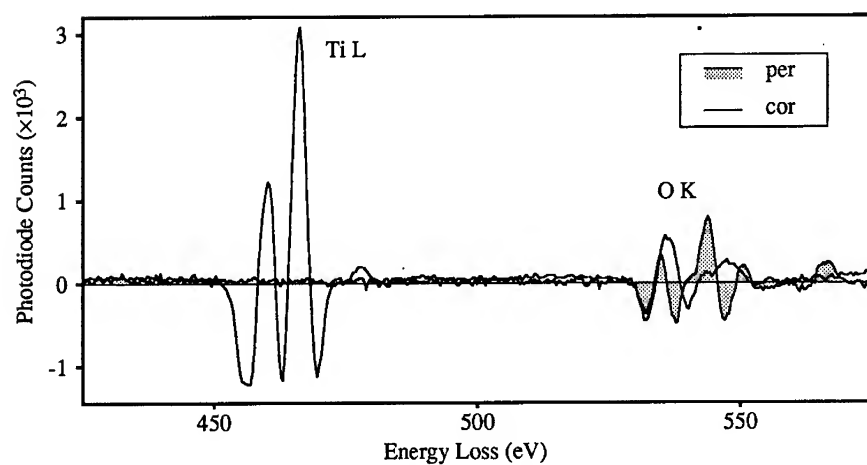


Figure 4. Electron energy-loss spectra, acquired in second-difference mode, showing the $\text{Ti L}_{2,3}$ and O K edges of the periclase-structured and corundum-structured phases. There is no $\text{Ti L}_{2,3}$ edge apparent in the spectrum of the periclase-structured phase.

containing the K_{α} lines of the 3d-transition-metals. For the analysis of GaAs-based heterostructures, copper or nickel masks would be appropriate. Copper, nickel, and gold masking washers are commercially available with a variety of aperture sizes. Optimally, a masking washer might be designed specifically for EDXS. Such a washer could have a beryllium layer facing the electron gun and layers of increasing atomic number thereafter, culminating with a gold layer adjacent to the specimen. In principle, such a masking washer would have a high absorbing power but would nevertheless contribute a low continuum background and no characteristic peaks to the measured spectrum. Moreover, such a masking washer could be used to mask any specimen, regardless of composition.

CONCLUSIONS

The masked self-supporting disc specimen yields a relatively modest secondary excitation contribution to the measured X-ray spectrum. In this study, the contributions of all secondary excitation effects to the measured $Ti\ K_{\alpha}$ intensity was only $\sim 0.5\%$ of the intensity of the measured $Ni\ K_{\alpha}$ intensity. A still lower secondary excitation intensity is expected if the specimen is masked with a washer having a small circular aperture.

Given a suitable choice of masking washer, the masked self-supporting disc is a versatile specimen-geometry for quantitative X-ray microanalysis. The commercial availability of copper, nickel, and gold masking apertures with a variety of aperture sizes makes the routine use of this specimen geometry a convenient one. This geometry could become even more versatile given a masking aperture designed specifically for EDXS.

ACKNOWLEDGMENTS

This research was supported by the Division of Materials Sciences, U.S. Department of Energy, under contract DE-AC05-84OR21400 with Martin Marietta Energy Systems, Inc. and through the SHaRE Program under contract DE-AC05-76OR00033 with the Oak Ridge Institute of Science and Education; and by the National Science Foundation through grant number DMR-8901218. This research is also supported in part by an appointment to the Oak Ridge National Laboratory Postdoctoral Research Associates Program, which is administered jointly by the Oak Ridge Institute for Science and Education and Oak Ridge National Laboratory.

REFERENCES

1. J. Bentley, in *Analytical Electron Microscopy - 1981*, edited by R. H. Geiss (San Francisco Press, San Francisco, CA, 1981), pp. 54-56.
2. E. A. Kenik and J. Bentley, in *Microbeam Analysis - 1990*, edited by J. R. Michael and P. Ingram (San Francisco Press, San Francisco, CA, 1990), pp. 289-292.
3. J. Bentley, P. Angelini, and P. S. Sklad, in *Analytical Electron Microscopy - 1984*, edited by D. B. Williams and D. C. Joy (San Francisco Press, San Francisco, CA, 1984), pp. 315-317.
4. D. B. Williams, *Practical Analytical Electron Microscopy in Materials Science* (Philips Electronic Instruments, Inc., Mahwah, NJ, 1984).
5. D. B. Williams, J. I. Goldstein, and C. E. Fiori, in *Principles of Analytical Electron Microscopy*, 2nd ed., edited by D. C. Joy, A. D. Romig, Jr., and J. I. Goldstein (Plenum Press, New York, 1986).
6. I. M. Anderson, Ph. D. thesis, Cornell University, 1993.
7. I. M. Anderson, J. Bentley, and C. B. Carter, *Microbeam Analysis* 2, pp. S230-S231 (1993).
8. I. M. Anderson, J. Bentley, and C. B. Carter, in preparation.
9. A. Muan, *J. Amer. Ceram. Soc.* 75, 1357-1360 (1992).
10. A. R. Spurr, *J. Ultrastr. Res.* 26, 31-43 (1969).
11. I. M. Anderson, J. Bentley, and C. B. Carter, these proceedings.

DETERMINATION OF THE NUMBER OF MOLECULES BONDED TO A CdSe NANOCRYSTALLITE SURFACE

SARA MAJETICH*, JENNIFER NEWBURY*, AND DALE NEWBURY**

*Department of Physics, Carnegie Mellon University, Pittsburgh, PA 15213

** National Institute of Standards and Technology, Surface and Microanalysis Science
Division, Gaithersburg, MD 20899

ABSTRACT

Electron excited energy dispersive X-ray spectrometry (EDS) was used to determine the atomic species present in 35 Å diameter CdSe nanocrystallites. Both theoretical modeling and experimental calibration with standard materials were used to relate the relative X-ray intensities to the atomic fractions present in the sample. The EDS results were normalized to those found by elemental analysis, which also detects light elements. With different surface models, and the atomic fractions found by EDS, the number of surface groups per nanocrystallite was determined.

INTRODUCTION

Under ambient conditions, nanocrystallites, which are small particles of 1- 50 nm in diameter, have chemically distinct surface layers which limit their size. While there has been considerable interest in these materials in recent years [1], the number of ligands or molecules involved in this surface coating is generally unknown. Here we present the results of an investigation using transmission electron microscopy (TEM) and quantitative EDS to study surface coverage in CdSe nanocrystallites, and compare it with other approaches. Semiconductor nanocrystallites (CdSe, CdS) can be grown with relatively narrow size distributions ($\pm 8\%$), and since these particles are nominally spherical, the number of surface sites per nanocrystallite can be estimated from the measured diameter. This is an important requirement in determining the degree of surface passivation.

EXPERIMENTAL

Sample Preparation

Thirty-five angstrom diameter CdSe nanocrystallites were grown using a modification of the reverse micelle method [2], and capped with various thiol ligands [3] (Fig. 1). They were treated with an extensive washing procedure to minimize the impurities present, as determined by NMR [4]. For EDS measurements, particles were prepared by dry deposition directly onto a thin (10 nm) carbon film carried on a copper TEM grid by dipping the grid into the powdered CdSe and shaking off the excess. For measurements on individual particles, a 0.0037 g/l methanol solution was prepared and sonicated, and then a drop was placed on the TEM grid. The size distribution was estimated from high resolution TEM of many nanocrystallites, and was found to be Gaussian. We expected the nanocrystallites in these samples to be partially covered with thiolate ligands bound to surface cadmium sites, with datively bonded pyridine ligands in the remaining sites. The EDS experiments were designed to determine the fraction of thiolate surface coverage.

Electron Microscopy Characterization

The particles were first imaged using a Vacuum Generators HB 501 field emission scanning transmission electron microscope (FE-STEM), located at the National Institute of Standards and Technology-National Institutes of Health Nanometer Analysis Facility in

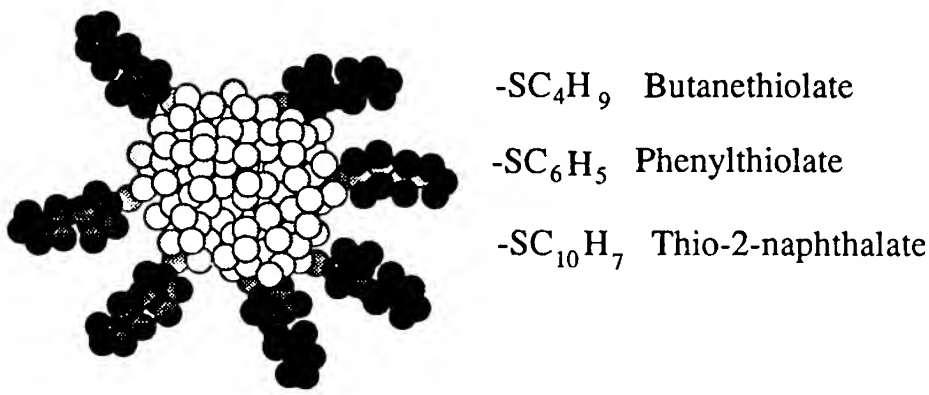


Fig.1. CdSe nanocrystallite showing attached butanethiolate ligands. The chemical formulas for the surface groups discussed in this work are shown on the right.

Bethesda, MD. For both imaging and energy dispersive X-ray spectrometry, the beam energy was 100 keV, and the incident beam was focused to 1 nm diameter with a beam current of 1 nA. Here the resolution was limited by the incident probe diameter (1 nm).

After imaging, the atomic components were determined using EDS to detect their characteristic x-ray fluorescence. To generate this signal, a beam electron with a precisely defined energy (100,000 eV \pm 0.3 eV from the field emission source) first scatters inelastically with a bound core shell electron, causing its ejection and leaving the atom in an excited state. An electron transition then occurs from an outer shell (L, M, etc.) to fill the K-shell vacancy, and the energy of the X-ray photon emitted is characteristic of the atomic species. Reabsorption was neglected due to the small size of the particles, relative to the X-ray penetration depth. The X-ray detector was a Noran windowless silicon (lithium) energy dispersive X-ray fluorescence spectrometer (EDS).

EDS RESULTS

X-ray analysis consists of first identifying which atom species create the characteristic X-ray peaks in the spectrum, and then relating the measured intensity of those peaks to the atomic concentration.

A representative example of the X-ray spectrum (Fig. 2) obtained by overscanning revealed Cd and Se as major components, and S and Si as minor species. The large Cu peaks were artifacts resulting from extraneous scattering of electrons into the 200 μm thick copper grid; the trace iron peak resulted from secondary electron scattering from the sample to the iron components of the microscope lens. Unexpectedly, silicon was found as a minor constituent, but was not homogeneously distributed. The source was presumably the trimethylsilylselenium reagent used in the sample preparation. The sulfur showed some variation as well, but the Cd and Se were evenly distributed. The results reported reflect averages over several hundred nanocrystallites.

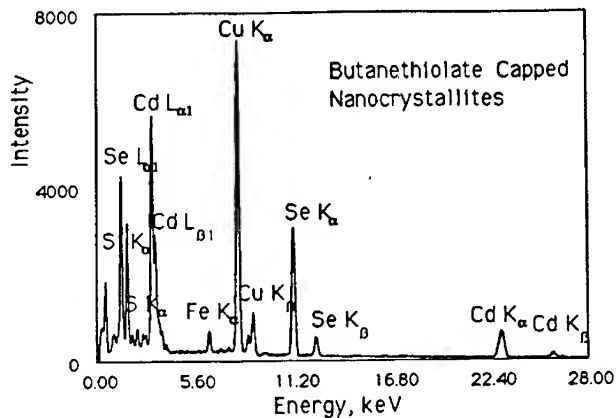


Fig. 2. EDS intensities for a sample of butanethiolate-capped CdSe nanocrystallites.

The absolute X-ray fluorescence intensity, I_A , for element A depends on a number of factors:

$$I_A \text{ (per beam } e^-) = C_A Q_A \omega_A (N_A v / A_A) \rho t (\Omega/4\pi) \epsilon, \quad (1)$$

where C_A is the mass concentration of the element, Q_A is the ionization cross-section (#ionizations/e⁻·atom·cm²), ω_A is the fluorescence X-ray yield, $N_A v$ is Avogadro's number, A_A is the atomic weight of element A, ρ is the mass density of the sample, t is the sample thickness, $\Omega/4\pi$ is the solid angle subtended by the detector, and ϵ is the detector efficiency, which is a function of the X-ray energy. Quantitative determination of the elemental mass or atomic ratios from the measured EDS intensities can be carried out either with standards of known composition or with "first principles" calculations. A ratio of measured X-ray intensities (I_A/I_B) for any two elements A and B can be converted into a ratio of concentrations (C_A/C_B) with the following relation:

$$(C_A/C_B) = (I_A/I_B) [(Q_B/Q_A) (\omega_B / \omega_A) (A_A/A_B) (\epsilon_B/\epsilon_A)]. \quad (2)$$

Note that several factors cancel when the intensity ratio is calculated. For these nanocrystallite samples there are no overlap or interaction factors which might invalidate equation (2). The first principles calculations used theoretical ionization cross sections with a hydrogenic approximation for the oscillator strength and relativistic kinematics [5]. For the empirical calculations, relative intensities from CdSe and CdS powder standards were used to determine the Cliff-Lorimer relative sensitivity factors, $k^w_{AB} = [(Q_B/Q_A) (\omega_B / \omega_A) (A_A/A_B) (\epsilon_B/\epsilon_A)]$ experimentally. Because an empirical Si standard was not used, k^w_{SiCd} was determined using the theoretical ionization cross-section for the Si peak at 1.74 keV, multiplied by the ratio of the empirical to theoretical values found for the nearby S peak at 2.3 keV. The NIST X-ray spectrum calculation engine, Desktop Spectrum Analyzer (DTSA), was used for all spectrum calculations. The characteristic x-ray intensities are extracted from the continuum background as well as from possible interferences from other nearby peaks by the "sequential simplex"

mathematical peak deconvolution procedure. This procedure optimized a synthesized fit to the experimentally measured spectrum based on an assumed Gaussian peak profile.

After the elemental ratios were calculated with equation (2), the absolute concentrations were determined by comparison with elemental analysis performed on an identical sample by Galbraith Laboratories, Knoxville, TN (Table I). This step was necessary since a number of light elements present in our samples could not be detected by EDS. The data were normalized to have the same total Cd + Se atomic fraction because these elements were most uniformly distributed. The uncertainty is specified only on the basis of the counting statistics, and does not include systematic errors due to limitations of the theoretical parameters.

TABLE I. Normalization of EDS and Elemental Analysis Atomic Fractions for the Butanethiolate-Capped Nanocrystallite Sample

Element	EDS, theoretical	EDS, empirical	Elemental Analysis
Cd	0.168 ± 0.008	0.162 ± 0.023	0.1643 ± 0.0006
Se	0.152 ± 0.010	0.157 ± 0.024	0.1547 ± 0.0006
S	0.014 ± 0.022	0.019 ± 0.011	0.0102 ± 0.00004
Si	0.048 ± 0.032	0.062 ± 0.035	0.0041 ± 0.0001
N	*	*	0.0473 ± 0.0003
C	*	*	0.290 ± 0.001
H	*	*	0.328 ± 0.004
Na	*	*	0.0009 ± 0.00002
Total	0.382 ± 0.041	0.400 ± 0.050	1.000 ± 0.004

* Element not detectable by EDS

DISCUSSION

The number of cadmium sites available for bonding was determined in order to relate the atom fractions to the nanocrystallite surface coverage. TEM images of single nanocrystallites show roughly spherical particles with an average diameter of 35 Å and a cubic lattice, but no evidence of faceting or surface ligands. From this we assumed that the 35 Å dimension reflected the size of the bare nanocrystallite, without surface groups. The average number of atoms per bare nanocrystallite equals the volume contained in a 35 Å diameter sphere, divided by the unit cell volume, a^3 , multiplied by the number of atoms per unit cell (8):

$$N = [4/3 \pi r^3] (8) / a^3 = 811. \quad (3)$$

We modelled the nanocrystallite in several ways, always requiring that the Cd:Se ratio agree with the experimentally measured value. Using a spherical shell model [6] with atoms tetrahedrally bonded in concentric shells about a central Se atom, we obtained agreement with the Cd:Se ratio, and 122 available Cd surface sites. However, when applied to Cd-centered spherical shells, the model predicts Se-rich nanocrystallites, inconsistent with the measured variations in the Cd:Se ratio. Experimental evidence based on the nanocrystallite growth dynamics [7] supports a shell model of some sort, and we propose a modification of the shell model, where charge neutrality is an important growth parameter. This model is supported by results from mass spectroscopy of small CdSe clusters, where the predominant mass peaks are interpreted in terms of approximately spherical clusters with equal numbers of Cd and Se atoms [8]. The ratio of Cd to Se atoms with dangling bonds is roughly 1:1 for these clusters. When this model is applied to nanocrystallites, we assume a neutral core with extra Cd atoms bonded to Se sites, consistent with the experimental Cd:Se ratio. With the shell approximation and equal numbers of Cd and Se atoms exposed, the number of Cd surface sites is ~126.

An upper limit for the number of surface groups was estimated from the elemental analysis data. Here we assumed that all elements in the butanethiolate-capped sample apart from the Si and Na impurities were part of the nanocrystallite, with all of the Cd and Se in the interior, all of the S as butanethiolate (SC_4H_9) ligands, and all of the N as pyridine ($\text{C}_5\text{H}_5\text{N}$) molecules. This accounts for almost all (99.16 %) of the elements observed and their relative abundances. This suggests a number of attached groups (26 butanethiolate and 120 pyridine) not inconsistent with the surface models. The extra pyridine groups need not be attached to the nanocrystallite surface; excess solvent impurities are often detected in samples evaporated from solution.

The fractional surface coverage for an average nanocrystallite was calculated from the ratio of sulfur atoms to surface cadmium sites, and Table II summarizes the results. Here we have assumed that the sulfur is present in the sample only as an attached thiol ligand, and we have used the charge neutrality model for the number of surface sites. The error in EDS measurement, which is shown, is greatly exceeded by the error due to variations in the nanocrystallite radius (~8%) and the estimated error involved in calculating the number of Cd surface sites (~20%).

TABLE II. Comparison of EDS Empirical and Theoretical Surface Coverage Results

Ligand	EDS empirical	EDS theoretical
Butanethiolate	$39.20 \pm 0.53\%$	$29.59 \pm 0.23\%$
Phenylthiolate	$40.83 \pm 0.46\%$	$30.08 \pm 0.95\%$
Thio-2-naphthalate	$69.71 \pm 6.47\%$	$51.55 \pm 4.60\%$

These results clearly indicate that the thiol surface coverage is far from complete passivation. Similarly low coverage has been reported for phenylthiolate-capped CdS nanocrystallites of comparable size probed by NMR [9]. Elemental analysis suggests that the portion of the nanocrystallite surface not bonded to thiolate ligands could be passivated with pyridine molecules, but the connection to surface coverage is less direct than for either EDS or NMR. The trend of increasing relative coverage despite increased steric hindrance indicates that another factor, such as bond strength, may be more important than the bulkiness of the ligand. This could potentially be measured from structure in the sulfur EELS peak. The significant quantitative difference in the surface coverage results for the empirical and theoretical analysis methods demonstrates the importance of using elemental standards. This is particularly important when the atomic fraction information is applied to problems on a molecular scale, such as nanocrystallite surface coverage.

CONCLUSIONS

Electron-excited energy dispersive X-ray spectrometry has been used to determine the atomic fractions present in CdSe nanocrystallites with different surface coatings. From the concentrations and a calculation of the available number of surface bonding sites, the degree of surface coverage was calculated. This problem has also been addressed by elemental analysis and NMR. While both elemental analysis and NMR are necessarily bulk measurements, the advantage of EDS is that it can be extended to measurements on individual nanocrystallites. In addition, EDS provides nanometer-scale elemental maps, verifying in this case that the Si impurity was not uniformly distributed. The inability of EDS to detect light elements can be overcome with renormalization to elemental analysis data. Finally it is important to use the empirical elemental sensitivity factors rather than theoretical cross-sections to complex issues such as surface coverage.

ACKNOWLEDGMENTS

S.M. would like to acknowledge the support of the ACS Petroleum Research Fund (#ACSPRF25025-G6), the National Science Foundation (#DMR-9258308), and the AT&T Foundation. In addition, help in sample preparation from A. C. Carter was greatly appreciated.

REFERENCES

1. R. P. Andres, R. S. Averback, W. L. Brown, L. E. Brus, W. A. Goddard, III, A. Kaldor, S. G. Louie, M. Moscovits, P. S. Peercy, S. J. Riley, R. W. Siegel, F. Spaepen, and Y. Wang, *J. Mater. Res.* **4**, 704 (1989).
2. M. L. Steigerwald, A. P. Alivisatos, J. M. Gibson, T. D. Harris, R. Kortan, A. J. Muller, A. M. Thayer, T. M. Duncan, D. C. Douglass, and L. E. Brus, *J. Am. Chem. Soc.* **110**, 3046 (1988).
3. S. A. Majetich and A. C. Carter, *J. Chem. Phys.* **97**, 8727 (1993).
4. S. A. Majetich, A. C. Carter, J. Belot, and R. D. McCullough, *J. Phys. Chem.* (under review).
5. R. F. Egerton, Electron Energy Loss Spectroscopy in the Electron Microscope, Plenum Press, New York, 1986, pp. 357-359.
6. P. E. Lippens and M. Lannoo, *Phys. Rev. B* **39**, 10935 (1989).
7. C. R. Kagan and M. J. Cima, in Microcrystalline Semiconductors: Materials Science and Devices, (*Mater. Res. Soc. Proc.* **283**, Pittsburgh, PA, 1993), p.841.
8. S. A. Majetich, J. H. Scott, S. Dougherty, and J. Amster (unpublished).
9. J. R. Sachleben, E. W. Wooten, L. Emsley, A. Pines, V. L. Colvin, and A. P. Alivisatos, *Chem. Phys. Lett.* **198**, 43 (1992).

TEM STUDY OF THE Pt-Ru BI-METALLIC CATALYST FORMATION

CHAOYING MA*, A. D. KOWALAK* AND CHANGMO SUNG**

*Department of Chemistry and **Center for Advanced Materials, University of Massachusetts - Lowell, Lowell, MA 01854

ABSTRACT

Pt colloidal particles with large surface areas are effective electrocatalysts which can be applied in methanol fuel cells. The efficiency of the Pt catalyst can be greatly increased if it is incorporated with a second component such as Ru. By applying TEM, EDXS and XRD, the chemical composition, particle size and crystallinity of Pt and Pt/Ru colloidal particles during synthesis procedure are investigated in this research.

INTRODUCTION

Different Pt-based bi-metallic catalysts [1-4] have been prepared in order to obtain higher catalytic efficiencies in fuel cell applications. The highly dispersed Pt-Ru electrocatalyst [1], which is studied in this research, is believed to be one of the effective catalysts for the methanol oxidation reaction in fuel cells. In this bi-metallic catalyst, platinum is the basic component, ruthenium is the second component. The incorporation of Ru into Pt colloidal particles can greatly increase the efficiencies of the catalysts which exhibit extremely high catalytic activities for the electro-oxidation reaction of methanol. According to a report [1], the pure Pt catalyst had a current density of 60 mA cm^{-2} at 0.4 V. However, Pt/Ru catalyst had a current density 200 mA cm^{-2} under the same conditions. Furthermore the limiting current increased from 0.3 A cm^{-2} (Pt) to 1 A cm^{-2} (Pt/Ru).

It has been reported that catalytic activity and chemical selectivity of the catalysts depend on the size of the colloidal metal particles [5]. Of same amount of catalysts, surface areas of expensive catalysts such as Pt, Pd, Ru increase as particle sizes of the catalysts decrease. Higher activities can be obtained with higher surface areas of the catalysts.

In order to explore the synthesis of highly active electrocatalysts for fuel cells which have potential applications in low pollution, high efficiency energy generation, it is necessary to conduct researches in depth on the formation and crystal growth of the catalysts and their structure-property relationship.

In the present work, by using the Pt-Ru catalyst as synthesized by Watanabe [1] as a model system, methodology of controlling the size, chemical composition and crystallization of Pt/Ru particles, were investigated. Different instrumentation including transmission electron microscopy, energy dispersive x-ray spectroscopy, x-ray diffraction as well as general chemistry analyses have been used.

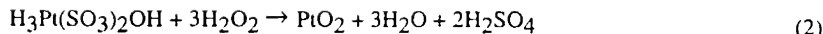
EXPERIMENTAL

The Watanabe method [1] was used to synthesize the Pt-Ru catalyst as illustrated in the following 3 steps.

Step 1: H_2PtCl_6 solution was reduced by NaHSO_3 at $\text{pH} \sim 5$.



Step 2: H_2O_2 solution (35 %) was used to oxidize the Pt(II) back to Pt(IV) at $\text{pH} \sim 5$.



Step 3: RuCl₃ was added into the solution from step 2 at pH ~ 5. Part of the Ru was oxidized by the excess H₂O₂ from step 2. The resulting dark brown colloidal solution was combined with Vulcan XC-72 (carbon black). H₂ gas was used to reduce the products. The resulting products were filtered and air dried at room temperature for further electrochemical analysis.

The microstructure and chemical composition of the materials at different stages of the crystal growth were characterized by analytical transmission electron microscope. TEM samples were prepared by placing a drop of the colloidal metal solution on a carbon film of copper grid. The sample analyses were performed on a Philips 400T scanning transmission electron microscope. The composition analyses were carried out on a Noran Instrument 5500 low-Z energy dispersive X-ray spectrometry system (EDXS). The various phases in the materials were identified by electron diffraction and EDXS with an electron diffraction simulation program. X-ray diffractometer was used to measure the crystallinity of bulk Pt-Ru/XC-72 catalysts.

RESULTS

Sample 1 was prepared from the yellow colloidal solution formed after the addition of H₂O₂ in step 2 followed by a period of reaction time. The effects of reaction time on particle size distribution are shown in Figure 1. Figure 2 shows the bright field image of crystalline particles and the EDXS confirming that the particles consisted of Pt and O (see Figure 2).

RuCl₃ solution was added into the reaction system 30 minutes after step 2 was completed. Sample 2 was prepared out of this solution and consisted of agglomerated grains which contained very small crystallites. EDXS analyses showed that two kinds of particles, Pt-O and Ru-O, were present in this step (see Figure 3). The preparation of sample 3 employed the same procedures as sample 2 except that the reaction time was 24 hours instead of 30 minutes. Both Pt and Ru peaks were observed from the resulting crystallites using EDXS (see Figure 4).

Samples 4 and 5 were prepared by combining Vulcan XC-72 carbon black with samples 2 and 3, respectively. The Pt-Ru colloidal particles seemed to be absorbed onto the carbon black. The morphology of these samples revealed that homogeneous distribution of Pt-Ru particles throughout the carbon black media had been achieved (see Figure 5). X-ray diffraction analyses were used to measure the crystallinity of sample 4 and sample 5 (see Figure 6). The color difference between samples 4 and 5 was also noticed. The solution of sample 5 was clear and colorless compared to that of sample 4 which was turbid. This suggests that in sample 5, Pt-O particles had a higher pick-up of Ru metal.

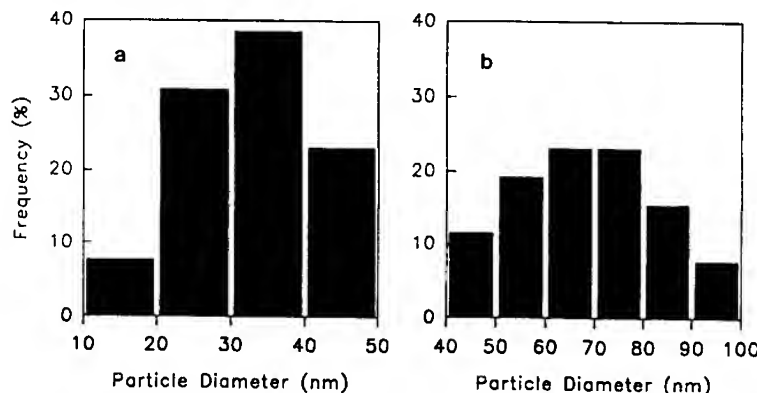


Figure 1. Particle size distributions of sample 1 for two different reaction times. (a) 30 minutes and (b) 48 hours.

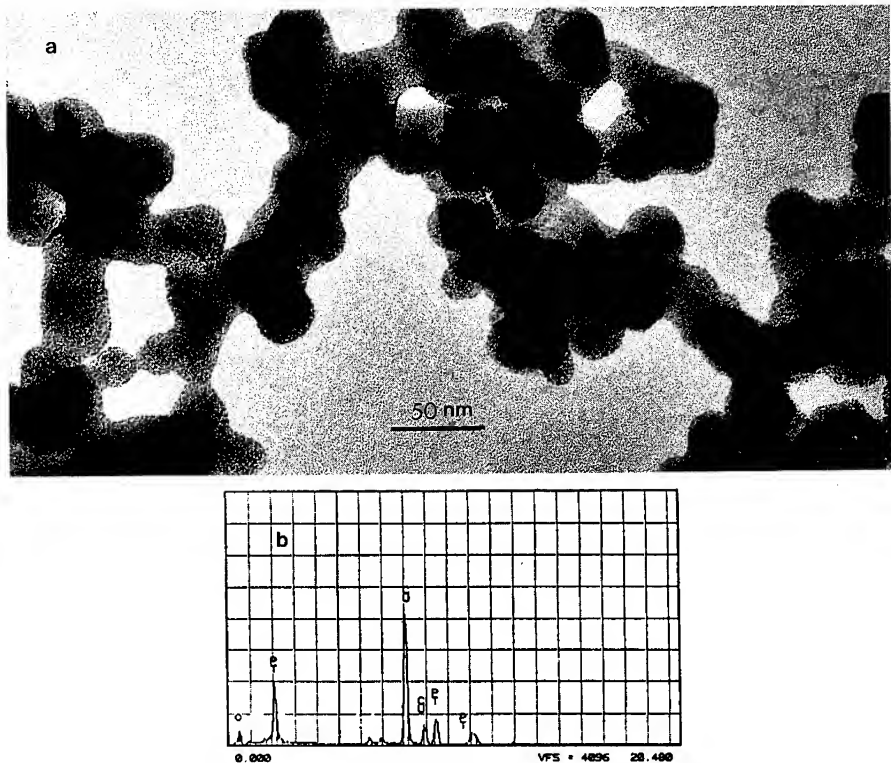


Figure 2. The TEM bright field image of crystalline particles of sample 1 (a). EDXS confirms that the particles are composed of Pt and O (b).

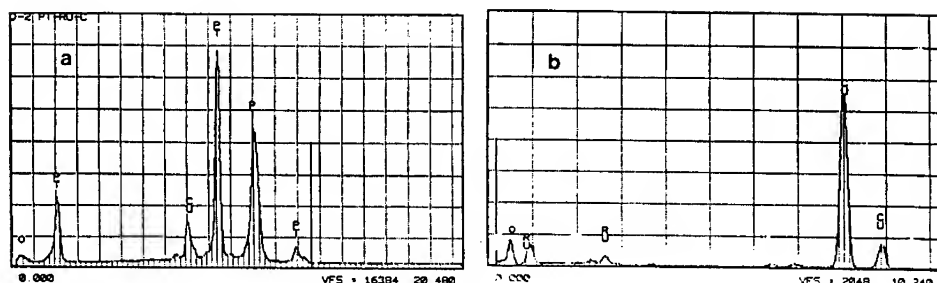


Figure 3. EDXS analyses show that there are two different kinds of particles, Pt-O (a) and Ru-O (b), in sample 2.

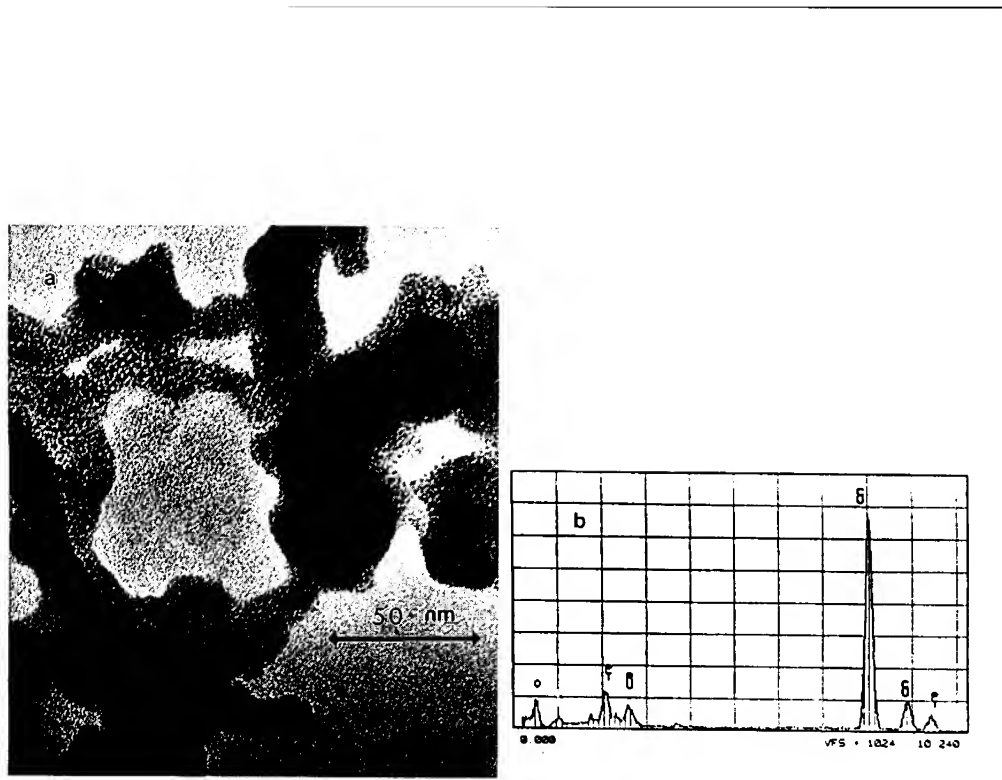


Figure 4. TEM picture of sample 3 (a). Both Pt and Ru peaks are observed in the EDXS of the Pt/Ru particles (b).

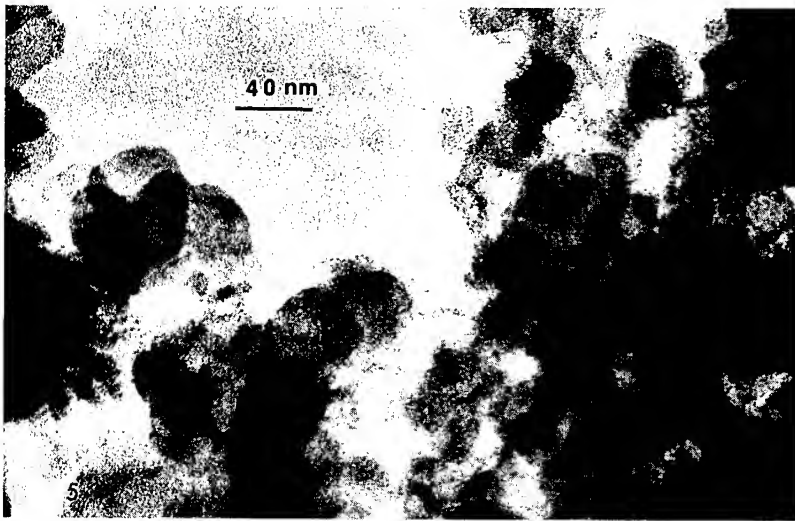


Figure 5. The morphology of the Pt-Ru/Valcun XC-72 samples (sample 5) reveals homogeneous distribution of Pt/Ru particles through the carbon black media.

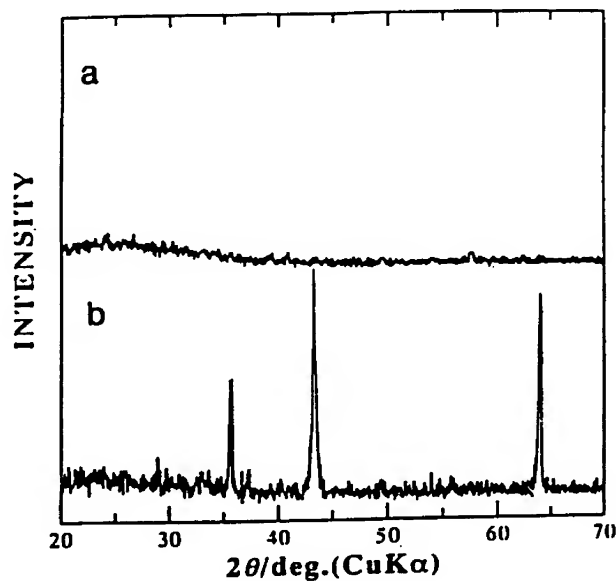


Figure 6. Powder XRD (CuK α) profiles of Pt-Ru bi-metallic particles supported on Vulcan XC-72 carbon black. Sample 4 corresponds to Pt-O products with 30 minutes reaction time in step 2 after the addition of H₂O₂. Sample 5 comes from the Pt-O products with 24 hours reaction time in step 2 after the addition of H₂O₂.

DISCUSSION

The effects of reaction time for Pt nucleation on the Pt-Ru particle formation were of interest in this study. In step 2, after the addition of H₂O₂, the Pt containing solution was kept stirring. The reaction time varied from 30 minutes to 24 hours. Particles which underwent 30 minutes reaction time had diameters around 30 - 50 nm. With 48 hours reaction time, particle size increased to 60 - 90 nm (see Figure 1). TEM results showed that the Pt-O colloidal particles were generated after the addition of H₂O₂ in step 2, and then did undergo crystal growth after incubation.

The reaction time of Pt-O particles in step 2 seemed to greatly influence the particle size, chemical composition and crystal structure of the following products. EDXS results of sample 2, in which Pt nucleation time was 30 minutes, revealed the presence of two different kinds of particles, Pt-O and Ru-O (see Figure 3). The added ruthenium formed its own oxide particles instead of combining with the Pt-O particles. EDXS and TEM results of sample 3, in which the Pt nucleation time took 24 hours under constant stirring, showed the existence of Pt-Ru bi-metallic particles rather than two separate particles of Pt-O and Ru-O (see Figure 4).

XRD results showed that the reaction time in step 2 was critical for the crystallization of the resulting Pt/Ru/C products. Sample 4 had amorphous features due to a short reaction time of 30 minutes in step 2. Sample 5, which reacted for 24 hours of Pt-O crystal growth, had obvious

crystallinity features (see Figure 6). It has been reported that the mechanism of methanol electro-oxidation reaction on a Pt electrode is greatly influenced by the crystallinity of the Pt electrode [6]. The catalysis efficiencies, namely, current density of fuel cells, of the above samples with different crystallinity features are going to be studied.

CONCLUSION

The reaction time after the addition of H_2O_2 in step 2 greatly influences the particle size, chemical composition, crystallinity of the products. The size of Pt-O colloidal particles is decided by the reaction time in step 2. The smaller Pt-O particles prepared in short reaction time (30 minutes) leads to the formation of separate particles of Pt-O and Ru-O when they are reacted with Ru. From this solution, amorphous Pt-Ru-C catalysts are produced. Pt-Ru bi-metallic crystallites can be synthesized by combining Pt-O colloidal particles prepared in longer reaction time (24 hours) with Ru. The solutions of Pt-Ru bi-metallic particles combine carbon black to form the catalysts which have crystallinity features. Further electrochemical experiments will be performed to determine the efficiencies of the catalysts corresponding to different particle sizes, chemical compositions and crystallinity features. The results of this research as part of the investigation of highly active electrocatalysts for fuel cells enrich the understanding of the Pt/Ru bi-metallic catalyst formation.

REFERENCES

- [1]. Watanabe, M., Uchida, M. and Motoo, S. J. Electroanal. Chem. **229**, 395-406 (1987).
- [2]. Gokagac, G. and Kennedy, B. J., Cashion, J. D. and Brown, L. J. J. Chem. Soc. Faraday Trans. **89** (1), 151-157 (1993).
- [3]. Nakajima, H. and Kita, H. Electrochimica Acta **35** (5), 849-853 , 1990.
- [4]. Swathirajan, S. and Mikhail, Y. J. Electrochem. Soc. **138** (5), 1321-1326 (1991).
- [5]. Metal Clusters in Catalysis; Gates, B. C. , Guczi, L., Knozinger, H., Eds.; Elsevier: New York, 1986.
- [6]. Moraallon, E., Vazquez, J. L. and Perrez, J. M., Beden, B., Hahn, F., Leger, J. M. and Lamy, C., J. Electroanal. Chem. **344**, 289-302 (1993).

RAMAN SPECTROSCOPY OF SIZE SELECTED, MATRIX ISOLATED Si CLUSTERS

A. OGURA^{a)}, E. C. HONEA, C. A. MURRAY, K. RAGHAVACHARI,
W. O. SPRENGER, M. F. JARROLD^{b)}, AND W. L. BROWN

AT&T Bell Laboratories, 600 Mountain Avenue, Murray Hill, NJ 07974

a) Resident Visitor from NEC Microelectronics Res. Labs., Tsukuba, Japan.

b) Department of Chemistry, Northwestern University, Evanston, IL 60208

ABSTRACT

We report results of Raman spectroscopy of size selected, matrix isolated Si clusters. Cluster ions produced by laser vaporization are size selected by a quadrupole mass spectrometer and co-deposited with cryogenic matrices onto a substrate at ~15K. A surface-plasmon-polariton-enhanced Raman geometry is used to gain adequate signal.

The observed vibrational frequencies from Si₄, Si₆ and Si₇ are compared with theoretically calculated Raman active modes based on the structures of planar rhombus, distorted octahedron and pentagonal bipyramid, respectively. The agreement is excellent. Cluster agglomeration is observed when cluster concentrations exceed ~0.3% by volume in the matrix and/or with annealing at ~28K, below the temperature of matrix evaporation.

INTRODUCTION

It is well known that the small Si clusters have quite different chemical and physical properties from those of bulk materials[1,2]. However, experimental information on cluster structure has been reported for clusters only as large as Si₄[3-5]. Raman spectroscopy can measure the vibrational modes of small molecules, therefore it is an attractive method for determination of Si cluster structures. However, for the small number of clusters that can be size selected and collected, the Raman signal is expected to be very weak. In the present paper, we discuss the use of surface plasmon-polariton-enhanced Raman spectroscopy on single size Si clusters isolated in matrices, and the successful determination of their structures by comparing obtained vibrational frequencies with *ab-initio* calculations. We also discuss observation of agglomeration of the single size clusters to material related to amorphous Si.

EXPERIMENTS

Cluster deposition

Figure 1 is a schematic of the cluster deposition system[6]. The Si clusters are formed from Si atoms evaporated from the rotating Si rod by XeCl laser ablation in continuously flowing He buffer gas. The electrons injected into the source chamber enhance the ionization of the Si clusters. The cluster ions are then focussed and injected into a quadrupole mass spectrometer. Finally, a single-size Si cluster ion beam is doubly deflected to reduce neutral contaminants coming from the source chamber and focused onto the collecting substrate kept at ~15K. The deposition energy is kept at 25eV. An

inert matrix gas such as N₂, Ar, Kr and Xe is deposited simultaneously with the clusters so that individual clusters are embedded and isolated. The substrate is a 550Å-thick Ag freshly deposited film on a sapphire hemi-cylindrical prism. Clusters are neutralized by electrons from a filament mounted underneath the substrate after the last ion optic. The base pressure of the deposition chamber is kept about 5×10^{-10} Torr, and the background during the cluster deposition consists mainly of He coming from the cluster source. The substrate, the mass spectrometer and the double deflection optics are surrounded by liquid N₂ cooled shields, to minimize the possibility of cluster reactions with contaminants such as carbon, oxygen or hydrogen. The matrix gas deposition rates were calibrated by using laser interferometry. The cluster ion deposition was calibrated by ex situ measurements of the deposited Si atoms using Rutherford back scattering. With these two calibrations, we can estimate the cluster concentrations in the matrix.

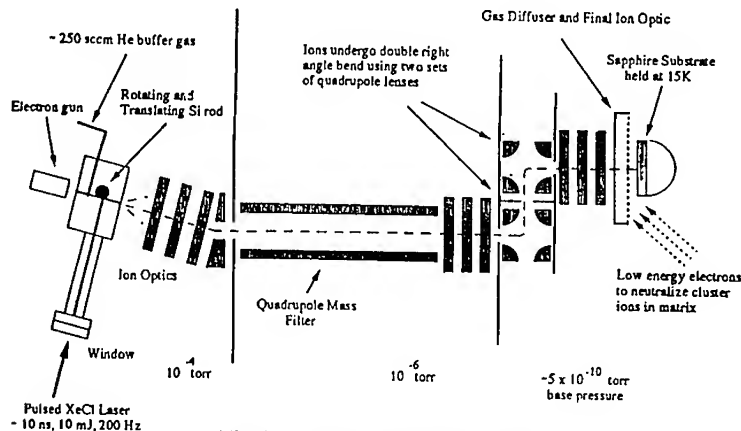


Fig.1 Cluster deposition system

Raman measurement

The Kretschmann configuration is used to obtain surface plasmon-polariton enhanced Raman spectroscopy[7-9]. The optical set up is shown in Fig. 2. The clusters and matrix are deposited onto a Ag film, which is on the flat surface of a hemi-cylindrical sapphire prism. The Ag deposition is carried out in the same UHV chamber at 200K at a deposition rate of $\sim 1\text{ \AA/sec}$. The film is annealed at room temperature for several hours to improve its quality prior to the cluster deposition[10].

For Raman measurement, the prism is rotated to an angle of incidence of the light at which the k vector of the light matches that of the surface plasmon. This depends on the optical constant of the matrix and the incident laser wave length (4880 or 5145Å are used here). At this angle, the reflection of the laser light is reduced dramatically and excitation of the surface plasmons in the Ag film occurs. The optical constants of the multilayer sample determine the enhancement of the local electric field in the matrix. The thickness of the matrix is made greater than 1μm although the thickness in which clusters are deposited is only 1000-1500Å since the enhancement effect decreases exponentially as a function of the distance from the Ag surface (1/e~700Å). Spectra are collected with a liquid N₂ cooled back-thinned CCD detector attached to a triple grating spectrometer. Raman spectra are obtained by binning vertical rows in the CCD image after proper signal

processing to remove the events produced by cosmic rays or residual radioisotopic decays which typically hit only one or two pixels of the CCD array.

Figure 3 shows the Raman intensity from an N_2 matrix as a function of the laser incident angle both on the spot at which clusters are deposited and on a background spot 3-4mm away from the cluster position. From Fig. 3 the Raman intensity is seen to be enhanced more than 100 times at the background position. A smaller enhancement, a broader peak and a shift in peak position are observed on the cluster spot due to the contribution of the Si clusters to the optical constant of the matrix.

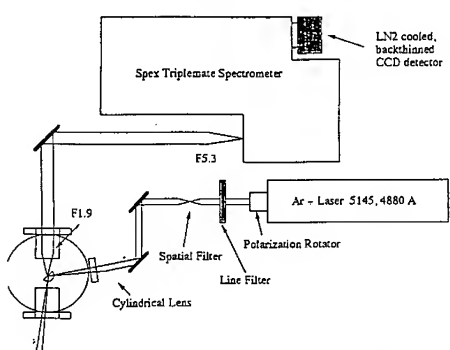


Fig.2 Optics for surface plasmon-polariton enhanced Raman measurement

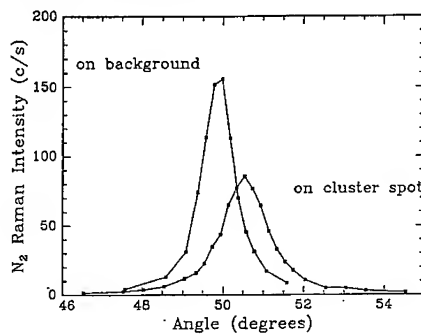


Fig.3 N_2 Raman intensity as a function of the laser incident angle both on the cluster spot and on the background (N_2 matrix without co-deposited clusters).

RESULTS AND DISCUSSION

Structure of small clusters

The measured Raman spectra from size selected Si_4 , Si_6 and Si_7 are shown in the Fig. 4, where the cluster concentrations are less than 0.1% by volume.[11]. Each plotted spectrum is obtained by averaging several spectra taken on the cluster spot, each of which is a 20-40 minute exposure, and subtracting a background spectrum taken 3-4mm away from the cluster spot. The calculated frequencies of Raman allowed vibrations, based on the structures shown at the right of the each spectrum in Fig. 4, are also shown. In the calculations, the vibrational properties of several isomers of each cluster were initially determined at the Hartree-Fock (HF) level with the polarized double-zeta 6-31* basis set. The structures and frequencies of the ground state isomers were then repeated by inclusion of electron correlation effects at second-order Moller-Plesset perturbation theory (MP2). The calculated results were then scaled down uniformly by 5% to take systematic deviations such as anharmonicity into account[12].

The predicted ground state structure of Si_4 is a planar rhombus (D_{2h}). The rhombus has three allowed Raman lines at $337(a_g)$, $440(b_{3g})$ and $463(a_g)$ cm^{-1} . The experimentally observed frequencies 345 and 470 cm^{-1} are in excellent agreement with two a_g modes. The b_{3g} is expected to be an order magnitude weaker than the nearby strong a_g modes. The distorted tetrahedral (D_{2d}), as a candidate for the Si_4 , has about 1eV higher in energy and five allowed Raman lines at 175 , 195 , 420 , 499 and 648 cm^{-1} , which don't agree with

the observed spectrum. Our result of the planar rhombus also agrees with the previous experiments[5].

The predicted ground state of Si_4 is a compressed octahedron (D_{4h}). The other candidate such as bicapped tetrahedron and capped trigonal bipyramidal collapsed to the same D_{4h} structure on optimization. It has five allowed Raman lines at $209(b_{2g})$, $298(a_{1g})$, $376(b_{1g})$, $425(e_g)$ and $457(a_{1g})$ cm^{-1} , which agree quite well with the experimental spectrum having peaks at 252 , 300 , 386 , 404 and 458 cm^{-1} . The b_{2g} mode, which has the largest deviation in the present work, involves the vibrations of the equatorial bonds which are unusually long (2.73\AA). Its calculated low value suggests that the extent of compression of the octahedron is probably overestimated in this level of theory. Reducing the compression will increase the frequency of the b_{2g} mode and decrease the frequency of the e_g mode, bringing both into better agreement with experiment. An alternative isomer such as a hexagonal chair (microcrystalline D_{3d} structure) with allowed Raman lines at 203 , 324 and 407 cm^{-1} is in poor agreement with the experiment. Other possible high energy isomers have lower symmetry and are predicted to have many more Raman lines.

For Si_7 the ground state is predicted to be a pentagonal bipyramid (D_{5h}), which has five allowed Raman lines at $300(e'_2)$, $339(e'_2)$, $346(e''_1)$, $352(a'_1)$ and $441(a'_1)$ cm^{-1} . Four lines at 289 , 340 , 358 and 435 cm^{-1} are observed experimentally. The relatively wide line at 340cm^{-1} suggests the possibility of the two predicted overlapping lines of e'_2 and e''_1 modes. The agreement between theory and experiment is excellent again. Another candidate, a C_{3v} isomer, has 9 allowed Raman lines and the agreement is much poorer (6 of them are less than 200 cm^{-1}). Other possibilities such as C_{3v} and C_{2v} symmetry are much higher in energy and have many more Raman allowed lines.

All of the spectra shown in Fig. 4 are taken for clusters in a N_2 matrix. Clusters in Kr , Ar and Xe matrices were also examined and no significant shift of the peak positions was observed. Since no Raman peaks of Si-H , Si-O and Si-N vibrations were observed, we can conclude the contaminant effect on the cluster structures was negligible.

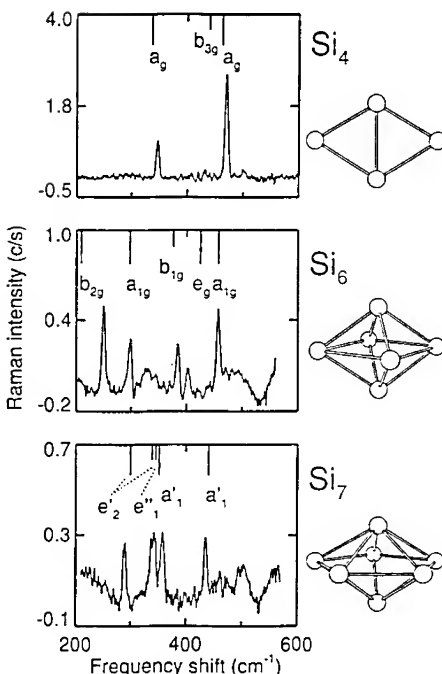


Fig.4 Raman spectra from Si_4 , Si_6 and Si_7 . The calculated vibrational frequencies based on the structure of the right side are also indicated at the top of each experimental one.

Cluster Agglomeration

When the cluster concentrations in the matrix were 0.1% by volume or lower, only sharp peaks are observed as shown above. With concentrations of $\sim 0.3\%$ or more, however, both sharp and broad peaks are observed in the as-deposited cluster spectrum as shown in Fig. 5 for Si_4 . The sharp peaks are at exactly the same frequencies as in the low concentration Si_4 . We assume the broad peaks come from aggregated clusters.

Figure 6 shows the various stages of the aggregation for Si_6 at concentration of $\sim 0.3\%$. The Raman spectrum of an as-deposited sample shows both sharp and broad peaks as shown in Fig. 6(a), in which the positions of the sharp peaks are the same as those of isolated Si_6 as shown in Fig. 4. After warming the matrix up to $\sim 28\text{K}$ for several hours, the sharp peaks disappear and only broad peaks are observed as shown in Fig. 6(b). For this case, where presumably the amount of Si is the same for both the Si_6 isolated clusters and what seem to be larger agglomerates, the stronger Raman signal observed after agglomeration indicates that the agglomerates have a relatively larger Raman cross section. The poor crystal quality of the N_2 matrix due to the low deposition temperature may enhance the cluster diffusion and coalescence in the matrix at the annealing temperature of nearly one third of the N_2 triple point.

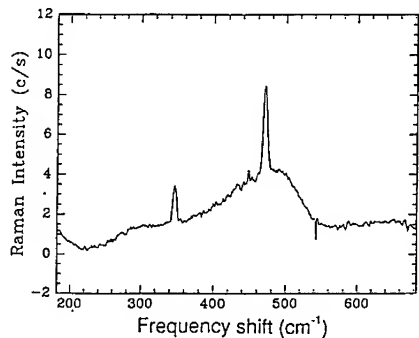


Fig.5 Raman spectra of as-deposited high concentration Si_4 $\sim 0.3\%$ by volume in an Ar matrix.

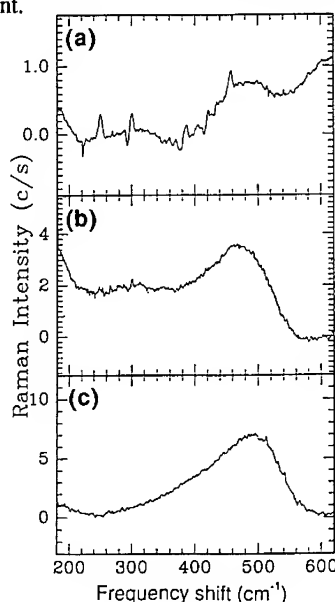


Fig.6 Raman spectra of (a) as-deposited Si_7 , (b) Si_7 after low temperature ($\sim 28\text{K}$) annealing for several hours and (c) Si_7 after matrix evaporation and another cap of matrix.

After warming the substrate over the matrix evaporation temperature (~60K in the case of N₂) followed by deposition of another matrix layer to obtain the Raman enhancement, the Si clusters which have now been deposited onto the Ag surface have a Raman spectrum with a broad peak which is similar to the Raman spectrum from amorphous Si as shown in Fig. 6(c)[13]. The systematic observation of the cluster coalescence and the detailed analysis of the Raman spectra compared with that of amorphous Si may provide some insight into the structure of amorphous Si.

ACKNOWLEDGEMENT

The authors thank E. Dons for RBS measurement, E. Bower for constructing the cluster equipment, D. Windt for the program for Fresnel multilayer calculation and J. Rowe, L. Brus, Y. Chabal and M. Hines for enlightening discussions.

REFERENCES

- 1) W. L. Brown, R. R. Freeman, K. Raghavachari and M. Schluter, *Science* **235**, 860(1991).
- 2) M. F. Jarrold, *Science* **252**, 1085(1991).
- 3) C. C. Arnold, T. N. Kitsopoulos and D. M. Neumark, *J. Chem. Phys.* **99**, 766(1993).
- 4) T. N. Kitsopoulos, C. J. Chick, A. Weaver and D. M. Neumark, *J. Chem. Phys.* **93**, 6108(1990).
- 5) C. C. Arnold and D. M. Neumark, *J. Chem. Phys.* **99**, 3353(1993).
- 6) J. E. Bower and M. F. Jarrold, *J. Chem. Phys.* **97**, 8312(1992).
- 7) E. Kretschmann, *Z. Physik* **241**, 313(1971).
- 8) Y. J. Chen, W. P. Chen and E. Burstein, *Phys. Rev. Lett.* **36**, 1207(1976).
- 9) K. Sakaoda, K. Ohtaka and E. Hanamura, *Solid St. Comun.* **41**, 393(1982).
- 10) W. Schlemminger and D. Stark, *Thin Solid Films* **137**, 49(1986).
- 11) E. C. Honea, A. Ogura, C. A. Murray, K. Raghavachari, W. O. Sprenger, M. F. Jarrold and W. L. Brown, *Nature* **366**, 42(1993).
- 12) R. F. Hout, B. A. Levi and W. J. Hehre, *J. Comput. Chem.* **3**, 234(1982).
- 13) H. Tanino, G. Ganguly and A. Matsuda, *Phys. Rev. B*, **46**, 15277(1992).

PART V

Elemental Imaging

ELEMENTAL MAPPING BY ENERGY-FILTERED ELECTRON MICROSCOPY

ONDREJ L. KRIVANEK*, MICHAEL K. KUNDMANN* and XAVIER BOURRAT**

*Gatan Research and Development, 6678 Owens Drive, CA 94588, USA

**LCTS, CNRS-SEP-UB1, 3 Allée de la Boëtie, 33600 Pessac, FRANCE

ABSTRACT

Energy-filtered imaging in a transmission electron microscope provides a fast and quantitative technique for mapping the distribution of elements in solids at nm-level resolution. The technique and its instrumental requirements are reviewed, and illustrated in the context of materials science.

INTRODUCTION

Quantitative elemental mapping with nm-level resolution requires a probe that penetrates into the material so that it samples the interior rather than the surface, and interacts with the material in a way that is element-specific and strong enough to give recognizable signals from nm-sized volumes.

Of the several possible candidates, electrons of 100-1000 keV energy are arguably the closest to the ideal probe. They are able to penetrate thin foils prepared from bulk materials, where they scatter both elastically and inelastically. 0.2 nm resolution images showing detailed atomic arrangements can be formed with the elastically scattered electrons [1]. Inelastic scattering is localized more poorly than the elastic scattering, and generally gives rise to nm-level resolution images. Some of the scattering is due to inner shell ionization edges, whose threshold energies are element-specific [2]. Images formed with electrons whose energy losses correspond to an ionization edge of a particular element show enhanced intensity in areas rich in that element. Combining several images taken with electrons of energy losses above and below an edge threshold leads to quantitative maps of the distribution of most elements present in concentrations greater than about 1%.

The energy-filtered images can be formed either in a fixed beam transmission electron microscope (TEM) equipped with an energy filter, or in a scanning transmission electron microscope (STEM) equipped with an electron spectrometer. In the STEM approach, a narrow probe is scanned over the sample, and an electron energy spectrum is recorded at every pixel. The advantage of this method is that all the channels of a spectrum can be recorded in parallel, resulting in a complete spectrum at each pixel with just one exposure of the sample by the electron beam. This minimizes radiation damage, and makes it possible to process the spectra using sophisticated quantitative algorithms.

In the TEM approach, the image information from all the image pixels is collected in parallel, but for only one pass-band of electron energies at a time. Simple elemental mapping requires a minimum of three energy-filtered images to be recorded per mapped element, resulting in an increased irradiation dose. More sophisticated mapping algorithms capable of providing error estimates or of separating closely spaced edges require an even larger number of energy-filtered images, and a correspondingly larger dose. However, because entire images are acquired in parallel, elemental maps with many pixels (there are 2.6×10^5 pixels in a 512 x 512 map) can be acquired much more quickly than in the pixel-by-pixel STEM approach.

The TEM and STEM approaches were initiated about 3 decades ago by Castaing's and Crewe's groups respectively [3,4]. Their wide-spread adoption was hindered by the available instrumentation, which was able to sort the electrons according to their energies, but lacked efficient electronic detectors and user-friendly software that could automatically quantify the collected data into elemental maps. These obstacles are now being overcome [5,6], permitting a fuller evaluation of the usefulness of the techniques. In this paper we describe the energy-filtered TEM approach, and illustrate it with several examples. The STEM approach is reviewed elsewhere in these proceedings [7].

ENERGY-FILTERED IMAGING IN A TEM

Energy-filtered transmission electron images are produced in a 3-stage process illustrated in Fig. 1. First, a non-filtered electron image is obtained as in conventional TEM: a thin sample is illuminated by a monochromatic beam of 100-1000 keV electrons, and an image is formed by one or more electromagnetic round lenses. Second, the image is transformed into a spectrum of electron energies in an energy filter, and a part of the spectrum is selected by an energy-selecting slit. Third, the selected part of the spectrum is transformed back into an image.

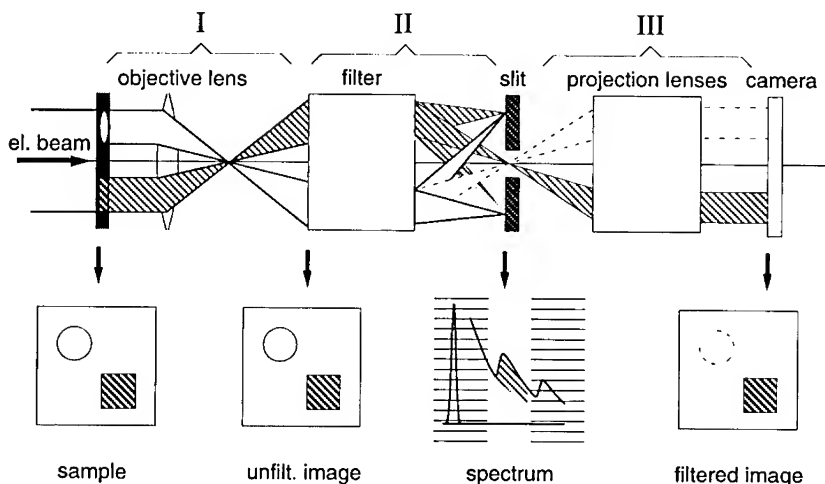


Fig. 1. Principle of energy-filtered TEM as used for chemical mapping. The shaded part of the spectrum is excluded by the energy-selecting slit. The square feature has an inner shell ionization edge in the energy interval selected by the slit, and is imaged with high intensity in the filtered image. The round feature contributes only spectrum background to these energies, and is therefore imaged weakly in the energy-filtered image.

Energy filters constructed so far fall into two categories: in-column filters that are typically located between the first and the second intermediate lenses of the microscope, and post-column filters located below the viewing chamber. The performance of the two types is broadly comparable. The largest difference between the two designs from the user's point of view is that post-column filters can be retrofitted in the field to most microscopes and can therefore take advantage of the many specialized capabilities provided by microscopes made by different manufacturers, whereas in-column filters must be incorporated into the microscope at the time the microscope is made.

Fig. 2 shows a schematic diagram of a recently developed post-column filter [8]. The parts of the instrument corresponding to the three separate stages of the formation of the energy-filtered image are indicated. The unfiltered image is projected by the microscope onto the microscope viewing screen (stage I). When the screen is lifted, a part of the image selected by the filter's entrance aperture enters the magnetic prism and its auxiliary quadrupoles, and is transformed into an energy-loss spectrum focused at the energy-selecting slit (stage II). The image information at this level is contained in the direction of the traveling electrons, and the spectrum begins to transform itself back into an image as soon as the electrons progress a short distance beyond the slit. The full transformation into an energy-filtered image is accomplished by an imaging assembly consisting of 4 quadrupole and 5 sextupole lenses (stage III). The assembly accepts the highly distorted image

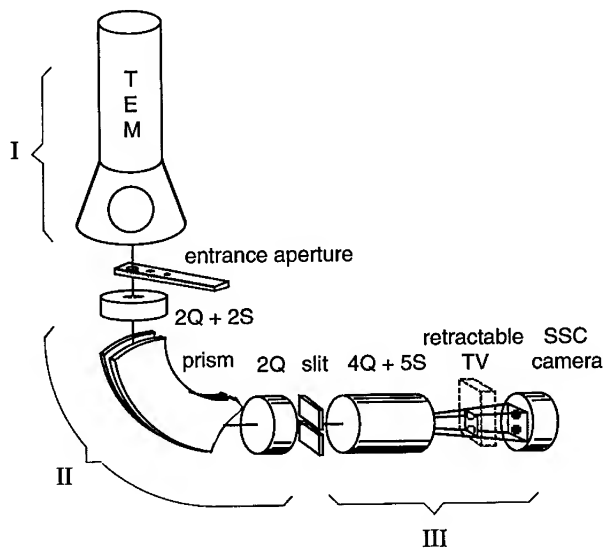


Fig. 2. Schematic diagram of the post-column imaging filter described in this article. Q = quadrupole lens, S = sextupole lens.

emerging from the slit, and transforms it into an achromatic image that shows no first-order dependence on the energy and is free of second-order aberrations and distortions.

As with an in-column imaging filter [9], there are several other modes of operation of the instrument besides energy-filtered imaging. If the excitations of the lenses of the microscope are modified so that a diffraction pattern is projected into the filter instead of an image, energy-filtered diffraction patterns are formed. Similarly, if the post-slit lenses of the filter are made to image the spectrum formed at the slit rather than to transform it into an image, the instrument performs as an electron spectrometer. Depending on which way the microscope and the filter are operating, four different modes of operation are therefore possible: energy-filtered imaging, energy-filtered diffraction, parallel-detection electron energy-loss (PEEL) spectroscopy with specimen area selection, and PEEL spectroscopy with scattering angle selection. The images, diffraction patterns and spectra are read out either by a TV-rate camera that can be pneumatically inserted into the electron beam, or by a slow-scan CCD camera that provides 1024×1024 independent pixels, and an excellent sensitivity for signals varying in intensity by up to 5 orders of magnitude. The whole instrument is controlled by software that permits a high degree of automation, flexibility and user friendliness.

Filters of the above design have been interfaced to microscopes operating at 100 keV to 1.25 MeV, and have produced a rich variety of experimental results, e.g. [10-14]. In the imaging mode of operation, the filters typically capture images of similar or better quality than the unaided microscope. In the spectroscopy mode, the filters improve on the performance of standard PEEL spectrometers, largely due to the superior performance of the slow scan CCD detector [15] compared to the photodiode arrays used in typical parallel-detection spectrometers [16]. In this paper we concentrate on applications of the filters to elemental mapping in materials science.

ELEMENTAL MAPPING IN A TEM

In order to ionize an atom by ejecting an inner shell (core) electron, the ionizing particle must supply the core electron with an energy greater than or equal to the energy needed for a transition to the first available unoccupied state. This rule is responsible for the threshold of each ionization edge. There is no limit on the maximum energy transferred to the core electron, which carries the excess energy away as its kinetic energy. This gives rise to a gradually weakening continuum above each edge threshold.

In a transmission electron microscope, the energy-loss events transform a monochromatic beam of 100-1000 keV electrons incident on a thin sample into a polychromatic beam that contains electrons of all energies up to the original primary energy. Depending on the element and the ionized shell, the energy losses corresponding to the edge thresholds range from a few tens of eV to tens of keV, and there is typically at least one edge for every element in the energy-loss range from 100 to 3000 eV, which is especially well suited for elemental mapping [2].

Because the edges always lie on a continuous background due to lower-energy edges, obtaining elemental maps requires that the background be taken into account. The standard method consists of fitting the pre-edge spectrum to a theoretical model described by AE^{-r} , where A is a constant, E is the energy loss expressed in eV, and r is a coefficient typically between 2 and 5 [17], and extrapolating and subtracting the fitted form from underneath each edge (see Fig. 4). In the typical energy-loss spectrum detected in parallel, there are many data points in both the background fit region and the edge region, enabling the background fitting and extrapolation to be performed with a high degree of precision.

In energy-filtered TEM imaging, each data point along the energy axis requires a separate image, and the background extrapolation and subtraction procedure must be performed at each pixel. In order to keep the irradiation dose of the sample and the processing time to minimum, the procedure is normally simplified so that it uses just two images separated by 30 to 100 eV in front of an edge to determine the shape of the background, and one image after the edge to determine the net contribution of the element to the spectrum. In order to maximize the signal in the images, they are collected with the slit selecting an energy interval equal to about 0.5 to 1 times the energy separation between the images.

The acquisition of the required three energy-filtered images as well as the processing necessary for an elemental map are performed automatically. The process is started when the user selects the command "Acquire elemental map" from the Filter menu which appears in the image acquisition software, and specifies which element is to be mapped. The software suggests appropriate energy intervals, which are either approved or modified by the user. The software then acquires the three images, processes them, and displays the elemental map. The processing options include automatic or manual alignment of the component images, which is useful for countering the effect of specimen drift between exposures, and noise reduction achieved by smoothing the variation of the slope of the fitted background between neighboring pixels [18]. The time per elemental map depends on the acquisition time of each image (typically 5 to 60 seconds) and the speed of the computer used for the processing. The total time is typically between 1 and 5 minutes for a 512 x 512 pixel map. The spatial resolution of the maps depends on the edge type and the microscope set-up. Attaining 1-5 nm resolution is routine, and < 0.5 nm is possible in especially favorable cases [6, 10].

PRACTICAL EXAMPLES OF ELEMENTAL MAPS

Figures 3-6 illustrate the elemental mapping with an example taken from the field of ceramics. Fig. 3 shows an elastic-only image of a thin cross-section of a ceramic composite consisting of coated SiC fibers embedded in a glass matrix consisting mostly of magnesia, alumina and silica [19]. The image was obtained with 200 keV electrons in a microscope equipped with a LaB₆ gun. The energy-selecting slit was set to exclude electrons that lost more than about 8 eV.

The image is shown twice: as-acquired (a), and "crispended" using a contrast-enhancement procedure in which the image was smoothed, multiplied by 0.6 times and then subtracted from the original image, and the contrast of the result stretched (b). The crispended image shows a number of morphological features not visible in the as-acquired image. However, neither image contains any information about the distribution of chemical elements among the various phases of the material.

Fig. 4 shows an energy-loss spectrum acquired from an area corresponding roughly to the part of the sample shown in Fig. 3. No objective aperture was used, thus maximizing the collection efficiency. Boron, carbon, nitrogen and oxygen K-edges are clearly resolved in the spectrum, with thresholds at 188, 284, 399 and 530 eV, respectively. The separation between them was sufficient for extrapolating and subtracting the background under each edge using the AE^r technique. The subtracted "net" edges are also shown in the figure. Quantifying the subtracted edges gave the elemental concentrations shown in the inset in the figure. The expected relative error of the concentrations is about 10%.

Fig. 5 shows maps from the four elements acquired with the automatic elemental mapping

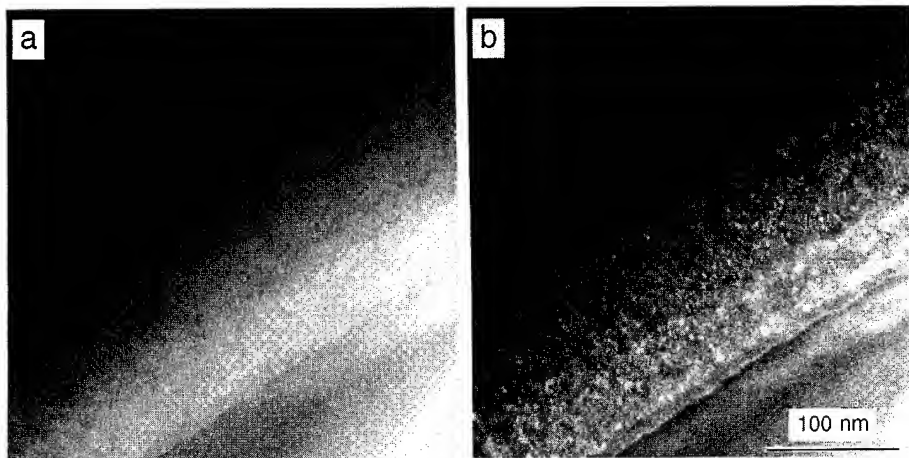


Fig. 3. Elastic-only energy-filtered images of a cross-section through a ceramic composite. (a) as acquired, (b) "crispened" by image processing. Part of a fiber core is visible at lower right, the glass matrix at upper left. The central part of the image shows the coating of the fiber.

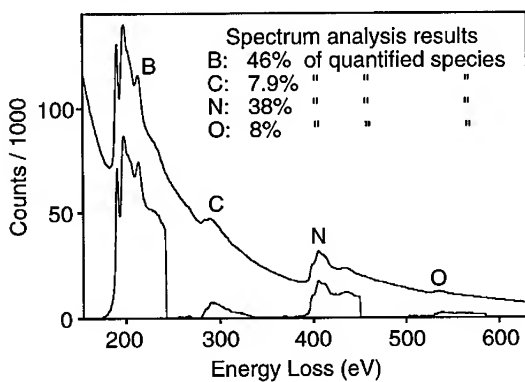


Fig. 4. As-acquired spectrum from the sample area shown in Fig. 3, subtracted (net) edges, and quantification results

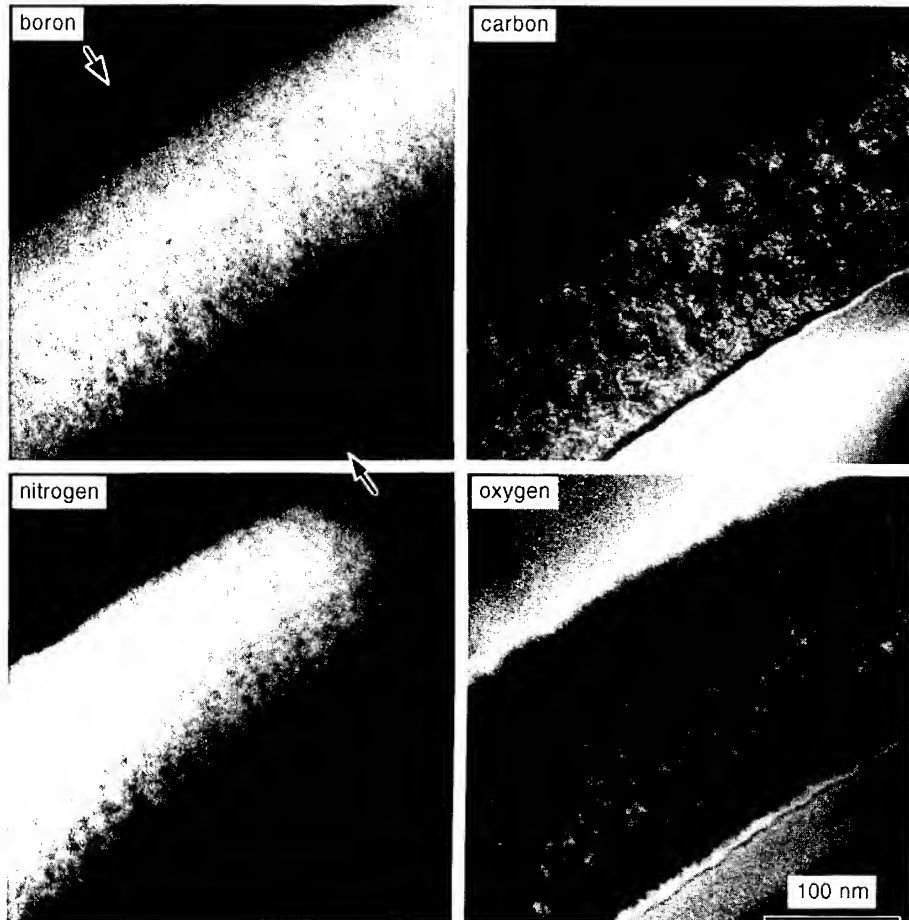


Fig. 5. 512 x 512 pixel chemical maps of boron, carbon, nitrogen and oxygen.

software, using the K-edges of the elements. The maps were obtained with the energy-selecting slit set to 20 eV width for boron, and 30 eV for the other elements. Combined exposure times for the three required images were 18, 60, 60 and 120 seconds for the boron, carbon, nitrogen and oxygen maps, respectively. Silicon maps of the same area are shown further on in this paper. Magnesium and aluminum maps were also collected [20], but are not shown here.

Comparing Fig. 5 to the elastic-only image of Fig. 3 reveals the great richness of additional information made available by elemental mapping. We leave a detailed discussion of the materials science behind the observed elemental concentrations to a future paper [20], and only summarize the main features discernible in the maps. As an aid to the description, in Fig. 6 we show line profiles drawn through identical locations of the four elemental maps shown in Fig. 5, plus profiles of magnesium and silicon maps of the same sample area obtained using K-edges. The aluminum profile followed closely the magnesium profile, and is not shown.

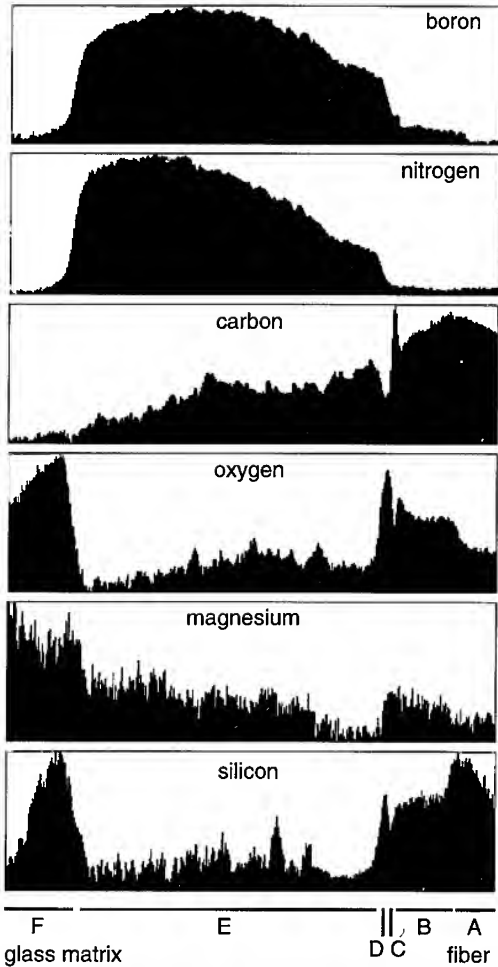


Fig. 6. Line profiles through the elemental maps of Fig. 5, and the corresponding magnesium and silicon maps. The location of the profile is indicated by arrows in the boron map. The profiles are "fat" profiles, obtained by integrating perpendicular to the profile line over 50 pixels.

The average composition of the as-received fibers was Si: 38 at.%, C: 43 at.%, O: 15 at.%, H: 3.7 at.% and N: 0.5 at.%. Accordingly, the elemental maps show the fiber to consist mostly of carbon, silicon and some oxygen (see region A in Fig. 6). The oxygen concentration is enhanced in a broad band near the fiber's outer boundary (B) that is also enriched in boron, magnesium and aluminum, and depleted in silicon. The outer surface of the fiber consists of two thin layers, the first one containing mostly carbon (C), and the second one enriched in silicon and oxygen (D). These are collectively known as the oxidation layer of the fiber. Next there is the fiber coating (E) consisting primarily of boron, nitrogen and carbon, with smaller concentrations of oxygen, magnesium and silicon. The boron and nitrogen maps of the coating are nearly identical, and have a filamentous appearance. The contrast in the carbon map of the coating is reversed compared to the boron and nitrogen maps. This indicates that boron and nitrogen formed a porous BN structure surrounded by a mostly carbon matrix. The oxygen map of the region shows many small particles. These correlate closely with particles appearing in silicon maps (Fig. 7). This demonstrates that there were particles containing silicon and oxygen (probably SiO_2) dispersed throughout the coating. The profiles

terminate in the glass matrix (F), which contains mainly oxygen, magnesium, aluminum and silicon, and is revealed to be a phase-separated magnesia-alumina-silica (MAS) glass by the magnesium, aluminum and silicon maps.

DISCUSSION

The example of an elemental map series given above illustrates most of the problems and advantages that arise with elemental mapping by energy-filtered imaging. The chief advantage of the technique is that it provides insights into the elemental composition of the sample which are not readily obtainable by any other means. Several of the results presented above are completely new, despite extensive previous studies of the material by TEM and X-ray microanalysis.

The most important problem is that collecting the map data requires the sample to be exposed to unusually large electron doses. This is because the probability of an inner shell ionization is about 10^3 to 10^6 times smaller than the probability of elastic scattering, which means that elemental maps require correspondingly higher beam doses than elastic imaging (but smaller doses than X-ray maps). The precise strength of the ionization events varies depending on the edge type and energy, and is the strongest for O_{4,5}, N_{4,5}, M_{4,5} or L_{2,3} edges occurring at 100 eV or lower energy loss, and weakest for K edges occurring above 1000 eV. Maps formed with edges situated between 100 and 500 eV energy loss typically require a dose of 10^6 to 10^8 primary electrons per pixel. Maps formed with higher energy-loss edges such as the silicon K-edge require doses of up to 10^{10} electrons per pixel, and acquisition times of hundreds of seconds. The sample examined here showed no readily discernible damage even under such a dose, but there are many other types of samples in which meaningful mapping using energy-filtered imaging will be made impossible by their susceptibility to radiation damage, even with a nearly 100% efficient instrument such as the one used here.

Provided that the sample is sufficiently resistant to radiation damage, optimizing the signal-to-noise ratio in the elemental maps usually means trying to maximize the intensity in the individual energy-filtered images. The best elemental maps are typically obtained using larger beam emission settings, larger condenser apertures, increased probe size and longer exposure time than those used in normal imaging.

Another technique useful for improving the signal-to-noise ratio in elemental maps is to simplify the signal processing by taking only one image before an edge and one image after an edge, and simply dividing the two images. The result is known as a jump ratio image. Jump ratio images do not permit the background fit to vary from pixel to pixel. This results in considerably reduced statistical noise in the image. However, they provide only a qualitative rather than quantitative depiction of an element's concentration, and can be rendered completely meaningless by a strong variation of the background due to another edge at a lower energy. Fig. 7 illustrates the advantages and the drawbacks of the technique by comparing jump ratio images with elemental maps taken from the sample of Fig. 5. The silicon jump ratio images closely resemble the silicon elemental maps, but their clarity is better due to an improved signal-to-noise ratio, even though they were recorded with only 0.67 of the electron dose needed for the proper maps. The silicon jump ratio image formed with the L_{2,3} edge also shows less contrast change due to thickness variation than the L_{2,3} map. The boron jump ratio image, on the other hand, contains spurious dark spots not present in the elemental map. These spots are due to the variation in the background in front of the boron edge caused by the silicon L_{2,3} edge originating from the SiO₂ particles.

Because of the possibility of artifacts with jump ratio imaging, proper elemental mapping requiring 3 or more energy-filtered images is generally the preferred technique. Nevertheless, jump ratio imaging can be very useful when closely spaced edges do not allow the correct background fitting and subtraction to be performed, and also when the proper elemental maps contain too much statistical noise to be useful. Pronounced artifacts with the jump ratio technique are less likely when the edge energy is high (above 500 eV), because variations in the pre-edge background tend to be small at higher energy losses.

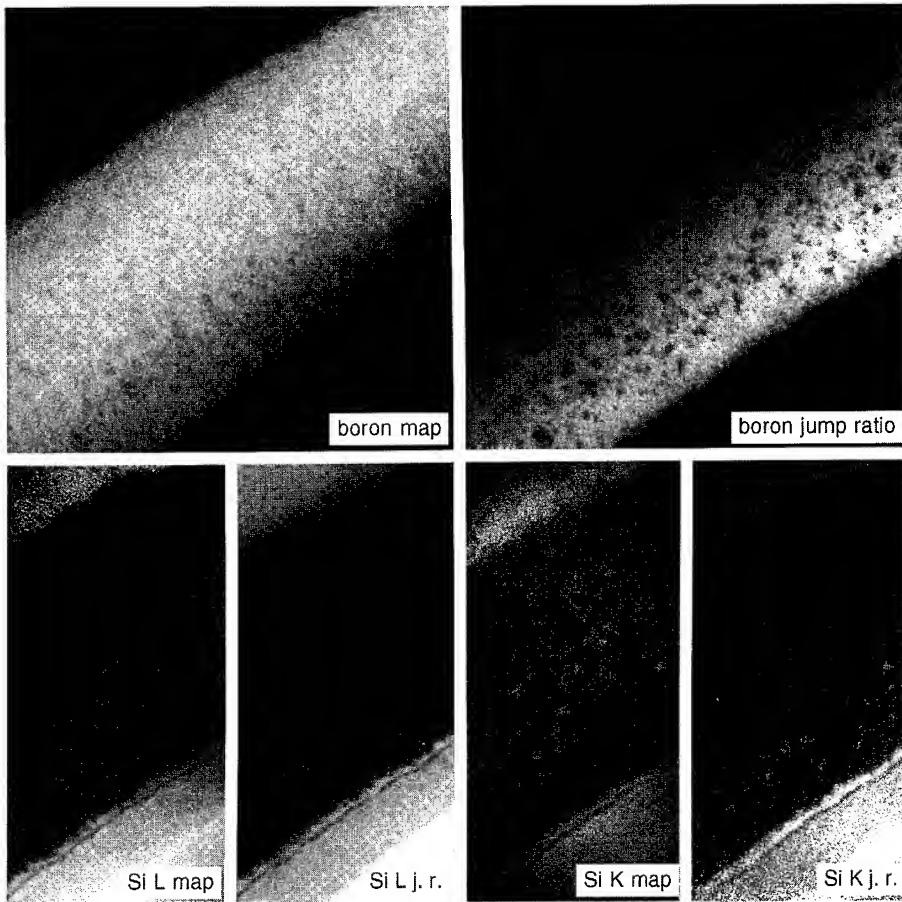


Fig. 7. Jump ratio images of boron and silicon compared with chemical maps of the two elements.

Other factors to note with the present form of elemental mapping are that in thin sample regions, the maps display the amount of the element per pixel rather than the elemental concentration, and that in specimen areas thicker than about 100 to 200 nm at 200 keV, multiple inelastic scattering makes the computed amount of each element smaller than the real amount. The effect of the multiple scattering is especially strong for low-energy edges located on a steeply descending background. This means that if there is a choice between a low-energy edge and a high-energy one to be used for mapping of a particular element, the low-energy edge will typically provide better sensitivity (because the edge cross-section is higher), but the high-energy edge will provide a more accurate value for the amount of the element present (because specimen thickness and edge overlap are typically less important at the higher energy loss). In the example given here, magnesium, aluminum and silicon maps and profiles could be produced using either the L_{2,3} edges or the K edges (see Fig. 7). In all cases, the more accurate results produced with the K-edges were preferred, despite their longer exposure times and larger amounts of statistical noise.

More minor concerns arise with crystalline samples in which elastic scattering can produce

contrast that affects the intensity of the elemental maps. However, this contrast can be largely accounted for if an elastic image is recorded at the same time as the series of energy-filtered images, and it is automatically cancelled in jump ratio images. Yet another practical difficulty arises if there is a drift of the specimen position, but this can be overcome by aligning the component images using cross-correlation prior to processing, and by dividing longer exposures into a series of shorter ones. Drift of the selected energy caused by high voltage or prism current fluctuations is another problem, but this can be cured by momentarily switching into a spectrum mode, and checking and correcting the position of the spectrum.

CONCLUSION

Depending on the element type and concentration, present-day imaging filters allow gray-scale elemental maps of 512×512 pixels to be obtained in a normal transmission electron microscope in about 1-5 minutes, at a resolution of typically 1-5 nm. The technique is at its most powerful for light and medium weight elements present in local concentrations greater than 1-5 at. %. It promises to find uses in all fields in which elemental concentrations of this type have an important influence on a material's properties, such as in semiconductor processing, composite and nano-engineered materials, mineralogical and geological materials, and also a broad range of biological and biomimetic materials.

ACKNOWLEDGMENT

We are grateful to N. Ricca of LCTS for preparing the composite samples used in this study.

REFERENCES

1. D.J. Smith and J.C. Barry, in *High Resolution Transmission Electron Microscopy*, edited by P.R. Buseck, J.M. Cowley and L. Eyring (Oxford University Press, New York and Oxford, 1988) p. 477.
2. C.C. Ahn and O.L. Krivanek, *EELS Atlas*, (Gatan, 780 Commonwealth Drive, Warrendale, PA 15086, 1983).
3. R. Castaing and L. Henry, *Compt. Rend. Acad. Sci. Paris* **255**, 76 (1962).
4. A.V. Crewe, M. Isaacs and D. Johnson, *Rev. Sci. Instr.* **42**, 411 (1971).
5. J.A. Hunt and D.B. Williams, *Ultramicroscopy* **38**, 47 (1991).
6. O.L. Krivanek, A.J. Gubbens, N. Dellby and C.E. Meyer, *Microsc. Microanal. Microstruct.* **3**, 187 (1992).
7. R.D. Leapman and J.A. Hunt, these proceedings.
8. O.L. Krivanek, A.J. Gubbens and N. Dellby, *Microsc. Microanal. Microstruct.* **2**, 315 (1991).
9. L. Reimer, I. Fromm and R. Rennekamp, *Ultramicroscopy* **24**, 339 (1988).
10. H. Hashimoto, Y. Makita and N. Nagaoka, *Optik* **93**, 119 (1992).
11. J.W. Steeds and R. Vincent, these proceedings.
12. A.J. Gubbens and O.L. Krivanek, *Ultramicroscopy* **51**, 146 (1993).
13. A.J. Gubbens and O.L. Krivanek, *Proceedings 13th International Congress on Electron Microscopy*, to be published (1994).
14. O.L. Krivanek, D.N. Bui, D.A. Ray, C.B. Boothroyd and C.J. Humphreys, *Proceedings 13th International Congress on Electron Microscopy*, to be published (1994).
15. O.L. Krivanek and P.E. Mooney, *Ultramicroscopy* **49**, 95 (1993).
16. O.L. Krivanek, C.C. Ahn and R.B. Keeney, *Ultramicroscopy* **22**, 103 (1987).
17. R.F. Egerton, *Electron Energy-Loss Spectroscopy in the Electron Microscope*, (Plenum Press, New York and London, 1986).
18. M.K. Kundmann and O.L. Krivanek, *MAS Journal*, Volume **2** Supplement (Proceedings 1993 MAS meeting), p. S276.
19. N. Ricca, Thesis N° 996, Univ. Bordeaux (1994).
20. X. Bourrat et al., to be published.

EELS IMAGING OF BIOLOGICAL MATERIALS

R.D. LEAPMAN*, S. SUN*, J.A. HUNT** AND S.B. ANDREWS***

*Biomedical Engineering and Instrumentation Program, National Center for Research Resources, National Institutes of Health, Bethesda, MD 20892; **Gatan R & D, Pleasanton, CA 94566;

***Laboratory of Neurobiology, National Institute for Neurological Diseases and Stroke, National Institutes of Health, Bethesda, MD 20892.

ABSTRACT

Parallel-detection electron energy loss spectroscopy (EELS) in the scanning transmission electron microscope provides a very sensitive means of detecting specific elements in biological systems. By analyzing EELS spectrum-image data recorded from rapidly-frozen and cryosectioned tissue it is possible to map quantitatively the distribution of the biologically important element, calcium, which is typically present at concentrations of only a few parts per million in cellular structures some tens of nanometers in diameter. A significant improvement (factor of four) in calcium detectability has been demonstrated for EELS compared with energy-dispersive x-ray spectroscopy. The spectrum-imaging technique has also been applied to map water distributions in hydrated biological specimens by utilizing the valence electron excitations.

INTRODUCTION

Developments in EELS techniques for applications to biological systems may be interesting to the materials scientist for several reasons. Firstly, the need to measure low elemental concentrations at the parts per million levels in cells has stimulated efforts to improve instrumentation and spectral processing techniques so that detection limits can be optimized. Historically, this trend started with the work of Isaacson and Johnson [1] who predicted nearly twenty years ago that single atom detectability should be feasible in biological specimens using EELS. Later on, Shuman et al. [2] developed parallel detection techniques for EELS and showed that trace analysis of biological systems could be achieved in practice. This has been followed by more recent work demonstrating that near single-atom sensitivity is indeed achievable for the analysis of individual macromolecules [3] as well as inorganic particles [4, 5]. Secondly, there have been new approaches to imaging biological structures with the so-called "spectrum-imaging" technique whereby entire spectra are acquired at each pixel in a two-dimensional map of the specimen [6-9]. Applications have included not only collection of elemental distributions but also the distributions of compounds, e.g., water and protein, in subcellular compartments [10]. This spectrum-imaging approach has proven extremely flexible in that optimal data processing methods can be applied off-line. Thirdly, the sensitivity of biological specimens to irradiation in the electron microscope [11] has required new methods for minimizing and characterizing the effects of beam damage [12]. EELS is particularly useful in this respect because it can detect the low atomic number elements that are lost under electron irradiation. Furthermore, it can also provide information about radiation-induced chemical changes that occur in the specimen through analysis of the fine structure. The applications of such techniques are likely to be valuable in the characterization of polymers [13]. Finally, the biological systems themselves may be relevant, e.g., for the characterization of biomimetic materials [14]. This paper discusses some recent "biology-inspired" developments in EELS in the context of the field-emission scanning transmission electron microscope (STEM).

EXPERIMENTAL APPROACHES AND PROCEDURES

The dedicated STEM has a number of features that are useful for performing EELS analysis on biological specimens. In particular, it has a high-brightness field-emission source that provides a

sub-nanometer diameter electron probe, and an annular dark-field detector that collects elastically scattered electrons with extremely high efficiency. The main biological applications of STEM have hitherto involved low-dose dark-field imaging whereby molecular weights of large protein assemblies can be accurately determined [15]. Apart from its use as a structural device, the STEM also offers exciting potential as a microanalytical tool because it is capable of providing very large currents (several nanoamperes) into probe diameters of around 5 nm. These conditions are optimal for microanalysis of subcellular structures by EELS, but it is only now that this possibility is being fully realized because of two other requirements: (i) it is essential to collect the energy loss spectrum in parallel so that detection limits can be optimized [2, 16], and (ii) the handling of cryosectioned tissue requires a stable cryotransfer specimen stage which has only recently become available [17].

Fig. 1 shows a simplified diagram of the system used in the present work, a VG Microscopes HB501 STEM which is operated at a beam energy of 100 keV and is equipped with a cryotransfer specimen stage as well as a Gatan model 666 electron energy loss spectrometer [18]. Electrons pass through the central aperture of an annular dark-field detector (ADF) and then into the magnetic field of the 90° sector after which the energy dispersion is magnified by a series of quadrupole lenses. An electrostatically isolated drift tube running through the spectrometer can be used to apply precise energy offsets to the spectrum. This feature is utilized for energy calibration and for acquiring difference-spectra. The energy loss spectrum is recorded in parallel by means of a 1024-channel photodiode array detector coupled to a yttrium aluminum garnet (YAG) scintillator by a fiber-optic plate. The ADF detector provides a morphological elastic image of the specimen simultaneously with the inelastic EELS data. An ultrathin window energy-dispersive x-ray detector (Noran Micro-ZHV) is also available to provide complementary information about concentrations of elements that are not suitable for EELS analysis.

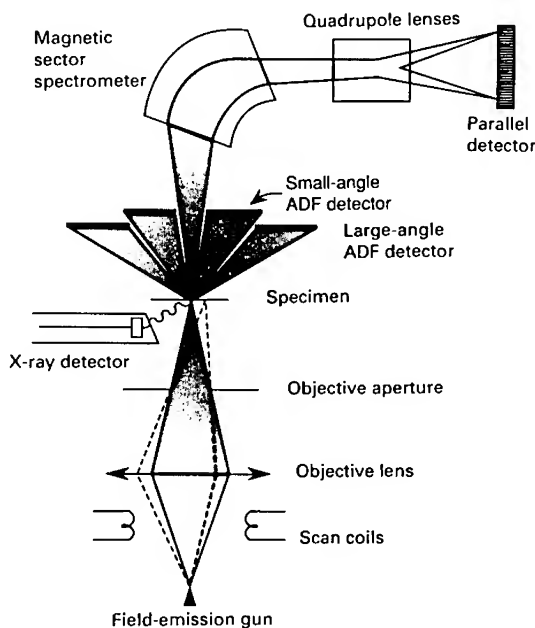


Fig. 1 Schematic diagram of STEM with parallel-EELS

The instrumentation for acquiring EELS spectrum-images has been described previously [7]. In brief, spectra are transferred to a PC-486 computer from the spectrometer photodiode interface via a direct memory access (DMA) unit in order to allow for high data transfer rates required for spectrum-imaging. The PC also controls the STEM deflection coils so that the probe can be digitally rastered on the specimen. The spectrum-images are stored on disk and then backed up on tape; a non-compressed 128x128 pixel EELS-image requires 32 Mbyte of storage. Annular dark-field images are acquired digitally either by feeding the pulse output of the scintillator / photomultiplier into a fast counter (low-dose conditions), or by digitizing the analog output of the detector (high-dose conditions). These images are then transferred to an Apple Macintosh II computer for analysis. EELS spectrum-images are processed by specially designed software running on the PC, whereas the spectra are processed on the Macintosh II computer using the Gatan EL/P program [19].

The raw energy loss spectrum from biological specimens typically only reveals the presence of the major core edges, carbon, nitrogen, and oxygen [20]. For example, the signal/background ratio at the calcium L₂₃-edge is below 0.1% for physiologically relevant concentrations in the millimolar range. The signal of interest is therefore hidden and special acquisition and processing techniques must be employed to extract it. At high electron fluxes the largest source of noise originates from channel-to-channel gain variations in the detector. One method to reduce these effects involves the use the difference acquisition technique [2-5, 21]. The first-difference spectrum is obtained by acquiring two spectra shifted electrically over the photodiode array by energies -Δ/2 and +Δ/2. In this way, the pattern noise stays fixed and is eliminated when the two spectra are subtracted,

$$I'(E) = I(E + \Delta/2) - I(E - \Delta/2) \quad (1)$$

This operation is similar to a first derivative and it enhances small spectral features situated on a large slowly-varying background. To optimize the signal-to-noise ratio in the first-difference spectrum we should set Δ to be somewhat greater than the energy width of the feature. For example, if we wish to detect a weak Ca L₂₃ edge we should select Δ in the range 6 eV to 10 eV, the measured width of the pair of white lines being approximately 4 eV. The main disadvantage of the first-difference acquisition is that the detective quantum efficiency is effectively decreased by a factor of two but this often is not a limiting factor. Recent papers discuss in detail the optimal parameters for difference acquisition [22, 23] as well as other iterative schemes for reduction of detector gain variations [24].

Difference spectra can be quantified by using multiple least squares to fit reference spectra from standards. This may be complicated for a general analytical problem because the detailed core edge shape depends on the type of chemical bonding. For calcium, however, the L₂₃ excitation is dominated by a white line resonance and its edge shape does not vary significantly from specimen to specimen. A calcium reference spectrum can simply be obtained from a specimen of calcium chloride and the background can be approximated by a spectrum recorded from a thin carbon film. Thickness effects can also be taken into account by incorporating plural scattering terms into the reference spectra [25]. The first-difference spectrum can thus be expressed as the sum of a calcium reference spectrum $X_{Ca}(E)$ with fitting coefficient a_{Ca} and contributions from the background $X_b(E)$ with fitting coefficient a_b ,

$$I'(E) = a_{Ca}X_{Ca}(E) + \sum_b a_bX_b(E) \quad (2)$$

where the calcium reference spectrum has been normalized by dividing by $S_{Ca}^{ref}(\Delta, \beta)$ the integrated signal in energy window Δ for collection semi-angle β,

$$X_{Ca}(E) = \frac{I_{Ca}^{ref}(E)}{S_{Ca}^{ref}(\Delta, \beta)} \quad (3)$$

A quantitative estimate for the atomic fraction N_{Ca}/N_C of calcium to carbon can then be obtained from the integrated carbon K-edge signal,

$$\frac{N_{Ca}}{N_C} = \frac{a_{Ca}}{S_C(\Delta, \beta)} \cdot \frac{\sigma_C(\Delta, \beta)}{\sigma_{Ca}(\Delta, \beta)} \quad (4)$$

where, $\sigma_{Ca}(\Delta, \beta)$ and $\sigma_C(\Delta, \beta)$ are the corresponding partial ionization cross section for calcium and carbon respectively.

RESULTS AND DISCUSSION

Elemental Mapping

The STEM spectrum-imaging approach is complementary to TEM energy-filtered imaging in which entire inelastic images are recorded in parallel by means of a two-dimensional detector (e.g., CCD array) but in which the spectral information must be recorded serially one energy loss at a time [26]. Energy-filtered imaging has a significant advantage when data from large numbers of pixels are required. Thus, a 512x512 pixel STEM spectrum-image would take two hours to acquire with a typical minimum integration time of 25 ms per pixel, whereas it might only take a few seconds in the energy-filtering microscope. Nevertheless, the STEM spectrum-imaging approach is essential for applications involving detection of physiologically relevant concentrations of trace elements like calcium in rapidly-frozen, cryosectioned tissue [27]. This is because precise background modeling must be used to extract the very weak signal. In the energy-filtering technique the post-edge background can only be extrapolated from other pre-edge images so that limited precision is available.

Table 1. Estimated number of Ca atoms at 1 mmol/kg wet wt concentration in a spherical organelle as a function of its diameter in a cryosection of thickness 100 nm; and the corresponding Ca atom fraction (excluding hydrogen) in the dehydrated specimen assuming 20% dry mass content.

Organelle diameter (nm)	Number of Ca atoms	Atom fraction of Ca
30	8	1.1×10^{-5}
50	36	1.8×10^{-5}
100	300	3.6×10^{-5}

Table 1 shows how few calcium atoms are contained within typical organelles when the Ca concentration is 1 mmol/kg wet weight of tissue ($10^{-3} \times 40$ g of Ca per kg). A 50 nm diameter organelle contains only 36 Ca atoms at an atomic fraction of around 18 ppm.

We have applied EELS spectrum-imaging to measure low calcium concentrations in brain where calcium is essential in the modulation of neuronal activity. Fig. 2a shows a dark-field STEM micrograph of a Purkinje cell dendrite in a rapidly-frozen, cryosectioned, and freeze-dried preparation of mouse cerebellar cortex. Two spectra, shifted in energy by $\Delta = \pm 3$ eV, were acquired at each pixel with a total recording time of approximately 1600 s (corresponding to a dwell time of 0.4 s per pixel). The maps were obtained with a probe current of approximately 5 nA and a collection semi-angle of 20 mrad. A nitrogen map was first generated by subtracting the background under the K-edge; this provided structural information about the distribution of proteins. By comparing the nitrogen map (Fig. 2b) with the corresponding dark-field image (Fig. 2a) recorded at low dose, it was possible to segment the EELS map into separate binary masks consisting of endoplasmic reticulum (ER) and mitochondria (Figs. 2c and 2d). By summing the first-difference spectra from these segmented spectrum-images and applying another high-pass digital filter to enhance further the visibility of the weak spectral features, the spectra in Fig. 3a and 3b were obtained. Quantitation of these spectra gave calcium concentrations of 4.9 ± 0.4 and 1.4 ± 0.4 mmol/kg dry weight in the ER and the mitochondria, respectively. These results support the conclusion that the ER and not the mitochondrion regulates intracellular calcium in neurons as in many other cell types [28].

The shorter acquisition times for EELS coupled with the spectrum-imaging capability make it feasible to sample exhaustively structures such as the Purkinje cell dendrites considered here. Using segmentation methods it then becomes possible to correlate changes that occur within a given structural unit, e.g., increase in cytoplasmic calcium with a decrease in ER calcium. Energy-dispersive x-ray spectra (EDXS) recorded with an ultrathin window detector (0.18 sterad solid-angle) under equivalent dose conditions indicate that the estimated calcium sensitivity of ± 3 mmol/kg (\pm standard deviation) is about four times lower than for EELS in agreement with earlier predictions [29]. However, several of the major elements (P, S, Cl and K) are more easily visible in the x-ray spectrum, demonstrating that the two techniques are complementary.

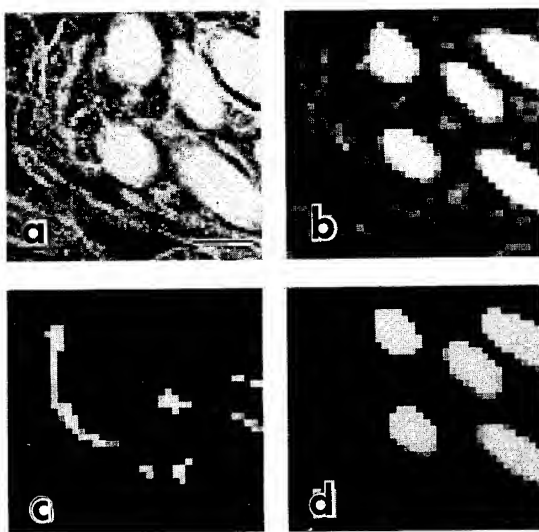


Fig. 2. Parallel EELS maps of Purkinje cell dendrite in mouse cerebellar cortex: (a) low-dose dark-field image, (b) high-dose nitrogen K-edge map segmented into (c) endoplasmic reticulum and (d) mitochondria. Bar = 200 nm.

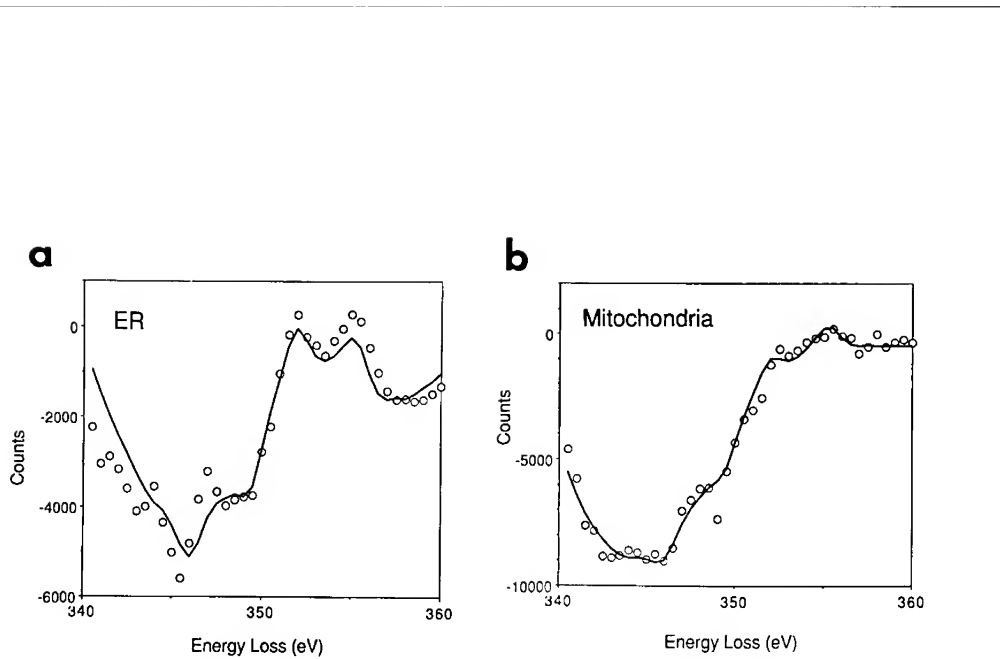


Fig. 3. Summed difference-spectra from four EELS-images of Purkinje cell dendrites: (a) endoplasmic reticulum and (b) mitochondria.

Chemical Mapping

The valence excitation spectrum, which includes energy losses in the range from zero to around 30 eV, can also be used to obtain useful information about the composition of cells. Although this spectral region has a much higher cross section than for the inner shell excitations, the expected variations due to compositional differences are more subtle [30]. Nevertheless, we have shown that the valence excitation technique does provide a practical basis for determining the water content of specific organelles in frozen-hydrated specimens [31]. The water content of subcellular compartments is an important physiological quantity that reflects how fluid and electrolyte concentrations are regulated both indirectly by osmotic effects following ion movements and directly through water-specific membrane channels in cells. Previously, analytical electron microscopy provided only an indirect determination of the subcellular water content in thin tissue sections because the measurements were made after dehydration [32].

The basis for the EELS water determination is evident in Fig. 4 which shows that significant differences exist between the energy loss spectra of water and protein. We see that the spectrum from ice has a plasmon maximum at 20.4 eV compared with 23.4 eV for the protein. Additionally, at lower energies the spectrum from ice contains zero intensity until a peak occurs at 9.1 eV which can be attributed to excitation of electrons across the band-gap, whereas a weaker peak at 6.7 eV in the protein can be attributed to excitation of π -states.

Experimentally we have found that the main contributions to the low-loss fine structure are due to intramolecular bonding and the interaction between these basic constituents are relatively unimportant. To determine the water mass fraction in an unknown specimen we can model its spectrum by expressing it as a linear sum of contributions from the constituent compounds. The spectra from these components can thus be treated as standard reference spectra and the coefficients can be determined by MLS fitting as described above for core-edge quantitation. First, we must remove effects of plural inelastic scattering by deriving the single-scattering distributions using the Fourier-logarithmic deconvolution procedure [30]. The single scattering distribution, $S_{\text{Hyd}}(E)$,

from the hydrated specimen is now given in terms of the single scattering distributions for the different components, $S_n(E)$, and the fitting coefficients, a_n , by the sum,

$$S_{\text{Hyd}}(E) = \sum_{n=1}^N a_n S_n(E) \quad (5)$$

In Eq. 5 all spectra have been corrected for the support film by subtracting an appropriate fraction of the carbon single-scattering distribution. In practice, we find that the experimental spectra can be modeled very well by a linear combination of just the protein and ice spectra. This is because protein is the major organic constituent and that spectra from other compounds are quite similar to each other. We find that the mass fraction of water F_{water} is given by,

$$F_{\text{water}} = \left(1 + K \frac{a_{\text{protein}}}{a_{\text{water}}} + \dots \right)^{-1} \quad (6)$$

where K is the ratio of cross section per unit mass for water to that for protein, which we have previously shown to be 0.89 ± 0.03 [31]. Eq. 6 can be generalized to take account of other organic constituents in the specimen such as nucleic acids, carbohydrates, and lipids by including additional reference spectra as indicated.

We have applied this method together with the spectrum-imaging technique to map the water distribution in hydrated cryosections of mouse liver that were cryotransferred into the STEM at liquid nitrogen temperature [10]. The images were acquired at low electron dose with an energy dispersion of 0.1 eV per channel and a dwell time of 0.15 s per pixel. By fitting the water and protein reference spectra at each pixel the water map in Fig. 5 was obtained. Values of $79 \pm 1\%$ (\pm standard error of the mean) and $56 \pm 1\%$ were obtained for the water content in the cytoplasm and mitochondria respectively, in good agreement with values obtained from other methods. The spatial resolution of the water maps is limited by radiolytic damage in the electron beam. Given a maximum allowed dose of 10^3 e/nm^2 [33], the minimum diameter of the specimen that can be analyzed is around 100 nm . Such a scale provides a useful resolution for analysis of hydrated cryosections; it is commensurable with the specimen thickness and also with the sizes of all but the smallest organelles. Higher resolution or greater precision in the EELS water measurement can be achieved by averaging spectra over many identical structures in the specimen.

CONCLUSION AND FUTURE PROSPECTS

The difficult demands of analyzing biological systems have helped to advance the technique of EELS with possible benefits for materials science. Instrumentation and processing techniques for EELS in the field-emission STEM have been developed to the stage where interesting biological applications are now feasible. The main difficulty with EELS microanalysis is the small core-edge signal/background ratio that is typically encountered but this can now be overcome with special processing techniques such as difference-acquisition. For biological applications parallel EELS provides an improvement in sensitivity by a factor of about four relative to EDXS for calcium detection. This capability of EELS is particularly significant because calcium is a very important element that is often present at levels that are only just detectable by EDXS. A similar advantage is found for other elements, including transition metals and lanthanides, and the EELS technique is likely to find materials science applications in the analysis of nanometer-scale particles [4]. Spectrum-imaging allows maximum flexibility in processing the data and segmentation techniques can be used to select the analysis region after acquisition. Detailed information is also obtainable from the valence excitation spectrum which can be used to map the water content in subcellular

compartments of frozen-hydrated cryosections. A similar approach may be useful for analysis of radiation-sensitive phases in materials such as polymers. One possible future improvement in the state of the art would be the development of parallel detectors with higher detective quantum efficiency and faster read-out so that data can be acquired more rapidly from beam-sensitive materials [34].

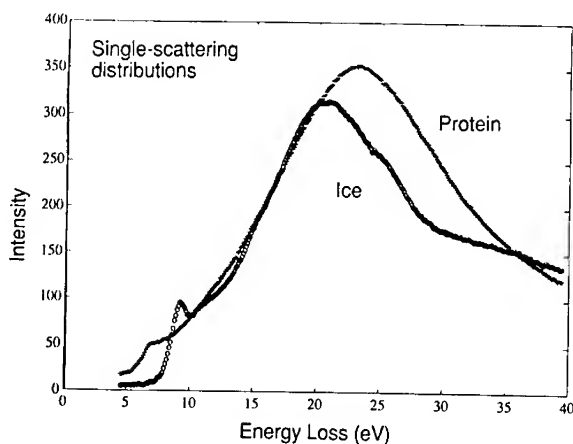


Fig. 4. Single-scattering distributions recorded at dispersion of 0.1 eV/channel from ice and from bovine serum albumin.

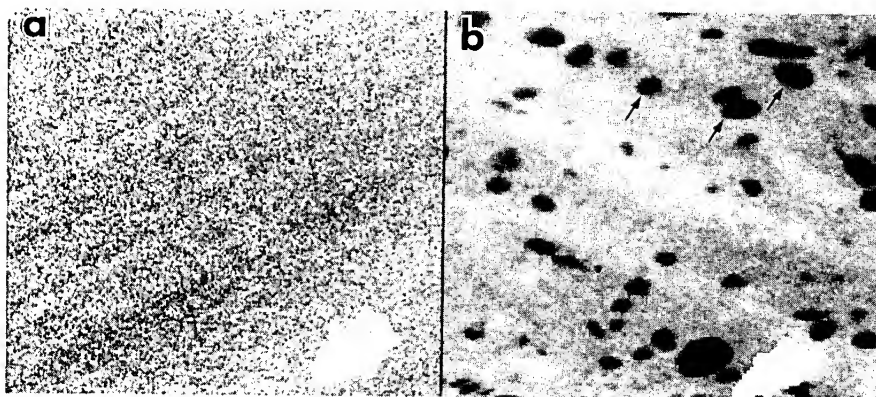


Fig. 5. Hydrated cryosection of vitrified liver maintained at temperature of -170°C . (a) Dark-field STEM with no structure visible. (b) Quantitative water distribution, obtained by fitting reference spectra at each pixel, shows strong contrast between mitochondria (arrows) and cytoplasm; brighter regions represent higher water content. Full image width = $10 \mu\text{m}$.

REFERENCES

1. M.S. Isaacson and D.E. Johnson, *Ultramicroscopy*, **1**, 33 (1975).
2. H. Shuman, *Ultramicroscopy*, **6**, 163 (1981); H. Shuman and P. Kruit, *Rev. Sci. Instrum.*, **56**, 231 (1985).
3. R.D. Leapman and S.B. Andrews, *J. Microsc.*, **165**, 225 (1992).
4. R.D. Leapman and D.E. Newbury, *Analytical Chem.*, **65**, 2409 (1993).
5. O.L. Krivanek, C. Mory, M. Tencé and C. Colliex, *Microsc. Microanal. Microstruct.*, **2**, 257 (1991).
6. C. Jeanguillaume and C. Colliex, *Ultramicroscopy*, **28**, 252 (1989).
7. J.A. Hunt and D.B. Williams, *Ultramicroscopy*, **38**, 47 (1991).
8. G. Botton and G. L'Espérance, *J. Microsc.*, in press (1993).
9. G. Balossier, X. Thomas, J. Michel, D. Wagner, P. Bonhomme, D. Ploton, A. Bonhomme, and J.M. Pinon, *Microsc. Microanal. Microstruct.*, **2**, 531 (1991).
10. S. Sun, S. Shi, J.A. Hunt and R.D. Leapman, to be published (1994).
11. M.S. Isaacson, in *Principles and Techniques of Electron Microscopy. VII*, edited by M.A. Hayat (Van Nostrand-Reinhold, New York) p. 1.
12. J.A. Hunt, R.D. Leapman and D.B. Williams, *Microbeam Analysis* **2**, S272 (1993).
13. A. Hitchcock, S. Urquhart and E. Rightor, *J. Phys. Chem.*, **96**, 96 (1992).
14. M. Sarikaya and I. Aksay, Proc. 51st Annual Meeting of Microscopy Society of America, San Francisco Press, p. 500 (1993).
15. J.S. Wall and J.F. Hainfeld, *Ann. Rev. Biophys. Biophys. Chem.*, **15**, 355 (1986).
16. O.L. Krivanek, C.C. Ahn and R.B. Keeney, *Ultramicroscopy*, **22**, 103 (1987).
17. S.B. Andrews and R.D. Leapman, *Microbeam Analysis*, San Francisco Press, p. 85 (1989).
18. R.D. Leapman and S.B. Andrews, *J. Microsc.*, **161**, 3 (1991).
19. M. Kundmann, X. Chabert, K. Truong and O.L. Krivanek (1990) EL/P software for Macintosh II computer, Gatan Inc., 6678 Owens Dr., Pleasanton, CA 94566, USA.
20. R.D. Leapman and R.L. Orberg, *Ultramicroscopy*, **24**, 251 (1988).
21. H. Shuman and A.P. Somlyo, *Ultramicroscopy*, **21**, 23 (1987).
22. Y.-Y. Wang, R. Ho, Z. Shao and A.P. Somlyo, *Ultramicroscopy*, **41**, 11 (1992).
23. N. Bonnet, J. Michel, D. Wagner and G. Balossier, *Ultramicroscopy*, **41**, 105 (1992).
24. P. Schattschneider and P. Jonas, *Ultramicroscopy*, **49**, 179 (1993).
25. R.D. Leapman, in *Transmission Electron Energy Loss Spectrometry in Materials Science*, edited by C. Ahn, M. Disko and B. Fultz (Minerals Metals Materials Society, Pittsburgh, 1992) p. 47.
26. O.L. Krivanek, A.J. Gubbens, N. Dellby and C.E. Meyer, *Microsc. Microanal. Microstruct.*, **3**, 187 (1992).
27. R.D. Leapman, J.A. Hunt, R.A. Buchanan and S.B. Andrews, *Ultramicroscopy*, **49**, 225 (1993).
28. A.P. Somlyo, M. Bond and A.V. Somlyo, *Nature (London)*, **314**, 622 (1985).
29. R.D. Leapman and J.A. Hunt (1991) Comparison of detection limits for EELS and EDXS. *Microsc. Microanal. Microstruct.* **2**: 231-244.
30. R.F. Egerton, in *Electron Energy Loss Spectroscopy in the Electron Microscope* (Plenum, New York, 1986).
31. S. Sun, S. Shi and R.D. Leapman, *Ultramicroscopy*, **50**, 127 (1993).
32. T. von Zglinicki, *J. Microsc.*, **161**, 149 (1991).
33. J. Dubochet, M. Adrian, J. Chang, J. Cl. Homo, J. Lepault, A.W. McDowall, and P. Schultz, *Quart. Rev. Biophys.*, **21**, 129 (1988).
34. Use of brand names does not constitute or imply endorsement.

ANNULAR DARK FIELD IMAGING IN STEM

SEAN HILLYARD AND JOHN SILCOX
School of Applied and Engineering Physics, Cornell University, Ithaca, N.Y., 14850

ABSTRACT

Annular dark field scanning transmission electron microscopy (ADF STEM) is chemically sensitive at high spatial resolution (e.g., 1.8 Å at 100keV). Images can be digitally acquired and recorded, permitting quantitative analysis. It is particularly powerful when used in combination with complementary analysis modes such as x-ray microanalysis and transmission electron energy loss spectroscopy. Critical to the interpretation of these data is an understanding and determination of the electron probe intensity, shape and propagation characteristics inside the specimen. Quantitative measurements of diffraction patterns and images in comparison with computer-based simulations (including phonon scattering) provide a basis for developing that information. Results of a series of studies are reviewed that address questions such as defocus and other instrumental factors, and also the formation of channeling peaks that appear on the atomic columns along zone axes. For example, along Si(100) a peak forms and penetrates over 500 Å whereas along Ge(100) it develops rapidly but disappears in less than 200 Å. In higher atomic number elements, the penetration is even less (e.g. 100 Å for In).

INTRODUCTION

Annular dark field scanning transmission electron microscopy (ADF STEM) [1] is now an accepted high resolution imaging approach [2-4] in materials research. Analytical studies such as electron energy loss spectroscopy (EELS) can be pursued in parallel with the dark field imaging mode and thus provide chemical and electronic structure information as well as the atomic structural information [see e.g., 5,6]. To a first approximation, the ADF STEM images are simple to interpret since they are not subject to the contrast reversals and shifts common with phase contrast bright field imaging. However, such interpretations do need to be tested so it is necessary to establish a good quantitative foundation and to probe the limits of the theoretical basis for this interpretation. Further, a solid theoretical basis is necessary for any attempt to use image enhancement techniques.

In this paper, we first introduce the ADF STEM approach with a simple description of the scattering and imaging processes. The paper reviews experimental arrangements for achieving expected performance limits and notes the importance of direct digital data recording [7] in determining instrumental parameters such as focal plane calibration with respect to objective lens current and the objective lens spherical aberration coefficient [8]. This permits quantitative modeling of the incident electron probe at the entrance surface of the sample. An outline of the approach used to model the interaction of the probe with the specimen and the subsequent scattering to form the image is provided. Quantitative comparisons between experimental convergent beam diffraction patterns and these theoretical simulations provide good agreement over four orders of magnitude in intensity [9,10]. This work introduces the "frozen phonon" approximation and provides the range of validity of the approximation. Comparisons between image measurements and the corresponding simulations demonstrate the validity of the incoherent imaging model [11]. Simulation studies demonstrate that the electron probe develops channeling

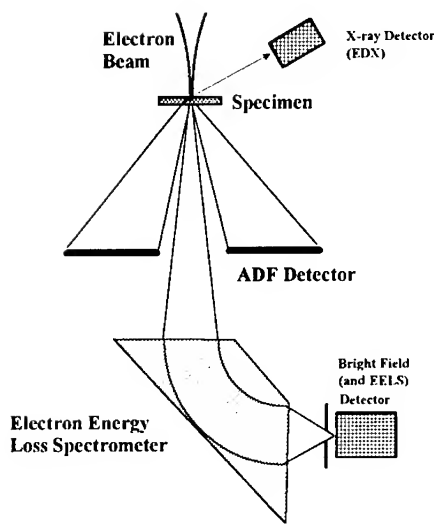


Fig. 1. Schematic of Scanning Transmission Electron Microscope (STEM)

peaks down the atomic channels within the specimen. It thus changes shape as it progresses through the sample, and the depth to which the channeling peak remains depends on the atomic number of the atoms constituting the columns [12, 13]. Scattering will depend on the electron intensity at the atom sites so this effect must be considered seriously in microanalysis at zone axis orientations. These studies also identify limits that arise in the imaging process from the virtual source size. This can be measured from the change of the image with the source demagnification [14].

PRINCIPLES AND IMPLEMENTATION

A very small (c. 2 Å) electron probe can be formed at the focal plane of a high quality objective electron lens by use of a cold field emission gun source. If the beam is rocked about the center of the lens, the probe can be scanned in a raster fashion across the specimen [1].

Strategically placed detectors pick up a signal from the scattered electrons or other radiation as illustrated in Fig. 1 which can then be displayed in a raster mode on a monitor. The magnification obtained is given by the ratio of the amplitude of the probe scan to the display scan and can be very high (e.g., 10 million times). Several signals can be acquired simultaneously and each image is in perfect registration since the pixel location in the image is determined by the location of the electron probe. The system is ideally suited for digital image acquisition (see e.g., 7) and is greatly improved by such facilities.

From fig. 1, a number of commonly used signals are shown schematically. The first, introduced by Crewe et al. [1], provides the annular dark field image and is formed by the elastic scattering outside the incident beam cone integrated over a detector of annular shape. Normally, the inner angular radius of this detector is significantly larger (e.g., 2 to 4 times) than the angular radius of the incident cone but it can be considerably larger (e.g., 8 to 10 times) when it is referred to as High Angle Annular Dark Field (HAADF). The image provided by this signal is

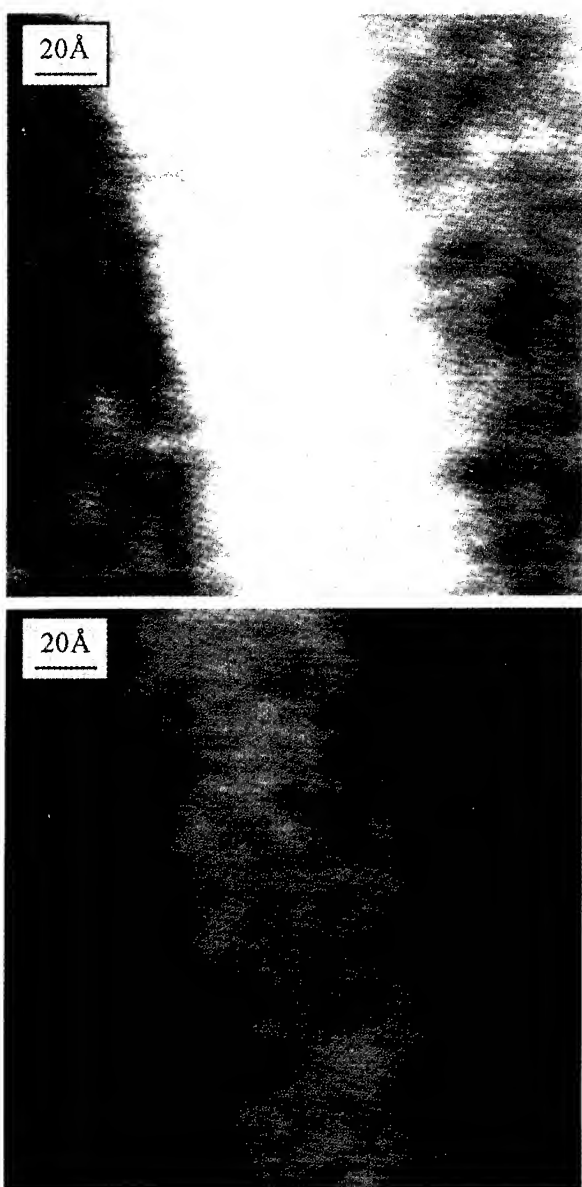


Figure 2. Annular Dark Field image of an 80Å wide GaAs/In_{0.2}Ga_{0.8}As/GaAs quantum well. The two pictures display the same digitally recorded data set. The (110) atomic columns are seen in the GaAs in the upper image and in the In_{0.2}Ga_{0.8}As quantum well in the lower image. The atomic structure is continuous through the quantum well (specimen courtesy of Y. Chen).

$$S(r, t) = \int |\Psi(r, t, k)|^2 D(k) dk \quad (1)$$

where $\Psi(r, t, k)$ is the wave function of the scattered electrons at a point on the detector given by the two dimensional vector k in the detector plane arising from a probe centered at a two dimensional position vector, r . $D(k)$ is the detector dimensions, and t is the specimen thickness. The scattering will be dependent on the atomic number of the atoms in the object and gives rise to "Z-contrast". Contrast can also arise from strain in the sample and, for example, it has been demonstrated that both arsenic (due to higher atomic number) and boron (due to the associated strain around the boron point defect) appear bright in silicon [15]. The spatial resolution in this mode of observation is generally taken as $0.43C_s^{1/2}\lambda^{1/2}$. In figure 2 an example of "Z-contrast" from an 80 Å quantum well of $In_{0.5}Ga_{0.5}As$ inside a matrix of GaAs is shown. The larger atomic number of the indium shows up as increased intensity. An advantage of the digital recording system is that the same image can be displayed in several intensity ranges depending on which features in that image are to be studied.

Those electrons passing through the hole in this detector also pass through an electron spectrometer permitting acquisition of energy selected images i.e., images recorded by scanning the beam across the sample at a particular energy window. If the zero loss is chosen, then the detector placed within the incident cone of illumination records a signal given by the interference between the incident beam and the elastically scattered beam. The principle of reciprocity [16,17] states that if the source and detector change places in a scattering experiment the same intensity is measured provided the dimensions remain the same i.e., the source size becomes the detector size and vice versa. In the present situation, for elastic scattering processes the energy filtered STEM bright field phase contrast image is identical with the TEM bright field phase contrast image for equivalent electron optical conditions. In line with this, the spatial resolution in this mode is $0.66C_s^{1/2}\lambda^{1/2}$, roughly 50% bigger than that cited for ADF STEM.

The sequential data acquisition of the STEM is well suited to digital recording as noted above [7]. Images from the separate detectors can be recorded simultaneously with the images in perfect registration since the pixel position is determined by the position of the probe. For each image, it is routine to record a bright field/dark field pair since different details can be identified in each image. If the images are recorded digitally prior to display, then it is possible to alter display conditions (e.g., fig. 2), to determine power spectra and to carry out extensive analysis of an image sequence (e.g., a through focal series) off-line. The first significant use of this at Cornell [8] was determination of the power spectra from defocus series of bright field phase contrast images of amorphous carbon films to measure the spherical aberration coefficients for two polepieces and to calibrate the associated defocus settings with lens current using Krivanek plots [18].

Several steps have been taken at Cornell to obtain data consistent with the intrinsic limitations of the instrument [19]. The experimental column was placed within a screened room to minimize vibrational, electrical and acoustic interference. Care had to be taken with the computer interfacing to isolate the computer from the column by optical isolation techniques [7]. The electronic controls were improved (e.g., an improved resolution potentiometer to obtain more finely set rocking points for diffraction studies [10] and higher thermal stability (factor of 10) operational amplifiers [8] have been installed). The bright field detector runs at a detection quantum efficiency of 90% (i.e., it is capable of single electron counting provided it is operated appropriately). The dark field detector is not at this level due to optical inefficiency in acquiring

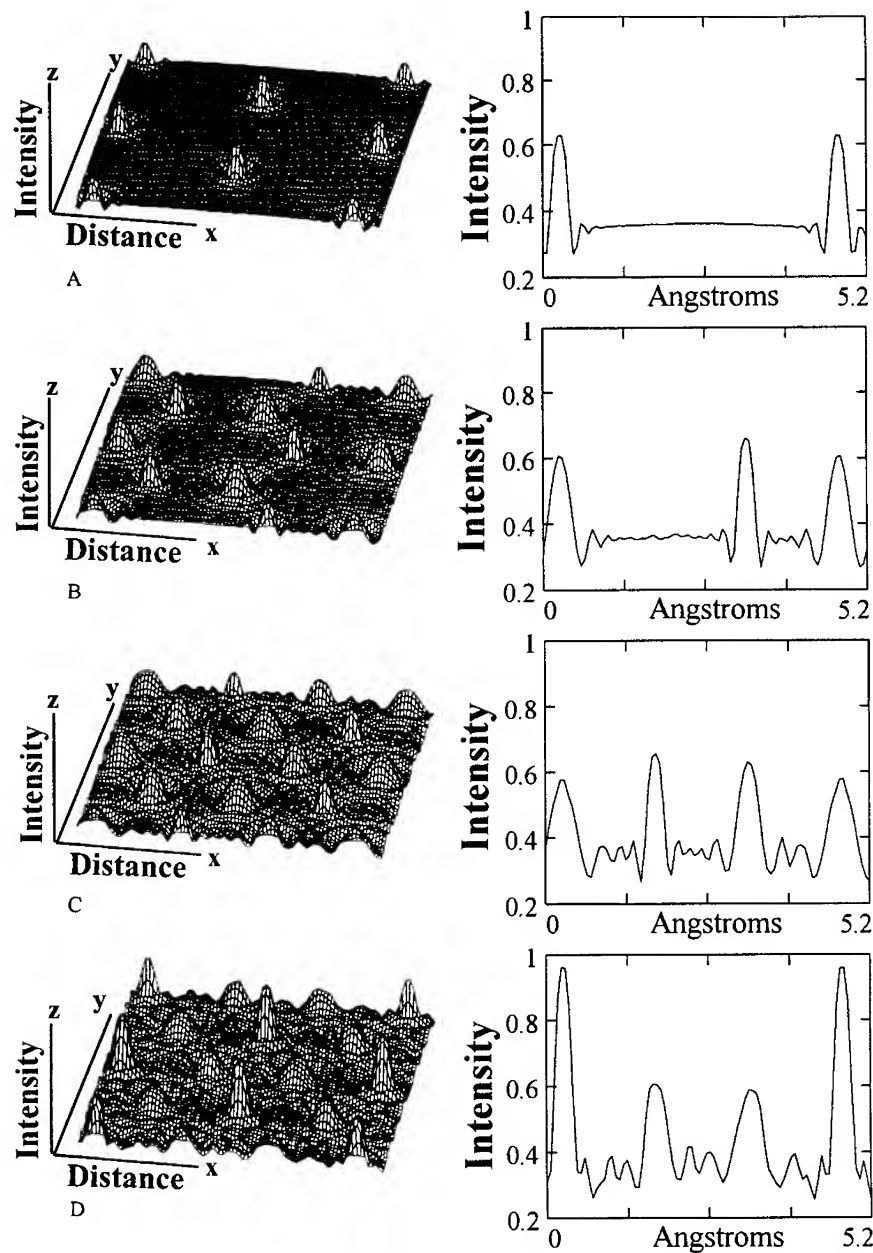


Figure 3. Simulated electron wavefunction intensity as it travels through the first four layers of Cu (111). The graphs on the right are line scans in x of the corresponding mesh plots for y halfway along the y-axis.

the optical intensity from the scintillator. Most recently, reduced thermal drift of the high voltage has been achieved by thermal stabilization of the high voltage tank [20].

THEORETICAL SIMULATION BASIS

The multislice theory initially put forward by Cowley and Moodie [21] and subsequently developed by many authors (see, e.g., [22-24]) forms the basis of the simulations relied upon in these studies. Although this model was originally developed in the context of conventional electron diffraction and microscopy, it is readily adapted to scanning probe microscopy [25,26] in three steps. The first step is simulation of the incident probe on the sample, followed by propagation of the probe through the sample by the multi-slice approach and finally evolution of the exit wave function from the specimen to the detector (essentially formation of the diffraction pattern). Integration over the detector dimensions gives a single image pixel. This has to be repeated for every pixel to provide an image. Implementation of algorithms based on this approach require substantial resources if they are to be sufficiently accurate, but these are increasingly available. Details of typical calculations are provided in the original papers [9,11,25,26] referenced in this article.

The multi-slice step involves repetition of two basic procedures for each slice (atomic layer). The first is calculation of the phase shift as the electron probe passes through the atom and the second is the evolution of the scattered wave by Fresnel diffraction towards the next layer. The size of the region in the atom over which the phase shift is significant is somewhat small. The phase shift can be written as

$$\phi(r) = \frac{\pi Z e^2}{\lambda E} \int f\left(\frac{R}{a}\right) dz \quad (2)$$

where Z is the atomic number, e the electronic charge, λ the electron wavelength, E the electron energy, R equal to $(r^2+z^2)^{1/2}$, where z is the coordinate along the direction of incidence and f is some spherically symmetric function varying in size with the atomic species. If the Wentzel model is used, i.e., $f(R/a) = e^{-Ra}/R$ with $a = a_0/Z^{1/3}$, where $a_0 = 0.53 \text{ \AA}$ is the Bohr radius, then for carbon and an electron energy of 100 keV a phase shift of 0.2 milliradians is calculated for a radius, r , equal to 0.1 \AA and for uranium the shift of 0.2 occurs at $r = 0.25 \text{ \AA}$. Thus, as far as the phase shift of the electron wave is concerned the atom appears rather small i.e., of order 0.5 to 0.2 \AA or about one tenth to one twentieth of the interatomic distance. The electron wave ($\lambda = 0.037 \text{ \AA}$) propagates towards the next atom via Fresnel diffraction.

This process is illustrated in figure 3 which shows the calculated form of an electron wavepacket at succeeding atomic layers down the (111) direction of copper. Passing through the first layer of atoms, the electron wavepacket (chosen to have 20 Angstroms fullwidth at half maximum) undergoes a phase shift calculated from the Doyle and Turner potentials [27]. The scattered wave resulting from this phase shift diffracts towards the next layer and is shown in figures 3a and 3e interfering with the incident wavepacket. It should be noted that the extra amplitude now appearing as an extra peak in the wavepacket at the atomic position will be reflected in a reduction of the amplitude in the incident wavepacket through normalization, i.e., the whole wave function still only contains one electron. Although the atomic potential is calculated throughout a single atomic layer, the dominant effect is that of scattering from one individual atom interacting with the incident wave i.e., from the relatively small (in spatial extent) atomic phase shift noted above.

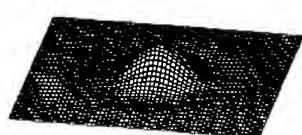
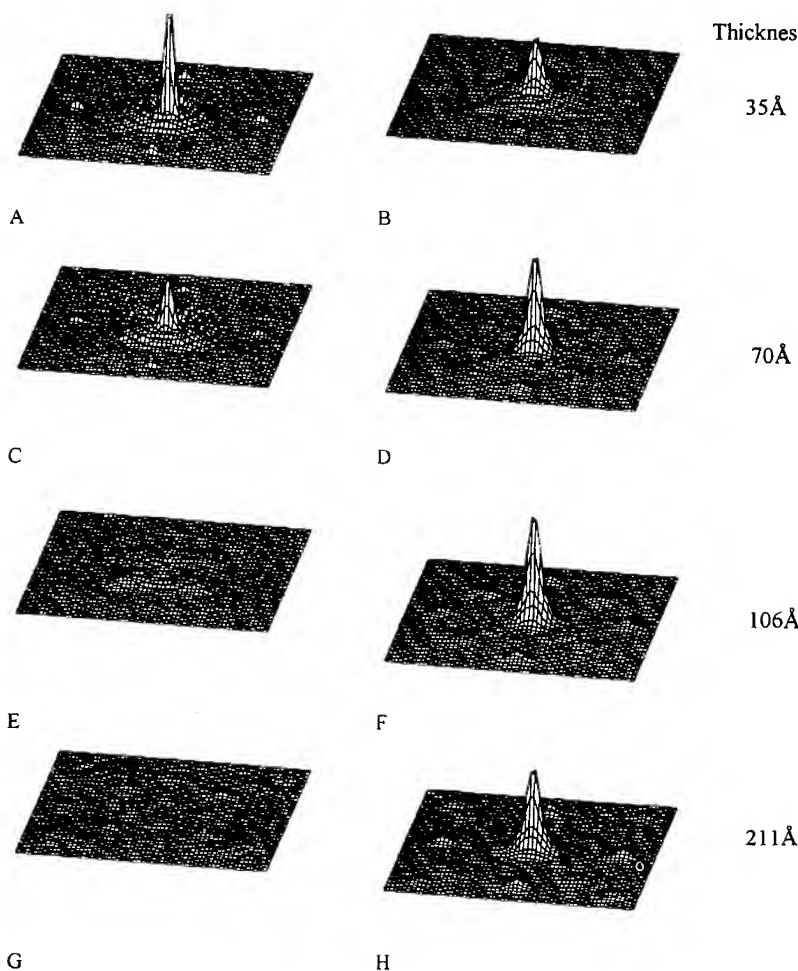


Figure 4. Simulated electron wavefunction intensity for a 100keV electron inside InP (100). The full scale is 8Å and the initial probe is shown to the left. A,C,E,G show the probe as it travels down an indium column and B,D,F,H as it travels down a phosphorus column.



Successive layers in the simulated crystal are shown until the packet has traveled to the fourth layer in the crystal in which the atoms lie directly underneath the initial layer. The wave scattered from the initial layers now undergoes a second phase shift and, on continued diffraction, appears as an enhanced or channeling peak. Note that the increased wave function amplitude depends on the incident amplitude. As the packet travels through the crystal, the atomic peaks increase and the remaining incident probe shrinks correspondingly. The latter disappears completely after perhaps 20 layers leaving strongly channeled peaks that are significantly sharper than the original probe and are located at the atomic sites (see, e.g., [26]).

The channeling effect noted in the large probe case becomes even stronger under high resolution, small probe conditions. In figure 4, the channeling of an incident probe of 2.2 Å diameter is illustrated for the case of an electron beam incident along the (100) zone axis orientation of InP [12]. In one column, the beam is located over the indium column and in the other, it is located over the phosphorus column. This figure shows that the simulations predict that the electrons will channel in zone axis orientations and that the extent and range of the channeling will depend on the atomic number of the elements in question. For example, in low Z elements (e.g., Si, Al and P) the channel width is about 0.7 Å, the channeling peak grows over a 100 to 200 Å distance and stays more or less level to a depth of several hundred Å. In heavier atoms (e.g., Ge, Sn or In) on the other hand, the channel width narrows (to 0.4 Å or less), it

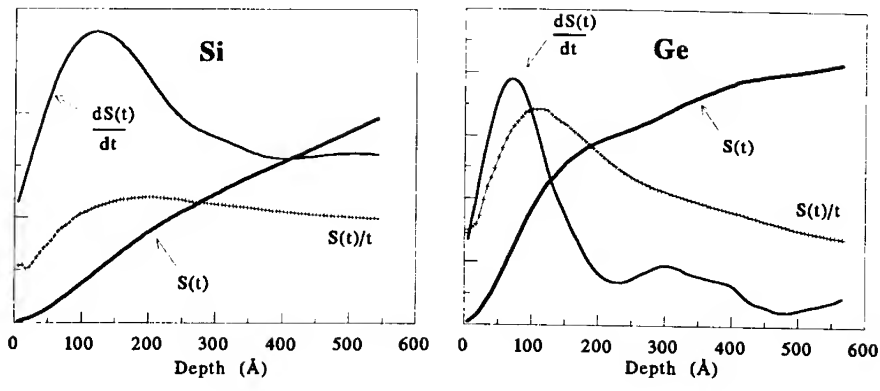
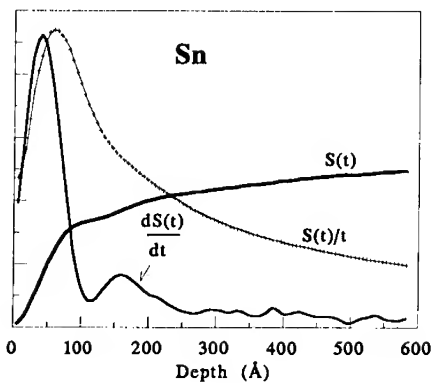


Figure 5. Simulated annular dark field signals $S(t)$ versus thickness for Silicon, Germanium and Tin (100) for a 2.8 Å probe located over an atom column. Also shown are its derivative $dS(t)/dt$ and thickness average, $S(t)/t$. For lower atomic number elements, such as Si, the annular dark field signal increases almost linearly for thickness greater than 500 Å. However, for higher Z elements such as Ge and Sn, the ADF signal saturates at about 200 Å and 100 Å respectively.



grows more quickly to full channel intensity (e.g., in 30 to 100 Å) and disappears quickly, presumably due to strong high angle scattering.

This effect is expected to be significant for analytical studies as well as ADF imaging. The annular dark field images integrate the scattering from the sample thickness i.e., $S(r,t)$. If the scattering (either the elastic dark field for the ADF image or the inelastic analytical signals) is proportional to the local wavefunction [12], then this effect will be present in the images. The integrated areas under the channeling peaks have been found to track closely with the simulated $S(r,t)$. In figure 5, we show curves of S , S/t and dS/dt for Si, Ge and Sn. The second of these identifies the average per layer ADF image intensity, while the third gives the contribution per layer to the image. For the higher Z elements, the contribution per atomic layer rises quickly and disappears just as quickly, suggesting that in these systems the observed image may arise purely from the uppermost layer of the sample. This is associated with the quick formation, and subsequent disappearance of the channeling peak for larger Z elements (as seen in fig. 4). For quantitative evaluation, this may be significant. Studies of X-ray excitation as a function of average thickness (i.e. $S(t)/t$) [28] are consistent with the general characteristics seen in fig 5. Additional experimental verification of this effect is important.

DIFFRACTION PATTERNS AND IMAGES

Intensity measurements were compared with image modeling [9-13, 25, 26, 29] that is accurate enough to provide a detailed interpretation of the intensity observations. The initial comparisons [29] between the model and experiment were convergent beam diffraction patterns recorded by direct photography of the diffraction pattern observation screen. At this stage the simulation did not include thermal scattering and thus did not predict such characteristic features as Kikuchi bands. Nevertheless the simulation gave a valuable comparison of the patterns observed in the first order Bragg reflections with those calculated as a function of the thickness as determined experimentally by plasmon intensities and the plasmon mean free path. The need to include thermal diffuse scattering to achieve an accurate description was pointed out by Wang and Cowley [30-32]. The 'frozen phonon' version of the simulation [9, 10] was then introduced as a first principles approach to introduce thermal effects as a random displacement of the atoms from the equilibrium lattice position. This calculation automatically includes multi-phonon effects and

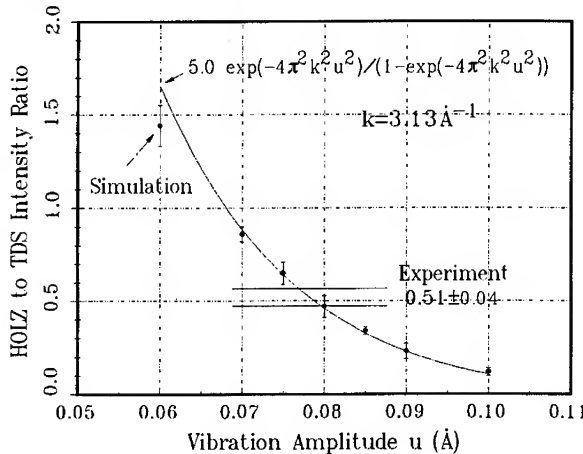


Figure 6. Ratio of the calculated HOLZ ring to TDS background intensities as a function of silicon vibration amplitude. The two horizontal lines indicate the experimentally measured HOLZ ring to TDS intensity ratio of 0.51 ± 0.04 . The corresponding rms vibration amplitude of $0.078 \pm 0.002 \text{ \AA}$ compares well [10] with the X-ray structure factor measurement of 0.0764 ± 0.0002 [34].

thus addresses criticisms [33] of the earlier calculations. The simulations (using an Einstein model) agree well with experiment [9,10] in good agreement with the X-ray determination of the mean atomic displacement [34]. Figure 6 shows the determination of the phonon amplitude from the ratio of the HOLZ ring to the background thermal diffuse intensity.

The study of model specimens such as (100) InP permits some insight into the image formation process [11]. Direct recording into digital memory makes Fourier transformation of the image intensities to determine the power spectra straightforward. Given the calibration of lens parameters [8], the electron optical conditions under which the images were recorded can be specified with some precision. Since (100) InP is a simple periodic specimen, the power spectra are dominated by strong fringes (at 2.1 Å and 2.9 Å). These vary in strength with defocus corresponding to predictable changes with the incident probe shape [11]. Good agreement between the focal variations of the experimental and the simulated images was obtained. The incoherent imaging model also gave a good description of the focal changes [11].

As a result of this analysis, it is now possible to understand the effects of the probe shape in the images and to address the thickness effects reviewed in the previous section. The intensity at the atomic columns associated with the channeling peaks is related to lattice fringe intensities measured in the power spectra. Both experimental and simulated images can be analyzed to recover the scattering associated with effects due to thickness for comparison. One complication became evident in the initial work [11]. The finite size of the virtual source of the incident electrons can limit the spatial resolution.

This effect was explored by changing the demagnification of the illumination system and found to be significant [14]. Accordingly, it must be included in analysis of the data. In figure 7, the dependence of fringe intensities with defocus is seen compared with the predictions of the incoherent imaging model including the effects of source size. Provided these are included, then it is feasible to analyze data from different thickness specimens and plot the ratio of the 2.1 Å fringe intensity to that of the 2.9 Å fringe intensity [13]. The simulations give a very specific form for this ratio as a function of thickness and this is compared with the experimental results in figure 8 (from ref. [13]). Good agreement is found providing evidence for the thickness effects described earlier.

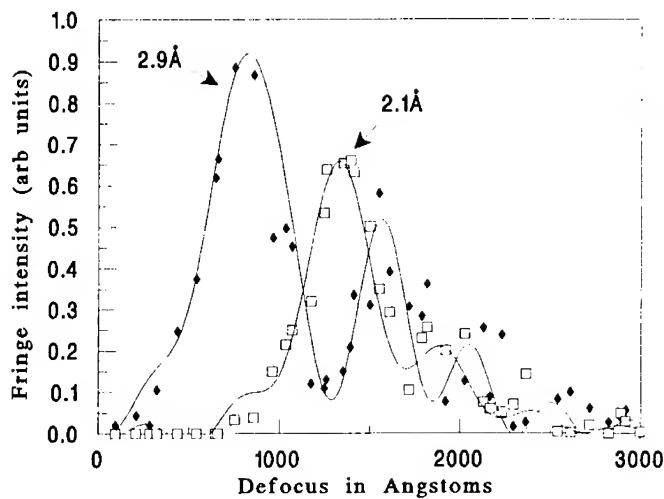


Figure 7. Fringe intensities vs defocus for the 2.9 Å and 2.1 Å fringes of InP(100). The lines are the calculated contrast transfer functions and the points are the experimentally measured values obtained from power spectra of a through focal series. [13]

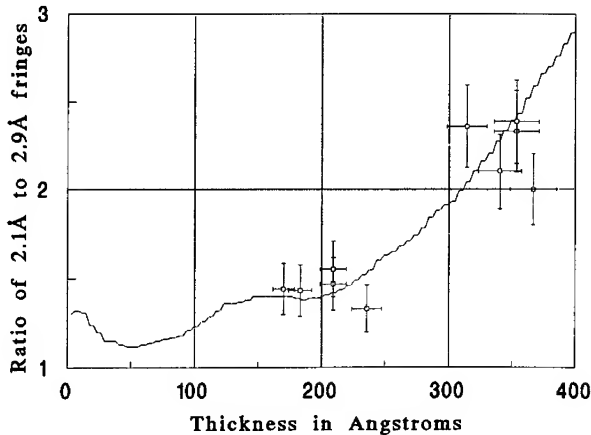


Figure 8. Plot of the ratio of the 2.1 and 2.9 Å fringes of InP(100) versus thickness. The solid line is that predicted with the multislice algorithm and the points are what is measured experimentally. [13]

PROSPECTS FOR THE FUTURE

From the results reported in the literature as cited above, it can be concluded that ADF STEM is an imaging approach capable of high resolution. It can be made intrinsically quantitative through digital image acquisition and the background simulation theory identifies the primary factors in the image formation process with high accuracy. An improvement of 40% over bright field phase contrast also permits high resolution at lower voltages than normal microscopy provides. It is very valuable as a way of locating the probe on the sample while exploiting energy loss analysis or other signals. For higher atomic number elements, however, it is advisable to remember that at zone axis orientations only a very thin layer at the entrance surface is sampled.

These factors suggest that this type of electron microscopy will see increasing use as the ease of use of the instrument improves. Digital image acquisition, storage and analysis will be a major factor in this. In addition, specimen handling should improve so that tilting and variable temperature stages can be made available for experimental use. No fundamental reason exists to forbid accessories of the same quality level as those available with conventional TEM.

Finally, the successful development of aberration corrected systems [35] should be as equally feasible in STEM as in TEM. Indeed it should be an easier task. Hence, resolution enhancement can be foreseen on a five to ten year time scale. Given a cold field emission gun, it is reasonable to anticipate that a resolution in the area of 0.5 Å might be attained as a result of recent designs. Such a system would open up vast areas of defect studies in crystals in which, for example it would be appropriate to ask questions about the three-dimensional structure of the defect. But that is a few years off!

ACKNOWLEDGEMENTS

Special thanks to E.J. Kirkland for his implementation of the STEM data acquisition system and to M. Thomas for keeping the STEM working. This research was supported through the award of a graduate fellowship to S.H. by the Department of Education and by the Department of Energy (DEFG028ER45322). Calculations were performed at the Cornell

Material Science Center computer facility. Funding for the purchase of the UHV STEM (DMR-8314255) and operation through the Materials Science Center (DMR-9121654) was provided by the National Science Foundation.

REFERENCES

1. A.V.Crewe, J.P.Langmore and M.S.Isaacson in *Physical Aspects of Electron Microscopy*, Eds. B.M.Siegel and D.K.Beaman (Wiley, New York 1975) 47
2. S.J.Pennycook and L.A.Boatner, *Nature* 336 (1988) 565
3. S.J.Pennycook, *Ultramicroscopy* 30 (1989) 58.
4. P.Xu, E.J.Kirkland, J.Silcox and R.Keyse, *Ultramicroscopy* 32(1990) 93
5. P.E. Batson, *Nature*, 366 (1993) 727
6. D.A. Muller, Y. Tzou, R. Raj and J. Silcox, *Nature*, 366 (1993) 725
7. E.J.Kirkland, *Ultramicroscopy* 32 (1990) 349
8. K.Wong, E.J.Kirkland, P.Xu, R.F.Loane and J.Silcox, *Ultramicroscopy* 40 (1992) 139
9. R.F.Loane, P.Xu and J.Silcox, *Acta Cryst. A*47 (1991) 267
10. P.Xu, R.F.Loane and J.Silcox, *Ultramicroscopy* 38 (1991) 127
11. R.F.Loane, P.Xu. and J.Silcox, *Ultramicroscopy* 40 (1992) 121
12. S.Hillyard, R.F.Loane and J.Silcox, *Ultramicroscopy*, 49 (1993) 14
13. S.Hillyard and J.Silcox, *Ultramicroscopy*, to appear (1993)
14. S.Hillyard and J.Silcox, to be submitted
15. D.D.Perovic and J.H. Paterson, *Proc. 49th Ann. Mtg E.M.S.A.* (San Francisco Press, San Francisco, 1991) 704
16. J.M.Cowley, *Appl.Phys.Lett.*, 15 (1969) 58
17. E. Zeitler and M.G.R. Thompson, *Optik* 31 (1970) 258, 359
18. O.L.Krivanek, *Optik*, 45 (1976) 97
19. J.Silcox, P.Xu and R.F.Loane, *Ultramicroscopy*, 47 (1993) 173
20. E.J.Kirkland, unpublished.
21. J.M.Cowley and A.F.Moodie, *Acta Cryst* 10 (1957) 609
22. P. Goodman and A.F. Moodie, *Acta Cryst. A* 30 (1974) 280
23. K. Ishizuka and N. Uyeda, *Acta Cryst. A* 33 (1977) 740
24. P.G. Self, M.A. O'Keefe, P.R. Buseck and A.E.C. Spargo, *Ultramicroscopy* 11 (1983) 35
25. E.J.Kirkland, R.F.Loane and J.Silcox, *Ultramicroscopy* 23 (1987) 77
26. R.F.Loane, E.J.Kirkland and J.Silcox, *Acta Cryst. A* 44 (1988) 912
27. P.A.Doyle and P.S.Turner, *Acta Cryst. A* 24 (1968), 390
28. D.Cherns, A.Howie and M.H.Jacobs, *Z. Naturforsch.* 28a (1973) 565
29. E.J.Kirkland, R.F.Loane, P.Xu and J.Silcox in *Computer Simulation of Electron Microscope Diffraction and Images* Eds.W.Krakow and M.O'Keefe (Minerals, Metals and Materials Society, New York 1989) 1315.
30. Z.L.Wang, *Acta Cryst. A* 45 (1989) 636
31. Z.L.Wang and J.M.Cowley, *Ultramicroscopy* 31 (1989) 437
32. Z.L.Wang and J.M.Cowley, *Ultramicroscopy* 32 (1990) 275
33. S.J.Pennycook, *Acta Metall. Mater.* 40 (1992) S149
34. S.J.E.Allred and M.Hart, *Proc. Roy. Soc., (London) A* 332 (1973) 239
35. H. Rose, *Optik* 85 (1990) 19

QUANTITATIVE HRTEM: MEASURING PROJECTED POTENTIAL, SURFACE ROUGHNESS AND CHEMICAL COMPOSITION.

P. Schwander, C. Kisielowski, F.H. Baumann, Y.O. Kim and A. Ourmazd
AT&T Bell Laboratories, Holmdel, New Jersey 07733, USA

ABSTRACT

We describe how general lattice images may be used to measure the variation of the potential in crystalline solids in any projection, with no knowledge of the imaging conditions. This approach is applicable to structurally perfect samples, in which interfacial topography, or changes in composition are of interest. We present the first atomic-level topographic map of a Si/SiO₂ interface in plan-view, and the first microscopic compositional map of a Si/GeSi/Si quantum well in cross-section.

1. INTRODUCTION

Lattice images, obtained by Transmission Electron Microscopy (TEM), are routinely used to infer the subsurface microstructure of crystalline materials. In principle, a lattice image is a map of the sample (Coulomb) potential, projected along a zone axis (see, e.g. [1,2]). In practice, it is difficult to extract quantitative information from lattice images. This stems from two primary reasons. First, electrons are multiply scattered during their passage through crystalline samples of realistic thickness ($\geq 10 \text{ \AA}$). This results in a complex, highly nonlinear relationship between the sample potential and the characteristics of the lattice image. This relationship changes rapidly with the sample thickness, and thus from point to point over the sample. Second, electromagnetic lenses have severe aberrations. The image details thus depend sensitively on the (contrast) transfer function of the microscope, and hence the lens defocus. As shown in Fig. 1, small changes in imaging conditions substantially alter the dependence of the image characteristics (e.g., intensity) on the projected potential (varied in Fig. 1 by changing the composition). It is not possible to establish a general relationship between the sample potential and the image features. This has led to the development of "image matching" procedures, whereby the sample structure is inferred by visually comparing simulated images of model structures with experimental results. Extraction of information by this procedure, even at the qualitative level, requires accurate knowledge of the imaging conditions (sample thickness, lens defocus, etc.) [3,4]. These are difficult to measure, and are often poorly known.

Here, we describe an approach, named QUANTITEM, which *measures* the variation of the potential over the sample from general lattice images of crystalline materials, requiring no knowledge of the imaging conditions [5]. In samples of uniform composition, QUANTITEM can be used to map the topography of buried interfaces in plan-view, with near-atomic resolution and sensitivity. Here, we demonstrate this capability for the Si/SiO₂ interface. We show that QUANTITEM topographic images of such *interfaces* are comparable with those obtained from

surfaces by the scanning tunnelling microscope. In samples with compositional non-uniformities, QUANTITEM may be used to map the compositional variation. We demonstrate this by presenting composition maps across Si/GeSi/Si quantum wells. Unlike chemical mapping, QUANTITEM does not rely on the presence of chemical reflections [6,7], and is thus applicable to general crystalline materials.

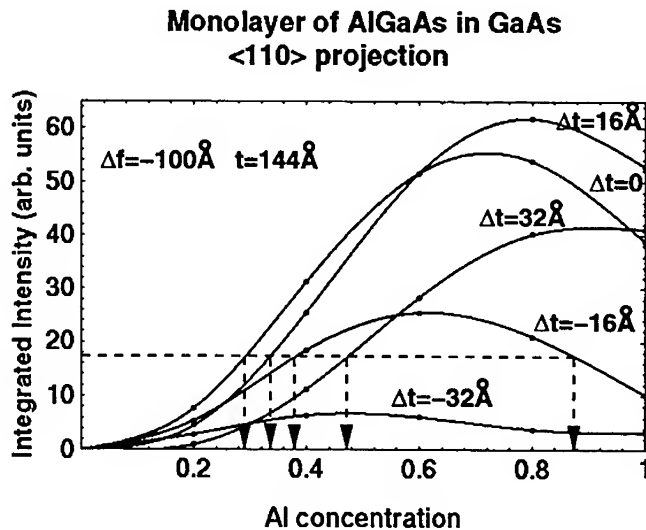


Fig. 1. Plot of image intensity vs Al concentration, (which changes the projected potential). The dependence of image characteristics on the projected potential changes rapidly with sample thickness. As an example, an intensity of 18 can correspond to an Al concentration of 0.28, 0.33, 0.39, 0.44, or 0.84, as the thickness changes by 32 Å.

2. PRINCIPLE OF APPROACH

To describe the principle of this approach, it is convenient to represent the information content of an image unit cell in vector notation [8]. All the available information in a lattice image is contained in the image intensity distribution. The periodicity of the lattice can be used to divide the image into unit cells, within each of which the intensity distribution is digitized. When a unit cell is sampled $n \times m$ times, its information content is contained in $n \times m$ numbers. We represent these numbers as the components of a (multi-dimensional) vector, whose position and length describe all the available information. (For a discussion of image localization¹, see [1,9]).

To measure the variation of the projected potential from a lattice image, one must discover how the image changes with the projected potential, under the particular conditions used to obtain the lattice image under analysis. In vector notation, this requires two steps. First, one

1. We have previously shown that under appropriate imaging conditions, the information content of an image unit cell is directly related to the projected potential of a region of the same cross-section in the sample. See: F.H. Baumann, M. Bode, Y.O. Kim and A. Ourmazd, Ultramicroscopy **47**, 167 (1992).

needs to determine the path traced by the unit cell image vector as the sample potential varies (Fig. 2). This path changes with imaging conditions, and must be determined afresh for each lattice image. Second, one must determine the rate at which this path is traversed as the sample potential changes. This rate need not be a linear function of the potential change. Determination of the path and the rate at which it is traversed quantify the way that changes in the sample potential affect the image.

The path of the image vector can be directly determined from the experimental image, by plotting the tips of the image unit cell vectors over the region of interest (Fig. 2). Since all TEM samples are wedge-shaped, this directly reveals the path described by the image unit cell vector as the projected potential changes. The rate at which this path is traversed can be measured in one of two ways. In the first, one assumes that no particular thickness is favored over the field of view². The density of points (vector tips) along the path is then inversely proportional to the local rate of path traversal. The total length of the path can be calibrated in terms of sample thickness, by recognizing that lattice images vary periodically with the pendellösung oscillations. This calibrates one period of the path in terms of a known change in thickness - the extinction distance³.

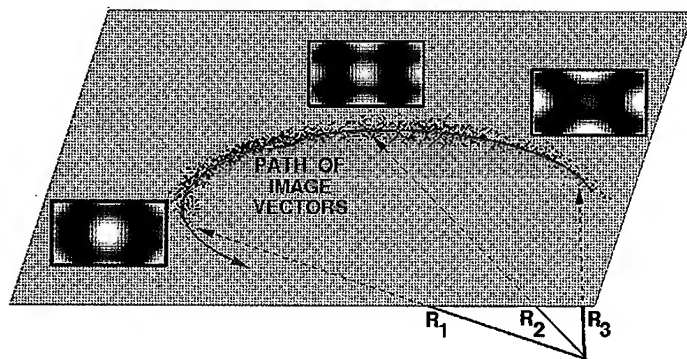


Fig. 2. Experimental lattice image unit cells, and their vector representation \mathbf{R}^i , for three different sample thicknesses. The cloud of points represents tips of vectors drawn from an experimental image of a (wedge-shaped) Si sample. The path described by the image vectors quantifies the way changes in the sample projected potential affect the lattice image.

The second approach to measuring the local rate of path traversal requires high signal-to-noise ratios. In the absence of noise, the atomic nature of the sample gives rise to discrete clusters of points along the path, each representing columns with a given number of atoms. Noise tends to smear these clusters into a continuous distribution. Nevertheless, the signal-to-noise ratio is sometimes adequate to reveal the presence of such clustering of points in Fourier trans-

2. This is not as restrictive as assuming a "linear" wedge with a constant slope. However, it does require that, on average, the sample not systematically deviate from a linear wedge.

3. In cases where the pendellösung oscillations cannot be characterized by a single extinction distance, a "local" extinction distance can be used to describe these oscillations.

forms of their density, or by autocorrelation techniques. This allows an absolute determination and calibration of the rate at which the path is traversed as a function of projected potential.

The above discussion notwithstanding, we show below that appropriate parameterization of the path can result in a highly linear relationship between the projected potential and the chosen parameter, obviating the need for local calibration of the rate of path traversal.

To summarize, the way that image characteristics change with sample projected potential is represented by the path traced out by the image unit cell vectors. This path and the rate at which it is traversed can be determined and calibrated directly from an experimental image, with no knowledge of imaging parameters. The projected potential at each point on the experimental image can then be measured from the position of its image unit cell vector on this path.

We now describe how QUANTITEM may be implemented in practice. The procedure is facilitated by an appropriate choice of reference frame in vector space. We derive a reference frame from the experimental image itself, by extracting a number of "template" vectors from the image. A general unit cell is then expressed in terms of its projections on planes defined by these template vectors. In general, three template vectors suffice, and their choice is not critical. This can be rationalized by the following argument. In most low-index zone axes, the image consists of three primary elements: the background (\mathbf{R}^B); the image due to interference of the central beam with the strongest set of reflections (single-periodic image, \mathbf{R}^S); and an image due to interference between these reflections themselves (double-periodic image, \mathbf{R}^D). This implies that a general lattice image consists of three large elements:

$$\mathbf{R}^G = a \mathbf{R}^B + b \mathbf{R}^S + c \mathbf{R}^D + \mathbf{r},$$

where a, b, \dots represent numbers, and the residue \mathbf{r} is small. Consider three (template) images \mathbf{R}_i^T ($i=1,2,3$) extracted from different areas of the lattice image. Since

$$\mathbf{R}_i^T \cong a_i \mathbf{R}^B + b_i \mathbf{R}^S + c_i \mathbf{R}^D, \quad \mathbf{R}^{B,S,D} = \sum_i p_i \mathbf{R}_i^T.$$

Substituting for $\mathbf{R}^{B,S,D}$ shows that the general vector \mathbf{R}^G can be written as:

$$\mathbf{R}^G \cong \alpha \mathbf{R}_1^T + \beta \mathbf{R}_2^T + \gamma \mathbf{R}_3^T.$$

Thus a general image can be conveniently expressed in terms of its projections on three template vectors extracted from the image. The primary requirement is that the choice of template vectors \mathbf{R}_i^T should provide an adequate description of the significant images present. This is easily achieved by extracting a template from areas of the image with distinctly different characteristics.

In general, the path described by the image vector for potential changes of more than half an extinction distance can be well-approximated by an ellipse⁴. Figure 2 shows the tips of experimental image unit cell vectors projected onto the plane defined by the three template vectors \mathbf{R}_i^T . We describe the path by fitting an ellipse to the experimental points, and parameterize it in terms of the ellipse phase angle Φ_e . For the samples we have investigated, this parameterization yields a universal and linear dependence on the sample potential, irrespective of the imaging conditions. Figure 3 is a plot of the variation of the ellipse angle $\Delta\Phi_e$ vs the projected potential for Si in the $\langle 100 \rangle$, $\langle 111 \rangle$ and $\langle 110 \rangle$ projections and for $\text{Ge}_x\text{Si}_{1-x}$ in the $\langle 110 \rangle$ projections over the defocus range $-100 - 700 \text{ \AA}$, and thickness range $80 - 420 \text{ \AA}$. These plots were obtained by

4. For larger thickness variations, the change of defocus due to the wedge shape of the sample can cause significant departures in the path from an ellipse. While convenient, it is not necessary that the path should be an ellipse. Any path can be parameterized, and the parameter related to the projected potential as described above. However, some parameterizations are more convenient than others, primarily because they lead to a more nearly linear relationship with the projected potential.

analyzing simulated images of Si and Ge_xSi_{1-x} . When present, such a universal relationship obviates the need for fresh measurement and calibration of the rate of path traversal in each lattice image.

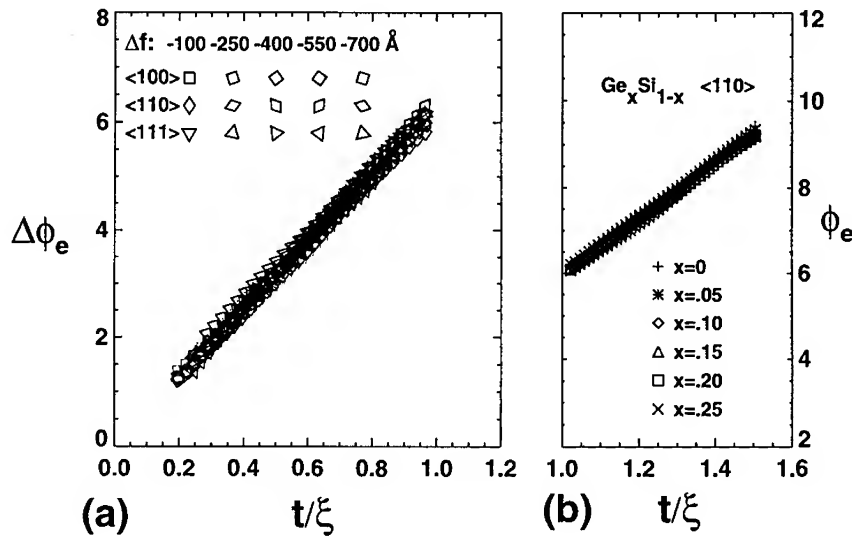


Fig. 3. Variation of ellipse phase angle Φ_e vs sample thickness t , normalized to the extinction distance ξ , for Si (a), and Ge_xSi_{1-x} (b). Note the strong overlap of the points, indicating a universal relation between the variation in Φ_e and the projected potential for these systems, irrespective of sample thickness, projection direction, and lens defocus.

3. TOPOGRAPHIC MAPPING: INTERFACIAL ROUGHNESS

By presenting experimental images of the atomic roughness at Si/SiO_2 interfaces in plan-view, we show that QUANTITEM may be used to reveal the topography of buried interfaces with high spatial resolution and sensitivity. Figure 4(a) is a $<100>$ lattice image of a Si sample, after a final rinse in an anisotropic etch (KOH in H_2O) and the formation of a native oxide ($\sim 15 \text{ \AA}$ thick on each surface). Figure 5(b) is a QUANTITEM map of the thickness variations in the crystalline part of the $SiO_2/Si/SiO_2$ sample⁵, with height representing thickness. Since the sample contains two Si/SiO_2 interfaces, the variations reveal the superimposed roughness of the two Si/SiO_2 interfaces in plan-view. The formation of pyramidal hillocks due to the anisotropic nature of the etch is clear. Such structures are absent when the Si surface is etched isotropically. Quantitative error analysis yields the sensitivity estimates shown in Table I. Figure 4(b) constitutes the first quantitative, high resolution, topographic image of a buried interface in plan-view.

5. For obvious reasons, QUANTITEM measures only the part of the sample that is crystalline.

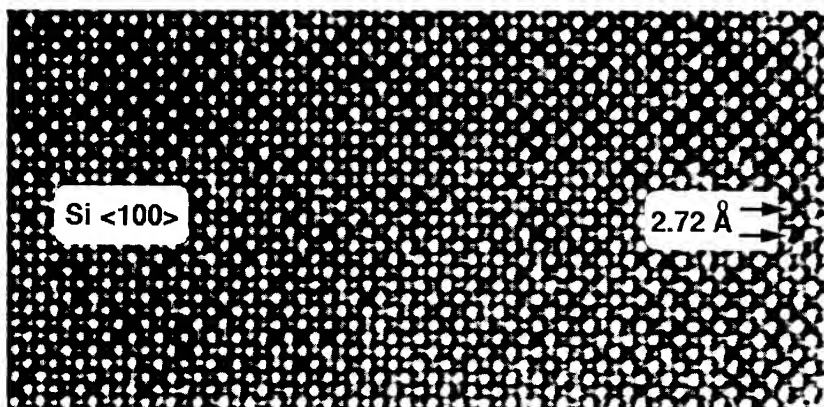


Fig. 4(a). Lattice image of SiO₂/Si/SiO₂ sample, viewed in <100> plan-view. The sample was formed by anisotropic etching of Si in KOH, followed by formation of a native oxide. Two Si/SiO₂ interfaces are seen superimposed.

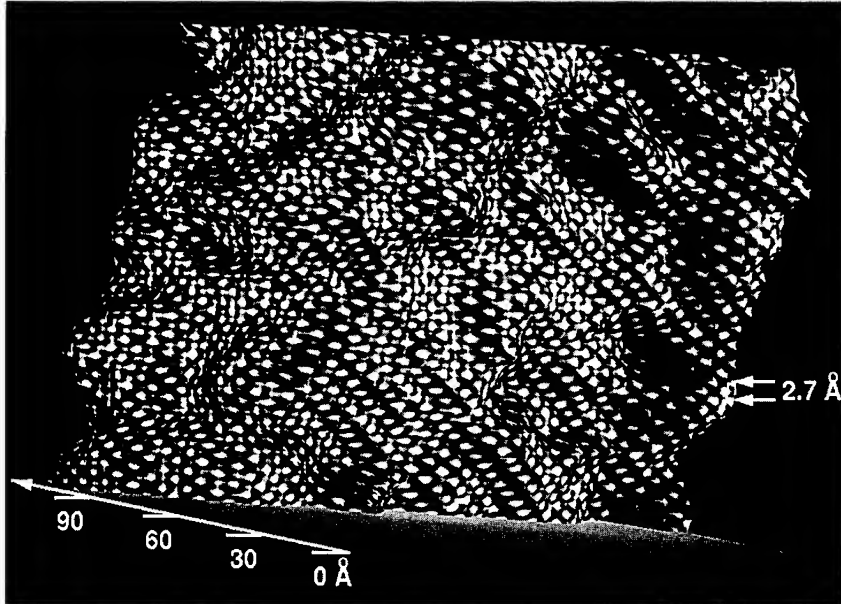


Fig. 4(b). QUANTITEM map of the thickness of crystalline Si sandwiched between the two SiO₂ layers. Height represents sample thickness. This topographic map, deduced from (a) above, directly reveals the superimposed roughness of the two Si/SiO₂ interfaces. Note the pyramidal hillocks produced by the anisotropic etch.

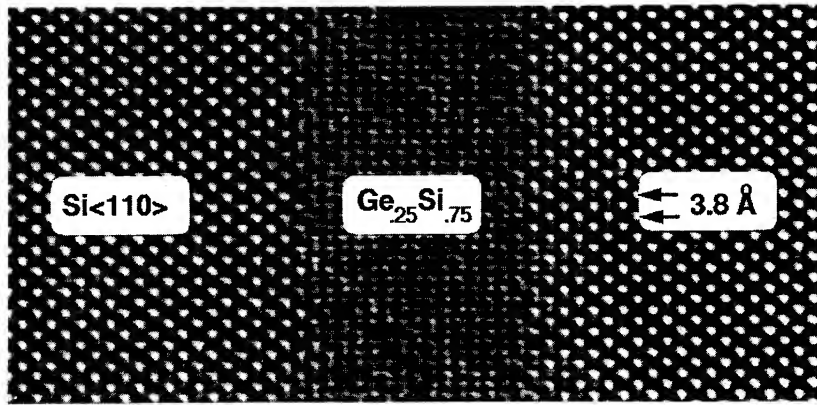


Fig. 5(a). Lattice image of Si/Ge_{0.25} Si_{0.75} /Si quantum well structure, viewed in <110> cross-section.

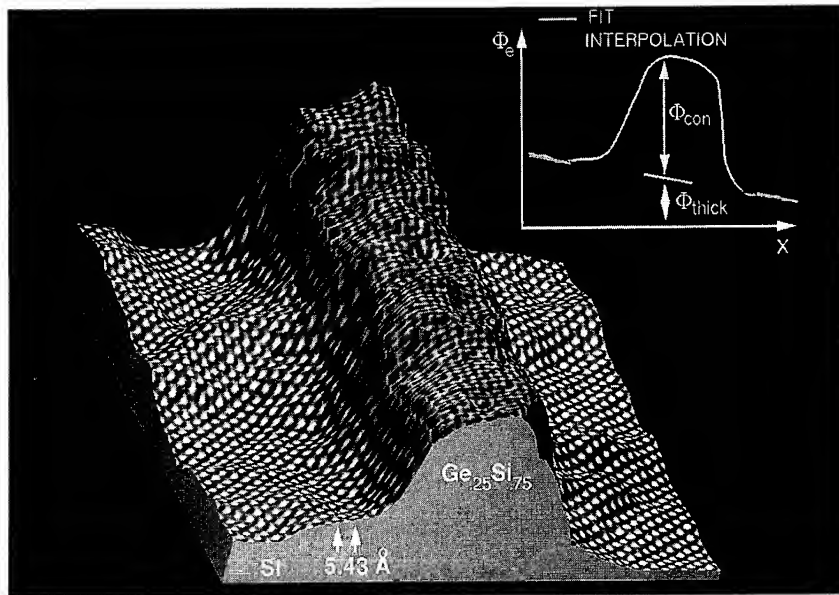


Fig. 5(b). Map of ellipse phase angle Φ_e across the image shown in (a) above. Note the variations in the Si region, indicating significant thickness changes. Inset: schematic representation of the effect of composition on Φ_e . The heavier GeSi causes Φ_e to advance more rapidly. The variation of thickness across the field of view means that part of the change in Φ_e is due to composition, part due to thickness change.

4. COMPOSITION MAPPING

We now describe how QUANTITEM may be used to measure the chemical transition between two regions of known composition in crystalline materials. In the absence of chemical reflections [7], a lattice image essentially measures the sample projected potential. Changes in sample thickness and composition must therefore be considered on the same footing. It is not possible to neglect changes in sample thickness over the field of view, and assign all changes in the image to compositional variations, for two reasons. First, changes in sample thickness mimic those brought about by changes in composition. Second, in the absence of chemical reflections, small changes in thickness radically alter the dependence of the image characteristics on composition (Fig. 1).

Changes in composition have two consequences. First, the path described by the vector can be changed. When present, this can be readily discerned by plotting the experimental vectors in regions of known composition. Second, the extinction distance is altered, which changes the rate at which the path is traversed in each material. QUANTITEM exploits this latter effect to determine the composition of an image unit cell. Consider a target unit cell of unknown thickness and composition, and assume for the moment that its thickness is known. In outline, QUANTITEM proceeds as follows (Fig. 5): (1) it measures the amount by which the ellipse phase angle Φ_e of the target unit cell is advanced from a reference unit cell in a region of known composition; (2) it subtracts the part $\Delta\Phi_e$ due to the thickness change; (3) it ascribes the remainder to changes in the extinction distance, and hence composition. Since the extinction distance can be easily calculated and/or measured, this directly yields the composition of the target unit cell.

To determine the sample thickness at the target unit cell, we map the sample thickness over regions of known composition and fit a two-dimensional model function (surface) to the data, so as to obtain an accurate description of the undulations in the sample thickness. We then infer the sample thickness at the target unit cell by interpolating the model function between the adjoining regions of known composition (Fig. 5(b), inset). Quantitative procedures are used to determine the uncertainty with which the thickness at the target cell has been inferred.

Figure 5(a) is a $<110>$ cross-sectional lattice image of a $\text{Si}/\text{Ge}_{.25}\text{Si}_{.75}/\text{Si}$ quantum well. Fig. 5(b) shows the variation of the ellipse phase angle Φ_e across the image, as determined by QUANTITEM⁶. The variation of Φ_e over the regions away from the interfaces clearly reveals significant thickness changes, both locally and across the $\sim 150 \text{ \AA}$ field of view. These variations can be reproduced by a model function with a (one-sigma) accuracy of $\sim 3.5 \text{ \AA}$. As shown in the inset of Fig. 5(b), once the sample thickness at a target cell is determined, its composition is deduced from the part of $\Delta\Phi_e$ not due to thickness change.

Figure 6 is a QUANTITEM composition map across a $\text{Si}/\text{Ge}_{.25}\text{Si}_{.75}/\text{Si}$ quantum well. The height represents the Ge concentration. This image represents the first quantitative microscopic map of the compositional change across the important $\text{Si}/\text{Ge}_x\text{Si}_{1-x}/\text{Si}$ interface, directly revealing its roughness at high resolution. (See Table I.)

We note in passing, that if the composition is known at two points on the sample, QUANTITEM allows an absolute determination of the sample thickness, point by point. This can be understood as follows. The image vector in each material describes its ellipse once every extinction distance $\xi_{1,2}$, where 1,2 refer to the two materials. Since ξ_1 and ξ_2 are different, the two

6. For this image, the Si and $\text{Ge}_{.25}\text{Si}_{.75}$ vectors follow the same path to within experimental noise.

Changes in composition are reflected in the extinction distance, and hence the rate at which the path is traversed. When the paths differ, Φ_e is referred to the path for each material.

ellipse periods are, in general, incommensurate. This creates a vernier effect between the Φ_e for the two materials. A given phase difference is then consistent with only a particular absolute thickness for the reference points in each material.

5. PRACTICAL LIMITS

Having outlined the principle of QUANTITEM and demonstrated its implementation, we briefly discuss a few of the factors that determine its practical limits. A more detailed discussion is reserved for a later publication.

5.1 Photographic Nonlinearities

QUANTITEM extracts the projected potential from the details of the image intensity distribution. By analyzing simulated images, we have demonstrated a linear relationship between the ellipse phase angle Φ_e and the projected potential. We have verified that this linear relationship also holds for experimental images, even when they are recorded on negatives and digitized by commercial video systems. First, QUANTITEM analysis of experimental images obtained from cleaved wedges yields wedges of correct constant slope. Second, analysis of simulated images of wedges after convolution with the measured nonlinearity of the (negative '+' video) system yields the input wedge. Third, QUANTITEM analysis of experimental images recorded directly on an *in situ* CCD camera, or by digitizing exposed negatives yields the same result. These establish that QUANTITEM is robust against recording nonlinearities⁷.

5.2 Distortions

A major source of uncertainty in QUANTITEM is the presence of image distortions due to the recording and digitizing instrumentation. Our procedure first corrects pin-cushion distortions, without which, the noise is overwhelming. Second, it resamples the image to remove moiré effects stemming from the often non-commensurate ratio of the unit cell size to the pixel size. Within this procedure each of the unit cells is also centered onto a rectangular grid. This improves the signal-to-noise ratio by a factor of ~2. Additional fine-tuning can be achieved by image filtering with a median filter and by restoration of the exact (e.g., four-fold) symmetry in each unit cell by appropriate averaging over its four quadrants. This improves the signal-to-noise by another factor ~1.3. This remaining noise is due to microbending in the sample, which causes systematic deviation of the data points from one particular path of the image vectors and can only be removed by reduction of the field of view. Reducing the field of view to ~50 Å square can improve the signal-to-noise ratio by a factor of ~2. At this level, monolayer changes in sample thickness are resolved (1.9 Å for silicon <110>).

5.3 Noise

The presence of amorphous overlayers introduces noise, creating a cloud of points (vector tips) about the path described with sample potential. We reduce this effect by projecting each point onto the path. In this way, only the component of noise that coherently changes the information content of the image unit cell in the direction of the path causes confusion. The ultimate sensitivity of QUANTITEM is limited by residual distortions, and colored noise, which cannot be eliminated by spatial averaging.

7. They also establish that inelastic scattering does not adversely affect analysis by QUANTITEM.

5.4 Spatial Resolution

The ultimate (lateral) spatial resolution of QUANTITEM is limited by three factors: spreading of information due to multiple scattering and imperfect lens information transfer¹; the size of the unit cell analyzed; and noise [8]. Typical spatial resolutions are summarized in Table I.

6. DISCUSSION AND CONCLUSIONS

We now discuss the more general implications of our work. There can be no single route to quantitative electron microscopy. However, we have described a means for direct measurement of the sample projected potential from general lattice images. This approach is based on the notion that imaging conditions do not need to be individually known. Their combined effect simply produces a relationship between the projected potential and the image features, which can be extracted directly from each experimental image. In view of the complexities of the image formation process, it is remarkable that such a conceptually simple approach can yield valuable information. In particular, the variation of the projected potential in crystals of uniform structure can be directly extracted from general lattice images, with no need for careful control or knowledge of the imaging conditions. Here, we have demonstrated the ability of QUANTITEM to yield high resolution topographic maps of *buried* interfaces in plan-view. This opens the way for the study of a variety of important interfacial reactions at the atomic level, such as surface roughening during oxidation. The ability to map compositional variations in general systems is a significant step toward investigating the relaxation of general multilayered systems and their point defect reactions [7]. More generally, QUANTITEM constitutes a rapid and robust means of extracting quantitative information from lattice images, which are generally obtained under poorly known conditions. It may thus help to transform high resolution transmission electron microscopy into a practically quantitative tool.

Table I:
Thickness and chemical sensitivity of QUANTITEM
Best values were obtained by median image filtering of 2x2 unit cells

SYSTEM	IMAGE CELL SIZE	SENSITIVITY TYPICAL	SENSITIVITY BEST
Si <100>	2.7 x 2.7 Å ²	15.1 Å	3.2 Å
Si <110>	3.8 x 5.4 Å ²	5.3 Å	2.0 Å
Si <111>	2.2 x 3.8 Å ²	11.0 Å	3.2 Å
Ge _{.25} Si _{.75} <110>	3.8 x 5.4 Å ²	5.4 at.% Ge	2.3 at.% Ge

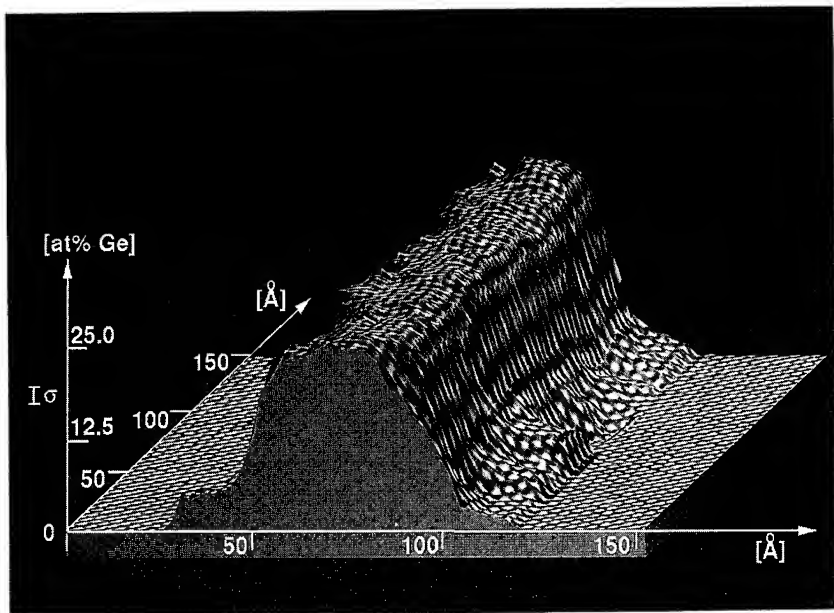


Fig. 6. QUANTITEM composition map deduced from Fig. 5. Height represents Ge concentration, the bar one-sigma accuracy.

ACKNOWLEDGEMENTS

We acknowledge valuable discussions with G. Higashi and Y. LeCun, expert technical assistance from J.A. Rentschler and efficient editorial help from C. Stiles-Canter. The GeSi/Si samples were kindly provided by J.C. Bean and J. Bevk.

REFERENCES

1. J.H.C. Spence, Experimental High Resolution Electron Microscopy (Clarendon Press, Oxford, 1981).
2. K.H. Downing, H. Meisheng, H.-R. Wenk and M.A. O'Keefe, *Nature* **348**, 525 (1990).
3. A. Bourret, J.-L. Rouvière and J.M. Penisson, *Acta Cryst. A* **44**, 838 (1988).
4. M.A. O'Keefe, U. Dahmen and C.J.D. Hetherington, *Mat. Res. Soc. Symp.* **159**, 453 (1990).
5. P. Schwander, C. Kisielowski, M. Seibt, F.H. Baumann, Y.O. Kim and A. Ourmazd, *Phys. Rev. Lett.*, accepted (1993).
6. A. Ourmazd, D.W. Taylor, J. Cunningham and C.W. Tu, *Phys. Rev. Lett.* **62**, 933 (1989).
7. A. Ourmazd, *Materials Science Reports* **9**, 201 (1993).
8. A. Ourmazd, D.W. Taylor, M. Bode and Y.O. Kim, *Science* **246**, 1571 (1989).
9. L.D. Marks, *Ultramicroscopy* **18**, 33 (1985).

COMPOSITIONS AND CHEMICAL BONDING IN CERAMICS BY QUANTITATIVE ELECTRON ENERGY-LOSS SPECTROMETRY

J. BENTLEY, L.L. HORTON, C.J. McHARGUE,[†] S. McKERNAN,^{*} C.B. CARTER,^{*} A. REVCOLEVSCHI,[‡] S. TANAKA,[§] and R.F. DAVIS[¶]

Metals and Ceramics Division, Oak Ridge National Laboratory, PO Box 2008, Oak Ridge, TN 37831-6376 († Now at: The University of Tennessee, Knoxville, TN 37993)

^{*} Department of Chemical Engineering and Materials Science, University of Minnesota, 421 Washington Ave. SE, Minneapolis, MN 55455-0132

[‡] Laboratoire de Chimie des Solides, CNRS UA 446, Université Paris-Sud, Bâtiment 414, 91405 Orsay Cedex, France.

[§] Department of Materials Science and Engineering, North Carolina State University, PO Box 7907, Raleigh, NC 27695-7907.

ABSTRACT

Quantitative electron energy-loss spectrometry was applied to a range of ceramic materials at a spatial resolution of <5 nm. Analysis of Fe L_{2,3} white lines indicated a low-spin state with a charge transfer of ~1.5 electrons/atom onto the Fe atoms implanted into (amorphized) silicon carbide. Gradients of 2 to 5% in the Co:O stoichiometry were measured across 100-nm-thick Co₃O₄ layers in an oxidized directionally solidified CoO-ZrO₂ eutectic, with the highest O levels near the ZrO₂. The energy-loss near-edge structures were dramatically different for the two cobalt oxides: those for Co₃O₄ have been incorrectly ascribed to CoO in the published literature. Kinetically stabilized solid solubility occurred in an AlN-SiC film grown by low-temperature molecular beam epitaxy (MBE) on α (6H)-SiC, and no detectable interdiffusion occurred in couples of MBE-grown AlN on SiC following annealing at up to 1750°C. In diffusion couples of polycrystalline AlN on SiC, interfacial 8H sialon (aluminum oxy-nitride) and pockets of Si₃N₄-rich β' sialon in the SiC were detected.

INTRODUCTION

Applications of electron energy-loss spectrometry (EELS) to ceramics have clearly demonstrated the powerfulness of this transmission electron microscopy (TEM) technique for characterization of such materials, especially those containing elements with atomic number Z < 10.¹ Examples described here illustrate the sensitivity, accuracy, and limitations of quantitative composition determination and chemical bonding information when applied at a spatial resolution of <5 nm to silicon carbide implanted with iron, to an oxidized directionally solidified CoO-ZrO₂ eutectic, and to aluminum nitride - silicon carbide diffusion couples.

EXPERIMENTAL

Analytical electron microscopy (AEM) was performed at ORNL with a Philips EM400T AEM equipped with a field emission gun (FEG), a Gatan 666 parallel-detection electron energy-loss spectrometer (PEELS) system, and an EDAX 9100 energy dispersive X-ray spectrometer (EDS). Philips CM12/STEM and CM30/STEM AEMs were also used. For microanalysis, specimens were usually cooled to -130°C in Gatan double-tilt cooling holders. High-spatial-resolution PEELS data were acquired in the scanning TEM (STEM) mode with probes of ~2-nm diameter (FWTM) containing ~0.8 nA, and incident and collection half-angles of 8 and 19 (or 30) mrad, respectively. Spectra were also recorded in the TEM mode with probe currents >3 nA, an incident beam divergence of 3 mrad, and probes of ~10-nm diameter.

Polished single crystal α -SiC platelets (Carborundum Company, Niagara Falls, NY) of predominately the 6H polytype, with the broad face parallel to the basal (0001) plane, were implanted at room temperature with 160 keV ⁵⁷Fe to a fluence of 6×10^{16} ions/cm² at the ORNL Surface Modification and Characterization Facility.²⁴

Directionally solidified cobalt oxide - zirconia eutectic material was grown at the Université Paris-Sud by a floating zone melting technique, described previously.⁵

Three AlN-SiC materials, each having α (6H)-SiC single crystal substrates (Cree Research, Raleigh, NC) oriented 3-4° from [0001] toward [1120], were examined in cross section: (1) an AlN-SiC solid solution grown at 1050°C by plasma-assisted, gas-source molecular beam epitaxy (MBE);⁶ (2) diffusion couples of MBE-grown AlN on SiC annealed for 70 h at 1700°C or 25 h at 1850°C; and (3) diffusion couples of polycrystalline sintered AlN (Dow Chemical) on the above specified SiC substrate, annealed at 1600 and 1700°C.

Specimens were prepared for AEM by standard dimpling and ion milling techniques.

IRON-IMPLANTED SILICON CARBIDE

Silicon carbide ion-implanted with iron has been previously characterized by AEM.^{2,4} Implanted iron depth profiles were measured by EDS; no clustering of the iron in the amorphized SiC was detected by TEM. Information about the bonding of the iron was sought from examination of the electron energy-loss near-edge structure (ELNES) for the Fe $L_{2,3}$ edge. Preliminary data^{2,4} have subsequently been supplemented and quantitatively analyzed. Figure 1 shows a comparison of the Fe $L_{2,3}$ ELNES in spectra measured with PEELS for a plan-view Fe-implanted SiC specimen sectioned to near the maximum Fe concentration (16 mol%), and for various other iron-based materials. The spectra are normalized so that the level of excitation to the continuum states (say $E > 735$ eV), which is a good measure of the quantity of iron analyzed, is identical for all spectra. The white lines, which arise from transitions to unfilled 3d levels, are much less intense for the Fe-implanted SiC than for the other materials; they are also slightly broader. In more quantitative terms, Pearson et al.⁷ have shown that the normalized white line intensity (WLI) ratio, relative to the intensity in a 50 eV window, 50 eV above the L_3 edge (continuum states), can be used as a measure of the 3d occupancy. Morrison et al.⁸ have derived expressions for measuring 3d hole concentrations from L_3 and L_2 white line intensities. Clearly, the marked differences in the white lines in the spectra of Fig. 1 imply gross changes in the 3d occupancies and thus of chemical bonding. Quantitative measurements of normalized WLI ratios⁷ for the spectra of Fig. 1 are shown in Table 1. The results imply a charge transfer of >1.5 electrons/atom onto the iron relative to metallic iron. Similarly, from the expressions of Morrison et al.,⁸ the ratio of the number of 3d holes for the implanted iron relative to that for metallic iron is 0.53, again implying ~1.4 electrons/atom charge transfer. Additionally, the small L_3/L_2 WLI ratio for the implanted iron implies a low spin state; the ratio of 5/2 to 3/2 state holes for the implanted iron is 20% lower than for metallic iron. The results suggest that the iron in the SiC is not primarily metallically bonded and support the conclusion of earlier conversion electron Mössbauer spectroscopy data that the iron is in covalently bonded sites.⁹

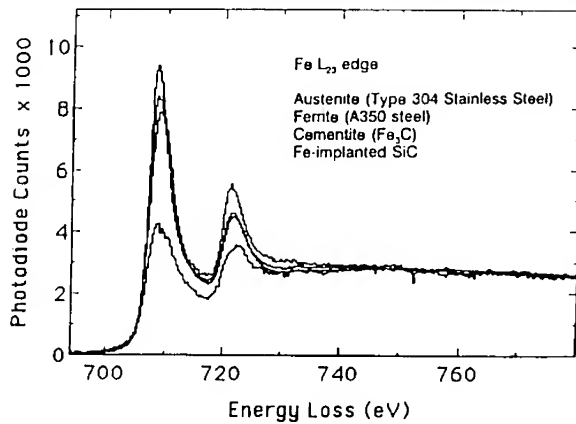


Fig. 1. Fe $L_{2,3}$ ELNES for Austenite, ferrite, cementite, and Fe-implanted SiC.

Table 1. Analysis of Fe $L_{2,3}$ white line intensities

	Normalized WLI	Implied 3d occupancy
Fe_2O_3	0.65	4.5
Fe_3C	0.41	6.5
Austenite	0.42	6.3
Ferrite	0.37	6.9
Fe in SiC	0.20	8.6

COBALT OXIDE - ZIRCONIA EUTECTIC

The morphology of directionally solidified eutectics (DSE) provides an excellent geometry for studying interfaces in materials, for example by high-resolution TEM.¹⁰ The thin, parallel plates which are formed in the ZrO_2/CoO system also produce flat interfaces on the microscopic scale. However, heat treatment of the eutectic in a high oxygen partial pressure results in a trilayer structure^{11,12} as the CoO transforms to Co_3O_4 . The microstructure consists of alternating lamellae of CoO and calcium-stabilized cubic- ZrO_2 , each with widths of up to 1 μm , and a thin (100 to 200 nm), irregular layer of Co_3O_4 spinel extending into the CoO from the flat ZrO_2 interface. The growth direction of the DSE is $[001]_{ZrO_2} // [1\bar{1}0]_{CoO}$ and the broad interface is $(100)_{ZrO_2} // (111)_{CoO}$. The Co_3O_4 is oriented cube-on-cube with the CoO .

Typical core-loss PEELS data for the stabilized cubic zirconia phase are shown in Fig. 2a. The proximity of the $Zr\ M_3$ and overlap with the $Zr\ M_2$ preclude accurate use of the $Ca\ L_{2,3}$ edge for composition determination but, fortunately, Ca/Zr ratios are easily obtained by EDS. Such measurements indicate that the Ca/Zr atomic ratio is 0.18. However, for other aspects of composition determination, secondary excitation¹³ in EDS gives misleading results, such as the apparent presence of zirconium in the cobalt oxides and higher than actual levels of cobalt in the zirconia. Also, strong X-ray absorption limits the accuracy of oxygen contents from EDS data.

Typical core-loss PEELS data for the cobalt oxide phases are shown in Fig. 2b. To determine compositions accurately,¹⁴ care has to be taken in the treatment of the energy-loss near-edge structure (ELNES), e.g., the $Co\ L_{2,3}$ "white lines." A simple approach, that of beginning the integration window just beyond the most pronounced ELNES was used. The measured values of composition depend upon the position of the integration window and the use of the white line correction in the Gatan EL/P (version 2.1) software. A 100 eV integration window offset from the edge threshold by 25 eV gave the most reliable results. Further work, at higher spatial resolution, indicated a reproducible 2 to 5% gradient in the $Co:O$ ratio across the Co_3O_4 phase, with the lowest values (highest oxygen content) near the ZrO_2 interface. This is consistent with the proposed mechanism of phase formation that is based on rapid diffusion of oxygen in the ZrO_2 lamellae and slower lateral diffusion into the cobalt oxide.⁵ The measurement of such composition gradients is possible because the precision of the data is much better than the absolute accuracy.

Inspection of the oxygen energy-loss near-edge structure (ELNES) reveals dramatic differences between the CoO and Co_3O_4 (Fig. 3a). Interpretation of such oxygen ELNES is complex and involves consideration of site symmetry and states arising from hybridization of oxygen 2p levels with metal 3d and 4s or 4p levels.¹⁵ Nevertheless, the differences in oxygen ELNES provide easily identifiable signatures for the two cobalt oxides. The cobalt $L_{2,3}$ white line ELNES (Fig. 3b) is superficially similar for the two phases, but there is a small shift to higher energies for the Co_3O_4 (~ 1.5 eV for L_3 , ~ 0.6 eV for L_2). The normalized WLI ratio, relative to the continuum states in a 50 eV window, 50 eV above the L_3 edge,⁷ is 0.53 ± 0.02 for the two cobalt oxides, implying similar 3d occupancies. The L_2/L_3 WLI ratios are 3.88 and 2.58 for the CoO and Co_3O_4 , respectively. From the type of analysis employed by Morrison et al.,⁸ the ratios of 5/2 to 3/2 state holes are 1.42 and 0.89 for CoO and Co_3O_4 , respectively, and the ratio of the total number of 3d holes in CoO to those in Co_3O_4 is 0.98, in agreement with the normalized WLI ratio analysis. Quantitative measurements were

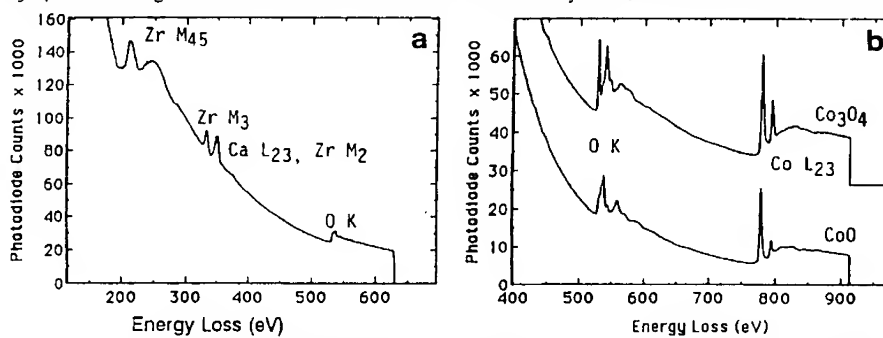


Fig. 2. Typical core-loss PEELS data for (a) ZrO_2 (CaO), (b) Co_3O_4 and CoO phases.

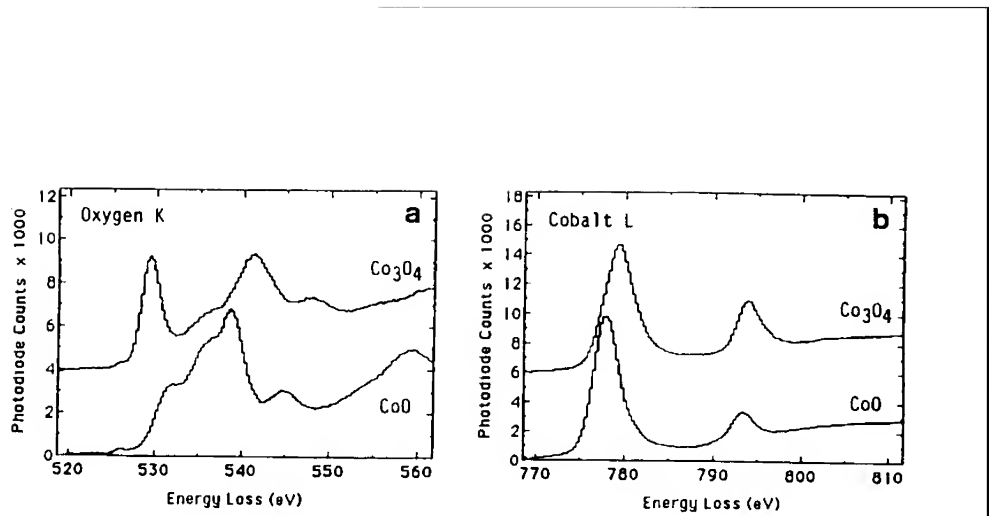


Fig. 3. (a) Oxygen K and (b) cobalt $\text{L}_{2,3}$ ELNES for Co_3O_4 and CoO phases.

made on single scattering profiles, but difficulty was experienced in implementing even the simple geometric approach used by Pearson et al.⁷ because of the edge shape just beyond the white lines.

Oxygen and cobalt ELNES (with slightly better energy resolution than our present results) for cobalt oxide have recently been published.¹⁶ The results were stated as being for CoO that was made by oxidizing thin evaporated metal films in air at 400°C. However, the published oxygen ELNES is not at all like our results for CoO ; instead, there is excellent agreement with our results for Co_3O_4 . Similarly, the positions of the published Co L white lines are more consistent with our data for Co_3O_4 than CoO . Phase diagram data indicate that Co_3O_4 is the stable oxide below ~900°C for oxygen partial pressures of >0.1 atm. Kurata and Colliex¹⁷ have noted similar discrepancies for ELNES of MnO and Mn_3O_4 .

Krivanek et al.¹⁸ extended the EDS-based ALCHEMI (atom location by channeling-enhanced microanalysis) method to demonstrate energy-loss with channeled electrons (ELCE) for MgAl_2O_4 spinel. Tafto and Krivanek¹⁹ further extended the method to demonstrate site-specific valence determination of Fe in a chromite spinel. Similar experiments were performed in an attempt to discriminate the signature of the di- and tri-valent cobalt ions in Co_3O_4 , but no difference in the Co ELNES was detected. The most likely explanation for this behavior is that Co_3O_4 has the inverse spinel structure.¹² There is some supporting evidence from X-ray diffraction data on bond lengths; in addition, Fe_3O_4 has the inverse spinel structure. Further experiments are planned.

ALUMINUM NITRIDE - SILICON CARBIDE

Aluminum nitride and silicon carbide are structural ceramics and wide bandgap semiconductors which have similar hexagonal structures and a lattice mismatch in the basal plane of only 0.9%. AlN-SiC materials are of interest as high temperature structural materials and as ceramic semiconductors for applications such as high power and ultraviolet optoelectronic devices, or for use in severe environments. The tentative AlN-SiC phase diagram of Zangvil and Ruh²⁰ shows a flat miscibility gap at ~1950°C between ~20 and 80 % AlN, with a 2H solid solution above this temperature. The existence of the miscibility gap has been confirmed by several investigators (see Kern et al.⁶), notably Chen et al.²¹ Interdiffusion data exist only for 1950°C and higher. High resolution PEELS was used to detect possible interdiffusion at lower temperatures.

Examination of the AlN-SiC solid solution epilayer grown by MBE at 1050°C revealed predominantly the 2H polytype. Planar defects about 40 nm long and separated by about 5 nm in the growth direction were present on the basal planes. Their formation appears to be linked to the presence of similar sized steps on the growth surface, which are in turn related to the misorientation of the SiC substrate.²² No compositional inhomogeneity was detected by PEELS, the solid solution presumably being kinetically stabilized at the low growth temperature. Quantitative analysis of PEELS data indicated N/C and Al/Si atomic ratios of 0.75 ± 0.05 , in contrast to published⁶ Auger measurements of ~0.43.

Similarly, high spatial resolution PEELS failed to detect any interdiffusion in the diffusion couples of AlN grown by MBE on α (6H)-SiC and annealed at 1700 or 1850°C, either near the substrate interface or at threading dislocations in the epilayer. Auger depth profiles had indicated apparent

substantial interdiffusion, but large growth-surface steps and concomitantly large variations in epilayer thickness (30%), explain the misleading Auger results.²²

In the diffusion couples of polycrystalline AlN on α (6H)-SiC annealed at 1600 and 1700°C, an additional phase, typically \leq 50-nm-thick, was present at the SiC-AlN interface, but only where the AlN was epitactic to the SiC. Typical PEELS data from this phase are shown in Fig. 4; the major constituents are N, O, and Al; there is also a small Si signal. The O/N ratio measured by PEELS ranged from 0.35 to 0.75; beam damage probably contributed to the variability. High-magnification images of the interface phase revealed a 2.3 nm periodicity along the c-axis. The interface phase was thus identified as the 8H sialon phase^{23,24} which is based on the 8H aluminum oxynitride polytypoid of nominal composition $(\text{AlN})_2\text{Al}_2\text{O}_3$.²⁴ With EDS, secondary excitation of the SiC precludes confident identification of the small Si signal as intrinsic to the 8H interface phase; with PEELS there

is no such concern. Sputtered films from the ion milling are also unlikely since no Si was detected by PEELS on the nearby AlN. The oxygen presumably originates as a surface impurity on the starting materials. The exact epitaxy of AlN grains with the SiC, strongly suggests recrystallization of AlN (2H) from the 8H sialon. Interestingly, this would mean that the dome defects, prevalent in the epitactically oriented grains, nucleate at the dome top, increase in diameter as the grain boundary advances, and eventually pinch off at the oxygen-rich basal fault.

No aluminum was detected in the SiC, even adjacent to the interface, but particles typically 250 nm in diameter, and occasionally up to 1 μm long, form within the SiC at distances up to several micrometers from the SiC-AlN interface. Quantitative analysis of typical PEELS data (Fig. 5) yields Si_3N_4 with small levels of O and Al. Diffraction patterns confirm the Si_3N_4 -rich β' sialon identification and show $[0001]_{\beta'} // [11\bar{2}0]_{\text{6H}}$ and $[10\bar{1}0]_{\beta'} // [0006]_{\text{6H}}$. Oxygen is suspected of playing an important role in the precipitate formation.

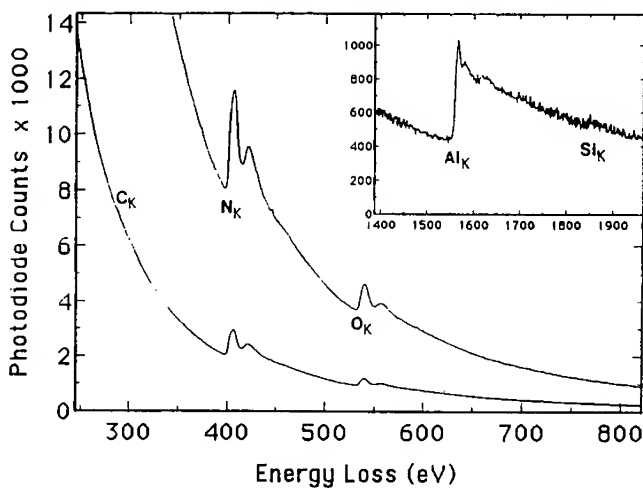


Fig. 4. PEELS data for 8H sialon interface phase.

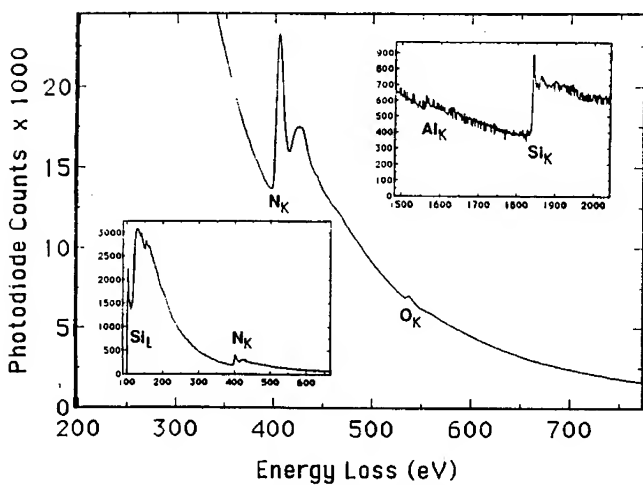


Fig. 5. PEELS data for Si_3N_4 -rich β' sialon particles.

CONCLUSIONS

The results vividly illustrate the efficacy of PEELS for the microanalysis of ceramics. Some questions remain regarding the validity of the normalized WLI ratio method for 3d occupancy measurement in 3d transition metal compounds. The method appeared useful for the Fe in amorphous SiC, but less so for differentiating Co^{2+} and Co^{3+} in cobalt oxides. The ability to measure compositions by PEELS, particularly for elements with $Z < 10$, at a spatial resolution of a few nanometers is unmatched. The absence of secondary excitation processes, which can plague EDS measurements of multi-phase materials, leads to greater confidence in the determined compositions. The Co:O stoichiometry gradients across the 100-nm-wide Co_3O_4 , the absence of AlN-SiC interdiffusion at low temperatures, and the importance of the minor constituents for sialon phase identification, are all examples where PEELS has clear advantages over any other technique.

ACKNOWLEDGEMENTS

This research was supported by the Division of Materials Sciences, U.S. Department of Energy under contract DE-AC05-84OR21400 with Martin Marietta Energy Systems, Inc. and through the SHaRE program under contract DE-AC05-76OR00033 with Oak Ridge Associated Universities, by NSF under grant #DMR-8901218, and by the Office of Naval Research.

REFERENCES

1. J. Bentley, in *Transmission EELS in Materials Science*, edited by M.M. Disko, C.C. Ahn, and B. Fultz (The Minerals, Metals and Materials Society, Warrendale, PA, 1992), pp. 155-181.
2. J. Bentley, L.J. Romana, L.L. Horton, and C.J. McHargue in *Phase Formation and Modification by Beam-Solid Interactions*, edited by G.S. Was, L.E. Rehn, and D.M. Follstaedt (Mater. Res. Soc. Proc. 235, Pittsburgh, PA, 1992) pp. 363-368.
3. L.L. Horton, J. Bentley, L. Romana, A. Perez, C.J. McHargue, and J.C. McCallum, *Nucl. Instr. and Meth.* **B65**, 345-351 (1992).
4. J. Bentley, L.J. Romana, L.L. Horton, and C.J. McHargue, in *Proc. 50th Ann. Meet. Electron Microscopy Soc. Amer.*, edited by G.W. Bailey, J. Bentley, and J.A. Small (San Francisco Press, San Francisco, 1992) pp. 346-7.
5. G. Dhalenne, F. d'Yvoire, P. Berthet, and A. Revcolevschi, *Solid State Ionics* **63-65**, 396-400 (1993).
6. R.S. Kern, L.B. Rowland, S. Tanaka, and R.F. Davis, *J. Mater. Res.* **8** 1477-80 (1993).
7. D.H. Pearson, B. Fultz, and C.C. Ahn, *Appl. Phys. Lett.* **53**, 1405 (1988).
8. T.I. Morrison, M.N. Brodsky, N.J. Zaluzec, and L.R. Sill, *Phys. Rev. B* **32**, 3107 (1988).
9. C.J. McHargue, A. Perez, and J.C. McCallum, *Nucl. Inst. and Meth.* **B59/60**, 1362-5 (1991).
10. V.P. Dravid, C.E. Lyman, M.R. Notis, and A. Revcolevschi, *Ultramicroscopy* **29**, 60-70 (1989).
11. J. Bentley, S. McKernan, C.B. Carter, and A. Revcolevschi, *Microbeam Analysis* **2**, S286-7 (1993).
12. J. Bentley, S. McKernan, C.B. Carter, and A. Revcolevschi, in *EMAG'93*, edited by A.J. Craven (Institute of Physics, Bristol, UK, 1993), in press.
13. J. Bentley, P. Angelini, and P.S. Sklad, in *Analytical Electron Microscopy 1984*, edited by D.B. Williams and D.C. Joy (San Francisco Press, San Francisco, 1984) pp. 315-7.
14. R.F. Egerton, *EELS in the Electron Microscope*, (Plenum, New York, 1986).
15. F.M.F. de Groot, M. Grioni, J.C. Fuggle, J. Ghijssen, G.A. Sawatzky, and H. Petersen, *Phys. Rev. B* **40**, 5715-23 (1989).
16. O.L. Krivanek and J.H. Paterson, *Ultramicroscopy* **32**, 313-8 (1990).
17. H. Kurata and C. Collie, *Phys. Rev. B* **48**, 2102-8 (1993).
18. O.L. Krivanek, M.M. Disko, J. Tafto, and J.C.H. Spence, *Ultramicroscopy* **9**, 249-254 (1982).
19. J. Tafto and O.L. Krivanek, *Phys. Rev. Lett.* **48**, 560 (1982).
20. A. Zangvil and R. Ruh, *J. Am. Ceram. Soc.* **71**, 884 (1988).
21. J. Chen, Q. Tian, and A.V. Virkar, *J. Am. Ceram. Soc.* **75**, 809-21 (1992).
22. J. Bentley, S. Tanaka, and R.F. Davis, in *EMAG'93*, edited by A.J. Craven (Institute of Physics, Bristol, UK, 1993), in press.
23. K.H. Jack, *J. Mater. Sci.* **11**, 1135-58 (1976).
24. J.W. McCauley et al., in *Ceramic Microstructures '86*, edited by J. Pask and A. Evans (Plenum, New York, 1988).

PART VI

Molecular Imaging

STM STUDIES AT ELECTROCHEMICALLY CONTROLLED INTERFACES

S.M. LINDSAY, J. PAN AND T.W. JING
Department of Physics and Astronomy, Arizona State University, Tempe, AZ 85287-1504

ABSTRACT

We use electrochemical methods to control the adsorption of molecules onto an electrode for imaging *in-situ* by scanning tunneling microscopy. Measurements of the barrier for electron tunneling show that the mechanism of electron transfer differs from vacuum tunneling. Barriers depend upon the direction of electron tunneling, indicating the presence of permanently aligned dipoles in the tunnel gap. We attribute a sharp dip in the barrier near zero field to induced polarization. We propose a 'tunneling' process consisting of two parts: One is delocalization of quantum-coherent states in parts of the molecular adlayer that hybridize strongly (interaction $\geq kT$) with Bloch states in the metal. This gives rise to a quantum-point-contact conductance, $G^c \leq 2e^2/h$ at a height z_0 . The other part comes from the exponential decay of the tails of localized states, $G = G^c \exp\{-2\kappa(z - z_0)\}$. Because measured decay lengths, $(2\kappa)^{-1}$, are small ($\approx 1\text{\AA}$), STM contrast is dominated by the contour along which $G[z_0(x, y)] = G^c$. Measured changes in z_0 are used to calculate images which are in reasonable agreement with observations. We illustrate this with images of synthetic DNA oligomers.

1. INTRODUCTION

The discovery that the scanning tunneling microscope (STM) could form images in water^{1, 2} has opened a new field of research^{3, 4}. The technique is often analyzed as though it were based on vacuum tunneling, although, until recently⁵ little was known about the mechanism of electron transport. In this paper, we will review the properties of the electrochemical interface briefly and describe what we know of the tunneling process.

Our interest in electrochemical STM (ECSTM) stems from developing methods for imaging DNA molecules in near-physiological conditions^{6, 7}. STM of biological molecules is controversial⁸. Images of DNA on graphite substrates which showed a 'double helix'⁹ or even 'atomic resolution'¹⁰ have been reproduced in experiments on *bare* graphite (no DNA was present)^{11, 12}. In addition, no mechanism for tunneling through large 'insulating' molecules is widely accepted¹³. We have continued to refine electrochemical deposition techniques^{14, 15}, and tested our method in a blind experiment¹⁶ which demonstrated clearly that DNA molecules can be imaged *in-situ* on an electrode surface using STM. Although we are far from a first-principles understanding of the contrast, our barrier-height measurements⁵ and modeling of images^{15, 16} suggest a mechanism which we will discuss in this paper also.

2. THE ELECTROCHEMICAL INTERFACE

The interface between an electrolyte and a metal is complicated when compared with the interface with a vacuum¹⁷. Nonetheless, it has at least two great advantages over uncontrolled or exposed surfaces. One is fundamental, and lies in the possibility of *potential control* of the electrode. The second is practical and is the relative ease with which contamination may be controlled.

Adsorption and the electric potential difference between the electrode and the bulk solution (i.e., outside the double layer region) are intimately connected. Adsorption involves a change of chemical potential for the adsorbing species which results in a change of the electric potential of the electrode. The Gibbs-Duhem equation is a quantitative statement of this relationship. The change in energy per unit area of a rigid surface of charge density σ on adsorption of a surface excess (with respect to the bulk concentrations) Γ_i of species i is

$$d\gamma = -\sigma d\phi - \sum_i \Gamma_i d\mu_i \quad (1)$$

where $d\phi$ is the change in potential of the surface with respect to the reservoir of particles and $d\mu_i$ is the change of chemical potential of species i on binding to the solid. In an ultrahigh vacuum (UHV) experiment, the adsorption (Γ) is controlled by isolating the surface from the reservoir of particles. In an electrochemistry experiment, the (conducting) surface is in contact with the source of particles, and adsorption is controlled using a feedback system to fix the electrode potential. Adsorption (and desorption) is carried out in thermodynamic equilibrium. Thus, the UHV and electrochemical environments are complementary ways of preparing controlled surfaces.

The second advantage is a practical one. The techniques outlined above only permits control to the extent that a reactive species (large $d\mu$) does not cover the surface. If a solid layer of the reaction product is in equilibrium with the dissolved (reactive) ions, attempts to alter the surface charge (or potential, $d\phi$) change only the relative amount of reactants and products, leaving the surface pinned at the Nernst potential for the reaction. Thus, the concentration of reactive atoms or molecules must be kept small. To take a concrete example, chlorine ions can react with gold, so electrolytes such as NaCl do not permit much variation of the interfacial potential at a gold electrode. Perchlorate electrolytes do not interact strongly with gold, but it is difficult to prepare perchlorate solutions with less than 10^{14} chlorine ions per cm^3 . In a vacuum, this concentration would correspond to a partial pressure of 10^{-3} Torr. However, in a liquid, ions move by diffusion, covering a distance ℓ cm in a time $t = \ell^2 / D$ seconds (D is the translational diffusion constant). In this example, about 10^{14} ions/ cm^2 would form a monolayer, so diffusion would have to transport ions over a distance of $\approx 1\text{cm}$. With D around 10^{-6} cm^2s^{-1} this would take 10^6 seconds (more than a month)! A UHV experiment would require a pressure of 10^{-12} Torr to achieve such results.

3. TUNNELING IN ELECTROCHEMICAL STM

Vacuum tunneling was identified by the exponential decay of conductance, G , with distance, z ,

$$G \approx G_0 e^{-2\kappa z} \quad (2)$$

and the observation of decay lengths, $(2\kappa)^{-1}$, on the order of 1\AA ¹⁸. Here,

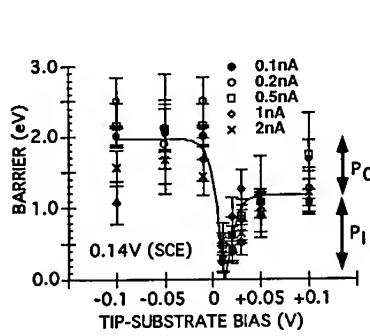


Figure 1. Tunneling barriers for Au(111) in NaClO_4 as a function of bias. Points are shown for several starting currents (as labeled). The line is a fit to a 2-level model of fixed (P_0) and induced (P_1) polarization in the gap.

$G_0 = 2e^2/h \approx 77.52 \mu\text{mho}$ ^{19, 20}. In a simple model $4\kappa^2 = \Phi$, the work function⁸. In practice²¹⁻²⁴ $4\kappa^2$ is found to be 1 to 3.5 eV less than Φ , owing to interactions between electrons at the small values of z used in STM^{19, 25, 26}. We will refer to the measured quantity, $4\kappa^2$, as the STM barrier.

Early attempts to measure this barrier in ECSTM^{6, 27} were plagued by contamination²⁸⁻³⁰. We have now constructed an ECSTM which is hermetically sealed, permits easy interchange of the sample in clean conditions and drifts very little. Using this, we have measured barriers for electron tunneling similar to those found in UHV experiments⁵. For example, we have measured values as high as 3.8 ± 0.6 eV (for tunneling through a cytosine adlayer). Such high values might be taken to indicate a process like vacuum tunneling. However, in contrast to vacuum tunneling, we find that the barriers are *strongly* dependent on the tip to substrate bias. This is illustrated in Fig. 1 which shows values for the STM barrier as a function of bias for a Pt-Ir tip and an Au(111) substrate in 0.4M NaClO_4 at 0.14V on the saturated calomel electrode (SCE) scale. Data were also taken as a function of the initial tip-to-substrate current, but this does not have much effect on the barrier.

The first point to notice is the asymmetry. It takes about 0.5 eV more energy for an electron to tunnel from the tip to the substrate than vice versa. This effect is seen with several electrolytes and adlayers and we attribute it to permanent molecular polarization in the tunnel gap⁵. More striking yet is the sharp dip near zero bias. It is not an electrochemical effect (the effects of changing substrate potential are relatively small) and it occurs at the same bias for a wide range of gap conductances. When we use a non-polar solvent, we do not find the sharp dip. We therefore attribute it to induced polarization in the tunnel gap. The solid line is a fit to a theory in which we model water alignment as a two-level system⁵.

In summary, we see that the arrangement of the molecules in the gap has a profound effect on the tunneling and that it is even possible that there are *liquid* water molecules in the gap at low electric fields. This is a very different situation from vacuum tunneling. This structure is summarized in Fig. 2.

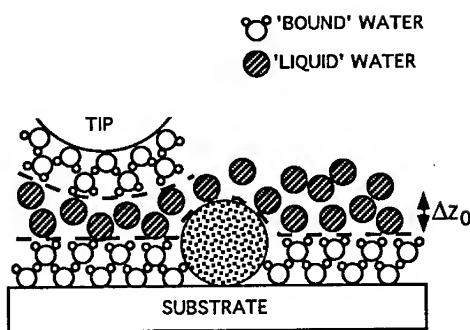


Figure 2. Model of the tunnel gap in ECSTM. The dashed line marks contours of quantum-point-contact.

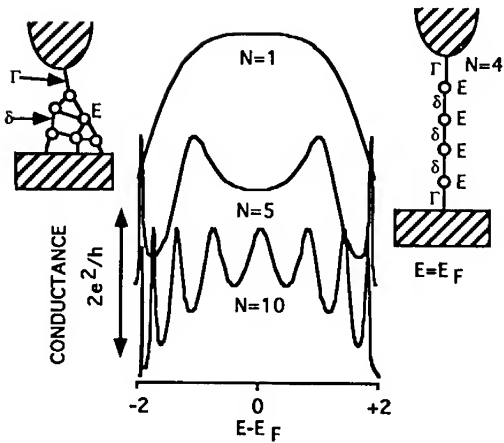


Figure 3. Conductance of some quantum-dot chains as a function of energy for chain model shown on right (curves are displaced vertically for clarity).

4. TUNNELING WITH METALS AND MOLECULES IN CLOSE PROXIMITY

4.1 Ab-initio calculations

We need to understand electron transport through molecular adsorbates so it is useful to review the few first-principles calculations. Examples are the local-density approximation calculation for xenon on a jellium model of nickel by Lang³¹, a scattering matrix procedure for benzene on Rh(111) by Sautet and Joachim³² and Car-Parrinello calculations for benzene on graphite by Fisher and Blöchl^{33,34}. In each case, the hybridization of molecular (or atomic states) with metal states at the Fermi energy was identified as the source of positive contrast, although interference between tunneling paths complicated the images³²⁻³⁴. Hybridization and resonant tunneling are equivalent descriptions of the same process, so we turn to a simple description of resonant tunneling.

4.2 A model for molecules

An atomistic picture of the tunnel gap is required for ECSTM and a tight-binding model, in our view, incorporates many of the important elements of the problem³⁵. The scattering matrix method of Sautet and Joachim³² is an equivalent approach which has been developed in a way that permits parameters to be extracted from LCAO calculations. Here we will present a simplified description based on a model by Sumetskii³⁶. We model the molecule connecting the tip and substrate as an interconnected assembly of quantum dots. Each dot is a point, i , at which the electron has an energy E_i , and a wavefunction φ_i . The partial flux of electrons from site i to electrode j is $\Gamma_i^{(j)}$ where

$$\Gamma_i^{(j)} = \frac{\hbar^2}{2m} \left| \int dP \left(\varphi_i \frac{\partial \varphi_i^*}{\partial s} - \varphi_i^* \frac{\partial \varphi_i}{\partial s} \right) \right|. \quad (3)$$

Here, s is the direction along the most probable tunneling path and P is a plane transverse to it. With matrix elements between dots

$$\delta_{ij} = \frac{\hbar^2}{2m} \left| \int dP \left(\varphi_i \frac{\partial \varphi_j^*}{\partial s} - \varphi_j^* \frac{\partial \varphi_i}{\partial s} \right) \right| \quad (4)$$

it is straightforward to write down a transfer matrix that yields transmission (i.e., conductance) between the electrodes^{36, 37}. A representation of a complicated assembly of dots is shown in Fig. 3 (inset on left). An analytical form is available for the conductance if we assume that the most probable tunneling path is dominated by a simple chain. It becomes particularly simple if we have all the matrix elements equal and set all widths (Γ_i) zero except the end dots for which we set $\Gamma = \delta$ ³⁶. This model is shown as the inset in the upper right of Fig. 3. We have calculated the conductance for up to 10 dots and the results are displayed in Fig. 3 for $N=1, 5$ and 10 and $\delta = 1$. The conductance is close to G_0 for dot energies that lie within $\pm 2\delta$ of the Fermi energy of the electrodes. In a long, homogeneous chain, a sharp conduction band develops but the cut-off is less sharp for a heterogeneous collection of dots (i.e., molecule). In general, N dots lead to $N-1$ resonances which, near their peaks yield a conductance for the k th resonance

$$G_k = \frac{2e^2}{h} \frac{g_{kk}^2}{4(E_k - E_F)^2 + g_{kk}^2} \quad (5)$$

where g_{kk} and E_k are the partial widths and energies after a transformation which diagonalizes the Hamiltonian³⁶. Thus, near a resonance, $G \approx G_0$. Away from a resonance G decreases slowly with N for almost any configuration. The exception is the long, homogeneous chain where decay is exponential for energies that lie outside $E_F \pm 2\delta$. In ignoring all but nearest neighbor interactions we have neglected important interference processes³². Note that equation (5) is the Breit-Wigner formula, derived for the conductance of a single atom by Kalmeyer and Laughlin²⁰. Our tight-binding calculations show a marked departure from this simple Lorentzian behavior far from resonances³⁵. Nonetheless, the conductance of an arbitrary collection of dots is close to G_0 almost independent of its size for a wide range of energies!

4.3 Quantum point contacts

This surprising result is supported by rather general arguments. When the STM tip contacts the surface, the tunnel current is *independent* of the local density of states and the gap conductance is given by the universal value, G_0 , that appears in equation 2. This result, implied by a result of Landauer³⁸ and verified in a calculation by Lang¹⁹, can be obtained simply as follows. Suppose that a constriction which connects two metals has a density of current carrying states at the Fermi energy $|dN/dE|_{E_F}$. The net number of current carrying electrons when a bias V is applied across the constriction is then $2 \times |dN/dE|_{E_F} \times e \times V$. The velocity of the electrons is $1/\hbar \times |dE/dk|_{E_F}$, so with the usual definition of current density, the density of states cancels out of the expression, leaving only the factor dN/dk . A constriction smaller than the Fermi wavelength can be treated as one-dimensional so $dN/dk = 1/2\pi$ and the conductance is given by G_0 for a single tunneling channel, independent of the size of any gap in the system. Since the gap may be made very large in vacuum STM, it is clearly possible to get into a regime where the tunnel gap does dominate (and limit) the tunnel conductance. In ECSTM, where the gap is filled with molecules in close contact, we must ask what stops indefinite propagation of current-

carrying states into the liquid?

4.4 What happens in a liquid?

Obviously, states on water molecules in the bulk are localized, so the problem is to find where states make a transition from delocalized to localized wavefunctions as one goes out into the liquid from the metal surface. Electronic states may become localized because of correlations (important in molecules³⁹), disorder (Anderson localization) or thermal fluctuations (which can be considered as a special case of Anderson localization⁴⁰). Localization lengths owing to static disorder can be quite large, while correlations do not necessarily lead to localization of all states in a complex system. We will restrict our discussion to thermal fluctuations, recognizing that this may be inappropriate in some cases.

To see how propagation of resonant states is destroyed by thermal fluctuations, one may consider the time-evolution of a delocalized state by solving the time-dependent Schrödinger equation for an incident flux on an isolated atom³⁷. Charge builds up on the localized state as the electron is reflected back and forth across the barrier many times. The weaker the coupling, Γ_{ij} between sites i and j , the longer this process takes (the time is on the order of \hbar/Γ_{ij}). If the potential changes during this time, the charge build-up can be destroyed. It is quite a complicated transition, in as much as many vibrational degrees of freedom may be required to destroy coherence^{41,42}. We do not know how to calculate a critical value for Γ_{ij} but will assume that localization occurs when Γ_{ij} becomes smaller than kT . Thus, there will be some distance $z_0(x,y)$ above the electrode surface at which the current carrying states begin to decay exponentially and $z_0(x,y)$ will be a function of the local electronic properties of the adlayer. We refer to $z_0(x,y)$ as the *contour of quantum-point-contact*. We expect that it (crudely) coincides with the point at which molecules cease to be strongly bound to the electrode by *direct* interactions with the metal. We arrive at the model depicted schematically in Fig. 2. The tip will scan at some distance above the substrate which is the sum of $z_0(x,y)$ (which may be many Ångstroms) and a gap set by the local exponential decay length (which is a few Ångstroms). $z_0(x,y)$ will be constant over a uniform adlayer, but will change as the tip passes over a molecule embedded in the adlayer (shown shaded in Fig. 2). The contrast of the embedded molecule, Δz_0 , will be a function of the difference between the electronic properties of the adjacent adlayer and the molecule. This is not simple to calculate. However, we know from measurements that the decay length for the region of exponential decay does not vary by more than a factor of two in our experiments ($0.5 \leq \kappa \leq 1 \text{ Å}^{-1}$), so the error in taking the *measured* contrast as the real Δz_0 is probably not big. Furthermore, we will assume that matrix elements change abruptly at the surface of the bound molecule, so that the contour of quantum-point-contact follows the surface of the molecule. We will also ignore interference effects. These last two assumptions are made for convenience and are unlikely to hold in many cases. Thus, our recipe for calculating an image is as follows: (a) We take the measured contrast and the known height of a molecule and use these to estimate $z_0(x,y)$ in the adjacent adlayer. (b) We cut out all of a model structure that lies below $z_0(x,y)$ in height and apply a Gaussian broadening to the remainder so as to simulate the effects of a finite tip radius or cluster of molecules on the tip.

4.5 Comparison with Tersoff-Hamman Theory

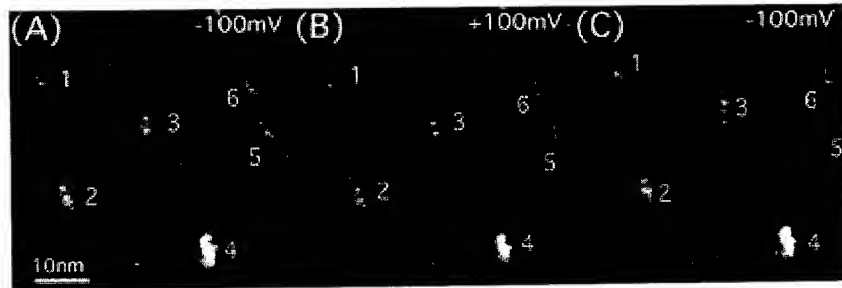


Figure 4. Images of six 20 base single-stranded DNA molecules (numbered) taken with the tip negative (A), then positive (B) then back to negative (C).

At first sight, our claim that the quantum-point-contact resistance is independent of the local density of states (LDOS) may appear to conflict with the Tersoff-Hamman theory⁴³ which has been so successful for vacuum STM. However, the LDOS and $z_0(x,y)$ are correlated because both depend upon some local effective interaction with the metal. The distinction is unimportant for imaging in a vacuum. It becomes important for imaging in a liquid medium.

5. DATA AND CALCULATIONS FOR ADSORBED DNA MOLECULES

5.1 Electron transport with DNA molecules in the tunnel gap

Here, we show that the preceding arguments can be used to analyze the contrast of DNA molecules. First, we show that DNA images are consistent with the tunneling processes we have discussed. Fig. 4 shows images of six 20 base single-strand DNA molecules taken with the tip negative (4A), then positive (4B) and then negative again (4C). The contrast is positive and does not change. This shows that (a) the electronic density of states is varying smoothly for at least $\pm 100\text{meV}$ around the Fermi energy, implying that the electronic bandwidth is greater than kT , (b) an electrochemical process involving localized charge transfer to or from the molecule is unlikely and (c) the tip-bias induced changes in the barrier have no significant effect on the contrast. Second, we show that decay lengths with DNA present are consistent with the range of barriers we have measured over homogeneous adlayers of the various chemical constituents. We have noted that the resolution is a strong function of the set-point tunnel current¹⁵ but the rather obvious ‘washing out’ of high frequency components in the image with decreased tunnel current is difficult to analyze quantitatively. We have measured the apparent height of whole DNA molecules as a function of the set-point tunnel current and found that it does decrease slightly as the set-point tunnel current is lowered. It is straightforward to use the Tersoff-Hamman theory⁸ to show that the contrast at a current i , $\Delta z(i)$, is related to the contrast at a current i_0 by

$$\frac{\Delta z(i)}{\Delta z(i_0)} = \left(\frac{i}{i_0} \right)^{\frac{\pi^2}{2k^2 a^2}} \quad (6)$$

where a is the spatial period of the image. Fig 5 shows data for this contrast ratio as a function of

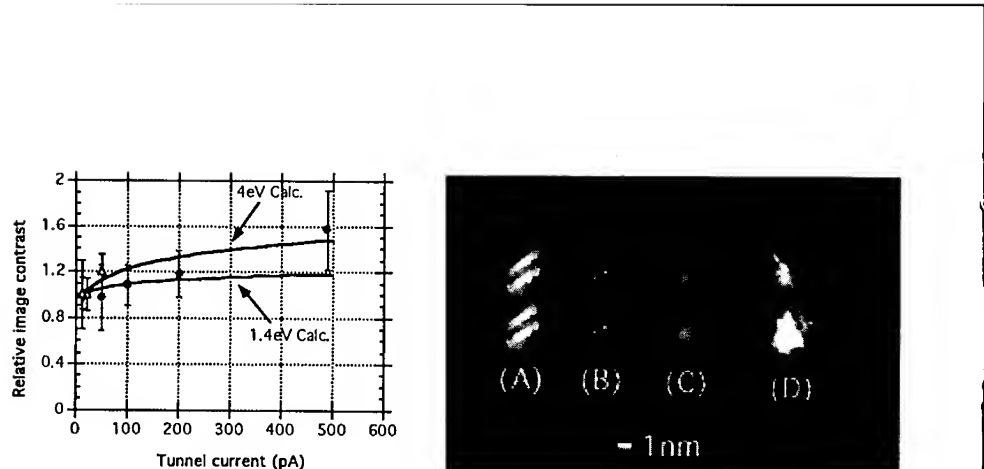


Figure 5. Measured height (normalized to 1.0 at lowest current) as a function of tunnel current. Lines are calculated according to equation (6) for the barrier values listed.

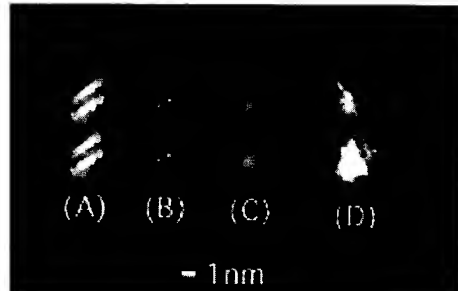


Figure 6. Steps in the calculation of contrast (A-C) for a 20 base double-stranded DNA molecule. D is an experimental image.

set-point current for a number of images. The solid lines are generated using equation (6), the range of barriers we have measured for the various constituents of the DNA and the surrounding phosphate adlayer and taking $a=2\text{nm}$. The weak dependence of contrast on current for a feature as large as these molecules precludes any convincing test, but we see that the data are consistent with a tunneling model.

5.2 Calculating the contrast for DNA molecules

Fig. 6 illustrates the various steps we outlined in section 4.4 above. A model structure (A) is first oriented with respect to the substrate. In this simple case of DNA oligomers, independent biochemical evidence⁴⁴ limits the choices to the orientation shown or one rotated azimuthally by π . The measured contrast is $2\pm1\text{\AA}$, and Fig. 6B shows what remains after the lower 18\AA of the structure is removed. These points are then blurred by a Gaussian of 7\AA radius to produce the final result shown in Fig. 6C. An experimental image is shown for comparison in Fig. 6D. Fig. 7 shows a series of models, and calculated and experimental images for a number of double-stranded and single-stranded oligomers. The imaging and samples are described in the paper by Jing et al.¹⁵ The calculated images were all obtained using a cut-off of 18\AA and a Gaussian blurring of 7\AA , as above. The agreement is generally good and these calculations account for the following anomalies: (1) The direction of the helical groove is not generally discerned in the images. (2) The 'sticky' ends of the 31 base sample are not seen. (3) If the image length is interpreted as the true length of the polymer, a range of base-stacking distances are obtained. However, comparison with these calculated images yields a consistent value of 3.3\AA as the effects of 'losing' some of the molecule under the adlayer are accounted for.

6. CONCLUSIONS

The ECSTM works by a quite different process from vacuum STM. Imaging occurs via a cluster of molecules in the gap. These molecules may be oriented by the electric field in the gap,

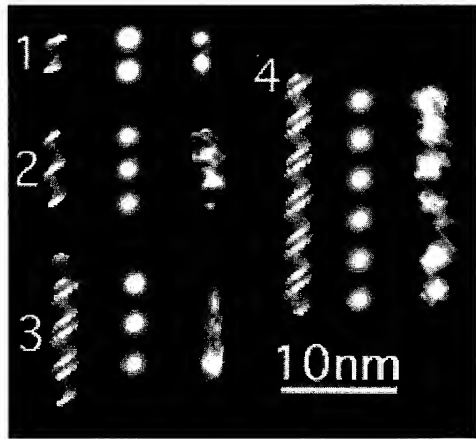


Figure 7. Showing (left to right) model, calculated image and experimental image for (1) 11 base single-stranded DNA, (2) 20 base single-stranded DNA, (3) 31 base DNA, 25 bases paired and 6 overhanging, (4) 61 base-pair double-stranded DNA.

but this does little to affect the images. The point at which wave functions become localized on the liquid or adlayer molecules plays a key role in the image which is quite well described as a contour which follows the height of quantum-point-contact. Reasonable agreement between measured and calculated images is obtained with a simple procedure based on this idea. If the sample is not flat, resolution is limited by the size of the cluster on the tip. In the images presented here, this effect leads to a Gaussian broadening width of 7 Å. Nonetheless, this structural probe provides useful information in an environment that has, hitherto, been inaccessible to direct imaging.

ACKNOWLEDGMENTS

We thank Jack Larsen, Andy Vaught and Dave Lampner for help in the lab and Kevin Schmidt, Otto Sankey and Andrew Chizmeshya for useful discussions. Financial support was received from the ONR (N00014-90-J-1455), NSF (Dir 89-20053) and NIH (1 R21 HG0081801A1).

REFERENCES

1. R. Sonnenfeld and P. K. Hansma, *Science* **232**, 211 (1986).
2. H.-Y. Liu, F. R. F. Fan, C. W. Lin and A. J. Bard, *J. Am. Chem. Soc.* **108**, 3838 (1986).
3. H. Seigenthaler in *Scanning Tunneling Microscopy II* edited by R. Wiesendanger and H. J. Güntherodt (Springer-Verlag, Berlin, 1992) p.7.
4. A. Bard and F. R. F. Fan in *Scanning Tunneling Microscopy, Theory, techniques and Applications* edited by D. A. Bonnell (VCH, New York, 1993) p.287.
5. J. Pan, T. W. Jing and S. M. Lindsay, *J. Phys. Chem.* (1993), submitted.
6. S. M. Lindsay and Barris, *J. Vac. Sci. Tech. A* **6**, 544 (1988).
7. S. M. Lindsay, T. Thundat, L. A. Nagahara, U. Knipping and R. L. Rill, *Science* **244**, 1063 (1989).
8. C. J. Chen, *Introduction to Scanning Tunneling Microscopy*, (Oxford University Press, NY.,

1993).

9. T. P. Beebe, T. E. Wilson, D. F. Ogletree, J. E. Katz, R. Balhorn, M. B. Salmeron and W. J. Siekhaus, *Science* **243**, 370 (1989).
10. R. J. Driscoll, M. G. Youngquist and J. D. Baldeschweiler, *Nature* **346**, 294 (1990).
11. C. R. Clemmer and T. P. Beebe, *Science* **251**, 640 (1991).
12. W. M. Heckl and G. Binnig, *Ultramicroscopy* **42-44**, 1073 (1992).
13. D. D. Dunlap, R. Garcia, E. Schabtach and C. Bustamante, *Proc. Natl. Acad. Sci. (USA)* (1993) in press.
14. S. M. Lindsay, N. J. Tao, J. A. DeRose, P. I. Oden, Y. L. Lyubchenko, R. E. Harrington and L. Shlyakhtenko, *Biophysical Journal* **61**, 1570 (1992).
15. T. Jing, A. M. Jeffrey, J. A. DeRose, Y. L. Lyubchenko, L. S. Shlyakhtenko, R. E. Harrington, E. Appella, J. Larsen, A. Vaught, D. Rekesh, F. X. Lu and S. M. Lindsay, *Proc. Natl. Acad. Sci. (USA)* **90**, 8934 (1993).
16. A. M. Jeffrey, T. W. Jing, J. A. DeRose, A. Vaught, D. Rekesh, F. X. Lu and S. M. Lindsay, *Nucleic Acids Research* (1993) in press.
17. E. M. Stuve and N. Kizhakevariam, *J. Vac. Sci. Technol.* (1993) in press.
18. G. Binnig, H. Rohrer, C. Gerber and E. Weibel, *Physica* **109/110B**, 2075 (1982).
19. N. D. Lang, *Phys. Rev. B* **36**, 8173 (1987).
20. V. Kalmeyer and R. B. Laughlin, *Phys. Rev. B* **35**, 9805 (1987).
21. G. Binnig, N. Garcia, H. Rohrer, J. M. Soler and F. Flores, *Phys. Rev. B* **30**, 4816 (1984).
22. R. Schuster, V. Barth, J. Wintterlin, R. J. Behm and G. Ertl, *Ultramicroscopy* **42-44**, 533 (1992).
23. J. K. Gimzewski and R. Möller, *Phys. Rev. B* **36**, 1284 (1987).
24. J. Wintterlin, J. Wiechers, H. Brune, T. Gritsch, H. Hofer and R. J. Behm, *Phys. Rev. Lett.* **62**, 59 (1989).
25. P. DeAndres, F. Flores, P. M. Echenique and R. H. Ritchie, *Europhys. Lett.* **3**, 101 (1987).
26. W. Schmickler and D. Henderson, *J. Electroanal. Chem.* **290**, 283 (1990).
27. M. Binggeli, D. Carmal, R. Nyffenegger and H. Seigenthaler, *J. Vac. Sci. Technol. B* **9**, 1985 (1991).
28. J. H. Coombs and J. B. Pethica, *IBM J. Res. Dev.* **30**, 455 (1986).
29. S. M. Lindsay, T. Thundat and L. Nagahara in *Biological and Artificial Intelligence Systems* edited by E. Clementi and e. H.S. Chin (ESCOM, Leiden, 1988) p.124.
30. S. M. Lindsay, T. Thundat and L. A. Nagahara, *J. Microscopy* **152**, Pt 1, 213 (1988).
31. D. M. Eigler, P. S. Weiss, E. K. Schweizer and N. D. Lang, *Phys. Rev. Lett.* **66**, 1189 (1991).
32. P. Sautet and C. Joachim, *Ultramicroscopy* **42-44**, 115 (1992).
33. A. J. Fisher and P. E. Blöchl in *Computations for the Nanoscale, NATO ARW* (1993) in press.
34. A. J. Fisher and P. E. Blöchl, *Phys. Rev. Lett.* **70**, 3263 (1993).
35. S. M. Lindsay, O. F. Sankey, Y. Li and C. Herbst, *J. Phys. Chem.* **94**, 4655 (1990).
36. Sumetskii, *J. Phys.: Condensed Matter* **3**, 2651 (1991).
37. S. M. Lindsay, O. F. Sankey and K. E. Schmidt, *Comments on Mol. Cell. Biophys.* **A7**, 109 (1991).
38. R. Landauer, *Philosophical Magazine* **21**, 863 (1970).
39. P. Fulde, *Electron correlations in molecules and solids*, (Springer-Verlag, Berlin, 1991).
40. A. D. Stone and P. A. Lee, *Phys. Rev. Lett.* **54**, 1196 (1985).
41. P. Hyldgaard and A. P. Jauho, *J. Phys: Condensed Matter* **2**, 8725 (1990).

42. M. I. Stockman, L. S. Muratov, L. N. Pandey and T. F. George, *Phys. Rev. B* **45**, 8550 (1992).

43. J. Tersoff and D. R. Hamann, *Physical Review B* **31**, 805 (1985).

44. D. Rhodes and A. Klug, *Nature* **286**, 573 (1980).

LOW VOLTAGE POINT PROJECTION MICROSCOPY AND TIME OF FLIGHT STM - TWO NEW MICROSCOPIES

J. C.H.SPENCE, W. QIAN, W. LO, S. MO, U. KNIPPING AND X. ZHANG

Department of Physics and Astronomy, Arizona State University,
Tempe, AZ 85287. USA.

ABSTRACT

The design of a low voltage point-projection field-emission transmission electron microscope is described and images showing 0.7nm resolution at 100 volts are given. A scheme for low voltage reflection electron holography from bulk samples in UHV is outlined. A new STM is described which allows atomic clusters to be transferred onto the tip, then introduced into a time-of-flight analyser for species identification.

POINT PROJECTION MICROSCOPY - TRANSMISSION AND REFLECTION.

The manipulation of individual atoms to form hand made structures with novel controllable properties has aroused wide interest (see [1] for recent work). Independent methods for imaging these and similar structures at atomic resolution are also needed, both to monitor the construction process and for structure determination, since image interpretation can be extremely complex due to the complexity of the quantum mechanical inversion problem, or difficulties in estimating the scattering potential at low electron energies. One of the earliest methods of forming electron images, both in field-emission and transmission microscopy, consisted of projection from a "point" source, distance z_1 from a transmission object [2, 3]. An image with magnification $M = z_2/z_1$ is then formed on a screen at distance z_2 from the object ($z_2 \gg z_1$). Under single scattering conditions, and in the absence of aberrations, it can be shown that this image is identical to a conventional image formed by an ideal lens which is out of focus by just z_1 [4]. The angular aperture of that lens should be equal to the coherence angle $\alpha = \lambda/d$ of the source, of size d . The image resolution is then approximately equal to the source size d , so that if a nanotip field-emitter is used as the source, atomic resolution images may be obtained with negligible aberrations from sufficiently thin films [5]. Similar electron shadow images known as Ronchigrams (or large-angle coherent nanodiffraction patterns) have been formed at high energies for many years using the stationary probe of a scanning transmission electron microscope (STEM) focussed a distance z_1 in front of a thin transmission object. These are severely affected by lens aberrations, unlike the low voltage point projection (PP) microscope (see [6] for a review).

We have recently constructed a low voltage point-projection instrument, as shown in figure 1. It has much in common with an STM. The tip to sample distance $z_1 = 100$ nm, and, with $z_2 = 10$ cm, the instrument gives a magnification of $M = 10^6$. The sample acts as the grounded anode, and the space between sample and channel-plate detector is field - free. Tips are prepared by chemical etching and in-situ sputtering, field-evaporation and heating, and examined by running the instrument as a field-ion microscope, using methods pioneered by H.W. Fink and co-workers [7]. A Burleigh ARIS UHV inchworm (I.W.) was chosen to support the tip because of its clamping action, which is maintained by stored charge during imaging when the leads are disconnected. A PZT deflection tube (T1) is also used for fine motion, and a single crystal [111] tungsten tip (T) is either welded to a tungsten heating loop or fitted directly to T1. The crystal axis is aligned with the center of the detector. Unlike STM design, the reduction of AC magnetic fields and vibration transmitted on tip heating wires are important, since both increase the effective source size and so reduce coherence. The microscope sits on a viton stack, enclosed in a mu-metal cylinder. An inertial stick-slip stage [8] which accepts a 3mm TEM grid (MG) was designed. The kinematic mounting uses three balls (two riding on sapphire rods (SR), one on a plate) to provide one-dimensional coarse motion in the direction

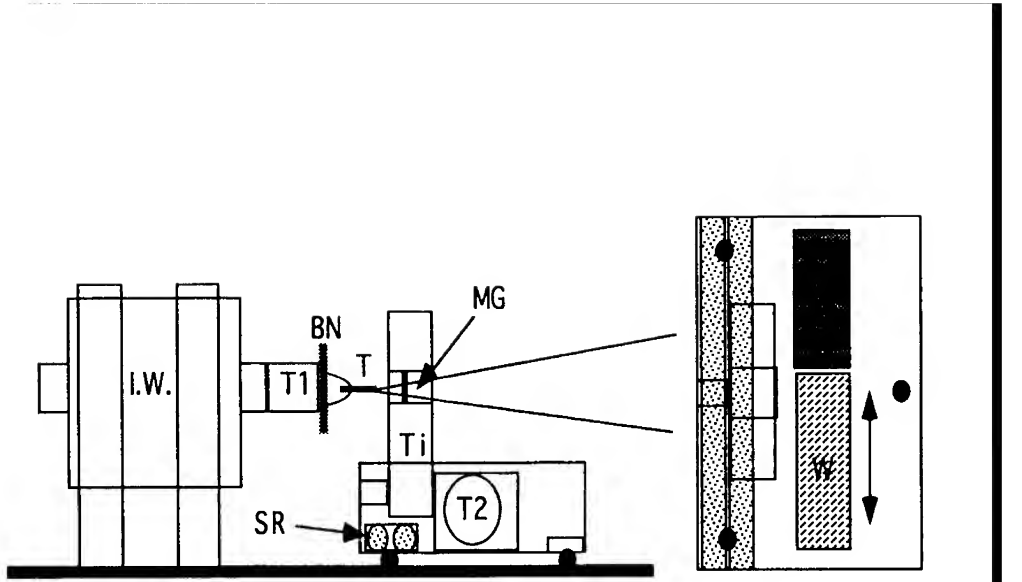


Figure 1. Point projection microscope. Stage T_1 moves normal to page. Top view of stage at right. Sapphire rods (SR), TEM Microscope grid (MG), Field emission tip T, Inch-worm (IW) Piezo tubes T_1 and T_2 and weight W are shown. The image is formed without scanning.

normal to the page in figure 1. Two-dimensional deflection of the tube T_1 then allows a three micron by 3 mm strip of the sample to be examined. The height of the sample can be preset. The stage is driven by a 100 volt ramp waveform applied to piezo tube motor T_2 operated in stretching mode against weight W. Differences between static and dynamic friction cause linear motion of the center of mass during the slow rise-time but not during the fast fall-time. This design has the advantage that no permanent magnets are used in the stage, however it will not operate well uphill. The (bakeable) microscope chamber is mounted on a pneumatic table which must therefore be accurately levelled. This table has a resonant frequency below $f_s = 2.5$ Hz. The resonant frequency of a 3 mm X 0.1mm tip is about $f_t = 2.3$ kHz, giving a total vibration amplitude attenuation for intermediate frequencies of $(f_s/f)^2 = 10^{-6}$. A higher value of f_t is desirable - by observing Fresnel edge fringes while supplying a sinusoidal voltage to the tip support piezo, the effect of the heating loop on f_t is being investigated (experience from high voltage STEM instruments is relevant here). Good (but unreliable) results have been obtained without tip heating, and indirect heating schemes are planned to improve tip stability. A single stage 75mm channel plate and screen are used as detector. A leak valve is fitted to the chamber to allow field-ion imaging of the tip during tip formation, with the tip held positive at several kilovolts.

For a suitably sharp tip emitting from a few-atom cluster the necessary magnification and electric field at the tip are obtained at about 100 volts. In the simplest model in which both the tip and detector are modelled as parabolic, the field at the tip (which needs to be about 0.4 V/A for field-emission from tungsten) is given by

$$E(z) = \frac{V}{z \ln(z_1/r)}$$

where r is the tip radius and z a coordinate along the axis measured from the center of the tip. Thus fixing z_1 (for given M), r and E fixes V . The properties of these nanotip field-emitters have been studied extensively; there have been reports of unusually narrow energy distributions [9], focussing effects due to diffraction through a single-atom tunneling barrier [10], and substantial increases in brightness [11], suggesting uses for second-order intensity interferometry with electrons [12]. We have studied the aberrations of the virtual source inside a nanotip, which we

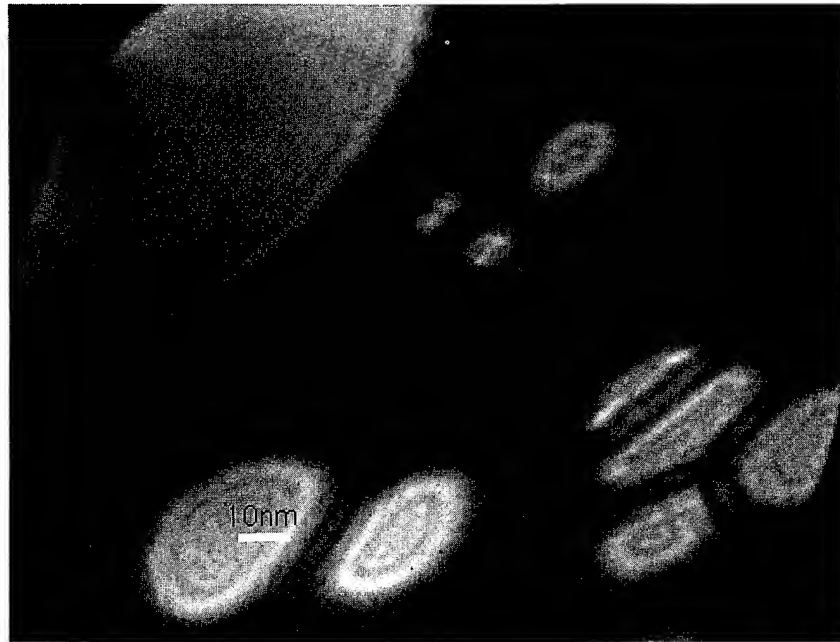


Figure 2. High magnification image showing Fresnel fringes at edges of holey carbon film. Beam current 1 nA, voltage 90 V.

find to be of Angstrom dimensions [13]. We find the measured brightness of our nanotip to be $3.3 \times 10^8 \text{ A cm}^{-2} \text{ str}^{-1}$ at 470 volts (or $7.7 \times 10^{10} \text{ A cm}^{-2} \text{ str}^{-1}$ when scaled to 100 kV), considerably higher than conventional cold field-emission tips (measurements for cold field-emission tips are average brightness values, however, made in the presence of lens aberrations, and so may not be comparable). Figure 2 shows an image from this instrument of a baked holey carbon film on a molybdenum TEM grid, obtained at 90 volts ($\lambda = 0.13 \text{ nm}$) with 1 nA beam current. Here $M=179,000$ (at the channel plate), so $z_1 = z_2 / M = 838 \text{ nm}$. This large defocus z_1 produces the many Fresnel fringes seen. From them, a rough estimate of the effective source size d (and hence the resolution (also d)) may be made if the transverse coherence width L_c is taken to be approximately equal to the total width of the band of Fresnel fringes. We measure $L_c = 51.1 \text{ nm}$, so that, using $d = \lambda / \pi \alpha = \lambda z_1 / (\pi L_c)$ from the Van-Cittert-Zernike theorem, we have $d \approx 0.68 \text{ nm}$. Alternatively, the resolution may be taken as the width of the smallest Fresnel fringe, which is given by the same expression. The rapid fall-off in DQE of the channel plate below 90 volts may also provide a beneficial energy filtering effect. Recently we have been successful, in collaboration with Dr. Y. Fujiyoshi, in obtaining a lattice image from the membrane protein purple membrane [14] at 100 volts by point projection. These results support the finding that, in certain classes of organic films, radiation damage results chiefly from inner shell excitations rather than valence excitations, so that this damage may be greatly reduced if the beam energy is less than the inner shell ionization energy [15]. In fact, due to multiple scattering, damage decreases well above this energy [15]. Thus the microscope may be useful for the study of Langmuir-Blodgett films and membrane proteins, or small molecules such as Bucky-balls. The interpretation of these images requires a solution to the

transmission low energy electron diffraction (TLEED) problem, which has now been analysed using both Bloch-wave [16] and Muffin-tin potential [17] methods. The treatment of these images as Fourier images has been discussed in detail [18]. If single scattering conditions could be obtained, the images of extended films (wider than the beam) could be interpreted as in-line electron holograms, so that methods for attacking the twin-image problem developed in photoemission "holography" may be useful [19]. At the boundary of opaque objects, the wave travelling in vacuo around the object acts as a reference wave, allowing the shapes of small molecules to be recovered, provided the twin image problem can be solved.

A much wider range of applications could be opened up for this instrument in surface science if point projection imaging could be applied to the reflection geometry for bulk samples. Two arrangements suggest themselves. The Lloyd's mirror interferometer provides a simple off-axis geometry [20], thus avoiding the twin image problem, but the image is foreshortened. Alternatively, the arrangement shown in figure 3 might be used. This requires an electron mirror, and a lens. Without a lens, electrons travel directly to the surface and become trapped beneath the tip. The mirror may be obtained by using the specular "RHEED" condition. The virtual source at P' then provides a geometry similar to in-line electron holography [21] for small particles lying on the surface, which produce elastic diffuse scattering to interfere with the specular reference beam. The twin image problem may then be solved by the Fraunhofer method of Thompson [22], since the interference pattern is recorded in the far-field of the particles. The main difficulty may be a-priori knowledge of the specular rocking curve amplitude and phase variation with angle, however this may be computed for substrates (such as silicon) of known structure. By comparison with the sub-nanometer resolution of modern field-emission SEM instruments, the advantages of the arrangement shown in figure 3 lie mainly in the higher resolution and three-dimensional information obtainable. Lens L may be a diverging lens as shown [23], in which case the large value of z_1 (and small M) require a second lens (not shown). Alternatively L may be a converging einzel minilens of micron dimensions [24] which

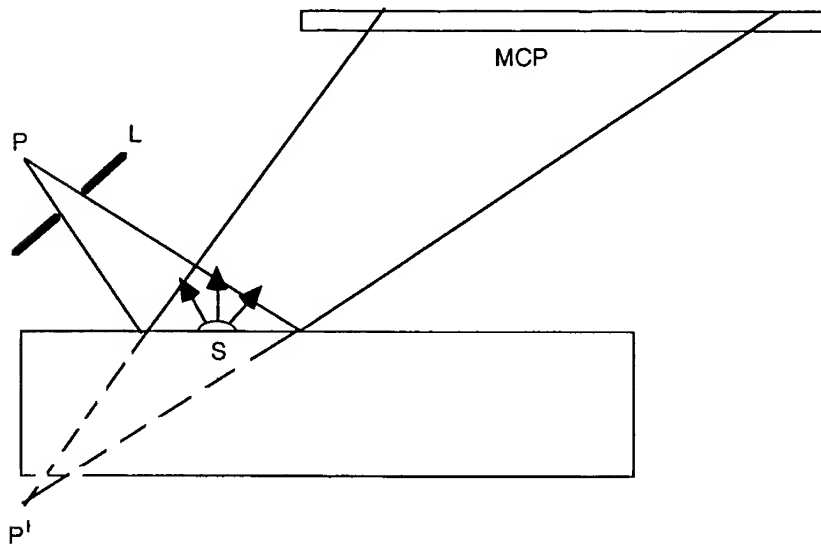


Figure 3. Scheme for point-projection reflection microscopy (holography). Particle S on atomically flat surface scatters diffusely, interfering with specular reference wave from virtual source P' . Image at MCP is out of focus by distance PS and is an in-line hologram.

forms a focussed probe just above the crystal surface, so that a second lens is not needed. The aberrations of these lenses, perhaps limited by the eccentricity of the hole, must then be considered. However lens aberrations scale roughly with lens dimensions, and the problem becomes one of accuracy in the lithography techniques used to make the lenses. The instrument shown lacks the simplicity of the transmission instrument, since many piezo motions are required, including those to align the tip with the lens and those which provide two-axis tilt and translation for the sample.

TIME OF FLIGHT SPECTROSCOPY FOR SPECIES IDENTIFICATION IN STM.

An STM has been constructed which will allow atomic clusters of interest to be transferred into a time-of-flight spectrometer for identification. Atoms will first be transferred onto the tip, using a small voltage pulse. The sample is then removed, and these atoms ejected into a time-of-flight (TOF) analyser for mass identification (see [25] for an excellent review of TOF methods). Figure 4 shows the experimental arrangement. The STM is based on a miniature Burleigh inchworm, to which two piezo tubes are directly attached. The outer one is used in bending mode to provide coarse stick-slip motion of the stage plate in the two lateral dimensions. The inner piezo provides fine z motion, and the inchworm accounts for the coarse approach. The sample holder sits on three balls, (to one of which the tunnel current amplifier is connected) and may be removed using a wobble-stick. Electrical insulation for 15 kV at the tip is provided. The tip is not cooled. A 75mm chevron dual channel plate is positioned $L = 200$ mm above the tip. This is used both as a time-of-flight detector, and to form field-ion images and electron field emission images of the tip. A D.C. voltage (up to 10 kV) is applied to the tip for TOF analysis, to which a small additional ten nanosecond wide pulse is applied to stimulate field evaporation of adatoms at the tip. The nanotip preparation techniques developed for the point projection microscope (above) are used to prepare especially sharp tips for STM and TOF. This keeps the field evaporation voltages low, as does the use of room temperature and the fact that the atoms to be desorbed may be weakly bonded. We use a Blumlien pulse generator and mercury reed switch [26]. The overall design is similar to the imaging atom probe of Panitz [27]. The output from the phosphor screen is led via a capacitor to a 2 ns sampling digital oscilloscope, whose trace is triggered by the tip pulse. For a total effective potential V_{eff} at the tip, the mass to charge ratio m/n is obtained in the usual way from the equation

$$n e V_{eff} = (1/2) m v^2 = (1/2) m (L/t)^2$$

where t is the flight time (typically about a microsecond for heavy elements and sharp tips). We take $L = 200$ mm on the assumption that the ions are accelerated to their final velocity within a few microns of the tip. At present the STM and TOF capabilities of the system are being evaluated, and atom transfer from a sample followed by TOF analysis has yet to be attempted. It remains to be seen whether adatoms collected from the sample will remain at the tip apex within the collection angle of the detector. Figure 5 demonstrates the excellent performance of this very small STM on the 2X1 cleavage surface of (111) Si. Figure 6 shows the TOF spectrum obtained from an undecorated tungsten tip. The ratio of the times (1.284 μ s and 2.025 μ s) suggest that these are W^{5+} and W^{2+} . The RF noise at the left of spectrum is due to inadequate RF shielding. By limiting the coarse lateral motion to one dimension we hope to be able to find the same region after removing the sample for analysis and returning the sample holder to the STM. This method of microanalysis is destructive.

Acknowledgements

We are most grateful to Drs. M. Scheinfien, G. D.W. Smith and D. Seidman for their generous advise and help with this work, supported by NSF awards DMR91-12550 and DMR91-16362.

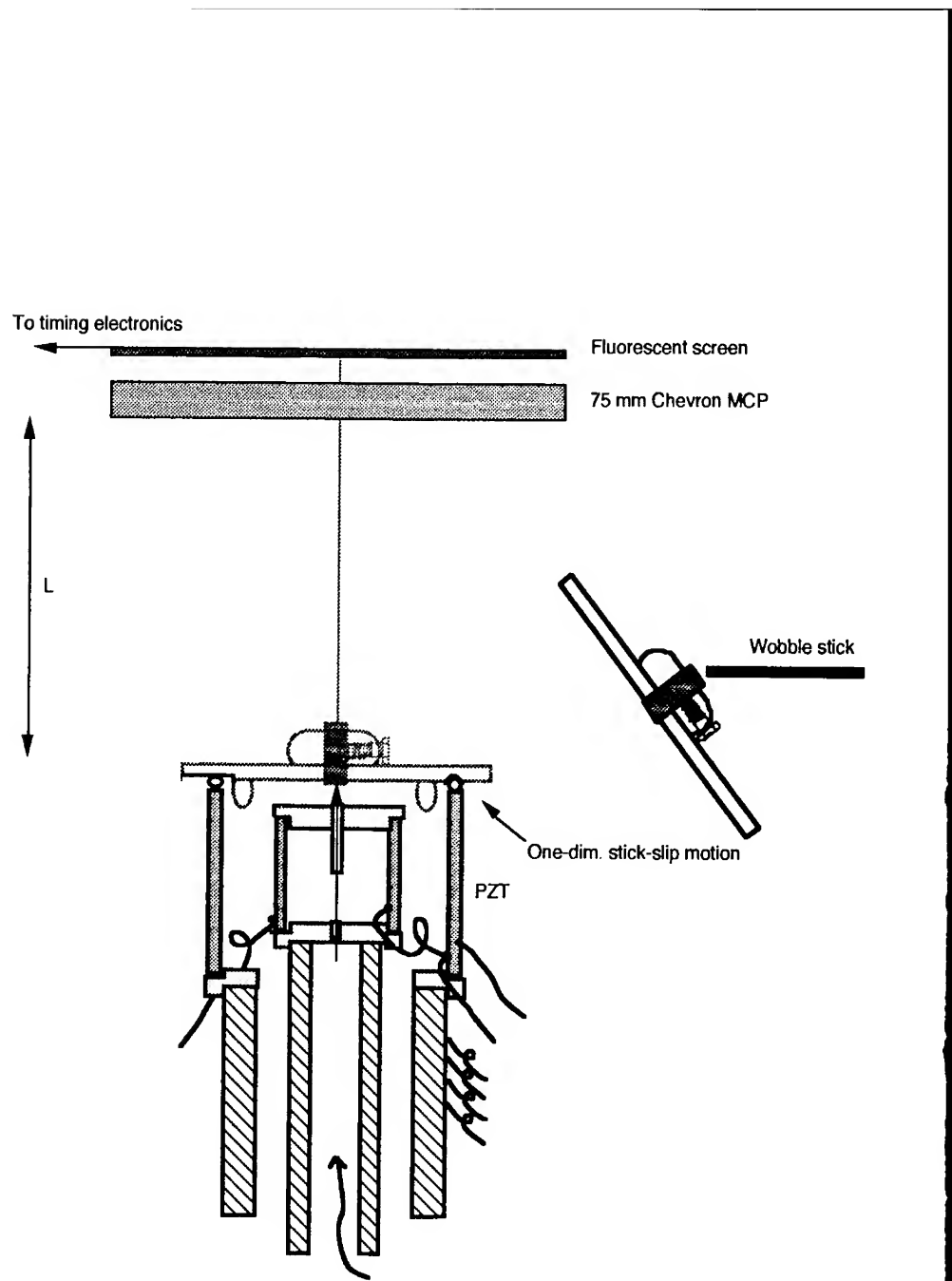


Figure 4. STM with time-of-flight spectrometer. The hatched region is an inchworm. Sample is removed (after transferring atoms to tip) for TOF analysis.

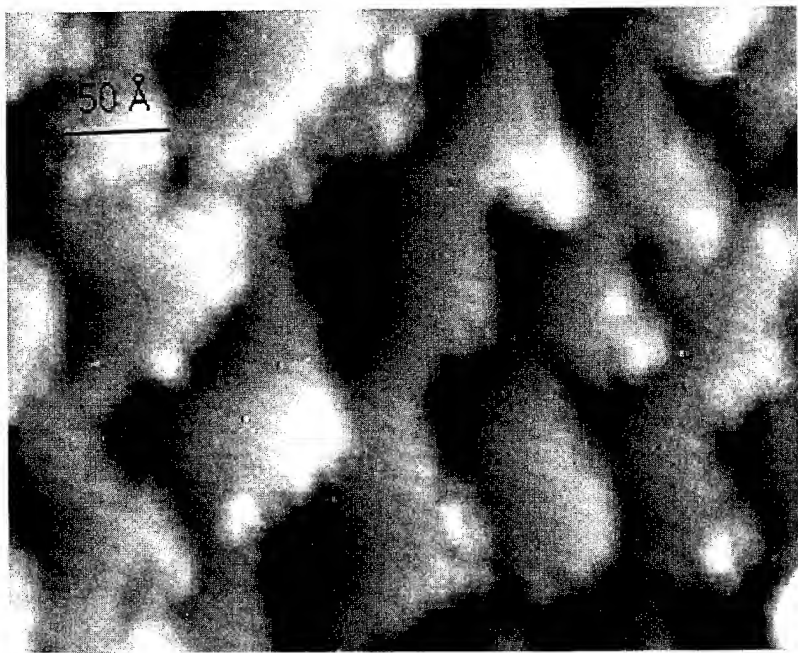


Figure 5. STM image of Si(111) 2X1 cleavage surface, showing dense cleavage steps.

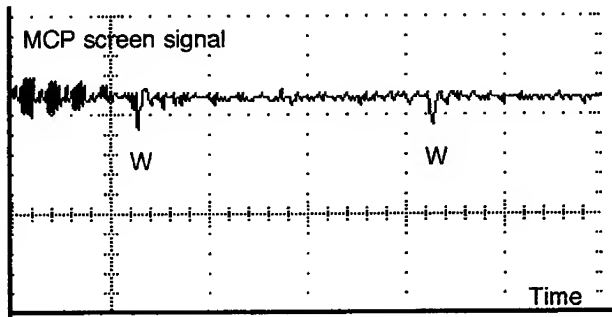


Figure 6. TOF spectrum from bare tungsten tip at about 5 kV. Two W ions are identified. Noise at left is direct RF pulse from tip which precedes ions. 250 ns per large division. The first dip occurs 1284 ns after the tip pulse.

References.

- [1] M. F. Crommic, C. P. Lutz and D. M. Eigler, *Science* 262 218 (1993).
- [2] G. A. Morton and E. G. Ramberg, *Phys. Rev.* 56 705 (1939).
- [3] H. Boersch, *Zeitschrift fur Techn Physik* (1939) 12 346 (1939).
- [4] J. C. H. Spence, *Optik* 92 57 (1992).
- [5] H. W. Fink, H. Schmid, H. J. Kreuzer and A. Wierzbicki, *Phys. Rev. Letts.* 67 1543 (1991).
- [6] J. C. H. Spence and J. M. Zuo, *Electron Microdiffraction* (Plenum, New York , 1992)
- [7] H. Fink, *Physica Scripta* 38 260 (1988).
- [8] D. W. Pohl, *Rev. Sci. Instr.* 58 54 (1986).
- [9] V. T. Binh, S. T. Purcell, N. Garcia and J. Doglioni, *Phys. Rev Letts.* 69 2527 (1992).
- [10] N. S. Garcia J., De Raedt. H. De, *J. Phys. Cond. Matter* 1 9931 (1989).
- [11] W. Qian, M. Scheinfein and J. C. H. Spence, *J. Appl. Phys.* 73 7041 (1993).
- [12] J. Spence, W. Qian and M. Silverman, *J. Vac. Sci. Tech.* in press (1993).
- [13] M. Scheinfein, W. Qian and J. C. H. Spence, *J. Appl. Phys.* 73 2057 (1993).
- [14] N. Unwin and R. Henderson, *J. Mol. Biol.* 94 425 (1975). Also J. Spence, W. Qian and Y. Fujioyoshi, submitted to "Science" (1994).
- [15] A. Howie, M. N. Muhid, F. J. Rocca, U. Valdre, *Inst. Phys. Conf. Ser.* 90 (EMAG 87) 155 (1987). See also H.W.Fink and H.J. Kreuzer, *Phys. Rev. Letts.* 68, 3257 (1992).
- [16] W. Qian, J. Spence and J. M. Zuo, *Acta Cryst. A* in press (1992).
- [17] H. Kreuzer, K. Nakamura, A.Wierzbicki, H. Fink and H. Schmid, *Ultramic.* 45 381 (1992).
- [18] J. Spence and W. Qian, *Phys. Rev. B*45 10271 (1992).
- [19] D. K. Saldin, X. Chen, N. C. Kothari and M. H. Patel, *Phys. Rev. Letts.* 70 1112 (1993).
- [20] J. Spence, W. Qian. *Proc. Micros. Soc. Amer. G. Bailey Ed.* San Francisco Press (San Francisco) (1992) p.938.
- [21] J. Munch, *Optik* 43 79 (1975).
- [22] J. B. DeVelis, G. B. Parrent and B. J. Thompson, *J. Opt. Soc. Am.* 56 423 (1966).
- [23] M. M. MacNaughton, *Proc. Phys. Soc.* B65 590 (1952).
- [24] M. A. McCord, T. Chang, D. Kern and J. Speidell, *J. Vac. Sci. B*7 1851 (1989).
- [25] M. Miller and D. A. Smith, *Atom Probe Microanalysis* (Materials Research Society) (1989)
- [26] A. R. Waugh, *J. Phys. E*14 615 (1981).
- [27] J. A. Panitz, *Rev. Sci. Instr.* 44 1034 (1973).

IMAGING SINGLE NACREOUS TABLETS WITH THE ATOMIC FORCE MICROSCOPE

R. Giles (1), S. Manne (1), C.M. Zaremba (2), A. Belcher (2), S. Mann (4) D.E. Morse (3),
G.D. Stucky (2), P.K. Hansma (1)

(1) Department of Physics, University of California, Santa Barbara CA 93106, (USA);

(2) Department of Chemistry, UCSB; (3) Marine Biotechnology Center, UCSB;

(4) School of Chemistry, University of Bath, Claverton Down, Bath BA2 7AY (UK).

ABSTRACT

After describing some recent developments in atomic force microscopy (AFM), a specific application to the study of shell ultrastructure is examined in detail. By embedding bleached nacreous tablets in epoxy and imaging them with the atomic force microscope (AFM) during *in situ* dissolution, it was possible to visualize the topography of both the top faces of the tablets and the impressions in epoxy made by the bottom faces of the tablets. This epoxy imprint reproduced tablet features down to the 10 nm scale. Using this technique it should be possible to measure correspondence between topographic features on the proximal and distal faces of tablets, which is necessary to form a three-dimensional picture of the nacreous region. In addition to these dissolution experiments, growth experiments (in modified sea water) on bleached, embedded tablets indicated that aragonite grows on a tablet as asperities oriented along the c axis, normal to the tablet surface. No change was seen on the surface of the epoxy, which confirmed that the crystals were growing on the tablet surface, not spontaneously nucleating out of solution.

INTRODUCTION

The atomic force microscope (AFM) [1,2,3] images surface topography by sensing the vertical deflections of a microfabricated cantilever which gently contacts the sample while it is raster-scanned over the surface. It has become an important tool in the characterization of many materials, including those of biological relevance. The AFM's ability to image processes *in situ* at the solid-liquid interface has been used to study a variety of crystal growth processes, e.g. on calcite [4,5], fluorite [6] and lysozyme [7]. The AFM has recently been used to image biominerals such as diatom shells [8], bone [9], teeth [10] and pressed powders of clam and sea urchin shells [11]. Please see [12] for a review of AFM applications to cell biology.

Recent progress in the development of the AFM has focused on combining it with other instruments, especially optical microscopes, and on using the AFM to measure forces with an unprecedented combination of sensitivity and spatial resolution. The development of "stand alone" AFMs which scan a mobile cantilever over a stationary sample rather than scanning the sample under a fixed cantilever allows the convenient imaging of large surfaces [13,14,15,16,17], such as silicon wafers or cells in a petri dish. Furthermore, such an arrangement, where all the AFM components typically line on the same side of the sample, allows the positioning of another microscope on the other side of the sample. Most commonly, this instrument is an optical microscope [13,14,15,18,19,20], including fluorescence microscopes. While the integration of AFM and optical microscopes does not require the stand alone geometry, it allows use of objectives with higher numerical aperture and, hence, resolution.

This combination of technologies is proving very useful for a wide variety of imaging applications. Particularly if the sample is transparent, or consists of small, dispersed particles, the optical microscope can be used to select points of interest for high resolution imaging by AFM. Also, the combination allows better identification of sample structure through the comparison of (for example) optical fluorescence and AFM topographic images of identical areas.

Other important advances have been made in the measurement of small forces. For instance, in studying the effects of solution chemistry on tip-sample interactions [21], quantization of the force required to break the adhesion between tip and sample as been observed [22]. In this case, the quantization (on the order of picoNewtons) is of the same order as would be expected for the breaking of individual hydrogen bonds. This observation suggests the exciting possibility of measuring properties and interactions of single molecules.

The ability to image with low forces is important in avoiding damage to delicate samples and in obtaining high resolution images. One major method of controlling tip-sample forces is imaging in a liquid environment which offers the advantages of reduced capillary [23,24] and van der Waals [25,26] forces as well as the ability to control electrostatic screening and surface chemistry. Another method, applicable to imaging in air or vacuum is the Tapping Mode AFM [27], which oscillates the cantilever so that it is in contact with the sample for only part of each cycle. Recently Tapping Mode AFM in water has been demonstrated. This method yielded stable, high resolution imaging of DNA molecules and proteins in water [28].

As a specific example of the novel ways the AFM can be used for investigations of a wide variety of materials, this paper will describe in detail a new sample preparation technique useful for examining particles from colloidal suspension: in this case, particles from the nacreous, (pearly) inner layer of molluscan shell.

Electron microscopy and x-ray diffractometry have proven powerful techniques for imaging and inferring structural relationships between mineral tablets in molluscan nacre; for examples see [29,30,31,32]. Nacre is known to consist of $\sim 0.5 \mu\text{m}$ thick layers of aragonite tablets ($\sim 10 \mu\text{m}$ across) bound by thin sheets of organic macromolecules. Each aragonite tablet is crystallographically coherent (although sometimes twinned), with the aragonite *c* axis normal to the tablet plane. In bivalves, tablets on a single layer as well as in several neighboring layers are oriented so that their *a* and *b* axes are roughly parallel [30]; in other words, crystallographic coherence extends to macroscopic regions of nacre beyond the domain of single tablets.

Since electron microscopy is limited to imaging single sections, it is not possible to visualize both the proximal (facing the animal) and distal (facing the ocean) surfaces of single nacreous tablets. Such imaging might provide insight into how tablets in neighboring layers fit together to give the nacreous region its characteristic strength and fracture resistance. We present a new technique for imaging both tablet surfaces, by etching nacreous tablets embedded in epoxy and examining the process *in situ* with the atomic force microscope. In the spirit of recent AFM investigation of biominerals, we also present first images of aragonite crystal growth on a nacreous tablet.

METHODS

The nacre for the experiments reported here came from the adult shell of the bivalve *Atrina sp.* (stored in bleach (dilute NaOCl solution)), kindly provided by Prof. S. Weiner at the Weizmann Institute of Science in Israel. The separation of single tablets from the normal "brick-and-mortar" structure was accomplished by sonicating a small chip of nacre in bleach (5% available chlorine) in an Eppendorf tube (0.4 ml) for about ten minutes. The bleach was removed from the suspension by repeated centrifugation followed by exchange of the supernatant solution with pure water. After the fifth wash cycle the suspension was pipetted onto a film of epoxy resin [33] which had been curing at room temperature for about an hour (full cure occurs in eight hours for this two-component epoxy). After allowing the tablets to settle under gravity for five minutes, the water was drawn off with a piece of filter paper. The epoxy was then allowed to cure overnight at room temperature before imaging.

For imaging, the epoxy film was placed directly in the fluid cell of a commercially available AFM [34]. Samples were first imaged in air to ensure that the tip was over a useful area; a saturated CaCO_3 solution was then added to the fluid cell. Once the initial appearance of the tablets (embedded in epoxy) had been established, growth and dissolution experiments were performed. Slow dissolution of the tablets occurred (over a period of a few hours) while flowing pure water through the cell, but addition of 1% HCl caused fast

and complete dissolution (in about 15 minutes) of the tablets, revealing impressions in the epoxy. For the growth experiment we used a supersaturated solution prepared by adding NaHCO_3 to filtered natural sea water [35] to give a 7 mM total concentration of $[\text{CO}_3^{2-}] + [\text{HCO}_3^-]$ and then raising the pH to 8.3 with the addition of dilute NaOH . Flow rates were approximately 10 $\mu\text{l/s}$, corresponding to a change of the total volume of the fluid cell about once every second.

For each scan of the sample two types of images were captured simultaneously, namely the height mode and error signal mode images [36]. In the height mode, the vertical translation of the sample in response to the feedback loop is displayed on a gray scale; brightness corresponds to true measured height. However, the feedback loop has a finite response time and cannot follow sharp changes in topography over small distances. Thus the error signal mode displays the small cantilever deflections that cannot be compensated by the feedback loop; these images show enhanced lateral contrast, which highlights steps and other features with large topographical gradients.

RESULTS AND DISCUSSION

Samples generally consisted of a mixture of single tablets, broken tablets, and aggregates of two or three. Figure 1a shows the initial appearance, with height mode (left) and error signal mode (right) images. The upper surface of the embedded tablets can be clearly distinguished from the smooth surface of the epoxy. Two complete tablets are visible in this view (indicated by arrows), together with several more that are partially submerged in the epoxy. The complete tablets show the central depression (lower left tablet) and the central bump (upper right tablet) characteristic, respectively, of the proximal and distal surfaces of bivalve nacre. The proximal side (with the depression) was the more common orientation overall, perhaps due to hydrodynamic effects during settling.

Figure 1b shows height (left) and deflection (right) images of the same area after the tablets had been completely dissolved (by flowing 1% HCl through the fluid cell). The impression of the features on the reverse side of the tablets can be seen in the epoxy. For the tablet in the upper right, the impression indicates that the opposite side was concave with a central depression, which is consistent with the convex top side. The tablet impression on the lower left shows a flatter surface with polygonal ridges; this is perhaps indicative of that face lying over a tablet boundary in the underlying nacreous layer, rather than over the center of another tablet.

This view of both sides of individual tablets provides some information about the structure of nacreous layers that is difficult to otherwise obtain. For many years, cross sections of nacre have been examined in with the electron microscope [31,37,38,39,40], resulting in much information about the spatial relationships between tablets, as well as the

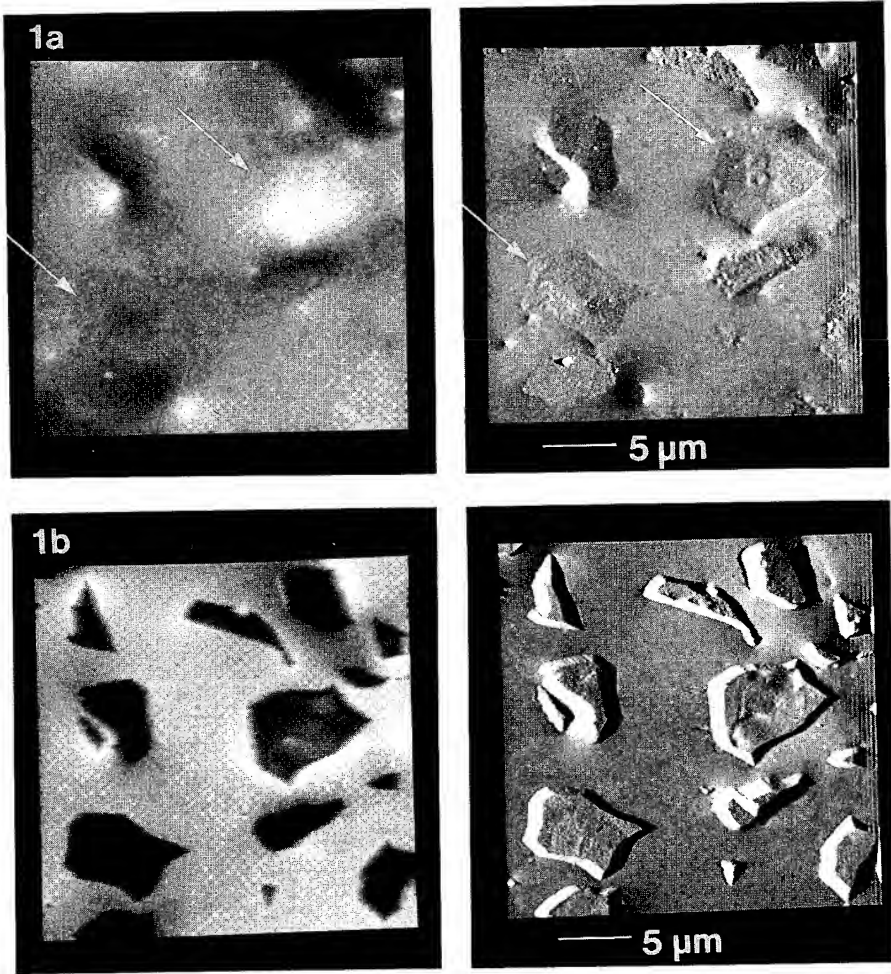


Figure 1: AFM images of nacreous tablets embedded in epoxy. The images are all 26 μm by 26 μm ; (a) shows height mode (left) and error signal mode (right) images, taken simultaneously, of the tablets as they initially appear in a solution saturated with CaCO_3 (to prevent etching). The arrows point out the two complete tablets with cleanly exposed surfaces. Note the central depression and concavity (lower left tablet) and the central bump and convexity (upper right) characteristic of the opposing sides of bivalve nacre. (b) shows height (left) and error signal (right) images of the same area after the tablets have been completely dissolved by flowing a 1% HCl solution though the fluid cell, leaving impressions of the opposite sides of the tablets. Note especially the impression of a concave surface with central depression in the upper right tablet impression, consistent with the convex surface in (a). The height mode images are shaded over 1.5 μm from black (lowest) to white (highest). The total acquisition time for each pair was 76 seconds.

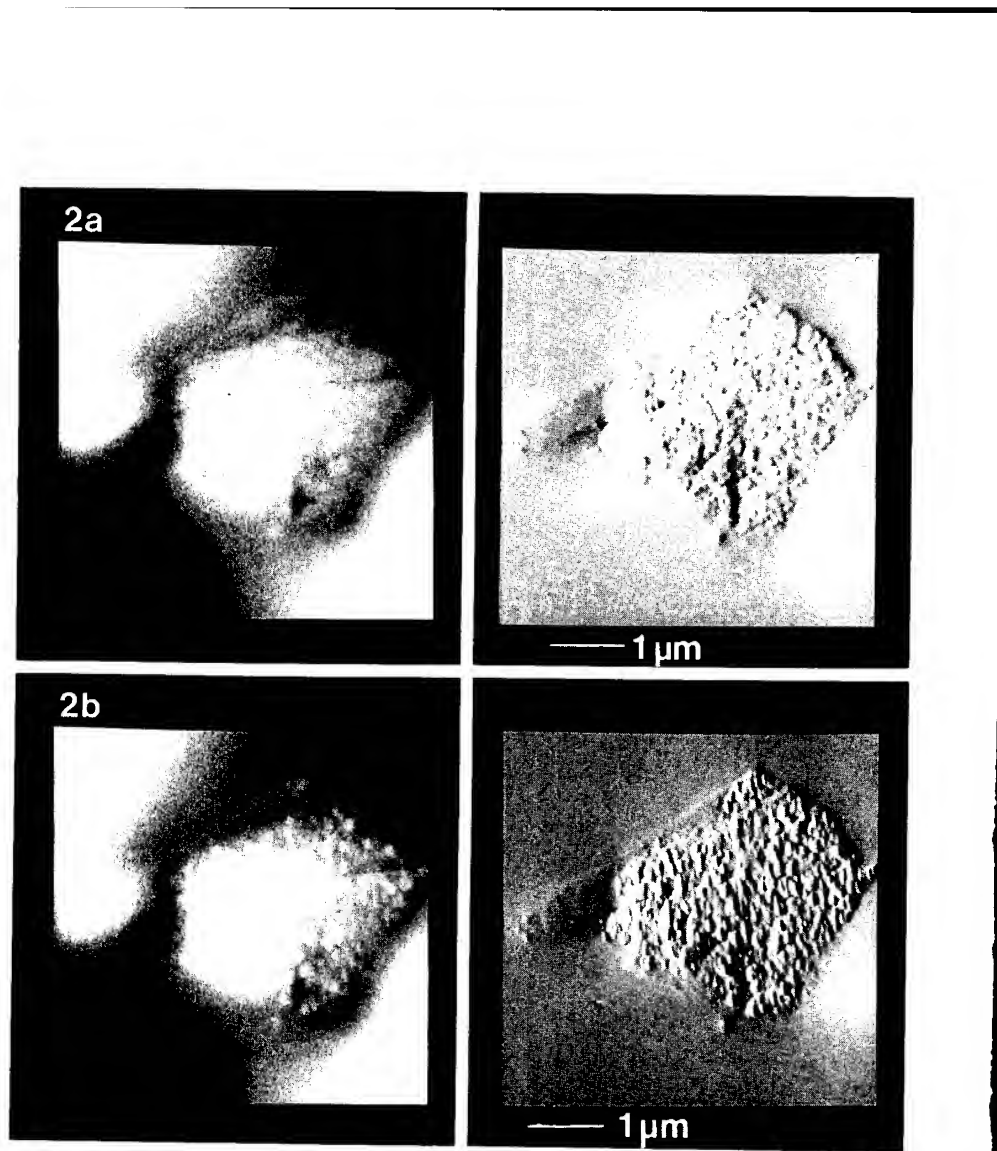


Figure 2: AFM images of a single nacreous tablet embedded in epoxy. The images are all 4.8 μm by 4.8 μm ; (a) shows height (left) and error signal (right) images of the tablet as it initially appeared in a solution saturated with CaCO_3 . (b) shows height (left) and error signal (right) images of the same area after flowing a solution based on natural sea water and supersaturated with CaCO_3 through the fluid cell. Surface changes indicative of growth can be seen on the free surface of the tablet, but not on the surrounding epoxy, demonstrating that the nacreous tablet alone is capable of nucleating growth on its surface. The height mode images are shaded over a range of 0.5 μm from black to white. The total acquisition time for Figure 2a was 42 seconds; the total acquisition time for Figure 2b was 50 seconds.

resolution of some fine structure of the organic matrix. This technique provides information about the topographical relationship between two sides of an individual tablet, divorced from its matrix, at resolutions comparable to transmission electron microscopy. Since bleach is required to separate the tablets, this technique does not allow study of the intertablet organic matrix; sonication does provide, however, a good way of separating the intratablet adsorbed organics for separate study. The two techniques offer complementary information about the nacreous structure.

An important issue is the faithfulness of the reproduction in epoxy, i.e., how small a feature on the tablet surface can be seen in the impression. This can be roughly quantified by measuring surface roughness values of small areas after subtracting out overall surface curvature. On similarly sized areas, we measured rms roughness values of ~30 nm on the tablet surface, ~25 nm on the epoxy impression, and ~5 nm on the undisturbed epoxy, indicating that tablet features larger than a few nm in size should be reproduced. We also observed specific small features, such as elongate rings (~10 nm in height) around the central depression of a tablet, reproduced in the epoxy. Use of a special resin, such as those employed in electron microscopy sections, it may allow further improvements in the resolution of impressions.

In addition to dissolution of nacreous tablets, it was possible to grow aragonite on embedded bleached tablets in the AFM fluid cell. Figures 2a and 2b show height mode (left) and error signal mode (right) images of a single tablet before and after flowing sea water supersaturated with CaCO_3 over the sample. The appearance in Figure 2b of many identical features of the same (vertical) orientation on the tablet implies that these are "tip images" [41] caused by sharp asperities imaging the AFM tip rather than vice versa. This in turn implies that growth on the tablet occurs as asperities oriented normal to the tablet plane, i.e., along the c axis. Since there is no evidence of crystals on the epoxy surface after introducing the growth solution, we conclude that the change on the tablet surface represents true crystal growth and not the results of spontaneous nucleation in solution. Since it is known that aragonite is the favored CaCO_3 polymorph for growth in sea water environments [42], we conclude that the asperities are aragonite needles oriented along the c axis and nucleated on the existing aragonite surface of the nacreous tablet, exposed by the oxidative removal of surface macromolecules.

CONCLUSION

Sonication of nacre in bleach allows the separation of individual nacreous tablets from their normal matrix of organic macromolecules. By drying a suspension of the tablets onto a film of epoxy and then dissolving away the mineral *in situ*, the topography of both sides of the same tablet may be examined, allowing direct comparison of features on each side.

These techniques also have usefulness outside this particular application and may prove valuable in preparing any sample that consists of small particles. Measurements of surface roughness and the observation of elongate rings in the impressions made by the tablets demonstrates reproduction of features down to ~10 nm. Embedding the bleached tablets in epoxy and flowing supersaturated CaCO₃ solution over the sample confirms that aragonite crystal growth occurs on the tablets; there is no spontaneous nucleation on the epoxy. The growth morphology appears to be that of needles elongated along the *c* axis and oriented normal to the plane of the tablet, parallel to the *c* axis of the tablet itself.

ACKNOWLEDGMENTS

This work was supported by the MRL program of the National Science Foundation under award DMR-9123048 (R.G.), the Materials Research Division of the National Science Foundation under award MCB-9202775 (G.D.S., P.K.H., D.E.M., C.M.Z.), the Office of Naval Research under award N00014-93-1-0584 (D.E.M., P.K.H., G.D.S., A.B.), Digital Instruments, and an AT&T fellowship (S. Manne).

REFERENCES

- [1] G. Binnig, C.F. Quate and Ch. Gerber, *Phys. Rev. Lett.* **56**, 930 (1986).
- [2] D. Rugar and P.K. Hansma, *Phys. Today* **43**, 23 (1990).
- [3] D. Sarid, *Scanning Force Microscopy: With Applications to Electric, Magnetic, and Atomic Forces*, (Oxford University Press, New York, 1991).
- [4] A.J. Gratz and P.E. Hillner, *J. Crystal Growth* **129**, 789 (1993).
- [5] P.M. Dove and M.F. Hochella Jr., *Geochem. et Cosmochem. Acta* **57**, 705 (1993).
- [6] P.E. Hillner, S. Manne, A.J. Gratz and P.K. Hansma, *Faraday Discuss.* **95**, 191 (1993).
- [7] S.D. Durbin and W.E. Carlson, *J. Crystal Growth* **122**, 71 (1992).
- [8] A. Linder, J. Colchero, H.-J. Apell, O. Marti and J. Mlynek, *Ultramicroscopy* **42-44**, 329 (1992).
- [9] N.J. Tao and S.M. Lindsay, *Biophys. J.* **63**, 1165 (1992).
- [10] S. Kasas, A. Berdal and M.R. Celio in *Scanning Probe Microscopies II*, edited by C.C. Williams (SPIE **1855**, Los Angeles, 1993), pp. 17-25.
- [11] G. Friedbacher, P.K. Hansma, E. Ramli and G.D. Stucky, *Science* **253**, 1261 (1991).
- [12] J.H. Hoh and P.K. Hansma, *Trends in Cell Biology* **2**, 208 (1992).
- [13] C.A.J. Putman, H.G. Hansma, H.E. Gaub and P.K. Hansma, *Langmuir* **8**, 3014 (1992).

[14] D.S. Sarid, P. Pax, L. Yi, S. Howells, M. Gallagher and T. Chen, *Rev. Sci. Instrum.* **63**, 3905 (1992).

[15] D.R. Baselt and J.D. Baldeschwieler, *Rev. Sci. Instrum.* **64**, 908 (1993).

[16] G. Meyer and N.M. Amer, *Appl. Phys. Lett.* **56**, 2100 (1990).

[17] M. Hipp, H. Bielefeldt, J. Colchero, O. Marti and J. Mlynek, *Ultramicroscopy* **42-44**, 1498 (1992).

[18] C.A.J. Putman, K.O. van der Werf, B.G. de Groot, H.F. van Hulst, F.B. Segesink and J. Greve, *Rev. Sci. Instrum.* **63**, 1914 (1992).

[19] M. Sander, *Rev. Sci. Instrum.* **64**, 2591 (1993).

[20] K.O. van der Werf, C.A.J. Putman, B.G. de Groot and F.B. Segerink, *Rev. Sci. Instrum.* **63**, 2892 (1992).

[21] J.H. Hoh, J.-P. Revel and P.K. Hansma, *Nanotechnology* **2**, 119 (1991).

[22] J.H. Hoh, J.P. Cleveland, C.B. Prater, J.-P. Revel and P.K. Hansma, *J. Amer. Chem. Soc.* **114**, 4917 (1992).

[23] B. Drake, C.B. Prater, A.L. Weisenhorn, S.A. Gould, T.R. Albrecht, C.F. Quate, D.S. Cannell, H.G. Hansma and P.K. Hansma, *Science* **248**, 1586 (1989).

[24] A.L. Weisenhorn, P.K. Hansma, T.R. Albrecht and C.F. Quate, *Appl. Phys. Lett.* **54**, 2651 (1989).

[25] U. Hartmann, *Phys. Rev. B* **43**, 2404 (1991).

[26] A.L. Weisenhorn, D. Maivald, H.-J. Butt and P.K. Hansma, *Phys. Rev. B* **45**, 11226 (1992).

[27] Q. Zhong, D. Inniss, K. Kjoller and V.B. Elings, *Surf. Sci. Lett.* **290**, 688 (1993).

[28] P.K. Hansma, J.P. Cleveland, M. Radmacher, D.A. Walters, P. Hillner, M. Bezanilla, M. Fritz, D. Vie, H.G. Hansma, C.B. Prater, J. Massie, L. Fukunaga, J. Gurley, and V. Elings, *Appl. Phys. Lett.* (in press).

[29] S. Weiner, *CRC Crit. Rev. Biochem.* **20**, 365 (1986).

[30] S.W. Wise, *Eclogae geol. Helv.* **63**, 775 (1970).

[31] K. Wada, *Biomineralisation* **6**, 141 (1972).

[32] H. Mutvei, *Calcif. Tiss. Res.* **24**, 11 (1977).

[33] "2 Ton Epoxy," Devcon Corporation, Danvers, MA 01923 USA.

[34] Nanoscope III from Digital Instruments, Santa Barbara, CA 93103 USA.

[35] The seawater was collected locally from the Pacific ocean near Santa Barbara, California, USA. It was irradiated with ultraviolet light, passed through a 0.2 μm filter and refrigerated until just before use.

[36] C.A.J. Putman, K.O. van der Werf, B.G. de Groot, N.F. van Hulst, J. Greve and P.K. Hansma in *Scanning Probe Microscopies*, edited by S. Manne, (SPIE **1639**, Los Angeles, 1992), pp. 198-204.

- [37] K. Wada, Bull. Natl. Pearl Res. Lab. **7**, 703 (1961).
- [38] G. Bevelander and H. Nakahara, Calc. Tiss. Res. **3**, 84 (1969).
- [39] H. Nakahara, G. Bevelander and M. Kakei, Venus **41**, 33 (1982).
- [40] H. Nakahara, in *Mechanisms and Phylogeny of Mineralization in Biological Systems*, edited by S. Suga and H. Nakahara (Springer-Verlag, Tokyo, 1991), pp. 343-356.
- [41] P. Grütter, W. Zimmermann-Edling and D. Brodbeck, Appl. Phys. Lett. **60**, 2741 (1992).
- [42] Y. Kitano and D.W. Hood, J. Oceanograph. Soc. Japan **18** (3), 35 (1962).

SCANNING TUNNELING MICROSCOPY (STM) AND SCANNING FORCE MICROSCOPY (SFM) OF LIQUID CRYSTALS AND POLYMERS

K. D. Jandt^{1*}, T. J. McMaster¹, D. G. McDonnell², J. M. Blackmore², M. J. Miles¹

¹H. H. Wills Physics Laboratory, University of Bristol, Royal Fort, Tyndall Avenue, Bristol, BS8 1TL, U. K.

²Defence Research Agency, St. Andrews Road, Great Malvern, Worcs WR14 3PS, U. K.

*To whom correspondence should be addressed.

ABSTRACT

Recent progress in the field of liquid crystal materials and oriented polymers studied by near-field scanned probe microscopies (SPM) is presented here. The investigations were focused on scanning tunneling microscopy (STM) results of antiferroelectric liquid crystalline molecules observed at different elevated temperatures corresponding to different bulk mesophases of the material, and on surface morphological studies of a liquid crystalline polymer by scanning force microscopy (SFM). In the field of oriented thermoplastic polymers, SFM images of the morphology and molecular packing in the outermost surface of poly(butene-1) films are presented.

INTRODUCTION

The main interest in liquid crystal materials (LCs) studied by scanned probe microscopies (SPM) is their molecular arrangement. The behaviour of LCs at surfaces is of scientific interest, and, because surface alignment is used in display devices (LCD), it is also of commercial importance. Order in the LC state of a polymer (LCP) caused by an electric or magnetic field can be frozen in by cooling the LCP to its crystalline state [1]. This makes LCPs suitable for storage devices.

Several STM papers (e.g. [2,3]) have been published on LC materials anchored to substrates such as graphite or similar compounds. In these cases the LC materials are bound to the surface through van der Waals interactions, allowing a molecular resolution of the LC surface lattice. For STM imaging of LCs, several different sample preparation methods are used [4]. However, these sample preparation methods do not allow the observation of one of the main characteristics of LC materials, the phase transitions associated with changes in molecular packing (mesophases) as a function of temperature. Here we present STM images of an antiferroelectric LC (AFEELC) showing a distinct two dimensional order. We have found evidence for a change in molecular arrangement of the AFEELC, when changing the temperature from that at which it exhibits a bulk smectic C_a mesophase to that at which it exhibits bulk smectic A mesophase.

Only few papers have been published about LCs investigated with scanning force microscopy (SFM) [5,6] owing to experimental difficulties, in particular the weak adhesion of these materials to the underlying substrate. More morphological studies of LCs have been performed using the transmission electron microscope (TEM) (for example [7]). These investigations have been carried out owing to a scientific and commercial need to gain knowledge of the morphological characteristics and structures of liquid crystalline polymers (LCPs) on a microscopic scale (1 nm to 100 μ m), since these molecular superstructures determine many of the LCP physical properties. Recent results of SFM investigations of a low molecular weight side-chain LCP, slow-cooled from the isotropic melt, are presented here. Images obtained from these investigations show the highly ordered 3-dimensional surface morphology of the LCP at a nanometre scale.

Contrary to the self-forming molecular order in LC materials, the order in ultra-thin melt-drawn poly(butene-1) (PB-1) films is caused by the drawing process of the material from the melt. The distinct surface topographic structures of these bare polymer films determine the interfacial properties (i.e. adhesion, orientation) in contact with other materials, as for example composite materials [8]. SFM was used in order to investigate the surface morphology of crystalline and semi-crystalline polymers. Morphological details and their molecular substructures were obtained.

EXPERIMENTAL

The chemical structure of the AFELC used in our studies is shown in Fig. 1a [9]. This material exhibits a smectic C_a mesophase between 313 K and 316 K and a smectic A mesophase between 316 K and 336 K. The molecule consists of three main sections shown in Fig. 1a. A longer alkyl chain at the one (left) end and two shorter alkyl chains (swallowtail) at the other (right) end of the molecule shown in Fig. 1a form the non-polar parts of this molecule. The main contribution to the dipole character of the molecule is given by its middle rigid part, consisting of three phenyl rings and polar carbonyl groups on each end of the biphenyl group. A further contribution to the antiferroelectric character of the material is steric based.

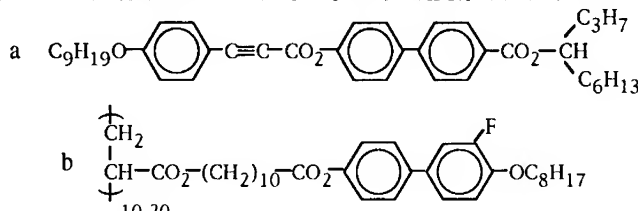


Fig. 1a, b: Chemical structures of the antiferroelectric LC (Fig. 1a) used in the STM investigations and the LCP (Fig. 1b) used in the SFM investigations presented here.

A small amount of the crystalline AFELC was deposited onto a freshly-cleaved surface of highly-oriented pyrolytic graphite (HOPG, ZYA grade). Subsequently the HOPG surface was heated above the isotropic phase ($T \geq 336$ K) of the AFELC over 20 minutes, using a STM heating stage. The sample was then allowed to cool down to the required temperature for the STM investigations. The temperature on top of the graphite surface (location of the AFELC monolayer) was controlled during the scan by a calibrated thermocouple within a tolerance range of ± 0.5 K.

A WA Technology STM (Cambridge, UK) operating in the constant-current mode was used for the STM investigations. The STM experiments were carried out at temperatures ranging between 315 K and 323 K, using mechanically cut Pt-Ir tips. A tunnel current I_t between 0.1 nA and 0.01 nA and bias voltage V_t between 100 mV and 1000 mV were used for the STM imaging. No significant changes of the images were observed for variation of I_t and V_t in these ranges. No filtering was applied to the feedback signal. All images presented here are flattened.

After depositing the side-chain LCP shown in Fig. 1b onto freshly cleaved mica, it was heated to the isotropic state (about 385 K) and spread on the mica surface, to form a thin liquid film (thickness ≈ 50 μ m). Subsequently, the sample was slowly cooled to room temperature at a rate of 0.01 K min⁻¹. The glass transition temperature T_g of the LCP material is 333 K.

Oriented semi-crystalline PB-1 substrates were prepared according to the method of Petermann and Gohil [10]: the polymer granulate was dissolved in xylene (w/w, 0.4 %), and some droplets of this solution were then deposited on the smooth surface of a glass slide where the solution itself disperses uniformly. On heating the sample to a temperature of about 420 K, the solvent evaporates. From the resulting melt, a highly-oriented ultra-thin film (thickness ≈ 0.1 μ m) was drawn by a motor driven cylinder ($v_x \approx 7$ cm/s). Immediately after the drawing process, the polymer films were fixed to freshly cleaved mica.

A Nanoscope III SFM (Digital Instruments, Santa Barbara, CA, USA) operating at room temperature was used for the SFM investigations. Experiments using the repulsive force mode of operation were carried out in air and under propanol (spectrophotometric grade). Propanol was chosen to minimize the capillary forces between the cantilever tip and the surface [11] and because it would not cause the samples to swell or soften. The cantilevers used were supplied by the microscope manufacturer, and had a nominal force constant of 0.06 N m⁻¹. The forces applied with the SFM tip were $\leq 10^{-9}$ N. The imaging force was adjusted to just above the pull-off point of the cantilever as soon as possible after the first contact in order to reduce the applied force to the minimum possible for stable imaging. From time to time it was checked that the set point was stable and still at the same location of the force curve. No filtering was applied to the feedback signal. All images presented here are flattened.

RESULTS AND DISCUSSION

During the slow cooling process described above, the AFELC physisorbed onto the HOPG surface, forming a monolayer [12]. At a temperature of 315 K, which corresponds to the smectic Ca mesophase of the bulk AFELC material, the monolayer self-assembles into a two dimensional structure. This can be seen in the STM image shown in Fig. 2a. As shown in Fig 2a, the AFELC forms a surface structure of alternating bright and dark bands. The identity period from the centre on one band, to the next band of the same intensity was found to be $6.9 \text{ nm} \pm 0.1 \text{ nm}$, whereas the identity period between two neighbouring bands was found to be half of this value. Within the bands, a structural modulation along the longitudinal axes of the bands is visible, pointing to the molecular substructure of the bands.

In contrast to the banding structure of the AFELC observed at 315 K, the bands observed at a temperature of 323 K shown in Fig. 2b exhibit no distinct alternating contrast. Another important distinction of the banding structure obtained at 323 K is the value measured for the inter-band distance, which was found to be $3.8 \text{ nm} \pm 0.1 \text{ nm}$ between neighbouring bands. In these images, the alkyl tails of the molecules are identifiable as fine bright lines running approximately perpendicular to the band direction whereas the biphenyl groups form the bright periodic bands. A detailed analysis of these and similar images revealed that the alkyl tails of the molecules make an angle of between 60° and 80° to the long axes of the bands. From the arrangement of the alkyl tails an average intermolecular distance of $1.4 \text{ nm} \pm 0.1 \text{ nm}$ has been obtained. A detailed analysis of the molecular packing of the AFELC molecules on the HOPG surface is in progress and will be published elsewhere [13].

As seen in Fig. 2b, the AFELC has formed two distinct two-dimensional domains, which consist of bands aligned parallel to each other. Further investigations revealed areas where many different orientations of the bands could be distinguished. A detailed measurement of the angles between the bands of different orientations, revealed angle values of 5° , 24° , 50° , 60° and $70^\circ \pm 3^\circ$. Further angular measurements in other regions of the surface revealed the last angle more often, but other angles were also found.

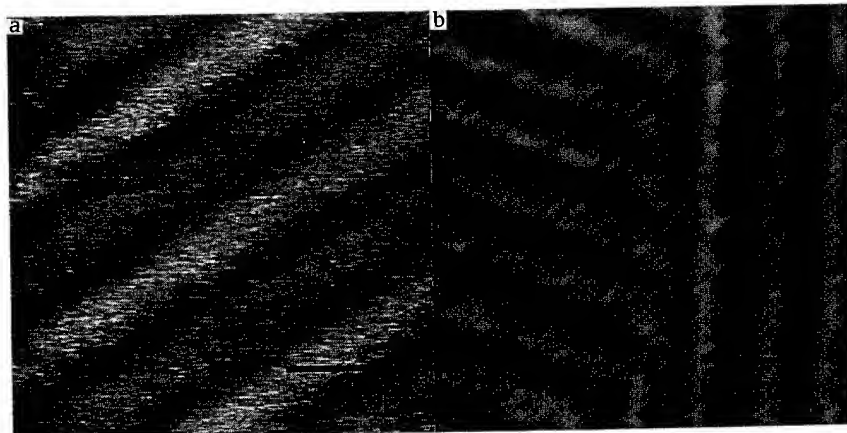


Fig. 2a, b: Fig. 2a shows a STM image of the AFELC on graphite imaged at a temperature of 315 K. The AFELC forms a surface structure of alternating bright and dark bands with an identity period of 6.9 nm . Note the structural modulation along the longitudinal axes of the bands, pointing to molecular substructure of the bands. Fig. 2b shows the banding structure of the AFELC at 323 K. In this image the alkyl tails of the molecules are identifiable as fine bright lines running at an angle of about 80° to the long axes of the bands, whereas the biphenyl groups form the bright periodic bands. The inter-band distance was found to be 3.8 nm .

The AFELC domains on the HOPG substrate do not show a simple three-fold symmetry as found for other organic materials, e.g., alkanes [14] on graphite substrates. The fact, that there is no simple angular relationship between the graphite substrate and the AFELC domains may presumably be due to a stronger, polar (electrostatic) interaction between the AFELC molecules than between the molecules and the substrate. This may lead to a molecular packing more independent of the underlying substrate and corresponding more closely with the structure in the bulk material immediately above the surface.

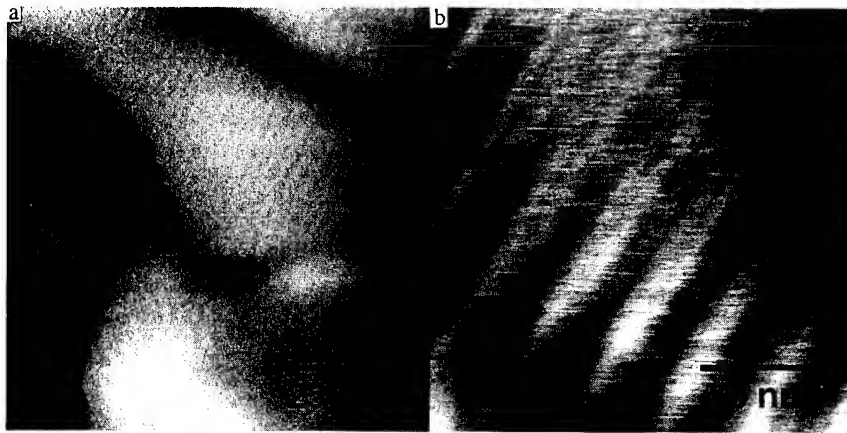


Fig. 3a, b: SFM image of the lamellar structures near a hedrite-core region (Fig. 3a). Note the fine banding structure and its texture within the lamellae. The repeat of the band structures was found to be about 30 nm. Fig. 3b shows the individual bands and their substructures. Each bright band of a thickness of about 20 nm consists of two narrow bright bands (diameter of each band is in the ranges of 7-8 nm) and a dark region (diameter 6 nm) separating these bands.

During the slow cooling process described above, the LCP film crystallizes onto the mica surface, forming distinct ordered structures at its surface [15]. In Fig 3a and b, the LCP can be seen to have formed distinct surface topography consisting of LCP lamellae. These lamellae of a thickness between 50 nm and 500 nm, are arranged in concentric superstructures similar to hedrites [16]. From other polymeric materials hedrites are well known as a precursor state of spherulitic growth [16]. The diameter of these hedrites was found to be between 7 μm and 10 μm . Fig. 2a shows the concentric growth of the lamellae around a common core (nucleus). The crystalline growth is believed to start at these cores which may consist of impurities.

The lamellar surfaces exhibit a fine substructure of bands, running approximately perpendicular to the long axes of the lamellae. The bands always cross the full diameter of the lamellae. At the regions where the domains change their direction, a great variety of sharp domain boundaries was obtained. Examples of these domain boundaries are shown in Fig. 3a.

As seen in Fig. 3b, the identity period of the bands is about 30 nm. A detailed analysis of the image shows that the bands exhibit a substructure. Each bright band of a thickness of about 20 nm consists of two narrow bright bands (diameter of each band is 7-8 nm) and one dark region (diameter 6 nm) separates these bands. The brightness of the band-substructure corresponds to a difference in height (bright regions higher than dark regions). A height difference of $0.3 \text{ nm} \pm 0.1 \text{ nm}$ was measured between the top of the bright subbands and the bottom of the dark subbands. The fact that a higher resolution of the LCP surface was not possible, presumably may be due to flexible dangling side- or main-chain ends of the LCP at the outermost surface.

The sizes of the structures in the bands are about double the length of the LCP main chain (between about 2.6 and 5.2 nm). Therefore the packing of the LCP molecules in the band structure can be only understood in terms of a superstructure of the molecular order.

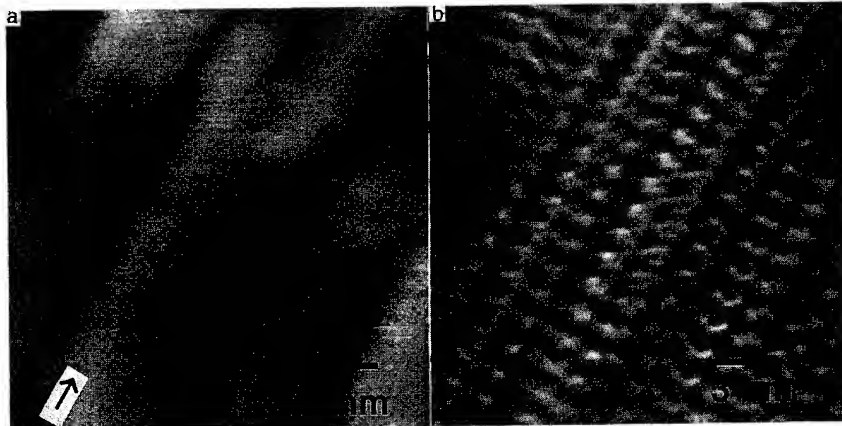


Fig. 4a, b: SFM image of a PB-1 substrate (Fig. 4a) shows four needle crystals arranged parallel to each other diagonally crossing the scan area. The arrow in the lower left corner indicates the direction of the molecular orientation. Note the fine structure of lines arranged parallel to the long axes of the needle crystals and the molecular orientation. At a higher magnification, the needle crystal surfaces (Fig. 4b) show individual PB-1 macromolecules (helices). Along the chain directions of the macromolecules a repeat (pitch height) of 0.7 ± 0.1 nm was obtained.

Earlier TEM investigations have shown the PB-1 polymer substrate surfaces produced by this technique exhibit a semi-crystalline morphology [17]. The crystalline areas of PB-1 substrates are built up of needle-like crystals aligned parallel to the drawing direction of the polymer film. The PB-1 surface planes are $\{hk0\}$ planes having only the $[001]$ direction, the direction of the molecular orientation, in common. This is well known as the fibre texture.

SFM imaging revealed structures as seen in Fig. 4a. The image shows four needle crystals arranged parallel to each other. All crystals are oriented approximately parallel to the drawing direction. Their length and their average diameter of 20–35 nm agree well with what is known from TEM dark-field investigations of needle crystals. Additionally, the needle crystals protrude out of the surface. The height from the region between the crystals to the top of the crystals was measured to be 0.5–4 nm (local values). In the upper part of the middle needle crystal, crystalline branching is visible. The surfaces of the needle crystals exhibit a molecular fine structure arranged parallel to the long axes of the needle crystals and the drawing direction.

When increasing the magnification further to a molecular scale, images like Fig. 4b were obtained. The image shows structures similar to PB-1 macromolecules (helices) with a repeat (pitch height) of 0.7 ± 0.1 nm along the molecular backbone. This value may be compared with the bulk value from X-ray diffraction data of 0.65 nm [18]. Structures shown in Fig. 4b were reproducible independent of scanning frequency, scanning direction and x-y range.

Although the determination of the pitch height (intramolecular distance) from images like Fig. 4b is straightforward, it is more difficult to obtain values for the intermolecular distances in planes parallel to the surface, due to the complex and detailed surface structure. It is assumed that linear uninterrupted structures oriented parallel to the drawing direction in Fig. 4b are the backbones of PB-1 macromolecules. The structures between these backbones may originate from interlocking ethyl side groups of the PB-1 macromolecules. A typical value obtained for the intermolecular distance in planes parallel to the surface is 1.2 ± 0.3 nm. This value may be compared with the intermolecular distance in the bulk of a PB-1-crystal; e.g., in the $\{100\}_{\text{PB-1}}$ planes the PB-1 helices are arranged in alternating distances of 0.59 nm and 1.18 nm. The difference in the observed intermolecular packing with the SFM compared to the bulk value may result from different molecular packing at surfaces compared with the bulk.

CONCLUSIONS

1. STM investigations of the AFELC revealed changes in band contrast and band identity period with increasing temperature, indicating a change in molecular packing of the material. This observation corresponds to a mesophase change from bulk smectic C_a to a bulk smectic A mesophase of the material at the temperatures used. The non-trivial angular relationship between the graphite substrate and the AFELC domains may be due to a stronger, polar (electrostatic) interaction between the AFELC molecules than between the adsorbate and the substrate.

2. SFM investigations of a low molecular weight LCP, slow-cooled from the isotropic melt revealed the hedritic surface morphology of the material. Higher-resolution SFM images show a regular fine structure of lamellae, consisting of band structures organized in domains with a band repeat distance of about 30 nm. Within the bands nanometer substructures were obtained.

3. SFM investigations of poly(butene-1) thin film surfaces revealed the close-packed needle crystal morphology of this substrate. Higher magnifications of needle crystals, their sub-structures show PB-1 macromolecules with a repeat along the axes of the PB-1 helix of 0.7 ± 0.1 nm. This value is consistent with data obtained from X-ray diffraction of 0.65 nm.

ACKNOWLEDGEMENTS

K. D. Jandt and M. J. Miles gratefully acknowledge the financial support of the SERC. M. J. Miles and T. J. McMaster gratefully acknowledge the financial support of the AFRC.

REFERENCES

- [1] L. M. Blinov, Electro-optical and Magneto-optical Principles of Liquid Crystals, (John Wiley and Sons, New York, 1983).
- [2] J. S. Foster, J. E. Frommer, *Nature* **333**, 542 (1988).
- [3] S. L. Brandow, J. A. Harrison, D. P. DiLella, R. J. Colton, S. Pfeiffer and R. Shashidhar, *Liquid Crystals* **1**, 163 (1993).
- [4] D. P. E. Smith, J. E. Frommer, STM and SFM in Biology, edited by O. Marti and M. Amreim, (Academic Press, London, 1993) and references cited therein.
- [5] H. Yamada, S. Akamine, C. F. Quate, *Ultramicroscopy* **42-44**, 1044 (1992).
- [6] B. D. Terris, R. J. Twieg, C. Nguyen, G. Sigaud, H. T. Nguyen, *Europhys. Lett.* **19** (2), 85 (1992).
- [7] S. D. Hudson, J. Lovinger, *Polymer* **6**, 1123 (1993).
- [8] J. Petermann, G. Broza, *J. Mater. Sci.* **22**, 1108 (1987).
- [9] The antiferroelectric LC was made at the Chemistry Dep. of the University of Hull by Issa Nishiyama, Nippon Mining Co., Tokyo, Japan, and was used without any further purification or solvent.
- [10] J. Petermann, R. M. Gohil, *J. Mater. Sci.* **14**, 2260 (1979).
- [11] H. G. Hansma, T. Vesenka, C. Siegerist, G. Keldermann, H. Momett, R. L. Sinsheimer, V. Eilings, C. Bustamante, P. K. Hansma, *Science* **256**, 1180 (1992).
- [12] K. D. Jandt, S. Tixier, J. M. Blackmore, M. J. Towler, M. J. Miles, submitted *Polym. Bull.*
- [13] K. D. Jandt, M. J. Miles, submitted to *Polymer Bulletin*.
- [14] G. C. McGonnigal, R. H. Bernhardt and D. J. Thomson, *Appl. Phys. Lett.* **57**, 28 (1990).
- [15] K. D. Jandt, J. M. Blackmore, D. G. McDonnell, M. J. Miles (submitted).
- [16] P. H. Geil, in: Growth and Perfection of Crystals, edited by R. H. Doremus, B. W. Roberts, D. Turnbull, (Wiley, New York, 1958), 579.
- [17] K. D. Jandt, T. J. McMaster, M. J. Miles, J. Petermann, *Macromolecules* (in press) (1993).
- [18] G. Natta, P. Corradini, I. W. Bassi, *Nuovo Cimento Suppl.* **15**, 52 (1960).

VISUALIZING LANGMUIR-BLODGETT FILMS WITH THE ATOMIC FORCE MICROSCOPE

RAVI VISWANATHAN*, D.K. SCHWARTZ**, L.L. MADSEN*, AND J.A. ZASADZINSKI*

*Dept. of Chemical & Nuclear Engineering, University of California, Santa Barbara, CA 93106

**Dept. of Chemistry and Biochemistry, University of California, Los Angeles, CA 90024

Abstract

The Atomic Force Microscope (AFM) has created exciting new possibilities for imaging thin organic films under ambient conditions at length scales ranging from tens of microns to the sub-molecular scale. We present images of thin organic films prepared by the Langmuir-Blodgett (LB) technique that demonstrate the possibilities of the AFM.

Introduction

Langmuir-Blodgett (LB) films, layered assemblies of amphiphilic molecules, have applications in the areas of nonlinear optics, molecular electronics, biosensors, and as models for cell membranes [1]. Most of these applications rely on the self-organization of amphiphilic molecules to form very thin and essentially perfect films. Hence, studies of the degree and type of order of these molecularly layered films are of critical importance. In addition, LB films are model systems for the crossover between two and three dimensions and can demonstrate aspects of the physics of two dimensions including hexatic phases. Ordering in LB films has been studied by several techniques, including electron diffraction [2-5], x-ray diffraction [6,7], reflectivity [8-10], and fluorescence [11], near-edge x-ray adsorption fine structure (NEXAFS) [12], the surface force apparatus [13], and various spectroscopies [14-16]. These experiments have given information about molecular order and orientation averaged over areas from square microns to square millimeters, and typically, averaged over all of the layers of the LB film.

Recently, the atomic force microscope (AFM) has been used to image LB films with molecular resolution [17,18], and has been shown to be able to identify local defects and inhomogeneities in ordered surfaces [19]. Most of the AFM studies in our lab revolve around thin fatty acid films that have divalent cations incorporated into them. Studies involving cadmium [20-23], lead [24,25], barium [25-27], manganese [24,25], and calcium [28] as cations have yielded distinct structural information for each system. In addition, the simple use of zinc as a cation in films of zinc arachidate (ZnA) yields structural information far different from any other LB system yet studied, including a greatly expanded lattice as well as a hexatic to crystalline order transition in the third dimension. In this paper, we shall examine several LB systems that have been visualized and characterized by the AFM. The common thread binding the systems is the notion that the substrate and cation plays an essential role in the molecular organization of LB films. The systems to be studied include reorganization of cadmium arachidate (CdA) films, substrate effects on lead stearate (PbSt) and manganese arachidate (MnA) films, and hexatic phases in zinc arachidate (ZnA) films.

Experimental

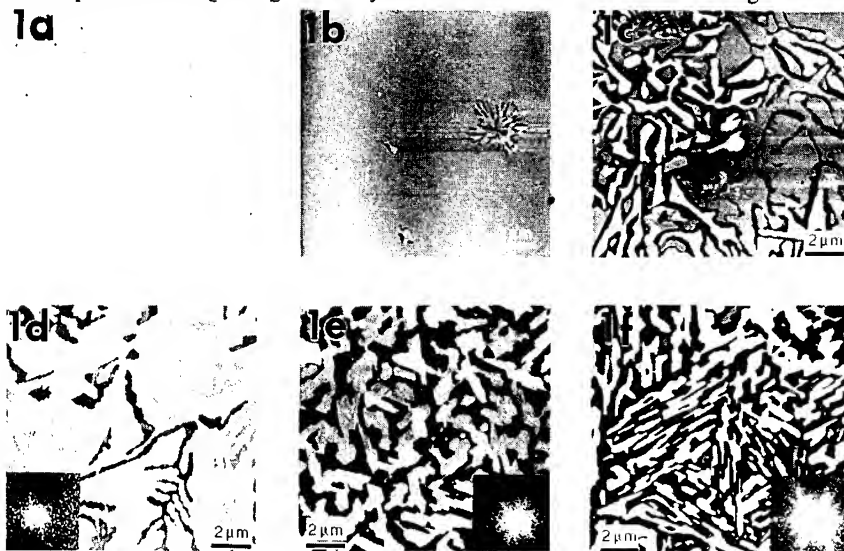
Arachidic acid ($\text{CH}_3(\text{CH}_2)_{19}\text{COOH}$, Aldrich, 99%) or stearic acid ($\text{CH}_3(\text{CH}_2)_{17}\text{COOH}$, Aldrich, 99%) (both 1.7-2.0 mg/ml) was spread from chloroform (Fisher spectrally analyzed) solution onto an aqueous (water from a Milli-Q [29] system was used) subphase in a commercial NIMA [30] trough. The subphase water included 5×10^{-4} M ZnCl_2 , CdCl_2 , $\text{Pb}(\text{CH}_3\text{COO})_2$, or MnCl_2 (Aldrich 99.99%) and was adjusted to a pH of 6.5-7 by addition of NaOH or NaHCO_3 (Aldrich 99%). Substrates were freshly cleaved mica or polished silicon wafers [31] (orientation (100), 3 ohm^*cm , n-type). LB films were deposited at a surface pressure of 30 mN/m using a

NIMA [38] trough at $22.00 \pm 0.1^\circ\text{C}$. AFM measurements were performed with a Nanoscope III [31] AFM at ambient temperature. A $1 \mu\text{m}$ by $1 \mu\text{m}$ scan head or $12 \mu\text{m}$ by $12 \mu\text{m}$ scan head and a silicon nitride tip on a cantilever with a spring constant of 0.12 N/m were used. The best molecular resolution was achieved in the "force mode," that is, scanning the tip at constant height and measuring spring deflection. Typical forces were 10^{-8} N .

Reorganization in CdA films

AFM studies were used to optimize the deposition parameters and substrates for CdA, the prototypical LB system, leading to very smooth and uniform LB films for investigation[19,20]. Using these films, we have shown that both orientational and positional order are long-ranged[21-23,26,27]. Surprisingly, even though the CdA films showed long-ranged positional order and very few defects, these uniform, homogeneous films were unstable to a dramatic reorganization in the presence of water [23]. Fig. 1 (bottom) shows an overview of the time evolution of the reorganization of a three layer cadmium arachidate LB film deposited on hydrophilic silicon when allowed to stay submerged under aqueous subphase. Fig. 1a shows a film submerged for only 4 minutes, the minimum time necessary for dipping to be completed. It appears to be flat and homogeneous except for some very small holes. After being submerged 10 minutes (Fig. 1b), small rough patches were observed which appeared to be nucleation sites for reorganization. Three heights can be observed, corresponding to 1, 3, and 5 layer regions. The nucleation site appears as though small bilayer sections have simply peeled off the first monolayer ("dewetted") and flipped over onto already covered areas of the film to form multilayer patches. The sizes and shapes of the holes in the film are consistent with the sizes and shapes of the multilayer regions.

After 30 minutes (Fig 1c), the process is so advanced that nearly the entire film is involved in the reorganization. There is an extensive random network of multilayered terraces, separated by heights that are a multiple of the bilayer spacing of $5.6 \pm 0.2 \text{ nm}$. From a rough analysis of a number of images, it is also apparent that the relative areas with less than the average number of layers is roughly equal to those with more than the average number of layers. Hence, little of the cadmium arachidate is being lost or solubilized, it is merely reorganizing on the surface. After 10 hours submerged (Fig. 1d), an interesting new feature begins to form; long fibrous shapes with straight edges overlay the rest of the film. The inset in Fig. 1d is a two-

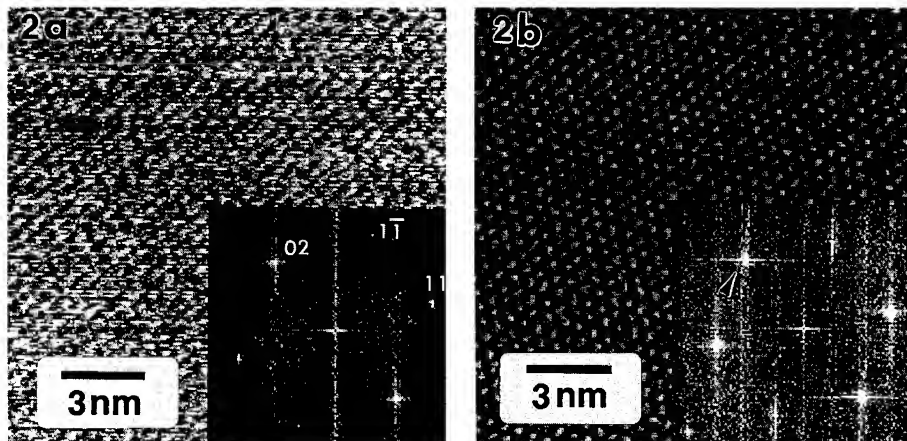


dimensional Fourier transform, which in this case is featureless since the image is still largely isotropic. After 25 hours submerged (Fig. 1e) the film has segregated into isolated islands, separated by regions of monolayer coverage. Not only do the islands have straight, sharp boundaries, but, as shown by the approximately hexagonal symmetry of the Fourier transform, the island edges have well defined absolute orientations. After 48 hours submerged (Fig. 1f) the hexagonal symmetry is even more pronounced and the islands can essentially be identified as isolated crystallites related by hexagonal "twinning". The approximately 2 μm distance between island centers is consistent with the approximately 2 μm size of the crystallites we measured in the films prior to reorganization. Hence, these LB films reorganized to form additional headgroup-headgroup interfaces that stabilized the films. The minimum size of the reorganized domains likely depends on the competition between the increase in adhesion energy of the newly folded regions and the extra energy associated with the increase in hydrocarbon-water contact at newly folded step edges. The kinetics of the reorganization were strongly dependent on the fatty acid chain length, with C16 reorganizing much faster than C22.

Substrate Effects - Lead Stearate and Manganese Arachidate

The choice of substrate does have a dramatic effect on the structure of monolayer films for both PbSt and MnA. Monolayers of PbSt deposited on crystalline mica have long range order while monolayers of MnA on mica show a distinct but short-ranged order. Otherwise identical lead stearate and manganese arachidate monolayers are completely disordered on amorphous oxidized silicon. Both PbSt and MnA monolayers on mica have a significantly larger lattice spacing and molecular area than do the corresponding multilayers on mica, indicating a strong coupling to the mica lattice [24]. For PbSt trilayers on mica, the molecular area and lattice parameters were significantly larger than those of PbSt trilayers on oxidized silicon [24]. However, by the seventh layer of PbSt, the lattice parameters had decreased to those of PbSt trilayers on oxidized silicon. Monolayers of both MnA and CdA were disordered, and for CdA no structural differences were observed between multilayer films deposited on oxidized silicon or mica. (MnA could not be deposited on oxidized silicon.)

Fig. 2 (below) shows molecular resolution images of (a) a monolayer LB film of PbSt deposited on mica and (b) the underlying mica lattice, along with their two-dimensional Fourier transforms (FT) inset. Note the similar orientations of the two images, indicating a coupling of the monolayer (and subsequent bilayers) to the mica lattice. While each alkyl chain in the 3 layer films of PbSt has 4 nearest neighbors at a relatively "close-packed" distance of 0.44-0.45 nm and 2 nearest neighbors at a distance of 0.48-0.51 nm, the alkyl chains in the monolayer films have only 2 nearest neighbors at a short distance of 0.45-0.46 nm and 4 nearest neighbors at a distance



of 0.49-0.51. This is a previously unreported sort of packing which does not correspond to any of the familiar types of alkane packing that are observed in all other ordered LB films we have imaged, although it may be related to a rectangular arrangement based on the "M" packing (which Kitaigorodskii rejects because of its low density) which has "ideal" cell dimensions of $a_1=0.42$ nm, $a_2=0.91$ nm [32].

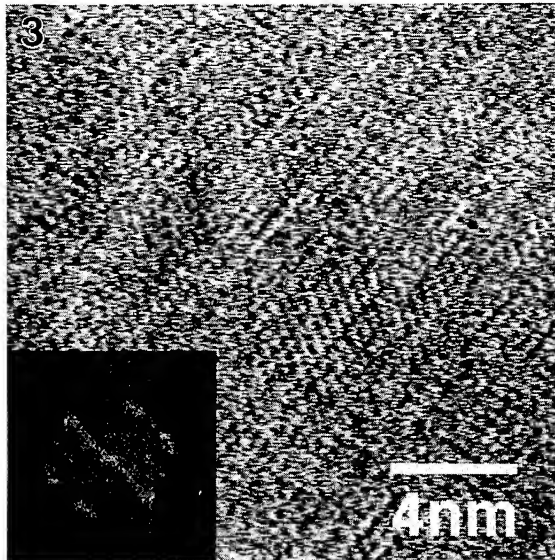
The nearest neighbor packing in the mica lattice is 0.52 nm, which indicates that all of the monolayer lattices are most likely expanding to match that of the mica. However, the overall symmetry difference between adsorbate and substrate makes for a rather poor match. Thus the PbSt films have chosen a middle ground between strained-layer epitaxy, in which the monolayer replicates the substrate structure exactly and gradually relaxes to the bulk structure with additional layers, and "van der Waals" epitaxy [33-35], in which the epitaxial crystal film takes on its bulk lattice constants even at submonolayer coverage, (although the adsorbate lattice constants can be quite different from those of the substrate) but is aligned with respect to the substrate.

Although the lattice structures of the monolayer and multilayers of PbSt and MnA are rectangular (with unit cell dimensions a and b), the monolayer lattice is qualitatively different from that of the multilayers. The monolayer lattice, characterized by a b/a ratio of about 2, is unusual for bulk aliphatic compounds, but has been seen in an LB monolayer [36] and has the same alkane chain packing as a tilted structure observed by x-ray diffraction in a fatty acid monolayer on an aqueous subphase [114]. The subsequent bilayers take on a more familiar type of lattice which is characteristic of the "herringbone" packing. From the comparison of the multilayer FT with the FT of the underlying mica substrate, we conclude that both the [02] and the [11] directions of the multilayer film are nearly aligned ($<1.5^\circ$) with the degenerate [11] and [11] directions of the monolayer, and that the [11] direction of the multilayer is aligned with a mica repeat direction [24]. The lattice constants of subsequent bilayers gradually relax while maintaining approximately the same b/a ratio until the bulk structure is reached at seven layers. This picture is consistent with previous x-ray diffraction measurements on thick (100 bilayers) PbSt films on mica [38] in which it was found that the [11] direction of the LB film was aligned with a mica repeat direction. Our results, which follow the growth from layer to layer, provide an explanation for this previously mysterious choice of alignment.

Hexatic phases in ZnA films

Hexatic phases emerged from two-dimensional melting transition theory [39,40] which predicted that two-dimensional crystals with triangular symmetry can melt continuously through a two-step process. This intermediate phase has long-range orientational order but short-range positional order and has been termed a "hexatic" phase [39-46]. In the hexatic phase, the long-range periodicity of the lattice is interrupted by point dislocations in the crystal. However, the orientational order is still preserved. Hexatic phases are common in smectic liquid crystals, which are distinguished from other liquid crystals by having an intermediate degree of positional order [19]. Analogies can be drawn between these liquid crystal systems and the ZnA films examined here, where a hexatic to crystalline order transition occurs in the LB films as they become thicker.

Figure 3 (top of next page) shows a molecular resolution image of a trilayer of zinc arachidate deposited on mica. The two-dimensional Fourier transform (FT) (inset of 3), shows the spots that correspond to the lattice row repeat distances. Qualitatively, the spots appear broad and diffuse, in contrast to the traditionally sharp spots associated with fatty acid films previously studied [21-28]. The relative positions and intensities of the spots give information on the positional and orientational order of the image. The positional correlation length is inversely proportional to the thickness of the spot. Hence, a sharp spot would correspond to long-range positional order. However, we cannot immediately ascribe the diffuse spots present in these trilayers to lack of positional order, as poor tips could have given these spots as well. To confirm this, we obtained 30-40 drift-free images from 2 independent samples using 5-7 different tips. From these results, tip effects were eliminated and the existence of the broad spots were attributed to the actual film structure. Hence, these films exhibited short-range positional order that extended only a few nanometers. Orientational order was preserved and maintained for domains extending up to a micron in size, thereby demonstrating hexatic order -- a hexatic phase.



Due to the expanded nature of the trilayers, thicker films were examined to check for evolution of the film, if any. Examination of 7 layer films of ZnA on mica gave dramatic results. These films show excellent molecular resolution and positional order that is long-range. In these films, the positional order extends well beyond the image size and the decay of order is much less than that for the trilayer. Hence, we see here a transition from hexatic at 3 layers, to crystalline at 7 layers. The crystallinity is induced in the third dimension.

Summary

The direct visualization of Langmuir-Blodgett films by Atomic Force Microscopy provides a great deal of information on the microstructure and macroscopic phenomena of organic thin films. The AFM gives the most easily understood atomic resolution images of organic and biomaterials. Both molecular resolution images [24-30] and larger scale images [19,20] have been important in answering questions on how the details of deposition affect the morphology of the films and the relationship between the molecular structure of the Langmuir film on the air-water interface and the Langmuir-Blodgett film on a substrate. The work presented in this paper emphasizes the effect of cation and substrate on the molecular organization of LB films.

References

1. G.G Roberts, *Advances in Physics*, **34**, 475 (1985)
2. A. Bonnerot, P.A. Chollet, H. Frisby, and M. Hoclet, *J. Chem. Phys.* **97**, 365 (1985);
3. S. Garoff, H.W. Deckman, J.H. Dunsmuir, and M.S. Alvarez, *J. Phys.* **47**, 701 (1986)
4. C. Böhm, R. Seitz, and H. Riegler, *Thin Solid Films*, **178**, 511 (1989)
5. I.R. Peterson, R. Seitz, H. Krug, and I. Voigt-Martin, *J. Phys. (France)*, **51**, 1003 (1990)
6. M. Seul, P. Eisenberger, and H. M. McConnell, *Proc. Natl. Acad. Sci.* **80**, 5795 (1983); M. Prakash, P. Dutta, J.B. Ketterson, and B.M. Abraham, *Chem. Phys. Lett.* **111**, 395 (1984)
7. P. Tippmann-Krayer, R. M. Kenn, and H. Möhwald, *Thin Solid Films*, **210**, 577 (1992).
8. M. Pomerantz and A. Segmüller, *Thin Solid Films*, **68**, 33 (1980)

9. R. F. Fischetti, V. Skita, A. F. Garito, and J. K. Blasie, *Phys. Rev. B* **37**, 4788 (1988); S. Xu, A. Murphy, S.M. Amador, and J.K. Blasie, *J. Phys. I (France)*, **1**, 1131 (1991)
10. V. Skita, W. Richardson, M. Filipowski, A. Garito, and J.K. Blasie, *J. Phys.*, **47**, 1849 (1986); V. Skita, M. Filipowski, A. F. Garito, and J. K. Blasie, *Phys. Rev B.*, **34**, 5826 (1986)
11. J.M. Bloch, W.B. Yun, and K.M. Mohanty, *Phys. Rev. B*, **40**, 6529 (1989)
12. D.A. Outka, J. Stöhr, J.P. Rabe, J.D. Swalen, and H.H. Rotermund, *Phys. Rev. Lett.* **59**, 1321 (1987)
13. P. M. Claesson and J. M. Berg, *Thin Solid Films* **176**, 157 (1989)
14. L. Rothberg, G.S. Higashi, D.L. Allara, and S. Garoff, *Chem. Phys. Lett.* **133**, 67 (1987); J.P. Rabe, J.D. Swalen, and J.F. Rabolt, *J. Chem. Phys.* **86**, 1601 (1987); T. Nakanaga, M. Matsumoto, Y. Kawabata, H. Takeo, and C. Matsamura, *Chem. Phys. Lett.* **160**, 129 (1989).
15. P. Stroeve, M. P. Srinivasan, B. G. Higgins, and S. T. Kowel, *Thin Solid Films*, **146**, 209-216 (1987).
16. R. Maoz and J. Sagiv, *J. Coll. Inter. Sci.*, **100**, 465 (1984); F. Kimura, J. Umemura, and T. Takenaka, *Langmuir*, **2**, 96 (1986); M. Shimomura, K. Song, and J.F. Rabolt, *Langmuir*, **8**, 887 (1992)
17. M. Egger et al, *J. Struct. Biol.*, **103**, 89 (1990); E. Meyer, et al, *Nature* **349**, 398 (1991); J.A.N. Zasadzinski et al, *Biophys. J.* **59**, 755 (1991); L. Bourdieu, P. Silberzan, and D. Chatenay, *Phys. Rev. Lett.* **67**, 2029 (1991).
- 18.. D. P. É. Smith et al, *Proc. Nat. Acad. Sci. USA*, **84**, 969-972 (1987); J. P. Rabe and S. Buchholz, *Phys. Rev. Lett.*, **66**, 2096-2099 (1991); J.K.H. Hörber et al, *Chem. Phys. Lett.* **145**, 151 (1988).
19. H. G. Hansma, S. A. C. Gould, P. K. Hansma, H. E. Gaub, M. L. Longo, and J. A. N. Zasadzinski, *Langmuir*, **7**, 1051 (1991).
20. R. Viswanathan, D. K. Schwartz, J. Garnaes, and J. A. N. Zasadzinski, *Langmuir*, **8**, 1603 (1992).
21. J. Garnaes, D.K. Schwartz, R. Viswanathan, and J.A.N. Zasadzinski, *Nature*, **357**, 54 (1992).
22. D.K. Schwartz, J. Garnaes, R. Viswanathan, and J.A.N. Zasadzinski, *Science* **257**, 508 (1992).
23. D.K. Schwartz, J. Garnaes, R. Viswanathan, S. Chiruvolu, and J.A.N. Zasadzinski, *Phys. Rev. E* **47**, 452 (1993).
24. R. Viswanathan, D.K. Schwartz, and J.A.N. Zasadzinski, *Science* **261**, 449 (1993).
25. D.K. Schwartz, R. Viswanathan, and J.A.N. Zasadzinski, *J. Am. Chem. Soc.*, **115**, 7374 (1993)..
26. D.K. Schwartz, R. Viswanathan, and J.A.N. Zasadzinski, *Phys. Rev. Lett.* **70**, 1267 (1993).
27. D.K. Schwartz, R. Viswanathan, and J.A.N. Zasadzinski, *Langmuir* **9**, 1384 (1993).
28. R. Viswanathan, D.K. Schwartz, and J.A.N. Zasadzinski, submitted to *Nature*.
29. Millipore Corporation, Bedford, MA.
30. NIMA Technology Ltd., Warwick Science Park, Coventry, CV4 7EZ, England.
31. Digital Instruments, Inc., Santa Barbara.
32. A.I. Kitagorodskii, Organic Chemical Crystallography, (Consultants Bureau, New York, 1961), Ch. 3.
33. K. Ueno et al, *J. Vac. Sci. Tech. A* **8**, 68 (1990).
34. A. Koma, K. Saiki, and Y. Sato, *Appl. Surf. Sci.* **41/42**, 451 (1989).
35. F.S. Ohuchi et al, *J. Appl. Phys.* **68**, 2168 (1990).
36. R. Steitz, E.E. Mitchell, and I.R. Peterson, *Thin Solid Films* **205**, 124 (1991).
37. D.K. Schwartz, M.L. Schlossman, and P.S. Pershan, *J. Chem. Phys.* **96**, 2356 (1992).
38. M. Prakash, J.B. Peng, J.B. Ketterson, and P. Dutta, *Chem. Phys. Lett.* **128**, 354 (1986).
39. J.D. Brock et al., *Z. Phys. B* **74**, 197 (1989).
40. B.I. Halperin and D.R. Nelson, *Phys. Rev. Lett.* **41**, 121 (1978); D.R. Nelson and B.I. Halperin, *Phys. Rev. B* **19**, 2457 (1979).
41. J. D. Brock et al., *Cont. Phys.* **30**, 321 (1989).
42. M. Cheng et al., *Phys. Rev. Lett.* **59**, 1112 (1987).
43. M. Cheng et al., *Phys. Rev. Lett.* **61**, 550 (1988).
44. R. Pindak, D.E. Moncton, S.C. Davey, and J.W. Goodby, *Phys. Rev. Lett.* **46**, 1135 (1981).
45. J.D. Brock et al., *Phys. Rev. Lett.* **57**, 98 (1986).
46. D.E. Moncton and R. Pindak, *Phys. Rev. Lett.* **43**, 701 (1979).

PART VII

Surface Structures and Physical Properties

POLARIZATION, INTERFERENCE CONTRAST, AND PHOTOLUMINESCENCE IMAGING IN NEAR FIELD OPTICAL MICROSCOPY

M. VAEZ-IRAVANI, R. TOLEDO-CROW, and J.K. ROGERS
Optical Sciences Group, Center for Imaging Science, Rochester Institute of Technology, P.O.
Box 9887, Rochester, N.Y. 14623-0887.

ABSTRACT

The design and operation of a number of techniques in near field optical microscopy are described. Specific attention is paid to the three modalities of polarization, interference contrast, and photoluminescence imaging. By premodulating the polarization state of the sample beam, pure, linear, polarizing microscopy is performed. In addition, polarization anomalies are observed in the focal plane of a high numerical aperture lens. Amplitude and phase contrast imaging is performed in a feedback stabilized Mach-Zehnder interferometer. Magneto-optically induced polarization shifts are detected interferometrically, resulting in linear sensitivity. Localized photoluminescence is induced in porous silicon, and the results are correlated with the topography of the sample.

1. INTRODUCTION

Despite the many recent innovative approaches in microscopy, optical microscopy continues to be widely used in a variety of applications. This popularity can be attributed to a number of factors, including the availability of a large number of contrast mechanisms, the possibility of using the technique with minimal sample preparation, operation in air, and the existence of a wealth of information on optical characteristics of materials. A disadvantage of optical microscopy, on the other hand, has always been the limited resolution of the technique as dictated by diffraction effects. However, by resorting to imaging in the near field [1-10], the diffraction-limited resolution can be exceeded. In essence, near field microscopy involves scanning an object in close proximity (i.e. at a distance $<< \lambda$) and capturing the high spatial frequency components of the object field, which contain information on a scale beyond the diffraction limit. In practice, the probe used is typically a pulled fiber tip, or a micro-pipette, made opaque everywhere except at the aperture with a layer of aluminum or gold. The size of the aperture, and the tip separation from the sample, determine the resolution.

It is an important feature of near field scanning optical microscopy (NSOM) that all the contrast mechanisms that are available in the conventional, far field, techniques, are also present in this regime. In this paper, we describe the application of NSOM in three imaging modalities of polarization, interference contrast, and luminescence.

2. POLARIZING MICROSCOPY IN THE NEAR FIELD

2.1. Linear Polarizing Microscopy

Polarization imaging in the near field can be performed by resorting to the usual far field

method of viewing the sample between a pair of crossed polarizers [11]. Indeed, this technique has successfully been exploited in imaging magneto-optic bits [12]. However, this approach presents two problems: (i) the detected signal is quadratically dependent on the sample birefringence, and (ii) the sample transmittance is superimposed on the output polarization image (see below). To avoid these problems, and to achieve a linear sensitivity with respect to the sample birefringence, we resort to the system of Fig. 1 [13], which embodies two separate probe microscopes. In the first branch, the output of a He-Ne laser, L1, is polarized, and is directed through an electro-optic modulator (a Pockels cell), driven at a frequency ω_p . The light is then launched into a single-mode-polarization-preserving fiber, which has been inserted into a micro-pipette with a small clear aperture at the end (as described above). The light through the sample is then analyzed and detected by a photomultiplier tube (PMT).

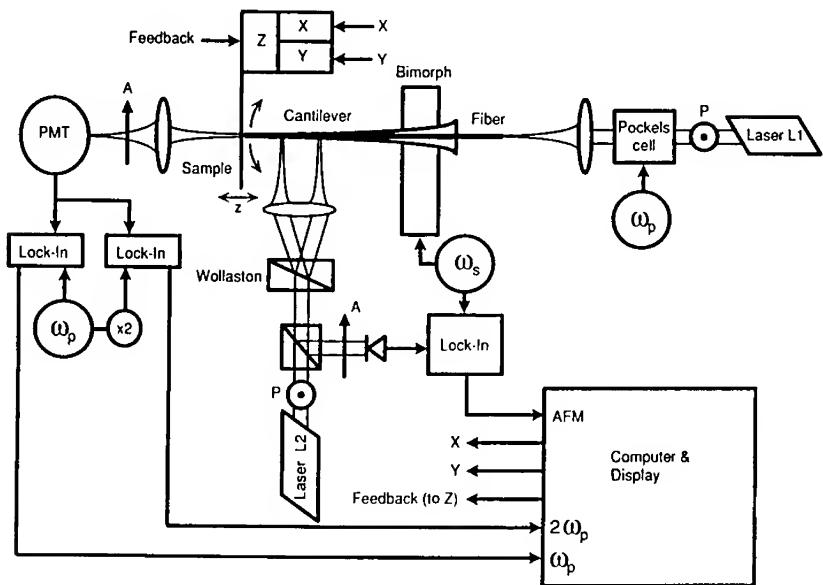


Fig. 1. Linear polarizing NSOM

The nominal distance of the tip from the sample in our experiments is of the order of 5-8 nm. To maintain this, we resort to a force regulation mechanism in which the variation of the lateral oscillation amplitude of a tip as a function of the position of the tip on the sample is monitored and is used as a feedback signal [14,8,9]. This is done by the second branch of the system, which consists of a differential interferometer, in which the light of a polarized He-Ne laser, L2, is split into two orthogonally polarized, angularly divergent beams by a Wollaston prism. The apparent plane splitting of the light is coincident with the focal plane of the lens, resulting in two foci on the shaft of the micro-pipette. The separation of the foci is 100 μm . Due to the lateral separation of the beams on the shaft, they receive a different amount of phase modulation at the oscillation frequency of the tip. Upon recombination, the state of polarization of the beam is altered with respect to that of the initial polarization, resulting in the passage of some light through the cross-polarized analyzer. An advantage of this method is that by adjusting the

lateral position of the Wollaston prism, one can obtain a signal whose strength is linearly dependent on the amount of phase modulation and, therefore, the tip movement [14].

Fig. 2 shows the arrangement of the polarization axes of the first branch of the system. Thus, the polarization of L1 is in the X direction, and the analyzer pass axis is along the Y-axis. The induced axes of the Pockels cell are along t_1 and t_2 which are at 45° with respect to the initial polarization. It can be shown that the output of the PMT for a given sample birefringence, $\delta\phi$, is given by [13]:

$$I_{out} \propto \{ t_1^2 + t_2^2 - 2t_1t_2[\cos(\delta\phi)J_0(\theta) - 2\sin(\delta\phi)J_1(\theta)\sin(\omega_p t) + 2\cos(\delta\phi)J_2(\theta)\cos(2\omega_p t) + \dots] \} \quad (1)$$

where t_1 and t_2 are the transmissivities of the sample along the two axes (Fig. 2), and θ is the amount of the phase modulation due to the Pockels cell, and J_i are the i th order Bessel functions of the first kind. In the absence of the Pockels cell, i.e. the normal approach, $\theta=0$, and Eq. (1) reduces to:

$$I_{out} \propto [t_1^2 + t_2^2 - 2t_1t_2\cos(\delta\phi)] \quad (2)$$

Assuming that $t_1=t_2$, we note that: (i) for a small $\delta\phi$, this represents a quadratically dependent signal on the birefringence, and (ii) the output is proportional to the sample transmittance. With the Pockels cell present, we detect the first two harmonics of f_p , and take their ratio. We have:

$$V_r = -\tan(\delta\phi) [J_1(\theta) / J_2(\theta)] \quad (3)$$

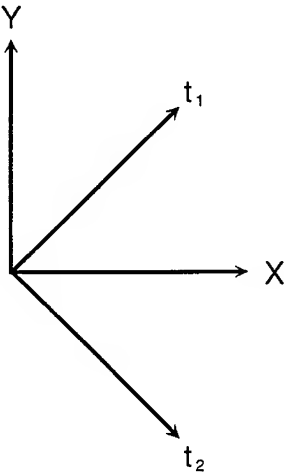


Fig. 2. Axes of polarizer and analyzer

Since for a small $\delta\phi$, $\tan(\delta\phi) \approx \delta\phi$, this ratio represents a linear, sample-transmittance-independent, polarization signal [13]. Using the system of Fig. 1, we have imaged a number of samples. Fig. 3 shows the transmittance (a), and pure polarization (b) images of a pattern in a 100-nm-thick layer of chromium on quartz. The bright areas in 3(a) correspond to the transparent regions on the sample. The polarization image shows variations due to changes in

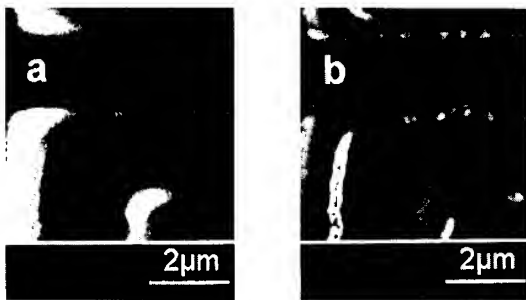


Fig. 3. Transmittance (a) and absolute polarization image (b) of a lithographic pattern

the boundary conditions at the edges. Fig. 3(b) is a rectified image; thus, the thin lines in the tracks represent regions where the sign of the birefringence changed. In general, the tracks in polarization images obtained this way appear wider than in the transmittance image, as even in those areas where the transmissivity may be limited, there can still be an appreciable amount of birefringence.

2.2. Anomalous behavior of polarized light in focal plane of lenses

As a second example of the use of high-resolution polarization imaging, we exploit the ability of the pulled fiber tip to preserve the polarization, to detect the polarization effects in the focal plane of lenses. Our interest in such work stems from the fact that, according to theory [15-17], when a lens of high numerical aperture (N.A.) is used to focus linearly polarized light, the light distribution in the focal plane also contains orthogonally polarized components. From a practical viewpoint, a direct consequence of this is that in high-resolution polarizing microscopy of weakly birefringent materials, care must be exercised in interpreting the data.

In order to observe directly the polarization effects in the focal plane of high N.A. lenses, one needs to have a high-resolution detector which preserves the polarization of the detected fields with very high accuracy. Both these criteria are met with a pulled, polarization-preserving fiber tip. Indeed, an approach similar to that of Fig. 1 could be used to collect the light in the focal plane of the lens under examination. However, since the expected value of the anomaly in the field is small, we decided not to use the Pockels cell, which could possibly have introduced small but appreciable phase errors. A He-Ne laser was expanded, linearly polarized, and was focused by a 0.6 N.A. lens. The fiber tip scanned the focal plane, and the light out of the other end of the fiber was analyzed. Images were obtained of the focal field in the parallel and crossed polarized directions. Fig. 4 (a) and (b) show the parallel and crossed polarized distributions, respectively. Fig. 4(a) is similar to the pattern expected from the scalar diffraction analysis. Fig. 4(b), however, is not predicted by scalar theory, and is in good qualitative agreement with vector diffraction theory [16,17]. In either case, there are some differences between the experimental results here, and theoretical patterns of Ref. [16]. These are thought to be primarily due to the residual birefringence that may exist in the lens, and slight imperfections in the lens body. The ratio of the peak power in 4(a) and 4(b) was 200:1. It

is clear that in high resolution applications of polarizing microscopy, including magneto-optic storage systems, one may need to place an upper limit on the N.A. of the lenses used, so as not to introduce appreciable errors in the detected signals.

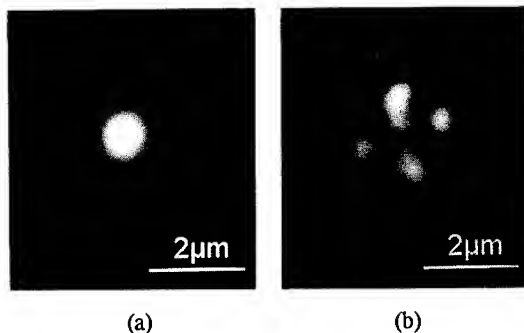


Fig. 4. Focal distribution of a 0.6 N.A. lens in the parallel (a) and crossed polarized (b) directions with respect to input polarization

3. NEAR FIELD INTERFERENCE CONTRAST MICROSCOPY

3.1. Pseudo-heterodyne interferometry in the near field

Interference contrast microscopy in the near field can be performed in a manner directly analogous to the conventional, diffraction limited, interferometric methods. In our system, which is depicted in Fig. 5, a Mach-Zehnder interferometer is set up in which the fiber tip and the sample are in one arm [18]. The tip/sample separation is force regulated by the action of the differential interferometer described in section 2.1 (shown here in block form to reduce the complexity of the diagram). The fiber length is sinusoidally stretched by a piezo-electric stretcher, operating at a frequency f_m , which results in the phase modulation of the sample light at the same frequency. Representing the complex amplitude of the sample light as E_s , and that of the reference as E_r , we have:

$$E_s = A \exp[j(\omega_0 t + \theta \sin \omega_m t + \phi + \gamma_1)] \quad (4)$$

$$E_r = B \exp[j(\omega_0 t + \gamma_2)] \quad (5)$$

where A and B are the amplitudes of the sample light and reference, respectively, ω_0 is the angular optical frequency, θ is the amount of phase modulation imparted by the piezo-stretcher and ω_m is its angular frequency, ϕ is the sample phase, and $\gamma_{1,2}$ are the environmentally dependent phase terms associated with the two branches of the interferometer. The output current of the detector is proportional to the intensity of the received light, and is given by:

$$I_{out} \propto [A^2 + B^2 + 2AB\cos(\theta\sin\omega_m t + \phi + \gamma)] \quad (6)$$

The interference signal is contained in the term $AB\cos(\theta\sin\omega_m t + \phi + \gamma)$, where $\gamma = \gamma_1 - \gamma_2$. Expanding this term further, we have:

$$AB\cos[\theta\sin\omega_m t + \phi + \gamma] = AB[\cos(\theta\sin\omega_m t)\cos(\phi + \gamma) - \sin(\theta\sin\omega_m t)\sin(\phi + \gamma)] \quad (7)$$

Only the first term on the right side of Eq. (7) includes a second harmonic signal (at $2f_m$). The presence of γ means that the entire interference signal is subject to fluctuations due to environmental variations. In order to stabilize the interference term, we resort to a feedback

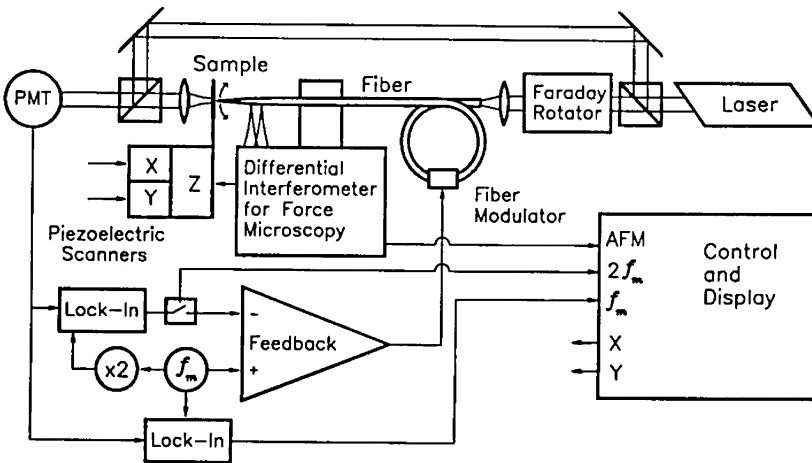


Fig. 5. Pseudo-heterodyne interference contrast NSOM

system, as shown in Fig. 5, which detects the signal at $2f_m$ in the output of the PMT, and feeds it back to the drive voltage to the phase modulator. The overall effect of this negative feedback system is to eliminate the second harmonic signal, and to keep the interferometer in quadrature [19]. In this system, therefore, we have two feedback loop responses: one due to the force regulation part (which determines the image bandwidth), and the other due to the fiber stabilization system. Depending on how we set the fiber stabilization response time with respect to that of the force feedback loop, we can have different regimes of operation. If the fiber stabilization loop bandwidth $>$ image bandwidth, then, through the elimination of the second harmonic signal, the stabilization system tends to set the term $\cos(\phi + \gamma)$ to zero. The interference signal at f_m is thus devoid of any sample phase, and is a pseudo-heterodyne amplitude signal (proportional to AB). If, on the other hand, the fiber loop bandwidth $<<$ image bandwidth, again the stabilization loop attempts to eliminate the second harmonic signal. However, since in normal operation the environmental fluctuation term (γ) varies much more slowly than the scanning rate, the result of this mode of operation is to eliminate the slow variations of the second harmonic signal, dominated by the term γ . This tends to set γ equal

to $\pi/2$. Therefore, the signal at f_m , $AB\sin(\phi+\gamma)$, becomes proportional to $AB\cos(\phi)$, which is a phase contrast signal [18].

Regardless of whether this method is used to detect amplitude or phase of the sample, we note that the signal amplitude is proportional to AB . In near field microscopy, the available light from the tip is usually quite small (of the order of a few nW or less). This implies that the normal, non-interferometric system is often not shot-noise limited. In the present pseudo-heterodyne interferometric system, by contrast, the reference beam can be many orders of magnitude greater than the sample light, resulting in a shot-noise-limited signal even with low sample light levels, and/or with the use of a simple photodiode, rather than a PMT, as the detector.

Fig. 6(a) and (b) show the image of a series of tracks, in a chromium-on-quartz substrate. The light out of the tip in both cases was of the order of 10 pW, and the image bandwidth was 1 kHz. Fig. 6(a) barely shows the tracks, and is dominated by the random fluctuations of the PMT output due to the low S/N. Fig. 6(b), on the other hand, was obtained by using the signal at f_m , when the same sample light level as in 6(a) was interfered with a 50 μ W reference beam. The improvement of the S/N is dramatic. The tracks and a number of characteristic interference effects are obvious. Fig. 7(a) shows the force image of a part of a chromosome, and 7(b) the

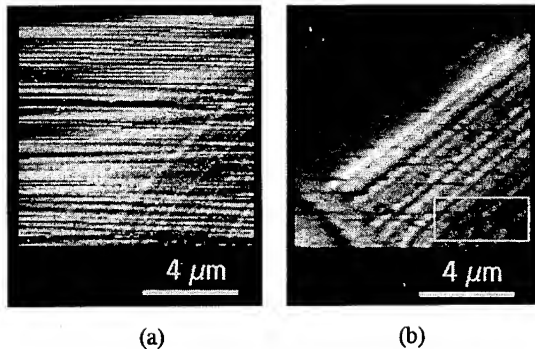


Fig. 6. Regular, intensity, image of tracks in chromium-on-quartz with low light level; (b) interference image of the same field.

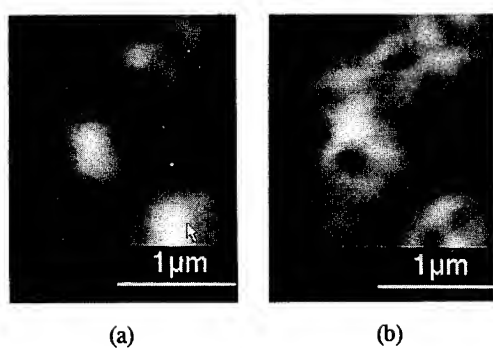


Fig. 7. Force (a) and interference (b) images of a part of a chromosome

simultaneously obtained interference contrast image of the same field. As can be seen, there are regions in the image that the force image alone, which reveals primarily the topography, is not able to show the structure of the sample. Currently, we are studying the possibility of using near field interference microscopy in an effort to alleviate the need for contrast agents in certain high-resolution biological imaging applications.

3.2. Interferometric detection of polarization effects

The fact that inference is inherently an amplitude rather than intensity effect enables us to use the system of Fig. 5 to detect minute polarization shifts in an unusual way. Let us suppose that the sample consists of regions which shift the plane of polarization of the interrogating light, such as would be the case for magneto-optic storage disks. If we arrange for the polarization of the reference and the sample beams (in the absence of any polarization shifts) to be orthogonal, no interference can take place. However, a small shift, θ , in the plane of polarization of the sample light would mean that it would have a component $A \sin(\theta) = A\theta$ along the polarization direction of the reference. The interference signal at f_i would have the amplitude $AB\theta$, i.e. it would represent a signal with a linear dependence on the polarization shift. At the same time, the basic pseudo-heterodyne nature of the system would imply shot-noise-limited performance even with small light levels, as would be the case in near field microscopy.

In our experiments, we used the system of Fig. 5 with a $\lambda/2$ plate inserted in the reference arm to rotate the polarization of this beam by 90° . Fig. 8 shows the resulting image, where the sample was a conventionally written magneto-optic disk, the sample light was 100 pW, and the bandwidth was 1 kHz. It should be noted that in this detection mechanism the detection bandwidth, and the resulting S/N are, of course, still limited by shot noise. By increasing the sample light level, which can be effected by using larger apertures, we hope to achieve much faster operation speeds, so as to establish the ultimate limits on the performance of this system.

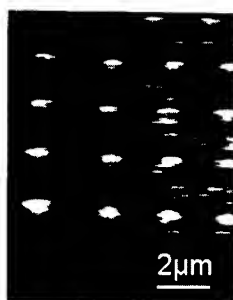


Fig. 8. Polarized interferometrically detected magneto-optic bits

4. PHOTOLUMINESCENCE STUDIES IN THE NEAR FIELD

Using radiation of appropriate wavelength, near field optical microscopy can be very effectively used in high-resolution luminescence studies [20]. Fig. 9 shows our experimental arrangement to perform near field photoluminescence studies on porous silicon (PS) [21], which is currently the subject of intense research due to its intriguing possibilities as a source compatible with silicon integrated circuit (IC) technology.

The experimental set-up has the basic framework of our force-regulated NSOM [9], except

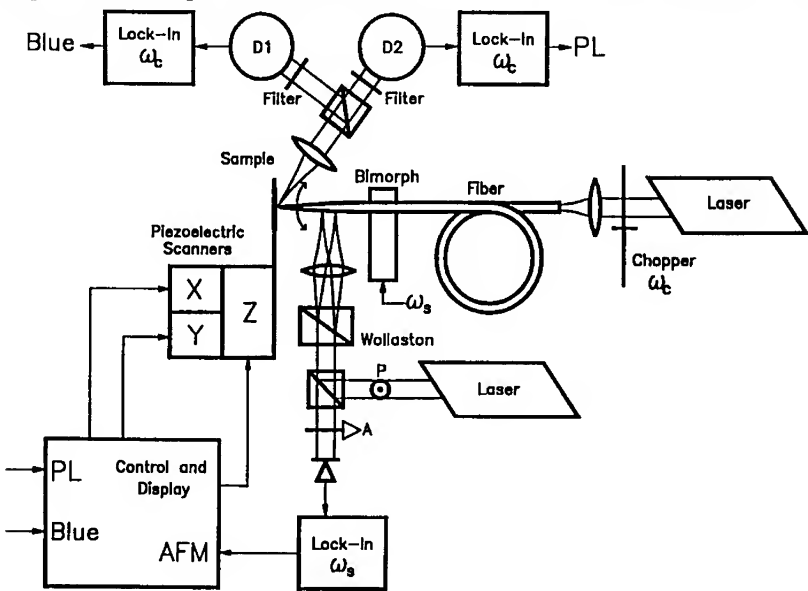


Fig. 9. Experimental set-up to perform near field photoluminescence imaging

that an Ar ion laser was used to illuminate the sample. The scattered blue, and the photoluminescence light were gathered by a collection lens, separated using filters, and detected. The porous silicon used was formed on an n-type, 5-15 Ω cm resistivity, [100] silicon wafer. The wafer was anodically etched, with white light assistance in a 1:1 solution of 49 wt% hydrofluoric acid and methanol. The current density was 6.3 mA/cm², and the total etching time was 40 minutes [22]. The sample had been stored in air at room temperature for several months prior to these experiments.

Fig. 10 shows a $12 \times 12 \mu\text{m}$ perspective view of the topography of the PS sample, as obtained with the force microscope part of the system. The image consists primarily of "hills and valleys" of the order of $1.0\text{--}1.5 \mu\text{m}$ in size. In common with earlier force images of porous silicon (obtained in contact mode) [23], we did not observe much evidence of the underlying wire structure. Fig. 11(a) shows the force image, and 11(b) the corresponding, simultaneously collected, photoluminescence image of a region of the PS sample. It appears that the PL is strongest in the regions between the macro-structures, as long as the separation between them is not large. The total variation of the PL intensity across this field was about 50%. Fig. 11(b), in addition to showing the PL image, is also affected by the underlying topography. If we assume a linear dependence between the two, we can normalize 11(b) by 11(a) to obtain 11(c), which does show the PL distribution with greater clarity. The significance of these results is that if porous silicon is eventually to be used as a small source, attention must be paid to the uniformity of its output. We are continuing work in this area in order to establish the



Fig. 10. $12 \times 12 \mu\text{m}$ force image of porous silicon showing the topography

relationship between the local photoluminescence and different porosities of samples prepared under different conditions.

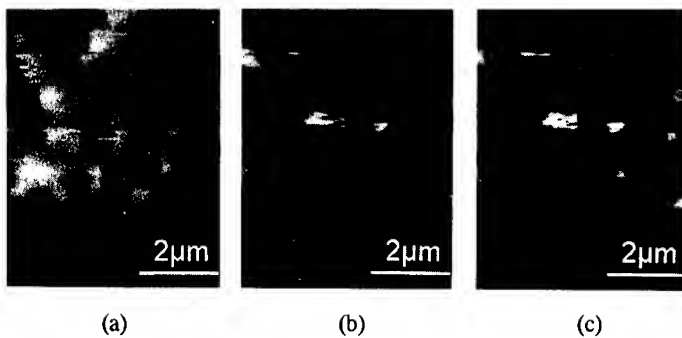


Fig. 11. Force (a), PL (b) and normalized PL (c) images of a region of porous silicon

5. CONCLUSIONS

In this paper the design of near field scanning optical microscopy in three modalities of polarizing, interference contrast, and photoluminescence, has been discussed, and a number of results have been presented. We have demonstrated pure, linear polarizing microscopy, and have imaged the focal field distribution of a high N.A. lens, showing polarization anomalies. We have shown that by resorting to a feedback stabilization technique, one can perform stable pseudo-heterodyne interference contrast microscopy in the near field. Furthermore, the fact that orthogonally polarized waves do not interfere has been used to image sample dependent polarization shifts with linear sensitivity. Finally, highly localized photoluminescence of a porous silicon sample has been imaged and correlated with the sample topography. We believe that these techniques and results are significant in a number of material and biological studies requiring optical contrast.

ACKNOWLEDGEMENTS

This work was supported in part by grants from the National Science Foundation and the Whitaker Foundation. We are indebted to C. Peng and F. Seiferth for the porous silicon sample.

REFERENCES

1. D.W. Pohl, W. Denk, and M. Lanz, *Appl. Phys. Lett.* 44, 651 (1984)
2. A. Harootunian, E. Betzig, M. Isaacson, and A. Lewis, *Appl. Phys. Lett.* 49, 674 (1986)
3. U. CH. Fischer, U.T. During, and D.W. Pohl, *Appl. Phys. Lett.* 52, 249 (1988)
4. R.C. Reddick, R.J. Warmack, and T.L. Ferrel, *Phys. Rev. B39*, 767 (1989)
5. D. Courjon, J.M. Vigoureux, M. Spajer, and K. Sarayeddine, *Appl. Opt.* 29, 3734 (1990)
6. M. Isaacson, J.A. Cline, and B.H. Barshatzky, *J. Vac. Sci. Tech. B9*, 3103 (1991)
7. N.F. van Hulst, F.B. Sergerink, and B. Bolger in: *Scanned Probe Microscopy*, Ed. H.K. Wickramasinghe (AIP, New York, 1992) p. 79
8. E. Betzig, P.L. Finn, and J.S. Weiner, *Appl. Phys. Lett.* 60, 2484 (1992)
9. R. Toledo-Crow, P.C. Yang, Y. Chen, and M. Vaez-Iravani, *Appl. Phys. Lett.* 60, 2957 (1992)
10. B. Yakobson, P. Moyer, and M.A. Paesler, *J. Appl. Phys.* 71, 7984 (1993)
11. E. Betzig, J.K. Trautman, J.S. Weiner, T.D. Harris, and R. Wolfe, *Appl. Opt.* 22, 4563 (1992)
12. E. Betzig, J.K. Trautman, R. Wolfe, E.M. Gyorgy, P.L. Finn, M.H. Kryder, and C.H. Chang, *Appl. Phys. Lett.* 61, 142 (1992)
13. M. Vaez-Iravani and R. Toledo-Crow, *Appl. Phys. Lett.* 63, 140 (1993)
14. P.C. Yang, Y. Chen, and M. Vaez-Iravani, *J. Appl. Phys.* 71, 2499 (1992)
15. B. Richards and E. Wolf, *Proc. Roy. Soc. A* 253, 353 (1959)
16. M. Mansuripur, *J. Opt. Soc. Amer. A3*, 2086 (1986)
17. M. Mansuripur, *J. Opt. Soc. Amer. A10*, 382 (1993)
18. M. Vaez-Iravani and R. Toledo-Crow, *Appl. Phys. Lett.* 62, 1044 (1993)
19. M. Vaez-Iravani, M. Nonnenmacher, and H.K. Wickramasinghe, *Opt. Eng.* 32, 1879 (1993)
20. E. Betzig and J.K. Trautman, *Sci.* 257, 189 (1992)
21. L.T. Canham, *Appl. Phys. Lett.* 57, 1046 (1990)
22. C. Peng, L. Tsybeskov, and P.M. Fauchet, *Proc. Mater. Res. Soc. Symp.* Vol. 283, 121 (1993)
23. G.B. Amisola, R. Behrensmeier, J.M. Galligan, F.A. Otter, F. Namavar, and N.M. Kalkoran, *Appl. Phys. Lett.* 61, 2595 (1992)

PHOTON TUNNELING MICROSCOPY APPLICATIONS

JOHN M. GUERRA

Polaroid Optical Eng. Dept., 38 Henry St., Cambridge, MA 02139

ABSTRACT

With photon tunneling microscopy (PTM), dielectric, semiconductor, and other surfaces are imaged by means of the phenomenon of photon tunneling (or evanescent waves). Vertical resolution is detector limited to one nanometer and the vertical range is $\lambda/2$. Lateral resolution is better than $\lambda/4$ with a field-of-view up to approximately 125 μm . PTM produces images of samples independent of size and thickness in real-time without metallization, shadowing, vacuum, electrons, or scanning probes. Tunneling images are analog processed for real-time 3-D topographic imaging with continuous viewpoint and magnification control. In this paper PTM images of a variety of samples are presented and briefly discussed.

INTRODUCTION

The photon tunneling microscope (PTM)¹ is a light microscope configured to make use of the evanescent waves that are lost in normal light microscopy. It shares the light microscope's power of parallel image formation, rather than serial as with scanning probe microscopes (SPM)²⁻⁶, that allows real-time and whole-field surveying of large and even dynamic sample topography, with redundant imaging for high data confidence. By employing the phenomenon of photon tunneling, it attains a lateral resolution (in blue light) of 0.1 μm , and provides height quantification with nanometer resolution. Development of PTM began at Polaroid Corp. in 1984^{7,8}, where it continues in proprietary service. In 1992 it became available commercially through a licensee²⁸, and there are now units at work in industry and research. The optical heritage of the photon tunneling microscope is the surface contact microscope pioneered by Ambrose⁹, used primarily in transmitted light biological studies, and the frustrated total internal reflection microscope (FTIRM) of McCutchen¹⁰. The former is still vital today primarily in biological imaging and surface microroughness inspection^{11,12}.

With the addition of video photometry, 3-D processing and display, and advancements in the transducer technology, the photon tunneling microscope transcends its heritage. Dielectric, semiconductor, and even strongly absorbing surfaces of any size are imaged and profiled with nanometer vertical resolution and lateral resolution better than $\lambda/4$, without the metallization, carbon shadowing, vacuum, electrons, time delay, or scanning probes inherent to other techniques. The easily obtained visual tunneling image is displayed in real-time topographic 3-D, with continuously variable viewpoint and magnification control that has been likened to flying about the topography. Single line profiles are electronically isolated for video height quantification and non-invasive cross-sectioning of the sample. These features make PTM a powerful tool for imaging and spatially quantifying a myriad of surfaces and the processes that give rise to them.

In addition, because PTM is a light microscope, it can be combined with spectroscopic, fluorescence, surface plasmon¹³, polarization, and other techniques, in transmission as well as in the normal reflection mode, with the efficient light throughput of a whole-field microscope.

Brief Theory

Light in a dielectric medium 1 with some index of refraction n_1 will experience total internal reflection (TIR) at its boundary with a dielectric medium 2 with a lower index of refraction n_2 , if the angle of incidence θ is equal to or greater than the critical angle defined as $\sin^{-1}(n_2 / n_1)$. Newton first observed that probing the rarer medium 2 near but not contacting the TIR surface with a dielectric surface of refractive index n_3 greater than n_2 couples light from the first medium¹⁴, indicating that light from medium 1 penetrates into medium 2. Later investigators showed that this penetration is an electromagnetic wave with the same frequency as its parent wave in the denser medium¹⁵, but is "evanescent" because it does not carry any energy from the TIR surface in averaged time if left unperturbed (Figure 1).

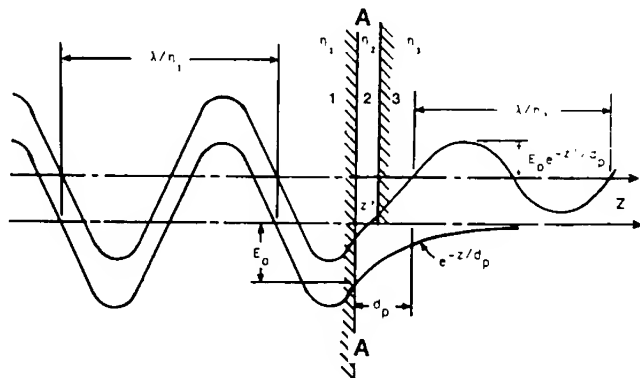


Figure 1. Evanescent field, associated with photons tunneling into medium 2, as a continuum of the parent field in medium 1. See also sample plane AA in Fig. 3.

The case for homogenous transparent dielectric media is chosen for brevity in illustration. The field strength of the evanescent wave in the direction normal to the TIR surface decays exponentially as:

$$E_{\text{Evanescent}} = E_0 \exp(-z/d_p) \quad (1)$$

where z is the distance normal to the TIR boundary and d_p is the penetration depth into medium 2 at which the field strength E falls to $1/e$ of its initial value E_0 :

$$d_p = \frac{\lambda_1}{2\pi (\sin^2 \theta - n_{21}^2)^{1/2}} \quad (2)$$

where n_{21} is the ratio n_2/n_1 and λ_1 is λ/n_1 , the illumination wavelength in medium 1.

Evanescent waves are fully explained with classical optics¹⁵⁻¹⁷ and one need not in-

voke quantum theory, but doing so adds to the intuitive understanding of the microscopy. The analogy to the electron barrier tunneling experiment has been elegantly made¹⁸⁻²², and the effect is known as optical or photon tunneling. In this modality, equation (1) describes the probability of encountering a photon from medium 1 in the tunneling gap at some distance Z normal to the TIR boundary.

Employing photon tunneling brings remarkable capabilities to microscopy. The Z -dependent exponential decay of the tunneling probability encodes topographic height information as a grayscale tunneling image; photometry of the grayscale tunneling image yields profilometry directly, after empirical calibration. The smoothly continuous decay of the tunneling probability yields vertical resolution limited in practice only by the photometric resolution, determined by the signal to noise ratio, of the detector (this also affects the vertical range).

The interrogating light is a continuum from medium 1, so the high lateral resolution of oil immersion is achieved with the sample remaining dry. In addition, the TIR illumination is inherently annular, which favors the higher spatial frequencies and amplifies lateral resolution by 1.3 to 1.6 times²³⁻²⁵. This "enhanced resolution" of optical systems with centrally obstructed apertures is used to advantage from microlithography to astronomy. The full numerical aperture (NA) remains available for imaging the sample. Further, evanescent waves generated in turn by the sample's microfeatures²⁶ are received and converted by the proximal transducer into propagating image-forming light. Described as a "super numerical aperture", the collection of the evanescent waves normally missed in a light microscope results in higher lateral resolution. There may also be contributions to the resolution from evanescent waves generated by the microroughness of the transducer itself, and this is being explored²⁷. The aforementioned features result in light microscope profilometry with nanometer vertical resolution and lateral resolution better than $\lambda/4$. The latter is evident in Figure 2.

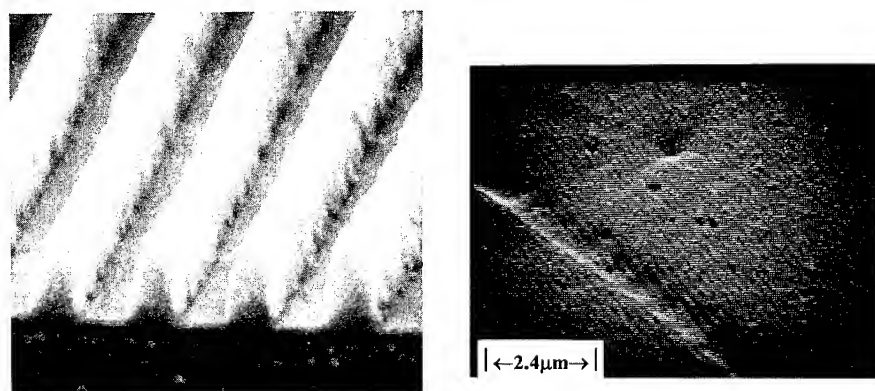


Figure 2. Scanning electron micrograph (a) of a grating in photoresist with $0.1 \mu\text{m}$ lines and spaces which is resolved (b) by PTM in blue light ($\lambda \approx 0.47 \mu\text{m}$), even though tunneling contrast was severely reduced by an unfavorable refractive index ratio of substrate and photoresist. (Grating and Fig.(a) courtesy of Dr. H. Smith, MIT Submicron Lab.)

Optical Configuration

Creating the condition required for photons to tunnel in a reflected light microscope is straightforward, in that the epi-illumination must be totally internally reflected at a surface in the object plane. This is accomplished as illustrated in Figures 3(a) and (b), where the objective is oil immersed to a transparent window whose distal surface is within the depth of focus. The numerical aperture of the objective is larger than one in order to contain the critical angle defined by the refractive indices of the transducer and the tunneling gap, so that TIR occurs at the distal surface. Accordingly, an aqueous tunneling gap, as with *in vivo* biological samples, requires the NA to be greater than 1.33. For high index windows that are hemispherical rather than plano-parallel, the required NA can be less than one.

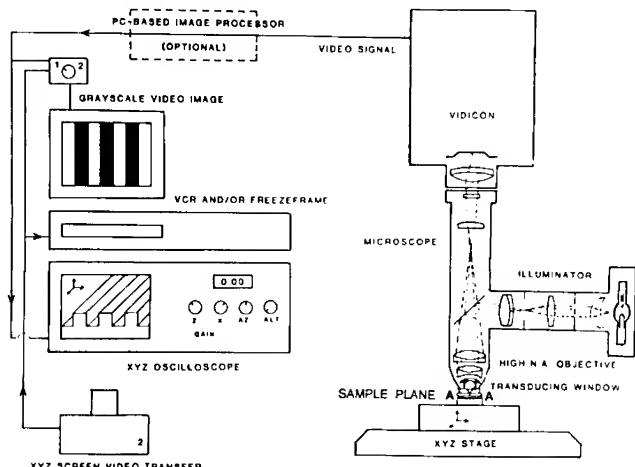


Figure 3(a). Photon tunneling microscope schematic. Sample plane AA is expanded in 3(b) below and also in Figure 1.

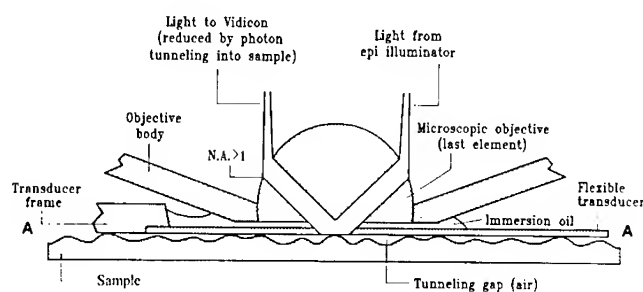


Figure 3(b). Sample plane AA: relationship of sample, transducer, and objective in PTM.

Partial coherence in the microscope is maintained by using the full numerical aperture of the objective, and by using broad band filters in the illumination with no restriction on polarization. This improves the lateral resolution, adjusts the system linearity for highest topographic fidelity, and also results in a tunneling response that is more tolerant of optical variations, if any, in the sample¹.

The sample is placed in proximity to the window, or *transducer* because it facilitates conversion of topographic height modulation into light modulation. Then the objective is oil immersed to the transducer/sample couple, with the sample remaining dry. In addition to providing the required optical unity for TIR, which is partially frustrated now in varying degrees by the sample, the immersion oil allows the sample and transducer to travel together with respect to the microscope. This eliminates damaging sliding contact, protects the sample from the oil, and allows complete freedom to move about the surface. A recent innovation is a proprietary (Polaroid Corp.) flexible transducer that is stiff and flat over the field of view of the microscope but flexible enough on a larger scale to accommodate curved surfaces and even dirt on the sample. It requires much less operator skill, can be made large enough to cover and protect any sample, is inherently clean, and is disposable and economical even though it has repeatable microroughness that is as low as the substrate to which it is cast. It is impervious to immersion oil, and is hydrophobic to allow tunneling on even the most humid days. Finally, it can be coated for surface plasmon studies, and height features can be embossed into it for calibration or other uses, such as control of the tunneling gap.

In practice, the vertical tunneling range is about $\lambda/2$, or $0.3 \mu\text{m}$ for red light, and depends upon the detector characteristics as well as the sample/transducer refractive indices, and the wavelength and angle of incidence of the illumination. Where the gap grows larger than this the tunneling image is lost; for this deeper topography, the transducer serves as a soft contact interference reference, with only refocussing and suppression of TIR illumination required for interferometry.

As stated previously, PTM gleans height information from the reflected light intensity modulation caused by the spatial modulation of the (optically homogenous) sample topography in reference to the transducer (Fig. 4(a)). This simple arrangement precludes the need for vertical control instrumentation and its limitation on speed and vertical resolution²⁶. However, height profilometry (rather than measuring optical variation in, for example, waveguides, latent images in photoresist, or biological samples) requires calibrating the photon tunneling response to the particular optical properties of the sample.

There are a number of possibilities for doing this, but empirical calibration to an identical material rendered in a known geometry, such as a spherical surface, allows the relation of sample height to the grayscale tunneling image to be directly determined with the video photometer for subsequent use on the actual sample (the rigid glass transducer is used for this), and also provides a check on optical homogeneity in the sample. Empirical calibration also broadens the application of PTM to samples for which equation (1) is not comprehensive¹⁵, such as strong absorbers or semiconductors. Materials that cannot be fashioned into a sphere are spin coated onto a spherical substrate. With the flexible transducer, alternately, the occasional dirt particle offers the opportunity to calibrate directly on the sample by using the PTM in contact interference mode, or calibration structures may be embossed into the transducer. Differences in film and bulk indices are rarely a problem because a $\approx 1\%$ variation

(rather large) has the same effect on the tunneling image as a 1 nm variation in topographic height, which is just resolved with the present detector, which is a form of vidicon tube.

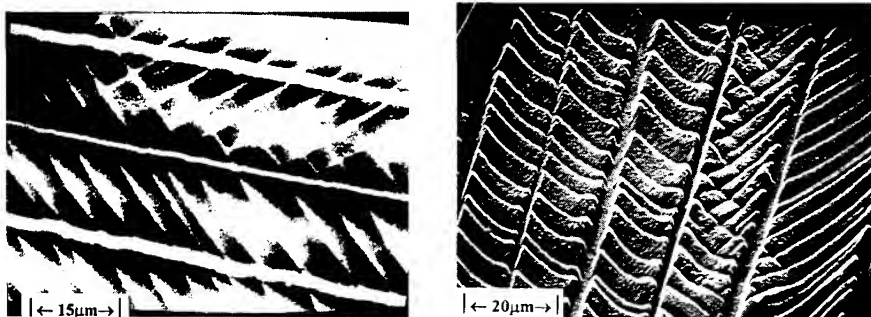


Figure 4. Conversion of (a) grayscale tunneling image into (b) 3-D image after analog processing.
Sample is a cracked latex film formed by drying an aqueous suspension of 50 nm diameter polystyrene spheres in air. Notice the diagonal features arising from close order packing of the polystyrene spheres.

Electronic Imaging Instrumentation

The tunneling image is projected onto either a photometric vidicon or a charge coupled detector (CCD) at the phototube of the microscope in the normal manner. Detector tradeoffs must be considered, in that while the CCD has the better signal to noise ratio and therefore higher vertical resolution and vertical range, the vidicon has higher lateral resolution at lower cost, and in the pasicon tube form, the vertical resolution is as high as one nanometer. Additionally, the nonlinear vidicon response to intensity largely nulls the exponential tunneling response to linear height, so that in the absence of image processing to rigorously correct the grayscale, the 3-D display of the topography is true. On the other hand, a cooled integrating 12 or 16 bit CCD would increase the vertical resolution, which in practice is the tunneling range divided by the number of resolvable gray levels, even further. Thus the resolution is convolved with the detector characteristics.

The video signal can be readily analyzed and displayed in any number of ways, including 3-D, by PC or workstation based image processing. However, at this writing, only analog processing has the speed to keep pace with the parallel optical imaging of this microscope and has a resolution advantage over digital in the 3-D display. A high resolution XY oscilloscope displays each of the video raster lines as amplitude traces, thus electronically mapping intensity back into height for a real-time 3-D image¹ (Fig. 4(b)). Analog circuits shear, expand, or collapse the multiple oscilloscope amplitude traces to control 3-D viewpoint with simple

turns of a few knobs. The reality and immediacy of this display helps the observer to understand and interpret the surface, and has been likened to flying around the sample terrain, with complete freedom to explore. A single trace can be isolated anywhere in the image for electronic cross-sectioning and height measurement. Also, left and right eye alternating perspectives can be generated and resolved by liquid crystal goggles for real-time stereopsis, an effect similar to virtual reality microscopy, for additional understanding of the topography. Figure 5 shows a commercial photon tunneling microscope²⁸.

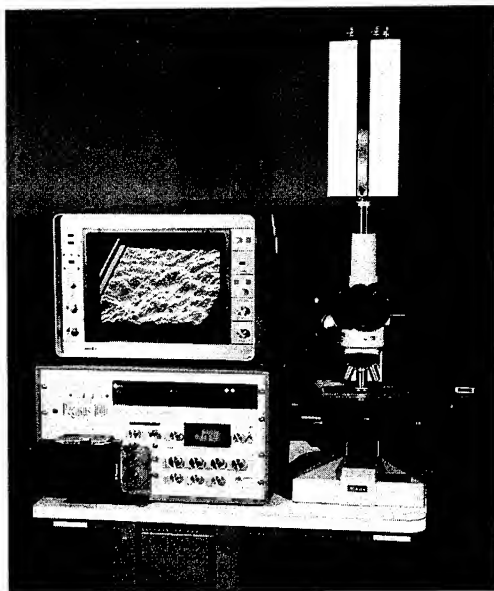


Figure 5. A commercial PTM (courtesy Dyer Energy Systems, Inc.).

RESULTS AND DISCUSSION

The following is a collection of PTM imaging solutions in a variety of applications presented to both demonstrate the scope and capabilities of PTM and suggest possible uses as well. Other applications are found in references [1] and [29]. None of these samples were coated, all were imaged in air (except the nematode in water) with light in the visible spectrum, and either the flexible or rigid transducer was in each case contacted to the sample.

Figure 6(a) shows a diamond tool used in the precision turning of optical surfaces to demonstrate the non-damaging inspection ability of PTM. A defect is seen near the edge. By orienting the edge nearly parallel to the single line profile in the 3-D display, one gets a Moiré-like edge magnification for precise radius measurement (this is not shown here). Only the top 0.3 μm of the diamond is seen, but the edge is all that is critical to its performance. On other tools, lapping marks (on the order of 2 nm peak to valley) on the top plane are evident, as seen in Figure 6(b).

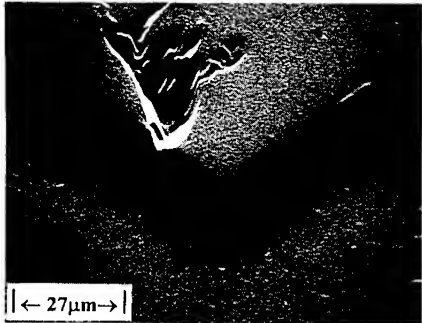


Figure 6(a). Diamond tool. Vertical black lines in scale bar are 0.30 μm high.

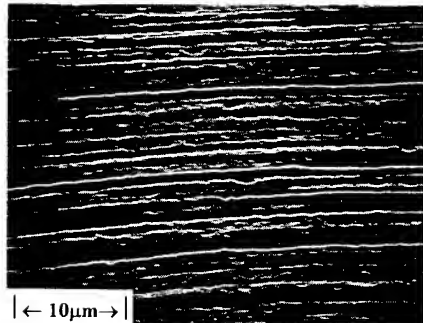


Figure 6(b). Lapping marks in diamond tool surface at higher Z magnification.

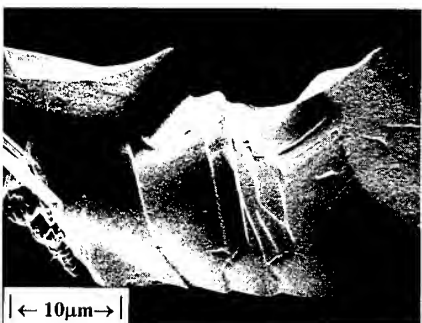


Figure 7. Two views of HOPG. Peak to valley topography is less than 0.3 μm on the 3mm thick sample.

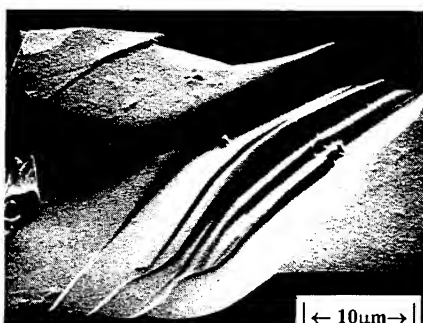


Figure 7 is a fractured area in highly ordered pyrolytic graphite (HOPG). This image is included to show that even absorbing non-dielectrics can be imaged because of the empirical calibration approach, as stated earlier.

Figure 8 illustrates the use of PTM in tribology: (a) a wear scar in a diamond-like carbon (DLC) coating on stainless steel and (b) fissures and a bubble-like feature are seen in a DLC coating on silicon. The high resolution profilometry of PTM and its non-destructive imaging of dielectric surfaces are key here, as is its imaging speed with resulting large survey capability as well. Real-time studies are possible. In scratch analysis, the profile of the scratch bottom is easily attained with the high resolution in combination with the edge-on 3-D perspective, with-

out having to precisely align a probe, for example, with the scratch direction (not shown here).

Figure 9(a) shows a thin film (magnesium fluoride) anti-reflection coating on acrylic that has cracked under compression due to substrate and coating thermal coefficient mismatch. Notice that, much like in plate tectonics, a central ridge remains. The missing film fragments were found far from this site, a task made trivial by the whole-field survey ability of PTM. In another thin film study of magnesium fluoride on acrylic seen in Figure 9(b), a transition edge was created by masking in order to illustrate how substrate roughness transfers into surface roughness on the coating. The ability of PTM to image and profile dielectric surfaces like these with high resolution and without further coatings or exposure to heat or vacuum is most useful.

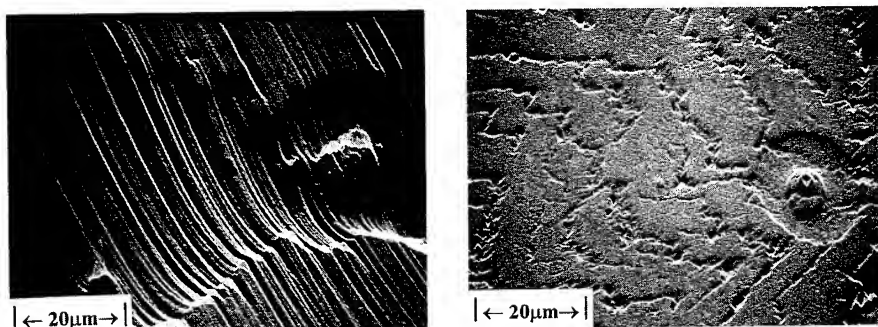


Figure 8. (a) Wear scar in DLC on stainless steel and (b) fissures in DLC on Si.

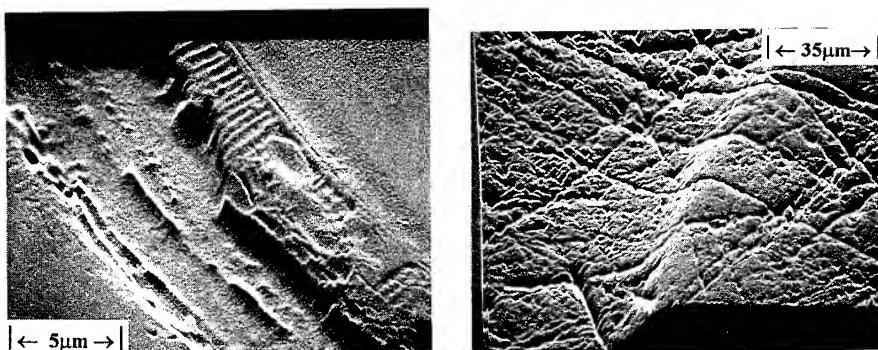


Figure 9. (a) Adhesion failure (vertical black lines in scale bar are 80 nm high) and (b) substrate roughness transfer in magnesium fluoride AR coatings on acrylic (vertical black lines in scale bar are 50 nm high).

Figure 10 demonstrates an interesting imaging problem in biological polymers, namely, viewing the attachment interface between cells and various surfaces. In this case human colon cells were critical point dried directly on the glass transducer, so that the attachment interface is also the tunneling gap (some of the topography in the nucleus is affected by optical inhomogeneity). In these images, therefore, the attachment surface is not that which the cells appear to be resting on but rather the plane above as indicated by the horizontal white line

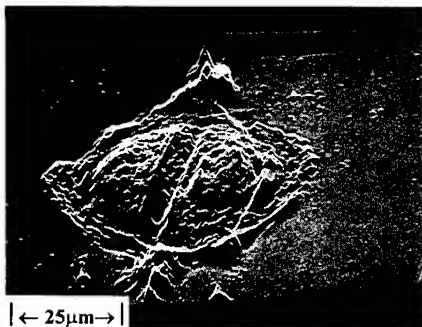


Figure 10(a). Cell attachment plane

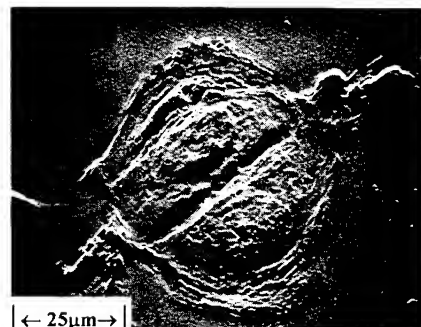


Figure 10(b). Overhead view.

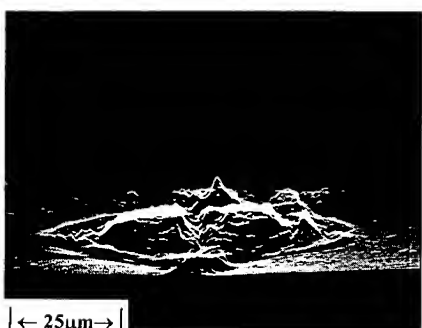


Figure 10(c). Edge-on view

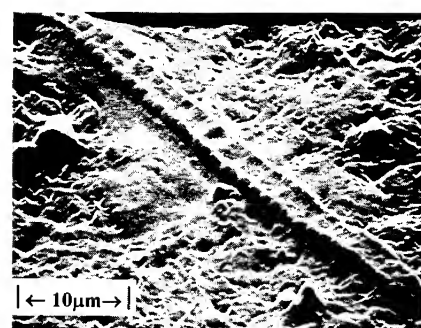


Figure 11. Nematode *in vivo*.

seen here in (a); (b) is an overhead view, and (c) is a very low elevation view, nicely showing the cleft in the cells and the attachment peaks that are the cell processes. (Sample is courtesy of Dr. S. Penman, M.I.T.) This surface is not directly accessible with other techniques. Sub-

sequent applications would include coating the transducer first with chemical/biological layers, and also viewing the attachment interface *in vivo*.

Figure 11 is an application involving tunneling into water, with a live nematode crawling along a soil sample. The degree to which the topography is convolved with optical mapping here is not known, but comparison to nematode images elsewhere with other techniques indicate that it is very small.

Figure 12 is an application where the transducer is part of the sample, in that the top surface of this mica was used to image voids just below it, without physically altering the sample. Even so, the unique ability of PTM to encode the enclosed topography in grayscale and then map it back into a 3-D topography allows these nearly edge-on views of the 100Å steps.

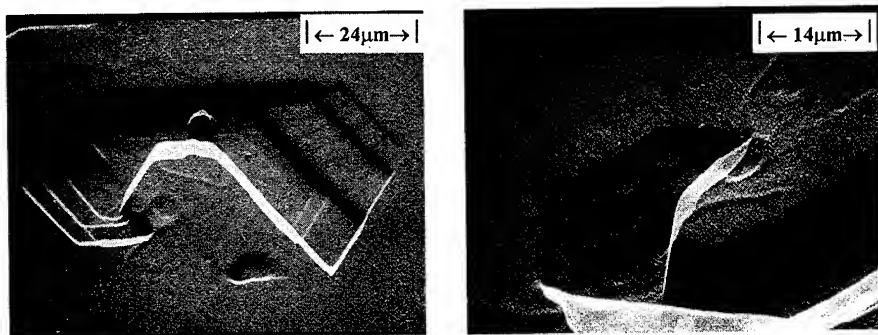


Figure 12. Two views of internal voids in mica. (a) Vertical black lines in scale bar are 28.5 nm high. (b) Vertical black lines in scale bar are 11.0 nm high.

FUTURE PLANS

As the photon tunneling microscope is at present limited (happily) by hardware, we look forward to incorporating the latest technology in detectors in order to extend the vertical range, vertical and lateral resolution to their limits, whatever they may be. New application exploration, extension into the ultra-violet and infra-red regions of the spectrum, and combining PTM with spectroscopic, surface plasmon, and other techniques, are ongoing or near term goals. Designing transducer surfaces and other sample-plane devices to handle the vast variety of samples remains an ever-present challenge.

ACKNOWLEDGMENTS

The author wishes to thank Dr. W. T. Plummer and colleagues at Polaroid Corp. for many helpful discussions and for supporting this work.

REFERENCES

1. J. M. Guerra, *App. Opt.*, **29**, 3741 (1990).
2. G. Binning and H. Rohrer, *Surf. Sci. (Netherlands)* **126**, No 1-3 (1983).
3. D. W. Pohl, U. Ch. Fischer, and U. T. Dürig, *SPIE* **897**, 84 (1988).
4. E. Betzig and J.K. Troutman, *Science*, **257**, 189 (1992) and references therein.
5. A. Harootunian, E. Betzig, M. Isaacson, and A. Lewis, *Appl. Phys. Lett.* **49** (11), 674 (1986).
6. R. C. Reddick, R. J. Warmack and T. L. Ferrell, *Phys. Rev.*, **B39**, 767 (1989).
7. J. M. Guerra and W. T. Plummer, U. S. Patent 4,681,451 (July, 1987).
8. J. M. Guerra, *Proc. of SPIE*, **1009**, 254 (1988).
9. E. J. Ambrose, *Nature*, **178**, 1194 (1956).
10. C. W. McCutchen, *Rev. Sci. Inst.*, **35**, 1340 (1964).
11. P. A. Temple, *Applied Optics*, Vol. **20**, No. 15, Aug, (1981).
12. D. Axelrod, in *Fluorescence Microscopy of Living Cells in Culture, Part B*, edited by D. L. Taylor and Y-L. Wang, (Academic Press, New York, 1989), Chap. 9.
13. W. Knoll, *MRS Bulletin*, **16**, 29 (1991).
14. Newton, Sir I., *Opticks*, (Dover, New York, 1979) Pt. 1, pp. 193-224.
15. N. J. Harrick, *Internal Reflection Spectroscopy*, (Harrick Scientific Corporation, Ossining, New York, 1979), pp. 1-65.
16. S. G. Lipson and H. Lipson, *Optical Physics*, 2nd ed., (Cambridge University Press, Cambridge, 1981), pp. 384-386.
17. J. Strong, *Concepts of Classical Optics*, (Freeman, San Francisco, 1958), pp. 124-126, 516-518.
18. D. D. Coon, *Am. J. Phys.*, **34**, 240 (1966).
19. D. Bohm, *Quantum Theory*, (Prentice-Hall, New Jersey, 1951) p. 240.
20. J. M. Vigoureux, C. Girard and D. Courjon, *Opt. Lett.*, **14**, 1039 (1989).
21. J. M. Vigoureux, F. Depasse, and C. Girard, *App. Opt.*, **31**, 3036 (1992).
22. S. Zhu, A. W. Yu, D. Hawley and R. Roy, *Am. J. Phys.*, **54**, 601 (1986).
23. S. G. Lipson, and H. Lipson, *Optical Physics*, (Cambridge University Press, London, 1969), pp. 79-109, 282-285.
24. C. Ma and R. W. Smith, *SPIE*, **1028**, Scanning Imaging, 45 (1988).
25. K. Matsumoto, and T. Tsuruta, *Opt. Eng.* **31**, 2657 (1992).
26. N. F. van Hulst, N. P. de Boer, and B. Bölger, *J. Microscopy* **163**, 117 (1991).
27. J. M. Guerra, unpublished research.
28. Dyer Energy Systems, Inc., Tyngsboro, MA.
29. J. M. Guerra, M. Srinivasarao, and R. S. Stein, *Science*, **262**, 1395 (1993).

THE FIELD EMISSION GUN SCANNING ELECTRON MICROSCOPE- HIGH RESOLUTION AT LOW BEAM ENERGIES

DAVID C JOY

EM Facility, University of Tennessee, Knoxville, TN 37996-0810
and Metals and Ceramics Division, Oak Ridge National Laboratory, Oak Ridge, TN 37831

ABSTRACT

The scanning electron microscope (SEM) is the most widely used, as well as the most versatile, of electron-optical instruments. In all of the imaging modes of the instrument it is now possible to achieve a spatial resolution on the nanometer scale from a bulk specimen, provided that the electron-optical performance of the instrument is of the necessary quality. In practice this means that a field emission gun (FEG) as well as a highly excited probe forming lens must be used. With state-of-the-art instrumentation, image resolutions as good as 4 - 5 nm at 1keV, and 1nm at 20keV, are now achievable. This paper outlines the design criteria for a high resolution FEG SEM and discusses the type of image information available. The performance achieved is compared to that of other types of microscope that offer similar capabilities.

INTRODUCTION

The scanning electron microscope is the most widely used, and the most versatile, of all electron beam instruments. The concept of a scanning electron microscope was first discussed in the 1930s ¹ at about the same time as the transmission electron microscope (TEM) was being developed. Although pioneering work by von Ardenne in Germany ², and by a group at RCA in the United States led by Zworykin³, succeeded in producing instruments that could image solid specimens with a resolution comparable to that of an optical microscope, the rapid improvements in TEMs overshadowed these achievements and further work on SEMs was abandoned. In 1948 Oatley and his group at Cambridge returned to this topic and within a few years constructed an instrument with a spatial resolution of 50 nm ⁴. The development of efficient detectors for secondary electrons ⁵, improved electron-optics and enhancements such as image processing ⁶, took the instrument resolution to better than 5nm and ultimately led to the first commercial scanning microscopes becoming available in 1965.

The factor that most strongly limited the performance of early SEMs was the brightness of the electron gun. High resolution imaging requires a small probe of electrons, but the current

in the electron beam falls rapidly as the probe diameter decreases so that for the smallest probes the current striking the specimen becomes too low to produce images of an acceptable quality. This problem was solved in 1969 when Crewe⁷ and his group at the University of Chicago developed a practical field emission gun (FEG) for the SEM. This device represented a factor of a thousand times improvement over existing electron sources and permitted currents large enough to give good images to be put into probes only a nanometer or less in size. Although application of this technology was at first hampered by the stringent requirements on the levels of vacuum that had to be obtained at the FEG, commercial field emission gun SEMs are now available from several manufacturers⁸. Even when the highest resolution is not required the advantages offered by the FEG SEM, such as low noise imaging at TV scan rates, high quality imaging of insulating specimens at low beam energies, superior microanalytical capabilities, and excellent reliability and productivity, have increasingly made it the instrument of choice.

THE HIGH RESOLUTION FEG SEM

The electron-optics of an SEM are simple. Electrons from a source of size s_0 are demagnified by some factor M , through one or more lenses to form a probe at the surface of the specimen of size $d_0 = M.s_0$. A variety of aberrations in the probe forming lens⁹ increase the probe size to an effective value d where

$$d^2 = d_0^2 + \left(\frac{1}{2}C_s\alpha^3\right)^2 + \left(\frac{\lambda}{\alpha}\right)^2 + \left(C_c\alpha\frac{\Delta E}{E}\right)^2 \quad (1)$$

C_s and C_c are the spherical and chromatic aberration coefficients of the lens respectively, α is the semi-convergence angle of the lens, λ is the electron wavelength = $1.226/\sqrt{E}$ nm where E is the energy of the electron beam in eV, and ΔE is the energy spread of the beam. If the chromatic aberration term can be ignored as is often the case at medium energies¹⁰ then the relationship between the current I_B in the probe striking the specimen and the probe diameter d is

$$I_B = 1.88 \beta \frac{d^{8/3}}{C_s^{2/3}} \quad (2)$$

where β is the brightness of the electron source (amps/cm²/sterad). Since a minimum 'threshold' current is required for the production of an image of acceptable quality⁹ equation (2)

shows that successful high resolution scanning microscopy requires two things, a high brightness electron source (large β), and a lens of low spherical aberration (small C_s). These two components in conjunction make it possible to put the largest amount of current into the smallest

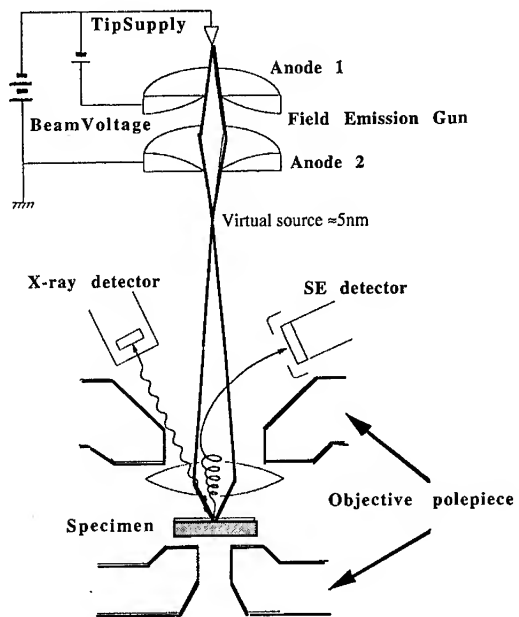


Figure 1. Schematic ray diagram and illustration of a field emission gun scanning electron microscope. The source of electrons at the gun is demagnified to give a final spot diameter at the specimen of the order of 1nm.

spot on the specimen. For a current commercial instruments the brightness of the field emission gun β at 20keV is of the order of 5.10^6 to 2.10^7 amps/cm 2 str, and C_s is 2mm or less, allowing currents of the order of 0.1nA or more to be put into probes 1nm in diameter.

Figure (1) shows schematically how an SEM which implements this arrangement is constructed. The FEG, most often using the gun design due to Crewe⁷, is housed in an ultra-high vacuum chamber pumped separately from the rest of the microscope column. Outside the gun the electron beam is focussed to give a cross-over with a diameter of about 5nm. This virtual source of electrons is then demagnified by the objective lens to produce the final probe. Since the magnitude of the spherical aberration coefficient scales with the physical size of the lens magnetic field, this field is confined within a region only a few millimeters in size by a magnetic pole piece. The sample, held on a rod inserted into the pole piece, is immersed in this field. This arrangement not only minimizes the aberration of the lens, but also effectively shields the specimen from external magnetic disturbances and, because the sample is physically clamped to the pole piece, it eliminates the effects of mechanical vibrations. The drawbacks of this arrange-

ment are that the specimen can only be a few millimeters in size and that the sample translation and tilt are limited in extent. Secondary electrons from the specimen are detected¹¹ by allowing them to spiral out of the lens in the magnetic field and then collecting them with a detector biased to about +10kV. Backscattered electron detectors¹² and energy dispersive X-ray detectors can also be positioned around the specimen to permit other modes of operation. A detector for transmitted electrons may be provided to permit scanning transmission electron microscopy (STEM) to be performed.

RESULTS

Figure (2) summarizes the calculated performance of an instrument of this type, using a numerical ray tracing method¹⁰ to compute the size and shape of the final probe, and assuming the lens parameters of the Hitachi S-5000 ultra-high resolution FEG SEM (focal length of 2.3mm, a spherical aberration coefficient of 1.9mm, and a chromatic aberration coefficient of 2.5mm). Over the energy range from 30keV to 1keV the probe diameter varies from about 0.6nm to about 3nm, with most of this variation occurring at the lowest energies where the effects of chromatic aberration begin to become significant. In practice this level of perfor-

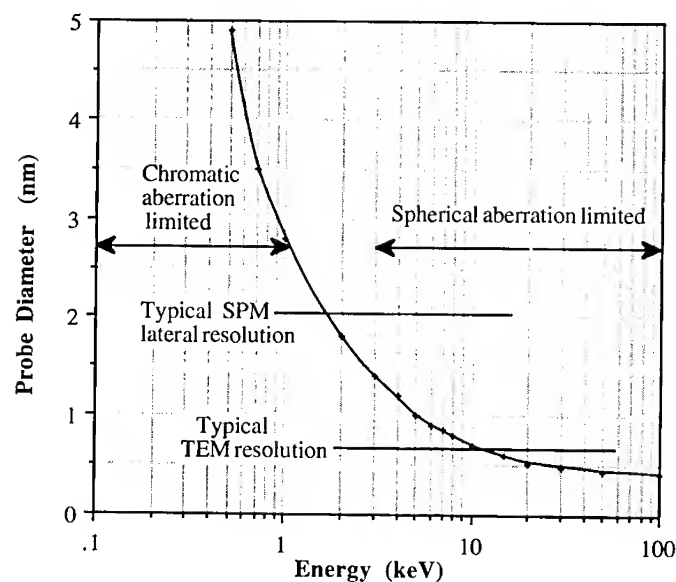


Figure 2. Calculated probe size as a function of beam energy for a high performance SEM with a field emission gun and an objective lens with C_s of 1.9mm and C_c of 2.5mm. For reference the typical resolution limits of a TEM and a scanned probe microscope are shown.

mance means that the usable resolution is almost independent of the accelerating voltage, and hence the beam energy can be chosen at will so as to define a beam interaction volume, or maximize a contrast effect of interest, rather than having to be fixed so as to guarantee a desired probe size as is invariably the case on less advanced machines.

Figure (3) illustrates a typical practical application of such a machine to the characterization of nanoscale materials. The sample is a magnetic oxide coating for an experimental computer hard disc device. This type of specimen demonstrates the particular advantages of the SEM approach to the imaging of micro- and nano-structure. For observation in the SEM a portion of the disk, which had actually been used in a test rig, was simply cut out with a saw, degreased with freon vapor, and placed in the microscope, a procedure which took in total only a few minutes. By comparison preparation of this material for the TEM would require either cross-sectioning and thinning, or embedding in epoxy resin and then sectioning, procedures which would take a couple of days of skilled activity. Similarly, the scanning tunneling microscope (STM) would have a problem with the poor conductivity of the sample, and both the atomic force microscope and the STM would find the extremely rough and irregular nature of the topography awkward to deal with. The FEG SEM shows the particles to be in the size range from a few tens of nanometers up to about $0.2\mu\text{m}$, and the secondary electron topograph-



Figure 3. High resolution secondary electron image of uncoated magnetic oxide particles. Image recorded at 10keV beam energy on Hitachi S-900 FEG SEM.

ic contrast image proves that the particles are mostly smoothly rounded, although small surface steps and roughness are visible. In such a specimen it is an advantage of the SEM that both low and high magnification images can be gathered with equal facility. This makes it possible to place the high resolution detail within the context of the larger scale microstructure and features of the specimen such as scratches and pits caused by mechanical wear during testing.



Figure 4. High resolution detail from figure (3) showing resolution of nanometer scale surface topography. Image recorded at 10keV on Hitachi S-900 FEG SEM.

At still higher magnifications, as in figure (4), surface detail is visible down to the nanometer scale on the surface of the particles. While, in general, the spatial resolution of the secondary electron image will generally be somewhat worse than the physical diameter of the probe, which here is about 1.0nm, because of the influence of the various beam interactions producing the contrast¹³, micrographs such as these confirm that nanometer scale detail is routinely observable on a wide range of specimens. Even under high resolution conditions the information content of the micrograph remains readily interpretable, even by unskilled observers.

If the FEG SEM is operated at lower beam energies then high resolution images may be obtained from fragile, beam sensitive, materials such as the surface of a cell infected with

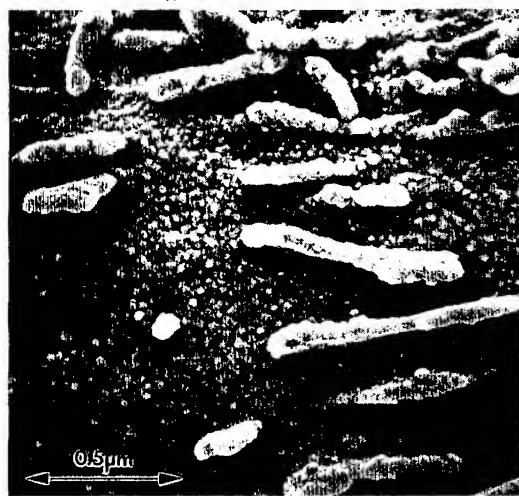


Figure 5. High resolution image of a cell surface infected with leukemia. The micrograph was recorded at 1keV on a Hitachi S-900 FEG SEM.

leukemia shown in figure (5). By optimizing the choice of operating voltage, and minimizing the intensity of the incident electron dose, such samples can usually be observed without the need to coat them with metal (to eliminate charging), or chemical fix them (to preserve the structure). In this particular image, integrated over a period of ten seconds at 2keV, the surface topography of the macromolecular protein structures bound to the cell surface is clearly displayed together with the larger scale viral structures. Under the conditions used for this micrograph the spatial resolution of the image is about 10nm. This figure is worse than that of the previous images because the microscope is operating at a lower energy and hence the probe is larger, and because the volume of the sample from which the secondary electrons are being generated and collected is larger in a low density, low atomic number, material such as dried biological tissue than in a compacted, inorganic, material,

In the backscattered (BSE) mode of observation direct imaging of individual crystallographic defects is possible ^{14,15}, as shown in figure (6). In this micrograph the sample of

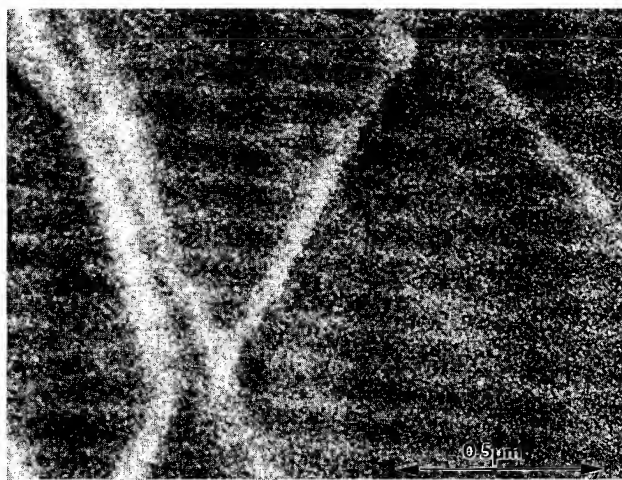


Figure 6. Images of individual crystallographic defects in bulk molybdenite, recorded in backscattered image mode at 20keV. Hitachi S-900 FEG SEM.

molybdenite has been oriented so as to place its c-axis parallel to the electron optical axis of the SEM. In this conditions electrons channel into the crystal and are only weakly backscattered. In the vicinity of a dislocation, however, the lattice strain and distortion de-channel the electrons producing contrast in the BSE image. The low level of contrast available from the channeling contrast, and the small probe size required to observe the dislocation, place severe demands on the performance of the instrument and only a field emission microscope is able to produce such images. The ability to combine high resolution surface topographic imaging with direct observations of defect structures in the same bulk sample again illustrates the power and convenience of the SEM approach in the study of materials.

DISCUSSION

Scanning microscopy is only one of the many imaging and microanalytical tools now available to the materials scientist for nanostructural characterization. Any survey of the SEM must therefore consider how the SEM compares to other potential techniques such as scanned probe microscopies (STM and AFM), transmission electron microscopy, and confocal and near field optical microscopy.

Sample Preparation

Samples for examination in an SEM require less preparative work than those for any other technique except light microscopy. Apart from a general requirement that the surface be free of significant contamination, any material that can be placed into the vacuum chamber of the machine can be imaged without further effort. Compared to the elaborate procedures needed to prepare samples for the TEM this represents a major saving of time while, at the same time, making much larger areas of the specimen available for examination. While both the STM and AFM can also look at bulk specimens, often without the need for a vacuum, these techniques are sensitive to surface conditions to a higher degree than the SEM, and irregular, or macroscopically rough, specimens (such as a fracture surface) are difficult to handle.

Types of information available

The SEM offers more varieties of information about a sample than any other technique. For example the microscopist can observe surface topography; determine the chemical composition of small selected areas of the specimen; study the elemental distribution within the sample; determine the crystallographic nature, type, and orientation of selected regions¹⁶; observe individual crystallographic defects^{14,15}; measure and observe the electrical and electronic properties¹⁷ of both materials and complete devices; and even derive data on the mechanical and thermal moduli of the sample¹⁸. These various signals and operational modes are available individually, or in combination, separately or simultaneously, and all from the same general volume of the specimen. The versatility and flexibility of the SEM is a major asset of the technique as compared to most other microscopies which offer only one or two modes of observation.

Lateral and Depth Resolution

As discussed above, the lateral resolution of a state-of-the-art FEG SEM is in the region of a few nanometers on metals, semiconductors, ceramics, composites and other inorganic samples. In practice this means that almost any microstructural detail that might be visible in a TEM image is resolvable in the corresponding SEM image. The lateral resolution of the SEM is also comparable to, and usually substantially better than, that of either the AFM or the STM. This is often misunderstood because of the ability of scanned probe instruments to produce atomic resolution images on a few, carefully selected, materials. On real, rough, surfaces the scanned probe resolution is limited by the profile of the tip to a few nm and on very complex surfaces may be tens of nanometers¹⁸. On the other hand, the sensitivity of the SEM to detail in the vertical direction is poor, and if surface steps and structures are the main area of interest then either the AFM/STM, or one of the optical microscopies, are more appropriate tools.

The information in the SEM image comes from a maximum depth which varies with the mode of observation but is typically some fraction of the incident electron range, and thus varies from micrometers at 30keV to tens of nanometers at a few keV. SEM micrographs are therefore images of the bulk of the material, although with increasing significant amounts of information from the surface at low energies. The SEM thus conveniently fills the gap between true surface techniques, such as Auger or ESCA and the AFM/STM methods, and true macroscopic bulk techniques such as X-ray topography or ultrasound imaging.

Ease of use

Of all of the major instruments commonly encountered the SEM is probably the easiest to use at a professional, but non-specialist, level of competence. This is due to the high degree of automation and optimization which has been built into current microscopes and to the widespread availability of these machines in laboratories. Even though operation of a state-of-the-art instrument at the limit of its capabilities remains a demanding and highly skilled task it is still true to say that the data produced from such a machine is more readily understood and interpreted than that from other technologies because the nature of the secondary electron image lends itself to convenient optical analogies⁹.

CONCLUSIONS

The SEM, and in particular the field emission SEM, is a powerful and versatile tool for the observation and characterization of materials on a nanoscale. In its current form the instru-

ment has a level of performance comparable with that available from any other type of microscopy while at the same time enjoying major advantages of convenience, ease of operation, ease of specimen preparation, and simplicity of image interpretation. Future developments promise still better performance and flexibility. The advent of 'nanotip' field emission sources²⁰, with a brightness another factor of a thousand times higher than current FEGs, may allow resolutions to be improved to levels approaching those required for direct lattice imaging; and the development of techniques for efficient operation at incident energies as low as a few eV²¹ should allow the observation of even the most fragile specimens without beam induced damage. Finally, the increasing use of digital image acquisition, processing, and enhancement, techniques will further improve the utility and productivity of the SEM.

ACKNOWLEDGEMENTS

Research partially supported by the U.S Department of Energy under contract DE-AC05-84OR21400 with Martin Marietta Energy Systems Inc.

REFERENCES

1. M. Knoll, *Z. Tech. Phys.*, **11**, 467, (1935)
2. M. von Ardenne, *Z.Tech. Phys.*, **109**, 553, (1938)
3. V.K.Zworykin, J.Hiller, and R.L.Snyder, *A.S.T.M. Bull.*, **117**, 15, (1942)
4. D. McMullan, Ph.D. Thesis, University of Cambridge, 1952
5. T.E.Everhart, and R.M.Thornley, *J.Sci.Instr.*, **37**, 246, (1960)
6. R.F.W.Pease, and W.C.Nixon, *J.Microsc.* **112**, 169, (1965)
7. A.V.Crewe, M.Isaacson, and D.E.Johnson, *Rev.Sci.Instr.*, **40**, 241, (1969)
8. T. Nagatani, S. Saito, M.Sato, and M. Yamada, *Scanning Microscopy*, **1**, 901, (1987)
9. J.I.Goldstein, D.E.Newbury, P.Echlin, D.C.Joy, A.D.Romig Jr., C.E.Lyman, C.E.Fiori, and E.Lifshin, Scanning Electron Microscopy and X-ray Microanalysis, 2nd ed. (Plenum:New York, 1992), p.59
10. Y.Jia, and D.C.Joy, *Acta Microscopica* **1**, 20, (1992)
11. H. Kimura, and H. Tamura, *Proc. 9th. Ann. I.E.E.E. Symp. on Electron, Ion, and Laser Beams*, **198**, (1967)
12. R. Autrata, and J.Henja, *Scanning*, **13**, 275, (1991)
13. D.C.Joy, *Ultramicroscopy*, **37**, 216, (1991)
14. J.T.Czernuszka, N.J.Long, E.D.Boyes, and P.B.Hirsch, *Phil.Mag.Letts.*, **62**, 227, (1990)

15. D.C.Joy, in High Resolution Electron Microscopy of Defects in Materials, edited by R Sinclair, D J Smith and U Dahmen, (Mater.Res.Soc.Proc. **183**, Pittsburgh,PA, 1990), pp.199-210
16. D.C.Joy, D.E.Newbury, and R.L.Davidson, *J. Appl. Phys.*, **53**, R81, (1982)
17. D.B.Holt, and D.C.Joy, SEM Microcharacterization of Semiconductors, (Academic Press, London, 1989), p132
18. A.Rosencwaig, in Microbeam Analysis-1983, edited by R.Gooley, (San Francisco Press, San Francisco, 1983), pp 137-141
19. T.Hashizume, I.Kamiya, Y.Hasegawa, N.Sano, T.Sakurai, and H.W.Pickering, *J.Microscopy*, **152**, 347, (1988)
20. M.R.Scheinfein, W.Qian, J.C.H.Spence, *J.appl.Phys.*, **73**, 2057, (1993)
21. I.Müllerova, and L.Frank, *Scanning*, **15**, 193, (1993)

STRUCTURAL AND MAGNETIC PROPERTIES OF EPITAXIALLY GROWN FCC Fe/Cu(100) and Fe/CaF₂/Si(111)

M.R. Scheinfein, S.D. Healy, K.R. Heim, Z.J. Yang, J.S. Drucker*, G.G. Hembree,
Department of Physics and Astronomy, *Center for Solid State Science, Arizona State University,
Tempe, AZ 85287-1504

ABSTRACT

We have used nanometer spatial resolution secondary electron and Auger electron imaging in an ultra-high vacuum scanning transmission electron microscope to characterize microstructure in ultrathin films of Fe/Cu(100) grown at room temperature and Fe/CaF₂/Si(111) grown at room temperature and 150 C. Thin film microstructure was correlated in situ with magnetic properties by using the surface magneto-optic Kerr effect.

INTRODUCTION

Ferromagnetic ultrathin epitaxial films grown on single crystal metal substrates display unusual properties characteristic of two-dimensional ferromagnetism stabilized by magnetic (surface) anisotropy [1]. The exchange coupling and crystalline anisotropy depend very sensitively on the lattice. Ultrathin films, grown epitaxially on templates which distort the bulk lattice are often highly strained enabling metastable film properties to be explored at room temperature. The most studied, and perhaps the most complex metal/metal epitaxial system is fcc Fe/Cu(100). The fcc phase of Fe, stable in bulk above 911° C [2], can be grown epitaxially on Cu(100) with 0.83% lattice mismatch. For fcc (fct) Fe, a non-magnetic, high and low spin, or an antiferromagnetic phase can be stable depending upon the lattice constant [3]. The magnetic properties of fcc Fe/Cu(100) have been investigated using the surface magneto-optical Kerr effect (SMOKE) [4,5], spin-polarized photoemission [6], spin-polarized secondary electron spectroscopy [7,8], conversion-Mössbauer spectroscopy [9], inverse photoemission [10] and spin-polarized scanning electron microscopy (SEMPA) [11]. The energy balance between surface anisotropy and shape anisotropy, both strong functions of film thickness, growth and measurement temperature [4,11-13], determine the easy axis of magnetization. Interest in this system is stimulated by rich structural properties present during various phases of film growth [12-18], including bilayer growth during initial phases of epitaxy [15-18], strain-relief at intermediate thicknesses, weak surface reconstructions [12], and fcc to bcc transitions [e.g. 13]. Extensive work has been devoted to correlating film microstructure with magnetic properties [12,13,19] with emphasis on the non-magnetic-to-magnetic transition at 1-2 ML (ML denotes a monolayer, 0.18 nm for fcc Fe(100) coverages and the polar-to-longitudinal transition in the easy axis of magnetization at 4-8 ML.

EXPERIMENTAL RESULTS

Our magnetic thin film growth and characterization facility is schematically depicted in Fig. 1. The foundation of this system, shown on the far left-hand side of Fig. 1, is a modified Vacuum Generators HB501-S, field-emission scanning transmission electron microscope (STEM) [24,25]. A magnetic parallelizer (P) [26] guarantees nearly 100% collection efficiency at SE energies, and nearly 50% collection efficiencies at intermediate Auger energies (300 eV to 500 eV) [27]. This high collection efficiency and the ability to form subnanometer 100 keV focused electron probes allows for the acquisition of nanometer transverse spatial resolution secondary and Auger electron images [20-23]. A secondary electron detector (SE) located below the sample facilitates in the study of bulk specimens (S). This electron microscope and the attached preparation chamber enables growth and characterization under UHV conditions using high resolution imaging and standard surface science techniques. A 24 hour, 170°C bakeout of the entire microscope and preparation chamber produces base pressures below 5×10^{-11} mbar. The specimen preparation chamber is equipped with a sample heater (H), a Surface Magneto-Optic Kerr Effect (SMOKE)

analysis chamber, a Perkin Elmer model 10-155 cylindrical mirror analyzer (CMA) broad-beam Auger analysis system, a scanning ion sputtering gun (Ar^+), a residual gas analyzer (RGA), various Knudsen cell evaporation sources (K1, K2, and K3), and an electron-bombardment Fe evaporator. The combination of *in situ* SMOKE measurements with nanometer-resolution microstructural characterization techniques makes this observation system ideal for correlating thin film surface microstructure (those structures with features larger than 1 nm) with macroscopic magnetic properties.

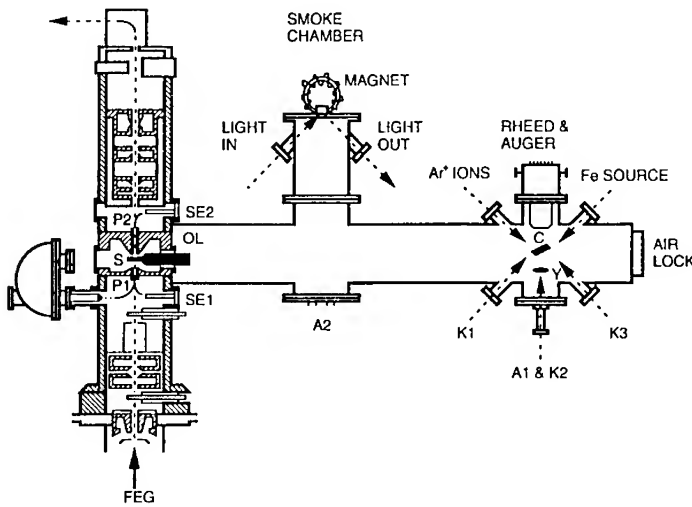


Fig. 1: Modified VG HB501-S thin film growth and characterization facility. The microscope column contains; P2, P1-upper and lower parallelizers, respectively, SE2, SE1-upper and lower secondary electron detectors, respectively, S-sample, OL-objective lens, and a FEG-field emission gun. The specimen preparation chamber consists of a SMOKE chamber for surface magnetism analysis, a CMA-cylindrical mirror analyzer for AES and RHEED, and sample surface preparation tools such as an Ar^+ ion sputtering gun, an Fe evaporator, annealing stages A1 and A2, and Knudsen cell evaporators K1, K2, and K3. Also shown are the Cu crystal, C, the YAG crystal, Y, and the air lock for fast sample entry.

Single crystal Cu(100) substrates were machined into 1 mm thick, 3 mm diameter shouldered disks and commercially electropolished [28]. After attaining pressures below 5×10^{-11} mbar the Cu specimens were sputtered with 600 eV Ar^+ ions at 45° from the surface normal. Typical ion currents were between 200 and 250 nA (current densities of $\sim 10 \text{ mA/cm}^2$) with an operational pressure of 6×10^{-7} mbar. Specifically, the Cu crystals were first sputtered at room temperature for 1 hour. Next, the Cu was heated to $\sim 330^\circ\text{C}$ and hot-sputtered for 4 hours. Following this, the Cu was annealed at $\sim 600^\circ\text{C}$ for 15 minutes to produce a well-ordered surface, as observed with RHEED. Recleaning samples with less than 10 ML (1 ML = 1.805 \AA) of Fe on them required a $\sim 330^\circ\text{C}$ sputter period of 1 hour. Any cleaned surface exposed to ambient vacuum conditions for more than several hours or exposed to an electron beam (Auger spectroscopy, RHEED, or electron microscopy) was, prior to Fe deposition, cycled through a $\sim 330^\circ\text{C}$, 15 minute sputter and a $\sim 600^\circ\text{C}$, 15 minute anneal. The crystal was allowed to cool for 1.5-2.0 hours after the last anneal such that a temperature below 40°C was obtained prior to Fe deposition.

Following the surface preparation and Fe deposition, surface structural characterization was performed using secondary electron (SE) microscopy. SE microscopy contrast is sensitive to topography [23,29] and local changes in the work function [30]. Several of the cleaned Cu surfaces observed with SE microscopy revealed small contaminant clusters which we believe to be Cu₂O (based upon the most likely copper oxide formed at these temperatures and pressures [31]) islands nucleated over the entire Cu surface. Analysis of these SE images indicates that oxygen coverages ≤ 0.0011 at.% are well below the sensitivity of the broad-beam AES (typically sensitive to no better than 1 at.%) used in the preparation chamber. In Figs. 2a-f we display corresponding broad-beam Auger spectra and SE images for two identically prepared Cu surfaces. Figs. 2a and 2b are the respective EN(E) and dN(E)/dE spectra acquired for a clean Cu(100) surface. These spectra clearly exhibit five Cu Auger peaks (58, 105, 776, 840, and 920 eV in the derivative mode) while not detecting the O (503 eV) peak (the sensitivity factors at 3 keV indicate that O is about two times more detectable than the 920 eV Cu signal, from which we conclude that the oxygen coverage is ≤ 2 at.%). The SE image shown in Fig. 2e represents a typical area of the clean Cu(100) crystal surface with less than 1.4×10^9 oxide particles/cm², thus yielding an oxygen coverage of 0.016 at.%. The typical terrace width on these Cu(100) surfaces vary from 25 nm to 75 nm, which, based on the uniform growth, is greater than the Fe atom diffusion length for this system. Thus, the effects of a rough and disordered surface on the magnetic properties have been reduced below a detectable level. Insulators and oxides, in general, have higher secondary electron yields than metals [32], and hence appear bright in SE micrographs. In contrast, the Auger spectra in Figs. 2c and 2d also imply a clean Cu surface, but the SE image of Fig. 2f shows larger, more numerous (3.6×10^{10} particles/cm² of 10 nm average radius and 3.75 at.%) oxide particles populating the entire Cu surface. In situ electron microscopy, with its high sensitivity for the detection of surface contamination, was used to guarantee the real space chemical and structural integrity of all Cu(100) substrates prior to Fe deposition. In particular, our cleanest Cu(100) surfaces had 1×10^9 particles/cm² of 3 nm average radius oxide clusters, implying an oxygen coverage of order ≤ 0.01 at.%, well below the detectivity of standard surface science techniques.

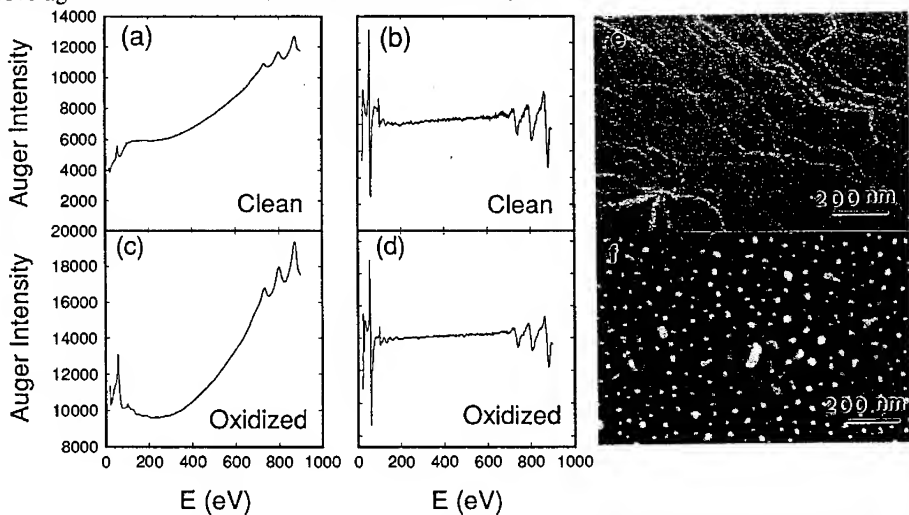
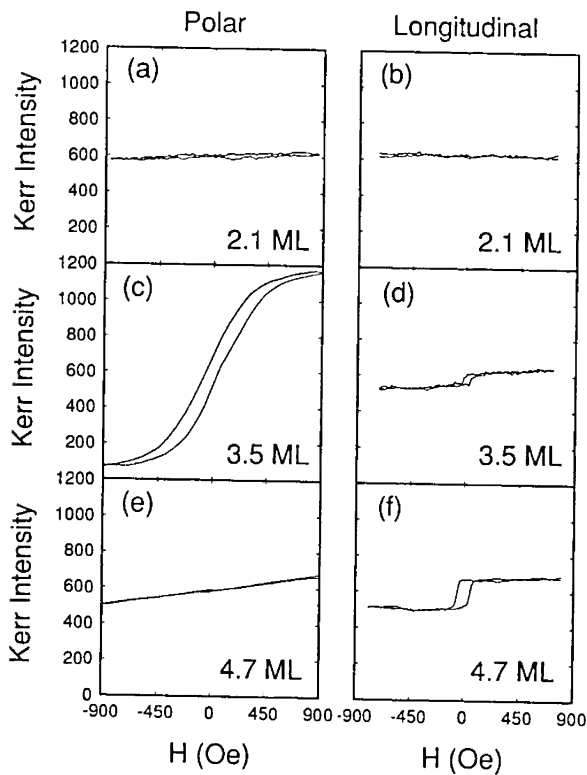


Fig. 2: Auger electron spectroscopy (AES) scans of clean copper in the (a) EN(E) and (b) dN(E)/dE mode with its corresponding (e) secondary electron (SE) image. The white curves are step bands separating terraces. The average terrace width lies within 25 nm and 75 nm. AES scans of oxidized copper in (c) EN(E) and (d) dN(E)/dE mode indicate no contamination while the (f) SE image reveals many oxide.

The thickness dependence of SMOKE hysteresis loops of as-grown fcc Fe/Cu(100) films are shown in Fig. 3. Fe film thicknesses below 2 ML displayed no magnetic response (not shown). Initial magnetic response is observed as a zero-remanence, linear hysteresis loop in the polar direction, with no magnetization in-plane, Figs. 3(a) and 3(b). At intermediate thicknesses, 3.5 ML, remanent polar, Fig. 3(c), and longitudinal, Fig. 3(d), SMOKE loops are observed. While the in-plane loop is square, the tilted polar loop displays the effects of shape anisotropy indicating a canted easy-axis. SMOKE loops from thicker films, 4.7 ML, shown in Figs. 3(e) and 3(f), lose polar remanence, but have square in-plane loops characteristic of an in-plane easy-axis. As-grown in-plane remanence and saturation magnetization both increase nearly linearly with thickness below 5 ML indicating that most of the film (above 2 ML) is magnetically active. Film thicknesses exceeding this range ($t > 10$ ML) become non-magnetic, in accordance with prior observations [13]. Films thinner than 10 ML had fcc structure with the transverse lattice constant of the substrate (our RHEED measurements permit an evaluation of the in-plane lattice constant to within $\pm 2\%$).



At low film coverages, supersurface island formation can be observed locally by correlating the SE images with the Cu and Fe AE images. One such set of spatially correlated images is displayed in Figure 4 for a 0.33 ML thick Fe film. SE images are sensitive to both the work function and topography of the surface. The SE image in figure 4a illustrates supersurface Fe islands with the corresponding contour plot shown in figure 4b. The large island (~ 45 nm in diameter) has intensity contours near its upper left quadrant indicating that this island is composed of more than one monolayer of Fe within the bulk of the island. The contrast of the smaller islands is identical to the contrast of the tip of the larger island (within the signal-to-noise limits of these measurements) indicating identical Fe island thicknesses. AE images and contour maps derived from the Cu (Figs. 4c and 4d) and Fe (Figs. 4e and 4f) Auger electron signals can be directly correlated with the SE

Fig. 3: Room temperature grown fcc Fe/Cu(100) polar and longitudinal surface magneto-optical Kerr effect (SMOKE) hysteresis loops. The incident angle is 45° for both longitudinal and polar SMOKE measurements. (a) polar - 2.1 ML, (b) longitudinal - 2.1 ML, (c) polar - 3.5 ML, (d) longitudinal - 3.5 ML, (e) polar - 4.7 ML and (f) longitudinal - 4.7 ML. All measurements made at room temperature.

image of the Fe islands. The AE images are produced by rastering the finely focused 100 keV incident electron beam across the sample surface and collecting most of the Fe (Cu) LMM peak Auger electrons using a spectrometer with a 1.5 eV window which is selected to pass electrons with the respective energy thus generating a two-dimensional surface map. A background map for each Auger map is subsequently acquired by selecting the pass band of the spectrometer to lie 20 eV higher than the Auger peak energy. The images shown in Figs. 4c and 4e result from subtracting the background map from the peak map, such that the intensity within each pixel of the image is proportional to the number of counts within a particular Auger peak, and, therefore, proportional to the number of atoms probed by the incident beam (the sensitivity factors for the Cu and Fe LMM peaks are almost identical). The black areas in Fig. 4c indicate the lack of a Cu signal, while the white areas in Fig. 4e indicate the presence of Fe. It is evident by correlating the contrast in the images and contour maps that the large island and several smaller islands are composed of Fe. Since the signal-to-noise ratio is much better in the SE image, the island density pictured in Fig. 4a likely characterizes the surface.

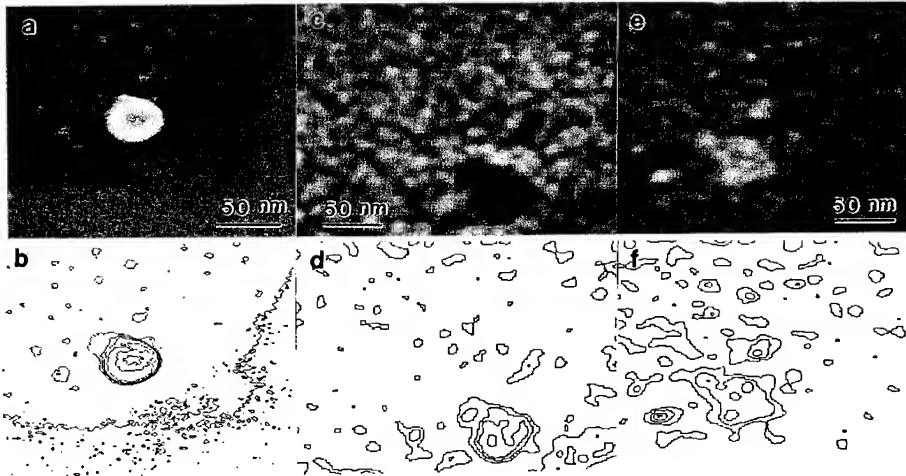


Fig. 4: After deposition of 0.33 ML of Fe at room temperature supersurface islands are observed: (a) secondary electron (SE) image, (b) contour map of SE image indicating island positions, (c) Cu LMM Auger electron (AE) image indicating Cu depletion (black) regions, (d) corresponding contour map of the Cu AE image, (e) Fe LMM AE image indicating Fe (white) islands, and (f) the corresponding contour map of the Fe AE image. The correlation of these three signals indicates that the islands have formed upon the Cu surface. These three images have identical scale factors.

Figure 5a-c displays SE, Cu AE and Fe AE images respectively, all in registry for a Cu substrate with 1.7 ML of Fe deposited at room temperature. The bright regions in the SE image are not correlated with any structure in the Cu (Fig. 5b) or Fe (Fig. 5c) AE images. However, these same Cu and Fe AE images with superimposed contour plots, shown in Figs. 5d and 5e respectively, indicate the regions depleted of Cu are rich in Fe. Since there is no contrast in the SE image, and the SE yield for fcc Fe and Cu are practically identical ($\delta_{\text{Fe}} = \delta_{\text{Cu}} = 0.38$ at 20 keV [33]), we conclude that there is no topographic structure on the surface in this region, indicating that the contrast observed in the AE images is a result of two-dimensional subsurface island formation. We have also observed both types of island growth as well as layer-by-layer growth in the same film at different positions along the film. This indicates that these phenomena are controlled by locally varying template surface conditions.

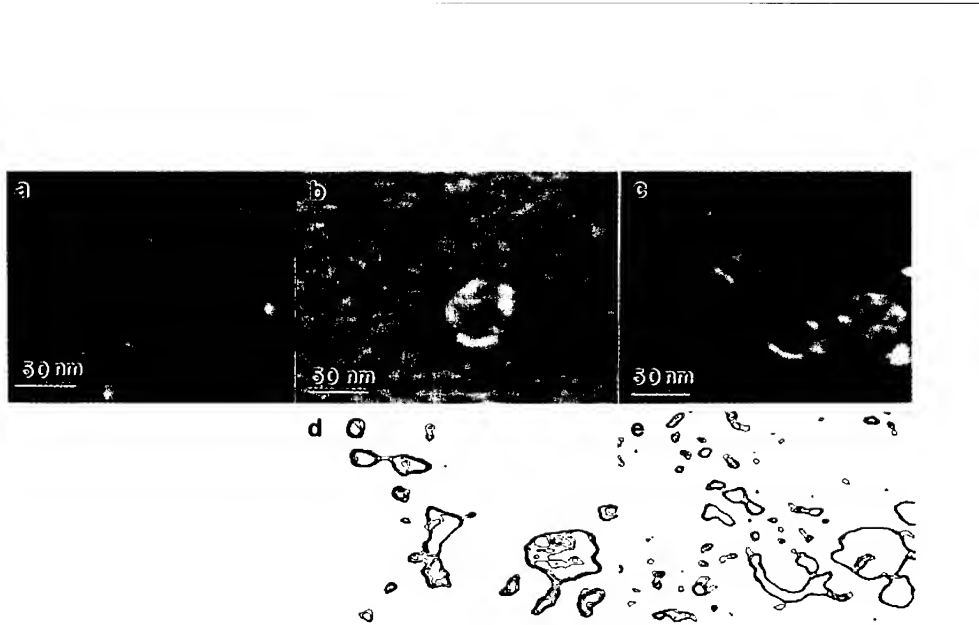


Fig. 5: After deposition of 1.7 ML of Fe at room temperature, subsurface islands are observed. (a) Secondary electron image, (b) Cu LMM Auger electron (AE) image indicating Cu depletion regions (black), and (c) Fe LMM AE image indicating Fe rich regions (white). The correlation of the structure in (b) and (c) and the lack of any contrast in (a) indicates that these islands are within the surface of the substrate. Contour plots for (b) and (c) are shown in (d) and (e) respectively, directly beneath the corresponding image. These three images have identical scale factors.

Our observations suggest that in the regions where subsurface islands occur, a vertical Fe-Cu atomic site exchange occurs. This process continues until the driving force causing the exchange diminishes. We observed this Fe coverage to be thicker than 2 ML, beyond which continuous Fe films grew. The lack of ferromagnetic ordering observed in this sub-2 ML regime is not inconsistent with the observed growth process. In order for the moment of an Fe island to be stable against thermal fluctuations, it must have a minimum size. Assuming a Boltzmann-type probability distribution, it is straight forward to show that most of the Fe islands, which are ~4 nm in diameter, are too small for the moments be unaffected by thermal energy..

We now turn our attention to the growth of Fe on CaF₂. Presently, the majority of solid state devices are fabricated using Si as the semiconducting material due to the existence of its native oxide, SiO₂. The lack of an atomically smooth SiO₂-Si interface does, however, impede the production of three dimensional Si-based devices. Rough interfaces not only decrease the mobility of carriers in devices, but can also destroy the three dimensional epitaxial ordering of subsequent depositions. CaF₂ has been noted as a suitable insulator which may be grown epitaxially and atomically smooth on Si(111) substrates. A small lattice mismatch (0.6% at 298 K) between CaF₂ and Si, a relatively large band gap (12.1 eV) for electronic isolation, and a larger dielectric constant (6.8) than SiO₂ (3.9) for an increased electric field at the insulator-semiconductor device interface are but a few of the many reasons for considering CaF₂ as an obvious replacement for the native SiO₂. In addition, CaF₂ layers may be used as a buffer region such that devices utilizing highly reactive metals such as Fe are not able to form compounds with the Si substrate. The deposition of Fe would enable the fabrication of fully integrated electronic and magnetic devices on a single substrate. Magnetic sensors, high speed microwave waveguides, and non-volatile memories are just three of the many applications which may result from constructing solid state devices using Fe, CaF₂, and Si.

For very slow growth rates the adsorbate topology is expected to approximate structures produced under equilibrium conditions. In this regime, the growth mode is controlled by surface energy imbalances. As Bauer has already set forth [34], a system in equilibrium can be characterized in terms of the surface energy of the adsorbate (γ_a), substrate (γ_s), and the interface between them (γ_i). When $\gamma_a + \gamma_i > \gamma_s$ the deposited material is not expected to spread evenly over the substrate's surface. Fe and CaF₂(111) are known to possess surface energies of 2475 erg/cm² [35] and 450-550 erg/cm² [36], hence, Fe island formation on CaF₂ is expected. We are interested in the formation of monodisperse transition metal island size distributions because ferromagnetic or paramagnetic granules embedded in a three-dimensional noble metal matrix have been shown to exhibit giant magnetoresistive behavior if the granules are properly spaced and smaller than some critical radius [37]. This leads to the natural extension whereby a two-dimensional array of isolated ferromagnetic particles, such as Fe islands on an insulating CaF₂ substrate, covered by a noble metal is expected to yield two-dimensional giant magnetoresistance (GMR) effects. In addition, since CaF₂ can be chemically altered by electron beam exposure [38], growth modes may be controlled for selected regions of the surface prior to metal deposition by modifying the surface composition with an electron beam. A further increase in electron irradiation and exposure to residual oxygen allows the CaF₂ to be used as an electron beam resist [38], thereby expediting the fabrication of nm-size and low dimensional magnetic devices.

SE microscopy (100 keV and ~10 pA incident beam current), performed before and after (radiatively) annealing the CaF₂/Si(111) substrates at 300 °C for 60 minutes, revealed that areas of obvious surface contamination were not reduced by heating. Broad-beam Auger electron spectroscopy (AES) displayed no statistically significant changes in the chemical composition of the CaF₂ surface after annealing for 60 minutes at temperatures up to 400 °C. Higher annealing temperatures do, however, produce significant changes in the surface morphology. These changes have been observed with SE microscopy. An unannealed CaF₂/Si(111) specimen is shown in Fig. 6a. The saw-toothed step edge visible in Fig. 6a is a typical surface feature of the many samples observed. Fig. 6b indicates that, after a 60 minute, 400 °C anneal, numerous, almost triangularly arranged pits are formed. These morphological changes may have resulted from the relief of stresses present during the growth of the CaF₂ [39]. In order to prevent severe surface modifications (pitting) during cleaning, the substrates were either annealed for 60 minutes at 300 °C or for 24 hours at 170 °C prior to the Fe deposition. Obvious contamination occupied small, localized regions of the total CaF₂ surface area (10-30%), such that Fe island size distributions could be determined from regions between the contaminated areas. Fe was deposited using an electron beam evaporator. The evaporation rate was confirmed by Rutherford backscattering, AES, and quartz-crystal microbalance techniques. The pressure during growth was typically less than 2×10^{-9} mbar with the substrates held at either room temperature or 140 °C.

The initial stage of Fe/CaF₂ growth proceeds by three dimensional islanding. Fig. 6c is an example of a 60 minute Fe deposition at a rate of 0.11 Å/min on a room temperature substrate. The relatively even distribution of 2.0 nm diameter Fe islands on a 100 Å thick CaF₂(111) surface is clearly displayed. Particle size analysis of the SE images revealed no statistical difference between the diameters and spatial distribution of Fe islands grown on 140 °C and room temperature CaF₂/Si(111) substrates. A post-growth anneal of 140 °C on room temperature grown films did not produce a noticeable change in the Fe island size distribution. Statistical analysis performed on a large variety of images yielded the following information for a 60 minute deposition of Fe (0.11 Å/min) on room temperature or 140 °C CaF₂/Si(111) substrates: (1) An average Fe island diameter of 2.0 ± 0.3 nm; (2) A range of Fe island diameters where 85% of the population will lie within 2.0 ± 1.0 nm; (3) An average Fe island separation of 2.0 ± 0.4 nm; (4) A 23% coverage of CaF₂(111) with Fe islands; (5) The number of Fe islands per unit area is 7.4×10^{12} islands/cm²; (6) The mean distance between Fe island centers is approximately 3.7 ± 0.6 nm; (7) No geometric ordering of the islands was observed based on fast Fourier transform image analysis.

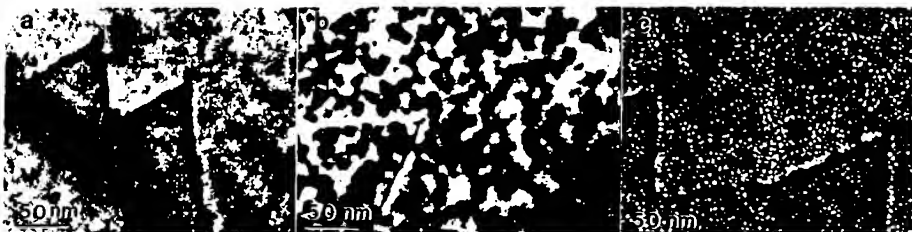


Fig. 6: (a) SE image of an unannealed $\text{CaF}_2/\text{Si}(111)$ surface. (b) SE image of $\text{CaF}_2/\text{Si}(111)$ surface that was annealed for 60 minutes at 400 $^{\circ}\text{C}$. Morphological changes are apparent by the many triangularly oriented pits now covering the entire surface. (c) A 60 minute deposition of Fe at a rate of 0.011 nm/min produces a monodisperse island size distribution.

A simple energy calculation indicates that a hemispherically shaped, unstressed, and magnetically ordered Fe particle must contain a single magnetic domain for diameters on the order of a few tens of nanometers. This transition is a result of domain formation becoming energetically unfavorable as the magnetic particle becomes smaller due to the domain boundary energy becoming a large percentage of the total energy. The islands observed in Fig. 6c are smaller than the critical single domain size and separated by less than the mean free path of conduction electrons in metals (near 30 nm at room temperature for Cu [40]). These properties make this system of nm-size Fe islands on an insulator, when covered by a noble metal, an excellent candidate for room temperature GMR studies [41].

CONCLUSIONS

In situ, magnetic and structural characterization of ultrathin films of Fe on Cu(100) was performed using SMOKE, RHEED, broad-beam AES, SE imaging, and AE imaging. Results indicate that room temperature grown films are non-magnetic below 2.1 ML, are ferromagnetic between 2.3 and 5 ML, and are no longer ferromagnetic greater than 5 ML but less than 10 ML. SE and AE images reveal localized alloying and simultaneous multilayered growth for films less than 2 ML and no gross structural changes for films of order 10 ML. AES reconfirms a simultaneous multilayered growth mode due to the lack of breaks in the normalized MVV Cu peak-to-peak height curve as a function of evaporation time. Broad-beam AES was determined to be inadequate for determining the oxide contamination of Cu crystal surfaces because of a lack of detection sensitivity, and may account for the variability in some growth/magnetic properties studies in the fcc Fe/Cu(100) system. Both supersurface islanding and subsurface islanding through vertical atomic site exchange in room temperature grown films of fcc Fe/Cu(100) in the 0-2 ML regime was observed. These observations are not inconsistent with the lack of ferromagnetism observed in room temperature grown sub-2 ML fcc Fe/Cu(100) ultrathin films. A narrow size distribution of 2.0 nm diameter Fe islands was grown on $\text{CaF}_2/\text{Si}(111)$ surfaces held at or near room temperature. This system, an arrangement of possibly single domain particles separated by less than the mean free path of conduction electrons in metals, is an exciting new candidate for GMR studies.

ACKNOWLEDGEMENTS

The authors wish to acknowledge thoughtful discussions with S. Bader, P. Bennett, M. Hart, D. Loretto, W. Petuskey and J. Venables. We are also indebted to D. Loretto of Lawrence Berkeley Laboratory for supplying the $\text{CaF}_2/\text{Si}(111)$ samples. This work is supported by the Office of Naval Research under grant No. N00014-93-1-0099 and the National Science Foundation under grant No. DMR 89-14761. The microscopy was performed at the National Science Foundation supported Center for High Resolution Electron Microscopy at Arizona State University, grant No. DMR-91-15680.

REFERENCES

1. N.D. Mermin, H. Wagner, Phys. Rev. Lett. **17**, 1133 (1966).
2. L.J. Schwartzendrubber, **Binary Phase Diagrams** : vol. 2, (Publisher, 1990).
3. O.N. Myrasov, A.I. Liechtenstein, L.M. Sandratskii, V.A. Gubanov, J. Phys.: Condens. Matter **3**, 7683 (1991); G.L. Krasko, G.B. Olson, Phys. Rev. **B40**, 11536 (1989); T. Kraft, M. Methfessel, M. van Schilfgaarde, M. Scheffler, Phys. Rev. **B47**, 9862 (1993); V.L. Moruzzi, P.M. Marcus, K. Schwarz, P. Mohn, Phys. **B34**, 1784 (1986).
4. C. Liu, E.R. Moog, S.D. Bader, Phys. Rev. Lett. **60**, 2422 (1988); C. Liu, E.R. Moog, S.D. Bader, J. Appl. Phys. **64**, 5325 (1988); C. Liu, S.D. Bader, J. Vac. Sci. Technol. **A8**, 2727 (1990); S.D. Bader, Proc. IEEE **78**, 909 (1990).
5. W.R. Bennett, W. Schwarzacher, W.F. Egelhoff Jr., Phys. Rev. Lett. **65**, 3169 (1990).
6. D. Pescia, M. Stampaconi, G.L. Bona, A. Vaterlaus, R.F. Willis, F. Meier, Phys. Rev. Lett. **58**, 2126 (1987).
7. D.P. Pappas, K.-P. Kamper, H. Hopster, Phys. Rev. Lett. **64**, 3179 (1990).
8. D.P. Pappas, K.-P. Kamper, B.P. Miller, H. Hopster, D.E. Fowler, A.C. Luntz, C.R. Brundle, Z.-X. Shen, J. Appl. Phys. **69**, 5209 (1991).
9. W.A.A. Macedo, W. Keune, Phys. Rev. Lett. **61**, 475 (1988).
10. F.J. Himpel, Phys. Rev. Lett. **67**, 2363 (1991).
11. R. Allenspach, A. Bishop, Phys. Rev. Lett. **69**, 3385 (1992).
12. P. Xhonneux, E. Courtens, Phys. Rev. **B46**, 5561 (1992).
13. J. Thomassen, F. May, B. Feldmann, M. Wuttig, H. Ibach, Phys. Rev. Lett. **69**, 3831 (1992).
14. W.A. Jesser, J.W. Mathews, Phil. Mag. **15**, 1097 (1967); Phil. Mag. **17**, 461 (1968).
15. S.A. Chambers, T.J. Wagener, J.H. Weaver, Phys. Rev. **B36**, 8982 (1987).
16. D.A. Steigerwald, W.F. Egelhoff Jr., Surf. Sci. **192**, L887 (1987); D.A. Steigerwald, F. Jacob, W.F. Egelhoff Jr., Surf. Sci. **202**, 472 (1988).
17. H. Glatzel, Th. Farster, B.M.U. Scherzer, V. Dose, Surf. Sci. **254**, 58 (1991).
18. A. Brodde, H. Neddermeyer, Ultramicrosc. **42-44**, 556 (1991).
19. H. Magnan, D. Chandesris, B. Villette, D. Heckmann, J. Lecante, Phys. Rev. Lett. **67**, 859 (1991).
20. G. Hembree, J. Drucker, L. Hong, M. Krishnamurthy, and J. A. Venables, Appl. Phys. Lett. **58**, 1991.
21. G. G. Hembree and J. A. Venables, Ultramicroscopy **47**, 109 (1992); J. Liu, G. G. Hembree, G. E. Spinnler, and J. A. Venables, Surface Science Lett. **262**, L111 (1992); J. Liu, G. G. Hembree, G. E. Spinnler, and J. A. Venables, Catalysis Letters **15**, 133 (1992).
22. M. Krishnamurthy, J. Drucker, and J. Venables, J. Appl. Phys. **69**, 6461 (1991).
23. J. Drucker, M. Krishnamurthy, and G. Hembree, Ultramicroscopy **35**, 323 (1991).
24. G. G. Hembree, P. A. Crozier, J. S. Drucker, M. Krishnamurthy, J. A. Venables, and J. M. Cowley, Ultramicroscopy **31**, 111 (1989).
25. J. A. Venables, J. M. Cowley, and H. S. von Harrach, Inst. Phys. Conf. Ser. **90**, 85 (1987).
26. P. Kruit and J. A. Venables, Ultramicroscopy **25**, 183 (1988).
P. Kruit, Adv. Opt. Electron Microsc. **12**, 93 (1991).
27. M. R. Scheinfein, unpublished.
28. Crystals were custom fabricated by Virgil Straughn, Monocrystals Inc. Cleveland, OH.
29. J. Drucker, J. Appl. Phys. **70**, 2806 (1991).
30. J. A. Venables, D. R. Batchelor, M. Hanbücken, C. J. Harland, and G. W. Jones, Phil. Trans. R. Soc. Lond. A **318**, 243 (1986).
31. F. Grønlund and P. E. H. Nielsen, Surface Science **30**, 388 (1972).
32. G. W. Goetze, A. H. Boerio, and M. Green, J. Appl. Phys. **35**, 482 (1964); G. W. Goetze, Adv. Electron. Electron Phys. **22**, 219 (1968).
33. L. Reimer, **Scanning Electron Microscopy**, (Springer-Verlag, Berlin, 1985).
34. E. Bauer, Z. Krist. **110**, 372 (1958).
35. F. R. de Boer, R. Boom, W. C. M. Mattens, A. R. Miedema, and A. K. Niessen, **Cohesion in Metals Transition Metal Alloys** (North-Holland Elsevier Science Publishers, NY, 1988).

36. J. J. Gilman, *J. Appl. Phys.* **31**, 2208 (1960). G. C. Benson and T. A. Claxton, *Can. J. Phys.* **41**, 1287 (1963). P. W. Tasker, *J. Phys. (Paris)* **41**, C6-488 (1980).
37. J. Q. Xiao, J. S. Jiang, and C. L. Chien, *Phys. Rev. Lett.* **68**, 3749 (1992).
38. T. R. Harrison, P. M. Mankiewich, and A. H. Dayem, *Appl. Phys. Lett.* **41**, 1102 (1982). P. M. Mankiewich, H. G. Craighead, T. R. Harrison, and A. H. Dayem, *Appl. Phys. Lett.* **44**, 468 (1984). M. Scheinfein and M. Isaacson, *J. Vac. Sci. Technol. B* **4**, 326 (1986).
39. Private communication with D. Loretto: Bright field transmission electron microscopy performed on the CaF₂/Si(111) samples revealed a non uniform distribution of line defects at the CaF₂-Si(111) interface. This is an indication that stress relief occurred during the CaF₂ growth. In comparison, an unrelaxed film will display a parallel array of line defects corresponding to the original steps on the Si(111) surface.
40. C. Kittel, *Introduction to Solid State Physics, fourth edition* (John Wiley & Sons, 1971), page 259.
41. C. L. Chien, *J. Appl. Phys.* **69**, 5267 (1991). A. E. Berkowitz, J. R. Mitchell, M. J. Carey, A. P. Young, S. Zhang, F. E. Spada, F. T. Parker, A. Hutton, and G. Thomas, *Phys. Rev. Lett.* **68**, 3745 (1992). A. E. Berkowitz, J. R. Mitchell, M. J. Carey, A. P. Young, D. Rao, A. Starr, S. Zhang, F. E. Spada, F. T. Parker, A. Hutton, and G. Thomas, *J. Appl. Phys.* **73**, 5320 (1993).

SURFACE MORPHOLOGY OF DIAMOND THIN FILMS USING PHOTO-INDUCED SCANNING TUNNELING MICROSCOPY

D.L. Carroll ^(a), T. Mercer ^(b), Y. Liang ^(a), N.J. DiNardo ^(b) and D. A. Bonnell ^(a)

^(a) Department of Materials Science and Engineering, University of Pennsylvania, Philadelphia Pa.

^(b) Department of Physics, Drexel University, Philadelphia Pa, 19104

ABSTRACT

Photo-induced conduction in thin insulating films of diamond was used to obtain STM images indicative of film morphology. UV light was used to generate carriers in the conduction band of diamond films grown on Si (111). Tunneling currents could only be established when the tunnel junction was illuminated. Without the light, no current was measured even with the tip in contact with the surface. Two types of films were studied. A CVD grown diamond film with nitrogen impurities and a diamond-like film grown by laser ablation of graphite. Topological detail was compared to that obtained with an AFM. The correspondence between AFM and photo-induced STM images suggests that the STM images are indicative of film morphology.

INTRODUCTION

The Scanning Tunneling Microscope (STM) has become accepted as an important probe of the local geometric and electronic structure of solid surfaces. [1] The applicability of the technique, however, is generally limited by the intrinsic conductivity of the samples of interest. [2, 3, 4] Therefore, STM studies have been predominately on systems which can provide carrier densities on the order of 10^{18} or greater. While this is easily obtainable for metals and semiconductors, imaging insulating materials is significantly more difficult. Low carrier mobility and density, create a space-charge buildup which prevents tunneling currents from being established. [5] Doping of wide bandgap materials such as boron in diamond thin films and niobium in bulk TiO_2 has been used to provide the conductivity needed to image surface features. In the case of oxide surfaces, chemical reduction has also been employed to increase carrier density and mobility. [6] As long as dopant levels can remain low, there is little alteration to the electronic structure of the material with the exception of the extra carriers. Clearly, high dopant levels will change electronic structure and, therefore, the properties which may have been of interest in the material. Likewise, it is not always certain that a chemically-reduced bulk crystal with a reoxidized surface is indicative of the fully stoichiometric system. In fact there is evidence that bulk reduction alters the geometric structure of the surface. The alteration of electronic properties becomes most pronounced for those situations in which all the carriers are provided by donor states deep within the electronic bandgap. This is the case, for instance, with nitrogen-doped diamond. Thus, it is not always feasible to induce conductivity through doping or reduction.

Conductivity in insulating materials may also be induced by the absorption of radiation. For photon energies at or above the band-gap energy, absorption cross-sections can become quite high, yielding carrier densities which are directly proportional to the illumination intensity with a proportionality constant dependent on electron-hole recombination rates. [7] This suggests that high conductivities may be obtained for materials with relatively light conduction electron effective masses. The effects of illumination on tunneling junctions in STM measurements have been investigated, primarily, with emphasis on heating and photovoltaic effects. Localized heating on illuminated GaAs surfaces and photovoltages on Si(111): 7x7 [8, 9] have been observed with the STM. Further, carrier density increases in wide band-gap oxides due to light absorption have been reported for oxides on which tunneling currents could be maintained without illumination. [10, 11]

In contrast to previous STM studies which involve light, this work demonstrates the use of photo-induced carriers to establish tunneling and to image. Insulating diamond thin films were illuminated with broad band light (180 - 700 nm) and imaged with a wide scan STM. Without

illumination tunneling could not be achieved. Two different thin film morphologies were imaged with the STM and the AFM. The high degree of correspondence between the images suggests that the photo-induced STM images reflect true surface topography.

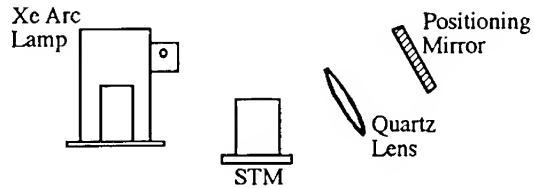
PROCEDURE

Two distinctively different types of diamond films were investigated. A $2.2 \mu\text{m}$ polycrystalline film was grown on a Si substrate using a standard hot-filament CVD technique. This provided a rough topography with which relative comparisons could be made. The second type of film was a $1 \mu\text{m}$ thick amorphous film produced by vacuum laser ablation of graphite. This technique produces extremely flat films with no apparent crystallite grains. The sheet resistance of both films exceeded 100 MW/cm^2 .

Each sample was ultrasonically cleaned in acetone and methanol before mounting into the STM. The 'in-air' STMs used in this experiment (Burleigh Aris 2200E; Digital Instruments Nanoscope III) have relatively open sample-tip geometries for satisfactory illumination of the tunnel junction. Images were obtained using both etched W tips and mechanically formed Pt-Ir tips. The W tips, which produced the best images, were prepared by electrochemical DC etching of 0.5 mm diameter polycrystalline wire.

A 400 W xenon arc lamp with a condenser housing and quartz lenses was used to illuminate the tunnel junction. This lamp produces a broad spectrum of light which extends into the ultraviolet (180 - 700 nm). The power curves provided with the lamp from the manufacturer (Oriel Corporation) shows that approximately 30% of the power is produced at wavelengths less than 225 nm (roughly 5.5 eV, the band-gap of diamond). An incident angle of approximately 45° was used to minimize shadowing at the junction by the upper portion of the tip and while maintaining a reasonably small spot size. Heating effects due to the high intensity light resulted in thermal drift. Temperatures at the diamond surface were measured to be around 80°C during illumination. It was therefore necessary to allow a minimum of 30 minutes for the device to come to thermal equilibrium before bringing the tip into tunneling. After tunneling was established, some thermal drift was still evident in the images but was manageable. A schematic diagram of the experimental setup and geometry is shown in Figure 1.

Figure 1. Experimental apparatus used for photostimulated Scanning Tunneling Microscopy. There is an estimated 80% loss in the optical system as shown.



AFM (Digital Instruments Nanoscope III) images of both films were obtained using microfabricated Si tips operating in the tapping mode. Since it is impossible to obtain images over exactly the same area of the surface with both microscopes, many areas of each surface were imaged and comparisons made between representative morphologies. It is not expected that the heating of the films should have effect on the measured surface topography, therefore, the AFM images were obtained without illumination and thus at room temperature.

Photoconductivity measurements were made on the polycrystalline film by making a mechanical contact to the film with silver print and measuring the I-V characteristics under illumination using a picoammeter. These were used to determine whether carrier densities sufficient for tunneling could be obtained. Without illumination there was no measurable current at

biases below 11.0 V. Under the light, however, a current of 3.0 nA was measured at 11.0 V. Further, the I-V characteristics were typical for a Schottky-type contact.

RESULTS AND DISCUSSION

The morphology of the CVD diamond films was typical of polycrystalline films in general. [12] Figure 2 shows a representative STM image of the surface acquired at a tunneling current of 0.6 nA and a sample bias of +10.0 V. Structures on the order of 0.1 μ m with height variations of approximately 200 nm are observed. The elongation along one direction was typical of the images collected with the STM and the AFM. Tunneling currents were generally maintained below 1 nA to avoid excessive tip crashes. Stable tunneling currents greater than 1 nA at biases as low as 2.0 V could however, be obtained.



Figure 2. 500 x 500 nm
STM image of the CVD
diamond film surface.
The z-scale shown
is 200 nm black to white.

For comparison, a typical AFM image is shown in Figure 3. Again, the image reveals corrugated, elongated structures of roughly 0.1 μ m in height. This is indicative of the topography observed over various areas of the surface of the CVD film. The small crystallite features are expected from this growth mechanism and thus it seems probable that the STM image truly reflects surface structure. Notice that the grain boundaries of the film have not been enhanced in the STM image. This effect might be expected due to photovoltaic effects across the boundary or an increased density of states at the interfaces of the grains. It is not observed, however, and considering tip induced space charge due to the low conductivity of the sample may smear the effect, the consequent spatial resolution may not be sufficient to observe the changes in the local density of states on this scale.



Figure 3. A 1250 x 1250 nm
AFM image of the
CVD diamond film surface.
The z-scale shown is
600 nm black to white.

The stability of the tunneling junction was highly dependent on the focus and intensity of the light at the tip. Small fluctuations in focus at the junction would affect whether or not tunneling currents could be established. Images at voltages around 5.0 V were possible but tip changes due to contact significantly reduced the quality of the image. This is because the scan speeds must be relatively high to avoid problems with thermal drift. The light in the source was generated by a plasma discharge through xenon which is not extremely stable in intensity. This may have also affected the long term stability of the junction during scanning.

The morphology of the laser-ablated films was significantly different from that of the CVD films and were extremely flat. This was reflected in both the AFM and STM images. The laser ablated film could be easily imaged with the STM at biases of 4.0 Volts and currents at 0.6 nA. It is likely that the difference in composition and surface morphology allows imaging at lower biases. Although the junction stability was still very sensitive to changes in the focus of the light, it seemed relatively easy to image the surface in comparison with the CVD diamond film. Given the less-ordered structure of the laser-ablated film and the differences in deposition conditions, it is reasonable to expect that the electronic nature and, therefore, the absorption characteristics of the two films are extremely different. This difference may be reflected in the tunneling characteristics of the films, though they both appear insulating without illumination.

To establish that the STM was tunneling, the tunnel current was measured as a function of tip-sample separation (I-S curves) for the CVD films. The logarithmic dependence of the current with separation expected for tunneling was obtained with the sample illuminated. Without the light, irreproducible I-S measurements were observed consistent with sample-tip contact.

As a comparison, tunneling on a single crystal diamond doped with nitrogen was attempted. The sample was polished to the (111) face by the suppliers. The dopant level in the diamond was approximately 0.001% and the crystal appeared yellow. Tunneling was established with great difficulty. Generally, the system was too unstable to image. This is currently under investigation.

CONCLUSIONS

This study presents evidence for STM image acquisition by tunneling solely from photo-induced carriers into an insulator. Illumination with broad spectrum light of insulating surfaces resulted in sufficient conductivity to achieve tunneling and the images corresponded in topographic detail to AFM images of the same surface. Three different diamond systems were used to demonstrate parameters important to the stability of the tunneling junction. The flat, laser ablated, amorphous, diamond films were the easiest to image. The CVD films were more difficult to image while obtaining a stable junction was essentially the same as on the ablated films. It is expected that the large height variations of the CVD film contributed to the problems with imaging at low biases; compositional differences in the films due to growth method undoubtedly also contribute. Although the band-gap and absorption properties of the two films should be roughly the same, the higher graphitic content of the amorphous material as well as impurity content may well lead to a higher density of donor states. The limit of these difficulties was illustrated in the behavior of the single crystal. The sharp band edges and low doping concentration implies that the majority of carriers are produced in direct bandgap transitions. Thus, only light above 5.5 eV is utilized in the process. This is in contrast to the films where impurities and grain boundaries (for the CVD film) are abundant and likely to produce states below the 5.5 eV threshold.

There is sufficient evidence that the STM is imaging the true morphology of the films suggesting that intrinsic local electronic properties of these insulating surfaces may be obtained. Extracting information about photovoltaics and interface states through tunneling spectroscopy is currently under investigation.

ACKNOWLEDGMENTS

We wish to thank Dr. Charles Beetz and the ATM Corp. for supplying the CVD films and Dr. Michael Seagal and Sandia National Labs for the laser ablated films. DAB acknowledges

support from the NSF Presidential Young Investigators Program under grant DMR 90-58557. NJD acknowledges financial support from NSF under grant DMR 91-20398.

REFERENCES

- 1 G. Binning and H. Rohrer, *Surf. Sci.* **126**, 236 (1983).
- 2 J. Wintterlin, J. Wiechers, H. Brune, T. Gritsch, H. Hofer and R. J. Behm, *Phys. Rev. Lett.* **62**, 59 (1989).
- 3 R. J. Hamers, *Annu. Rev. Chem.* (1989) 531.
- 4 M. P. Everson and M. A. Tamor, *J. Mater. Res.* **7**, 1438 (1991).
- 5 R. Feenstra and J. Stroscio, *J. Vac. Sci. Technol.* **B5**, 923 (1991).
- 6 G. S. Rohrer, V. E. Henrich and D. A. Bonnell, *Science* **250**, 1239 (1990).
- 7 R. Bube, *Photoelectric Properties of Semiconductors*, Cambridge University Press. (1992).
- 8 R. J. Hamers and K. Markert, *Phys. Rev. Lett.* **1051** (1990).
- 9 R. J. Hamers and D. G. Cahill, *Appl. Phys. Lett.* **57**, 2031 (1990).
- 10 G. S. Rohrer and D. A. Bonnell, *J. Am. Ceram. Soc.* **73**, 3257 (1990).
- 11 D. A. Bonnell, *J. Vac. Sci. Technol.* **B9**, 551 (1991).
- 12 K. Okano, H. Kiyota, T. Iwasaki, T. Kurosu, M. Iida and T. Nakamura, *Appl. Phys. Lett.* **58**, 840 (1991).

ATOMIC SCALE CHARACTERIZATION OF (NH₄)₂S_x-TREATED GaAs (100) SURFACE

NAOKI YOKOI, HIROYA ANDOH AND MIKIO TAKAI

Faculty of Engineering Science and Research Center for Extreme Materials,
Osaka University, Toyonaka, Osaka 560, Japan

ABSTRACT

The geometric structure of GaAs (100) surfaces, treated in a (NH₄)₂S_x solution and annealed in N₂ environment, has been studied in an atomic scale using high-resolution Rutherford backscattering (RBS), X-ray photoemission spectroscopy (XPS) and scanning tunneling microscopy (STM). RBS analysis using medium energy ion scattering (MEIS) could provide the thickness of the sulfur layer on the GaAs surface of about 1.5 monolayers. RBS channeling spectra indicated that the disorder of atoms in the surface region of S-terminated samples was smaller than that of untreated one. XPS spectra showed that S atoms on the surface bonded only As atoms. STM observation revealed that S atoms had a periodicity of 4 Å corresponding to that of Ga or As atoms in the (100) plane.

INTRODUCTION

Native oxide layers on semiconductor surfaces have undesirable effects on device fabrication processes. In particular, formation of surface / interface states and pinning of Fermi level cause serious problems for GaAs surfaces. These problems can be solved by means of surface termination by other species of atoms after removal of the oxide layer and such terminated surfaces are stable for a long time even in the air. Surface termination by chalcogen atoms (e.g., S, Se and Te) is successfully applied to GaAs surfaces to overcome the problems mentioned above. Some investigators have been studying on the electronic structures and characteristics of GaAs surfaces terminated by chalcogen atoms. Ohno et al. have theoretically studied the electronic structures of S-, Se- and Te-terminated surfaces and predicted that S on the bridge site on Ga- or As-terminated (100) surface is stable [1, 2]. Fan et al. have measured the capacitance-voltage (C-V) characteristics and interface state densities of metal-insulator-semiconductor (MIS) structures fabricated on (NH₄)₂S- / (NH₄)₂S_x-treated surfaces [3]. Other investigators have been interested in geometric structures. Shigekawa et al. have observed Se-treated GaAs surfaces by field ion scanning tunneling microscopy (FI-STM) with an atomic resolution [4]. Richter and Hartnagel observed GaAs (100) surfaces by scanning tunneling microscopy (STM) in a scale of hundreds of nm after various treatment including S-passivation [5]. They also studied similar samples by X-ray photoemission spectroscopy (XPS), but the bonding between S and substrate atoms (Ga or

As) was not investigated.

The three-dimensional geometric structures in an atomic scale must be clarified as well as electronic structures in order to practically use this surface termination technique for device fabrication. However, there are few experimental studies to determine atomic structures of such terminated surfaces.

In this study, XPS, STM and high-resolution Rutherford backscattering (RBS) analysis using medium energy ion scattering (MEIS) were performed on S-terminated GaAs (100) surfaces to clarify the atomic structures.

EXPERIMENTAL PROCEDURES

S-termination of GaAs (100) surfaces was accomplished by dipping substrates into a $(\text{NH}_4)_2\text{S}_x$ solution of pH 8.5 including excess reactive sulfur at room temperature for 16 hr after chemical etching for 1 min in an etchant of $\text{H}_2\text{O}_2 : \text{H}_2\text{SO}_4 = 1 : 1 : 5$ at 60 °C to remove native oxide layers. Subsequently, the samples were annealed at 200 °C for 10 min in N_2 environment so that excess sulfur atoms were removed, leaving only one monolayer of sulfur on the sample surfaces. Different samples were prepared in the same way for each analysis.

The MEIS measurement was performed using a 100 keV He^+ beam at a base pressure of 10^{-10} Torr. The energy resolution ($\Delta E/E$) of a toroidal electrostatic analyzer was 4×10^{-3} , corresponding to 0.4 keV for the incident energy 100 keV [6]. The incident beam was aligned along $\langle 110 \rangle$ axis and the analyzer was located at 60 degrees of a scattering angle when the channeling spectra were measured.

The XPS spectra were measured using an Al K_α line at a base pressure of 10^{-9} Torr. It took about 30 min after annealing to transfer the samples into each vacuum chamber for MEIS and XPS measurements.

The STM observation was also performed using PtIr tips for 10 - 40 min after annealing. The current image was obtained with a tip bias voltage of -2.0 V. The details of our STM equipment were described elsewhere [7, 8].

RESULTS AND DISCUSSION

RBS Analysis

Figure 1 shows the RBS channeling spectra of S-terminated and untreated GaAs (100) surfaces. According to the comparison of surface peak widths and maximum normalized yields between two samples, the disorder of Ga or As atoms in the surface region of S-terminated sample is smaller than that of untreated one, since incident ions in a disordered lattice impact more atoms and are easily scattered, giving rise to larger surface peak width and yield.

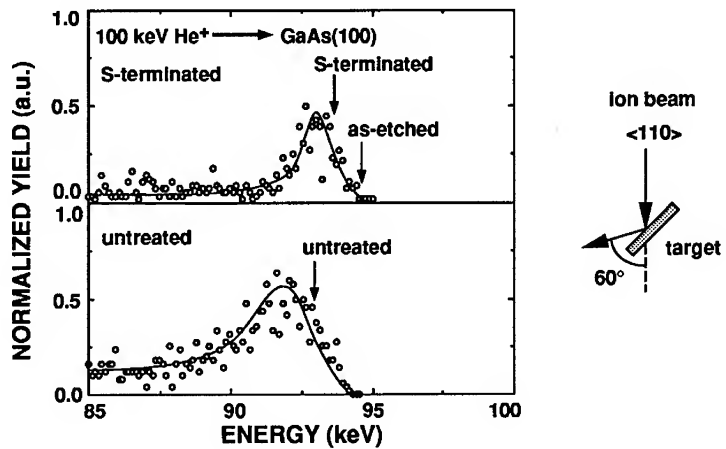


Fig. 1. RBS channeling spectra of S-terminated (upper) and untreated (lower) GaAs (100) surfaces obtained using 100 keV He⁺. The incident beam was aligned along the <110> axis and the detector was located at 60 degrees of a scattering angle.

The thickness of the sulfur layer can be estimated by comparing the leading edge energy of the random spectrum of the S-terminated sample to that of as-etched one. Their leading edge energy, calibrated by random spectra of carbon and gold, were 93.5 and 94.6 keV, respectively. These leading edge energies are represented by the arrows in the figure. Therefore, the estimated thickness of the sulfur layer on the GaAs (100) surface was about 1.5 monolayers.

XPS Analysis

Figure 2 shows the XPS spectra of S-terminated and untreated samples. The first and the second columns show the spectra for Ga 3d and As 3d, respectively. The large peaks at 19.3 eV for Ga 3d and 41.2 eV for As 3d are due to the bonding between Ga and As [9]. The peaks at about 20.5 eV for Ga 3d and about 45 eV for As 3d, representing the bonding to O, are remarkably large in the spectra for untreated sample and can be hardly seen in those of S-terminated one. This suggests that S-termination of GaAs (100) surface can suppress the growth of native oxide layer. The shoulder at 43.1 eV in the As 3d spectrum of S-terminated sample corresponds to the chemical shift due to As₄S₄ [9], while Ga 3d spectrum seems to consist of only one peak.

The third column shows the spectrum of S 2s for S-terminated sample. This spectrum also seems to consist of only one peak which represents the bonding of S to another species of atoms with smaller electronegativity. Therefore, it can be said that S atoms on the GaAs (100) surface

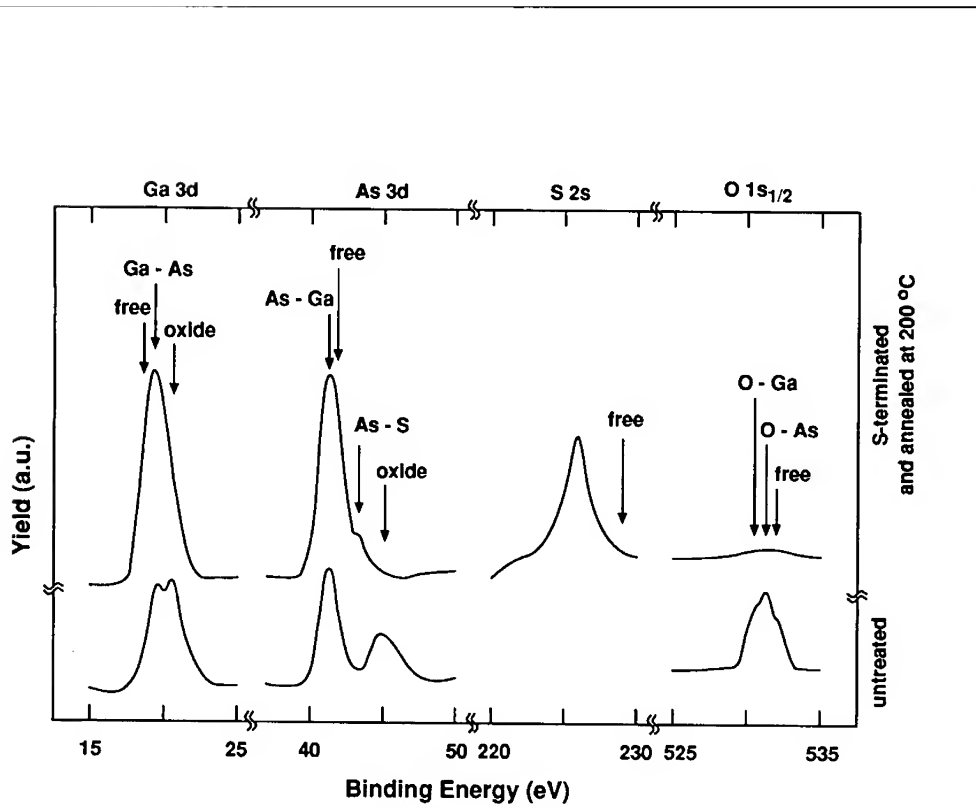


Fig. 2. XPS spectra of S-terminated (upper) and untreated (lower) GaAs (100) surfaces. Each column represents the spectra of Ga 3d, As 3d, S 2s and O 1s_{1/2}, respectively.

bond only As atoms. This result is in good agreement with the model by Nannichi and Oigawa[10] in the case of annealing below 250 °C.

The fourth column shows the spectra of O 1s_{1/2} for S-terminated and untreated samples. The spectrum for untreated one contains three peaks, representing the bonding to Ga, As and O itself. On the other hand, slight peak of O 1s_{1/2} can be seen even in the spectrum for S-terminated sample. This peak does not seem to be due to residual oxygen in the XPS chamber because such a peak could not be observed for a GaAs substrate sputtered by 1 keV Ar⁺ in the same chamber. Thus, oxidation might already start for S-terminated sample during exposure to the air for about 30 min.

STM Observation

Figure 3 shows the 1.5 nm x 1.5 nm STM image of a S-terminated GaAs (100) surface. Bright spots in this image are considered to represent S atoms on the surface. Both aligned and disordered spots exist in the image. The disordered spots suggest that exposure of the sample to

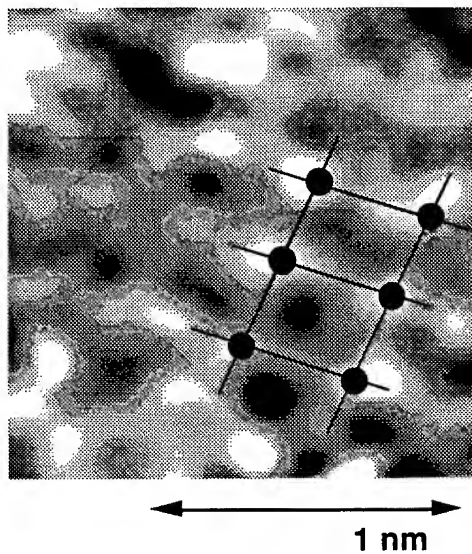


Fig. 3. 1.5 nm x 1.5 nm STM current image of a S-terminated GaAs (100) surface. The bias voltage on the tip is -2.0 V. Bright spots correspond to S atoms. The solid lines and circles represent the periodic structure of S.

the air may cause desorption of S atoms and oxidation of GaAs. The slight O 1s_{1/2} peak in the XPS spectrum of S-terminated sample supports this. S-As bonds on the GaAs surfaces may not be perfectly stable in the air. On the other hand, the aligned spots have a periodicity of 4 Å, corresponding to that of Ga or As in the (100) plane, i.e., S atoms on the GaAs (100) surface are aligned in the 1 x 1 structure. This periodic structure is represented by the solid lines and circles in the image. According to the theoretical prediction by Ohno, chalcogen atoms in the bridge construction are most stable on the GaAs (100) surface [1]. Therefore, S atoms on the GaAs (100) surface presumably replace Ga atoms in a bridge construction in the case of annealing at 200 °C. The distance between S plane and upper most As plane, however, may be different from that between Ga and As planes in bulk GaAs.

CONCLUSIONS

S-terminated GaAs (100) surfaces were studied by high-resolution RBS, XPS and STM. The RBS channeling spectra showed that the disorder in the surface region of S-terminated surface was smaller than that of untreated one. The thickness of the S layer on the GaAs substrate could be estimated to about 1.5 monolayers by the RBS random spectra. The XPS spectra showed that S atoms on the GaAs surface bonded only As atoms. STM observation revealed that

S atoms on the GaAs surfaces were aligned in the rectangular periodic structure with a periodicity of 4 Å. Thus, S atoms on the GaAs (100) surface are considered to be in a bridge construction replacing Ga atoms. However, the XPS analysis and the STM observation also suggest that even S-terminated surfaces can be slightly oxidized by exposure to the air. Further information on atomic sites of S can be obtained by combining other kind microscopies or spectroscopies. For example, the distance between the S layer and the upper most As layer can be estimated by MEIS using blocking.

ACKNOWLEDGMENTS

The authors are indebted to K. Kawasaki of Osaka University for his help during XPS analysis, to M. Taketani for his help during RBS analysis and to A. Inagaki for his help during STM observation.

REFERENCES

1. T. Ohno, *Surf. Sci.* **255**, 229 (1991).
2. T. Ohno and K. Shiraishi, *Phys. Rev. B* **42**, 11194 (1990).
3. J. -F. Fan, H. Oigawa and Y. Nannichi, *Jpn. J. Appl. Phys.* **27**, L1331 (1988); J. -F. Fan, Y. Kurata and Y. Nannichi, *Jpn. J. Appl. Phys.* **27**, L2255 (1989).
4. H. Shigekawa, T. Hasizume, H. Oigawa, K. Motai, Y. Mera, Y. Nannichi and T. Sakurai, *Appl. Phys. Lett.* **59**, 2986 (1991).
5. R. Richter and L. Hartnagel, *J. Electrochem. Soc.* **137**, 2879 (1990).
6. A. Kinomura, M. Takai, S. Namba and Y. Agawa, *Nucl. Instrum. Methods B* **64**, 576 (1992).
7. N. Yokoi, S. Ueda, S. Namba and M. Takai, *Jpn. J. Appl. Phys.* **32**, L129 (1993).
8. N. Yokoi, S. Namba and M. Takai, *Advanced Materials for Optics and Electronics* **2**, 71 (1993).
9. Eds D. Briggs and M. P. Seah, Practical Surface Analysis by Auger and X-ray Photoelectron Spectroscopy (John Wiley & Sons, Chichester, 1983).
10. Y. Nannichi and H. Oigawa, *Ext. Abst. 22nd Conf. SSDM*, 453 (1990).

RELATIONSHIPS BETWEEN PHOTOLUMINESCENCE SPECTRA AND POROSITY OF POROUS SILICON

H.Z. SONG*, L.Z. ZHANG*, B.R. ZHANG* AND G.G. QIN**

* Department of Physics, Peking University, Beijing 100871, P.R.China

** Department of Physics, Peking University, Beijing 100871, P.R.China and International Center for Material Physics, Academia Sinica, Shenyang 110015, P.R.China

ABSTRACT

It was found that porous silicon (PS) layers formed on $0.01 \Omega\text{cm}$ (111) and $0.02 \Omega\text{cm}$ (100) Si substrates show high photoluminescence (PL) peak energies on both lower and higher porosity sides and a minimum of PL peak energy at the moderate porosity, while those formed on 0.8 and $10 \Omega\text{cm}$ (111) p-type Si substrates show an increase of PL peak energy with porosity on the lower side and a saturation of PL peak energy with porosity on the higher side. These experimental facts are not consistent with the quantum confinement model for light emission of PS, which predicts a monotonous increase of PL peak energy with PS porosity.

INTRODUCTION

At present, many models of the luminescence mechanism of porous silicon (PS) have been proposed. The quantum confinement (QC) model¹ is one of the widely accepted points of view. Some experimental results were considered supporting of this model.²⁻⁷ Porosity is an important parameter characterizing the PS and is considered to relate to the sizes of nanoscale silicon quantum dots or wires, which are referred to as nanoscale silicon units (NSUs) hereafter, in PS. It is usually thought that, the higher the porosity of PS is, the smaller the NSUs, and the larger the emitting photon energy is according to the QC model. This letter shows our systematic research of the relationship between the photoluminescence (PL) and porosity of PS and the results are not consistent with the QC model for light emission of PS.

EXPERIMENTS AND RESULTS

The substrates used were p type (boron doped) silicon wafers, (100) oriented with different resistivities of about 10 and $0.02 \Omega\text{cm}$, and (111) oriented with three resistivities of about 0.01 , 0.8 and $10 \Omega\text{cm}$. They were polished on one side, and deposited with aluminum on the other side in vacuum and then alloyed at 530°C for 5 min in N_2 to make

Ohmic contacts. The PS layers were formed by electrochemical anodization. In order to obtain different porosity values in the current density range from 30 to 200mA/cm² while keep PS layers luminescent throughout and not polished, different anodization conditions were used on different substrate materials. In detail, in electrolyte HF(48wt.%)H₂O=1:1, PS samples on (111)10Ωcm substrates were anodized for 2 min in light, those on (111) 0.8 Ωcm and (100) 10 Ωcm for 2min in dark and those on (111) 0.01 Ωcm substrates for 4 min in dark. The samples on (100) 0.02 Ωcm substrates are formed in HF:H₂O=1:2 for 4 min in dark. In PL measurements, the excitation source was 4880Å line of Ar laser. The porosity of the PS sample was gotten from measuring the weights m_1 , m_2 and m_3 respectively before and after the formation and after removal of the PS layer in a NaOH solution. The porosity ϵ is expressed as:

$$\epsilon = (m_1 - m_2) / (m_1 - m_3) .$$

In the QC model for the light emission of PS, NSUs with smaller sizes have larger energy gaps, so they emit photons with higher energy, if the NSUs are small enough, the emission light is in the visible range. Since there is a correlation between the porosity and the pore size in PS layers, i.e., the lower porosity corresponds to smaller pores, while the higher porosity to larger pores,⁸ porosity has been widely used to characterize the NSU sizes in PS layer. Voos et al³ have investigated the PL for PS formed on p type, (100) oriented, 1 Ωcm Si substrates. In the meantime, they proposed a theory about the relationship between the porosity and the pore size in PS layer, and got the theoretical curves of confinement energy E_{CON} versus porosity of PS based on the QC model, and the PL peak energy E_{PL} equals

$$E_{\text{PL}} = E_{\text{CON}} + E_{\text{G}} - E_{\text{TO}}$$

where E_{G} and E_{TO} are the energy gap and TO phonon energy of bulk silicon respectively. They found that the PL energy increases monotonically with increasing PS porosity and the quantitative results are in good agreement with their theoretical curves deduced from the QC model. However, much evidence shows the shortcoming of the QC model, so we want to know whether there is such a coincidence generally. Since no dependence on substrate resistivity was illustrated in this theory, it may be helpful to do experiments on PS substrates with other resistivities. Using (100) orientation Si materials with resistivity of ~0.02 Ωcm, which is much lower than what Voos et al used, as substrate to prepare PS, we found an anomalous relationship between PL peak energy and the porosity of PS samples. FIG.1 shows the typical PL spectra, from which we see that both the highest porosity of 85% and the lowest one of 60% correspond to larger PL peak energies of 1.66eV and 1.80eV respectively than that of 1.58 eV corresponding to a moderate porosity of 70%, although the PL intensity always increases with porosity. The case of higher substrate resistivity, about 10 Ωcm, than Voos et al adapted was also investigated, somewhat similar PL variation trend to what Voos et al observed was obtained. The

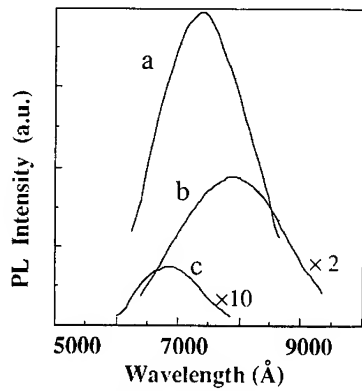


FIG.1. Typical PL spectra for PS layer formed on $0.02 \Omega\text{cm}$ (100) oriented Si substrates, where a, b and c correspond to 180 , 80 and 40 mA/cm^2 and $\epsilon=85$, 70 and 60% respectively.

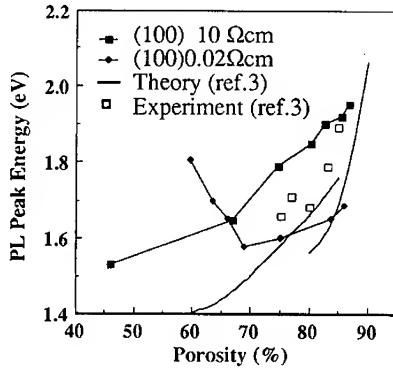


FIG.2. The variation of PL peak energy with porosity for PS layers formed on (100) oriented Si substrates with different doping levels. Also shown in solid lines and open squares are the theoretical and experimental results from Ref.3.

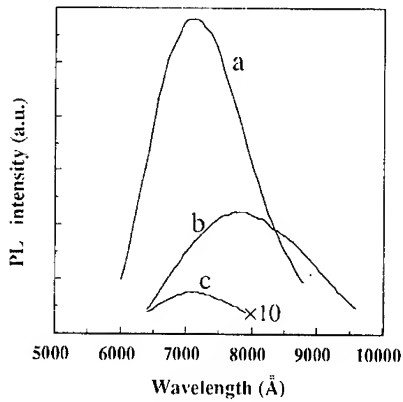


FIG.3. Typical PL spectra for PS layer formed on $0.01 \Omega\text{cm}$ (111) oriented Si substrates, where a, b and c correspond to 200 , 100 and 30 mA/cm^2 and $\epsilon=90$, 80 and 55% respectively.

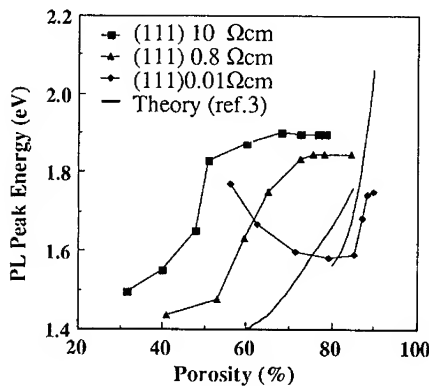


FIG.4. The variation of PL peak energy with porosity for PS layers formed on (111) oriented Si substrates with different doping levels. Also shown in solid lines are the theoretical results from Ref.3.

concrete results are displayed in FIG.2. The similar trend but quantitative difference between the results of $10 \Omega\text{cm}$ substrates and the theoretical curves suggest further that the agreement of Voos et al.'s results on (100) $1 \Omega\text{cm}$ Si wafer, shown in open squares in FIG.2, to their theory may be an accident.

In order to elucidate the relationship between PL energy and porosity more system-

atically, we did work on PS fabricated on (111) oriented Si substrates. As shown in FIG.3, both the lowest and highest porosity of 55% and 90% correspond to the largest PL peak energy of 1.78eV, and the porosity of 80% to 1.58eV, the lowest PL energy as directly shown in FIG.4. Unexpected phenomena were found even in the case of moderately doped substrates. As shown in FIG.4, the PL peak position for 10 Ωcm substrate blueshifts, from a low value of 1.5eV corresponding to porosity of 30%, with the increasing porosity at first, and pins at a fixed position of 1.9eV when porosity is higher than ~60%. Similar to 10 Ωcm (111) case, the PL peak position corresponding to 0.8 Ωcm (111) substrate blueshifts from a lower value of 1.43eV with porosity and then tends to saturate at 1.85eV with porosity higher than 70%.

DISCUSSION

As stated above, the PL peak energy versus porosity relationships deduced from the QC model are not consistent with experimental results in most cases. We consider there are two possible origins: (1) Beale et al⁹ had researched the functions of dopant atoms in PS formation processes and found two kinds of microstructures, branching buds in heavily doped and randomly distributing pores in lightly doped PS. Smith and Collins¹⁰ thought that dopants can steer or impose a bias on the direction of pore propagation. We consider maybe both microstructures and porosity play roles on band gaps of NSUs in PS. In another word, this macroscopic parameter, porosity, cannot alone characterize perfectly the sizes and shapes of NSUs in PS. (2) In some recent models for PS luminescence, e.g., the quantum confinement and luminescence center (QCLC) model suggested by Qin and Jia¹¹, the photo emission is not directly related to the band gap of NSUs. In the QCLC model, QC effect is considered as a necessary but not sufficient condition for visible light emission, the electron-hole pairs in NSUs can have energies much larger than the energy gap of bulk Si due to the QC effect. However, porosity only reflects the sizes of NSUs and is related to the photo excitation process, but does not determine the photo emission energy. In this model, light emission is through the luminescence centers outside NSUs. Therefore, such models as the QCLC and that suggested by Koch et al¹² etc. about luminescence mechanism of PS are compatible in principle with the experimental facts reported in this letter.

CONCLUSION

To summarize, we found that porous silicon formed on moderately doped and heavily doped Si wafers show different relationships between the photoluminescence peak energy and the porosity. In the moderately doped Si substrate, the photoluminescence peak energy blueshifts with increasing porosity first and then keeps at a constant position. For porous silicon formed on (111) oriented Si substrates,

it blueshifts continuously within the current density range used in this letter for porous silicon formed on (100) oriented substrates; in the heavily doped Si substrate case, it redshifts first until a certain porosity and then blueshifts with the porosity. There is not any simple relationship between the photoluminescence peak energy and the porosity of porous silicon as predicted by the quantum confinement model about the luminescence mechanism of porous silicon.

This work is supported by NFSC.

REFERENCES

1. L.T. Canham, *Appl. Phys. Lett.* **57**, 1046 (1990).
2. V. Lehmann and U. Gosele, *Appl. Phys. Lett.* **58**, 856 (1991).
3. M. Voos, Ph. Uzan, C. Delalande, G. Bastard and A. Halimaoui, *Appl. Phys. Lett.* **61**(10), 1213 (1992).
4. A. Halimaoui, C. Oules, G. Bomchil, A. Bsiesy, F. Gaspard, R. Herino, M. Ligeon, and F. Muller, *Appl. Phys. Lett.* **59**, 304 (1991).
5. R. Tsu, H. Shen, and M. Dutta, *Appl. Phys. Lett.* **60**, 112 (1992).
6. S. Gardelis, J.S. Rimmer, P. Dawson, B. Hamilton, R.A. Kubiak, T.E. Whall, and E.H.C. Parker, *Appl. Phys. Lett.* **59**, 2118 (1991).
7. R. Behrensmeier, Fereydoon Namavar, G.B. Amisola, F.A. Otter, and J.M. Galligan, *Appl. Phys. Lett.* **62**, 2408 (1993).
8. R. Herino, G. Bomchill, K. Barla, C. Bertrand and J.L. Ginoux, *J. Electrochem. Soc.* **134**, 1994 (1987).
9. M.I.J. Beale, N.G. Chew, M.J. Uren, A.G. Cullis and J.D. Benjamin, *Appl. Phys. Lett.* **46**(1), 86 (1985).
10. R.L. Smith and S.D. Collions, *J. Appl. Phys.* **71**(8), R1 (1992).
11. G.G. Qin and Y.Q. Jia, *Solid State Commun.* **86**, 559 (1993).
12. F. Koch, V. Petrova-Koch, T. Maschhik, A. Nikolov and V. Gavrilko, *MRS Symp. Proc.* **283**, 197 (1993).

EXPERIMENTAL AND SIMULATED SCANNING TUNNELING MICROSCOPY OF THE CLEAVED $\text{Rb}_{1/3}\text{WO}_3$ (0001) SURFACE

WEIER LU AND GREGORY S. ROHRER
Carnegie Mellon University
Department of Materials Science and Engineering
Pittsburgh PA 15213

ABSTRACT

Atomic-scale resolution scanning tunneling microscope (STM) images of cleaved (0001) surfaces of the hexagonal tungsten bronze, $\text{Rb}_{1/3}\text{WO}_3$, show two distinct contrast patterns. We have interpreted these images using simulated constant current STM topographs. These simulations are constructed based on calculations of the tunnel current as a function of the lateral and vertical position above the surface. By calculating simulated images for the limiting cases of different termination layers, different tip sizes, and different electronic structures, it is possible to systematically explore the important parameters and choose a model that most closely matches the experimental observations. In this case, we conclude that two distinct termination layers have been imaged, a W-O terminated surface and a Rb-O terminated surface. Also, we have found that the O atoms on the W-O surface relax to new positions nearer the 6-fold axis of rotational symmetry. Some of the advantages and disadvantages of this model are discussed.

INTRODUCTION

The ability of the scanning tunneling microscope (STM) to record real-space, atomic-scale resolution images of metal oxide surfaces has been clearly demonstrated in recent publications [1-4]. However, experience shows that interpreting STM images from complex binary or ternary oxide surfaces can be considerably more challenging than recording the observations. Although the problem is somewhat simplified for the surfaces of two-dimensional materials that are formed by cleavage at a van der Waals gap [4], the quantitative interpretation of images from the surfaces of cleaved three-dimensionally bonded compounds is frustrated by uncertainties regarding the multiple termination layer possibilities, the inability to form images from both the bonding and anti-bonding bands (due to their large energy separation), uncertainties with respect to the electronic structure of the surface, and ill-defined tip structures [5].

We have recently reported experimental STM images of the cleaved (0001) surface of the hexagonal tungsten bronze (HTB), $\text{Rb}_{1/3}\text{WO}_3$ [5]. The structure of this compound, originally determined by Magnéli [6], is most easily visualized as a network of corner sharing WO_6 octahedral units, as shown in Fig. 1. In planes parallel to (0001), the octahedra link in a hexagonal pattern which leaves cavities in the structure. The layers are then stacked so that the cavities form tunnels parallel to the c axis and Rb ions occupy the 12-fold sites within the tunnels. Contrast in images of these surfaces, which exhibited two distinct patterns, was interpreted on the basis of qualitative arguments. We have assumed that variations in the termination layer are responsible for the different types of contrast. In the present paper, we attempt to quantify this interpretation and to learn more about the relationship between the surface atomic positions and the atomic-scale image contrast by simulating images within the framework of a simple model.

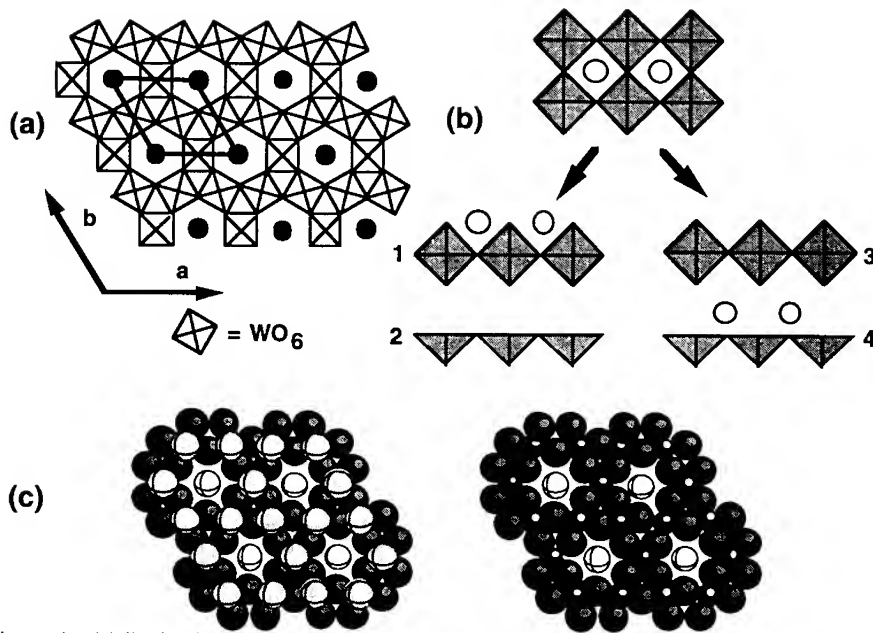


Figure 1. (a) Projection of the HTB structure along [0001]. The 3-dimensional structure is formed by stacking these layers so that each O at the apex of an octahedron is shared by one W above and one below. (b) When a corner-sharing network is broken, one surface consists of octahedra and the other of square pyramids. Depending on the fate of the alkali, there are four limiting cases. (c) Hard sphere models of the (0001) surface with apical O atoms in place (left) and with them, removed (right). The Rb are the spheres in the center of the rings, W are black, and the spheres representing O are shaded according to their height.

PROCEDURE

Fresh (0001) surfaces were formed by cleavage in air immediately before insertion into the vacuum chamber which had a base pressure of less than 1×10^{-9} torr. The tips used in these experiments were formed by clipping Pt-10% Ir wire and all of the images were acquired in the constant current mode using a 0.3 to 0.5 V sample bias (tunneling to unoccupied sample states) and a tunnel current of 0.6 to 0.8 nA. Details of the sample preparation and imaging can be found in ref. [5].

It is generally assumed that STM image contrast is determined primarily by the convolution of two factors: the surface electronic structure and the relative vertical positions of the surface atoms. In order to simulate these two effects within the framework of a simple, but physically valid model, we calculate the tunneling current as a function of the tip's lateral and vertical position over the sample assuming that each atom in the model contributes independently to the tunneling current and that at any specific coordinate, the tunneling current is given by a superposition of these contributions as follows.

$$I = \sum_i D_i \exp(-1.025 S_i \sqrt{\phi}) \quad (1)$$

For the tunnel barrier height, ϕ , we used the value of 1.6 eV which was determined from an experimental measurement of the dependence of I on S_i . S_i is defined as the distance between the surface of the tip (a sphere with radius r_{tip}) and the surface of the i^{th} atom which is a hard sphere whose size is defined by the ionic radius. Although not explicitly in the equation for the tunneling current, the tip radius influences the current through its effect on the separations, S_i . D_i is the relative contribution of the i^{th} atom to the total density of electronic states in the conduction band (the band being probed in the STM images). This term is meant to represent, in the simplest possible way, the lateral variation of the surface density of states. For example, for a surface terminated by a single element, all D_i would be equal. For a binary surface layer, on the other hand, we would expect the density of conduction band states to be higher at the electropositive element and would weight the values of D_i appropriately. Once the current is determined at each position, constant current images can be easily extracted.

The computational simplicity of the model makes it possible to generate many possible images based on different experimental parameters such as termination layer, atomic structure, tip size, and the contribution of each atom to the density of electronic states at the energy level being probed by the tip. Considering the fact that many of these parameters are ill-defined in most experiments, there is a considerable advantage to being able to systematically and rapidly explore the effects of the most important parameters.

The parameters that were found to have the most significant effect on the images are the termination layer, the relative contribution of the atoms to the band being probed by the STM (D_i), and the tip size (r_{tip}); choice of the constant current level or the barrier height influence only the total vertical corrugation and do not substantially alter the appearance of the image or the shapes of features, since images are normalized to maximize contrast. Our termination models are based on the fact that when the crystal is cleaved, only the longitudinal W-O bond that connects the apical oxygen anion and the W cation is broken. This creates four distinct limiting cases (illustrated schematically in Fig. 1b) based on the presence or absence of the apical O and the alkali atoms.

We considered two possible sets of values for D_i . The first is that all atoms contribute equally ($D_W = D_O = D_{Rb}$) and the second is that the values are weighted ($D_W = 9D_O = 90D_{Rb}$). We propose the weighting scheme based on the knowledge that the images were formed by tunneling to the conduction band and the assumption that this band is formed by the overlap of O 2p and W 5d orbitals and that Rb 5s orbitals make only a weak contribution. Although details of the electronic structure of this compound have not been studied, our numerical choices for the values of D_i were guided by the results of Bullett's [7] calculation of the electronic structure of cubic NaWO₃, a chemically similar compound.

RESULTS AND DISCUSSION

Figure 2 shows the two characteristic constant current STM images. Both have the hexagonal symmetry of the bulk structure and even preserve the bulk unit cell dimensions. However, the 6-fold symmetry axes of these two images are at contrary positions: at protrusions (white) in Fig. 2a and at depressions (black) in Fig. 2b. In the bulk structure, this axis of 6-fold rotational symmetry is located at the center of the hexagonal channel where the Rb cations reside. Thus, the point of 6-fold symmetry on the images must also represent this point.

Simulated images of the four possible termination layers, calculated under the assumption that the radius of the tip is equal to the radius of a Pt atom and that all of the D_i are equal, are shown in Fig. 3. The simulated images of the Rb-O (3a) terminated surface and of the Rb (3d) terminated surface both produce white contrast at the position of the 6-fold rotational axis and thus bear some resemblance to the experimental image in 2a. Of the two possibilities, we consider the simulated image of the Rb-O terminated surface to be the best match because the round areas of white contrast are approximately the same size as those in the

experimental image and there is some background gray contrast, as we also observe in the image.

None of the simulations in Fig. 3 produce the rings of white contrast that are characteristic of the experimental image in 2b. Assuming that the difference between the experimental image and the simulated images is due to the relaxation of the surface atoms to new positions, we note that on the W-O terminated surface (Fig. 3c), where O atoms create the bright contrast, the relaxation of these atoms toward the center of the tunnel could produce the characteristic rings of bright contrast while conserving the size of the surface repeat unit. A simulated image calculated under the same assumptions as in Fig 3c, but with the O atoms in sites displaced 0.3 Å toward the center of the tunnels, is shown in Fig 4a. A second calculation, using a tip with twice the radius of that in 4a is shown in 4b. Both images produce the characteristic white ring of contrast but it is the image in 4b that most closely resembles the experimental data in Fig. 2b.

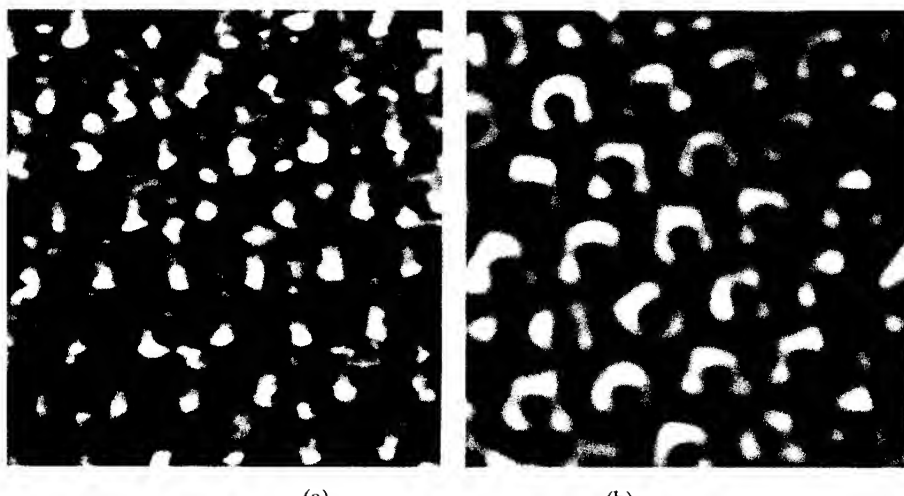


Figure 2. $41 \text{ \AA} \times 41 \text{ \AA}$ constant current STM images with a repeat unit equal to that of the bulk unit cell. (a) The vertical height (black-to-white contrast) is 2 \AA . The raised white features are arranged in a pattern with 6-fold rotational symmetry. (b) The vertical height is 0.8 \AA

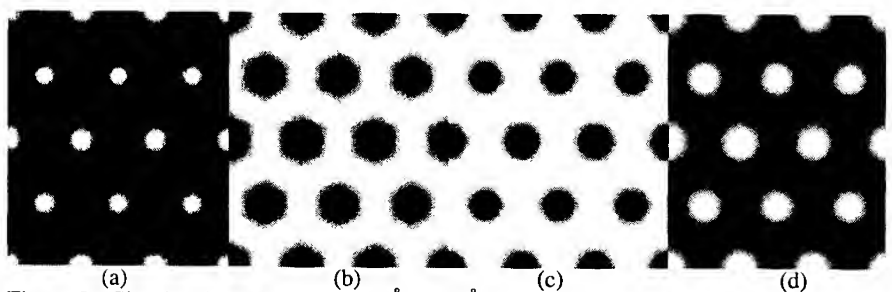


Figure 3. Simulated STM images, $22 \text{ \AA} \times 26 \text{ \AA}$. (a) Rb-O surface, case 1 in Fig. 1b. (b) O surface, case 2 in Fig. 3. (c) W-O surface, case 3 in Fig. 1b. (d) Rb surface, case 4 in Fig. 1b. For all cases, $r_{\text{tip}} = r_{\text{Pt}} = 1.38 \text{ \AA}$ and $D_w = D_O = D_{\text{Rb}}$

Based only on the simulations presented above, we would conclude that the image in 2a is of the Rb-O terminated surface and that the one in 2b is the W-O terminated surface, with

the surface O atoms in relaxed positions. It is, however, enlightening to consider other simulations using an alternate weighting scheme for the contribution of each atom to the surface density of states. Specifically, we assume that the contributions are weighted in such a way that $D_w = 9D_O = 90D_{Rb}$, values that seem chemically realistic assuming that polar-ionic bonding dominates in this material. Simulations of the Rb-O surface, the W-O surface with O atoms in relaxed positions, and the Rb terminated surface are shown in Fig. 5. We note that in the simulation of the Rb-O terminated surface the bright contrast is now dominated by the O atoms and that in the simulation of the W-O surface the bright contrast is now dominated by the W atoms position. Thus, using the weighted contributions, the simulated images of these surfaces no longer resemble any of the experimental images. On the other hand, in the simulated image of the Rb terminated surface, the size of the areas of white contrast shrink to sizes nearer those in Fig. 2a.

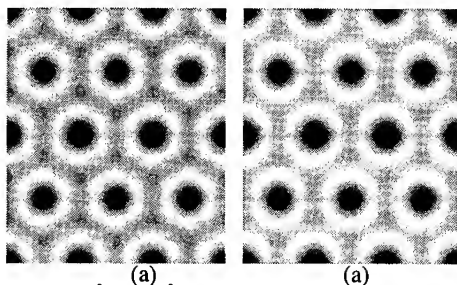


Figure 4. Simulated images, $22 \text{ \AA} \times 26 \text{ \AA}$, of the W-O surface. (a) This is the same as Fig. 3c, but the O atoms occupy relaxed positions. (b) this is the same as a, but r_{tip} equals twice r_{Pt} .

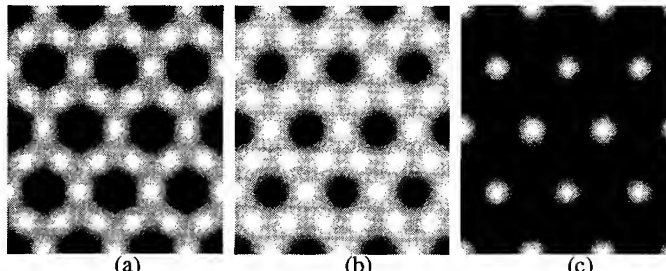


Figure 5. Simulated images, $22 \text{ \AA} \times 26 \text{ \AA}$, with $r_{\text{tip}} = r_{\text{Pt}} = 1.38 \text{ \AA}$ and $D_w = 9D_O = 90D_{Rb}$
(a) The Rb-O surface. (b) The W-O surface. (c) The Rb surface.

The agreement between the experimental images and the simulated images is better when the contributions from all atoms are weighted equally. Although the reasons for this are not clear, we take this to be the appropriate model and conclude that Fig. 2a is an image of the Rb-O terminated surface and that Fig. 2b is an image of the W-O terminated surface with the atoms in relaxed positions. While it is possible that simulations which account for the lateral variations in the surface density of electronic states based on tight binding model calculations, which have been successfully used to interpret images of chalcogenides [8], might resolve this issue, we believe that our simplified model offers certain advantages. First, because of its simplicity, it allows a range of possible termination layers or surface structures to be easily examined. This is especially important for surfaces of complex ternary materials. Second, it includes effects related to the finite size of the tunneling tip, as shown in Fig. 4. As the tip gets larger, contributions from more and more tunneling sources become significant and affect the image contrast.

Finally, we comment on the O relaxation on the W-O surface. While this relaxation suggests unusually short O-O separations, they are nearly identical to the in-plane oxygen positions in the metastable hexagonal WO_3 which also has the HTB structure, but contains no alkali [9]. Thus, such a relaxation should not be unexpected because the surface layer can be viewed as a local approximation of the empty tunnel structure where at least half of the coordinating alkali atoms are missing. We also note that STM images of the cubic tungsten bronze $\text{Na}_{0.82}\text{WO}_3(100)$ surface demonstrated that surface atoms relaxed to form a 1x2 surface structure in response to the local ordering of sub-surface sodium [10]. These results, taken together with the results presented here, suggest that the alkali atoms play an important role in determining how the surfaces of the tungsten bronzes relax.

CONCLUSION

Based on simulated constant current STM images of the hexagonal tungsten bronze $\text{Rb}_{1/3}\text{WO}_3$ (0001) surface, we conclude that different termination layers are responsible for the different types of contrast in the experimental images. Also, within the framework of our model, we conclude that the best agreement is obtained when it is assumed that all atoms contribute equally to the tunnel current. In other words, the effect of surface geometry dominates the effect of the local variations in the density of electronic states. Also, based on the simulations, we conclude that the O atoms on the W-O surface relax to positions closer to the six-fold symmetry axis. Based on a comparison to the structure of hexagonal WO_3 , it seems that this relaxation is driven by broken alkali-oxygen bonds at the surface. While the results here suggest the need for more testing, we note that the proposed model provides tangible manifestations of the often used qualitative arguments regarding the origin of contrast in STM images and, because of its simplicity, provides some advantages for the interpretation of STM images from complex materials.

ACKNOWLEDGMENTS

This work was supported under National Science Foundation Grant DMR-9107305.

REFERENCES

- [1] G. S. Rohrer, V. E. Henrich, and D. A. Bonnell, *Science* **250**, 1239 (1990).
- [2] R. Wiesendanger, I. V. Shvets, D. Bürgler, G. Tarrach, H. J. Güntherodt, J. M. D. Coey, and S. Gräser, *Science* **255**, 583 (1992).
- [3] T. Matsumoto, H. Tanaka, T. Kawai, and S. Kawai, *Surface Science Letters*, **278**, L153 (1992).
- [4] G. S. Rohrer, W. Lu, R. L. Smith, and A. Hutchinson, *Surface Science* **292**, 261 (1993).
- [5] W. Lu, N. Nevins, M. L. Norton, and G. S. Rohrer, *Surface Science* **291**, 395 (1993).
- [6] A. Magnéli, *Acta Chem. Scand.* **7**, 315 (1953).
- [7] D. W. Bullett, *J. Phys. C: Solid State Phys.* **16**, 2197 (1983).
- [8] J. Ren, M.-H. Whangbo, H. Bengel, H.-J. Cantlow, and S. N. Magonov, *Chem. Mater.* **5**, 1018 (1993).
- [9] J. Oi, A. Kishimoto, and T. Kudo, *J. Solid State Chem.* **96**, 13 (1992).
- [10] G. S. Rohrer, W. Lu, M. L. Norton, M. A. Blake, and C. L. Rohrer, *in press J. Solid State Chemistry*.

IMAGING THE ATOMIC-SCALE STRUCTURE OF MOLYBDENUM AND VANADIUM OXIDES BY SCANNING TUNNELING MICROSCOPY

GREGORY S. ROHRER, WEIER LU, AND RICHARD L. SMITH
Carnegie Mellon University
Department of Materials Science and Engineering
Pittsburgh PA 15213

ABSTRACT

Single crystals of $\text{Na}_{0.003}\text{V}_2\text{O}_5$ and $\text{Mo}_{18}\text{O}_{52}$ were grown by chemical vapor transport and cleaved surfaces were imaged in ultrahigh vacuum using scanning tunneling microscopy (STM). Because the $\text{Mo}_{18}\text{O}_{52}$ (100) and $\text{Na}_{0.003}\text{V}_2\text{O}_5$ (010) surfaces of these layered materials have a bulk terminated structure, the atomic-scale contrast in constant current images can be directly compared to components of the bulk structure. Among the structural features identified in the STM images are the surface/crystallographic shear plane intersections, the different MoO_x coordination polyhedra on the $\text{Mo}_{18}\text{O}_{52}$ (100) surface, and the VO_5 square pyramids that make up the $\text{Na}_{0.003}\text{V}_2\text{O}_5$ (010) surface. In each of these cases, it was found that the atoms closest to the tip dominate the image contrast.

INTRODUCTION

The catalytic properties of transition metal oxides such as MoO_3 and V_2O_5 are known to be influenced by the structure of their surfaces [1,2]. Unfortunately, our ability to establish useful relationships between the surface structure and properties of these materials has been limited by our incomplete knowledge of the surface structure. It is expected that this information will soon become available through the use of the scanning tunneling microscope (STM), which allows the structure of surfaces to be visualized at micron to the angstrom length scales. However, although many transition metal oxides have already been imaged at atomic-scale resolution, correlating the contrast in an STM image of a complex binary or ternary compound surface with specific structural features remains a challenge [3-6].

Layered compounds, which have strong primary bonds between atoms within layers, but weak van der Waals bonding between the layers, are excellent models for the study of contrast in STM images because cleavage parallel to the layer breaks only the weak bonds and creates a low energy surface with little or no driving force for relaxation or reconstruction. Thus, topographic features in STM images can be correlated with bulk crystallographic data. The two compounds described here, V_2O_5 and $\text{Mo}_{18}\text{O}_{52}$ (an oxygen deficient relative of MoO_3), both have layered structures. It is the goal of this work to identify the contrast that arises from specific structural features on the surfaces of these layered compounds so that in the future, the contrast on inhomogenous or defective oxide surfaces can be identified.

The vanadium and molybdenum oxides exhibit a number of structural and chemical similarities. Both have O ions in 1-, 2-, and 3-fold coordination and both materials are very labile, with high oxygen diffusivities and easily accessed reduced valence states. The specific structural features that we wish to identify are the different coordination polyhedra (the $\text{Mo}_{18}\text{O}_{52}$ surface has both octahedral and tetrahedral groups on the surface), the orientation of the polyhedra (the V_2O_5 surface is terminated by square pyramids with opposite vertical orientations), and the surface/crystallographic shear (CS) plane intersections (the CS planes intersect the $\text{Mo}_{18}\text{O}_{52}$ surface periodically along the [010] direction).

EXPERIMENTAL

The single crystals used in this study were prepared by chemical vapor transport. The growth of $\text{Mo}_{18}\text{O}_{52}$ crystals involves heating, in a horizontal tube furnace with a small temperature gradient, at approximately 677 °C for several days, an evacuated quartz ampoule containing a stoichiometric mixture of Mo and MoO_3 together with a small amount of I_2 that acts as a transporting agent [7, 8]. Powder X-ray diffraction was used to identify platey black crystals found throughout the tube as $\text{Mo}_{18}\text{O}_{52}$.

Because crystals of pure V_2O_5 are too insulating to permit high resolution STM measurements, we increased the conductivity by intercalating them with a small amount of Na [9]. In order to insure uniformity, the Na was added during the crystal growth. The single crystals of $\text{Na}_{0.003}\text{V}_2\text{O}_5$ were prepared by sealing $\text{Na}_x\text{V}_2\text{O}_5$ (prepared by treating V_2O_5 in an aqueous $\text{Na}_2\text{S}_2\text{O}_4$ solution) in a quartz ampoule with a small amount of TeCl_4 to act as a transporting agent. The ampoule was then heated in a 30 °C temperature gradient (530 °C to 500 °C) for seven days after which crystals were harvested from the cooler end of the tube. Powder X-ray diffraction was used to show that the structure of these crystals was essentially identical to that of pure V_2O_5 , with no extra peaks. Analysis of the sodium content by flame emission spectroscopy indicated a chemical composition of $\text{Na}_{0.003}\text{V}_2\text{O}_5$. The electronic conductivity, determined using a four-point probe method, is $0.04 \Omega^{-1}\text{-cm}^{-1}$. These structural, chemical, and electrical measurements are all consistent with the model that the single crystals grown by chemical vapor transport are essentially V_2O_5 with a small amount of sodium intercalated into the interlayer spaces that increases the electronic conductivity by donating electrons to the V_2O_5 framework, but does not significantly alter the structure.

STM imaging was carried out in ultrahigh vacuum (UHV) on cleaved surfaces. Surfaces of $\text{Na}_{0.003}\text{V}_2\text{O}_5$ were prepared either by cleavage in the vacuum chamber, or by cleavage in a N_2 filled glove bag connected to the chamber's load-lock. $\text{Mo}_{18}\text{O}_{52}$ surfaces were cleaved in air immediately before transferring them to the UHV environment. Constant current images were obtained using current levels between 0.6 and 1.0 nA. Images of $\text{Mo}_{18}\text{O}_{52}$ were recorded at -1.6 V sample bias (tunneling from filled states) using a clipped Pt-Ir tip. Images of $\text{Na}_{0.003}\text{V}_2\text{O}_5$ were recorded in the range of 2 to 3 V sample bias (tunneling to empty states) using a similar tip. The images presented here are representative of many observations on several crystals.

RESULTS

Topographic STM images showed that the cleavage surfaces of $\text{Mo}_{18}\text{O}_{52}$ (100) and $\text{Na}_{0.003}\text{V}_2\text{O}_5$ (010) are flat over hundreds to thousands of angstroms in each direction. For each material, higher resolution images reveal contrast that has, within the errors caused by thermal drift, the periodicity of the planar repeat unit of the bulk structure.

A characteristic image from a $50 \times 50 \text{ \AA}$ area of the $\text{Na}_{0.003}\text{V}_2\text{O}_5$ (010) surface is shown in Fig. 1c. The primary contrast in this image is due to the elevated (white) areas oriented along [100] separated by approximately 11 \AA . The height of this corrugation is 2 \AA . There is additional contrast along these rows with an approximately 3.7 \AA period. The primary contrast in images of the $\text{Mo}_{18}\text{O}_{52}$ (100) surface (see Fig. 2a) is caused by a series of steps and terraces oriented along the [010] direction with a 26 \AA period. Typically, the steps were very straight and evenly spaced, but occasional curves and variations in terrace width were observed. There is a series of bright features at the edge of each step which has an 11.8 \AA average frequency along the direction of the step. The topographic variation over these features is less than 1.0 \AA . There is also a series of rows within each step which have a periodicity of 3.8 \AA and a corrugation height of 0.4 \AA . Any additional features within these rows are incompletely resolved.

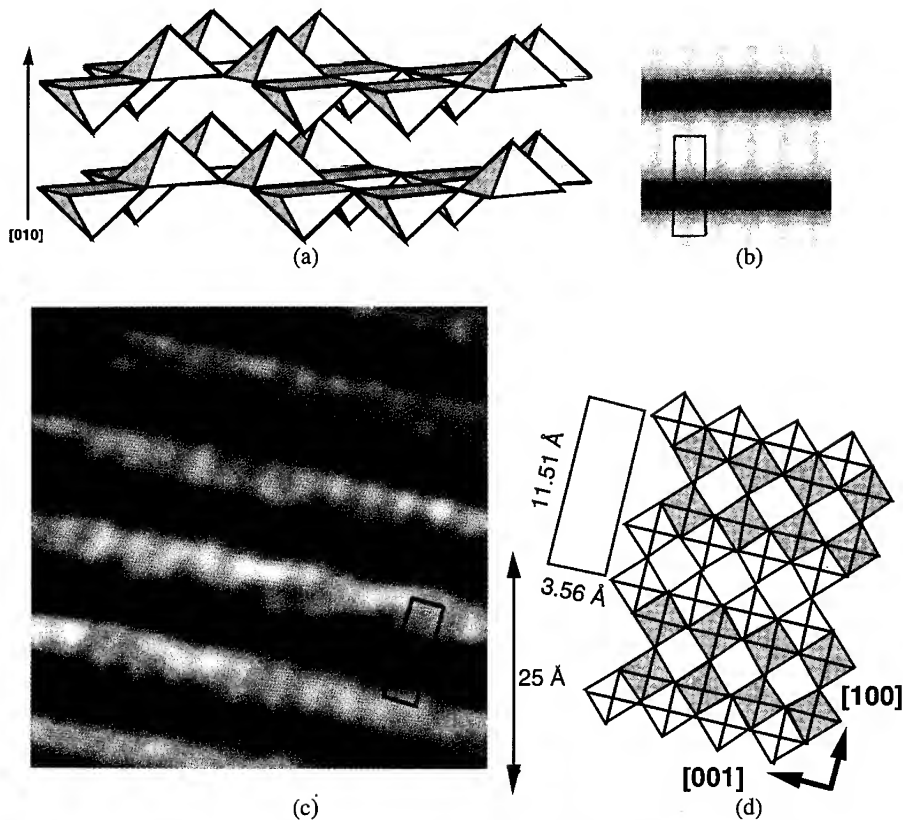


Figure 1. (a) A 3-dimensional rendering of the idealized V_2O_5 structure, composed of layers of edge- and corner-sharing square pyramids in up and down orientations. (b) A simulated constant current image of the V_2O_5 surface, $23 \text{ \AA} \times 21 \text{ \AA}$. The rectangle marks the unit cell, as in c & d. (c) A $50 \text{ \AA} \times 50 \text{ \AA}$ constant current image of the $Na_{0.003}V_2O_5$ (010) surface. The vertical resolution from black-to-white is 2 \AA . (d) A projection of the structure along [010] (not to scale). Lighter pyramids have the upward orientation, darker ones point downward.

DISCUSSION

Contrast in an STM image is determined by a convolution of the geometric positions of atoms on the surface and lateral variations in the surface density of states. Although the atomic positions are known on the basis of bulk crystallographic data, our knowledge of the electronic structure of the surface is incomplete. We can, however, assume that in both cases images were formed using electrons coming from (in the case of $Mo_{18}O_{52}$) or going to (in the case of $Na_{0.003}V_2O_5$) states in a partially filled conduction band formed by the overlap of metal d and O 2p orbitals. Considering the polarity of these materials, this band should be predominantly "d" in character and, therefore, we might expect the metal atoms to represent the bright contrast. However, we find that in each case the geometric structure of the surface is important for a consistent interpretation.

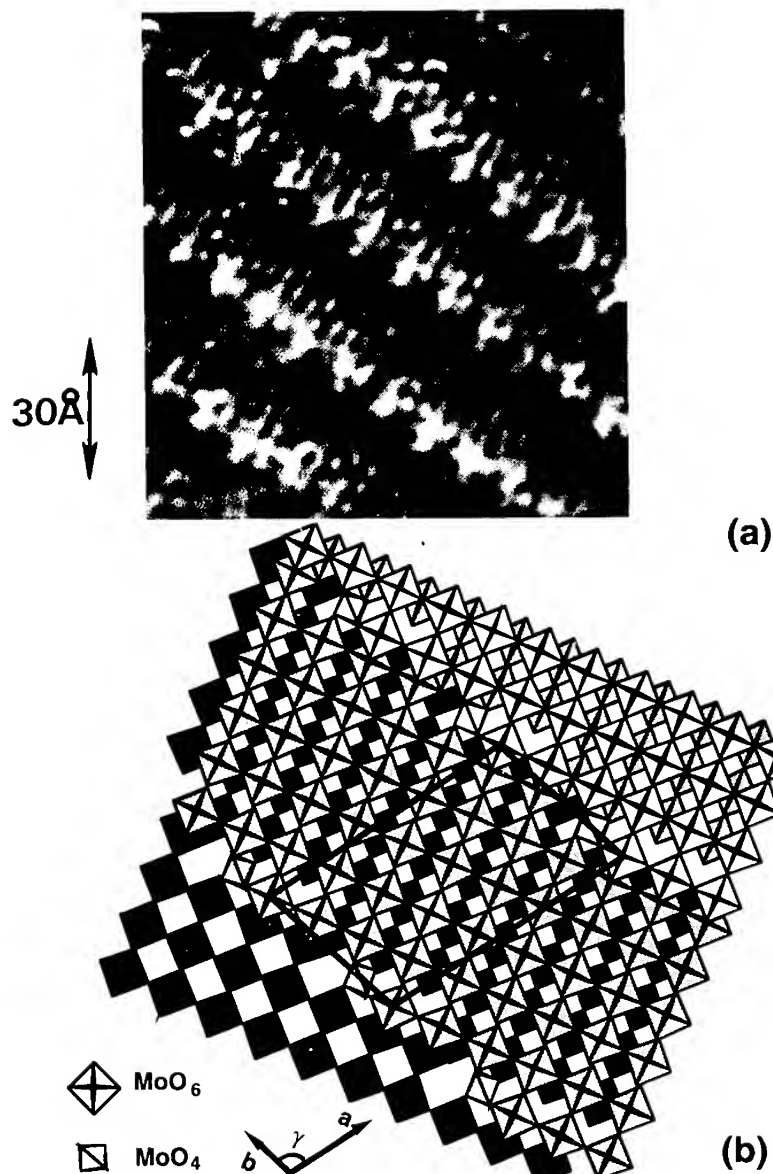


Figure 2. (a) A constant current STM image of a $110 \text{ \AA} \times 110 \text{ \AA}$ area of the $\text{Mo}_{18}\text{O}_{52}$ (100). The vertical resolution is 2.5 \AA from black-to-white, the planar repeat unit is 26 \AA along the long axis (the distance between CS planes) and 11 \AA along the short axis (the distance between tetrahedral groups at the edge of the shear step). The fine corrugations are 3.8 \AA apart, the distance between adjacent corner-sharing octahedra. (b) A structural model (not to scale) of the surface with polyhedra shaded according to their vertical height, darker ones being lower.

Considering the projection of the $\text{Na}_{0.003}\text{V}_2\text{O}_5$ (010) surface shown in Fig 1d, there are two structural features that could cause the white contrast in the image. The first are the pairs of vanadyl O that cap the square pyramids in the upward orientation. The second are the pairs of exposed V atoms at the bases of the inverted pyramids. Based only on the electronic structure, one might conclude that it is the V atoms. However, based on the facts that the O 2p states make some contribution to the conduction band, that the O ions are larger than the V ions, and that the O ions are elevated 2.5 Å above the plane of the V atoms, we expect the O ions to make a greater contribution to the tunneling current than the V. In order to quantify these suggestions, we have calculated the tunnel current as a function of the lateral and vertical position over the surface assuming that the tunnel current is given by the sum of contributions from each atom according to:

$$I = \sum_i D_i \exp(-1.025 S_i \sqrt{\phi}) \quad (1)$$

For the tunneling barrier height, ϕ , we take a characteristic value determined by measurements of the dependence of I on S_i . This variable acts as a scale factor and changes only the overall vertical corrugation of the image without effecting its appearance after normalization. S_i is defined as the distance between the surface of the tip (a sphere with radius r_{tip} = the radius of a Pt atom) and the surface of the i^{th} atom which is a hard sphere whose size is defined by the ionic radius. Although not explicitly in the equation for the tunneling current, the tip radius influences the current through its effect on the separations, S_i . Based on the polarity of the structure, D_i , the relative contribution of the i^{th} atom to the total density of electronic states in the conduction band, was taken to be 1 for V and 0.1 for O. A more complete explanation of this model appears in ref. [10]. After the current has been determined at each position, constant current images can be easily extracted and displayed as shown in Fig 1b. In this simulated image, the white contrast corresponds to the O atoms at the peaks of the square pyramids. Based on the qualitative similarity of the experimental and computed image, we conclude that the white contrast comes from pairs of incompletely resolved square pyramids in the upward orientation.

Contrast in images of the $\text{Mo}_{18}\text{O}_{52}$ surface can be interpreted based on the bulk crystal structure which has been specified by Khilborg [11]. Based on their spacing and orientation with respect to other features, we conclude that the lines of contrast with the 26 Å periodicity are the surface/CS plane intersections that define the boundaries of the unit cell. Between the CS planes the structure of $\text{Mo}_{18}\text{O}_{52}$ is nearly identical to MoO_3 . The small O deficiency of $\text{Mo}_{18}\text{O}_{52}$ with respect to MoO_3 is accommodated by these structural elements. Using the bulk structure as a model, the vertical displacement between two terraces separated by a surface/CS plane intersection should be 1.7 Å. Measured vertical displacements on the image vary from 1.5 to 2.5 Å, depending on the point of measurement.

The 3.8 Å period of the contrast within the terraces correlates with both the positions of the Mo atoms and the apical O atoms that cap the MoO_6 octahedra. Without attempting to deconvolute the competitive effects of the greater contribution of the Mo atoms to the conduction band states and closer proximity of the O atoms to the tunneling tip, we will simply assume that it is the MoO_x group as a whole that is responsible for the contrast. This interpretation is consistent with explanations of the contrast in STM images of alkali molybdate bronzes, related compounds which can also be considered as arrangements of MoO_x polyhedra [12-14]. Thus, we assign the 3.8 Å periodicity to the rows of corner sharing MoO_6 octahedra in each terrace (see Fig. 2b). This assignment leads to an explanation of the bright contrast that occurs with an 11.8 Å period at the end of every third row of octahedra. The position and frequency of these spots correspond to the only positions on the surface where MoO_4 tetrahedral units occur. One possible reason for the pronounced contrast difference between the tetrahedral and octahedral units, based solely on geometric considerations, is that while a Mo atom in the octahedral environment is well shielded from the tip by the apical oxygen, in the tetrahedral unit there is a direct line between it and the tip which might lead to

an enhanced local density of electronic states and the enhanced corrugations. In any case, the two coordination polyhedra are clearly discriminated.

CONCLUSION

The contrast in STM images of the surfaces of layered oxides such as $\text{Na}_0.003\text{V}_2\text{O}_5$ and $\text{Mo}_{18}\text{O}_{52}$ can be interpreted based on comparisons with the bulk structure. Through such comparisons, we have determined that square pyramids with the upward orientation (oxygen atoms) are the source of white contrast on the STM images of the $\text{Na}_0.003\text{V}_2\text{O}_5$ (010) surface and that the surface/CS plane intersection, octahedral MoO_6 groups, and tetrahedral MoO_4 groups can all be distinguished on the (100) surface of $\text{Mo}_{18}\text{O}_{52}$. In each of these cases, it was found that the atoms closest to the tip dominate the image contrast. The identification of contrast from the structural elements of these ordered surfaces will aid in the interpretation of contrast from images of defective surfaces.

ACKNOWLEDGMENTS

This work was supported by the National Science Foundation under Grant DMR-9107305.

REFERENCES

- [1] J. E. Germain, in Adsorption and catalysis on Oxide Surfaces, edited by M. Che and G. C. Bond (Elsevier, Amsterdam, 1985) p. 355.
- [2] J. Haber, in Solid State chemistry in Catalysis edited by R. Grasselli and J. Brazdil (American Chemical Society, Washington D.C., 1985) p. 1.
- [3] G. S. Rohrer, V. E. Henrich, and D. A. Bonnell, *Science* **250**, 1239 (1990).
- [4] R. Wiesendanger, I. V. Shvets, D. Bürgler, G. Tarrach, H. J. Güntherodt, J. M. D. Coey, and S. Gräser, *Science* **255**, 583 (1992).
- [5] T. Matsumoto, H. Tanaka, T. Kawai, and S. Kawai, *Surface Science Letters*, **278**, L153 (1992).
- [6] W. Lu, N. Nevins, M. L. Norton, and G. S. Rohrer, *Surface Science* **291**, 395 (1993).
- [7] G. S. Rohrer, W. Lu, R. L. Smith, and A. Hutchinson, *Surface Science* **292**, 261 (1993).
- [8] O. Bertrand, N. Floquet and D. Jacquot, *J. of Crystal Growth* **96**, 708 (1989).
- [9] P. Hagenmuller, J. Galy, M. Pouchard, and A. Casalot, *Mat. Res. Bull.* **1**, 45 (1966).
- [10] G. S. Rohrer, W. Lu, M. L. Norton, M. A. Blake, and C. L. Rohrer, in press *J. Solid State Chemistry*.
- [11] L. Kihlborg, *Ark. Kemi* **21**, 443 (1963).
- [12] J. Heil, J. Wesner, B. Lommel, W. Assmus, and W. Grill, *J. Appl. Phys.* **65**, 5220 (1989).
- [13] E. Garfunkel, G. Rudd, D. Novak, S. Wang, G. Ebert, M. Greenblatt, T. Gustafsson, and S. H. Garofalini, *Science* **246**, 99 (1989).
- [14] U. Walter, R. E. Thomson, B. Burk, M. F. Crommie, A. Zettl, and J. Clarke, *Phys. Rev. B* **45**, 11474 (1992).

CHARACTERIZATION OF InP/GaInAs NANOMETER SIZED COLUMNS PRODUCED BY AEROSOL DEPOSITION AND PLASMA ETCHING

I. MAXIMOV, K. DEPPERT, L. MONTELius, L. SAMUELSON, S. GRAY*,
M. JOHANSSON*, H.-C. HANSSON**, and A. WIEDENSOHLER**

Department of Solid State Physics, Lund University, Box 118, S-221 00 Lund, Sweden

*Department of Synchrotron Radiation Research, Lund University, Box 118, S-221 00 Lund,
Sweden

**Department of Nuclear Physics, Lund University, Sölvegatan 14, S-223 62 Lund, Sweden

ABSTRACT

We present a technique for the fabrication of InP nano-columns and GaInAs/InP quantum-dots based on the use of sintered aerosol Ag particles as a mask in an electron cyclotron resonance etching process. The sintered particles have much more regular shapes than the unsintered ones used in previous studies and are more resistant to the etching environment, which results in the formation of more regular and reproducible structures. For example, we have been able to produce columns 100 nm in height which have an average diameter of 24 nm and a density of 10^9 cm^{-2} . We have investigated the shape of the etched columns as a function of the Ag particles' size, and characterized their electrical and optical properties using a combination of scanning electron microscopy, scanning tunneling microscopy, atomic force microscopy, and photoluminescence.

INTRODUCTION

Recently we reported a technology for production of quantum-dot (QD) structures without using lithographic methods. This technique allowed the fabrication of QD structures in large quantities, reaching densities of 10^9 cm^{-2} [1]. We demonstrated the feasibility of fabricating QD structures using GaInAs/InP heterostructures containing several quantum-wells (QW) and have shown that QDs produced in this way are optically active [2,3]. However, the typical size of these columns was about 80 nm which is too large for quantum-confinement effects to be pronounced. Attempts to reduce the size by using an additional wet etching procedure were only partly successful. The main obstacle was the irregular shape of the aerosol particles which lead to a large variability in the diameters of the columns.

In this work we have characterized InP columns produced using a technique which introduces a sintering step to reshape the aerosol particles in a nitrogen atmosphere before depositing them onto the InP surface. The reshaped Ag particles have a higher stability during plasma etching than the unsintered ones observed previously [3]. Low energy dry etching in a methane/hydrogen/argon plasma produces columns of correspondingly uniform size and shape which have a "survival rate" (the ratio of the number of columns to the number of particles) close to 100%. We have produced columns with diameters which vary between 20 and 40 nm and which have heights of about 100 nm.

EXPERIMENTAL

We performed the present experiments using an aerosol generator set-up similar to that used in previous studies [1-3], based on the generator described in ref. 4. We modified the previous set-up by introducing a second tube furnace which sinters the aerosol particles after particle size selection has occurred in the first differential mobility analyzer (DMA). Also, a second DMA was added after the new furnace to ensure a narrow size distribution of the reshaped particles. Finally, the whole process was run with nitrogen as the carrier gas to avoid oxidation of the silver particles. Fig. 1 shows a schematic diagram of this improved set-up.

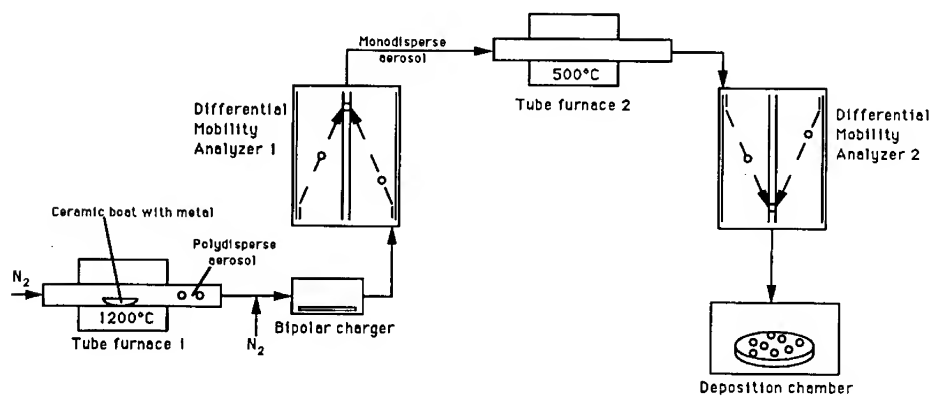


Figure 1. Schematic diagram of the improved aerosol set-up.

Tube furnace 1 was kept at a temperature of 1200°C so as to produce a sufficient concentration of Ag particles with a size below 50 nm. Tube furnace 2 was operated between room temperature and 600°C. Before entering the second furnace, aerosol particles with a certain mobility diameter were selected by the first DMA. The second DMA was used both for measuring the size distribution of the sintered, monodispersed aerosol and for selecting a narrow size range for particle deposition. Both DMAs were run at 10 l/min sheath N₂. The particles were deposited on the substrate in the deposition chamber by a perpendicular electric field.

For substrates we used both (001)-oriented, n-type InP and GaInAs/InP QW structures with two QWs of different thickness grown by low pressure metal organic vapor-phase epitaxy. Growth was performed at a pressure of 50 mbar and with a temperature in the range 560-600°C.

The samples were etched using an electron cyclotron resonance metal organic reactive ion etching (ECR-MORIE) system described in detail elsewhere [3]. The etching was carried out with a radiofrequency bias of -90V, a microwave power of 300 W, and CH₄, H₂ and Ar flow rates of 3.2, 3.0 and 1.2 ml/min respectively. These conditions gave a controllable and smooth etching rate of 5 nm/min.

The silver particles and etched out columns were characterized using a combination of high resolution scanning electron microscopy (SEM), atomic force microscopy (AFM) and scanning tunneling microscopy (STM).

RESULTS AND DISCUSSION

Sintering fuses the microcrystallites within the particles [2], thereby leading to particle shrinkage. Sintering temperatures as low as 200°C result in a shift of the particles' size distribution to smaller diameters; for example, unsintered particles of 40 nm are reduced in size to 33 nm. However, the most important effect of sintering is to change the particles' shape from irregular to spherical, as has been observed by SEM [5].

Fig. 2.a shows an SEM image of aerosol Ag particles 33 nm in diameter deposited on InP. These particles were produced by sintering at 500°C followed by size selection in the second DMA. The particles are remarkably spherical, in contrast to previous results [2,3]. ECR-MORIE of these structures for 15 min resulted in InP columns about 100 nm high with an average diameter of 24 ± 5 nm. Fig. 2.b shows a side view of the columns. The "survival rate" was found to be close to 100% compared to the 50-60% found for unsintered particles etched under similar conditions [3].

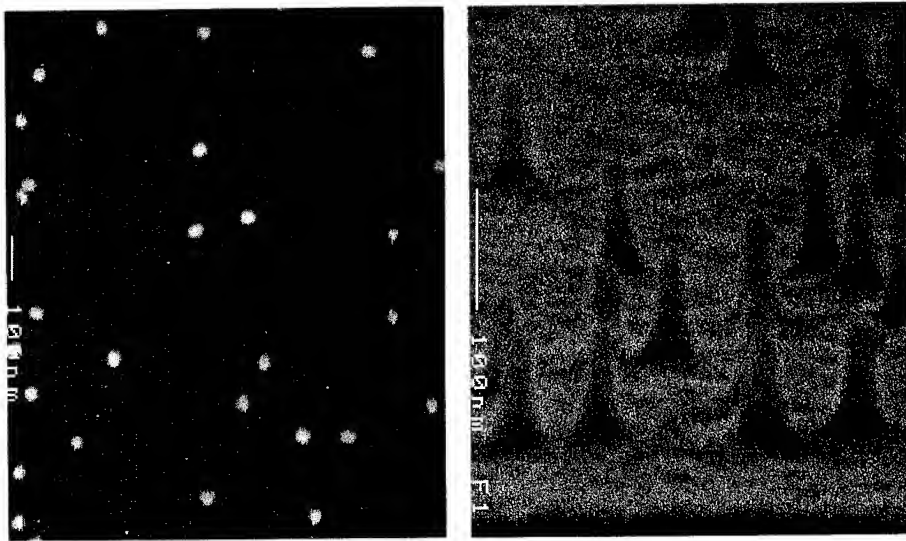


Figure 2. a) SEM picture of sintered (500°C) 33 ± 2 nm aerosol Ag particles deposited onto InP.
b) ECR-MORIE produced columns 24 ± 5 nm in diameter and about 100 nm in height.

The stability of the sintered aerosol Ag particles was found to be critically dependent on the presence of oxygen during the sintering process. Sintering in air did produce spherical particles, but their survival rate during etching was low, probably due to the formation of silver oxide which is less stable in the etching environment.

The size of the aerosol particles determines the diameter and shape of the etched out columns. Fig. 3 illustrates the dependence of mean column diameter on particle size. For sizes about or below 30 nm the etched columns are conical, indicating that thinning of the top part of the column has taken place. In contrast, a predominantly cylindrical shape was observed for particles in the 40-50 nm range. The mean diameter of columns produced using ≈ 30 nm Ag particles is about 20 nm while under the same etching conditions ≈ 40 nm particles result in columns 40 nm in diameter. Etching the samples containing GaInAs QW structures produced columns similar in shape to those with InP substrates.

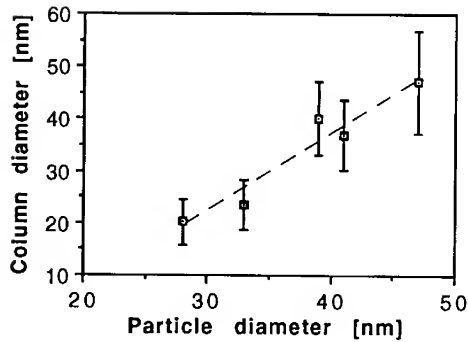


Figure 3. Mean diameter of the InP columns Vs. diameter of the Ag particle-masks. For particles of 30 nm or smaller the column diameter is in the 20 nm range indicating some degree of thinning during the 15 minute long etching process.

One would expect there to be a difference between the optical and electronic properties of these nanometer-scale columns and those of the bulk semiconductor. In the InP columns surface-induced depletion of electrons should occur, as well as some widening of the band gap caused by quantum confinement. The QW structures should display QD characteristics since the wells are laterally constrained by the walls of an etched column.

We used STM and AFM to characterize an etched InP sample. Both microscopy techniques suffer from the fact that the normal 100 nm columns are sharper than the macroscopic profile of the tip, and thus the topographs produced often contain artifacts which are images of the tip rather than the surface. Worse, if the columns are too tall or densely packed the tunnel tip or force probe never images the substrate, since some part of the tip or probe is always in contact with the top of a column. To avoid this problem a sample was made which had shorter columns: this used 29 nm Ag particles as a mask to produce columns that were approximately 50 nm tall.

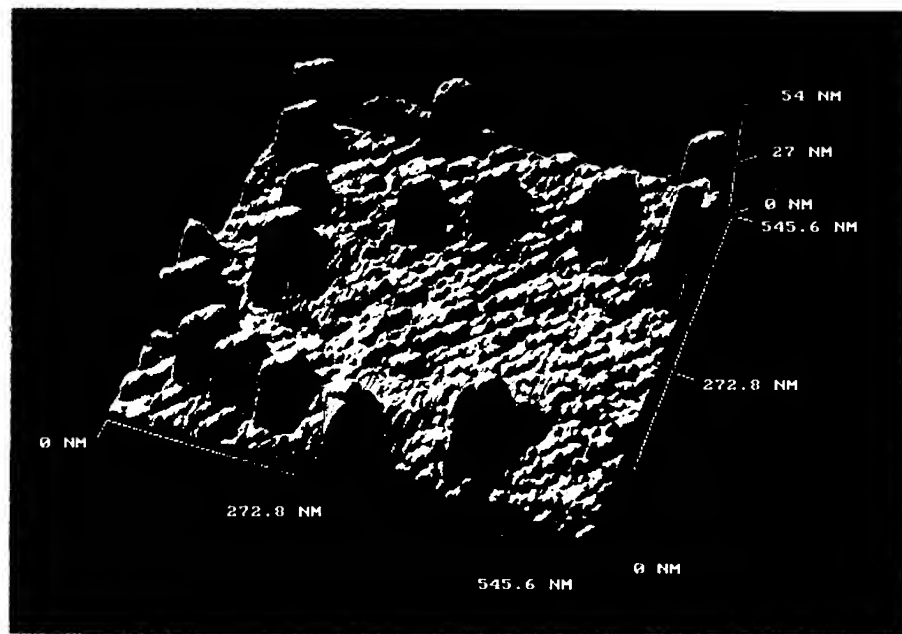


Figure 4. AFM view of the etched sample with InP columns.

Fig. 4 illustrates the topography of the sample as observed by AFM. The measured size and density of the columns agree well with SEM measurements, and although the profiles of the sides of the columns are distorted by the tip-imaging mentioned above, their measured heights are not, and can be measured with a greater accuracy than with the SEM.

With the STM we were also able to observe features whose morphology agrees well with that seen in the SEM (Fig. 5.a), although again the measured topography is a convolution of the tip and sample, and here what look like substrate grains are in fact mostly images of the tip. Despite this distortion, we can use the topograph unambiguously to identify the columns for spectroscopic analysis.



Figure 5. a) 200nm x 200nm STM topograph of the InP column ($I_{tip}=0.05$ nA, $V_{tip}=-2.1$ V, Black-White = 50nm) b) Barrier height image of the same area. ($Z_{mod} = 0.025\text{\AA}$, Black-White = 0.6V).

Fig. 5.b shows barrier height data taken simultaneously with the topograph using a tunnel-gap modulation technique [6]. This measurement gives an estimate of the sample's work function, but is also affected by the slope of the surface. As expected, the grains of the substrate appear brighter on one side, but the much steeper slope of the side of the column is not nearly so bright, and the whole column is obviously darker than the surrounding substrate. The data indicate that the column has a barrier height that is on average only 60% of that of the substrate.

I-V curves were taken on both the columns and the substrate surface using a "fast" spectroscopy method, in which the feedback loop is momentarily disabled and the tip-sample bias ramped. Fig. 6 shows $d(\ln I)/d(\ln V)$ plots formed by averaging the logarithmic differential of IVs taken at four different set point currents. The individual IVs were themselves the average of 400 separate curves, measured at different positions on the substrate or column.

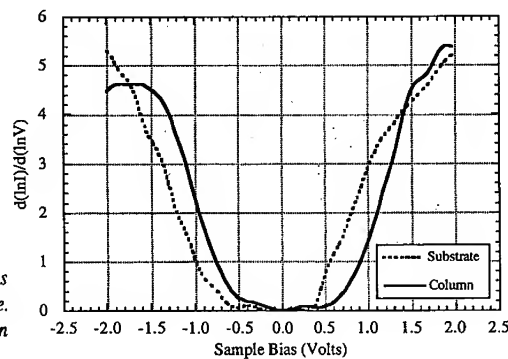


Figure 6. Current - voltage characteristics obtained on the column and the InP substrate. Curves are averages of $d(\ln I)/d(\ln V)$ data taken at $V_{tip}=-2.0$ V, $I_{tip}=0.1, 0.5, 1.0$ and 5.0 nA.

Both the column and the substrate display a clear band gap, as well as some evidence of states in the gap, as would be expected from a relatively rough surface. The band gap of the column appears to be slightly larger than that of the substrate. The Fermi level ($V_{sample} = 0$) has also shifted down with respect to the band edges, which is consistent with electron depletion within the column. This data therefore confirms the expected change in electronic properties of the InP columns, although more investigation is required to show that the observed differences are due to the shape of the columns and not simply to differences in the structure or chemical composition of the immediate surface layer. What is certain is that the IVs are not indicative of tunneling to metallic silver, which implies that the Ag particle was destroyed during the etching process, in agreement with SEM observations.

An InP/GaInAs QW structure was used as the starting material for making QDs using sintered Ag particles and ECR-MORIE. Preliminary photoluminescence data has shown that 40 nm QDs are optically active. Details of optical measurements will be reported elsewhere.

CONCLUSIONS

A sintering technique has been used to reshape aerosol Ag particles in order to produce stable etching masks for ECR-MORIE. Previous studies of aerosol-defined columns have suffered from the fact that the particles are irregularly shaped and do not resist the etching process well. The sintered particles have a more spherical shape and are more effective when used as masks. The stability of sintered Ag particles which are more than 33 nm in size is sufficient to produce 70-100 nm high columns without severely thinning their tops. SEM was used to investigate the dependence of the column diameter on particle size. STM spectroscopy revealed that in InP nano-columns both electron depletion and a slight widening of the band gap occur. PL data show that GaInAs QDs embedded in 40 nm wide InP columns are optically active.

ACKNOWLEDGEMENTS

The work was performed within the nm-Structure Consortium in Lund and supported by grants from the Swedish National Board for Industrial and Technical Development (NUTEK). The authors wish to thank W. Seifert for supplying the QW samples and D. Hessman for photoluminescence measurements.

REFERENCES

1. A. Wiedensohler, H.-C. Hansson, I. Maximov, and L. Samuelson, *Appl. Phys. Lett.*, **61**, 837 (1992).
2. L. Samuelson, I. Maximov, A. Gustafsson, X. Liu, W. Seifert, H.-C. Hansson, and A. Wiedensohler, *Mat. Res. Soc. Proc.*, **283**, 789 (1993).
3. I. Maximov, A. Gustafsson, H.-C. Hansson, L. Samuelson, W. Seifert, and A. Wiedensohler, *J. Vac. Sci. Technology A*, **11**, 748 (1993).
4. H. G. Scheibel and J. Porstendörfer, *J. Aerosol Sci.*, **14**, 113 (1983).
5. K. Deppert, H.-C. Hansson, I. Maximov, L. Samuelson, and A. Wiedensohler, submitted to *Appl. Phys. Lett.* (November 1993).
6. J. Tersoff and N. D. Lang in *Scanning Tunneling Microscopy*, edited by J. A. Stroscio and W. J. Kaiser (Academic Press, San Diego, 1993) p. 20.

NANOMETER SCALE STRUCTURES RESULTING FROM GRAPHITE OXIDATION

Marilyn J. Nowakowski*, John M. Vohs**, and Dawn A. Bonnell*

*Department of Materials Science and Engineering, **Department of Chemical
Engineering, University of Pennsylvania, Philadelphia, PA 19104

ABSTRACT

Scanning tunneling microscopy (STM) and spectroscopy (STS) were used to characterize highly oriented pyrolytic graphite (HOPG) which was oxidized by two different methods, furnace heating in atmosphere and immersion in oxygen plasma. The character of the surfaces was found to be dissimilar on a micron scale but comparable on a nanometer scale, at which both appear to be comprised of sharp step edges. Variations in local electronic structure near a step edge were compared.

INTRODUCTION

The many forms of carbon, including graphite, fibers, and carbon-carbon composites, have great potential in industrial applications that is limited by instability in oxidizing environments. Early work on the gasification of graphite as studied by transmission electron microscopy (TEM) and scanning electron microscopy (SEM) has been extensive [1-3], shedding light on the oxidation process. It has been observed that atomic oxygen will affect the basal plane directly. The atomic oxygen attacks in an isotropic fashion, resulting in comparable rates of interplanar and planar graphite recession, whereas molecular oxygen will mostly affect edges and defects. This previous work is based on observations on the micron scale. More recently, the modes of plane recession from molecular oxygen exposure have been categorized basically as attack at point defects causing monolayer pit formation, and attack at line defects forming deep hexagonal holes [4].

The rates of oxidation at edges of the basal planes are sensitive to the local structure of the edge site. Multilayer pits are likely to have a different edge geometric and electronic structure than do monolayer pits. Additionally, different methods of gasification are expected to result in different types of surface morphology. In this study, the effects of oxidation by immersion in oxygen plasma are compared to the effects resulting from heating graphite in air, comparing effects resulting from atomic and molecular oxygen. Scanning tunneling microscopy (STM) is used in order to characterize the surface features on both the micron and nanometer scale. Scanning tunneling spectroscopy (STS) is used to examine the differences in electronic structures of the basal plane and near a monolayer step edge.

EXPERIMENTAL PROCEDURES

Oxidized samples of highly oriented pyrolytic graphite (HOPG) were prepared by two different methods: furnace heating and exposure to an oxygen plasma. In the first method, freshly cleaved samples of HOPG were placed in a preheated furnace at 1000°C and heated in air for 3 min., and at 950°C for 4 min. The second method was invoked to expose HOPG samples to atomic oxygen. A freshly cleaved HOPG sample was placed in an evacuated chamber, which was then filled to approximately 10⁻⁶ torr O₂ at room temperature. An RF voltage was applied across the chamber to create a plasma, in which the sample was immersed for 15 min.

Topographical STM (Digital Instruments Nanoscope III) data was acquired on both samples using a 1.6 nA tunneling current and 50mV bias voltage for the furnace heated sample, and at 300 pA tunneling current and 30mV bias voltage for the plasma treated sample. Spectroscopy data was acquired in UHV (WA Technology) using 700pA and 70mV for the setpoint at which the feedback circuit operated between acquisitions. Current data collected as a function of voltage was converted to $dI/dV^*(V/I)$ format and then smoothed.

RESULTS AND DISCUSSION

The production of pits in the surface of graphite as a function of heating in an oxidizing environment has been observed by STM [4,5]. Figure 1 shows a constant-current image of HOPG heated for 3 min. at 1000°C. Along with a large multilayer hexagonal pit, many monolayer steps can be seen which appear as scalloped edges. These were believed to be initiated from steps formed during the cleaving process. These edges were attacked in a circular form in contrast to the relatively straight edge recession seen by Chu et al. [4]. The difference in morphology is probably due to the higher temperature treatment in our case.

The growth rate of hexagonal multilayer pits has been observed to be approximately 4 times higher than that of circular monolayer pits [4]. The image in Figure 2 shows a circular pit formed at the bottom of a hexagonal multilayer pit. Assuming this hexagonal pit has formed through recession perpendicular to a line defect, as suggested by Chu, this image is evidence that in this case the line defect has terminated, allowing a vacancy in the bottom layer to be exposed and subsequent monolayer growth to occur. If the line defect had not terminated, the growth of the hexagonal pit would have obscured the observation of the monolayer pit growth.

Figure 3 shows a HOPG sample treated by oxygen plasma. On the micron scale it appears that the character of the surface is significantly different than that of furnace treated samples, i.e., uniform pits are not observed. Rather, depressions of isotropic dimensions on the order of 100 nm are observed with no distinct shape. This type of surface morphology is consistent with direct basal plane attack. Figure 4 displays the same sample on a smaller scale. It is clear from this image that the treated surface exhibits the same type of step and edge character on the nanometer scale as does the heat treated samples. Distinct sharp step edges are observed, as opposed to any amorphization of the surface, as might be inferred from Figure 3. Examination of line



Figure 1. STM image of HOPG heated to 1000°C for 3 min.

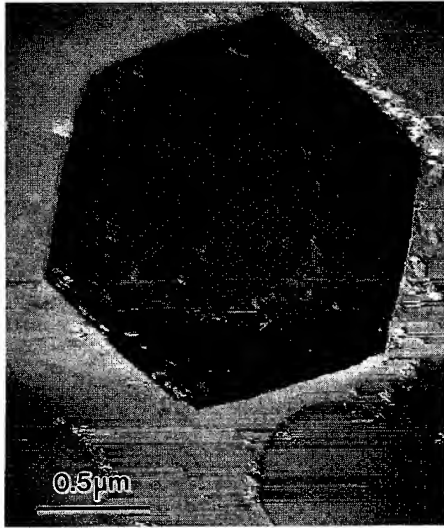


Figure 2. STM image of HOPG heated to 950°C for 4 min.

profiles reveals that the steps are up to 20 atomic layers high, with the most being around 10 layers high. The edges of these holes, then, most likely recede in the multilayer fashion.

Previous high resolution electron energy loss spectroscopy (HREELS) studies of plasma treated HOPG show that the predominant oxygen surface complex existing above 727°C involves a carbon-oxygen double bond [6]. Because of the similarity in the topographies on the nanometer scale of the heated and plasma treated HOPG surfaces, it is likely that this same species exists on the furnace heated sample.

Tunneling spectroscopy is used to reveal information about spatial variation in electronic structure. As has been seen previously [7], spectra taken on cleaved graphite exhibit anisotropy about zero volts in the range -1.0 to +1.0 V. Figure 5 shows tunneling spectra for an oxidized HOPG sample heated to 1000°C for 5 min. Figure 5(a) was acquired near a single monolayer step on the surface, and (b) on the step terrace. There is a distinct difference in features, and the difference is likely due to the changes in electronic structure associated with configuration of a step and the possible presence of an oxygen species. Atamny et al. [7] have associated increases in state densities with graphite structural defects.



Figure 3. STM image of oxygen plasma treated HOPG.



Figure 4. STM image of oxygen plasma treated HOPG

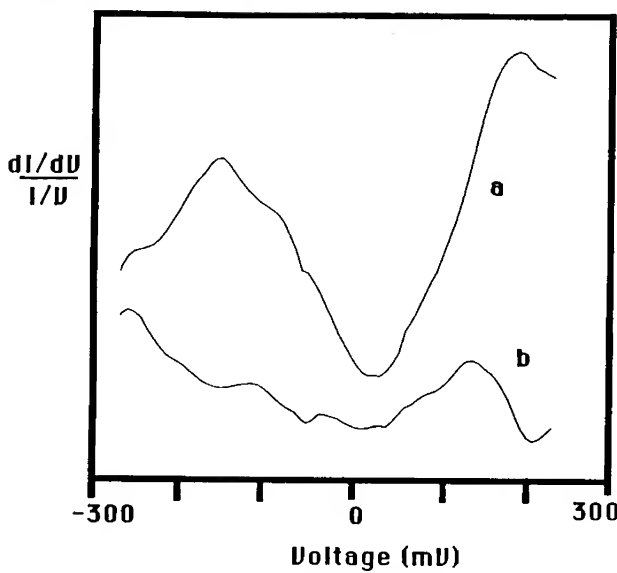


Figure 5. Current-voltage curves acquired (a) near a monolayer step, and (b) on the step terrace, of a heat treated HOPG surface.

SUMMARY

The surface morphologies of HOPG oxidized by two different processes, furnace heating in air and exposure to an oxygen ion plasma, were compared using STM. On a micron scale, the heat treatment resulted in pitting of the surface, causing multilayer hexagonal pits and circular monolayer pits, while the plasma treatment resulted in deep isotropic holes. Although the surfaces appear to be different on that scale, both are seen to exhibit a distinct sharp edge character on the nanometer scale. It is likely then that the plasma pitting is caused by atomic oxygen attacking the basal plane, and proceeds by multilayer recession. Local electronic structural variations near a step edge were observed.

ACKNOWLEDGMENTS

This work was supported by the Air Force Office of Scientific Research, Division of Chemistry and Materials under grant #AFOSR-91-0103.

REFERENCES

1. R. T. Yang, in Chemistry and Physics of Carbon, edited by P. L. Walker, Jr., and P. A. Thrower, Vol. 19 (Marcel Dekker, New York , 1984), pp.163-210.
2. G. R. Hennig, in Chemistry and Physics of Carbon, edited by P. L. Walker, Jr., Vol. 2 (Marcel Dekker, New York , 1966), pp.1-50.
3. G. R. Hennig, *J. Chem. Phys.* **40**, 2877 (1964).
4. X. Chu and L. D. Schmidt, *Surf. Sci.* **268**, 325 (1992); *Carbon* **29** (8), 1251 (1991).
5. H. Chang and L. J. Bard, *J. Am. Chem. Soc.* **112**, 4598 (1990); *J. Am. Chem. Soc.* **113**, 5588 (1991).
6. M. J. Nowakowski, J. M. Vohs, and D. A. Bonnell, *J. Am. Ceram. Soc.* **76** (2), 279 (1993).
7. F. Atamny, R. Schlogl, W. J. Wirth, and J. Stephan, *Ultramicroscopy* **42-44**, 660 (1992).

GRAZING INCIDENCE X-RAY REFLECTANCE MEASUREMENT OF SURFACE AND INTERFACE ROUGHNESS ON THE SUB-NANOMETRE SCALE

M. Wormington^{*†}, K. Sakurai^{*†}, D.K. Bowen^{*†} and B.K. Tanner[§]

**Centre for Nanotechnology and Microengineering, Department of Engineering, University of Warwick, Coventry CV4 7AL, UK*

†Bede Scientific Software Division, University of Warwick Science Park, Coventry CV4 7EZ, UK

§Department of Physics, University of Durham, Durham DH3 1LE, UK, and Bede Scientific Instruments Ltd, Bowburn, Durham DH6 5PF, UK

†On leave from National Research Institute for Metals, Tsukuba, Japan

ABSTRACT

Grazing incidence X-ray reflectivity may be used to measure surface topography including roughness and correlation lengths to sub-nanometre precision. A study is made of a technically important surface, a carefully-polished specimen of Zerodur glass-ceramic, which has been measured by diffuse scatter of CuK_α X-radiation and atomic-force profilometry methods. The data have been analysed in terms of a fractal representation of the surface correlation function. Results from the two methods agreed within their estimated errors, with the X-ray data showing roughnesses of 1.3 nm, correlation length of 1 μm and fractal parameter (bandwidth) of 0.35. The X-ray methods have a lower cut-off length, are much more rapid for averaged information and are both non-contacting and non-destructive. They also show potential for the study of interface roughness in thin films.

INTRODUCTION

The measurement of surface topography is fundamental to engineering metrology. With the development of nanotechnology, methods are required that have sensitivity at nanometre levels and below. Both vertical and lateral sensitivity are required, thus the traditional stylus and optical instruments are no longer adequate; they provide sub-nanometre vertical resolution, but their lateral resolution is of the order of micrometres. Instruments based upon atomic-force microscopes do have sufficient resolution, but have a lower cut-off of dimensions comparable to the tip radius and hence are unsuited to the measurement of surfaces with high spatial bandwidth, for example bearing surfaces with intentionally deep cracks to retain lubricant. Methods of X-ray diffuse scatter have been shown to possess suitable sensitivity^{1,2} and are particularly useful when averaged information is required. This is increasingly becoming the case as the connections are being made between surface topography and surface function. However, the theory of diffuse scatter is mathematically quite complex, and computational methods for its interpretation have been slow, requiring some hours on a fast PC.

We have made a study of one material important to precision engineering, the ultra-stable glass-ceramic Zerodur (™ Schotts), which is widely used for astronomical telescope mirrors, metrological instruments, ultraprecision slideways and components for precision machines³. The X-ray diffuse scatter at grazing incidence has been measured, and interpreted using new high-speed algorithms which give rapid results (within seconds on a fast PC). We have also made a comparison with atomic-force profiler measurements on the same specimen as a test of the methods of interpretation. In each case we have extracted correlation functions that describe the surface topography. Finally, we show the potential of the method for interface studies.

GRAZING INCIDENCE X-RAY SCATTERING EFFECTS

Figure 1 summarises the many effects that are caused when an X-ray beam strikes the surface at grazing incidence⁴. These comprise fluorescence, diffraction, specular reflection, diffuse scatter and the evanescent wave into the surface. All of these give different information about the surface structure, but in this work we concentrate upon the diffuse scatter around the specular reflected beam. This gives information about surface topography, namely the roughness, correlation lengths and spatial bandwidth

over a range of approximately 0.1 nm to 10 μ m in lateral dimension and about 0.1 to 2 nm in vertical dimension. (There is actually no difficulty in measuring surfaces much rougher than 2 nm, but the interpretative theory is not yet available.) The lower cut-off length for X-ray information will be some fraction of the X-ray wavelength, which was 0.15 nm in this case. The upper lateral cut-off length is related to the transverse spatial coherence length of the X-ray beam, which is of the order of tens of micrometres.

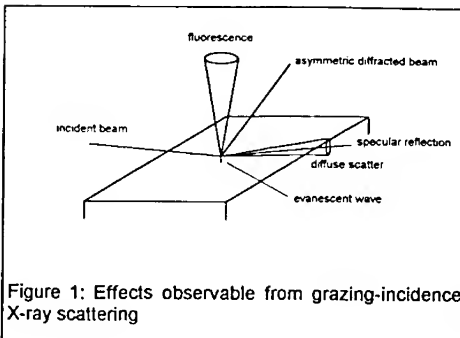


Figure 1: Effects observable from grazing-incidence X-ray scattering

EXPERIMENTAL PARAMETERS

The specimen and its preparation

The specimen was a disc of Zerodur glass-ceramic, 25 mm diameter and 5 mm thick. It was lapped with 6 μ m alumina particles on a Lapmaster 48" machine, then pitch-polished with 700 nm ceria particles on a Lapmaster 24" air-bearing polishing machine. It was then cleaned with filtered and demineralised water. No further preparation or mounting was required, either for the X-ray or AF profiler measurements.

X-ray reflectometry

The Bede GXR1 X-ray reflectometer was used⁵. This employs a CuK α conventional tube, run at 1.4 kW (40 kV, 35 mA). The novel Bede high-power asymmetric channel-cut silicon beam conditioner can provide about 10⁷ cps intensity incident on the sample after slit selection of CuK α 1 radiation, and the Bede EDR detector gave a linear range of 0.1 - 5.10⁵ cps, which was extendable with deadtime correction to about 5.10⁶ cps. The incident beam divergence was 25 arc seconds and the angular acceptance of the detector slit was set at 100 arc seconds. This instrument has a very small beam height of 40 μ m, which means that good intensities may be obtained on small samples. The instrument has automatic alignment, and ultraprecision coaxial location of specimen and detector axes.

Atomic force profiler

The Warwick University long-range AFM profiler was used. This was developed using a Rank Taylor Hobson Nanostep with the normal differential transformer sensor replaced with a capacitance-gauge AFM head of our own design. This gives AFM profiling capability over 50 mm though the scan was restricted in this case to 60 μ m, in order to get good lateral resolution with a tractable data set. The vertical and horizontal resolution were both approximately 0.7 nm, using a Berkovitch diamond tip, approximately 20 nm radius.

MEASUREMENTS OF DIFFUSE SCATTER

Figure 2 shows a full data set of scattering around the specular reflection region. The specular scattering itself occurs along the ridge at $\theta_i = \theta_s$. Diffuse scatter extends from the critical angle for incident beam to the critical angle for the exit beam, and hence occurs over a wider angle as the scattering angle increases. The secondary ridges on either side of the specular ridge are the 'Yoneda wings', due to the increased intensities found just at the critical angles for entrance and exit caused by constructive interference of the entrance and exit beams at these angles⁶. The shape of the diffuse scatter, for example the sharpness of the Yoneda wings, is governed by the roughness, correlation length and spatial bandwidth of the surface. The theory has been treated by a number of authors^{7,8}.

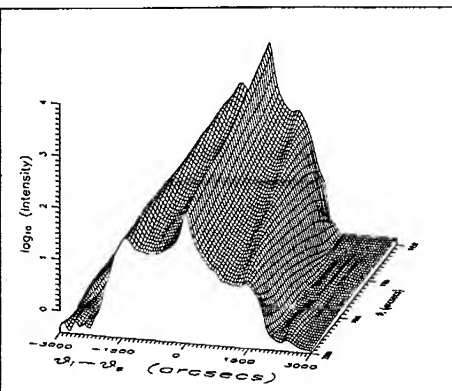


Figure 2: Diffuse scatter of Cu K α_1 X-rays from the polished Zerodur specimen. Logarithmic vertical scale.

MATCHING X-RAY THEORY WITH EXPERIMENT

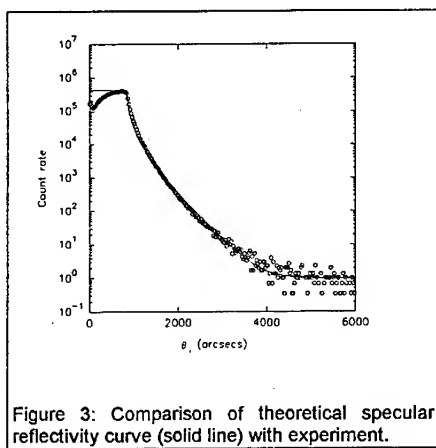


Figure 3: Comparison of theoretical specular reflectivity curve (solid line) with experiment.

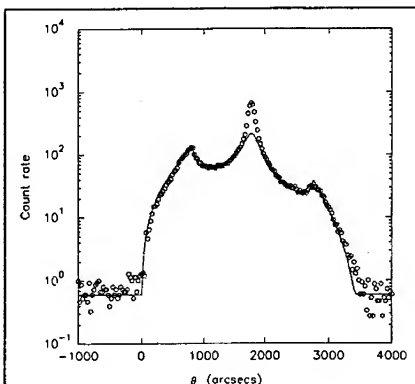


Figure 4: Comparison of theoretical diffuse scattering model (solid curve) with experiment, at one value of the scattering angle (3575 arcsecs). The data fit a fractal height-height correlation function (see Table 1).

Figure 3 shows the match between the specular reflectivity and the theoretical model, and figure 4 shows a comparison between one cross-section of the full plot of figure 2 (this is all that is needed for parameter extraction) and the theoretical model. New, rapid algorithms are used for the calculation, which enable the diffuse scatter simulations to be carried out in seconds, rather than hours, on a fast PC (these will be published separately). The model uses the distorted wave Born approximation and the detailed match takes into account specimen and beam sizes, beam

divergence and receiving slit height. Specular reflectivity is not included in the theoretical curve, hence the differences in the centre of the plot.

The simulation requires the height-height correlation function of the surface, which, following Sinha, we represent in principle by a three-parameter modified self-affine fractal model. The surface topography is described by a correlation function with a characteristic correlation length ξ and corresponding fractal parameter (bandwidth) h , i.e.

$$C(x) = \exp(-|x|/\xi^{2h}) \quad [1]$$

This function is then inserted in the key expression in the calculation of the diffuse scatter, the surface structure factor for a given scattering vector q_t , $S(q_t)$, given by:

$$S(q_t) = \frac{1}{|q_t|^2} e^{-[(q_t^x)^2 + (q_t^y)^2]\sigma^2/2} \int (e^{|q_t|^2 \sigma^2 C(x)} - 1) e^{i q_t x} dx \quad [2]$$

in which the r.m.s. roughness σ also appears. Unfortunately, the integral is difficult and time-consuming to evaluate by normal computational methods, and it is this integration that has now been implemented with high efficiency, making this simulation a practical engineering method.

ATOMIC FORCE PROFILOMETRY

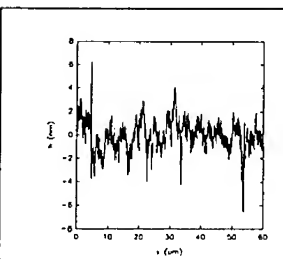


Figure 5: Typical atomic-force profiler data for the Zerodur specimen, taken over a 60 μm scan.

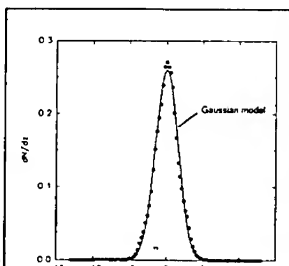


Figure 6: Height distribution function dN/dz obtained by AF profilometry.

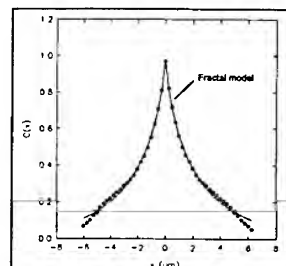


Figure 7: Height-height correlation function obtained by AF profilometry.

Figure 5 shows a typical trace on the AF profiler over a 60 μm scan. The traces are highly reproducible on this instrument. The data were used to plot the height distribution data shown in figure 6. A Gaussian model gives a good fit to the data as shown by the solid line in figure 6. The correlation function may be extracted directly from AF profiles, and is shown in figure 7. The solid line is a fractal model, as in equation 1.

There are other correlation models that will also fit these data, and the above fits are not unambiguous. We should need a large number of scans to distinguish between the models.

COMPARISON OF AFM AND X-RAY RESULTS

The parameters deduced from the two methods are shown in the table. It is encouraging that they all agree within the estimated errors.

Errors in the parameters deduced from AF profilometry arise primarily through the limited number of scans of the profiler (five 60 μm scans were taken and averaged). Those from the X-ray measurements are dominated by the detector slit size (controlling the acceptance divergence) of 40 μm in the X-ray instrument. These are not fundamental limitations. We expect to improve the profilometry in the near future by a better data-handling capability, and to sharpen the resolution

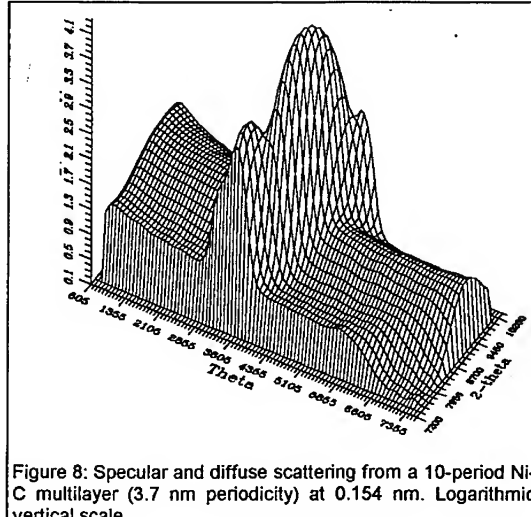
of the X-ray instrument by the use of Soller slits or an analyser crystal (of course, standard triple-axis instruments will perform these measurements with high resolution). It is encouraging that both models, dependent on quite different measurement processes and physical theory, give similar results. It may be noted that the estimated errors on the X-ray data are substantially lower than those on the AF profiler, even though the latter represents some 40,000 data points and the former only 200.

Table 1. Comparison of parameters deduced from diffuse X-ray scattering and atomic force profilometry

Parameter	Diffuse X-ray scatter	AFM profiler
Roughness σ , nm	1.3 ± 0.2	1.5 ± 0.4
Correlation length ξ , nm	1000 ± 200	2100 ± 1000
Fractal parameter h	0.35 ± 0.05	0.38 ± 0.09

INTERFACES IN MULTILAYERS

Figure 8 shows specular and diffuse scatter from a multilayer of Ni-C⁹. The large peak in the specular scattering is the first Bragg peak of the multilayer. There is a clear ridge in the diffuse scatter at the same scattering angle. This may be interpreted qualitatively as evidence of conformal roughening, on the argument that the diffuse scatter is caused by the roughening, and a peak in the diffuse scatter at the same point as the Bragg scattering indicates that the topography of one layer conforms to that of the layer below. The quantitative interpretation of the diffuse scattering data from multilayers is considerably more complex than that from simple surfaces. We shall report on this in a later paper.



with tip radius. In the AF methods, the best that can be achieved is the cross-correlation of the tip profile with the surface profile, which will clearly result in data loss.

The AFM profiles were taken over single line scans of 60 μm , whereas the X-ray data came from about 1 cm^2 . To measure the same area with AFM would require the acquisition and processing of about 100 terabytes of data! Of course, X-ray methods provide averaged information, and AFM methods provide highly localised information. The two techniques are thus complementary. Where averaged data are required, for example for predicting tribological and optical properties, and for monitoring production processes, the X-ray methods are clearly more appropriate. They are also non-contacting and non-destructive.

ACKNOWLEDGEMENTS

We acknowledge with gratitude the skilled work of Mr Rhod Mortimore in specimen preparation. We thank also Professor D.J. Whitehouse for valuable discussions on surface topography. This work was sponsored by Bede Scientific Instruments Ltd. and by the Department of Trade and Industry and the Science and Engineering Research Council under the UK LINK Nanotechnology Programme.

REFERENCES

- ¹ W. Weber and B. Lengeler, *Phys. Rev. B* **46** 7953 (1992)
- ² S.K. Sinha, E.B. Sirota, S. Garoff and H.B. Stanley, *Phys. Rev. B* **38** 2297 (1988)
- ³ S.T. Smith and D.G. Chetwynd, *Fundamentals of Ultraprecision Mechanism Design*, Gordon and Breach 1992
- ⁴ D.K. Bowen, *Advances in X-ray Analysis* **36** 171 (1993)
- ⁵ N. Loxley, A. Monteiro, M.L. Cooke, D.K. Bowen and B.K. Tanner, *Mat. Res. Soc. Symp. Proc.* **240**, 219-224 (1992)
- ⁶ Y. Yoneda, *Phys. Rev.* **131** 2010 (1963)
- ⁷ S.K. Sinha, *Physica* **B173**, 25 (1991)
- ⁸ R. Pynn, *Phys. Rev. B* **45**, 602 (1992)
- ⁹ B.K. Tanner and J.M. Hudson, *IEEE Trans. Magnetics* **MAG28** 2736 (1992)
- ¹⁰ D.J. Whitehouse, *Annals of CIRP* **1** 641 (1993)
- ¹¹ B. Lengeler, *Advances in X-ray Analysis* **35A** 127 (1993)

Size-effect Stabilization of the Low-T Ferroelectric Phase in Nanocrystalline WO_3

Xiang-Xin Bi¹, W. T. Lee¹, Kai-An Wang², D. F. Collins³, S. Bandow⁴ and P. C. Eklund^{1,2}

¹Center for Applied Energy Research, ²Department of Physics and Astronomy, University of Kentucky, Lexington, KY40511-8433, USA

³Department of Physics, Warren Wilson College, Asheville, NC 28815, USA

⁴Instrument Center, Institute for Molecular Science, Myodaiji, Okazaki, 444 Japan

Abstract *Using a CO_2 laser to drive the pyrolysis of $W(CO)_6$ and O_2 , we have synthesized nanocrystalline WO_{3-x} particles. These nanopowders are found to exhibit a narrow size distribution with an average particle size produced in the range 5 to 10 nm, depending on the experimental conditions. Typical production rates are ~ 2 g/h. Results from a Raman scattering study on WO_3 nanopowder samples annealed in O_2 indicate that a smaller particle size appears to stabilize the low-T ferroelectric phase (< -40 °C) at room temperature.*

CO_2 Laser pyrolysis (LP)^[1] involves the nucleation and growth of particles from a gas phase reaction in a small reaction zone defined by the intersection of a vertical reactant gas stream and a horizontal laser beam, as indicated in Fig. 1. Thermal energy is provided by a CO_2 laser beam which is coupled optically to a rotational/vibrational band in at least one of the gas species present. This approach to ultrafine particle synthesis utilizes the unique advantage of a spatially well defined laser beam to form a reaction zone as small as $1 \times 1 \times 0.1$ mm³ which is isolated from the walls of the reaction chamber by argon gas. The flow rate of the reactant gases through the reaction zone leads to heating and cooling rates on the order of 10^5 - 10^6 °C/s, so it is reasonable to expect that particle growth may not in many instances occur by equilibrium thermodynamics^[2]. Also the high cooling rates might be expected to result in the production of crystallographic phases which might be difficult, or impossible, to obtain from conventional oven-based synthesis routes. Despite the early indication that LP might be an important general technique to produce high quality, crystalline nanoparticles in relatively large quantities, very few reports of particle production by this technique have been made: Si, SiC, Si_3N_4 ^[1, 3, 4], ZrB_2 ^[5], TiO_2 ^[6], and Fe_3C ^[7, 8]. Recently, we have been able to demonstrate that LP is generally applicable to the synthesis of a wide variety of nanocrystalline powders, and the powders exhibit a narrow particle size distribution. The typical particle size and production rate is ~ 10 nm and 1 - 5 g/hr, respectively. Using carbonyls as a source for the elemental metals Fe, Ti, W and Mo, we have, for example, synthesized nanocrystalline oxides, sulfides, carbides and nitrides: Fe_3C , Fe_7C_3 ^[9], Mo_2C , W_2C , Mo_2N , W_2Ni ^[10], $Fe_{1-x}S$, Fe_3N , Fe_4Ni ^[11], MoS_2 and WS_2 ^[12], Fe_3O_4 , TiC , and TiO_2 . In this paper, we discuss the LP synthesis of nanocrystalline WO_3 , an important electrochromic material^[13, 14]. The structure and chemical bonding in these particles have been studied by X-ray diffraction(XRD), transmission electron microscopy(TEM) and Raman scattering spectroscopy.

Bulk WO_3 has been studied extensively, in part, because of the potential application of its electrochromic properties, discovered first by Deb^[13] in H_xWO_3 . The optical transmission of WO_3 can be controlled by the diffusion of cations (e.g. Li^+ , H^+ , Na^+ , etc) via an applied electrical field into vacancies in the anion sublattice. The diffusion is quite rapid, and therefore WO_3 has been investigated, for example, for display devices and electronically controlled window coloration^{[15][14][16]}. WO_3 also exhibits an array of interesting phase transitions, and has therefore been studied for fundamental reasons as well. It has at least 7 crystallographic phases

existing in several temperature ranges^[17], a metal-insulator phase transition^[18], and exhibits ferroelectric behavior in its low-T triclinic phase ($T < -40^{\circ}\text{C}$ or 233 K)[19][20]. Numerous studies have also been made on amorphous WO_3 prepared by vacuum evaporation^[21], rf sputtering^[22], anodic oxidation^[23] and sol-gel synthesis^[24]. These amorphous materials also possess good electrochromic properties, including fast response capabilities, high coloration efficiency, and a long life time^[25].

As far as we are aware, no studies have been carried out to determine the electrochromic behavior of *nanocrystalline* WO_3 particles. This behavior might be enhanced due to the small particle size, particularly in regard to the device response time, which is controlled by the diffusion constant. It is well known that the diffusion constant is generally found to be larger in nanoscale materials than in the bulk solid^[26]. Also, it should be kept in mind that these nanopowders might be applied by spray pyrolysis, for example, to large area substrates. Other nanoparticle size effects, as they pertain to the optical dielectric function or to the stabilization of a particular crystallographic phase, may also be important^{[27][17][28][2]}. For example, the ferroelectric transition temperature T_c in PbTiO_3 nanoparticles (dia $\sim 50\text{ nm}$) was found to decrease from the bulk value of 500°C to $\sim 420^{\circ}\text{C}$. Closely related to the present work, is the Raman scattering study of Hayashi et al.^[20] on microcrystals of WO_3 (avg. particle size 100 nm) prepared by burning tungsten wire in an O_2 atmosphere. Similar to what we observe in the spectra for our nanoparticles, they identified, at room temperature, several Raman modes of WO_3 associated with the low T (-40°C) ferroelectric phase. However, at $T = 300\text{ K}$ they found a mixture of the monoclinic and ferroelectric phases. Results of this study suggest this phase mixture might be due to their large particle size distribution ($20 - 180\text{ nm}$). In the present study, our particles have typically an average size in the range $5 - 10\text{ nm}$, with $\sim 2/3$ particles exhibiting diameters that deviate less than 1 nm from the average.

Our laser pyrolysis system is shown schematically in Fig. 1. O_2 is introduced at the input to a cell containing solid $\text{W}(\text{CO})_6$ powder (Aldrich, 99.9%), whose temperature is regulated at a value close to the sublimation point ($T = 150^{\circ}\text{C}$) of this carbonyl compound. $\text{W}(\text{CO})_6$ vapor was carried into the reaction zone by flowing O_2 through the cell. C_2H_4 (or SF_6), which have rotational/vibrational bands matching the photon energy of the P20 emission line from a cw CO_2 laser (Laser Photonics Model 150), is mixed into the reactant gas stream above the sublimation cell, as shown in the figure. Flow rates of the various gases are controlled by electronic monitors. The reactant gas mixture then flows vertically out of a central stainless steel tube (or nozzle) surrounded by a second, larger diameter stainless steel tube used to establish a concentric flow of Ar gas around the nucleating nanoparticles. The particles are thereafter entrained in inert gas and flow upward into a pyrex trap. Similar to our studies of the formation of Fe_{1-x}S ^[11], MoS_2 and WS_2 ^[12], we propose that the reaction pathway involves the thermal decomposition of $\text{W}(\text{CO})_6$ to elemental W and CO, the metal (W) then reacts with the oxidizing gas (O_2) to form the binary compound, and the C_2H_4 (or SF_6) acts as a passive, heat absorbing species. Minute amounts of a highly disordered carbon coating were detected by Raman scattering when the particles were produced with C_2H_4 , and this carbon coating was not detected when SF_6 was used as the chemically passive absorbing gas. This point is discussed further below. We point out here, however, that since the carbon coating does not appear to form when SF_6 was used as the optically absorbing gas indicates that the source of this carbon is not the CO coming from the carbonyl. The nanoparticle production rate is found to be reasonably high when compared with most other techniques, i.e., $\sim 2\text{ g/h}$ using a 5 mm dia. nozzle. This large production rate makes it possible to evaluate these nanoparticles for practical applications requiring more material. It should be noted that under our experimental conditions, the "as synthesized" WO_3 nanopowders

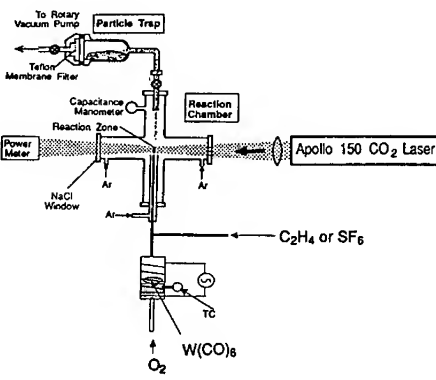


Fig. 1 CO₂ laser pyrolysis system.

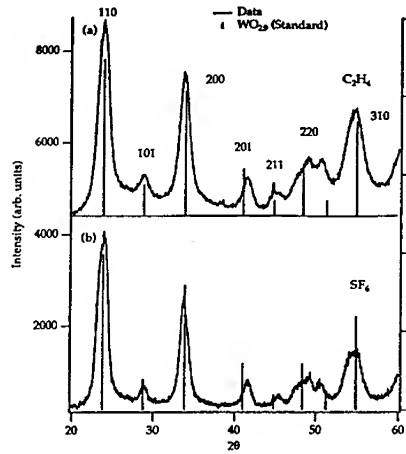


Fig. 2 Cu(K α) X-Ray diffraction data for nanocrystalline "as synthesized" WO_{2.9} particles produced with C₂H₄ (2a) and SF₆ (2b). Vertical lines are from standard powder diffraction data for tetragonal phase WO_{2.9}.

exhibit a bluish color due to an oxygen deficiency.

In Fig. 2 we show the XRD data for the "as synthesized" nanocrystalline powders produced using C₂H₄ (Fig. 2(a)) or SF₆ (Fig. 2b) as the chemically passive absorber. The data, corrected for the instrumental zero shift in 2 θ , were collected using Cu(K α) radiation using a Phillips 3100 powder diffractometer. Vertical lines in the figure represent data from the standard powder diffraction file for the tetragonal phase of W-oxides(WO_{2.9}), which is oxygen deficient. It is clear from the figure that most peaks in both figures match well with the standard file for WO_{2.9}, and this identification is consistent with the observed bluish color of the "as synthesized" particles. Thus the crystallographic phase does not depend on the "chemically passive" absorber(i. e. C₂H₄ or SF₆), as anticipated. From the width of the {110} peak, an average crystallite size was estimated to be ~ 5 nm using the Debye-Scherrer (DS) equation[29].

In Fig. 3, we show a bright field TEM image for the WO_{2.9} nanoparticles, whose XRD data appeared in Fig. 2a. The average particle size, as determined directly from this image is ~ 8 nm, exceeding the DS estimated size (5 nm) by 3 nm, similar to the case of LP-produced MoS₂ and WS₂ particles[12]. The closeness of the TEM- derived and XRD-derived values for the particle size indicates that the particles are highly crystalline; i.e., there does not appear to be much disorder-induced broadening of the x-ray lines.

We next present XRD results on the effects of O₂ annealing(~ 1 atm.)of the "as synthesized" WO_{3-x} nanopowders. In Fig. 4 we show data for nanoparticles heat treated in flowing O₂ at 150 °C (Fig. 4(a)) and 400 °C (Fig. 4(b)) for 24 hrs. These data are compared to bulk WO₃ powder (Aldrich, 99.9%) in Fig. 4(c). Vertical lines in the figures represent the standard powder diffraction data for the triclinic WO₃ phase (Fig. 4a), and the monoclinic phases (Fig. 4(b) and 4(c)). The structural phase of the nanoparticles annealed at 400 °C (Fig. 4(b)) can be clearly identified with the expected bulk (T=300 K) monoclinic WO₃ phase (as also shown in Fig. 4(c)). It is difficult to determine the crystalline phase for the nanocrystalline WO_{3-x} annealed

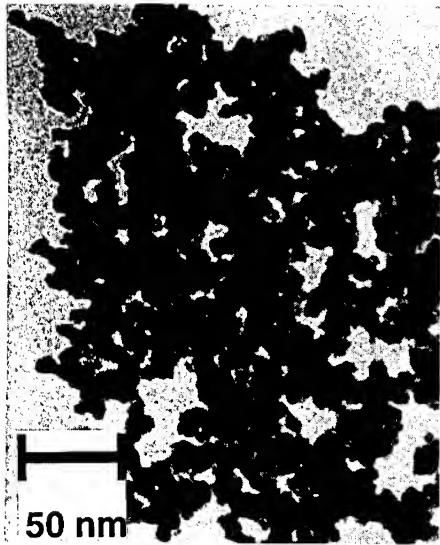


Fig. 3 Bright field TEM image for “as synthesized” nanocrystalline $\text{WO}_{2.9}$ particles.

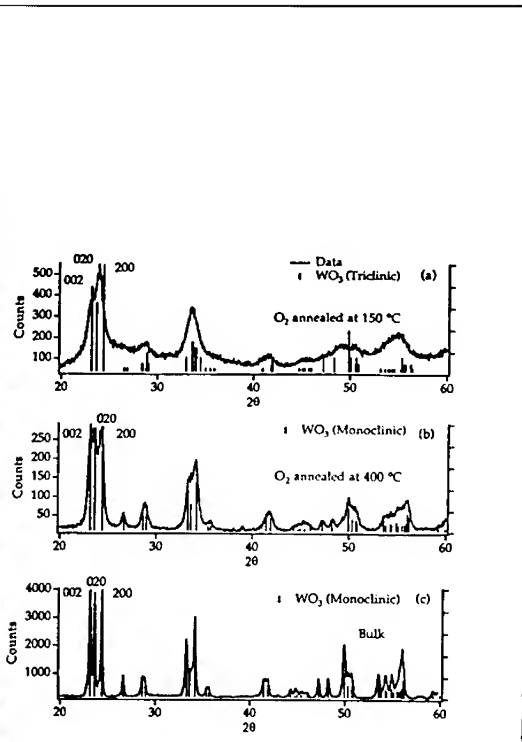


Fig. 4 $\text{Cu}(\text{K}\alpha)$ X-Ray diffraction data for nanocrystalline powders annealed at 150 °C (4a) and 400 °C (4b), and unannealed bulk WO_3 powders (4c). Vertical lines represent standard powder diffraction data for monoclinic (4b and 4c) and triclinic (4a) WO_3 phases.

in O_2 at 150 °C due to the broad nature of the diffraction lines. However, the best match was obtained for triclinic WO_3 . The structural identifications made above on the basis of XRD are supported by Raman scattering experiments discussed below. It is clear from the decreased linewidth of the diffraction peaks of these three samples that significant sintering has occurred in 24 hours. We next discuss the results of Raman scattering measurements on these three samples.

Raman scattering data ($T = 300$ K) were taken on the “as synthesized” $\text{WO}_{2.9}$ particles using the 488 nm Argon ion laser line in a backscattering configuration with the powder in a He atmosphere. Using Raman spectroscopy we were able to detect easily the presence of a carbon coating when C_2H_4 was used as the absorber, as shown in Fig. 5. In this case, broad bands centered around 1375 and 1580 cm^{-1} are observed and identified with pyrolytic carbon [30]. This carbon coating probably forms via the catalytic decomposition of C_2H_4 on the hot particle surface. SF_6 , on the other hand, is considered to be much more inert. The particles obtained with SF_6 as the absorber clearly do not exhibit this carbon coating (Fig. 5), which further supports the view that the carbon for this coating is being supplied by the C_2H_4 , and not from the CO in the carbonyl [9]. We next turn to the discussion of the effect of O_2 annealing on the vibrational spectrum of WO_{3-x} . In Fig. 6, we display the $T = 9$ (dashed lines) and 300 K (solid lines) Raman spectra (in the range of 600 - 900 cm^{-1}) for the three WO_3 samples whose XRD data appear in Fig. 4 (a-c). Other Raman active modes appear at lower frequencies and will be addressed in a separate paper [31]. Two prominent peaks are observed at 715 and 808 cm^{-1} in bulk WO_3 spectrum at 300 K (Fig. 6a, solid line) and are associated with the A_{1g} modes of the monoclinic WO_3 phase [32][33]. The spectrum taken at 9 K is similar to that reported for bulk WO_3 .

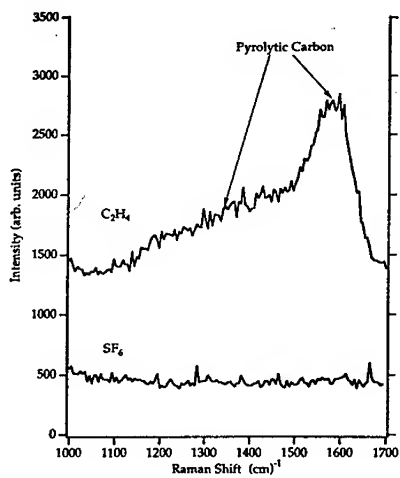


Fig. 5 300 K Raman spectra of "as synthesized" $\text{WO}_{2.9}$ particles produced with C_2H_4 (5a) and SF_6 (5b). The presence of a pyrolytic carbon coating on the particles produced with C_2H_4 is responsible for the broad bands at ~ 1350 and 1580 cm^{-1} .

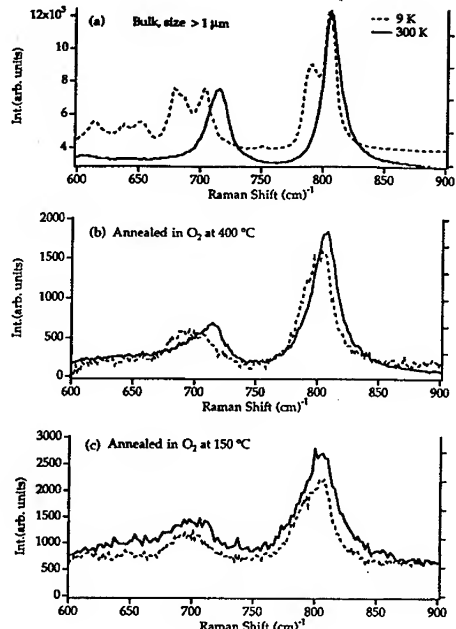


Fig. 6 Raman spectra at $T = 9 \text{ K}$ (dashed) and 300 K (solid) for bulk WO_3 (6a), nanocrystalline WO_3 powders annealed in O_2 (1 atm.) at $400 \text{ }^\circ\text{C}$ (6b) and $150 \text{ }^\circ\text{C}$ (6c).

in the low temperature, triclinic phase ($T < -40 \text{ }^\circ\text{C}$ or 233 K) [17, 20, 28]. Furthermore, the lower symmetry of the triclinic phase is seen to activate more Raman modes. We now compare the Raman spectra of the annealed nanopowders to that of the bulk. First, the Raman lines for the nanopowders are broadened relative to those in the bulk. This may be due to a particle size effect, although it is possible that this broadening is also due to disorder (probably in the anion sublattice). A change from monoclinic to triclinic phase with reduced temperature is still observable in the nanopowder annealed in O_2 at $400 \text{ }^\circ\text{C}$ (Fig. 6(b)). However, the nanopowder annealed in O_2 at $150 \text{ }^\circ\text{C}$ appear on the basis of the Raman spectrum in this range to be stabilized at room temperature in the low-T triclinic ferroelectric phase. This can be seen in Fig. 6(c), where little T-dependence is observed in the Raman spectrum, and also the features there can be assigned to broadened versions of the narrow triclinic features in Fig. 6(a). This interpretation supports the tentative assignment of the triclinic phase in the $T=300 \text{ K}$ XRD data (Fig. 4(a)).

Acknowledgement

This work was supported, in part, by a grant from the United States Department of Energy (DOE#DE-FC22-90PC90029) and the Center for Applied Energy Research.

References

1. J. S. Haggerty, *Sinterable Powders from Laser-Driven Reactions*, in *Laser-induced Chemical Processes*, J.I. Steinfeld, Editor, 1981, Plenum Press: New York.
2. R. P. Andres, R. S. Averback, W. L. Brown, I. W. A. Goddard, A. Kaldor, S. G. Louie, M. Moscovits, P. S. Peercy, S. J. Riley, R. W. Siegel, F. Spaepen, and Y. Wang, *J. Mater. Res.*, **4**: p. 704, 1989.
3. P. R. Buerki, T. Troxler, and S. Leutwyler, *Synthesis of Ultrafine Si₃N₄ Particles by CO₂ laser Induced Gas Phase Reactions* in *High Temperature Science*, Vol. 27. 1990, Humana Press Inc. 323.
4. F. Curcio, G. Ghiglione, M. Musci, and C. Nannetti, *Applied Surface Science*, **36**: p. 52-58, 1989.
5. G. W. Rice and R. L. Woodin, *J. Am. Ceram. Soc.*, **71**: p. C181, 1988.
6. F. Curcio, M. Musci, and N. Notaro, *Applied Surface Science*, **46**: p. 225-229, 1990.
7. R. A. Fato, G. W. Rice, S. Miseo, and S. L. Soled, United States Patent, 4,637,753, 1987.
8. G. W. Rice, R. A. Fato, and S. L. Soled, United States Patent, 4,659,681, 1987.
9. Xiang-Xin Bi, B. Ganguly, G. P. Huffman, F. E. Huggins, M. Endo and P. C. Eklund, *Journal of Materials Research*, Vol. 8(7), 1666(1993).
10. Xiang-Xin Bi, W. T. Lee, S. Bandow, B. Davis and P. C. Eklund, to be published, 1993.
11. Xiang-Xin Bi and P. C. Eklund, *Proc. of Mater. Res. Society Meeting*, Boston, Mass., Dec. 2 - 6, 1992.
12. Xiang-Xin Bi, Y. Wang, W. T. Lee, K.-A. Wang, S. Bandow, and P. C. Eklund, *Proceedings of Material Research Society*, in press, 1993.
13. S. K. Deb, *Phil. Mag.*, **27**: p. 801, 1973.
14. S. K. Deb, *Solar Energy Mater.*, **25**: p. 327, 1992.
15. W. C. Dautremont-Smith, *Displays*, **4**: p. 3, 1982.
16. J.-G. Zhang, D. K. Benson, C. E. Tracy, and S. K. Deb, *J. Mat. Res.*, **8**: p. 2649, 1993.
17. A. Anderson, *Spectroscopy Letters*, **9**(11): p. 809-819, 1976.
18. R. Gehlig and E. Salje, *Phil. Mag. B*, **47**(3): p. 229 - 245, 1983.
19. R. L. Bihan and C. Vacherand, *J. Phys. Soc. Japan*, **26**, *Suppl.*: p. 158 - 161, 1970.
20. S. Hayashi, H. Sugano, H. Arai, and K. Yamamoto, *J. Phys. Soc. Jpn.*, **61**(3): p. 916-923, 1992.
21. T. Shimomura, T. Furuta, and T. Maki, *Jpn. J. Appl. Phys.*, **26**: p. L299, 1987.
22. D. H. Mendelsohn and R. B. Goldner, *J. Electrochem. Soc.*, **131**: p. 857, 1984.
23. P. Delichere, P. Falaras, M. Froment, A. H.-L. Goff, and B. Agius, *Thin Solid Films*, **161**: p. 35, 1988.
24. A. Takase and K. Miyakawa, *Jpn. J. Appl. Phys.*, **30**(8B): p. L1508 - L1511, 1991.
25. H. Kaneko and K. Miyake, *J. Appl. Phys.*, **66**: p. 845, 1989.
26. R. W. Siegel, *Processing of Metals and Alloys of "Materials Science and Technology - A comprehensive Treatment"*, (VCH Verlagsgesellschaft, Weinheim), 1991.
27. K. Ishikawa, K. Yoshikawa, and N. Okada, *Phys. Rev. B*, **37**: p. 5852, 1988.
28. M. Arai, S. Hayashi, K. Yamamoto, and S. S. Kim, *Solid State Commun.*, **75**: p. 613, 1990.
29. B. D. Cullity, *Elements of X-Ray Diffraction*. 1967, Addison-Wesley Publishing Company, Inc.
30. Xiang-Xin Bi, M. Jagtoyen, F. J. Derbyshire, P. C. Eklund, M. Endo, D. Chowdhury, and M. S. Dresselhaus, to be published, 1993.
31. Xiang-Xin Bi, W. T. Lee, and P. C. Eklund, in preparation, 1993.
32. M. F. Daniel, B. Desbat, J. C. Lassegués, B. Gerand, and M. Figlarz, *Journal of Solid State Chemistry*, **67**: p. 235 - 247, 1987.
33. E. Salje, *Acta Cryst.*, **A31**: p. 360, 1975.

STRENGTH-FLAW RELATIONSHIP OF CORRODED PRISTINE SILICA STUDIED BY ATOMIC FORCE MICROSCOPY

QIAN ZHONG, DARYL INNISS, AND CHARLES R. KURKJIAN
AT&T Bell Laboratories, Murray Hill, NJ 07974

ABSTRACT

Glass strength is controlled by microscopic surface flaws. Attempts to quantify the strength-flaw relationship for corroded silica fibers have been unfruitful, principally because of the difficulty in identifying the nanometer-sized, strength-controlling flaws on a uniformly corroded surface. In this paper, studies on corrosion of pristine silica optical fibers by HF vapor are presented. The HF-treated fibers exhibit strength degradation and contain well-defined, spatially-resolved surface flaws, which are characterized with an atomic force microscope. Excellent strength agreement is obtained for all chemically corroded fibers when the flaws are modeled as partially embedded hemispheres (i.e., blunt flaws). The implication of these results to the corrosion and fatigue process of silica glasses is discussed, since all previous analyses have assumed the strength-controlling flaws to be sharp.

INTRODUCTION

Microscopic surface flaws have long been known to influence the strength of glass [1]. Understanding the strength of silica glass fiber is particularly important because strength retention is critical to the long-term reliability of telecommunication fibers. Although the phenomenon of glass weakening as it ages is well-known, microscopic characterization of surface flaws on glass fibers, and in particular, quantification of the strength-flaw relationship, is in its infancy.

It is well-established experimentally that the tensile strength of silica fibers in liquid nitrogen (~12.5 GPa) and in air at room temperature (~5.5 GPa) are essentially single-valued [2]. Because the intrinsic strength (i.e., the liquid nitrogen strength) of pristine silica fibers is sufficiently close to its theoretical prediction (≥ 17 GPa), these fibers have been described as flaw-free [2]. On the other hand, based upon the assumption that the flaws are sharp, the Griffith criterion [1], as shown in Eqn. 1,

$$\sigma = \frac{K_f}{Y\sqrt{c}} \quad (1)$$

where σ = applied stress, Y is a geometrical factor, which is about 1.76 for an edge flaw in an optical fiber, K_f is the stress intensity factor, and c is the flaw length, indicates that the flaw length is on the atomic scale.

However, the validity of the assumption that the flaw is sharp, i.e., $c \gg a$, where $2a$ is the width of the flaw, has not been verified experimentally. Although flaws produced by abrasion are often considered "sharp", their initial sharpness and the ability of these flaws to become blunt has been debated [3]. Furthermore, several reports have suggested that flaws developed by corrosion are "blunt" [4-7]. The behavior of silica glass fibers during a corrosion process and the resultant surface structure is, therefore, the subject of this study.

As a model system, bare silica fibers are corroded by aging in the vapor of a hydrofluoric acid (HF) solution. This results in strength degradation and a surface topography which contains well-defined, spatially-resolved etched pits. The inert strength is determined and the flaw with the highest aspect ratio, which defines the highest stress concentrator, is characterized. Based on the measured inert strength and flaw dimension, a strength-flaw relationship is proposed. Furthermore, the implication of the proposed model on the glass fiber fatigue mechanism (i.e., the behavior of the flaw under stress) is discussed. Although it is well-known that the fatigue process of silica glass fibers results in time-dependent strength degradation, current analyses, based on the study of bulk silica, have simply assumed that the flaw propagation is the rate-dependent step. This, in turn, implies that the flaws are sharp and can readily grow further to catastrophic failure. This assumption is, therefore, further examined in the present study.

EXPERIMENTAL

Standard 125- μm diameter fused silica glass (Amersil TO8) fibers coated with a 62.5 μm thick polymer coating were used in this study. The polymer coating was removed by dipping the coated fiber in hot ($T \geq 185^\circ\text{C}$) sulfuric acid for ~ 30 seconds. This treatment was followed by rinsing the fiber in acetone. The uncoated fibers were aged by exposure to the vapor of a 1 vol. % HF solution. The resulting strength is sensitive to the aging time and the relative humidity (R.H.) of the environment. The strength decreases at a faster rate at higher humidities, and at a given R.H., it decreases with increasing aging times. The corrosion was controlled by varying the aging time and/or the relative humidity of the aging environment (i.e., 30% to 40% R.H. was typically used).

The inert strength of silica glass fibers is dependent on the flaws in the glass, the bond density and the cohesive bond [8]. However, since water reacts with silica while the fiber is being stressed (i.e., during the strength measurement), the failure stress in air is also a function of the test environment [9] and the rate at which the stress is applied. It is, therefore, necessary to determine the strength in an essentially water-free environment. In the present experiment, the failure strain was measured by fracturing the fibers at room temperature and 30% to 40% R.H. or at 77 K in a liquid nitrogen reservoir with a two-point bender [10, 11]. When the measurement was performed in air, the inert strength (strain) is derived by using an experimentally determined 2.1 multiplicative factor. The failure strength was calculated from the stress-strain relationship, $\sigma = E \epsilon$, where E is Young's modulus, and ϵ is the failure strain. The modulus was corrected by $E = E_0 (1 + 3\epsilon)$ [12], where E_0 is the zero stress modulus (70.3 GPa), for fibers with failure strains below 6.5%. The zero stress modulus was corrected by 10%, to calculate the strength for fibers which failed above 6.5% strain [13].

A MultiMode NanoScope III (Digital Instruments) atomic force microscope (AFM) was used to characterize the topography of the glass surface. The data were obtained by scanning the surface with an etched silicon tip with an end radius of approximately 10 nm and an aspect ratio of about 3:1. The instrument was operated in both the tapping and the contact mode. The tapping mode was used to minimize surface/probe degradation [14]. Except for plane fitting and removal of the intrinsic curvature of the fiber, all images are presented as acquired.

RESULTS

One of the difficulties in earlier work [15-18] of characterization of glass surfaces is to locate the strength-defining flaw(s) on a generally rough surface. An example of such is illustrated in Fig. 1a, which shows an AFM micrograph of a bare silica fiber aged in 90 °C water for 23 days. However, for the model system described in the present study, where the bare silica glass fiber surface was corroded by exposing to HF vapor, well-defined surface flaws are generated. Fig. 1b illustrates the surface topography of the fiber exposed to the vapor of 1 vol.% HF for 10 mins. In contrast to the general roughness, there are distinct etched holes on the surface, some much wider than others. The surface next to these holes appears smooth, especially when compared to the sample aged in water. The feature with the highest aspect ratio is identified as the highest stress concentrator, and therefore, the strength controlling feature.

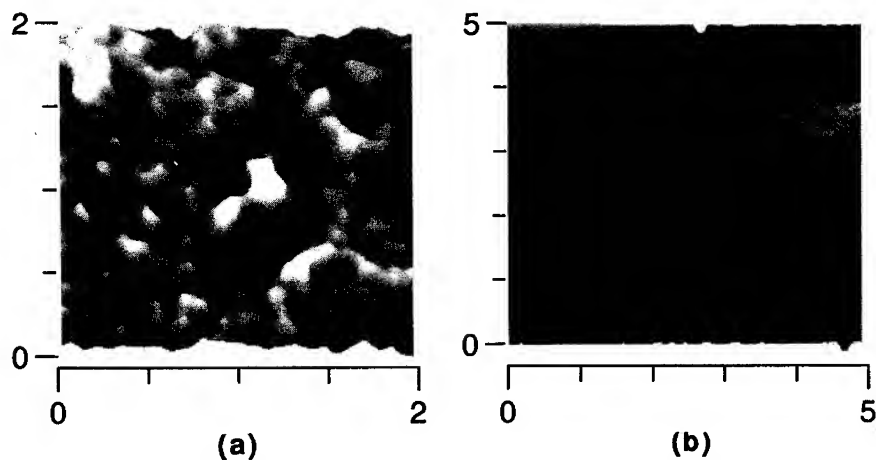


Fig. 1 The surface topography of a bare fiber aged in (a) 90 °C water for 23 days, and (b) HF vapor for 10 mins. Note that the x-y scale is in μm for both, while the z-scale is 50 nm for (a) and 20 nm for (b).

The measured failure strength (inert) of fibers exposed to HF for various times is shown in Table 1. The strength value is based upon an average of at least 20 measurements for each sample. The respective flaw geometry, characterized by c and a , is also illustrated in Table 1.

Table 1 The measured failure strength (inert) of various bare silica fibers aged in HF vapor for different times.

Strength (GPa)	12.3	12.2	10.8	10.6	10.6	10.6	7.88	7.48	5.36
c (nm)	1.0	1.3	3.5	3.9	3.9	10	9.0	9.5	30
a (nm)	50	50	65	160	115	100	25	25	100

DISCUSSION

The measured geometry of the surface flaws developed by HF-vapor exposure clearly illustrates that the flaws are not sharp, i.e., they do not follow the assumption used in the Griffith criterion, $c > a$. Furthermore, reexamining the results presented in the literature [15-18] also indicate that flaws on corroded silica glass fibers are blunt ($c \leq a$), independent of the aging environment. These results suggest that the Griffith criterion may not be appropriate in assessing the surface flaws developed via this mechanism. In fact, a compilation of all available strength/flaw geometry data for corroded silica glass fibers, including those in the literature, shows that the $\sigma \sim c^{-1/2}$ dependence is not followed.

A more general treatment is given following Inglis [19], who defines, independent of geometry, the maximum stress concentrator (β) of a surface flaw as

$$\beta = \frac{\sigma_a}{\sigma_t} - 1 \quad (2)$$

where σ_a is the applied stress and σ_t is the theoretical strength at the crack tip. Assuming that the geometry of the surface flaws is essentially a partially embedded hemisphere, β is given [20] as,

$$\beta = \frac{1}{1.62} \left[\frac{1}{0.27} \frac{c}{\rho} \right]^{0.85} \quad (3)$$

where ρ is the radius of the assumed hemisphere and can be calculated based on c and a as follows

$$\rho = \frac{c^2 + a^2}{2c} \quad (4)$$

In Fig. 2, the data set includes samples aged in the HF environment, in water, results presented by Yuce et. al. [16], where the presented line trace of an AFM image was reevaluated to determine the half-width of the flaw (i.e., a), and the data (i.e., c and a) reported by Kennedy et. al. [17, 18] for both silica and titania silicate glasses. The solid curve illustrated in Fig. 2 is based on Eqns. 2-4, with 12.5 GPa as the theoretical strength. Good agreement is observed between the measurements and the prediction, suggesting that the strength-defining flaws are blunt and can be modeled as partially embedded hemispheres.

The blunt flaw model has an important consequence in understanding the fatigue mechanism, since all fatigue analyses of silica glass fibers assume that sharp flaws are responsible for the strength degradation. This assumption is largely based on the knowledge from the bulk silica studies. However, numerous studies indicate that pristine and corroded glass fibers behave differently from the bulk silica [21]. Based on a chemical kinetics model [21], it is shown that for both pristine and corroded silica fibers, whose surface flaws are blunt, the time required to introduce a sharp flaw, which allows the propagation of the flaw, is much greater than the time for the flaw growth. The crack initiation process is proposed to involve chemical reactions which break bonds locally, and therefore, lead to the formation of a sharp crack. Increasing the local stress at the crack tip (i.e., fatigue or stress-accelerated corrosion) effectively lowers the activation energy for the hydrolysis of silica; therefore facilitates the formation of a sharp crack. Therefore, for corroded silica fibers, the rate limiting step in the

fatigue process is the time necessary to form flaws which are sufficiently sharp to propagate, but not by the time required for crack propagation as previously assumed.

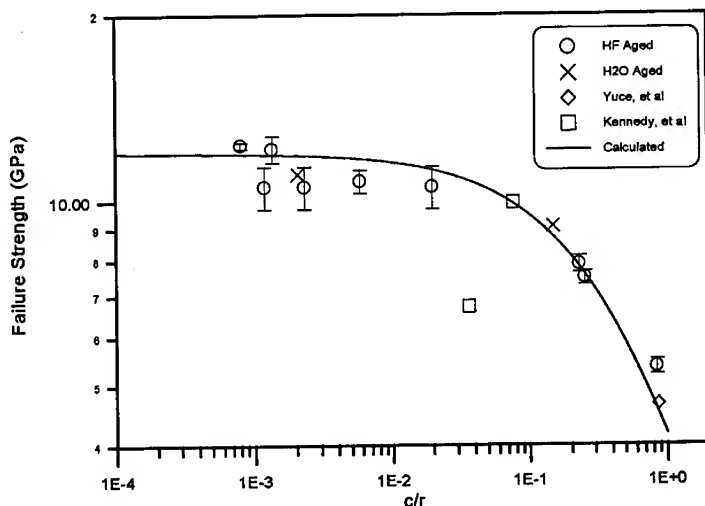


Fig. 2 The maximum stress concentrator, c/p , is plotted vs. the measured inert strength at failure. The data are compared to the model assuming a partially embedded hemisphere.

SUMMARY

An atomic force microscope is used to characterize the surface topography of fibers after they are aged in an HF environment. This treatment produced well-defined, spatially-resolved flaws whose geometry, i.e., depth and width, can be accurately characterized. In contrast to commonly assumed sharp flaw geometry, it is found that the maximum stress concentrator is blunt, independent of the chemical environment in which the fibers are aged and the flaw geometry follows, in general, $c \leq a$. For corroded fibers, the surface flaws can be modeled as partially embedded hemispheres. This result further indicates that when fibers are subjected to stress, the stress-accelerated corrosion (fatigue) process is dictated by the time necessary to form flaws that are sufficiently sharp to propagate, not by the crack propagation time as previously assumed.

ACKNOWLEDGMENT

The authors thank their colleagues at AT&T Bell Laboratories, D. L. Brownlow, F. V. DiMarcello, L. Shepherd, and K. L. Walker for critical comments on this work.

REFERENCES

1. A. A. Griffith, *Philos. Trans. Roy. Soc. London*, **A221**, 163 (1920).
2. C. R. Kurkjian and U. C. Paek, **42[3]**, 251 (1983).
3. W. Han and M. Tomozawa, *J. Non-Cryst. Solids*, **122**, 90 (1990).
4. D. M. Martin, M. Akinc, and S. M. Oh, *J. Am. Ceram. Soc.*, **61**, 308 (1978).
5. F. M. Ernsberger, *Proc. 8th Intl. Congress on Glass*, London 1968 (Soc. of Glass Technol., Sheffield, England, 1969).
6. C. R. Kurkjian, J. T. Krause and U. C. Paek, *J. de Phys. Coll (Les Ulis, Fr.)*, **43[12]**, C9-585, (1982).
7. P. C. P. Bouting and G. de With, *J. Appl. Phys.*, **64**, 3890 (1988).
8. C. R. Kurkjian, *J. Non-Cryst. Solids*, **102**, 71 (1988).
9. B. A. Proctor, I. Whitney, and J. W. Johnson, *Proc. Roy. Soc.*, **297A**, 534 (1967).
10. P. W. France, W. J. Duncan, D. G. Smith, and K. J. Beales, *J. Mater. Sci.*, **18**, 785, (1983).
11. M. J. Matthewson, C. R. Kurkjian, and S. T. Gulati, *J. Am. Ceram. Soc.*, **69[11]**, 815 (1986).
12. J. T. Krause, L. R. Testardi, and R. N. Thurston, *Phys. Chem. Glasses*, **20[6]**, 135 (1979).
13. S. Gao (private communication).
14. Q. Zhong, D. Inniss, K. Kjoller, and V. B. Elings, *Surf. Sci. Lett.*, **290**, L688 (1993).
15. R. S. Robinson and H. H. Yuce, *J. Am. Ceram. Soc.*, **74[4]**, 814 (1991).
16. H. H. Yuce, J. P. Varachi, Jr., J. P. Kilmer, C. R. Kurkjian and M. J. Matthewson, *Optical Fiber Comm. Conf., Post-Deadline Papers*, (OSA, Washington, DC, 1992) PD-21.
17. M. T. Kennedy, E. Cuellar, and D. R. Roberts, *SPIE Proceedings*, **1580**, 152 (1991).
18. M. T. Kennedy, E. Cuellar, D. R. Roberts, and M. M. Stipek, *SPIE Proceedings*, **1791**, 67 (1991).
19. C. E. Inglis, *Trans. Inst. Nav. Archit.*, **55**, 219 (1913).
20. D. H. Roach, and A. P. Cooper, in *Strength of Inorganic Glass*, edited by C. R. Kurkjian (Plenum, New York, 1985).
21. D. Inniss and Q. Zhong, *J. Appl. Phys.* (submitted).

Photon Scanning Tunneling Microscopy of Optical Waveguide Structures

Ahn Goo Choo, Mona H. Chudgar, and Howard E Jackson

Department of Physics, University of Cincinnati, Cincinnati, OH 45221-0011
and

Gregory N. De Brabander, Mukesh Kumar, and Joseph T. Boyd

*Department of Electrical and Computer Engineering,
University of Cincinnati, Cincinnati, OH 45221-0030*

Abstract

Photon scanning tunneling microscopy (PSTM) has been used to obtain effective refractive indices of optical channel waveguide structures. The local evanescent field intensity associated with the propagation modes of optical channel waveguides are measured at two different wavelengths. Both a tapered optical fiber tip and a semiconductor heterostructure tip are employed for detection. Local values of effective refractive index are measured for both TE and TM polarizations and compared to model calculations.

Introduction

The idea of measuring the exponential decay of evanescent field in the near field by a tapered optical fiber tip is of current interest due to the advantage of subwavelength spatial resolution compared to the far field detection¹⁻⁴. The basic idea is to form evanescent field by total reflection at the surface of a transparent object and to detect this evanescent field intensity by a tapered optical fiber tip whose resolution is defined by the aperture of the tip. Thus this method allows local measurement of the effective refractive index⁵⁻⁶. In this paper, we demonstrate the use of both a tapered optical fiber tip and a cleaved semiconductor heterostructure tip to measure the effective refractive index in a $\text{Si}_3\text{N}_4/\text{SiO}_2$ optical channel waveguide at the two different wavelengths of 632.8 nm and 830 nm.

Experiment

Optical channel waveguides were formed using partially etched $\text{Si}_3\text{N}_4/\text{SiO}_2$ ridge structure as shown in Fig. 1. A 120 nm thick layer of Si_3N_4 is deposited on a 3.5 μm layer of SiO_2 which was thermally grown on a Si substrate. The upper cladding layer consists of SiO_2 with a thickness of 100 nm (δ_1) away from the ridge and of 310 nm (δ_2) under a ridge which has varying widths. Each channel waveguide supported single mode propagation at a He-Ne laser wavelength of 632.8 nm and a semiconductor diode laser wavelength of 830 nm. The values of the effective refractive index were calculated by the effective index approximation^{7,8}.

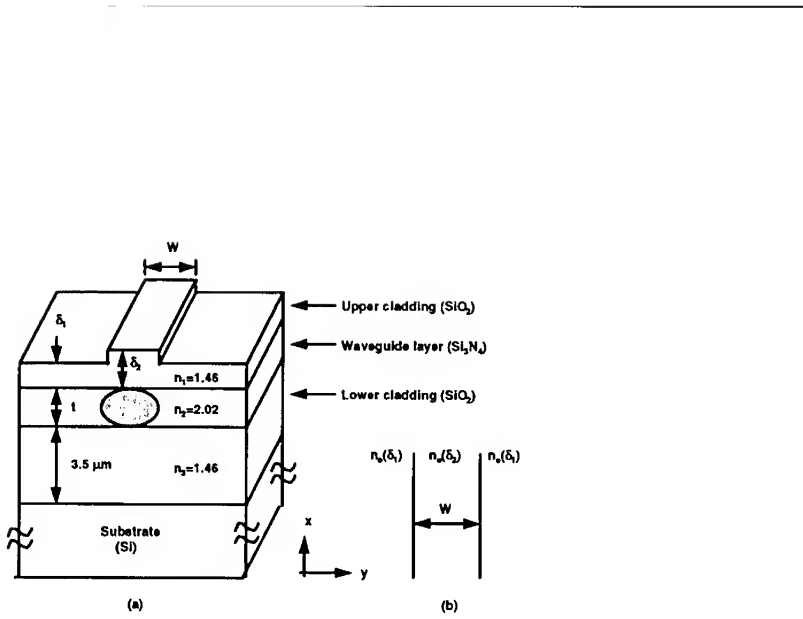


Fig. 1. $\text{Si}_3\text{N}_4/\text{SiO}_2$ optical channel waveguide formed by a partially etched ridge structure.

A conventional PSTM experimental setup was employed with an additional infrared camera system used to view the coupling of 830 nm light to the waveguide and to position the fiber tip above the channel waveguide region.

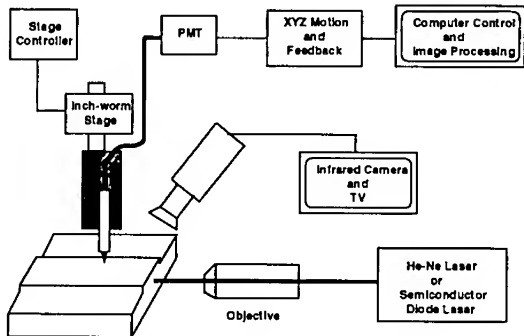


Fig. 2. Schematic of the PSTM.

Two different detection tips were used to probe the evanescent field intensity. The first is an uncoated tapered multimode fiber tip with a refractive index of 1.4815 and a tip diameter of 0.7 μm . The second tip was a cleaved semiconductor heterostructure fabricated using a MOCVD grown heterostructure consisting of a 2.0 μm $\text{Al}_{0.24}\text{Ga}_{0.76}\text{As}$ guiding layer grown on top of a 3 μm $\text{Al}_{0.3}\text{Ga}_{0.7}\text{As}$ isolation layer itself grown on the GaAs substrate. This structure supports planar waveguiding of two modes at a wavelength of 830 nm. The heterostructure was thinned down to 100 μm in thickness from the substrate, cleaved to a size of 0.5 mm x 2.5 mm, and carefully attached to a well-cleaved optical fiber. The edge opposite the optical fiber was used to probe the evanescent field intensity.

Results and Discussion

The PSTM is used to probe the evanescent field intensity of the optical waveguide mode by using a tapered optical fiber tip. If an optical fiber tip is brought within the exponentially decaying evanescent field associated with an optical waveguide mode, a small portion of the guided photons are transmitted into the aperture of a fiber tip. The collected intensity is proportional to the evanescent field intensity expressed by⁵

$$I(x) = I(0) \exp\left(-\frac{x}{\beta}\right) + I_s \quad (1)$$

where $I(0)$ is the intensity at the surface, x is the height above the waveguide surface, I_s is the stray scattered light intensity, and β is given as

$$\beta = \frac{\lambda}{4\pi} (n_e^2 - 1)^{-\frac{1}{2}} \quad (2)$$

where λ is the excitation wavelength, and n_e is effective index of refraction. A measurement of the evanescent field intensity as a function of x yields the decay length β which, in turn, provides a value of the effective refractive index by using Eq. (2). By plotting the derivative of measured intensity as a function of distance on a log scale, a linear variation is obtained due to the exponential dependence. Performing a linear fit to the data and obtaining the slope then gives a direct measure of decay length of the evanescent field intensity. Fig. 3 shows example of such data, taken with an optical fiber tip at an excitation wavelength of 632.8 nm. The measured values of the effective refractive index for TE and TM modes are 1.69 and 1.58, compared to the calculated values of 1.6919 and 1.5802, respectively. Table 1 summarizes the effective refractive indices from Figs. 3(a) and 3(b) for the channel waveguide.

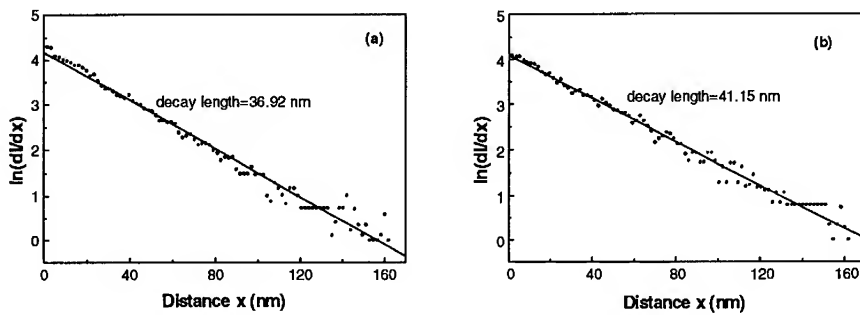


Fig. 3. Measured values (points) using an optical fiber tip and linear fit (solid line) at a wavelength of 632.8 nm. (a) TE mode and (b) TM mode.

Polarization	n_e Effective refractive index calculation	n_e measured by PSTM 632.8 nm
TE	1.6919	1.69 \pm 0.01
TM	1.5802	1.58 \pm 0.01

Table 1. Comparison of theoretical and experimental values of effective refractive indices at a wavelength of 632.8 nm.

We measured the same channel waveguide with the same fiber tip at a wavelength of 830 nm, and display the data in Figs. 4(a) and 4(b). The measured values of the effective refractive index for TE and TM modes are 1.64 and 1.51, compared well to the calculated values of 1.626 and 1.523, respectively. Note that the data fits a linear variation very well as above, particularly in the region close to the waveguide surface.

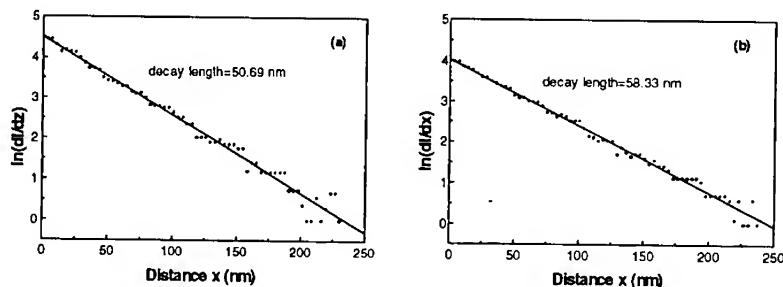


Fig. 4. Measured values (points) using an optical fiber tip and linear fit (solid line) at a wavelength of 830 nm. (a) TE mode and (b) TM mode.

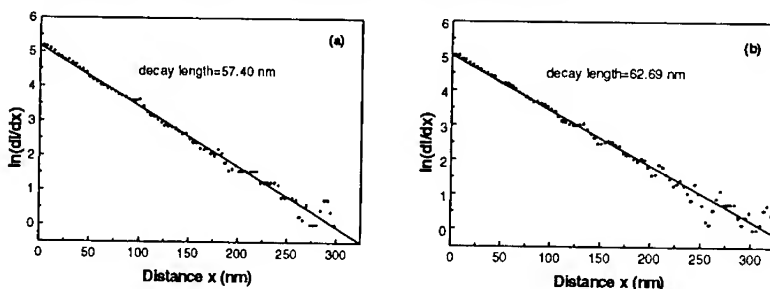


Fig. 5. Measured values (points) using a heterostructure tip and linear fit (solid line) at a wavelength of 830 nm. (a) TE mode and (b) TM mode.

Polarization	n_e Effective refractive index calculation	n_e measured by PSTM, 830 nm	
		Fiber tip	Semiconductor tip
TE	1.626	1.64 ± 0.01	1.52 ± 0.01
TM	1.523	1.51 ± 0.01	1.45 ± 0.01

Table 2. Comparison of theoretical and experimental values of effective refractive index using both an optical fiber tip and a semiconductor heterostructure tip at a wavelength of 830 nm.

Now we attached a semiconductor heterostructure tip to the optical fiber, and excited the same channel waveguide at a wavelength of 830 nm. Preliminary data using this tip is shown in Figs. 5(a) and 5(b). The measured values of TE and TM modes are 1.52 and 1.445 compared to the calculated values of 1.626 and 1.523, respectively. Note that the quality of fit similar to that obtained using an optical fiber tip with notably lower effective refractive indices. Table 2 summarizes the values of effective refractive index calculated from Figs. 4(a) and (b) and Figs. 5(a) and (b) for the channel waveguide.

Summary

We have shown that the PSTM enables a local measurement of the effective refractive index of $\text{Si}_3\text{N}_4/\text{SiO}_2$ channel waveguides formed by a partially etched ridge structure. The measured values at two different wavelengths and using an optical fiber tip to probe evanescent field are found to be in excellent agreement with model calculations for the effective refractive indices of optical channel waveguides. The measured values using a semiconductor tip show the exponential behavior of evanescent field intensity with lower effective refractive indices compared to the calculated values.

Acknowledgments

We gratefully acknowledge the financial support of the Army Research Office and the National Science Foundation.

References

1. R. C. Reddick, R. J. Warmack, and T. L. Ferrell, *Phys. Rev. B* **39**, 767 (1989).
2. D. Courjon, K. Sarayeddine, and Spajer, *Optics Comm.* **71**, 23 (1989).
3. M. A. Paesler, P. J. Moyer, C. J. Jahncke, C. E. Johnson, R. C. Reddick, R. J. Warmack, and T. L. Ferrell, *Phys. Rev. B* **42**, 6750 (1990).
4. T. L. Ferrell, J. P. Goudonnet, R. C. Reddick, S. L. Sharp, and R. J. Warmack, *J. Vac. Sci. Technol. B* **9**, 525 (1991).
5. D. P. Tsai, H. E. Jackson, R. C. Reddick, S. H. Sharp, and R. J. Warmack, *Appl. Phys. Lett.* **56**, 1515 (1990).
6. Y. Wang, M. H. Chudgar, H. E. Jackson, F. S. Miller, G. N. De Brabander, and J. T. Boyd, Integrated Optics and Microstructures, Eds. D. Polla and T. Azar, SPIE **1793**, 66 (1993).
7. A. G. Choo, M. H. Chudgar, H. E. Jackson, G. N. De Brabander, M. Kumar, and J. T. Boyd, *Ultramicroscopy* (accepted for publication).
8. See, for instance, R. G. Hunsperger, Integrated optics: Theory and Technology, 3rd Edition, (Springer-Verlag, New York, 1991), and H. Nishihara, M. Haruna, and T. Suhara, Optical Integrated Circuits, (McGraw-Hill, New York, 1989).

SPECTROSCOPIC CHARACTERIZATION OF NANOSCALE MODIFICATION OF PASSIVATED Si(100) SURFACE BY STM.

F. PÉREZ-MURANO, N. BARNIOL AND X. AYMERICH.
Dept. Física-Electrònica. Universitat Autònoma de Barcelona. 08193-Bellaterra. SPAIN.

ABSTRACT

The electrochemical modification of H-passivated Si(100) surface is produced and characterized by Scanning Tunneling Microscopy and Spectroscopy (STM/STS) operating in air. In order to better understand this nanometer scale modification, we have characterized spectroscopically the modified region. From the current-voltage (I/V) curves, dI/dV versus V curves and tip to sample spacing versus voltage (s/V) curves (at constant current) we have concluded that the modification induces a local electrochemical change on the surface, which in turn produces both, a decrease of the local density of surface states and a variation of the band bending in the silicon surface.

INTRODUCTION

The potential of scanning tunneling microscopy (STM) as a nanofabrication tool has been widely shown in the literature: from the direct manipulation of individual atoms normally under very severe conditions (ultra high vacuum [1], low temperatures [2]) to the simple modification of metal surfaces under room conditions by field evaporation of tip material to the surface [3], there are a great number of techniques which demonstrate its capability. These experiments have in mind the purpose to fabricate a nano-structure that could take advantage of its small size. In this context, it is interesting to study several techniques to produce the modification of a widely studied and technologically important surface as Si(100), and several papers have been published describing different methods of fabrication [4-7]. In this paper, we deal with the modification of Si(100) surface produced with STM in air at room temperature. The surface is passivated by an etching with HF, which is one of the most common technological process. In this sense, we will study a local electrochemical modification of the surface under very low restrictive experimental conditions.

On the other hand, STM gives us the capability not only to acquire images of metal and semiconductor surfaces with high resolution, but also additional information about the local electronic structure of the surface can be obtained making several type of local electrical measurements. We have used this possibility to characterize the as-modified Si(100) in order to better understand which are the properties of the changes induced by STM on the surface.

ELECTROCHEMICAL NANO-MODIFICATION OF Si(100) SURFACE

All the experiments have been performed in air over n-type Si(100) surface with a high surface doping level ($N_D = 2 \times 10^{18} \text{ cm}^{-3}$). In order to achieve the H-passivation of

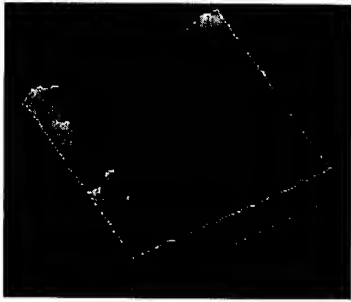


Figure 1. STM image of a 550 nm x 550 nm Si(100) surface where it has been produced a modification consisting on a square of 300 nm X 300 nm and 1 nm depth.

fluorine.

The method to produce the modification on the surface consists of scanning with the STM a selected region under normal imaging conditions (that is, tunneling voltage between 1 V and 1.6 V, sample negative, and tunneling current between 0.5 nA and 4 nA). Then, a greater area which includes the selected region is scanned at the same or higher scanning frequency: when acquiring this last image it can be observed that the selected region first

scanned appears now as a depression typically around 1 nm depth. The depth of the depression depends on the voltage and tunneling current chosen to perform the modification (the higher the current and the lower the voltage, the deeper the modification, what implies that the modification depends on the electrical field between tip and surface, as we have shown before [6]). Also, the depth depends on the time the tip has been over the same region of the surface: this is why an area scanned at higher scanning rate is not so much modified (condition used for imaging). In Figure 1, it is shown a typical modification produced on the surface: the previously scanned region appears as a squared depression at the upper part of the image. The lateral dimensions of the square are 300 nm X 300 nm and the depression depth is 1 nm. Moreover, the lateral dimensions of the modified regions can be as small as 10 nm, as it is shown in Figure 2. The line produced in

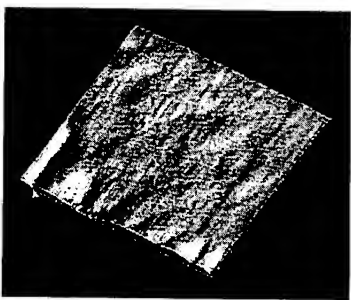


Figure 2. STM image (600 nm x 600 nm) of a Si(100) surface where it has been produced a modification consisting on a line of dimensions 200 nm x 10 nm and 1 nm depth.

the bottom left of the image has dimensions of 200 nm long by only 10 nm width.

SPECTROSCOPICAL CHARACTERIZATION

The ability of STM to perform spectroscopic measurements is of a great utility in this case, where we want to study the electrical properties of the modified region, which in fact is a nanometer scale structure.

The first class of measurements that can be performed consists of performing current voltage (I/V) curves at constant tip-surface distance on selected points of the sample surface. As the tip to surface distance is kept constant (cutting the feed-back loop and applying a voltage ramp), different behaviour in the I/V curves (that is, different current level for the same tunneling voltage) means that differences in some electrical property of the surface exist. This is shown in the image of Figure 3, where the tunneling current for the same tunneling voltage are displayed at every spatial point where the voltage ramp has been made (this is known as current image tunneling spectroscopy (CITS)). It is found that, in the modified regions, the current level is higher for the same polarization. It indicates that a chemical change on the surface has been produced.

One problem related with the CITS images is that the tip to sample distance is settled by the feedback loop to maintain the tunneling current constant. This condition does not

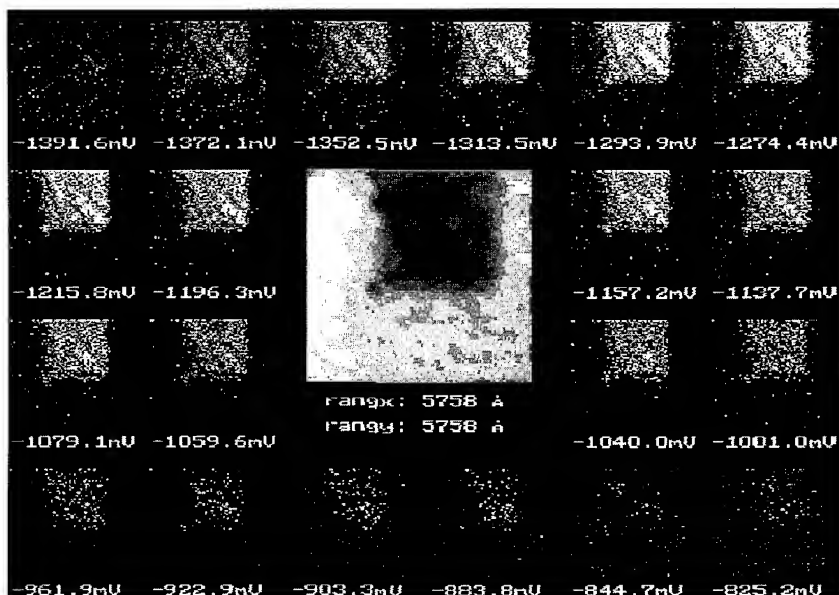


Figure 3. CITS image acquired simultaneously to the topographic image of figure 1, which is represented here as the central image.

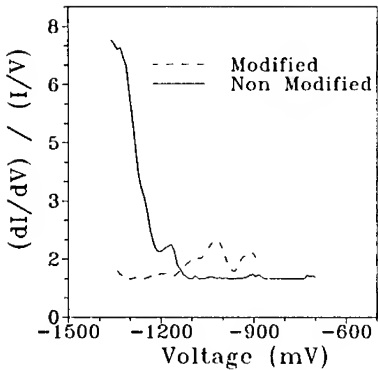


Figure 4. Normalized conductance $(dI/dV)/(I/V)$ for the non modified region (solid line) and the modified region (dashed line).

states presents an exponential decrease in the non-modified region which corresponds to a band bending effect at the silicon surface. This decrease disappears at the modified region, remaining the density of states approximately constant.

This behaviour is compatible with the assumption that the modified regions are oxidized regions, appearing charged interface states which produces both, a reduction of the density of states and the pinning of the Fermi level, decreasing the band bending effect.

In order to corroborate this framework, additional measurements can be performed. Specifically, the presence or absence of band-bending would produce two clearly distinctive dependencies of the voltage versus tip to sample distance curves keeping the tunnelling current constant (that is, under feedback control), a phenomenon similar to the reduction of the apparent barrier height due to band bending, as explained by Weimer et al. [11]. The tunnelling current can be conveniently written as [12]:

$$I \propto V \rho_s(0, E_F) e^{-1.025\sqrt{\phi} s} \quad (1)$$

where I is the tunneling current, V the voltage between tip and sample, $\rho_s(0, E_F)$ the local density of surface states near the fermi level of the sample, ϕ the barrier height in eV between tip and sample and s the distance between tip and sample in Å. This equation gives, for the case that the sample is a clean metal, an exponential dependence of the voltage with tip to surface spacing s . On the other hand, when band bending exists, several authors [6,13-14] have found good agreement between experimental current voltage curves and the MIS theory [15]. Under these circumstances, and assuming that the surface states are passivated, the above expression becomes:

$$I \propto e^{(V_{do} - V_d)/V_T} e^{-1.025\sqrt{\phi} s} \quad (2)$$

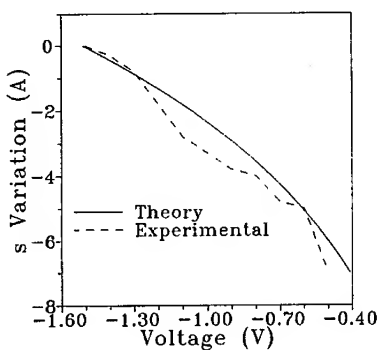


Figure 5. Tip to sample variation (s) as a function of the voltage applied to the sample.

tip to sample distance versus voltage curves on conventionally passivated silicon surfaces. It is shown a good agreement between the experimental curve (solid line) and the predicted by the MIS theory.

CONCLUSIONS

In conclusion, it has been shown that the electrochemical modification of Si(100) surfaces can be produced with a lateral resolution of 10 nm. Information about the electrical properties of the modified region has been obtained from spectroscopic measurements performed with STM (I/V curves, $(dI/dV)/(I/V)$ curves and s/V curves), showing that the modified region presents different electrical characteristics consisting of a lower density of states and a lower effect of the band bending.

ACKNOWLEDGMENTS

This work has been performed with the financial support from the DGICYT under project number PB92-0587.

REFERENCES

- [1] Ph. Avouris and I.W. Lyo. *Appl. Surf. Sci.* **60**, 426 (1992).
- [2] D.M. Eigler, C.P. Lutz, W.E. Rudge. *Nature* **352**, 600 (1991).
- [3] H.J. Mamin, S. Chiang, H. Birk, P.H. Guethner and D. Rugar. *J. Vac. Sci. Technol. B* **9**, 1371 (1991).
- [4] L.A. Nagahara, T. Thundat and S.M. Lindsay. *Appl. Phys. Lett.* **57**, 270 (1990).

[5] N. Barniol, F. Pérez-Murano and X. Aymerich. *Appl. Phys. Lett.* **61**, 462 (1992).

[6] F. Pérez-Murano, N. Barniol and X. Aymerich. *J. Vac. Sci. Technol. B*, **11**, 651 (1993).

[7] E.S. Snow, P.M. Campbell, P.J. McMarr. *Appl. Phys. Lett.* **63**, 749 (1993).

[8] F.J. Grunthaner and P.J. Grunthaner. *Mater. Sci. Rep.* **1**, 69 (1987).

[9] M. Grundner, D. Graf, P.O. Hahn and A. Snegg. *Solid State Technology*. 69 (February 1991).

[10] R.M. Feenstra, J.A. Stroscio and A.P. Fein. *Surf. Sci.* **181**, 295 (1987).

[11] M. Weimer, J. Kramer and J.D. Baldeschweiler. *Phys. Rev. B* **39**, 5572 (1989).

[12] See for example C. Julian Chen. *Introduction to Scanning Tunneling Microscopy*. (Oxford University Press) 1993.

[13] L.D. Bell, W.J. Kaiser, M.H. Hecht and F.J. Grunthaner. *Appl. Phys. Lett* **52**, 278 (1988).

[14] J. Jahanmir, P.E. West, A. Young and T.N. Rhodin. *J. Vac. Sci. Technol A* **7**, 2741 (1989).

[15] H.C. Card and E.H. Rhoderick. *J. Phys. D* **4**, 1589 (1971).

INVESTIGATION OF THE VICINAL Ge(001) SURFACE WITH STM

BART A.G. KERSTEN, LIANDA SJERPS-KOOMEN, HAROLD J.W. ZANDVLIET,
AND DAVE H.A. BLANK
University of Twente, Department of Applied Physics, P.O. Box 217, 7500 AE Enschede,
The Netherlands

ABSTRACT

The morphology of Ge(001) has been investigated with a UHV - Scanning Tunneling Microscope. The Ge(001) surface was misoriented towards the [011] direction with a miscut angle varying from 0.4° to 5° . The surface stress was found to have considerable influence on the step edge configuration as well as the position of the steps with respect to each other.

INTRODUCTION

Recently there is increased interest in the morphology of vicinal crystal surfaces i.e. surfaces slightly misoriented with respect to a low index direction. The misorientation is typically accommodated by single or double height steps which separate terraces of the low index direction. This interest rises from the important role steps play in phenomena as crystal growth chemistry, catalysis and the growth of epitaxial overlayers.[1-3] Most attention has been focused on the Si(001) surface with a small miscut θ towards the [011] direction.

Both, the Ge(001) and the Si(001), surface reconstruct by forming dimers that are arranged in parallel rows. Depending on the plane where the crystal is cut either a (2 x 1) or (1 x 2) reconstructed domain is formed, which are related to each other by a 90° rotation. If the surface has a slight miscut θ towards the [011] direction, single height steps are formed, which separate terraces with alternatingly a (2 x 1) and (1 x 2) reconstruction. In this configuration two types of steps denoted SA and SB occur.

For Si(001) it is observed that with increasing θ the SB step shifts towards the lower lying SA step [4,5]. For θ greater than 2° this leads to the formation of double height DB steps and for $\theta > 4^\circ$ the SL steps have almost disappeared and a primitive (2 x 1) surface is formed. Here we present and discuss the transition we have measured for Ge(001), from SL to SB steps and show that its behaviour is in some extent similar to silicon. The transition from SL to DB steps is especially influenced by surface strain [4-7]. In this paper we will show that the surface strain also has a large impact on the configuration of steps. We have observed a type of SB steps that has not been reported before and will present a configuration that incorporates strain effects.

EXPERIMENTAL

All experiments were carried out in a stainless steel ultra high vacuum chamber with a base pressure of 1.10^{-10} Torr. The chamber contains an Omicron UHV STM, a CMA Auger apparatus, an ion gun as well as facilities for gas handling. The 5×10 mm Ge(001) substrates

were miscut towards the [110] direction by 0,4,1°, 2°, 3° and 5° respectively.

Before loading in the UHV system they were ultrasonically rinsed in isopropyl alcohol. No further chemical treatments were used. The sample could be heated resistively by passage of a DC current. A clean surface was obtained by cycles of sputtering (1000 eV, Ar ions $2\mu\text{A}/\text{m}^2$ 30 min., angle of incidence 20°) and annealing ($800\pm50\text{K}$, 20 min.). The temperature during annealing was measured with an infrared pyrometer. After annealing the samples were radiation quenched to room temperature by disconnecting the heating current. STM images were taken in the constant current mode with a sample bias between -1 and -2V and a typical tunnelling current of 5 nA. Scan ranges varied between $700 \times 700\text{\AA}$ and $1000 \times 1000\text{\AA}$ (0,8 to 1,0 Å/pixel). The scanning direction was oriented 45° to the dimer rows.

To get reasonable statistics several images were taken to achieve a total length of the SB step greater than 3600 a (a is raster constant) for each miscut angle.

RESULTS AND DISCUSSION

An interesting feature of the Ge surface is that the SB steps are much rougher i.e. have more thermally excited kinks than the SA steps (see fig. 1.) which is consistent with measurements on Si(001) [7-9]. Analysis of the kink distributions have been used to determine step- and interaction-energies.

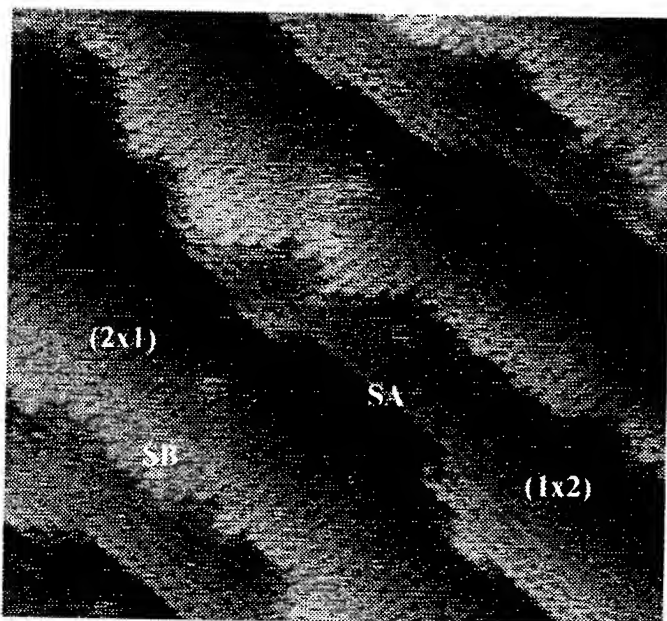


Fig. 1 STM measurements of Ge(001) misoriented towards the [001] direction by 1°. SA steps and (1 x 2) terraces alternate with SB steps and (2 x 1) terraces. Scan range is $400 \times 400\text{\AA}$. $I = 3.5\text{ nA}$, $V = -0.5\text{ V}$.

In contradiction with Si(001) the Ge(001) surface exhibits two kinds of SB steps. In principle there are two different geometries for the SB step depending on the way the SB step ends with respect to the lower lying terrace (see fig. 2). The SB step can be rebonded or non-bonded, the latter configuration being rare on Si(001) [7-11]. Chadi [10] performed calculations on Si(001) steps which showed the rebonded SB step to be more stable than the non-bonded.

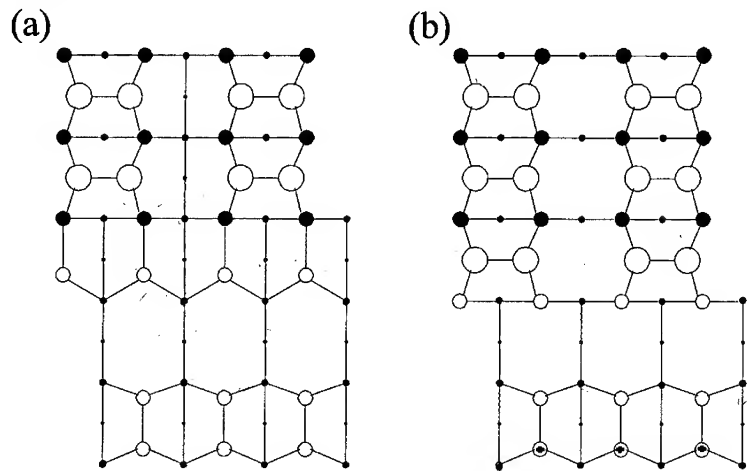


Fig. 2. (a) - (b) Top views of the rebonded (a) and the non-bonded (b) SB step, respectively, after ref. [10]. Larger circles denote atoms with a dangling bond. A crossing is used to indicate buckling away from the substrate.

The energy difference between them is roughly equal to the energy difference between the rebonded SB and SA step ($0,16 \text{ eV}/a$). For the lowest miscut angle the effect of strain is the smallest, resulting in an equal population of the rebonded and non-bonded SB steps. This indicates that for germanium the energy difference is much smaller than for silicon.

To understand the morphology of steps, the surface stress must be taken into account. The dimer bond induces considerable stress, a tensile stress in the direction of the dimer bond and a compressive one in the perpendicular direction, i.e., a single domain say (2×1) surface can lower its energy by contraction in the direction of the dimer bond and expansion in the direction along the dimer rows [12]. This anisotropy in surface stress is partly responsible for the energy difference between the rebonded and the non-bonded SB step. The rebonded SB step has stretched bonds at the step edge, which can be stabilised by a relaxation of the dimer row in the direction along the dimer row.

Our measurements show two clear examples of the influence of the anisotropy of the surface stress. First, consider in fig. 2b the dimer at the edge of the SB step. The two dimers that lie in front of it on the lower (1×2) terrace show the same kind of buckling in all our measurements. The two dimers are buckled in the same direction and the buckling is such that the dimers closest to the SB step are the lower ones. This buckling can be explained by the tendency of the (2×1) dimer row to expand itself, which tends to shift the atoms on the lower (1×2) terrace away from the step edge. Second we have found a deviant configuration for the non-bonded SB step which has not been reported so far. In figs. 3a,b this

configuration can clearly be seen. This configuration occurs together with the normal configuration of the non-bonded SB step of fig. 2b: the ratio being about 1 to 1. It was observed for all miscut angles in all measurements and is characterised by a single dimer that ends two dimer rows of the (2 x 1) terrace.

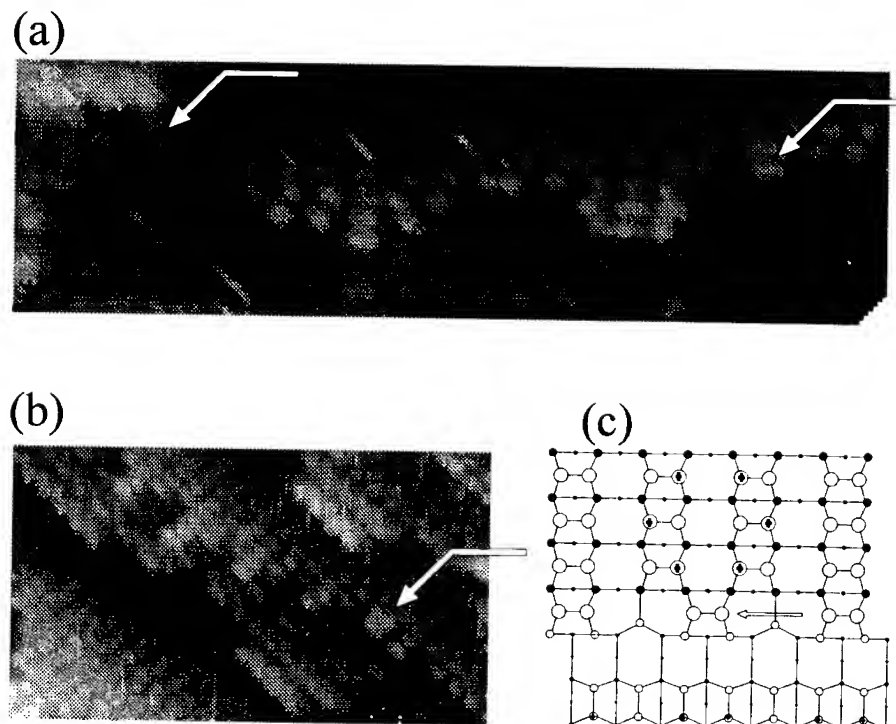


Fig. 3 (a) - (b) Close-ups of a 3° misoriented surface, $I = 5$ nA, $V = -2$ V. Scan range is about 80×30 Å for (a) and 100×50 Å for (b). Both rebonded, non-rebonded, and deviant-non-bonded SB steps occur. The arrows point to the "end dimer". Note the buckling of the (1 x 2) terrace dimers in front of the non-bonded SB edge-dimer.

(c) Proposed configuration for the non-bonded SB step. Open circles denote atoms with dangling bonds, larger circles denote atoms of the upper terrace, a cross indicates buckling upwards from the substrate. The arrow points to the "end dimer". The atoms next to the end-dimer are rebonded.

We have two arguments that this "end dimer" is a dimer and not an effect caused by two buckled dimers. First, height differences at both sides of the end dimer are 1,0 Å. Height differences caused by buckling are rarely higher than 0,5 Å. Second, as mentioned above, the dimer at the edge of a non-bonded SB step is always accompanied by the same kind of buckling at the lower (1 x 2) terrace. In the measurement of fig. 3a,b only the dimers of the (1 x 2) terrace in front of the "end dimer" have this buckling. The configuration is a mixture of a rebonded and non-bonded SB step and has a periodicity of 3a along the step edge.

Table 1

θ	p	% DB	% rebonded SB
1	0.249	2.0	51.0
2	0.388	4.1	52.2
3	0.338	11.2	59.6
5	0.305	37.7	80.3

With increasing θ we observe an increase of the percentage of rebonded SB step over the non-bonded one (see Table 1). Further, the percentage of DB steps increases and a shift of the SB step towards the lower lying SA terrace is observed. Let 2ℓ be the average distance between the SA steps and $(1+p)\ell$ the size of the (2 x 1) terrace, so p describes the asymmetry between the 2 x 1 and the 1 x 2 terrace sizes. In Table 1 the percentage of double steps DB and p are presented as function of θ . These measurements show roughly the same behaviour as those for silicon. From measurements on silicon a theoretical framework has been developed [5,6,13-15] that takes into account step energies and surface stress. The influence of surface stress has been described in terms of monopole-monopole and dipole-monopole interactions. Following Phelke and Tersoff [6] the energy of a SB + SA pair is :

$$E = \lambda_0(SA + SB) - 2\lambda_\sigma \cdot \ln\left(\frac{\ell}{\pi a} \cos\left(\frac{p\pi}{2}\right)\right) + \lambda_d \left(\frac{a}{2\ell}\right)^2 - (3\lambda_\sigma \cdot \lambda_d)^{1/2} \frac{a}{\ell} \tan\left(\frac{p\pi}{2}\right)$$

The first term is the step energy of the SA and SB step excluding strain contribution to the energy. The second term is the Alerhand's energy and describes the force-monopole-monopole interaction. The third and fourth term describe the monopole-dipole interaction.

Calculations [10] for silicon show that $\lambda(DB) < \lambda(SA) + (SB)$. In the case of Ge(001) only for $\theta = 5^\circ$ a sharp increase of the percentage of DB steps is observed. This contradiction can be explained by the Alerhand's [13] energy and the rebonding of the SB steps. The first states that the strain energy of a surface with alternatingly (1 x 2) and (2 x 1) domains is lower than the strain energy of a single domain surface consisting exclusively of DB step. The rebonding of the SB steps induces a dipole-monopole interaction and a lowering of the strain energy by a shift of the SB terrace towards the lower lying SA terrace [5,6]. This accounts for the increase of p in Table 1 for small θ , but also for the increase of the percentage of rebonded SB steps we observe. The dipole-monopole interaction becomes stronger with decreasing terrace width.

The force dipole is ascribed to the rebonding of the SB step. For the non-bonded or partly bonded configuration we have proposed, the force dipole may be assumed to be lower. Hence with increasing θ the rebonded SB step will be energetically more favourable than the non-

bonded. The decrease of p for $\theta > 3^\circ$ is caused to by the relatively small terrace width ; kinks of length $2a$ already have a large impact on p .

In conclusion, we have found that the surface stress is an important factor in the morphology of the vicinal Ge (001) surface. It influences the configuration of the step-edges, as well as the position of the steps with respect to each other.

REFERENCES

- [1] Tomonobu Nakayama, Yasumasa Tanishiro and Kunio Takayanagi, *Surf. Sci.* **273**, 9-20 (1992).
- [2] Y.-W. Mo and M.G. Lagally, *Surf. Sci.* **248**, 313-320 (1991).
- [3] S. Sharan and J. Narayan, *J. Appl. Phys.* **66**, 2376 (1989).
- [4] B.S. Swartzentruber, N. Kitamura, M.G. Lagally, M.B. Webb, *Phys. Rev. B* **47**, 1432 (1993).
- [5] Tze Wing Poon, Sidney Yip, *Phys Rev. Lett* **65**, 2161 (1990).
- [6] E. Pehlke, J. Tersoff, *Phys. Rev. Lett* **67**, 465 (1991).
- [7] H.J.W. Zandvliet, H. Wormeester, D.J. Wentink, A. van Silfhout, H.B. Elswijk, *Phys. Rev. Lett.* **70**, 2122 (1993).
- [8] H.J.W. Zandvliet, H.B. Elswijk, E.J. van Loenen, D. Dijkkamp, *Physical Rev. B* **45**, 5965 (1992).
- [9] B.S. Swartzentruber, Y.W. Mo, R. Kariotis, M.G. Lagally, M.B. Webb, *Phys. Rev. Lett.* **65**, 1913 (1990).
- [10] D.J. Chadi, *Phys. Rev. Lett* **59**, 1691 (1987).
- [11] J.A. Kubby, J.E. Griffith, R.S. Becker, J.S. Vickers, *Phys. Rev. B* **36**, 6079 (1987).
- [12] M.C. Payne, N. Roberts, R.J. Needs, M. Needels, J.D. Joannopoulos, *Surf. Sci.* **211/212**, 1-20 (1989).
- [13] L. Alerhand, D. Vanderbilt, R.D. Meade, J.D. Joannopoulos, *Phys. Rev. Lett* **61**, 1973 (1988).
- [14] O.L. Alerhand, A. Nihat Berker, J.D. Joannopoulos, David Vanderbilt, R.J. Hamers, J.E. Demuth, *Phys. Rev. Lett* **64**, 2406 (1990).
- [15] B. Kersten, D. Blank to be published.

PART VIII

**Cross-Sectional and 3-D Imaging
at Atomic Resolution**

3-D IMAGING OF CRYSTALS AT ATOMIC RESOLUTION

M.A. O'KEEFE^o, K.H. DOWNING[◊], H-R. WENK^{*} and HU MEISHENG^{*}

^oNational Center for Electron Microscopy, UCLBL, Berkeley, CA 94720.

[◊]Donner Laboratory, UCLBL, Berkeley, CA 94720.

^{*}Department of Geology and Geophysics; University of California, Berkeley, CA 94720.

ABSTRACT

Electron crystallography has now been used to investigate the structures of inorganic materials in three dimensions. As a test of the method, amplitudes and phases of structure factors were obtained experimentally from high resolution images of staurolite taken in a number of different projections. From images in five orientations, a three-dimensional Coulomb potential map was constructed with a resolution of better than 1.4Å. The map clearly resolves all the cations (Al, Si, Fe) in the structure, and all of the oxygen atoms. This method promises great potential for structure determinations of small domains in heterogeneous crystals which are inaccessible to x-ray analysis. Three-dimensional structure determinations should be possible on small domains only approximately 10 unit cells wide, and may resolve site occupancies in addition to atom positions. Given a microscope stage with a suitable range of tilt and enough mechanical stability, the method could also be applied to small crystalline particles larger than about 50Å to 100Å. In addition, it may be possible to apply the method to derive the two-dimensional structure of periodic defects.

INTRODUCTION

With recent advances in electron microscope instrumentation, high resolution electron microscopy has become routine, and point resolutions of better than 2Å have been obtained in images of many inorganic crystals. Although this resolution is sufficient to resolve interatomic spacings, interpretation generally requires comparison of experimental images with calculations[1]. Since the images are two-dimensional representations, or *projections*, of full three-dimensional structures, information in the images is often lost due to overlapping images of atoms at various heights. We have explored the technique of three-dimensional electron crystallography as a way to circumvent this limitation. In three-dimensional electron crystallography, information from several views of a crystal is combined to produce a three-dimensional data set that can provide images of atoms in single atomic layers.

Electron crystallography was originally developed to obtain three-dimensional information on proteins[2,3]. The resolution in images of proteins is severely limited by effects of radiation damage; however, in principle, three-dimensional reconstructions should be obtainable at atomic resolution from specimens that are resistant to damage. The most serious problem would appear to be in obtaining high-resolution images from areas that are thin enough that dynamical scattering effects can be ignored without significant degradation of accuracy, although to some degree dynamical effects can be reduced by slight off-axis tilts of the specimen[4].

To demonstrate the potential of the method for materials, we have used electron crystallography to carry out a determination of the three-dimensional structure of staurolite. The first determination[5] was to a resolution of 1.6Å, and was produced by using data from images taken at Scherzer defocus in five different directions. A later determination[6] achieved a resolution of 1.4Å by including data from through-focus series of images obtained in each of the five directions previously used. Staurolite, a silicate mineral for which the complex structure is well known[7], is typical of many oxide structures with close-packed oxygen atoms surrounding different types of cations in tetrahedral and octahedral coordination; it thus provides a good test of the methodology.

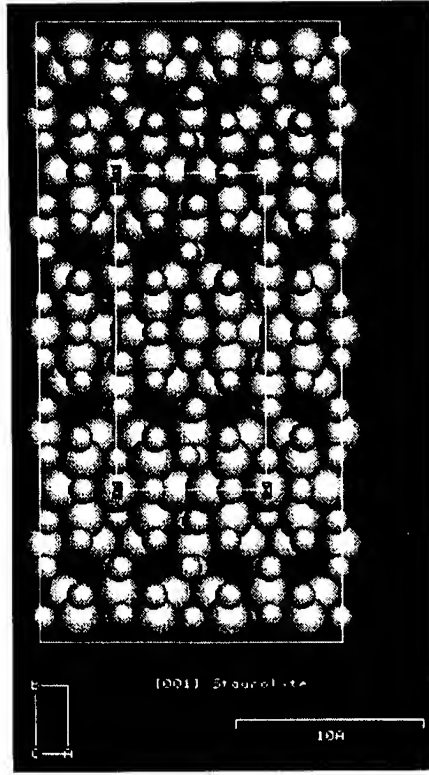


Figure 1 shows the structure of staurolite projected in the [001] direction, displaying the large number of overlapping atoms from the four layers (lying 1.4 Å apart along the c axis) that make up the unit cell of staurolite. This overlapping of atoms is typical of many materials, including alloys, minerals, and ceramic structures, and leads to difficulty in image interpretation in terms of atomic arrangement. For comparison, figure 2 shows how much more easily the structure can be discerned when the four layers are separated out as individual layers.

In the sections shown in figure 2, all the atoms can be clearly distinguished because no two can be much closer together than the metal-oxygen bond distances. In the $xy0$ and $xy\frac{1}{2}$ sections the distance of closest approach of any two atoms is 1.8 Å, whereas in the $xy\frac{1}{4}$, and $xy\frac{3}{4}$ sections, the oxygen atoms lie slightly above and below the $z=\frac{1}{4}$, and $z=\frac{3}{4}$ planes, and the projected distance is 1.6 Å.

It is obvious that the improvement in the visibility of atoms in sections compared with those in projections will extend to high-resolution electron microscope images. Image simulation can be used to confirm this supposition, and to show just how visible the atoms will be at various

Figure 1. Projection of the structure of staurolite in the [001] direction. The unit cell (marked) has dimensions $a = 7.82\text{ \AA}$, $b = 16.52\text{ \AA}$, and $c = 5.63\text{ \AA}$.

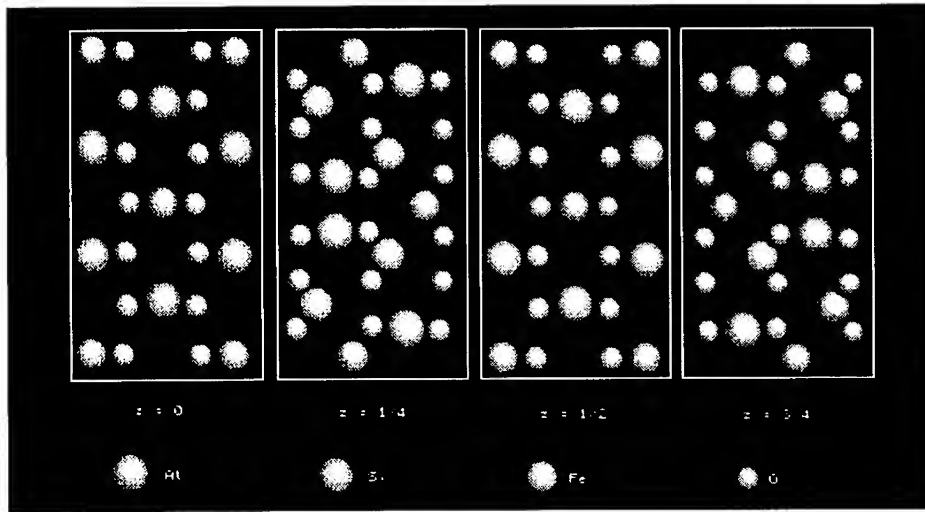


Figure 2. The four sections making up a unit cell of staurolite. Heights in the [001] direction are $z=0$, $z=\frac{1}{4}$, $z=\frac{1}{2}$, and $z=\frac{3}{4}$. The $z=0$ and $z=\frac{1}{2}$ are identical, and $z=\frac{1}{4}$ and $z=\frac{3}{4}$ mirrors.

electron microscope resolutions. For the thin crystals used in three-dimensional reconstruction, a simple weak-phase-object image formation theory can be used to demonstrate visibility as a function of resolution. Figure 3(a) shows weak-phase-object image simulations for electron microscope images from thin specimens of staurolite viewed in [001] orientation over a range of microscope resolutions. The simulations demonstrate that individual atoms are difficult to discern in images that are a projection of the full unit cell, even at a resolution as good as 1.4 Å.

On the other hand, when simulations are computed from just the $xy0$ and $xy\frac{1}{4}$ sections (fig. 3b,c), it is clear that atoms may be distinguished clearly in these sections at 1.6 Å resolution (and even at 1.8 Å for the $xy0$ section). Of course, it is not possible to obtain experimental section images directly from the electron microscope, but it is possible to derive approximations to them from a three-dimensional reconstruction derived from projections (images). To form

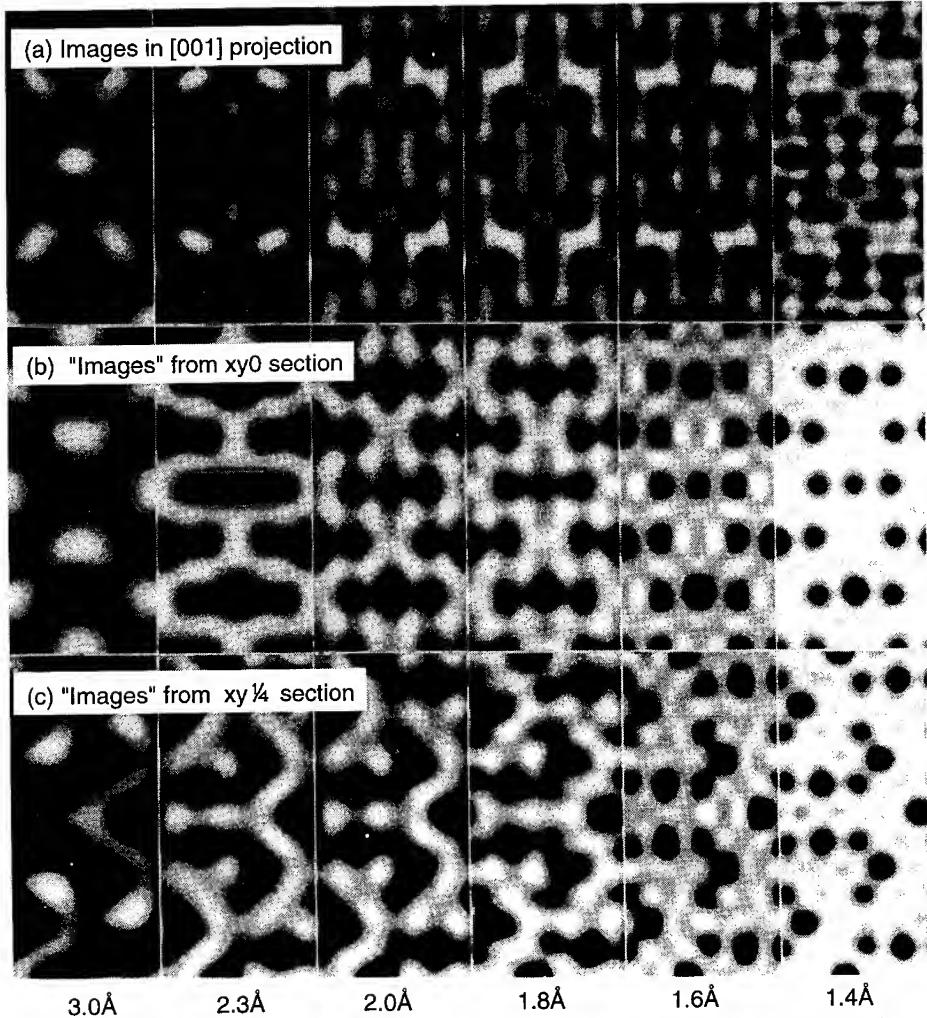


Figure 3. Weak-phase-object simulations of [001] images of staurolite for the full unit cell (a), the $xy0$ section (b), and the $xy\frac{1}{4}$ section (c). Resolutions (marked in Å) run from 3.0 Å to 1.4 Å.

such a three-dimensional reconstruction requires combining images obtained in several different directions. Figure 4 demonstrates how sets of images are obtained from the three-dimensional specimen over a range of objective lens defocus in each of several directions. The information in the sets of images is then combined to produce a three-dimensional representation of the specimen unit cell.

EXPERIMENTAL

Using the JEOL ARM-1000 at the National Center for Electron Microscopy, we obtained focus series of images at atomic resolution in the three main projections ([100], [010], and [001]). We also used the high angle tilt stage ($\pm 40^\circ$ on two axes) to obtain images perpendicular to [101] and [310]. All the micrographs used for processing came from very thin areas, equivalent to $<40\text{\AA}$ in the matching simulations (crystal thicknesses derived from matching on-axis simulations to experimental images form a lower limit to experimental specimen thicknesses[4]). In these thin areas, the scattering contribution from the overlying amorphous film is considerable, but the crystalline image component is resolved with sufficient signal-to-noise ratio to enable the structure factors to be extracted reliably. Initially, we selected only micrographs close to Scherzer focus for analysis. Images in the five projections were digitized, and structure factors were extracted from the Fourier transforms, allowing calculation of unit cell projections. Multibeam dynamical scattering image-contrast calculations for the microscope conditions and specimen parameters were computed as a check on the image processing, and agree well with the observed images and the unit cell projections (figure 5). The same is true for diffraction patterns and the optical diffractograms of the images used to extract

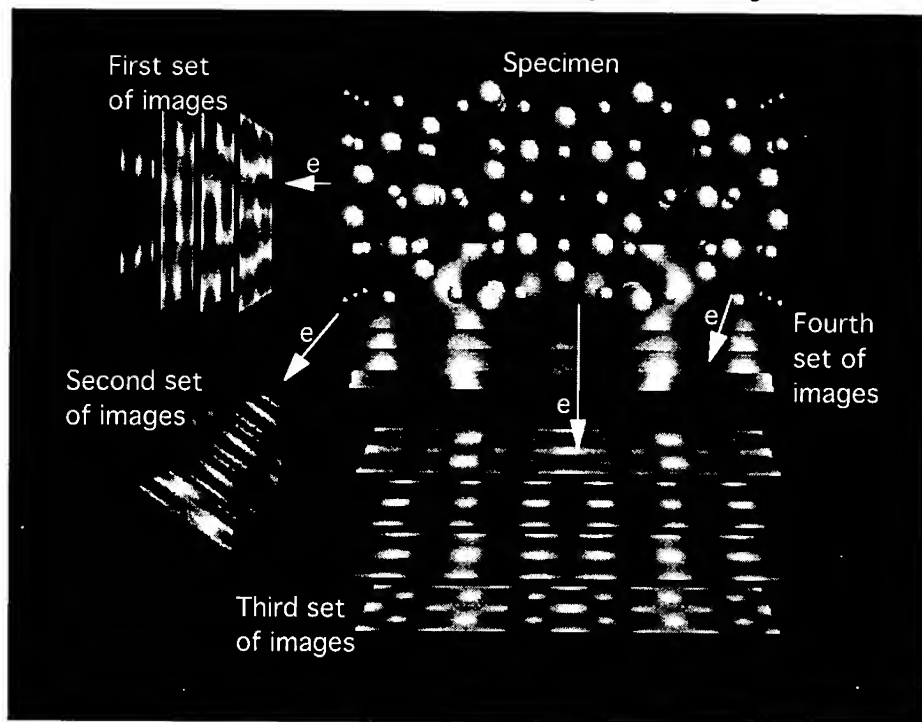


Figure 4. Illustration of the method of obtaining three-dimensional data in the form of sets of two-dimensional projections (images) of the crystalline specimen.

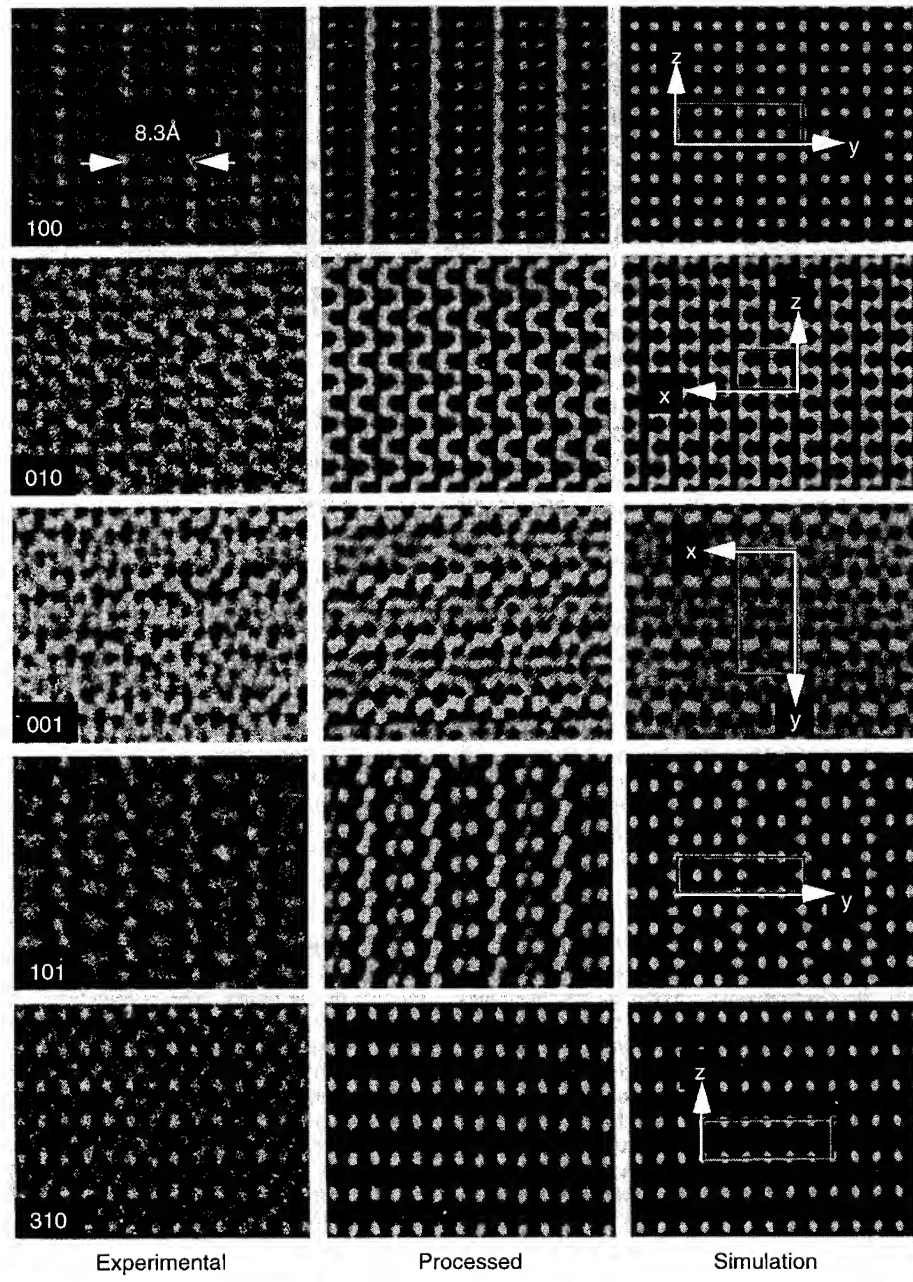


Figure 5. Scherzer-focus images (left) taken in five directions (marked), processed (center) by Fourier filtering, and compared with simulations (right) for the ARM at 800keV and 50Å crystal thickness.

experimental structure factors (figure 6). The experimental optical diffractograms show intensity extending to 1.38\AA , the value at which the envelope of the contrast transfer function of the JEOL ARM-1000 approaches zero.

In our first determination, we used the five Scherzer-focus images (figure 5) to produce reflections with $d > 1.6\text{\AA}$ because of the uncertainty in determining the sign of the CTF at higher resolution. Symmetry-related reflections within each projection were averaged. Data from the five projections were then combined, using equivalent reflections in different projections for scaling, resulting in measurement of 30 of the 80 unique, non-extinct reflections out to $d = 1.6\text{\AA}$. Symmetry operators expanded these 30 structure factors to 72 in half space.

The second structure determination used eight to ten images (in a focal series) from each projection direction, and produced 59 reflections out to 1.38\AA , out of 93 possible reflections; these 59 reflections expanded to give 162 structure factors in half space. However, this result did not significantly improve the resolution in the three-dimensional reconstruction because the additional reflections were strongly damped by the actions of the objective lens contrast transfer function (CTF) and the damping functions associated with the effects of partial coherence[8,9].

In the third determination, we included a correction for the fall-off in intensity-spectrum amplitudes due to the objective lens CTF and its damping function[6]; this determination showed improved resolution.

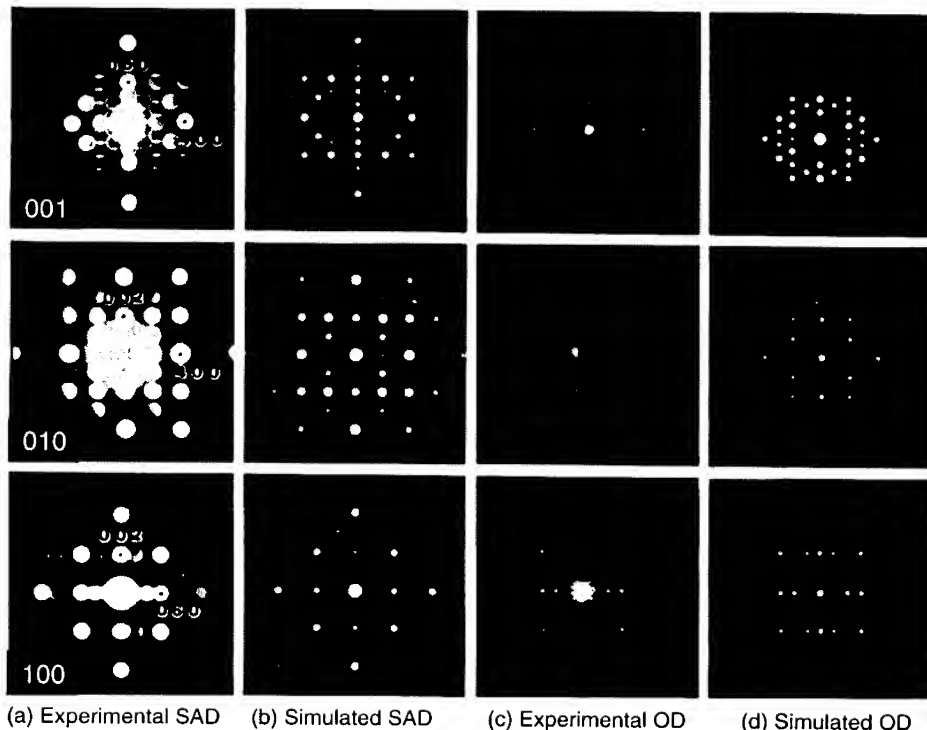


Figure 6. Diffraction patterns and intensity spectra in the three main directions. (a) experimental selected area diffraction pattern (SAD), (b) simulated SAD, (c) experimental image intensity spectrum (optical diffraction pattern) from image at Scherzer focus, (d) simulated intensity spectrum.

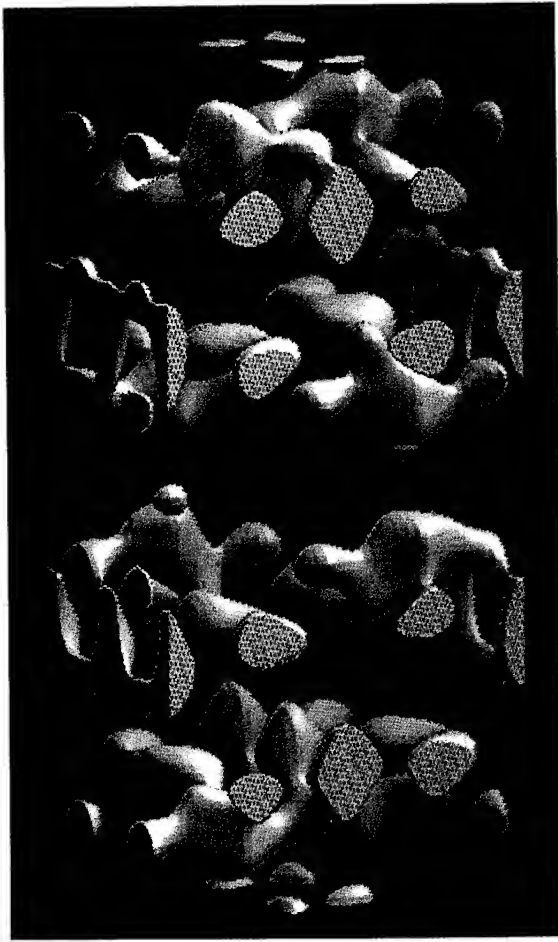


Figure 7. Surface representation of the three-dimensional Coulomb potential in a full unit cell of staurolite, at a density level that displays all fully occupied cations and oxygens; the view is close to [001].

Since all atoms are located near planes equivalent to $z = 0$ and $z = \frac{1}{4}$ and because of the assumed orthorhombic symmetry, most of the information is contained in these two xy sections. Figure 8 compares the experimental results obtained from the three determinations, displayed in the [001] direction, both as projections of the unit cell, and as xy sections. There is excellent correspondence between the experimental results and the weak-phase object (WPO) simulations of figure 3. While the second determination (at a nominal resolution of 1.38\AA) shows a slight improvement over the first (at 1.6\AA), most improvement occurs in the third determination, in which CTF correction was included. The results of the third determination match the 1.4\AA WPO simulation for the full unit cell projection, and clearly resolve all atom positions in the xy sections. Note that the partially occupied octahedral Al site at $1/2 1/2 0$ has a much lower potential than the fully occupied sites (e.g., $1/2 1/6 0$).

Because the five projections of staurolite that we used were centrosymmetric, structure factor phases were either 0° or 180° . They were determined directly from the Fourier transform of the image (image intensity spectrum) after shifting to the proper phase origin[2]. Amplitudes could be obtained either directly from electron diffraction patterns or from the transform of the image. We have used the latter. Because electron diffraction patterns average over large areas of varying thickness, it is advantageous to obtain amplitude information from images, even though they are affected by the contrast transfer function. Image simulations for staurolite show that dynamical effects should not be significant in our data. Amplitudes vary linearly with thickness up to an on-axis simulation thickness of 50\AA ; above that, changes become irregular due to dynamic scattering. In the centrosymmetric case, phases derived from the images are less affected by dynamical effects, and are reliable for thickness up to 100\AA .

RESULTS

The three-dimensional potential map calculated from our third determination of the experimental structure factors is illustrated in figure 7 as a three-dimensional surface enclosing all of the cations and associated oxygen atoms that are present at full occupancy.

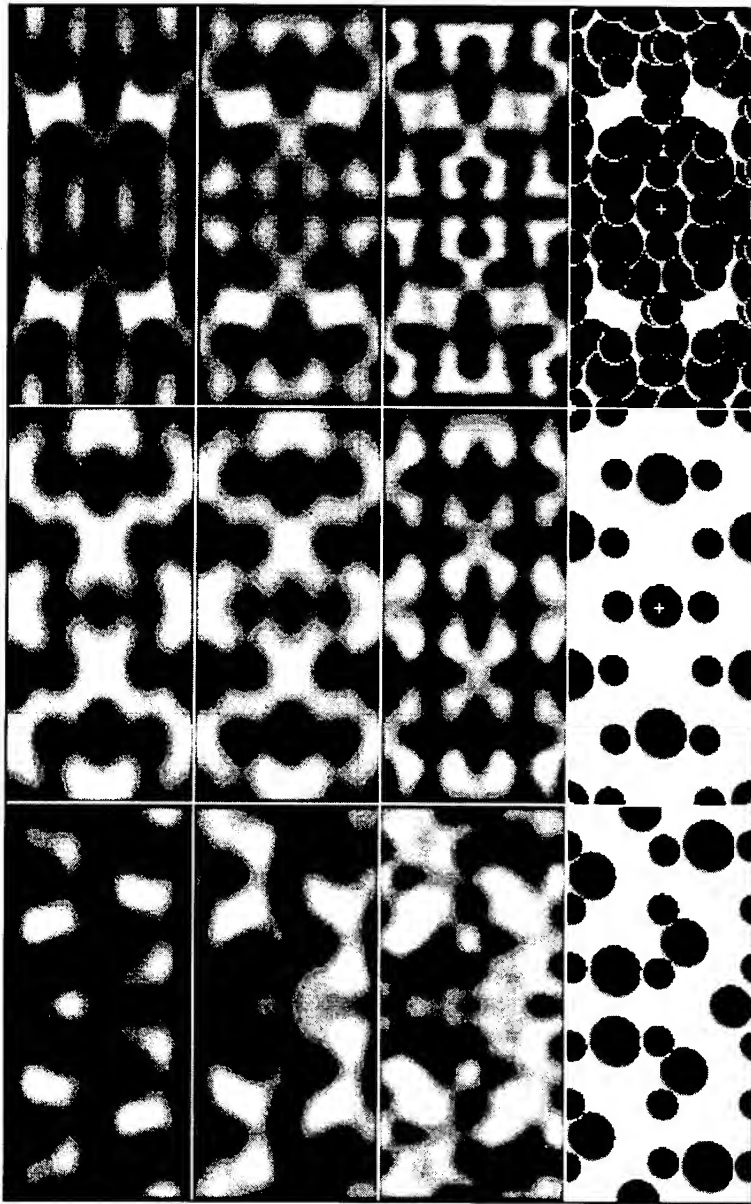


Figure 8. Projections (upper), and sections at $z=0$ (center) and $z=\frac{1}{4}$ (lower) from the three experimental determinations. The first column shows results from the determination from 30 reflections to 1.6\AA , the second from 59 reflections to 1.38\AA , and the third includes CTF correction. Note the correspondence of the 1.38\AA projection to the 1.4\AA WPO image from the model (top right in figure 3). The fourth column shows the model for comparison.

DISCUSSION

We have demonstrated the procedure of three-dimensional reconstruction for staurolite in order to show the steps required. It is clear that three-dimensional reconstruction can enable us to construct images which resolve atoms that are normally overlapped in any one electron microscope image, including lighter atoms such as oxygen in the presence of heavier metal atoms; the fact that individual atoms in a close-packed structure, including the oxygen atoms, can be separated is attributed to the three-dimensional reconstruction. The technique has obvious application to the oxide-superconductor structures.

In addition, once the process of image processing is routinely applied, it becomes simple to extend the microscope resolution by reconstruction from a focal series; in our third structure determination (even before applying any three-dimensional reconstruction) CTF correction and reconstruction from focal series produced images from the ARM-1000 with a full 1.4 Å resolution instead of the routine 1.6 Å available at Scherzer defocus. Such resolution-extension will become of much greater importance as high-resolution electron microscopes equipped with field-emission guns become more prolific.

CONCLUSIONS

We see great potential for three-dimensional electron crystallography in determination of unknown crystal structures, particularly where homogeneous regions exist only in submicrometre-sized domains. Such heterogeneous crystals have been increasingly recognized in metals, ceramics and minerals. We estimate that a three-dimensional structure determination should be possible on areas only about 10 unit cells across, provided only that a sufficient number of projections can be recorded. In addition, where defects are periodic, the technique should be applicable to the supercell created by the periodic defects. Our own efforts are proceeding into applying three-dimensional reconstruction to the case of periodic defects such as grain boundaries in metals and periodic oxygen vacancies in superconductors.

ACKNOWLEDGMENTS

The authors wish to thank J.H. Turner for assistance with the figures and David J. Smith with the text. NCEM facilities are available to qualified microscopists at no cost; they and this work are supported by the Director, Office of Energy Research, Office of Basic Energy Sciences, Materials Science Division of the U.S. Department of Energy under contract no. DE-AC03-76SF00098. In addition, KHD is supported in part by NIH grant GM 36884. Support from the National Science Foundation (EAR88 16577 to HRW), the University of California Education Abroad Program (to HM and HRW) is also gratefully acknowledged.

REFERENCES

1. M. A. O'Keefe, P. R. Buseck, & S. Iijima, *Nature* **274**, 322-324 (1978).
2. L. A. Amos, R. Henderson, & P. N. T. Unwin, *Prog. Biophys. Molec. Biol.* **39**, 183 (1982).
3. R. M. Glaeser, *Ann. Rev. Phys. Chem.* **36**, 243-275 (1985).
4. M.A. O'Keefe and V. Radmilovic, in 51st Ann Proc. MSA, Cinc., Ohio, 980-981 (1993).
5. K. H. Downing, Hu Meisheng, H.-R. Wenk & M. A. O'Keefe, *Nature* **348**, 525 (1990).
6. H-R. Wenk, K.H. Downing, Hu Meisheng, & M.A. O'Keefe, *Acta Cryst. A* **48**, 700 (1992).
7. J. V. Smith, *Amer. Mineral.* **53**, 1139-1155 (1968).
8. M.A. O'Keefe, in 37th Ann. Proc. EMSA, San Antonio, Texas, 556-557 (1979).
9. M.A. O'Keefe, *Ultramicroscopy* **47**, 282-297 (1992).

ELECTRONIC STRUCTURE OF LAYERED AND LINEAR CHAIN MATERIALS BY SCANNING PROBE MICROSCOPY

**R.V. COLEMAN, Z. DAI, Y. GONG, C.G. SLOUGH, AND Q. XUE, University of
Virginia, Charlottesville, VA 22901**

ABSTRACT

Transition metal impurities such as Fe, Ni, and Co can be intercalated into the van der Waals gap of layer structure dichalcogenides and these modify the charge-density wave (CDW) structure and CDW energy gaps. Ordered superlattices associated with antiferromagnetic phases can be detected by both scanning tunneling microscopy (STM) and atomic force microscopy (AFM). STM spectroscopy indicates the formation of a mixed spin-density-wave (SDW) and CDW (SDWCDW) in the doped materials. The quasi-one dimensional trichalcogenide NbSe_3 exhibits two CDW transitions and the presence of dilute transition metal impurities produces ordered superlattices due to long range screening of the impurities.

INTRODUCTION

The layer structure transition metal dichalcogenides and the linear chain transition metal trichalcogenides both form charge-density wave (CDW) phases due to the favorable Fermi surface nesting caused by the lower dimensional structure of these materials. The introduction of interstitial impurities into the chalcogenides is observed in many cases to produce an ordered superlattice of impurities. In the case of the layer structure dichalcogenides the impurities enter the octahedral holes in the van der Waals gap and exhibit an ordered occupancy as the impurity concentration increases, reaching almost perfect ordering for specific fractional occupancies of the octahedral holes. In the case of the transition metal trichalcogenide, NbSe_3 , a long range modulation develops along the chains at very dilute interstitial impurity concentrations. This indicates an ordered spacing of impurities along the chains, but this is occurring through a quite different mechanism from that driving the impurity ordering in the layer structure crystals. The ordering of impurities in both types of materials relates to the low dimensional structure and this modifies the CDW structure in various ways. However, direct

impurity-impurity interactions develop in different ways in the layer structures versus the linear chain structures.

In the layer structure dichalcogenides the impurities in the van der Waals gap order at high concentrations and develop magnetic phases. This indicates a direct interaction between impurities at close range, possibly mediated by the conduction electrons of the chalcogenide. The formation of the ordered impurity phase modifies the CDW structure and we present evidence that a mixed spin-density wave (SDW) charge-density wave (CDW) phase can be formed. In the case of NbSe_3 the long range modulation develops at very low impurity concentrations and results from preferred interstitial impurity sites that result from long range impurity screening effects. This relates to the susceptibility anomalies which exist at high temperature and drive the CDW formation at low temperature. However, the formation of the long range impurity modulation at high temperature does not appreciably affect the CDW structure in contrast to the layer structure chalcogenides.

We have used the atomic force microscope (AFM) to detect the formation of the ordered superlattices and long range modulations at room temperature. For the chalcogenides considered in this paper, the CDWs form at temperatures well below room temperature, and we have used a scanning tunneling microscope (STM) operating at 4.2 K to measure energy gaps associated with the CDW forming in the doped crystals.

The formation of superlattices in the layer structure chalcogenides will be demonstrated with results on 2H- Fe_xNbSe_2 and 2H- Fe_xTaSe_2 . The formation of the long range modulation due to interstitial impurities in NbSe_3 will be demonstrated for a range of impurities including Mn, V, Cr, Fe, Co and Gd.

EXPERIMENTAL TECHNIQUES

The quasi-two-dimensional layer structure dichalcogenide crystals were grown using iodine vapor transport in sealed quartz tubes. The quasi-one-dimensional trichalcogenide crystals were grown in vacuum using sealed quartz tubes. In both cases a specified amount of impurity metal powder was introduced into a stoichiometric powder of metal and chalcogenide. The mixed powder was then sintered and the crystals were grown at a temperature in the range of 650-700°C with a gradient of ~ 25°C per inch.

For crystals listed for example as M_xNbSe_2 , x refers to the concentrations of M_x

relative to Nb in the original powder. The final concentrations in the crystals are determined by the precise way in which the impurities enter the crystal lattice. For the layer crystals the impurities enter the van der Waals gap and x in the crystal is comparable to x in the growth powder. For the linear chain crystals the impurities are interstitial and enter preferred sites between the chains. In general, this means that x in the crystal is substantially less than x in the starting powder. The quantitative amounts of impurity in the as grown linear chain crystals have only been measured for Fe by secondary ion emission [1]. However, the relative changes in impurity concentration as a function of x in the powder have been monitored in all crystals by measuring residual resistance ratios, CDW onset temperatures, and the amplitude and frequency of magnetoquantum oscillations. These properties show a systematic change as a function of the starting concentration of impurity in the powder and these changes are reproducible. However, the rate of change is significantly different for each impurity.

EXPERIMENTAL RESULTS

A. Impurity Superlattice Formation in Fe_xNbSe_2 and Fe_xTaSe_2

The pure 2H phases of NbSe_2 and TaSe_2 exhibit CDW transitions at 35 and 122 K and STM scans [2] at 4.2 K show $3a_0 \times 3a_0$ superlattices as expected. In the dilute concentration range with $x = 0.01$ to $x = 0.10$, the Fe impurities produce Kondo-like resistance minima in the resistance versus temperature curves [3,4], but the CDW structure is not destroyed and can be detected in STM scans [5] at 4.2 K as indicated in the profiles shown in Fig. 1 for Fe_xNbSe_2 . STM spectroscopy shows that the CDW energy gap is reduced from $\Delta_{\text{CDW}} = 59.0 \pm 2.0$ meV in pure 2H- NbSe_2 to $\Delta_{\text{CDW}} = 28.0 \pm 3.4$ meV in $\text{Fe}_{0.10}\text{NbSe}_2$ as shown in Fig. 2(a). For higher concentrations of Fe the energy gap decreases slowly reaching $\Delta_{\text{CDW}} = 25.4 \pm 1.0$ meV at $x = 0.20$ and $\Delta_{\text{CDW}} = 25.3 \pm 1.5$ meV at $x = 0.33$ as shown in Figs. 2(b) and 2(c).

At Fe concentrations of $x = 0.20$ the AFM and STM scans on 2H- $\text{Fe}_{0.20}\text{NbSe}_3$ detect the formation of superlattice regions of the form $2a_0 \times 2a_0$. For $x = 0.33$ in the starting powder the $2a_0 \times 2a_0$ lattice formation is complete and corresponds to a local concentration of $x = 0.25$ in the single crystal. An example of an AFM scan at 300 K on $\text{Fe}_{0.33}\text{NbSe}_2$ showing the strong $2a_0 \times 2a_0$ superlattice is shown in Fig. 3(a).

The behavior of 2H- TaSe_2 as a function of Fe doping is very similar to that of 2H-

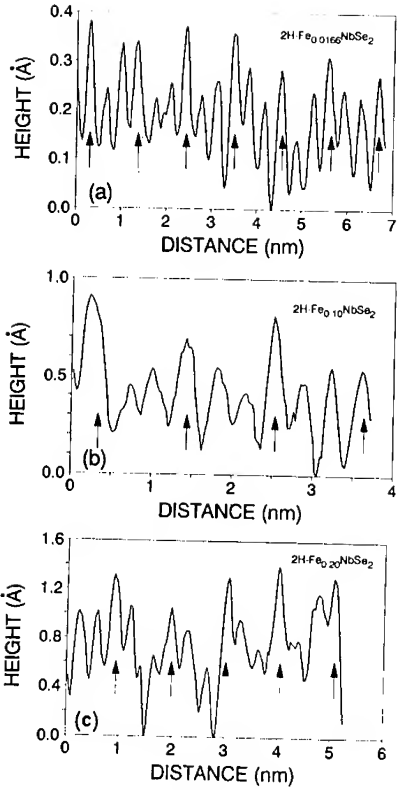


Fig. 1. Profiles of z deflection taken from STM images at 4.2 K for (a) $2\text{H-Fe}_{0.016}\text{NbSe}_2$, (b) $2\text{H-Fe}_{0.10}\text{NbSe}_2$, and (c) $2\text{H-Fe}_{0.20}\text{NbSe}_2$. All three profiles show the $\sim 3a_0 \times 3a_0$ CDW modulation. (From reference 5)

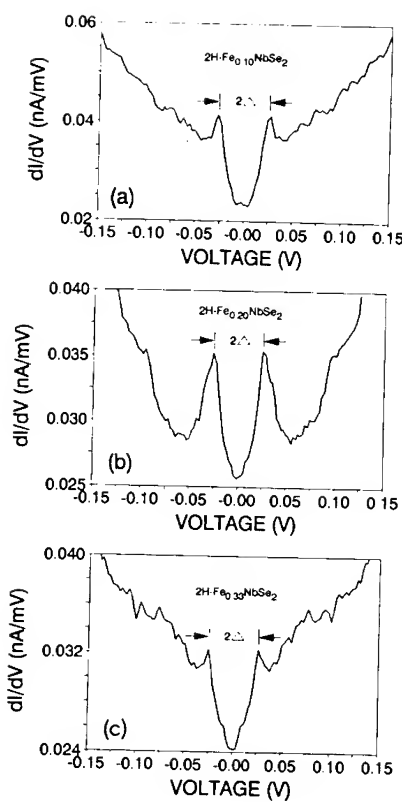


Fig. 2. Conductance versus bias-voltage curves measured at 4.2 K for $2\text{H-Fe}_x\text{NbSe}_2$. They indicate that the CDW energy gap remains relatively constant for concentrations of Fe greater than $x=0.10$. (From reference 5)

NbSe_2 . At low concentrations of Fe the CDW energy gap is substantially reduced, but then remains relatively constant as the Fe concentration is increased and an ordered $2a_0 \times 2a_0$ superlattice of Fe impurities is formed. An AFM scan at 300 K on $\text{Fe}_{0.33}\text{TaSe}_2$ as shown in Fig. 3(b) shows a perfectly ordered $2a_0 \times 2a_0$ superlattice corresponding to a local Fe concentration of $x = 0.25$. As shown in the STM spectroscopy curves of Figs. 4(a) and 4(b) the CDW gap in the pure 2H-TaSe₂ is 89.9 ± 2.8 meV and is reduced to 54.6 ± 1.1 meV in 2H- Fe_xTaSe_2 with $x = 0.05$. Over the concentration range $x = 0.05$ to $x = 0.33$ in the starting powder the measured CDW gaps in Fe_xTaSe_2 remain approximately constant as

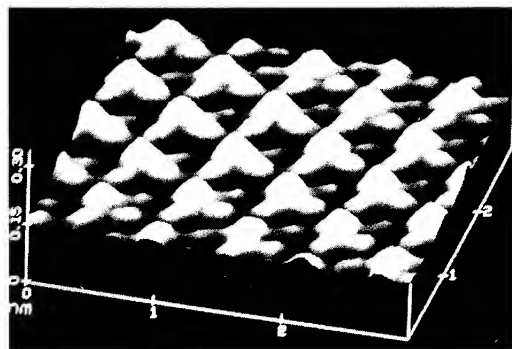


Fig. 3(a). Three-dimensional projection of the AFM scan on 2H-Fe_{0.33}NbSe₂ at room temperature. The image was recorded using the constant force mode. The image shows a basic $2a_0 \times 2a_0$ structure. (From reference 5).

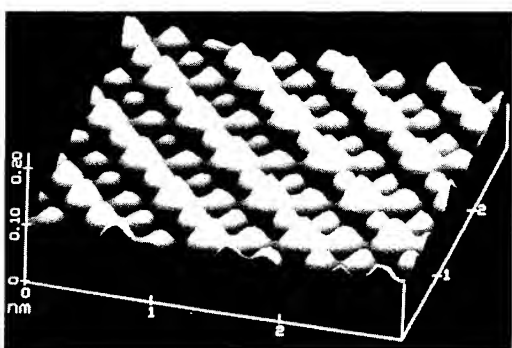


Fig. 3(b). The three-dimensional projection of the AFM scan of 2H-Fe_{0.33}TaSe₂ at room temperature. The scan shows a $2a_0 \times 2a_0$ superlattice similar to the one observed in (a). (From reference 5).

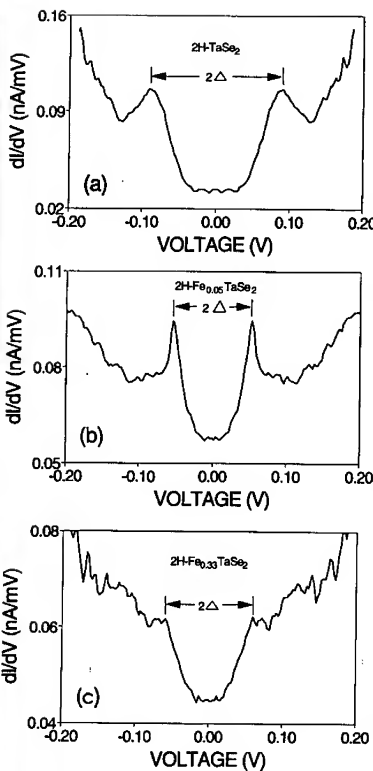


Fig. 4. Conductance versus bias-voltage curves measured at 4.2 K. (a) Pure 2H-TaSe₂ shows peaks above CDW gap edges at $\sim \pm 89.9$ mV. (b) 2H-Fe_{0.05}TaSe₂ shows peaks above CDW gap edges at $\sim \pm 54.6$ mV. (c) 2H-Fe_{0.33}TaSe₂ shows peaks above CDW gaps edges at $\sim \pm 58.8$ mV.

indicated by the STM spectroscopy curve in Fig. 4(c) for $x = 0.33$ which gives a measured value of $\Delta_{\text{CDW}} = 58.8 \pm 4.6$ meV.

For $x < 0.10$ in Fe_xTaSe_2 a Kondo-like resistance minimum is also observed at low temperature. For crystals of both Fe_xNbSe_2 and Fe_xTaSe_2 with $x > 0.20$ the resistance minima disappear and the resistance versus temperature curves show a monotonic decrease of resistance as a function of decreasing temperature with a pronounced break in slope. For

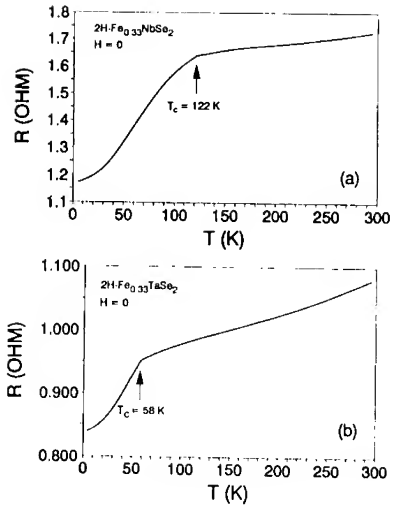


Fig. 5. (a) Resistance versus temperature curve measured for 2H- $\text{Fe}_{0.33}\text{NbSe}_2$. An antiferromagnetic phase transition is indicated at ~ 122 K. (b) Resistance versus temperature curve measured for 2H- $\text{Fe}_{0.33}\text{TaSe}_2$. An antiferromagnetic phase transition is indicated at ~ 58 K.

concentration as well as the same development of a $2a_0 \times 2a_0$ Fe superlattice. We conclude that both materials develop an antiferromagnetic phase at high Fe concentration and that these phases exhibit a spin-density wave component associated with the measured energy gaps. Additional discussion is given in Section IV.

B. Long Range Impurity Screening Modulation in NbSe_3

The quasi-one-dimensional metal NbSe_3 exhibits two CDW phase transitions, with onset temperatures $T_{C1} = 144$ K and $T_{C2} = 59$ K. Pure NbSe_3 is monoclinic with six chains per unit cell. The introduction of dilute interstitial impurities into NbSe_3 produces an immediate long range modulation parallel to the chain direction [7]. The wavelength of this modulation depends on the impurity concentration in the as grown crystal. The wavelength is many unit cells at very dilute concentrations and decreases to a wavelength of two unit cells at high

crystals grown from powders with $x = 0.33$ the pronounced breaks in slope occur at 122 K in $\text{Fe}_{0.33}\text{NbSe}_2$ and at 58 K in $\text{Fe}_{0.33}\text{TaSe}_2$ as shown in Figs. 5(a) and 5(b).

The breaks in slope are associated with transitions to an antiferromagnetic phase clearly associated with the existence of the well-ordered $2a_0 \times 2a_0$ lattice of Fe atoms located in the van der Waals gap. Susceptibility data [6] on Fe_xNbSe_2 clearly establish a transition to an antiferromagnetic phase for Fe concentrations above $x = 0.20$. For $x = 0.33$ a well-defined susceptibility maximum is observed at ~ 130 K in reasonable agreement with the break in slope observed in the resistance curve at 122 K. Susceptibility data is not available for Fe_xTaSe_2 , but the resistance curves show the same range of behavior as a function of Fe

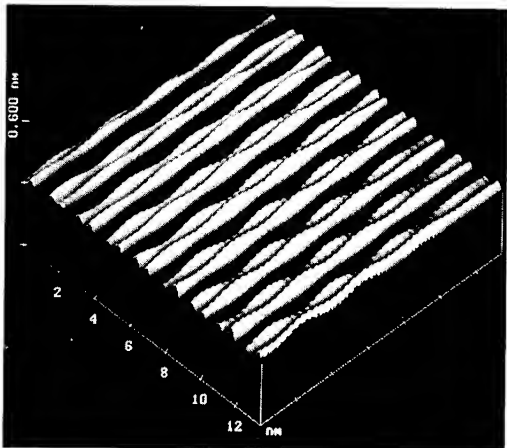


Fig. 6(a). 3-dimensional projection of an AFM scan on $\text{Gd}_{0.01}\text{NbSe}_3$ recorded in the constant force mode at room temperature. An impurity induced modulation of wavelength $10b_0$ is observed.

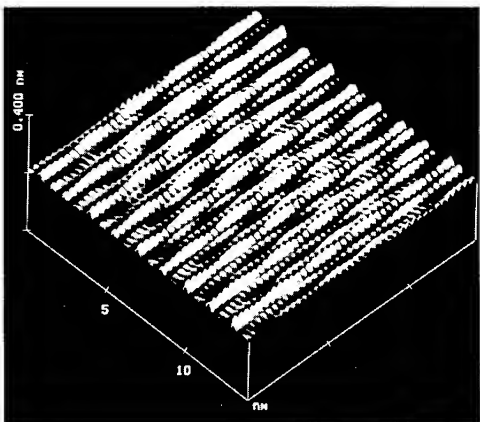


Fig. 6(b). 3-dimensional projection of an AFM scan on $\text{Mn}_{0.03}\text{NbSe}_3$ recorded in the constant force mode at room temperature. The wavelength of the impurity induced modulation is $8b_0$.

concentrations. The initial wavelength observed is characteristic of each impurity and is consistent with differences in the impurity charge and the resulting screening charge. The long distance ripples in the screening charge produce, in turn, a long range interaction between impurities and a disturbance of the total charge density that can propagate over macroscopic distances. This is a different mechanism than the one that produces ordering of the impurities in layer structure crystals. It is unique to the one-dimensional chain structure and is related to the existence of the stronger susceptibility anomalies that lead to the formation of CDW's at low temperature. Further discussion of the mechanism will be given in section IV.

The long range modulations produced by the dilute interstitial impurities in NbSe_3 can easily be detected in AFM scans at room temperature. Examples of the longest wavelength modulations observed for two different impurities in NbSe_3 are shown in the AFM scans of Fig. 6. The longest wavelength modulations as shown in Fig. 6 all occur for crystals

grown from powders with impurity concentrations of $x \leq 0.01$. The impurity spacing and concentration taken up by the crystal is governed by the charge screening and impurity

interaction and is different for each impurity. In most cases the concentration of impurity in the crystal is substantially less than in the starting growth powder although the impurity concentration in the crystal can be systematically increased by increasing the concentration in the growth powder and this is, in turn, correlated with a systematic decrease of the observed modulation wavelength.

For Gd doping in the most dilute range the modulation wavelength is $\Lambda = 10 b_0$ as shown in Fig. 6(a). For Mn doping in the most dilute range the modulation wavelength is $\Lambda = 8b_0$ as shown in Fig. 6(b). For V doping in the most dilute range the modulation wavelength is $\Lambda = 6 b_0$. For Cr doping in the most dilute range the modulation wavelength is $\Lambda = 5b_0$. As the concentration of impurity is increased in all cases, the wavelength changes to a shorter wavelength in crystals grown from powders with x above certain critical values.

In the case of Gd the observed wavelength series is $10b_0, 6b_0, 4b_0$, and $2b_0$. For Mn, the wavelength series is $8b_0, 5b_0, 3b_0$ and $2b_0$. For V, the wavelength series is $6b_0, 4b_0$ and $3b_0$. For Cr, the wavelength series is $5b_0, 4b_0, 3b_0$ and $2b_0$. The critical values of impurity concentration x required in the growth powder in order to induce the various modulation wavelengths is substantially different depending on the specific impurity. For Cr and Gd the entire series is observed in the range $x = 0.0$ to 0.04 . For V and Mn, the series of wavelengths is observed over a much larger range with $x = 0.0$ to 0.30 .

In NbSe_3 doped with dilute interstitial impurities, the CDW energy gaps can show an initial rapid change, but remain well-defined for the range of impurity modulations studied here [8]. For Fe doping the energy gaps are decreased on the order of 30%, while for Co doping they are increased on the order of 30%. At this level of doping both Fe and Co produce a high temperature modulation of wavelength $2b_0$. The changes in CDW gaps observed do not have a major effect on the Fermi surface nesting, but correlated effects are observed in the relative intensities of the CDWs observed with STM, the details of the resistance anomalies associated with the CDW's, and the frequencies of the magnetoquantum oscillations. The correlations will be presented in more detail in other publications [9] [10].

DISCUSSION

The addition of interstitial impurities to the quasi-two-dimensional layer structure crystals and the quasi-one-dimensional linear chain crystals produces interesting ordered states

of the impurity atoms. These result from unusual impurity interactions that are distinctly different in the two cases. In the case of the layer structures the impurity atoms occupy the octahedral holes in the van der Waals gap, and at high concentrations the direct impurity interactions create an ordered occupancy of the octahedral holes. In the case of Fe impurities these ordered superlattices form magnetic phases at low temperatures. In the linear chain material, NbSe_3 , very dilute interstitial impurities form an ordered occupancy along the chains and create a long range electronic modulation along the chains. This modulation is associated with the impurity screening which develops long range "ripples" due to the presence of strong susceptibility anomalies in the quasi one-dimensional crystals. The two different cases will be discussed below.

The AFM images presented above have been processed through Fourier filtering in order to remove noise in the original scan. However, the original scans used clearly show the superlattice modulation in the layer structure crystals and the long range impurity modulation in the doped NbSe_3 crystals. The Fourier transforms of the data used for this filtering also show extremely strong peaks at the appropriate wave vectors in the cases used, and these can be reproduced on different crystals of the same material.

The energy gap spectroscopy has all been carried out at 4.2 K and within experimental error we have not observed any spatial variation of the magnitude of the energy gap. In general the dominant structure would be determined by the abrupt change in the density-of-states as the bias voltage exceeds the critical value corresponding to CDW gap energy. This would be a property of the band structure as modified by the CDW and for a given tunneling direction relative to the crystal axes would not be expected to depend on surface topography. The slope of the general conductance curve might depend on topography, but this has not been studied in any detail.

A. Ordered Antiferromagnetic Phases in 2H- Fe_xNbSe_2 and 2H- Fe_xTaSe_2

Previous x-ray diffraction experiments on 2H- Fe_xNbSe_2 and 2H- Fe_xTaS_2 have established the existence of ordered superlattices of Fe with the Fe atoms occupying the octahedral holes in the van der Waals gap below the Nb or Ta atoms. The present experiments also establish that 2H- Fe_xTaSe_2 forms an ordered superlattice similar to that forming in 2H- Fe_xNbSe_2 .

The AFM results at room temperature reported in this paper confirm the formation of

a $2a_0 \times 2a_0$ superlattice of Fe atoms in the octahedral holes of the van der Waals gap. The STM scans at low temperature show that the $3a_0 \times 3a_0$ CDW superlattices persist until the Fe concentration approaches $x = 0.20$ and is quenched when the full $2a_0 \times 2a_0$ Fe lattice is formed corresponding to $x = 0.25$.

However, the STM spectroscopy results at 4.2 K show that a well-defined energy gap in the electronic spectrum exists throughout the entire range of Fe doping and shows very little change as the crystal makes the transition from a $3a_0 \times 3a_0$ CDW superlattice to a $2a_0 \times 2a_0$ superlattice exhibiting antiferromagnetic properties.

The continued presence of the energy gap in the antiferromagnetic phase suggests the presence of a density wave associated with the antiferromagnetism. The stabilization of a static SDW would drive the formation of the antiferromagnetic phase, or the formation of a mixed SDWCDW could characterize the antiferromagnetic phase. The mixed density wave state has been discussed by Denley and Falicov [11] who studied a variety of electron correlated density wave states in hexagonal layers. Mechanisms for density wave formation in antiferromagnetic alloys were also previously discussed by Overhauser [12] and by Antoniou [13]. The development by Antoniou [13] was specifically applied to Fe doped 2H-TaSe₂ in order to explain the susceptibility data in terms of a type of spin-glass developing out of the CDW phase.

B. Impurity Screening in NbSe₃

Charge-density wave systems in their normal phase exhibit a wavevector-dependent electric susceptibility that has striking and unusual features. In particular the susceptibility is very large for the vector \mathbf{Q} that, at lower temperatures (in the CDW phase), becomes the characteristic wavevector of the oscillatory electronic charge connected with the CDW. The high temperature susceptibility at the \mathbf{Q} vector in quasi-one-dimensional metals such as NbSe₃ can be expected to be extremely large and this in turn can affect the electronic screening of the impurity charge at high temperature.

In general the \mathbf{Q} is arbitrary and is determined by the properties of the Fermi surface, the phonon spectrum, and the electron-phonon interaction. In the case of NbSe₃ the susceptibility has a maximum associated with the high temperature CDW phase at a \mathbf{Q} given by

$$\mathbf{Q} = (0 \mathbf{G}_a, 0.243 \mathbf{G}_b, 0 \mathbf{G}_c) \quad (1)$$

where \mathbf{G}_a , \mathbf{G}_b , and \mathbf{G}_c are the three reciprocal-lattice vectors of the monoclinic structure; \mathbf{G}_b is along the two-fold axis. \mathbf{Q} is directed along the monoclinic b -axis (chain axis) and is incommensurate with it with a period of approximately $4.11 b_0$.

The interstitial impurities will be located in one or a few sites in the unit cell corresponding to lower energy compared to other high energy sites. The atomic (ionic) potential associated with the impurity produces an excess (defect) in the electronic charge of the metallic solid. This excess (defect) charge, a result of the Coulomb and local fields, is the screening of the impurity atom. For normal metals the screening charge is restricted to a Thomas-Fermi-length which is relatively short with no perceptible long-range effects on the electronic structure.

In CDW solids, especially the quasi-one-dimensional types with large susceptibility anomalies above the CDW transition temperature, the impurity screening charge produces large "ripples" in the charge and these can propagate over long distances. These long-distance "ripples" produce a long-range interaction between impurities and a disturbance in the total charge density that can propagate over macroscopic distances. As a result of the interaction and long range charge disturbance, the impurities try to distribute themselves during crystal growth so that the total free energy of the system is a minimum. Contributions to the free energy will come from the local energy of the impurities, the total charge-density distribution, the compatibility of the impurity location in the unit cell, and the "intrinsic" charge oscillation.

The final impurity configuration and charge oscillation depend on competing factors such as, the value or values of \mathbf{Q} for which the susceptibility is a maximum, the favored position of the impurity in the unit cell, and the strong interaction between impurities due to the long range "ripple" in the screening charge. The resulting impurity spacing is such that the charge oscillations, and the attended periodic lattice distortions, give a free energy minimum. Since this is a balance of many competing factors, small changes in the impurity concentration would be expected to change the impurity spacing and charge oscillation wavelength as observed in the AFM experiments.

The long range charge oscillations discussed here are observed at 300 K, well above the CDW transition temperatures. The presence of these impurity induced oscillations does not have a very strong effect on the low temperature CDW formation. The CDW transitions

have been studied in the resistance versus temperature curves [9] and in measurements of the magnetoquantum oscillations [10] as well as direct STM images of the CDW structure at 4.2 K.

At very dilute concentrations of impurity corresponding to the longest wavelength charge oscillations observed at high temperature, the characteristic CDW properties at low temperature show little or no change other than an increased pinning and a reduction of the energy gap. As the impurity concentration increases and the high temperature oscillation wavelength decreases, the T_C 's of the CDW's can slowly decrease and the quantum oscillation frequencies become less anisotropic. The magnitude and concentration dependence of these changes is a function of each specific impurity. Overall the Fermi surface nesting and CDW phases show only relatively small changes due to the interstitial impurities and charge oscillations due to the impurity screening at high temperature. This is consistent with the overall picture in which the impurity screening oscillations and CDW formation are independent effects except for the fact that both arise from the very strong susceptibility anomalies expected for quasi-one-dimensional metals with strong Fermi surface nesting.

CONCLUSIONS

These experiments have shown that the AFM and STM can be used to discover subtle changes in the electronic structure of low dimensional metals induced by impurities. In the case of Fe_xNbSe_2 and Fe_xTaSe_2 STM spectroscopy has been used to show the existence of a mixed density wave and in $NbSe_3$ doped with a wide range of impurities a new type of long range impurity screening has been discovered.

Research supported by DOE Grant DE-FG05-91ER45072 and NSF Grant DMR92-23576.

REFERENCES

- [1] R.V. Coleman, M.P. Everson, Hao-An Lu, and A. Johnson, Phys. Rev. B **41**, 460 (1990).
- [2] R.V. Coleman, B. Giambattista, P.K. Hansma, A. Johnson, W.W. McNairy, and C.G. Slough, Adv. Phys. **37**, 559 (1988).
- [3] D.A. Whitney, R.M. Fleming, and R.V. Coleman, Phys. Rev. B **15**, 3405 (1977).
- [4] S.J. Hillenius, R.V. Coleman, E.R. Domb, and D.J. Sellmyer, Phys. Rev. B **19**, 4711 (1979).
- [5] Z. Dai, Q. Xue, Y. Gong, C.G. Slough, and R.V. Coleman, Phys. Rev. B **48**, 14543 (1993).
- [6] S.J. Hillenius and R.V. Coleman, Phys. Rev. B **20**, 4569 (1979).
- [7] Y. Gong, Q. Xue, Z. Dai, C.G. Slough, R.V. Coleman, and L.M. Falicov, Phys. Rev. Lett. **71**, 3303 (1993).
- [8] Zhenxi Dai, C.G. Slough, and R.V. Coleman, Phys. Rev. B **45**, 9469 (1992).
- [9] Q. Xue, Y. Gong, C.G. Slough, and R.V. Coleman (unpublished).
- [10] C. G. Slough, Z. Dai, Y. Gong, Q. Xue, D.L. Drake, and R.V. Coleman (unpublished).
- [11] D. Denley and L.M. Falicov, Phys. Rev. B **17**, 1289 (1978).
- [12] A.W. Overhauser, Phys. Rev. B **29**, 7023 (1984).
- [13] P.D. Antoniou, Phys. Rev. B **20**, 231 (1979).

ATOM PROBE MICROSCOPY AND ITS FUTURE

T. F. KELLY^{1,2,3}, P. P. CAMUS^{2,3}, D. J. LARSON^{1,3}, AND L. M. HOLZMAN^{1,3}

¹Materials Science Program, ²Department of Materials Science and Engineering

³Applied Superconductivity Center, University of Wisconsin, Madison, WI 53706.

ABSTRACT

Much of the current activity and excitement in materials science involves processing and understanding materials at the atomic scale. Accordingly, it is necessary for materials scientists to control and characterize materials at the atomic level. There are only a few microscopies that are capable of providing information about the structure of materials at the atomic level: the atom probe field ion microscope, the high resolution transmission electron microscope, and the scanning tunneling microscope. The three-dimensional atom probe (3DAP) determines the 3D location and elemental identity of each atom in a sample. It is the only technique that provides 3D information at the atomic scale.

The origin and underlying concepts behind the 3DAP are described. Several examples of actual images from existing 3DAPs are shown with emphasis on nanometer-scale analysis. Current limitations of the technique and expected future developments in this form of microscopy are described. It is our opinion that 3D atomic-scale imaging will be an indispensable tool in materials science in the coming decades.

1. INTRODUCTION

In the last decade or so, atomic-scale microscopy and microanalysis have blossomed. For examples, consider the invention of the scanning tunneling microscope (STM) or developments in high resolution transmission and scanning transmission electron microscopy (HRTEM and HRSTEM). In each of these atomic-scale microscopies, however, the image is either two dimensional (STM) or it is a two-dimensional projection of a three-dimensional object (HRTEM and HRSTEM).

Atom probe microscopy [1], which is based on the first ever atomic-scale imaging technique, field ion microscopy (FIM), has entered a new era in its development. Three-dimensional atom probes (3DAP) are now operating which produce 3D images with atomic scale resolution. The 3DAP brings atomic-scale microscopy into the next dimension. Indeed, 3DAP may fairly be considered an entirely new genre of high resolution analytical microscopy.

Though not all of the capabilities are yet realized, it appears that the technology will soon be at hand to make 3DAPs do everything that their predecessor, the conventional atom probe, now does and also reach the third dimension. These microscopes will be simpler, smaller, faster, and much more powerful than the conventional atom probe.

The ability to analyze atomic-scale structure is becoming a necessity in order to optimize a wide variety of materials systems which come from both traditional fields (e.g., ferrous metallurgy) and emerging technologies (e.g., multilayer thin films). In the future, this ability will be requisite. In this paper, we take stock of the present technology of atom probe microscopes and explore the future promise of this fascinating instrument.

How the Atom Probe Works

The 3DAP evolved from the conventional atom probe [1] which evolved from the FIM [2] which evolved from the field electron emission microscope [3]. Some background on the operation and capabilities of an APFIM is provided in an excellent review of conventional AP by Miller [4]. Essentially, the FIM is capable of producing a static two-dimensional image of atoms on the surface of a sharply pointed specimen. These surface atoms can also be removed in a controlled fashion by field evaporation which makes it possible to image successive atomic layers and thus gain three-dimensional information about the internal structure of the specimen.

The Conventional Atom Probe

The process of field evaporation results in ionization of the surface atoms, which are accelerated to the imaging screen by the applied field. In the APFIM, shown schematically in Figure 1, pulsed field evaporation removes a fraction of a monolayer from the specimen surface. The standing high voltage is kept low enough that the initial evaporation rate is negligible. A very short duration (<10 ns) high voltage (15% of standing voltage) pulse is applied which causes evaporation of a small number of ions (0.01 to 10 detected ions per pulse). The time-of-flight (TOF) of the evaporated ions from the specimen to a single-particle detector is measured and used to identify the ions. This approach is known as "voltage pulsing" or "field pulsing". In conventional voltage pulsing, the ions evaporate over a range of voltages during the pulse. The resulting range in kinetic energy leads to a large variation in the total TOF for any given ion. This uncertainty in the TOF directly limits the mass resolution of an AP.

It is also possible to momentarily increase the field evaporation rate by pulsing the temperature of the tip, which is known as "thermal pulsing". In the late 1970's, Tsong [5] and Kellogg and Tsong [6] described the use and advantages of thermal excitation by a pulsed laser for inducing field evaporation. By holding the field just below the critical evaporation field and then heating with a short duration (7 ns) laser pulse, they were able to induce controlled evaporation in a pulsed mode. The major advantage of this approach over voltage pulsing is that the applied field is constant during the pulse ($\Delta V \approx 0$) and the mass resolution is therefore not degraded by a large spread in kinetic energy as in voltage pulsing.

In a conventional AP, an aperture is placed in the image screen to allow the ions from a specific location on the specimen to pass into a long-flight-path TOF mass spectrometer. This long flight path makes for long TOFs which improves the timing resolution and therefore the mass resolution. It is also possible to build devices, for example a Poschenrieder lens [7] and a reflectron lens [8], which compensate for variations in the kinetic energy of the ions for the case of voltage pulsing so that ions of like mass-to-charge ratio have the same time of flight.

Because elemental identification is based on TOF, all elements are detected simultaneously and there are no mass limitations either at low or high masses. However, the TOF detector is typically only a few atom diameters wide at the image plane, and it does not record any positional information about the ions. Thus conventional AP data are inherently one-dimensional. The lateral resolution varies from about 0.2 nm to 10 nm depending on the sample, and the depth resolution varies from about 0.2 to 1.0 nm depending on the image plane.

One serious limitation of conventional AP is that it makes inefficient use of the sample: over 99.9% of the specimen atoms that are evaporated are never analyzed. The imaging atom probe [9] and the wide-angle atom probe [10] have developed in response to this inefficiency. They

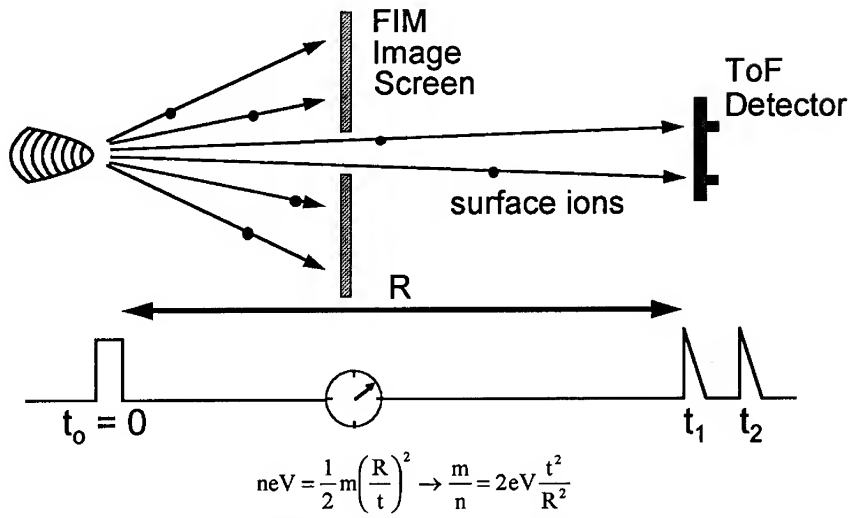


Figure 1. Schematic of an APFIM which shows microchannel plates for amplification of the image and a central aperture which is an entrance to a time-of-flight mass spectrometer. The magnification for both imaging and analysis depends on specimen radius of curvature and the location of the microchannel plate amplifiers.

both make it possible to image and analyze a very large amount of the surface with similar depth resolution but reduced lateral resolution.

The 3DAP

By measuring the TOF of each ion to the wide-angle image plane (FIM image screen) and the arrival position on that plane, then the benefit of large area analysis with good lateral resolution would be obtained. This is what is done in 3DAP. In this way, both the position of the atoms on the surface of the tip and their identity are determined.

The group at the University of Oxford was the first to apply a wide-angle position-sensitive detector (PSD) to an AP [11, 12]. Figure 2, which they call the position-sensitive atom probe (PoSAP). Incoming ions strike a microchannel plate (MCP) and the electron charge cloud that is produced is accelerated onto a position-sensitive anode. The PoSAP uses a wedge-and-strip anode that divides the charge, depending on location, among three geometrically-arranged interpenetrating electrodes [13].

3DAP Images

Using voltage pulsing, the Oxford group has produced numerous nanometer-scale PoSAP images [14]. Each spot in the images corresponds to a single detected ion. Note that not every atom in a sample is detected; the microchannel plates amplify only about 60% of the ions which

hit them. In addition, the detection system will have a finite error rate though this should typically be very low ($<10^{-3}$).

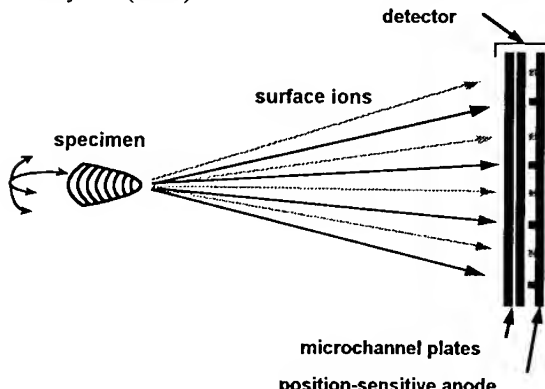


Figure 2 Schematic of a PoSAP which shows microchannel plates for amplification of the image and a PSD. Note that the effective aperture is the entire detector and that the flight path is limited to the distance between the specimen and the microchannel plates.

distance between the specimen and the detector. The trade-off is that this decreases the lateral width of the 3D image. The best mass resolution in a 3DAP to date has been achieved by the group at the Université de Rouen in their tomographic atom probe (TAP) which has a one-meter long flight path [17]. An image recorded by the TAP from a nickel-base superalloy which shows both a γ and γ' phase is shown in Figure 3. The mass resolution of the TAP is one part in 300 which is adequate for nearly all materials analysis work. Presently, both the Oxford and the French 3DAPs are moving to a flight path length of about 500 mm as a compromise between image width and mass resolution.

2. PRESENT CAPABILITIES AND DEVELOPMENTS

Because 3DAPs are much newer and more powerful than conventional atom probes, the examples in this paper will concentrate on results from 3DAPs.

3D Quantitative Microanalysis -- The composition at any location in a sample is determined simply by counting the number of each type of atom in a given volume. This is a great advantage of 3DAP; 3D microanalysis may be performed for a volume of any shape, location and size, from a few atoms to the entire data set. The statistical precision of the analysis, of course, depends on the size of the analyzed volume.

Composition Imaging -- As an approach to composition imaging, 3DAP is clearly very powerful and flexible. For example, Figure 4 shows a 3D rendering of an Fe-Cr spinodal structure [18]. The local composition is determined by mathematically smoothing small volumes of about less than 10 atoms throughout the image and an isoconcentration surface is fit during

Since conventional atom probes may be fitted with devices which compensate for the kinetic energy spread of the ions in voltage pulsing [7, 8], their mass resolution can be as high as one part in 2000. At this time, there is no demonstrated approach which will make it possible to achieve high mass resolution in 3DAPs without unduly sacrificing image size. This is a topic which has received attention recently [15] and is clearly a goal for further development of 3DAP. The PoSAP achieves a mass resolution of about one part in 75 [16] which makes it difficult to separate some elements (or their isotopes) in common analyses.

It is possible to improve the mass resolution of 3DAP by increasing the

post-collection computation. The real power of 3DAP in showing the true 3D nature of the composition distribution becomes more apparent in this image. Furthermore, these images may be analyzed, transformed, and rendered after recording, in any manner which may optimally extract and illustrate the desired information.

Since the images are three-dimensional, it is desirable to be able to display them as such. For example, dynamic stereo image presentation on a computer monitor and holographic rendering are two possibilities which can make the presentation of this information more effective.

Applications -- The AP is at its best when more than one of the unique capabilities of the AP can be exploited. Some of the unique capabilities of 3DAP include atomic-scale composition imaging, detectability of all elements and isotopes and even molecular species at atomic resolution, and a minimum detectable mass of one atom. Other techniques may be able to match one or more of these capabilities but only 3DAP can provide them simultaneously. These analysis capabilities would be useful for their low-mass detection capabilities (as in carbon distribution in ferrous metallurgy or boron segregation in intermetallics), the high lateral spatial resolution (as in segregation to interfaces) and/or the high depth resolution (as in composition and structure quantification of fine precipitates). Typical materials studies that could use the 3D capabilities of 3DAPs include segregation at and near interfaces, fine-scale composition variations (< 1 nm) and light-element analyses. In addition, when high data collection rates are employed in 3DAP, then analysis of large numbers of atoms make it possible to quantify low concentrations and analyze features on a larger scale. The possibility of high speed 3DAP will be discussed below.

An illustration of the unique power of 3DAP images comes from studies of interfaces in multilayer structures. Fine-scale multilayer structures are used in many important materials technologies such as information storage, quantum effect devices, and high speed electronics. A problem which is common to all of these materials systems is that there has not been a characterization technique which can provide compositional and morphological information about the layers and their interfaces at the atomic scale in 3D. HRTEM has been the most useful imaging technique for studying these materials but it is limited by the fact that the information is integrated in one dimension for both imaging and local composition determinations.

3DAP is likely to make significant contributions to this characterization problem. Some early work by the Oxford group [19] illustrates the promise of this technique. They have found that the interface roughness in a GaInAs/InP multilayer is greater at the InP/GaInAs interface than at the GaInAs/InP interface as the structure grows. This interface roughness may be quantified after fitting an isoconcentration surface to the interface. This work shows that 3DAP holds great promise for providing the feedback that is needed to optimize these multilayer structures.

Materials studies are most effective when multiple techniques are used to investigate a phenomenon. Each technique provides information that is either unique or is corroborative in nature. Typical techniques that are used in conjunction with AP are SIMS, SEM, SAM, and (S)TEM.

3. IMPROVING THE 3DAP

There are improvements in 3DAP which are needed to make it realize its full potential. Current 3DAPs suffer from two primary limitations: low data collection rate (due to a low pulsing rate and single-event detection) and low mass resolution (due to the use of voltage pulsing with a short flight path). The data collection rate is a product of the pulsing rate (number of

pulses per second) and the detection proficiency (number of ions detected per pulse). The detection proficiency is a product of the probability of detecting an incoming ion (detection efficiency) and the number of concurrent events that can be deciphered by the detector. Each of these may be considered for improvement.

Increased Pulsing Rate -- In field-pulsed atom probes, the data collection rate is primarily limited by the repetition rate of the pulsing system. In a conventional AP, the field is pulsed from a capacitor bank through a mercury-wetted reed switch that can be operated at a maximum of about 200 pulses per second. This pulsing rate severely limits the rate of data collection in voltage-pulsed APs especially since the duty cycle of the analysis permits frequencies up to 1 MHz.

Thermal pulsing has been considered for rapid pulsing. The first requirement is that the achievable evaporation pulse width be less than about one nanosecond. Pulse widths of this magnitude may be achieved if a small enough volume of the tip (less than one micron in length) is heated [20, 21]. Small heated volumes have the added benefit that the total deposited energy is small and the repetition rates may be high.

The possibility of increasing the pulsing rate by several orders of magnitude by using an electron beam to thermally pulse the field evaporation rate has been modeled [20, 22, 23]. Detailed theoretical calculations [20, 21] indicate that up to 10^6 pulses per second will be achievable with electron beam pulsing. Thus much larger quantities of material can be studied in a short time (one billion atoms or about one micron in length will take 27 hours at 10^4 atoms per

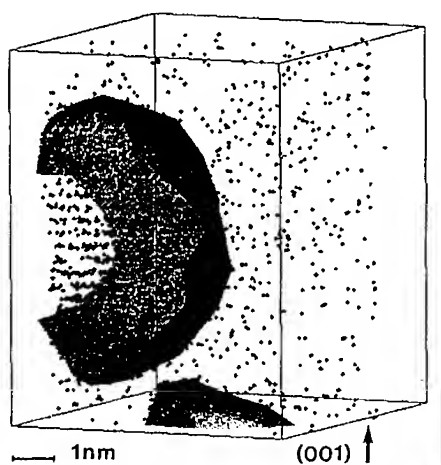


Figure 3 3DAP image from the TAP which shows the spatial distribution of aluminum (nickel has been recorded but is not shown for clarity) near a γ/γ' interface [17]. γ is a disordered face-centered cubic phase and γ' is an ordered $L1_2$ cubic phase. This image shows that the aluminum atoms in the base planes of the ordered structure can be resolved as distinct planes.

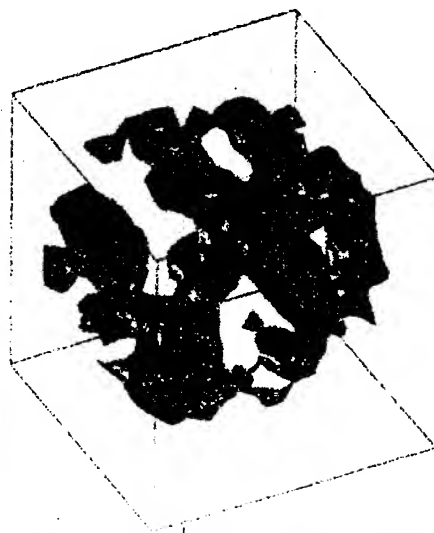


Figure 4. Three-dimensional PoSAP image of an Fe-Cr spinodal structure which has been determined by fitting an isoconcentration surface. Local concentrations were determined from cubic volumes which contain on average 10 atoms. The isoconcentration fit has been smoothed and rendered [18].

second and only 17 minutes at 10^6 atoms per second). With these large volumetric capabilities, the 3DAP would become a more generally useful analytical instrument.

Improvements in Mass Resolution -- The quality of the data from 3DAPs is compromised by a field-pulsing as currently practiced. The uncertainty in the acquired kinetic energy, which limits mass resolution, derives primarily from an uncertainty in the voltage at the moment of evaporation. Thermal pulsing, however, greatly reduces the troublesome energy spread of ions. Furthermore, thermal pulsing may, in principle, have a much shorter pulse width. Both of these effects lead to inherently better timing and therefore, mass resolution. Thus a thermal-pulsed 3DAP may achieve both high repetition rates and high mass resolution in a single instrument.

Increased Detection Efficiency -- Currently MCPs are used for most AP detectors, as well as for single-particle detectors in many fields of study. However, their detection efficiency is limited by the amount of open area on the entrance side of the assembly, typically 60%. As the identification of each and every atom in an AP or 3DAP specimen is preferred, increasing the overall detection efficiency towards 100% would significantly increase the quality and quantity of information acquired and reduce errors in small-volume composition determinations. Development of 100% efficiency detectors for 3DAP remains one of the key needs of this field.

Detection of Multiple Concurrent Events -- Large increases in the data generation rate may be realized by devising a detector that can decipher concurrent events. The wedge-and-strip anode, used in the PoSAP, can detect only a single event at a time. In order to ensure that there is a negligible (about 10^{-4}) chance of two like atoms evaporating in any one pulse, the average number of detected ions per pulse must be kept lower than about one detected ion per 250 pulses. At about 250 pulses per second in a field-pulsed 3DAP, only about one atom per second is detected. At this rate, it takes more than 10 days to collect a small volume of one million atoms (about 20 nm on a side).

If a PSD can be devised that accepts two events simultaneously, then the pulse magnitude may be increased such that the probability of three events is negligible. At this rate, there may be two atoms perhaps every 250 pulses and one atom every 25 pulses. An order of magnitude increase in the data generation rate is therefore expected by utilizing a dual-event detector. Three-event detectors would offer another order of magnitude increase in data collection rate, and so on. Currently, three other groups have designed and built multi-hit detectors [24, 25, 26] and a 100x increase in the data collection rate has been reported [24]. This permits the acquisition of the million atom data set in under 3 hours. Thus a significant increase in the data collection rate will greatly benefit 3DAP analysis.

Increased Lateral Image Resolution -- The ultimate in 3DAPs would be a system which has sufficient spatial resolution that the crystal structure of a material can be determined directly in real space from the atomic position information. Aberrations in the trajectories of ions emanating from the specimen are the primary limitation on the lateral resolution of AP analysis. It is not likely that these aberrations may be corrected physically. However, if they can be described theoretically, then they might be deconvoluted from the data. It is not likely that this theoretical task will be solved in the immediate future. However, it does not appear to be an impossible task. Furthermore, there are some possibilities that progress can be made either by assigning a lattice to the 3D image and forcing atoms to pick their nearest lattice point or by using statistical pattern

recognition techniques to determine what information about the lattice is present in the 3D image and then assigning atoms to the nearest lattice point.

One such method involves Fourier transform (FT) techniques to reconstruct the original lattice structure from the data. A common example of using the FT for image processing is the removal of noise from a HRTEM lattice image using filtering in the frequency domain [27]. This method will find and sort the underlying periodic information contained in the image.

In order to get a first order estimate of the possibilities of utilizing FT techniques on 3DAP images, a small 2D collection of 16 by 16 atoms on a square lattice was used. The atom positions were smeared by a Gaussian probability in distance from the exact location at random orientations in 2D to simulate the effect of random trajectory aberrations in the data. Figure 5a shows this data set. Figure 5b shows the same data set with 40% of the atoms missing at random to simulate the effect of the 60% detection efficiency of microchannel plates. If the atoms are taken to be 0.20 nm apart, then the full width at half maximum (FWHM) of the Gaussian distribution is $\sigma = \pm 0.05$ nm in Figure 5.

The data of Figures 5a and b were Fourier transformed. Only peaks in the 2D frequency domain that were greater than a threshold intensity were retained. All other components were set to zero to reduce noise. The inverse transform of these thresholded-frequency domain data sets

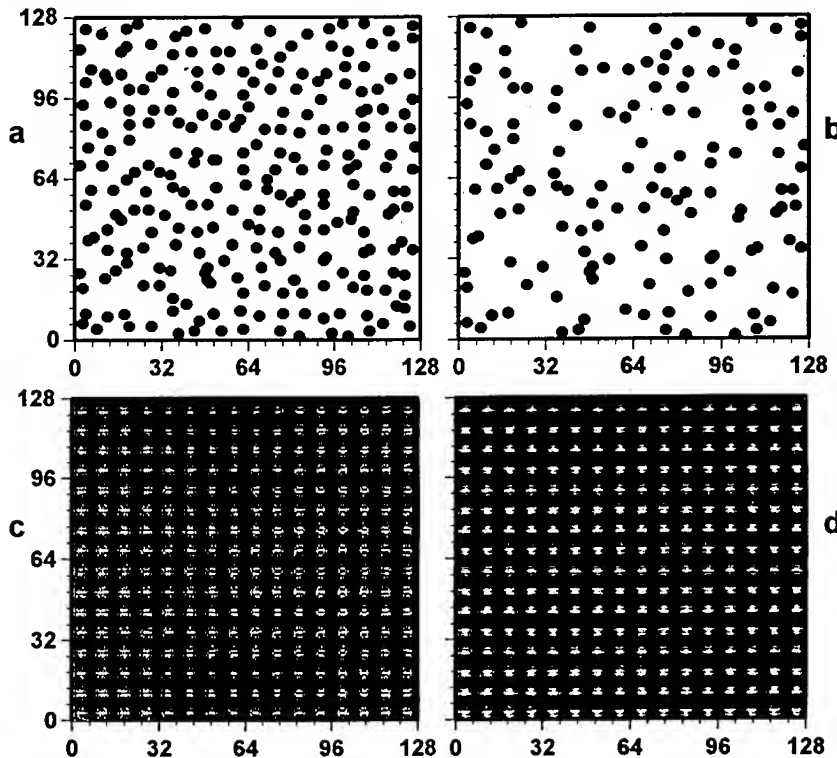


Figure 5. Simulated 2D atom probe data from random variation about a square lattice with (a) 100% efficiency and (b) 60% efficiency. Calculated lattice using masked Fourier transform technique for (c) 100% efficiency and (d) 60% efficiency.

are shown in Figures 5c and d, respectively. The real space 16 by 16 square lattice is clearly visible in these inverse transforms for both the 100% and 60% occupancy cases.

As the magnitude of σ increases to simulate greater trajectory aberration magnitude, it becomes more difficult to recover the original lattice. It was observed that a smaller array of atoms (7 by 7) was not sufficient to extract the original lattice for the $\sigma = \pm 0.05$ nm case, yet the original lattice was recovered for a 16 by 16 array. The size of the data set therefore has a direct impact on the magnitude of the smearing that can be tolerated before the original lattice becomes unrecoverable. With the 16 by 16 array, the original lattice was not recovered with this technique for $\sigma = \pm 0.10$ nm.

The above "quasi-optical" filtering technique may be readily extended to 3D. However, correlation averaging techniques will likely be more successful at this type of pattern recognition [28] and this type of processing is currently being studied by us as well.

It may be that trajectory aberrations are not completely random in orientation. If this is the case then the directionality of the aberrations could show up in the above analysis techniques. This approach may therefore provide experimental data on trajectory aberrations which could eventually lead to a theoretical understanding and description.

Although actual images have not yet been analyzed, these analysis procedures clearly hold promise for real space structure determination in 3DAP.

Increased Volume Sampling -- Historically, an AP analysis has been performed on needle-shaped specimens which imposes two major limitations: a very limited specimen sampling or field of view and a very small analyzed volume. The field of view is limited by the lateral extent of the specimen to about 50-200nm diameter. Rapid specimen analysis and rapid sample exchange can also increase the total volume of material available for analysis.

Nishikawa and Kimoto [29] have recently described a concept which should make atom probe analysis much more accessible to non-experts because it greatly simplifies and expedites sample preparation. A flat specimen surface is masked with circular objects like micron sized spheres from liquid solution and then it is ion milled from normal incidence. Pointed spikes protruding from the surface will be formed by this process. There would be thousands of spikes on any given sample. These spikes are shaped correctly for atom probe work but it is necessary to apply the high electric fields only to one spike at a time. In what they call the Scanning Atom Probe, Nishikawa and Kimoto suggest using a local extraction electrode which is mounted on a translatable stage to pick one spike at a time. With this idea, one can envision an instrument where flat samples are put into an ante chamber and are masked and ion milled in the course of 15 minutes and a nearly unlimited amount of atom probe data could then be obtained.

4. THE ATOM PROBE MICROSCOPE

At the University of Wisconsin, we are building a 3DAP which incorporates the above improvements. This instrument is a 3DAP built inside a scanning electron microscope (donated by NORAN Instruments) so that the electron beam may be used for rapid thermal pulsing. By rastering the beam across the specimen, we expect to achieve very high data collection rates (up to 10^6 atoms/second) and high mass resolution (one part in 300). In addition to thermal pulsing, the electron beam may be used to form an image and obtain analytical information such as x-ray spectroscopy and electron diffraction patterns.

This large increase in pulsing rate must be accompanied by attention to the capabilities of the position-sensitive detection system. Accordingly, we have developed new PSDs based on centroid-finding charge separation techniques [26] which feature multiple concurrent event capability (up to four simultaneous events) and short cycle times (up to 10^6 pulses/second). These detectors will have high image resolution (up to 5000 by 5000) which means we can record perhaps 500 by 500 atoms per specimen plane. Thus the instrument will record more of the sample and do it at much higher rates than in previous instruments.

5. THE ATOM PROBE OF THE NEAR FUTURE

Conventional atom probes, despite their unique capabilities and huge success in many difficult applications, have been utilized by only a small number of groups in the world. In order to project what the AP of the future should look like, it is instructive to ask why atom probes have not been more widely adopted. The answers seem to lie with several key factors.

- (i). Sample preparation for atom probe work has historically been perceived as being tedious and artful. Single samples are prepared one at a time, a process that is truly analogous to sample preparation for TEM work. The samples thus prepared are delicate and so require careful handling. Such samples do not lend themselves to automated preparation, especially inside the atom probe instrument which will be used to analyze them. Furthermore, it is difficult to know whether any one sample will succeed and so usually several samples must be prepared. The sample geometry (a sharp needle with radius of curvature at the tip of about 100 nm) constrains the number of applications which can readily be studied by atom probe.
- (ii). Features of large spatial extent ($>1 \mu\text{m}$) cannot be surveyed or analyzed readily in conventional atom probe. This constraint is related, in part, to the sample geometry.
- (iii). Even when the sample preparation and geometry do not pose problems, the data collection rate of conventional atom probes is low. It is difficult to get more than 10^5 atoms in an analysis with 10^6 being about the practical upper limit. These are, unfortunately, small volumes.
- (iv). The small number of atoms analyzed limits the sensitivity of the conventional atom probe. Even though single atoms can be detected and studied, statistically, composition determinations for any given volume are limited by the small lateral extent of the linear swath which is analyzed in a material.
- (v). There have been no easy-to-use, highly automated atom probes. Without high demand, it is difficult to develop such a user-friendly instrument.

So, is the atom probe poised for a major upswing in usability and popularity? These authors think so. Consider this vision of the atom probe of the near future: You, as a user, walk into a office sized room at 9 a.m. with samples in your pocket. The main vacuum chamber and ante chambers are collectively a table top unit about the size of a microwave oven. The electronics, including vacuum controls, are all integrated into a floor standing personal computer. After logging in to the computer, you open a small door in an ante chamber and put your six flat samples onto a turret. The door is closed and you go for coffee while the instrument automatically deposits spheres onto the samples and ion mills them. Alternatively you could have used the patterning system to deposit masks across a grain boundary of interest. When you return, the six samples are ready with thousands of tips each and the turret has been inserted into the main chamber. You turn on the SEM image and move the extraction electrode around until you have picked a good looking tip. The instrument will also automatically find tips if you prefer.

You begin data collection and see a 3D image of the sample form so rapidly it looks like a high speed video fly-by from STAR WARS. The small precipitates in your sample appear as golden rocks floating in a sea of blue. The average composition is displayed in real time for all phases detected. You have found the one part per million of oxygen and it is primarily located in the precipitates. After analyzing about three tips from the first sample, you move on to the second. By noon you have finished all samples and you walk away with the entire results, video and all with annotation, on a CD ROM. You have analyzed 20 billion atoms total. It is only 50 GB of data.

Is this the stuff of the twenty-fourth century? Hardly; we believe this will all be possible by the twenty-first century.

6. SUMMARY

3DAP is one of a variety of microscopies that has near-atomic resolution analysis capabilities. However, it is the only microscopy that attempts to identify each atom in its correct spatial location.

Some current technological limitations are being addressed to further enhance the capabilities of 3DAP. Thermal pulsing of a FIM specimen by an electron beam is likely to produce high repetition rates and also good mass resolution. Multi-hit detectors for 3DAP must be developed to increase data acquisition rates. Determination of the exact location of each atom in a sample appears feasible, but more analysis is required.

High speed, 3D atom probes will push the mass detectability limits and spatial resolution of analytical instrumentation.

7. CONCLUSIONS

Because the physical properties of many modern materials are determined by microstructural features with near-atomic dimensions, atomic-scale analytical techniques are required for characterization. 3DAP combines the capabilities of standard AP analysis with significant new capabilities for imaging. Technological advances promise to bring high speed ($>10^6$ atoms/second) and high mass resolution ($>$ one part per 300) to the technique.

In the future, 3DAP should be the technique of choice for compositional studies of nanometer structures. It may eventually also provide 3D structural information truly at the atomic scale.

8. ACKNOWLEDGMENTS

This work is sponsored by the National Science Foundation under grant #DMR-8911332 (Dr. John Hurt) and the Electric Power Research Institute under agreement #RP8009-5 (Dr. Thomas Schnieder).

9. REFERENCES

- [1] E. W. Müller, J. A. Panitz and S. B. McLane, *Rev. Sci. Instrum.*, **39** (1968) 83.
- [2] E. W. Müller, *Z. Phys.*, **131** (1951) 136.

[3] E. W. Müller, *Z. Phys.*, **106** (1937) 541.

[4] M. K. Miller, *Int. Metals Rev.*, 1988.

[5] T. T. Tsong, *Surf. Sci.*, **70** (1978) 219.

[6] G. L. Kellogg and T. T. Tsong, *J. Appl. Phys.*, **51** (1980) 1184.

[7] W. P. Poschenrieder, *Int. J. Mass Spectrom. Ion Phys.*, **6** (1971) 413.

[8] V. I. Karataev, B. A. Mamyrin and D. V. Shmikk, *Sov. Phys. Technol. Phys.*, **16** (1972) 1177.

[9] J. A. Panitz, *Prog. Surf. Sci.*, **8** (1978) 219.

[10] A. J. Melmed, M. Martinka and R. Klein, *Proc. 29th Intern. Field Emission Symp.*, eds H-O. Andrén and H. Nordén, 243 (1982).

[11] G. D. W. Smith and A. Cerezo, International Patent Application PCT/GB86/00437, publication no. W087/00682, July 24th, 1987.

[12] A. Cerezo, T. J. Godfrey and G. D. W. Smith, *Rev. Sci. Instrum.*, **59** (1988) 862.

[13] C. Martin, P. Jelinsky, M. Lampton and R. F. Malina, *Rev. Sci. Instrum.*, **52** (1981) 1067.

[14] A. Cerezo, T. J. Godfrey, C. R. M. Grovenor, M. G. Hetherington, R. M. Hoyle, J. P. Jakubovics, J. A. Liddle, G. D. W. Smith and G. M. Worrall, *J. of Microscopy*, **154** (1989) 215.

[15] Summary of first Workshop on 3D Atom Probes at the 40th Annual International Field Emission Symposium, Nagoya, Japan, to appear in proceedings of this meeting, *Applied Surface Science* (1993).

[16] A. Cerezo, personal communication (1991).

[17] B. Deconihout, A. Bostel, P. Bas, S. Chamberland, L. Letellier, F. Danoix and D. Blavette, Accepted for publication in *App. Surf. Sci.* (1993).

[18] A. Cerezo, J. E. Brown, T. J. Godfrey, C. R. M. Grovenor, M. G. Hetherington, J. M. Hyde, B. A. Shallock, W. Sha and G. D. W. Smith, "The Anatomy of Alloys," commercial brochure for Kindbrisk, Ltd. of Oxford, England, 1990.

[19] J. A. Liddle, N. J. Long, A. K. Petford-Long, *Materials Charac.*, **25** (1990) 157.

[20] T. F. Kelly, Nuri A. Zreiba, B. D. Howell and F. G. Bradley, *Surf. Sci.*, **246** (1991) 31.

[21] P. P. Camus, D. J. Larson and T. F. Kelly, *App. Surf. Sci.*, **67** (1993) 467.

[22] T. F. Kelly, J. J. McCarthy and D. C. Mancini, US patent #5,061,850, issued October 29, 1991.

[23] T. F. Kelly, D. C. Mancini, Jon J. McCarthy and N. A. Zreiba, *Surf. Sci.*, **246** (1991) 396.

[24] B. Deconihout, A. Bostel, A. Menand, J. M. Sarrau, M. Bouet, S. Chamberland and D. Blavette, *App. Surf. Sci.*, **67** (1993) 444.

[25] M. K. Miller, *Surf. Sci.*, **246** (1991) 428.

[26] L. M. Holzman, T. F. Kelly and P. P. Camus, Patent application submitted July 1993 by Wisconsin Alumni Research Foundation.

[27] J. C. Russ, *The Image Processing Handbook*, (CRC Press, Boca Raton, FL, 1992), p. 207.

[28] M. Van Heel, private communication (1993).

[29] O. Nishikawa and M. Kimoto, Accepted for publication in *App. Surf. Sci.*

Cross-Sectional Scanning Tunneling Microscopy of III-V Quantum Structures

M.B. Johnson, M. Pfister,* S.F. Alvarado and H.W.M. Salemink

IBM Research Division, Zurich Research Laboratory, CH-8803 Rüschlikon, Switzerland

*Also at: Institut de Micro- et Optoélectronique, EPFL,
CH-1015 Lausanne, Switzerland

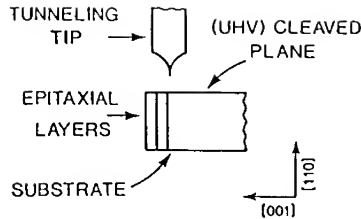
Abstract

In this paper, we report on the use of cross-sectional scanning tunneling microscopy (XSTM) to analyze several aspects of MBE-grown III-V quantum structures on an atomic scale. In particular, we discuss our recent work to identify various atomic species within the same chemical group (e.g. Al and Ga within the group III sublattice of AlGaAs) thereby allowing the determination of atomic roughness at GaAs/AlGaAs interfaces and alloy clustering in AlGaAs. We demonstrate and discuss the sensitivity of the STM to individual dopants in the near surface layers, as well as to the local carrier concentration. Lastly, we use XSTM to obtain images of cross-sectioned GaAs/AlGaAs quantum well wires with atomic detail.

1. Introduction

The ongoing downscaling of semiconductor structures requires novel analysis tools with atomic-scale chemical and structural resolution, and near-atomic-scale resolution of electronic properties in the lateral and depth dimensions [1]. Conventional analysis techniques spatially average over several nanometers in one or more dimensions. For example, high-resolution transmission electron microscopy (HRTEM) [2] averages structural and chemical information along the electron beam direction over the thickness of the sample (20-50 nm); secondary ion mass spectroscopy (SIMS), which is used for dopant profiling, is a chemical-sensitive technique with a depth resolution limit near 5 nm, but it is a large-area technique [3]; and photoluminescence and photoluminescence excitation yields properties that are averaged over the size of an exciton, typically 20 nm in diameter [4]. In contrast, the scanning tunneling microscope (STM) measures structural chemical and electronic properties with atomic or near-atomic resolution in the lateral and depth dimensions (all three spatial dimensions) [5]. However, the STM is primarily associated with atomically resolved studies of semiconductor and metallic surfaces, while far less work has been done to exploit the STM to analyze cross-sectional surfaces, thereby accessing subsurface layers and buried interfaces, on an atomic or near-atomic scale [6-13]. In this paper we describe our recent work on the ultrahigh vacuum (UHV) cleaved (110) surface of III-V compound multilayers. In particular we discuss the atomic-scale chemical sensitivity in GaAs/AlGaAs material, which allows the observation of clustering and interface roughness, the observation of individual doping sites in GaAs and the sensitivity to carrier concentration, and the first atomically resolved images of MBE-grown GaAs/AlGaAs quantum well wires.

Figure 1. Schematic view of the XSTM of a multilayer heterostructure. MBE growth is in the [001] direction and the UHV cleaved (110) face is exposed to the STM tip [from Ref. 12].



2. Experimental Technique

A simplified schematic view of XSTM is shown in Fig. 1. For the samples discussed in this paper, the planar epitaxial layers are grown by MBE on slightly misoriented [001] substrates (for details see the cited references) and the quantum wires were grown using MBE on prepatterned V-groove GaAs substrates (for details see Ref. [14]). For STM analysis small, thinned, pre-scribed bars of these wafers are inserted in the UHV-STM system via an airlock. There they are cleaved to expose the (110) surface just prior to the STM measurement [12]. In early work, an UHV-SEM in the STM chamber was used to observe the cross-sectional surfaces and to guide the STM tip rapidly towards the small region of interest [12], whereas in recent work a smaller UHV-STM is used and a step-and-search technique guides the tip to the layers of interest [13]. Both STMs are equipped with removable tunneling tips, which allows the tip preparation – including annealing and sputtering – to be done in a separate interconnected UHV preparation chamber. The ambient operating pressure in the STM chamber is below 3×10^{-11} mbar. Such a low operating pressure is necessary to avoid the buildup of contamination on the Al-containing layers.

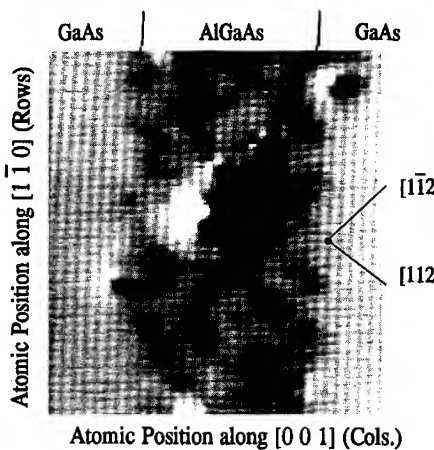
The clean, atomically flat, UHV cleaved GaAs (110) is a nonpolar 1×1 surface without surface states in the semiconductor band gap. It has been demonstrated by Feenstra et al. that voltage-dependent imaging on GaAs (110) can be used to resolve separately the respective group III and V sublattices [15]. Using negative sample voltage the filled valence-band-related states (group V) are imaged; using positive sample voltages the empty conduction-band-related states (group III) are imaged. Thus, to first order, the topographic images at these respective voltages can be used to map the group V (e.g. As and P) and group III sites (e.g. Al, Ga, and In) [16].

3. Atomically Resolved GaAs/AlGaAs Interfaces

Typical III-V multilayer samples in our studies contain several sets of layers with changes in alloy composition, layer thickness, or doping density. Thus by virtue of cross-sectioning we have convenient access to many layers and interfaces with varying specifications. Figure 2 is a topographic image of the filled (group V) As states across a GaAs/Al_{0.3}Ga_{0.7}As/GaAs structure with atomic resolution; it is a section of an image of many layers [17]. In this As-related image, the clean homogeneous GaAs layers are seen on both sides of an inhomogeneous AlGaAs layer. The variation of the As charge density within the ternary layer is the result of fluctuations of the Al content [17]. This mottled

appearance is the result of clustering of the Al which is on a scale of 3-4 lattice spacings (about 2 nm), and preferentially aligned in the $[1\bar{1}2]$ and $[\bar{1}12]$ directions. Such Al clustering also gives rise to roughness of the GaAs/AlGaAs interface on the same 2 nm scale. Note that this roughness and clustering is more than that expected for a random AlGaAs alloy. In fact, in our MBE-grown AlGaAs, we see such a tendency for clustering and roughness [18].

Figure 2. Cross-sectional STM view of the UHV cleaved (110) face of a GaAs-Al_{0.3}Ga_{0.7}As multilayer stack. Tunneling sample voltage is -2.2 V, imaging the filled state (As) sublattice. The inhomogeneous topography in the AlGaAs is due to clustering in this material [from Ref. 17].



4. Al-Ga Identification within Group III Lattice

Figure 3 displays an empty state group III image (Al_xGa_{1-x} sublattice) at the (inverted) AlGaAs-GaAs interface grown by MBE. Tunneling involving the energetically higher Al-related states (see Fig. 3a) requires the tip to approach the surface compared with tunneling into the lower lying Ga-related states [16]. For this reason the Al sites are darker (lower) than the Ga sites. In this particular image, a row of five Al sites is seen at the nominal AlGaAs/GaAs interface and a single Al site across the GaAs material. In further work we have imaged *n*-type AlGaAs with both polarities (group III and V

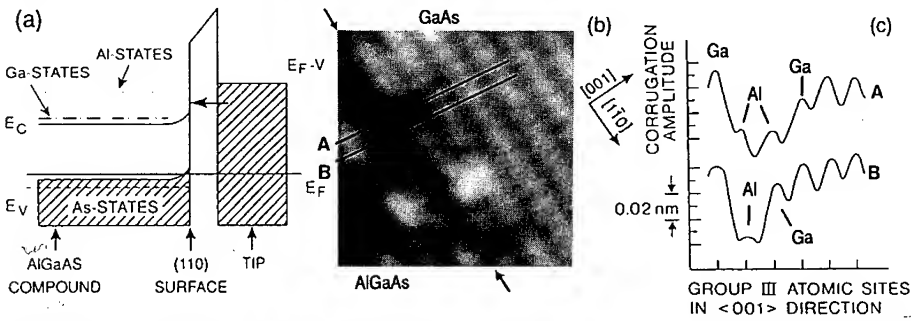


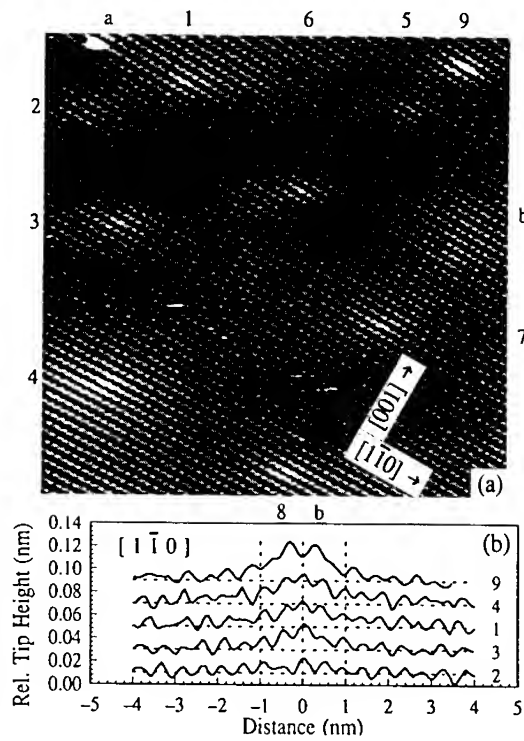
Figure 3. (a) Potential energy diagram for tunneling into conduction band states, showing different empty state positions for Al and Ga sites. (b) Empty state image of the group III sublattice containing the atomic-scale charge density contributions from the (Al,Ga) sites. The darker sites are due to Al, the brighter ones to Ga. (c) Line scans along A and B in (b) clearly showing the different Al and Ga sites. [From Ref. 16].

sublattices). Here the dark sites in both polarities (Al in the group III image, and As bonded to Al in the group V image) are well correlated as expected [19]. Similar chemical sensitivity has also been demonstrated for InGaAsP/InP [16] and for GaInP/GaAs material [20].

5. Direct Observation of Doping Sites in III-V Compounds

Figure 4 shows the filled-state charge density of a GaAs buffer layer doped with a Be density of $1 \times 10^{19} \text{ cm}^{-3}$. Nine hillock features are observed with varying amplitudes and typically 2-3 nm in diameter and heights up to 0.01 nm. These features are due to dopants on or near the surface. Such dopants are ionized and result in an enhancement of the surface density of states over an area given by the Bohr radius of a dopant (1.2 nm), the extent of which diminishes with the depth of the dopant. This gives rise to a slowly varying envelope that modifies the As atomic corrugation as observed. Nine hillocks in the area shown for the doping concentration of $1 \times 10^{19} \text{ cm}^{-3}$ indicate a sensitivity to dopants in the top five atomic layers or 1 nm, in agreement with calculations. A detailed analysis was recently published [21]. Not only is the STM sensitive to the individual dopants as described above, it is also sensitive to the local carrier density due to the depletion layer at the unpinned semiconductor surface. Less doped regions require the tip to approach the surface to maintain constant current conditions. Scanning tunneling spectroscopy is a particularly sensitive probe of this effect. This effect has been modeled and analyzed

Figure 4. (a) STM image of a (110)-cleaved, $1 \times 10^{19} \text{ cm}^{-3}$, Be-doped GaAs surface. Image displays 31×29 nm of the As sublattice taken with sample voltage of -2.1 V and demand current of 0.1 nA. The relative tip height is given by a gray scale, from 0 (black) to 0.2 nm (white). Nine hillocks (dopants) are identified using numbers at the closest point on the perimeter. Features marked "a" and "b" are an adatom and a vacancy, respectively. (b) Tip-height traces along the $[1\bar{1}0]$ direction of a selection of the hillocks identified in (a). [From Ref. 21].



[22]. Such modeling is important for the advancement of such techniques to ultra-small device structures. In subsequent work on Be modulation-doped GaAs multilayers, a quantitative analysis of the XSTM data, including both individual dopant counting and local doping density sensitivity, was made and shows very good agreement when compared with the results of SIMS analysis [23].

6. GaAs Quantum Wires on V-Grooved GaAs Substrates

The growth on prepatterned substrates by epitaxial techniques is a promising method to fabricate nanostructures such as quantum wires. Although the analysis of such small structures is usually done by TEM, SEM, and photoluminescence, XSTM can also be used to analyze these structures in atomic detail by preparing suitable cross sections. Figure 5 is a montage of several XSTM topographic images showing a set of GaAs quantum well wires, nominally 5 nm thick, embedded in $(\text{AlAs})_4\text{-}(\text{GaAs})_8$ superlattice barriers [13]. These structures were grown by MBE on a pre-etched V-groove in a GaAs substrate. The wires are thicker than the nominal 5 nm thickness due to a growth interruption after the wire is grown, which allows diffusion of material to the concave valley of the V-groove and thereby forming the laterally confined well wire itself. This sample was also studied using STM-induced electroluminescence which determines the luminescence efficiency of the individual wells by probing the well wires on length scales dictated by the diffusion of carriers within the well wires (10 nm) barriers [24,25]. Numerous features regarding the structure's growth are visible with atomic detail: 1) The superlattice barrier acts as an atomic record of the growth history which allows interesting properties such as the rate of lateral mass flow to be determined. For example, the first superlattice barrier is far from uniform. Instead, at certain points on the V-groove wall, several periods are missed in the superlattice. Also, various zones show different growth rates depending on subtle differences in the index of the growth surface, e.g. between wire 2 and 3 on the left side. 2) The superlattice itself is not uniform in texture. In fact there appears to be intermixing of the AlAs and GaAs layers especially on the high indexed planes but also on the (001) growth plane not shown in this image. 3) Doping sites as discussed in Section 5 are visible throughout the structure – with uniform distribution in this case. Thus the detailed dopant distribution even in a complicated nanostructure can be determined with atomic resolution. 4) Finally, the electroluminescence in combination with STM allows the determination of the luminescence efficiency of the wires on a wire-by-wire basis and can elucidate the reasons for such different efficiencies. In the wire set shown, wire 3 shows the highest luminescence efficiency, while wire 1 shows very poor efficiency. This is presumably due to the proximity of the etched V-groove interface which gives rise to a higher concentration of nonradiative recombination centers. This work will be discussed in detail in a forthcoming publication [26].

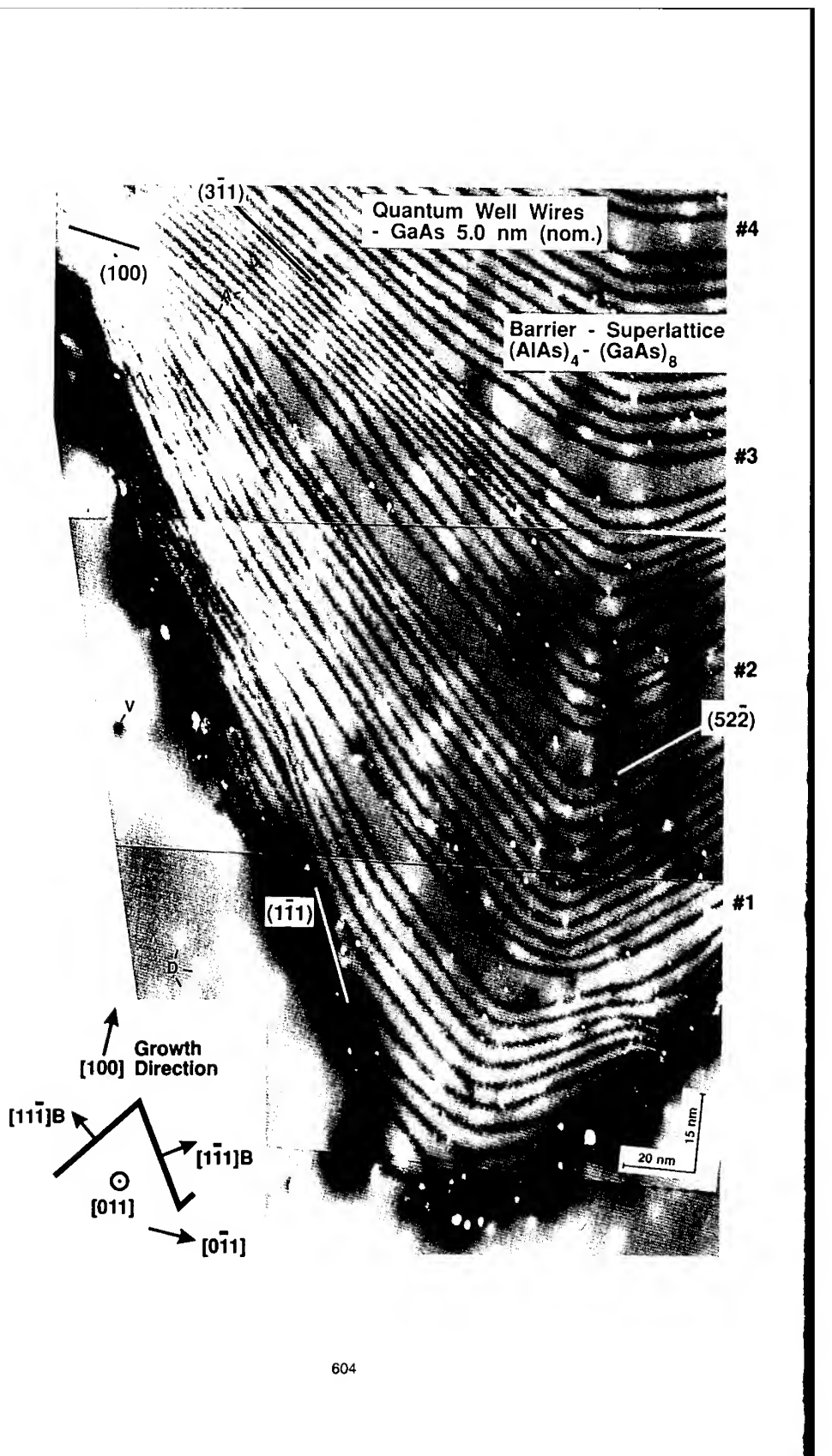


Figure 5. (Previous page) Atomically resolved XSTM filled-state (As site) image of a (110) UHV-cleaved plane through a quantum wire structure. The GaAs wires (numbered) and $(\text{AlAs})_4(\text{GaAs})_8$ superlattice stacks are grown by MBE over a prepatterned V-groove GaAs substrate [26]. Small white hillocks marked "D" are dopant sites (see Fig. 4) while the sharper white dots "A" and black dots "V" are adatoms and vacancies, respectively. Note the superlattice barrier acts as a record of the growth history of the nanostructure.

7. Conclusions and Outlook

Cross-sectional STM has been used to study (110) cross sections of MBE III-V compound multilayers and nanostructures. As the STM is highly surface-sensitive and provides lateral atomic resolution, the spatial averaging of properties with conventional techniques does not occur. Chemical analysis within group III or group V sites can be done on a near-atomic or atomic basis. This allows epitaxial interfaces and ternary alloys to be analyzed with atomic detail. In fact, in our MBE-grown GaAs/AlGaAs layers, such analysis shows more clustering and roughness than expected for random alloys and abrupt interfaces. The distribution of dopants through the layers can be observed in two different ways: first, by the direct observation of dopants near the surface (about 5 layers deep); and second, by the tip/sample distance (or measured by the tunneling current turn-on in spectroscopy), which is sensitive to the local carrier density. This technique is extremely well suited to the analysis of the active dopant distribution in III-V semiconductor structures. Finally, novel results on sections of MBE-grown GaAs/ $(\text{AlAs})_4(\text{GaAs})_8$ quantum wires demonstrate the ability to quantify the complex growth phenomena on prepatterned surfaces in a very direct way with unprecedented spatial resolution, and to link this directly to luminescence properties. In closing, it has been shown that XSTM is a powerful technique to analyze III-V quantum structures with atomic resolution. This success hinges on the properties of the (110) cleavage plane. The ability to perform similar cross-sectional experiments on group IV and II-VI structures – including quantum structures – requires similar suitable cross-sectional surfaces.

Acknowledgments. We gratefully acknowledge L. Perriard and H. Richard for material processing, H.P. Meier for MBE growth, P. Roentgen for MOVPE growth, as well as U. Marti, D. Martin, F. Morier-Genoud, and F.K. Reinhart of IMO, EPFL for MBE growth of the quantum wires. We are indebted to many discussions with R. Feenstra relating to III-V compounds as well as his modeling of ionized dopants. We have profited from software by B. Michel and J. Jorgensen. Finally, we acknowledge the use of a spectroscopy simulation program by P. Koenraad and the HETMOD program, kindly provided by A.C. Warren.

References

1. For a review see Proc. 2nd Int'l Workshop on Ultra Shallow Doping Profiles, MCNC 1992, to be published in *J. Vac. Sci. Technol. B*, Jan/Feb. 1994.
2. A. Ourmazd, D.W. Taylor, J. Cunningham and C.W. Tu, *Phys. Rev. Lett.* **62**, 933 (1989).
3. See papers on SIMS depth profiling in Ref. 1.
4. D. Gammon, B.V. Shanabrook and D.S. Katzer, *Phys. Rev. Lett.* **67**, 1547 (1991).
5. G. Binnig, Ch. Gerber, H. Rohrer and E. Weibel, *Phys. Rev. Lett.* **49**, 57 (1982); R.J. Hamers, R.M. Tromp and J.E. Demuth, *Phys. Rev. Lett.* **56**, 1972 (1986).
6. O. Albrektsen, D.J. Arent, H.P. Meier and H.W.M. Salemink, *Appl. Phys. Lett.* **57**, 31 (1990).
7. S. Kordic, E.J. van Loenen, D. Dijkkamp, A.J. Hoeven and H.K. Moraal, *J. Vac. Sci. Technol. A* **8**, 549 (1990).
8. Proc. of NATO ARW on *Semiconductor Interfaces at the Sub-Nanometer Scale*, NATO ASI Series E **243**, edited by H.W.M. Salemink and M.D. Pashley (Kluwer, Dordrecht, 1993).
9. M.B. Johnson and J.M. Halbout, *J. Vac. Sci. Technol. B* **10**, 508 (1992).
10. E.T. Yu, M.B. Johnson, and J.-M. Halbout, *Appl. Phys. Lett.* **61**, 201 (1992).
11. R.M. Feenstra, E.T. Yu, J.M. Woodall, P.D. Kirchner, C.L. Lin and G.D. Pettit, *Appl. Phys. Lett.* **61**, 795 (1992).
12. S. Gwo, K.J. Chao, C.K. Shih, K. Sadra and B.G. Streetman, *Phys. Rev. Lett.* **71**, 1883 (1993).
13. H.W.M. Salemink, M.B. Johnson and O. Albrektsen, in Ref. 1.
14. U. Marti, M. Proctor, D. Martin, F. Morier-Genoud, B. Senior and F.K. Reinhart, *Microel. Engineering* **13**, 391 (1991).
15. R.M. Feenstra, J.A. Stroscio, J. Tersoff and A.P. Fein, *Phys. Rev. Lett.* **58**, 1192 (1987).
16. H.W.M. Salemink and O. Albrektsen, *Phys. Rev. B* **47**, 10644 (1993).
17. M.B. Johnson, U. Maier, H.P. Meier and H.W.M. Salemink, *Appl. Phys. Lett.* **63**, 1273 (1993).
18. See paper by Salemink et al. in Ref. 8, page 151.
19. M.B. Johnson, and H.W.M. Salemink, unpublished.
20. M.B. Johnson and H.W.M. Salemink, to be submitted to *Appl. Phys. Lett.*
21. M.B. Johnson, R. Feenstra, O. Albrektsen and H.W.M. Salemink, *Appl. Phys. Lett.* **63**, 2923 (1993).
22. H.W.M. Salemink, O. Albrektsen and P. Koenraad, *Phys. Rev. B* **45**, 6946 (1992), and unpublished.
23. M.B. Johnson, H.P. Meier and H.W.M. Salemink, *Appl. Phys. Lett.* **63**, 3636 (1993).
24. D. Abraham, A. Veider, Ch. Schönenberger, H.P. Meier, D.J. Arent and S.F. Alvarado, *Appl. Phys. Lett.* **56**, 1564 (1990).
25. Ph. Renaud and S.F. Alvarado, *Phys. Rev. B* **44**, 6340 (1991).
26. M. Pfister, M.B. Johnson, S.F. Alvarado, H.W.M. Salemink, U. Marti, D. Martin, F. Morier-Genoud, F.K. Reinhart, to be submitted to *Appl. Phys. Lett.*

INCOHERENT IMAGING BY Z-CONTRAST STEM: TOWARDS 1 \AA RESOLUTION

S. J. PENNYCOOK, D. E. JESSON, AND A. J. MCGIBBON
Solid State Division, Oak Ridge National Laboratory, Oak Ridge, Tennessee 37831-6030

ABSTRACT:

By averaging phase correlations between scattered electrons a high angle detector in the scanning transmission electron microscope (STEM) can provide an incoherent, Z-contrast image at atomic resolution. Phase coherence is effectively destroyed through a combination of detector geometry (transverse incoherence) and phonon scattering (longitudinal incoherence). Besides having a higher intrinsic resolution, incoherent imaging offers the possibility of robust reconstruction to higher resolutions, provided that some lower frequency information is present in the image. This should have value for complex materials and regions of complex atomic arrangements such as grain boundaries. Direct resolution of the GaAs sublattice with a 300kV is demonstrated.

INTRODUCTION

Figure 1 compares contrast transfer functions for coherent and incoherent imaging conditions under the same electron optical parameters, specifically a 300 kV accelerating voltage and an objective lens of 1mm C_s . The Scherzer resolution condition [1] in each case is marked, and it can be seen that the incoherent mode has a higher intrinsic resolution, given by $0.43 C_s^{1/4} \lambda^{3/4}$ compared to $0.66 C_s^{1/4} \lambda^{3/4}$ for the phase contrast case. More importantly perhaps, even beyond the Scherzer limit the incoherent transfer function shows no contrast reversals, so that it is always possible to identify the atomic sites directly by inspection of the image. In a region such as a grain boundary, atomic column separations are often significantly altered from those in the bulk. With coherent imaging this can result in the contrast of a column being reversed from that of an identical column in the bulk, so that image interpretation must necessarily rely on simulations of atomic structures derived for example from coincidence site lattice models. With incoherent imaging, if columns become closer together at the boundary they will simply merge together into one bright feature of elongated shape. They will still be identifiable by eye as two atomic columns, and in principle the resolution function could be deconvoluted from the image to extract atomic positions from such features. Since we can invert an incoherent image directly we are therefore no longer restricted to working from model structures. We have effectively bypassed the phase problem of electron diffraction and also avoided the problems of non-linear and non-local imaging associated with phase contrast methods.

Below we first show how the high angle detector destroys long-range phase correlations allowing us to consider each atom as scattering independently with a cross section that is close to the Rutherford value. This leads to an object function description of the imaging process, in which dynamical diffraction and anomalous absorption effects can be included in a straightforward manner. Finally, preliminary results from a 300 kV STEM are presented showing the direct resolution of the GaAs sublattice.

PHONON-MEDIATED DESTRUCTION OF COHERENCE

It was realized very early that because the annular detector covers an angular range much larger than the separation between diffraction discs, interference effects in the transverse plane are effectively averaged, leading to images of single atoms and clusters that do not reverse contrast and show the resolution expected from the probe intensity profile [2-6]. For low inner

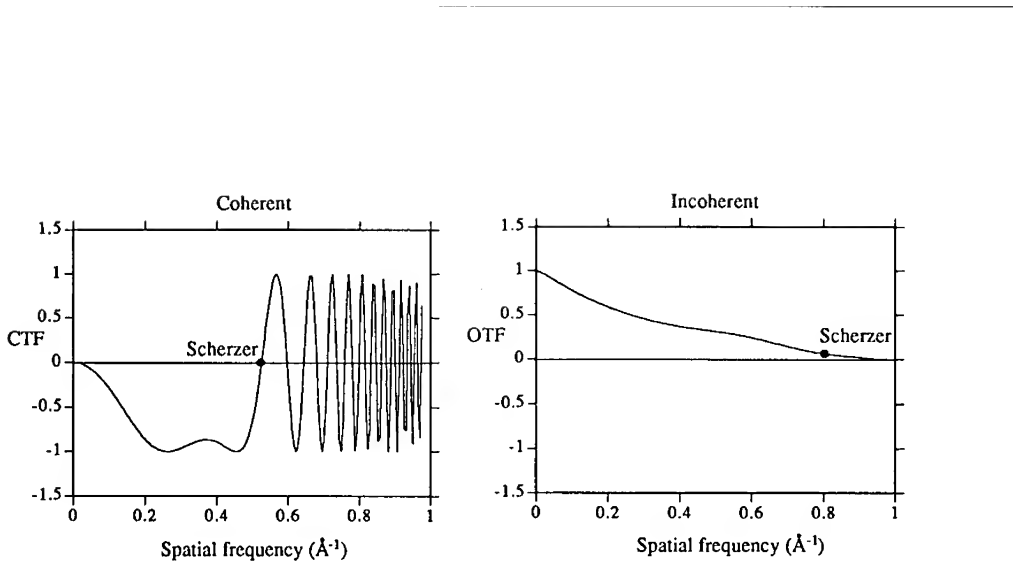
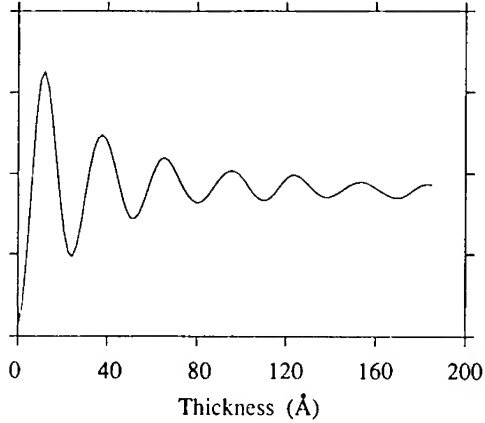


Fig. 1. Comparison of coherent and incoherent contrast transfer functions for a 300 kV microscope with 1 mm C_s .

Fig. 2. The intensity of zero-layer coherent scattering reaching a 50-150 mrad annular detector shows an oscillatory thickness behavior. Calculated on a kinematic model for a 100 kV probe of 10.3 mrad semiangle located over a dumbbell in Si {110}.



detector angles, some residual transverse coherence effects remain [7]. This led to the widespread misconception that to achieve incoherent imaging *all* the scattered radiation had to be detected, so that at high resolution incoherent imaging would break down because of the so-called "hole in the detector" problem [8]. However, incoherent imaging of thin specimens can be achieved at atomic resolution simply by increasing the inner angle of the detector so as to collect a constant *fraction* of the total scattered radiation. [9]

Interference effects between atoms separated along the beam direction cannot however be destroyed by the geometry of the detector alone, as shown strikingly by Fig. 2. From a thin crystal, the intensity of zero layer coherent scattering increases initially as n^2 , where n is the number of atoms along the column, but destructive interference rapidly sets in resulting in strong intensity oscillations, the intensity never rising above that scattered by a very thin slab [9]. It is this long range destructive interference that is destroyed by thermal vibrations, and leads to a thickness dependence that in the absence of dynamical effects and absorption would be linear. HOLZ diffraction also has a linear thickness dependence, and this has led to suggestions that the Z-contrast image might represent a HOLZ image [10,11]. However, it is easy to determine experimentally if the HOLZ contribution is significant, and for Si at room temperature it was found to be of the order of 1% of the total diffuse scattering detected [12]. Calculated HOLZ intensities are shown in Fig. 3, for three different Debye-Waller factors [13].

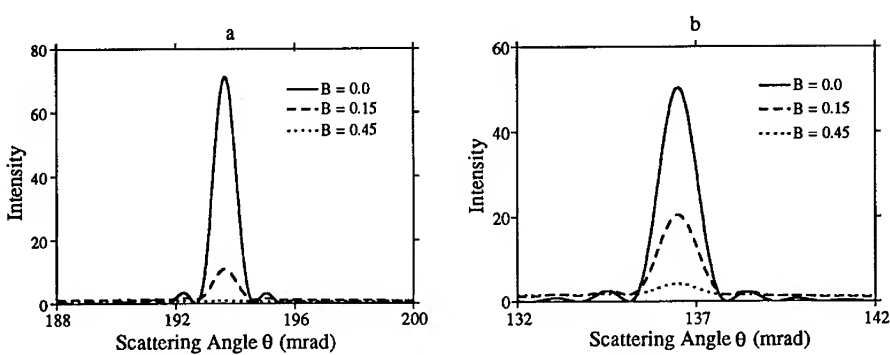


Fig. 3. Comparison of HOLZ ring intensities, azimuthally integrated, for stationary atoms with $B = 0$ (solid line), atoms at absolute zero, $B = 0.15$ (dashed line) and atoms at room temperature, $B = 0.45$ (dotted line). The atoms are spaced (a) 2 \AA and (b) 4 \AA apart along a column of length 200 \AA .

$B = 0$ corresponds to stationary atoms, and predicts very strong HOLZ diffraction. However it is important to realize that stationary atoms are non-physical; even at absolute zero atoms are vibrating significantly due to zero point energy, and the curves with $B = 0.15$ represent the appropriate Debye-Waller factor for Si at absolute zero. Now to obtain a strong HOLZ image would require a thin annular detector centered on the HOLZ ring; for typical annular detector angles the HOLZ contribution is still only $\sim 10\%$. Note that a HOLZ image could be very different from a diffuse scattering image, since it is sensitive to the atomic arrangement along the string, whereas the diffuse image is much less sensitive. At room temperature the HOLZ peaks are dramatically reduced.

Thermal diffuse scattering is normally described in terms of the Einstein model [14-16], in which atoms are treated as independently vibrating oscillators as indicated schematically in Fig. 4. This is a mathematically convenient but rather drastic representation of the effect of phonons. It means that each atom is treated as a separate independent source of thermal diffuse

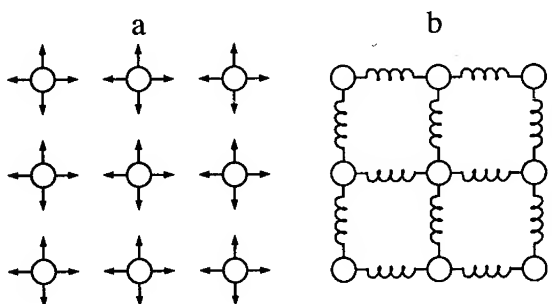


Fig. 4. Schematic comparing the (a) Einstein (or early Debye) model with (b) a phonon model of correlated vibrations

Fig. 5. Schematic comparing the correlation lengths of the coherent and diffuse components on an Einstein model of thermal vibrations.



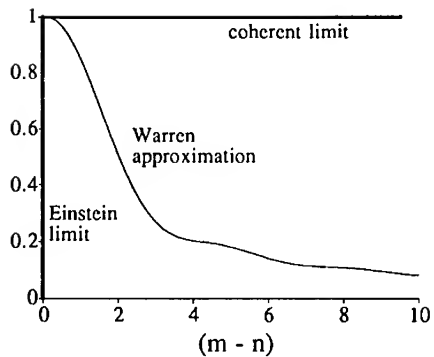


Fig. 6. Degree of coherence between an atom m spacings away from one at the origin, in the coherent scattering limit, the Einstein limit, and in the Warren approximation.

scattering, completely uncorrelated with any other atom in the crystal. The convenience of this approach arises from the fact that the scattering from a crystal splits into two components, one of which is completely coherent (a coherence volume comprising the entire sample), the other, the diffuse component, which is perfectly incoherent (the coherence volume around an atom contains only that atom), as indicated in the schematic of Fig. 5. The ratio between the two is controlled by the Debye-Waller factor. In order to examine the degree of incoherence in the thermal diffuse scattering, it has been suggested that a weighted average of the coherence volumes can be used [17]. However, it is clearly preferable to go beyond the Einstein model in which total incoherence is assumed. A convenient model of thermal diffuse scattering including all orders of phonon scattering has been given by Warren [18] for the x-ray case, and recently developed for electron diffraction [13]. The most important result of this analysis is that it quantitatively describes the degree of coherence between atoms different distances apart in a column, as shown in Fig. 6. Changing scattering angle or Debye-Waller factor the correlation envelope changes smoothly from full coherence (horizontal line at unity) towards the Einstein model (a δ -function at the origin). For the angles generally used for Z-contrast imaging, partial coherence remains between near neighbor atoms.

The physical interpretation suggested by this analysis is that a column of n atoms can be considered as n independently vibrating packets of atoms, as shown in Fig. 7. If the column is shorter than the packet size then coherent scattering dominates, (low angles and/or very short columns), but if the column is much longer than a packet then the column scatters incoherently, but with an atomic scattering cross section that is increased or decreased over the Einstein value depending on the phase of the residual correlations within the packet. For example, for columns greater than $\sim 20\text{\AA}$ in length and a detector inner angle of 75 mrad, an Einstein model will underestimate the scattering from a column of atoms 1\AA apart by 25%, but overestimate the scattering from a column of atoms 2\AA apart by 15%. It is worth noting however that these changes in cross section will only be noticeable if they are different for different columns, ie. if columns have different atomic spacings along the beam direction, otherwise these effects will just scale the overall image intensity.

Fig. 7. Schematic showing a column scattering as n independently vibrating packets of atoms.



s-STATE PROBE PROPAGATION

Now that we have established that an incoherent scattering description is valid for high angles, we must next determine the illumination of each atom, which is controlled by the dynamical diffraction of the incoming probe. It has been noted previously that a STEM probe propagating along a low index zone axis tends to form narrow spikes around each atomic column having the envelope of the incident probe profile [19,20]. The reason for this is the special nature of the STEM illumination, a coherent probe having a rather large angular spread. Tightly bound *s*-type Bloch states add constructively as we integrate over this large angular range to construct the focussed probe, whereas other less localized states interfere destructively. The result is a great reduction in beam broadening and for a small enough incident probe we can achieve column-by-column illumination. This tendency is further enhanced for scattering processes that are *localized* at the atomic cores, high angle diffuse scattering or inelastic scattering with large energy losses, which preferentially selects these localized *s* type states. Dynamical diffraction manifests simply as a columnar channeling effect, and the image intensity can be written as a simple convolution with an object function peaked at each atomic site [12,21]. The object functions contains to first order the effects of dynamical diffraction and absorption, and predicts thickness behavior that agrees with experiment (Fig. 8.) The *s* states themselves are highly localized around each atomic column, with a diameter less than that of the incident probe, even for a 300 kV STEM. Closely spaced identical columns lead to molecular orbital like Bloch states, but under most conditions, the *s* states are insensitive to the nature and distribution of surrounding atoms. The object function is highly localized because only the intensity of the *s*-state is involved, not its emergent phase, (see Fig. 9). No supercell calculations are necessary, in fact, with complex materials or interfaces small model unit cells may be used to determine columnar channelling effects and an object function constructed in a column-by-column manner [21]. In thin specimens, the dominant contribution to the intensity of a column is always its composition; we have never found a situation in which the heavier columns are not the brightest in the image, although due to the higher absorption of the heavy strings the contrast does decrease with increasing specimen thickness. In very thick crystals there is no longer a high resolution image. Eventually, the intensity detected from the heavy material must become less than that detected from a lighter material, as multiple scattering sends electrons outside the range of the annular detector.

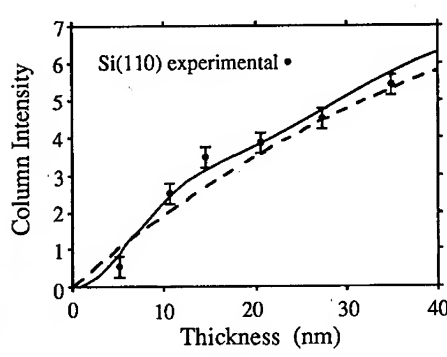


Fig. 8. Thickness dependence of image intensity from Si (110) on the *s*-state model (dashed line), and using all states (solid line), compared to experimental measurements (points).

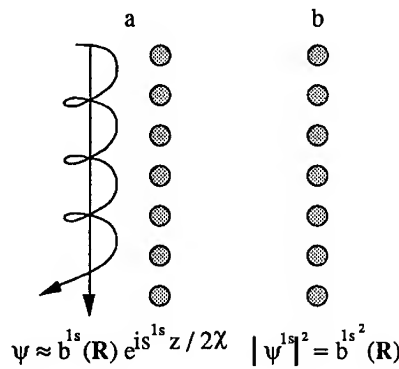


Fig. 9. (a) Coherent imaging measures the phase of the emergent *s*-state which is sensitive to tails of potentials from surrounding strings. (b) Incoherent imaging measures *s*-state intensity which is more local.

Incoherent imaging in perfect crystals is well explained in this picture, but a defect such as a dislocation that destroys the continuity of a column, through its associated strain fields, will alter the channeling effect of columns in the vicinity. Dislocations induce transitions to and from other Bloch states and can appear dark or bright depending on their depth in the sample and the inner-detector angle (22,23). Even end-on dislocations can induce strain fields that can bend nearby columns because of surface relaxation. The strain fields extend several atomic spacings, but within the strained region the positions of the heaviest columns can still be picked by inspection to an accuracy much better than one spacing, but further study of the effect of strain fields on the image is needed to extract dislocation core structures accurately.

MAXIMUM ENTROPY IMAGE ANALYSIS

Incoherent imaging not only allows an intuitive first order structure determination, it also opens up the possibility of quantitative and robust image analysis and reconstructions via maximum entropy methods [24,25]. Although it has been suggested that higher resolutions can be achieved through higher defocus values [26], the use of a non-Scherzer probe results in non-intuitive imaging and a return to a dependence on structure models, thus negating one of the key advantages of incoherent imaging. Figure 10. shows probe profiles and simulated images for Si {110} as a range of defocus, and although increasing the defocus from the Scherzer optimum probe increases the resolution from 1.25\AA to 1.0\AA at a defocus of 700\AA , a strong subsidiary maximum appears around the central sharp peak resulting in a loss of image contrast and interpretability. A more robust approach is to use the optimum Scherzer probe and reconstruct the higher resolution information by maximum entropy. A probe near optimum is readily found experimentally by focussing for maximum contrast in the image.

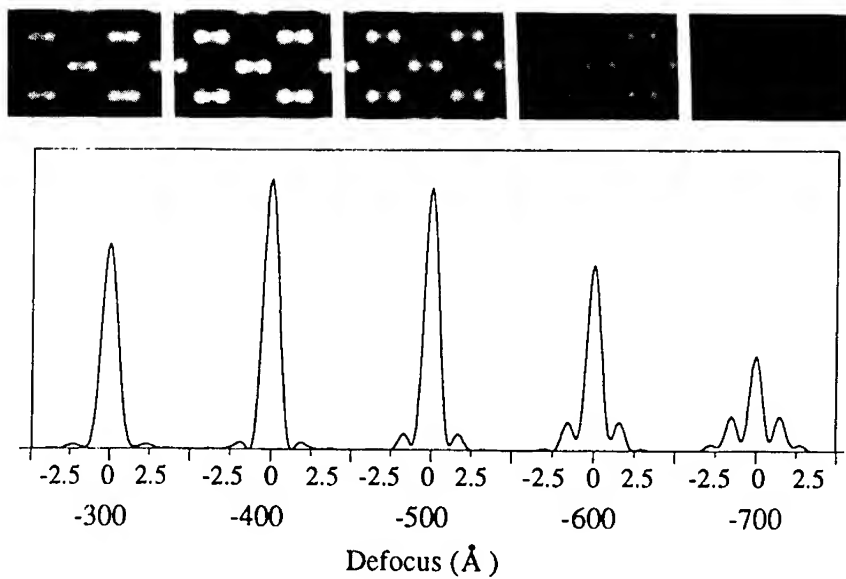


Fig. 10. Simulated focal series for Si {110} with corresponding probe intensity profiles, calculated for a 300 kV STEM with 1mm C_s and a 9.3 mrad objective semiangle.

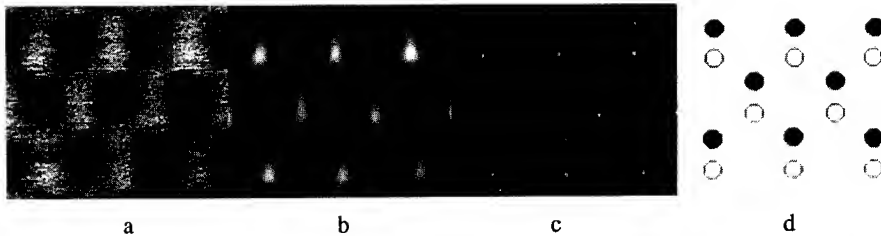


Fig. 11. (a) Z-contrast image of GaAs showing direct resolution of the sublattice with a 300 kV STEM, with maximum entropy restorations for 25 (b), and 100 (c) iterations, compared to the projected structure (d).

As an example of this approach we show in Fig. 11. an image of GaAs [27] to which maximum entropy restoration has been applied. The reconstruction works from a point spread function defined by the user, in this case a Lorentzian with a FWHM of 1.3\AA , and attempts to account for the experimental image intensity distribution by an array of point scatterers. This is clearly ideal for our situation, and depending on the number of iterations employed, the method can be used either as an efficient noise reduction technique or as a means of image quantification, providing positions and strengths of atomic columns together with individual error bars. 25 iterations produce significant sharpening of the image features (b) but 100 iterations are required to reduce the data to points (c). In all cases the polarity of the GaAs sublattice can be determined visually, even though the two columns are only two atomic numbers apart, and differ by only $\sim 10\%$ in their scattering power. The noise in the original image is translated into errors in position and intensity of the final points. From the region shown we find an intra-dumbbell separation of $1.46\text{\AA} \pm 0.16\text{\AA}$ and an inter-dumbbell spacing of $1.37\text{\AA} \pm 0.21\text{\AA}$, which differ by less than 0.1\AA from the correct (400) spacing of 1.41\AA .

FUTURE DIRECTIONS

The maximum entropy method offers an attractive means to quantify column positions and compositions at interfaces and grain boundaries, although further work is required to determine the best probe profiles to use. We have yet to try a realistic probe profile as shown in Fig. 10., and it would also seem attractive to attempt to extract the actual resolution function from a region of perfect crystal adjacent to an interface. This might allow the effects of astigmatism and residual crystal tilts to be corrected for by the reconstruction.

A second attractive direction is to utilize the probe channeling phenomenon and localised inelastic scattering events to obtain column-by-column spectroscopic information [28]. We have recently demonstrated a resolution of 2.7\AA at a CoSi_2/Si {111} interface using the Co-L edge [29]. With increasing accelerating voltage, although the range of the inelastic excitation increases, the probe size decrease at a faster rate and a resolution of 1.5\AA at the Co-L edge is indicated for a 300 kV STEM. Combining Z-contrast imaging, maximum entropy analysis, and bonding information from parallel detection EELS offers much promise for the study of interface structure and chemistry.

ACKNOWLEDGMENTS

The authors are grateful to S. L. Carney, J. T. Luck, and T. C. Estes for technical assistance. This research was sponsored by the Division of Materials Sciences, U.S. Department of Energy, under contract DE-AC05-84OR21400 with Martin Marietta Energy Systems, Inc.

REFERENCES

1. O. Scherzer, *J. Appl. Phys.* **20**, 20 (1949).
2. A. V. Crewe, J. Wall and J. Langmore, *Science* **168**, 1338 (1970).
3. A. Engel, J. W. Wiggins, and D. C. Woodruff, *J. Appl. Phys.* **45**, 2739 (1974).
4. A. V. Crewe, J. P. Langmore, and M. S. Isaacson, in Physical Aspects of Electron Microscopy and Microbeam Analysis, edited by B. M. Siegel and D. R. Beaman (Wiley and Sons, New York, 1975), p. 47.
5. J. Wall, J. Langmore, M. Isaacson, and A. V. Crewe, *Proc. Nat. Acad. Sci.* **71**, 1 (1974).
6. M. S. Isaacson, M. Ohtsuki, and M. Utlaut, in Introduction to Analytical Electron Microscopy, edited by J. J. Hren, J. I. Goldstein, and D. C. Joy, (Plenum Press, New York, 1979), p. 343 .
7. J. M. Cowley, *Ultramicroscopy* **2**, 3 (1976).
8. G. Ade, *Optik* **49**, 113 (1977).
9. D. E. Jesson and S. J. Pennycook, *Proc. R. Soc. Lond.* **A441**, 261 (1993).
10. J. C. H. Spence, J. M. Zuo, and J. Lynch, *Ultramicroscopy* **32**, 233 (1989).
11. R. F. Loane, P. Xu, and J. Silcox, *Acta Cryst. A47*, 267 (1991).
12. S. J. Pennycook and D. E. Jesson, *Ultramicroscopy* **37**, 14 (1991).
13. D. E. Jesson and S. J. Pennycook, *Proc. R. Soc. Lond.* submitted (1993).
14. C. R. Hall and P. B. Hirsch, *Proc. Roy. Soc. A* **286**, 158-177 (1965).
15. D. M. Bird and Q. A. King, *Acta Cryst. A46*, 202 (1990).
16. L. J. Allen and C. J. Rossouw, *Phys. Rev. B* **42**, 11644 (1990)
17. M. M. J. Treacy and J. M. Gibson, these proceedings.
18. B. E. Warren, X-Ray Diffraction, (Dover Publishing, New York, 1990).
19. J. Fertig and H. Rose, *Optik* **59**, 407 (1981).
20. R. F. Loane, E. J. Kirkland, and J. Silcox, *Acta Cryst. A44*, 912 (1988).
21. S. J. Pennycook and D. E. Jesson, *Acta Metall. Mater.* **40**, Suppl. S149 (1992).
22. J. M. Cowley, and Y. Huang, *Ultramicroscopy* **40**, 171 (1992).
23. D. D. Perovic, A. Howie and C. J. Rossouw, *Phil. Mag. Letts.* **67**, 261 (1993)
24. S. F. Gull, and J. Skilling, *IEE Proc. 131F* 646 (1984).
25. S. J. Pennycook, D. E. Jesson, M. F. Chisholm, A. G. Ferridge and M. J. Seddon, *Proc. 10th Pfeifferkorn Conf. on Signal and Image Processing*, Cambridge, U. K. (Scanning Microscopy International, AMF O'Hare, in press).
26. P. Xu, E. J. Kirkland, J. Silcox, and R. Keyse, *Ultramicroscopy* **32**, 93 (1990).
27. A. J. McGibbon, S. J. Pennycook and Z. Wasilewski in Growth Processing and Characterization of Semiconductor Heterostructures, edited by G. Gumbus, S. Luryi, B. Weiss, and G. W. Wicks (Mater. Res. Soc. Proc. **326**, Pittsburg, PA, 1994, in press)
28. N. D. Browning, and S. J. Pennycook, *Microbeam Analysis* **2**, 81 (1993).
29. N. D. Browning, M. F. Chisholm, and S. J. Pennycook, *Nature* **366**, 143 (1993).

Author Index

Alvarado, S.F., 599
Amrein, M., 189
Anderson, Ian M., 309, 315
Andoh, Hiroya, 489
Andres, Ronald P., 99, 195
Andrews, S.B., 351
Aymerich, X., 549
Bandow, S., 531
Barniol, N., 549
Barton, J.J., 141
Batson, P.E., 275
Baumann, F.H., 373
Belcher, A., 413
Benson, W.E., 65
Bentley, Jim, 309, 315, 385
Bhushan, Bharat, 93
Bi, Xiang-Xin, 207, 531
Blackmore, J.M., 423
Blank, Dave H.A., 555
Bonevich, John E., 219, 231
Bonnell, Dawa A., 483, 519
Bourrat, Xavier, 341
Bowen, D.K., 525
Boyd, Joseph T., 543
Brown, W.L., 333
Browning, N.D., 297
Bruley, J., 169
Camus, P.P., 587
Carroll, D.L., 483
Carter, C. Barry, 309, 315, 385
Cerrina, F., 87
Chang, Y.-C., 65
Chepin, James, 267
Cheyssac, P., 109
Chisholm, M.F., 297
Choo, Ahn Goo, 543
Chudgar, Mona H., 543
Coleman, R.V., 573
Collins, D.A., 15
Collins, D.F., 531
Cramer, C., 189
Cruickshank, Brandon J., 121
Dai, Z., 573
Davis, R.F., 385
De Brabander, Gregory N., 543
Del Rio, L. Beltran, 177
Deppert, K., 513
DiNardo, N.J., 483
Downing, K.H., 563
Drucker, J.S., 473
Duan, X.F., 129
Edelman, Piotr, 201
Eklund, P.C., 531
El-Egili, K., 189
Feenstra, R.M., 15
French, R.H., 169
Funke, K., 189
Garbini, Joseph L., 25
Garg, A., 65
Gewirth, Andrew A., 121
Giles, R., 413
Glaunsinger, W.S., 115
Gomez, A., 177
Gong, Y., 573
Gray, S., 513
Guerra, John M., 449
Hadjipanayis, G.C., 303
Hansma, P.K., 413
Hansson, H.-C., 513
Harada, K., 219
Healy, S.D., 473
Heim, K.R., 473
Hellman, Olof C., 237
Hembree, G.G., 473
Henderson, D.O., 243
Herring, Rodney A., 231
Hillyard, Sean, 361
Holzman, L.M., 587
Honea, E.C., 333
Horton, L.L., 385
Howe, James M., 65
Hunt, J.A., 351
Inniss, Daryl, 537
Inoue, S., 293
Jackson, Howard E., 543
Jandt, K.D., 423
Jarrold, M.F., 333
Jesson, D.E., 607
Jin, F., 243
Jing, T.W., 393
Johansson, M., 513
Johnson, M.B., 599
Joy, David C., 461
Kakibayashi, H., 213
Kasai, H., 219
Kawami, H., 293
Kelly, T.F., 587
Kersten, Bart A.G., 555
Kim, Gyeung Ho, 151
Kim, Y.O., 373
Kisielowski, C., 373
Knipping, U., 405
Kofman, R., 109
Koinkar, Vilas N., 93
Kontkiewicz, Andrzej M., 201
Kontkiewicz, Anna, 201
Kowalak, A.D., 327
Kowalewski, Tomasz, 201

Krivanek, Ondrej L., 341
Kuech, T.F., 249
Kulnis, Jr., W.J., 105
Kumar, Mukesh, 543
Kundmann, Michael K., 341
Kurkjian, Charles R., 537

Lagally, M.G., 249
Lagowski, Jacek, 201
LaGraff, John R., 121
Lapiano-Smith, D.A., 141
Larson, D.J., 587
Leapman, Richard D., 287, 351
Lee, W.T., 531
Li, Z.G., 303
Liang, S., 87
Liang, Y., 483
Lindsay, S.M., 393
Liu, J., 303
Lo, W., 405
Lu, Weier, 501, 507

Ma, Chaoying, 327
Madsen, L.L., 429
Majetich, Sara, 321
Mann, S., 413
Manne, S., 413
Marie, A., 115
Matsuda, T., 219
Maximov, I., 513
McCartney, M.R., 43
McDonnell, D.G., 423
McGibbon, A.J., 607
McGill, T.C., 15
McHargue, C.J., 385
McKelvy, M., 115
McKernan, S., 385
McMaster, T.J., 423
Meisheng, Hu, 563
Mercer, T., 483
Merli, P.G., 109
Midgley, P.A., 129
Migliori, A., 109
Miles, M.J., 423
Mo, S., 405
Montelius, L., 513
Morris, P.A., 169
Morse, D.E., 413
Mu, R., 243
Müllejans, Harald, 169
Muller, David A., 163
Murray, C.A., 333

Nagata, F., 213
Nayak, S., 249
Newbury, Dale E., 287, 321
Newbury, Jennifer, 321
Ng, W., 87
Ni, Hengfei, 207
Nowakowski, Marilyn J., 519

Ogura, A., 333
O'Keefe, M.A., 563

Okitsu, Yoshitaka, 255
Otsuka, N., 195
Ourmazd, A., 373

Paithankar, Dilip Y., 99
Pan, J., 393
Papaefthymiou, Georgia C., 261
Parkinson, Bruce A., 79
Patil, A.N., 195
Pennycook, S.J., 297, 607
Pérez-Murano, F., 549
Petersen, B.L., 141
Pfister, M., 599
Pozzi, G., 219

Qian, M., 3
Qian, W., 405
Qin, G.G., 495

Raghavachari, K., 333
Raj, Rishi, 163
Ray-Chaudhuri, A.K., 87
Redwing, J.M., 249
Reichelt, R., 189
Reifenberger, R., 225
Revcolevschi, A., 385
Reyes-Gasga, J., 183
Rogers, J.K., 437
Rohrer, Gregory S., 501, 507
Ross, Jr., Joseph H., 267
Ruan, J., 93

Sakurai, K., 525
Salemink, H.W.M., 599
Samelson, L., 513
Sarikaya, Mehmet, 3, 151
Savage, D.E., 249
Schaefer, D.M., 225
Scheinfein, M.R., 473
Schwander, P., 373
Schwartz, D.K., 429
Sen, Sidhartha, 201
Sharma, R., 115
Shirley, D.A., 141
Sidles, John A., 25
Sidorov, M., 115
Silcox, John, 163, 361
Sjerps-Koomen, Lianda, 555
Slough, C.G., 573
Smith, David J., 43
Smith, Richard L., 507
Song, H.Z., 495
Spellward, P., 129
Spence, J.C.H., 405
Sprenger, W.O., 333
Steeds, J.W., 129
Stella, A., 109
Stencil, John M., 207
Stern, E.A., 3
Stucky, G.D., 413
Sun, S., 351
Sung, Changmo, 327

Takagi, Yasuo, 255
Takai, Mikio, 489
Talbot, Julian, 99
Tanaka, S., 385
Tanji, Takayoshi, 231
Tanner, B.K., 525
Tehuacanero, S., 177, 183
Terminello, L.J., 141
Toledo-Crow, R., 437
Tonomura, Akira, 55, 219, 231
Tsoukatos, A., 303
Tsuneta, R., 213
Tzou, Yujun, 163
Ukena, Toshiyasu, 255
Unertl, W.N., 105
Vaez-Iravani, M., 437
Vaterlaus, A., 15
Vincent, R., 129
Viswanathan, Ravi, 429
Volhs, John M., 519
Wan, H., 303

Wang, Kai-An, 531
Wenk, H-R., 563
Wesolowski, Marek, 201
Wiedensohler, A., 513
Woodall, J.M., 15
Wormington, M., 525
Xue, Q., 573
Yacaman, M. Jose, 177
Yang, Z.J., 473
Yao, T., 293
Yokoi, Naoki, 489
Yoshida, T., 219
Yoshimura, M., 293
Zandvliet, Haroild J.W., 555
Zaremba, C.M., 413
Zasadzinski, J.A., 429
Zhang, B.R., 495
Zhang, L.Z., 495
Zhang, X., 405
Zhong, Qian, 537
Zorrilla, C., 183

Subject Index

ab-initio calculations, 333
aerosol, 513
agglomeration, 333
Al-Cu-Si alloy thin films, 87
alloys, 267
AlN, 385
amorphous-Ge/Si (111), 237
analytical electron
 microscope, 287
 microscopy, 303
angle-dependent electron diffraction, 141
annular dark field (ADF) imaging, 361
antiferromagnetic phases, 573
anti-phase boundary, 267
atom probe, 587
atomic(-) force
 microscope (AFM), 201, 225, 413, 429, 537
 microscopy, 93, 121, 573
 level topographic map, 373
 resolution, 563, 607
 scale, 15
Atrina, 413
Au films, 225
Auger electron imaging, 473
barrier for electron tunneling, 393
B₃C-Al, 151
Bi-metallic catalyst, 327
biological systems, 351
biomolecular imaging, 25
blunt flaws, 537
bonding, 163
buried surface, 237
cantilever, 25
ceramic-metal (cermet), 151
cermets, 151
channeling-enhanced microanalysis, 309
characterization, 287
charge-density wave, 573
chemical
 bonding, 385
 composition, 373
clustering, 243
clusters, 99
CO₂ laser, 531
 pyrolysis, 531
coherent electron diffraction, 129
composition
 and strain, 213
 determination, 385
compositional map, 373
conductivity spectroscopy, 189
convergent beam electron
 diffracted beams, 231
 diffraction, 151
CoO-ZrO₂ eutectic, 385
copper, 121
corrosion, 537
Cu(001), 141
Cu-Au, 267
Cu-rich phase, 87
CVD diamond, 163
dark field images, 275
dedicated scanning transmission electron
 microscope, 169
defect structures, 43
deintercalation processes, 115
depth profiles, 213
diamond thin films, 483
diffraction arcs, 255
digital image
 processing, 177
 recording, 43
direct observation, 255
DNA oligomers, 393
doping, 599
dynamic high-resolution transmission electron
 microscopy, 115
EELS, 163, 275, 309
elastic, 225
 deformation, 99
 modulus, 99
electrical properties, 275
electrocatalysts, 327
electrochemical, 393, 549
electron, 231
 diffraction, 213
 energy
 dispersive x-ray spectrometry (EDS), 321
 loss
 spectrometer, 3
 spectrometry (EELS), 287, 385
 spectroscopy, 297, 351
 holography, 55, 219
 microscope, 405
 microscopy, 183
 electronic
 spectroscopy, 15
 structure, 169, 275
 elemental mapping, 341
ELNES, 309
energy(-)
 dispersive spectrometry, 287
 filter, 341
 filtered
 electron microscopy, 341
 imaging, 341
etching, 513
evanescent waves, 449
extended
 energy loss fine structure (EXELFS), 3
 x-ray absorption fine structure (EXAFS), 3
fatigue, 537
fatty acid, 429

Fe-carbide, 207
ferroelectric, 531
field(-)emission, 405
 gun scanning electron microscope, 461
film, 55
flux(-)line(s), 55, 219
force microscope, 25
Formvar films, 207
Fourier transform infrared spectroscopy, 201
friction, 93
frustrated total internal reflection
 microscope, 449
GaAs, 607
GaAs (100), 489
gas aggregation source, 195
giant magnetoresistance, 303
grain boundaries, 177
granular magnetic films, 303
grazing incidence x-ray reflectance, 525
guest-layer behavior, 115
hardness, 93
height quantification, 449
heterostructures, 213
hexagonal tungsten bronze, 501
hexatic, 429
high(-)
 angle detector, 607
 resolution, 461
 electron microscopy, 43, 183
 imaging, 361
 TEM, 177
higher order Laue Zone (HOLZ) line, 151
highly oriented pyrolytic graphite (HOPG), 519
holographic atom imaging, 141
holography, 231
HREM images, 183
image
 processing, 183
 simulation(s), 43, 183
imaging plate, 255
imperfections, 231
InAs/GaSb superlattices, 15
incoherent imaging, 607
indentation, 99
inelastic behavior, 225
in situ hot-stage high-resolution, 65
interband transition strength, 169
interface(s), 163
 dynamics, 65
 roughness, 525
interfacial structure, 237
interference contrast, 437
intermetallics, 267
internal spin structure, 261
ion implanted Si, 231
iron aggregates, 261
Knight shift, 267
Langmuir-Blodgett, 429
lattice
 images, 373
 strain, 151
layered
 compound(s), 293, 507
 semiconductor, 15
lead nanoparticles, 109
liquid crystals, 423
local
 atomic structure, 3
 residual stresses, 151
localized corrosion, 87
long range screening, 573
Lorentz
 micrograph, 55
 microscopy, 219
low(-)
 beam energies, 461
 temperature-grown GaAs, 15
magnetic
 properties, 473
 resonance force microscopy (MRFM), 25
 structural parameters, 261
magnetization, 473
MBE, 599
measurement, 231
mechanical properties, 93
melting, 109
mercury titanium disulfide, 115
metal oxide surfaces, 501
methanol fuel cells, 327
metrology, 525
microanalysis, 587
microstructural evolution, 87
microstructure, 303
Mo d₂ state, 293
Moire patterns, 183
molecular
 aggregates, 243
 arrangement, 423
 dynamics, 99
MoO₃, 507
morphology, 423
MoS₂, 293
Mössbauer spectroscopy, 261
multilayer, 599
multiple-wavenumber, 141
nacre, 413
nano-columns, 513
nanocrystalline, 531
nanocrystallites, 321
nanodiffraction, 303
nanoindentation, 225
nanometer scale modification, 549
nanoparticles, 177
nanoscale
 heterogeneities, 189
 structure studies, 105
nanostructural, 261
nanostructured particles, 195
nanotechnology, 529

Nb, 55
near field optical microscopy, 437
 $(\text{NH}_4)_2\text{S}_x$, 489
niobium, 219
NMR, 267
optical channel waveguide structures, 543
ordered superlattices, 573
organic films, 429
oxidation, 519
oxide, 121
oxygen plasma, 519
parallel electron energy loss, 3
phase
 contrast, 437
 fluctuations, 109
 separation, 303
 transitions, 423
phased summing, 141
photoelectron holography, 141
photo-induced STM, 483
photoluminescence (PL), 201, 437
 peak energies, 495
photon
 scanning tunneling microscopy (PSTM), 543
 tunneling microscopy, 449
point-projection, 405
polarization, 437
polymers, 423
polystyrene spheres, 105
porosity, 495
porous, 243
 silicon (PS), 201, 495
precipitates, 255
pristine silica optical fibers, 537
projected potential, 373
Pt(111), 141
quantification, 43
quantitative
 critical point (CP) modelling, 169
 HRTEM, 373
 maps, 341
QUANTITEM, 373
quantized vortices, 219
quantum-
 dots, 513
 point-contact conductance, 393
radiation damage, 3, 341
Raman
 scattering, 531
 spectroscopy, 333
randomly staged, 115
RBS, 489
reflection electron holography, 405
 S_{p_2} state, 293
S-terminated, 489
scanning
 force microscope, 105
 probe microscopy, 423
transmission electron
 microscope, 297, 351, 473
 microscopy (STEM), 361
tunneling
 microscope, 501, 555
 microscopy (STM), 15, 393, 483, 519, 549, 573, 599
 spectroscopy (STS), 519
scattering, 341
secondary
 electron, 473
 excitation, 315
selective imaging, 293
self-supporting disc specimen, 315
SEM, 189
Si clusters, 333
Si(100) surface, 549
sialon, 385
SiC, 385
Si-Ge alloys, 275
silicon, 93, 163
silver-iodide/silver-borate glass, 189
simulated images, 501
single spin detection, 25
size distribution, 207
sodium nitrate, 243
solid(-)
 electrolytes, 189
 liquid interfaces, 121
 state phase transformations, 65
spatial resolution, 461
spectromicroscopy, 87
spectrum-imaging, 351
spin relaxation phenomena, 261
spinel, 309
SR-EEL spectroscopy, 169
steels, 255
STEM, 163, 341
STM, 189, 489, 549
STM/STS, 293
strength-flaw relationship, 537
structure determination, 43
superconductor(s), 55, 219
superlattice, 599
surface(s), 429
 magneto-optic Kerr effect, 473
 models, 321
 photovoltage, 201
 roughness, 525
 states, 549
 structure, 507
 topography, 525
synchrotron radiation, 141, 255
synthesis of two component clusters, 195
TEM, 207, 237, 341
termination layers, 501
thermal stage, 105
thickness fringes, 213
3-D
 electron crystallography, 563
 imaging, 563
 reconstructions, 563

three-dimensional atom probe (3DAP), 587
time of flight STM, 405
topography, 449
trace
 analysis, 287, 351
 nanoanalysis, 287
transition metal oxides, 507
transmission electron
 microscope, 3, 151, 213
 microscopy, 65, 195
tribological properties, 93
tunneling images, 449
two-dimensional ferromagnetism, 473
ultrafine particles (UFP), 207
valence electron
 energy-loss (EEL) spectroscopy, 169
 excitations, 351
vertical resolution, 449
vibrational frequencies, 333
vicinal crystal surfaces, 555
 V_2O_5 , 507
wear, 93
 WO_3 , 531
XPS, 489
x-ray
 absorption fine structure (XAFS), 3
 diffraction (XRD), 531
 microanalysis, 309, 315
Z-contrast, 275
 image, 297
 STEM, 607
Zerodur, 525